JOURNAL OF UNDERGRADUATE RESEARCH

U.S. DEPARTMENT OF ENERGY

A Message from the
Under Secretary for Science

The publication of the 8th Volume of the *Journal of Undergraduate Research* presents striking evidence of the Department of Energy's support for the next generation of scientists and engineers. The body of knowledge contained in this issue of the *Journal* reflects the creativity and commitment of hundreds of young minds. We hope the excitement of discovery they have experienced will inspire them to continue their scientific studies. If our Nation is to remain at the forefront of science and technology, a condition for our continued economic vitality and energy security, it is essential that we develop this reservoir of talent.
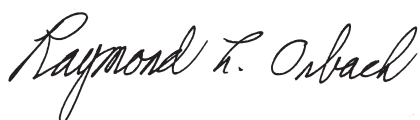
This issue of the *Journal* contains an impressive collection of articles and abstracts. Research topics range from high energy physics to genomics to nanoscience, and include many other leading areas of modern scientific inquiry. These contents reflect only a portion of the support the Department of Energy's Office of Science provides to basic research. In addition, the quality of the papers attests to the importance of Office of Science contributions to scientific discovery.

Office of Science supported research enables the U.S. to maintain its competitive edge. It transforms our energy future, supports our national security, and elucidates the fundamentals of matter and energy. All of the research described in this *Journal* was conducted at the Department of Energy's 17 national laboratories, a critical resource for our Nation's scientific needs.

The nurturing and recruitment of extraordinary scientific and technical talent is essential if the Department is to continue to serve our Nation. This 8th Volume of the *Journal of Undergraduate Research* reflects but one of the Department's ongoing efforts to develop this critical resource.

More than 650 undergraduate women and men were awarded research internships at the Department of Energy's national laboratories during 2007. These men and women will become the nucleus of our Department's and Nation's scientific and technical work force. This issue of the *Journal* summarizes and makes available to the scientific and lay communities the results of their research. In addition, these contributions demonstrate the skills and accomplishments of these young scientists.

As Under Secretary for Science, I again express my pride in the achievements of these extraordinary young minds. I thank them for their dedication to science and for their accomplishments. I wish them well for an exciting future.

Raymond L. Orbach
Under Secretary for Science
U.S. Department of Energy

Disclaimer

Mentorship: The Education-Research Continuum

Mentoring of science students stems naturally from the intertwined link between science education and science research. In fact, the mentoring relationship between a student and a scientist may be thought of analogically as a type of double helix forming the "DNA" that defines the blueprint for the next generation of scientists. Although this analogy would not meet the rigorous tests commonly used for exploring the natural laws of the universe, the image depicted does capture how creating and sustaining the future science workforce benefits greatly from the continuum between education and research. The path science students pursue from their education careers to their research careers often involves training under an experienced and trusted advisor, i.e., a mentor. For many undergraduate science students, a summer research internship at a DOE National Laboratory is one of the many steps they will take in their Education-Research Continuum.

Scientists who choose to be mentors share a commitment for both science education and science research. This commitment is especially evident within the research staff found throughout the Department of Energy's National Laboratories. Research-based internship opportunities within science, technology, engineering and mathematics (STEM) exist at most, if not all, of the Laboratories. Such opportunities for students are helping to create the next generation of highly trained professionals devoted to the task of keeping America at the forefront of scientific innovation. The *Journal of Undergraduate Research* (JUR) provides undergraduate interns the opportunity to publish their scientific innovation and to share their passion for education and research with fellow students and scientists.

> *Scientists who choose to be mentors share a commitment for both science education and science research.*

The theme of this issue of the JUR (Vol. 8, 2008) is "Science for All." Almost 20 years have passed since the American Association for the Advancement of Science published its 1989 report, *Science for All Americans—Project 2061*. The first recommendation for learning science stated: "The Nature of Science includes the scientific world view, scientific methods of inquiry, and the nature of the scientific enterprise." All three elements of the "Nature of Science" are pivotal aspects of a research internship under the mentorship of an experienced and trusted advisor. In addition to internships for undergraduates, an important ingredient in realizing "Science for All" is collaboration involving educators and scientists as they engage science students and the public at large to promote science literacy and to develop the next generation of STEM professionals. The DOE National Laboratories, individually and collectively, form an ideal nexus for nurturing these complementary collaborations.

My "Science for All" experiences at Lawrence Livermore National Laboratory (LLNL) over the last 30 years have spanned pre-college, college, and postdoctoral activities, including mentoring of undergraduate students. Early in my mentoring career, I became aware that undergraduates in particular needed help in answering the question

"what path (or paths) will lead to a challenging and rewarding STEM career?" For many, a successful path included a research internship that would result in expanded skills and training in addition to those received from their academic education. These internship skills were helpful whether the student's next Education-Research Continuum decision was graduate school or STEM employment. My experience at LLNL mirrors that of my colleagues at other DOE National Laboratories—internships with a dedicated mentor provide undergraduates with a unique set of skills that can underpin their future options and serve to improve the number, quality, and successful outcomes of students who enter STEM careers.

"Science for All" can also be found in the goals of "The America COMPETES Act," which calls for renewed efforts to increase investments in scientific research and development, strengthen education, and encourage entrepreneurship. Mentoring is an important ingredient in reaching these goals because the success of future endeavors will require a diverse workforce of scientists, technicians, engineers, mathematicians, and STEM educators. A small, but not insignificant, metric of how well the nation is doing to create the next STEM generation can be measured by the abstracts and articles published in the *Journal of Undergraduate Research*. At the "heart" of the JUR is the professional commitment of the DOE National Laboratory workforce to mentor the next STEM generation and to realize "Science for All."

Don Correll

Chief of Staff, Physical Sciences Directorate

Director, Institute for Laser Science & Applications

Lawrence Livermore National Laboratory

TABLE OF CONTENTS

About the Cover

Throughout the year, undergraduate students from across the country come to a U.S. Department of Energy national laboratory facility to engage in a mentored research experience.

———————

Map image courtesy of the National Oceanic and Atmospheric Administration

---

Selected Student Papers

Marcus S. Allegood was born in Des Moines, IA and grew up in both Pensacola, FL and Dublin, GA. He attended North Georgia College and State University, majoring in Physics. During his undergraduate career he held two SULI internships and a CCI internship at the Oak Ridge National Laboratory during the summers of 2005 to 2007. He was recently accepted into the masters program at the Georgia Institute of Technology in the Medical Physics program and hopes to pursue a career as a Medical Physicist. His interests included collecting books, football, and kayaking.

Justin S. Baba is a staff research scientist and development biomedical engineer in the Engineering Science & Technology Division at Oak Ridge National Laboratory (ORNL), Tennessee. He received his Ph.D. in Biomedical Engineering, 2003 from Texas A&M University, College Station, TX and joined ORNL in Sept. 2003. His primary research focus is in non-invasive diagnostics using both ionizing and non-ionizing radiation sources. He has additional interests in the development of non-invasive optical and electronics based sensors for medical and non-medical applications.

Extension of the Inverse Adding-Doubling Method to the Measurement of Wavelength-Dependent Absorption and Scattering Coefficients of Biological Samples

Marcus S. Allegood and Justin S. Baba

ABSTRACT

Light interaction with biological tissue can be described using three parameters: the scattering and absorption coefficients (μ_s and μ_a), as well as the anisotropy (*g*) which describes the directional dependence of the scattered photons. Accurately determining these optical properties for different tissue types at specific wavelengths simultaneously would be beneficial for a variety of different biomedical applications. The goal of this project was to take a user defined *g*-value and determine the remaining two parameters for a specified wavelength range. A fully automated computer program and process was developed to collect data for all wavelengths in a timely and accurate manner. LabVIEW® was used to write programs to automate raw intensity data collection from a spectrometer equipped integrating sphere, conversion of the data into a format for analysis via Scott Prahl's Inverse Adding-Doubling (IAD) C code execution, and finally computation of the optical properties based on the output from the IAD code. To allow data to be passed efficiently between LabVIEW® and C code program modules, the two were combined into a single program (OPT 3.1). OPT 3.1 was tested using tissue mimicking phantoms. Determination of the absorption and scattering coefficients showed excellent agreement with theory for wavelengths where the user inputted single *g*-value was sufficiently precise. Future improvements entail providing for multi-wavelength *g*-value entry to extend the accuracy of results to encompass the complete multispectral range. Ultimately, the data collection process and algorithms developed through this effort will be used to examine actual biological tissues for the purpose of building and refining models for light-tissue interactions.

INTRODUCTION

In recent years, the need for accurate models for light-tissue interaction has led to the development of several methods for characterizing the optical properties of biological tissue samples. Of these, one that is widely utilized is an integrating sphere in conjunction with the Inverse Adding-Doubling program (IAD) developed by Scott Prahl [1]. The integrating sphere method is a process by which raw light intensity data for a particular sample can be collected. By positioning the sample at either the front or the rear port of the sphere, transmitted or reflected intensity from an incident light source can be recorded within the sphere using an appropriately mounted photo-detector. The IAD program can then take this data and apply a brute force iterative process to determine the desired values. Essentially, the numerical process entails accepting raw intensity data as inputs and then repeatedly guessing the scattering and absorption coefficients until an appropriate match is attained [1].

To date, the vast majority of methods that have been investigated, including the method developed by Prahl, are designed to collect the respective optical properties at a single wavelength via a monochromatic laser light source. The process that we have developed addresses this limitation by using a collimated white light source to allow for user specified spectral data collection. System generated multi-wavelength data is analyzed by a program that computes the respective optical properties for each wavelength within the spectrum. Because scatter and absorption theories are well established for visible wavelengths, our system is only limited by its wavelength response and resolution for the individual wavelengths emitted by the light source.

Wavelength dependent light propagation through biological tissue can be described with three parameters: the anisotropy (*g*)

the scattering coefficient μ_s and absorption coefficient μ_a. The anisotropy describes the fraction of light forward scattered from an initial propagating direction s to s'. The reciprocal of the scattering (or absorption) coefficient is the average distance that a photon will travel before being scattered (or absorbed) [1]. It is these parameters that the IAD program does a particularly good job of determining. For this reason, the IAD program implemented for a single integrating sphere serves as the building block of our system. In this paper we present and discuss our developed system and the accuracy of results using tissue mimicking phantoms to test it, the underlying theory used, and the issues that arose over the course of data collection and optical property determination.

THEORY

Four raw light intensity measurements are needed for each sample. The collection of the required light intensity measurements along with the corresponding variable names are illustrated in Figures 1 and 2. Figure 1 depicts collection of sample transmitted light, variable: *samp_t* (Figure 1A) and sample reflected light, variable: *samp_r* (Figure 1B). Figure 2 depicts collection of two system characterization readings that are used to remove system optical response from measured sample readings. These are variable: *tot* (Figure 2A) — accounts for total internal reflection within the sphere, and variable: *dark* (Figure 2B) — accounts for non-perfect collimation of the input light source, i.e., slight divergence of light source output rays from parallel. Figure 3 depicts collection of the system baseline parameter, variable: *base* — accounts for system electronic noise, primarily from the charge coupled device (CCD) array in the detection spectrometer.

Once raw intensity data is collected for each required variable, two new variables are created, T and R, which represent the baseline corrected and normalized light transmission and reflection intensities respectively (Equations 1 and 2). Essentially, any light not recorded as either transmitted or reflected intensity, as captured by T and R, is assumed by the program to be absorbed by the sample [1].

$$T = \frac{[(sam\_t - base) - (dark - base)]}{[(tot - base) - (dark - base)]} \qquad (1)$$

$$R = \frac{[(sam\_r - base) - (dark - base)]}{[(tot - base) - (dark - base)]} \qquad (2)$$

The conservation of energy condition that the sum of R and T must be equal to or less than one, in Equation 3, is implemented in the program. Therefore, all values outside this range are returned as errors by the program.

$$R + T \leq 1 \qquad (3)$$

Anisotropy (g), is a value that must be predetermined and provided by the user [1]. The g-value implemented in this system, g_{HG}, is determined by the Henyey-Greenstein phase function $p(\theta)$, which describes the amount of light scattered at a particular angle. As shown in Equation 4, it varies by a factor, β, from the anisotropy, g, as determined by Mie theory for a single scattering event [3]. β is known as the isotropic factor and it accounts for the randomization of scatter that occurs due to multiple scattering events that occur in thicker samples. For simplicity, from this point forward the Henyey-Greenstein anisotropy, g_{HG}, is referred to as anisotropy unless otherwise specified.

$$g = g_{HG}(1 - \beta) \qquad (4)$$

The phase function is often expressed in terms of the cosine of the scattering angle $p(\cos\theta)$ [1].

Figure 1. A. Light transmission reading. Rear port is closed (variable: *samp_t*). B. Sample reflectance reading (variable: *samp_r*).

Figure 2. A. Total internal reflection. Rear port is closed (variable: *tot*). B. Optical dark reading. Both rear and front ports are open, allowing collimated beam to pass through unscattered and unabsorbed (variable: *dark*).
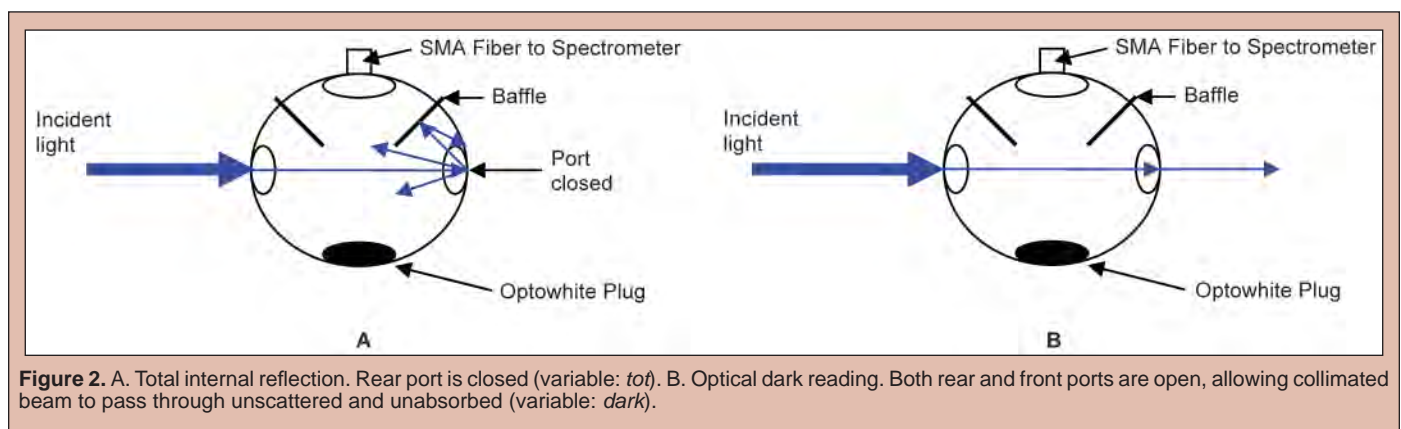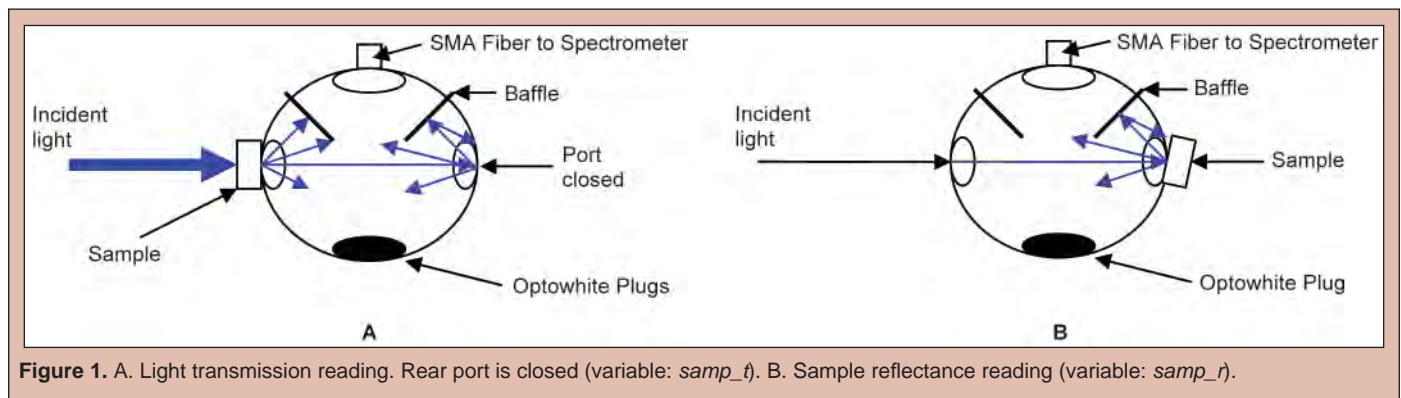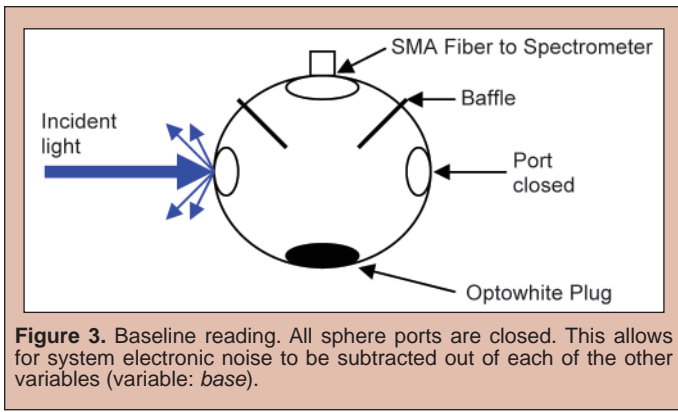
Figure 3. Baseline reading. All sphere ports are closed. This allows for system electronic noise to be subtracted out of each of the other variables (variable: *base*).

$$p(\cos\theta) = \frac{1 - g_{HG}^{2}}{4\pi(1 + g_{HG}^{2} - 2g_{HG}\cos\theta)^{3/2}} \tag{5}$$

The function is normalized, so that the total light intensity scattered over all angles is equal to unity.

$$\int_{4\pi} p(\cos\theta)d\omega = 1 \tag{6}$$

Calculating the expectation value of $p(\cos\theta)$ yields the anisotropy, which ranges from total isotropic scattering, i.e., $g_{HG} = 0$, and complete forward scattering, i.e., $g_{HG} = 1$.

$$\int_{4\pi} p(\cos\theta)\cos\theta d\omega = g_{HG} \tag{7}$$

The photon path is also influenced by the refractive index of both the sample holder and the sample itself. Two separate formulas are incorporated in the program for this purpose. The Cauchy equation, Equation (8), is used to determine the multispectral refractive index for the glass sample holder, while the Sellmeier equation, Equation (9), is used for actual tissue samples.

$$n(\lambda) = A + \frac{B}{\lambda^{2}} + \frac{C}{\lambda^{4}} + \ldots \tag{8}$$

$$n^{2}(\lambda) = 1 + \frac{A\lambda^{2}}{\lambda^{2} - B^{2}} + \ldots \tag{9}$$

In both cases only the first two terms are needed as the affect due to additional terms is negligible within the visible wavelengths of interest. The Cauchy equation works extremely well for non-absorbing materials. However, it breaks down for wavelengths in the vicinity of an absorption band [6]. The Sellmeier equation begins to address this issue and was developed to account for absorption, with the second coefficient, *B*, being a wavelength equal to that of the medium's natural — i.e., primary absorptive — frequency [6]. As with anisotropy, the user must provide the coefficients for both equations. Each equation is incorporated into OPT 3.1 in order to provide the IAD program with a proper refractive index for each wavelength within the user defined range.

Normalized reflection and transmission values, *R* and *T*, and the anisotropy value, g_{HG}, provide the three main input variables for the IAD program. Given these inputs and the refractive indexes, the program applies an iterative process to arrive at a set of optical variables that match the corresponding values of *R*, *T*, and *g* that it received as inputs [1].

The optical variables output from the IAD program are the albedo (*a*) and the optical thickness (τ). Albedo, presented in Equation 10, is the ratio of the scattering coefficient to the sum of the scattering and absorption coefficients μ_{s} and μ_{a}. Highly scattering samples are dominated by μ_{s} and approach a limit of one, while highly absorbing samples are dominated by μ_{a}, and thus approach a limit of zero.

$$a = \frac{\mu_{s}}{(\mu_{s} + \mu_{a})} \tag{10}$$

The optical thickness, presented in Equation 11, is the product of the sample thickness, *d*, and the sum of the scattering and absorption coefficients. It is a measure of how far a photon travels into a sample before it is either scattered or absorbed.

$$\tau = d(\mu_{s} + \mu_{a}) \tag{11}$$

With the albedo and optical thickness outputs from the IAD program as inputs, OPT 3.1 calculates μ_{a} and μ_{s} using the relationships in Equations 12 and 13.

$$\mu_{a} = \frac{\tau(1 - a)}{d} \tag{12}$$

$$\mu_{s} = \frac{a\tau}{d} \tag{13}$$

The units of both the scattering and absorption coefficients are in inverse millimeters and the reciprocal of these values represents the respective mean free paths, i.e. the distance a photon travels before being either scattered or absorbed.

The results for absorption and scattering coefficients can be verified against predictions by the Beer-Lambert (Beer's) law and Mie theory respectively. The exponential form of Beer's law is presented in Equation (14) with I_{0} and I_{1} as the input and output intensities respectively.

$$\frac{I_{0}}{I_{1}} = e^{-A} \qquad A = \ln\left(\frac{I_{1}}{I_{0}}\right) \tag{14}$$

Absorbance, A, is related to the absorption coefficient as presented in Equation 15.

$$A = \varepsilon \cdot c \cdot l \qquad \mu_{a} = \varepsilon \cdot c \tag{15}$$

Here ε is the molar absorptivity [M^{-1}mm^{-1}] at a specific wavelength, *c* is the molar concentration [M], and *l* is the sample path length [mm]. The absorption coefficient is the product of the molar absorptivity and the concentration [4]. Mie theory is used to predict the expected values for the scattering coefficient and a well documented and free online applet is provided by Scott Prahl [5].
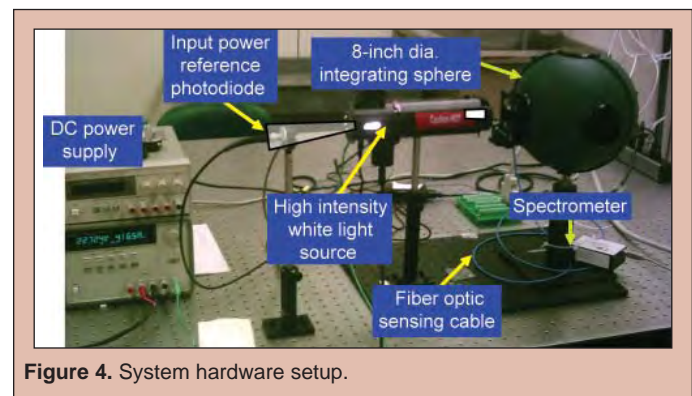
Figure 4. System hardware setup.

Experimental Setup

Figure (4) depicts the complete hardware system. It consists of a hollow 8-inch diameter sphere (SphereOptics Inc.) with a side mounted SMA fiberoptic cable that connects to an external spectrometer that utilizes a CCD detector (Ocean Optics, USB 2000). The interior walls of the sphere are coated with Optowhite (BaSO$_4$) [2] to ensure minimal absorbance and uniform photon diffusivity. By positioning a sample at the front or rear of the sphere, scattered or reflected light intensity can be recorded from an incident light source respectively. The system employs a collimated, high intensity, white light source providing a wide spectrum of wavelengths within and beyond the visible region (SphereOptics Inc., CL-100). A photodiode is also implemented externally to monitor light source power fluctuations. It provides a means to reduce intensity measurement errors via normalization of detected intensity by the corresponding light source output intensity.

LabVIEW® was used to create our OPT 3.1 program, which automated data collection over a user specified wavelength range — including a step size to extract specific wavelengths within the range. OPT 3.1 automatically calls up the IAD C code when needed, and transfers the necessary input variable data to it. Upon completion of IAD code execution, OPT 3.1 resumes control and performs the final calculations to produce the desired optical properties for each individual wavelength. The entire process is completed in a matter of minutes.

Tissue Phantoms

Tissue mimicking phantoms were produced using Trypan Blue (Sigma, T8154) to provide for absorption along with polystyrene spheres (Duke Scientific, 5100A and 5153A) to act as a scattering agent. These phantom materials were selected due to the readily available literature on their optical properties. Polystyrene sphere sizes of 1.0 and 1.5 micron diameters were utilized to mimic the strong forward scattering of biological tissues, which range in anisotropy values from 0.8 to 0.95 and are well characterized by Mie theory [1]. Sphere concentrations were chosen to be 2.97×10^9 and 1.08×10^9 parts per million (ppm) for the 1.0 and 1.5 micron spheres respectively. This was sufficient to produce accurate results and prevent skewed values seen in higher concentrations due to the level of multiple scattering events.

Samples were prepared in distilled water using different combinations of sphere sizes with varying Trypan Blue concentrations. Three sets of phantom mixtures were created. The first two sets contained only Trypan Blue or polystyrene spheres. These were used to test the system's ability to characterize samples that were either purely absorbing or scattering. They also served as reference data for comparison with samples that included both Trypan Blue and polystyrene spheres. In samples that included Trypan Blue, ten different molar concentrations were prepared ranging from 4.16×10^{-5} to 6.25×10^{-4} M. Testing was repeated three times for Trypan Blue only samples, nine times for polystyrene sphere only samples, and nine times for combination samples. All data were collected using a 1.0 mm path length sample holder constructed out of borosilicate glass.

All data presented in the following figures to be discussed were based on nine repetitions. For each, the standard deviation (σ) bars are not depicted because there are over 1,140 wavelengths sampled between 400 and 800 nm, moreover the maximum σ for all of the plotted data was determined to be ~ 4% of the nominal mean value. All spectral data were filtered to remove hot pixel values from the CCD detector output, i.e. consistently excessive spikes, and a 5 point moving average was applied for smoothing.

Absorption Coefficient, μ_a

Table 1 shows a comparison of system determined μ_a to that determined theoretically by implementing the known molar absorptivity of 6,900 M^{-1}mm^{-1} at 606 nm into Equation 15 ($\mu_a|_{606}$) for ten concentrations of Trypan Blue in distilled water ranging from 4.16×10^{-5} to 6.25×10^{-4} M that were tested [7]. The results show excellent agreement to theory throughout the range of concentrations with a mean error of 2.3%. To validate system derived μ_a across the complete system spectral range, the absorbance of each solution was measured independently and modeled using Beer's law by applying

Molar Concentration [M]	Absorption coefficient, μ_a		% Error
	Theoretical	Experimental	
4.16×10^{-5}	0.287	0.277	3.5
8.33×10^{-5}	0.574	0.540	5.9
1.25×10^{-4}	0.862	0.868	0.7
1.67×10^{-4}	1.149	1.148	0.1
2.08×10^{-4}	1.437	1.413	1.7
2.50×10^{-4}	1.724	1.667	3.3
2.91×10^{-4}	2.011	1.921	4.5
3.33×10^{-4}	2.298	2.243	2.4
4.16×10^{-4}	2.872	2.808	2.2
6.25×10^{-4}	4.309	4.284	0.6
Mean			2.3

Table 1. Absorption coefficient comparison as a function of concentration for samples of Trypan Blue in distilled water. Theoretical values were determined from known molar absorptivity of 6,900 M^{-1} mm^{-1} at 606 nm.[13]
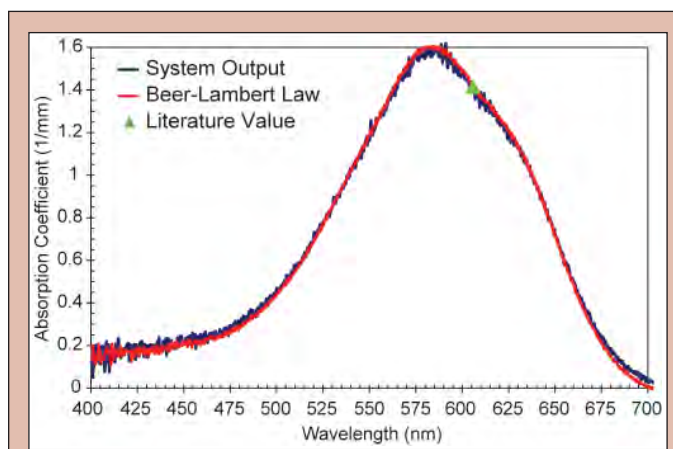
Figure 5. Absorption coefficient of Trypan Blue solution vs. wavelength comparison with a molar concentration of 2.08×10^{-4} M. The green triangle shows the value determined from the known molar absorptivity of 6,900 M^{-1} mm^{-1} at 606 nm for Trypan Blue.

Equations 14 and 15 [4]. Figure 5 shows results from a 2.08×10^{-4} M solution for the system spectral range of 400–700 nm. Beer's law results are represented in red, the system derived values in blue, and the green triangle shows $\mu_a|_{606}$. Again, the data shows good agreement with theory with a mean error of 2%. It should also be noted in Figure 5 that both methods converge at the $\mu_a|_{606}$ value, thus further strengthening the validity of these results. Though not presented, we consistently saw this repeated for all microsphere-Trypan Blue combinations studies. However, there are erratic values at both ends of the spectrum resulting in increased errors. These are due to hardware limitations that result in lower signal-to-noise ratios .

Data for samples that contained both an absorbing agent and a scattering agent (polystyrene microspheres) are presented in Figures 6–9. Two different samples were created using a 2.08×10^{-5} M concentration of Trypan Blue dye: one with 1.0 μm mean diameter spheres and the other with 1.5 μm diameter spheres. Figures 6 and

7 are the raw absorbance data for each of the samples. The red square in each figure depicts the expected value determined from the known molar absorptivity of Trypan Blue dye at 606 nm [7]. The system determined absorption coefficient values of 0.0930 and 0.0877 mm^{-1} for 1.0 and 1.5 μm diameter spheres at 606 nm. These values are in good agreement with the expected values, varying by only 4% and 0.5% respectively. Figures 8 and 9 are qualitative comparisons of normalized system absorbance values versus those determined using Beer's law.

Scattering Coefficient, μ_s

The two samples containing only polystyrene spheres, along with the two that contained both polystyrene spheres and Trypan Blue, as introduced in the absorption coefficient discussion, were utilized for investigating μ_s. The samples containing 1.0 μm spheres had a concentration of 2.97×10^9 parts per mL and those with 1.5
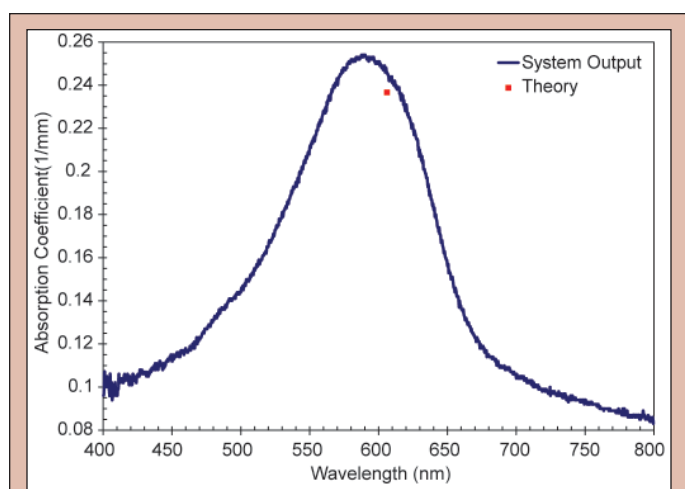
Figure 6. Absorption coefficient spectrum of Trypan Blue solution with a molar concentration of 2.08×10^{-4} M combined with 1.0 μm diameter polystyrene spheres. The red square shows the value determined from the known molar absorptivity of 6,900 M^{-1} mm^{-1} at 606 nm for Trypan Blue.
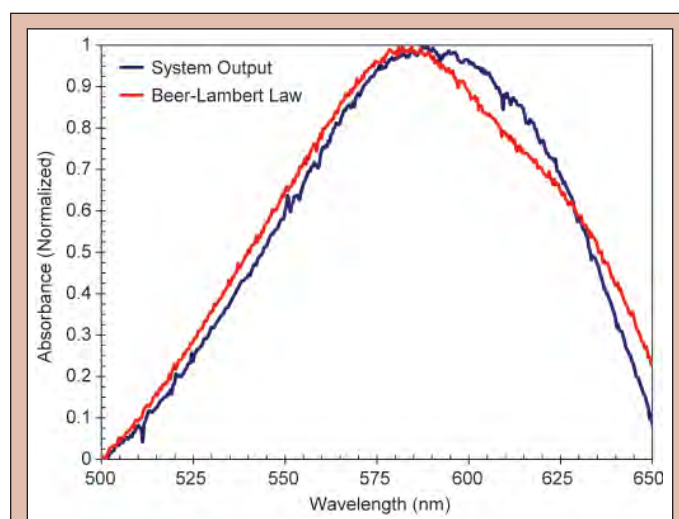
Figure 8. Normalized absorbance vs. wavelength. A comparison of system output and Beer-Lambert law modeled data for a sample consisting of a molar concentration of 2.08×10^{-5} M Trypan Blue combined with 1.0 μm diameter polystyrene scattering spheres.
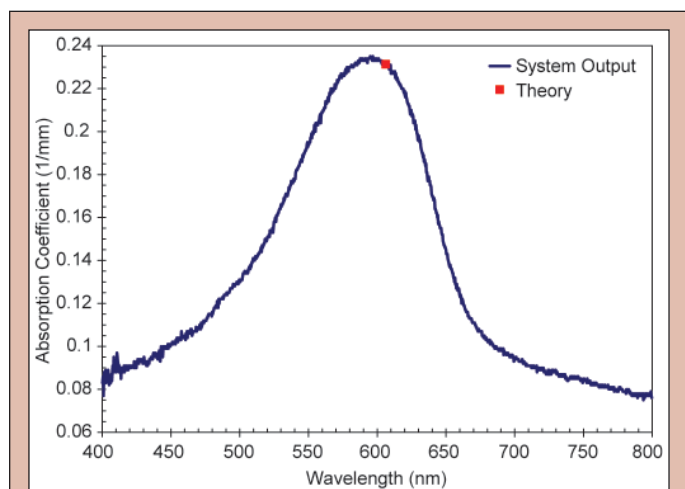
Figure 7. Absorption coefficient spectrum of Trypan Blue solution with a molar concentration of 2.08×10^{-4} M combined with 1.5 μm diameter polystyrene spheres. The red square shows the value determined from the known molar absorptivity of 6,900 M^{-1} mm^{-1} at 606 nm for Trypan Blue.
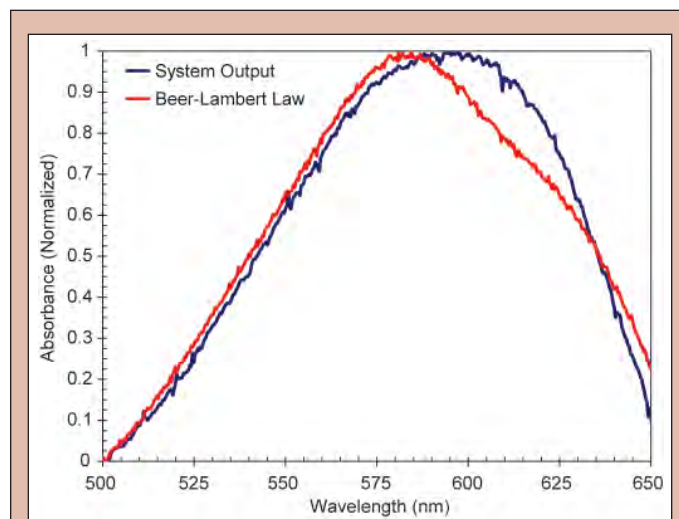
Figure 9. Normalized absorbance vs. wavelength. A comparison of system output and Beer-Lambert law modeled data for a sample consisting of a molar concentration of 2.08×10^{-5} M Trypan Blue combined with 1.5 μm diameter polystyrene scattering spheres.

U.S. Department of Energy Journal of Undergraduate Research

μm sphere solutions contained 1.08 x 10⁹ parts per mL. Figures 10 and 11 show data collected for the polystyrene spheres only samples. The red squares in these figures depict the expected values as determined by Mie theory [5]. The notable deviations from Mie theory are due to the current system limitation of only allowing a single anisotropy value to be specified for all wavelengths within the spectrum. However, it is well established that anisotropy varies with wavelength and this issue will be addressed in future work. The anisotropy value that was chosen for each sample was the value at 600 nm because it fell in the middle of the spectral ranges that were being examined. As such, in these figure, the best fit of the system outputted values to Mie theory occurs here.

A large deviation can be seen in the data for the 1.5 μm sphere samples. This is due to photons at the lower wavelengths approaching the geometric limit of the scattering cross section [8]. Figures 12 and 13 are the data for scattering samples that also contain a 2.08 x 10⁻⁵ M concentration of Trypan Blue. Again, the same deviations from theory can be seen for lower wavelengths, but

there is good agreement for wavelengths that fall within the Mie regime and below the geometric limit [8].

Conclusion and Future Work

Overall, the program performed exceptionally well for each sample tested. The system was able to reliably determine the scattering and absorption coefficients for a wide range of sample mixture concentrations. Currently, the lack of a wavelength dependent anisotropy variable in our OPT 3.1 software program is the limiting factor for accurate simultaneous characterization of a sample's multispectral optical properties. Because anisotropy varies with wavelength, as do the other parameters, accurate results are currently restricted to the wavelength range where the user-defined single g-value is valid. Implementing anisotropy as a wavelength dependent variable into the analysis portion of the OPT 3.1 program is the next issue to be addressed.
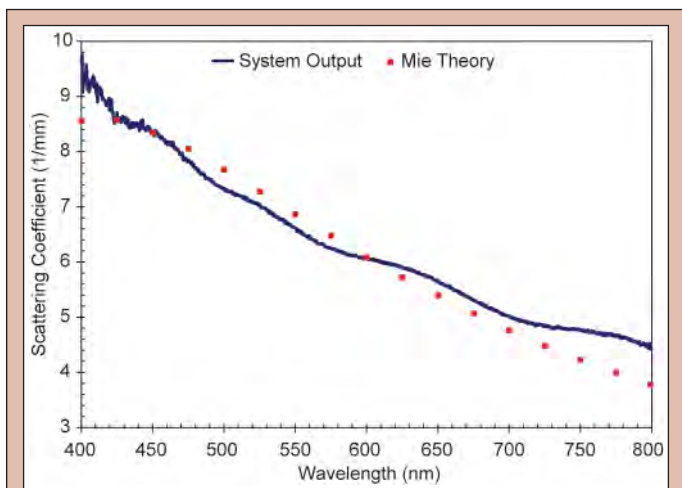
Figure 10. Scattering coefficient vs. wavelength for a sample of 1.0 μm diameter polystyrene scattering spheres with a concentration of 2.97 x 10⁹ parts per mL. The red squares depict expected values computed from Mie theory. (g_{HG} = 0.916).
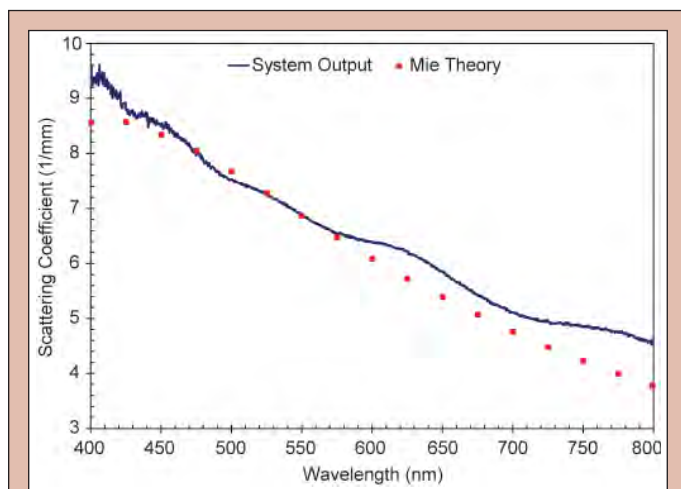
Figure 12. Scattering coefficient vs. wavelength for a sample mixture consisting of 1.0 μm diameter polystyrene scattering spheres with a concentration of 2.97 x 10⁹ parts per mL and a 2.08 x 10⁻⁵ M concentration of Trypan Blue. The red squares depict expected values computed from Mie theory. (g_{HG} = 0.916).
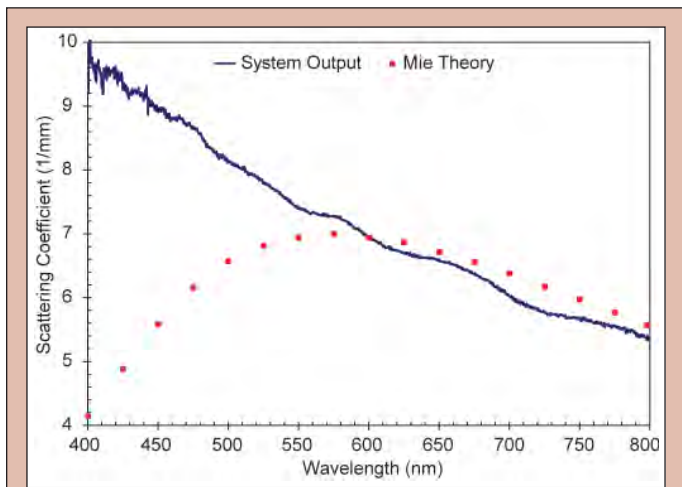
Figure 11. Scattering coefficient vs. wavelength for a sample of 1.5 μm diameter polystyrene scattering spheres with a concentration of 1.08 x 10⁹ parts per mL. The red squares depict expected values computed from Mie theory. (g_{HG} = 0.933).
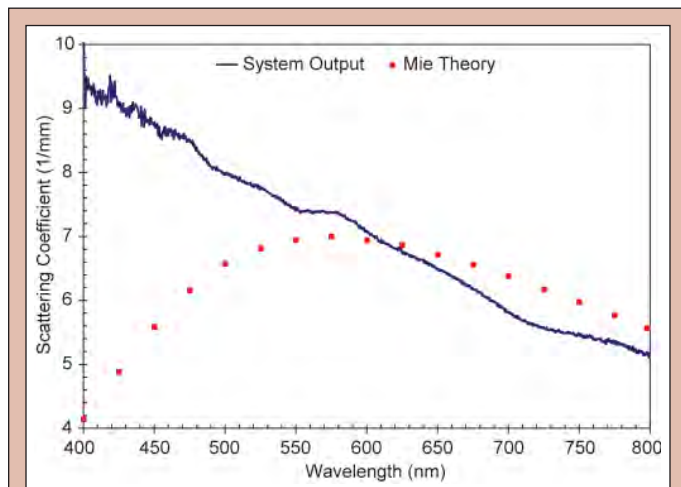
Figure 13. Scattering coefficient vs. wavelength for a sample mixture consisting of 1.5 μm diameter polystyrene scattering spheres with a concentration of 1.08 x 10⁹ parts per mL and a 2.08 x 10⁻⁵ M concentration of Trypan Blue. The red squares depict expected values computed from Mie theory. (g_{HG} = 0.933).

In summary, the automation provided by OPT 3.1 allows determination of desired optical properties in a matter of minutes within system hardware limits. Once the aforementioned outstanding issues have been resolved, the next phase of testing will be performed on actual biological tissue. Eventually the data collected using this system will be used to model light interaction with biological tissue.

References

[1] S. Prahl, "Optical Property Measurements Using the Inverse Adding-Doubling Program," [Online document], http://omlc.ogi.edu/pubs/pdf/man_iad.pdf, Accessed 03/19/08.

[2] SphereOptics, "Integrating Sphere Design and Applications," [Online Product Documentation], http://www.sphereoptics.com/assets/sphere-optic-pdf/sphere-technical-guide.pdf, Accessed 03/19/08.

[3] S. Prahl, Light Transport in Tissue, Dissertation, The University of Texas, Austin, 1988. Available: http://omlc.ogi.edu/pubs/pdf/prahl88.pdf, Accessed 03/19/08.

[4] Wikipedia, "Beer-Lambert law," Wikipedia. The Free Encyclopedia., [Online document], http://en.wikipedia.org/wiki/Beer-Lambert_law, Accessed 03/19/08.

[5] S. Prahl, "Mie Scattering," [Online resource], http://omlc.ogi.edu/calc/mie_calc.html, Accessed 03/19/08.

[6] F.A. Jenkins and H.E. White, Fundamentals of Optics, 4th ed., McGraw Hill, Inc., 1976.

[7] Dojindo, "Cellstain-Trypan Blue, Product code: T375-10," [Online documentation], http://www.dojindo.com/products/alphasearch/dojindodtl1.cfm?alphafield=Trypan%20Blue&ProdName=-Cellstain-%20Trypan%20Blue, Accessed 03/19/08.

[8] T. Vo-Dinh, Biomedical Photonics Handbook, Boca Raton, CRC Press, pp. 2.1–2.10, 2003.

Janilee Y. Benitez graduated from the University of California, Berkeley with a B.A. in anthropology and an emphasis in archaeology in 2005. She completed the B.S. physics major requirements at California State University, East Bay in 2007. During her undergraduate career, she held an internship at the University of California, San Diego's Research Experience for Undergraduates (REU) program, and a second internship at Lawrence Berkeley National Lab's (LBNL) SULI program. She continues to work with her mentor Daniela Leitner at LBNL and plans to attend graduate school to earn a PhD in either Nuclear Physics or Nuclear Engineering.

Daniela Leitner got her PhD in experimental physics from the University of Technology in Vienna, Austria, in 1995. Her thesis was focused on aspects to advance the Li plasma edge diagnostic technique used on fusion reactor experiments. In 1996 she was awarded with the "Schrödinger Fellowship" administered by the Austrian Academy of Science to conduct the research project "Development of multiply-charged ion sources" at the Lawrence Berkeley National Laboratory. This research project led to the design and construction of a compact ECR ion source, which was used for the online production of radioactive ion beams, resulting in record intensities of low energy ^{14}O ion beams (consequently used for a precision measurement of the ^{14}O lifetime). After completion of her fellowship year she joined the Lawrence Berkeley National Laboratory, where she has been working as a staff scientist since 2000 and was promoted to senior scientist in 2006. Currently she is heading the accelerator physics and ECR ion source development group at the 88-Inch Cyclotron. This group has designed and built the next generation superconducting ECR ion source VENUS, which is presently the most advanced ECR ion source worldwide. Under her lead, the 88-Inch accelerator physics group is currently working on the development of advanced simulation tools to model the transport of multi species heavy ion beams extracted from ECR ion sources.

ANALYSIS OF X-RAY SPECTRA EMITTED FROM THE VENUS ECR ION SOURCE

JANILEE BENITEZ, DANIELA LEITNER

ABSTRACT

The Versatile Electron Cyclotron resonance ion source for Nuclear Science (VENUS), located at Lawrence Berkeley National Lab's 88-inch cyclotron, extracts ion beams from a plasma created by ionizing a gas with energetic electrons. Liquid-helium cooled superconducting coils produce magnetic fields that confine the plasma and high microwave frequencies heat the electrons enough to allow for successive ionizations of the neutral gas atoms. The combination of strong plasma confinement and high microwave frequencies results in VENUS' production of record breaking ion beam currents and high charge state distributions. While in operation, VENUS produces significant quantities of bremsstrahlung, in the form of x-rays, primarily through two processes: 1) electron-ion collisions within the plasma, and 2) electrons are lost from the plasma, collide with the plasma chamber wall, and radiate bremsstrahlung due to their sudden deceleration. The bremsstrahlung deposited into the plasma chamber wall is absorbed by the cold mass used to maintain superconductivity in the magnets and poses an additional heat load on the cryostat. In order for VENUS to reach its maximum operating potential of 10 kW of 28 GHz microwave heating frequency, the heat load posed by the emitted bremsstrahlung must be understood. In addition, studying the bremsstrahlung under various conditions will help further our understanding of the dynamics within the plasma. A code has been written, using the Python programming language, to analyze the recorded bremsstrahlung spectra emitted from the extraction end of VENUS. The code outputs a spectral temperature, which is relatively indicative of the temperature of the hot electrons, and total integrated count number corresponding to each spectra. Bremsstrahlung spectra are analyzed and compared by varying two parameters: 1) the heating frequency, 18 GHz and 28 GHz, and 2) the ratio between the minimum magnetic field and the resonant magnetic field, .44 and .70, at the electron resonant zone.

INTRODUCTION

The Versatile Electron Cyclotron resonance ion source for Nuclear Science (VENUS), located at Lawrence Berkeley National Laboratory's 88-inch cyclotron, is the most advanced superconducting ion source capable of using high frequencies and high magnetic fields to produce a plasma from which ion beams are extracted [1,2]. The capability VENUS has to produce high charge state ion beams at record intensities makes it a vital instrument in nuclear science research. Ion beams, like the ones produced by VENUS, are used to conduct research in various realms such as astrophysics, heavy elements and nuclear chemistry studies, and weak interactions. Fully understanding its production mechanisms will allow it to be run at its maximum potential and should be done before its ion beams can be used as a source for such research.

Most Electron Cyclotron Resonance (ECR) ion sources, including VENUS, rely on the superposition of solenoid and sextupole magnetic fields for plasma confinement. VENUS, in particular, has a strong plasma confinement since its magnetic fields are produced using liquid-helium cooled superconducting coils. The plasma electrons are resonantly heated up to several hundred keV using microwave heating. In VENUS, the electron heating is done using 18 GHz energy, produced by a klystron, or 28 GHz energy, produced by a gyrotron, or dual frequency 18

and 28 GHz heating. Heating occurs as the free electrons absorb the microwave energy. When the electrons have gained enough energy, through microwave heating, they are capable of ionizing by impact. Plasma ions are created through a step by step ionization process involving collisions with the electrons. In addition to the bremsstrahlung produced via electron-ion collisions, electrons that are not perfectly confined in the plasma will collide with the wall producing bremsstrahlung in the form of x-rays due to their sudden deceleration. High energy x-rays can penetrate the plasma chamber wall and be partially absorbed by the liquid helium surrounding the coils. The cryogenics system can remove only a limited amount of the heat from the cryostat. If more heat is added to the system than can be removed, the temperature of the liquid helium rises and can cause the superconducting coils to quench. The heating induced into the cryostat by the absorption of the x-rays can reach several W/kW. However the cryostat cooling system can only dissipate up to 3 W. Therefore, careful attention must be given to the amount of heat posed by the emitted bremsstrahlung before VENUS is run at its maximum operating potential of 10 kW at 28 GHz.

As a result of previous studies of the VENUS emitted bremsstrahlung, modifications have already been made to the plasma chamber. A plasma chamber surrounded by 2mm of Ta shielding was designed and implemented, and this reduced the bremsstrahlung heat load by a factor of 10. However, the 2 mm of Ta becomes transparent for x-rays with energies above 300 keV [2]. Data presented in this paper shows that under certain conditions the bremsstrahlung far surpasses 600 keV where the 2 mm of tantalum provide no shielding. The energy spectrum of the emitted bremsstrahlung is indicative of the energy of the electrons within the plasma and, as such, can reveal a lot of information about the plasma's properties, which are yet to be fully understood.

This paper presents studies done on the axially emitted bremsstrahlung. The bremsstrahlung spectra and their spectral temperatures, which are used as a relative indication of the temperature of the electron energy distribution function [3], are compared for different source parameters. In particular, microwave power input, magnetic mirror configuration and confinement, and resonant frequency heating are varied. Conclusions regarding their effect on the electron heating are presented.

<center>MATERIALS AND METHODS</center>

Electron Heating in VENUS

The combination of three superconducting axial coils and six superconducting radial coils surrounding the plasma chamber in the VENUS design produce a plasma containment zone composed of axial fields of up to 4T at injection and 3T at extraction, and radial fields increasing radially outward everywhere to 2T at the chamber wall. The superposition of the magnetic fields produced by the three superconducting axial coils, an injection, middle, and extraction solenoid, form the magnetic mirror structure. The magnetic mirror structure shown in Figure 1a, characterized by the values B_{INJ}, B_{MIN}, and B_{EXT} that create the desired confinement structure, is of particular interest in this study. For the data presented, the current through the three axial coils (at injection, center and extraction) was varied to create the desired axial magnetic field in the center of the source (B_{MIN}) as shown in Figure 6 while keeping the mirror peak fields
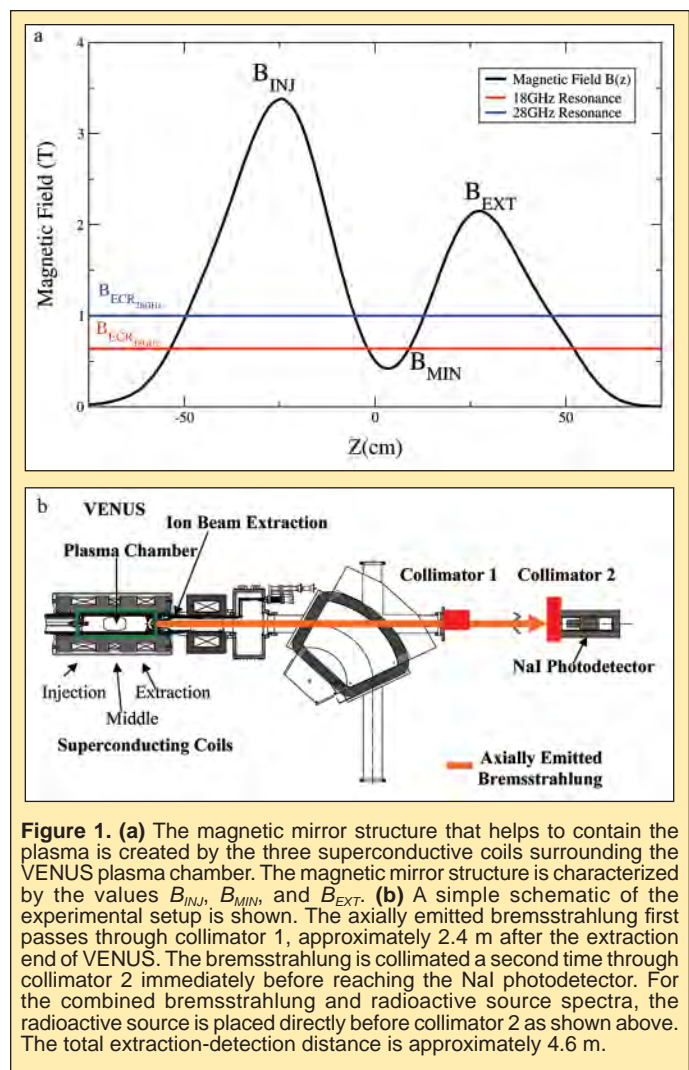
Figure 1. (a) The magnetic mirror structure that helps to contain the plasma is created by the three superconductive coils surrounding the VENUS plasma chamber. The magnetic mirror structure is characterized by the values B_{INJ}, B_{MIN}, and B_{EXT}. **(b)** A simple schematic of the experimental setup is shown. The axially emitted bremsstrahlung first passes through collimator 1, approximately 2.4 m after the extraction end of VENUS. The bremsstrahlung is collimated a second time through collimator 2 immediately before reaching the NaI photodetector. For the combined bremsstrahlung and radioactive source spectra, the radioactive source is placed directly before collimator 2 as shown above. The total extraction-detection distance is approximately 4.6 m.

(B_{INJ} and B_{EXT}) constant (see Figure 1a). Also varied were the heating frequency and the power input at each heating frequency.

The electron's Larmor frequency is shown in Equation 1:

$$B_{ECR} = \frac{m_{e-}\omega}{Q_{e-}} \qquad (1)$$

where Q_{e-} is the electron charge, m_{e-} is the electron mass, and ω is the microwave heating frequency. Since VENUS uses 18 GHz or 28 GHz heating frequencies the electron resonant magnetic fields, $B_{ECR_{18GHz}}$ or $B_{ECR_{28GHz}}$, according to Equation 1, are 0.64 T or 1 T, respectively, and are also shown in Figure 1a. In other words, as the electrons spiral along the magnetic field lines in the magnetic mirror structure, when they encounter the resonant magnetic field they can absorb energy and be heated. The heating of electrons is necessary in order to ionize atoms and multiply ionize ions through collisions. The recorded axially emitted bremsstrahlung spectra primarily results from these ionizing collisions as well as electron collisions with the chamber wall.

Bremsstrahlung Spectra Collection

The experimental set-up of the VENUS source and NaI detector is shown in Figure 1b. The ions are extracted from the plasma at an extraction energy of approximately 20 keV and transported through

the analyzing magnet, after which the charge state distribution of the ion species are measured. The x-ray radiation is observed axially through the straight port of the analyzing magnet and collimated by Collimator 1 about 2.4 m after the extraction aperture of the plasma chamber, with which it is carefully aligned. Collimator 1 has an acceptance angle of 0.2 degrees which represents a 14 mm diameter at the extraction aperture. Since the extraction aperture is only 8 mm, we are also detecting bremsstrahlung from electron collisions with the plasma chamber extraction wall. Collimator 2 follows Collimator 1 by about 2 m. The sodium iodide (NaI) detector used to detect the bremsstrahlung is placed directly behind Collimator 2. In sum, the axially emitted bremsstrahlung is measured approximately 4.6 m after the extraction aperture of the ion source.

The NaI detector is comprised of a 3x3 inch NaI scintillator and a photomultiplier tube. In order to avoid detecting background radiation, the NaI detector is surrounded by lead bricks. The NaI scintillator absorbs the incident bremsstrahlung and, in turn, emits photons proportional to the deposited energy. Each emitted photon is collected by the photomultiplier which converts it into an electrical pulse and amplifies it through a series of stages. Finally, the amplified pulse is recorded by a multi-channel analyzer (MCA). The MCA sorts each pulse according to its amplitude, which is proportional to the energy of the initial photon, and assigns each pulse to a channel. As pulses, referred to as counts, continue to arrive they are assigned to the appropriate channel depending on the amplitude of the pulse. The final output of the MCA is a channel versus count graph and in order to obtain the desired energy versus count graph, calibration of the detector is required. The detector is calibrated by placing a radioactive isotope source with known energy peaks directly before the detector. Although the temperature drift of the detector was measured to be less than 2% for a temperature change of 10 degrees, and the change of the detector's internal energy calibration due to count rate change was found to be less than 1% when varying the count rates from 800 Hz to 30,000 Hz, the internal energy calibration of the detector can drift by a few percent over several days of operation, which we were unable to eliminate. As a result, the detector is recalibrated for each measured spectrum to avoid errors and two spectra are recorded at each setting: 1) a combined bremsstrahlung and radioactive source spectrum, similar to that shown in Figure 2a, and 2) a pure bremsstrahlung spectrum, similar to that shown in Figure 2b.

The recorded bremsstrahlung spectra are analyzed using a code written in Python [5]. In order to obtain a calibrated bremsstrahlung spectrum the code subtracts the bremsstrahlung spectrum from the combined bremsstrahlung and source spectrum, leaving a radioactive source spectrum as shown in Figure 2c. The subtraction is one-to-one with respect to channel and assumes that the NaI detector's internal energy calibration has not drifted in the short amount of time between recording the combined spectrum and the pure bremsstrahlung spectrum. In order to find the maxima on the radioactive source spectrum's peaks a number of things must be done. First, corrections must be made to the height of each peak since the peak is superimposed on a continuum of background counts. The background counts that appear in the spectra may be due to a number of things, including the radiation emitted from the adjacent Advanced ECR source (AECR), and

Compton scatter peaks, plateaus and backscatter peaks resulting from the partial absorption of the bremsstrahlung by the NaI scintillator and surrounding materials. Future work will focus on correcting the spectra for detection efficiencies. The code makes a linear approximation to the background surrounding each peak and subtracts it, as shown in Figure 3. Once the background has been subtracted, a Gaussian fit is applied to the source spectrum peaks. Since there is a large amount of fluctuation in the photon energy emitted by the NaI scintillator for every incident photon energy, a Gaussian fit is appropriate [6]. Due to statistical fluctuations,
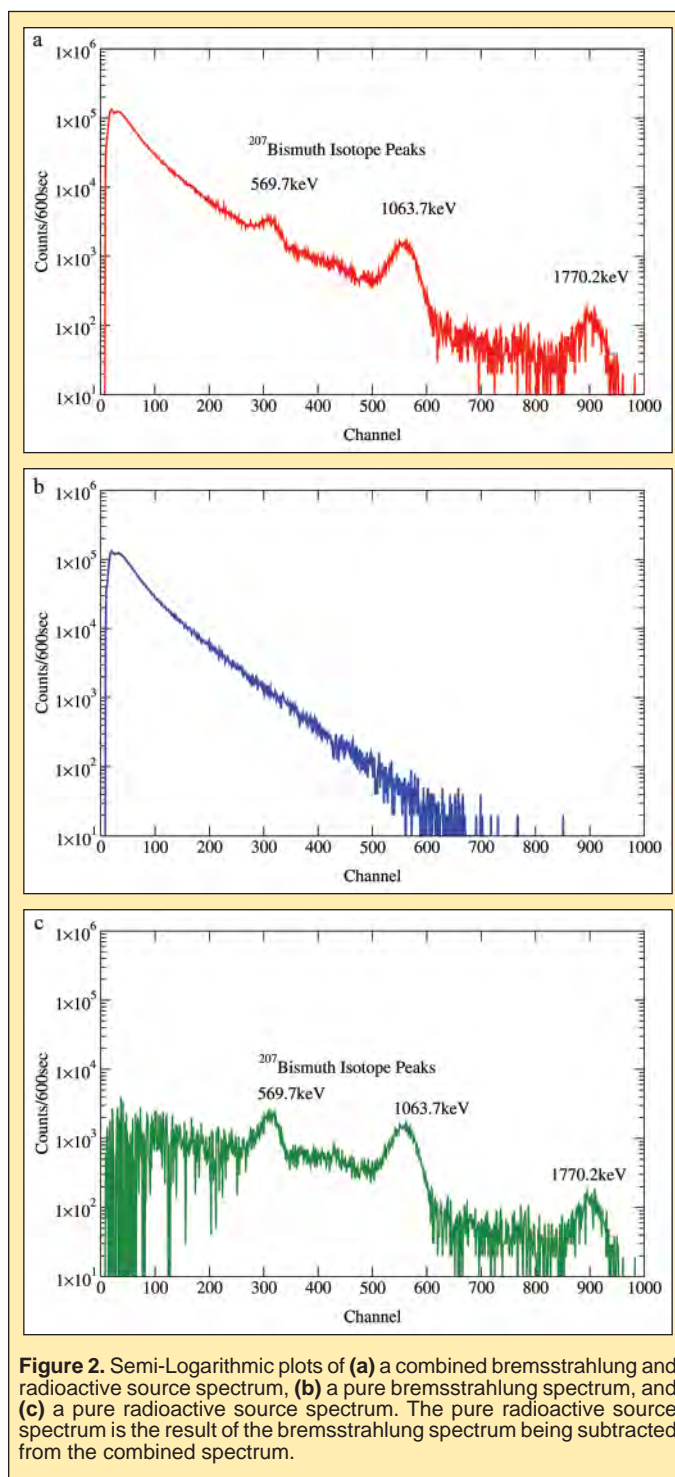
Figure 2. Semi-Logarithmic plots of **(a)** a combined bremsstrahlung and radioactive source spectrum, **(b)** a pure bremsstrahlung spectrum, and **(c)** a pure radioactive source spectrum. The pure radioactive source spectrum is the result of the bremsstrahlung spectrum being subtracted from the combined spectrum.
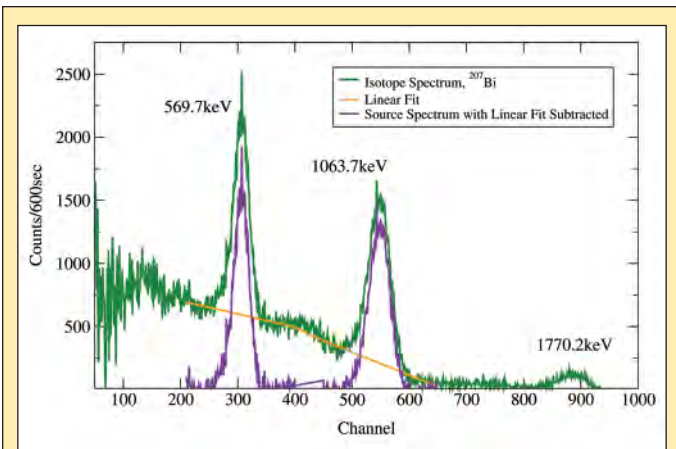
Figure 3. Linear plot of a pure radioactive source spectrum. The Python code calibrates the bremsstrahlung spectrum using the source spectrum. Before determining the peak positions on the source spectrum a linear fit is made to the background and subtracted from it.
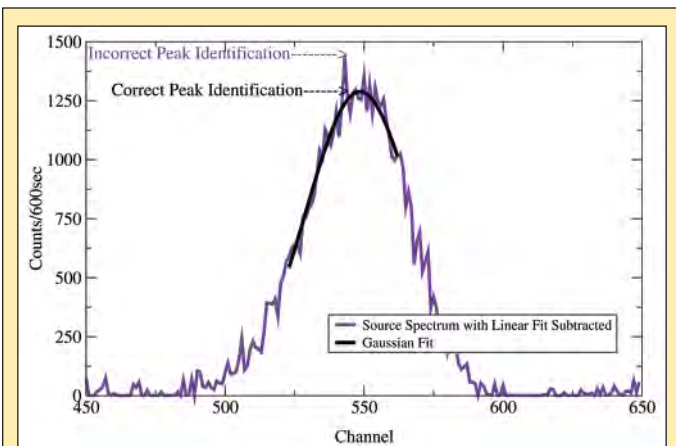
Figure 4. Once the linear approximation to the background is subtracted from the source spectrum a Gaussian fit is applied to the peaks. The Gaussian fit is used to determine the correct position of the peaks.
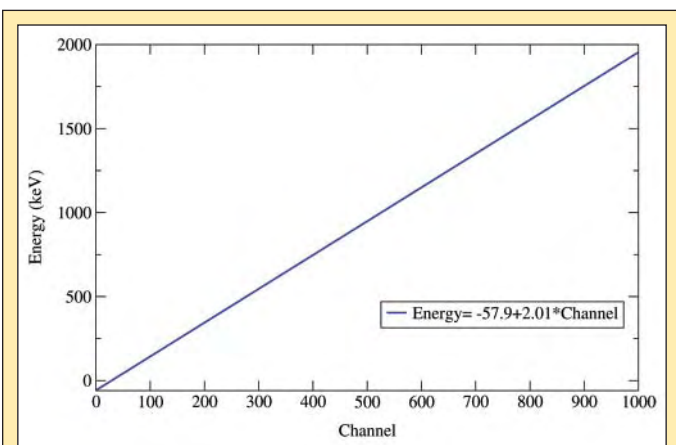
Figure 5. The Python code calibrates the bremsstrahlung spectra. The calibration is a linear relationship between channel and energy as shown here.

simply searching for the channel with the highest count number would lead to an incorrect calibration. Using the Gaussian fit to the peaks, the program finds the correct radioactive source peaks and assigns the appropriate energies to the corresponding channels. An example of an incorrect peak determination and a Gaussian fit used to correctly identify the peak is shown in Figure 4. Since each channel represents an energy value a linear calibration is then obtained, such as shown in Figure 5. The data presented in this paper was calibrated using only the 569.7 keV and 1063.7 keV gamma peaks of Bismuth-207.

Once a spectrum has been calibrated, its spectral temperature, T_S, is obtained. The spectral power, j, emitted is proportional to frequency:

$$j(\omega) \propto \exp[\frac{-\hbar\omega}{kT_S}]$$

where $\hbar$ is Planck's constant, ω is the photon frequency, and k is Boltzmann's constant [7]. Using a semi-logarithmic representation of the data a least-squares fit is applied, from which the inverse of the slope is taken to represent the spectral temperature, T_S. For the spectra discussed in this paper, two energy ranges are used to find T_{S_1} and T_{S_2}: 1) 60–120 keV and 2) 120–200 keV, respectively. In addition to the T_S, the Python code also integrates the spectra for each energy range to give the total counts.

<div align="center">

RESULTS

</div>

Electron Heating as a Function of Magnetic Field Gradient at Resonance Zone

The plasma is confined by the axial and radial magnetic fields. Together the B_{INJ}, B_{MIN}, and B_{EXT} axial magnetic fields make up the magnetic mirror structure. In order to see the effect that varying one of these parameters has on the hot electron population, the minimum B-Field, B_{MIN}, was varied while B_{INJ} and B_{EXT} were held constant. While B_{MIN} was varied, only 28 GHz heating was used. Using two B_{MIN} values, 0.44 T and 0.70 T, we obtained two $\frac{B_{MIN}}{B_{ECR_{28GHz}}}$ ratios: 1) .44 and 2) .70. The .44 ratio represents a steep magnetic field gradient at the resonant magnetic field surface while a 0.70 ratio
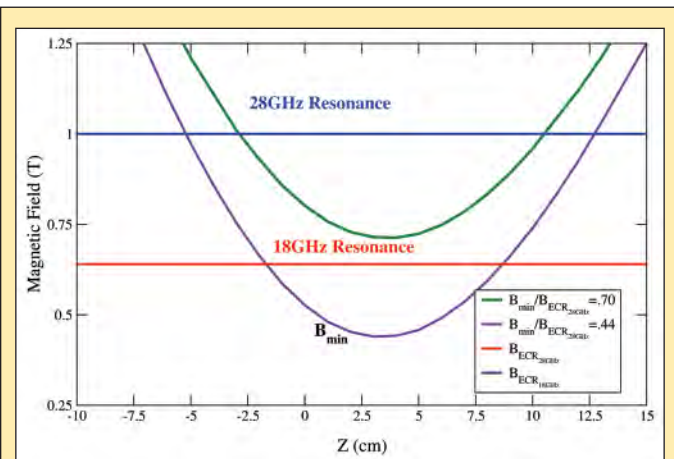
Figure 6. A close look at where the magnetic mirror structures for $\frac{B_{MIN}}{B_{ECR_{28GHz}}}$=.44 and $\frac{B_{MIN}}{B_{ECR_{28GHz}}}$=.70 intersect the 28 GHz resonance zone shows that the .70 ratio has a shallow gradient relative to the steeper .44 ratio.

represents a shallow magnetic field gradient. Figure 6 shows the magnetic mirror structure for these two values and from this figure one can see that the gradient at resonance for a .70 ratio is more shallow than the .44 ratio. Table 1 shows the coil current settings used to produce the magnetic mirror configurations for each ratio. The recorded spectra are shown in Figure 7.

Electron Heating as a Function of Microwave Frequency

In order to see the effect that increased microwave frequency has on the hot electron population, spectra for both 18 GHz and 28GHz were taken at $\frac{B_{MIN}}{B_{ECR_{18GHZ}}}$ and $\frac{B_{MIN}}{B_{ECR_{28GHZ}}}$ ratios of .47 and .70.

.44	Inj	Min	Ext	.70	Inj	Min	Ext
Current (A)	185	153	154	Current (A)	185	113	154
B-Field (T)	3.38	0.44	2.16	B-Field (T)	3.46	0.70	2.23

Table 1. Solenoid current and magnetic field parameters used to compare 28 GHz spectra for $\frac{B_{MIN}}{B_{ECR_{28GHz}}}$ ratios of .44 and .70. The fields B_{INJ} and B_{EXT} are held constant to see the effect varying B_{MIN} has on the hot electron population.
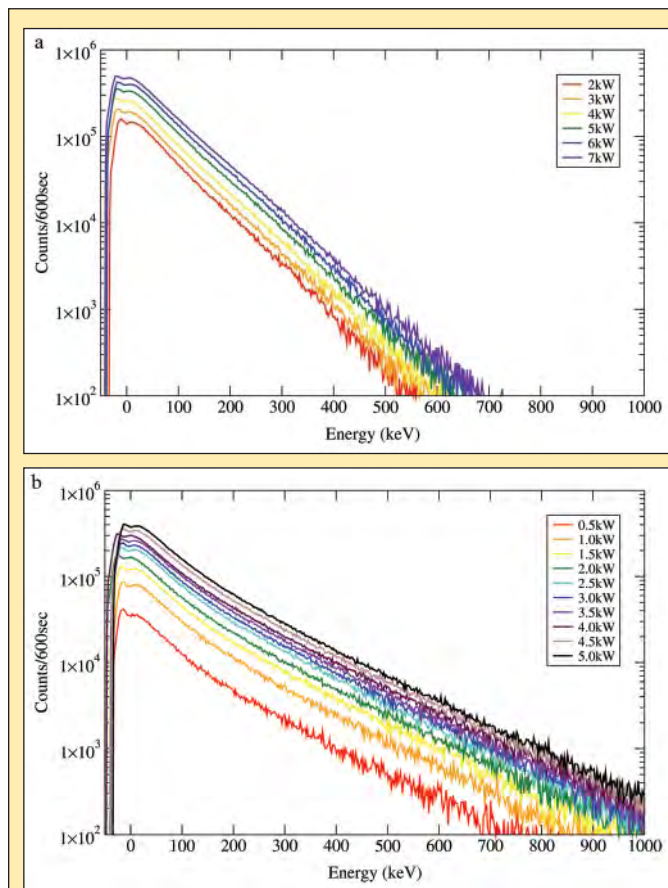
Figure 7. (a) Bremsstrahlung spectra for $\frac{B_{MIN}}{B_{ECR_{28GHz}}}$=.44 with 28 GHz power input varied from 2 kW to 7 kW. **(b)** Bremsstrahlung spectra for $\frac{B_{MIN}}{B_{ECR_{28GHz}}}$=.70 with 28 GHz power input varied from 0.5 kW to 5 kW. The .70 ratio shallow magnetic field leads to more efficient heating since more electrons reach higher temperatures at lower 28 GHz power inputs.

The .70 ratio spectra are shown in Figure 8 and the .47 ratio spectra are shown Figure 9. The 18 GHz spectra are compared to 28 GHz spectra at equivalent ratios. So that the 18 GHz power input remains comparable to the 28 GHz power input in terms of magnetic mirror structure, the 18 GHz current settings used to create the magnetic fields where scaled down by a factor of $\frac{18}{28}$. Table 2 shows the coil current settings used to produce magnetic mirror structures for each ratio at 18 and 28 GHz power inputs.

DISCUSSION AND CONCLUSIONS

Electron Heating as a Function of Magnetic Field Gradient at Resonance Zone

A comparison of the spectra obtained with steep and shallow gradients, or $\frac{B_{MIN}}{B_{ECR_{28GHz}}}$ ratios of .44 and .70, respectively, suggests that a shallow gradient at resonance leads to more efficient electron heating. Therefore, higher electron energies can be reached. A shallow gradient allows the electron to remain in the vicinity of the resonance zone for a longer period of time, allowing it to gain more energy. Simulations have shown that the amount of speed gained by an electron in the resonance zone seems to decrease as the square-root of the gradient [8].
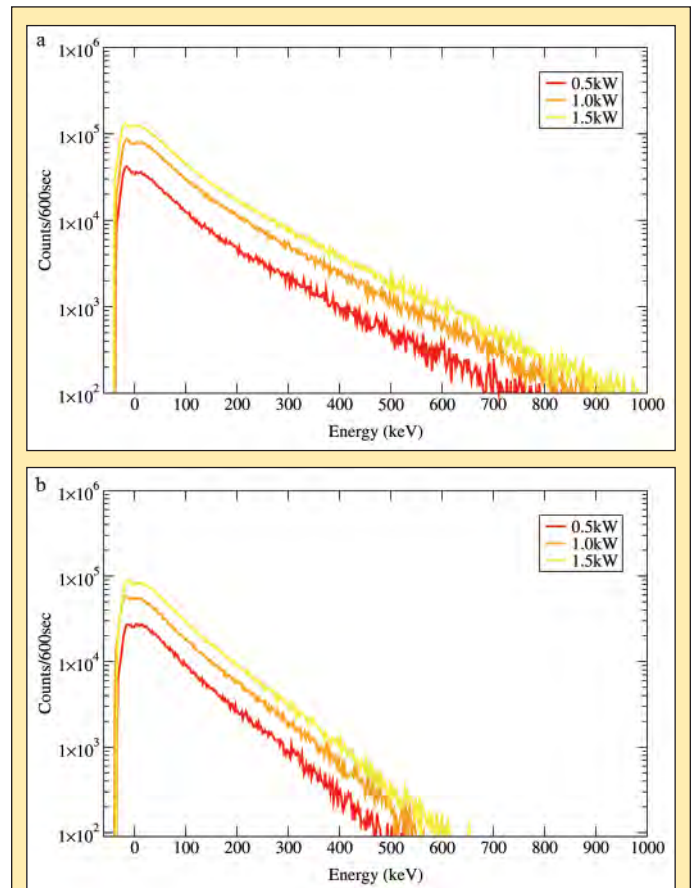
Figure 8. (a) 28GHz bremsstrahlung spectra for $\frac{B_{MIN}}{B_{ECR_{28GHz}}}$=.70. **(b)** 18 GHz bremsstrahlung spectra for $\frac{B_{MIN}}{B_{ECR_{18GHz}}}$=.70. The 18 GHz magnetic fields are scaled down from 28GHz by a factor of $\frac{18}{28}$ in order to achieve equivalent magnetic mirror structures.
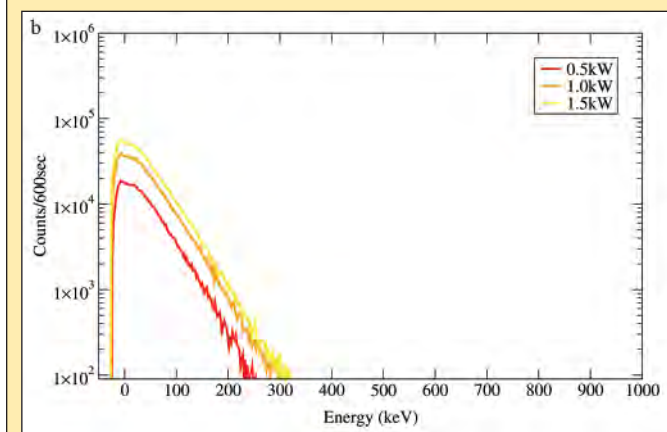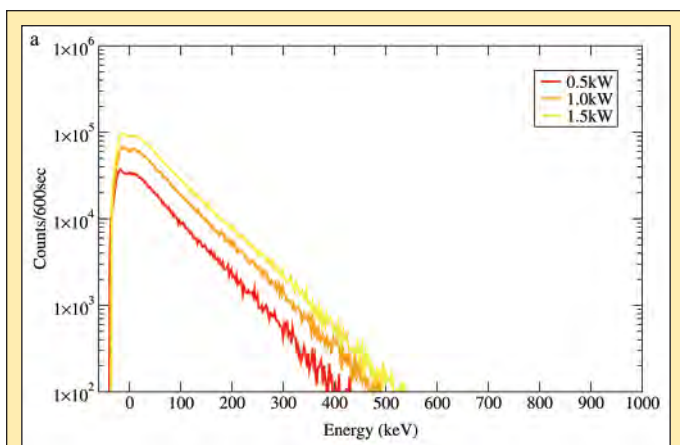
Figure 9. (a) 28 GHz bremsstrahlung spectra for $\frac{B_{MIN}}{B_{ECR_{28GHz}}}$=.47. **(b)** 18 GHz bremsstrahlung spectra for $\frac{B_{MIN}}{B_{ECR_{18GHz}}}$=.47. The 18 GHz magnetic fields are scaled down from 28 GHz by a factor of $\frac{18}{28}$ in order to achieve equivalent magnetic mirror structures.

.44	Inj	Min	Ext	.70	Inj	Min	Ext
28GHz Current (A)	189	158	163	28GHz Current (A)	185	113	154
28GHz B-Field (T)	3.48	0.46	2.29	28GHz B-Field (T)	3.46	0.70	2.23
18GHz Current (A)	122	102	105	18GHz Current (A)	118.6	72.4	98.7
18GHz B-Field (T)	2.23	0.30	1.47	18GHz B-Field (T)	2.22	0.46	1.43

Table 2. Solenoid current and magnetic field parameters used to compare spectra for 18 GHz and 28 GHz heating frequencies. 18 GHz and 28 GHz spectra are recorded for $\frac{B_{MIN}}{B_{ECR}}$ ratios of .47 and .70. The 18 GHz magnetic fields are scaled down from 28 GHz by a factor of $\frac{18}{28}$ for each $\frac{B_{MIN}}{B_{ECR}}$ ratio in order to achieve equivalent magnetic mirror structures.
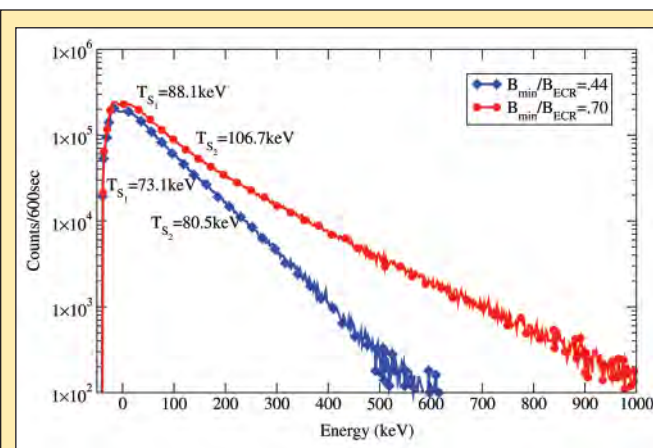
Figure 10. Shown is a direct comparison of a steep magnetic field gradient, $\frac{B_{MIN}}{B_{ECR}}$=.44, and a shallow magnetic field gradient, $\frac{B_{MIN}}{B_{ECR}}$=.70, at equivalent power inputs. The comparison shows that the shallow magnetic field gradient leads to more efficient heating. The spectral temperatures, T_{S_1} (60–120 keV) and T_{S_2} (120–200 keV), for each ratio are indicated and show that electrons present in a shallow magnetic field achieve higher temperatures.

Figure 10 directly compares a .44 ratio spectrum to a .70 ratio spectrum, each at 3 kW of 28 GHz, by indicating the spectral temperature. The spectral temperatures for both ranges, T_{S_1} (60–120 keV) and T_{S_2} (120–200 keV), for the .70 shallow ratio at resonance are greater than the .44 steep ratio by about 17% and 25%, respectively. In addition, the increase in spectral temperature when going from a steep to a shallow magnetic field gradient presents an increased amount of heat deposited onto the cryostat surrounding the plasma chamber. The increase in the amount of heat deposited is supported by the increased counts observed for .70 shallow ratio at each input power, shown in Figure 11. The integrated number of counts for a .70 shallow ratio spectrum is greater by about 50%, or more, at 2 kW of 28 GHz power, and by about 200% at 4 kW of 28 GHz power. These results support simulations which show that electron energy increases with decreasing magnetic field gradient at the resonance zone [9].

Electron Heating as a Function of Microwave Frequency

New generations of ion sources strive for higher microwave frequency capabilities. Since plasma density scales with the square of microwave frequency and magnetic field confinement scales linearly with microwave frequency, higher frequencies are desired [10]. A consequence of increased plasma density at higher frequencies is an increased hot electron population and, as such, an increase in the amount of electrons lost from the plasma. 18 and 28GHz bremsstrahlung spectra recorded for $\frac{B_{MIN}}{B_{ECR}}$ ratios of .47 and .70 show that the difference in emission between 18 and 28 GHz is significant. For both $\frac{B_{MIN}}{B_{ECR}}$ ratios of .47 and .70 the number of hot electrons increases significantly when going from 18 to 28 GHz heating frequencies. This is shown in Figures 8 and 9 where the 28 GHz spectra extend to higher energies.

Figure 12 shows that for a $\frac{B_{MIN}}{B_{ECR}}$ ratio of .70 the spectral temperature does not change when power input is increased. This is also true for the .47 ratio spectral temperatures. As power is increased, the spectrum shape does not change but only shifts upward, suggesting an increase in plasma density, and the slope remains the same, reflecting a constant spectral temperature. Interestingly, when the ratio of 28 GHz to 18 GHz counts is taken for the range 60–120 keV, the .47 ratio case shows a constant increase in counts by a factor of about 2.3 as power input increases, while the .70 case shows an increase in counts by a factor of 1.6. The reason for this remains unclear. Figure 13 shows a direct comparison

between 18 and 28 GHz heating, each at 1.5k W of input power, for both $\frac{B_{MIN}}{B_{ECR}}$ ratios of .47 and .70. For both cases, the spectral temperature in either range increases significantly for 28 GHz heating, indicating an increased hot electron population. These results support simulations which have concluded that electron energy increases with microwave frequency [9].

Concluding Remarks

VENUS, which has already produced record breaking ion beam currents and high charge state distributions, has yet to reach its maximum operating potential. In order to prevent failures as its performance is gradually improved and tested, it is important to take advantage of the diagnostic capabilities the emitted bremsstrahlung can provide. The information provided by the bremsstrahlung is most valuable when accurately analyzed. As such, computer code was developed to extract values such as spectral temperatures and integrated count numbers under various operating conditions. Future work will focus on correcting the spectra for detector efficiencies which may affect these values.

The presented axially emitted bremsstrahlung spectra primarily represent electrons which have been lost from the plasma at the extraction end of the plasma as well as bremsstrahlung emitted from the plasma in the direction of the extraction aperture. Although the axially emitted bremsstrahlung is not an adequate representation of the bremsstrahlung emitted at all surfaces of the plasma, it does give insight into the electron energy distribution of the plasma. The setup of VENUS prevents studies of radially emitted bremsstrahlung, and so an overall determination of the electron losses is not yet known. However, a few conclusions can be drawn from the experimental data obtained. First, a small magnetic field gradient at the electron resonant zone leads to more efficient electron heating. Increasing the power input increases the density of electrons, but has no or very little effect on the electron energy distribution function. Increasing the microwave heating frequency also leads to more efficient electron heating and increases the mean electron energies.

Figure 11. The integrated counts, for the energy range of 60–120 keV, increases with increasing power input as well as with a decreasing magnetic field gradient.
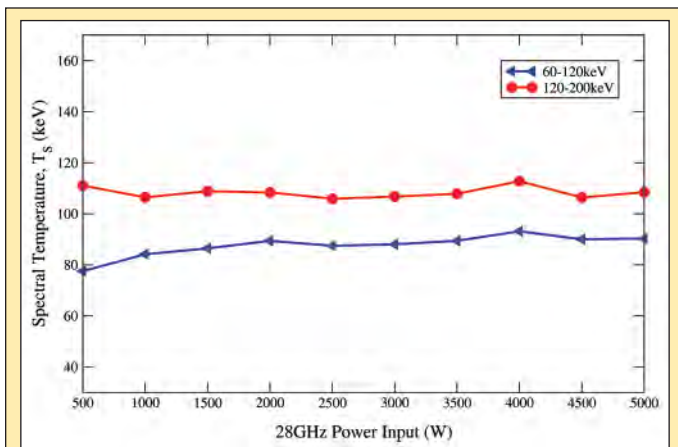
Figure 12. The spectral temperatures, T_{S_1} (60–120 keV) and T_{S_2} (120–200 keV), for a $\frac{B_{MIN}}{B_{ECR_{28GHz}}}$=.70 ratio are shown. As the 28 GHz power input increases the spectral temperature remains constant.
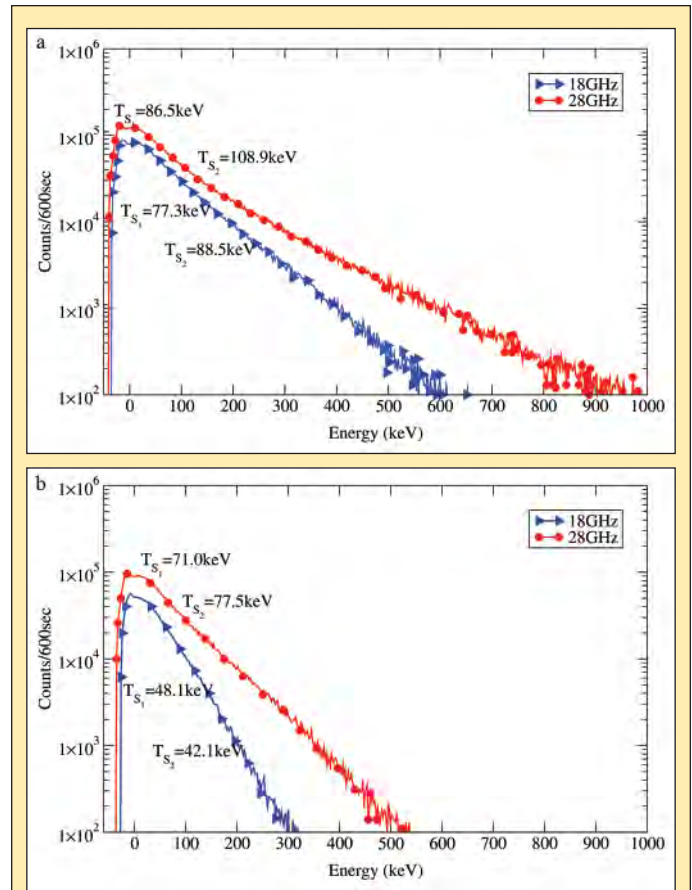
Figure 13. (a) 18 and 28 GHz bremsstrahlung spectra with 1.5 kW power input at $\frac{B_{MIN}}{B_{ECR}}$=.70. **(b)** 18 and 28 GHz bremsstrahlung spectra with 1.5 kW power input at $\frac{B_{MIN}}{B_{ECR}}$=.47. The 18 GHz magnetic fields are scaled down from 28 GHz by a factor of $\frac{18}{28}$ in order to achieve equivalent magnetic mirror structures. The spectral temperatures, T_{S_1} (60–120 keV) and T_{S_2} (120–200 keV), for each heating frequency are indicated.

REFERENCES

[1] D. Leitner, C.M. Lyneis, T. Loew, D.S. Todd, S. Virostek, and O. Tarvainen, "Status Report of the 28GHz Superconducting Electron Cyclotron Resonance Ion Source VENUS," *Review of Scientific Instruments*, vol. 77, 03A302, February 2006.

[2] C. Lyneis, D. Leitner, D. Todd, S. Virostek, T. Loew, A. Heinen, and O. Tarvainen, "Measurement of Bremsstrahlung Production and X-Ray Cryostat Heating in VENUS," *Review of Scientific Instruments*, vol. 77, 03A342, March 2006.

[3] C. Barue, M. Lamoureux, P. Briand, A. Girard, and G. Melin, "Investigation of hot electron-cyclotron resonance ion sources," *Journal of Applied Physics*, vol. 76, no. 5, September 1994.

[4] D. Leitner, C.M. Lyneis, S.R. Abbott, D. Collins, R.D. Dwinell, M.L. Galloway, M. Leitner, and D.S. Todd, "Next Generation ECR ion sources: First Results of the superconducting 28 GHz ECRIS-VENUS," *Nuclear Instruments and Methods in Physics Research B*, vol. 235, 486–496.

[5] "Python Programming Language-Official Website," [cited 2007 Aug 09], http://www.python.org/.

[6] G. F. Knoll, *Radiation Detection and Measurement, 2nd Edition*, New York: John Wiley & Sons, Inc., 1989: 114–117.

[7] R. Geller, *Electron Cyclotron Resonance Ion Sources and ECR Plasmas*, Bristol: Institute of Physics Publishing, 1998: 252.

[8] Y. Jongen. "E.C.R. Electron Acceleration", *Proceedings of the Sixth International Workshop on ECR Ion Sources*, January 17th–18th, 1985, Berkeley, California, USA.

[9] H. Koivisto, "The effect of microwave frequency and grad B on the energy of electrons in an electron cyclotron resonance ion source," *Review of Scientific Instruments*, vol. 70, no. 7, July 19.

[10] D. Leitner and C.M. Lyneis, "ECR Ion Sources," *The Physics and Technology of Ion Sources, 2nd Edition*, Ian G. Brown (ed.), Weinheim: Wiley-VCH, 2004: 203–227.

Blaine Carter was born in Kirkland, Washington and grew up in Sammamish. He attended Northwest Nazarene University, majoring in chemistry. During his undergraduate career he held a SULI internship at Pacific Northwest National Laboratory in Sequim, Washington. Blaine hopes to enter a PhD program in the field of chemistry and become a research associate. In his spare time, Blaine loves to play basketball and explore the outdoors.

Michael Huesemann is a Staff Research Engineer at PNNL Marine Sciences Laboratory, Sequim, Washington. He has conducted both experimental and theoretical research in environmental and marine biotechnology for more than fifteen years. Dr. Huesemann has conducted experimental research in diverse areas such as photosynthetic hydrogen production, biofixation of carbon dioxide from flue gases by marine microalgae, the effects of ocean carbon sequestration on nitrogen cycling, PCB phytoremediation of marine sediments using sea-grasses, and hydrocarbon bioavailability in aged petroleum contaminated soils undergoing bioremediation treatment. In addition, Dr. Huesemann has published policy-related journal articles on climate change mitigation, sustainable development, environmental remediation, and professional ethics. He received his M.S. and Ph.D. in 1989 in biochemical engineering from Rice University, Houston, Texas.

HYDROGEN PRODUCTION BY THE CYANOBACTERIUM *PLECTONEMA BORYANUM*: EFFECTS OF INITIAL NITRATE CONCENTRATION, LIGHT INTENSITY, AND INHIBITION OF PHOTOSYSTEM II BY DCMU

BLAINE CARTER AND MICHAEL HUESEMANN

ABSTRACT

The alarming rate at which atmospheric carbon dioxide levels are increasing due to the burning of fossil fuels will have incalculable consequences if disregarded. Fuel cells, a source of energy that does not add to carbon dioxide emissions, have become an important topic of study. Although significant advances have been made related to fuel cells, the problem of cheap and renewable hydrogen production still remains. The cyanobacterium *Plectonema boryanum* has demonstrated potential as a resolution to this problem by producing hydrogen under nitrogen deficient growing conditions. *Plectonema boryanum* cultures were tested in a series of experiments to determine the effects of light intensity, initial nitrate concentration, and photosystem II inhibitor DCMU (3-(3,4-dichlorophenyl)-1,1-dimethylurea) upon hydrogen production. Cultures were grown in sterile Chu. No. 10 medium within photobioreactors constantly illuminated by halogen lights. Because the enzyme responsible for hydrogen production is sensitive to oxygen, the medium was continuously sparged with argon/CO_2 (99.7%/0.3% vol/vol) by gas dispersion tubes immersed in the culture. Hydrogen production was monitored by using a gas chromatograph equipped with a thermal conductivity detector. In the initial experiment, the effects of initial nitrate concentration were tested and results revealed cumulative hydrogen production was maximum at an initial nitrate concentration of 1 mM. A second experiment was then conducted at an initial nitrate concentration of 1 mM to determine the effects of light intensity at 50, 100, and 200 µmole m^{-2} s^{-1}. Cumulative hydrogen production increased with increasing light intensity. A final experiment, conducted at an initial nitrate concentration of 2 mM, tested the effects of high light intensity at 200 and 400 µmole m^{-2} s^{-1}. Excessive light at 400 µmole m^{-2} s^{-1} decreased cumulative hydrogen production. Based upon all experiments, cumulative hydrogen production rates were optimal at an initial nitrate concentration of 1 mM and a light intensity of 100 µmole m^{-2} s^{-1}. DCMU was shown in all experiments to severely decrease hydrogen production as time progressed. With the information acquired so far, future experiments with reducing substances could determine maximum rates of hydrogen production. If maximum hydrogen production rates proved to be large enough, *Plectonema boryanum* could be grown on an industrial scale to provide hydrogen gas as a renewable fuel.

INTRODUCTION

While greenhouse gases are responsible for making Earth's surface temperature supportable for life, the rate at which carbon dioxide is being emitted into the atmosphere is increasing. Even with the most stringent mitigation practices, the Intergovernmental Panel on Climate Change predicts a 1.4° to 5.8°C increase in global average surface temperature by the year 2100 [1]. While temperature changes of this magnitude have both foreseeable and unforeseen consequences, it could take hundreds of years for the full consequences of these carbon dioxide levels to take effect. Even if carbon dioxide emissions were significantly reduced and atmospheric carbon dioxide levels were allowed time to stabilize, increases in temperature and sea level would be seen for approximately 1,000 years [1]. Since energy demands will only continue to increase with time, renewable energy has become an important area of research.

Increasing atmospheric carbon dioxide levels are largely due to the burning of fossil fuels, therefore technology that aims at finding sources of renewable energy directly address this problem. Virtually all sources of renewable energy are directly or indirectly driven by

the sun, making them fundamentally different than other sources of energy such as fossil fuels or nuclear power. Because of this, renewable sources of energy produce far less pollution and release fewer greenhouse gases. Some of the major renewable technologies include wind power, hydro power, solar energy, geothermal energy, and biofuels. Although biofuels are most commonly associated with the conversion of biomass to liquid biofuels, another valuable source of renewable energy is hydrogen produced by photobiological systems. Hydrogen, with an extremely high energy density, has the potential to positively impact fossil fuel reduction and global warming by providing a means of sustainable energy generation. Major discoveries have been made with fuel cell related technologies, but a large problem still remains: cheap hydrogen production.

There are many different ways to produce hydrogen, such as natural gas reformation, renewable electrolysis, gasification, renewable liquid reforming, nuclear high temperature electrolysis, and high temperature thermochemical water splitting [2]. All of these methods have potential, but only a few are efficient enough at this point to meet demands. Natural gas reformation and electrolysis, methods which can currently meet production demands, do not solve any problems because they require large amounts of energy, which is inevitably generated by the burning of fossil fuels. A resolution to this problem is hydrogen production from a renewable source, in this case photobiological systems.

Photobiological H_2 production by microalgae has been investigated since the early 1970s [3]. The fundamental concept is to use microalgae to catalyze the conversion of solar energy and water into H_2, with O_2 as by-product. Most current research is focusing on the direct biophotolysis approach, in which water is split into H_2 and O_2 without intermediate CO_2 fixation [3]. As shown in Figure 1, during direct biophotolysis, electrons flow "directly" from water via photosystem II (PSII) and photosystem I (PSI) to the hydrogenase enzyme, which transfer these electrons to protons, thereby causing the release of hydrogen gas. However, this reaction is limited by the strong inhibition of the process by the simultaneously produced O_2. Searching for, or protein engineering of, hydrogenases that exhibit an O_2 resistant H_2 evolution reaction has been, and continues to be, a major field of research, but has not

Figure 1. Electron transport in the light reactions of photosynthesis [4].

yet been successful. Indeed, achieving the levels of oxygen resistance required in a practical process may well be problematic, with perhaps a million-fold improvement required. The alternative approach, to use irreversible (e.g., glucose-glucose oxidase) or reversible (e.g. hemoglobin) O_2 absorbers, does allow sustained direct biophotolysis. However, the irreversible O_2 absorbers contain, and thus dissipate, as much energy as contained in the H_2, resulting in essentially zero net energy gain. Even if O_2 inhibition were somehow overcome, direct biophotolysis would still suffer from the practical problems of generating explosive H_2:O_2 mixtures as well as requiring very expensive photobioreactors to contain such a reaction.

These various problems of direct biophotolysis led to proposals for indirect, two-stage light-driven processes, with CO_2 fixation and O_2 release occurring in the first stage followed by H_2 production reactions in the second stage [5]. In the indirect biophotolysis process (see Figure 1), reduced substrates (i.e., carbohydrates, such as starch or glycogen) accumulate during the photosynthetic O_2 production and CO_2 fixation stage, and these are then used in a second stage for H_2 production. By temporarily separating the photosynthetic oxygen production phase from the hydrogen production phase, indirect biophotolysis overcomes the two major problems associated with direct biophotolysis, oxygen inhibition of the hydrogenase and the generation of highly explosive H_2:O_2 mixtures.

In green microalgae such as *Chlamydomonas reinhardtii*, starch accumulates within the cells under nutrient-limited culture conditions such as sulfur or nitrogen deficiency [6]. As shown in Figure 1, during indirect biophotolysis, the electrons from the accumulated starch are donated to plastoquinone (PQ). Then they flow down-gradient through the electron transport chain to photosystem I (PSI) to be energized again and transferred to ferredoxin (Fd). The hydrogenase enzyme then accepts the electrons from ferredoxin and combines them with protons from the medium to generate hydrogen gas. The relative contributions of hydrogen production from direct and indirect biophotolysis can be quantified by challenging the culture with DCMU (3-(3,4-dichlorophenyl)-1,1-dimethylurea), which shuts down the water splitting, oxygen-generation activity of photosystem II (PSI II) by inhibiting the transfer of electrons between electron carriers Q and PQ (see Figure 1). For example, the addition of DCMU will have no effect on hydrogen production rates if hydrogen is generated solely by indirect biophotolysis but will completely inhibit any hydrogen production by direct biophotolysis.

The non-heterocystous nitrogen-fixing blue-green microalga (cyanobacterium) *Plectonema boryanum* is capable of producing hydrogen only by indirect biophotolysis. During the daytime, this organism carries out photosynthetic oxygen production and CO_2 fixation. The depletion of nitrogen in the culture results in glycogen-accumulation within the cells. At night, the cells respire the remaining dissolved oxygen and the medium becomes anaerobic. If the culture is both nitrogen-limited and anaerobic, the nitrogenase enzyme is induced to fix nitrogen from the atmosphere according to the following reaction [7]:

$$N_2 + 8H^+ + 8e^- + 16\,ATP \rightarrow 2NH_3 + H_2 + 16ADP + 16Pi$$
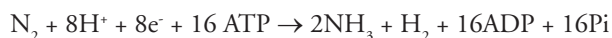
It can be seen that one mole of hydrogen is produced as a byproduct of the fixation of one mole of nitrogen into two moles of
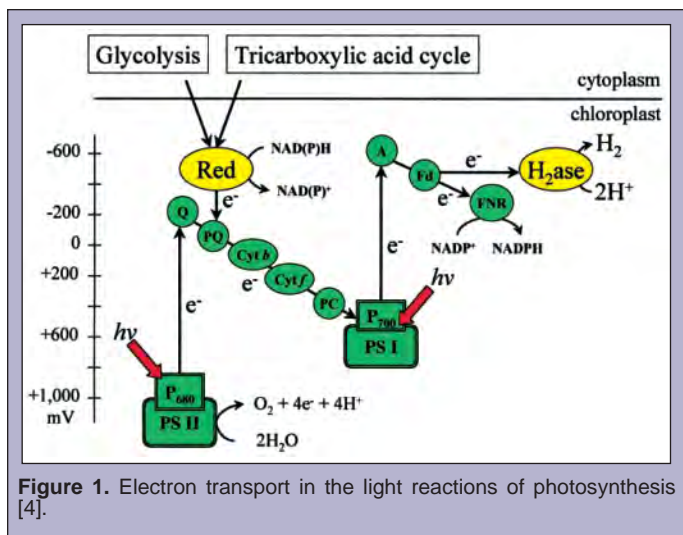
ammonia [8]. It is also important to note that this reaction is very energy intensive since it requires 8 moles of high-energy electrons, which are donated from the accumulated glycogen, per mole of hydrogen generated [7]. While this nitrogen-fixation reaction occurs in the dark, it is enhanced in the light because electrons are energized at photosystem I, resulting also in cyclic ATP generation. Because of its extreme sensitivity to oxygen, the nitrogenase, as the hydrogenase, is only active under strict anaerobic conditions.

The hydrogen yield of this reaction can be increased by eliminating dinitrogen gas from the medium and replacing it with an inert gas such as argon. The nitrogenase will then use the high energy electrons that are donated from the accumulated glycogen to produce hydrogen (instead of ammonia), as long as the medium remains anaerobic and nitrogen-deficient. Challenging the culture with DCMU should have no effect on the rates of hydrogen generation since it proceeds entirely by indirect biophotolysis. However, since DCMU inhibits photosynthetic CO_2 fixation, the intracellular glycogen reserves cannot be restored after their depletion during the hydrogen production phase.

In addition to hydrogen generation by the nitrogenase enzyme, cyanobacteria also have the ability to generate hydrogen via hydrogenase-catalyzed reactions. Hydrogenases occur as two distinct types in cyanobacteria. One of them, the uptake hydrogenase, has the ability to oxidize hydrogen to generate energy (ATP) and reducing equivalent (NAD(P)H) while at the same time removing oxygen via respiration, thereby protecting the oxygen-sensitive nitrogenase enzyme from inhibition [7]. The other type of hydrogenase is the reversible or bidirectional hydrogenase and it can take up or produce hydrogen, depending on the redox status of the culture [9]. Generally, the contribution to hydrogen evolution by the reversible hydrogenase is neglible [9]. Therefore, the net hydrogen generation rate in cyanobacteria is the sum of the hydrogen production rate by nitrogenase and the hydrogen consumption rate by the uptake hydrogenase.

Cyanobacterium *Plectonema boryanum* has been shown by Weave and Benemann to produce hydrogen under nitrogen deficient conditions [10]. In their study, oxygen was found to be a strong and irreversible inhibitor of the enzyme responsible for hydrogen production at very low concentration (>0.5%) [10]. This problem was overcome by continually flushing cultures with an argon/carbon dioxide gas mixture, or by adding reducing substances that encourage hydrogen production.

It is the objective of this experiment to determine the effects of initial nitrate concentration, light intensity, and photosystem II inhibitor DCMU upon hydrogen production by the cyanobacterium *Plectonema boryanum*.

Materials And Methods

Strain Selection and Medium Composition

Cyanobacterium *Plectonema boryanum*, acquired from American Type Culture Collection (Catalog #18200), was used in a series of experiments to determine the effects of nitrogen concentration, light intensity, and photosystem II inhibitor DCMU upon hydrogen production. Cultures were grown in sterile Chu No. 10 medium.

Compound	Mass (mg/L)
Ca(NO$_3$)$_2$·4H$_2$O	Variable (Growth Medium = 232)
K$_2$HPO$_4$	10
MgSO$_4$·7H$_2$O	25
Na$_2$CO$_3$	20
Ferric Citrate	3.5
Sodium Citrate	5.4
Na$_2$SiO$_3$·9H$_2$O	58.9

Table 1. Chu No. 10 medium ingredients.

To prepare sterile Chu No. 10 media, concentrated stock solutions containing all of the medium ingredients except calcium nitrate tetrahydrate were created (See Table 1). Separate concentrated calcium nitrate tetrahydrate solutions were prepared as well, and were always made fresh or frozen, in order to prevent degradation. The stock solutions were mixed together in appropriate ratios for the specific experiment and diluted to one liter. After the appropriately mixed solutions were adjusted to a pH of 7.5 with hydrochloric acid, solutions were sterile filtered using 0.2 µm nitrocellulose filters. After filtration, the sterile solutions were ready for inoculation.

Bioreactor Setup

Roux bottles were used for carrying out all experiments and were continuously sparged with argon/CO$_2$ (99.7%/0.3% vol/vol) at 60 mL/min by gas dispersion tubes immersed in the culture. The culture medium within the Roux bottle was constantly stirred by a magnetic stir bar. Continuous illumination was maintained by 300 or 500 W halogen bulbs in a Regent PN PQS45 light housing.

Measurement of Light Intensity

Whenever the light intensity illuminating the Roux bottles was measured, lightmeter readings were taken at five evenly distributed points at the face of the Roux bottle. The average of these values approximated the overall light intensity selected for the specific experiment. Whenever photon absorbance was measured, readings at the five points were taken both in front of and behind the bottle, relative to the light source. All readings were taken using a Hansatech Quantitherm Lightmeter.

Measurement of Optical Density (OD) and Nitrate Concentration

During the initial active growth phases, nitrate concentration and optical density (OD) were frequently measured. Nitrate concentration was determined via cadmium reduction using Hach NitraVer packets. A 10 mL culture sample was taken from the Roux bottle and spun in a centrifuge at 2500 rpm for three minutes. The supernatant was then poured off into a sealable test tube. A single Hach NitraVer packet was added to the supernatant and was mixed for one minute by continuous inversion. After mixing, the solution was allowed to react for precisely five minutes. The cuvette was rinsed with the sample solution twice and then an absorbance reading

was taken at 500 nm using a UNICO 1100 spectrophotometer. Based upon a previously constructed calibration curve, the nitrate concentration was determined by the absorbance. Because this method is technique sensitive, results were merely looked upon in a qualitative manner. The optical density of the culture samples was measured at 595 nm. Culture samples were diluted to ensure that observed readings were within the linear range of acquisition ($0 < OD_{590} < .5$), in accordance with Beer's law.

Measurement of AFDW

Ash free dry weight (AFDW), another measurement of cell biomass, was determined by vacuum filtering a measured volume of culture through a Whatman, 55mm, GF/F glass microfibre filter. The filter was dried overnight in a 105°C oven and the mass was measured. At this point the filter was combusted in a 550°C furnace for 30 minutes and then weighed. The difference in these weights represents the combustible organic cellular materials. AFDW, with units of mg/L, is calculated by dividing the difference of the dried and combusted weights by the measured volume of the sample. Filters were pre-vacuum rinsed with 25ml of de-ionized water and pre-ashed in a 550°C furnace for 15 minutes to ensure accuracy.

Gas Composition Analysis

Although all culture bottles were continuously sparged with argon/CO_2 (99.7%/0.3% vol/vol) at 60 mL/min for the duration of all experiments, the gas flow was reduced to 10 mL/min to allow for hydrogen measurements. Once flow rates were reduced, a minimum of three hours was allocated to allow hydrogen concentration within the headspace of the Roux bottle to stabilize (as seen in Figure 2). After this time period, the gas composition was analyzed using an SRI 8610C gas chromatograph equipped with a thermal conductivity detector. The carrier gas used in all measurements was argon. The cumulative hydrogen production (V_{H2}) was calculated using the following equation:

$$V_{H2} = \Sigma f_{H2} \bullet F_G \bullet \Delta T$$

where f_{H2} is the measured fraction of hydrogen, F_G is the flow of the sparge gas, and ΔT is the time interval between measurements.

Glycogen Assay

In order to monitor glycogen concentration within the cells, glycogen measured as glucose was determined by the method described by Gfeller and Gibbs [6]. One mL samples were drawn from the culture and spun down at 13,000 rpm for two minutes. The supernatant was discarded and the pellet was then washed two times with 1 mL of methanol and two times with 1 mL of sodium acetate (pH 4.5). The samples were sonicated and spun down for each stage of the wash. These wash cycles broke apart the cells and removed components that could interfere with future absorbance readings. After completing the two wash cycles, the pellet was resuspended in 1.7 mL acetate buffer and 0.02 mL of α-amylase (Sigma Aldrich Catalog # A4582) was added to solution. The samples were autoclaved for 10 minutes to solubilize the glycogen. After autoclaving, 0.05 mL of amyloglucosidase (Sigma Aldrich
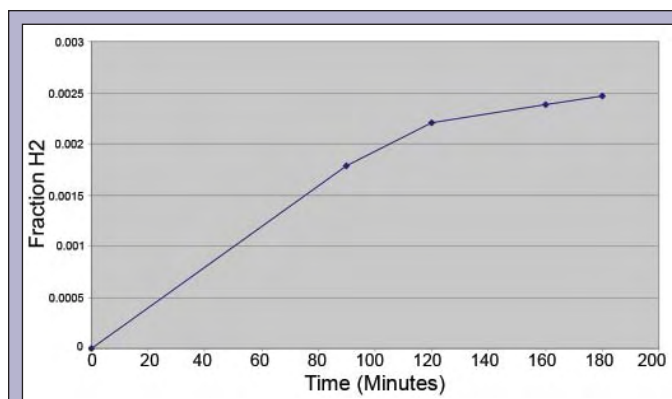
Figure 2. The graph above shows the fraction of hydrogen changing within the Roux bottle headspace as a function of time. At an initial sparge rate of 60 mL/min, the fraction of hydrogen within the headspace is below the detection limit of the gas chromatograph. When the gas flow is reduced to 10 mL/min, the fraction of hydrogen increases to a detectable level, but as seen above, it takes approximately three hours for the value to stabilize. During the stabilization period, equilibrium is being established between the amount of hydrogen produced by the algae and the amount of hydrogen being expelled from the headspace due to the sparge gas.

Catalog # S9144) was added to solution and the samples were incubated at 55°C for 14 hours to convert glycogen to glucose. Sample volumes were then readjusted to 2.0 mL with distilled water. At time zero, a reaction period was initiated by adding 2.0 mL of glucose assay reagent (Sigma Aldrich Catalog # G3666 and # D2679) followed by mixing. Sixty second time intervals were allocated between the additions of glucose assay reagent to each subsequent tube. Immediately after mixing, each tube was incubated for thirty minutes at 37°C. The reaction was stopped at the end of the thirty minute incubation by adding 2.0 mL of 6 M H_2SO_4. Each tube was mixed thoroughly and the absorbance was measured at 540 nm. Chemically, when glucose oxidase contained within the glucose assay reagent reacts with glucose, hydrogen peroxide and gluconic acid are formed. The hydrogen peroxide then reduces dianisidine, which turns a brown color. The strength of the absorbance is directly related to the glucose concentration. In order to normalize glycogen concentrations to biomass concentrations, AFDW was always taken the same time glycogen samples were withdrawn. Based upon a calibration curve, glucose concentration was calculated based upon the absorbance.

Chlorophyll Concentration

Chlorophyll concentration was measured spectrophotometrically in experiments to observe possible changes with varying nitrate concentration or light intensity. Chlorophyll was extracted from 1 mL of cells in boiling methanol following the procedure described by Tett [11]. One mL of algae culture was transferred to an amber glass centrifuge tube and 0.2 mL of 1% (w/v) $MgCO_3$ was added. A boiling chip was placed in the tube along with 9 mL of 90% (v/v) methanol/water. The sample was vortexed and then boiled in a water bath at 90°C for two minutes. In this process the cell walls of the algae were broken apart and the chlorophyll was extracted into solution. The tubes were then spun down at 1,500 rpm for four minutes to remove particulates from the solution. Sample volume was readjusted to 10 mL using 90% (v/v) methanol/water. Blanks of

90% (v/v) methanol/water were measured at 663 nm and 750 nm, followed by the chlorophyll samples. The chlorophyll concentration was then calculated in mg/L from the following equation:

$$Chla = DF*(1/77)*((C_{663}-B_{663})-(C_{750}-B_{750}))*1000$$

where DF is the dilution factor (10), C_{663} and C_{750} are the absorbance of the extract at 663 and 750 nm respectively, and B_{663} and B_{750} are the absorbance of the blank at 663 and 750 nm, respectively.

RESULTS AND DISCUSSION

Effects of Nitrogen Concentration and Inhibition of Photosystem II by DCMU

In the first experiment, the effects of nitrogen concentration and DCMU upon *Plectonema boryanum* hydrogen production were observed. Four cultures within Roux bottles were grown at a light intensity of 100 μmole m^{-2} s^{-1} in the following initial medium nitrate concentrations: Bottle A=0.5 mM NO$_3$, Bottle B=1.0 mM NO$_3$, Bottle C=1.0 mM NO$_3$, and Bottle D=2.0 mM NO$_3$. When nitrate concentrations approached zero in culture C, 10 μmol of DCMU was added to inhibit photosynthetic oxygen production.

As seen in Figure 3, after approximately 70 hours, bottles A, B, and C reached a stationary growth phase. At this point, DCMU was added to bottle C. Bottle D reached a stationary growth phase at approximately 100 hours of growth. Nitrate concentrations were estimated to approach zero when the optical density no longer increased, because readings obtained with the Orion nitrate probe proved to be inaccurate and imprecise. It was observed that the maximum optical density, which was reached during stationary phase, was directly related to the initial nitrate concentration. Since nutrients available within the media decrease as the cells continue to grow, a maximum biomass concentration is reached when the nutrients are depleted. For this experiment, the maximum biomass concentration, measured as optical density, is directly related to the initial nitrate concentration.

As each respective bottle reached the stationary growth phase, the sparge gas flow was reduced to 10 mL/min to allow for gas
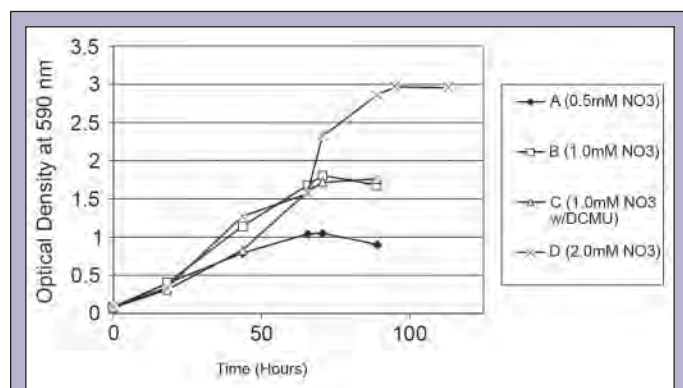
composition analysis. For an unknown reason, the sparge gas flow rates had an occasional problem of slowly approaching and then reaching zero. When this occurred, the average flow rate could not be accurately calculated and hydrogen production values became uncertain. While most of the bottles did not have this problem most of the time, bottle C had the particular problem of reaching zero sparge gas flow overnight. Daytime measurements, where the flow was closely monitored, resulted in a different rate of hydrogen production than the overnight readings. A new system was devised to sparge the cultures at high flow rates overnight to keep them anaerobic, accurately set the flow during the day, and then analyze the gas composition once with the accurately calculated flow rates. This method eliminated the degree of uncertainty and provided a more accurate and precise measurement of hydrogen production. After reviewing the data, a revised curve for bottle C was constructed to estimate the hydrogen production values based upon the rates obtained during daytime measurements (Figure 4).

From Figure 4 it is evident that at a light intensity of 100 μmole m^{-2} s^{-1}, an initial nitrate concentration of 1.0 mM is optimal for hydrogen production. After 500 hours, culture B (1.0 mM nitrate) produced 395 mL of hydrogen, followed by cultures A and D, which produced 298 and 165 mL of hydrogen, respectively. Although hydrogen production should be normalized to ash free dry weight (biomass), the only time an AFDW measurement was taken was at the end of the experiment (Table 2). The cultures had undergone considerable lysis and decomposition by this point, so hydrogen production rates normalized to biomass were not
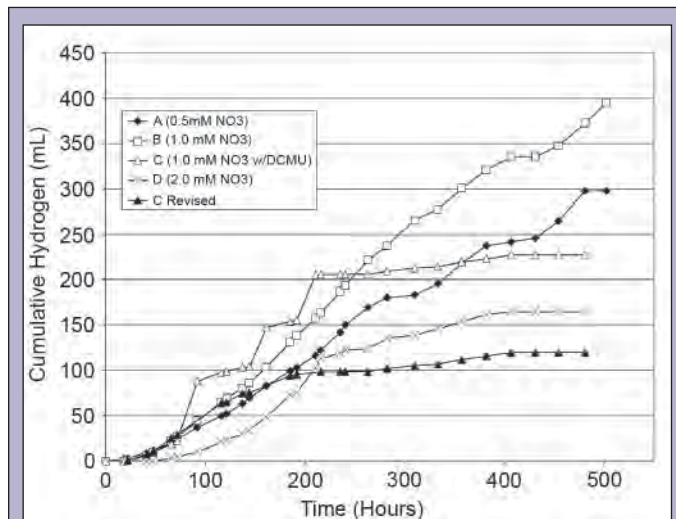
Figure 4. Cumulative hydrogen production in cultures with varying initial nitrate concentrations as a function of time.

Culture	AFDW (mg/L)
A (0.5 mM NO$_3$)	145
B (1.0 mM NO$_3$)	240
C (1.0 mM NO$_3$ w/DCMU)	30
D (2.0 mM NO$_3$)	165

Table 2. AFDW measurements taken at the end of the experiment.

Figure 3. Optical Density measured at 590 nm as a function of time in cultures with varying initial nitrate concentrations.

calculated. Cumulative hydrogen production should therefore be looked upon only in a comparative manner.

It is also apparent from Figure 4 that DCMU has a latent effect of severely decreasing hydrogen production. Once glycogen energy stores are used up by all the cells, the cells begin to deteriorate and DCMU inhibits new culture growth within the medium. This means that as time progresses, the DCMU culture continues to deteriorate and produces very little hydrogen. Before this occurs however, hydrogen production rates are very similar in the culture with the same initial nitrate concentration not inhibited by DCMU. Another important observation was a cyclic pattern of hydrogen production in bottle A after approximately 250 hours. Culture A, at an initial nitrate concentration of 0.5 mM, the most nitrogen deficient, shows alternating periods of fast and slow hydrogen production. It is possible these cycles indicate a synchronized culture, where periods of photosynthesis for glycogen synthesis alternate with nitrogenase based hydrogen production.

Effects of Light Intensity and Inhibition of Photosystem II by DCMU

In a second experiment, the effects of light intensity and DCMU upon hydrogen production by *Plectonema boryanum* were observed. Four cultures were grown in Roux bottles at an initial nitrate concentration of 1.0 mM with the following light intensities: Bottle A = 50 µmole m^{-2} s^{-1}, Bottle B = 100 µmole m^{-2} s^{-1}, Bottle C = 100 µmole m^{-2} s^{-1}, and Bottle D = 200 µmole m^{-2} s^{-1}. When nitrate concentrations approached zero in culture C, 10 µmol of DCMU was added to inhibit photosynthetic oxygen production.

As seen in Figure 5, after approximately 48 hours, all nitrate had been removed from the media in bottles B (100 µmole m^{-2} s^{-1}), C (100 µmole m^{-2} s^{-1} w/DCMU), and D (200 µmole m^{-2} s^{-1}). It was not until 70 hours that all nitrate had been removed from the medium in bottle A (50 µmole m^{-2} s^{-1}). Even when all nitrate was removed from the media, the cultures continued to grow for a short time (Figure 6). Bottle D (200 µmole m^{-2} s^{-1}) reached a stationary growth phase at 67 hours, followed by bottles B (100 µmole m^{-2} s^{-1}) and C (100 µmole m^{-2} s^{-1} w/DCMU), reaching stationary phases at 86 hours. At this point DCMU was added to bottle C. As seen from figures 6 and 7, bottle A (50 µmole m^{-2} s^{-1}) never reached a stationary phase before entering hydrogen production.

As shown in Figure 7, cumulative hydrogen production increased with increasing light intensity. After approximately 470 hours, bottle D (200 µmole m^{-2} s^{-1}) produced 589 mL of hydrogen, the highest cumulative amount. Bottle B (100 µmole m^{-2} s^{-1}) produced 491 mL of hydrogen by 470 hours, followed by bottle A (50 µmole m^{-2} s^{-1}), which produced 271 mL of hydrogen. When hydrogen production values were normalized to biomass, bottle B (100 µmole m^{-2} s^{-1}) had the greatest rate of hydrogen production. All of the hydrogen production rates were calculated based upon a line of best fit for the cumulative hydrogen production curves as a function of time and were standardized to biomass concentration based upon the AFDW taken at the onset of hydrogen production.

As shown in Figure 8, the cumulative volume of hydrogen produced was also plotted as a function of the total number of photons absorbed. In this regard, bottle A (50 µmole m^{-2} s^{-1}) had the
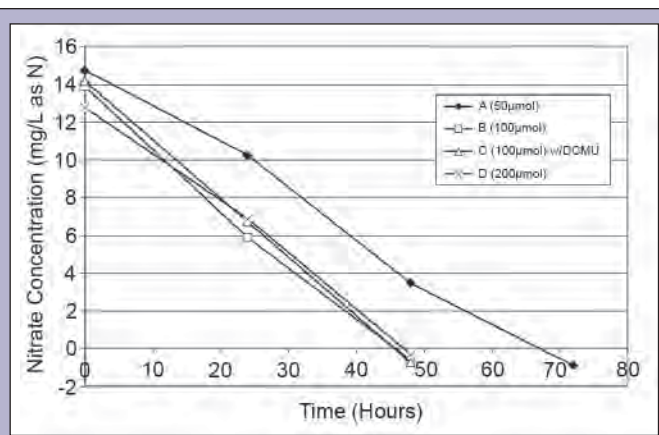
Figure 5. Nitrate concentration as a function of time in cultures grown at varying light intensities.
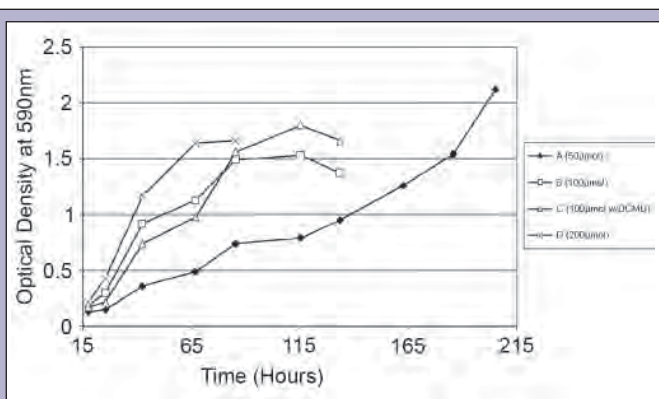
Figure 6. Optical Density at 590 nm as a function of time in cultures grown at varying light intensities.
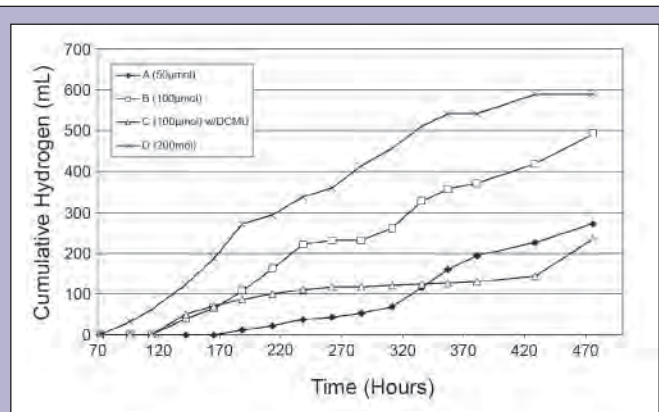
Figure 7. Cumulative hydrogen production in cultures at varying light intensities as a function of time.

greatest rate of hydrogen production in terms of photon absorption, followed by bottles B (100 µmole m^{-2} s^{-1}), D (200 µmole m^{-2} s^{-1}), and C (100 µmole m^{-2} s^{-1} w/DCMU), respectively.

Light measurements taken periodically throughout the experiment revealed an overall decrease in photon absorption as the experiment progressed (Figure 9). The major contributor to this decrease was the considerable cell lysis and decomposition that occurred. At the end of the experiment, when chlorophyll
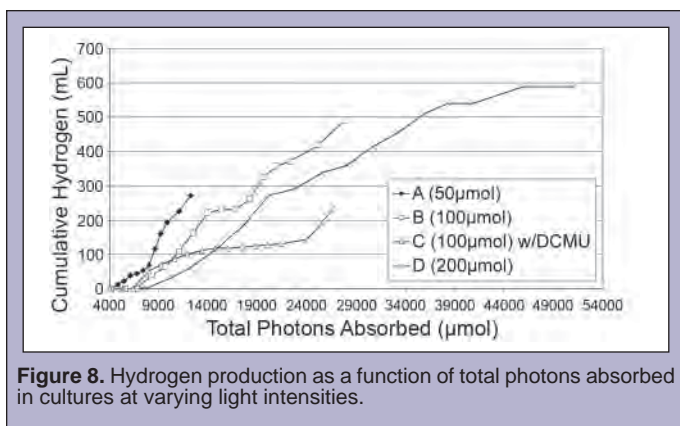
Figure 8. Hydrogen production as a function of total photons absorbed in cultures at varying light intensities.

Figure 10. Chlorophyll concentration and photons absorbed at varying light intensities.

concentration was measured, a direct correlation could be seen between the light intensity and the chlorophyll concentration (Figure 10). At higher light intensities, the chlorophyll content was lowest. At low light intensities, the chlorophyll content was highest. From an efficiency perspective, it would make sense that chlorophyll content would decrease as light intensity increases. If large numbers of photons are being projected, less chlorophyll is needed to effectively utilize the light. At low light intensities however, more chlorophyll is synthesized to capture light and adequately drive photosynthesis. Although culture A has the highest chlorophyll content, the number of photons absorbed is the lowest because it is only being grown at a light intensity of 50 µmole $m^{-2} s^{-1}$ (Figure 10). Bottle D however, with the lowest chlorophyll content, is still absorbing the greatest number of photons, for it is being illuminated with a light intensity of 200 µmole $m^{-2} s^{-1}$. These observations also relate back to hydrogen production, which shows that the larger number of photons a culture absorbs, the higher their cumulative hydrogen production, the exception being cultures inhibited by DCMU (Figure 8).

It is evident in this experiment, just as in the previous one, that DCMU has a severe effect on decreasing hydrogen production as time progresses. Bottles B (100 µmole $m^{-2} s^{-1}$) and C (100 µmole $m^{-2} s^{-1}$ w/DCMU) showed similar rates of hydrogen production until approximately 190 hours, at which point bottle C (100 µmole $m^{-2} s^{-1}$) with DCMU showed dramatic decreases in hydrogen production. Because DCMU inhibits photosystem II and thus prevents any further accumulation of glycogen within the cell, once glycogen
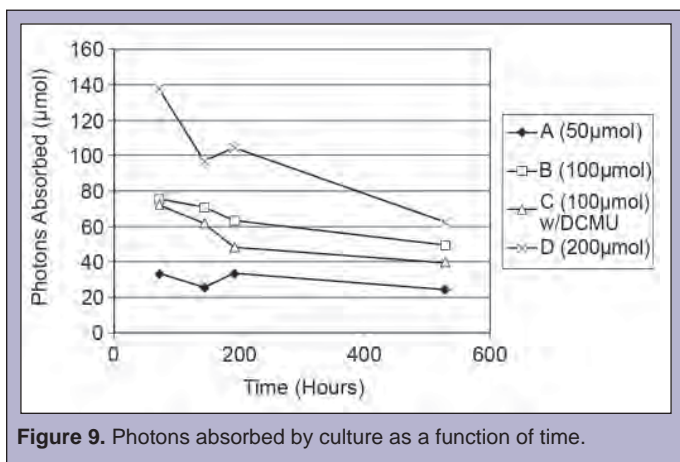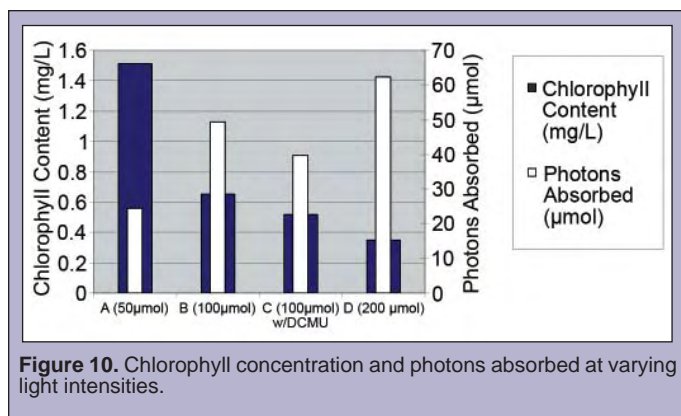
stores are depleted in the DCMU culture, there is no source of electrons remaining for hydrogen production. Cultures not inhibited by DCMU can continue photosynthesis and accumulate glycogen as necessary. This is why bottle B (100 µmole $m^{-2} s^{-1}$), not inhibited by DCMU, continued to produce hydrogen at the initial rate. After 240 hours however, bottle B (100 µmole $m^{-2} s^{-1}$) showed the cyclic pattern of hydrogen production that was also seen in the previous experiment.

Glycogen content (measured as glucose) was measured for all cultures at the onset of hydrogen production and at the end of the experiment. Results revealed an overall decrease in glucose concentration for all cultures during this time period, especially in culture C inhibited by DCMU (Figure 11). When glucose concentrations were normalized to biomass concentrations, it appears that the glycogen content of the cells also decreases. During the initial growth phase, cells accumulate stores of glycogen. When nutrients are depleted within the medium, the cells then use glycogen to produce hydrogen. Cultures not inhibited by DCMU can continue to accumulate glycogen via photosynthesis and carbon fixation, but cultures inhibited by DCMU can no longer synthesize any glycogen stores. This may be why culture C, inhibited by DCMU, decreased in glycogen fraction by 20 percent (Figure 12). Both cultures A and B, not inhibited by DCMU, showed a glycogen fraction decrease of only 10%. Culture D, which produced the largest cumulative amount of hydrogen, appeared not to change its glycogen fraction. An important observation to note is that at the point this final glycogen measurement was taken, bottle D is possibly entering a cyclic phase of hydrogen production. The cyclic patterns of hydrogen production observed suggest the entire culture is entering a growth phase, which is then followed by a hydrogen production phase. The cycle continues as cells accumulate glycogen for a given period of time and then enter a hydrogen production phase until glycogen stores are depleted. No hydrogen production was observed in bottle D the day the glycogen sample was taken, so it is possible bottle D was entering a growth phase. Future experiments could attempt to monitor glycogen concentration during these cyclic phases of hydrogen production.

Figure 9. Photons absorbed by culture as a function of time.
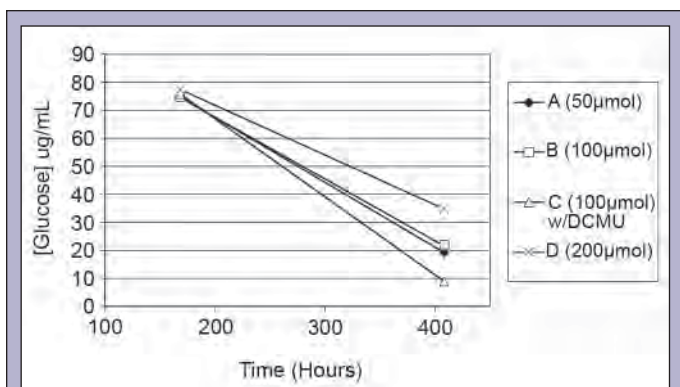
Figure 11. Glucose Concentration as a function of time in cultures grown at varying light intensities.
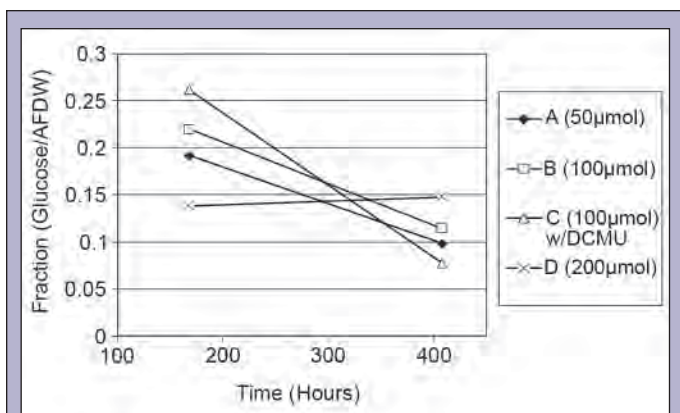
Figure 12. Fraction of Glucose/AFDW as a function of time in cultures grown at varying light intensities.

Effects of High Light Intensity and Inhibition of Photosystem II by DCMU

In a final experiment, the effects of high light intensity and DCMU upon hydrogen production by *Plectonema boryanum* were observed. Four cultures were grown at an initial nitrate concentration of 2.0 mM and were grown at two different light intensities. Cultures A and B were grown at a light intensity of 200 µmole m^{-2} s^{-1}, while cultures C and D were grown at a light intensity of 400 µmole m^{-2} s^{-1}. When nitrate concentrations approached zero in cultures B and D, 10 µmol of DCMU was added to inhibit photosynthetic oxygen production.

As seen in Figure 13, the nitrate concentration approached zero in all of the cultures after approximately 68 hours of growth. All of the cultures continued to grow for another 48 hours until the stationary phase was reached, as shown in Figure 14. Based upon the nitrate concentration and optical density curves, increasing the light intensity above 200 µmole m^{-2} s^{-1} does not increase the growth rate of the cultures at initial nitrate concentration of 2 mM.

As seen in Figure 15, cumulative hydrogen production was greatest in culture A, which was grown at light intensity of 200 µmole m^{-2} s^{-1} and not inhibited by DCMU. While culture A produced over a total of 300 mL of hydrogen, all other cultures failed to produce more than 110 mL of hydrogen. It can be concluded that excessive light intensity decreases cumulative hydrogen production, possibly by photoinhibition. This is confirmed by hydrogen production rates normalized to biomass. (These rates were calculated based upon a line of best fit for cumulative hydrogen production as a function of time and the AFDW taken at the onset of hydrogen production). Both cultures grown at a light intensity of 200 µmole m^{-2} s^{-1} had higher rates of hydrogen production than any of the cultures grown at a light intensity of 400 µmole m^{-2} s^{-1}.
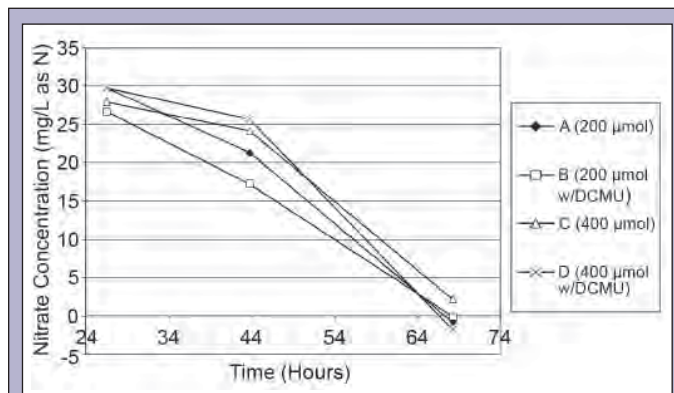
Figure 13. Nitrate Concentration as a function of time with cultures grown at two different light intensities.
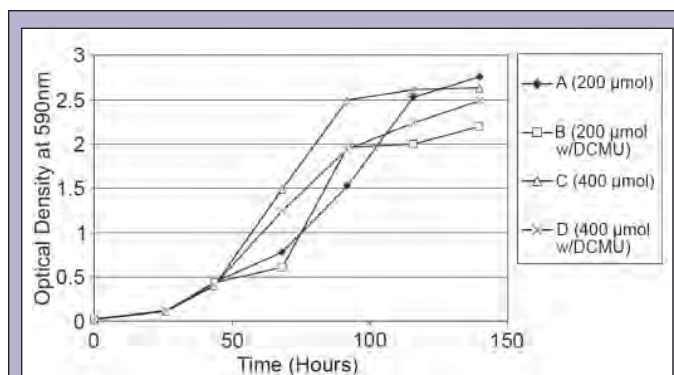
Figure 14. Optical Density at 590 nm as a function of time with cultures grown at two different light intensities, with and without DCMU, respectively.
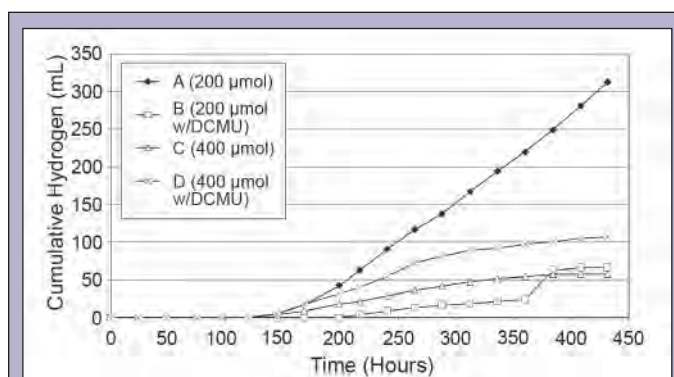
Figure 15. Cumulative Hydrogen Production as a function of time in cultures grown at two different light intensities, with and without DCMU, respectively.

As seen in Figure 16, glycogen concentration decreased in all of the cultures as a function of time. It is also apparent that the final glycogen concentration very closely correlates to cumulative hydrogen production. Culture A, which produced the largest amount of cumulative hydrogen, ended with the highest glucose concentration. Culture D, which produced the second largest amount of cumulative hydrogen, had the second highest final glucose concentration. Cultures B and C, which were very close in producing the lowest amount of cumulative hydrogen, ended with the lowest glucose concentrations.
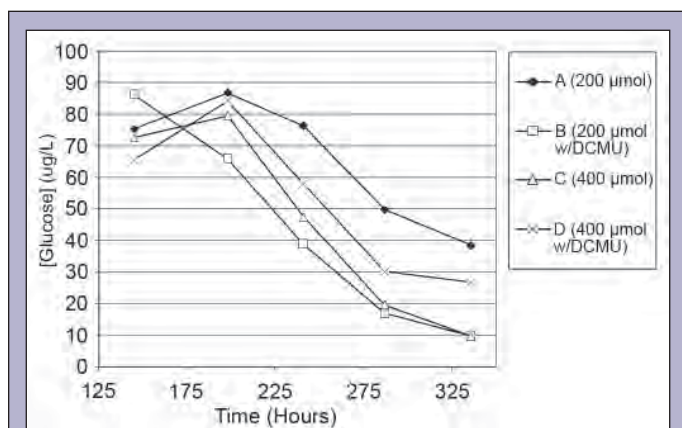
Figure 16. Glycogen measured as glucose as a function of time in cultures grown at two different light intensities, with and without DCMU, respectively.

Conclusion

After testing the effects of initial nitrate concentration, light intensity, and photosystem II inhibitor DCMU upon hydrogen production by *Plectonema boryanum*, it can be concluded that *Plectonema boryanum* is a suitable candidate for future studies on renewable hydrogen production. In the first experiment, where the effects of initial nitrate concentration were tested, results showed cumulative hydrogen production was maximum at an initial nitrate concentration of 1 mM. With this information, a second experiment was conducted at 1 mM initial nitrate concentration to test the effects of light intensity at 50, 100, and 200 μmole m^{-2} s^{-1}. Cumulative hydrogen production was shown to increase with increasing light intensity. A final experiment was then performed at high light intensity with an initial nitrate concentration of 2 mM. Excessive light at 400 μmole m^{-2} s^{-1} decreased cumulative hydrogen production, possibly because of photoinhibition, thus optimal cumulative hydrogen production occurred at an initial nitrate concentration of 1 mM and a light intensity of 200 μmole m^{-2} s^{-1}. Hydrogen production rates, normalized to biomass, were shown to be optimal at an initial nitrate concentration of 1 mM with a light intensity of 100 μmole m^2 s^{-1}. When compared to values reported in literature [12], hydrogen production rates by *Plectonema boryanum* were measured to be at most 0.12 μmole H$_2$/hr/mg without reducing substances. In this experiment however, *Plectonema boryanum* was shown to produce 0.16 μmole H$_2$/hr/mg without reducing substances. When reducing substances are added,

hydrogen production rates can be increased by up to six times [12]. If other variables such as temperature, pH, and salinity were optimized, hydrogen production by *Plectonema boryanum* could prove to be a viable source of renewable hydrogen. Results from all DCMU challenged experiments support the idea that glycogen is the source of electrons for hydrogen production within *Plectonema boryanum*.

References

[1] Intergovernmental Panel on Climate Change (IPCC): 2001a, *Third Assessment Report – Climate Change 2001: The Scientific Basis, A Report of Working Group I – Summary for Policymakers*, www.ippcc.ch.

[2] McHugh, Kathleen, "Hydrogen Production Methods", *MPR Associates*, 2005. http://www.mpr.com/pubs/hydroprod.pdf

[3] Prince, R.C., and H.S. Kheshgi, "The Photobiological Production of Hydrogen: Potential Efficiency and Effectiveness as a Renewable Fuel", *Critical Reviews in Microbiology*, **31(1)**:19–31, 2005.

[4] Melis A., and T. Happe, "Hydrogen Production: Green Algae as a Source of Energy", *Plant Physiology*, **127**:740–748, 2001

[5] Hallenbeck, P.C., and J.R. Benemann, "Biological Hydrogen Production: Fundamentals and Limiting Processes", *International Journal of Hydrogen Energy*, **27**:1185–1193, 2002.

[6] Gfeller, R., and M. Gibbs, "Fermentative Metabolism of *Chlamydomonas reinhardtii*", *Plant Physiology*, **7(75)**:212–218, 1984.

[7] Madamwar, D., N. Garg, and V. Shah, "Cyanobacterial hydrogen production", *World Journal of Microbiology and Biotechnology*, **16(1)**:757–767, 2000.

[8] Dutta, D., D. De, S. Chaudhuri, and S.K. Bhattacharya, "Hydrogen Production by Cyanobacteria", *Microbial Cell Factories*, **4**:36, 2005.

[9] Rao, K., and D. Hall, "Hydrogen production by cyanobacteria: Potential, problems and prospects", *Journal of Marine Biotechnology*, **4(1)**: 10–15, 1995.

[10] Weare, N.M., and J.R. Benemann, "Nitrogenase Activity and Photosynthesis in Plectonema boryanum", *Journal of Bacteriology*, **119(1)**:258–265, 1974.

[11] Tett, P., M.G. Kelly, and G.M. Hornberger. "A Method for the Spectrophotometric Measurement of Chlorophyll a and Pheophytin a in Benthic Microalgae", *Limnology and Oceanography*, **20(5)**:887–896, 1975.

[12] Kashyak, A.K., K.D. Pandey, and S. Sarkar, "Enhanced Hydrogen Photoproduction by Non-Heterocystous Cyanobacterium Plectonema Boryanum", *International Journal of Hydrogen Energy*, **21(2)**:107–109, 1996.

Rebecca Christopfel was born and raised in Seattle, Washington. She earned a Bachelors degree in physics with minors in math and astronomy from Western Washington University. During her undergraduate career, she participated in a SULI internship at Stanford Linear Accelerator Center during the summer of 2007. She hopes to enter a PhD program in physics. Her interests include cooking, playing team sports and music.

Apurva Mehta is a staff scientist at SLAC. He received is Ph.D from Lehigh University, in 1990, on investigating point defects in LiNbO3 and its effect on electronic and optical properties. His current research is focused on using high brightness x-rays beams to probe materials at the interatomic level. Current projects include, understanding micromechanical deformation in nanocrystalline metals and biomaterials, corrosion of medical devices /in vivo, /interaction of aqueous ions with graphitic surfaces and nanostructures, and use of x-ray scattering, spectroscopy and microscopy to better understand art and archaeological objects.

Characterizing Surface Layers in Nitinol using X-ray Photoelectron Spectroscopy

Rebecca Christopfel and Apurva Mehta

ABSTRACT

Nitinol is a shape memory alloy whose properties allow for large reversible deformations and a return to its original geometry. This nickel-titanium (NiTi) alloy has become a material used widely in the biomedical field as a stent to open up collapsed arteries. Both ambient and biological conditions cause surface oxidation in these devices which in turn change its biocompatibility. The thickness of oxidized layers can cause fractures in the material if too large and can allow for penetration if too thin. Depending on the type and abundance of the chemical species on or near the surface, highly toxic metal ions can leak into the body causing cell damage or even cell death. Thus, biocompatibility of such devices is crucial. By using highly surface sensitive x-ray photoelectron spectroscopy to probe the surface of these structures, it is possible to decipher both layer composition and layer thickness. Two samples, both of which were mechanically polished, were investigated. Of the two samples, one was then exposed to a phosphate buffered saline (PBS) solution to mimic the chemical properties of blood, while the other remained unexposed. Although both samples were found to have oxide layers of appropriate thickness (on the order of a few nm), it was found that the sample exposed to the saline solution had a slightly thicker oxide layer and more significantly, a phosphate layer very near the surface suggesting toxic metal components are well contained within the sample. These are considerable indications of a biocompatible device.

Introduction

The equiatomic nickel-titanium alloy (Nitinol) is an advanced material, increasingly used as a biomedical device [4]. It is critical that a foreign body implant is biocompatible. Understanding the nature of the surface oxide layers on these devices helps determine the biocompatibility and, consequently, the usability of such materials. Biocompatibility is "the ability of a material to perform with an appropriate host response in a specific application" [1]. A device under investigation is tested both *in vitro* and *in vivo* to examine the degree of toxicity of the devices to cells of the material. Materials that are not biocompatible induce many complications in the body. Specifically, corrosion of metals can create toxic metal ions inducing cell damage [2]. In the case of Nitinol, nickel and nickel compounds are the components that are at the center of toxicity concerns.

In this experiment the NiTi alloy tested is used to manufacture stents to open collapsed arteries. Several different alloys whose production processes vary are being tested to better understand the surface oxidation that occurs and what affects such oxidation can have when implanted.

By probing the surface of these metallic structures it is possible to determine the composition and layer formation of the samples under investigation. The comparison of titanium vs. titanium oxide and nickel vs. nickel oxide can be used to determine abundance and location of species within a sample. The technique used is x-ray photoelectron spectroscopy (XPS), a highly surface sensitive, non-destructive method which involves irradiating a material with x-rays while measuring the kinetic energy and number of emitted photoelectrons. The binding energy of the core electron is then determined as the difference between the incident x-ray energy and the kinetic energy of the photoelectron. Analyzing the position and intensity of spectrum allows determination of the amount of different chemical species in the material. Escape depth of electrons from a material is very small: ~1–2 nm and is strongly dependent on the kinetic energy, therefore by varying the energy of the incident photon (and thus the kinetic energy) and/or changing the angle of incidence, it is possible to determine the location of the identified species as a function of depth from the surface. This technique is used to understand the character of the oxidation/corrosion layer on NiTi when exposed to different chemical environments including a liquid that mimics the chemical properties of blood. This technique

is also unique in its tunability of incident x-ray beams, allowing for a specific range of energies to be examined. Moreover, by changing the sample/detector orientation it is possible to identify depths of species within a sample. Compared to other surface analysis techniques that offer structural information about a sample, XPS allows for a determination of the atomic compositions of a sample or the chemical state of a certain element, as well as a comparative depth analysis.

MATERIALS AND METHODS

The samples of interest in this experiment include two different Nitinol substrates. Nitinol is a shape memory alloy (SMA). If it undergoes some deformation from its original crystalline structure, it has the ability to regain its original geometry when heated or cooled. The property that enables such processes is the superelasticity of a material, the amount of strain a material can handle before the atomic structure is permanently altered.

Both samples were mechanically polished, a process that strips away surface materials. This was followed by cleaning with acetone and then distilled water in an ultrasonically agitated bath to ensure a clean, uncontaminated surface [3]. One of the samples was then soaked in a simulated biological fluid known as phosphate-buffered saline (PBS) that consists of 0.154 M NaCl, 0.0003 M Na_2HPO_4 and 0.004 M KH_2PO_4 (pH 7.4), and PBS with an addition of 0.0013 M $CaCl_2$ [4]. This solution acts as a liquid that mimics the chemical properties of blood, enabling a determination of the biocompatibility of such devices. The other sample has not exposed to the saline solution.

Measurements were carried out at beam line 5-1 at Stanford Synchrotron Radiation Laboratory (SSRL), a station designed to carry out the specific needs of XPS. The end-station is equipped with two interconnecting ultra high vacuum chambers with operation pressure in the low 10^{-11} Torr range. One chamber is dedicated to surface preparation and contains an ion gun for ample sputtering, mass spectrometer for residual gas analysis and thermal desorption spectroscopy (TDS), pulsed gas dosing system and low-energy electron diffraction (LEED) optics. The other chamber, dedicated to core level spectroscopy, houses a hemispherical SES-100 electron analyzer (VG-Scienta) and a multi-channel plate partial electron yield detector as well as a collimated beam gas-doser regulated by the backing pressure at the backside of an array of multi-channel plates.

The sample rod allows the mounting of several different samples at the same time, each having a grazing incident angle of the photon beam to the sample of about 5° or less. The sample rod can be rotated around the photon beam axis allowing for variation of the escape angle of the electron and therefore variation of escape depth. The manipulator onto which the sample rod is attached is equipped with computer controlled stepper motors for easy alignment in the spectroscopy chamber and transport between the two chambers [4].

Samples were irradiated with x-rays at a known energy of approximately 1,080 eV. For the Nitinol samples under investigation, this incident energy is sufficient to excite different core electrons of interest, that is, titanium, nickel, oxygen and phosphorus. The

detector and sample orientation were varied to provide information about the structure and chemistry of the sample, namely species identification and depth of the various surface elements. The rod and affixed sample were rotated such that the detector was at 0, 18, 48, 60 and 70 degrees from the surface normal of the sample.

An overview scan was taken at the beginning of each of the detector/sample orientations to ensure an appropriate scan range of the different species. Knowing the binding energies of a particular elemental core electron and thus their specific kinetic energies, a spectrum was then obtained to show peaks in a particular range. The Ni3p electron has binding energies of 68 and 66.2 eV due to spin-orbit splitting, while the Ti3s electron has a binding energy of 58.7 eV and thus showed peaks in the kinetic energy range of approximately 1,015 eV and 1,025 eV, respectively. See Figure 2. Each species and associated core electrons were subject to smaller range scans such that each peak with a specific energy was well defined. This was done at each of the five detector/sample orientations in six different energy ranges. Depending on the resolution of the spectrum, each energy range was swept by the x-ray beam for a certain number of frames, whereby the length of the sample is scanned by the beam, and the intensity of each spectra are summed. Final intensities and corresponding kinetic energies are recorded. See Figure 1. This was done separately to both the sample exposed to the saline solution and the sample left unexposed.
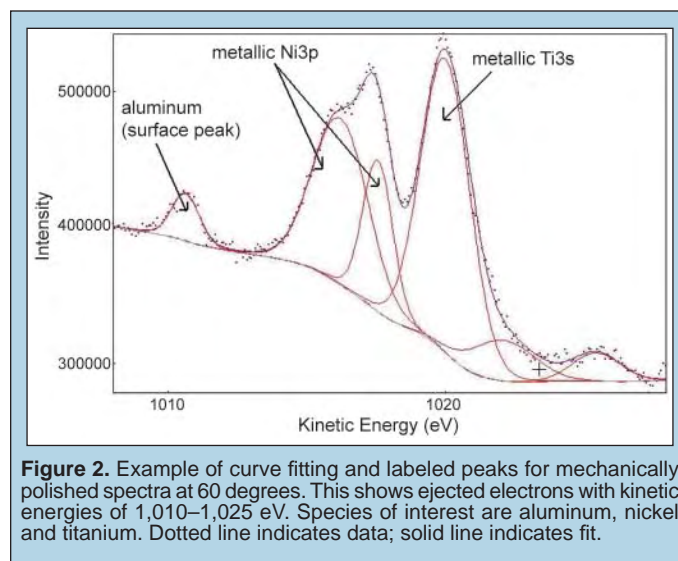
Figure 2. Example of curve fitting and labeled peaks for mechanically polished spectra at 60 degrees. This shows ejected electrons with kinetic energies of 1,010–1,025 eV. Species of interest are aluminum, nickel and titanium. Dotted line indicates data; solid line indicates fit.

To come up with a physical model of the speciation and location of said species that exist on the surface of Nitinol, a theoretical model is first called upon. To excite core electrons, sufficient incident energy is required. The intensity of photoelectrons collected by the detector then becomes a function of this incident photon flux, and the combination of parameters associated with the irradiated material as well as the detector position and geometry. Thus, an equation for number of counts from a given signal, S, for a given layer of finite thickness is given by an adapted equation for measuring counts in a given spectra [8].

$$S(\alpha,\beta) = I_\circ [e^{-\frac{\mu d}{\cos\beta}}(\frac{h}{\cos\beta})Df\,]e^{-\frac{d}{\lambda\cos\alpha}}\,Gt \qquad (1)$$
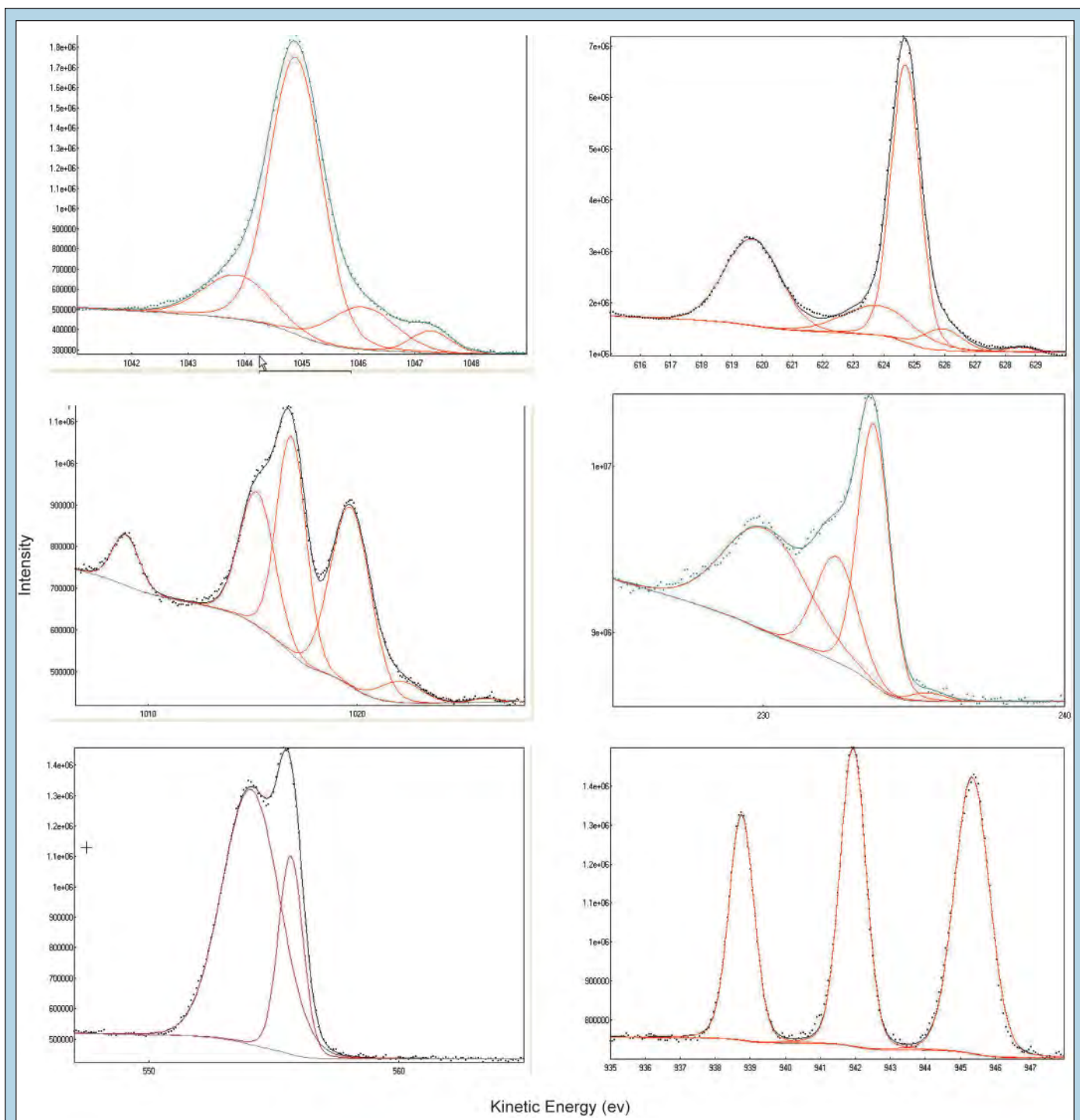
Figure 1. Spectra and fitted peaks for the six small range energy scans. These energy ranges include core electrons of interest: Ti3p, Ti2p, Ni3p, Ni2p, O1s and P2p from left to right, top to bottom. Dotted lines indicate data; solid lines indicate fits.

Where α = angle of detector with respect to surface normal of sample (in degrees), β = angle of incident x-ray (in degrees), $I_\circ$ = intensity (W · m^{-2}), μ_x = property of incident x-ray traveling through material which depends on energy of photon and material (m^{-1}), d = depth (m), h = width of area probed by x-ray (m), D = concentration of species, f = rate at which electrons are ejected from sample (cross section), λ = function of material that depends on KE of electron and material in which it propagates (m), G = detector geometry and t = time (s).

Under some constraints and by making some assumptions [6], a signal to signal ratio of peaks whose energies are very close allows for elimination of many of the unknowns and can provide a qualitative model of the structure by locating surface and near surface layers with respect to one another.

$$\frac{S^1}{S^2} = Ce^{-\frac{1}{\lambda \cos\alpha}(d_1-d_2)} \tag{2}$$

where C is a collection of constants and parameters whose values do not depend on detector angle α while d_1 and d_2 are depths of a certain species from the surface of the sample. By taking the natural log of Eq. (2) we get a linear relationship where the natural log of the signal ratio is inversely related to $\cos\alpha$.

$$\ln\left(\frac{S^1}{S^2}\right) = \ln(C) - \frac{1}{\cos\alpha}\left(\frac{d_1-d_2}{\lambda}\right) \tag{3}$$

The line has a y-intercept equal to $\ln(C)$ and a slope equal to $-\left(\frac{d_1-d_2}{\lambda}\right)$. Thus, when the natural log of the signal ratio is plotted against $\frac{1}{\cos\alpha}$, the length d_1-d_2 can be calculated and the distance between two different species in a sample is estimated. The value for λ, the inelastic mean free path of electrons in a sample, is known and assumed to be the same for species whose energies are very close.

Results and Discussion

Once plotted, information regarding depth and abundance of species was determined. A large positive slope implies that the depth of species relative to the surface species is very deep, while a small positive slope implies a species closer to the reference species, but still below it. A negative slope implies a species above the reference. If we pick a reference species, say alumina, which we assume is remnant from the mechanical polishing and therefore very near the surface and determine the depth of the other layers with respect to that, we can get a reasonable picture of the composition of surface layers.

Theory tells us that purely metallic peaks occur at lower binding energies and will therefore have higher kinetic energies. Oxidized peaks, whose valence electrons are paired with an oxygen molecule, have more tightly bound core electrons and thus a higher binding energy. The signals used to come up with the relevant signal-to-signal ratio are the areas under the fitted curves of the plotted spectrum. The peaks were fit with a series of curves which had a small and fixed amount of Lorentzian component and a large variable Gaussian component. The widths, energies and areas under the various peaks in the specific energy range of the P2p electron are listed in Table 1 and show the data acquired at various angles. Data shows multiple peaks for a given core level and therefore imply surface layers contain species with various oxidation levels, including the stable oxidation states of titanium oxide, TiO_2 and nickel oxide, NiO, as well as partially oxidized nickel peaks. The number of peaks becomes evident in the fitting process; however the identification of all peaks has not been possible. Further investigation and an alternative experimental approach is needed for completion. To come up with helpful information regarding the structure of these two samples, specific signal to signal ratios were taken, metallic peak to a sum of the oxidized peaks — or more generally, a reference peak to a series of other peaks, at multiple angles. See Figure 2 for an example of a spectrum and labeled peaks. Lines are fit to the data points and structural information about the composition of the mechanically polished sample and the mechanically polished sample exposed to the PBS solution is revealed. Comparisons between samples can then be made.

Phosphorus (P2p)–MPPBS	Peak 1	Peak 2	Peak 3
Angle			
		AREA	
0 deg	5.46E+05	7.48E+05	9.16E+05
18 deg	5.79E+05	7.79E+05	9.79E+05
48 deg	3.33E+05	4.48E+05	6.88E+05
60 deg	2.01E+05	2.73E+05	5.18E+05
70 deg	91258	1.28E+05	3.48E+05
		ENERGY	
0 deg	938.7615	941.9441	945.3409
18 deg	938.8604	942.0377	945.4329
48 deg	938.8463	942.03	945.4292
60 deg	938.765	941.9416	945.3619
70 deg	938.753	941.9194	945.3792
		GAUSS	
0 deg	0.7627	0.7926	1.092
18 deg	0.7777	0.7951	1.087
48 deg	0.7661	0.7834	1.09
60 deg	0.7554	0.7894	1.064
70 deg	0.7637	0.7843	1.075

Table 1. Sample of data collected from P2p electron energy range for the sample exposed to the PBS solution, including area under various peaks, energy, and Gaussian width.

By analyzing the slopes of these lines from a series of different spectra it is possible to formulate a layer-by-layer model of each of the samples without necessarily knowing the composition of each layer or the arrangement of the constituents between layers. Regardless, an understanding of the configuration of oxide layers can help determine the biocompatibility of these devices. The plot of $\ln\left(\frac{S^1}{S^2}\right)$ vs. $\frac{1}{\cos\alpha}$ yields lines whose slopes are indicative of depth from surface or separation distance from that of another species. In Figures 3 and 4, linear fits and R^2 values are shown from both the
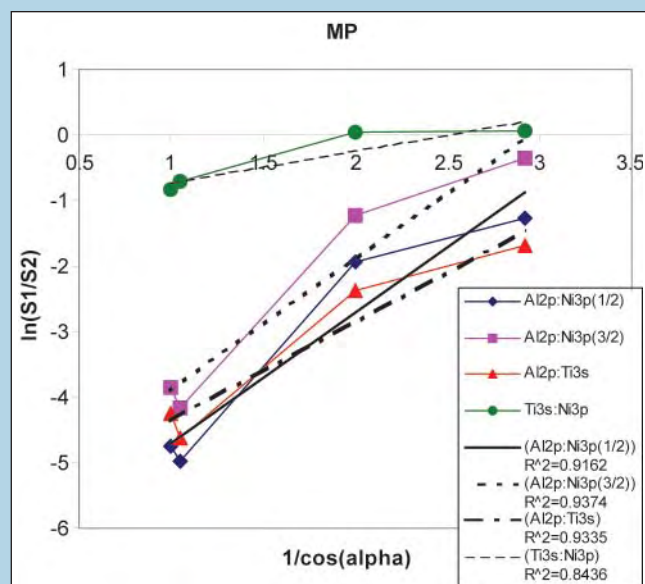
Figure 3. Plots, best fit lines and R^2 values for the mechanically polished sample. Signal to signal ratios were taken of the spectrum whose energy range spans electrons ejected with kinetic energies of 1,010–1,025 eV as detector/sample orientation was rotated through a series of angles.

mechanically polished sample and the mechanically polished sample exposed to solution over several angles in a particular energy range. The results from these plots (as well as all others not shown) are presented in Table 2. Using the surface aluminum signal and that of the metallic nickel signal(s), a surface to substrate depth can be calculated. Since the slopes of these lines are positive, it is clear that the nickel lies beneath the aluminum. See Table 2. Similar depth analyses were done between all relevant signals to build a layer-by-layer model. See Figure 6.

The mechanically polished (MP) sample appears to have a thicker oxide layer than that of the mechanically polished sample exposed to the PBS solution (MPPBS). However, the different forms of nickel oxides are further from the bulk material suggesting they are closer to the surface in the unexposed mechanically polished sample. The mechanically polished sample and the mechanically polished sample in PBS solution have an approximate 5 nm surface-to-substrate thickness. This was determined by comparing the surface aluminum signal to that of metallic titanium whose depth is associated with that of the Nitinol substrate. In both samples, the majority of the 5 nm thickness was titanium oxide, with some metallic nickel and nickel oxide very near the base of this titanium oxide. In addition, the PBS exposed sample included a thin layer of oxidized phosphorus near the surface.
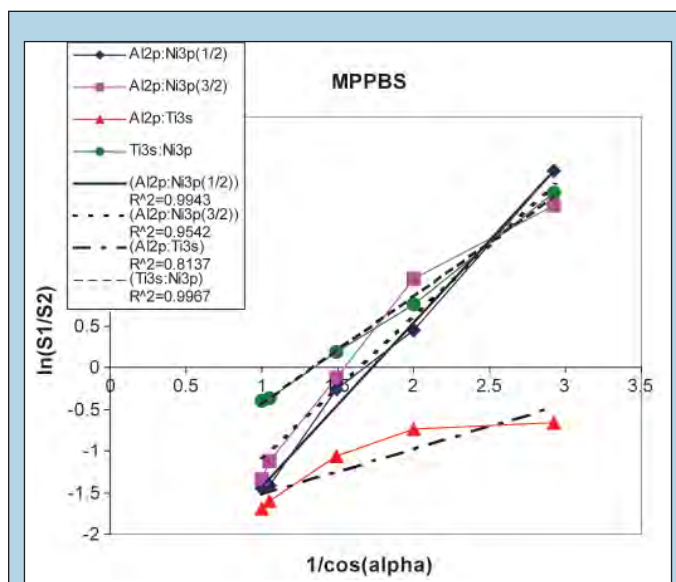
Figure 4. Plots, best fit lines and R^2 values for the mechanically polished sample exposed to the PBS solution. Signal to signal ratios were taken of the spectrum whose energy range spans electrons ejected with kinetic energies of 1,010–1,025 eV as detector/sample orientation was rotated through a series of angles.

	MP	MPPBS	KE (avg.)	Lambda (nm)	Thickness (MP)	Thickness (MPPBS)
Ni3p						
Al2p:Ni3p(1/2)	1.9943	1.9701	1020	2	3.9886	3.9402
Al2p:Ni3p(3/2)	2.0072	1.7247	1020	2	4.0144	3.4494
Al2p:Ti3s	1.5122	0.5418	1020	2	3.0244	1.0836
Ti3s:Ni3p	0.4856	1.2927	1020	2	0.9712	2.5854
Ni2p						
metallic:partially	-0.6162	4.3377	233	0.8	-0.49296	3.47016
metallic:oxidized	-0.4214	-2.4838	233	0.8	-0.33712	-1.98704
partially:oxidized	0.1949	-6.8217	233	0.8	0.15592	-5.45736
Ti3p						
metallic:oxide	-0.6549	-1.8966	1047	2	-1.3098	-3.7932
Ti2p					0	
metallic:oxide	-0.1296	-0.5714	626	1.4	-0.18144	-0.79996
O1s						
oxide:hydroxide	0.5425	1.0021	555	1.2	0.651	1.20252
P2p						
p2:p0		0.431	950	1.8		0.7758
p2:p1		0.415	950	1.8		0.747
p1:p0		0.016	950	1.8		0.0288
TiO:p2		-0.549		1.9		-1.0431

Table 2. Column 1 (far left) describes which signal-to-signal ratio that was taken. Columns 2 and 3 give the slope of the best-fit line. Lambda is the inelastic mean free path of the electron. The product of the slope and lambda yields thickness separation between said species in nanometers. MP is the sample mechanically polished while MPPBS is the sample mechanically polished and exposed to the PBS solution. Note the MP sample (without solution) shows no phosphorus. Positive slope implies the species foremost in the ratio given in Column 1 lies above. A negative slope implies the species foremost in the ratio given in Column 1 lies below.
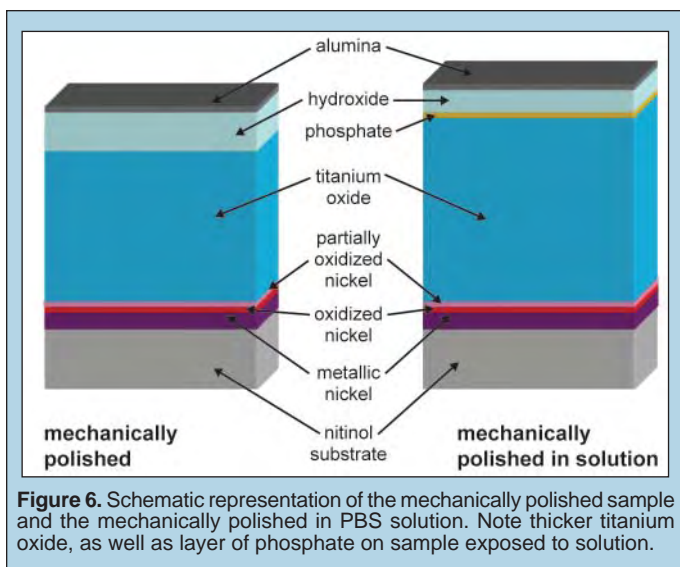
Figure 6. Schematic representation of the mechanically polished sample and the mechanically polished in PBS solution. Note thicker titanium oxide, as well as layer of phosphate on sample exposed to solution.

Conclusion

From quantitative analysis, the data shows oxidation layers of sufficient thickness to prevent harmful nickel ions from leaking into the body. However the sample that was treated with the PBS solution appeared to have a slightly thicker titanium oxide layer and also included phosphorus and phosphate layers near the surface, but below the alumina. An exciting conclusion from this analysis is the fact that the phosphorus lies above the oxide very near the surface. This implies that the potentially harmful nickel and nickel-oxide ions are well contained within the sample exposed to the PBS solution. Moreover, the sample left unexposed experienced less oxidation suggesting that merely by placing such a device in the body allows for slightly thicker oxide layers, leaving the harmful components impenetrable by the phosphate layer. Thus, when exposed to bodily fluids, Nitinol devices improve their biocompatibility.

References

[1] Ratner, Buddy D., et al. *Biomaterials Science: An Introduction to Materials in Medicine.* Academic Press: San Diego, 1996.

[2] Lim, Issel A., *Biocompatibility of Stent Materials.* MURJ. 11, 34 (2004).

[3] Private Communication with Valeska Schroeder.

[4] V. Schroeder, A. Mehta, A. R. Pelton, and P. Pianetta. *An Investigation of the Passive Film on Nitinol in Simulated Biological Fluids.*

[5] Anderson, K. *"Structure, Bonding and Chemistry of Water and Hydroxyl on Transition Metal Surfaces,"* PhD Thesis, Stockholm University, Sweden, 2006.

[6] Assumptions made include: keeping incident photon beam at a fixed angle; peaks are very close together in energy such that the elastic mean free path for each species in a given spectra is the same; layers are very thin and homogeneous.

[7] S. Geng, S. Zhang, and H. Onishi. *XPS Applications in Thin Films Research.*

[8] A. I. Martin-Concepci, F. Yubero, J. P. Espinos, J. Garcia-Lopez and S. Tougaard. *Determination of amount of substance for nanometrethin deposits: consistency between XPS, RBS and XRF quantification.*

Robert Citron was born in Silver Spring, MD and grew up in Overland Park, KS. He attended the University of Chicago, majoring in physics and math. As an undergraduate, he completed a SULI internship with the DOE and another internship with NASA. He plans to attend graduate school and study planetary science. His interests include science fiction, mountain biking, and Krav Maga.

Jeremy Kropf is a physicist in the Chemical Sciences and Engineering Division at Argonne National Laboratory. He received his Ph.D in Physics from the University of Notre Dame in 1997 for a study of interfacial structure in thin films and epitaxially-grown superlattices. His current research activities focus on applying X-ray absorption spectroscopy to energy-related challenges in the areas of catalysis, lithium-ion batteries, and the nuclear fuel cycle. He serves on the board of directors for the Materials Research Collaborative Access Team beamline at the Advanced Photon Source and the Beamline Advisory Team that is developing the plans for a new X-ray absorption spectroscopy facility at the proposed NSLS-II X-ray storage ring.

X-ray Absorption Spectroscopy of Yb³⁺-Doped Optical Fibers

Robert Citron and A. Jeremy Kropf

ABSTRACT

Optical fibers doped with Ytterbium-3+ have become increasingly common in fiber lasers and amplifiers. Yb-doped fibers provide the capability to produce high power and short pulses at specific wavelengths, resulting in highly effective gain media. However, little is known about the local structure, distribution, and chemical coordination of Yb^{3+} in the fibers. This information is necessary to improve the manufacturing process and optical qualities of the fibers. Five fibers doped with Yb^{3+} were studied using Extended X-ray Absorption Fine Structure (EXAFS) spectroscopy and X-ray Absorption Near Edge Spectroscopy (XANES), in addition to Yb^{3+} mapping. The Yb^{3+} distribution in each fiber core was mapped with 2D and 1D intensity scans, which measured X-ray fluorescence over the scan areas. Two of the five fibers examined showed highly irregular Yb^{3+} distributions in the core center. In four of the five fibers Yb^{3+} was detected outside of the given fiber core dimensions, suggesting possible Yb^{3+} diffusion from the core, manufacturing error, or both. X-ray absorption spectroscopy (XAS) analysis has so far proven inconclusive, but did show that the fibers had differing EXAFS spectra. The Yb^{3+} distribution mapping proved highly useful, but additional modeling and examination of fiber preforms must be conducted to improve XAS analysis, which has been shown to have great potential for the study of similar optical fibers.

Introduction

Rare earth (RE) doped optical fibers have rapidly been gaining attention for use in fiber lasers and amplifiers. Yb^{3+}-doped fibers are particularly effective because their higher doping levels result in higher output power and efficiency [1, 2]. But, despite their advantages, Yb-doped fibers are still prone to problems. Clustering is a problem when higher concentrations of REs are present [3–5] and can lead to concentration quenching [6] and reduction in radiative transitions [7]. Higher Yb^{3+} concentration can also reduce gain by means of cooperative upconversion [1].

Many of the problems associated with Yb-doped fibers result from the manufacturing process, which determines the local structure of Yb^{3+} in the fibers. Determining and understanding the local structure of Yb^{3+} in the fibers is critical to finding ways to improve fiber manufacturing and increasing the optical qualities of the fibers.

The aim of this experiment was to examine the distribution and local structure of Yb^{3+} in fibers using Extended X-ray Absorption Fine Structure spectroscopy (EXAFS), X-ray Absorption Near Edge Spectroscopy (XANES), and Yb^{3+} concentration mapping. The distribution of Yb^{3+} should display radial symmetry; any asymmetrical behavior, diffusion into the cladding, or a concentration depression towards the center of the core could have detrimental effects on the efficiency of the fibers [8].

Prior studies of RE doped fibers examined the fiber glass preforms or the fibers themselves. Some used instruments such as the ion microprobe [9] or Raman confocal microscope [8]. Previous studies also included EXAFS [3, 6, 10–12] and XANES [4, 13, 14], but most investigated other REs such as erbium. Some X-ray Absorption Spectroscopy (XAS) studies have investigated the Yb^{3+} local structure in glass [5], but, to the best of our knowledge, this is the first EXAFS and XANES measurement of Yb^{3+} in fibers.

Materials And Methods

X-ray Fluorescence Mapping

X-ray fluorescence mapping is a useful tool for finding the distribution of elements, such as Yb, in materials. Incident x-rays are set to an energy equal to, or slightly above, the absorption edge of the targeted element. At this energy, there will be a sharp rise in

absorption. Excited electrons will move to higher energy levels and quickly decay, releasing photoelectrons and fluorescence photons [15]. An x-ray fluorescence detector will measure higher or lower count rates depending on the concentration of the targeted element at each point in the mapped region. By focusing the beam to a small area (<9 μm^2) and moving the beam in a grid pattern or a simple line scan, the x-ray fluorescence at each point can be measured. This will display the distribution and concentration of the targeted element in the sample. In this experiment, line and grid scans were taken of Yb^{3+} X-ray fluorescence from the core of the fibers. The germanium distribution was also mapped in one fiber.

XAS

X-ray Absorption Spectroscopy (XAS) is well-suited for determining the local structure and chemical coordination of Yb^{3+} ions in optical fibers. XAS can be divided into two main categories: Extended X-ray Absorption Fine-Structure (EXAFS) and X-ray Absorption Near Edge Spectroscopy (XANES). EXAFS is suitable for determining the distance, coordination number, and the neighboring species of the Yb^{3+} ion. XANES is useful for detecting the coordination chemistry, bond structure, molecular orbitals, and multiple scattering from the Yb^{3+} ions.

The Advanced Photon Source synchrotron facility at Argonne National Laboratory produces a steady X-ray source well suited for XAS experiments. The experiment was conducted at Sector 10-ID, MR-CAT.

Sample Preparation

Five optical fibers provided by Southampton Photonics were examined. The fibers had varying core diameters and Yb^{3+} concentrations (Table 1). Before being examined with XAS, the fibers were cut into thin cross-sections suitable for X-ray measurements.

Fiber Number	Fiber ID	Core Diameter (µm)	Cladding Diameter (µm)	Yb^{3+} Concentration (ppm)
1	T0084 L30058	43	670	4500
2	P004 F01	12	125	5500
3	T0075 P120	30	400	13000
4*	F125 FI24	30	375	6500
5**	T0072 ROD2	25	290	20000

*Contains a central dip.
**Inter cladding contains GeO_2

Table 1

The x-rays will penetrate through <100 µm of the fiber samples, but, in order to obtain improved results, the fibers had to be cut to a thickness of significantly less than 100 µm. The ideal thickness would be less than 20 µm. The faces of the fiber were polished to reduce surface disturbance and further improve the results.

Each sample was first embedded in an epoxy made from Buehler Epoxicure/Epoxide resin and hardener. This created a cylindrical stub with the fiber along the vertical axis (Figure 1a). The top of the stub was then cut with a low speed diamond saw to create a flat surface for polishing. The top face was then polished using 320 and 600 grit paper and ending with a 15 µm diamond polish which leaves grooves <2 µm deep.
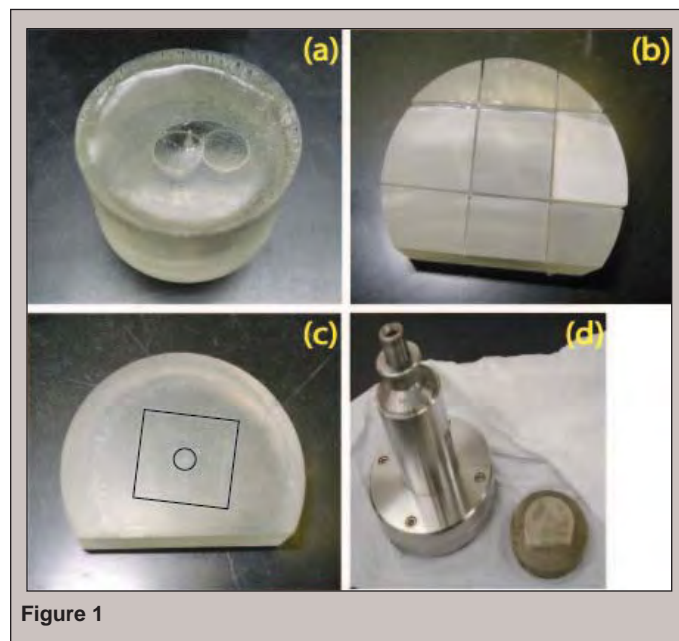
Figure 1

After polishing the top face, a thin square about 1 cm^2 and less than 1 mm in thickness was cut from the polished face of the stub (Figure 1b). The thickness of the square was precisely measured before it was re-embedded in epoxy. It was re-embedded so that its unpolished side was facing down, at the very bottom of the sample holder (Figure 1c). After the epoxy hardened, the sample was again cut so that it could fit in a polishing mount to be precisely polished/re-polished (Figure 1d). The goal was to orient the precisely measured square section at the bottom of the new epoxy stub so that it could be precisely ground. For example, if the square section had an average thickness of .8 mm, the goal would be to remove .700–.780 mm of material so that a very thin fiber section could be examined with XAS.

The sample was fixed to a polishing fixture that could be used to remove a specific amount of material. A small amount of epoxy seeped under the sample during preparation, so first the sample was polished until the epoxy that seeped under the square section was removed (i.e. when the bubbles that formed under the square section disappeared). This position was noted as the zero position and the thickness of the stub was measured with a micrometer. Since the exact thickness of the square section containing the fiber was measured before re-embedding, it was possible to measure the thickness of the embedded fiber sample during polishing by measuring the amount of material removed using a micrometer. In this manner the sample could be polished to a thickness of 50–100 µm (20 µm proved too risky) using 400, 800, and 1200 grit paper with a final polish using 15 µm diamond. It was noted that coarser paper caused too much damage to the fiber.

Fibers 1–3 were prepared in this manner. Fiber 4 ripped out during polishing when it became too thin and there was insufficient time to prepare samples 5–7 in this manner. The initial epoxy-embedded stubs of fibers 4 and 5 were cut and polished so they could be examined using XAFS, even though they were not thin sections.

XAS and X-ray mapping setup

The fibers were examined using x-ray fluorescence. They were placed so that the incident X-rays were parallel to the fiber axis. A germanium detector (Canberra Industries, Ultra-LEGe 19 element array) was used in the configuration seen in Figure 2. The beam energy was set to 11.500 KeV to excite both Yb^{3+} and Ge atoms as well as to allow for Yb L3 absorption edge measurements. The X-ray beam was focused to 3 μm² using total external reflection mirrors in the Kirkpatrick-Baez geometry, which allowed for high resolution intensity scans of the fiber core.

Figure 2
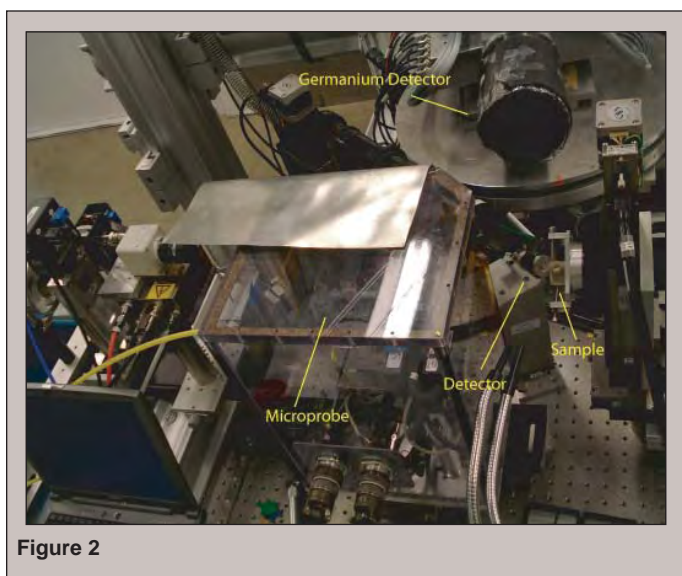
After locating each fiber, a 2D intensity grid scan was taken of the core to measure the ytterbium concentration in the core. Line scans were then taken on the orthogonal axes through the center of the core. After noting the distribution from the 2D map, 1–4 locations were selected for EXAFS and XANES scans. Due to time constraints, some samples were scanned only once, while others were given multiple scans at different locations. The locations were chosen so they best reflected the entire fiber core. Scans were taken at sites of high and low Yb^{3+} concentration for comparison.

Results and Discussion

Ytterbium Distribution

Figure 3 displays contour plots from the 2D intensity scans of each fiber. The scans show that the Yb^{3+} distribution in the cores of the fibers is not uniform. The Yb^{3+} distribution concentrates at a peak and then spreads outward. Fibers 2 and 5 show fairly

symmetrical cores, with higher intensity peaks towards the center of the core. Fiber 4 also contains an almost symmetrical peak at the center of the core. Fibers 1 and 3, however, display crescent shaped Yb^{3+} distributions. After scanning Fiber 1, the fiber was rotated 180 degrees and rescanned to ensure that the crescent distribution was not a result of the experimental setup and geometry. The resulting scan displayed the same image as before, but rotated 180 degrees, confirming that the lopsided nature of the image is due to the Yb^{3+} distribution in the core. Fibers 1 and 3 both display similar crescent peaks that appear to be a result of manufacturing error. During manufacturing, fibers are drawn out at high temperature to form the thin fibers of the final product. This process is prone to error because it is difficult to maintain a circular cross-section, sometimes the cladding of the fiber will collapse into the fiber core. Such a collapse seems the most likely explanation for the irregular distributions observed in fibers 1 and 3.

The germanium distribution in the inner cladding of Fiber 5 is shown in Figure 3f. There is a narrow space between the core and the inner cladding where the Yb^{3+} and Ge concentrations both dip. This is emphasized in the overlay of the Yb^{3+} and Ge grid maps (Figure 5). The germanium distribution is slightly lopsided, but this does not seem to have affected the symmetrical Yb^{3+} distribution in the core.

Linescans taken through the center of each core along the X and Y axes better display the shape of the Yb^{3+} peaks (Figure 4). Yb^{3+} distributions with flat-topped peaks would be preferred and show the most uniform distribution of Yb^{3+} in the fiber core. Most peaks display a rounded point(s) at the top. Fiber 5 displays the flattest peak, which is also observed in the broad red area in the Fiber 5 contour plot. The linescans were used to accurately measure the width of the Yb^{3+} distribution in the fiber cores. Measurements were made at the turning point where the peak begins to meld into the background. Full-width half-maximum (FWHM) measurements were also made. Both were compared to the widths of the cores provided by the manufacturer (Table 2). With the exception of Fiber 4, the Yb^{3+} distribution peaks were wider than the fiber core diameters provided by the manufacturer. This implies that either the fiber cores were wider than the given dimensions or the Yb^{3+} ions diffused outside the fiber cores. The irregular pattern of the Yb^{3+} concentration towards the edge of the Yb^{3+} peak seen in the contour plots (Figure 3) suggest that the Yb^{3+} diffused from the core. The cores would not be expected to stretch into the irregular shapes seen in Figures 3a–e due to manufacturing error. However,

Fiber number	Given core width (μm)	Avg. Yb^{3+} width (μm)	Fwhm (μm)	Difference* (μm)	Yb^{3+} concentration (ppm)
1	43	57.0 ± 4	38.2 ± 0.9	14	4500
2	12	29.0 ± 3	12.9 ± 0.3	17	5500
3	30	76.5 ± 4	52.7 ± 0.9	46.5	13000
4	30	25.5 ± 5	15.1 ± 0.3	-4.5	6500
5	25	34.5 ± 4	25.1 ± 0.2	9.5	20000

*Difference between the experimental Yb^{3+} peak width and the fiber core diameter (from Table 1).

Table 2

inaccuracies in the manufacturing process mean that the cores could differ from the provided dimensions. The distributions could result from manufacturing error, diffusion (the difference between the experimental and given core widths), or both. Further studies should include refractive index measurements to see the exact dimensions of the core and to see how the core mixes with the cladding.

No real correlation between Yb^{3+} concentration and possible diffusion was found. The full-width half-maxima also display no
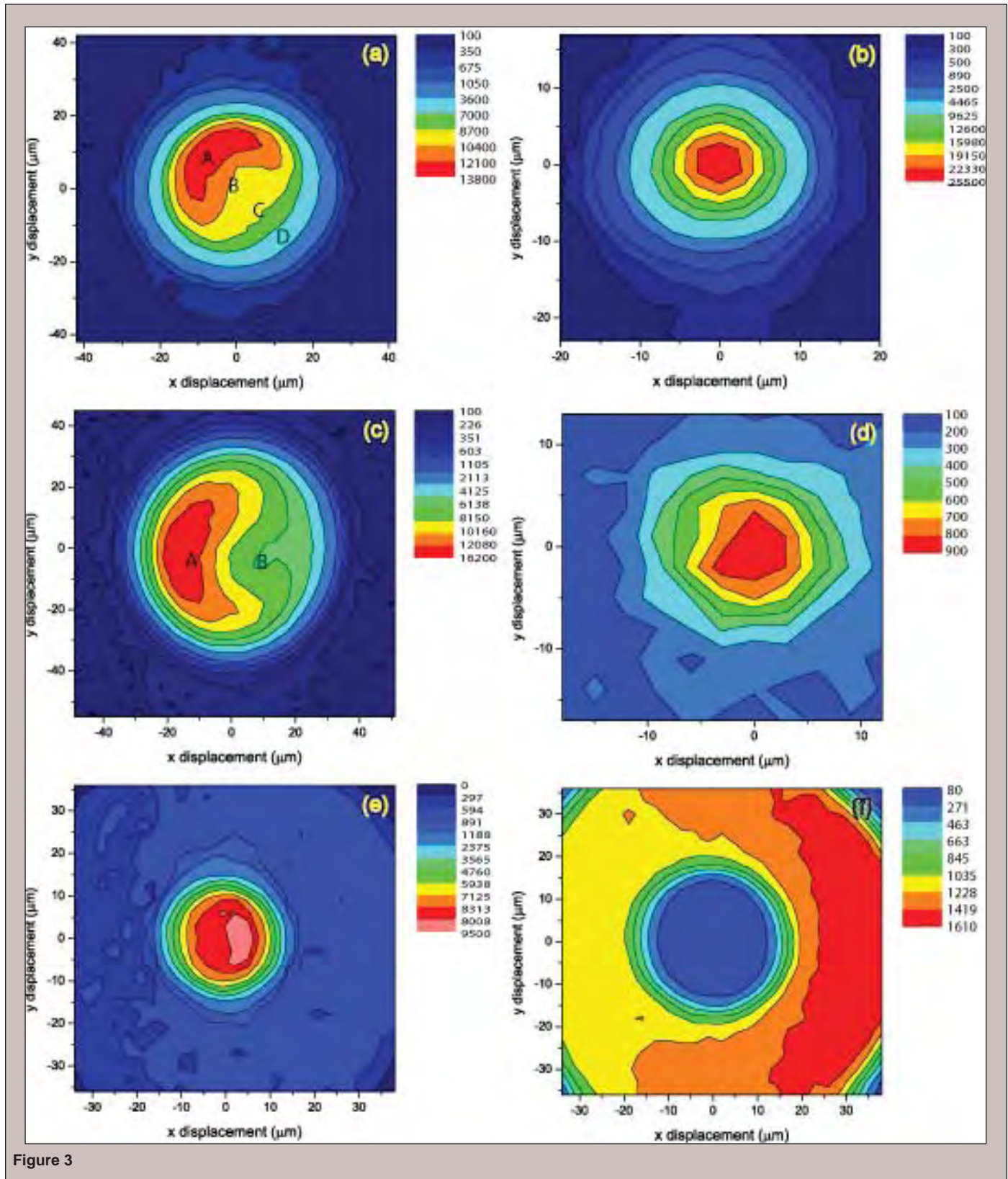
Figure 3

clear relation to the Yb^{3+} concentrations or given core widths. Fibers 1–3 display an almost linear relation between Yb^{3+} concentration and possible diffusion, but Fibers 4 and 5 display no such correlation. This may be because of their unique properties (central dip and cladding Ge content, respectively).

EXAFS and XANES Interpretation

The EXAFS data was analyzed using standard methods with the IFEFFIT program suite. ATHENA was used for background subtraction and summing multiple data sets. ARTEMIS was used
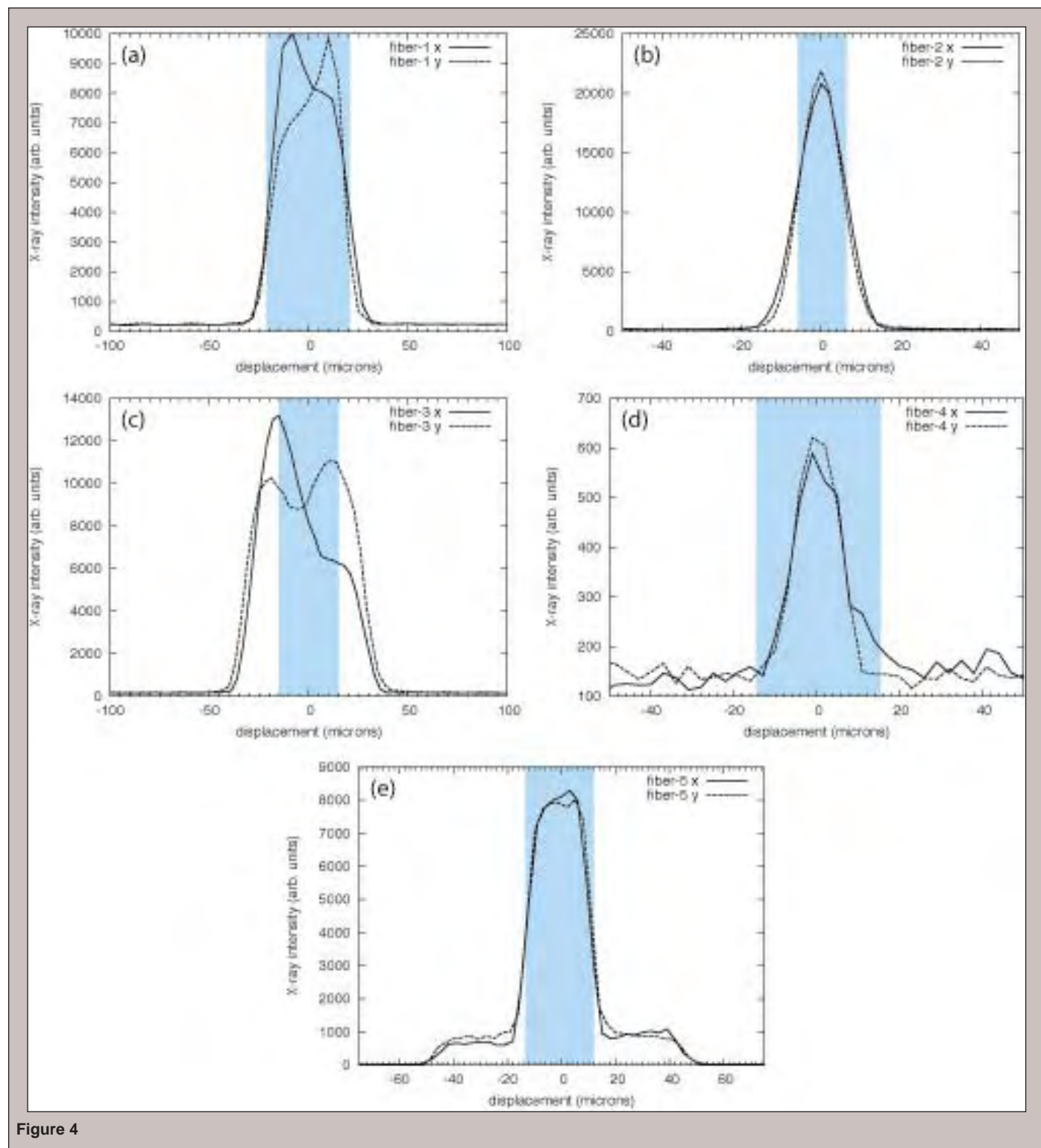
Figure 4
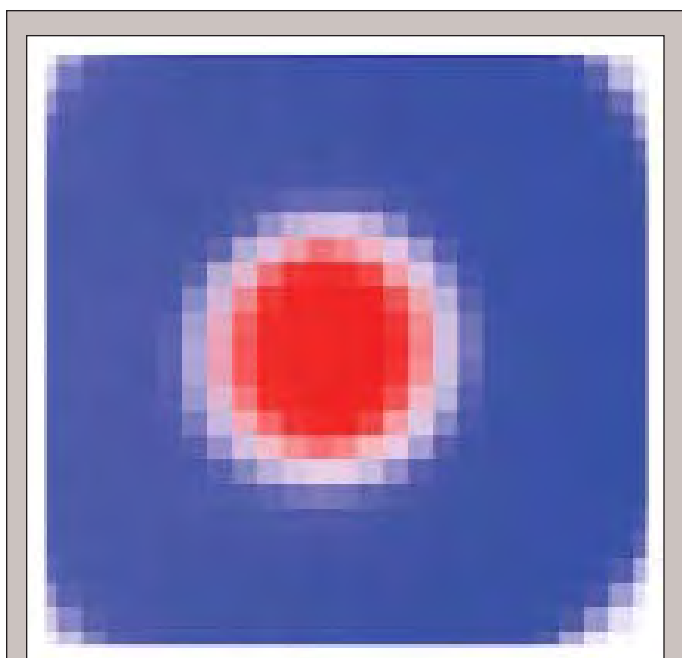
Figure 5

to fit the data using theoretical models made with FEFF. The basic EXAFS equation is:

$$\chi(k) = \sum_j \frac{N_j e^{-2k^2\sigma^2_j} e^{-2R_j/\lambda(k)} f_j(k)}{kR^2_j} \sin[2kR_j + \delta_j(k)]$$

where N_j is the number of neighboring atoms at a distance of R_j with a disorder in the neighboring distance of σ_j^2, and $f_j(k)$ and $\delta_j(k)$ represent neighboring atom and excited atom scattering properties [15].

Using plots of $\chi(k)$ and $\chi(R)$, the different EXAFS spectra between the different fibers (Figure 6) and between different locations in the same fiber (Figure 7) were compared. The data from Fibers 2 and 4 were too noisy, but fibers 1, 3, and 5 were comparable. Each of the fibers displays a modestly different EXAFS spectrum. The Fiber 5 spectrum appears to be a mix of the fiber 1 and 3 spectra, having an average amplitude between that of fiber 1 and 3.

The different locations in the cores of Fiber 1 and 3 (Figure 7) display very similar plots in k-space, though position C contains less noise and has a smaller amplitude. In R-space the spectra have more drastic differences. This could be caused by differences in Yb^{3+} concentrations within the fiber core. In Fiber 1, from position A to C the Yb^{3+} concentration decreased as seen in Figure 3. In Figure

Figure 6

U.S. Department of Energy Journal of Undergraduate Research
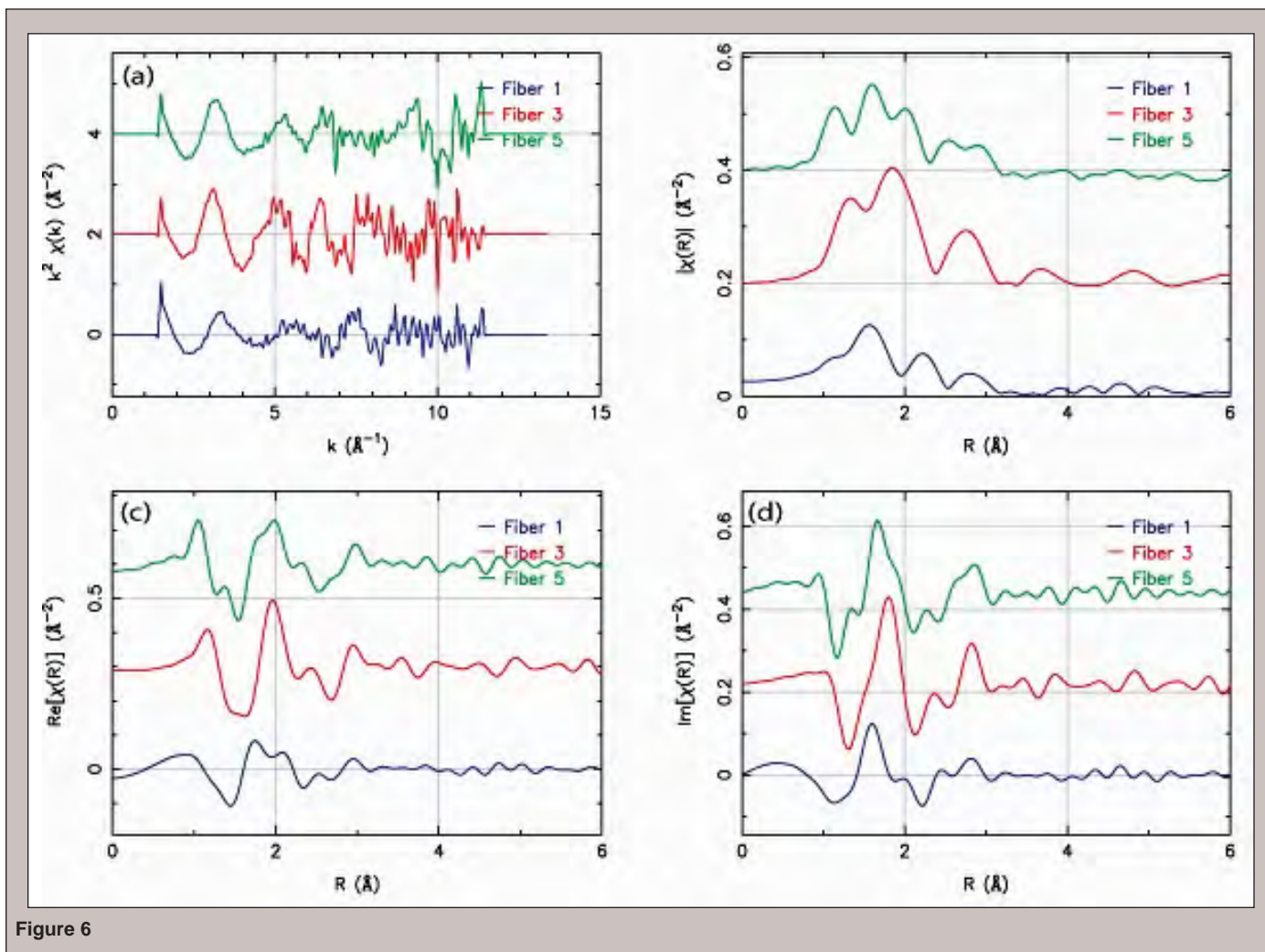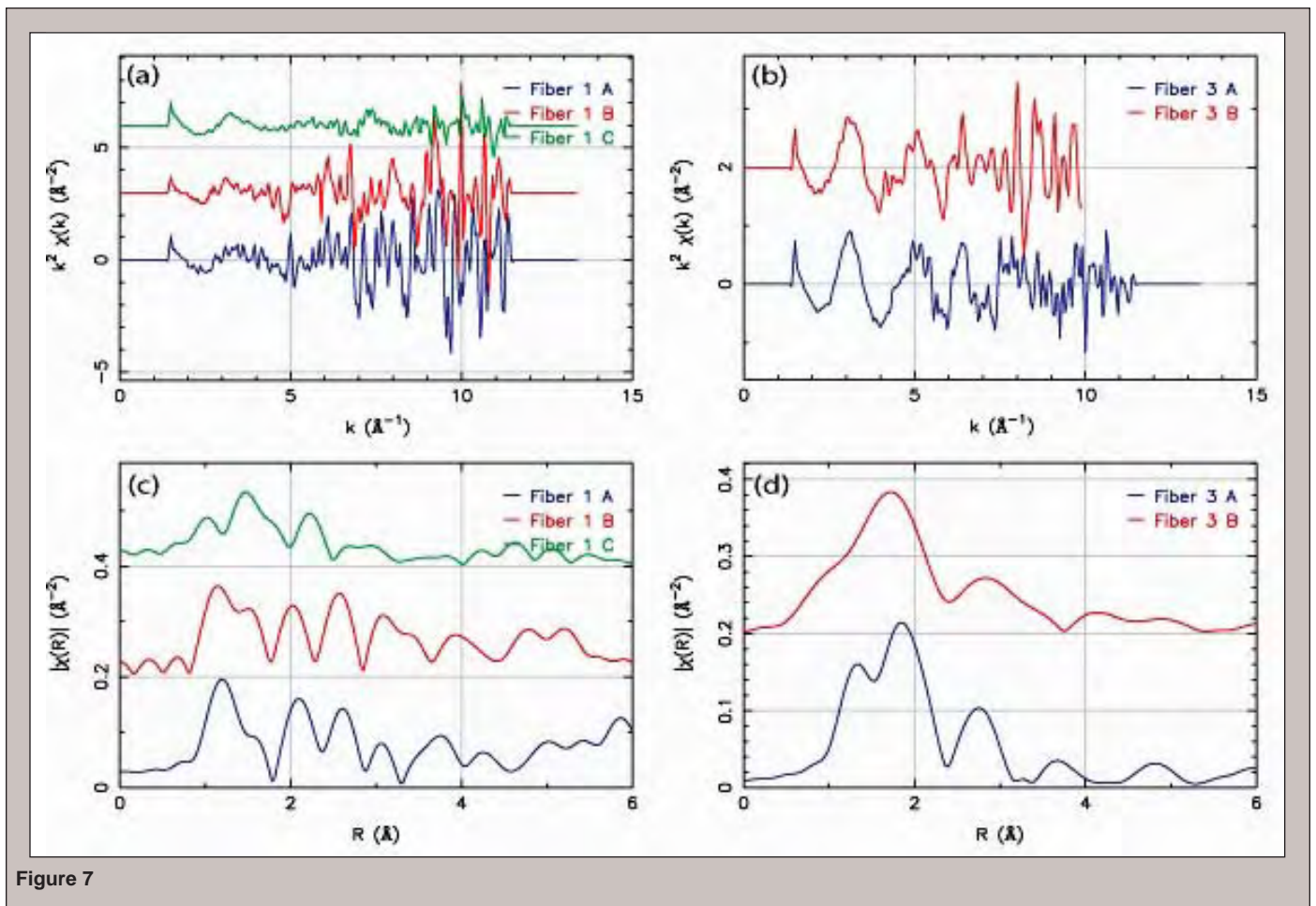
Figure 7

7c, from positions A to C, it appears that the larger first peak at 1.1 Å diminishes as the peak at 1.7 Å takes over. A similar effect is seen in Fiber 3 (Figure 7d).

Unfortunately, no conclusive fit was made to the measured EXAFS data. The data from Fiber 4 and Fiber 2 were too noisy. Fibers 1 and 5 had unexpectedly low initial amplitudes and the fits did not produce realistic results. This resulted from interference in spectra from different photoelectron scattering paths. If this persists, then the problem may not be solvable using EXAFS. However, Fiber 3 had a better initial amplitude and less peak interference. It produced unrealistic but improved results. Work is still being conducted to refine the fitting process and to produce interpretable results.

Figure 8 displays the XANES spectra for Fibers 1, 3 and 5, and for separate locations within the core of Fiber 1 and 3. Each fiber displays a unique spectrum, which is important information
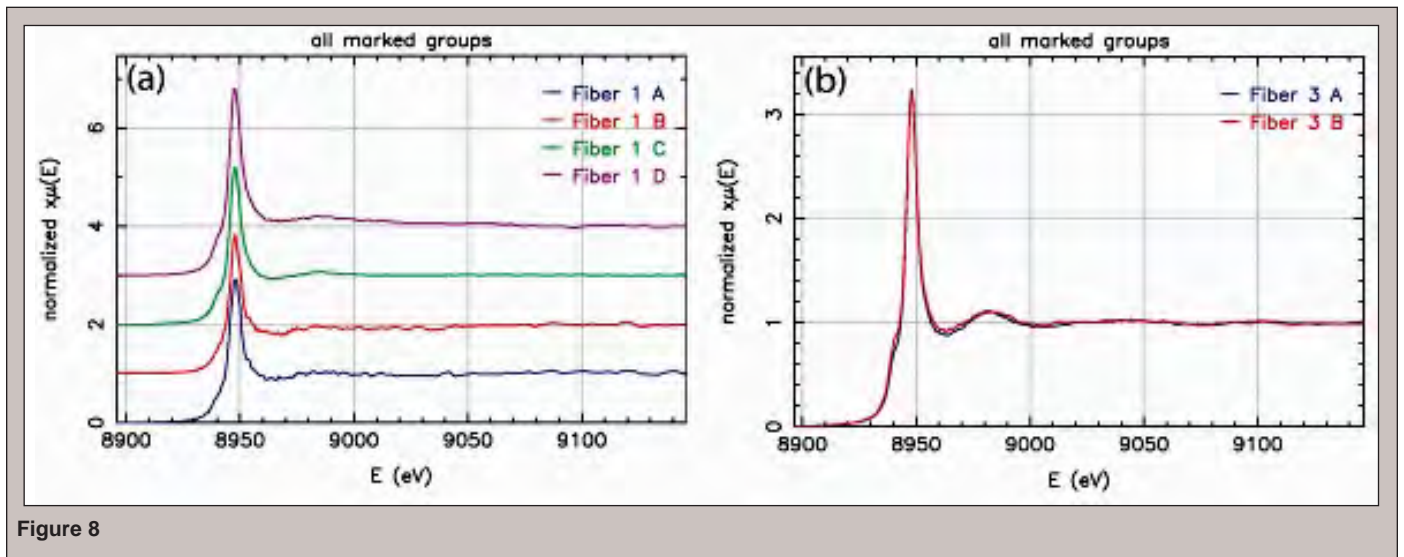
Figure 8

itself, showing that the differences in Yb^{3+} concentration and fiber production do produce different local structures. In Fiber 1, a bump in the upwards slope at 8940 eV appears at locations A and B, which are at higher Yb^{3+} concentrations than locations C and D. In Fiber 3, this feature appears to become larger from position B to A, or from lower to higher Yb^{3+} concentration. The bump may possibly be a characteristic of higher Yb^{3+} concentrated regions. As for the specific interpretation of the XANES spectra, further analysis cannot be completed until XANES measurements are made of the fiber optic preforms so that comparisons between the experimental data and known configurations can be made.

Conclusion

Five fibers were analyzed using X-ray absorption spectroscopy. The fibers were made into thin sections and analyzed with 1D and 2D X-ray fluorescence mapping scans in addition to EXAFS and XANES scans. There was no significant difference in the spatial resolution for the Yb maps for fibers that were prepared 50–100 μm thick and those that were much larger. Future studies should find methods to obtain samples less than 20 μm thick. The 2D intensity scans of the fiber cores were extremely useful, revealing information on the fiber cores. The cores were found to be diffusing Yb^{3+} into the cladding, larger than manufacturer dimensions, or both. The extent of diffusion can be resolved through a comparison of the linescans with refractive index as done in a previous study using a Raman confocal microscope [8]. Two fibers also displayed signs of collapse during manufacturing. The scan of Fiber 5 also displayed a depression between the Yb^{3+} and the GeO_2 in the core and cladding. The grid scans and line scans proved a useful tool to search for fiber collapse and diffusion, though future studies should include refractive index measurements.

Each fiber displayed a unique EXAFS and XANES spectrum, suggesting there is much to be learned from studying the fiber cores further. There were also slight variations in the XANES and EXAFS scans within the individual fiber cores. These variations could be caused by drops in the Yb^{3+} concentration. EXAFS fitting was unsuccessful due to the low amplitude of the spectra and interference between peaks. In order to produce a comprehensive XANES analysis, fiber preforms must be obtained to compare to the fiber core XANES data. Different samples may produce more easily fit results for EXAFS analysis. The distribution maps were highly successful, and the described enhancements to XANES and EXAFS analysis could make XAS a very useful tool for optical fiber analysis.

Acknowledgments

References

[1] R. Paschotta, J. Nilsson, A. C. Tropper, and D. C. Hanna, "Ytterbium-doped fiber amplifiers," *IEEE Journal of Quantum Electronics*, vol. 33, no. 7, pp. 1049–1056, Jul. 1997.

[2] H. M. Pask, R. J. Carman, D. C. Hanna, A. C. Tropper, C. J. Mackechnie, P. R. Barber, and J. M. Dawes, "Ytterbium-doped silica fiber lasers — versatile sources for the 1-1.2 MU-M region," *IEEE Journal of Selected Topics in Quantum Electronics*, vol. 1, no. 1, pp. 2–13, Apr. 1995.

[3] J. C. Du and A. N. Cormack, "The structure of erbium doped sodium silicate glasses," *Journal of Non-Crystalline Solids*, vol. 251, no. 27-29, pp. 2263–2276, Aug. 2005.

[4] R. M. Almeida, H. C. Vasconcelos, M. C. Goncalves, and L. F. Santos, "XPS and NEXAFS studies of rare-earth doped amorphous sol-gel films," *Journal of Non-Crystalline Solids*, vol. 234, pp. 65–71, Jul. 1998.

[5] J. A. Sampaio and S. Gama, "EXAFS investigation of local structure of Er^{3+} and Yb^{3+} in low-silica calcium aluminate glasses," *Physical Review B*, vol. 69, no. 10, p. 104203, Mar. 2004.

[6] P. M. Peters and S. N. HoudeWalter, "X-ray absorption fine structure determination of the local environment of Er^{3+} in glass," *Applied Physics Letters*, vol. 70, no. 5, pp. 541–543, Feb. 1997.

[7] B. J. Ainslie, "A review of the fabrication and properties of erbium-doped fibers for optical amplifiers," *Journal of Lightwave Technology*, vol. 9, no. 2, pp. 220–227, Feb. 1991.

[8] F. Sidiroglou, S. T. Huntington, and A. Roberts, "Micro-characterisation of erbium-doped fibers using a raman confocal microscope," *Optics Express*, vol. 13, no. 14, pp. 5506–5512, Jul. 2005.

[9] F. Sidiroglou, S. T. Huntington, A. Roberst, R. Stern, and I. R. Fletcher, "Simultaneous multidopant investigation of rare-earth-doped optical fibers by an ion microprobe," *Optics Letters*, vol. 31, no. 22, pp. 3258–3260, Nov. 2006.

[10] S. Gurman, R. J. Newport, M. Oversluizen, and E. J. Tarbox, "An extended x-ray absorption fine-structure study of the rare-earth sites in a neodymium doped glass," *Physics and Chemistry of Glasses*, vol. 33, no. 1, pp. 30–32, Feb. 1992.

[11] D. T. Bowron, R. J. Newport, J. S. Rigden, E. J. Tarbos, and M. Oversluizen, "An X-ray absorption study of doped silicate glass, fibre optic preforms," *Journal of Materials Science*, vol. 31, no. 2, pp. 485–490, Jan. 1996.

[12] M. A. Marcus and A. Polman, "Local-structure around Er in silica and sodium-silicate glasses," *Journal of Non-Crystalline Solids*, vol. 136, no. 3, pp. 260–265, Dec. 1991.

[13] T. Haruna, J. Iihara, K. Yamaguchi, Y. Saito, S. Ishikawa, M. Onishi, and T. Murata, "Local structure analyses around Er^{3+} in Er-doped fiber with Al co-doping," *Optics Express*, vol. 14, no. 23, pp. 11 036–11 042, Nov. 2006.

[14] M. R. Antonio, L. Soderholm, and A. J. G. Ellison, "Local environments of erbium and lutetium in sodium silicate glasses," *Journal of Alloys and Compounds*, vol. 250, no. 1-2, pp. 536–540, Mar. 1997.

[15] M. Newville. (2004, Jul.) Fundamentals of XAFS. Consortium for Advanced Radiation Sources. [Online]. Available: http://xafs.org/Tutorials

Ying Yi Dang grew up in New York City and majored in applied physics as an undergraduate engineering student at Columbia University. Her internship experiences at University of Michigan, Columbia University, and then Oak Ridge National Laboratory encompass physics, materials, nanoscience, and engineering, thus representing her varied interests and development of a multidisciplinary approach to scientific research. Ying Yi fantasizes about helping to solve the global energy problems in the future, but for now she plans on pursuing graduate studies in materials science. Any free time she finds in the interstices of work is usually devoted to fiction novels, music, or community service.

M. Parans Paranthaman is a distinguished scientist and a leader of the Materials Chemistry Group of the Chemical Sciences Division at the Oak Ridge National Laboratory. He received his PhD in Materials Science and Solid State Chemistry from the Indian Institute of Technology, Madras, in 1988. He was a postdoctoral fellow (with Professor John Goodenough) at the University of Texas at Austin and a research associate (with Professor Allen Hermann) at the University of Colorado at Boulder. He joined Oak Ridge National Laboratory in 1993. His research activities have focused on developing novel substrates and buffers for growing high temperature superconductor oxide films. He has also researched in the following areas: semiconductors for solar energy conversion, hydrogen generation and storage, catalysis for energy conversion, solid state fast ionic conductors, fuel cells, magnetic materials, and dielectric materials. He has authored or co-authored more than 300 publications and issued 20 U.S. Patents in his area and has over 4000 citations to his work. He has won several awards including two R&D 100 Awards and two National Federal Laboratory Consortium (FLC) Awards for developing high performance second generation superconducting wires for electric-power applications.

ZIRCONIUM OXIDE NANOSTRUCTURES PREPARED BY ANODIC OXIDATION

YING YI DANG, M.S. BHUIYAN, AND M. PARANS PARANTHAMAN

ABSTRACT

Zirconium oxide is an advanced ceramic material highly useful for structural and electrical applications because of its high strength, fracture toughness, chemical and thermal stability, and biocompatibility. If highly-ordered porous zirconium oxide membranes can be successfully formed, this will expand its real-world applications, such as further enhancing solid-oxide fuel cell technology. Recent studies have achieved various morphologies of porous zirconium oxide via anodization, but they have yet to create a porous layer where nanoholes are formed in a highly ordered array. In this study, electrochemical methods were used for zirconium oxide synthesis due to its advantages over other coating techniques, and because the thickness and morphology of the ceramic films can be easily tuned by the electrochemical parameters, such as electrolyte solutions and processing conditions, such as pH, voltage, and duration. The effects of additional steps such as pre-annealing and post-annealing were also examined. Results demonstrate the formation of anodic porous zirconium oxide with diverse morphologies, such as sponge-like layers, porous arrays with nanoholes ranging from 40 to 75 nm, and nanotube layers. X-ray powder diffraction analysis indicates a cubic crystallographic structure in the zirconium oxide. It was noted that increased voltage improved the ability of the membrane to stay adhered to the zirconium substrate, whereas lower voltages caused a propensity for the oxide film to flake off. Further studies are needed to define the parameters windows that create these morphologies and to investigate other important characteristics such as ionic conductivity.

INTRODUCTION

The fabrication of large areas of porous, high aspect-ratio nano-sized structures has attracted considerable scientific interest as its potential applications, which range from nanoscale templating to optical, electronic, and micromechanical devices, are being realized. The challenge is to overcome the difficulties of conventional lithographic processes in the production of such structures. One promising approach is to use electrochemical techniques [1]. They are generally straightforward and relatively inexpensive, can be performed near room temperature on a large scale, can deposit uniformly on complex shapes, and the morphology and thickness of the structures can be tuned by the electrochemical parameters and processing conditions such as electrolyte solutions, pH, voltage, temperature and duration.

Zirconium oxide possesses many highly desired materials qualities useful for structural and electrical applications such as fracture toughness, chemical robustness, thermal stability, and biocompatibility. It is already used as catalyst supports [2, 3], chemical sensors [4], thermal barrier coatings, and transformation-toughened materials. If highly-ordered porous zirconium oxide membranes can be successfully formed, this will expand its real-world applications, such as further enhancing solid-oxide fuel cell (SOFC) technology. In the case of the SOFC, it would improve the efficiency as a catalytic material by increasing its surface area with porous nanostructures. To this end, efforts have been placed

on finding ways to create porous zirconia with methods such as template synthesis [5] and electrolytic deposition [6–9].

Anodic oxidation is one particular electrochemical method that has generated significant research effort [10–12] towards investigating the synthesis of ordered oxide structures on metallic surfaces other than zirconium, like Al_2O_3 on aluminum [13, 14]. In this method, two electrodes (one electrode is the metallic surface to be anodized, and the other, usually platinum, serves as the counter and/or reference electrode) are immersed in an electrolyte bath and suspended from wires connected to a DC power supply. Achieving the desired reaction products at the exposed surface is highly dependent on the details of manipulating the chemistry of the metal-electrolyte interface with various combinations of electrochemical parameters. Recent studies have achieved various morphologies of porous zirconium oxide using anodic oxidation [15–18], but they have yet to create a porous layer where nanoholes are formed in an extremely highly ordered array, e.g. a honeycomb structure. Additionally, many questions remain open about the evolution of the nanostructures' morphology and the establishment of the self-organization process [19]. The purpose of this research was to study the formation of porous zirconium oxide structures via anodization, gain an understanding of the formation mechanisms, explore the properties of anodized zirconium, and to continue to test the effects of different permutations of the processing conditions. Plots of anodization current versus, XRD scans and SEM images are used for this discussion.

MATERIALS AND METHODS

Zirconium (99.98% purity, Aldrich, USA) substrates of 0.75 cm x 2.5 cm were cut from a zirconium sheet of 100 or 25 micron thickness. They were prepared for the electrochemical anodization by first sonicating in acetone for degreasing purposes, then rinsing with deionized water, and finally dried with nitrogen gas. A pure platinum foil served as the counter electrode in the electrochemical cell. Electrolyte bath of 1M $(NH_4)_2SO_4 + 0.5\%\ NH_4F$ was prepared at room temperature from analytical grade chemicals and deionized water.

The electrochemical treatment was carried out at room temperature and consisted of the two electrodes immersed in the electrolyte and externally connected to a DC power supply (Agilent E3612A or VersaSTAT 3). Figure 1 shows the basic experimental set-up used for this study. The anodizing area of the zirconium foils is approximately 1.4 cm^2. Current-time measurements were recorded during the treatment. After the electrochemical deposition, the sample surface was immediately rinsed with de-ionized water and then streamed with nitrogen gas to prepare for characterization.

X-ray diffraction (XRD) was used to identify the crystal structure of the resulting ZrO_2 films. XRD was performed with a scanning rate of 0.05 degrees per minute using CuKα radiation with a wavelength of approximately 1.5 Å. The 2θ measurement range varied from 25° to 85°. The actual structure and surface morphology were characterized using scanning electron microscopy (SEM). The cross-section of the samples was also examined. For investigating the effect of annealing, samples were either pre-anodization annealed with Ar at 900°C for 1 hour, or post-anodization annealed with O$_2$

Figure 1. The anodization setup features a DC power supply, an electrolyte bath, and two electrical wires suspending two electrodes in the electrolyte bath. The black lead holds the Pt counter electrode, and the red one holds the zirconium foil to be anodized.

also at 900°C for 1 hour, and then compared to samples that were processed under identical conditions without annealing.

RESULTS AND DISCUSSION

Analysis of Transient Current

By observing the transient current for different runs, a better understanding of the mechanics of anodization can be obtained. Figure 2 shows the current-time behavior for three different anodization runs. All show that after extended constant potential anodization times, all systems experience a decline in current due to the increase in both the oxide layer as an electrical barrier and the diffusion length for the ionic species in the electrolyte bath [20]. Comparing plots for two different voltages, 30 volts (Figure 2a — plot a) and 50 volts (Figure 2a — plot b), it shows that the higher the applied voltage, the longer it takes for the current to die off and the higher the current at all times because the rates of oxidation are higher and the drift of ions are faster under higher applied potentials. It is evident from the particularly rapid fall-off
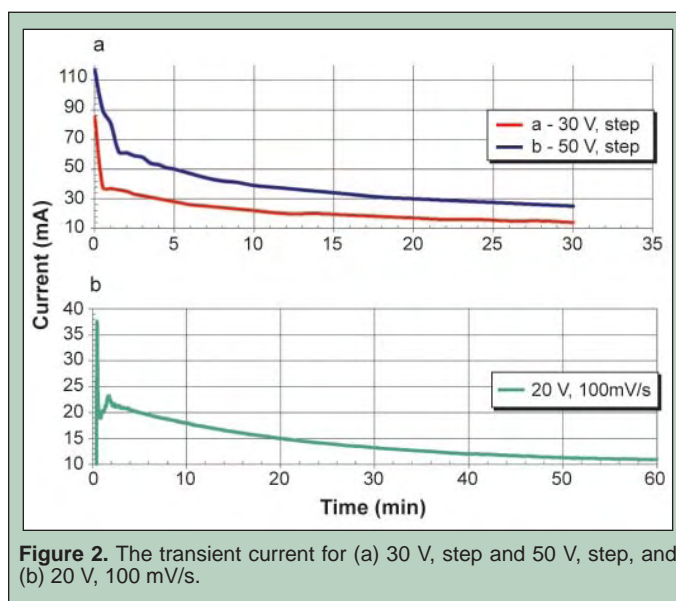
Figure 2. The transient current for (a) 30 V, step and 50 V, step, and (b) 20 V, 100 mV/s.

in current during the first few minutes that the formation of a non-porous compact layer of oxide is the dominant process and hence acts as a barrier layer before any nanostructures have begun to form and compete with the barrier. After those few minutes, the current behavior declines more steadily, thus signifying that it has entered the stage where the compact oxide layer gives way to the porous structures that are taking shape.

In order to better discern the stages of anodization, the electric potential was applied by sweeping from an open circuit potential to a final value of 20 volts at a rate of 100 mV/s and then followed by holding the potential at 20 volts. As seen in Figure 2b, the current during this type of application deviates twice from exponential decay. It initially increases as the applied potential is ramped and then quickly drops and increases again, which marks the transition to a perforated and porous oxide layer. The second increase can be explained by the oxide layer being weakly dissolvable in the presence of the fluoride additives, which creates locally varying film thicknesses. A self-catalyzing effect occurs where the pits or perforations that are created concentrate the electric fields that spur local acid corrosion and also enhance ion drifts [21]. Only after this random growth stage and the pores begin to compete with each other do we observe the usual steady decrease in current, so this second spike in current readings followed by the return to steady decline indicates that the system has entered the pore formation regime [14, 21, 22], which continues until the system is turned off or the pores have reached a final geometry.

XRD Analysis

With XRD analysis, the various signature peaks like ZrO_2 (111) and ZrO_2 (220) as shown in Figure 3 indicate that all the non-annealed ZrO_2 films developed a cubic crystallographic structure directly after anodization. This is consistent with previous literature
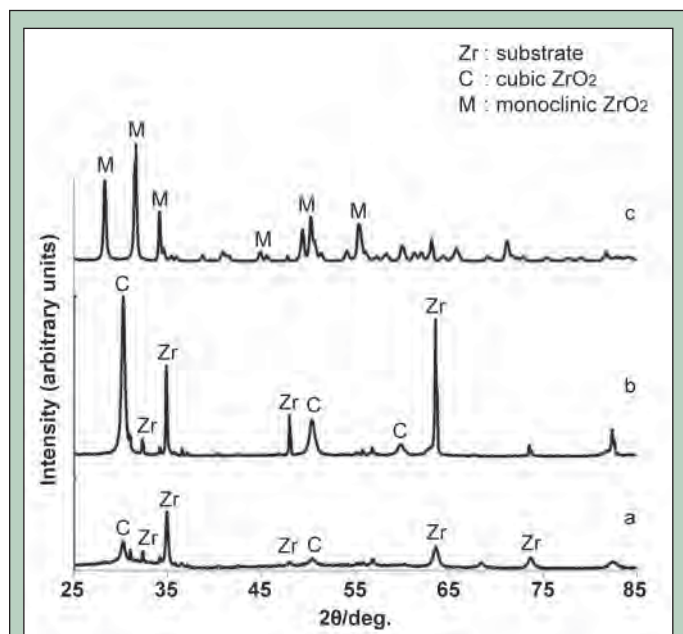
that reported that the cubic zirconia structure was predominant in compact oxide layers formed in a variety of electrolytes [23]. This is noteworthy because zirconia's naturally occurring form at room temperature is monoclinic and would usually require the addition of dopants such as yttrium to stabilize the cubic phase. Hence, the fact that the zirconia nanostructures have a cubic crystalline structure directly after anodization (Figure 3a) without the need for stabilizers or annealing is of a particular advantage in applications that are sensitive to thermal treatments because cubic zirconia has low thermal conductivity.

In the same figure, the XRD plot of Ar pre-anodization (Figure 3b) annealing shows more intense peaks. This signifies that pre-annealing with argon gas is successful in re-crystallizing and removing the deformities and internal stresses of the pure zirconium foils because if all other conditions are identical, these higher peaks of the ZrO_2 and its parent substrate can only be explained by fewer crystal defects and a more organized structure. However, post-anodization annealing with O_2 reveals completely different peaks (Figure 3c) and corresponds to ZrO_2 that is monoclinic. This indicates that during the annealing process, grain growth and the associated volume expansion causes the cubic phase to convert to monoclinic. The sample has been observed, however, after O_2 annealing to be extremely brittle or cracked after it has cooled from the high annealing temperature, which indicates that the transformation from cubic to monoclinic induces significant stresses on the crystalline structure.

SEM Analysis

Results of SEM analysis reveal a variety of nanostructures (Figures 4–5), from porous array-like structures, to tubular, to sponge-like, to "mixed". TEM images of the cross section of two particular samples that were anodized for 30 minutes but created at different voltages are shown in Table 1. It indicates the formation of ZrO_2 film on both sides of the substrate. Work is ongoing to define which parameters are specific to the types of structures that have been observed, however, the samples with morphologies possibly viable for application can be seen in Figures 4a and 4b: the semi-ordered nano-hole porous arrays of approximately 40 nm (10 volts, 30 min) and 75 nm (20 volts, 30 min). This may suggest that higher voltages produce nano-hole membranes with bigger holes.

Figure 3. XRD chart for the zirconia (a) without annealing, (b) with pre-anodization annealing with Ar, and (c) post-anodization annealing with O_2.
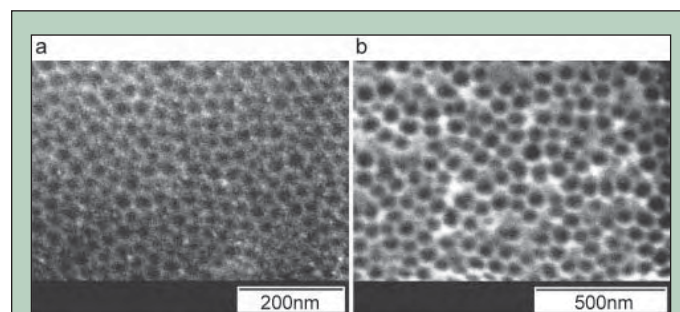
Figure 4. SEM images of semi-ordered nano-hole porous arrays. The pores range from 40 to 75 nm. (a) 10 volts, 30 min. (b) 20 volts, 30 min.

Figure 5. SEM images of (a) sponge-like ZrO$_2$ film and (b) mixed morphology. Note in (b) that underneath the sponge-like strips there are tubular nanostructures.
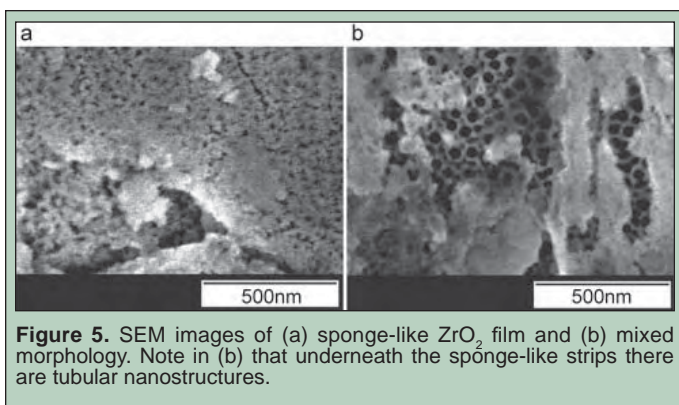
Samples with mixed morphologies (Figure 5) have been correlated to those that have been anodized for only a relatively short time. In this example, the samples were anodized for only 10 minutes, which was probably not enough time for the structure to fully and uniformly develop. From a mechanistic standpoint, those non-porous strips of oxide are remnants of the barrier oxide layer that is first formed when anodization is activated before it becomes a nanoporous or nanotubular structure. Since it usually takes very long anodization times to create a uniform nanoporous array, it makes sense that a sample anodized for 10 minutes shows remnants of the barrier oxide layer that has yet to begin seeding the growth of nanotubes.

Figure 6. TEM images of the cross section of the samples made under 10 volts for 30 minutes (left column), and 30 volts for 30 minutes with a re-used Zr substrate (right column).
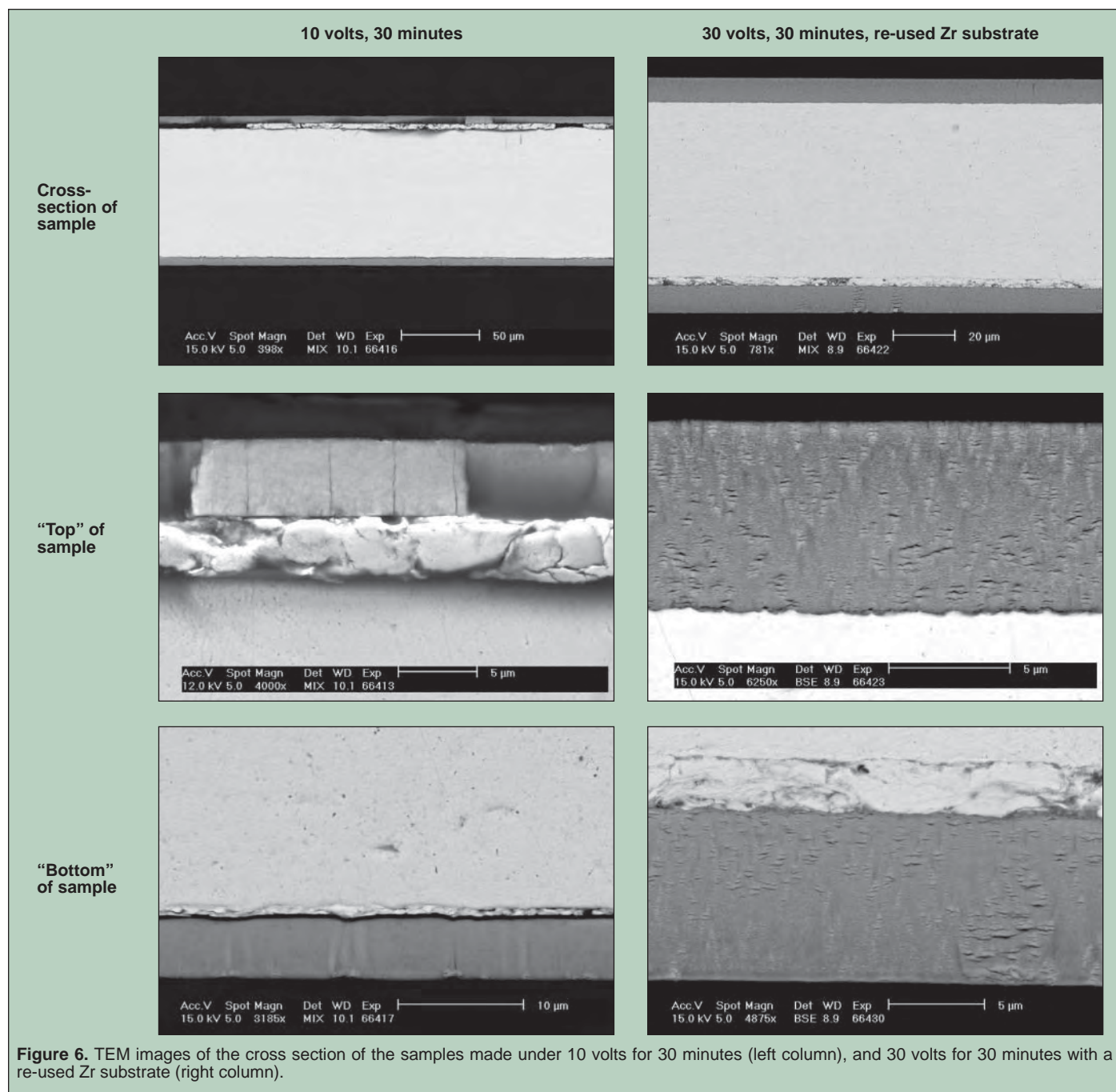
Finally, when analyzing the cross sections of the samples (Figure 6), ZrO_2 film can be observed on both sides of the zirconium substrate, which is logical because both sides of the zirconium are exposed in the electrolyte bath. The ZrO_2 film on the "top" layer of the 10 volts sample has cracks. The 30 volts sample on the left hand column exhibit interesting striations on the "top" and "bottom" ZrO_2 that indicate that the pores of the film are more penetrating. The thickness of the leftover substrate, which is the pale middle layer in the top row of pictures, is considerable in relation to thickness of the ZrO_2 film. On the other hand, it should be noted that the sample with the higher voltage has thicker ZrO_2 films. Both samples were anodized for half an hour, but the sample that was only anodized for 10 minutes created 4.4 µm thick ZrO_2 film, whereas the 30 minute sample produced ZrO_2 film that was approximately 9.6 µm thick. This is a logical relationship since higher applied voltages stimulate stronger and faster anodization, which is simply a type of electrochemical method.

CONCLUSION

Further research is needed to define and correlate the various ZrO_2 nanostructure morphologies to the specific processing variables. This way, one may be able to obtain the desired nanostructure morphology by simply tuning the parameters of the electrochemistry to the correct values. More studies should also be done on investigating the morphological results of different deposition regimes via permutations of voltage, duration, different electrolytes that can anodize zirconium. Meanwhile, additional steps that can refine the structure of the resulting ZrO_2 film like argon pre-anodization annealing to remove deformities should be capitalized in the future. The vertical profiles of the ZrO_2 film also deserve a closer look because the cracks and striations that are found give more information to the usefulness of ZrO_2 film applications. All of this may also be furthered with similar studies using "doped" Zr and compared with the pure Zr. Finally, investigation of other important characteristics such as ionic conductivity of the ZrO_2 is essential, especially because solid oxide fuel cells using ZrO_2 would operate by having oxygen ions flowing through it in order to convert chemical energy to electricity and heat.

REFERENCES

[1] N. Kanani, *Electroplating: Basic Principles, Processes, and Practice.* Oxford, UK: Elsevier Ltd, 2004.

[2] T. Yamaguchi, "Application of ZrO_2 as a catalyst and a catalyst support," *Catalysis Today*, vol. 20, pp. 199–218, Jun 1994.

[3] K. Tanabe and T. Yamaguchi, "Acid-base bifunctional catalysis by ZrO_2 and its mixed oxides," *Catalysis Today*, vol. 20, pp. 185–198, Jun 1994.

[4] R. H. Zhang, X. T. Zhang, and S. M. Hu, "Nanocrystalline ZrO_2 thin films as electrode materials using in high temperature-pressure chemical sensors," *Materials Letters*, vol. 60, pp. 3170–3174, Nov 2006.

[5] B. T. Holland, C. F. Blanford, T. Do, and A. Stein, "Synthesis of highly ordered, three-dimensional, macroporous structures of amorphous or crystalline inorganic oxides, phosphates, and hybrid composites," *Chemistry of Materials*, vol. 11, pp. 795–805, Mar 1999.

[6] P. Stefanov, D. Stoychev, M. Stoycheva, J. Ikonomov, and T. Marinova, "XPS and SEM characterization of zirconia thin films prepared by electrochemical deposition," *Surface and Interface Analysis*, vol. 30, pp. 628–631, Aug 2000.

[7] I. Zhitomirsky and L. Gal-Or, "Characterization of zirconium, lanthanum and lead oxide deposits prepared by cathodic electrosynthesis," *Journal of Materials Science*, vol. 33, pp. 699–705, Feb 1998.

[8] I. Zhitomirsky and A. Petric, "Electrolytic deposition of zirconia and zirconia organoceramic composites," *Materials Letters*, vol. 46, pp. 1–6, Oct 2000.

[9] I. Valov, D. Stoychev, and T. Marinova, "Study of the kinetics of processes during electrochemical deposition of zirconia from nonaqueous electrolytes," *Electrochimica Acta*, vol. 47, pp. 4419–4431, Oct 2002.

[10] T. Tsukada, S. Venigalla, and J. H. Adair, "Low-temperature electrochemical synthesis of ZrO_2 films on zirconium substrates: Deposition of thick amorphous films and in situ crystallization on zirconium anode," *Journal of the American Ceramic Society*, vol. 80, pp. 3187–3192, Dec 1997.

[11] H. Tsuchiya, J. M. Macak, A. Ghicov, L. Taveira, and P. Schmuki, "Self-organized porous TiO_2 and ZrO_2 produced by anodization," *Corrosion Science*, vol. 47, pp. 3324–3335, Dec 2005.

[12] B. Cox, "Factors affecting growth of porous anodic oxide films on zirconium," *Journal of the Electrochemical Society*, vol. 117, pp. 654–663, 1970.

[13] H. Masuda and K. Fukuda, "Ordered metal nanohole arrays made by a 2-step replication of honeycomb structures of anodic alumina," *Science*, vol. 268, pp. 1466–1468, Jun 1995.

[14] O. Jessensky, F. Muller, and U. Gosele, "Self-organized formation of hexagonal pore structures in anodic alumina," *Journal of the Electrochemical Society*, vol. 145, pp. 3735–3740, Nov 1998.

[15] H. Tsuchiya and P. Schmuki, "Thick self-organized porous zirconium oxide formed in H_2SO_4/NH_4F electrolytes," *Electrochemistry Communications*, vol. 6, pp. 1131–1134, Nov 2004.

[16] H. Tsuchiya, J. M. Macak, L. Taveira, and P. Schmuki, "Fabrication and characterization of smooth high aspect ratio zirconia nanotubes," *Chemical Physics Letters*, vol. 410, pp. 188–191, Jul 2005.

[17] H. Tsuchiya, J. M. Macak, I. Sieber, and P. Schmuki, "Self-organized high-aspect-ratio nanoporous zirconium oxides prepared by electrochemical anodization," *Small*, vol. 1, pp. 722–725, Jul 2005.

[18] H. Tsuchiya, J. M. Macak, I. Sieber, and P. Schmuki, "Anodic porous zirconium oxide prepared in sulfuric acid electrolytes," in *Advanced Structural and Functional Materials Design, Proceedings*. vol. 512, 2006, pp. 205–210.

[19] K. Yasuda, J. M. Macak, S. Berger, A. Ghicov, and P. Schmuki, "Mechanistic aspects of the self-organization process for oxide nanotube formation on valve metals," *Journal of the Electrochemical Society*, vol. 154, pp. C472–C478, 2007.

[20] K. Yasuda and P. Schmuki, "Control of morphology and composition of self-organized zirconium titanate nanotubes formed in $(NH_4)(2)SO_4/NH_4F$ electrolytes," *Electrochimica Acta*, vol. 52, pp. 4053–4061, Mar 2007.

[21] F. Y. Li, L. Zhang, and R. M. Metzger, "On the growth of highly ordered pores in anodized aluminum oxide," *Chemistry of Materials*, vol. 10, pp. 2470–2480, Sep 1998.

[22] R. B. Wehrspohn, "Pits and Pore II: Formation Properties and Significance for Advanced Materials," Pennington, NJ, 2000, p. 168.

[23] R. A. Ploc and M. A. Miller, "Transmission and scanning electron-microscopy of oxides anodically formed on zircolay-2," *Journal of Nuclear Materials*, vol. 64, pp. 71–85, 1977.

Siva Darbha was born in Ottawa, ON and attended the University of Toronto, where he majored in engineering science. During his undergraduate career, he held an internship at the European Organization for Nuclear Research in the summer of 2006, and a SULI internship at the Stanford Linear Accelerator Center in the summer of 2007. He seeks to enter a PhD program in nuclear science and engineering and to conduct research at a national laboratory. His interests include literature, film, and graphic novels.

Lewis Keller is an engineering physicist at the Stanford Linear Accelerator Center (SLAC). He received a B.S. degree from Valparaiso University and a Ph.D. from Oklahoma State University in 1969. Following a post-doc appointment at Argonne National Laboratory, he joined SLAC as head of the Experimental Facilities Department in 1973. He collaborated on numerous fixed target and colliding beam experiments, and participated in the design of the Stanford Linear Collider and the BaBar Detector at PEP-II. He is currently working on design of the International Linear Collider and the LHC Accelerator Research Project.

Takashi Maruyama is a staff physicist at the Stanford Linear Accelerator Center. He received his Ph. D. in high energy physics from Tohoku University, Japan. His research interests include high energy e+e- interactions, particle tracking and radiation shielding, and polarized electron source based on semiconductor photocathodes.

SIMULATION OF NEUTRON BACKGROUNDS FROM THE ILC EXTRACTION LINE BEAM DUMP

SIVA DARBHA, LEWIS KELLER, AND TAKASHI MARUYAMA

ABSTRACT

The operation of the International Linear Collider (ILC) as a precision measurement machine is dependent upon the quality of the charge-coupled device (CCD) silicon vertex detector. An integrated flux of 10^{10} neutrons/cm^2 incident upon the vertex detector will degrade its performance by causing displacement damage in the silicon. One source of the neutron background arises from the dumping of the spent electron and positron beams into the extraction line beam dumps. The Monte Carlo program FLUKA was used to simulate the collision of the electron beam with the dump and to determine the resulting neutron flux at the interaction point (IP). A collimator and tunnel were added and their effect on the flux was analyzed. A neutron source was then generated and directed along the extraction line towards a model of the vertex detector to determine the neutron flux in its silicon layers. Models of the beampipe and BeamCal, a silicon-tungsten electromagnetic calorimeter in the very forward region of the detector, were placed in the extraction line and their effects on scattering were studied. The IP fluence was determined to be 3.7×10^{10} +/- 2.3×10^{10} neutrons/cm^2/year when the tunnel and collimator were in place, with no appreciable increase in statistics when the tunnel was removed. The BeamCal was discovered to act as a collimator by significantly impeding the flow of neutrons towards the detector. The majority of damage done to the first layer of the detector was found to come from neutrons with a direct line of sight from the first extraction line quadrupole QDEX1, with only a small fraction scattering off of the beampipe and into the detector. The 1 MeV equivalent neutron fluence was determined to be 9.3×10^8 neutrons/cm^2/year from the electron beam alone. The two beams collectively contribute double to this fluence, which is 19% of the threshold value in one year. Future work will improve the detector model and other sources of neutron backgrounds will be analyzed.

INTRODUCTION

The Large Hadron Collider (LHC) operating at CERN will probe a new energy scale using 14 TeV center of mass energy proton-proton collisions and will produce a wealth of new physics, including searches for the Higgs boson and Supersymmetry [1]. The International Linear Collider (ILC) is a proposed linear electron-positron collider that will be 31 km in length and will have a center of mass energy of 500 GeV. It will have a cleaner signal to noise ratio than the LHC and will provide precision measurements for some of the physics discovered there.

The electron and positron beams in the ILC will have 2×10^{10} particles per bunch and a bunch separation of 370 ns with 2,625 bunches in 1 ms trains at a repetition rate of 5 Hz. The bunches will collide at the interaction point (IP) at a 14 mrad crossing angle [2]. The Beam Delivery System (BDS) in the ILC is responsible for transporting the electron and positron beams from the main linacs, colliding them at the IP, and discarding the spent beams to the extraction line beam dumps [Figure 1]. The beam dumps are stainless steel cylindrical containers of 75 cm radius and 7.5 m length with a titanium window of 15 cm radius and 1 mm thickness through which the beams enter. The dumps contain water at a pressure of 10 bar [3]. Water's high specific heat capacity makes it ideal to dissipate the energy of the beams. Only a minute fraction of the particles in any bunch crossing will interact, leaving on the order of 10^{14} high energy electrons and positrons to be extracted from the IP and discarded in the water dumps each second. The

dumps are designed to absorb 17 MW of beam power at a 500 GeV center of mass energy [3].

The extracted beams will interact with the H_2O molecules in the dump, leading to electromagnetic showers in which the resulting photons will produce a flux of neutrons through photonuclear interactions. The shower maximum, the locus of neutron production, occurs roughly 2 m into the water dump [4]. Though the majority of this 'gas' of neutrons will be forward directed, some will be backward directed and will reach the detector, a phenomenon called neutron backshine. The backshine creates unwanted backgrounds in the tracking devices and calorimeters that will obscure the physics processes observed from collision of the beams and may even cause displacement damage in the silicon atoms in the charge-coupled device (CCD) vertex detector if the integrated flux reaches a level higher than 10^{10} neutrons/cm^2, leading to charge traps [5, 6]. The accumulation of charge traps would degrade the performance of the detector by reducing the charge transfer along the CCD and by causing junction leakage [5, 6]. The CCD vertex detector is the innermost tracking system in the SiD detector model, one of the four detector models under consideration for the ILC. Such degradation would hinder the performance of the ILC as a precision machine and would require frequent repairs, which should be minimized to allow continuous and robust recording of data.

This paper investigates the neutron detector backgrounds from the extraction line beam dump through Monte Carlo simulations. The program FLUKA was used for the simulations due to its robustness with low energy neutron cross sections. Only the electron beam was used for the analysis, with the positron beam

having symmetric and analogous results. The neutron fluxes at the dump and at the detector were studied first without material near the beam line to provide a benchmark estimate. Concrete tunnel walls and a concrete collimator were then added to the simulation and their effect on the flux was studied. Information gathered on neutron distributions at the dump during this work was used to simulate an isotropic and uniformly distributed neutron source. The source was positioned in the bore of the extraction line quadrupole QDEX1 and incident upon the beryllium beampipe and the five layers of the CCD silicon vertex detector central barrel to obtain an estimate of the neutron flux at the vertex detector. These values were integrated over a year into annual fluences. Particle biasing techniques were used to increase statistics on the simulated events, and the effectiveness of each bias was studied.

MATERIALS AND METHODS

The Monte Carlo program FLUKA was used for the simulations. The spent electron beam was given an initial position at the origin and was directed in the positive z-direction with 250 GeV of energy. The beam was directed into the water dump, which was placed at z = 300 m and was modeled by a circular cylinder of water with a radius of 75 cm and a length of 5 m (see Figure 2). The stainless steel container and Ti window were ignored since they would not impede an outward flux of neutrons from inside the dump and would increase the computation time.

Although the ILC will have on the order of 10^{14} electrons incident on the water dump per second, only between 10^3 and 10^7 electrons can be simulated in FLUKA per run to maintain reasonable computation times. Performing subsequent runs to increase the statistics would be ineffective, for that approach would provide
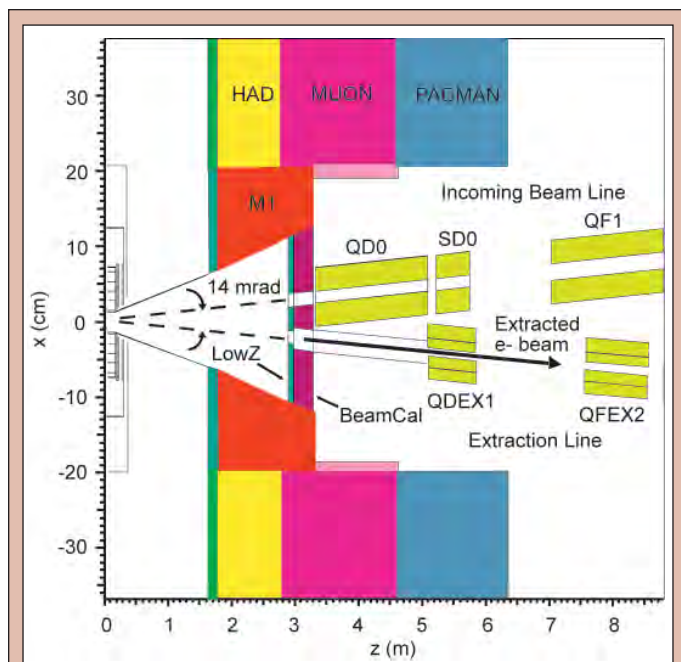
Figure 1. A Geant4 model of the extraction line. M1 is an instrument mask, HAD is the endcap hadronic calorimeter, MUON is the endcap muon calorimeter, and PACMAN is a beamline shielding ring to provide radiation shielding to the endcap detectors. In the incoming beam line, QD0 and QF1 are the final doublet quadrupole magnets and SD0 is the final sextupole. QDEX1 and QFEX2 are the first doublet quadrupoles in the extraction line. The water dump is located 300 m down the extraction line.
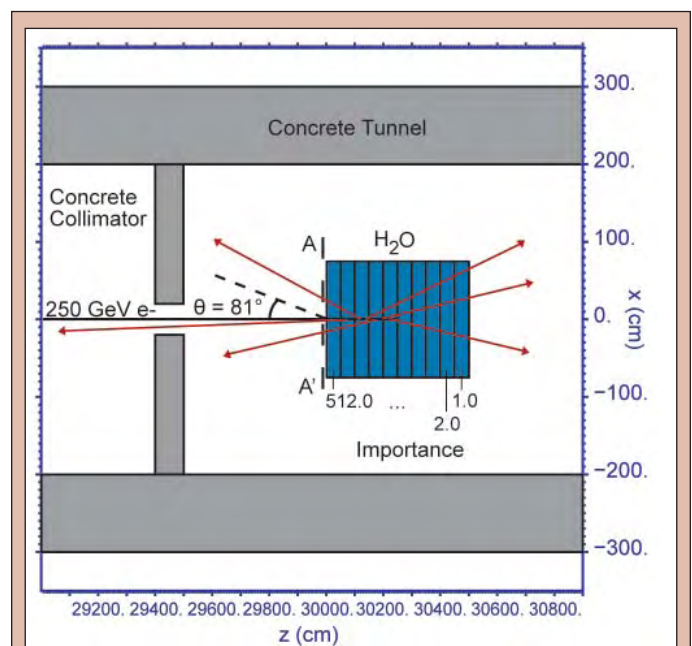
Figure 2. The FLUKA model of the beam dump with a concrete collimator and concrete tunnel in place. The 250 GeV input electron beam acts as a line source in the water dump, and the red arrows symbolize possible trajectories of the neutrons produced in the dump along that source.

an unnecessary level of precision at too great of a computation time. As a result, three particle biasing techniques were used to shift computation time towards simulating interesting events at the expense of uninteresting ones, effectively increasing the statistics on the fluence scoring by using computation time effectively and providing sufficient precision. First, leading particle biasing was activated for electrons, positrons, and photons with energy below 2.5 GeV. Since simulating a full electromagnetic shower requires long computation time, leading particle biasing traces only the most energetic secondary created by the electrons, positrons, or photons below 2.5 GeV and eliminates all others, adjusting the 'weight' of the most energetic particle accordingly. Secondly, the interaction cross section for neutron production by photonuclear interactions was increased by a factor of 50, and the 'weight' associated with each neutron produced this way was decreased by a factor of 50 to preserve particle multiplicity. Finally, the cylindrical water dump was divided into 10 adjacent regions as in Figure 3. The region at the back of the dump was given an 'importance' of 1.0, and each region progressively closer to z = 0 was given a factor of 2.0 larger importance. Photons crossing a region boundary from lower importance to higher importance were reloaded onto the particle transport stack an integer number of times, such that on average 2.0 photons exited the boundary for every one that entered; this sampling is called splitting. FLUKA adjusted the 'weight' associated with the new photons on the stack to conserve particle multiplicity when the bias was applied. The increase in photon multiplicity exacerbated the electromagnetic showering and increased neutron production through photonuclear interactions. Photons crossing a region boundary in the opposite direction were terminated similarly, a sampling called Russian Roulette [7]. The application of splitting and Russian Roulette focused the computation time on increasing statistics on backward directed neutrons at the expense of ignoring forward directed one, which do not contribute to backshine. The effectiveness of each type of bias was studied with 6,000 incident electrons (see Table 1).

Production and transport cutoffs were activated to decrease simulation time. A 50 MeV cutoff on both was applied to electrons and positrons, and a 10 keV cutoff on both was applied to photons. A transport cutoff of 1.0332×10^{-5} GeV was applied to neutrons. This value was chosen from Non-Ionizing Energy Loss (NIEL) scaling studies which show that neutrons below 10 keV do not have sufficient energy to create displacement damage, which are mostly from point defects and defect clusters, in the silicon bulk of the vertex detector [8]. The NIEL stopping power for neutrons in silicon also decreases with decreasing kinetic energy, and consequently neutrons below 10 keV were not a concern [9].

The neutron fluence decays exponentially as a function of cos θ for neutrons leaving the water dump in the negative z-direction, where θ is the zenith angle with respect to the z-axis. The distribution was measured on the surface of the dump at A-A' in Figure 2 and was partitioned into bins covering small ranges of cos θ, over each of which the fluence can be viewed as isotropic (see Figure 3) [10]. The fluence was assumed to be isotropic in the first bin, which corresponds to the range -1 < cos θ < -0.99 and an 8.1° spread around the negative z-direction from the surface of the water dump. This spread was sufficiently large that the expected scattering from the tunnel walls would be observed.

The relevant fluence value was that measured in a circle of 1.5 cm radius at z = 0, concentric with the z-axis and parallel to the xy-plane, which is the IP fluence. The neutrons that reach this circle are the ones that will reach the vertex detector, since they have passed through the bore of the first extraction line quadrupole, which has a radius of 1.5 cm and have not been impeded by collimators, magnets, or the tunnel. However, when a scoring plane that size was used, small fluence values with large errors were measured.
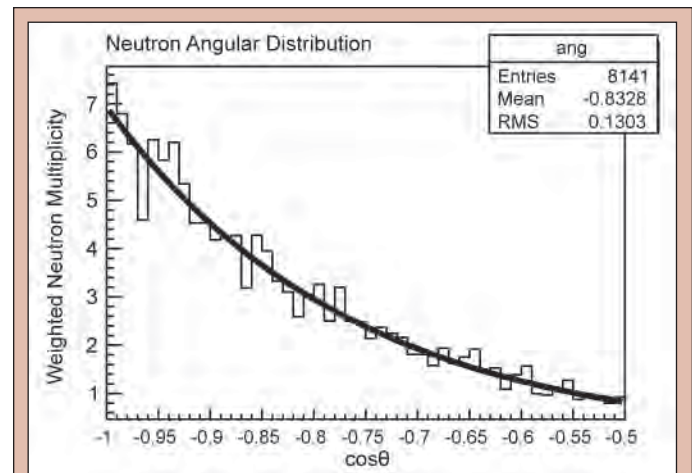
Figure 3. The neutron angular distribution at A-A' in Figure 2. The neutron fluence can be treated as isotropic in each bin [10]. The fluence was scored at z = 0 m with a 2 m radius scoring plane with the assumption of the isotropy in the first bin (-1 < cosθ < -0.99).

Run Number	Type of Bias	Computation Time	Neutron total 'weight'		Neutron total number	
			At z = 300 m	At z = 0	At z = 300 m	At z = 0
1	No biasing	23 hours 35 min	82	2	82	2
2	Leading particle biasing activated for EMF particles (for e-,e+ < 2.5 GeV and γ < 2.5 GeV)	1 hour 36 min	103	0	87	0
3	Decay length biasing activated for photonuclear interactions (biasing factor = 0.020)	6 hours 46 min	103	0.781	5008	49
4	Splitting in waterdump activated for photons (10 regions in waterdump, factor of 2 for each region boundary)	6 hours 22 min	96.4	1.09	16619	117

Table 1. Computation time and effectiveness of each bias. All runs were made with 6,000 electrons incident on the water dump and each run contains the biases of all previous runs.

This was a consequence of the relatively small number of incident electrons that were simulated compared to the large rates of incident electrons expected at the ILC and did not accurately reflect the IP fluence. To obtain better statistics, a circular scoring plane 2 m in radius at z = 0 was used. Due to the isotropic fluence assumption, the fluence calculated with this scoring plane, per square centimeter, was assumed to be the same as that measured with a 1.5 cm radius circle after a sufficiently long time.
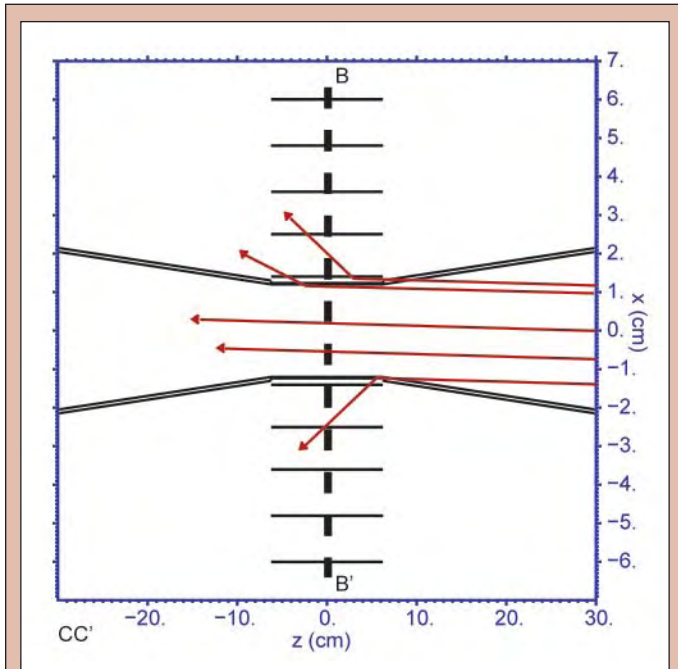
Figure 4. The CCD silicon vertex detector in the SiD detector model. The five layers of the detector were modeled by concentric cylinders, each 0.01 cm thick. The beampipe barrel was made 0.04 cm thick and the conical section was made 0.1 cm thick. The left and right conical sections of the beampipe extend outward to -167.9 cm and +167.9 cm respectively, but have been truncated here at -30 cm and +30 cm [11].

As a primary benchmark estimate, 10^4 electrons were collided into the water dump and the IP fluence was measured with no material in the beamline. A concrete collimator and a concrete tunnel wall were then added to the simulation, as shown in Figure 2. The number of incident electrons was increased to 5×10^4 to overcome the anticipated drop in statistics from the addition of the collimator, and the IP fluence was measured again. Finally, the tunnel was removed, the collimator was kept in place, and the IP fluence was measured with 5×10^4 incident electrons to study neutrons which scatter off of the tunnel walls and towards the detector.

Once the IP fluence was determined, the neutron fluence from the quadrupole QDEX1 to the five layers of the CCD silicon vertex detector, the detector fluence, was studied, since the neutrons that reach the IP do not necessarily collide with the detector elements. The central barrel beryllium beampipe and the five layers of the Si barrel vertex detector were placed around the IP, as shown in Figure 4, and were based on the geometry specified at the Snowmass conference [11]. Figure 5 shows the full model of the detector and the nearest section of the extraction line, which consists of QDEX1
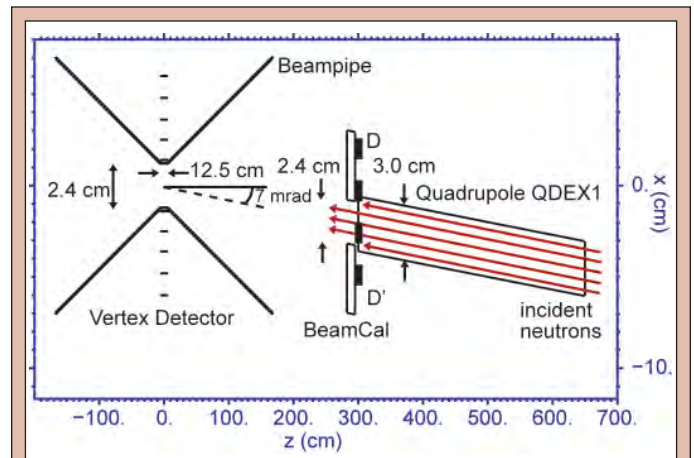
Figure 5. The full model of the extraction line. The BeamCal was modeled by a 12.5 cm thick slab of tungsten. The neutron source was evenly distribution on the surface of the quadrupole at D-D' and the neutrons were given a trajectory of 7 mrad towards the detector.

and the BeamCal. The BeamCal was modeled by a 12.5 cm thick slab of tungsten; the Si layers in it were ignored since they have a low probability of scattering the incident neutrons.

The neutron energy and 'weight' distributions at A-A' in Figure 2 were recorded from the previous simulations and were sampled from and used to generate a neutron source. Figure 6 shows the energy distribution. The initial positions of the neutrons in the source were generated randomly in the bore of QDEX1 at D-D' in Figure 5 in a circle of 1.5 cm radius centered at x = -2.1 cm and y = 0 cm. This starting point modeled the neutrons from the water dump that would reach the surface of the quadrupole from the dump without being blocked by collimators, magnets, or other material. All neutrons in the source were given a 7 mrad trajectory from the z-axis.

The detector fluence was measured and combined with the IP fluence when the tunnel and collimator were in place, to provide an estimate of the total fluence at the vertex detector. The total

fluence values were converted to annual fluxes to obtain a temporal picture of the neutron displacement damage. The measurement was performed twice more, when the BeamCal was removed and when it was replaced with an infinitely absorbing material, in order to give an estimate of the BeamCal scattering. The BeamCal was then returned and the flux as a function of the BeamCal aperture radius was studied.

Finally, a normalized and comparable value was obtained for the amount of damage done to the first layer of the vertex detector by neutron backshine. Previous research has studied the amount of displacement damage done to CCD silicon detectors by neutrons as a function of neutron energy and has produced a 1 MeV equivalent silicon displacement damage scale (see Figure 7) [12]. The total fluence in the first silicon layer was scaled according to this distribution. Although the neutron energy distribution in Figure 6 extends beyond the upper bound of the experimental data, which occurs at $2x10^7$ eV, the data reaches a plateau above 10^7 eV, and this trend was used to scale the neutrons above 0.01 GeV. The calculated fluence would underestimate the damage if highly energetic neutrons require a higher scaling factor than this, though it does at least provide a lower bound. In addition, the calculated fluence provides an upper bound on the fluences in the other layers and, as such, they were left unscaled, but would also have a greater scaled flux due to their similar input neutron energy distributions.

RESULTS

The IP flux with no objects in the extraction line was measured to be $8.3x10^{10}$ +/- $1.5x10^{10}$ neutrons/cm^2/year. When the tunnel and collimator were added for a more accurate estimate, the flux dropped to $3.7x10^{10}$ +/- $2.3x10^{10}$ neutrons/cm^2/year. When the tunnel was removed, there was no appreciable change in the flux given the current level of statistics, as it remained at $3.7x10^{10}$ +/- $3.3x10^{10}$ neutrons/cm^2/year. The computation time and effectiveness of the biasing techniques used in the IP flux scoring are shown in Table 1.
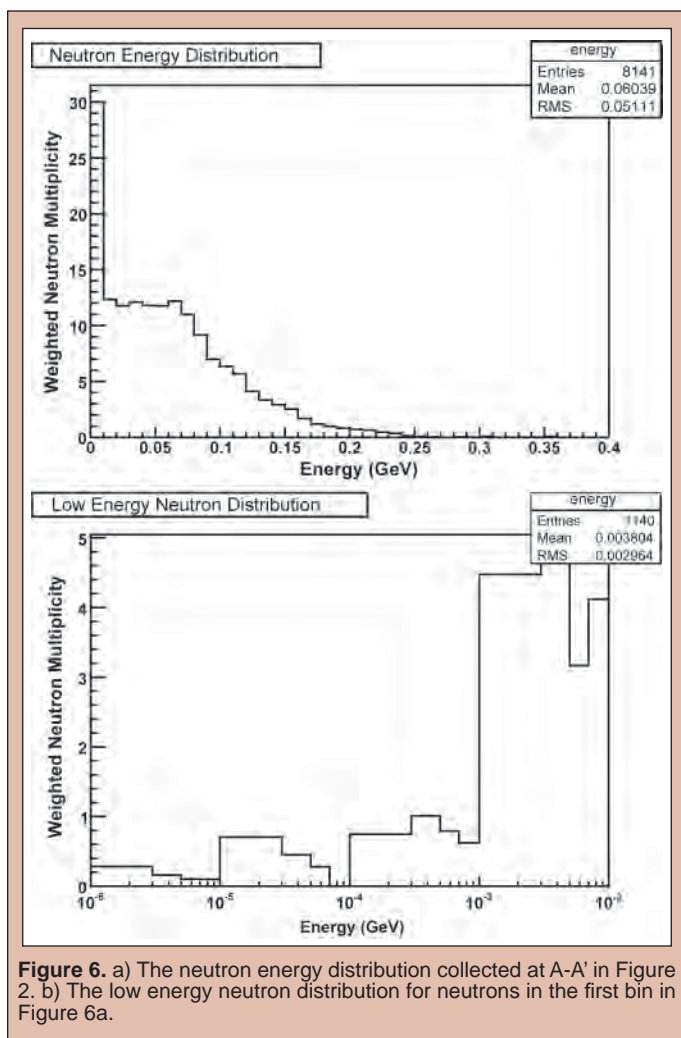
Figure 6. a) The neutron energy distribution collected at A-A' in Figure 2. b) The low energy neutron distribution for neutrons in the first bin in Figure 6a.
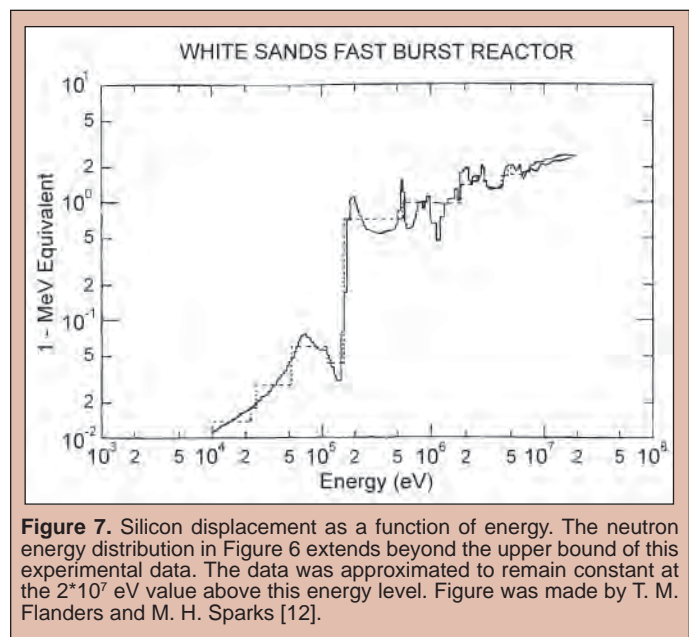
Figure 7. Silicon displacement as a function of energy. The neutron energy distribution in Figure 6 extends beyond the upper bound of this experimental data. The data was approximated to remain constant at the $2*10^7$ eV value above this energy level. Figure was made by T. M. Flanders and M. H. Sparks [12].
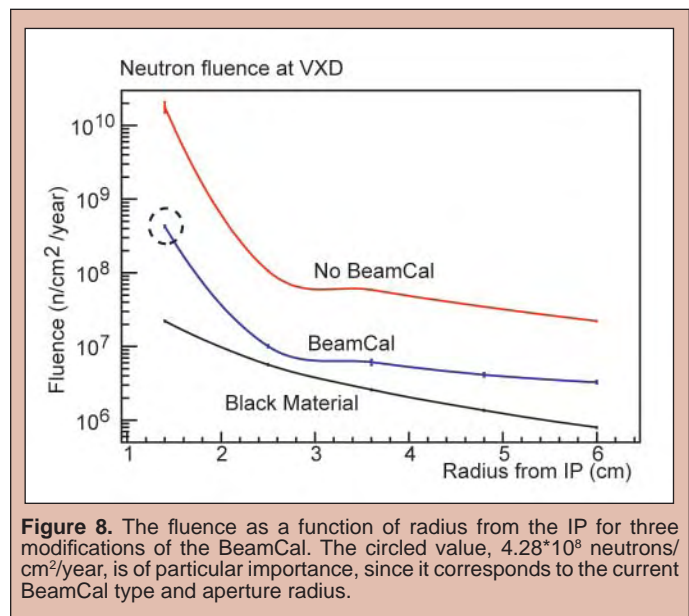
Figure 8. The fluence as a function of radius from the IP for three modifications of the BeamCal. The circled value, $4.28*10^8$ neutrons/cm^2/year, is of particular importance, since it corresponds to the current BeamCal type and aperture radius.

Figure 8 shows the fluence at the five layers of the inner detector for the three different modifications of the BeamCal. For the first layer, there was over an order of magnitude difference between the cases when there was a BeamCal and when there was no BeamCal, the former having a fluence of 4.3×10^8 neutrons/cm²/year and latter having one of 1.8×10^{10} neutrons/cm²/year. There was a larger difference between the cases when there was a BeamCal and there was black absorbing material, the latter having a fluence of 2.2×10^7 neutrons/cm²/year. In all three cases, the fluence in layers two to five dropped far below that in layer 1. The neutron fluence of 4.3×10^8 neutrons/cm²/year at the first layer when the BeamCal was in place is of particular importance, since it was found for the present status of the extraction line, and is shown circled in Figure 8. This neutron fluence at the detector is 1.2% of the fluence that reaches the IP, with the rest of the neutrons passing through the empty space in the detector or scattering off the Be beampipe harmlessly (see Figure 4).

The energy distribution of the neutrons that contribute to this fluence shows a large number of neutrons with energy greater than 10 MeV, implying that the current nominal fluence underestimates the displacement damage power (see Figure 9). This distribution, corrected with the information from Figure 8, gives the 1 MeV damage equivalent neutron fluence to be 9.3×10^8 neutrons/cm²/year, which is a factor of two larger than the unscaled value.

The symmetric positron beam contributes the same amount of displacement damage, meaning the final corrected fluence is 1.9×10^9 neutrons/cm²/year. In one year, this amounts to 19% of the 10^{10} neutrons/cm² flux that would degrade the vertex detector to the point of repair or replacement.

Figure 10 shows the fluence at the five layers of the detector as the BeamCal aperture was expanded; the fluence increases as the aperture is opened.

DISCUSSION AND CONCLUSIONS

The neutron fluence at the IP when there is no material in the extraction line, which was 8.3×10^{10} +/- 1.5×10^{10} neutrons/cm²/year, is the highest level of background that is possible at the detector from backscattering from the beam dump if one assumes that every particle that reaches the IP will damage the vertex detector. The collimator in front of the dump blocked roughly half of this flux, since the fluence decreased by a factor of two to 3.7×10^{10} +/- 3.3×10^{10} neutrons/cm²/year when the collimator was added. There was no appreciable increase in fluence when the tunnel was added given the current level of statistics, as it remained at 3.7×10^{10} +/- 2.3×10^{10} neutrons/cm²/year. This should not be interpreted to mean that there is no scattering off the tunnel walls, as the root-mean-square (RMS) deviation in the fluences once the collimator was added was more than 50% of the fluence itself. The amount of scattering is an important value to know when looking for potential solutions to reduce the backscattering problem. One solution being considered is to move the water dump out of a direct line of sight from the detector and to place a dipole immediately before the collimator to bend the trajectory of the beam towards the dump. If neutrons do not scatter off the tunnel walls, this would be an effective solution. However, if the neutrons do scatter off the tunnel walls and act like

a gas of particles moving back towards the detector, as suspected, then bending the beam would not reduce this background source. A further study of neutron scattering is being conducted.
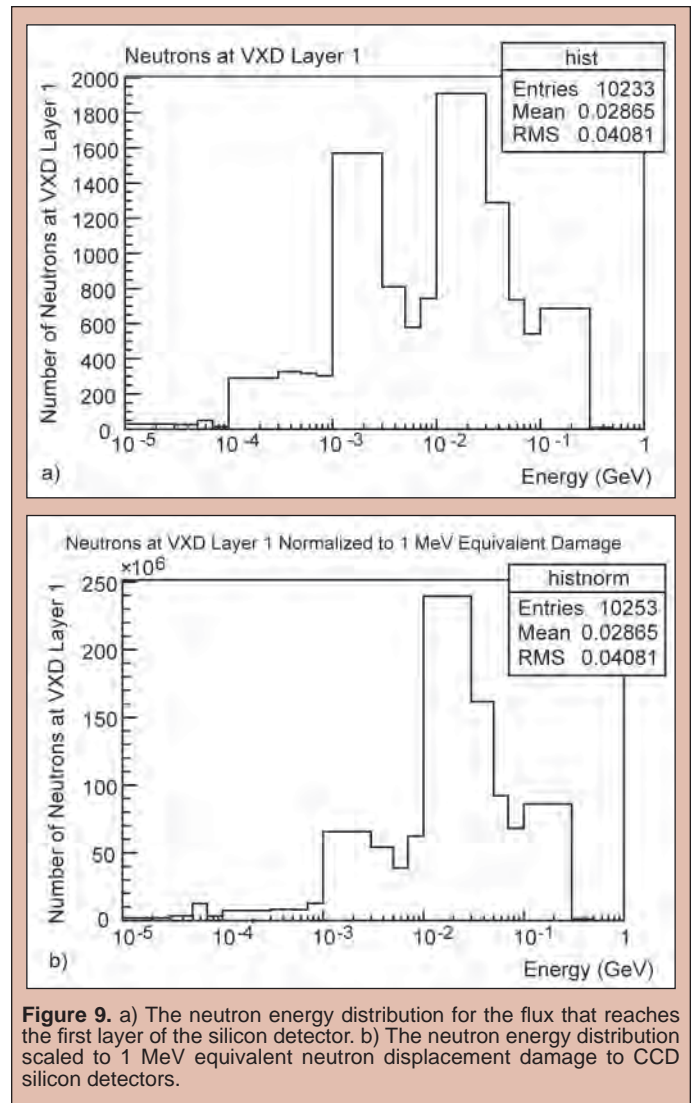
Figure 9. a) The neutron energy distribution for the flux that reaches the first layer of the silicon detector. b) The neutron energy distribution scaled to 1 MeV equivalent neutron displacement damage to CCD silicon detectors.
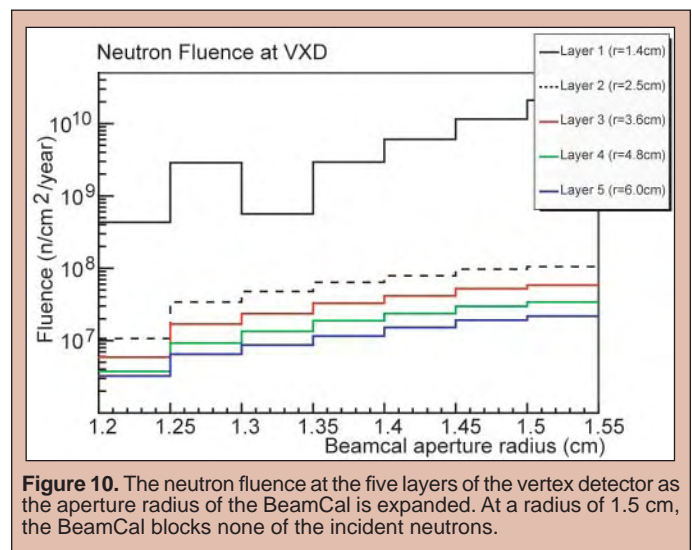
Figure 10. The neutron fluence at the five layers of the vertex detector as the aperture radius of the BeamCal is expanded. At a radius of 1.5 cm, the BeamCal blocks none of the incident neutrons.

The computation time and effectiveness of the biasing techniques for 6,000 incident electrons are shown in Table 1. As columns 6 and 7 show, statistics increased by a factor of 203 at the surface of the dump and by a factor of 59 at the IP. This allowed the estimation of a more stable IP fluence and provided a large distribution from which to sample in order to produce the neutron source. The total 'weight' of the neutrons recorded at z = 300 m and z = 0 m, shown in columns 4 and 5, was preserved as the different biases were applied, meaning that the biases did not obscure the underlying physics when improving the statistics. This validated the use of these biases with 10^4 and $5x10^4$ incident electrons when estimating the IP fluence.

The sharp drop in the fluence at layer 1 of the vertex detector from $1.8x10^{10}$ to $4.3x10^8$ neutrons/cm^2/year, shown in Figure 8, implies that the BeamCal acts like a collimator and impedes the flow of neutrons through it by 97%. Since this large amount of collimation is not the intent of the BeamCal, the effect of the fluence on its tungsten and silicon layers are being studied in further detail. When the black absorbing material is in place, there is no direct line of sight from the quadrupole bore to the detector, and the only neutrons that can hit the detector are those that scatter off of the beryllium beampipe. Thus, the further drop in the fluence, to $2.2x10^7$ neutrons/cm^2/year, for the case of the black absorbing material gives the estimate that 5.2% of the neutrons that hit the detector have scattered off of the beampipe, and the rest have hit it along their direct line of sight. Furthermore, the order of magnitude drop in the fluence between layer 1 and layers 2 to 5 of the silicon detector show that the outer layers are well shielded from the neutron fluence and are not a concern; attention should be focused on the innermost layer which takes the bulk of the displacement damage. The endcap sections of the silicon detector are being added and their effect on the fluence at all of the layers is being studied.

The neutron energy at the vertex detector is more heavily distributed above 10 MeV, as shown in Figure 9, which implies that the damage to the detector is greater than the nominal fluence. The corrected 1 MeV equivalent neutron fluence of $9.3x10^8$ neutrons/cm^2/year is properly normalized and can be compared to the threshold value of 10^{10} neutrons/cm^2. When the positron beam is considered and the fluence doubles to $1.9x10^9$ neutrons/cm^2/year, the neutron backscattering from the dump contributes 19% of the threshold value in one year. Even if this were the only background, the detector would degrade within 6 years; a longer lifetime is desired.

Although the current background level is not overwhelming, the relationship in Figure 10 is an important consideration when analyzing the effect of other neutron backgrounds in the detector. Two particularly important neutron backgrounds arise from electron-positron pairs produced from beam-beam interactions and synchrotron radiation produced from the quadrupoles used to focus the beams immediately before the IP; both products can hit the BeamCal and produce neutrons through electromagnetic showers [13]. This is the dominant source of neutron background, as the neutrons produced at the BeamCal are located near the vertex detector and cannot be shielded. A simple method to reduce this flux would be to open the BeamCal aperture to prevent interactions. However, as Figure 10 shows, a tradeoff exists, since doing so would increase the neutron background from the extraction line beam dump. In the extreme case, the BeamCal could be opened up larger than the extraction line quadrupole aperture, and the dump background would equal $2.1x10^{10}$ neutrons/cm^2/year, which would require the vertex detector to be replaced every six months.

These results have directed further studies towards the main sources of neutron backgrounds, including electron-positron pairs, Bremsstrahlung photons, and radiative Bhabha scattering, in order to obtain a complete picture of the overall neutron damage done to the vertex detector and to understand the tradeoffs that exist in attempting to suppress it. The detector model will also be improved and the effect of the neutron flux on the endcap tracking chambers and other elements will be studied. The neutron damage in the CCD silicon detector must be minimized in order to ensure detector longevity as well as minimal repairs of the detector components, allowing the ILC to effectively perform measurements and discover new fundamental physics.

REFERENCES

[1] ATLAS Collaboration, "ATLAS Detector and Physics Performance Technical Design Report," ATLAS TDR 14, CERN/LHCC 99–14, Vol. 1, pp. 3, 25 May 1999.

[2] G. Aarons *et al.*, "International Linear Collider Reference Design Report," ILC Global Design Effort and World Wide Study, Vol. 3: Accelerator, pp. 2.1-1 to 2.1-5, August 2007.

[3] G. Aarons *et al.*, "International Linear Collider Reference Design Report," ILC Global Design Effort and World Wide Study, Vol. 3: Accelerator, pp. 2.7-1 to 2.7-18, August 2007.

[4] R. B. Neal Editor, "The Stanford Two-Mile Accelerator," pp. 706–709, 1968.

[5] W. R. Dawes, Jr., "Overview of Radiation Hardening for Semiconductor Detectors," *Nuclear Instruments and Methods in Physics Research*, A 288, pp. 54–61, 1990.

[6] J. E. Brau and N. Sinev, "Operation of a CCD Particle Detector in the Presence of Bulk Neutron Damage,"

IEEE Transactions on Nuclear Science, vol. 47, no. 6, pp. 1898–1901, December 2000.

[7] The FLUKA team, *Online FLUKA manual*, INFN and CERN, version 2006.3b, March 2007.

[8] G. Lindstrom, "Radiation damage in silicon detectors," *Nuclear Instruments and Methods in Physics Research*, A 512, pp. 30–43, 2003.

[9] A. Chilingarov, J. S. Meyer, and T. Sloan, "Radiation damage due to NIEL in GaAs particle detectors," Nuclear Instruments and Methods in Physics Research, A 395, pp. 35–44, 1997.

[10] R. B. Neal Editor, "The Stanford Two-Mile Accelerator," pp. 1035–1040, 1968.

[11] N. Graf, SLAC Confluence, sidaug05, July 23, 2005, http://confluence.slac.stanford.edu/display/ilc/sidaug05

[12] T. M. Flanders and M. H. Sparks, "Monte Carlo calculations of the neutron environment produced by the White Sands Missile Range Fast Burst Reactor," *Nuclear Science and Engineering*, vol. 103, pp. 265–275, 1989.

[13] T. Abe *et al.*, "SiD Detector Outline Document," pp. 30, 19 May 2006.

Pearl E. Donohoo grew up in Cuyahoga Falls, Ohio. She earned a Bachelors of Science in mechanical engineering from the Franklin W. Olin College of Engineering where she was a member of the second graduating class. During her undergraduate career, she held two SULI internships at the National Renewable Energy Laboratory over the summers of 2006 and 2007. Pearl is currently a Masters student in the Technology and Policy Program at the Massachusetts Institute of Technology where she is researching alternative aviation fuels. She enjoys urban cafes and is a keen outdoorswoman.

Jason Cotrell is a Senior Project Leader at the National Renewable Energy Laboratory's National Wind Technology Center (NWTC). During his 11 year tenure at the NWTC, he has researched wind turbine drivetrains, advanced wind turbine rotors, wind-to-hydrogen systems, and equipment for wind turbine blade testing. His present focus is leading the effort to develop large blade testing facilities to be built in Massachusetts and Texas. Prior to the NWTC he obtained a BSME and MSME at UT Austin in 1995 and 1997.

Characterization of a Mobile Oscillatory Fatigue Operator for Wind Turbine Blade Testing

Pearl E. Donohoo and Jason Cotrell

ABSTRACT

Laboratory testing of wind turbine blades is required to meet wind turbine design standards, reduce machine cost, and reduce the technical and financial risks of deploying mass-produced wind turbine models. Fatigue testing at the National Wind Technology Center (NWTC) is currently conducted using Universal Resonance Excitation (UREX) technology. In a UREX test, the blade is mounted to a rigid stand and hydraulic exciters mounted to the blade are used to excite the blade to its resonant frequency. A drawback to UREX technology is that mounting hydraulic systems to the blade is difficult and requires a relatively long set-up period. An alternative testing technology called the Mobile Oscillatory Fatigue Operator (MOFO) has been analyzed. The MOFO uses an oscillating blade test-stand rather than a rigid stand, avoiding the need to place hydraulic systems on the blade. The MOFO will be demonstrated by converting an existing test-stand at the NWTC to an oscillating stand that can test blades up to 25 m in length. To obtain the loads necessary to design the MOFO, the system motion is modeled using rigid body and lumped mass dynamics models. Preliminary modeling indicates the existing stand can be converted to a MOFO relatively easily. However, the blade dynamic models suggest that blade bending moment distributions are significantly different for UREX and MOFO testing; more sophisticated models are required to assess the implication of this difference on the accuracy of the test.

INTRODUCTION

Over their lifetimes, wind turbine blades are exposed to uneven loadings. These result from varying wind distributions and uneven loading across the blade itself. Repetitive loading cycles stress blade materials and can cause failure. To certify that blades can withstand the forces and to test new blade concepts, they are first subjected to controlled fatigue and static tests. During fatigue testing, blades are preloaded with masses. They are then oscillated, both flapwise and edgewise, through approximately one million cycles to simulate field operating conditions. Testing is performed at the resonant frequency to minimize the input energy required by the test. The amplitude of oscillations is chosen to achieve a strain distribution in the blade required to accelerate conditions experienced in the field.

Fatigue testing is currently conducted at the National Renewable Energy Laboratory's National Wind Technology Center

Symbology	
θ_{b0}:	Initial angle to the center of gravity of the blade from the horizontal
θ_b:	Perturbation from θ_{b0}
θ_{ts0}:	Initial angle to the center of gravity of the test stand from the horizontal
θ_{ts}:	Perturbation from θ_{b0}
θ_h:	Angle from the horizontal to the actuator attachment point
m_b:	Mass of blade and added weights
m_{ts}:	Test stand mass
I_{ts}:	Test stand rotational moment of inertia about pivot
I_b:	Blade rotational moment of inertia about pivot
F_h:	Actuator force
k:	Spring constant of blade
ζ:	Damping ratio
c:	Damping coefficient

(NREL NTWC) using blade mounted testing apparatus (UREX); however, several sizes of UREX are required to accommodate a full range of blade sizes. The size of the UREX is limited by the weight it adds to the blade. Additionally, the hydraulic actuators require 3,000 psi fluid lines which travel with the UREX on the blade. The constant motion of the lines can cause leaks which require time to repair and are a safety hazard.

An oscillating test-stand would provide a universal testing mechanism, eliminate the need for moving hydraulic lines, and minimize the amount of setup time required. In addition, an oscillating stand could be used as a rigid stand for UREX testing by locking out the rotating degree of freedom. This paper explores the possibility of oscillating a current NWTC test-stand, here titled the Mobile Oscillatory Fatigue Operator (MOFO), to replace the blade mounted UREX apparatuses (Figure 1). To be a successful replacement, the MOFO must be able to generate testing loads and displacements

at the natural frequency of wind-turbine blades, and these loads must be generated with standard hydraulics. This paper discusses two dynamic models of the NWTC test-stand, their results, and preliminary design and component selection.
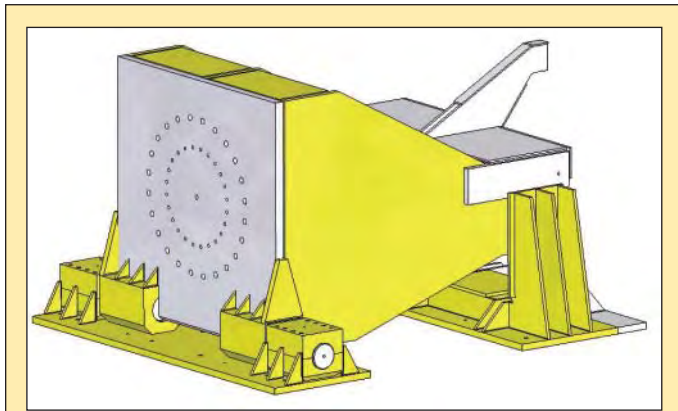
Figure 1. Model of existing NWTC test-stand.

Dynamic Load Models

Rigid body and lumped mass models were considered to determine the dynamic loading of the system at the hydraulic attachment point (Figure 2). In each model, the blade moment of inertia was calculated about the pivot point (A), the hydraulic force was constrained to act only in the vertical direction, and θ_{ts} and θ_b were decomposed into an initial angle (θ_{x0}) and a perturbation (θ_x).

Rigid Body Model

The rigid body model was analyzed first due to its simplicity. It is a single degree of freedom system with a forced angular displacement. In the rigid body model, the elasticity of the blade is assumed to be infinite such that perturbations of the blade and test-stand are equal. The perturbations (θ) are driven at a given amplitude (B) and the natural frequency of the blade (ω, Equation 1). The unknown term in Equation 1 is the hydraulic force (F_h), and time is the independent variable. The first two terms represent the moments due to the gravitational force on the blade and test stand. The second two terms represent moments due to the rotational inertias. The derivation of the equation of motion is found in Appendix A1.

$$\theta = B\sin(\omega t)$$
$$F_h(t) = \frac{-1}{l_b\cos(\theta_{b0})}(m_b gl_b\cos(\theta_{b0}-\theta)-m_{ts}gl_{ts}\cos(\theta_{ts0}+\theta)+\ddot{\theta}I_h+\ddot{\theta}I_{ts})$$

Equation 1: Rigid body governing equation of motion.

Elastic Lumped-Mass Model

The more complicated lumped mass model was analyzed to determine how blade elasticity affects the system. The lumped mass model is a base excitation model with two degrees of freedom. It
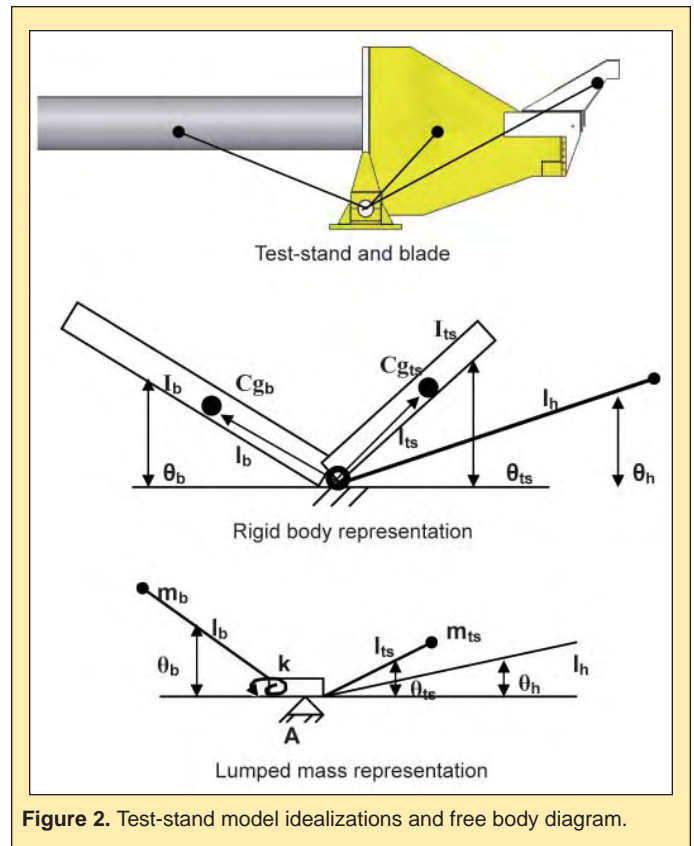
Figure 2. Test-stand model idealizations and free body diagram.

assumes the same perturbations as the rigid body model; however, it incorporates viscous damping and a torsion spring located at the pivot point to model the blade's elasticity (Equation 2). The derivation of the equation of motion is found in Appendix A2. As in Equation 1, the unknown term is the hydraulic force (F_h), and time is the independent variable. The additional fifth and sixth terms in the equation of motion represent the elasticity of the blade and aerodynamic viscous damping.

$$F_h(t) = \frac{-1}{l_b\cos\theta_{b0}}(m_b gl_b\cos(\theta_{b0}+\theta_b)-\ddot{\theta}_b I_h-m_{ts}gl_{ts}\cos(\theta_{ts0}+\theta_{ts})$$
$$+\ddot{\theta}_{ts}I_{ts}-k(\theta_b-\theta_{ts})-c(\dot{\theta}_b-\dot{\theta}_{ts}))$$

Equation 2: Lumped mass governing equation of motion

With the addition of the torsion spring, the amplitude and phase of motion of the test-stand are no longer equal. The hydraulic driving function and blade response functions are determined by solving the corresponding base excitation differential equation at the blade's natural frequency (Equation 3).

$$\theta_b = B\cos(\omega t - \frac{\pi}{2} - \arctan(\frac{1}{2\varsigma}))$$
$$\theta_h = \theta_{ts} = B\sqrt{\frac{1+(2\varsigma)^2}{(2\varsigma)^2}}\sin(\omega t)$$

Equation 3: Base excitation response and input functions

Loads

Model Inputs

The model is used to calculate forces for the worst case scenario, a hypothetical 25 m blade and a 9 m experimental blade (TX) currently being tested at the NWTC. The characteristic blade constants are derived from generalized equations and from past experience with blade testing (Table 1). Constants for the 9 m blade are drawn from current fatigue testing when available. In both cases a conservative 2% viscous damping ratio is used. The effective torsion spring constant, k, is determined by assuming the blade has constant mass and stiffness matrices. Using known natural frequency values and computed rotational inertia values, the spring constant is calculated using Equation 4. The rotational moment of inertia, center of gravity, and mass of the test-stand were determined using the SolidWorks model of the stand.

$$k = \omega^2 I$$

Equation 4: Definition of spring constant value.

Model Outputs

As shown in Table 2, the forces required in the lumped mass model are considerably lower than those in the rigid body model. Additionally, the amplitude, or ½ the difference between the maximum and minimum hydraulic force, is reduced by more than a factor of 100. This reduction of forces in the lumped mass model is a result of the blade oscillating at its natural frequency. As shown in Figure 3, the moment due to the elasticity of the blade and the moment due to the rotational inertia of the blade cancel.

The moment due to the rotational inertia of the test-stand is also reduced. Because the base excitation model includes the elastic properties of the blade, the test-stand displacement (O_h, Equation 3) required to produce a displacement on the blade (B) is lowered from 2° to 0.08°. This small angular displacement appears unintuitive. To ensure that the angular displacement is reasonable, displacements from an ongoing 9 m blade fatigue test were measured (Table 3). The 0.06° displacement at the center of gravity validates the result that only very small displacements are required to produce desired tip displacements and corresponding strains. The small angular

Model Constants					
	9 m			**25 m**	
m_b	(kg)	454	[1]	5440	[1]
m_{ts}	(kg)	4400	[2]	4400	[2]
r_b	(m)	2.4	[3]	8.2	[4]
r_{ts}	(m)	1.1	[2]	1.1	[2]
r_h	(m)	3.2	[2]	3.2	[2]
ω	(Hz)	1.2	[3]	1	[1]
I_b	(kg m²)	7.5e3	[5]	6.5e7	[5]
I_{ts}	(kg m²)	8590	[2]	8590	[2]
θ_b	(rad)	±0.035	[1]	±0.035	[1]
k	(Nm)	11e3	[6]	4.2e15	[6]
ζ	(Nms²)	0.02	[1]	0.02	[1]
c	(Nms)	0.048	[7]	0.040	[7]

[1] NWTC Estimate from current blades
[2] Measured from SolidWorks model of test-stand
[3] Measured from current blade fatigue test
[4] r_b=0.327(blade length), W. Musial and D. White, *Final Report for Large Blade Test Facility Scaling Study*. August 9, 2004.
[5] I=(1/12)m(blade length)²+$m_b r_b^2$
[6] k= $\omega^2 I$
[7] c=2$\omega\zeta$

Table 1. Constants in 9 m and 25 m models.

25m Blade	Rigid Body	Lumped Mass
Maximum Hydraulic Force (kN)	-58.9	-130.7
Minimum Hydraulic Force (kN)	-203.6	-131.9
Amplitude of Force Curve	144.7	1.2
Actuator Stroke (cm)	±11.2	±0.4

Table 2. Comparison of hydraulic forces and stroke from rigid body and base excitation models of NWTC test-stand and 25m blade. Negative numbers indicate that the actuator is pulling.

Figure 3. Comparison of rigid body and base excitation models for hypothetical 25 m blade. Note that in the base excitation model, the moment due to the rotational inertia of the test stand and moment due to damping overlap along the x-axis.

displacement translates into a short required stroke from the forcing hydraulic actuators (Table 2).

The elastic lumped-mass model is also used to compute forces for an experimental 9 m blade (Figure 3, Table 4). In this case, the magnitude of the required force is reduced because the moment due to the gravitational force on the blade is significantly reduced. The force is also reduced because the blade and test stand are in close to static equilibrium. In order to reduce the loads required by a 25 m blade, the test stand was also modeled with a large counterweight. The counterweight addition significantly lowers the loads required from the hydraulic actuator (Table 5).

	9m TX Blade Test	Model
Displacement at CG	± 0.060°	± 2.0°
Displacement at root		±0.078
Displacement at Tip	± 1.3°	± 2.0°

Table 3. Comparison of displacements on NWTC test-stand from base excitation model and 9 m TX blade fatigue test.

9m TX Blade	Rigid Body	Lumped Mass
Maximum Hydraulic Force (kN)	4.38	1.64
Minimum Hydraulic Force (kN)	-1.22	1.59
Amplitude of Force Curve	2.8	0.025

Table 4. Comparison of hydraulic forces from rigid body and base excitation models of NWTC test-stand and 9m blade. Negative numbers indicate that the actuator is pulling.

25m blade	Base Excitation	Statically Balanced Base Excita-
Maximum Hydraulic Force (kN)	-130.7	1.1
Minimum Hydraulic Force (kN)	-131.9	-1.1
Amplitude of Force Curve (kN)	1.2	1.1

Table 5. Comparison of hydraulic forces on NWTC test-stand from base excitation and statically balanced base excitation models.

Component Considerations

Hydraulic Actuators

The hydraulic actuators should be sized to exceed the maximum loads imposed by base oscillation of a 25 m blade. For a successful certification test, actuators must supply a smooth sinusoidal input force; double ended actuators ensure this input force. Additionally, actuators should be oversized to ensure a sufficient margin of safety to avoid damage. Fatigue rated cylinders should be used for the longevity of the system. The prototype test-stand will use 14.7 kN (3.3 kip) fatigue rated actuators already owned by the laboratory.

Load Cell

A load cell is placed in line with the hydraulic actuators to measure the supplied force; however, the rigidity of the stand cannot be compromised. A stand which is not rigid will distort test results.

Lash should be removed from the system using spiral washers or another like system.

Bearings

Unlike the UREX, the MOFO requires the test-stand to oscillate. Radial loads dominate the test-stand, but axial loads are also present as a result of twist bending in blades and possibly dual axis testing; bearings must carry both loads. The bearings chosen must also avoid lubrication issues with repetitive small angular displacements.

Safety System

Although displacements on the test-stand are small, the center of gravity of the system with large blades lies outboard of the test-
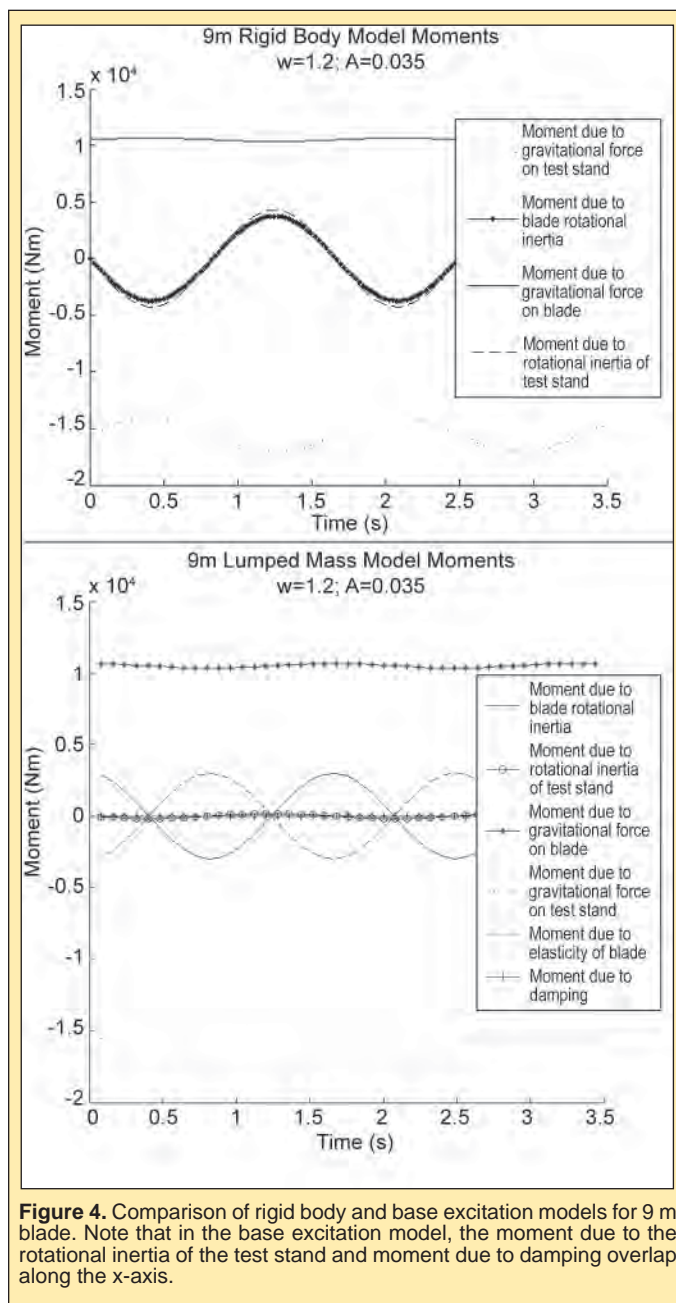
Figure 4. Comparison of rigid body and base excitation models for 9 m blade. Note that in the base excitation model, the moment due to the rotational inertia of the test stand and moment due to damping overlap along the x-axis.

stand. If the hydraulic pressure is cut, or if user-error occurs, the test-stand will rotate forward until the blade contacts the floor or rotate backward until the blade either contacts the ceiling or the actuator retracts enough to hit the cushion. This may damage the blade and poses a serious safety risk. Using the hydraulic actuator's cushion, dampers on the test stand, and blade straps should be incorporated to the stand's design.

Blade Moment Distributions

For simplicity and design characterization, the above modeling assumes that the blade has a constant bending moment distribution. Real blades, however, have complex bending moment distributions based on the individual design, materials, and construction. With previous blade mounted testing designs, loads have been applied at the center of mass of the test stand. Using the MOFO, however, loads will be applied at the root of the blade. A basic model comparing the load application showed differences in internal bending moment distributions. This finding has implications for the individual blade testing but does not affect the overall loads and characterization of the test stand.

CONCLUSIONS AND FUTURE WORK

Through the preceding modeling and conceptual design process, it has been concluded that creating a 25 m prototype Mobile Oscillatory Fatigue Operator (MOFO) from a current NWTC test-stand will be able to generate loads and displacements required to replace the current UREX testing system. The MOFO will simplify testing as a universal test stand. Two dynamic models were completed for 9 m and 25 m blades to size hydraulics. For the project to proceed, the dynamic model should be validated. This can be achieved through further dynamic modeling using software such as SIMPACK or ADAMS or by completing a fatigue test on the 9 m TX blade and comparing the results. Further modeling should also be completed to determine the moment distribution within blades using the new test methodology.

ACKNOWLEDGEMENTS

A.1 Derivation of Rigid Body Model

The torques are summed about the pivot, A.

$$\Sigma\tau_A = \tau_{ts} - \tau_b + \tau_{Fh}$$

Each torque can be written in terms of its dependent terms.

It is assumed that the actuator acts only in the vertical direction.

$$\tau_{Fh} = F_h(t)r_h = F_h(t)l_h\cos\theta_{h0}$$

The test stand and blade perturbations are driven at the natural frequency of the blade, ω and desired amplitude, *B*.

$$\theta = B\sin(\omega\tau)$$
$$\dot\theta = B\omega\cos(\omega\tau)$$
$$\ddot\theta = B\omega^2\sin(\omega\tau)$$

The resulting torque from the blade can be split into two a static torque due to gravity and a dynamic torque due to rotational inertia, as well as an initial angle θ_{b0} and the perturbation, θ.

$$\tau_b = \tau_{b\text{-}static} + \tau_{b\text{-}dynamic}$$
$$\tau_{b\text{-}static} = -m_b gr_b = -m_b gl_b\cos(\theta_b) = -m_b gl_b\cos(\theta_{b0}-\theta)$$
$$\tau_{b\text{-}dynamic} = \ddot\theta_b I_b = -\ddot\theta I_b$$

The negative sign results from the blade being fastened on the opposite side of the pivot point as the actuators.

The same procedure is followed for the torque from the test stand.

$$\tau_{ts} = \tau_{ts\text{-}static} + \tau_{ts\text{-}dynamic}$$
$$\tau_{ts\text{-}static} = -m_{ts} gr_{ts} = -m_{ts} gl_{ts}\cos(\theta_{ts}) = -m_{ts} gl_{ts}\cos(\theta_{ts0}+\theta)$$
$$\tau_{ts\text{-}dynamic} = \ddot\theta_{ts} I_{ts} = \ddot\theta I_{ts}$$

Substituting back in terms yields

$$F_h(t) = \frac{-1}{l_h\cos(\theta_{h0})}\left(m_h gl_b\cos(\theta_{b0}-\theta) + \ddot\theta I_b - m_{ts} gl_{ts}\cos(\theta_{ts0}+\theta) + \ddot\theta I_{ts}\right)$$

A.2 Derivation of Lumped Mass Model
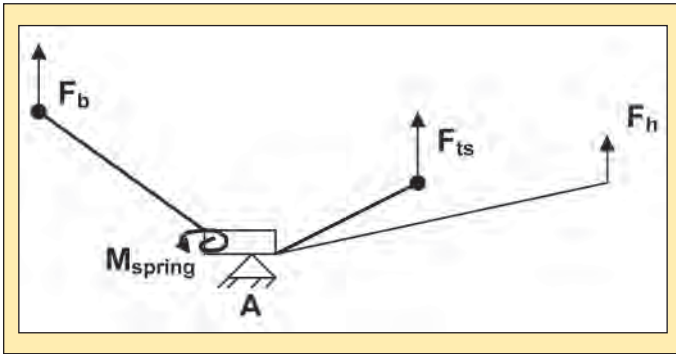
The same governing equation can be derived for the lumped mass model as the rigid body model with the addition of a spring and a damping term.

$$F_h(t) = \frac{-1}{l_h \cos\theta_{h0}}(m_b \, gl_b \cos(\theta_{b0} + \theta_b) - \ddot{\theta}_b I_b - m_{ts} \, gl_{ts} \cos(\theta_{ts0} + \theta_{ts})$$
$$+ \ddot{\theta}_{ts} I_{ts} - k(\theta_b - \theta_{ts}) - c(\dot{\theta}_b - \dot{\theta}_{ts}))$$

However, the input and response functions, θ_b and θ_{ts}, are no longer governed by the simple $\theta = \sin(\omega t)$. The governing equation describing the base excitation vibration of the blade with a given sinusoidal input is a second order linear differential equation[1].

$$\theta_{ts} = Y \sin(\omega t)$$
$$I\ddot{\theta}_b + c(\dot{\theta}_b - \dot{\theta}_{Fh}) + k(\theta_b - \theta_{ts}) = 0$$

The solution for the response function, θ_b, is dependent only the system damping when driven at the blade's natural frequency. When the damping coefficient is small ($\varsigma \approx < 0.05$), the blade trails the test stand approximately 90° out of phase.

$$\theta_b = \omega Y \left[\frac{\omega^2 + (2\varsigma\omega)^2}{(2\varsigma\omega^2)^2}\right]^{1/2} \cos(\omega t - \frac{\pi}{2} - \arctan(\frac{1}{2\varsigma}))$$
$$= Y \left[\frac{1 + (2\varsigma)^2}{(2\varsigma)^2}\right]^{1/2} \cos(\omega t - \frac{\pi}{2} - \arctan(\frac{1}{2\varsigma}))$$

The coefficient, Y, is unknown; however, the amplitude of the blade displacement is driven. The desired amplitude B is known. From the above equation, the amplitude of the input function Y can be solved.

$$Y = B \left[\frac{\omega^2 + (2\varsigma\omega)^2}{(2\varsigma\omega^2)^2}\right]^{-1/2} = B \left[\frac{1 + (2\varsigma)^2}{(2\varsigma)^2}\right]^{-1/2}$$

The governing equation is reduced to one unknown, $F_h(t)$.

$$F_h(t) = \frac{-1}{l_h \cos(\theta_{h0})}(m_b \, gl_b \cos(\theta_{b0} + B\cos(\omega t - \frac{\pi}{2} - \arctan(\frac{1}{2\varsigma})))$$
$$+ B\cos(\omega t - \frac{\pi}{2} - \arctan(\frac{1}{2\varsigma}))I_b$$
$$- m_{ts} \, gl_{ts} \cos(\theta_{ts0} + B\left[\frac{1 + (2\varsigma)^2}{(2\varsigma)^2}\right]^{-1/2} \sin(\omega t) - \omega^2 B\left[\frac{1 + (2\varsigma)^2}{(2\varsigma)^2}\right]^{-1/2} \sin(\omega t)I_{ts}$$
$$- kB(\cos(\omega t - \frac{\pi}{2} - \arctan(\frac{1}{2\varsigma})) - B\left[\frac{1 + (2\varsigma)^2}{(2\varsigma)^2}\right]^{-1/2} \sin(\omega t))$$
$$+ cB\omega(\sin(\omega t - \frac{\pi}{2} - \arctan(\frac{1}{2\varsigma})) - \left[\frac{1 + (2\varsigma)^2}{(2\varsigma)^2}\right]^{-1/2} \sin(\omega t)$$

The value of k is calculated from the known natural frequency of the blade and rotational moment of inertia.

$$k = \omega^2 I_b$$

The blade rotational inertia and spring term dependent on θ_b cancel.

$$F_h(t) = \frac{-1}{l_h \cos(\theta_{h0})}[m_b \, gl_b \cos(\theta_{b0}) + B\cos(\omega t - \frac{\pi}{2} - \arctan(\frac{1}{2\varsigma})) +$$
$$- m_{ts} \, gl_{ts} \cos(\theta_{ts0}) + B\left[\frac{1 + (2\varsigma)^2}{(2\varsigma)^2}\right]^{-1/2} \sin(\omega t))$$
$$- \omega^2 B\left[\frac{1 + (2\varsigma)^2}{(2\varsigma)^2}\right]^{-1/2} \sin(\omega t)I_b + cB\omega(\sin(\omega t - \frac{\pi}{2} - \arctan(\frac{1}{2\varsigma})))]$$

If the test stand is balanced, the static terms also cancel, leaving a simplified equation.

$$F_h(t) = \frac{-1}{l_h \cos(\theta_{h0})} [-\omega^2 B\left[\frac{1 + (2\varsigma)^2}{(2\varsigma)^2}\right]^{-1/2} \sin(\omega t)I_{ts}$$
$$+ cB\omega(\sin(\omega t - \frac{\pi}{2} - \arctan(\frac{1}{2\varsigma}))$$
$$- \left[\frac{1 + (2\varsigma)^2}{(2\varsigma)^2}\right]^{-1/2} \sin(\omega t)) + kB(-B\left[\frac{1 + (2\varsigma)^2}{(2\varsigma)^2}\right]^{-1/2} \sin(\omega t))]$$

---

1 Daniel J Inman, *Engineering Vibration.* Prentice-Hall Inc. Englewood Cliffs, NJ: 1994.

Amy Gao is a resident of the beautiful Washington State. Growing up around the natural paradox of water and desert, she lives for nature and loves contradictions. As a child, she vastly enjoyed running between the evergreen trees with her beloved twin brother, letting their imaginations roam free. Now, Amy is studying mechanical engineering at Olin College in Needham, MA, and hopes to earn her Ph.D. in engineering one day. She held one SULI internship at Pacific Northwest National Laboratory in the summer of 2007. Amy likes chocolate, adventuring, design, running, and all things bright and shiny.

Robert Heck is a senior research scientist at the Pacific Northwest National Laboratories (PNNL). He received his Ph.D. from the University of Florida in 1996 for a study of the structure and function of murine carbonic anhydrase isozyme V. His postdoctoral research at the University of Pennsylvania focused on using xray crystallography to explore carbonic anhydrase isozymes and several other proteins. His research activities as PNNL have focused on using solid state NMR techniques to investigate the structure and function of zinc, magnesium, copper, and calcium metalloproteins.

Large Scale Production, Purification, and ^{65}Cu Solid State NMR of Azurin

Amy Gao and Robert W. Heck

ABSTRACT

This paper details a way to produce azurin with an efficiency over 10 times greater than previously described and demonstrates the first solid state nuclear magnetic resonance spectrum of ^{65}Cu(I) in a metalloprotein. A synthetic gene for azurin based upon the DNA sequence from *Pseudomonas aeruginosa* including the periplasmic targeting sequence was subcloned into a T7 overexpression vector to create the plasmid pGS-azurin, which was transformed into BL21 (DE3) competent cells. The leader sequence on the expressed protein causes it to be exported to the periplasmic space of *Escherichia coli*. Bacteria grown in a fermentation unit were induced to overexpress the azurin, which was subsequently purified through an endosmotic shock procedure followed by high performance liquid chromatography (HPLC). 1,500 mg of azurin were purified per liter of culture. ^{65}Cu(II) was added to apo-azurin and then reduced. The ^{65}Cu metal cofactor in azurin was observed with solid state nuclear magnetic resonance (NMR) to determine any structural variations that accompanied copper reduction. This is the first solid state NMR spectra of a copper(I) metalloprotein. Analysis of the NMR spectra is being used to complement hypotheses set forth by x-ray diffraction and computational calculations of electron transfer mechanisms in azurin.

INTRODUCTION

Pseudomonas aeruginosa has been shown to be highly cytotoxic to certain cancer cells. It produces the protein azurin in the presence of cancer cells, which stabilizes the tumor suppressor p53, inducing apoptosis [1]. However, *P. aeruginosa* is an opportunistic bacterium that is often lethal to immunosuppressed patients, including those with AIDS, cystic fibrosis, severe burns, and cancer. The bacterium thwarts cancer from claiming the life of the patient, but it may live on as a parasite, ultimately killing the patient. However, it is the protein azurin, produced by *P. aeruginosa*, not the bacterium itself, that cancerous cells find deadly. Previous reports show up to 100 mg of recombinant azurin have been produced per liter of culture [2]. With slight alterations to a method provided by Karlsson *et al.* [3], we found that the yield can be increased over tenfold. These methods are described in this paper.

The structure and function of the redox copper metalloprotein azurin has been studied extensively by redox biochemistry, x-ray diffraction, and computational approaches. Azurin is a 14-kilidalton (kDa) protein, composed of a beta barrel backed by an alpha helix. It is a blue-copper metalloprotein characterized by a deep azure hue when Cu(II) is bound to the protein by its three planar trigonal ligands — two histidines and a cysteine. An axial methionine and an axial glycine backbone carbonyl complete the trigonal bipyramidal ligand sphere around the copper atom [4] (Figure 1).

The reduced copper azurin has been shown to have a similar structure to the oxidized form by Crane *et al.* [4] (Figure 2), but the postulated changes in copper-ligand bond lengths and angles are less than the experimental errors of x-ray crystallographic structure determination for the oxidized and reduced forms. The ability of azurin to lose and gain electrons gives it the role of an electron-transfer protein in *P. aeruginosa*, possibly one that donates electrons to nitrite reductase under stress. The redox reactions cause some slight structural changes in the protein but cause a large change in the visible absorption spectrum of the bound copper ion. Although much is known about the chemical environment around the copper in oxidized azurin, solid state NMR of ^{65}Cu provides some valuable new insights into the previously spectroscopically silent reduced form of azurin.

1. Chemicals and Solutions

Isopropyl-β-D-thiogalactopyranoside (IPTG), Antifoam 204 and Terrific Broth (TB) from Sigma-Aldrich, Rainbow Markers from Amersham (Buckinghamshire, United Kingdom), *E.coli* strain BL21(DE3) from Novagen (Merck KGaA, Darmstadt, Germany) were used . Buffer A was composed of 20% sucrose, 0.3 M Tris, 1 mM EDTA, pH 8. Buffer B was 1 mM $MgCl_2$. Solution C was 0.5 M ammonium acetate (pH 4.1). Solution D was 0.05 M ammonium acetate. All solutions were prepared at 20°C. Cobalt substituted recombinant human carbonic anhydrase II was obtained from Robert Heck (PNNL) and prepared as described in Lipton *et al*. Briefly, the carbonic anhydrase was purified from cobalt supplemented and zinc depleted minimal media cultures of a pET/ *E.coli* expression system [5].

2. Cloning and expression system construction

A synthetic gene was constructed by GenScript Corporation (Piscataway, NJ) from the amino acid sequence of *P. aeruginosa* azurin including the N-term targeting sequence. The codon frequency was optimized for expression in *E. coli*, and the gene was cloned into Genscript's pET expression plasmid, pGS-21A, at the NdeI and HindIII restriction sites to give plasmid pGS-azurin. Plasmid DNA was transformed into BL21 (DE3) competent cells.

3. Fermentation and protein overexpression

E. coli transformants containing pGS-azurin were initially grown on LB/Agar (100 mg/L ampicillin) plates and then used to inoculate 50 mL Terrific Broth (TB) shaken cultures (with 100 mg/L ampicillin) at 37°C overnight. 200 mL of overnight culture was used to inoculate a 2 liter New Brunswick Scientific (Edison, NJ) Bio Flow 110 Fermentor filled with 1.6 L TB (100 mg/L ampicillin). Pumps for antifoam, 5 M ammonium hydroxide, and 40% w/v glucose were attached to the system. The temperature, pH, glucose level, and dissolved oxygen level were monitored through the program BioCommand Plus. Temperature was kept at 35°C and pH at 7. Glucose was delivered to the system as necessary, determined through the effect of glucose pulses on the dO_2 level similar to the methods of Akesson [6]. Glucose feed rates increased from 0 to 0.46 mL/min during the six hours prior to induction. A dO_2 level of 30% was maintained through adjustment of first the agitation and, subsequently, the oxygen gas distributed to the system. Cell growth was presumed if motor agitation continually increased. When growth appeared to be stunted at 2.5 hours and without glucose being rate limiting, 10 mL of a mineral solution (0.5 M ammonium sulfate, 1 M KH_2PO_4, 1 M Na_2HPO_4) were added. Cell growth was monitored through the performance of an optical density (OD) measurement every hour after start and before induction.

Induction was performed at 6 hours, when the optical density of the culture was approximately 20, by the addition of 0.1 mM IPTG. Following induction, the glucose feed was reduced to 0.17 mL/min
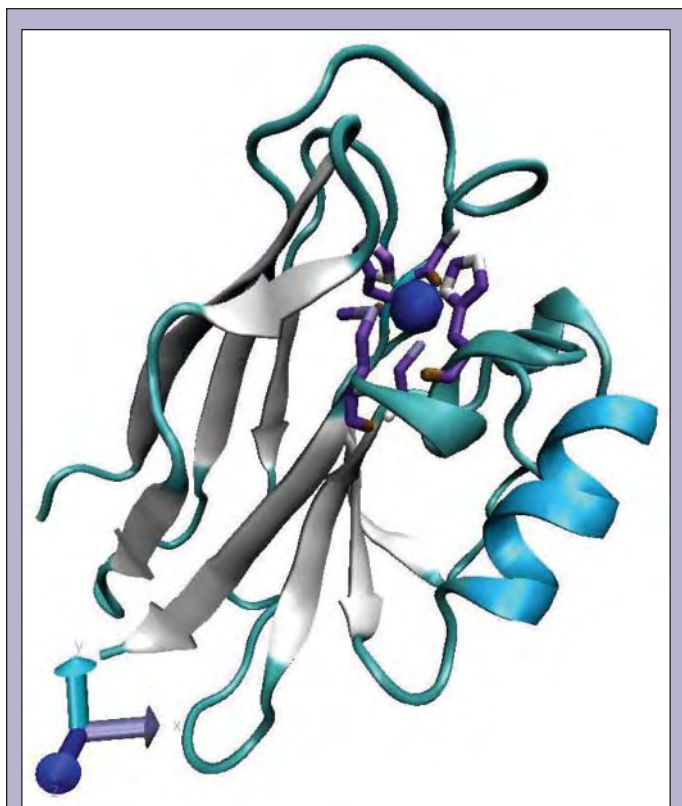
Figure 1. A structural model of the oxidized-copper azurin molecule. The copper ion is bound by his 46 and 117, cys 112, met 121, and gly 45. (Crane et. al., 2001.)
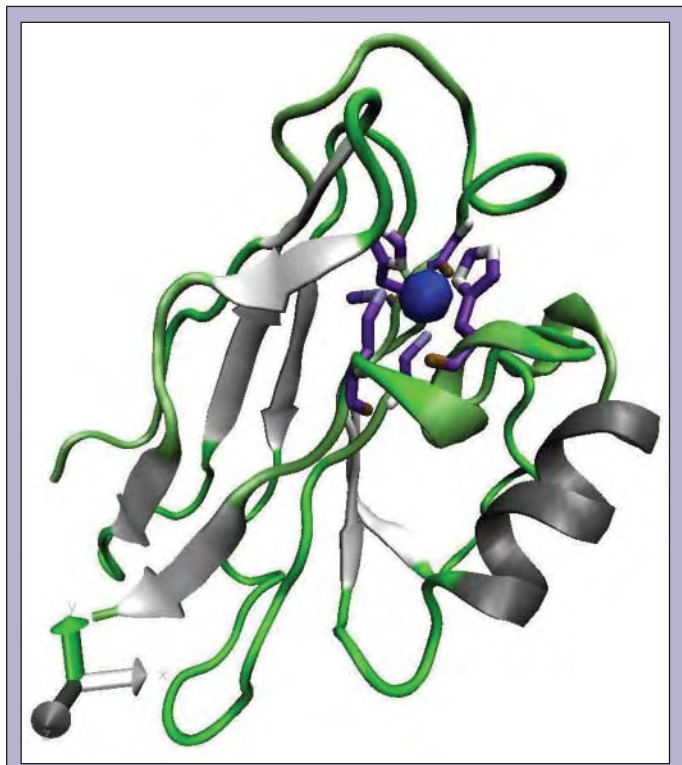
Figure 2. A structural model of the reduced-copper azurin molecule. (Crane et. al., 2001.)

and temperature was reduced to 25°C. Cells were harvested 17 hours after induction, and used immediately for isolation of protein.

4. Azurin purification

The leader sequence on the azurin protein causes *E. coli* to export the protein to the periplasmic space of the cell [7]. By performing an endosmotic shock procedure on the cells, the azurin can be extracted in a lightly contaminated form, and further purified.

The fermentor cell culture was centrifuged at 3,000 x G for 30 minutes at 4°C to harvest the cells. Wet weight of cells was about 200 grams. The cell pellets were washed twice with 300 mL of buffer A and centrifuged at 6,250 x G for 25 and 30 minutes at 4°C. Because a distinct cell pellet was not formed after the second wash, the cell suspension was centrifuged an additional 20 minutes at 7,000 x G (4°C). The supernatant was decanted once again, and cells were resuspended in 300 mL of buffer B, placed into a -20°C chamber for 10 minutes, then at 4°C for an hour to release periplasmic protein by osmotic shock. This mixture was then centrifuged at 17,000 x G for 20 minutes (4°C) and the supernatant containing azurin was collected. Solution C was added in an amount equal to 1/10 the total volume of supernatant to precipitate out unwanted proteins and the resulting mixture was allowed to settle at 4°C for 24 hours.

At this point two tests were performed to detect the presence of azurin. First, sodium dodecyl sulfate polyacrylamide gel electrophoresis (SDS-PAGE) was executed using a Mini Protean II system (Bio-Rad, Hercules, CA) with 10–20% tris-tricine polyacrylamide gels, at a constant current of 40 amps for approximately 1 hour. Samples were run against Amersham Rainbow Markers. Secondly, a $CuCl_2$ addition test was performed as described below. The SDS-PAGE revealed a dark band at the expected 14 kDa for the mature form of azurin lacking the periplasmic targeting sequence.

The $CuCl_2$ test consisted of adding 0.08 mL of a 0.2 M $CuCl_2$ solution to 30 mL periplasmic extract and observing the ensuing color change. The extract slowly darkened to a deep blue color over the course of 24 hours, indicating azurin presence. Analysis of the sample with a Beckman Model 640 DU spectrophotometer allowed us to form preliminary estimates as to the size of the sample. Due to the size of the sample, it was now split into two equal parts. Half was frozen and stored at -20°C, while we continued our experiments with the other half.

For the solid state NMR experiments, it was necessary to add highly enriched ^{65}Cu to the azurin. 20 mg of 97% isotopically enriched ^{65}Cu Oxide (Isotec, Sigma-Aldrich, St. Louis, MO) was dissolved with 0.6 mL of 12 M hydrochloric acid, dried under a stream of N_2 gas, then reconstituted in water for a 0.1 M concentration. All of the 0.1 M $CuCl_2$ solution was added to the azurin sample, and allowed to sit overnight.

The extract was further purified by high performance liquid chromatography (HPLC) through a 10 x 1.6 cm column with Poros 20 CM weak cation exchange resin (Boehringer Mannheim, Mannheim, Germany). A gradient from pH 4.1 to 5.1 in solution D was used to elute the sample with the major azurin peak eluting at pH 4.75. Fractions exhibiting high absorbance at 625 nm were pooled. The pH was adjusted to 8 with 1.5 M ammonium hydroxide. The

sample was concentrated with an Amicon ultrafiltration unit (76 mm 1,000 nominal molecular weight limit (NMWL) membrane, filter code: YM1), dialyzed against 4 L of water overnight, then freeze-dried. A small amount of freeze dried ^{65}Cu azurin was overloaded onto SDS-PAGE to estimate purity (Figure 3). A few milligrams of freeze dried azurin were accurately weighed out, resuspended in dH_2O, and absorbance was measured at 625 nm to determine an accurate extinction coefficient.
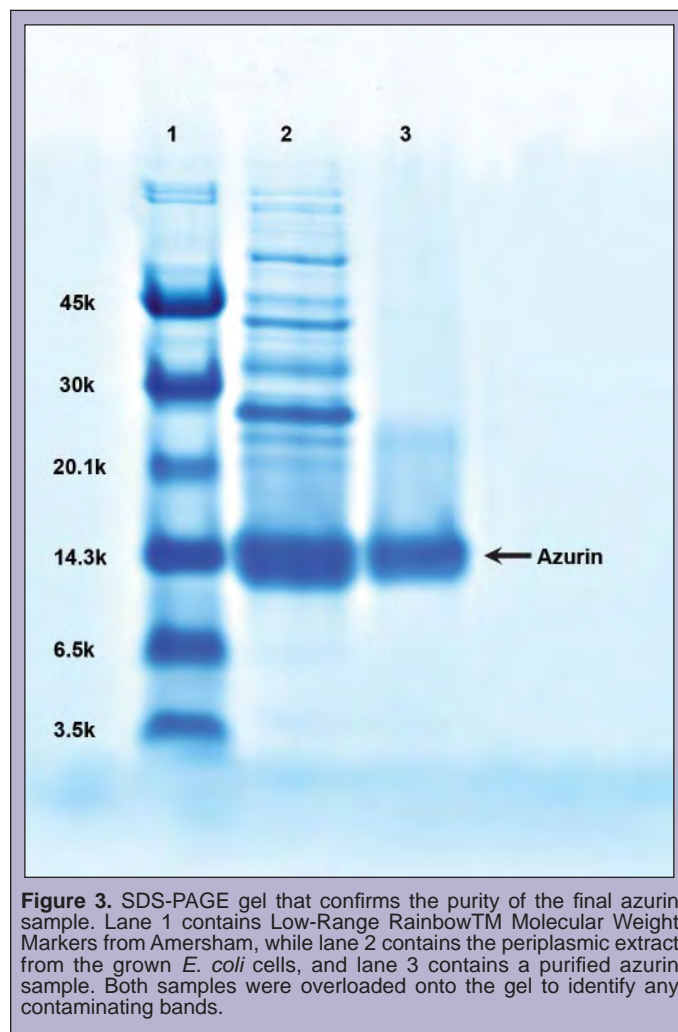
Figure 3. SDS-PAGE gel that confirms the purity of the final azurin sample. Lane 1 contains Low-Range RainbowTM Molecular Weight Markers from Amersham, while lane 2 contains the periplasmic extract from the grown *E. coli* cells, and lane 3 contains a purified azurin sample. Both samples were overloaded onto the gel to identify any contaminating bands.

5. NMR Analysis

70 mg of azurin were weighed out and mixed with 20 mg of cobalt carbonic anhydrase as a dopant [8] in 150 μL of 50 mM ascorbate and 30% glycerol. The ascorbate solution, which is used to reduce the copper in the azurin sample, had been previously sparged with N_2 gas for 20 minutes to eliminate any dissolved oxygen. The final sample of approximately 0.2 mL faded from a dark blue to a clear light purple solution, which was pipetted into a 5x20 mm glass NMR tube for analysis.

A Varian $^{UNITY}INOVA$ spectrometer with a medium-bore (63 mm) Oxford Instruments magnet and an Oxford Instruments

continuous flow cryostat was used to collect NMR data at 18.8 T (227.144 MHz for ^{65}Cu and 799.691 MHz for ^{1}H) and a sample temperature of 10 K. Zinc RF coils were built for this experiment to eliminate interference from the previous copper coils in the probe described in Lipton et al. [9]. Solid-state nuclear magnetic resonance was performed as previously described [5, 10] with the following parameters: The proton $\pi/2$ pulse width used for cross polarization (CP) was 7 μs with a 30 ms contact time and a 30 s recycle delay. The ^{65}Cu π pulses used in the quadrupole Carr-Purcell-Meiboom-Gill (QCPMG) train were 19 μs with a τ of 150 μs with a decoupling field of 44 kHz for 512 transients. The ^{65}Cu RF frequency was offset for each experiment to trace the overall pattern of the lineshape.

RESULTS

Azurin production was maximized by fermentation to a high cell density with glucose limited growth and oxygen supplementation and a lengthened post-induction incubation at a reduced temperature (25°C). The average growth rate was 3.3 AU·h^{-1} and the culture was allowed to grow to a density of approximately 10.4 g dry cell weight/L (dcw/L) before induction.

The overnight post-induction incubation, as opposed to a 3 hour post-induction incubation, was shown to result in a higher azurin yield, as well as a lower retention of azurin within the cell membrane where it would be more difficult to harvest.

In the harvest procedure, the wash and endosmotic shock procedures have been streamlined. Centrifuging the cell tubes for 20–30 minutes at 6,250 x G was found to be ineffective in forming a distinct cell pellet a majority of the time. For future methods, it is recommended to centrifuge the tubes at 7,000 x G for a minimum of 20 minutes per step.

Azurin has been previously shown in our lab [11] to be mostly apoprotein following the endosmotic shock procedure. This apo-azurin readily takes up Cu(II) ions, resulting in a strong absorbance maximum appearing at 625 nm with an extinction coefficient of 8400 M^{-1} cm^{-1}. Thus, a preliminary estimate as to the total amount of azurin produced was determined at this point by measuring the absorbance of the dark blue azurin sample resulting from the CuCl$_2$ addition with a Beckman DU 640 spectrophotometer. Absorbance was measured to be 2.10 AU at 625 nm, which amounts to between 1,600 and 2,000 mg of azurin, by the estimated extinction coefficient.

Regarding purification of the azurin sample through HPLC, it was noted that the column equilibration time is unacceptably lengthy. This is likely due to the high buffering capacity of the column in conjunction with inadequate buffer strength of the chosen buffers. Therefore, additional experiments must be conducted to determine an appropriate buffer or a more suitable column.

Ultimately, 1.20 grams of ^{65}Cu labeled azurin were obtained. Figure 3 shows the results of SDS-PAGE of the purified protein. By overloading the purified azurin sample, several contaminating bands become visible, but they are estimated to be less than 5% of the total protein present in the azurin preparation. This amounts to approximately 1,500 mg of azurin per liter of culture, and approximately 11.8 mg of azurin per gram of wet cells. In

addition, an extinction coefficient of 5,240 M^{-1} cm^{-1} was obtained for azurin.

The composite spectrum or skyline projection of the resulting frequency offset NMR experiments is depicted in Figure 4. The lineshape spans from +1.33 MHz to -2.11 MHz relative to CuCl at 0 Hz (0 ppm). Assuming a quadrupole dominated lineshape, extracted parameters are C_q of 71.2 MHz, η_q of 0.2 and an isotropic shift of 50 kHz from CuCl. The calculated NMR lineshape from these parameters is shown in Figure 4 above the experimental spectrum. The region of intensity at the center of the experimental spectrum is an artifact or impurity and not due to the azurin. This was confirmed by a series of Bloch decay experiments directly observing the copper and the region was found to be more consistent with the simulated spectrum (data not shown).
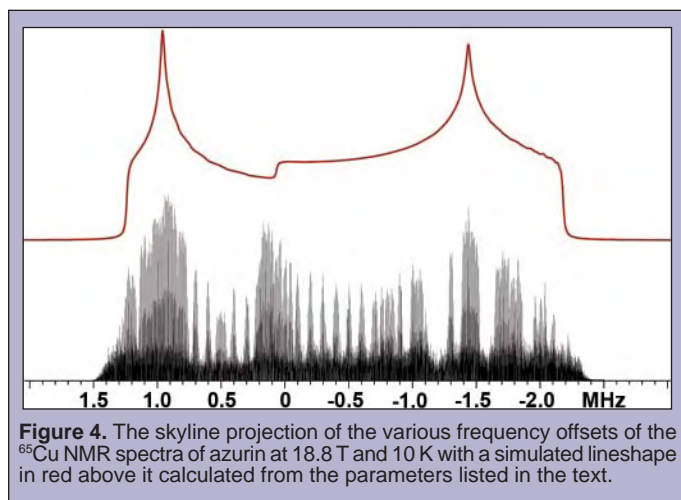
Figure 4. The skyline projection of the various frequency offsets of the ^{65}Cu NMR spectra of azurin at 18.8 T and 10 K with a simulated lineshape in red above it calculated from the parameters listed in the text.

DISCUSSION

1. Optimization of Azurin Production

In past years, much has been done regarding the field of azurin research. Karlsson et al. have found a way to easily produce it outside of its host organism [3]. His methods have been improved by Harris et al. [2], and the structure of azurin has been defined through x-ray diffraction techniques reported by Crane et al. [4]. Our results show that azurin can be produced in higher quantities than before through fermentation.

While manual control of fermentation succeeded in growing E. coli to a high cell density, this procedure could be optimized even further. Clearly, there is a limit on the density to which the cells can grow, but there are several examples in the literature of efficient recombinant protein production in E. coli to cell densities over twice the level we achieved [12]. The six hour growth before induction could be shortened through a more highly automated fermentation procedure. In the methods described above, antifoam, ammonium hydroxide, temperature, and agitation/oxygen level were automated through proportional-integral-derivative (PID) control, but the glucose feed had to be controlled manually due to limitations in the software and hardware used. The manual control of the glucose feed required a human presence during a majority of

the fermentation procedure. Automation would not be exceedingly challenging. It may be possible for a program to be written within the interface of the BioCommand software, developed separately, or a different system used so that *E. coli* growth would not merely be more efficient, but not require constant supervision. Such a program might give the system a 5–10% glucose pulse every 10 minutes, and adjust the glucose feed according to the methods described by Akesson. That is to say, when the *E. coli* are underfed, the glucose pulse will result in a growth surge and resultant drop in dO_2, while if they are overfed, the pulse will not cause any reaction. This is due to the theory that specific oxygen uptake reaches a maximum at the onset of acetate formation [6]. Acetate formation is crippling to the system, as it has been shown to both inhibit growth and recombinant protein production, possibly even causing the latter to be halted entirely at acetate concentrations between 33 and 167 mM [12]. Therefore, the program might offer the condition that IF the dO_2 level drops below 25%, then the glucose feed will be increased by 2%. Following glucose pulses, a plunge in dO_2, representing normal cellular respiration, would then result in increased feed, while slight or no change in dO_2, representing onset of acetate formation, would not. Such a feedback mechanism would ensure that a glucose level that sanctioned acetate formation would never be reached. The BioCommand program has proved difficult to manipulate to perform this, but it would not be a formidable program to write in a standard programming language, such as Matlab or Visual Basic. One other concern must be taken into account. The Bio Flow 110 is particularly prone to dO_2 oscillations, especially when the glucose level is unusually high. A program to regulate glucose level, then, must offer a safeguard against automatic increases in glucose feed during dO_2 oscillations, such as an alarm or termination in glucose feed.

Due to the blue-green color of the pelleted cells following periplasmic protein extraction during previous preparations, we believed that a fair amount of azurin was not exported to the periplasm of the cell following induction. By reducing the post-induction temperature and not adding Cu(II) until later in the purification we achieved a large increase in azurin which could be recovered from the periplasmic extract. Further optimization of the yield might be achieved by further increasing the cell density at which induction is initiated.

2. Interpretation of NMR results

Sensitivity is a substantial concern in all NMR experiments. A balance must be achieved between high and low sensitivity, for high sensitivity may have high signal, albeit accompanied with high noise. In previous experiments, low signal-to-noise resulted in an inability to detect the copper ion within azurin at all. To circumvent the sensitivity issue, we have made several alterations to our experimental protocol. First, a large amount (70 mg) of azurin was used. A new probe coil, composed of zinc rather than copper (which interferes with the azurin copper signal) was made. To further reduce the possible background signal the magnetization was generated utilizing cross polarization with spin temperature alternation. The sample was brought down to a temperature of 10 K, which increases the Boltzmann distribution of observable spins. While all of these alterations increase the signal-to-noise ratio, the last can potentially increase the T_1 relaxation time to hours. To counteract this, cobalt-substituted carbonic anhydrase is added to the sample as a dopant. The dopant significantly reduces the T_1 relaxation time of the proton bath to the order of seconds or minutes. Any nucleus in the vicinity of the paramagnetic cobalt senses the unpaired electrons within it, which provide efficient nuclear-relaxation pathways [13].

Furthermore, to increase signal, a spikelet echo technique (or QCPMG) is used to continually refocus the signal with a train of pulses. Each complete echo is recorded and a Fourier transform on them produces a series of discrete spikes, whose envelope reveals information about the specific binding site for copper. The timing was set such that the spikes have a 5 kHz spacing between them. A finer distribution leads to more spikes, but a lower signal-to-noise ratio.

The azurin spectrum with its C_q of 71.2 MHz generated a lineshape that is over 3 MHz wide. With the proton $\pi/2$ at 7 μs for CP and the ^{65}Cu π pulse at 19 μs (limited by the voltage handling of the components) the observable bandwidth for each experiment was only 20 kHz. To acquire a complete data set, filling in the lineshape completely would have been time prohibitive. Each frequency offset was acquired with 512 transients, pulsing every 30 s for a total time for each block of 4.25 hours. The spectrum shown in Figure 4 is the result of approximately 3.5 weeks of instrument time.

3. Future directions

While we have obtained an NMR spectrum for the copper (I) in azurin, molecular and quantum mechanical modeling of the site must be performed and the results reconciled with our data. This will tell us whether the proposed models are reasonable and possibly elaborate on key points of the model.

This work demonstrated the feasibility of studying copper in many other metalloproteins by solid state NMR. The trigonal bipyrimidal ligand geometry and axial oxygen ligand of Cu(I) within azurin caused extreme distortions that made it one of the hardest proteins to study with NMR. The extremely large field gradient and the broad NMR spectrum that was generated by it is presumably as large as is likely to be generated by any copper protein, giving promise to the future study of other proteins. The spectra that could be obtained from several other intriguing copper proteins such as superoxide dismutase (21.65 MHz C_q from NQR [14]) should be far simpler to obtain and analyze. Further development on the NMR probe could also lead to a reduction of experiment time making these types of experiments less demanding and more generally applicable to other systems.

REFERENCES

[1] T. Yamada, M. Goto, V. Punj, O. Zaborina, M. L. Chen, K. Kimbara, D. Majumdar, E. Cunningham, T. K. Das Gupta, and A. M. Chakrabarty, "Bacterial Redox Protein Azurin, Tumor Suppressor Protein p53, and Regression of Cancer," PNAS, vol. 99, 14098–14103, 2002.

[2] R. L. Harris, M. Prudêncio, S. S. Hasnain, R. R. Eady, and R. G. Sawers, "Heterologous Metalloprotein Biosynthesis in *Escherichia coli*: Conditions for the Overproduction of Functional Copper-containing Nitrite Reductase and Azurin from *Alcaligenes xylosoxidan*s," Journal of Synchrotron Radiation, vol. 12, 13–18, 2004.

[3] B. G. Karlsson, T. Pascher, M. Nordling, R. H. A. Arvidsson, and L. G. Lundberg, "Expression of the blue copper protein azurin from *Pseudomonas aeruginosa* in *Escherichia coli*," FEBS Letters, vol. 246, 211–217, 1989.

[4] B. R. Crane, A. J. Di Bilio, J. R. Winkler, and H. B. Gray, "Electron Tunneling in Single Crystals of *Pseudomonas aeruginosa* Azurins," J. Am. Chem. Soc, vol. 123, 11623–11631, 2001.

[5] A. S. Lipton, R. W. Heck, and P. D. Ellis, "Zinc Solid-State NMR Spectroscopy of Human Carbonic Anhydrase: Implications for the Enzymatic Mechanism," J. Am. Chem. Soc, vol. 126, no. 14, 4735–4739, 2004.

[6] M. Akesson, E. N. Karlsson, P. Hagander, J. P. Axelsson, and A. Tocaj, "On-line Detection of Acetate Formation in *Escherichia coli* Cultures Using Dissolved Oxygen Responses to Feed Transients," Biotechnology and Bioengineering, vol. 64, 590–598, 1999.

[7] T. K. Chang, S. A. Iverson, C. G. Rodrigues, C. N. Kiser, A. Y. C. Lew, J. P. Germanas, and J. H. Richards, "Gene Synthesis, Expression, and Mutagenesis of the Blue Copper Proteins Azurin and Plastocyanin," Proc. Natl. Acad. Sci. USA, vol. 88, 1325–1329, 1991.

[8] A. S. Lipton, S. S. Mason, S. M. Myers, D. L. Reger, and P. D. Ellis, "Cd-113 Shielding Tensors of Monomeric Cadmium Compounds Containing Nitrogen Donor Atoms .3. CP/MAS Studies on 5-Coordinate Cadmium Complexes Having N(3)X(2) (X=H,N,O, and S) Donor Atoms," Inorganic Chemistry, vol. 35, no. 24, 7111–7117, 1996.

[9] A. S. Lipton, R. W. Heck, J. A. Sears, and P. D. Ellis, "Low Temperature Solid-State NMR Experiments of Half-Integer Quadrupolar Nuclides: Caveats and Data Analysis," Journal of Magnetic Resonance, vol. 168, 66–74, 2004.

[10] A. S. Lipton, J. A. Sears, and P. D. Ellis, "A General Strategy for the NMR Observation of Half-Integer Quadrupolar Nuclei in Dilute Environments," Journal of Magnetic Resonance, vol. 151, 48–59, 2001.

[11] G. Harbison, unpublished data, 2007.

[12] W. Johnston, R. Cord-Ruwisch, and M. J. Cooney, "Industrial Control of Recombinant *E. coli* Fed-batch Culture: New Perspectives on Traditional Controlled Variables," Bioprocess. Biosyst. Eng., vol. 25, 111–120, 2002.

[13] I. Bertini, C. Luchinat, R. Pierattelli, and A. J. Vila, "The Interaction of Acetate and Formate with Cobalt Carbonic Anhydrase. An NMR Study," Eur. J. Biochem., vol. 208, 607–615, 1992.

[14] G. S. Harbison, R. Subramanian, and M.-Y. Liao, "Pure Nuclear Quadrupole Resonance of the Copper Site in (Cu, Zn) Superoxide dismutase," Biophysical Journal, vol, 78(1), 9A-9A, 2000.

[15] M. Y. Liao, R. Subramanian, R. L. Yung, and G. S. Harbison, "Two and three dimensional nuclear quadrupole resonance in the investigation of structure and bonding," Zeitschrift Fur Naturforschung Section a-a Journal of Physical Sciences, vol. 55, no. 1–2, 29–36, 2000.

[16] V. Punj, S. Bhattacharyya, D. Saint-Dic, C. Vasu, E. A. Cunningham, J. Graves, T. Yamada, A. I. Constantinou, K. Christov, B. White, G. Li, D. Majumdar, A. M. Chakrabarty, and T. K. Das Gupta, "Bacterial cupredoxin azurin as an inducer of apoptosis and regression in human breast cancer," Oncogene, vol. 23, 2367–2378, 2004.

[17] M. Goto, T. Yamada, K. Kimbara, J. Horner, M. Newcomb, T. K. Das Gupta, and A. M. Chakrabarty, "Induction of Apoptosis in Macrophages by Pseudomonas aeruginosa Azurin: Tumour-Suppressor Protein p53 and Reactive Oxygen Species, but not Redox Activity, as Critical Elements in Cytotoxicity," Mol. Microbiol., vol. 47(2), 549–559, 2003.

Michael Hvasta, a physics major at The College of New Jersey, held a SULI internship at the Princeton Plasma Physics Laboratory during the summer of 2007. He hopes to enter a PhD program in plasma physics and become an experimentalist. His interests include racquetball and cooking for friends. More information about his ongoing experiments can be found at www.DustyPlasma.org.

Andrew Zwicker is the Head of the Science Education Program at the Princeton Plasma Physics Laboratory. He received a bachelor's degree in physics from Bard College and a Ph.D. in physics from Johns Hopkins University in 1993, developing spectroscopic diagnostics for fusion energy experiments. From 1993-1997, he conducted post-doctoral research for Oak Ridge National Laboratory at PPPL and in Germany. In 1997 he joined the Science Education Program at PPPL and became Head in 2004. He was named an "Outstanding Undergraduate Mentor" in 2003 by the Office of Workforce Development at the Department of Energy. In 2006, the American Association of Physics Teachers included him in its list of 75 leading contributors to physics education. In 2008, he became the Chair of the American Physical Society's Forum on Physics and Society. His current research interests are in dusty plasmas, plasma processing, and plasma education. He and a collaborator won the 2006 Art of Science competition at Princeton University for a photograph entitled "Plasma Table." He also teaches a writing seminar at Princeton University, "The Ethics of Human Experimentation."

Ultraviolet Induced Motion of a Fluorescent Dust Cloud in an Argon Direct Current Glow Discharge Plasma

Michael George Hvasta and Andrew Zwicker

ABSTRACT

Dusty plasmas consist of electrons, ions, neutrals and nm-μm sized particles commonly referred to as dust. In man-made plasmas this dust may represent impurities in a tokamak or plasma etching processing. In astrophysical plasmas this dust forms structures such as planetary rings and comet tails. To study dusty plasma dynamics an experiment was designed in which a 3:1 silica (<5 μm diameter) and fluorescent dust mixture was added to an argon DC glow discharge plasma and exposed to UV radiation. This fluorescent lighting technique offers an advantage over laser scattering (which only allows two-dimensional slices of the cloud to be observed) and is simpler than scanning mirror techniques or particle image velocimetry. Under typical parameters (P=150 mTorr, V_{anode}= 100 V, $V_{cathode}$= -400 V, I_{total} < 2mA) when the cloud is exposed to the UV light (100W, λ = 365 nm) the mixture fluoresces, moves ~2mm towards the light source and begins rotating in a clockwise manner (as seen from the cathode). By calibrating a UV lamp and adjusting the relative intensity of the UV with a variable transformer it was found that both translational and rotational velocities are a function of UV intensity. Additionally, it was determined that bulk cloud rotation is not seen when the dust tray is not grounded while bulk translation is. This ongoing experiment represents a novel way to control contamination in man-made plasmas and a path to a better understanding of UV-bathed plasma systems in space.

INTRODUCTION

Dusty plasmas (sometimes referred to as complex plasmas) are comprised of electrons, ions, neutrals and comparatively large particles (dust). On Earth, dusty plasmas are seen in plasma processing facilities and tokamaks where the dust is typically considered to be contamination. Therefore, it is important to learn how to control and limit the negative effects of these particles. In space, astrophysical dusty plasmas create comet tails, planetary rings and are a major component of the interstellar medium. These dusty plasmas, outside of our protective atmosphere, are bathed in ultraviolet (UV) light and must be better understood if we are to comprehend most of the visible universe [1, 2, 3]. To this end, the aim of the Dusty Plasma experiment (DPX) is to investigate the dynamics of dusty plasma systems and their interactions with UV light.

Traditionally, laboratory dusty plasmas are illuminated with a laser-sheet that reveals two-dimensional cross-sections of the cloud. In this experiment, in order to study the three-dimensional structure of the dust cloud, a fluorescent dust mixture is used that enables the entire cloud structure to become visible when exposed to UV light. Beyond uniformly illuminating the entire cloud, the experiment serendipitously provided a method of making the cone shaped dust cloud move and rotate. The following details the progress made in characterizing and explaining this motion.

MATERIALS & RESEARCH

The majority of our research was carried out in a 13.5" long cylindrical chamber with a 6" diameter. Figure 1 depicts the six-way cross configuration that was used.

Figure 1. A schematic depicting the experimental setup.
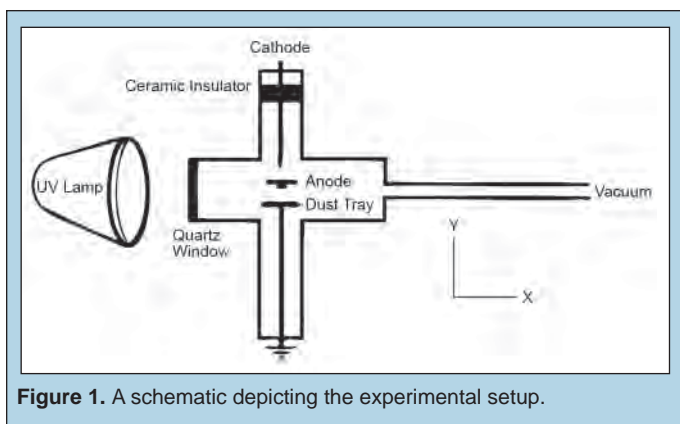
The dust tray consisted of a 1.9" x 0.25" stainless steel disc that was screwed onto a 0.5" diameter stainless steel shaft. The electrodes in the experiment were made from 0.5" diameter stainless steel rods. All of the stainless steel shafts were installed through Wilson-seals that allowed for the adjustment of their location and orientation. The tray and the chamber were grounded.

The negatively biased cathode (V = ⁻400 Volts) was positioned parallel to the Y-axis 2.0–2.5" above the dust tray. The positively biased anode (V = +100 Volts) was installed parallel to the Z-axis 1.0–1.5" above the dust tray. On top of the anode, near the tip of the electrode was another 1.9" x 0.25" stainless steel disc. This geometrical setup proved useful in creating distinct cone shaped clouds as seen below in Figure 2.

Figure 2. Three distinct dust clouds formed above the dust tray. The third cloud, on the far right, is cut-off. The diameter of the central cloud is ~ 2mm.
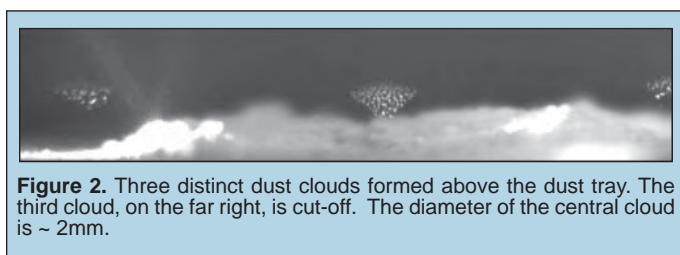
Typically, the dust was deposited on the dust tray after the chamber had been cleaned. The electrodes were scrubbed with acetone while the walls were washed with alcohol to prevent ruining the vacuum compatible paint used to add contrast during observation. The chamber pressure was then reduced to ~10^{-6} Torr before the volume was backfilled with 150 mTorr of argon. The experiment would begin by applying 1–3 kV to the anode to produce an electrical arc down towards the grounded dust tray that would excite the dust into the plasma.

Once the dust was excited into the plasma, electron capture would allow the dust grains to obtain a negative charge. The resulting attraction between the negative particles and the anode would offset downward gravitational forces and allow the particles to float within the plasma [4, 5]. The clouds could then be exposed to UV light which would cause the dust cloud to fluoresce, translate towards the light source and begin rotating in a clockwise manner (as seen from the cathode).

Dust dynamics were captured using a CCD camera with 640 x 480 resolution at 30 fps. After filming, the camera would be rotated

to face a ruler and, without touching the focus controls, its distance from a ruler would be adjusted until the etchings on the ruler were clearly in focus. Once the ruler was in focus the width and height of the frame could be determined. The width would be divided by 640 and the height would be divided by 480 to give us the dimensions of an individual pixel. A program called ImageJ was used to determine the number of pixels between two points and this information could then be converted into displacement. Since each frame represented 1/30th of a second, the average velocity between two points could be obtained by dividing the displacement by (n/30), where n is the number of frames between the two measurements.

RESULTS AND DISCUSSION

The research consisted of two primary studies. The first was designed to investigate the relationship between dust cloud motion and UV light intensity. The second was designed to determine whether or not chamber wall outgassing was responsible for cloud movement.

The UV lamp was calibrated by connecting it to a Variac variable transformer and measuring the relative UV intensities at varying voltages with a spectrometer. Conveniently, the UV intensity's dependence on voltage was linear as seen below in Graph 1.
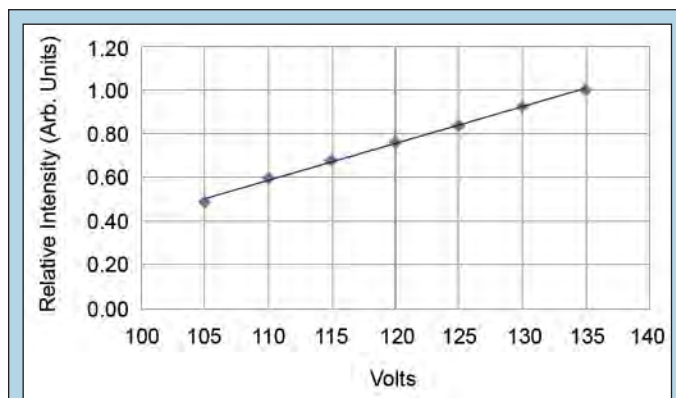
Graph 1. The UV intensity of the lamp scaled linearly with voltage.

Using the above calibration curve, the dust clouds suspended above the electrically grounded dust tray could be exposed to specific relative intensities of UV light. It was then determined that the velocity of the rotating cloud's particles at any given focal length was linearly dependent on UV intensity. Particle velocity decreased towards the center of the dust cloud and no rotation occurred when the dust tray was not grounded.

The cloud's translation towards the light tended to be more extreme as UV intensity increased and was unaffected by the floating or grounding of the dust tray.

A second study was needed to ensure that the observed effects in the first study were electrical in nature and not simply due to the paint on the chamber walls out-gassing and pushing the cloud towards the light. To this end, another series of experiments was performed to see if neutral particles or some other form of out-gassing could provide a mechanism for cloud translation [6, 7].

Graph 2. The linear relationship between particle velocity within the rotating cloud and UV intensity.
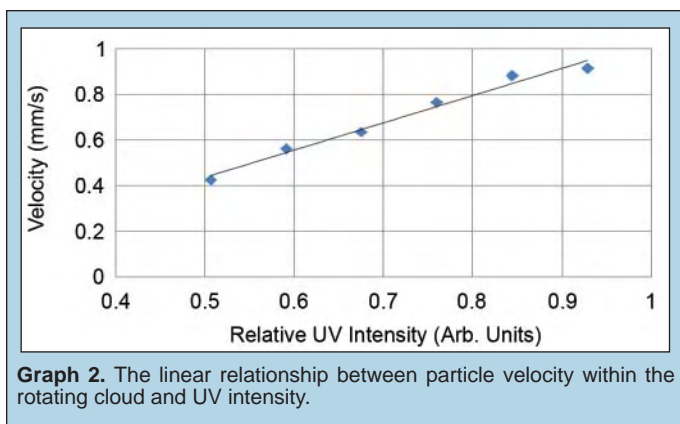
When the pressure in the chamber was at 1.5×10^{-5} Torr the chamber was isolated from the vacuum system and the pressure was monitored. Without any outside influence the chamber would slowly leak and/or out-gas and raise the pressure. This pressure vs. time reading became the benchmark for the next portion of the experiment.

In the next step, a focused beam of UV light, with three times the intensity of the regular lamp, was aimed at the dust on the tray and then the paint on the back wall of the chamber, opposite the UV lamp. For both scenarios the pressure was monitored as a function of time. Graph 3 depicts the results showing almost no differences in pressure due to UV related out-gassing.

Graph 3. There is almost no difference in the rate of rising pressure within the chamber due to UV induced outgassing.
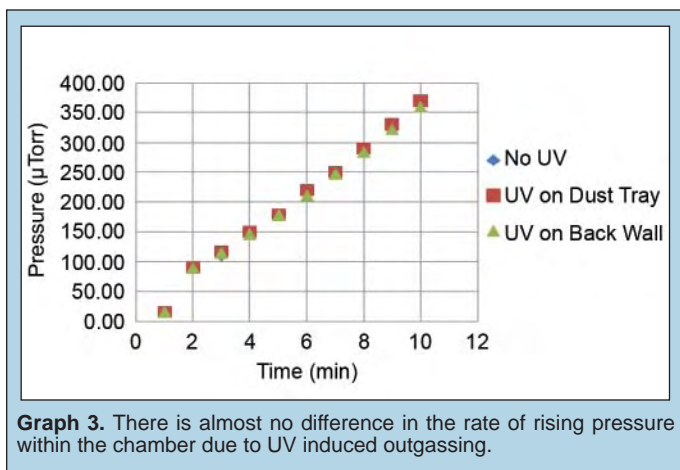
Another step was needed to see if heat from the UV lamp played a significant role in increasing the pressure within the chamber. The system was heated using the UV lamp in its regular position and with heating tape at 100°F on the back wall of the chamber. Prolonged UV lamp heating lasting 10 minutes provided little more than a .1 mTorr increase in pressure. The heating tape proved to be effective at increasing the pressure but on a level that was unobtainable with the UV lamp alone.

As a final test, the chamber was opened and the 3:1 dust mixture was replaced with pure silica. Upon repeating the same experiments with the UV lamp on the silica none of the same rotational or translational effects were seen.

CONCLUSION

The linear dependence on UV light intensity in the first study coupled with the lack of convincing evidence for out-gassing in the second study leads to the conclusion that the cause of the observed motion is due primarily to UV photoionization and its corresponding electrical effects [8].

Future microgravity work aboard NASA's 'Vomit-Comet' is scheduled for early June, 2008. Without gravity, the research group hopes to find the relationship between dust cloud movement and its proximity to the grounded dust tray.

More information about this and future work is available at www.DustyPlasma.org.

REFERENCES

[1] Edward Thomas Jr., and Michael Watson, "First experiments in the dust plasma experiment device," in Physics of Plasma, Vol. 6, October 1999, pp. 4111–4117.

[2] Li-Wen Ren, Zheng-Xiong Wang, Xiaogang Wang, Jin-Yuan Liu and Yue Liu, "The dust acoustic solitary waves in dusty plasmas: effects of ultraviolet radiation," in Physics of Plasmas, Vol. 13, September 20, 2006, pp. 1–5.

[3] Edward Thomas Jr., "Observations of high speed particle streams in dc glow discharge dusty plasmas," in Physics of Plasmas, Vol. 8, January 2001, pp. 329–333.

[4] V. Land and W.J. Goedheer, "Can we use UV light to control dust charging? An investigation using particle-in-cell/Monte Carlo simulations," Institute for Plasma Physics Rijnhuizen, the Netherlands, www.rijnh.nl.

[5] A. Barkan, N. D'Angelo and R.L. Merlino, "Charging of dust grains in a plasma," in Physical Review Letters, Vol. 73, December 5, 1994, pp. 3093–3096.

[6] Phil Danielson, "Sources of water vapor in vacuum systems," in R&D Magazine, September 2000.

[7]   Marshal Dhayal, Morgan R. Alexander and James W.
      Bradley, "The surface chemistry resulting from low-
      pressure plasma treatment of polystyrene: The effect of
      residual vessel bound oxygen," in <u>Applied Surface Science</u>,
      Vol. 252, September 15, 2006, pp. 7957–7963.

[8]   Victor Land and Wim J. Goedheer, "Manipulating dust
      charge using ultraviolet light in a complex plasma," in
      <u>IEEE Transactions on Plasma Science</u>, Vol. 35, April 2007,
      pp. 280–285.

Elissa Knoff was born in Bartlett, IL and grew up in Algonquin, IL. She attended Northwestern University, majoring in physics. While she was an undergraduate, she participated in a PST internship at Fermi National Accelerator Laboratory during the summer of 2007. She hopes to eventually obtain a master's degree in education and to teach high school physics. She enjoys reading and tutoring high school students.

Robert Peterson is an Education Program Leader at the Fermi National Accelerator Laboratory. Bob comes to the QuarkNet project with entrepreneur zeal, so he never misses an opportunity to talk up cosmic ray research for high school students. He came to the Education Office from Bartlett High School as a physics and engineering teacher where the challenges of the classroom convinced him there must be a better way. So, he's always glad to promote Inquiry Based learning as an alternative to text-book, rote education. Bob also knows the research world having worked on the Sloan Digital Sky Survey and basic research for the US Navy. Still, because he ran his own business, he leads with a marketing sense to win teachers over to a new way of being in the classroom. Robert holds two engineering degrees in Aerospace Engineering and Naval Architecture from the University of Michigan.

Plateauing Cosmic Ray Detectors to Achieve Optimum Operating Voltage

Elissa N. Knoff and Robert S. Peterson

ABSTRACT

Through QuarkNet, students across the country have access to cosmic ray detectors in their high school classrooms. These detectors operate using a scintillator material and a photomultiplier tube (PMT). A data acquisition (DAQ) board counts cosmic ray hits from the counters. Through an online e-Lab, students can analyze and share their data. In order to collect viable data, the PMTs should operate at their plateau voltages. In these plateau ranges, the number of counts per minute remains relatively constant with small changes in PMT voltage. We sought to plateau the counters in the test array and to clarify the plateauing procedure itself. In order to most effectively plateau the counters, the counters should be stacked and programmed to record the number of coincident hits as well as their singles rates. We also changed the threshold value that a signal must exceed in order to record a hit and replateaued the counters. For counter 1, counter 2, and counter 3, we found plateau voltages around 1V. The singles rate plateau was very small, while the coincidence plateau was very long. The plateau voltages corresponded to a singles rate of 700–850 counts per minute. We found very little effect of changing the threshold voltages. Our chosen plateau voltages produced good performance studies on the e-Lab. Keeping in mind the nature of the experiments conducted by the high school students, we recommend a streamlined plateauing process. Because changing the threshold did not drastically affect the plateau voltage or the performance study, students should choose a threshold value, construct plateau graphs, and analyze their data using a performance study. Even if the counters operate slightly off their plateau voltage, they should deliver good performance studies and return reliable results.

Introduction

The QuarkNet project [1] connects high school students to high-energy physics projects and facilitates learning the scientific process [2]. As part of the project, high school students across the world use detectors to gather data about cosmic rays, uploading data to the Cosmic Ray e-Lab [3]. Using the online e-Lab, students further study the data they, and others, have collected [4]. Even schools without detectors can research cosmic rays using the data uploaded by other schools. The detectors utilize technology similar to that used by professional scientists [5]. However, their simplified construction makes them highly usable in a classroom setting. Their primary components include plastic scintillator, photomultiplier tubes [PMTs], a Data Acquisition board (DAQ), and a power distribution unit (PDU) [6]. The PDU delivers a range of 0.3 V to 1.8 V to the PMT. The PMT operates at a voltage 1,000 times that delivered by the PDU (a range of 300 V to 1,800 V). The DAQ coordinates data collection, placing a timestamp on the events

detected by the counter [7]. The detector also includes a Global Positioning System (GPS) unit which delivers precise 1-pulse-per-second (1PPS) signals [8]. Students can connect the DAQ board to a computer and use a terminal emulation program such as ZTerm (which was used for this experiment) to view their data [9]. Each participating school receives one DAQ board and the components needed to construct four counters.

Using a terminal emulation program, a user can program the DAQ board to record different types of cosmic ray detections. Students can track the number of cosmic ray "hits" each individual counter receives. They can also utilize the board's coincidence logic to gather data only when a certain number of counters receive a hit [7]. Students can choose to stack counters or arrange them in different configurations to research different properties of cosmic rays. Using the e-Lab, they can perform flux studies to examine the number of cosmic rays passing through their counters in a certain time, look for cosmic ray showers, and investigate muon lifetime [3].

In order to maximize the accuracy of their results, users must minimize background noise while retaining necessary sensitivity to detect the cosmic rays. Users address this issue in two ways: they must determine the appropriate threshold voltage for their counters and they must optimize the voltage the PDU delivers to the PMT [9]. An appropriate threshold voltage allows the detector to recognize real cosmic ray hits while not counting background noise. A correct operating voltage allows the counts recorded to maintain steady even if the PMT tube voltage drifts to either a higher or lower level. In order to achieve optimal operating voltage, users must "plateau" the counters. Each PMT has a different optimum operating voltage that must be determined. In this experiment, we sought to determine the optimum plateau voltage for the counters in the Fermilab Test Array. The Fermilab Test Array is a complete detector set-up that is located on the fifteenth floor of Wilson Hall at Fermilab. QuarkNet staff use this detector for prototyping changes to counters and the DAQ board as well as other non-standard uses. Concurrently, this experiment explored the effects of the threshold setting on the plateau voltage of the counters. This allowed for deeper understanding of the plateau process. Ultimately, we wanted to understand the the plateauing process and to understand how operating at the plateau voltage affects measurements. Through this understanding, we hoped to make the plateauing process more efficient and effective for students and teachers.

Methods and Materials

Detector Setup

For this experiment, we used a complete setup of a cosmic ray detector, which included four counters. Each cosmic ray counter (comprised of a piece of scintillator with a light-channeling "cookie" attached, a PMT, and a base) records the number of cosmic ray hits it receives [9]. As a cosmic ray encounters a scintillator, it produces scintillation light, which is transmitted through the cookie to the PMT. The PMT converts the light signal it receives into an electrical signal [7]. The DAQ board then measures the time that a signal, or pulse, is larger than a certain (user-determined) threshold voltage. This measured time over threshold (TOT) crudely estimates the energy of the incident cosmic ray [9]. The threshold value must be set low enough that the energy of the cosmic rays is "counted" but high enough that background "noise" will not be counted [9].

Determining Optimum Operating Voltage

Each PMT has an optimal operating voltage, which must be determined by plateauing the counters. This step establishes a voltage at which the counter records incoming cosmic rays but little background noise. At the plateau voltage small changes in PMT voltage will not drastically affect the number of cosmic rays recorded by a counter, minimizing the effects of drifts in the tube gain or power supply during the experiment [10]. The plateau voltage is so named because the shape of the graph that plots counts per minute with respect to PMT voltage displays a "plateau" region with approximately equal counts per minute over a range of PMT voltage. Two approaches can be adopted for identifying the plateau

region. Plotting the number of counts a single counter receives ("singles rate") with respect to its operating voltage produces a small plateau. The DAQ board can also record the number of coincidence hits ("coincidence rate") between multiple counters. For plateauing purposes, we programmed the DAQ board to respond when two counters received a hit. We kept one counter at a constant voltage while we changed the other counter's (the one being plateaued) voltage. Plotting the coincidence rate with respect to the voltage of the counter being plateaued produced a long, flat plateau [10].

To best determine the operating voltage for a counter, we considered both the singles rate and the coincidence rate [10]. We stacked two counters (for example, counters 1 and 2) so that the same cosmic rays could be tracked as they hit the two counters. To study counter 1, we programmed the DAQ board to record the singles rate for counters 1 and 2, while not recording information from counters 3 and 4. We also programmed the DAQ board to record coincidence rates from a coincident hit on counters 1 and 2 [10]. To make data collection easier, the DAQ board was also programmed to provide counts at one-minute intervals [11]. We recorded all data in terms of PMT voltage (1,000 times the PDU voltage).

To study counter 1, we kept the voltage on counter 2 at a constant, appropriate potential of about 1,000 V. We set counter 1 to a low voltage (600 V–800 V), and we collected at least two data lines (two minutes of data). Using adjacent lines, we subtracted the starting count for channel 1 from the ending count for channel 1 to produce a "total" singles rate. We also used this method for the coincidence rate. This "singles total" as well as the "coincidence total" were recorded. We repeated this process for increasing voltages in 20 V increments, until our singles rates reached approximately 1,200 counts per minute [9]. Our PMTs did not operate effectively with counts higher than this level. When the data were plotted, we explored areas of interest in 10 V increments. Because we cannot operate the PMTs below 300 V, we only plotted values above this voltage.

To determine a good plateau voltage, we plotted the singles rate and the coincidence rate simultaneously with respect to the different PMT voltages. While the singles rate increased, plateaued, and then continued to increase, the coincidence rate increased, plateaued, and did not increase again in the domain of our data. The operating voltage should be located above the "knee" on the singles graph where the graph levels off. The operating voltage should also be located on the plateau of the coincidence graph. Ideally, the PMT setting should be on both plateaus [10]. Furthermore, data from all counters must be considered when determining the correct operating voltages. Each of the four counters should read similar singles rates [11].

Examining the Effects of Threshold

In order to better understand the process of plateauing, we implemented different thresholds and replateaued the counters. We also varied threshold voltages in an attempt to receive consistent singles rates for the four counters. If a counter's plateau voltage corresponded to a higher than expected singles rate, we raised the threshold voltage. If the counter's plateau voltage corresponded to a lower than expected singles rate, we lowered the threshold voltage.

We also adjusted thresholds if a counter was more or less sensitive than the other counters. Particularly for counters that recorded high singles rates at comparatively low operating voltages, we raised the threshold. Similarly, if a counter recorded low singles rates at high operating voltages, we lowered the threshold.

After the counters were plateaued, we then set them at their determined PMT and threshold settings. Data were collected for at least 30 minutes. We then uploaded data to the Cosmic Ray e-Lab [3]. The e-Lab contains different experiments for analyzing data. One experiment, the "performance study" allows groups to evaluate the quality of their data [3]. The e-Lab performs the necessary calculations to deliver a histogram that shows the distribution of the energies of the cosmic rays collected during a data capture. Ideally, the graph should be a Poisson shape [9]. We used these graphs to evaluate choices of operating voltage and threshold.

RESULTS

Plateau Voltages for the Counters

Counter 1 was plateaued using counter 2 as a reference for recording coincidence rates. Counter 2 was then plateaued using counter 1 as a reference. We determined the initial threshold and operating voltage for the "reference" by using the standard threshold setting used by classroom teachers and using the operating voltage determined for that PMT by a previous plateauing attempt. The counters exhibited very low count rates until PMT voltages of approximately 900 V were exceeded. Counter 1 showed somewhat defined plateaus on graphs of singles rates with respect to PMT voltage at various threshold voltages. Plateaus for the coincidence rates were longer and more defined. For each threshold voltage, a plateau PMT voltage was chosen to be located on both the singles rate plateau and the coincidence rate plateau. Counter 2 also showed somewhat defined plateaus on the singles rate and more defined coincidence plateaus. Again, we chose a plateau PMT voltage to be located on the plateaus of both the singles graph and the coincidence graph.

We used both counters' graphs to determine the appropriate threshold voltage and PMT voltage combination. We looked for graphs that showed similar singles rates at the chosen plateau voltage. For counters 1 and 2, we chose 2.0 V as the appropriate threshold. 2.0 V gave reasonable (approximately 1 V) plateau voltages and similar singles rates between counters 1 and 2.

Figure 1 shows counts per minute with respect to PMT voltage at a 2.0 V threshold. The coincidence plateau began at around 990 V. The coincidence rate in this plateau region wavered somewhat but remained around 400–500 counts per minute. Using the singles graph, we determined that the plateau voltage was between 1020 V and 1030 V. This range was located above the "knee" on the singles graph where the counts per minute rate began to level off. This range is also located on the long coincidence plateau. In its plateau range, counter 1 recorded singles rates of 710–734 counts per minute.

Figure 2 shows counts per minute with respect to PMT voltage at the 2.0 V threshold. Two small plateaus are visible on the singles rate. The first plateau corresponds to a voltage of 1,100 V–1,120 V.
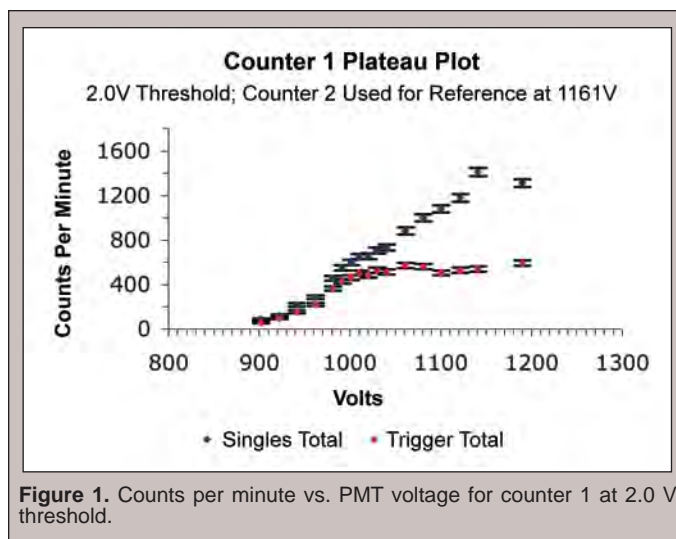
Figure 1. Counts per minute vs. PMT voltage for counter 1 at 2.0 V threshold.
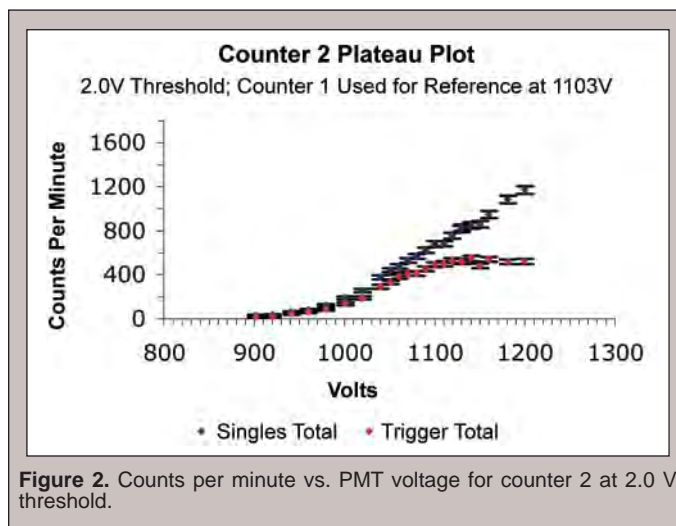
Figure 2. Counts per minute vs. PMT voltage for counter 2 at 2.0 V threshold.

The second plateau corresponds to a voltage of 1,130 V–1,150 V. The long coincidence plateau began at approximately 1,070 V. This plateau had more variation than counter 1's plateau. Again, the coincidence rate ranged from 400–500 counts per minute. We chose the operating PMT voltage to be between 1,100 V and 1,120 V. In this range, counter 2 received 682–757 counts per minute. This plateau corresponded to a more consistent singles rate with counter 1.

Counter 3 and counter 4 were plateaued together in the same manner as counter 1 and counter 2. We used the singles rates we obtained from counters 1 and 2 as reference to judge our data from counters 3 and 4. We looked for plateaus where counters 3 and 4 had singles readings of 700-800 counts per minute.

Counter 3 was more sensitive in that it had higher singles rates at lower PMT voltages. We chose a threshold voltage of 2.5 V so that counter 3 would have a singles rate in the appropriate range at its plateau voltage. Figure 3 shows counter 3's count rate with respect to PMT voltage. Counter 3 showed a small but defined plateau on its singles graph. Again, the coincidence plateau was extended and defined. The coincidence plateau began at 960 V. We determined counter 3's singles plateau to be in the range of 1,000 V–1,020 V.
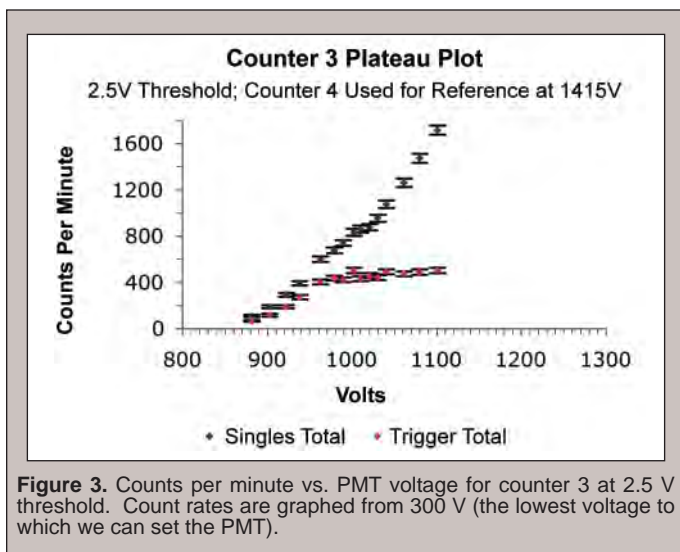
Figure 3. Counts per minute vs. PMT voltage for counter 3 at 2.5 V threshold. Count rates are graphed from 300 V (the lowest voltage to which we can set the PMT).
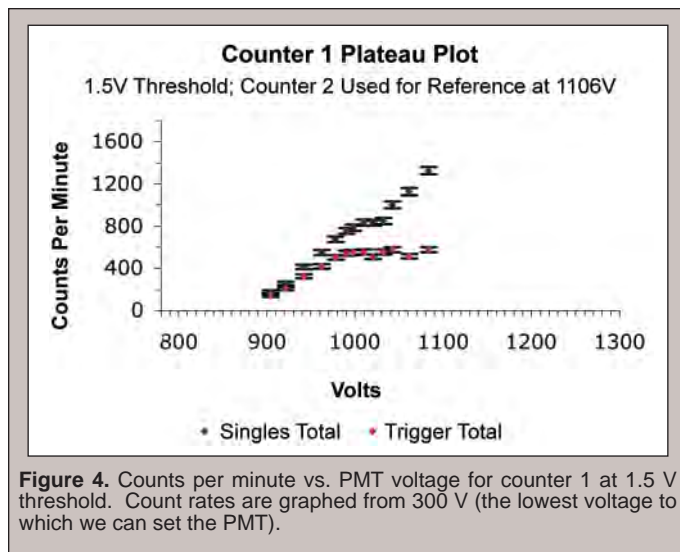
Figure 4. Counts per minute vs. PMT voltage for counter 1 at 1.5 V threshold. Count rates are graphed from 300 V (the lowest voltage to which we can set the PMT).

Figure 5. Counts per minute vs. PMT voltage for counter 1 at 2.8 V threshold. Count rates are graphed from 300 V (the lowest voltage to which we can set the PMT).

We chose an operating voltage in this range. Here, the singles rate was between 836 and 839 counts per minute.

Counter 4 exhibited very erratic behavior. Even with a low (1 V–1.5 V) threshold, the PMT voltage needed to be very high (1,400 V–1,500 V) in order to receive comparable singles rates to the other three counters. Furthermore, very small changes in voltage would cause either tremendous increases or drastic decreases in singles rates. We determined that counter 4 was faulty and required repair.

Relationship between Threshold Setting and Plateau Voltage

Figure 4 shows counter 1's plot of counts per minute with respect to voltage at a threshold of 1.5 V. Figure 5 shows counts per minute with respect to voltage for counter 1 at a threshold of 2.8 V. At a 1.5 V threshold, the coincidence plateau began at approximately 980 V. In the plateau, the coincidence values were approximately 500–600 counts per minute. The singles plateau occurred from 1010 V–1030 V. In this range, the singles rate was 834–850 counts per minute. At a 2.8 V threshold, the coincidence plateau began at approximately 1050 V. This plateau had a coincidence rate of 400–440 counts per minute. A small singles plateau occurred from 1070 V–1080 V. Here, the singles rate was 788–801 counts per minute.

Discussion and Conclusions

Analyzing Determined Plateau Values

Overall, plateaus were difficult to identify on graphs of singles rates per minute with respect to PMT voltage. Singles plateaus were especially hard to identify given random variations in counts per minute. To determine a rough estimate of this variation, we recorded the singles rates for different one-minute time frames with PMT voltage and threshold voltage remaining constant. In our small sample, we found up to 5 percent variation from our recorded value. This could substantially affect our graphs and the apparent plateaus. Furthermore, the counting error (the square root of each count
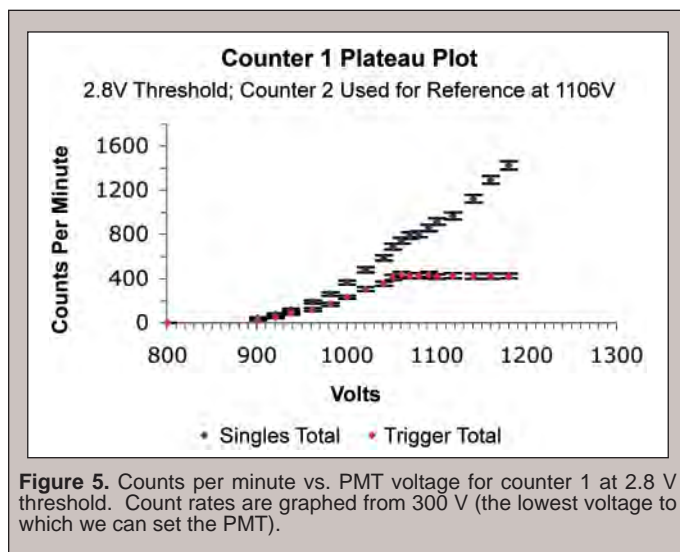
rate) creates more difficulty in identifying the plateau. As expected, coincidence rate plateaus were very long and easy to identify. The coincidence plateau was not very useful without the singles plateau, however. Because the coincidence plateau was so long, the singles rate varied widely within the plateau range.

Further difficulties arose from uncertainties about the proper singles rate reading for the QuarkNet counters. Adams's guide places the appropriate reading at approximately 300 counts per minute [10]. The user's manual illustrates a plateau value closer to 700–800 counts per minute [9]. This experiment did not find a plateau in the range of 300 counts per minute. In most cases, even the coincidence rate did not plateau in the singles range of 300 counts per minute. Our plateaus were much closer to the 700–800 counts per minute range.

Although our values vary substantially from those prescribed by Adams, our plateau voltages (Table 1) produced good performance graphs (Figure 6). The three counters have very similar counts. Furthermore, their shapes are alike and they have peaks at very similar values. We also tried different combinations of PMT settings and threshold value. Most notably, we tested the counters at the values

summarized in Table 2. We chose these values to focus the singles rates more closely at about 800 counts per minute. These settings, however, produced worse performance graphs (Figure 7). These results were somewhat unexpected. We expected that, as long as the chosen plateau value corresponded to the threshold setting, the performance graphs would have the desired Poisson shape. The variation between the two graphs, however, is relatively minor.

Overall, we plateaued the counters effectively. Our singles rates were consistent, and our operating voltages were reasonable. In fact, at thresholds of 1.5 V and 2.5 V, counter 1's plateau corresponded to singles rates closer to 800 counts per minute. This would indicate that the singles rates obtained at the 2.0 V threshold were unusually low. Because these experiments were conducted on different days, this could be due to temporal variation in the number of cosmic rays.

Analyzing the Plateauing Process

Experience with the counters indicates that they deliver consistent count rates during a given time and show very little background noise, especially compared to the well-defined cosmic ray pulses. As shown in Figures 1, 4, and 5, changes in threshold affected the PMT setting but had little effect on the singles rate obtained at the plateau voltage. Even these variations in PMT voltage were fairly small. For use in a classroom, any plateauing procedure must be consistent and efficient. Our experiment indicates that an extremely high level of precision is not necessary to produce good readings from the counters. A good reading in the context of the counters' purpose provides consistency among the counters and leads to a performance graph with only one peak. Keeping this in mind, teachers and students should choose a threshold voltage and produce graphs of counts per minute with respect to PMT voltage. If one counter obtains a widely varying singles rate, i.e. the rate varies by more than 100 or 200 counts per minute, from the other counters, the experimenters can adjust the threshold and re-plateau. The plateauing process is important in that it allows for both elimination of noise and consistent readings. However, since most counter experiments will focus on changes in coincidence rates, the plateauing process should be completed effectively and efficiently.

Counter	PMT Setting (Volts)	Threshold (Volts)
1	1,024	2.0
2	1,114	2.0
3	1,009	2.5

Table 1. Settings for plateaued counters.

Counter	PMT Setting (Volts)	Threshold (Volts)
1	1,023	1.5
2	1,140	2.0
3	1,009	2.5

Table 2. Settings that produce plateaus at singles rates of approximately 800 counts per minute.
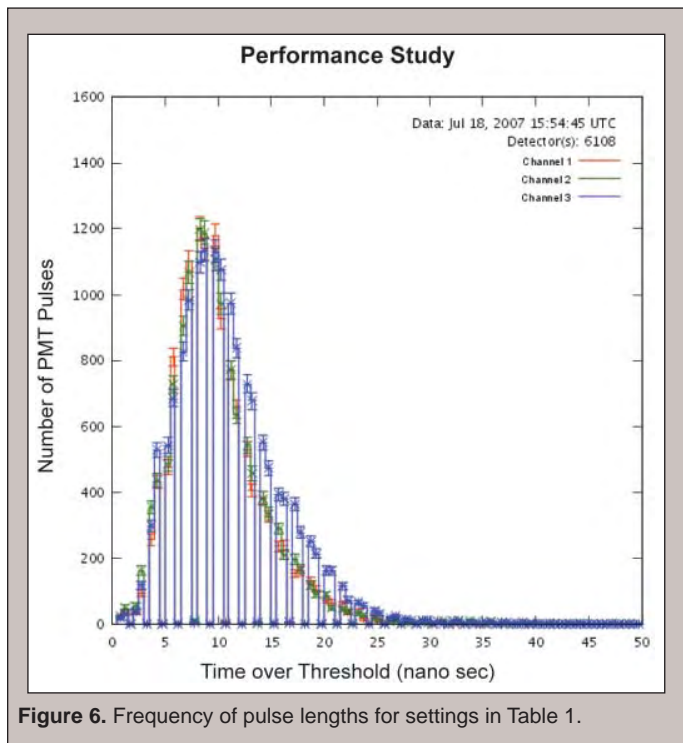
Figure 6. Frequency of pulse lengths for settings in Table 1.
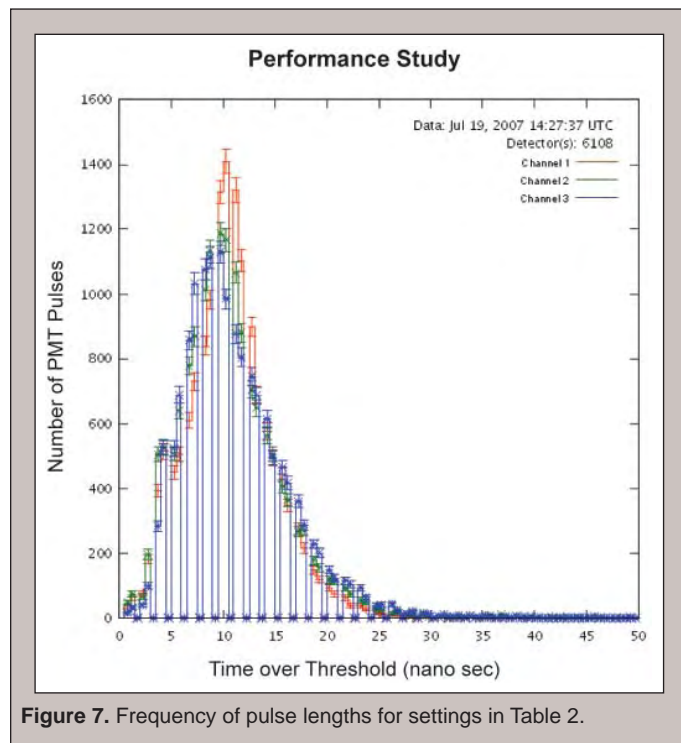
Figure 7. Frequency of pulse lengths for settings in Table 2.

REFERENCES

[1] QuarkNet [Online]. Available: http://quarknet.fnal.gov

[2] R. D. Ruchti (2002, Jan. 10). Quarknet: A Particle Physics Program of Education and Outreach in the U.S.A. *World Scientific*, pp. 1–10. [Online]. Available: http://villaolmo. mib.infn.it/Manuscripts/10_generalities/Ruchti.ps

[3] Cosmic Ray e-Lab. [online]. Available: http://www.i2u2. org/elab/cosmic and http://quarknet.fnal.gov/e-lab

[4] M. Bardeen, E. Gilbert, T. Jordan, P. Nepywoda, E. Quigg, M. Wilde, and Y. Zhao. (2006). The QuarkNet/ Grid Collaborative Learning e-Lab. *Future Generation Computer Systems*, 22, pp. 700–708. [Online]. Available: http://quarknet.fnal.gov/talks/clag_paper.pdf

[5] R. Graue, T. Stuffler, T. Gobel. (1996, Aug. 5–7). A Compact Gamma Ray Detection System for Space Applications Based on Photodiodes and CsI(TI) Scintillation Crystals. *Gamma-ray and cosmic-ray detectors, techniques, and missions: 5–7 August 1996, Denver, Colorado, Presented at the Proceedings of the SPIE, 2806*, pp. 400–414. [Online]. Available: http://spiedigitallibrary. aip.org

[6] B. Baumbaugh, et al. (1999, Oct. 24–30). A portable cosmic ray detector and display. *Conference Record of the 1999 Nuclear Science Symposium*, pp. 783–785. [Online]. Available: http://ieeexplore.ieee.org/xpls/abs_all. jsp?arnumber=845784

[7] S. Hansen, T. Jordan, T. Kiper, D. Claes, G. Snow, H. Berns, T. H. Burnett, R. Gran, and R. J. Wilkes. (2004, June). Low-Cost Data Acquisition Card for School-Network Cosmic Ray Detectors. *IEEE Trans. Nuclear Sci., 51*, pp. 926–930. [Online]. Available: http://arxiv.org/abs/ physics/0311060

[8] H. Berns, T. H. Burnett, R. Gran, J. Wilkes. (2004). GPS time synchronization in school-network cosmic ray detectors. *IEEE Trans. Nucl. Sci., 51*, pp. 848. [Online]. Available: http://arxiv.org/abs/physics/0311079

[9] J. Rylander, R. J. Wilkes, R. Gran, and T. Jordan, "Quarknet/Walta/CROP Cosmic Ray Detector User's Manual," Aug. 2004.

[10] M. Adams. "Plateauing Counters."

[11] R. S. Peterson, "Plateau Cookbook," Mar. 2007.

Andrea Montgomery was born in Fort Dodge, IA and grew up in Omaha, NE. She attend Butler University in Indiana, majoring in physics, and minoring in math and music. After graduation, she participated in a SULI internship at Lawrence Berkeley National Lab. She currently is enrolled in a PhD program at the University of Wisconsin, Madison, studying plasma physics. Her hobbies include singing and cooking.

Carl Schroeder is a staff scientist at the Lawrence Berkeley National Laboratory (LBNL). He received his Ph.D. in physics from the University of California at Berkeley in 1999 for his study of intense, short-pulse, laser-plasma interactions. Following postdoctoral work studying x-ray free-electron lasers at UCLA and SLAC, he joined the Accelerator and Fusion Research Division of LBNL in 2002. At LBNL his research activities have focused on the development of laser-driven plasma-based accelerators and novel radiation sources.

Studies of a Free Electron Laser Driven by a Laser-Plasma Accelerator

Andrea Montgomery, Carl Schroeder, and William Fawley

ABSTRACT

A free electron laser (FEL) uses an undulator, a set of alternating magnets producing a periodic magnetic field, to stimulate emission of coherent radiation from a relativistic electron beam. The Lasers, Optical Accelerator Systems Integrated Studies (LOASIS) group at Lawrence Berkeley National Laboratory (LBNL) will use an innovative laser-plasma wakefield accelerator to produce an electron beam to drive a proposed FEL. In order to optimize the FEL performance, the dependence on electron beam and undulator parameters must be understood. Numerical modeling of the FEL using the simulation code GINGER predicts the experimental results for given input parameters. Among the parameters studied were electron beam energy spread, emittance, and mismatch with the undulator focusing. Vacuum-chamber wakefields were also simulated to study their effect on FEL performance. Energy spread was found to be the most influential factor, with output FEL radiation power sharply decreasing for relative energy spreads greater than 0.33%. Vacuum chamber wakefields and beam mismatch had little effect on the simulated LOASIS FEL at the currents considered. This study concludes that continued improvement of the laser-plasma wakefield accelerator electron beam will allow the LOASIS FEL to operate in an optimal regime, producing high-quality XUV and x-ray pulses.

Introduction

As researchers work to understand properties of materials on the molecular and atomic level, new instruments must be developed that are both accurate and powerful at nanometer and femtosecond scales. One option is the free electron laser (FEL), a device that uses a periodic magnetic field and electromagnetic radiation (either from a seed laser or spontaneous emission) to stimulate the emission of coherent radiation from a relativistic beam of electrons. The Lasers, Optical Accelerator Systems Integrated Studies (LOASIS) group at Lawrence Berkeley National Laboratory (LBNL) is developing such an instrument. An FEL must be driven by an energetic, high-quality, relativistic electron beam in order to lase at the desired wavelengths. Over the past several years, the LOASIS group has developed laser-plasma wakefield accelerator (LWFA) technology, allowing compact generation of these electron beams [1]. The LWFA electron beam is ultra-short (approximately 50 fs) with a mean energy up to 1 GeV, and a small projected energy spread [2]. With the LWFA electron beam, the FEL will be able to produce ultra-short laser pulses at UV and x-ray wavelengths. A laser with these properties will allow researchers to explore ultra-fast phenomena such as chemical reactions and phase-transitions of materials using pump-probe experiments.

As the LWFA is being tested and developed at LBNL, the FEL is being designed. Consequently, members of LOASIS must not only optimize the performance and improve the analysis of the electron beam from the laser-plasma accelerator, but also must address any problems or non-ideal conditions that might seriously affect the FEL performance. The FEL simulation program GINGER is used to model a wide range of FELs, including those with certain non-ideal effects. It can predict how the FEL will perform and identify problem issues prior to running the experiment.

Modeling of the LOASIS FEL is focused on optimizing its performance at wavelengths and powers compatible with the LWFA, and also predicting the effects of phenomena such as wakefields and mismatched beams. Some important electron beam parameters include energy spread, transverse emittance, and the interrelated quantities of current, charge, and pulse length. Knowledge of what type of electron beam creates good FEL performance provides LWFA researchers with realistic benchmarks for success. Wakefields, the electromagnetic fields caused by high-current electron bunches moving through the slightly resistive vacuum chamber, have the potential to reduce the output power of the laser. Consequently, it is useful to study the scaling of wakefields with FEL parameters and determine at what point they will become a severe detriment to the laser performance. Another possible problem is electron beam

mismatch to the undulator focusing lattice. This could occur when the electron beam entering the FEL system has the wrong transverse size or when it is diverging or converging. The magnitude of the effects caused by these imperfections can help determine the types of transport optics to be used between the LWFA beam source and the FEL beam entrance.

Analysis has also included effects on the output at the third harmonic of the resonant wavelength. Although it produces much lower power than the fundamental wavelength, the third harmonic emission provides a way to reach shorter wavelengths while still operating within the range of the current LWFA and FEL experimental configuration (i.e., beam energy and undulator wavelength).

This paper presents an overview of the simulation code GINGER, including the approximations used, and analysis of the results obtained from this code for the LOASIS FEL. These analyses include a range of optimal values for energy spread and emittance, a discussion of the most effective method for reaching short wavelengths, and an overview of the predicted effects of wakefields and mismatched beams.

Materials and Methods

GINGER is a multidimensional simulation code that tracks macroparticles, each of which represents numerous actual electrons. These macroparticles interact with electromagnetic fields which vary both radially and along the undulator axis. GINGER uses the slowly-varying envelope approximation of Maxwell's equations (also known as the eikonal approximation) and undulator-period averaged FEL equations for advancing the electromagnetic fields. The code simultaneously determines the value of the bunched transverse electron current and advances the macroparticles' energies and longitudinal phases as they move along the undulator. For more information on GINGER, see Fawley [6].

GINGER has the capability to run in two different modes. The first is a simple, monochromatic approximation that requires relatively little computational expense, allowing the user to scan over a large number of parameters in a short amount of time. This mode uses only one slice of macroparticles to model the entire duration of the pulse. GINGER tracks this single slice as it moves down the length of the undulator. By recording the fundamental and third harmonic power output at the end of the undulator for series of runs in which individual parameters are varied, the functional dependence of the FEL performance upon these parameters can be determined. Sample parameters include the energy spread, normalized transverse emittance, peak current, and matching parameters of the electron beam and the resonant wavelength of the system. Scanning in time-independent mode helps define a reasonable range of parameter values that result in lasing. A more accurate simulation can then be run in the second, more accurate GINGER mode.

The second mode in GINGER is fully time-dependent (and polychromatic) with respect to the electron pulse and radiation field, tracking multiple slices of macroparticles and fields in order to cover the full duration of the electron pulse. Using predictions and measurements of the LOASIS LWFA electron source, it is estimated that electron pulse durations will be approximately

30 fs long. To model the FEL, GINGER subdivides this pulse longitudinally, with each slice on the order of half a femtosecond long. These slices are then tracked as they move down the undulator. Time-dependent mode allows proper simulation of self-amplified spontaneous emission (SASE). SASE, which is initiated by random microbunching (i.e. shot noise) on the electron beam as it enters the undulator, does not require a seed laser at a specified wavelength, and is tunable by changing the initial electron energy or the magnitude of the undulator magnetic field. The spontaneous emission is created in the simulation using two user-input random number seeds for the microbunching. For most cases, the $RANDOM function in UNIX was used to generate these seeds.

Time-dependent mode is also needed to study the effects of vacuum chamber wakefields as they vary in time. To create realistic wakefields, a separate code generates the electric field in the longitudinal direction as a function of time relative to the passing electron bunch. GINGER then uses this additional electric field as it advances Maxwell's equations for the macroparticles' energies along the undulator axis.

Results

Studies of the proposed FEL center around one nominal case, the parameters of which are shown in Table 1 [3]. The GINGER runs presented use these parameters unless specified otherwise. For further information on the undulator construction and configuration, see Robinson et al [5]. The first parameter to be studied was energy spread. This value is defined as the ratio of the RMS variation in energy to the peak energy of the electron beam. Ideally, the energy spread will be as small as possible. The measured projected energy spread of the LOASIS LWFA electron beam is on the order of one percent [1]. The instantaneous energy spread may be much smaller than the projected spread, which is integrated over time. In addition, refinements in the LWFA design should allow

LWFA electron beam:	
Beam energy, γmc^2	0.5 GeV
Peak current, I (seeded/SASE)	5 kA / 10 kA
Longitudinal bunch shape	parabolic
Bunch duration (Full width)	30 fs
Charge	0.15 nC
Energy spread (slice, RMS), σ_γ/γ	0.25%
Normalized transverse emittance	1 mm mrad
Undulator:	
Undulator wavelength, λ_u	2.18 cm
Minimum magnetic gap	4.8 mm
Resonant wavelength, λ_s	31 nm
Seed Laser (when applicable):	
Radiation wavelength	31 nm
Radiation power	15 MW

Table 1. Nominal Parameters for GINGER Simulations.

production of electron beams with less than 0.5% energy spread. The range examined for FEL simulations went from 0.01% to 0.7%, with 0.25% being the value used for GINGER scans of other parameters (see Table 1). The output power for the fundamental wavelength and the third harmonic as a function of initial energy spread are shown in Figure 1(a,b). The second electron parameter scanned was normalized transverse emittance. Transverse emittance is a measure of the beam's area in transverse phase space (as shown in Figure 2) and is related to the product of the beam's radius and its transverse kinetic temperature. A large transverse emittance can affect the beam size as it is focused and also leads to an increase in the spread of beam particles' longitudinal velocity. Normalized transverse emittance is defined as $e_n = \gamma \sqrt{\langle \theta^2 \rangle} \sqrt{\langle r^2 \rangle}$. The nominal value for the LOASIS beam is 1 mm mrad, and the range of values scanned was from 0.2 mm mrad to 4.0 mm mrad. The output powers are shown in Figure 3(a,b).

Studies of the effects of a mismatched electron beam were also performed in the quick, time-independent mode of GINGER. The first parameter, α-Twiss, ranges from -1 to 1, and is a measure of the divergence of the beam, with -1 indicating a diverging beam, and +1 indicating a converging beam. The resulting output radiation power for the fundamental is shown in Figure 4. The second mismatch parameter is the scaled β-Twiss, which is a factor related to the cross-sectional size of the beam. Specifically, for these simulations, RMS beam size = $60 \mu m \cdot \sqrt{\beta_{Twiss}}$. When β-Twiss = 1, the beam is ideally matched to the undulator focusing, with an RMS beam size of 60 μm, which stays constant for the length of the undulator. When β-Twiss < 1, the beam is too small, and when β-Twiss > 1, the beam is too large. Here, β-Twiss is varied from 0.25 to 4.0 (with RMS beam size ranging from 30–120 μm), as shown in Figure 5.
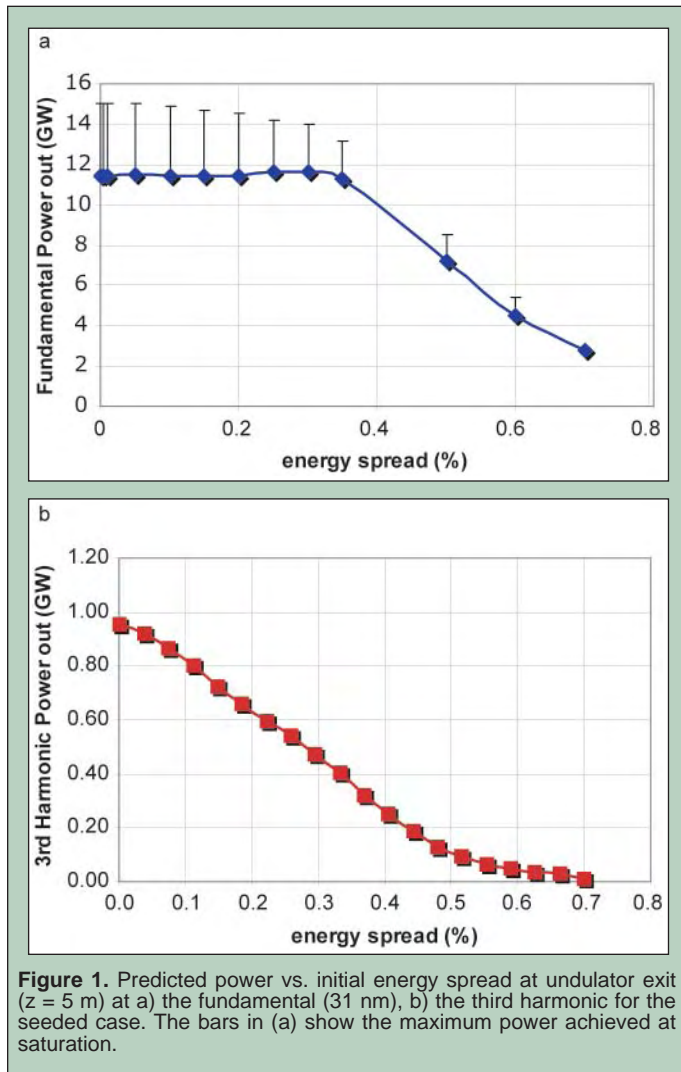
In order to study the possibilities for using the third harmonic to reach shorter wavelengths than are possible with the fundamental only, two series of runs were performed. In the first, the fundamental resonant wavelength varied from 12 nm to 31 nm. In order to change the resonant wavelength, λs, the strength of the normalized peak magnetic field of the undulator, a_w, was increased, in accordance with the FEL resonance relationship: $\lambda_s = \lambda_u (1 + a_w^2) / (2\gamma^2)$, where γ is the energy of the beam in units of mc^2 and λ_u is the undulator wavelength. The radiation power output for both the fundamental as it ranges from 12 nm to 31 nm and the associated third harmonic, ranging from 4 nm to 10.3 nm are plotted in Figure 6. In order to reach third harmonic wavelengths exceeding 10.3 nm, a different variable in the FEL resonant relationship may be varied. The maximum undulator magnetic field is limited by the allowed magnetic gap in the configuration, so for fundamental wavelengths larger than 31 nm, the energy of the beam must be decreased to increase the wavelength. Similar runs were performed using SASE as the initial radiation source instead of a seed laser (see Figure 7). In order to simulate SASE, the time-dependent mode of GINGER was used. In these cases, changing the magnitude of the undulator magnetic field was the only method explored to vary the resonant fundamental wavelength.

The final studies concerned the effects of wakefields in the vacuum chamber of the undulator. Using a vacuum chamber radius

Figure 1. Predicted power vs. initial energy spread at undulator exit (z = 5 m) at a) the fundamental (31 nm), b) the third harmonic for the seeded case. The bars in (a) show the maximum power achieved at saturation.
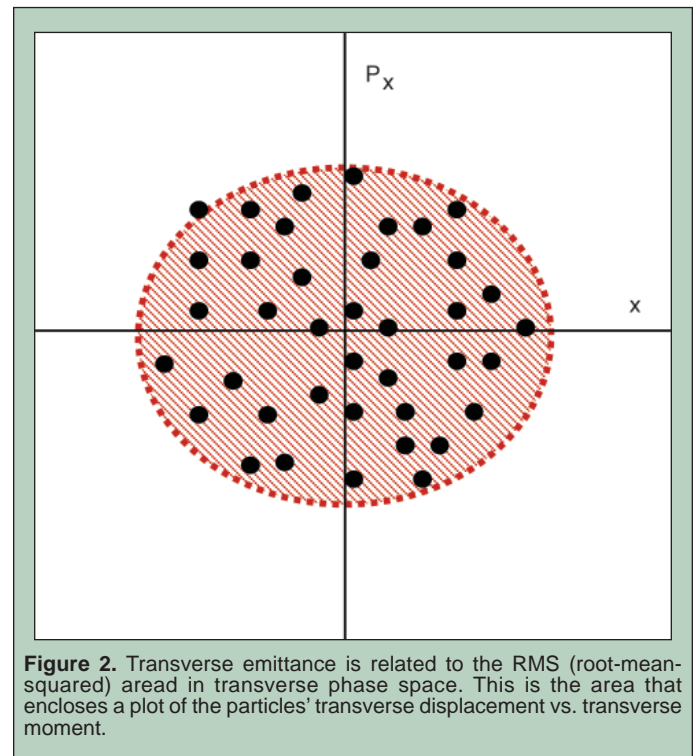
Figure 2. Transverse emittance is related to the RMS (root-mean-squared) aread in transverse phase space. This is the area that encloses a plot of the particles' transverse displacement vs. transverse moment.

of 2 mm, several cases were considered. A basic approximation, for which the conductivity parameters are well known, is to treat the chamber as an aluminum cylinder with AC conductivity. The resulting wakefield from 300 pC of beam charge contained within a bunch length of 30 fs is shown in Figure 8. The actual vacuum chamber for the undulator to be used by LOASIS is constructed from stainless steel 303, for which the DC conductivity is well documented, but for which the AC conductivity relaxation time, τ, is unknown. To deal with this, it was presumed that 303 stainless steel has the same τ as iron, which is well known [4]. Figure 8 also shows the computed wakefields for a stainless steel vacuum chamber with both AC and DC conductivity models. To obtain basic statistical data on the expected effects of wakefields, a series of

32 SASE runs with different random number seeds were compared with 64 statistical SASE runs with no wakefields included. In these runs, the aluminum AC conductivity model was used to compute the wakefield. The resulting RMS values and relative differences are shown in Table 2.

In order to model the effects of current on wakefields, and how that, in turn, affects the electron beam, a series of different wakefields were created for varying currents, I. The pulse length, τ_p, was kept constant, and the charge, Q, was varied to satisfy the equation I τ_p = Q. The resulting output energies are compared with the equivalent runs without wakefields in Figure 9.
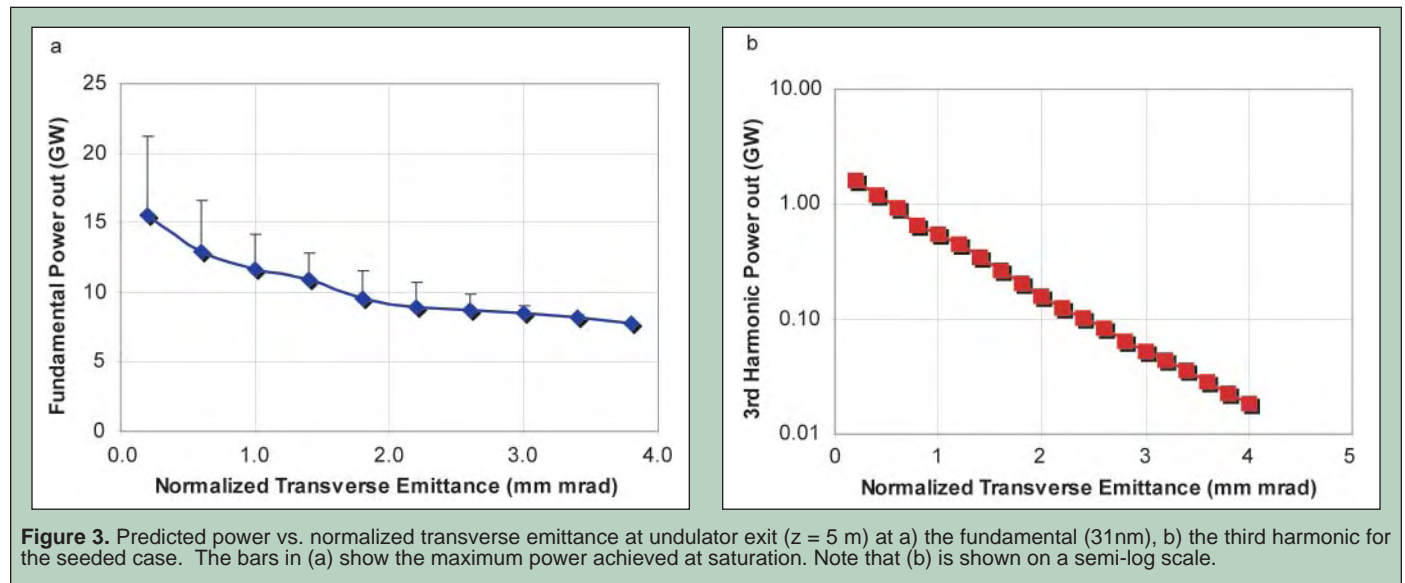
Figure 3. Predicted power vs. normalized transverse emittance at undulator exit (z = 5 m) at a) the fundamental (31nm), b) the third harmonic for the seeded case. The bars in (a) show the maximum power achieved at saturation. Note that (b) is shown on a semi-log scale.
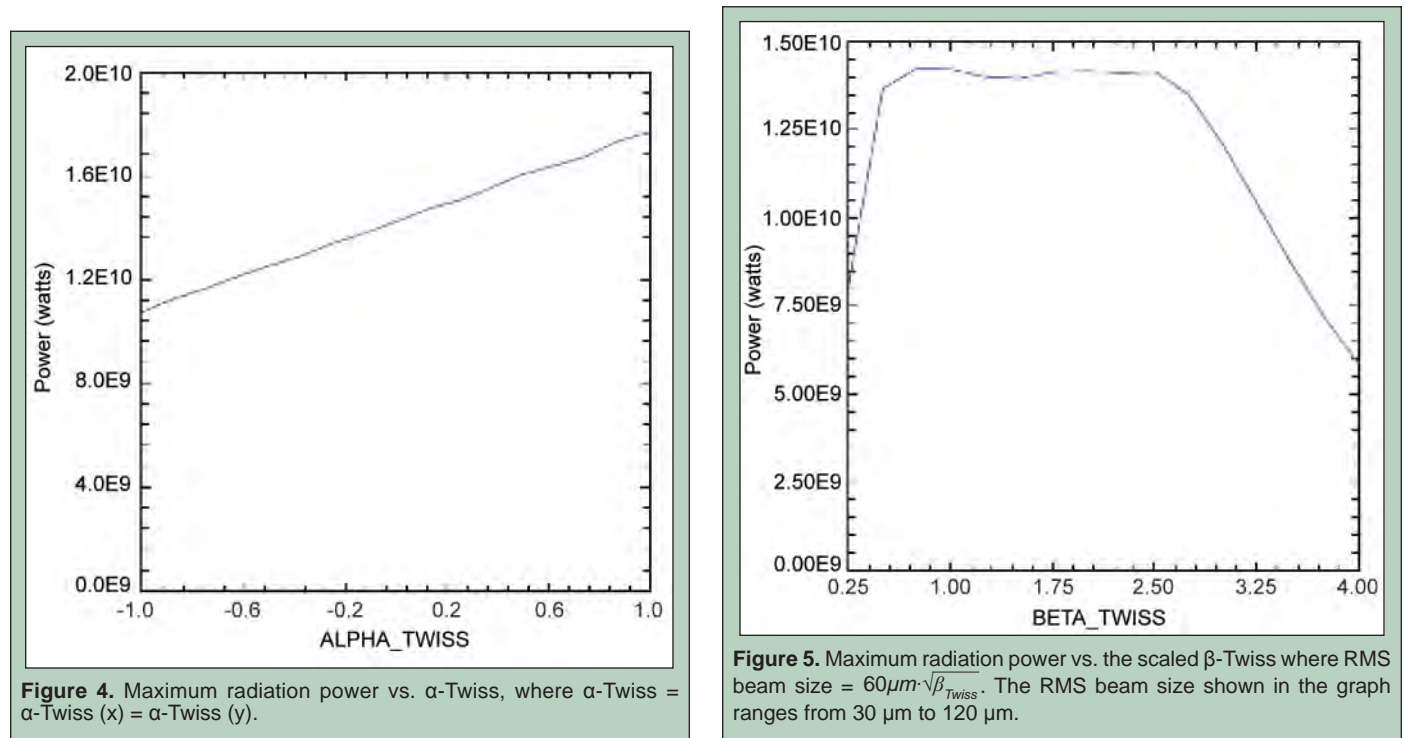
Figure 4. Maximum radiation power vs. α-Twiss, where α-Twiss = α-Twiss (x) = α-Twiss (y).

Figure 5. Maximum radiation power vs. the scaled β-Twiss where RMS beam size = $60\mu m \cdot \sqrt{\beta_{Twiss}}$. The RMS beam size shown in the graph ranges from 30 μm to 120 μm.
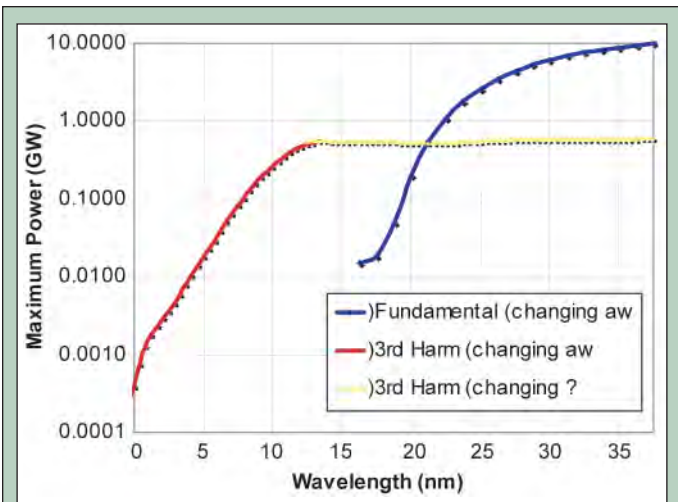
Figure 6. Maximum power at a given wavelength reached using fundamental (blue) and or the third harmonic (red and yellow).
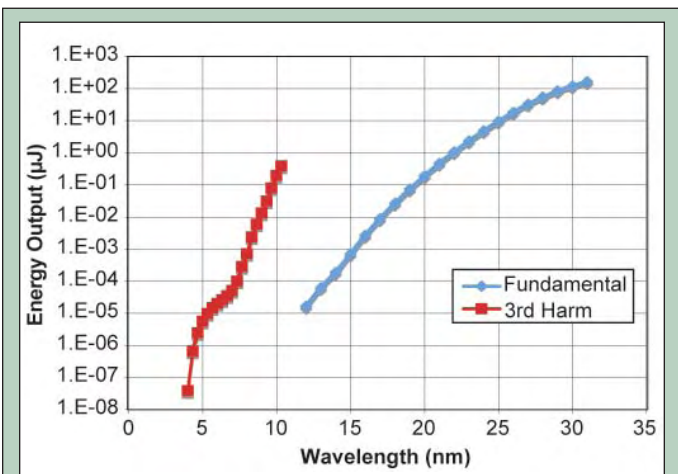
Figure 7. Average energy output vs. resonant wavelength from 4 SASE runs.
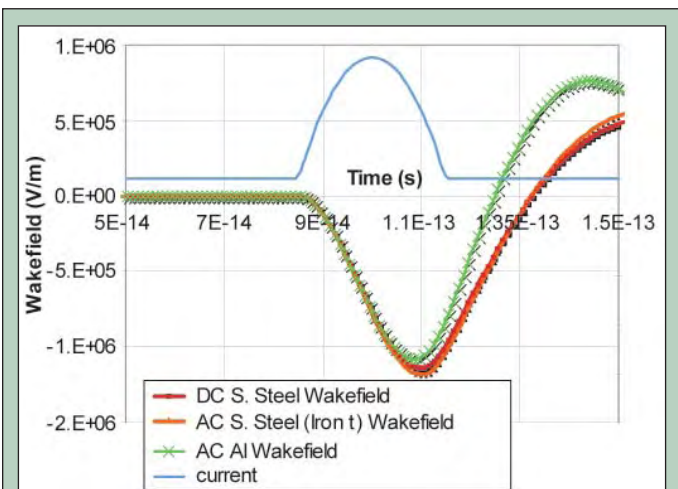
Figure 8. Computed wakefields for DC and AC models for stainless steel (using stainless steel 303 DC conductivity and τ for iron) and aluminum. The current profile is also shown, with peak value of 10 kA. The head of the electron bunch is on the left and the tail is on the right.
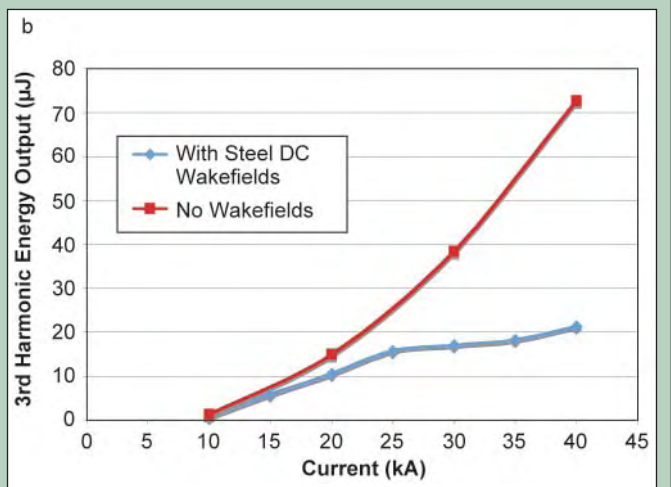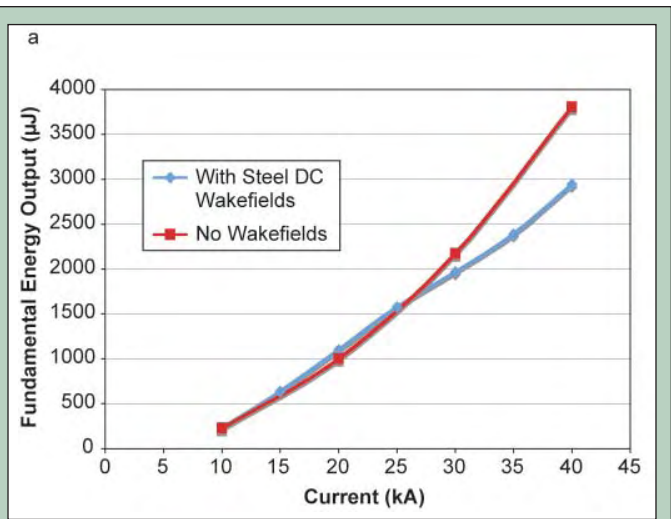
Figure 9. Output energies for a) the fundamental, and b) the third harmonic as current is varied (and pulse length kept constant). This is shown for the case with stainless steel DC wakefields and the case where no wakefield effects were included.

	Fundamental (31 nm)	3rd Harmonic (10.3 nm)
Avg. Output Energy (with wakefields) (µJ)	211.6	0.819
Std. Deviation (with wakefields) (µJ)	61.3	0.443
Avg. Output Energy (no wakefields) (µJ)	238.0	1.173
Std. Deviation (no wakefields) (µJ)	58.8	0.532
Percent Difference between output energies $(E_{no\,wake} - E_{wake}) / \frac{1}{2} (E_{no\,wake} + E_{wake})$ (100%)	11.8	35.6

Table 2. Statistical Analysis of Wakefield Effects for Nominal Case.

DISCUSSION AND CONCLUSIONS

These studies help provide a better understanding of the parameters needed to obtain successful FEL with the LOASIS electron beam and some of the expected properties of the resulting laser. The relative energy spread per slice has a clear effect on the fundamental power, as seen in Figure 1a. For an energy spread less than 0.35%, the laser can saturate (reaching its maximum power) before the end of the undulator, and then slowly oscillates near that power until the undulator exit. For an energy spread of greater than 0.35%, the laser does not saturate by the time it reaches the end of the undulator, and the output power drops linearly as energy spread increases. The third harmonic (as shown in Figure 1b), however, does not have a maximum energy spread below which the power stays approximately constant. Instead, the approximately linear dependence of output power on energy spread continues even for very small energy spreads. The difference in performance between a beam with 0.5% energy spread and 0.25% energy spread was noted for several other cases where other parameters, such as resonant wavelength, were varied.

Examining the scans in emittance in Figure 3, there is no clear cut-off point as there is for energy spread, nor is there a linear dependence of fundamental power on emittance. The nominal value for emittance, 1 mm mrad, gives an acceptable output fundamental power of approximately 12 GW in this seeded run. The third harmonic output power does have an interesting exponential correspondence of output power with emittance that is not yet fully understood.

The maximum power shown in the α-Twiss scan in Figure 4 shows that the FEL performance is relatively insensitive to beam divergence for the parameters considered. Varying β-Twiss gives a definite but large range of beam sizes that will allow the FEL to saturate in the undulator. The results shown in Figure 5 indicate that the RMS beam size could range from 40–100 μm without an appreciable loss of power. Beam mismatch appears to have less of an effect on FEL performance than beam emittance and energy spread.

Even with a matched beam with ideal emittance and energy spread, it is difficult to operate at wavelengths shorter than 31 nm without decreasing the output power. Figure 6 shows that the most effective way to reach wavelengths below 13 nm is to use the third harmonic. Although the maximum power for these is still under a gigawatt, the number of photons reaches a maximum of 7×10^{11}. In the equivalent SASE runs, as shown in Figure 7, we see that wavelengths between 7 nm and 10 nm are best obtained by using the third harmonic. Below 7 nm, the output energy appears to be dominated by spontaneous emission, indicating that no significant bunching (i.e., coherent emission) has occurred.

Wakefields are the final issue addressed in this paper. As can be seen in Figure 8, the three types of wakefields examined (AC aluminum, AC stainless steel, and DC stainless steel) have nearly identical values over the time span occupied by the current. Because of this, all three types of wakefield models yield similar results. All wakefield simulations were run as SASE cases, so numerous runs were done with different random seeds. In Table 2, one sees that a) the third harmonic was affected more by wakefields than the fundamental, and b) that, although there is a statistically important percent difference between the RMS value for the cases with wakefields and those without, both RMS values lie within a standard deviation of each other. Some individual cases with wakefields had better performance than some cases without wakefields, but, on average, output energy was greater for the case without wakefields, as expected. The uncertainty introduced by the randomness of the SASE runs is large enough that it makes the energy loss caused by wakefields experimentally insignificant.

Improvements in the LWFA performance may allow for larger currents, which would in turn create larger wakefields. Figure 9 shows at what current wakefields will begin to have a significant effect on the energy output for the fundamental and third harmonic. In Figure 9a, one can see that wakefields cause a decrease in output energy only at high currents (i.e., above 35 kA). Wakefields have a more significant effect on the third harmonic as seen in Figure 9b, where they significantly decrease the output energy at currents as low as 25 kA.

The results and analysis presented in this paper provide a range of parameters for which the FEL will perform best. The most significant of these parameters is energy spread, which must be small to ensure FEL saturation. It has also been shown that beam mismatch and vacuum chamber wakefields will not have a large effect when the standard input parameters are used. Continued improvement of the LWFA electron beam will allow the LOASIS FEL to operate in an optimal regime and produce a high-quality x-ray laser pulse.

REFERENCES

[1] C.G.R. Geddes, Cs. Toth, J. van Tilborg, *et al*, "High-quality electron beams from a laser wakefield accelerator using plasma-channel guiding," *Nature*, Vol. 431, 538–541 (Sep 2004).

[2] W.P. Leemans, B. Nagler, A.J. Gonsalves, *et al*, "GeV electron bemas from a centimeter-scale accelerator," *Nature Phys.*, Vol. 2, 696–699 (Oct 2006).

[3] C.B. Schroeder, W.M. Fawley, E. Esarey, and W.P. Leemans, "Design of an XUV FEL Driven by the Laser-Plasma Accelerator at the LBNL LOASIS Facility," in *Proceedings of FEL 2006*, 455–458, JACoW (Sep 2006).

[4] D. Scott, "Longitudinal Resistive Wall Wakefields for the ILC Positron Undulator Vessel," ASTEC-ID-040 (May 2006).

[5] K.E. Robinson, D.C. Quimby, and J.M. Slater, "The Tapered Hybrid Undulator (THUNDER) of the Visible Free-Electron Laser Oscillator Experiment," *IEEE Journal of Quantum Electronics*, Vol. QE-23, 1497–1513 (Sep 1987).

[6] W.M. Fawley, Technical Report LBNL-49625, Lawrence Berkeley National Laboratory, (2002).

Robert Pasquarelli was born in Pittsburgh, PA. He obtained in B.S. in Chemistry from the Rochester Institute of Technology. During his undergraduate career, he held two SULI internships at the National Renewable Energy Laboratory (NREL) in the summers of 2006 and 2007. He is currently pursuing a Ph.D. in materials science at the Colorado School of Mines and is conducting his thesis research at NREL under David Ginley and Ryan O'Hayre. He enjoys hiking, biking, and graphic design.

Calvin Curtis is a senior scientist at the National Renewable Energy Laboratory (NREL). He earned his BS in chemistry at Harvey Mudd College and his Ph.D. in inorganic chemistry from the University of California at Berkeley. After postdoctoral work at CalTech, he joined the technical staff at the Solar Energy Research Institute (now NREL) in 1980. His research interests include the synthesis of photovoltaic materials and semiconductor nanostructures from organometallic precursors, inkjet printing of electronic materials and metals using organometallic inks, hydrothermal synthesis of novel metal oxide nanostructures, and transition metal hydride thermodynamics. He is a co-inventor on 10 patents in the areas of synthesis and surface modification of nanoparticles, ink formulation and film deposition, and the author of over 50 refereed publications.

Inkjet Printing of Nickel and Silver Metal Solar Cell Contacts

Robert Pasquarelli, Calvin Curtis, and Maikel Van Hest

ABSTRACT

With about 125,000 terawatts of solar power striking the earth at any given moment, solar energy may be the only renewable energy resource with enough capacity to meet a major portion of our future energy needs. Thin-film technologies and solution deposition processes seek to reduce manufacturing costs in order to compete with conventional coal-based electricity. Inkjet printing, as a derivative of the direct-write process, offers the potential for low-cost, material-efficient deposition of the metals for photovoltaic contacts. Advances in contact metallizations are important because they can be employed on existing silicon technology and in future-generation devices. We report on the atmospheric, non-contact deposition of nickel (Ni) and silver (Ag) metal patterns on glass, Si, and ZnO substrates at 180–220°C from metal-organic precursor inks using a Dimatix inkjet printer. Near-bulk conductivity Ag contacts were successfully printed up to 4.5 μm thick and 130 μm wide on the silicon nitride antireflective coating of silicon solar cells. Thin, high-resolution Ni adhesion-layer lines were printed on glass and zinc oxide at 80 μm wide and 55 nm thick with a conductivity two orders of magnitude less than the bulk metal. Additionally, the ability to print multi-layered metallizations (Ag on Ni) on transparent conducting oxides was demonstrated and is promising for contacts in copper-indium-diselenide (CIS) solar cells. Future work will focus on further improving resolution, printing full contact devices, and investigating copper inks as a low-cost replacement for Ag contacts.

Introduction

With about 125,000 terawatts of solar power striking the earth at any given moment, solar energy may be the only renewable energy resource with enough capacity to meet a major portion of our future energy needs [1]. However, the key issue is cost. In order to compete with conventionally coal-based electricity, the U.S. Department of Energy's Solar America Initiative seeks to drive down the price of solar electricity to less than $0.10 per kWh by 2015. Second-generation solar cells seek to reduce manufacturing costs through thin-film technology, process optimization, and minimizing material usage. In these devices, liquid precursor deposition methods (including spin coating, spray deposition, and inkjet printing) are attractive because the equipment required is simple and inexpensive, the methods are scalable to large substrate sizes, and they are carried out under atmospheric conditions. Inkjet printing, as a derivative of direct-write processing, offers further advantages including high material usage efficiency, non-contact processing for use with fragile thin-film substrates, and the elimination of photolithography [2].

Inkjet printing is quickly becoming an alternative to existing deposition methods and has wide-range potential in both inorganic and organic photovoltaic and electronic materials. With the appropriate inks, all the features of a solar cell, including the absorber, dopants, transparent conductor, and front and rear metal contacts, could be sprayed or directly printed. Advances in contact metallizations are important because they can be employed on existing silicon technology and in future-generation devices. As such, the initial thrust and focus of this paper is on the materials used for front metal contacts. At present, inkjets are capable of line resolutions less than 20 μm, which is two to four times better than the current method of screen printing [3]. High resolution (narrower contact lines) means more absorber material is exposed to sunlight and thus higher conversion efficiency can be obtained. Additionally, unlike screen printing, direct-write is a no-waste approach, which is both environmentally- and cost-friendly.

The ink consists of two major components: the appropriate precursor and the carrier (an organic solvent). The precursor is the compound that decomposes into the desired material or

metal. Additionally, the content of the ink can be easily tailored by addition of binders, adhesion promoters, surfactants, reducing agents, and dopants. Composition is important because it influences the way in which the ink is jetted and adheres to the substrate, the profile and resolution of the line, and the material/metal formation. The ink is printed onto a heated substrate in the desired pattern. At the appropriate temperature, the metallic film forms following decomposition of the precursor and evaporation of the solvent. Byproducts of decomposition leave as gases, resulting in contaminant-free films.

Inkjet printing allows for multilayer structures and thus is well-suited for contact layers, which are often multicomponent. Silver (Ag) is primarily used as the contact metal because of its high conductivity. Ideally, less expensive copper (Cu) would replace Ag as the contact. The printing approach for these contacts is dependent on the surface material. As such, surface modifying agents and adhesion inks have been developed to improve contact formation and surface adhesion. For example, silicon (Si) cells are coated with an anti-reflective (AR) layer of silicon nitride. The Ag contact can be printed onto a previously printed layer of fire-through ink, which when heated etches through the AR coating to expose the Si to the contact [4]. In next-generation copper-indium-diselenide (CIS) cells, the top layer is a transparent conducting oxide (TCO), which acts as both a conductor and a window to allow light to pass through to the absorbing layer. For these devices, a thin layer of nickel (Ni) is first applied to the TCO to create good adhesion between the TCO and contact. A typical CIS structure is depicted in Figure 1. Ag diffusion into the absorber layer can detrimentally affect efficiency, particularly for CIS. Therefore, in addition to acting as an adhesion layer, the Ni serves the essential role of a diffusion barrier [5].

We report on the inkjet printing of the Ag contact and Ni adhesion layer from proprietary inks developed at the National Renewable Energy Laboratory (NREL). Inkjet printing was chosen

over spray deposition because it is spatially selective and drop-on-demand, which is ideal for depositing contact grid patterns. The specific goals of this research were to optimize printing parameters and ink formulations to achieve highly conductive lines with good adhesion and high resolution. For the Ni adhesion layer, the target was to make each line as thin and narrow as possible while maintaining uniformity (no breaks, beading, or large profile variations). For the Ag contact layer, the target was a thicker (10 μm), narrow line with near bulk-material conductivity. The supporting Ni layer would ideally govern the Ag line width and profile.

MATERIALS AND METHODS

Inkjet System. Printing was performed using a Dimatix Materials Printer (Fujifilm Dimatix, Santa Clara, CA), as shown in Figure 2. The ink cartridge contains a piezoelectric material behind each ink nozzle. When a voltage is applied to the material, it changes shape, which results in a pressure pulse that forces a droplet of ink out of the nozzle. The cartridge consists of 16 nozzles with 10-picoliter drop volume. The Dimatix system consists of a print head positioned above a heatable platen on a moving stage. A programmable hotplate was constructed and mounted to the platen to provide a wider range of substrate temperatures (up to 400°C). The user has control over several parameters to optimize printing, including ink and substrate temperature, individual jet firing voltage (to tune drop velocity), firing frequency, and drop spacing.

Figure 2. Dimatix Materials Printer inkjet system.

Inks. Metallization inks consisted of the precursor and additives dissolved in organic solvents (NREL proprietary compositions). Inks were filtered through a 0.2 μm syringe filter to remove particulates that would clog the nozzles and stored in their respective cartridges at room temperature. The Ni ink was stable for several months. The Ag ink was stored away from light to avoid decomposition, and the cartridge was covered with aluminum foil to avoid exposure to light during printing. The Ag ink began to discolor, indicating gradual decomposition, after a couple of weeks.

General Procedures. The Ni ink was printed over a substrate temperature range of 140 to 180°C, over a drop spacing range of 10 to 50 μm, and from 1 to 10 layers. Two printing approaches

Figure 1. Schematic cross-sectional view of a substrate configuration device.

were explored. The Ni Wet Print approach consists of printing a wet line at 140°C, and after printing, increasing to 180°C to induce decomposition and solvent evaporation. The Ni Hot Print approach involves printing the line at sufficient temperature (180°C) to simultaneously produce decomposition and evaporation as printing occurs. Glass microscope slides and thin films of ZnO on glass were used as substrates. The Ag ink was test printed between 155 and 220°C, over a drop spacing range of 20 to 70 μm, and from 1 to 200 layers. The ink was printed on four separate surfaces: (a) glass slides, (b) Ni printed lines, (c) 0.125 mm thick Ni foil, and (d) the silicon nitride AR coated side of Evergreen Solar silicon string ribbon.

Two printing patterns were used. Initial studies were performed on a pattern consisting of five lines with increasing incremental widths of 20 μm. The second pattern was used to test device features, consisting of single-drop-row lines for fine resolution tests and wider lines with square pads at the ends for performing conductivity measurements (Figure 3).
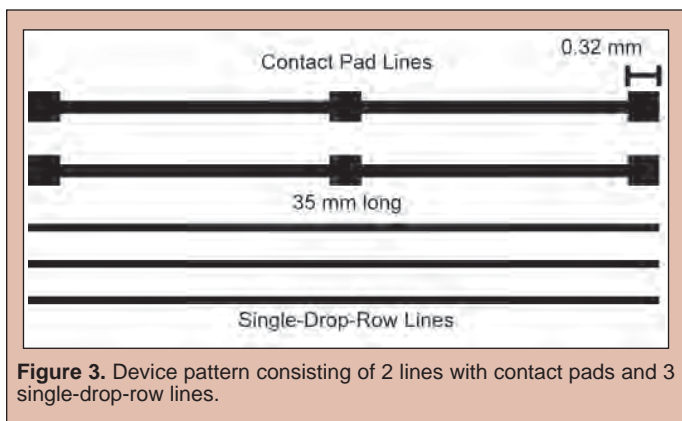
Figure 3. Device pattern consisting of 2 lines with contact pads and 3 single-drop-row lines.

Substrate surface temperature was monitored with a type-J thermocouple thermometer prior to printing. Line thickness, width, and cross-sectional area were measured using a Dektak 8 profilometer. A Nikon Eclipse LV 100 camera equipped microscope was used to image lines and assess line quality. X-ray diffraction (XRD) studies were performed on a Bruker AXS D8 Discovery System. Resistivity, calculated using the equation below, was determined by using a four-point probe microscope station to measure voltage (V) and current (I).

$$Resistivity \ (\Omega \cdot cm) = \frac{V}{I} \cdot \frac{cross\text{-}sectional \ area \ of \ line}{length \ of \ line \ between \ probes}$$

RESULTS

Four layers of Ni ink were printed on glass using the five-line pattern to observe changes in line profile as a function of drop spacing. Drop spacing was varied in 5-μm increments from 10 to 50 μm. The average line width and thickness of Hot and Wet printed Ni ink at the determined optimal drop spacing of 30 μm was plotted in Figure 4. Using this drop spacing and the Hot Print approach, Ni was printed from 1 to 10 layers using the device pattern. The average width and thickness of these single-drop-row lines on glass was plotted in Figure 5A as a function of the number of layers

printed. For the line profile data, width refers to the resolution (narrowness) of the line, and thickness refers to line height. Line width and thickness measurements from the five-line pattern are averages of profilometry readings at two points per line. Device pattern data with single-drop-row lines represent the average of six measurements, two per line over three lines to test variation within a line and reproducibility of lines. Microscope images of Ni contact pad lines Hot printed on glass and ZnO are provided in Figure 6.

Ag was printed from 1 to 200 layers using the device pattern on AR coated Si ribbon at 215°C with an optimized 35-μm drop spacing and an initial ink temperature of 45°C. The average width and thickness of the single-drop-row lines was plotted in Figure
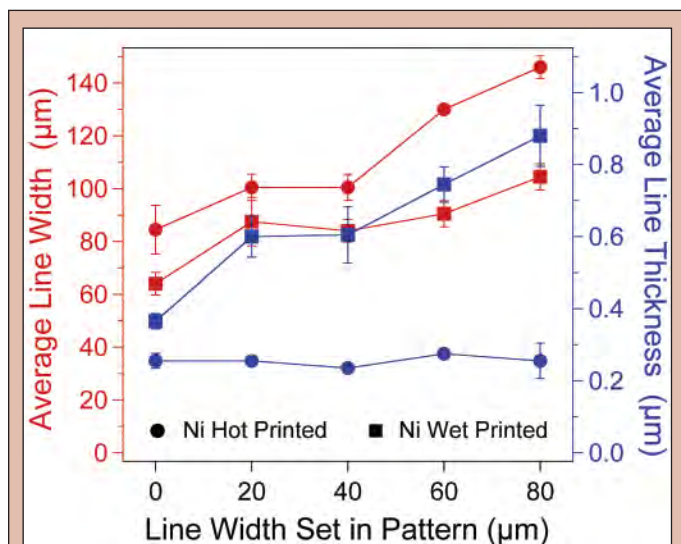
Figure 4. Line width (red) and thickness (blue) of Hot and Wet printed Ni ink at optimized 30-μm drop spacing. Single-drop-row lines printed on glass (4 layers).
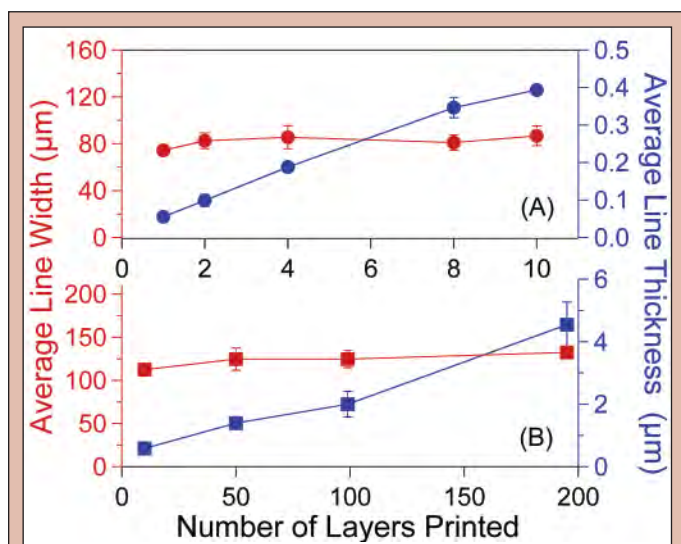
Figure 5. Line width (red) and thickness (blue) of single-drop-row lines of optimized Ni Hot Print on glass (A) and Ag on AR coated Si ribbon (B) as a function of the number of layers.

5B as a function of the number of layers printed. Figure 7 shows high-resolution Ag lines printed on glass, on inkjet printed Ni lines, on Ni foil, and on AR coated Si ribbon. The Ag ink was initially printed on glass to find the optimum drop spacing. Single rows of individual 50-μm wide Ag drops on glass at 45-μm drop spacing, just prior to line formation, is shown in Figure 7A. In Figure 7B, the fine line demonstrates that Ag can be printed on top of printed Ni lines. The wider lines are printed offset to show the Ag and Ni lines stacked.

The X-ray diffraction (XRD) patterns of the spray-printed inks for Ni, Ag, and Cu are depicted in Figure 8. The resulting metal coatings are consistent with the expected intensities and scattering angles (given by two-theta) for the pure, bulk material (included in the figure for comparison). Resistivities for the optimized Ni and Ag printed as a function of the number of layers are represented in Figure 9. The target resistivities of the pure, bulk material for Ni and Ag are $7.12 \times 10^{-6}\ \Omega \cdot cm$ and $1.59 \times 10^{-6}\ \Omega \cdot cm$ respectively [6]. Measurements were based on Ni and Ag printed using the contact pad pattern on glass and AR coated Si substrates respectively. The Si was assumed not to interfere with the resistivity measurements because the silicon nitride AR coating is a good electrical insulator.

Discussion and Conclusions

Inkjet temperature trials for the Ni ink revealed two potential avenues, referred to as the Wet and Hot Print approaches. At 140°C, the lines printed clear and were still wet. They only decomposed into black lines after secondary heating. From 150 to 170°C, the lines printed black but were still wet, suggesting that decomposition occurred without solvent evaporation. Poor quality lines that tended to bead and bubble were produced when the solvent was evaporated via secondary heating. Thus, this range was not pursued. At 180°C, dry, decomposed lines formed on contact with the heated substrate. No secondary heating was required. Above this temperature, lines tended to bubble due to the rapid evaporation of the solvent. The temperatures used for the Ni Wet and Hot Print experiments were selected with these results in mind. Generally, the Hot Print was the preferred route since it is a simpler, single-step process. Likewise, difficulty in controlling the rate of the secondary heating for the Wet Print resulted in bubbling and line breaks.

Drop spacing was a critical parameter in the printing process because it affected line formation. At larger drop spacings (exceeding 40-μm for Ni), individual drops formed. As the drop spacing was decreased, more drops and thus material was used to create a line, which affected line thickness and width. It was crucial to find the spacing that used the least material and at which drops still merged to form a uniform line. From the experiments, the optimal drop spacing was determined to be 30 μm, at which a key difference between the two printing approaches was revealed. The thickness of the Hot Print remained unaffected by the number of rows printed next to each other while the Wet Print thickness increased (Figure 4). Ideally, one controls width only by printing more rows and controls thickness only by printing more layers.

The Ni Hot Print at 30-μm drop spacing was the superior approach because it was one-step, consistently produced continuous lines, and had more degrees of control. Hot Print Ni line width was only dependent on the number of rows printed and independent of the number of layers printed (Figure 5A). Line thickness was only dependent on the number of layers and behaved linearly, each layer adding ~50 nm of material (Figure 5A). Likewise, it met the desired features for Ni, with a width of 80 μm and thickness of 55 nm at 1 layer. The profile was consistent within each line and reproducible between lines. Figure 6 demonstrates the line quality and resolution control of features achieved on glass and ZnO. Printing parameters on ZnO were the same as on glass. Results on ZnO are promising for printing on the TCO layer in a CIS cell.

Wetting, the amount a drop spreads out on a substrate, was a critical parameter for printing Ag. Various wetting situations are illustrated in Figure 10. Initial experiments varying the drop spacing on glass revealed that individual drops formed at 45-μm (Figure 7A) and pairs of drops merged at 40-μm into larger drops. The fact that drops of ink only beaded into larger drops instead of
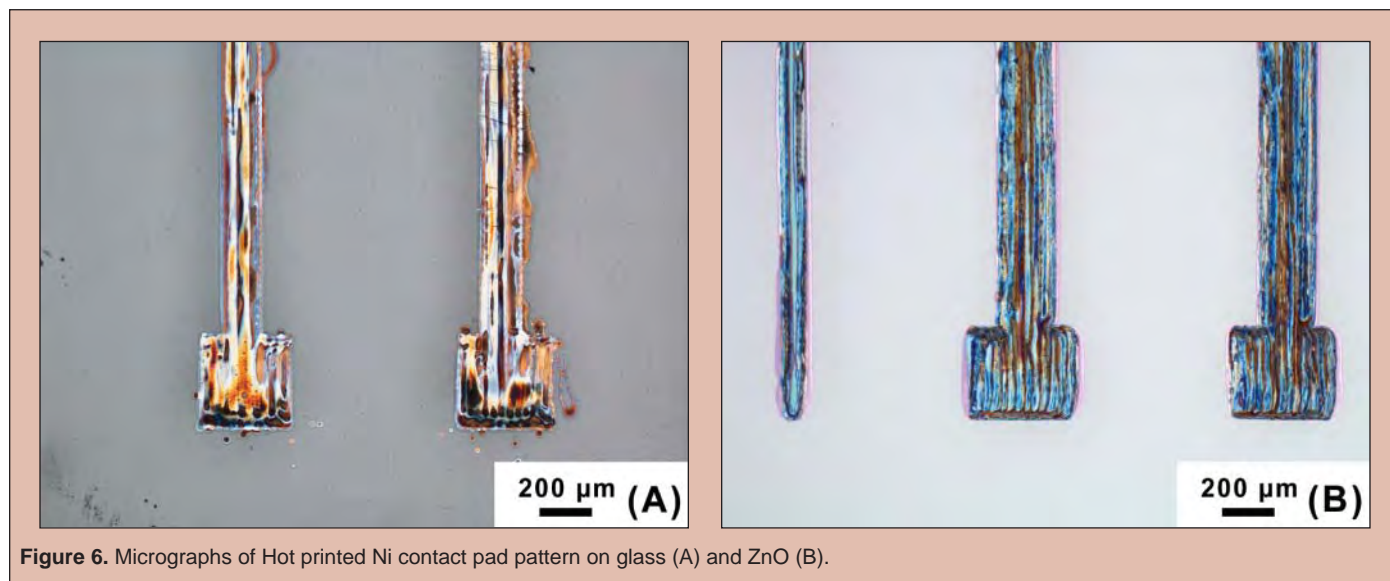
Figure 6. Micrographs of Hot printed Ni contact pad pattern on glass (A) and ZnO (B).
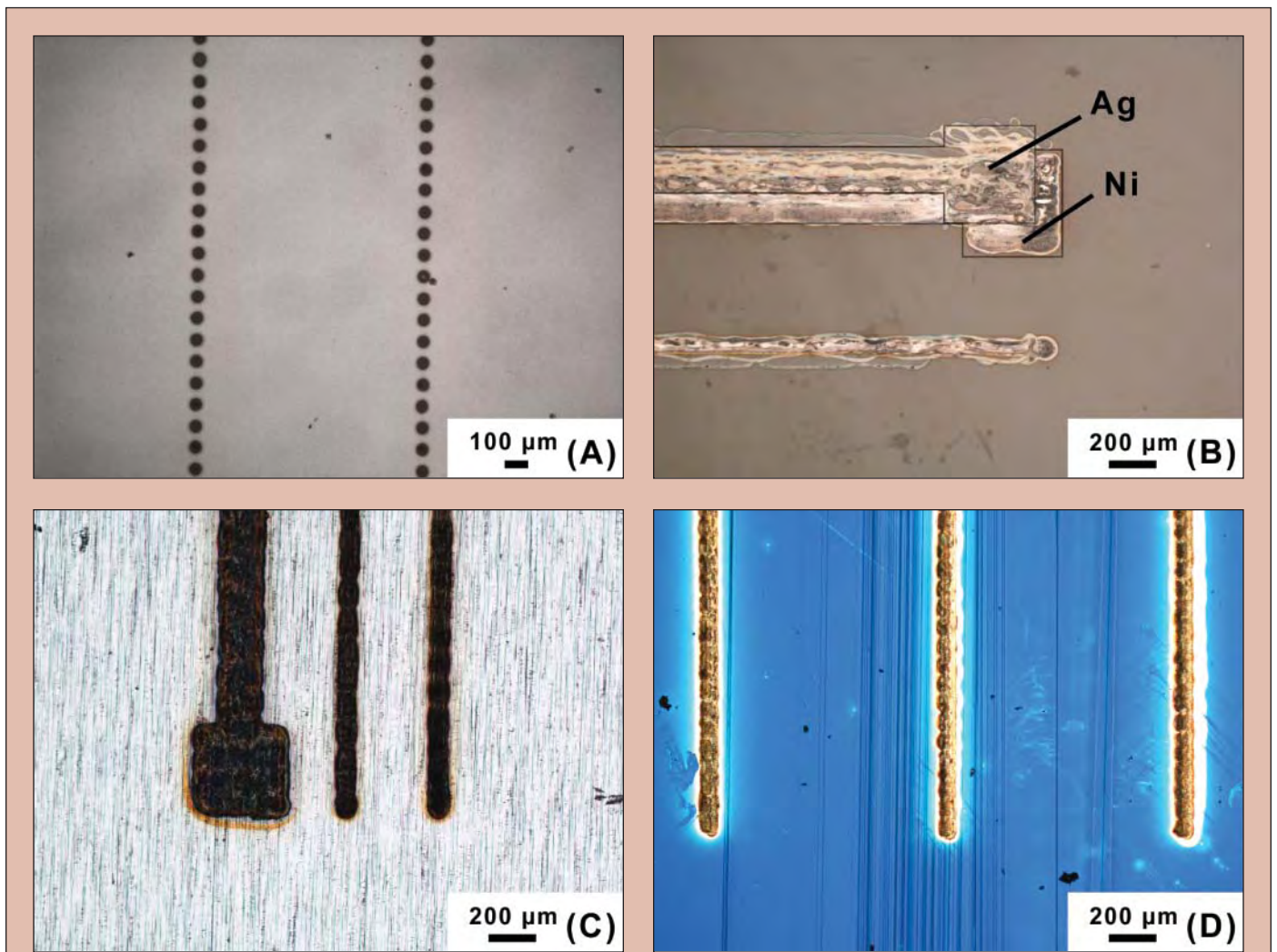
Figure 7. Micrographs of individual 50-μm wide Ag drops on glass at 45-μm drop spacing (A), Ag lines printed on top of printed Ni lines (B) and Ni foil (C), and Ag lines on AR coated Si ribbon (D).
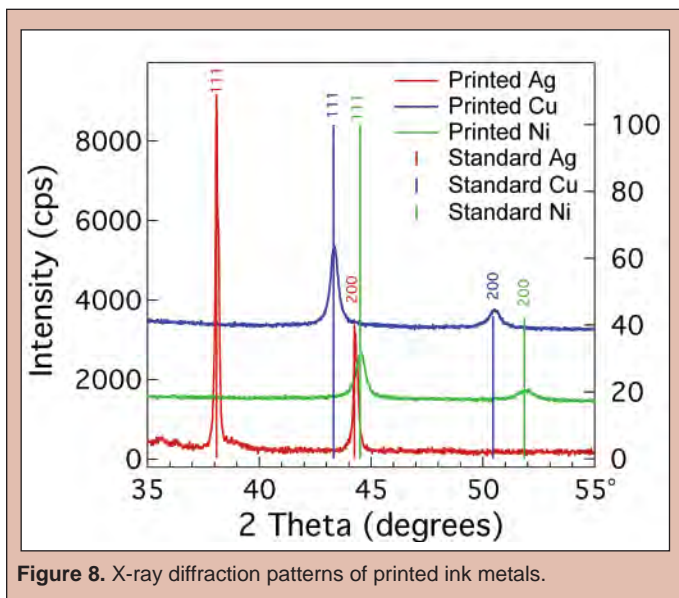
Figure 8. X-ray diffraction patterns of printed ink metals.
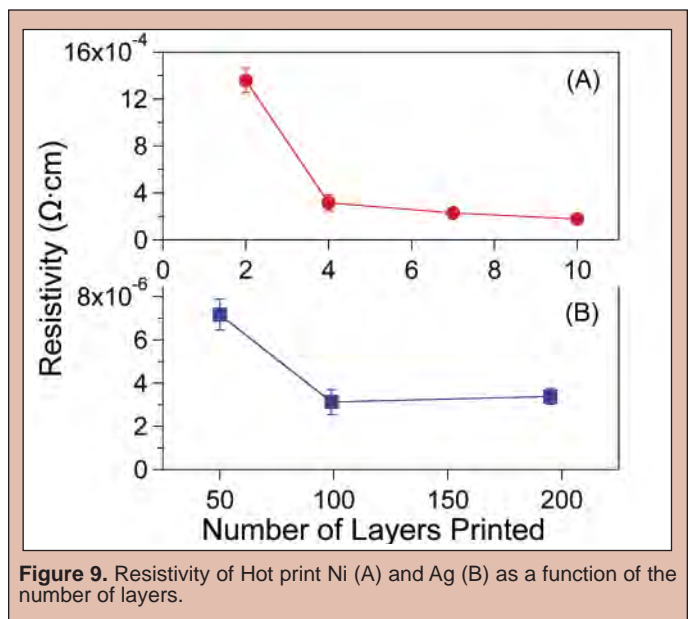
Figure 9. Resistivity of Hot print Ni (A) and Ag (B) as a function of the number of layers.
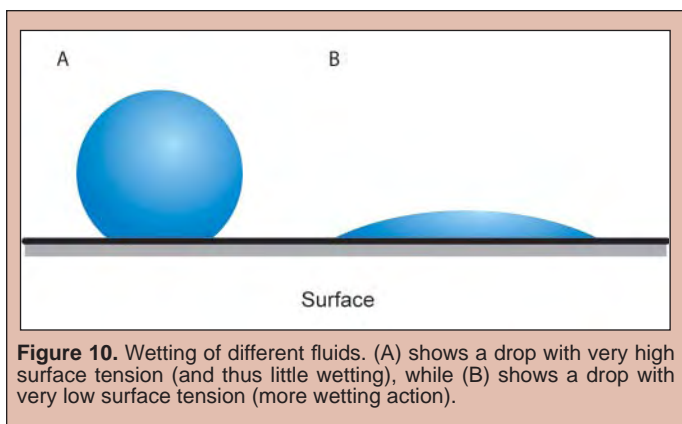
Figure 10. Wetting of different fluids. (A) shows a drop with very high surface tension (and thus little wetting), while (B) shows a drop with very low surface tension (more wetting action).

spreading to form a line indicated there was a problem with the Ag ink wetting on glass. Thus, Ni and Si were explored as substrates to observe wetting effects on materials specific for solar cell devices. Increasing the initial ink temperature by just 10°C to 45°C decreased ink viscosity, resulting in better wetting and line formation on these materials (at 35-μm drop spacing). Figure 7B shows that Ag can be printed on top of printed Ni lines. On Ni foil (Figure 7C), a smaller drop spacing (23-μm) was required to produce a single-layer line, although 30-μm printed well after 4 layers. Figure 7D shows lines form well on the AR coated Si ribbon. Results are promising for printing on the Ni layer in a CIS cell and on Si solar cells.

Ag on AR coated Si printed at a line width of ~125 μm and was unaffected by the number of layers printed (Figure 5B). Line thickness reached half its target at ~200 layers (4.5 μm). It should be noted that the Ag ink used was a week old and gray in the cartridge, suggesting some of the ink decomposed and that the ink printed had a lower-than-prepared precursor concentration. While the older ink still printed well, fresh ink would require fewer layers to achieve the thicknesses reported.

Metallic lines printed from the inks were consistent with the pure material and had no detectable traces of carbon or oxide contaminates, as confirmed by XRD (Figure 8). It was noted that, in addition to the purity of the metal deposited, resistivity was affected by the profile of the line. Narrow and thin features in the line limit the flow of electrons through them like a bottleneck. Therefore, uniformity in the line was an important criterion in printing contacts. Resistivity of the Ni lines decreased as more layers were printing, leveling off at ~$1.7 \times 10^{-4} \ \Omega \cdot$ cm at 10 layers (Figure 9A). While the value is two orders of magnitude greater than bulk Ni, the resistivity requirement of the Ni layer is relaxed since it only serves as an adhesion layer. Electrons only need to flow through the thin region of material to reach the primary Ag contact. Low resistivity is more important for the Ag since electrons must flow through the length of the contact line, similar to a wire. Ag was printed with about twice bulk resistivity at ~$3.4 \times 10^{-6} \ \Omega \cdot$ cm above 100 layers (Figure 9B). The Ag lines appeared white and not metallic. However, it was highly conductive like its metallic counterpart. Under certain conditions and treatment (proprietary), the white line transforms into a metallic appearance. The identity of the white material and the cause of the transformation require further study.

In summary, we have developed atmospheric direct-write depositions of Ni and Ag metals. Inkjet printing produced line resolutions and thicknesses comparable to current screen printing technologies. Narrow (80 μm) and thin (55 nm) Ni lines were printed with a resistivity two orders magnitude more than bulk. Ag was successfully printed up to 4.5 μm thick and 125 μm wide with about twice bulk resistivity. We have shown how ink based deposition can improve the contact processing via a non-contact approach. Additionally, the ability to print on various substrates for photovoltaic applications was demonstrated on glass, AR coated Si, TCOs, and multi-layered metallizations. Future work will focus on improving Ag resolution and Ni conductivity and on printing full contact devices (TCO-Ni-Ag/Cu and Si-BurnThrough-Ag). Printing Cu will be investigated as a low-cost replacement for Ag contacts.

REFERENCES

[1] A. Slaoui, R.T. Collins, "Advanced Inorganic Materials for Photovoltaics," *MRS Bulletin*, vol. 32, no. 3, p. 211, 2007.

[2] K.F. Teng, R.W. Vest, *IEEE Electron Device Lett.*, vol. 9, p. 591, 1988.

[3] M. Ghannam, S. Sivoththaman, J. Poortmans, J. Szlufcik, J. Nijs, R. Mertens, R. Van Overstraeten, *Solar Energy*, vol. 59, no. 1-3, pp.101–110, 1997.

[4] T. Kaydanova, M. van Hest, A. Miedaner, C.J. Curtis, J.L. Alleman, M.S. Dabney, E. Garnett, S. Shaheen, L. Smith, R. Collins, J.I. Hanoka, A.M. Gabor, D.S. Ginley, "Direct Write Contacts for Solar Cells," Paper presented at 31st IEEE Photovoltaics Specialists Conference, Lake Buena Vista, Florida, 2005.

[5] A.M. Abdul-Lettif, "Investigation of Interdiffusion in Copper–Nickel Bilayer Thin Films," *Physica* B, vol. 388, pp. 107–111, 2007.

[6] *Handbook of Chemistry and Physics*, 65th edition, CRC Press.

Alexander Nikolich Patananan was born in Los Angeles, California and grew up in Palmdale. After graduating from Antelope Valley College Summa Cum Laude at the age of 18 with an Associates of Science degree in Biological Sciences, Alexander attended the University of California at Los Angeles, majoring in Microbiology, Immunology, and Molecular Genetics. During his undergraduate career, he has held one CCI fellowship and two SULI internships at the Pacific Northwest National Laboratory in the summers of 2005, 2006, and 2007. His research projects have focused on Arabidopsis thaliana *and soybean cyst nematode proteomics, in addition to analyzing the surface-mediated unfolding kinetics of globular proteins on cationic surfaces. He has also been involved in the UCLA Undergraduate Research Consortium in Functional Genomics, conducting research associated with the genome-wide clonal analysis of lethal mutations in* Drosophila melanogaster*, as well as the development of a novel* in vivo *cell-lineage tracing system. Alexander is the author of nine science editorials, manuscripts, and books. In the Fall of 2008, he plans to enter a PhD program in genetics and protein biophysics, and ultimately intends to become a researcher in the field of medicine.*

Steven C. Goheen has worked at Pacific Northwest National Laboratory as a scientist for approximately 20 years. He is currently in the Chemical and Biological Sciences group. He received a Ph.D. from Northwestern University in 1978 and has continued to be interested in the interactions between proteins and surfaces. His most recent research in this area has been using chromatographic techniques, as reflected in this manuscript.

THE SURFACE-MEDIATED UNFOLDING KINETICS OF GLOBULAR PROTEINS IS DEPENDENT ON MOLECULAR WEIGHT AND TEMPERATURE

ALEXANDER N. PATANANAN AND STEVEN C. GOHEEN

ABSTRACT

The adsorption and unfolding pathways of proteins on rigid surfaces are essential in numerous complex processes associated with biomedical engineering, nanotechnology, and chromatography. It is now well accepted that the kinetics of unfolding are characterized by chemical and physical interactions dependent on protein deformability and structure, as well as environmental pH, temperature, and surface chemistry. Although this fundamental process has broad implications in medicine and industry, little is known about the mechanism because of the atomic lengths and rapid time scales involved. Therefore, the unfolding kinetics of myoglobin, β-glucosidase, and ovalbumin were investigated by adsorbing the globular proteins to non-porous cationic polymer beads. The protein fractions were adsorbed at different residence times (0, 9, 10, 20, and 30 min) at near-physiological conditions using a gradient elution system similar to that in high-performance liquid chromatography. The elution profiles and retention times were obtained by ultraviolet/visible spectrophotometry. A decrease in recovery was observed with time for almost all proteins and was attributed to irreversible protein unfolding on the non-porous surfaces. These data, and those of previous studies, fit a positively increasing linear trend between percent unfolding after a fixed (9 min) residence time (71.8%, 31.1%, and 32.1% of myoglobin, β-glucosidase, and ovalbumin, respectively) and molecular weight. Of all the proteins examined so far, only myoglobin deviated from this trend with higher than predicted unfolding rates. Myoglobin also exhibited an increase in retention time over a wide temperature range (0°C and 55°C, 4.39 min and 5.74 min, respectively) whereas ovalbumin and β-glucosidase did not. Further studies using a larger set of proteins are required to better understand the physiological and physiochemical implications of protein unfolding kinetics. This study confirms that surface-mediated unfolding can be described by experimental techniques, thereby allowing for the better elucidation of the relationships between the structure and function of soluble proteins as well as other macromolecules.

INTRODUCTION

In 2004, 478,000 knee and 234,000 hip replacement procedures were conducted in the United States, accounting for a total cost of $18.2 billion [1]. Autographs, allografts, xenografts, and metal implants are commonly used such procedures. However, these procedures have biocompatibility limitations. Metal implants, typically composed of stainless steel, cobalt-chromium alloys, and titanium-based alloys, are frequently rejected by the body's host tissue once they contact biological fluids [2]. These rejection processes are initiated primarily by the adsorption and unfolding of blood proteins [3]. As a result of being rejected, implants typically have an average lifespan of ten to fifteen years. In addition to biological implants, the surface-mediated unfolding of proteins is important in cellular processes (e.g. enzyme activity and protein translocation), food processing, paper manufacturing, biosensors, maritime construction, and diseases such as Creutzfeldt-Jakob, Alzheimer's, amyotrophic lateral sclerosis, cancer, and osteoporosis. However, little is known about the mechanisms behind this type of protein unfolding. Modeling the rates at which proteins unfold has become one of the most prominent challenges in computational biology and chemistry.

Adsorption and unfolding processes are related to the molecular configuration and dynamics of the bound macromolecule. More emphasis has recently been placed on the unfolding of soluble proteins than other bio-macromolecules because proteins are far more diverse in structure than DNA, RNA, or lipids [4, 5]. Many soluble proteins are globular and composed of internalized hydrophobic domains joined by hydrogen bonds, disulfide bridges, and hydrophobic interactions [6]. To remain soluble in aqueous media, hydrophilic functional groups enclose the hydrophobic inner core. Because of functional variability, many proteins must be dynamic and flexible, transforming into different conformations to facilitate environmental adaptation at the cost of intramolecular bonding [7, 8].

Adsorption to solid supports occurs due to favorable entropic increases in hydrophobic interactions induced by dehydration between the protein and surface [9]. To assist adsorption and environmental adaptation, proteins unfold and expose more active sites that participate in subsequent interactions [10]. In general, proteins of higher molecular weight have more surface contacts, more flexibility because of the increased total degrees of freedom, and therefore unfold faster than smaller proteins [11].

Unfolding kinetics models have been developed for proteins in solution [12–15]. The structure of globular proteins is commonly based on a rigid sphere composed of network glass due to similarities in high packing density values [16–19]. Computational models have determined the maximum distance over which interactions can occur between a solid surface and a protein functional group to be between 20 and 30 Å [20]. This distance defines a zone of influence to help us better understand the surface-mediated unfolding process. After the protein functional groups within this zone of influence have responded to attractive forces and diffused onto the interface, reversible protein denaturation (rupture of the internal bonds) occurs [21, 22]. Because of adsorption and the initial unfolding at the interface, structural stability and solubility decrease, resulting in the release of side chain groups [23]. Solvent molecules then enter the interior of the protein core, further reducing secondary structure [24, 25]. Following the passage through one or more transition states, irreversible spreading leads to proteins becoming fully denatured and relaxed [26]. In fibrinogen, spreading on hydrophobic surfaces results in an increase in footprint size from 100 nm^2 to 500 nm^2 during a single-exponential decay of 1735 s [27]. Finally, interfacial protein aggregation, multiple film formation, and/or gelation may result depending on protein structure and function [28, 29]. It is important to note that these models do not apply to surface-mediated unfolding because the physical processes differ significantly.

Although much is still to be learned about surface-mediated protein unfolding, models describing such mechanisms are important because many biochemical reactions are surface-mediated, such as cellular processes taking place at membranes. We are also aware that surfaces catalyze protein unfolding such that unfolding on surfaces occurs at a lower temperature than it would in bulk solution [30]. The rates of unfolding on most synthetic, rigid surfaces are slow because only the protein is allowed flexibility relative to the solid surface [31, 32]. It is likely that unfolding or relaxation of a protein at a membrane surface is much faster because both components

are flexible [33]. And, it is easy to imagine that at physiological temperatures, flexibility is optimal to match performance.

The separation, quantification, and partial characterization of proteins by liquid chromatography is a highly respected and common process. Hydrophobic interaction high-performance liquid chromatography (HPLC) has proven to be not only a good means by which to separate proteins, but also a method to determine their relative hydrophobic properties [34, 35]. It is now well accepted that the retention properties of cytochrome c increase with time and temperature on ionic and hydrophobic supports [36, 37]. Furthermore, loss of protein by HPLC has implications on the usefulness of this method for quantification in addition to studying surface-mediated unfolding. With the use of ion-exchange and hydrophobic interaction HPLC of fibrinogen, cytochrome c, bovine serum albumin (BSA), and immunoglobulin G (IgG), Goheen and Gibbins identified a logarithmic relationship between protein loss and molecular weight [11]. In the present study, the protein losses for the globular proteins myoglobin, ovalbumin, and β-glucosidase were compared with earlier findings. We investigated this by absorbing proteins to non-porous cationic polymer beads under different gradient residence time conditions and tested the null hypothesis that protein loss, and hence unfolding kinetics, is independent of molecular weight.

Materials and Methods

The Bio-Rad Laboratories (Hercules, CA, USA) HPLC dual piston, dual-pump gradient system was used for protein separation. The 2.5 mL mixer of this system was replaced with a low volume Lee Co. 250 µL visco-jet micro-mixer (Westbrook, CT, USA). Ultraviolet/visible absorbance was obtained with a 9 µL flow cell at 280 and 409 nm to detect proteins. Microsoft-based BioRad ValueChrom software recorded chromatograms and integrated peak areas.

A MA7Q (quaternary amine) anionic exchange column from Bio-Rad was used and included nonporous, spherical, polymeric beads. The column has a loading capacity range of 5–10 mg for static proteins and 1–2 mg for dynamic proteins. For residence time studies, the temperature was kept constant at 37°C. The temperature was varied for select experiments using a Bio-Rad column heater. The column was kept in an ice bath for 0°C sorption experiments.

Chemicals and reagents were of the highest purity available from Sigma (St. Louis, MO, USA) unless otherwise indicated. Water used was deionized and purified with a Milli-Q filtration system (Milliport, Bedford, MA, USA). Buffer A contained 20 mM tris (hydroxyl-methyl) aminomethane (Tris)-HCl base (Trizma, reagent grade). After filtration through a 0.2-µm membrane (Whatman, Maidstone, UK), the pH was brought to 8.5 using 0.1 M NaOH. Buffer B contained 20 mM Trizma base and 500mM NaCl (≥99% purity, ACS grade). After filtration through a 0.2-µm membrane, the pH was brought to 8.5 using 1 M HCl.

Sample preparation for myoglobin (horse heart, ≥90% purity, Sigma), ovalbumin (turkey egg, Grade VI, Sigma), and β-glucosidase (almond, 30 units/mg, Sigma) consisted of solubilizing the protein in Buffer A (pH 8.5), unless otherwise noted. Protein solutions

were prepared daily to concentrations of 1 mg/mL. Solutions were stored at 8°C when not in use and warmed to room temperature prior to analysis.

HPLC gradients initiated with Buffer A and ended with Buffer B. The time between sample injection and the start of the gradient varied between gradients (Table 2). 100% recovery was determined using a low-dead-volume (LDV) connector (and 0.5 M NaCl) in place of a column. Gradient 0 was a control in which an isocratic gradient of 0.5 M NaCl should have prevented all protein binding to the cationic support and 100% recovery was anticipated. For all gradients, with the exception of gradient 0, NaCl concentrations increased linearly over 15 min from 0 M to .5 M (0.03 M/min). The column was washed for 5 min with Buffer B after the completion of the gradient in order to ensure elution of all recoverable proteins. The flow-rate was kept at 1 mL/min and a sample injection volume of 20 µL was used for all experiments.

For each experiment, absorbance readings at 280 nm and 409 nm were recorded using a Gilson 118 ultraviolet/visible detector (Gilson, Middleton, WI, USA). These recordings monitored protein loss and ensured the elution of all proteins from the column. Absorbance at 409 nm was used to verify the components of myoglobin. Protein peaks were integrated using the Bio-Rad ValueChrom system. The adjusted retention time was calculated as the time difference between protein injection and elution. In order to calculate and compare protein recovery, a 9 min elution time was arbitrarily chosen to measure protein levels. Consequently, protein recovery was calculated as the ratio of $(area_{9min})$ / $(area_{dead\ volume})$.

The column was rejuvenated periodically by eluting a 0.1 M NaCl and/or 0.1 N NaOH solution for 1 hour. Afterward, Buffer A was eluted until equilibrium was reached between the mobile and stationary phases before another experiment could be conducted.

RESULTS

Protein Retention and Recovery

The unfolding kinetics of myoglobin, β-glucosidase, and ovalbumin were examined in this study. Some characteristics of these proteins are shown in Table 1. Protein-support residence times were varied in order to examine surface-mediated protein unfolding kinetics on the cationic support. Protein loss with respect to molecular weight was calculated as described in the Materials and Methods. Subsequent data will help delineate the mechanisms of protein adsorption and unfolding at the protein-surface interface.

When a 15 min (1.0 mL/min) linear gradient was started immediately after each

of the proteins in Table 1 was injected, profiles shown in Figure 1 resulted. Ovalbumin and β-glucosidase were each characterized by a single primary peak eluting from the column approximately 6.5 min after the start of the gradient. Myoglobin had two prominent peaks, with the first peak eluting either as a doublet or a singlet with a left-side shoulder component. At a wavelength of 409 nm, the first peak to elute from the column during gradient 1 (37°C) had a retention time equivalent to the second component of this doublet (approximately 4.53 min). This peak was assigned as holo-myoglobin. The first member of the doublet (or shoulder component) was assigned apo-myoglobin. The peak eluting after the doublet was assigned as a dissociated heme prosthetic group because the retention and area of this peak did not change significantly throughout our experiment, and its absorbance was strong at 409 nm.

Figure 2 shows the absorption spectrum of myoglobin, ovalbumin, and β-glucosidase when gradients 1, 2, 3, and 4 were used at 37°C. See Table 2 for a description of the different gradients used. For myoglobin, increasing the residence time reduced the distance separating the two major peaks and increased retention time (4.87 min and 5.49 min, 0 min and 30 min, respectively). Initial exposure to the column (gradient 1) resulted in a protein loss of 62.1% to the surface when compared to the LDV connector (gradient 0). At the longest residence time (gradient 4), the initial holo-myoglobin peak was almost absent, with an 84.7% loss.

Protein	MW (kDa)	pI	Function	% α-helices and β-sheets	Internalized Disulfide bonds?
Fibrinogen	330	5.1	Blood coagulation	Chain A,D: 23% helical, 0% beta sheet; Chain B,E: 33% helical, 18% beta sheet; Chain C,F: 33% helical, 19% beta sheet.	Yes
Immunoglobulin G	150	6.1-8.5	Antibody in the blood against bacteria and viruses	3% helical, 43% beta sheet	Yes
Bovine Serum Albumin	69.9	4.9	Lipid binding	67% helical, 0% beta sheet	Yes
β-glucosidase	60.4[a]	4.5	Cellulose digestion	40% helical, 16% beta sheet	No[b]
Ovalbumin	42.9	4.5-4.9	Unknown	28% helical, 31% beta sheet	Yes
Myoglobin	17.1	6.9/7.35	Oxygen storage	71% helical, 0% beta sheet	No
Cytochrome C	11.8	9.1	Electron carrier involved in aerobic energy generation	20% helical, 11% beta sheet	Yes

[a,b] β-glucosidase is a homodimer consisting of two monomers of approximately 65,000 Da molecular weight. The native molecular weight of the enzyme is 130,000 Da. Although no disulfide bonds maintain its internal structure, a disulfide bond links the two dimers to form the native structure.

Table 1. Representative characteristics of the proteins analyzed in this study. Protein data are from modeling tools available at the ExPASy proteomics server (http://ca.expasy.org/tools/), unless otherwise noted.
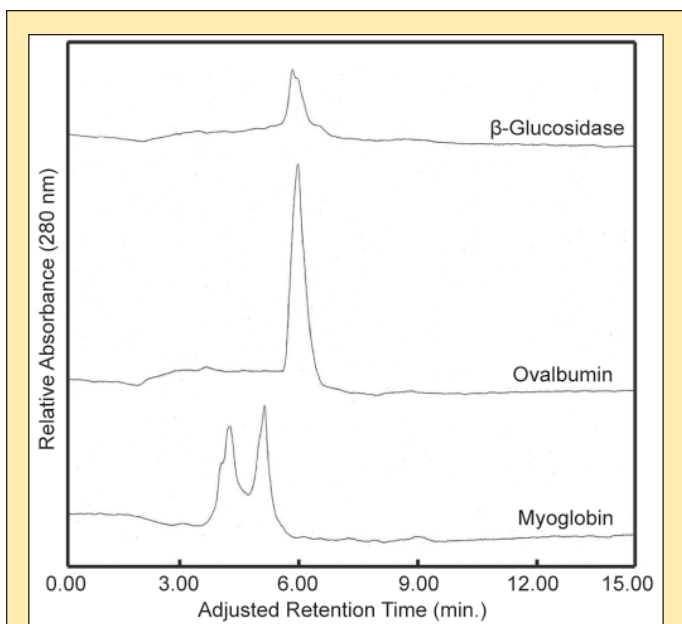
Figure 1. Representative chromatographic profiles of myoglobin, ovalbumin, and β-glucosidase adsorbed to a cationic surface using gradient 1 at 37°C.

Increasing the residence time did not increase the retention times of either ovalbumin or β-glucosidase. However, both exhibited a loss in protein to the surface. For ovalbumin, 33.7% of the protein was initially lost at gradient 1. After a 30 min gradient delay, protein levels were further reduced, resulting in a 43.3% total loss. Overall, ovalbumin exhibited a slight decrease in retention time with increasing residence (6.59 to 6.33 min, 0 to 30 min, respectively). Similarly, β-glucosidase yielded an initial reduction of 29.6% at gradient 1. For gradient 4, a total of 56.3% of protein was lost.

At 9 min, 71.8%, 31.1%, and 32.1% of myoglobin, β-glucosidase, and ovalbumin were lost to the column surface, respectively. The trends in protein loss with respect to residence time over the 30 min time range are illustrated by an exponential relationship in Figure 3 (R^2 values for myoglobin, β-glucosidase, and ovalbumin are 0.997, 0.997, and 0.957, respectively).

A comparison of protein recovery was performed. The logarithm of the molecular weights of myoglobin, β-glucosidase, and ovalbumin, in addition to cytochrome c, BSA, IgG, and fibrinogen, were plotted against their respective percent losses to the surface at 9 min. A positively increasing linear relationship (R^2 value of 0.970) was observed for most proteins, with higher molecular weights resulting in lower recovery (Figure 4). Myoglobin was the only protein which significantly differed from this trend.
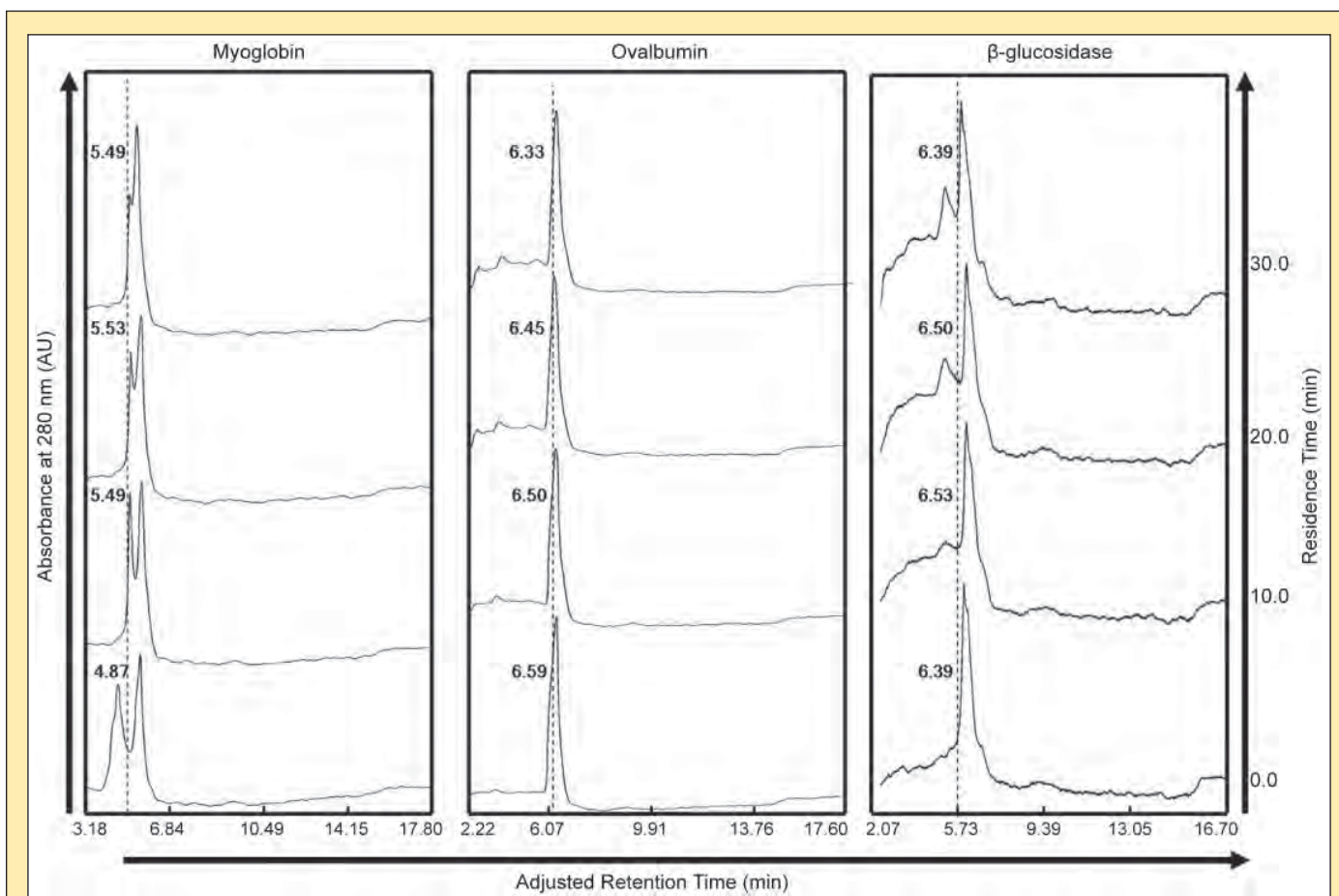
Figure 2. Chromatographic profiles of myoglobin, ovalbumin, and β-glucosidase adsorbed to a cationic support using gradients (bottom to top) 1, 2, 3, and 4 (37°C). The variable residence time, t_r, subtracted from the elution time, normalized the data relative to the start of the Buffer B (0.5 M NaCl) linear gradient. An increase in retention time is observed as the adjusted residence time is increased for myoglobin.

U.S. Department of Energy Journal of Undergraduate Research

Gradient No.	t_1 (min)	Retention at 37°C (min)		
		Myoglobin	Ovalbumin	β-glucosidase
0	N/A	~0	~0	~0
1	0	4.81–4.87	6.52–6.59	6.39–6.60
2	10	15.49–15.51	16.43–16.50	16.53
3	20	25.53–25.55	26.41–26.45	26.39–26.51
4	30	35.44–35.49	36.32–36.33	36.28–36.39

aGradients used in these experiments are labeled 0-4. t_1 is the delay in time between sample injection and the start in a linear gradient of Buffer B (0.5 M NaCl). All gradients were 15 min in length (1 mL/min) and for each a range of retention times were observed for the three studied proteins. Total protein amounts (100% recovery) for each sample were determined by an isocratic condition of Buffer B only (gradient 0) using a LDV connector in place of a column

Table 2. Variable time t_1 for gradients[a].

Myoglobin Unfolding and Temperature

The effects of temperature on surface-induced losses were investigated with myoglobin. Figure 5 shows that as the temperature increased, retention time also increased (0°C to 55°C, 4.39 min to 5.77 min, respectively), bringing the elution of myoglobin and apo-myoglobin closer to that of the heme-prosthetic group. At the highest examined temperature of 55°C, approximately 89% and 63% of apo-myoglobin and myoglobin were recovered respectively using an anion exchange column compared to the lowest temperature (0°C).

Figure 3. Recovery percentages of myoglobin, ovalbumin, and β-glucosidase as a function of variable residence time. Protein recovery, the total concentration eluted from the column, was calculated by taking the integral of obtained peaks. For myoglobin, ovalbumin, and β-glucosidase, a decrease in eluted protein occurred as variable residence time increased from gradient 1 to 4 at 37°C. Myoglobin exhibited high surface-mediated unfolding rates, with recovery decreasing shortly after exposure to the cationic support.
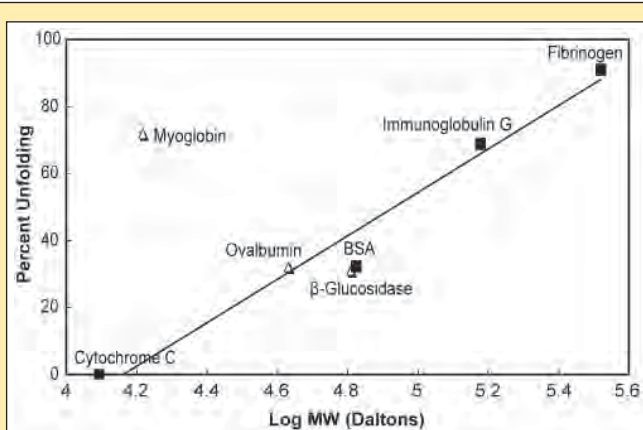
Figure 4. The unfolding percentage as a function of molecular weight for proteins adsorbed to cationic surfaces at 37°C. The percentage of protein unfolded was determined by the percent of protein loss. Losses were calculated at an arbitrary 9 min elution time for each protein. A linear relationship exists between the proteins, with an R^2 value of 0.970.

Figure 5. Myoglobin (horse heart) separation on a cationic surface as a function of temperature using gradient 1. Retention times of the myoglobin peak increased with elevated temperatures, indicating higher levels of surface-mediated unfolding.

Discussion

In the present work, the unfolding kinetics of β-glucosidase, ovalbumin, and myoglobin were studied to determine if unfolding rates were related to protein molecular weight. These proteins were chosen because of their wide range of structural and functional properties. β-glucosidase assists cellulose digestion by cleaving the breakdown products of endoglucanase and exocellobiohydrolases into two glucose molecules [38]. Ovalbumin is a glycoprotein abundant in avian eggs (comprising 60% of the total protein in egg whites) whose function is yet to be deciphered [39]. Myoglobin, found typically in muscle tissue, is a small monomeric protein involved in oxygen storage.

The retention time for myoglobin on a cationic support increased with temperature (Figure 5). This alteration in retention time may be the result of increased exposure to ionized regions of the protein. Khechinashvili et al. suggest that at room temperature, globular proteins are stabilized by the entropy of non-polar group hydration and enthalpy as a result of internal interactions [40]. Because of the substantial heat capacity associated with nonpolar group hydration, high temperatures lead to the decrease in its stabilizing capacity and an increase in destabilizing forces such as conformational entropy and vibrational effects. The side chains of a protein will rotate and bend more as the temperature is raised, resulting in an increase of exposed sites for attachment.

The observed increases in retention time and decreases in percent recovery for myoglobin are contrary to previous studies which illustrate higher elution temperatures result in decreased retention times [41]. These experiments were conducted under acidic conditions using silica-based supports. The experiments discussed in the present study were performed at near-physiological conditions to explore biologically significant protein behavior rather than developing optimal separations.

Other than temperature, the recovery of proteins as a function of sorbent residence time was also analyzed. A comparison of the proteins revealed a correlation between recovery and molecular weight. Increases in the logarithm of molecular weight led to lower recovery in a linear correlation for all proteins with the exception of myoglobin (Figure 4).

Previously we suggested the surface acts as a catalyst for protein unfolding. As residence time is increased before the start of each gradient, the proteins have increasing amounts of time to find the surface-aqueous interface. However, whether surface-mediated unfolding is solely related to protein flexibility and stability is still not certain. Further experiments should be carried out to more fully describe the unfolding phenomena on solid supports.

All of the proteins examined fit the linear trend between unfolding and molecular weight except myoglobin. On average, the retention time of myoglobin differs significantly from ovalbumin and β-glucosidase for all gradients (Table 2). Myoglobin also exhibited a high degree of unfolding, with an increase in retention time and decreased percent recovery as residence times were extended (Figures 3 and 4). This result may be related to the structure and function of myoglobin. Although myoglobin contains only 153 residues, 71% of its secondary structure is alpha helices (eight right handed alpha helices). While BSA has a similar percentage of helices (67%), its internal structure is maintained by disulfide bridges, which are absent in myoglobin. Disulfide bridges can be vital in maintaining structural integrity [42]. Although the combination of these two characteristics may result in a relatively flexible structure for myoglobin, they may not be the only factors involved. β-glucosidase also does not possess internal disulfide bridges, yet its structural flexibility is consistent with the general unfolding trend. Another reason for the deviation may be due to the relatively high isoelectric point (pI) of myoglobin (6.9/7.35) compared to the other proteins (approximately 5.0). Because the buffers used were equilibrated to pH 8.5, myoglobin could have had a disproportionately stronger affinity for the cationic surface. This affinity would unlikely be the sole result of net charge since myoglobin (-1.3) is not as negatively charged as other proteins at this pH (-15.2, -35.2, and -17.1 for ovalbumin, β-glucosidase, and BSA, respectively), and consequentially will not be as attracted to the positively charged surface. The charges of IgG and fibrinogen could not be calculated due to the lack of structural knowledge.

Interestingly, although myoglobin and cytochrome c are both low molecular weight proteins, their unfolding rates differ significantly. Under our experimental conditions, cytochrome c, which is a soluble protein associated with the mitochondrial inner membrane, has almost no unfolding on the cationic support (Figure 4). It is possible that this is also related to the pI of the proteins because cytochrome c has a charge of 6.6 under our variables. Another factor involved may be the protein's hydrophobic characteristics. Myoglobin and cytochrome c have different relative hydrophobicity values of 0.23 and 0.0, respectively [43]. Because hydrophobic interactions are entropically favored by protein adsorption, this may lead to increased unfolding. These relationships need to be examined in greater detail in order to develop a more comprehensive model.

Recent studies have suggested numerous reasons and models for the unfolding of proteins under various conditions such as temperature, pH, and pressure [44, 45]. In a related analysis, the adsorption and unfolding of proteins at interfaces was investigated based on computational models. It was found that the process of unfolding occurs via a generic, rapid loss of native contacts, rather than as a gradual event [46]. Although other theoretical approaches have occurred, only a few studies have experimentally examined surface-mediated protein unfolding [47]. Of these, most deal with the examination of a single protein and not a comprehensive comparison between many different proteins.

In the present investigation, HPLC was used to analyze and compare a wide range of proteins with various molecular weights, structures, and functions. It has been demonstrated that there is a positively increasing linear trend between molecular weight and the rate of unfolding. This may be due either to the surface acting as a catalyst or protein destabilization as a result of sorbent binding. The present study confirms that surface-mediated unfolding can be described by experimental techniques, thereby allowing for the better elucidation of the relationships between the structure and function of soluble proteins as well as other macromolecules. In practical application, this knowledge will assist in unraveling the origins of protein-related diseases such as Creutzfeldt-Jakob, Alzheimer's, amyotrophic lateral sclerosis, and cancer.

References

[1] U.S. Department of Health and Human Services. *National Hospital Discharge Survey, 1991–2004*. U.S. Department of Health and Human Services, Centers for Disease Control and Prevention, National Center for Health Statistics 1991–2004.

[2] Jones, F.H., Teeth and bones: applications of surface science to dental materials and related biomaterials, Surface Science Reports, **42**, Page 75–205, 2001.

[3] Gray, J.J., The interaction of proteins with solid surfaces, Curr. Opin. Struct. Biol., **14**, Page 110–115, 2004.

[4] Gromiha, M.M., Selvaraj, S., and Thangakani, A.M., A Statistical Method for Predicting Protein Unfolding Rates from Amino Acid Sequence, J. Chem. Inf. Model., **46**, Page 1503–1508, 2006.

[5] Bippes, C.A., Janovjak, H., Kedrov, A., and Muller, D.J., Digital force-feedback for protein unfolding experiments using atomic force microscopy, Nanotechnology., **18**, Page 1–7, 2007.

[6] Damodaran, S. and Paraf, A., Food proteins and their application, New York, Marcel Dekker, Inc, 1997.

[7] Tan, J.S. and Martic, P.A., Protein adsorption and conformational change on small polymer particles, J. Colloid Interface Sci., **136**, Page 415–431, 1990.

[8] Norde, W., MacRitchie, F., Nowicka, G., and Lyklema, J., Protein adsorption at solid-liquid interfaces: Reversibility and conformation aspects, J. Colloid Interface Sci., **112**, Page 447–456, 1986.

[9] Norde, W. and Lyklema, J., The adsorption of human plasma albumin and bovine pancreas ribonuclease at negatively charged polystyrene surfaces, J. Colloid Interface Sci., **66**, Page 257–265, 1978.

[10] Engel, M.F.M., dissertation, Wageningen Universiteit, 2004.

[11] Goheen, S.C. and Gibbons, B.M., Protein losses in ion-exchange and hydrophobic interaction high-performance liquid chromatography, J. Chromatogr. A., **890**, Page 73–80, 2000.

[12] Bakk, A., Hoye, J.S., and Hensen, A., Apolar and polar salvation thermodynamics related to the protein unfolding process, Biophys. J., **82**, Page 713–719, 2002.

[13] Bakk, A., Hoye, J.H., and Hansen, A., Specific heat upon aqueous unfolding of the protein interior: a theoretical approach, Physica A, **304**, Page 355–361, 2002.

[14] Holmberg, M., Stibius, K.B., Ndoni, S., Larsen, N.B., Kingshott, P., and Hou, X.L., Protein aggregation and degradation during iodine labeling and its consequences for protein adsorption to biomaterials, Anal. Biochem., **361**, Page 120–125, 2007

[15] Otzen, D.E., Protein unfolding in detergents: effects of micelle structure, ionic strength, pH, and temperature, Biophys. J., **83**, Page 2219–2230, 2002.

[16] Graziano, G., Cavity size distribution in the interior of globular proteins, Chem. Phys. Lett., **434** , Page 316–319, 2007.

[17] Fang, Y., Surface tension, volume, area, hydrophobic core, and protein folding, Centre for Bioinformation Science, Mathematical Sciences Institute, ANU, 2003.

[18] Rader, A.J., Hespenheide, B.M., Kuhn, L.A., and Thorpe, M.F., Protein unfolding: rigidity lost, PNAS, **99**, Page 3540–3545, 2002.

[19] Thorpe, M.F., *et al.*, in Rigidity Theory and Applications, Eds., Springer, New York, 1999.

[20] Lee, S.J. and Park, K., Protein interaction with surfaces: separation distance-dependent interaction energies, J. Vac. Sci. Technology A, **12**, Page 2949–2955, 1994.

[21] Ybert, C. and di Meglio, J.M., Study of protein adsorption by dynamic surface tension measurements: diffusive regime, Langmuir., **14**, Page 471–475, 1998.

[22] Wustneck, R., Kragel, J., Miller, R., Fainerman, V.B., Wilde, P.J., Sarker, D.K., and Clark, D.C., Dynamic surface tension and adsorption properties of b-casein and b-lactoglobulin, Food Hydrocolloids., **10**, Page 395–405, 1996.

[23] Wang, H. and Ben-Naim, A., Solvation and solubility of globular proteins, J. of Phys. Chem. B., **101**, Page 1077–1086, 1997.

[24] Finkelstein, A.V., Can protein unfolding simulate protein refolding, Protein Eng., **10**, Page 843–845, 1997.

[25] Williams, M.A., Thornton, J.M., and Goodfellow, J.M., Modelling protein unfolding: hen egg-white lysozyme, Protein Eng, **10**, Page 895–903, 1997.

[26] Fukunishi, Y., Folding-unfolding energy change of a simple sphere model protein and an energy landscape of the folding process, Proteins Struct., Funct., Genet., **33**, Page 408–416, 1998.

[27] Santore, M.M. and Wertz, C.F., Protein spreading kinetics at liquid-solid interfaces via an adsorption probe method, Langmuir, **21**, Page 10172–10178, 2005.

[28] Freer, M.E., Yim, K.S., Fuller, G.G., and Radke, C.J., Interfacial rheology of globular and flexible protein at the hexadecane/water interface: a comparison of shear and dilatational deformation, J. Phys. Chem. B., **108**, Page 3835–3844, 2004.

[29] Graham, D.E. and Phillips M.C., Proteins at liquid interfaces, J. Colloid Interface Sci., **70**, Page 403–414, 1979.

[30] Somasundaran, P, Encyclopedia of Surface and Colloid Science, CRC, New York, Ed. 2, 2006.

[31] Regnier, F.E., The role of protein structure in chromatographic behavior, Science, **222**, Page 245–252, 1983.

[32] Lu, X.M., Benedek, K., Karger, B.L., Conformational effects in the high-performance liquid chromatography of proteins Further studies of the reversed-phase chromatographic behavior of ribonuclease A, J. Chromatogr., **359**, Page 19–29, 1986.

[33] Canale, C., Torrassa, S., Rispoli, P., Relini, A., Rolandi, R., Buccianitini, M., Stefani, M., and Gliozzi, A., Natively Folded HypF-N and Its Early Amyloid Aggregates Interact with Phospholipid Monolayers and Destabilize Supported Phospholipid Bilayers, Biophys. J. **91**, Page 4575–4588, 2006.

[34] Goheen, S.C., and Hilsenbeck, J.L., High-performance ion-exchange chromatography and adsorption of plasma proteins, J. Chromatogr. A., **816**, Page 89–96, 1998.

[35] Goheen, S.C., and Engelhorn, S.C., Hydrophobic interaction high-performance liquid chromatography of proteins, J. Chromatogr., **317**, Page 55–65, 1984.

[36] Herbold, C.W., Miller, J.H., and Goheen, S.C., Cytochrome c unfolding on an anionic surface, J. of Chromatogr A, **863**, Page 137–146, 1999.

[37] Ingraham, R.H., Lau, S.Y.M., Taneja, A.K., and Hodges, R.S., Denaturation and the effects of temperature on hydrophobic-interaction and reversed-phase high-performance liquid chromatography of proteins, J. Chromatogr., **327**, Page 77–92, 1985.

[38] Lymar, E.S., Li, B., and Renganathan, V., Purification and characterization of a cellulose-binding β-glucosidase from cellulose-degrading cultures of Phanerochaete chrysosporium, Appl. Environ. Micrbiol., **61**, Page 2976–2980, 1995.

[39] Huntington, J.A., and Stein, P.E., Structure and properties of ovalbumin, J. of Chromatogr. B, **756**, Page 189–198, 2001.

[40] Khechinashvili, N.N., Janin, J.J., and Rodier, Thermodynamics of the temperature-induced unfolding of globular proteins, Protein Sci., **7**, Page 1315–1324, 1995.

[41] Yang, X., Ma, L., and Carr, P.W., High temperature fast chromatography of proteins using a silica-based stationary phase with greatly enhanced low pH stability, J. of Chromatogr. A., **1079**, Page 213–220, 2005.

[42] Zavodszky, M., Chen, C., Huang, J., Zolkiewski, M., Wen, L., and Krishnamoorthi, R., Disulfide bond effects on protein stability: Designed variants of *Cucurbita maxima* trypsin inhibitor-V, Protein Sci., **10**, Page 149–160, 2001.

[43] Goheen, S.C., in *Methods for Protein Analysis*, American Oil Chemist Society, Champaign, Ill, USA, 1988.

[44] Bismuto, E., Colonna, G., and Irace, G., Unfolding pathways of myoglobin. Evidence for a multistate process, Biochemistry, **22**, Page 4165–4170, 1983.

[45] Fandrich, M., Forge, V., Buder, K., Kittler, M., Dobson, C.M., and Diekmann, S., Myoglobin forms amyloid fibrils by association of unfolded polypeptide segments, PNAS, **100**, Page 15463–15468, 2003.

[46] Chakarova, S.D. and Carlsson, A.E., Model study of protein unfolding by interfaces, Phys. Rev. E, **69**, Page 1–9, 2004.

[47] Kopachiewicz, W., Rounds, M.A., and Regnier, F.E., Stationary phase contributions to retention in high-performance anion-exchange protein chromatography: ligand density and mixed mode effects, J. of Chromatogr., **318**, Page 152–172, 1985.

Stephanie M. Patterson was born and raised in Corpus Christi, Texas. She received her Associate's degree in mathematics from Del Mar College in May 2007. During the summers of 2006 and 2007, Stephanie participated in the FaST internship at the Lawrence Berkeley National Laboratory where she has continued her research through the fall of 2007 and spring of 2008. She plans to receive a Bachelor's Degree in Physics and a PhD in Biophysics. Her interests include philosophy and active participation in the University Students Cooperative Association.

Steve Yannone is currently a staff scientist at Lawrence Berkeley National Laboratory in the department of Molecular Biology. He completed his undergraduate studies in biochemistry at the University of California at Riverside, his Ph.D. in biochemistry at UC Irvine and spent two years of postdoctoral training at Los Alamos National Laboratory. Steve began his research career with an undergraduate research scholarship to study insect kairomones in the department of entomology at UC Riverside. His graduate studies focused on the roles of metalloproteins in mediating cellular stress responses and redox status in the nitrogen fixing bacteria Azotobacter vinelandii. His graduate studies lead him into the field of DNA repair and he now leads an active research program at LBNL studying the biochemistry of DNA repair enzymes.

EXPRESSION, PURIFICATION, AND SMALL ANGLE X-RAY SCATTERING OF DNA REPLICATION AND REPAIR PROTEINS FROM THE HYPERTHERMOPHILE *SULFOLOBUS SOLFATARICUS*

STEPHANIE M. PATTERSON, J. ROBERT HATHERILL, MICHAL HAMMEL, GREG L. HURA, JOHN A. TAINER, AND STEVEN M. YANNONE

ABSTRACT

Vital molecular processes such as DNA replication, transcription, translation, and maintenance occur through transient protein interactions. Elucidating the mechanisms by which these protein complexes and interactions function could lead to treatments for diseases related to DNA damage and cell division control. In the recent decades since its introduction as a third domain, Archaea have shown to be simpler models for complicated eukaryotic processes such as DNA replication, repair, transcription, and translation. *Sulfolobus solfataricus* is one such model organism. A hyperthermophile with an optimal growth temperature of 80°C, *Sulfolobus* protein-protein complexes and transient protein interactions should be more stable at moderate temperatures, providing a means to isolate and study their structure and function. Here we provide the initial steps towards characterizing three DNA-related *Sulfolobus* proteins with small angle X-ray scattering (SAXS): Sso0257, a cell division control and origin recognition complex homolog, Sso0768, the small subunit of the replication factor C, and Sso3167, a Mut-T like protein. SAXS analysis was performed at multiple concentrations for both short and long exposure times. The Sso0257 sample was determined to be either a mixture of monomeric and dimeric states or a population of dynamic monomers in various conformational states in solution, consistent with a flexible winged helix domain. Sso0768 was found to be a complex mixture of multimeric states in solution. Finally, molecular envelope reconstruction from SAXS data for Sso3167 revealed a novel structural component which may function as a disordered to ordered region in the presence of its substrates and/or protein partners.

INTRODUCTION

Transient protein complexes and assemblies perform many essential biological processes in organisms. Elucidating the precise mechanism by which these processes are carried out will give valuable insight into how cells function. Of particular interest is how cells efficiently replicate, repair, translate and transcribe their DNA. In humans and other mesophiles, these processes involve dynamic protein complexes, which can be difficult to study due to their transient nature. Instead, researchers have looked to hyperthermophilic Archaea to provide more tractable model systems for the more complicated eukaryotic processes.

A growing number of archaeal genomes have recently been sequenced, revealing that Archaea process information similarly to Eukaryotes [1,2,3,4]. Archaeal DNA translation, transcription, and replication resemble eukaryotic processes, but with Archaea-specific characteristics. In particular, the archaeal transcription initiation complex shares many important characteristics with the more complicated eukaryotic complexes [5,6,7,8]. In addition to providing a simpler model, many Archaea are hyperthermophiles implying that their transient protein complexes will be more physicochemically stable at moderate temperatures, potentially allowing researchers to thermally-trap protein complexes that are unstable in their eukaryotic homologs.

Sulfolobus solfataricus (S. so) is a broadly researched crenarchaeon, whose proteins have been used to model molecular mechanisms in the cell cycle, chromosomal maintenance, transcription, translation, RNA processing, and DNA replication [9, 10]. *S. so* has an optimal growth temperature of 80°C, is aerobic and heterotrophic, can be

grown on liquid or solid media, and is relatively easy to work with in the lab.

Here we present the expression, purification, and low-resolution structural characterization using small angle X-ray scattering (SAXS) for three *S. so* proteins involved in nucleic acid metabolism.

Sso0257, Cell Division Control 6 (CDC6), Origin Recognition Complex 1 (ORC1) homolog

S. so contains open reading frames (ORFs) encoding eukaryotic-like initiation factors including three cell division control 6 (CDC6)/ origin recognition complex 1 (ORC1) homologs: CDC6-1, CDC6-2, and CDC6-3 [4,10]. In Eukaryotes, ORC1 recognizes and binds to origins of replications in an ATP-dependent mechanism, then recruits the prereplication complexes, including CDC6, to the replication origin. CDC6 helps to assemble the minichromosome maintenance (MCM) proteins. Based on sequence similarity, She *et al*. have suggested that the three *S. so* CDC6 homologs combine the functions of the eukaryotic CDC6 and ORC1 proteins [4]. Sso0257 is the 45 kilodalton (kDa) CDC6-1 protein. Sso0257 has been biochemically characterized reporting the formation of monomers in solution and the ability to auto-phosphorylate *in vitro* [11]. Additionally, Sso0257 binds DNA, with a preference for bubble and fork substrates and stimulates *S. so* MCM protein binding to oligonucleotides with bubble or fork structure [11]. Recently, Sso0257 was crystallized in complex with CDC6-3 and replication origin DNA displaying an independent yet consorted deformation of the DNA where both the ATPase and the winged helix domain bind DNA [12].

Sso0768 Replication Factor C (RFC), Activator 1, small subunit

Replication factor C is a clamp-loader protein known to load the polymerase processivity factor (Proliferating Cell Nuclear Antigen, PCNA in Eukaryotes) onto DNA. In *S. so*, two RFC proteins were identified: a large (47 kDa) and a small subunit (38 kDa) [4]. Sso0768, the small subunit, cannot alone bind DNA effectively or initiate DNA polymerase B1 in the presence of either *S. so* PCNA-like proteins, 039p and 048p [13].

Sso3167 Mut-T like protein

A member of the base excision repair family, Mut-T proteins repair endogenous oxidative damage to dGTP nucleotides prior to incorporation in the genome during replication. Mut-T was originally discovered in bacterial cells; however a similar protein has been partially purified from human cells [14]. Sso3167 is an 18 kDa polypeptide.

MATERIALS AND METHODS

One liter LB media containing 0.1 mg/ml ampicillin was inoculated from frozen stocks of *E. coli* Rosetta cells (Novagen) transformed with the pet21a vector (Novagen) containing the *S. so* gene of interest fused to a C-terminal six-histidine tag. Cultures were grown at 37°C while shaking at 250 revolutions per minute (rpm) to an optical density of 0.5 at 600 nm (logarithmic phase). Protein expression was induced by the addition of isopropyl ß-D-1-thiogalactopyranoside (IPTG) to a final concentration of 1 mM at 20°C while shaking at 225 rpm for 8 hours.

Cells were harvested by centrifugation at 4500 x g at 4°C. Packed cell volume (PCV) was approximately 7 ml and cell pellet mass was about 7 g. Cell pellets were resuspended and lysed by sonication in four to five times the PCV of 25 mM TRIS, pH 8.0, 10% glycerol, 250 mM NaCl (buffer A). Samples were heated at 65°C for 25 minutes to denature *E. coli* proteins, and then centrifuged at 14,500 x g and soluble extract was retained for purification. Protein expression was confirmed by visualization of appropriately sized bands on sodium dodecyl sulfate — polyacrylamide gel electrophoresis (SDS-PAGE) stained with Coomassie Brilliant Blue (CBB) dye.

Ni-NTA Superflow beads (QIAGEN) were equilibrated with buffer A in a one to one ratio. Three milliliters of the buffer A and bead resin was added to each soluble protein extract and tumbled gently at 4°C for one hour. The beads were washed three times with buffer A, then loaded onto a column (15 mm x 150 mm, KONTES) previously rinsed with buffer A. Protein was eluted using a linear imidazole gradient from 0 to 250 mM over 30 ml in a Fast Protein Liquid Chromatography (FPLC) system (Pharmacia). Protein elution was monitored by UV absorbance at 280 nm (Pharmacia LKB, Optical Unit UV-1) and collected in 1 ml fractions. Purity and yield were determined by protein visualization on CBB stained SDS-PAGE. Uncontaminated fractions were pooled and concentrated using Amicon Ultra-4 centrifugal filter devices (Millipore).

Experimental SAXS data of protein samples in buffer A were collected at the SIBYLS Beamline 12.3.1 of the Advanced Light Source (Lawrence Berkeley National Laboratory). Three proteins, lysozyme (14.3 kDa), bovine serum albumin (66.2 kDa), and glucose isomerase (172 kDa), were used to estimate molecular weights with respect to zero angle scattering intensity and concentration. All samples were exposed at 12 KeV for 5 seconds, 50 seconds, and then 5 seconds again to check for radiation damage. Sso0257 data were collected at concentrations of 6.9, 3.5, and 1.8 mg/ml. Sso0768 data were collected at concentrations of 2.3, 1.1, and 0.6 mg/ml. Sso3167 data were collected at concentrations of 6.0, 3.0, and 1.5 mg/ml. CRYSOL [15] software was used to generate theoretical scattering curves from crystal structures of homologs. OLIGOMER [16] was used to predict multimeric composition from solved structures to best fit the experimental data. DAMMIN [17] was used to generate *ab initio* envelope predictions.

RESULTS

Recombinant Protein Expression

Induced protein expression and solubility was evaluated for all three proteins by visualization of soluble extract fractions on a CBB stained SDS-PAGE (see Figure 1). Other heat-stable proteins were observed, most of which were common to all samples; however, the over-expression of an approximately 30 kDa polypeptide was clearly evident and unique to Sso0257. Another contaminating polypeptide of about 20 kDa was observed exclusively in the

over-expression of Sso0768 (see Figure 1). The over-expression of Sso3167 was visualized by SDS-PAGE as a small band; however, because of the low molecular weight (18 kDa), the protein ran with the dye front, making it difficult to resolve (see Figure 1). All three recombinant proteins (Sso0257, 0768, and 3167) were abundantly over-expressed in *E. coli* and resulted in heat stable and soluble recombinant proteins.

Figure 1. SDS-PAGE shows heat stable protein extracts for uninduced and induced cultures. Target proteins are circled in red.
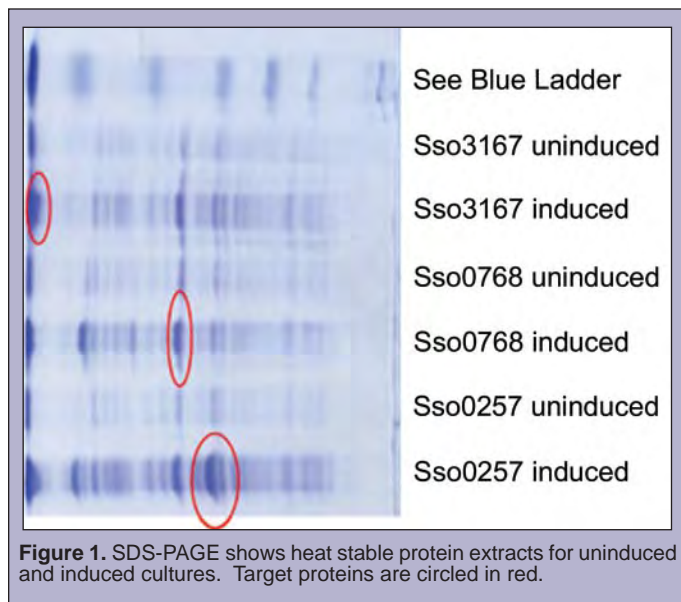
Sso0257 CDC6/ORC1

Large scale purification of Sso0257 was carried out and purity and abundance were determined by CBB SDS-PAGE. Peak elution fractions were pooled and concentrated to 6.9 mg/ml. Dilutions were then made using buffer A to concentrations of 3.5 mg/ml and 1.8 mg/ml.
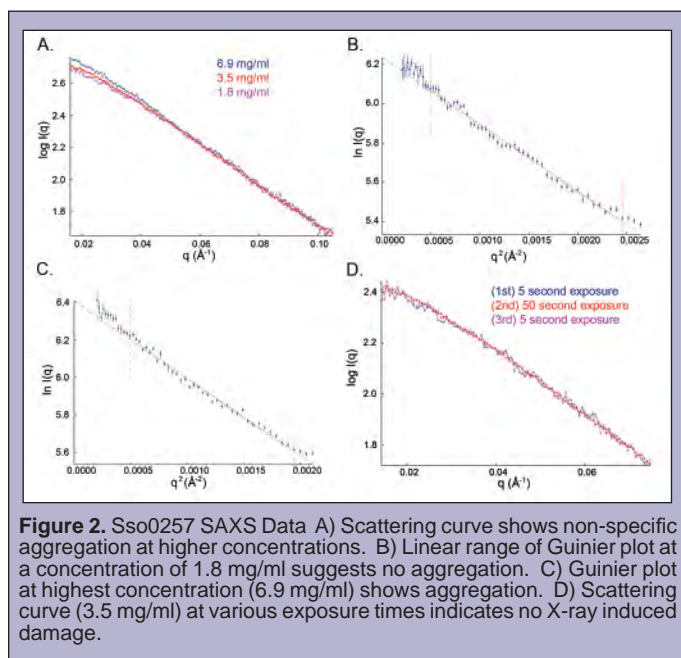
Scattering curves for the different concentrations suggest non-specific aggregation at higher concentrations (see Figure 2A). This is also evident in the Guinier plots. At a low concentration (1.8 mg/ml) the Guinier plot is linear (see Figure 2B) but at the highest concentration (6.9 mg/ml) the plot lacks linearity (see Figure 2C). Scattering curves for multiple exposure times show no X-ray induced damage at the lower angles (see Figure 2D) nor is there damage evident in the higher angles (see Figures 4A–B). The radius of gyration determined by the linear range of the Guinier plot at a concentration of 1.8 mg/ml is 32.0 Å. The molecular weight of Sso0257 was experimentally determined from SAXS data by extrapolation on a standard curve generated from three known proteins with respect to zero angle intensity and sample concentration (see Figure 3). This experimental data is most consistent with the monomeric state of the recombinant Sso0257, which has a molecular weight of 46 kDa, including six-histidine tag (see Figure 3). The crystal structure of the homologous *Pyrobaculum aerophilum* CDC6p protein (1FNN.pdb) was used for comparison with experimental data [18]. This homolog shares 27% sequence identities with the Sso0257 protein and forms a dimer in the crystal structure. CRYSOL was used to generate scattering curves from the entire structure as well as the single chain A to provide dimer and monomer theoretical scattering curves to compare with the Sso0257 scattering data. However, neither theoretical curve was in good agreement with the experimental data (see Figures 4A–B). Therefore, the OLIGOMER program was used to estimate mulitimeric composition. The best fit to the experimental data was a 50/50 mixture of monomer and dimer states (see Figure 5). DAMMIN was used to construct an *ab initio* shape prediction for the SAXS data, which was superimposed on the CDC6p dimer structure as well as the single chain A (monomer) structure; however, the *ab initio* shape did not agree with either form of the crystal structure (see Figures 4C–D).

Figure 2. Sso0257 SAXS Data A) Scattering curve shows non-specific aggregation at higher concentrations. B) Linear range of Guinier plot at a concentration of 1.8 mg/ml suggests no aggregation. C) Guinier plot at highest concentration (6.9 mg/ml) shows aggregation. D) Scattering curve (3.5 mg/ml) at various exposure times indicates no X-ray induced damage.

Figure 3. Sso0257 molecular weight estimation. Red line indicates standard curve based on three proteins with respect to known molecular weight, zero angle intensity and sample concentration.

Figure 4. Sso0257 SAXS data compared with homologous crystal structure. A) Experimental scattering curve superimposed on theoretical scattering curve for *P. aerophilum* CDC6p, chain A (monomer). B) Experimental scattering curve superimposed on theoretical scattering curve for *P. aerophilum* CDC6p dimer structure. C) Sso0257 DAMMIN *ab initio* shape prediction superimposed on *P. aerophilum*, chain A crystal structure in three orientations. D) Sso0257 DAMMIN *ab initio* shape prediction superimposed on *P. aerophilum* CDC6p dimer crystal structure in three orientations.
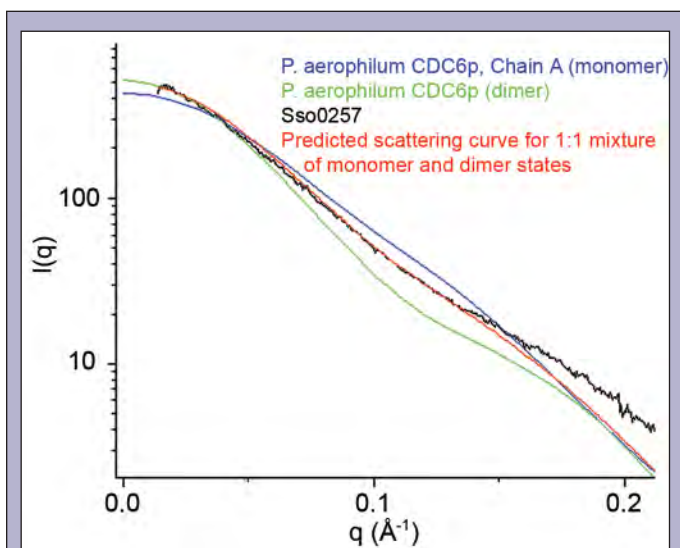
Figure 5. Scattering curves for Sso0257 experimental data, *P. aerophilum* CDC6p theoretical curves for monomer and dimer, and OLIGOMER best fit curve.

Sso0768 Replication factor C (RFC), Activator 1, small subunit

Protein purity and abundance from the over-expression of Sso0768 were determined by CBB SDS-PAGE, and then peak elution fractions were pooled and concentrated to 2.3 mg/ml. Dilutions were then prepared in buffer A to concentrations of 1.1 mg/ml and 0.6 mg/ml.

SAXS curves for the lower concentrations (1.1 mg/ml and 0.6 mg/ml) show different oligomerization states for different concentrations (see Figure 6A). A Guinier plot is not linear for the 1.1 mg/ml sample concentration suggesting aggregation (see Figure

6B). The radius of gyration approximated from the Guinier plot is 34.3 Å. An archaeon RFC small subunit crystal structure from the hyperthermophile *Pyrococcus furiosus* [19] with 59% sequence identities to Sso0768 was available for comparison with the experimental scattering curves. The *P. furiosus* RFC small subunit crystal structure (1IQP.pdb) is a hexamer, therefore theoretical scattering curves were predicted using CRYSOL from the six chains of the structure (monomer based on chain A, dimer based on chains A and B, trimer based on chains A, B, and C, tetramer based on chains A, B, C, and D, pentamer based on chains A, B, C, D, and E, hexamer based on complete crystal structure) [19]. Neither the monomer nor the hexamer theoretical curves coincide with the experimental curve (see Figures 7A–B). OLIGOMER was used to estimate the composition of oligomeric states. The best fit to the experimental data was to a mixture of 69% monomer, 13% trimer, 3% tetramer, and 15% hexamer (see Figure 7C).
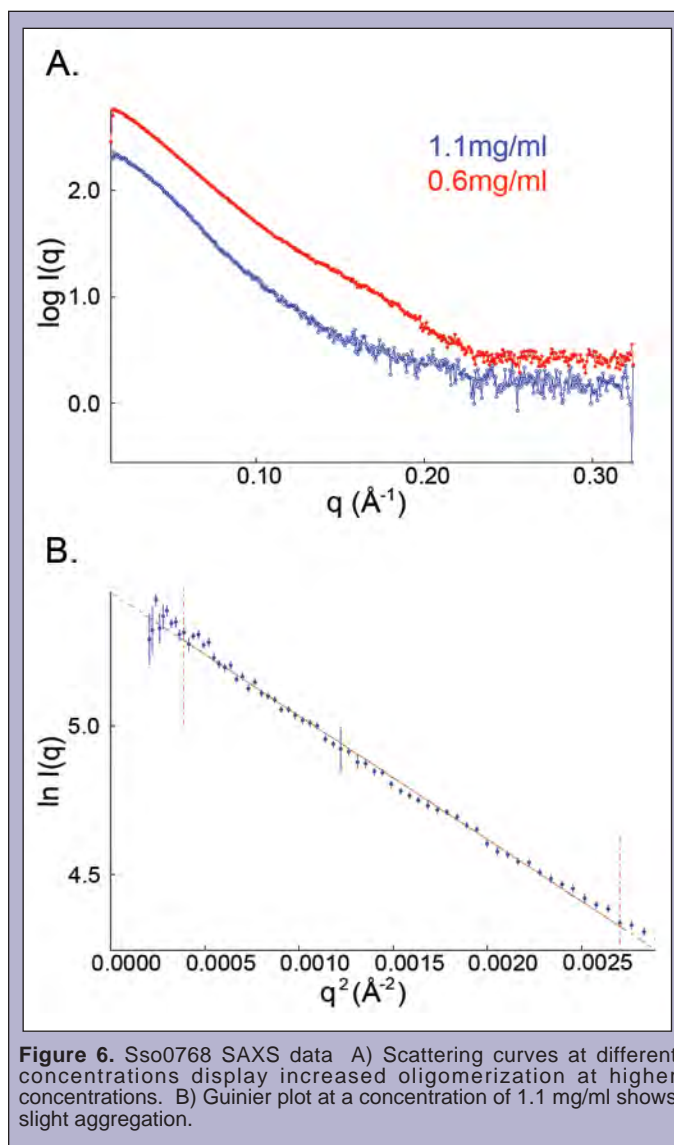
Figure 6. Sso0768 SAXS data A) Scattering curves at different concentrations display increased oligomerization at higher concentrations. B) Guinier plot at a concentration of 1.1 mg/ml shows slight aggregation.

U.S. Department of Energy Journal of Undergraduate Research
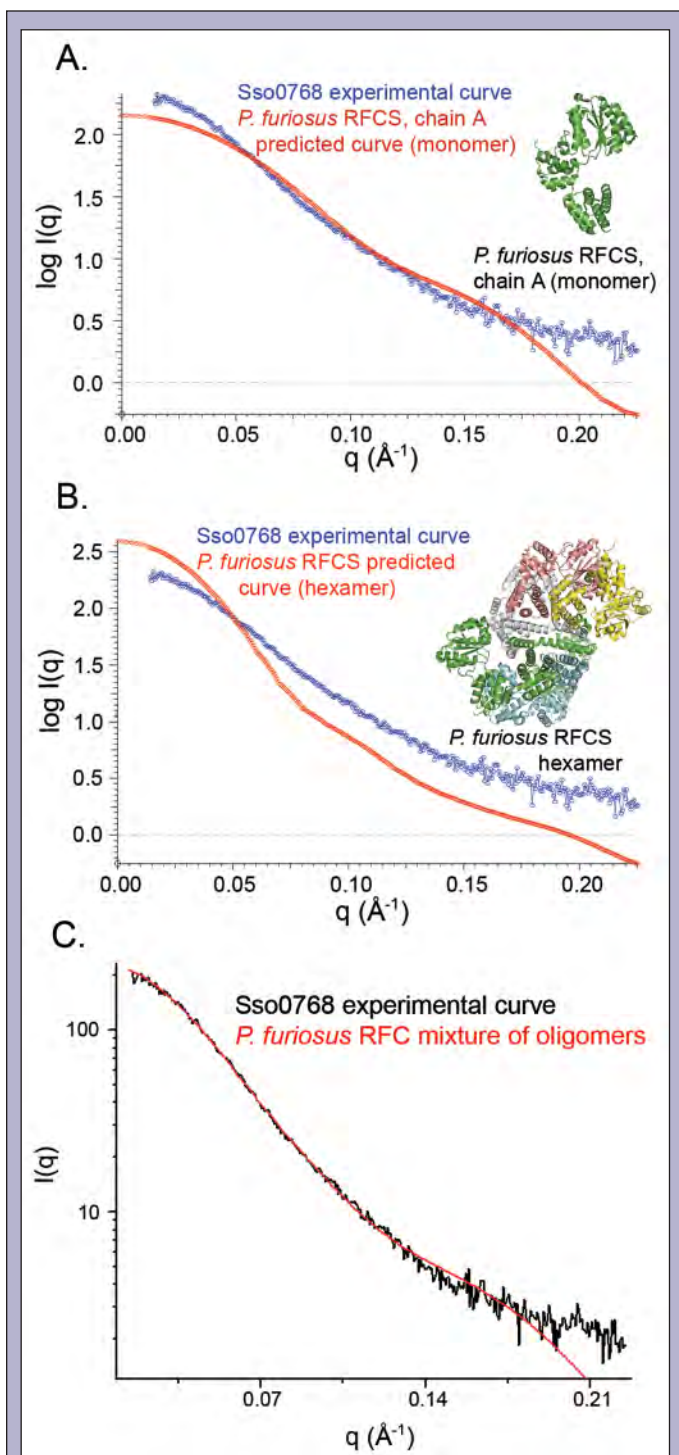
Figure 7. Sso0768 SAXS data compared with *P. furiosus* homologous crystal structure. A) Experimental data superimposed on the theoretical scattering curve for the *P. furiosus* RFC small subunit, chain A (monomer). Also shown is the crystal structure from which the theoretical curve was derived. B) Experimental data superimposed on the theoretical scattering curve for the *P. furiosus* RFC small subunit hexamer. Also shown is the crystal structure used to generate the theoretical curve. C) Sso0768 experimental data overlaid with OLIGOMER best fit for *P. furiosus* RFC small subunit complex mixture of oligomeric states.

Sso3167 Mut-T like protein

Protein purity and abundance were determined by CBB SDS-PAGE after large scale protein preparations. Fractions corresponding to the elution peak were pooled and concentrated to 6.0 mg/ml and dilutions were then prepared in buffer A to concentrations of 3.0 mg/ml and 1.5 mg/ml.

Experimental scattering curves for various concentrations and exposure times are in agreement suggesting no concentration dependence or radiation damage (see Figures 8A–B). At a low concentration (1.5 mg/ml), the experimental data fits linearly on a Guinier plot of the lower angles indicating sample homogeneity (see Figure 8C), but at high concentration (6.0 mg/ml), the data begins to lack linearity suggesting slight aggregation or an elongation within the protein (see Figure 8D). The radius of gyration given by the linear range of the Guinier plot is 18.7 Å at a concentration of 1.5 mg/ml and 19.7 Å at a concentration of 6 mg/ml.
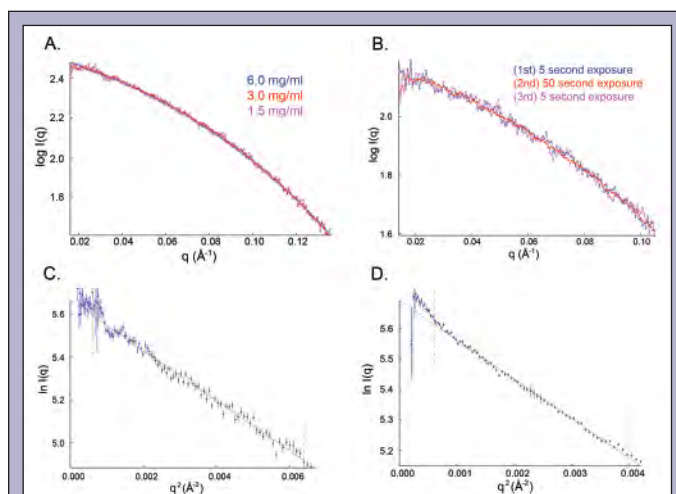
Figure 8. Sso3167 SAXS data. A) Scattering curves for various concentrations are consistent with each other suggesting no concentration dependence. B) Scattering curve of low angles for consecutive exposure times shows no X-ray induced damage. C) At a low concentration (1.5 mg/ml) the Guinier plot is linear suggesting sample homogeneity. D) At a higher concentration (6 mg/ml), the Guinier plot begins to lack linearity, which may correspond to slight aggregation or an elongated portion of the protein.

The *Deinococcus radiodurans* Mut-T/NADIX, chain A crystal structure [20] was used for comparison with the Sso3167 experimental data. The *D. radiodurans* homolog (1NQY.pdb) shares 27% sequence identities to Sso3167 including a similar large region of disorder. A theoretical scattering curve was generated from the crystal structure using CRYSOL. When overlaid with the experimental data, the theoretical curve is similar, but offset at higher angles indicating a deviation in overall protein shape (see Figure 9A).

DAMMIN was used to generate *ab initio* shape predictions from the experimental scattering curves. Ten individual runs using the q range up to 0.21 Å consistently predicted an extension in various orientations. These ten individual runs were averaged to generate the final shape prediction (See Figure 9B). The *D. radioduran* crystal structure was superimposed on the shape prediction for

the Sso3167 data. The crystal structure is missing eleven residues which may fit in the elongated potion of the envelope (see Figure 9B). Although normalized spatial discrepancy has previously been suggested to determine goodness of fit for three-dimensional objects [21], statistical methods have proven unreliable in accessing the fit of a model. Instead, best fit of the shape prediction is based on experimental repetition and visually comparing the final models [22].

Sso0257 CDC6-1

Scattering data at higher concentrations (6.9 mg/ml) shows non-specific aggregation (see Figure 2A). Although the homologous *P. aerophilum* CDC6p crystal structure is dimeric, its theoretical scattering profile is not in good agreement with the experimental data (see Figure 4A). Interestingly, the theoretical curve for the single chain A (monomer) also did not agree with the SAXS data (see Figure 4B). Using a standard curve based on three proteins, the estimated molecular weight for Sso0257 is 46kDa, which is consistent with a monomeric state (see Figure 3); however the *ab initio* shapes appear

Figure 9. Sso3167 experimental data compared with homologous crystal structure. A) Sso3167 scattering curve superimposed on the theoretical curve for the *D. radiodurans* Mut-T crystal strucutre shows slight deviation at the higher angles. B) Sso3167 DAMMIN *ab initio* shape prediction superimposed on the *D. radiodurans* Mut-T crystal structure in three orientations.

too large to be monomeric when compared with the *P. aerophilum* monomer structure (see Figure 4C). The shape also conflicts with the *P. aerophilum* dimer structure (see Figure 4D). It is probable that the discrepancy in the predicted low resolution shape and the homologous crystal structures is attributed to a flexible winged helix domain within the protein. The flexibility of this domain in solution may cause the shape reconstructions to be larger than the monomeric crystal structure. The functional relevance of this domain is evident in the recently published crystal structure of CDC6-1 complexed with CDC6-3 and origin DNA (2QBY.pdb) where the winged helix domain is deeply inserted into the DNA grooves and effectively deforms the duplex [12]. Another possibility for the inconsistency in the shape predictions and the crystal structures is that the sample is a mixture of monomer and dimer states. This is supported by the best fit curve from the OLIGOMER analysis based on predicted scattering profiles for the *P. aerophilum* monomer and dimer (see figure 5). In order to discriminate between these two possibilities, the protein sample will be further purified by size exclusion. This will ensure monodispersity in the sample and will eliminate the possibility of a mixture of oligomeric states. The protein will then be analyzed with SAXS and again compared to the homologous crystal structure to determine whether the size difference between *ab initio* shape and the crystal structure is attributed to the flexibility of the winged helix domain.

In a separate article published at the same time as the CDC6-1, CDC6-3 and origin DNA complex, the *A. pernix* ORC1 protein was crystallized with a 22bp canonical origin of replication sequence [23] showing DNA-binding activity for both the expected winged helix domain, but also, surprisingly, for the ATPase domain as well. Therefore, further studies will be conducted using SAXS on the conformational changes assumed in presence of bubble or forked DNA and ATP.

Sso0768 RFC6, Activator 1, small subunit

Comparison of scattering data at 1.1 mg/ml and 0.6 mg/ml shows different scattering curves, which indicates aggregation and higher oligomerization of this protein at higher concentrations (see Figure 6A). The *P. furiosus* RFC small subunit crystal structure is a hexamer, but neither the theoretical scattering curve derived from the hexamer nor the monomer state agree with the experimental scattering curve for Sso0768 (see Figures 7A–B). The hexameric crystal structure has two-fold symmetry and can be viewed as two trimer states (see Figure 10). This view supports the OLIGOMER fit of mostly monomers, trimers and hexamers to the SAXS data (see Figure 7C). It is likely that at higher concentrations the Sso0768 protein forms trimers, which then assemble into hexamers because of interactions between the proteins. As a clamp loader, this oligomeric state may also serve a functional purpose loading the polymerase onto DNA. Sso0768 will be further purified by size exclusion and will be analyzed by SAXS at increased temperature (40°C and 60°C) to study what affect temperatures closer to biological conditions will have on the oligomerization state. These methods will elucidate the functional and physiological relevance of the oligomeric state and should resolve whether trimers and hexamers are only formed at high concentrations or if they are functionally significant. Also, Sso0768

will be co-expressed with the RFC large subunit to investigate any conformational or oligomeric changes brought about by interactions between the subunits in solution.
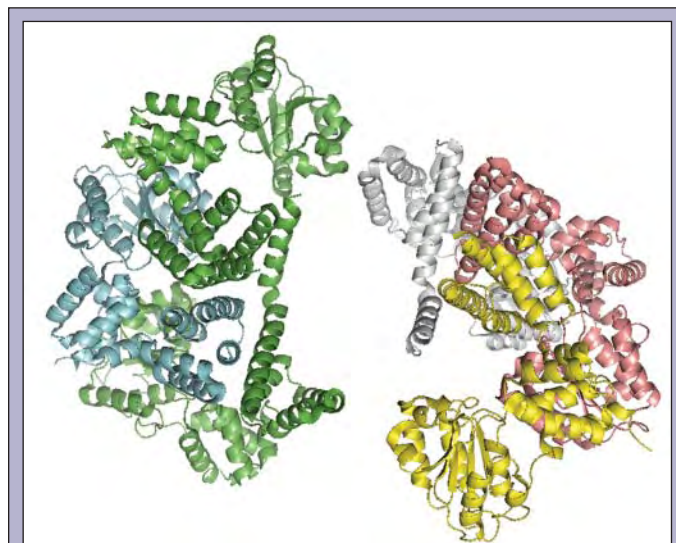
Figure 10. *P. furiosus* RFC small subunit hexamer arranged into two trimers.

Sso3167 Mut-T like protein

The predicted scattering curve from the *D. radiodurans* homolog and the experimental scattering curve are analogous but do not overlay completely at larger angles (see Figure 9A). This discrepancy may be caused by an extended region of the protein that is not resolved in the crystal structure. This possibility is further supported by the *ab initio* shape prediction for Sso3167, which contains a protrusion that may correspond to the eleven missing residues in the crystal structure of the *D.radiodurans* homolog (see Figures 9B). Both Sso3167 and the *D. radiodurans* Mut-T protein contain large regions of disorder based on sequence as predicted by PONDR [24,25,26] (data not shown). It is likely that these disordered regions occupy the extension in the shape prediction, transitioning from a floppy domain in solution to a functional region in the presence of a substrate. This feature may also help to recognize oxidized dGTP and catalyze the reaction to remove it from the free nucleotide pool. Possible changes in conformation and oligomeric states in the presence of oxidized dGTP and other nucleotides will be studied using SAXS to evaluate the functional role of the elongation in enzymatic activity.

These three archaeal proteins were chosen because of their involvement in processes that are similar to and representative of more complicated processes in Eukaryotes and their preliminary characterization emphasizes the utility of hyperthermophilic proteins as models for higher eukaryotic processes. Sso0257 is an essential component in origin recognition and has also been implicated in cell division control [18]. Understanding how this protein recognizes origins and initiates replication will help to shed light on how and why mutations occur during this process. Sso0768 is a RFC subunit thought to help load the processivity factor onto DNA. The mechanism for this is still unclear as is the role of the large

subunit and its possible interaction with Sso0768, the processivity factors and DNA. Sso3167 is a Mut-T like protein. This family of proteins is important in preventing mutated nucleotides from being incorporated into DNA. The expression, purification and initial SAXS analysis of these proteins demonstrates the applicability of thermo-stable archaeal proteins to provide simplified model systems for transitory eukaryotic processes.

REFERENCES

[1] C.J. Bult, O. White, G.J. Olsen, L. Zhou, R.D. Fleischmann, G.G. Sutton, J.A. Blake, L.M. Fitzgerald, R.A. Clayton, J.D. Gocayne, A.R. Kerlavage, B.A. Dougherty, J.F. Tomb, M.D. Adams, C.I. Reich, R. Overbeek, E.F. Kirkness, K.G. Weinstock, J.M. Merrick, A. Glodek, J.L. Scott, N.S. Geoghagen, and J.C. Venter, "Complete Genome Sequence of the Methanogenic Archaeon, *Methanococcus jannaschii*," Science, vol. 273, no. 5278, Aug., 1058–1073, 1996.

[2] H.P. Klenk, R.A. Clayton, J.F. Tomb, O. White, K.E. Nelson, K.A. Ketchum, R.J. Dodson, M. Gwinn, E.K. Hickey, J.D. Peterson, D.L. Richardson, A.R. Kerlavage, D.E. Graham, N.C. Kyrpides, R.D. Fleischmann, J. Quackenbush, N.H. Lee, G.G. Sutton, S. Gill, E.F. Kirkness, B.A. Dougherty, K. McKenney, M.D. Adams, B. Loftus, S. Peterson, C.I. Reich, L.K. McNeil, J.H. Badger, A. Glodek, L. Zhou, R. Overbeek, J.D. Gocayne, J.F. Weidman, L. McDonald, T. Utterback, M.D. Cotton, T. Spriggs, P. Artiach, B.P. Kaine, S.M. Sykes, P.W. Sadow, K.P. D'Andrea, C. Bowman, C. Fujii, S.A. Garland, T.M. Mason, G.J. Olsen, C.M. Fraser, H.O. Smith, C.R. Woese, and J.C. Venter, "The Complete Genome Sequence of the Hyperthermophilic, Sulphate-reducing Archaeon *Archaeoglobus fulgidus*," Nature, vol. 390, Nov., 364–370, 1997.

[3] Y. Kawarabayasi, Y. Hino, H. Horikawa, K. Jin-no, M. Takahashi, M. Sekine, S. Baba, A. Ankai, H. Kosugi, A. Hosoyama, S. Fukui, Y. Nagai, K. Nishijima, R. Otsuka, H. Nakazawa, M. Takamiya, Y. Kato, T. Yoshizawa, T. Tanaka, Y. Kudoh, J. Yamazaki, N. Kushida, A. Oguchi, K. Aoki, S. Masuda, M. Yanagii, M. Nishimura, A. Yamagishi, T. Oshima, and H. Kikuchi, "Complete Genome Sequence of an Aerobic Thermoacidophilic Crenarchaeon, *Sulfolobus tokodaii* Strain 7," DNA Research, vol. 8, 123–140, 2001.

[4] Q. She, R.K. Singh, F. Confalonieri, Y. Zivanovic, G. Allard, M.J. Awayez, C.C.Y. Chan-Weiher, I.G. Clausen, B.A. Curtis, A. De Moors, G. Erauso, C. Fletcher, P.M.K. Gordon, I. Heikamp-de Jong, A.C. Jeffries, C.J. Kozera, N. Medina, X. Peng, W.F. Doolittle, M. Duguet, T. Gaasterland, R.A. Garrett, M.A. Ragan, C.W. Sensen and J. Van der Oost, "The Complete Genome of the Crenarchaeon *Sulfolobus solfataricus* P2," Proceedings of the National Academy of Sciences, vol. 98, no. 14, July, 7835–7840, 2001.

[5] W. Zillig, K.O. Stetter, and D. Janekovic, "DNA-dependent RNA Polymerase from the Archaebacterium *Sulfolobus acidocaldarius*," European Journal of Biochemistry, vol. 96, June, 597–604, 1979.

[6] J.N. Reeve, K. Sandman, and C.J. Daniels, "Archaeal Histones, Nucleosomes, and Transcription Initiation," Cell, vol. 89, June, 999–1002, 1997.

[7] M. Thomm, "Archaeal Transcription Factors and Their Role in Transcription Initiation," FEMS Microbiology Review, vol. 18, May, 159–171, 1996.

[8] S.A. Qureshi and S.P. Jackson, "Sequence-specific DNA Binding by the *S. shibatae* TFIIB Homolog, TFB, and its Effect on Promoter Strength," Molecular Cell, vol. 1, Feb., 389–400, 1998.

[9] F. Pfeifer, K.H. Schleifer, P. Palm, Eds., Molecular Biology of Archaea, Munich: John Wiley & Sons, 1994.

[10] M. Ciaramella, F.M. Pisani, and M. Rossi, "Molecular Biology of Extremophiles: Recent Progress on the Hyperthermophilic Archaeon *Sulfolobus*," Antonie van Leeuwenhoek, vol. 81, 85–97, 2002.

[11] M. De Felice, L. Esposito, M. Rossi, and F. Pisani, "Biochemical Characterization of Two Cdc6/ORC1-like Proteins from the Crenarchaeon *Sulfolobus solfataricus*," Extremophiles, vol. 10, 61–70, 2006.

[12] E.L. Cunningham Dueber, J.E. Corn, S.D. Bell, J.M. Berger, "Replication Origin Recognition and Deformation by a Heterodimeric Archaeal Orc1 Complex," Science, vol. 317, 1210–1213, 2007.

[13] F. Pisani, M. De Felice, Fl. Carpentieri, and M. Rossi, "Biochemical Characterization of a Clamp-loader Complex Homologous to Eukaryotic Replication Factor C from the Hyperthermophilic Archaeon *Sulfolobus solfataricus*," Journal of Molecular Biology, vol. 301, 61–73, 2000.

[14] J.Y. Mo, H. Maki, M. Sekiguchi, "Hydrolytic Elimination of a Mutagenic Nucleotide, 8-oxoGTP, by Human 18-kilodalton protein: Sanitization of Nucleotide Pool," Proceedings of

the National Academy of Sciences, vol. 89, 11021–11025, 1992.

[15] D.I. Svergun, C. Barberato, and M.H.J. Koch, "CRYSOL — a Program to Evaluate X-Ray Solution Scattering of Biological Macromolecules from Atomic Coordinates," Journal of Applied Crystallography, vol. 28, 768–773, 1995.

[16] P.V. Konarev, V.V. Volkov, A.V. Sokolova, M.H.J. Koch, and D.I. Svergun, "PRIMUS: a Windows PC-based system for Small-Angle Scattering Data Analysis," Journal of Applied Crystallography, vol. 36, 1277–1282, 2003.

[17] D.I. Svergun, "Restoring Low Resolution Structure of Biological Macromolecules from Solution Scattering Using Simulated Annealing," Biophysical Journal, vol. 76, June, 2879–2886, 1999.

[18] J. Liu, C.L. Smith, D. DeRyckere, K. DeAngelis, G.S. Martin, J.M. Berger, " Structure and Function of Cdc6/Cdc18: Implications for Origin Recognition and Checkpoint Control", Molecular Cell, vol. 6, 637–648, 2000.

[19] T. Oyama, Y. Ishino, I.K.O. Cann, S. Ishino, and K. Morikawa, "Atomic Structure of the Clamp Loader Small Subunit for *Pyrococcus furiosus*," Molecular Cell, vol. 8, Aug., 455–463, 2001.

[20] L. Kang, S.B. Gabelli, M.A. Bianchet, W.L. Xu, M.J. Bessman, and L.M. Amzel, "Structure of a Coenyme A Pyrophosphatase from *Deinococcus radiodurans*: a Member of the Nudix Family," Journal of Bacteriology, vol. 185, no. 14, July, 4110–4118, 2003.

[21] M.B. Kozin and D.I. Svergun, "Automated matching of low- and high-resolution structural models," Journal of Applied Crystallography, vol. 34, no. 1, Feb., 33–41, 2001.

[22] C.D. Putnam, M. Hammel, G.L. Hura, and J.A. Tainer, "Solution scattering (SAXS) combined with crystallography and computation: defining accurate macromolecular structures, conformations and assemblies in solution," Quarterly Reviews in Biophysics, vol. 40, no. 3, Aug., 191–285, 2007.

[23] M. Gaudier, B.S. Schuwirth, S.L. Westcott, D.B. Wigley, "Structural Basis of DNA Replication by an ORC protein," Science, vol. 317, Aug., 1213–1216, 2007.

[24] X. Li, P. Romero, M. Rani, A.K. Dunker, and Z. Obradovic, "Predicting protein disorder for N-, C-, and internal regions," Genome Informatics, vol. 10, 30–40, 1999.

[25] P. Romero, Z. Obradovic, X. Li, E. Garner, C. Brown, and A.K. Dunker, "Sequence complexity of disordered protein," Proteins: Structure, Function, and Genetics, vol. 42, no. 1, Jan., 38–48, 2001.

[26] P. Romero, Z. Obradovic, and A.K. Dunker, "Sequence data analysis for long disordered regions prediction in the calcineurin family," Genome Informatics, vol. 8, 110–124, 1997.

Guilhem Ribeill was born in Vitry-sur-Seine, France, and has lived in France, England and most recently Raleigh, NC. He attended North Carolina State University, majoring in physics and chemistry. During his undergraduate career, he held a SULI internship at the Thomas Jefferson National Accelerator Facility in the summer of 2007. He hopes to earn a doctoral degree in physics and continue a career in research. His interests include improvisational comedy and photography.

Charles Reece is a Senior Scientist at the Thomas Jefferson National Accelerator Facility (Jefferson Lab). He received his Ph.D. from the University of Rochester in 1983 for a study exploring the use of a superconducting cavity parametric converter for periodic gravitational force detection. He spent several years at Cornell University working on accelerator applications of superconducting rf (SRF) cavities. Since 1987 he has worked at Jefferson Lab, leading technical facility development, SRF cavity testing, accelerator system optimization in CEBAF, accelerator cryomodule prototyping, and more recently R&D on SRF materials and conditioning processes pushing to fundamental limits with familiar and new materials. He presently serves as Deputy Director of the Institute for Superconducting RF Science and Technology at Jefferson Lab.

Roughness Analysis of Variously Polished Niobium Surfaces

Guilhem Ribeill and Charles Reece

ABSTRACT

Niobium superconducting radio frequency (SRF) cavities have gained widespread use in accelerator systems. It has been shown that surface roughness is a determining factor in the cavities' efficiency and maximum accelerating potential achievable through this technology. Irregularities in the surface can lead to spot heating, undesirable local electrical field enhancement and electron multipacting. Surface quality is typically ensured through the use of acid etching in a Buffered Chemical Polish (BCP) bath and electropolishing (EP). In this study, the effects of these techniques on surface morphology have been investigated in depth. The surface of niobium samples polished using different combinations of these techniques has been characterized through atomic force microscopy (AFM) and stylus profilometry across a range of length scales. The surface morphology was analyzed using spectral techniques to determine roughness and characteristic dimensions. Experimentation has shown that this method is a valuable tool that provides quantitative information about surface roughness at different length scales. It has demonstrated that light BCP pretreatment and lower electrolyte temperature favors a smoother electropolish. These results will allow for the design of a superior polishing process for niobium SRF cavities and therefore increased accelerator operating efficiency and power.

Introduction

Superconducting radio frequency (SRF) cavities are widely used to achieve high quality particle beams for nuclear physics research. Their usefulness rests mainly on their high quality factor, low power dissipation and potential for continuous wave operation. The most common material for the construction of these cavities is solid niobium, due to the availability of high-purity niobium and the ease of machining it into cavities [1,2]. Surface roughness has been shown to be a critical factor in determining the efficiency and maximum accelerating potential these cavities can achieve. The quality of the niobium surface directly impacts such undesirable effects such as field enhancement, the creation of 'hot spots' and electron multipacting [3]. The surface is typically polished using an acid etch Buffered Chemical Polish (BCP) consisting of HNO_3, HF and H_3PO_4 or EP in a HF/H_2SO_4 solution [4, 5].

Characterizing the surface morphology of the Niobium surfaces is a challenging task as it is unknown at what scale roughness is important to SRF performance. Pending such an analysis, the roughness of niobium must be looked at across a range of sizes and resolutions, which can only be accomplished using several different instruments. A method of combining the measurements from different instruments is therefore needed. A powerful tool for this kind of analysis is the power spectral density (PSD) [6]. From the PSD, one can easily obtain the characteristic length of surface features as well as the fractal dimension of the surface [7].

Sample Preparation

Chemical reagents used for polishing in this study were a BCP acid etch solution and an EP solution. The BCP solution was a 2:1:1 solution of 85% H_3PO_4, 49% HF and 70% HNO_3. The EP solution was a 1:9 mixture of 49% HF and 96% H_2SO_4. The samples that were used in this study were reactor-grade polycrystalline niobium slabs (CBMM, Sao Paulo, Brazil) with dimensions of 22 mm x 22 mm x 4 mm. All samples were mechanically polished using 1 μm grit prior to any chemical treatment. The sample used as a reference for an "untreated" sample was placed in a BCP acid etch for 5 minutes in order to remove any residual surface contamination. In this paper, the samples we refer to as having undergone a "Light BCP" treatment were placed in a BCP bath for 20 minutes. As measured by weight loss, the acid etch removed 30 μm. Those

samples we refer to as having undergone "Heavy BCP" were placed in the BCP bath for 90 minutes which resulted in a 150 µm etch of the surface.

To electropolish the samples, the niobium sample and an aluminum counter electrode were held in place by Teflon clamps in the EP solution a distance of 100 mm apart. This setup was also used for taking EIS data with a mercury-amalgam reference electrode placed halfway between the niobium and counter-electrode. To prevent damage to the reference electrode, it was immersed in a solution of 1 N sulfuric acid, which was separated from the EP bath by a glass frit at the end of a Teflon tube. Samples having undergone no BCP treatment, as well as those having undergone light and heavy BCP treatment were subjected to 30 minutes of EP at 6 V, with electrolyte temperatures of 24°C and 30°C. These treatments removed approximately 100 µm from the surface, as measured using a stylus profilometer.

METHOD

Profilometry measurements were obtained with a stylus profilometer (KLA-Tencor: P-15) equipped with a tip with a diameter of two µm. The samples were scanned in two different regions with a scan size of 200 x 200 µm and 1000 x 1000 µm. The 200 µm scan was taken as an array of 101 traces with 401 points in each trace, and the 1000 µm as an array of 251 traces with 2501 points each. AFM measurements were performed using a commercial AFM (Digital Instruments: Nanoscope II) in tapping mode using silicon tips with a diameter of 10 nm. The samples were each scanned in three different regions with scan sizes of 20x20 µm, 50x50 µm, and 100x100 µm. The AFM images were captured as arrays of height values with 256x256 points.

There exist several measures of surface roughness. The typical measure is the root mean square roughness, defined by (1):

$$\bar{R}_q = \sqrt{\frac{1}{n}\sum_{i,j}(z_{i,j}-\bar{z})^2} \tag{1}$$

Another way to characterize roughness is the Power Spectral Density (PSD). It can easily be computed as the square of the Fourier transform (2),

$$PSD(f) = \frac{1}{L}\left|\int_0^L dx z(x) e^{2\pi f/s}\right|^2 \tag{2}$$

or in the case of discrete data consisting of N points separated by Δx, equation (3),

$$PSD(m) = \frac{\Delta x}{N}\left|\sum_{n=1}^{N-1} z(n) e^{i2\pi mn/N}\right|^2 \tag{3}$$

A more complete mathematical treatment can be found in Elson and Bennett [8]. The PSD represents the squared amplitude of surface features plotted against the spatial frequency of those features. This provides information about both the lateral and vertical size of features; data from different instruments can also be combined, taking care that the range of spatial frequencies over which the PSD is valid for a certain scan size is determined by the Nyquist limits. To simplify calculations, in this study the power spectral density for all traces in the fast scan direction were averaged to approximate the true 2D PSD. This assumption is valid in the case of a surface with isotropic roughness [9]. For all the samples, all the PSDs from a sample were averaged together and the PSDs

from the profilometer data were filtered using a 4-sample moving average in order to eliminate high-frequency noise.

RESULTS AND DISCUSSION

Figure 1 represents the 50 µm AFM data from the surface with five minutes of BCP and the surface that was treated with both heavy BCP and EP. The former shows very pronounced peaks and valleys, as well as a very non-uniform surface, whereas the latter is much smoother.
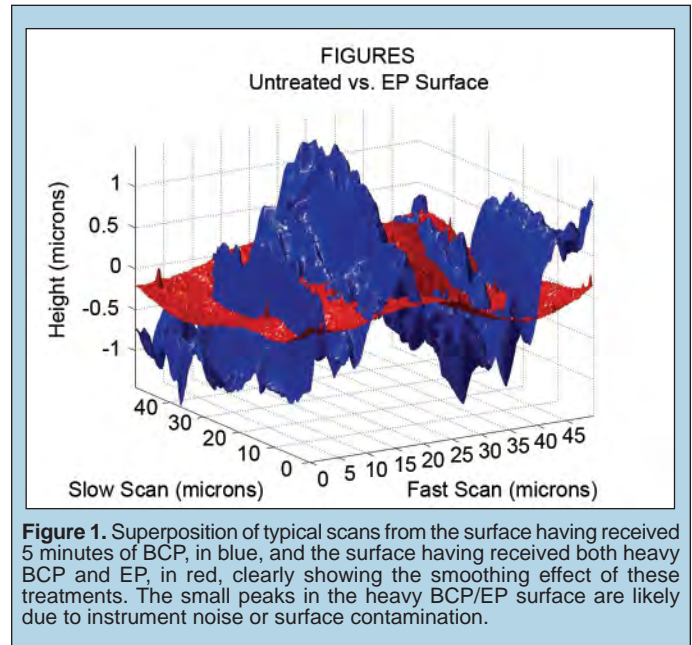
Figure 1. Superposition of typical scans from the surface having received 5 minutes of BCP, in blue, and the surface having received both heavy BCP and EP, in red, clearly showing the smoothing effect of these treatments. The small peaks in the heavy BCP/EP surface are likely due to instrument noise or surface contamination.

Figure 2 shows a plot of different R_q values computed from the data at all of the scan sizes. While R_q is a useful and widely used measure of surface roughness, it is dependent on the scan size and the particularities of the area being scanned. The data shows different values of R_q for each surface; at small scan lengths, light BCP + EP
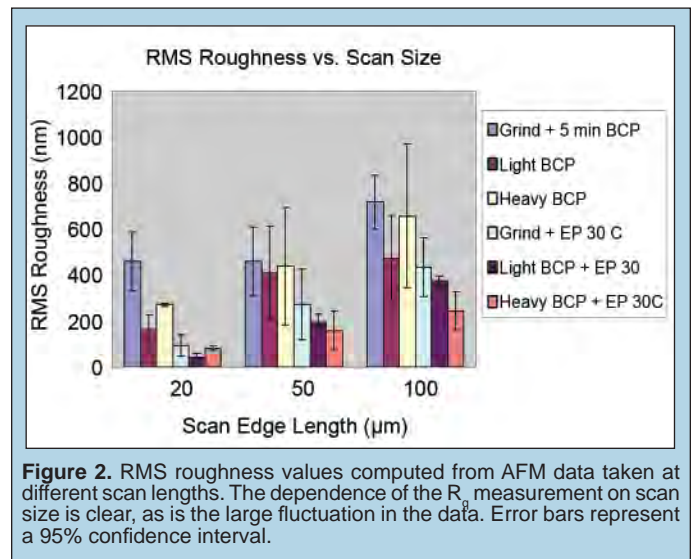
Figure 2. RMS roughness values computed from AFM data taken at different scan lengths. The dependence of the R_q measurement on scan size is clear, as is the large fluctuation in the data. Error bars represent a 95% confidence interval.

is smoother than heavy BCP + EP, but it is rougher at large scan lengths. While this may indicate that heavy BCP followed by EP promotes smoothing only at large scales, large error bars associated with the R_q measurements, make it difficult to draw conclusions.

It is also difficult to compare roughness values taken using different instruments, especially when one considers that the range of frequencies that any one instrument can resolve is necessarily limited and unique to that instrument [6, 8]. Furthermore, since this roughness measurement considers only vertical information, it does not give any information about the lateral morphology of surface features.

In order to overcome these limitations, we have used the PSD, defined in equation 3, of the surface profile as a tool to combine measurements from different scales and different instruments.

Figure 3 shows the combined AFM and profilometer data from the sample with five minutes of BCP treatment. The measurements using the two techniques agree very closely over the range of frequencies that are common to both instruments. This shows that the PSD is a method which can combine information from different instruments in a consistent and useful manner. At the high-frequency end of the spectra, the slope of all the graphs shows a marked decrease and they begin to level off. This is likely due to the effects of limited resolution for the AFM, and the finite tip size for the profilometer data [10]. Of particular interest in this graph is the change of slope that occurs at a spatial frequency of approximately 0.04 μm. (From Fig.3 it is hard to tell the slope change around 0.04 μm^{-1}.) Changes in slope of the PSD are related to the inverse of the correlation length of the sample. The correlation length sets the scale at which surface features are similar [7, 9]. For this data, the correlation length is approximately 25 μm s, which is on the order of the size of niobium grains in the polycrystalline crystals studied.

For clarity, the rest of the graphs in this paper only show data from the 1000 μm profilometer scans and the 20 μm AFM scans. The differences between these scans and the others are minor, as can be seen in Fig. 3.
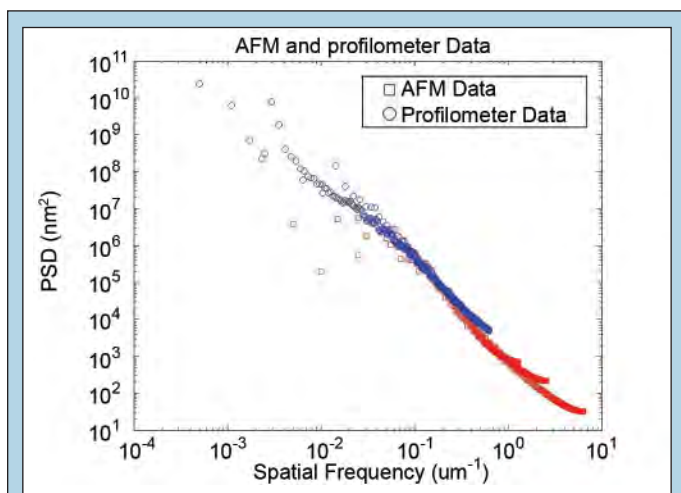
A comparison of the different methods of polishing a ground sample can be found in Figure 4. The smaller amplitude of the PSD for the electropolished sample supports the conclusion from R_q data that it is the technique that produces the smoothest surface. The slope change at 0.04 μm^{-1} from the ground sample is no longer visible, indicating that differences between grains have been greatly reduced, unlike with BCP. Furthermore, the greater slope of the PSD in the mid to high frequency region as compared to the other polishing techniques indicates that EP provides the best micropolish. The EP PSD also shows a change in slope at the smallest frequency, corresponding to EP producing a surface with the longest correlation length. This also supports the conclusion that EP produces the smoothest surface, since surface features are self-similar on larger scales. Interestingly, the light BCP treatment seems to produce a smaller PSD at low frequencies than the heavy BCP treatment, but the situation is reversed at high frequencies. Quite right, I took it out! This effect would be impossible to analyze if using only R_q as a measure of roughness; it indicates that a longer BCP treatment produces a better micropolish, but a rougher macropolish. This effect is likely due to the differential etching by BCP of grains with different crystallographic orientations [3]. As more material is etched, and the damage caused by the mechanical polish is removed, material from different grains is removed at different rates, leaving a rougher surface.
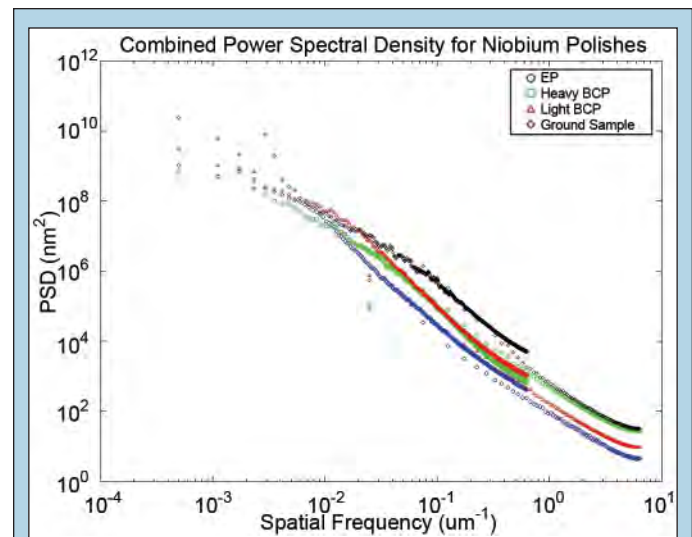
Figure 4. PSD spectra for the different polishing methods performed on a mechanically ground sample. Electropolishing was performed at 24°C.

Figure 5 compares the PSD of samples that have undergone different pretreatments before the electropolish. Light BCP again has the smallest amplitude, and the longest correlation length which corresponds to the smoothest surface. This result is not surprising in the context of the results previously discussed; a longer BCP treatment produces a rougher surface at large scales which has not been smoothed out by EP. Figure 6 presents the power spectra of ground samples treated with EP at two different electrolyte temperatures. The overlap of the two plots in the high-frequency region indicates that there is no significant difference in the quality of the polish at small scales. There is some evidence for a difference

Figure 3. Combined AFM and profilometer PSD from all scan sizes from the untreated sample.

U.S. Department of Energy Journal of Undergraduate Research

at low frequencies, since the graphs take on a different shape. The longer correlation length of the 24°C sample, as indicated by the smaller inverse length at which the graph levels off, suggests that the lower temperature may cause a smoother finish of the sample, a conclusion also supported by the RMS roughness values, 84 nm for the 24°C niobium sample and 94 for the 30°C sample, at a scan size of 20 x 20 μm s. However, while suggestive, such a small temperature difference does not fully explore the effect of temperature on EP treatment and this merits further study.
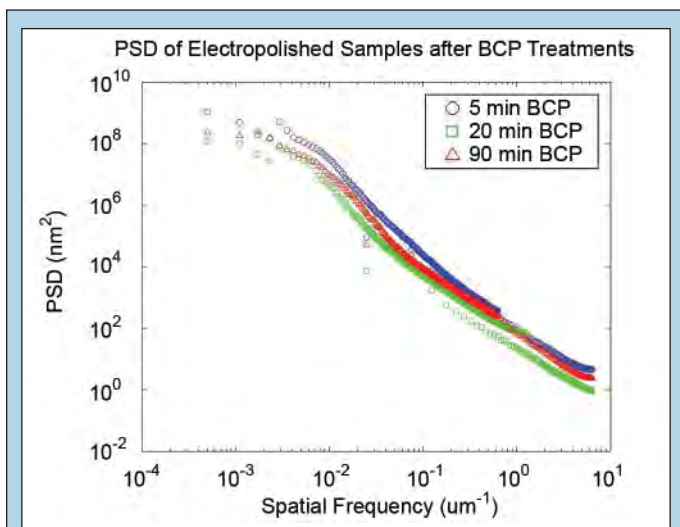
Figure 5. Power spectral density plots of niobium samples that have undergone different treatments before being electropolished.
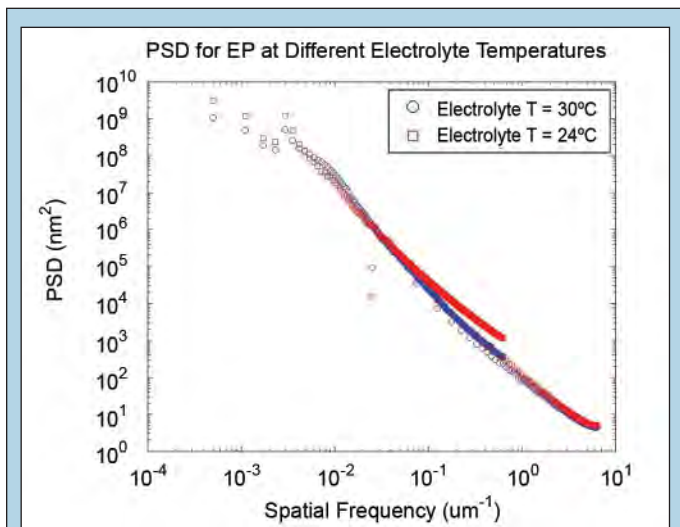
Figure 6. PSD graphs for EP of a ground sample at different electrolyte temperature.

CONCLUSION

We have demonstrated the use of spectral analysis techniques and, specifically, the power spectral density in quantitatively characterizing the surface roughness of niobium. This tool will therefore allow for improved monitoring and analysis in the production of SRF cavities. PSD curves can also be analyzed to determine fractal dimension, an alternative measure of surface roughness [7, 12]. In certain cases, this fractal dimension can be related to impedance spectra which show power-law dependence at low frequencies [13]. If this holds true in the case of niobium, it may be possible to use EIS to monitor surface roughness *in situ* during electropolishing.

The spectral technique has allowed us to make preliminary observations about the use of BCP and EP on niobium samples. We have conclusively shown that electropolishing produces the best surface polish, and is most effective when following a short BCP treatment. (Actually, in this manuscript, only one set of data (Fig. 2, scan size 20 × 20 μm) shows the sample with EP + light BCP gives best polishing. No other figures or PSD data demonstrate this point. So, more convincing data and explanation need be given.) Our data also suggests that a lower electrolyte temperature promotes a better EP at larger scales. However, our data is preliminary and merits much further study. The most important future work will be to determine at length scales roughness is most important to cavity performance. This information will allow for the development of a polishing process that optimizes the performance of SRF cavities and thereby accelerator systems.

REFERENCES

[1] H. Padamsee, *et al.*, <u>RF Superconductivity for Accelerators</u>. 2nd ed. Ithaca, NY: John Wiley & Sons, 1998.

[2] H. Padamsee, "The science and technology of superconducting cavities for accelerators," <u>Supercond. Sci. Technol.</u>, vol. 14, R28–R51, 2001.

[3] H. Tian *et al.* "Surface studies of niobium chemically polished under conditions for superconducting radio frequency (SRF) cavity production," <u>Appl. Surf. Sci.</u> vol. 253, no. 3, 1236–1242, 2006.

[4] Y. Uzel *et al.* "Improvement of the polishing treatment for niobium surfaces of superconducting cavity resonators," <u>Appl. Phys A.</u> vol. 30, no. 3, 185–187, 1982.

[5] K. Saito. <u>Particle Accelerator Performance: Proceedings of the PAC 2003</u>. 1 462–466 (2003)

[6] A. Duparré *et al.* "Surface Characterization Techniques for Determining the Root-Mean-Square Roughness and Power Spectral Densities of Optical Components," <u>Appl. Optics</u>. vol. 41, no. 1, 154–171, 2002.

[7] O. Vatel *et al.* "Roughness Assessment of Polysilicon Using Power Spectral Density," Jpn. J. <u>Appl. Phys.</u> vol. 32, 5671–5674, 1993.

[8] J. M. Elson, J. Bennett. "Calculation of the Power Spectral Density from Surface Profile Data," <u>Appl. Optics</u>. vol. 34, no. 1, 201–208, 1995.

[9] F. Biscarini *et al.* "Scaling Behavior of Anisotropic Organic Thin Films Grown in High Vacuum," <u>Phys. Rev. Lett.</u> vol. 78, no. 12, 2389–2392, 1997.

[10] K. Westra, D. Thomson. "Effect of tip shape on surface roughness measurements from atomic force microscopy images of thin films," <u>J. Vac. Sci. Technol. B</u>. vol. 13, no. 2, 344–349, 1995.

[11] F. Eozénou, A. Aspart, C. Antoine, B. Maliki. CARE Report 06-10-SRF. EU contract number RII3-CT-2003-506395. (2006)

[12] Macdonald, J. Ross., ed. <u>Impedance Spectroscopy: theory, experiment and applications</u>. New York: John Wiley & Sons, 1987.

[13] M. Matlosz, *et al.* "Impedance Analysis of a Model Mechanism for Acceptor-Limited Electropolishing," <u>J. Electrochem. Soc.</u> vol. 141, no. 2, 410–418, 1994.

Idaykis Rodriguez was born in Habana, Cuba in the little harbor town of Mariel. She came to the United States when she was seven years old with her mother from Cuba. She grew up in Miami, Florida and attends Florida International University majoring in physics and a minor in math. During her undergraduate career, she held a summer SULI internship at Jefferson National Laboratory in the summer of 2007. She has been accepted into the PhD program in physics at Florida International University and she hopes to specialize in Physics Education Research and become a professor. Her interests include reading, hiking and teaching.

Douglas W. Higinbotham is an experimental nuclear physicist at the Thomas Jefferson National Accelerator Facility in Newport News, Virginia. He received his Ph.D. from the University of Virginia in 1999 for his work on internal target physics at NIKHEF in Amsterdam, the Netherlands and did his postdoctoral work for the Massachusetts Institute of Technology. Higinbotham's research is currently focused on studying short-range correlations to understand how protons and neutrons behave in nuclear matter. He has twice been awarded the SULI outstanding mentor award for his work with summer students.

REVIVING AND UPGRADING OF THE eP DEVICE

IDAYKIS RODRIGUEZ AND DOUGLAS W. HIGINBOTHAM

ABSTRACT

At Thomas Jefferson National Accelerator Facility, an electron beam is used to probe the fundamental properties of the nucleus. In these experiments, it is essential to know the precise energy of the beam. An important instrument along the beamline to measure the beam energy is the eP device. The device measures the scattered electron angle and the recoil proton angle of an elastic collision. From these angle measurements, the beam energy can be calculated. Many eP device components such as computer software, controls, and mechanical parts needed to be upgraded and/or replaced in order for the eP device to be operational again. A research study was conducted of the current hydrogen target and its properties as well as alternate targets for better performance. As the maximum electron beam energy incident on the eP device will soon be upgraded from 6 GeV to 12 GeV, an analysis was also done on potential changes to the position of the electron and proton detectors in order to accommodate this change. Calculations show that for the new energy upgrade, electron detectors need to be positioned at 5° above and below the beamline to measure the energy of 12 GeV. New proton detectors need to be placed at an angle of 49.2° above and below the beamline to measure energies of 6.6 GeV and 8.8 GeV. With these changes the eP device will measure the range of new energies from 2.2 GeV to 12 GeV. From the target research studies it was found that a carbon nanotube mixture with polypropylene could be the ideal target for the eP device because of its high thermal conductivity and its high hydrogen content. The changes made to the eP device demonstrate the importance of continued research and new technologies.

INTRODUCTION

Thomas Jefferson National Accelerator Facility, also known as Jefferson Lab, hosts some of the most innovative experiments in nuclear physics. Jefferson Lab is a United States Department of Energy National Laboratory dedicated to basic research into the fundamental properties of the atomic nucleus. Experiments conducted within the experimental halls use a high-energy electron beam to probe the nucleus. Jefferson Lab's electron beam currently can reach a maximum energy of about 6 billion electron volts (6 GeV) and a proposed upgrade will increase the maximum energy to 12 GeV. For many experiments, accurate and precise measurements of the beam's energy need to be made.

The energy of the electron beam can be measured by several different methods. A simple method of measurement is through elastic scattering. Elastic scattering occurs when one particle collides with another and then both scatter with the energy and momentum of the system conserved. The simplest elastic reaction is between an electron and a proton, denoted as *H(e,e´p)*. In this reaction, an incoming electron collides with a hydrogen nucleus and they scatter in different directions, as shown in Figure 1. The beam energy E is determined by measuring the scattered electron angle θ_e and the recoil proton angle θ_p in the elastic collision using the following formula:

$$E = M_p \frac{\cos(\theta_e) + \sin(\theta_p)/\tan(\theta_p) - 1}{1 - \cos(\theta_e)} + \Theta \frac{m_e^2}{E^2}$$

where M_p is the mass of the proton and m_e is the mass of the electron [1]. In practice, this is done with the Jefferson Lab eP device which makes use of this formula by precisely measuring the scattered electron angle and the recoil proton angle from a thin hydrogen rich target.

Figure 1. Shown is a schematic of the electron and proton elastic collision where the vertex indicates the location of the target.

Figure 2. Schematic layout of the eP device showing example scattered electron and proton tracks. Electrons are detected in silicon-strip detectors (SSD), scintillator (S3), and a Cherenkov for particle identification. Proton are detected in silicon-strip detectors (SSD) and a pair or scintillators (S1 & S2) which can identify protons by time-of-flight.

Figure 3. Shown is a schematic of the polypropylene rotary target system along with the location of the ceramic bearings.

MATERIALS AND METHODS

The eP device is composed of three types of particle detectors to identify the electron-proton elastic collision: scintillators, silicon strip detectors, and Cherenkov detectors. Scintillators, which produce light when a particle passes through them, are attached to photomultiplier tubes (PMT) that transform the light into amplified electrical signals that can then be analyzed. Silicon micro-strip detectors are high-resolution spatial detectors ideal for identifying the position of the particles. The third kind of particle detector used in eP is Cherenkov detectors, which are chambers filled with gas. Cherenkov light is emitted and detected by PMTs when a charged particle moves faster than the speed of light in the gaseous medium [2] and is used to identify the relativistic electrons.

All detectors in the eP device are strategically placed at specific angles to detect elastically scattered particles. The scintillator's position coincides with the solid angle of the silicon strip detectors (SSD) within the eP device as shown in Figure 2. Scintillators S1 and S2 detect charged particles at a fixed angle of 60° detect charged particles and, by measuring the time between S1 and S2, can determine by time-of-flight if the particle is a proton. A coincidence between the S1 and S2 scintillators, a corresponding electron S3 scintillator, and the Cherenkov detector must happen simultaneously for an event to be counted. The eP device is thus designed to detect the electron-proton elastic collisions and any additional reactions which trigger the device will fall within the background noise and will be statistically deleted.

In order to have elastic collisions, the electron beam needs to hit a target. The target for the eP device is a thin film of polypropylene (C_3H_6). The device is designed for the electrons to elastically collide with a proton in a hydrogen nucleus. Certain polymers, like polypropylene, have the high hydrogen ratio that is needed in a target but are unstable in vacuum and melt if the electron beam passes continuously through one spot. The target control was designed to keep the polymer film constantly moving to keep it from melting. The melting is caused by heating due to energy loss as particles travel through matter. The energy that the electrons lose as they pass through the hydrogen target transforms into heat at a rate defined by the Bethe-Bloch equation [3]. To keep the heat generated by an electron beam passing through from melting the target, material must be thermally conductive or have a high melting point. Polypropylene, which has been used as the eP target, has neither of these properties and can melt in the electron beam extremely easily. Thus, finding a better thin target material became the second part of upgrading the eP device.
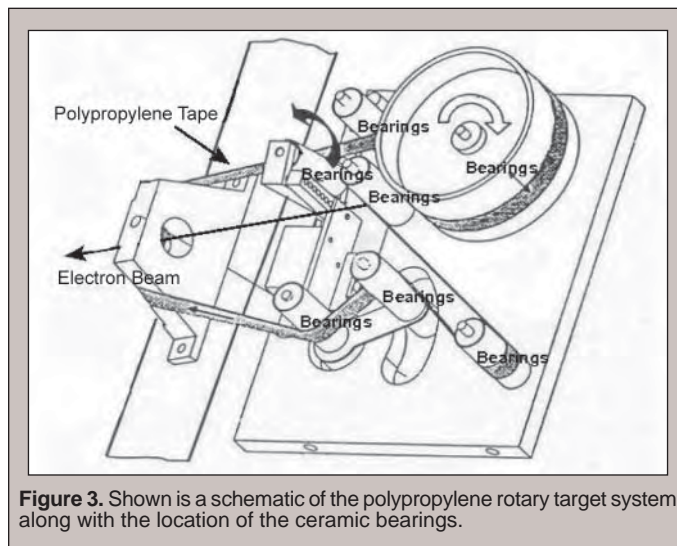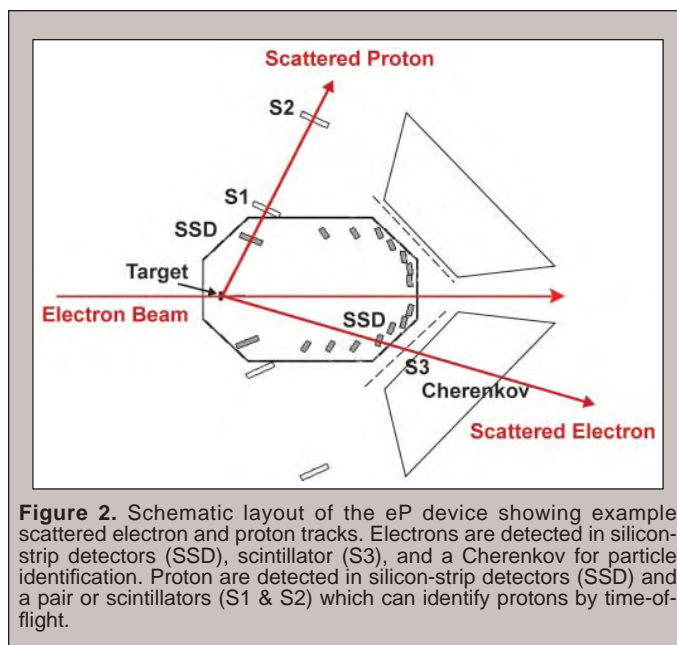
RESULTS

Reviving the eP Device

The eP device was built over ten years ago [1] and had not been operated successfully for several years. To revive the eP device, extensive upgrades and repairs were done to the machine and to its computer. The computer controls all of the mechanical functions of the eP device and also records the data. The original computer was obsolete and needed to be replaced. The programs and software were transferred from the old computer to the new computer, though there were some difficulties in running the data acquisition

program. This program, CODA, was reviewed and debugged to run on the new computer.

Mechanical parts of the eP device, such as bearings, were checked and replaced. The bearings are part of the target rotary system as seen in Figure 3. The target film rolls on the bearings, which are powered by a small motor on the largest of the cylinders. The bearings used were ceramic ball bearings with steel races. In general, steel is a material that at a microscopic level still has edges and ridges. When rough surfaces rub together, friction will deaden the motion quickly. Any part of the bearing that is made with steel will require some type of lubricant for smooth rolling and to give the bearings a longer lifespan. But for polypropylene, the target rotary system is inside a very high vacuum system and any type of grease or lubricant can disintegrate at low pressures, leaving the steel bearings without lubrication. The old steel bearings were discarded and more robust bearings were used. The replacement bearings were made with ceramic balls on ceramic races since this type of bearing does not require a lubricant and thus works well in vacuum [4]. This new, more efficient and tolerant ceramic bearing should keep the rotary system operational for much longer periods of time before needing maintenance.

Studies of Targets

The current eP device target is polypropylene (C_3H_6) due its high ratio of hydrogen to carbon. This is important since the ratio of hydrogen to other materials in the eP target directly affects the signal to noise ratio of eP device measurements. Previous use of this thin polymer as a target has shown it can work for proton-electron scattering; but the films often break, usually during a measurement, and need to be replaced. This led to a research study on alternate targets for the eP device. The ideal target for this elastic scattering experiment would be a thin, solid piece of pure hydrogen that can conduct heat to its edges for cooling and can move in and out of the beam. Since the ideal target is non-physical, compromises must be made.

Organic polymers, such as polypropylene have been widely used as targets for elastic scattering because they have a high hydrogen-material ratio. Naturally, to keep the 2:1 hydrogen ratio, a good alternate could be water. Liquid water has a higher thermal conductivity than polypropylene. The water could be made to flow through a small container so it does not overheat. A similar target has been used in other experiments at Jefferson Lab as seen in Figure 4. The problem with a target like this is the required thickness of the containment material. The thickness of water along with the thickness of the cell walls creates a significant electron beam energy loss and would compromise the precision of the energy measurements.

The organic compound, Kapton® polyimide, was considered for its high melting point [5]. However, Kapton's chemical formula ($C_{22}H_{10}N_2O_5$) [6] shows that hydrogen is lost amongst the other elements. The approximate

1:4 hydrogen ratio for Kapton® polyimide film disqualifies it as an ideal alternative.

A commonly used target material is carbon. It has high thermal conductivity and can resist the electron beam without moving constantly like the polypropylene film. More recently, the popular carbon material has been chemical vapor deposition (CVD) diamonds. In this research study it was found that the properties of CVD diamonds as a backing material for the original polypropylene are exceptional [7]. The only concern for CVD diamond backing is its thickness and the high carbon content decreases the total hydrogen ratio of the target. Carbon still remains the best known material for use in an electron beam; the difference is the form of carbon. As seen in Table 1, the thermal conductivity of carbon nanotubes is twice that of CVD diamonds [8]. Carbon nanotube technology is proving to be a promising field.

A study was done on polymer carbon nanotube composite that shows the ability to blend the two materials and change their physical properties significantly [9]. The experiment only included 10% by weight of carbon nanotubes while 90% of the original organic polymer remained. This means the density of this new material, as well as the hydrogen ratio, are still approximately the same as the

Figure 4. Photograph of flowing water target used in Jefferson Lab experiments.

Target Material	Density (g/cm³)	Thickness (cm)	Ratio of H nucleons	Thermal Conductivity (Wm⁻¹K⁻¹) @300K	Energy loss dE (MeV)
Polypropylene (C_3H_6)	0.95	0.003	2:1	0.20	8.8x10⁻³
Water (H_2O)	1.00	0.5	2:1	0.60	1.49
Kapton® Polyimide ($C_{22}H_{10}N_2O_5$)	1.42	0.0025	~1:4	0.12	9.6x10⁻³
CVD Diamond foil	3.52	0.015	0	3320	1.41
C_3H_6 and Carbon Nanotube Mixture	~1.00	~0.005	~2:1	6600	9.3x10⁻³

Table 1. Shown are the physical properties of the possible target materials. The ideal material is thin to minimize energy loss, has high ratio of hydrogen to minimize background events, and has a high thermal conductivity to prevent melting or boiling of the target. The composite mixture with 90% C_3H_6 and 10% carbon nanotubes clearly best satisfies these requires.

original polymer. If such a composite blend can be manufactured with polypropylene film, then this polymer carbon nanotube composite would be the ideal target, not only for the eP device, but also for many elastic scattering experiments. A summary of the physical properties of all these targets is given in Table 1.

Upgrade Proposal

Scientists are trying to discover new physics as they go deeper into the proton to learn more about quarks. Quarks manifest themselves at very small scale, less than a femtometer. In order to study physics phenomena at such a small scale, large beam energies are needed since the de Broglie wavelength is inversely proportional to the momentum of the particle. Therefore, Jefferson Lab has proposed to upgrade the accelerator facility from a 6 GeV to a 12 GeV. Along with the changes of the beam energy, changes in the eP energy calibration device also need to be done.

The eP device has electron detectors at angles of 9.5°, 12.25°, 15.5°, 24.0°, 35.5° and 38.5° symmetric about the beamline. The position of the electron detectors is determined by the elastic scattering equation for a fixed proton angle of 60°. The positions of the electron detectors are currently designed to measure a range of energy from 0.5 GeV to 5.5 GeV. By manipulating the equation to have the proton angle fixed, it becomes evident that as the energy increases, the scattered electron angle decreases.

The desired energies for the 12 GeV upgrade are 2.2, 4.4, 6.6, 8.8, and 12 GeV. The current geometry of the eP device only allows energies of 2.2 and 4.4 GeV to be detected with a fixed proton angle of 60°. It is proposed to make two major changes to the position of four electron detectors in order to detect the whole range of desired energies. In order to reuse as much equipment as possible, it is proposed to move the two electron detectors from the 30.5° positions symmetric about the beamline to a 5.0° position

symmetric about the beamline. They would detect the 11 GeV electrons. It was calculated that given the electron angle, both 6.6 GeV and 8.8 GeV could be detected at the single proton angle of 49.2°. It is also proposed to move the remaining electron detectors from the 38.5° to the 49.2° positions symmetric about the beamline. Given this new proton angle of 49.2°, the electrons scattered from beam energies of 6.6 GeV and 8.8 GeV will be detected at 12.25° and 9.5° respectively as seen in Figure 5. The newly upgraded eP device will have an energy detecting range from 1.3 GeV through 6 GeV, and 6.6 and 8.8 GeV exactly, and 10.1 GeV through 13 GeV. These relatively minor changes to the eP device transform it to a useful device for current experiments and future experiments at higher energies.

CONCLUSION

The results show that the eP device can be a proficient energy calibration device. The new upgrades and changes in the computer control system, as well as the mechanical parts, will make the eP device more efficient. The substitution of full ceramic bearings for steel-ceramic ball bearings will reduce maintenance on the target rotary system because ceramic bearings are more effective in a vacuum environment. From the research done on targets, it is evident that the new polymer carbon nanotube composite may be the best thin hydrogen target for elastic scattering experiments. Further research of carbon nanotubes as electron beam targets is needed, but the properties of the polymer carbon nanotube composite show that it may be an ideal target. Testing of the eP device with its new detector upgrade is to be pursued, to determine how accurately and precisely the new electron detectors at 5.0° and the new proton detectors at 49.2° will measure the incoming beam energy. Reviving the eP device demonstrated the importance of continued research and new technologies.

Figure 5. The points indicate the eP energy acceptance at a proton angle of 60° and for the proposed 49.2°. The electron angle of 5° will require installing a new detector. The vertical lines indicate the available energies after the accelerator upgrade (2.2, 4.4, 6.6, 8.8, and 11 GeV) and show that the proposed changes will cover all future energies.

REFERENCES

[1] O. Ravel. "Mesure Absolue de L'Energy du Faisceau d'Electrons de TJNAF (hall A) par Diffusion Elastique *p(e.e'p)*." Thesis from Universite Blaise Pascal. 1997.

[2] W.R. Leo. Techniques for Nuclear and Particle Physics Experiments. Second Revised Edition. Berlin Heidelberg: Springer-Verlag. 1994.

[3] S. Eidelman *et al.* Physics Letters. B592, 1, 2004. http://pdg.lbl.gov

[4] Champion Bearings technician (private communication), 2007.

[5] Dupont. Summary of Properties Kapton® Polyimide Film. http://www2.dupont.com/Kapton/en_US/index.html

[6] Y.Q. Wang. "Hydrogen Standards in Elastic Recoil Detection Analysis." Nuclear Instruments and Methods in Physics Research Section B: Beam Interactions with Materials and Atoms, vol. 219–220. 2004. pp. 115–124.

[7] A.V. Sukhadolau *et al.* "Thermal Conductivity of CVD Diamond at Elevated Temperatures." Diamond & Related Materials, vol. 14. 2005. pp. 589–593.

[8] S. Berber, Y.K. Kwon, and D. Tomanek. "Unusually High Thermal Conductivity of Carbon Nanotubes." Physical Review Letters, vol. 84, number 20. 2000.

[9] T. McNally *et al.* "Polyethylene Multiwalled Carbon Nanotube Composites." Polymer, vol. 46. 2005. pp. 8222–8232.

Matthew Seidman participated in the Science Undergraduate Laboratory Internship (SULI) program during the summer of 2007, completing the internship with the Center for Transportation Technologies and Systems at the National Renewable Energy Laboratory in Golden, Colorado. He recently graduated from California State Polytechnic University, Pomona with a Bachelor of Science degree in mechanical engineering. He currently works for Alternative Energy Systems Consulting in Pasadena, California.

Tony Markel joined NREL in 1996. He received his M.S. degree in mechanical engineering from University of Colorado in 2005 and a B.S.E degree in mechanical engineering from Oakland University in 1995. He was instrumental in the development of the ADVISOR software tool for vehicle systems simulation and is skilled at using analysis and optimization tools to address real-world problems. He has supported simulations for setting requirements of batteries for advanced vehicles for the USABC. Mr. Markel's research is focus on plug-in vehicle technology in support of the DOE Vehicle Technologies Program.

Plug-in Hybrid Electric Vehicle and Hybrid Electric Vehicle Emissions under FTP and US06 Cycles at High, Ambient, and Low Temperatures

Matthew R. Seidman and Tony Markel

ABSTRACT

The concept of a Plug-in Hybrid Electric Vehicle (PHEV) is to displace consumption of gasoline by using electricity from the vehicle's large battery pack to power the vehicle as much as possible with minimal engine operation. This paper assesses the PHEV emissions and operation. Currently, testing of vehicle emissions is done using the federal standard FTP4 cycle on a dynamometer at ambient (75°F) temperatures. Research was also completed using the US06 cycle. Furthermore, research was completed at high (95°F) and low (20°F) temperatures. Initial dynamometer testing was performed on a stock Toyota Prius under the standard FTP4 cycle, and the more demanding US06 cycle. Each cycle was run at 95°F, 75°F, and 20°F. The testing was repeated with the same Prius retrofitted with an EnergyCS Plug-in Hybrid Electric system. The results of the testing confirm that the stock Prius meets Super-Ultra Low Emission Vehicle requirements under current testing procedures, while the PHEV Prius under current testing procedures were greater than Super-Ultra Low Emission Vehicle requirements, but still met Ultra Low Emission Vehicle requirements. Research points to the catalyst temperature being a critical factor in meeting emission requirements. Initial engine emissions pass through with minimal conversion until the catalyst is heated to typical operating temperatures of 300–400°C. PHEVs also have trouble maintaining the minimum catalyst temperature throughout the entire test because the engine is turned off when the battery can support the load. It has been observed in both HEVs and PHEVs that the catalyst is intermittently unable to reduce nitrogen oxide emissions, which causes further emission releases. Research needs to be done to combat the initial emission spikes caused by a cold catalyst. Research also needs to be done to improve the reduction of nitrogen oxides by the catalyst system.

Introduction

The development of hybrid electric vehicles (HEV) reduces the use of gasoline and its associated side-effects. While still completely powered by gasoline, the HEV uses an optimized power train system of an IC engine, a battery pack, and an electric motor. A HEV is able to reduce fuel consumption by using regenerative braking to recover energy from braking and running the engine at its highest level of performance, to charge the vehicle's battery or directly power the wheels.

A plug-in hybrid electric vehicle (PHEV) goes one step further in conserving gasoline. The vehicle stores electricity from the grid in its battery pack. A PHEV still has an IC engine and is capable of operating like an HEV when necessary, but is programmed to use as much of the stored electric energy as possible. Using more battery and less fuel further reduces gasoline consumption and

green house gas emissions, assuming the electricity from the grid comes from a renewable source. HEVs and PHEVs are bridging the gap between internal combustion engine vehicles and alternative energy vehicles.

Currently there are no PHEVs in production by any of the major automotive companies. As a result, not much is known about the emission characteristics of PHEVs. Initial studies have been done by Argonne National Laboratory using a dynamometer running Federal Test Procedure (FTP) cycles at ambient (75°F) temperatures [2]. The purpose of this research is to expand on Argonne National Laboratory's research by 1) presenting emission data on PHEVs under the FTP cycle and the more demanding US06 cycles, 2) presenting emissions data on PHEVs at high (95°F), ambient (75°F), and low (20°F) temperatures of operation for both cycles, 3) finding out if the Toyota Prius HEV and PHEV meet the Super-Ultra Low Emission Vehicle standards at all three temperatures mentioned

above during a FTP cycle, and 4) looking at the emission trends for both systems under these real world operating conditions.

The Toyota Prius hybrid electric vehicle utilizes a hybrid transmission with a power-splitting device using a planetary gear system [3]. The engine drive shaft is connected to the planetary gear carrier, which allows power to be simultaneously supplied through the outer ring gear to the wheels and through the sun gear to the generator [3]. The electricity produced by the generator can then be directed to the electric motor to increase the power available to drive the car or through the inverter to be converted into direct current to charge the battery [3]. The standard Prius has a 6-Ah 1.3-kWh battery pack. The EnergyCS PHEV modification replaces the smaller battery pack with a 9-kWh battery pack and performance software. The larger battery pack allows the Prius to travel close to 50 miles on one charge in charge depletion mode.

The stock Prius operates in a charge-sustaining (CS) mode that constantly maintains the battery state of charge (SOC) by running the engine intermittently. The EnergyCS modified Prius, at full charge, will run in charge-depletion (CD) mode using as much battery as possible and will not enter CS mode until a low SOC is reached. In both modes the engine will turn on only when needed for speeds above 34 mph or on steep sections of road, when more power is needed. If the battery is able to supply all the power to drive the vehicle, the possibility for large gaps between engine uses may cause the catalytic converter to cool, resulting in higher levels of emissions during operation.

The environmental protection agency (EPA), up to the year 2003, used an emissions standard for all new vehicles called Tier I. The EPA is currently phasing in their new emission standard called Tier II. The California Air Resource Board (CARB) is also phasing in their new, more stringent emission standards as well. The three CARB emission standards applied to the Toyota Prius HEV and PHEV are the minimum low emission vehicle (LEV), the 50 percent cleaner than LEV ultra low emission vehicle (ULEV), and the 90 percent cleaner than LEV super low emission vehicle (SULEV). The emission values for all three CARB standards are displayed in Table 1. All emission testing is performed using the FTP cycle at ambient temperatures.

	LEV (grams/mile)	ULEV (grams/mile)	SULEV (grams/mile)
HC	0.09	0.055	0.01
CO	4.2	2.1	1.0
NO$_x$	0.07	0.07	0.02

Table 1. CARB emission standards.

The current Toyota Prius HEV has been certified to meet the new Super Ultra-Low Emission Vehicle (SULEV) standard set by CARB. This standard reduces most emissions by 70 to 97 percent from the current federal Tier 1 standards [1]. Under SULEV standards, vehicles must emit less than 0.01 grams/mile of hydrocarbons (HC), 0.02 grams/mile of nitrous oxides (NO$_x$), and 1.0 grams/mile of carbon monoxide (CO) [1]. Hydrocarbons

are volatile organic compounds that cause smog and are toxic and carcinogenic [1]. Carbon monoxide is a poisonous gas that impairs the flow of oxygen to the brain and other parts of the body [1]. Nitrogen oxides aggravate respiratory problems, both directly and indirectly, by forming PM and smog; NO$_x$ also causes acid rain and damages aquatic environments [1].

In standard vehicles, emissions are controlled by a catalytic converter that uses the heat from the engine's exhaust to activate the catalyst. The minimum catalyst operating temperature is 300°C and maximum operating efficiency is achieved at 400°C. The exhaust gases must alternate rapidly between high CO content, to reduce NO$_x$ emissions, and high oxygen content, to oxidize the HC and CO emissions [5]. A rich air-to-fuel ratio (A/F ratio) will produce more CO while a lean A/F ratio will produce more oxygen.

Materials and Methods

The emission testing was performed using a dynamometer and emission testing systems at Environmental Testing Corporation in Aurora, Colorado. The vehicle was fitted with emissions sensors at the engine, the catalyst outlet, and the tailpipe. All the exhaust is collected in emission bags that can be analyzed for specific emissions and fuel economy. The facility was also capable of producing high, low, and ambient temperatures around the vehicle during testing.

An initial analysis called a coast down was performed to determine the rolling resistance of the vehicle. The dynamometer is capable of reproducing specific drive cycles using the vehicle's rolling resistance, the road's percent grade, and the vehicles aerodynamic drag at any speed. The operator must then reproduce the specific cycle by accelerating or braking the vehicle.

The (FTP) cycle is used for emission certification of passenger vehicles. This cycle has three separate phases: a cold-start (505-second) phase known as bag 1, a hot-transient (870-second) phase known as bag 2, and a hot-start (505-second) phase known as bag 3 [4]. These three test phases are referred to as bag 1, bag 2, and bag 3 because exhaust samples are collected in separate bags during each phase [4]. During a 10-minute cool-down between the second and third phase, the engine is turned off [4]. The 505-second driving trace for the first and third phases is identical. The 870-second driving trace for the second and fourth phases is identical. The fourth phase is not performed during the test because it is assumed that phase two and four begin at the same operating conditions where phase one and phase three do not because of cold and hot start conditions. The top speed for the cycle is 56.7 mph and the average speed is 21.4 mph. The distance traveled is approximately 15 miles [4].

When FTP testing HEVs and PHEVs, it is necessary to perform and record phase four during testing. The reason for the fourth phase is that the engine in HEVs and PHEVs does not operate the entire time like a standard vehicle. Based on the hybrids SOC and mode of operation, CD or CS, the emissions will vary between phase two and phase four negating the previous assumption that phase two and four are identical.

The US06 cycle is more representative of aggressive, rapid speed fluctuation, high speed, and high acceleration driving. The cycle is an eight mile drive with an average speed of 48.4 miles per hour

and a maximum speed of 80.3 miles per hour over 596 seconds using one bag.

After collecting all the data, Microsoft Excel was used to graph the total emissions of hydrocarbon and nitrogen oxide for the HEV and PHEV under the FTP and US06 cycles. The resulting graphs showed emissions greater then SULEV, ULEV and even LEV standards at times. To further explore where the emissions were occurring cumulative emissions graphs were generated over the distances traveled in each cycle. These graphs revealed the common theme of emission spikes within the first few minutes of operation. To better understand these emission spikes a final set of graphs were constructed. These graphs looked at the speed trace, fuel consumption, SOC, engine exhaust temperature (CAT IN), first catalyst exhaust temperature (CAT MID), tailpipe exhaust temperature (CAT OUT), first catalyst's operating temperature (CAT 1), cumulative hydrocarbon emissions and the cumulative nitrogen oxide emissions over the first 600 seconds of testing.

RESULTS

Bar graphs were generated based on the HEV and PHEV total bag calculated emissions in grams per mile for each cycle. The green line represents SULEV, the blue line represents ULEV, and the pink line represents LEV. Figures 1 and 2 show the hydrocarbon emissions for the HEV and PHEV respectively, under the FTP cycle. Figure 1 illustrates that the HEV meets the SULEV standard except during the cold run. Figure 2 shows that the PHEV fails the SULEV standard in CD mode and fails the ULEV standard in the cold run. The figure also shows that the PHEV meets the SULEV standard in CS mode but fails to meet SULEV during the cold run. Figures 3 and 4 present the nitrogen oxide emissions for the HEV and PHEV respectively, under the FTP cycle. Figure 3 illustrates that the HEV meets the SULEV standard during hot and ambient runs, but just misses the standard during the cold run. Figure 4 exhibits that the PHEV fails the SULEV standard, but meets the ULEV standard on all but one instance.

Figures 5 and 6 display the hydrocarbon emissions for the HEV and PHEV respectively, under the US06 cycle. Figure 5 demonstrates mild HC emissions for hot and ambient temperatures with large

emissions for the cold temperature. This correlates with Figure 1, where the cold emissions are higher than the others. Figure 6 shows that HC emissions are higher when the PHEV is in CD mode. This figure also reveals that as the temperature decreases the emissions increase. Figures 7 and 8 represent the nitrogen oxide emissions for
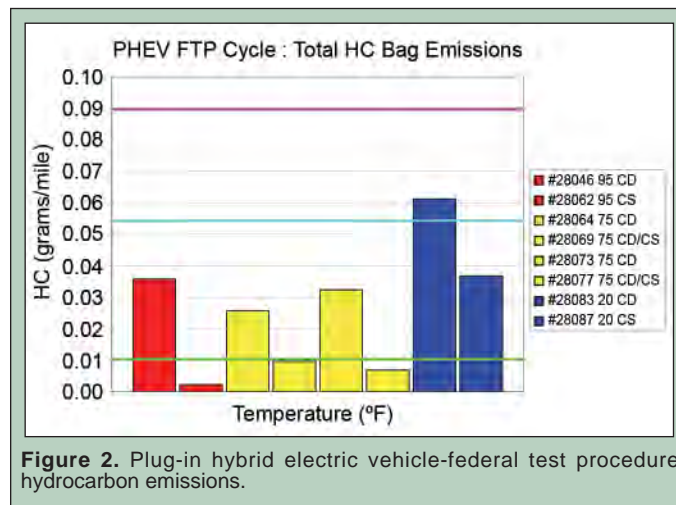
Figure 2. Plug-in hybrid electric vehicle-federal test procedure hydrocarbon emissions.
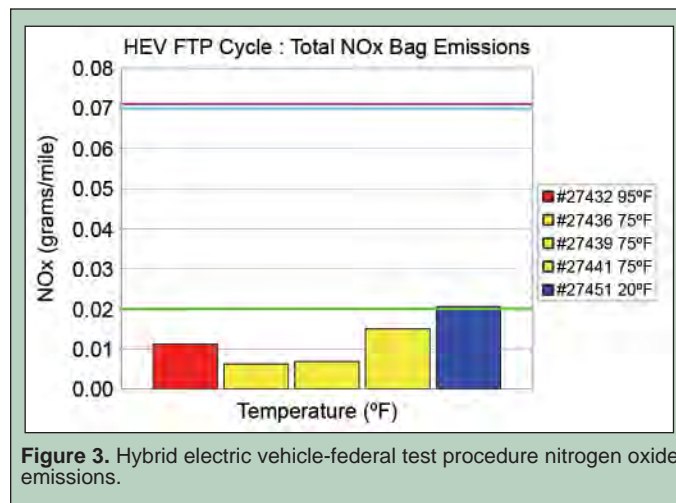
Figure 3. Hybrid electric vehicle-federal test procedure nitrogen oxide emissions.
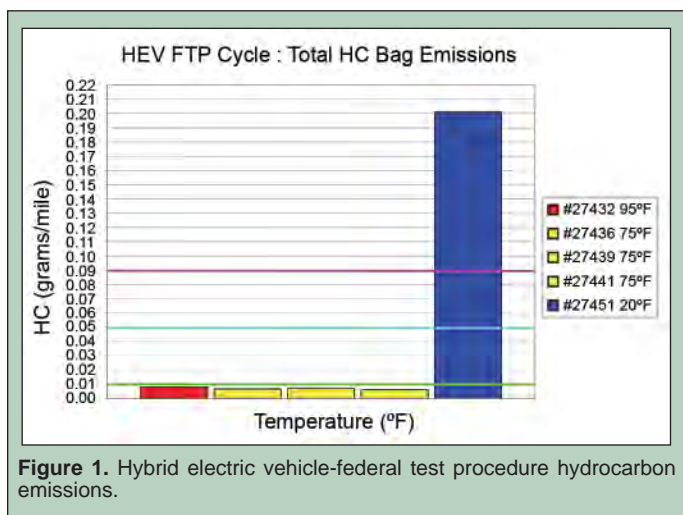
Figure 1. Hybrid electric vehicle-federal test procedure hydrocarbon emissions.
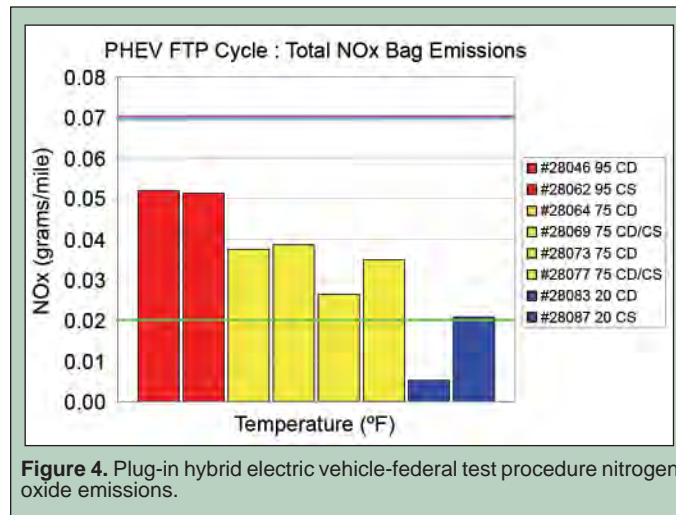
Figure 4. Plug-in hybrid electric vehicle-federal test procedure nitrogen oxide emissions.

U.S. Department of Energy Journal of Undergraduate Research

the HEV and PHEV respectively, under the US06 cycle. Figure 7 illustrates consistent NO_x emissions except at the lower temperature. Figure 8 depicts higher NO_x emissions at high and low temperatures with a decrease in emissions at ambient temperature.

Figures 9 and 10 represent the HEV and PHEV cumulative hydrocarbon emissions respectively, under the FTP cycle. Figure 9 shows a sharp spike in emissions, then a leveling out during the first mile. After the 10 minute cool-down at mile 7 another emissions spike occurs, then a leveling out during the first half-mile. Figure 10 reveals that the CD mode emissions have a sharp spike in the first mile, but never level off as much as the CS mode. After the 10-minute cool-down the emissions spike again, but never level off like in the CS mode. Figures 11 and 12 impart the HEV and PHEV cumulative nitrogen oxide emissions respectively, under the FTP cycle. Figure 11 illustrates a stair-step function with a small slope, while Figure 12 reveals a stair-step function with a larger slope. Figure 12 also shows a large spike, which flat-lines in the first mile for the two cold runs.

Figures 13 and 14 represent the HEV and PHEV cumulative hydrocarbon emissions respectively, under the US06 cycle. Figure 13 displays various sizes of emission spikes within the first mile with a leveling off for the rest of the cycle. Figure 14 also displays

various sizes of emissions spikes, but the slope after the emissions level off is greater than Figure 13. Figures 15 and 16 divulge the HEV and PHEV cumulative nitrogen oxide emissions respectively, under the US06 cycle. Figures 15 and 16 both exhibit stair-step function emissions curves.
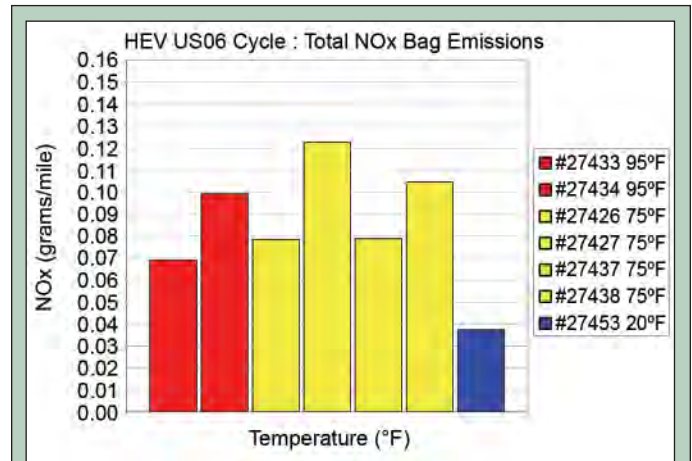
Figure 7. Hybrid electric vehicle-US06 nitrogen oxide emissions.

Figure 8. Plug-in hybrid electric vehicle-US06 nitrogen oxide emissions.
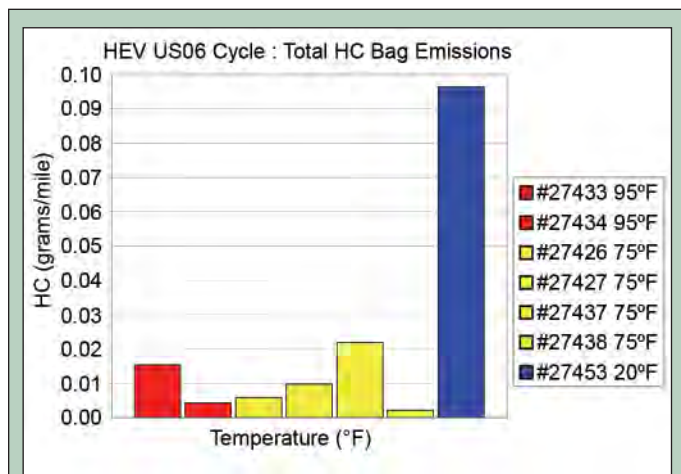
Figure 5. Hybrid electric vehicle-US06 hydrocarbon emissions.
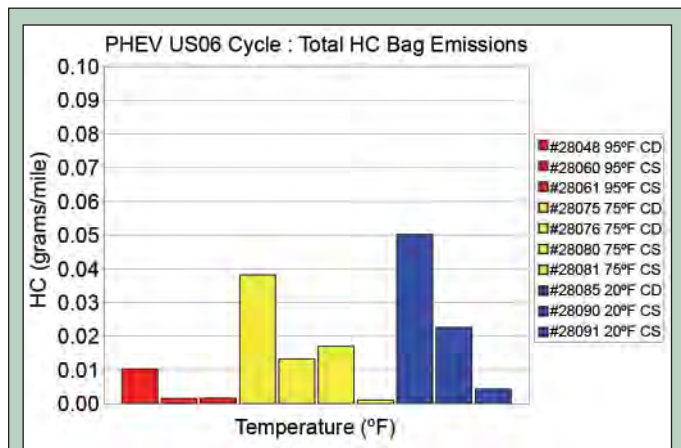
Figure 6. Plug-in hybrid electric vehicle-US06 hydrocarbon emissions.
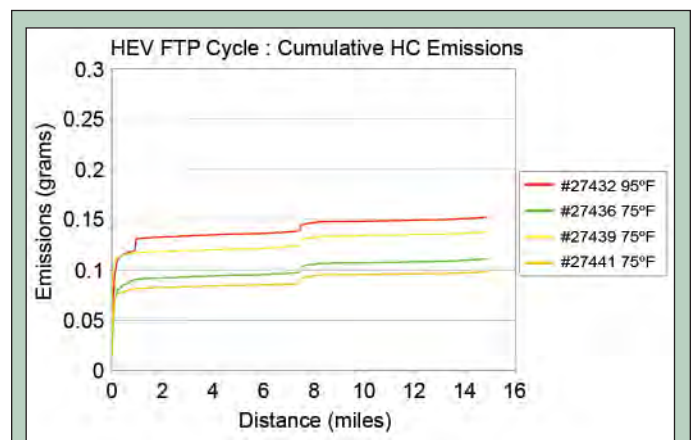
Figure 9. Hybrid electric vehicle-FTP cumulative hydrocarbon emissions.
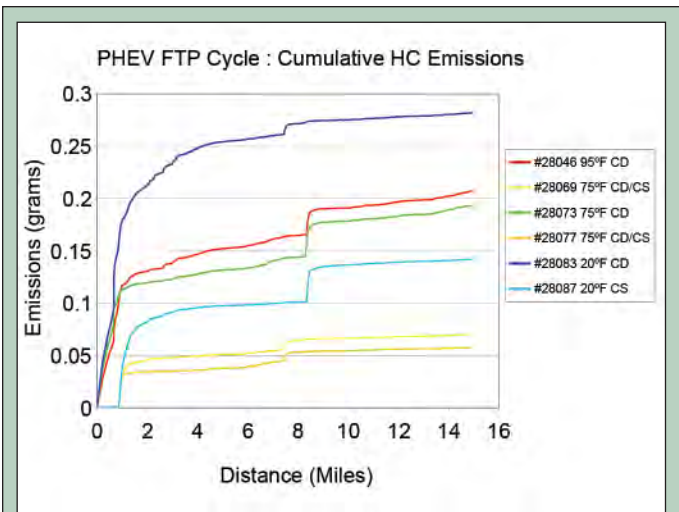
Figure 10. Plug-in hybrid electric vehicle-FTP cumulative hydrocarbon emissions.

Figure 11. Hybrid electric vehicle-FTP cumulative nitrogen oxide emissions.

Figure 12. Plug-in hybrid electric vehicle-FTP cumulative nitrogen oxide emissions.

Figure 13. Hybrid electric vehicle-US06 hydrocarbon emissions.

Figure 14. Plug-in hybrid electric vehicle-US06 hydrocarbon emissions.
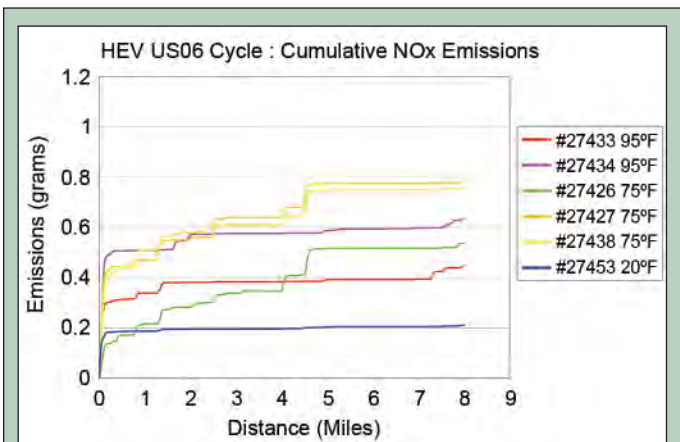
Figure 15. Hybrid electric vehicle-US06 nitrogen oxide emissions.

Figures 17 and 18 both depict the HEV operating under a FTP cycle at 75°F. The two graphs have a good correlation between exhaust and CAT 1 temperatures, fuel consumption, and HC emissions. The NO_x emissions vary in size and location of emission spike occurrences. Figures 19 and 20 illustrate the PHEV operating in transition from CD to CS mode under FTP cycles at 75°F. Because the PHEV is still in CD mode throughout the 600 seconds, the engine does not turn on until speeds reach 34 mph at about 200 seconds into the trace. In Figure 20 emissions and temperatures are close, considering the engine does not operate as much in the middle of the trace because no fuel is being consumed. Figure 21 is a PHEV at full charge in CD mode under a FTP cycle at 75°F. The engine turns on right away for this test instead of using only the battery. The fuel consumption is greater than the CD/CS mode tests and less than the HEV tests. The cumulative HC emissions are greater than all the similar tests. The cumulative NO_x emissions are the same as the HEV, much less than CD/CS mode.

Figures 22 and 23 show the HEV operating under US06 cycles at 75°F. The two graphs have a strong correlation between exhaust and CAT 1 temperatures, fuel consumption, and emissions. A sharp spike in NO_x emissions is produced because of the rapid acceleration of the engine with a cold catalyst. Figures 24 and 25 are both the PHEV in CD mode under US06 cycles at 75°F. The two graphs maintain a close correlation between the exhaust temperatures, CAT 1 temperatures, and fuel consumption. Even with the same fuel consumption, Figure 24 shows a larger spike in HC and NO_x emissions than Figure 25. The PHEV also consumes less gasoline and produces less NO_x emission for the US06 cycle.
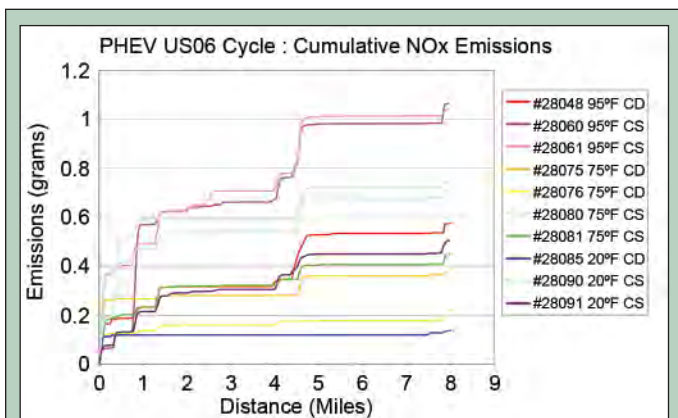
Figure 16. Plug-in hybrid electric vehicle-US06 nitrogen oxide emissions.
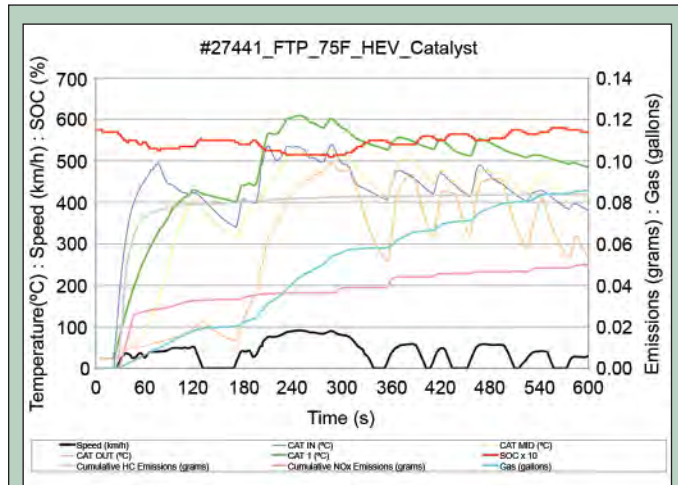
Figure 18. Hybrid electric vehicle-federal test procedure at ambient temperature.
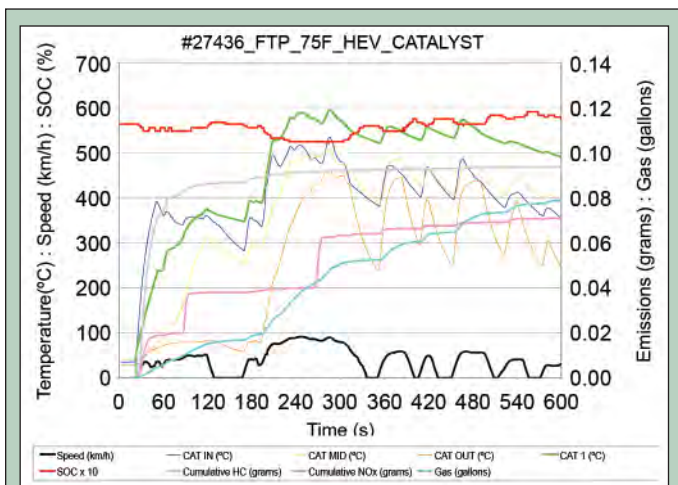
Figure 17. Hybrid electric vehicle-federal test procedure at ambient temperature.
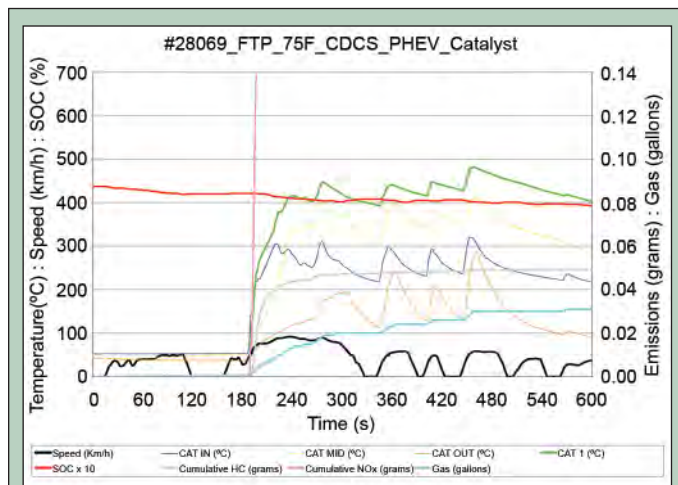
Figure 19. Plug-in hybrid electric vehicle-federal test procedure at ambient temperature.
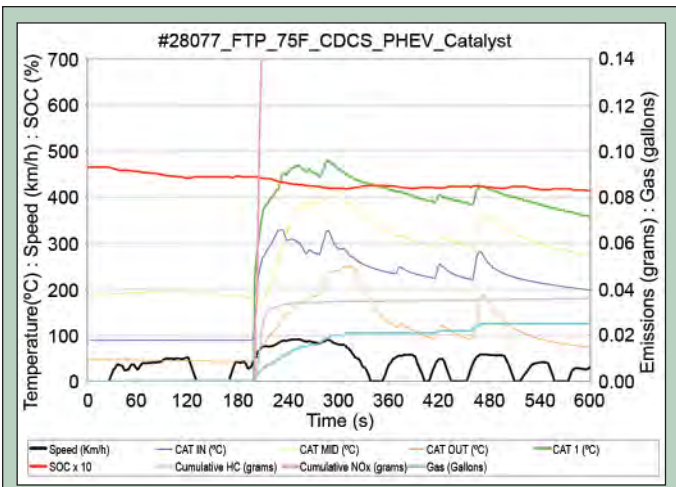
Figure 20. Plug-in hybrid electric vehicle-federal test procedure at ambient temperature.
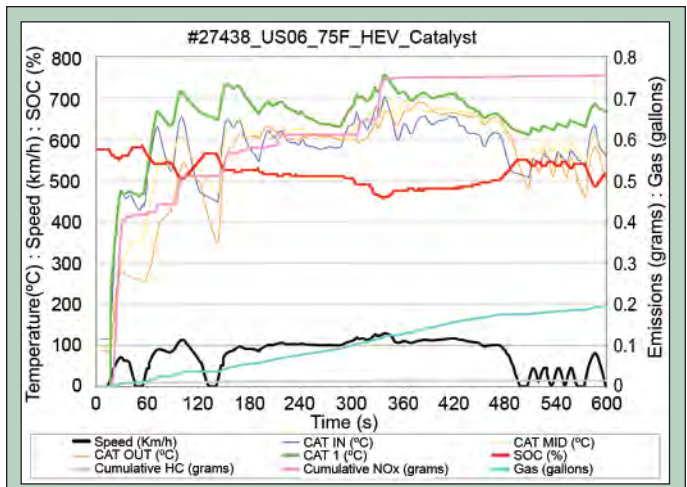
Figure 23. Hybrid electric vehicle-US06 cycle at ambient temperature.
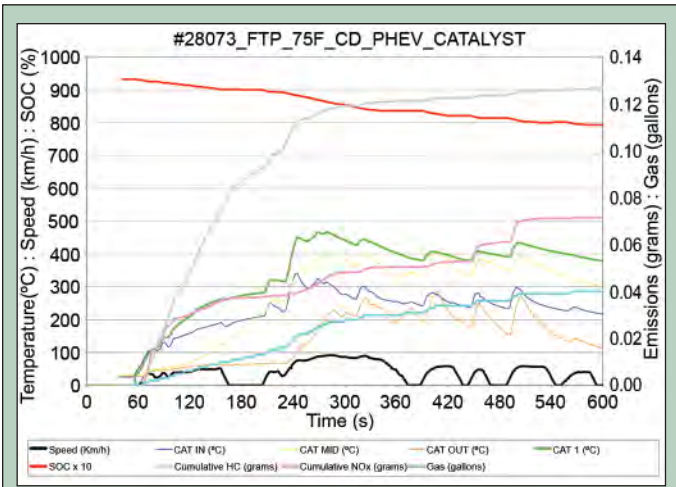
Figure 21. Plug-in hybrid electric vehicle-federal test procedure at ambient temperature.
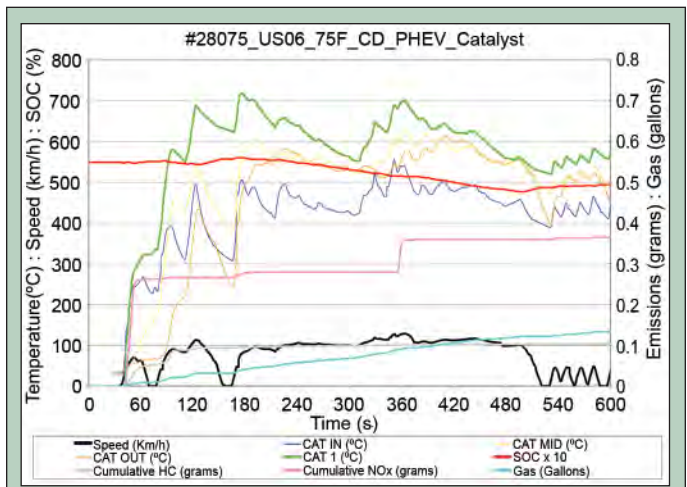
Figure 24. Plug-in hybrid electric vehicle-US06 cycle at ambient temperature.
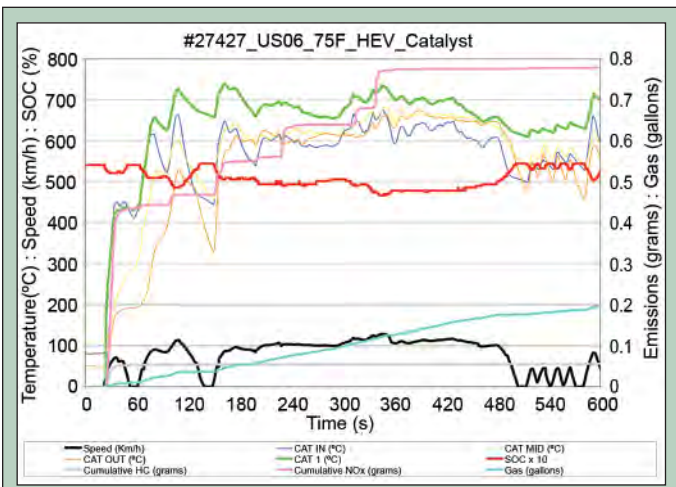
Figure 22. Hybrid electric vehicle-US06 cycle at ambient temperature.
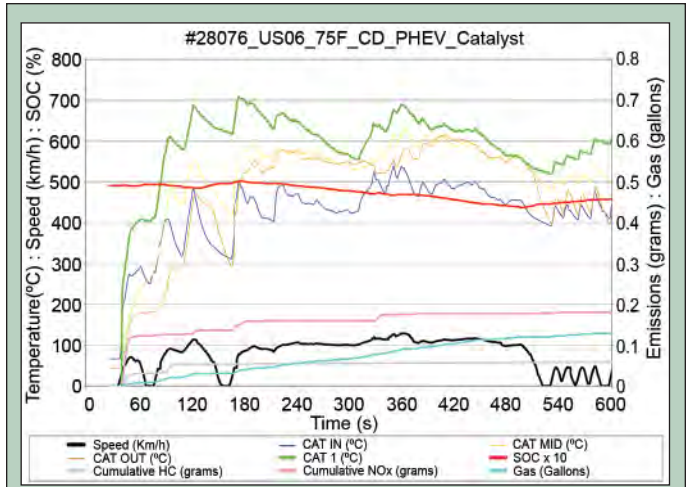
Figure 25. Plug-in hybrid electric vehicle-US06 cycle at ambient temperature.

U.S. Department of Energy Journal of Undergraduate Research

DISCUSSION

Testing confirmed that the Toyota Prius HEV met SULEV standards under the EPA's FTP cycle at ambient temperatures. Figure 2 illustrates that when the PHEV operates in CD mode, the HC emissions are higher than CS mode. It would be expected that the transition from CD to CS produces emissions between the CD and CS modes, and Figure 2 demonstrates this. When looking at the PHEV in Figure 2, it makes sense that the CS mode produces similar HC emissions as the HEV in Figure 1 because the software defaults back to normal HEV operation. The PHEV meets the ULEV standard under the FTP cycle at all temperatures except at 20°F. Figure 4 showed high NO_x emissions over the entire cycle. After looking at Figures 19 and 20, it was found that NO_x spikes when the PHEV's engine turns on at 50 km/h. Under the large initial load with a cold catalyst the resulting emissions can be expected. If the catalyst was at operating temperature like in Figures 17 and 18 the spike in emissions caused by the large engine load might have been eliminated by the catalyst. The stair-step emissions displayed in Figure 12 account for half the emissions produced during the cycle. For some reason the catalyst is not eliminating NO_x emissions at different times during the cycle. The PHEV also failed the SULEV HC standard under the FTP cycle in CD mode. Figure 21 represents a PHEV fully charged at home beginning its daily commute. From Figure 21, the cumulative HC emissions climbs steadily until the catalyst warms up to the maximum efficiency temperature of 400°C. While the figure shows fuel consumption, the engine is running at low loads and is unable to produce high temperature exhaust. The emissions fail to flat-line because the catalyst is unable to achieve the maximum efficiency temperature and drops below the minimum operating temperature further into the cycle. The initial engine usage in CD mode is part of a battery protection strategy employed by EnergyCS in this prototype conversion. Future PHEVs will likely incorporate alternatives to protect the battery at high SOC.

The cumulative HC emission decreases for the US06 cycle in Figures 13 and 14 compared to the FTP cycle, Figures 9 and 10. The aggressive initial acceleration in the US06 cycle quickly heats the catalyst up keeping the HC emissions low for the US06 cycle. Conversely, when looking at the cumulative NO_x emission graphs for the US06 cycle, Figures 15 and 16, the emissions increase compared to the FTP cycle, Figures 11 and 12. Within the US06 cycle, the HEV experiences a larger spike in NO_x emissions than the PHEV even though its engine exhaust and CAT1 temperatures are greater by about 100°C, Figures 22–25. The HEV's engine appears to be under more load because the SOC in Figures 22 and 23 show the engine is charging the battery. The PHEV's engine appears to be under less load because the SOC in Figures 24 and 25 do not change, which suggests that the PHEV's software is better utilizing the battery and engine. NO_x continues to stair-step throughout the cycle for the HEV, even after reaching maximum efficiency temperature.

The PHEV's emissions did increase. However, they are still 50 percent lower than the minimum LEV standards. The EnergyCS conversion and other aftermarket conversions are only prototypes. There are technology options available to address emissions issues in production vehicles. The PHEV also experienced reduced fuel consumption during testing. A vehicle designed as a stand alone PHEV, not a modified HEV, could further reduce fuel consumption. In conclusion, PHEVs hold promise in reducing gasoline consumption and meeting emission standards.

FUTURE WORK

The most important lesson from these emission tests is that a cold catalyst is unable to effectively control emissions. No matter the load size on the engine, a hot catalyst will eliminate emission spikes. Research needs to find cost-effective solutions to the initial cold catalyst problem. Research has been conducted by NREL on variable conductance catalyst technology in the past and may be of value in reducing HEV and PHEV emissions [6]. Once the cold catalyst problem is solved, focus should be placed on the NO_x stair-step problem. Even though the engine exhaust is monitored to regulate A/F ratios, the catalyst is failing to control NO_x emissions consistently. Research needs to explore richer A/F ratios to provide the catalyst with emissions to reduced NO_x. To counteract the richer A/F ratios, an extra air intake may need to be incorporated to oxidize HC emissions. Next generation HEVs and PHEVs will need to address these issues to meet real world driving conditions.

ACKNOWLEDGEMENTS

REFERENCES

[1] Clean Car Campaign, "Emissions," http://www.cleancarcampaign.org/emissions.shtml [Accessed: June 25, 2007].

[2] Richard W. Carlson, Michael J. Duoba, Theodore P. Bohn, Anantray D. Vyas "Testing and Analysis of Three Plug-in Hybrid Electric Vehicles," SAE Technical Papers., 2007-01-0283.

[3] M. H. Westbrook, The Electric and Hybrid Electric Car. London: The Institution of Electrical Engineers, Warrendale, PA: Society of Automotive Engineers, 2001.

[4] http://www.avt.nrel.gov/emis_tour/ftp-75.html [Accessed: July 18, 2007].

[5] Toyota Motor Sales, U.S.A., "Emission Sub Systems – Catalytic Converter," http://www.autoshop101.com/forms/h64.pdf [Accessed: July 26, 2007].

[6] Steven D. Burch, Matthew A Keyser, Chris P. Colucci, Thomas F. Poter, and David K Benson "Applications and Benefits of Catalytic Converter Thermal Management," SAE Technical Papers., 961134.

Jesse St. Charles was born in Chattanooga, TN and grew up on nearby Signal Mountain. He attended the University of Tennessee at Chattanooga, receiving a Bachelor of Science with dual concentrations in Computer Science: Scientific Applications and Software Systems and a minor in mathematics in December 2007. He is currently in his second SULI appointment with the ASER group at Oak Ridge National Laboratory. He hopes to begin a doctoral program in computer science in the fall of 2008. His research interests include emergent behavior, complex systems, self-organizing systems, and swarm intelligence.

Dr. Xiaohui Cui is an associate research scientist in the Computational Sciences & Engineering Division of Oak Ridge National Laboratory. He received his Ph.D. degree in Computer Science and Engineering from University of Louisville in 2004. His research interests include swarm intelligence, agent based modeling and simulation, emergent behavior in complex system, high performance computing, information retrieval and knowledge discovering. His current research focuses in developing new computational algorithms inspired from biological models. His research works include collective intelligence of multi-agent system, parallel and distributed knowledge discovering, swarm based social simulation, and adaptive agent cognitive modeling.

FLOCKING-BASED DOCUMENT CLUSTERING ON THE GRAPHICS PROCESSING UNIT

JESSE ST. CHARLES, ROBERT M. PATTON, THOMAS E. POTOK, AND XIAOHUI CUI

ABSTRACT

Analyzing and grouping documents by content is a complex problem. One explored method of solving this problem borrows from nature, imitating the flocking behavior of birds. Each bird represents a single document and flies toward other documents that are similar to it. One limitation of this method of document clustering is its complexity $O(n^2)$. As the number of documents grows, it becomes increasingly difficult to receive results in a reasonable amount of time. However, flocking behavior, along with most naturally inspired algorithms such as ant colony optimization and particle swarm optimization, are highly parallel and have experienced improved performance on expensive cluster computers. In the last few years, the graphics processing unit (GPU) has received attention for its ability to solve highly-parallel and semi-parallel problems much faster than the traditional sequential processor. Some applications see a huge increase in performance on this new platform. The cost of these high-performance devices is also marginal when compared with the price of cluster machines. In this paper, we have conducted research to exploit this architecture and apply its strengths to the document flocking problem. Our results highlight the potential benefit the GPU brings to all naturally inspired algorithms. Using the CUDA platform from NVIDIA®, we developed a document flocking implementation to be run on the NVIDIA® GEFORCE 8800. Additionally, we developed a similar but sequential implementation of the same algorithm to be run on a desktop CPU. We tested the performance of each on groups of news articles ranging in size from 200 to 3,000 documents. The results of these tests were very significant. Performance gains ranged from three to nearly five times improvement of the GPU over the CPU implementation. This dramatic improvement in runtime makes the GPU a potentially revolutionary platform for document clustering algorithms.

INTRODUCTION

Analysts are continually faced with the extremely difficult task of extracting relevant data from thousands to millions of documents at a time. This problem is exacerbated by the large quantities of data generated through the use of computing systems, information systems, and sensor systems. The need for fast, efficient document analysis has driven the research community to develop and improve document clustering methods. One method, document flocking [4], is a nature-inspired computational model for simulating the dynamics of a flock of entities. This method takes an agent-based approach and relies on emergent organization to effectively cluster documents. The effectiveness of this approach relies on the organization that arises through a group of agents interacting through simple rules. In the case of document clustering, similar documents flock together, loosely organizing themselves according to subject. This method

has met with success in clustering documents quickly, performing better than traditional methods such as K-means [4]. Unfortunately it needs to be implemented on expensive cluster computers when trying to analyze more than a few hundred documents at a time. Not only are these cluster-computers expensive, but they also lack portability and are impractical in certain environments. Our research investigates the possibility of implementing this algorithm on more portable machines, thereby bringing the clustering ability to the analyst. In our work, we compared the runtime performance of sequential and parallel versions of the document flocking algorithm. Using an NVIDIA® GPU platform we saw a dramatic fivefold improvement over the sequential CPU implementation. Ultimately, we are working toward illustrating a low-cost, high-capacity parallel computational platform suitable for most naturally inspired cooperative applications.

Document Clustering

Cluster analysis is a descriptive data mining task, which involves dividing a set of objects into a number of clusters. The motivation behind clustering a set of data is to find its inherent structure and expose that structure as a set of groups [1]. The data objects within each group should exhibit a large degree of similarity while the similarity among different clusters should be minimal [2]. Document clustering is a fundamental operation used in unsupervised document organization, automatic topic extraction, and information retrieval. It provides a structure for efficiently browsing and searching text.

There are two major clustering techniques: partitioning and hierarchical [2]. Many document clustering algorithms can be classified into these two groups. In recent years, it has been recognized that the partitioning techniques are well suited for clustering large document datasets due to their relatively low computational requirements [10]. The best-known partitioning algorithm is the K-means algorithm and its variants [11]. This algorithm is simple, straightforward and based on the firm foundation of analysis of variances. One drawback of the K-means algorithm is that the clustering result is sensitive to the selection of the initial cluster centroids and may converge to local optima, instead of global ones. Another limitation of the K-means algorithm is that it requires a prior knowledge of the approximate number of clusters for a document collection. Flocking-based clustering is classified as a type of partitioning algorithm.

Flocking Behavior

Social animals in nature often exhibit a form of emergent collective behavior known as '*flocking*.' The flocking model is a biologically inspired computational model for simulating the animation of a flock of entities. It represents group movement as seen in flocks of birds and schools of fish. In this model each individual makes movement decisions without any communication with others. Instead, it acts according to a small number of simple rules, dependent only upon neighboring members in the flock and environmental obstacles. These simple local rules generate a complex global behavior of the entire flock. The basic flocking model was first proposed by Craig Reynolds [5], in which he referred to each individual as a "boid". This model consists of three simple steering rules that each boid needs to execute at each instance over time: separation (steering to avoid collision with neighbors); alignment (steering toward the average heading and matching the velocity of neighbors); cohesion (steering toward the average position of neighbors). These rules describe how a boid reacts to other boids' movement in its local neighborhood. The degree of locality is determined by the range of the boid's sensor. The boid does not react to the flock mates outside its sensor range. These rules of Reynolds' boid flocking behavior are sufficient to reproduce natural group behaviors on the computer.

It has been shown, however, that these rules alone are not sufficient to simulate flocking behavior in nature [4]. A Multiple Species Flocking (MSF) model was developed to more accurately simulate flocking behavior among a heterogeneous population. MSF includes a feature similarity rule that allows each boid to discriminate among its neighbors and only flock with those similar to itself. The addition of this rule allows the use of flocking behavior to organize groups of heterogeneous documents into homogenous subgroups.

The Graphics Processing Unit

The GPU serves as a specialized processor that is tailored to make extremely fast graphics calculations. Demands for increasingly realistic visual representations in simulation and entertainment have driven the development of the GPU. As is evident in Fig. 1, the most recent iteration of NVIDIA®'s GPU has a theoretical performance of over 100 times more floating point operations per second than the current top-of-the-line desktop CPU (the 3.0 GHz Intel Core2 Duo). This difference arose from the evolution of the GPU on highly parallel, computationally intensive calculations rather than data caching and flow control [6].
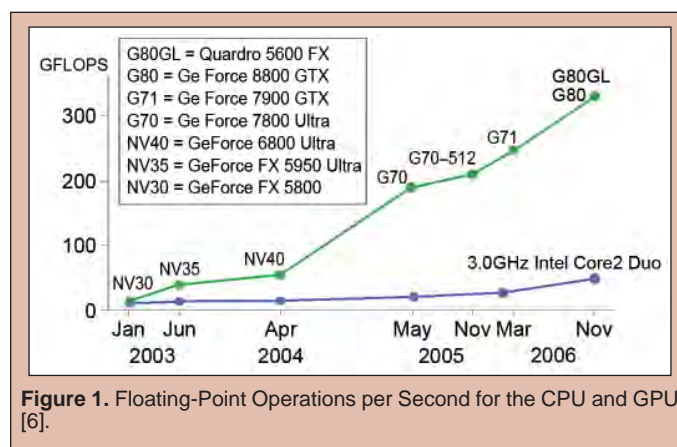
Figure 1. Floating-Point Operations per Second for the CPU and GPU [6].

The immense computational power of the GPU was noticed by developers and a move to exploit this power was made. A community of general-purpose GPU programmers quickly arose (www.gpgpu.org) and pioneered programming on the GPU. In the early stages, programming for the GPU was non-intuitive. Vertex shader languages, such as Sh, Cg, and OpenGL, were the only ones available for general use with the GPU and these focused entirely on the graphics paradigm. Consequently, they did not have appropriate naming constructs for general use and therefore were not particularly programmer friendly. Also, early GPU architectures had basic limitations that prevented some common programming operations [3]. To solve some of these problems and encourage general use of the GPU, NVIDIA® developed the GPU language CUDA as well as a more robust architecture for its GPUs.

NVIDIA® CUDA

CUDA stands for Compute Unified Device Architecture [6]. It is a C-like language that allows programmers to easily write programs to run on certain NVIDIA® GPUs. CUDA 1.0, used in this research, was released in July 2007. CUDA programs can

run using any graphics cards that use the G8x architecture [6]. Depending on the model number, members of the G8x family will have between two and sixty-four SIMD (Single Instruction stream Multiple Data stream) processors. Each SIMD processor contains eight processing elements and has access to 16KB of fast, locally shared memory, 64KB of locally cached texture memory, and 64KB of locally cached constant memory. All multiprocessors also have access to slower main device memory.

Since CUDA was developed to be run on a parallel architecture, certain parallel programming constructs and limitations are inherent to the language. Execution on this architecture is thread-based. Threads are organized into *blocks* and executed in groups of 32 threads called *warps*. Blocks are organized in groups called *grids*. All threads in a single block will execute on a single multi-processor and can exchange data through that processor's shared memory. The algorithm that is executed on the GPU directly is called a *kernel*. To run a kernel on the GPU, dimensions for the number of blocks and the number of threads per block must be specified. The unique ID of each thread and block is then used to access data unique to it. The relationship between grids, blocks, threads, and memory is illustrated in Fig. 2. A thread running on the GPU does not have access to CPU main memory. Once a kernel is run by the host (CPU), its GPU blocks all communication to and from the host, until all threads spawned by the kernel die. During kernel execution the host does not spin and can spawn additional kernels in other graphics cards present in the system.
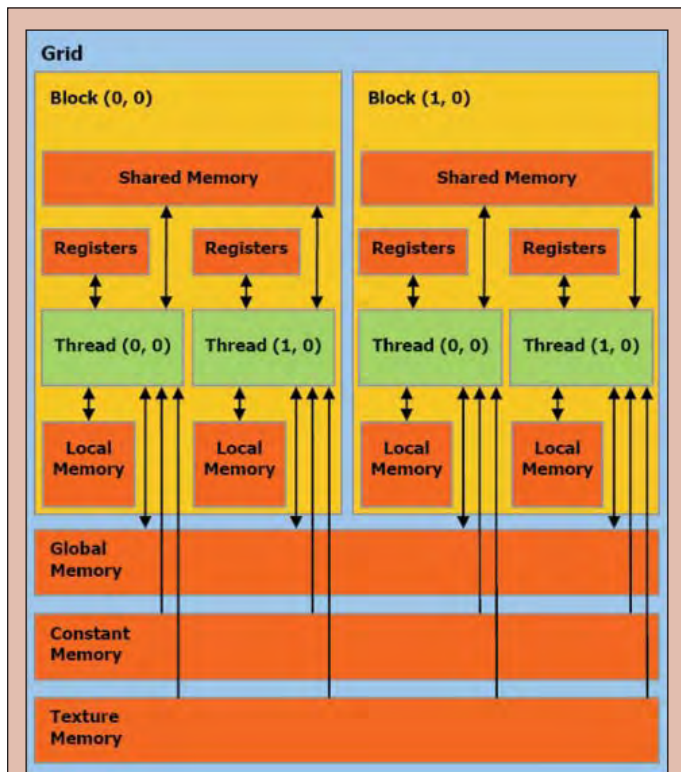
Figure 2. Thread, Block, and Grid memory relations [6].

Experimental Environment

In setting up our research we made an attempt to use low cost, commercially available equipment to help highlight the cost and performance benefits of our approach. All tests were run on a single desktop workstation, the Dell Precision 370. This machine houses 4GB of RAM and a single 3.6 GHz Intel processor with hyper-threading. We added an NVIDIA® Geforce 8800GTS graphics card to the workstation to enable the use of CUDA. The 8800GTS contains 14 SIMD processors and has 648 MB of device memory. All experiments were run under Windows XP Service Pack 2, and CUDA programs ran under CUDA 1.0.

Challenges

One fundamental challenge of programming in CUDA is adapting to the Single Program Multiple Data (SPMD) paradigm. SPMD is different from traditional parallel paradigms in that multiple instances of a single program act on a body of data. Each instance of this program uses unique offsets to manipulate pieces of that data. Data parallelism fits well in this paradigm while operational parallelism does not. Figure 6 provides a visual representation of the data flow in our implementation.

Once the programming paradigm is understood, there are additional difficulties in using the CUDA language. Since each warp is executed on a single SIMD processor, divergent threads in that warp can severely impact performance. To take advantage of all eight processing elements in the multiprocessor, a single instruction is used to process data from each thread. However, if one thread needs to execute different instructions due to a conditional divergence, all other threads must wait until the divergent thread rejoins them. Thus, divergence forces sequential thread execution, negating a large benefit provided by SIMD processing. Another limitation in CUDA is the lack of communication and, consequently, the lack of synchronization between blocks. This creates possible problems of data consistency, typical of parallel modification of singular values. Currently, all functionality must be written into the kernel code. In the future, libraries could be written for CUDA as device functions to help streamline the development process.

Debugging can be difficult in CUDA. A debug mode is available in the CUDA compiler which forces sequential execution on the CPU by emulating the GPU architecture. While this mode is useful for most general types of debugging, some errors are not exposed. The emulator cannot detect any concurrency problems as its execution is sequential. Write and read hazard behavior is undefined during thread execution on the GPU, so the programmer must be cautious to avoid these errors. While running a kernel on the GPU, no access is provided to the standard output. This effectively turns the GPU into a black box when it comes to runtime behavior.

The largest constraint for us in our work was the shortage of fast, local memory. The large amount of document information and the method of document comparison forced frequent reading from global device memory. This memory is not cached and has a penalty of hundreds of clock cycles per read associated with it.

We tried to reduce the impact of this problem by caching some document terms in shared memory for fast access. Another less costly problem we ran into was the requirement of thread divergence in the implementation. Certain conditional statements could not be avoided. This seemed to have some effect on the performance, but not a significant one when compared with the performance degradation of global memory reads.

In an effort to improve the speed of position retrieval and distance calculation, all document positions were stored in texture memory. This design decision did improve the performance of our implementation on the GPU, but it put a hard limit on the number of documents that could be compared (roughly 3,600).

Implementation

The document flocking algorithm that we used in our research was developed by Cui and Potok [4]. This approach treats documents as boids and uses the MSF model to cluster based on a similarity comparison between documents. Rather than use the feature similarity rule, we nullified the alignment and cohesion rules for documents that were not similar. Thus, for dissimilar documents, separation is the only active rule, causing them to repel one another. This algorithm was implemented in CUDA 1.0 and was run on the GPU of our test workstation. Another similar but sequential implementation was written in C and run on the CPU of the same machine.

Adapting the document flocking algorithm used in an SPMD environment is not overly difficult. We implement the algorithm in two kernels. The first kernel creates a thread for each document pair (n^2 threads in total) and compares their locations to determine if the distance between them is within the neighborhood threshold. If the distance is small enough, a document comparison is initiated. This comparison computes the linear distance between the two documents' feature vectors. If that distance is small enough, the documents are deemed similar and treat each other as flock mates. Similar documents contribute to the final velocity of each using the separation, cohesion, and alignment rules discussed earlier. Dissimilar documents contribute to the final velocity of each using only the separation rule. Once each document's influence on the rest of the population is calculated, the second kernel is run. This kernel spawns n threads, each updating the final velocity and position of a single document. Limitations are in place in this kernel to prevent velocity from changing drastically in each generation. This forces each document to make gradual turns, exposing them to a larger number of neighbors and more accurately simulating the behavior of birds. When this kernel is finished executing, a generation is finished and the cycle begins again.

Testing

We conducted testing on populations of documents ranging from 200 to 3,000 documents in increments of 200 documents. We tested each population size 30 times and then averaged the runtime of each. We used randomly generated values for the initial position and velocity of each document for each test to prevent accidental

initial seeding optimization. Each test ran the flocking simulation for 200 generations. This means that documents updated their positions and velocities 200 times based on other documents present in their neighborhood. Based on our observations, 200 generations was an adequate number to allow the documents to converge into stable clusters of similar documents (Fig. 3).
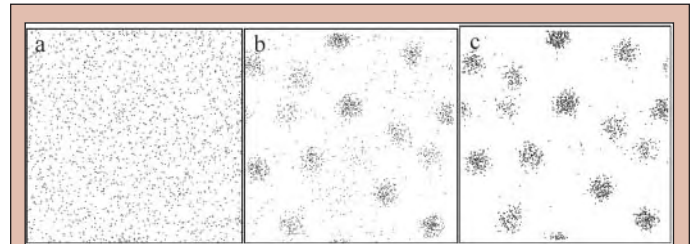
Figure 3. Snapshots of Document Flocking running on the GPU with 2,000 documents at generations 2(a), 55(b), and 200(c).

Flock Parameters

The flock parameters of each simulation were identical. The "flying" space of the documents was 300x300 units. This size space was selected to allow adequate room for each document to move. Each document had a static neighborhood radius of 30 units and a constant speed of 3 units per generation. These parameters were selected based on the flying space size and the observed behavior of the flocks. Each document had a maximum limit of a 0.35 radian deviation from its old velocity. We gave each rule a weight that encouraged system behavior typical of flocking birds. The use of these weights is described in Cui [4]. We assigned a weight of 3 to the alignment rule, 5 to the separation rule, and 3 to the cohesion rule. The document feature vector linear distance threshold was 2.50. This value was selected as it was small enough to clearly differentiate groups in the flock while not being so small that it prevented flocking altogether.

Documents

We compiled the documents used for clustering in our experiments from RSS news feeds and press releases from February 20–28, 2006 in no particular order. We initially processed the documents by stripping out HTML tags, stop words, numbers, and punctuation. We then stemmed the document content using a Porter Stemming algorithm [16]. Finally, we generated a term frequency list using TF-ICF [7] and normalized these frequencies for direct document comparison.

Timing

In the CUDA implementation, we used the timer in the *cutil* library to measure the execution time of each test. Similarly, the CPU implementation uses the Windows XP high precision timer in the *windows* library.

RESULTS

Through our experiments we observed that document flocking on the GPU is many times faster than its CPU counterpart (see Fig. 5). We observed that with 200 documents the GPU implementation is roughly three times faster than the CPU version. As we increased the number of documents in our test set, the improvement increased. For 1,000 documents, we saw an improvement of four times over the CPU. From 1,400 to 3,000 documents the improvement levels off and remains constant at approximately 4.6 times improvement of the GPU over the CPU. Figure 4 uses a logarithmic scale to illustrate that while the performance has drastically improved the complexity of each implementation remains equivalent. The runtime of each grows at the same rate, though at different magnitudes.
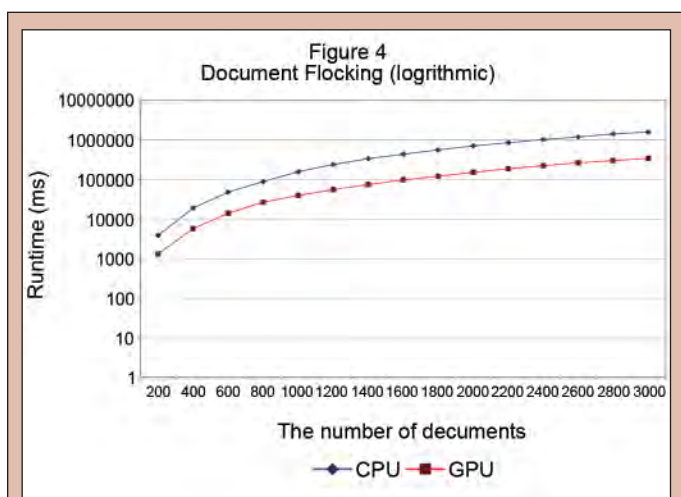
Figure 4. Document Flocking runtime, CPU vs. GPU, logarithmic.
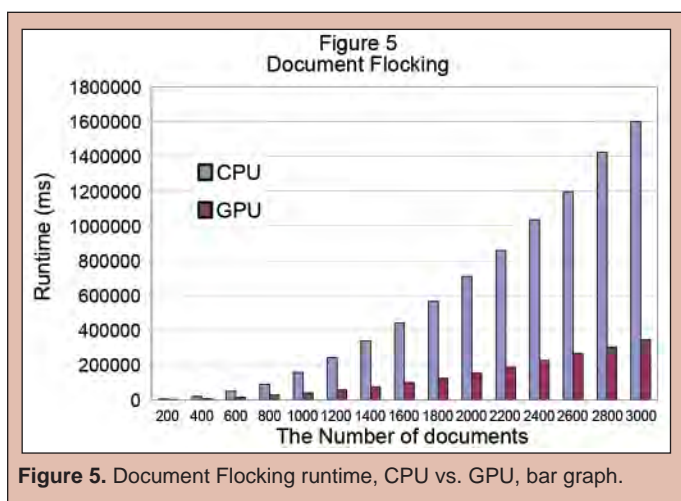
Figure 5. Document Flocking runtime, CPU vs. GPU, bar graph.

DISCUSSION AND CONCLUSION

The results that we have presented here add to the already substantial body of work that supports the GPU as a powerful, general computational device. This power is especially evident when applied to highly parallel algorithms. Other biologically inspired algorithms should benefit when implemented on the GPU. We believe that with continued development, document flocking on the GPU would be an extremely versatile data clustering solution. The low cost and portability of the GPU could allow analysts to cluster large data sets anywhere they are needed. The low cost could also encourage small businesses to use document clustering techniques in new ways. In future work, performance could be increased further if a faster document-to-document comparison technique was implemented. This was our most substantial bottleneck to additional performance gains. Distributing the document flocking algorithm across many GPU's could also substantially improve the number of documents that can be handled during a simulation, possibly allowing millions of documents to be clustered quickly. We did not conduct our tests on the fastest graphics card available from NVIDIA®. The currently unreleased Tesla architecture has 52 additional multiprocessors with over twice the amount of device memory. These additional capabilities would greatly enhance the already high performance we saw in our tests.
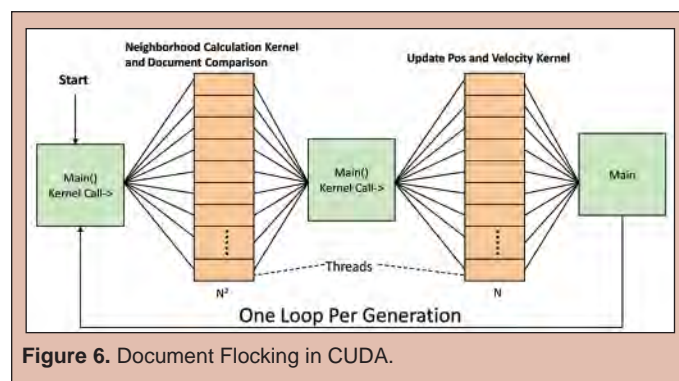
Figure 6. Document Flocking in CUDA.

RESEARCH

Oak Ridge National laboratory is managed by UT-Battelle, LLC, for DOE under contract DE-AC05-00OR22725.

References

[1]   Anderberg, M.R., Cluster Analysis for Applications, Academic Press, Inc., New York, 1973.

[2]   Jain, A.K., Murty, M.N., and Flynn, P.J., Data clustering: a review. *ACM Computing Surveys*, 31 (1999), pp. 264–323.

[3]   Owens, J.D., *et al.*, "A Survey of General Purpose Computation on Graphics Hardware," 2007 *Computer Graphics Forum* Volume (26), pp. 80–113.

[4]   Cui, X., and Potok, T., "A Distributed Flocking Approach for Information Stream Clustering Analysis," *snpd-sawn, Seventh ACIS International Conference on Software Engineering, Artificial Intelligence, Networking, and Parallel/ Distributed Computing (SNPD'06)*, 2006, pp. 97–102.

[5]   Reynolds, C.W., "Flocks, Herds, and Schools: A Distributed Behavioral Model," *Computer Graphics* (ACM), Volume 21, (1987), pp. 25–34.

[6]   NVIDIA®, "NVIDIA® CUDA: Compute Unified Device Architecture" *NVIDIA®*, http://developer.NIVIDA®.com/cuda, Version 1.0, 2007. Accessed July 2007

[7]   Reed, J., *et al.*, "TF-ICF: A New Term Weighting Scheme for Clustering Dynamic Data Streams," in *Proc. Machine Learning and Applications*, 2006, ICMLA *'06*, pp. 258–263.

[8]   Fang, R., *et al.*, "GPUQP: query co-processing using graphics processors," in *Proceedings of the 2007 ACM SIGMOD international conference on Management of data*, 2007, pp. 1061–1063.

[9]   Xu, Z., and Bagrodia, R., "GPU-accelerated Evaluation Platform for High Fidelity Network Modeling," in *2007 Proceedings of the 21st International Workshop on Principles of Advanced and Distributed Simulation*, pp. 131–140 .

[10] Steinbach, M., Karypis, G., and Kumar, V., "A comparison of document clustering techniques," KDD Workshop on Text Mining, 2000

[11] Selim, S.Z., and Ismail, M.A., "K-Means-Type Algorithms: A Generalized Convergence Theorem and Characterization of Local Optimality," *IEEE Transactions on Pattern Analysis and Machine Intelligence PAMI-6* (1984), pp. 81–87.

[12] Chitty, D., "A Data Parallel Approach to Genetic Programming Using Programmable Graphics Hardware," *Proceedings of the 9th annual conference on Genetic and evolutionary computation*, 2007, pp. 1566–1573.

[13] Rick, T., and Mathar, R., "Fast Edge-Diffraction-Based Radio Wave Propagation Model for Graphics Hardware," *Proceedings of ITG INICA*, 2007.

[14] Rodríguez-Ramos, J., *et al.*, "Modal Fourier wavefront reconstruction on graphics processing units," *Proceedings of the SPIE*, Volume 6272, 2006, pp. 627215.

[15] Yamagiwa, S., *et al.*, "Data Buffering Optimization Methods toward a Uniform Programming Interface for GPU-based Applications," *Proceedings of the 4th international conference on Computing frontiers*, 2007, pp. 205–212.

[16] Porter, M.F., "An algorithm for suffix stripping," *Program*, 14 no. 3, July 1980, pp. 130–137

Michael Wiczer was born in Albuquerque, NM and grew up partly in Albuquerque followed by Buffalo Grove, IL. He studied engieering physics with an interest in mathematics at the University of Illinois at Urbana-Champaign where he was involved with molecular spectroscopy research in the physical chemistry department. He held a SULI internship at the Stanford Linear Accelerator Center in summer 2007. He plans to pursue a Ph.D. in some incarnation afterwards.

Aaron Lindenberg is an assistant professor with joint appointments at Stanford University in the Materials Science and Engineering Department and in the Photon Science Department at the Stanford Linear Accelerator Center. He received his Ph.D. from the University of California, Berkeley in 2001 for the development of picosecond x-ray techniques and the study of ultrafast structural properties in semiconductors at atomic-scale resolution. His current research activities are focused on the ultrafast properties of materials, probed using light from the THz to the x-ray spectral range.

Measurements of High-Field THz Induced Photocurrents in Semiconductors

Michael Wiczer and Aaron Lindenberg

ABSTRACT

THz pulses have provided a useful tool for probing the time-resolved dynamics of free carriers in a system. However, the development of methods to produce intense THz radiation has been slow. We have developed a method for producing intense ultra-short THz pulses, which have a full width at half maximum of 300 fs — approximately a half cycle of THz radiation. These intense half cycle pulses (HCPs) allowed us to use THz radiation as a source of excitation. By exposing the semiconductor indium antimonide (InSb) to intense THz HCP radiation, we have observed non-linear optical effects which suggest the generation of new free carriers by below band-gap THz photons. This generation of free carriers appears to be due to an avalanche multiplication process which then induces a current in the time-scale of our THz pulse. This amplification on such a short timescale suggests the possibility of an ultra-fast detector of weak above band-gap radiation. We constructed a device which detects these currents by painting an electrode structure on the surface of the semiconductor. The currents induced across the electrodes by this avalanche multiplication process were measured and compared with other measurements of this non-linear optical process. We successfully measured THz induced currents in InSb, suggesting promise towards the development of an ultra-fast detector. Further, we have gained insight into a possible physical explanation of the THz induced free carriers we observe in InSb.

Introduction

Ultra-fast THz (10^{12} Hz) radiation has proved tremendously useful for probing time-resolved dynamics in a variety of systems [1]. Traditionally, a sample is excited or set into motion in some way (i.e., by a "pump" such as an IR-laser pulse or synchrotron radiation pulse) and at various times following this excitation, a THz pulse passes through the sample and "probes" its state at that instant. THz radiation is an extremely good probe of systems because each THz photon has very low energy (1 THz photon ~ 4 meV). Thus, the radiation is absorbed by free electrons in the system (a detectable effect), but the small increase in the energy of the free electron has no discernible effect on the system. Although this has been a powerful tool for studying dynamics for some time, we are beginning to learn that — at high enough intensity — THz radiation can act as a valuable source of excitation ("pump") for a system.

Promising new techniques generate THz radiation by optical rectification [2] not limited in intensity by a threshold for damaging a non-linear optical crystal. We have developed one such experimental setup which uses a plasma in air as a nonlinear optical element. For our purposes, the THz radiation generated by this method is only limited by the intensity of incident 800 nm and 400 nm laser light. With this tool, we can begin to study ultra-fast dynamics using THz radiation as a pump.

One such experiment employing this high intensity THz radiation studies its interaction with semiconductors. In an experiment which preceded this work [3], indium antimonide (InSb) was placed in the path of the THz beam and absorption was measured. Since the photons had much lower energy than the band-gap of the semiconductor (4 meV << 170 meV), one would not expect the THz radiation to increase the number of free carriers in the semiconductor. Instead, the THz absorption should provide a measure of the number of free carriers currently present in the semiconductor (due to thermal excitation). However, we observed that THz radiation at high enough intensity generates new free carriers. This phenomenon was measured by using the THz pulse as a probe of its own interactions. To supplement the previous experiment, the work presented here attempts to understand the process by observing a current generated by the new free carriers.

Our THz radiation is short enough (~300 fs FWHM) to be considered a half-cycle pulse [4]. In this case, the integral of electric (or magnetic) field over all time is 0, but one half-cycle of the electric field is much stronger than all others (Figure 1). This half cycle peak

is strong for long times compared to certain free electron processes in InSb and therefore shares some properties with an applied DC field. Accelerated from this quasi-DC field, free electrons can collide with valence electrons and, if there is enough energy, create new electron-hole pairs. The new conduction band electrons can now feel the electric field and accelerate into valence electrons to produce even more electron-hole pairs [4–6]. Upon investigating this process — avalanche multiplication — we observe that the ultra-fast, high intensity THz radiation provides for an experiment which isolates certain physical processes extremely well. While in bulk systems electron-electron collisions in the conduction band and electron-phonon coupling prove significant, both of these processes occur on much longer time-scales than our experiment. Furthermore, fields this intense are generally unable to penetrate the surface of the semiconductor material, which breaks down at much lower fields. The ultra-fast nature of the pulse once again allows for the pulse to excite the sample before it breaks down and the field is not screened.
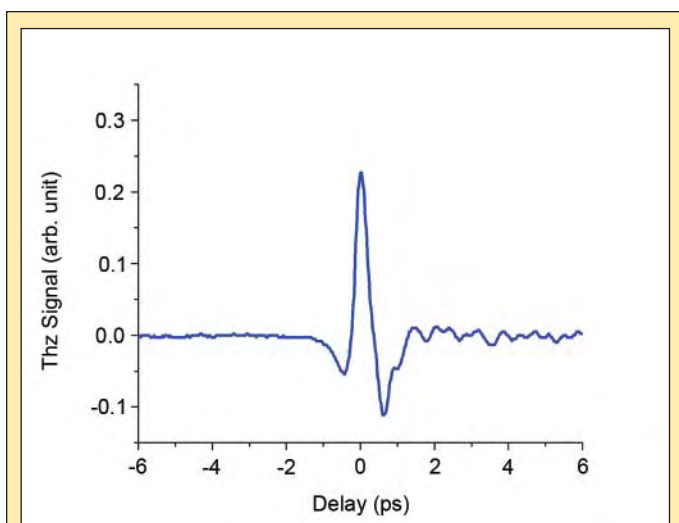
Figure 1. A half-cycle pulse of THz radiation acts as a directional electric field for short times.

This setup may assist the development of an ultra-fast detector. Our THz radiation can multiply the number of free carriers in the semiconductor and produce a current in very short timescales. This amplification can be harnessed by the construction of a photoconductive dipole antenna [7–8]. By placing two electrodes on the surface of the sample with the polarization of the THz beam pointing across the electrodes, the THz beam will sweep and multiply any newly generated free carriers (i.e. by an above band-gap photon). This device, which generally uses a known pulsed laser to detect small THz signals, can use a known THz signal to detect small laser signals with high gain and very fast response — as fast as the THz pulse length. As yet, no detection method this fast exists.

MATERIALS AND METHODS

We generate high-intensity THz pulses with a Ti:Sapphire laser system. A mode-locked Ti:Sapphire oscillator produces weak, 25 fs pulses, which are then sent to a regenerative amplifier to be amplified using chirped pulse amplification (CPA) [10]. The final laser pulses have total energy of approximately 1 mJ, pulse length of 50 fs, wavelength centered at 800 nm (full width half maximum spanning from about 775–825 nm), and a repetition rate of 1 KHz. These laser pulses are then passed through a β-barium borate (BBO) frequency-doubling crystal to produce 400 nm light collinear with the original 800 nm light. As described by Bartel *et al*, if this beam is focused to a small enough waist to ionize air — and has an appropriate divergence angle for optimal phase matching — a 3rd order non-linear optical effect will produce a quasi-DC electromagnetic field. Since the pulse duration for the incoming laser beams are so short, this quasi-DC field takes the form of an ultra-short THz pulse [4].

A sample photoconductive antenna is constructed in order to test both the physics of the interaction between intense THz radiation and semiconductor samples as well as the potential development of an ultra-fast photoconductive switch. Using silver paste two vertical electrodes, approximately 5 mm in length and separated by 500 μm, were painted onto the InSb sample. Although InSb is a semiconductor, its extremely narrow band-gap allows for a high density of free carriers even at room temperature (2×10^{16} cm^{-3}). Thus, it has a relatively low resistivity, and the resistance across the two electrodes was measured to be approximately 50 Ω. Since the heat of a soldering iron damages the semiconductor material, wires were attached to the surface of the semiconductor with epoxy, and electrical contact with the electrodes was ensured with additional silver paste. In order to minimize the amplification of ambient electrical noise, wire directly from a coaxial cable was mounted to the sample and cable length was minimized (Figure 2). The current across these electrodes was input to a current amplifier (Stanford Research Systems SR570) set to a gain of 1 pA/V. This was the most sensitive gain setting on the current amplifier, and thus the output from the amplifier was slow (output time constant
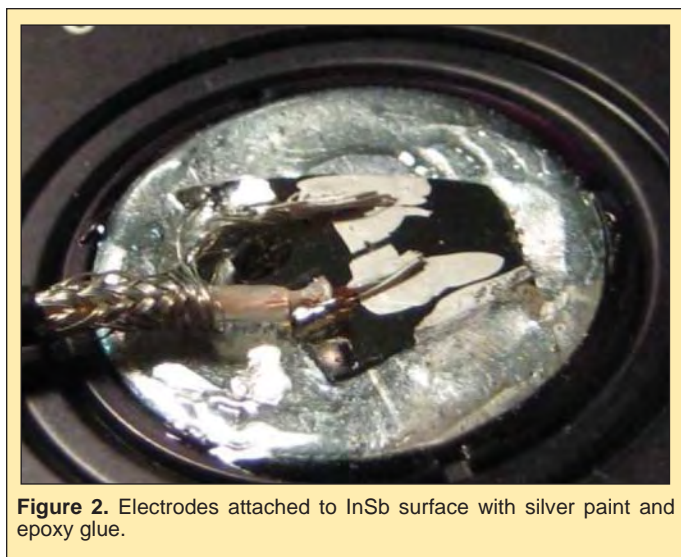
Figure 2. Electrodes attached to InSb surface with silver paint and epoxy glue.

of 3.5 s). An optical shutter (Thorlabs SH05 shutter with Thorlabs SC10 controller) modulated the beam at 0.2 Hz. A reference signal from this shutter and the output of the current amplifier were synchronized using a lock-in amplifier (SR830) acquiring with a time constant of 100 s.

This type of device has been used extensively in the past to detect THz radiation [8]. When used with a semiconductor having carrier lifetimes of approximately the width of the THz pulse or less, the current induced across the electrodes increases linearly with electric field amplitude for low fields. If the carrier lifetimes are much longer than the width of the THz pulse (as in InSb) and no new free carriers are induced, a free carrier feels the electric field of the THz pulse for a very long time, and the current across the electrodes is approximately zero. If, however, new free carriers are induced, then the average conduction band electron loses energy at every collision. The electron no longer feels the electric field uninterrupted for the entire width of the pulse. Rather, during the positive portion of the pulse, the energy decreases. The now slower free carrier then feels the rest of the field, which reduces its velocity further until the net velocity of free carriers is in the direction opposite the direction the charge was accelerated during the THz pulse. This results in a net current indicative only of the free carriers generated during the positive portion of the THz pulse (Figure 3). The expectation at high THz intensity is that, once the field reaches an impact-ionization threshold, additional free carriers will be generated and a current will form. We measure the dependence of current on incident electric field by focusing our THz beam to a small waist and translating the sample along the direction of propagation of the THz beam. At the beam waist, the electric field amplitude will be greatest and, as the sample is translated away from the waist, the amplitude decreases.
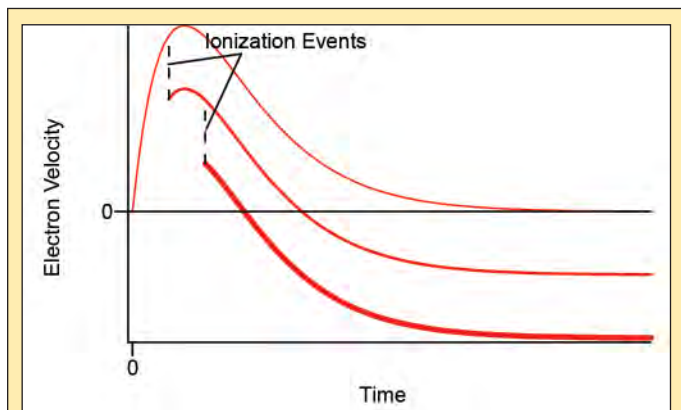
Figure 3. A free electron which is subject to a THz HCP for long times has velocity qualitatively depicted in the top trace. For every ionization event, not only are total free carriers doubled, but the net velocity after long times becomes non-zero (bottom two traces).

The intention is that we acquire data as the photoconductive antenna translates along the propagation axis of the focusing THz beam. This data then needs to be calibrated to be expressed against peak electric field instead of position. To this end, we mapped the THz beam as it propagates. We use a bolometer, which measures the total THz intensity incident on the detector. Spatial resolution is provided by blocking all THz radiation except that which passes through a narrow slit (Figure 4). The slit is open to a small portion

of the THz beam's longitudinal profile at a particular propagation distance; the THz intensity incident on the bolometer is a measure of the THz intensity at the position of the slit.
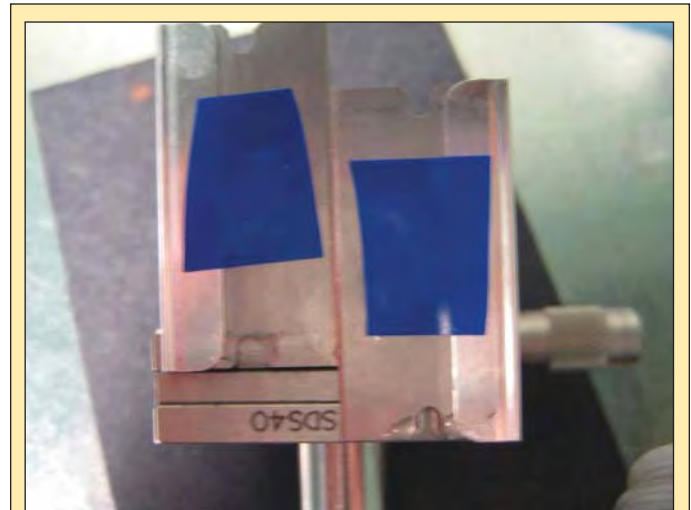
Figure 4. Width between narrow slits is adjusted by micrometer position. Only THz radiation at a specified position reaches the bolometer when the slits are positioned in front of the THz beam.

RESULTS

Modeling

In order to characterize the physical processes involved in our experiment, we must produce a model which predicts a signature of the suspected physical process which might be measurable. We produce a simple "order-of-magnitude" model for the current generated by avalanche multiplication induced by THz radiation in InSb. Since the THz wavelength is long and the pulses intense, it is an accurate picture to consider the effect of the bulk electric field created by the THz radiation as opposed to multi-photon absorption — which is a much more complex description of the process. The traditional treatment of semiconductors exposed to fields as high as the peak field of the THz HCP we generate (approximately 200 KV/cm) is to suggest that a free electron reaches a saturation velocity because of the increased number of collisions at fields this high. Furthermore, avalanche breakdown will occur, the semiconductor will become a conductor and fields will be screened. However, the THz pulses we generate are short enough that relatively few collisions occur. Hence, the electron can — for this short duration — transport through the semiconductor at velocities much greater than the saturation velocity, and fields much greater than the breakdown field of the semiconductor can penetrate the sample. Thus, a "hot-electron" transport model — one where the electron has a fixed energy incident on the material — appears more appropriate than a high-field transport model — one where the electron starts at rest and then is accelerated. Kane developed a model for the rate of impact ionization collisions — collisions with valence electrons which create new electron-hole pairs — as a function of a hot electron's kinetic energy [5]. Based on Kane's "random-k" approximation, we find that — if the hole effective mass

U.S. Department of Energy Journal of Undergraduate Research

is much greater than the free carrier effective mass — the collision rate, ω(E), is related to the following integral expression [5]:

$$\omega(E_1) \propto \int_{E_g}^{E_1-E_g} \int_{E_g}^{E_1-E_g} \varphi_v(E_2)\varphi_c(E_3)\varphi_c(E_4)dE_2dE_3$$

where E_1 is the energy of the initial hot electron and E_4 is the energy of the valence electron which interacts with the initial hot electron. Once the hot electron interacts with the valence electron, the hot electron loses energy and the valence electron gains enough energy to enter the conduction band. This produces two final electrons in the conduction band with energies E_2 and E_3. The conservation of energy condition is that $E_1=E_2+E_3-E_4$. All energies are measured from the valence band edge, and the band gap energy is E_g (E_g = 0.17 eV for InSb ($E_4<0$; $E_1,E_2,E_3>E_g$). φ_c is the density of states function of the conduction band and φ_v is the density of states for the valence band. If we assume a parabolic band structure, these functions become:

$$\varphi_c(E) = \frac{1}{2\pi^2}\left(\frac{2m_c}{\hbar^2}\right)^{3/2}\sqrt{E-E_g}, \; \varphi_v(E) = \frac{1}{2\pi^2}\left(\frac{2m_v}{\hbar^2}\right)^{3/2}\sqrt{-E}$$

where m_c is the effective mass of a free electron (0.014 m_e in InSb) and m_v is the effective mass of a hole (0.43 m_e in InSb). This integral was evaluated and the constant of proportionality was determined by calibrating our results to previous Monte-Carlo calculations of low-energy impact ionization rates in InSb [6]. The calculated collision rate is given in Figure 5.
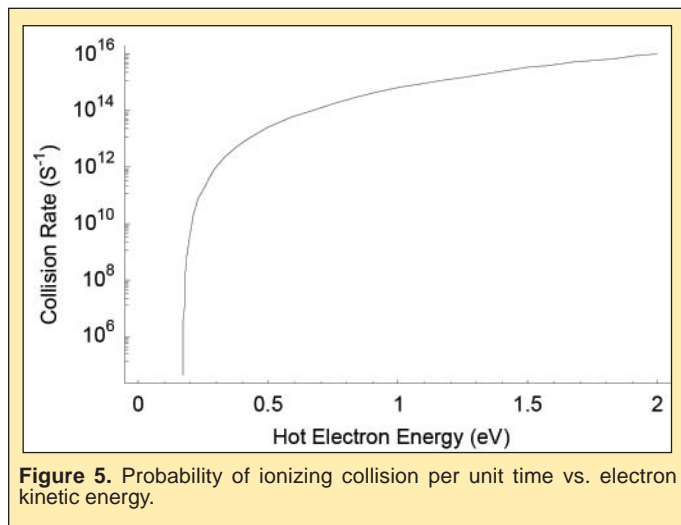
Figure 5. Probability of ionizing collision per unit time vs. electron kinetic energy.

Using this, we must now consider that the electron, in fact, starts at rest and is accelerated. The instantaneous collision probability per unit time, P(t), must satisfy:

$$P(t) = \left(1 - \int_{t_0}^{t}P(s)ds\right)\omega(E(t)),$$

where t_0 is the time for the electron to accelerate to the threshold energy and E(t), under a constant field, is given by $E(t)=\frac{1}{2m^*}(qFt)^2$. For various field strengths, P(t) and, in turn, the average times for the first ionizing collision were calculated. The dependence of collision time on applied field (assuming a constant field) τ(F) was found to be given by $\tau(F) \propto (F-F_t)^{-0.9}$ (Figure 6), where F_t is the threshold field for impact ionization. If we approximate our THz

pulse as a square wave, we can generate an approximation for the multiplication factor:

$$M(F) = 2^{t_p/\tau(F)},$$

where t_p is the width of the pulse. It is important to note that many assumptions have been made which result in considerable uncertainties in the multiplication factor. However, this rough modeling is likely sufficient for purposes of distinguishing between distinct potential underlying processes. For instance, one might suggest an alternative scenario that free electrons are generated by the THz field distorting the band-gap of the semiconductor. In this case, the THz field would interact with valence band electrons, which have effective masses nearly 30 times that of the conduction band electrons. Clearly these physical processes would have to be very different and order-of-magnitude discussions provided here may prove useful in clarifying the physical situation.
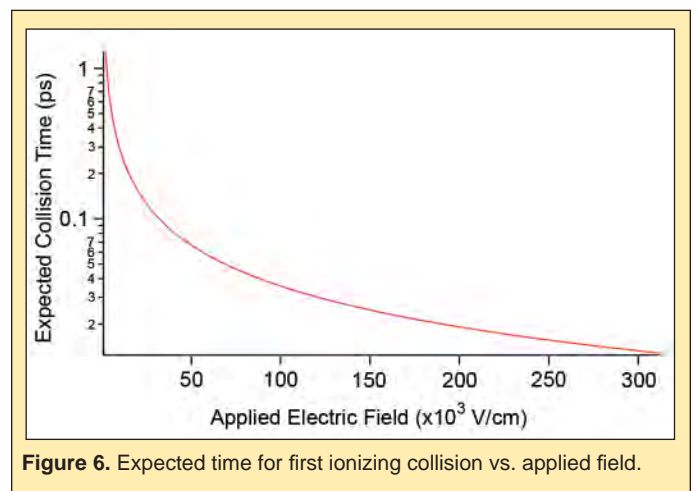
Figure 6. Expected time for first ionizing collision vs. applied field.

Experiment

Using slits to provide spatial resolution to our bolometer measurement (as described in Materials and Methods section), we acquired a map of the intensity profile of the THz beam as it propagates (Figure 7). After extracting the intensity peak at each position along the propagation axis (and then taking the square root of intensity) we were able to extract the relative peak electric field as a function of position along the propagation axis (Figure 8).

Once the THz beam profile was achieved, the electrode structure (Figure 2) was placed at the focus of the THz beam. Current was measured where the electrodes were placed at various longitudinal positions along the beam profile (Figure 9). The width of the current profile was approximately 750 μm FWHM, which is comparable to the width of the THz intensity profile at the focus. This suggests that the current measured is, in fact, induced by the THz beam. We then placed the electrode structure at various positions along the propagation axis of the THz beam (Figure 10). The current profile was much broader than the intensity profile of the THz beam. Some current was found when no THz radiation was generated but 800 nm IR radiation was incident on the electrode gap. This suggests that the current profile of the THz beam may have been broadened by scattered IR radiation.
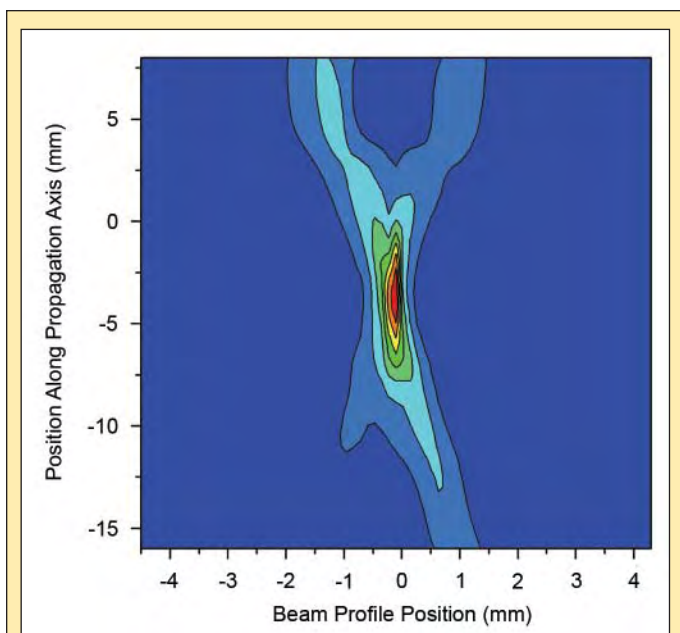
Figure 7. THz beam intensity contour plot.
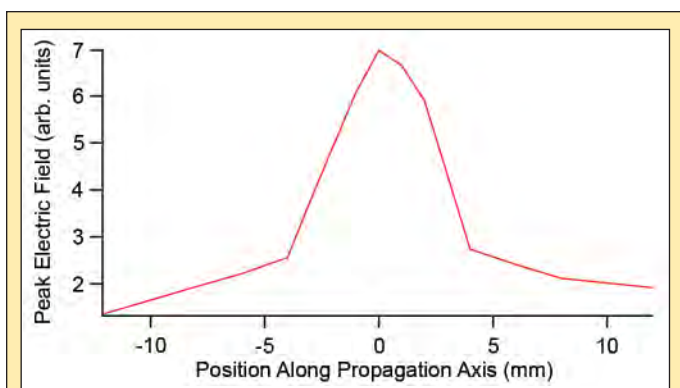
Figure 8. Peak THz electric field vs. propagation distance as beam is focused.
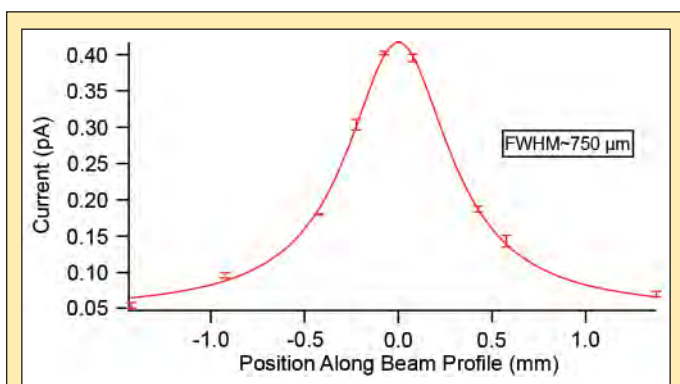
Figure 9. THz induced current vs. position along beam profile at focus of THz beam.
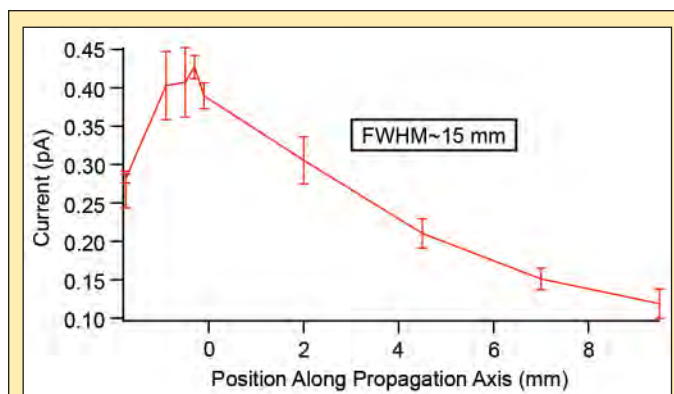
Figure 10. THz induced current vs. propagation distance as beam is focused. This trace is about twice as broad as the non-linear features observed in absorption measurements.

DISCUSSION AND CONCLUSIONS

We have tentatively observed THz induced photocurrents on 300 fs timescales. The mere existence of this photocurrent is valuable as it shows promise as an ultra-fast, high gain photoconductive switch — a fast detector of weak above-band-gap radiation. Although these data have not yet been related to similar absorption measurements, we expect that after repeating our photocurrent measurements with improved scattered light cancellation the relation between absorption and photocurrent measurements will become apparent.

The differences between the field dependence of photocurrent and absorption measurements should be caused by differences in the frequency dependence of the two measurement schemes. Thus, in order to attempt to describe these differences, it is valuable to speculate about frequency dependences. The frequency response of the bolometer that was used for absorption measurements favors higher frequencies. Furthermore, in low-intensity conditions, InSb absorbs low frequency THz radiation considerably more than higher frequency THz. This suggests that our absorption measurements, which indicate an increase in free carriers, are mostly providing insight in the response of InSb to higher frequency THz radiation. Based on the impact ionization model, we understand that the width of the HCP is extremely significant to the gain generated by avalanche multiplication. Lower frequency components help to broaden the HCP. Our understanding of the photoconductive antenna, on the other hand, suggests that it can provide insight into the response of InSb to low as well as high THz frequencies. This is because the electrodes are on the surface of the sample, so absorption effects through the depth of the sample are insignificant. Furthermore, our understanding of the mechanism which generates photocurrents suggests that the current is much more sensitive to the properties of the electric field of the THz pulse as a function of time as opposed to the frequency components. The lack of frequency discrimination in the photoconductive antenna and the observation that the effects of impact ionization are amplified by the present of low frequency THz radiation suggest that the photoconductive antenna should be more sensitive to these non-linear effects than the absorption measurements. Thus, currents should begin to develop at lower peak intensity than increased absorption began. This seems

to support our tentative results that the current profile is broader than the absorption profile of the THz beam. It does not change the fact that scattered IR light may have played a significant role in broadening the current profile, but a broader profile is expected nevertheless.

Necessary further investigation includes the repetition of our measurement of the photocurrent profile with the effects of scattered IR light being reduced. Furthermore, we would like to repeat our measurements at low temperatures. This will provide direct evidence for whether the non-linear effects we observe are produced by conduction band electrons or valence band electrons since, as the conduction band electrons are reduced, the effect will be either enhanced or reduced. Finally, we should refine our photoconductive antenna design for use as an ultra-fast photoconductive detector.

REFERENCES

[1] C.A. Schmuttenmaer, "Exploring Dynamics in the Far-Infrared with Terahertz Spectroscopy," in Chemical Reviews, Vol. 104, 2004, pp. 1759–1779.

[2] T.J. Carrig, *et al.*, "Scaling of Terahertz Radiation Via Optical Rectification in Electrooptic Crystals," in Applied Physics Letters, Vol. 66, 1995, pp. 121–123.

[3] Wen, Haidan, "Table-Top, High-Power Terahertz Source and Its Applications," presented at SSRL seminar at Stanford Linear Accelerator Center, Menlo Park, CA, July 12, 2007.

[4] T. Bartel, *et al.*, "Generation of single-cycle THz transients with high electric-field amplitudes," in Optics Letters, Vol. 30, 2005, pp. 2805–2807.

[5] E.O. Kane, "Electron Scattering by Pair Production in Silicon", in Physical Review, Vol. 159, 1967, pp. 624–631.

[6] R.C. Curby and D.K. Ferry, "Impact Ionization in Narrow Gap Semiconductor", in Physica Status Solidi (a), Vol. 15, pp. 319–328.

[7] S.A. Jamison and A.V. Nurmikko, "Avalanche formation and high-intensity infrared transmission limit in InAs, InSb, and $Hg_{1-x}Cd_xTe$", in Physical Review B, Vol. 19, 5185–5193.

[8] P.R. Smith, D.H. Auston, and M.C. Nuss, "Subpicosecond Photoconducting Dipole Antennas" in IEEE Journal of Quantum Electronics, Vol. 24, 1988, pp. 255–260.

[9] M. van Exter, C. Fattinger, and D. Grischkowsky, "High-brightness terahertz beams characterized with an ultrafast detector", in Applied Physics Letters, Vol. 55, 1989, pp. 337–339.

[10] U. Keller, *et al.*, "Femtosecond pulses from a continuously self-starting passively mode-locked Ti:sapphire laser" in Optics Letters, Vol. 16, 1991, pp. 1022–1024.

Kelsey Winsor is from Rhode Island and went to Smith College in Massachusetts, where she majored in geology and minored in philosophy. Through SULI, she interned at the Pacific Northwest National Laboratory in the spring of 2007, and worked there as a research associate during the following year. She plans to attend grad school to study ocean-climate interactions, and hopes to apply her research to identifying causes of regional changes in water resources and ecology. Outside of science, she likes to backpack and is trying to learn kung fu.

George V. Last is a senior research scientist at the Pacific Northwest National Laboratory. He received his B.S. degree in Geology and M.S degree in Environmental Science (Hydrogeology Option) from Washington State University. He is a registered professional geologist and hydrogeologist in the states of Washington and Oregon. Throughout his 32 year career, his research has focused on applied subsurface science aimed at improving our understanding of the geologic controls on contaminant fate and transport and methodologies for predicting the spatial distribution of hydrologic and geochemical properties.

STRATIGRAPHIC CONTROL ON CCl_4 AND $CHCl_3$ CONCENTRATIONS IN THE 200 WEST AREA, HANFORD SITE

KELSEY WINSOR AND GEORGE V. LAST

ABSTRACT

An extensive subsurface contaminant plume of carbon tetrachloride (CCl_4) is the focus of a remedial effort in the 200 West Area of the U.S. Department of Energy's Hanford Site in eastern Washington. Remediation requires a high-resolution understanding of the region's spatially variable lithofacies and of the effect these lithofacies have on CCl_4 migration through the unconfined aquifer. To increase the level of detail of our current understanding, a transect was chosen along the primary groundwater flow path in the most heavily contaminated area. Borehole logs of wells along this 3.7 km-long transect were standardized and used to create a cross section displaying the depth and continuity of lithofacies. Natural and spectral gamma geophysical logs were examined to pinpoint the depths of geologic units. Depth discrete concentrations of CCl_4 and its reductive dechlorination product, chloroform ($CHCl_3$), were overlain on this cross section. Comparison of stratigraphy to contaminant levels shows that peaks in CCl_4 concentration occur in thin, fine-grained layers and that other fine-grained layers frequently form lower boundaries to regions of high concentration. Peaks in CCl_4 concentrations are frequently located at different depths from those of $CHCl_3$, suggesting that these concentrations are affected by dechlorination of CCl_4. Transformation of CCl_4 to $CHCl_3$ appears to be more prevalent within reduced, iron-containing sediments. The influence of thin, fine-grained layers within the larger aquifer unit indicates that characterization of contamination in this locality should consider subsurface geology with at least as much resolution as provided in this study.

INTRODUCTION

Enormous volumes of waste water, which included a range of chemical and radioactive contaminants, have been disposed in the 200 West Area of the U.S. Department of Energy's Hanford Site in eastern Washington [1]. Without complete natural attenuation and/or remediation, contaminants reaching the groundwater will eventually enter the Columbia River [2, 1]. The river is vital to regional salmon and is an important water resource for human developments in the Pacific Northwest. Of particular interest to this study is tetrachloromethane, or carbon tetrachloride (CCl_4). This liquid was used during the plutonium finishing process between 1955 and 1973, and 750,000 kg of CCl_4 was disposed of in cribs and trenches in the 200 West Area [3]. Subsequent drainage through the thick vadose zone has released an estimated 132,000 kg of this contaminant into the unconfined aquifer, creating a large groundwater plume [4, 5]. Found in concentrations above the drinking water standard (5 µg/L) over an area of 10.78 km², the

CCl_4 plume has spread significantly in the past 15 years and several remediation treatments are being conducted to restrict the plume [6]. Background levels of CCl4 in Hanford Site sediments are below the 5 µg/L drinking standard [6].

Subsurface geology and groundwater flow are the primary determinants of contaminant migration in this arid region [7]. While the Hanford Site's geology has been studied extensively [8, 1], uncertainties remain regarding variation in depths and extent of sedimentary units below the site. Stratigraphic complexity is greatly influenced by spatially variable fluvial and flood deposits and erosional features. General stratigraphy in the 200 West Area includes some 160 m of fluvial, lacustrine, and eolian deposits above basalt bedrock. The lowermost formation, the Ringold, is a fluvial/lacustrine deposit and locally consists of three major units; sands and gravels (Ringold A), overlain by an impermeable but discontinuous mud and sand (Ringold Lower Mud), overlain in turn by a thick sequence of sands and gravels (Ringold E). Both confined and unconfined aquifers are located in the Ringold

Formation. Groundwater in the Ringold A unit is confined by the overlying Lower Mud unit. Upper, vadose zone units are the silty, calcium carbonate-rich Cold Creek Unit, sand-dominated facies of the Hanford formation, and gravel-dominated facies of the Hanford formation. The latter two units are moderate- to high-energy ice age flood deposits, respectively, and are in places overlain by more recent Holocene sands [9, 10].

Above the water table, variations in these vadose zone units have influenced the downward migration of CCl_4, and have trapped CCl_4 in both its dense, non-aqueous phase and its aqueous phase. This trapped CCl_4 acts as a source for further contamination [5]. Within the saturated zone, a small volume of aqueous CCl_4 has been transformed to chloroform ($CHCl_3$), creating a relatively low-concentration plume of $CHCl_3$ associated with CCl_4 groundwater contamination. Modeling $CHCl_3$ can therefore provide additional information regarding behavior of the CCl_4 plume.

In the 200 West Area, groundwater travels in a general eastward direction, flowing more toward the east-northeast in the northern portion of the Area, and more toward the east-southeast in the southern portion. Groundwater levels range between an elevation of about 139 m above sea level (asl) in the west, to 133 m asl in the east, and are slowly decreasing [6]. Flow rates vary, but tend to be less than 0.1 m/day [5]. Recent remediation has involved installation of pump and treat wells, with extraction wells in the heavily-contaminated central 200 West and injection wells about 1 km to the west. This treatment has altered groundwater levels and thus groundwater flow in the central 200 West Area.

Because of spatial variations in subsurface geology and spatiotemporal variations in groundwater flow, high-resolution spatial hydrogeological modeling is necessary to depict current (and predict future) contaminant migration. Sources providing information for such models include drillers' records, geologists' records, geophysical logs of boreholes, as well as groundwater monitoring data that provide contaminant concentrations and water levels. This study attempts to create a geological model along the primary flowpath of CCl_4 in the northern half of the 200 West Area, displaying the present-day extent of the plume and its interaction with subsurface geology.

MATERIALS AND METHODS

A northeast-trending transect through the 200 West Area incorporating nineteen wells was identified. This transect begins near the source of carbon tetrachloride contamination and follows the curve of the plume's primary flow path (Fig. 1).

Drillers', geologists', and geophysical logs from wells along this transect were used, requiring systematization of the data recorded in these logs. Systematization follows PNL Procedures DO-6, DO-7, and DO-8, respectively, as detailed in Last et al., 2007 [10, 12]. For drillers' and geologists' logs, this procedure involves gleaning out information related to sediment class and composition, particle size, calcium carbonate content, color, moisture, roundness, and any relevant drilling procedures or other geologic characteristics associated with a certain depth. Sediment class and size were based on the Folk/Wentworth schemes. A total of 14 geologists' and drillers' logs (comprising 13 wells) were systematized and entered

into the Hanford Borehole Geologic Information System (HBGIS), adding to the 6 transect wells already in the system. From HBGIS, sedimentary data were exported into LogPlot, graphing software that stratigraphically displays geologic information. Figure 4 displays a stratigraphic column created using LogPlot.

Geophysical data, primarily natural gamma (12 wells) along with spectral gamma (5 wells), were also entered into HBGIS. Data originated from three sources: recent digital records from the Hanford Site Groundwater Remediation Project, older digital records from the Pacific Northwest National Laboratory (PNNL) Log Database, and hard copy originals of graphical logs. Hard copy graphical logs were manually digitized using Engauge Software. Using a paired t-test, results from manual digitization were compared to digital records from wells 299-W6-10 and 299-W11-30 to determine accuracy of the manual process. Digital geophysical data from the three sources were entered into HBGIS, then graphed using LogPlot and compared to lithologic descriptions of the same wells. Using these data, a cross section along the primary groundwater flow path was modeled.

Special depth discrete and routine measurements of CCl_4 and $CHCl_3$ concentrations for all available wells were taken from the Hanford Virtual Library and the Hanford Environmental Information System (HEIS). Both types of data are presented in
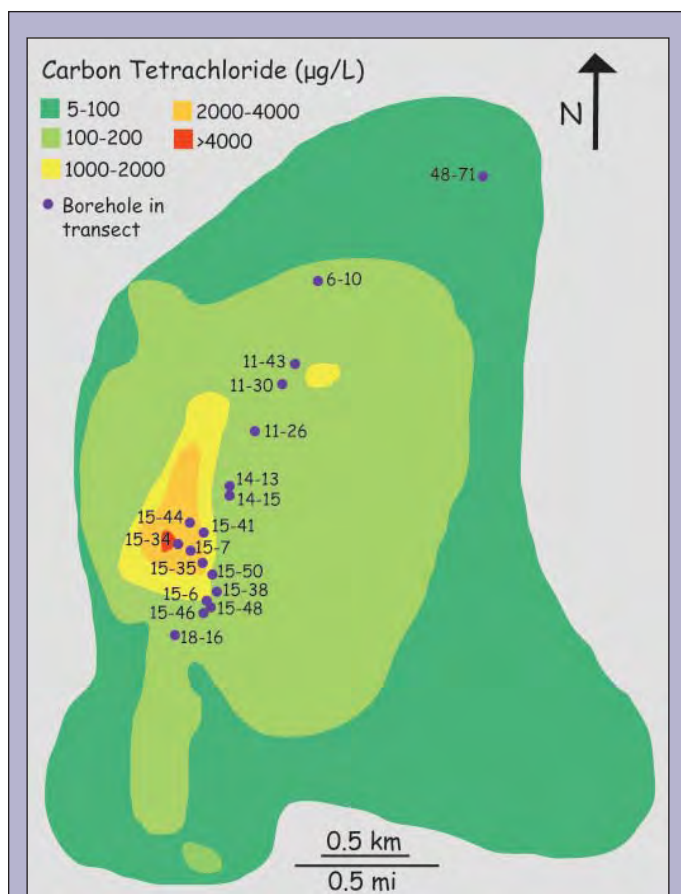
Figure 1. Carbon tetrachloride contaminant plume in 200 West Area aquifer, with boreholes included in this study's transect. All wells are located in the 200 West Area and are prefixed with 299-W, except for the most northern borehole (48-71), which is located just outside this Area and is prefixed 699-. Modified from Hartman et al., 2006 [6].

<table>
</table>

Well	Date	Depth (ft bgs)	[CCl$_4$] (µg/L)	[CHCl$_3$] (µg/L)
299-W18-16	11/22/2004	250.0	670	81
	12/9/2004	326.0	850	44
	12/15/2004	339.9	1.5	120
299-15-46	1/31/2006	226.5	1342	18
	2/1/2006	275.5	4096	37
299-W15-6	10/28/2004	318.2	110	1100
	11/14/2005	368.1	834	146
	11/14/2005	406.1	1003	235
299-W15-50	2/2/2005	285.0	1540	115
	2/7/2005	318.0	2000	52
299-W15-35	2/22/2006	254.0	2200	13
299-W15-7	8/14/1996	211.6	720	29
	8/14/1996	309.3	730	99
	2/22/2007	SI	2100	13
299-W15-34	2/22/2006	258.5	3200	18
	12/21/2005	280.6	3358	12
299-W15-41	2/15/2007	SI	1300	11
299-W15-44	2/15/2007	SI	2100	13
299-W14-15	-	-	-	-
299-W14-13	8/2/2006	SI	110	1.6
299-W14-1	-	-	-	-
299-W11-26	-	-	-	-
299-W11-43	6/1/2005	298.0	900	13
	6/9/2005	363.8	450	54
	6/21/2005	449.1	1100	46
299-W6-10	9/1/2005	SI	200	4.5
699-48-71	1/12/2007	SI	20	2.7

Well	Date	Depth (ft bgs)	[CCl$_4$] (µg/L)	[CHCl$_3$] (µg/L)
299-W15-46	1/31/2006	226.5	1342	18
	9/14/2004	229.2	330	150
	10/13/2005	232.5	1248	18
	10/13/2005	242.5	2116	22
	10/14/2005	253.5	2362	23
	10/11/2004	257.0	120	220
	2/1/2006	275.5	4096	37
	2/1/2006	286.5	2567	25
	10/19/2004	292.0	2918	413
	10/25/2004	297.5	286	1039
	10/28/2004	318.2	110	1100
	11/2/2004	338.9	32	690
	11/8/2004	357.0	258	353
	11/10/2004	365.6	1300	180
	11/15/2004	378.2	470	280
	11/23/2004	399.9	8.7	290
	11/30/2004	419.0	206	482
	1/13/2005	482.0	2.2	36
	1/26/2005	522.5	3	217

Table 1. a) Representative CCl$_4$ and CHCl$_3$ concentrations for all wells with available data in the transect. Concentrations are from depth discrete intervals except where marked SI, which are average concentrations over the screened interval of the well, and b) more detailed resolution of CCl$_4$ and CHCl$_3$ concentrations from well 299-W15-46. Peaks in CCl$_4$ and associated peaks in CHCl$_3$ are highlighted in blue.

Table 1a. Where more than one routine measurement was available, data from the closest date to February, 2007 was used. Although depth discrete contaminant concentrations for some wells are available at higher spatial resolutions, only select depths are displayed in Table 1a. Table 1b shows CCl$_4$ and CHCl$_3$ concentrations in well 299-W15-46 in more detail. Using these data, extent and concentrations of the CCl$_4$ and CHCl$_3$ plumes were estimated. Only aqueous CCl$_4$ within the unconfined aquifer was identified, and both plumes were interpreted to have failed to permeate the Lower Mud unit where the unit is continuous.

RESULTS

Data from manual digitization of geophysical logs is consistent with data regarding stratigraphic depths of peaks evident in digital geophysical records. However, actual counts per second values vary, sometimes considerably, between the two record types (Fig. 2). Discrepancies between the records appear clustered by depth, suggesting a systematic error in digitization.

Subsurface geology is modeled in a curvilinear transect through the central to northeastern 200 West Area, as displayed in Figure 3. Units generally dip toward the southwest, but vary in thickness and continuity; a short summary of lithofacies trends are presented. The Ringold Lower Mud unit thins toward the northeast, eventually pinching out shortly beyond well 299-W11-43. However, the underlying Ringold A unit thickens toward the northeast, contacting the Ringold E unit where the Lower Mud is absent and thus connecting the confined and unconfined aquifers. The water table in this portion of the 200 West Area generally decreases in elevation along the transect toward the northeast.

Above the water table and the Ringold E unit, the Cold Creek Unit extends throughout the transect, ranging in thickness from approximately 4 to 16 m. A thin, discontinuous caliche layer is found at the bottom of this unit. A lower sand-dominated and an upper gravel-dominated subunit of the Hanford formation are present throughout the transect, with the transition from the lower to upper subunits nearly always a sharp contact. Holocene sand,
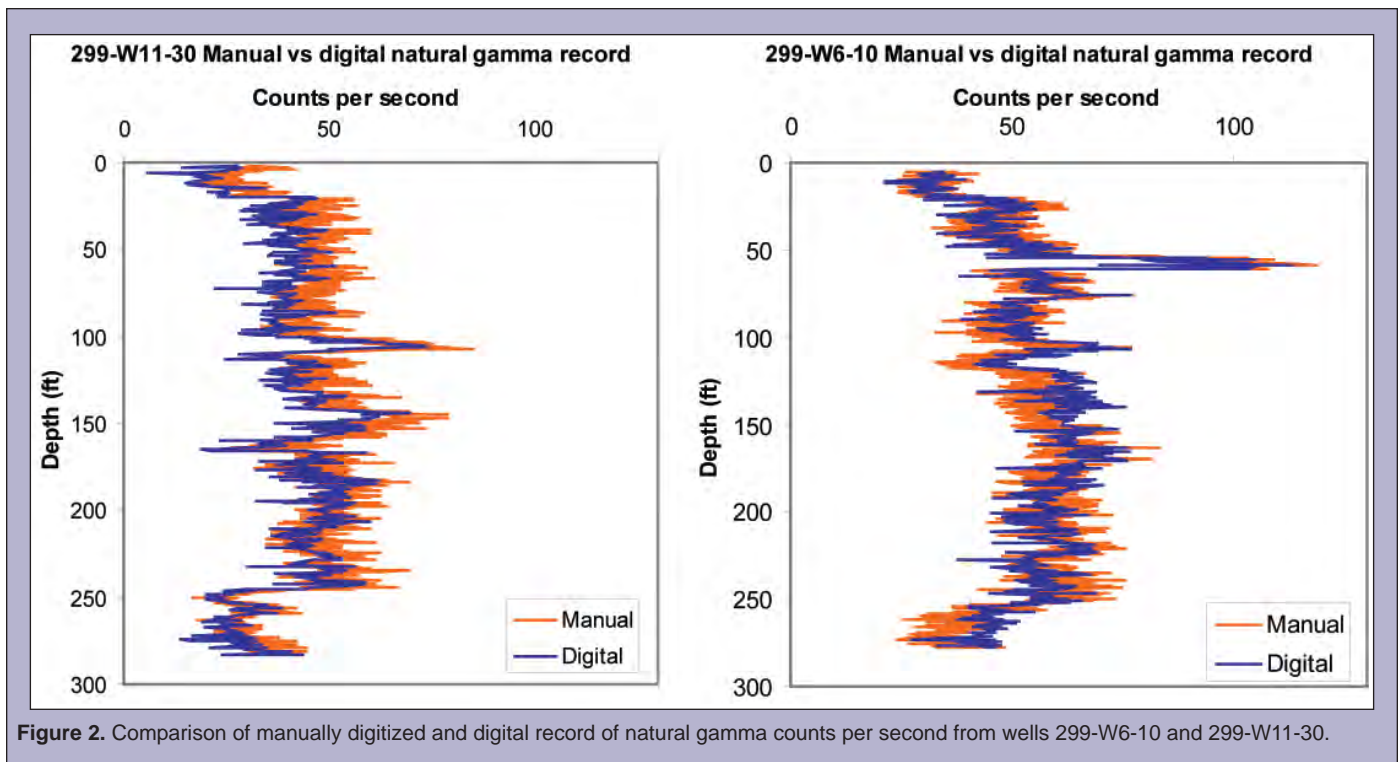
Figure 2. Comparison of manually digitized and digital record of natural gamma counts per second from wells 299-W6-10 and 299-W11-30.

as it is elsewhere in the 200 West Area, is discontinuous along the transect.

Results show an extensive low-concentration area (greater than 5 µg/L) of the CCl_4 plume, with increasing concentrations (greater than 1000 µg/L) extending over 1200 m along the transect (Fig. 3). While the CCl_4 plume sits above the Lower Mud sequence where the unit is present, discontinuities in the unit to either side of the transect have permitted CCl_4 to permeate into the confined (Ringold A) aquifer in the northeast of the 200 West Area. Highest CCl_4 concentrations are located around well 299-W15-46 and wells 299-W15-34 through 299-W15-44; both 299-W15-34 and 299-W15-44 are groundwater extraction wells for the pump and treat remediation system. Finer-grained sand or mud layers frequently form the bottom boundary of these high concentration areas (Fig. 3).

Chloroform concentrations are usually one to two orders of magnitude less than those of CCl_4, with the exception of $CHCl_3$ concentrations of up to 1,100 µg/L around well 299-W15-46 in central 200 West. When considering sample records from discrete depths within individual wells, higher concentrations of $CHCl_3$ are generally located near higher concentrations of CCl_4. Furthermore, in many instances peaks in $CHCl_3$ concentrations occur stratigraphically lower (by less than 8 m) than the associated peak in CCl_4 concentration (Table 1b, Fig. 3). This trend is well represented by depth discrete CCl_4 and $CHCl_3$ concentrations from well 200-W15-46 (Table 1b).

DISCUSSION AND CONCLUSION

Concentrations of carbon tetrachloride in the groundwater of the 200 West Area appear to be affected by a combination of sediment type and unit continuity, down-gradient groundwater
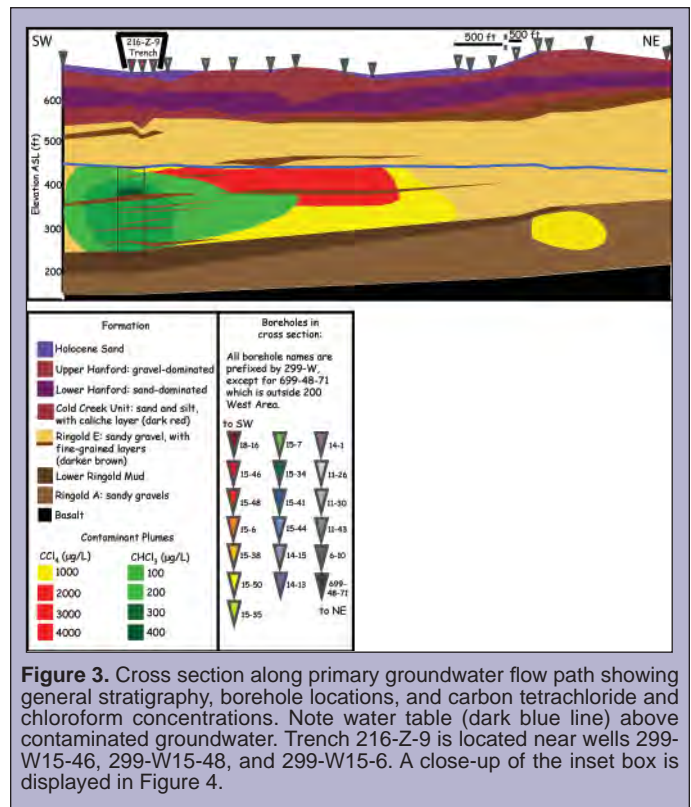
Figure 3. Cross section along primary groundwater flow path showing general stratigraphy, borehole locations, and carbon tetrachloride and chloroform concentrations. Note water table (dark blue line) above contaminated groundwater. Trench 216-Z-9 is located near wells 299-W15-46, 299-W15-48, and 299-W15-6. A close-up of the inset box is displayed in Figure 4.

flow, injection and extraction wells, and to a lesser extent reductive dechlorination of CCl_4 to $CHCl_3$. At present, the two areas of highest CCl_4 concentration along this study's northeast-southwest transect are located below the 216-Z-9 trench (Fig. 3) and at extraction wells. Those locations are precisely where highest concentrations would be expected during a successful remediation
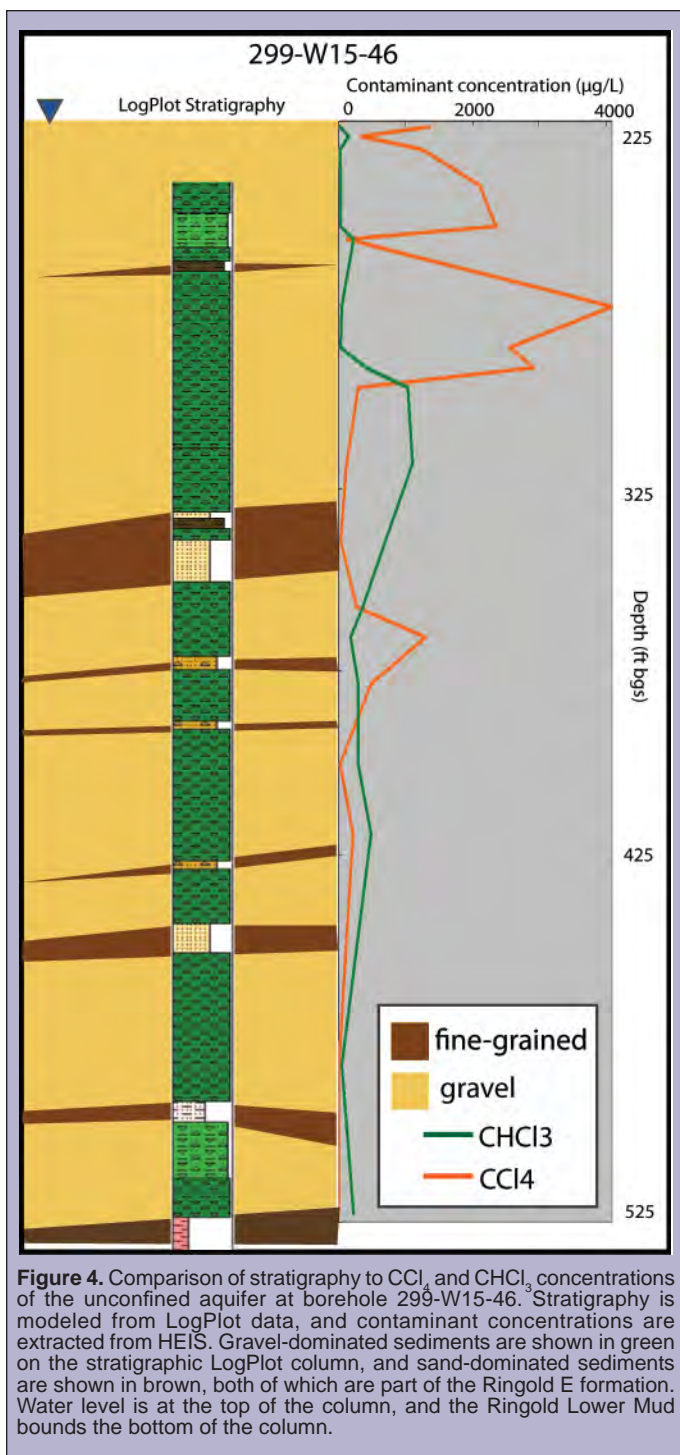
Figure 4. Comparison of stratigraphy to CCl_4 and $CHCl_3$ concentrations of the unconfined aquifer at borehole 299-W15-46. Stratigraphy is modeled from LogPlot data, and contaminant concentrations are extracted from HEIS. Gravel-dominated sediments are shown in green on the stratigraphic LogPlot column, and sand-dominated sediments are shown in brown, both of which are part of the Ringold E formation. Water level is at the top of the column, and the Ringold Lower Mud bounds the bottom of the column.

process, and this pattern was found in other, larger-scale studies of CCl_4 in the 200 West Area [6]. This demonstrates some success in the pump and treat remediation effort.

During discussion of contaminant concentrations presented in this report, it should be remembered that data was collected over a 2.5 year time span. Thus, some changes in concentrations by depth are partially an artifact of the sampling time.

Stratigraphic control on downward migration of CCl_4 is evident at several layers of fine-grained sediment (Figs. 3, 4). The depth discrete record of well 299-W15-46, which exhibits the highest CCl_4

concentration along this transect, shows that all concentrations above 2000 µg/L are confined between two thin layers of sand (Figs. 3, 4). Highest recorded CCl_4 concentrations for wells 299-W18-16, 299-W15-6, and 299-W15-50 are all located at thin (less than 2 m) layers of relatively fine-grained material. With the exception of 299-W15-7, all other wells in this transect with a depth discrete record of CCl_4 concentration were sampled over a saturated interval that only included gravels. This indicates that thin, fine-grained layers within the generally coarse-grained Ringold E unit partially inhibit downward CCl_4 migration.

Frequent presence of $CHCl_3$ peaks stratigraphically below those of CCl_4 suggest that if $CHCl_3$ is present primarily because of CCl_4 dechlorination, variations in sediment grain size have a strong effect on this reaction. Alternative sources of $CHCl_3$ include past waste discharges into a nearby tile field [6] and impurities in the originally disposed CCl_4. If $CHCl_3$ and CCl_4 have different source locations, comparison between the stratigraphic controls on the two contaminants is less accurate. Additionally, sampling resolution is generally coarse, with records 5–10 m apart, resulting in uncertainty in actual peak values and locations. Therefore, peaks in concentrations for both contaminants may be stratigraphically closer than they appear at this sampling resolution.

Despite these uncertainties, data from several wells in this transect (e.g. 299-W15-46, 299-W15-50, and 299-W18-16) indicate that peaks in $CHCl_3$ are associated with the transformation of CCl_4 (Table 1b). Carbon tetrachloride is rapidly dechlorinated into $CHCl_3$ when reacted with Fe^{2+}:

$$CCl_4 + 2Fe^{2+}(Porph) + H^+ \rightarrow CHCl_3 + Fe^{3+}(Porph) + Cl^- \quad (1)$$
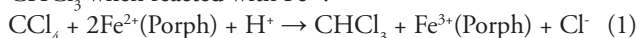
where Fe^{2+}(Porph) is a reduced iron porphyrin hydroxide found under iron-reducing conditions [13, 14]. In borehole samples, these reducing conditions are indicated by green, gray, blue, or olive brown sediments. Sediments in the 200 West Area possessing iron necessary for the above reaction to occur include carbonates and those incorporating iron-rich basalt.

For individual wells with sufficient data, the presence of reducing conditions and iron-containing minerals can tentatively be related to CCl_4 and $CHCl_3$ concentrations at a given depth. The borehole record for well 299-W18-16 identifies olive brown sediment at the only recorded depth at which $CHCl_3$ concentrations are greater than those of CCl_4. The record for well 299-W15-46 shows that the highest ratio of $CHCl_3$ to CCl_4 above the Lower Mud Unit is found in greenish to gray sediment. While these few examples cannot conclusively indicate a correlation between reduced, iron-containing sediments and high transformation rates of CCl_4 to $CHCl_3$, they do suggest that further study of this relationship is warranted.

Most studies documenting the stratigraphy of the Hanford Site describe sedimentary units that are generally between 10 and 100 m thick [1, 10]. While the scale of these divisions is useful in predicting low-resolution contaminant migration, heterogeneities in mineral composition, grain size, and a layer's capability to provide a reducing environment vary on the scale of decimeters to meters (Fig. 3). These heterogeneities appear to strongly influence transport of $CHCl_3$ and CCl_4, and dechlorination of CCl_4. To accurately predict future contaminant migration, small-scale subunits of the accepted sedimentary units should be identified and mapped throughout

the CCl$_4$ plume area. The stratigraphic model presented in this study provides a guide for beginning this work, but is limited in its coverage. During mapping, particular attention should be paid to sediment color and composition (indicators of reducing conditions), and to grain size. In addition, prediction of contaminant transport would be benefited by geochemical studies comparing sediment color to reducing conditions on the Hanford Site.

REFERENCES

[1] G.W. Gee, M. Oostrom, M.D., Freshley, M.L. Rockhold, and J.M., Zachara, "Hanford Site vadose zone studies: an overview," Vadose Zone Journal, v. 6, no. 4, p. 899-905, 2007.

[2] H.G. Wilshire and I. Friedman, "Contaminant migration at two low-level radioactive waste sites in arid western United State- a review", Environmental Geology, v. 37, no. 1-2, p. 112-123, 1999.

[3] M.J. Truex, C.J. Murray, C.R. Cole, R.J. Cameron, M.D. Johnson, R.S. Skeen, and C.D. Johnson, "Assessment of carbon tetrachloride groundwater transport in support of the Hanford carbon tetrachloride innovative technology demonstration program," PNNL-13560, Pacific Northwest National Laboratory, Richland, Washington, 2001.

[4] C.J. Murray, Yi-Ju Bott, and M.J. Truex, "Persistence and Inventory of Carbon Tetrachloride in the 200 West Area of the Hanford Site," Pacific Northwest National Laboratory, Richland, Washington, 2007.

[5] W.L. Bratton, K.R. Moser, and J.D. Doughty, "Carbon Tetrachloride Dense Non-Aqueous Phase Liquid (DNAPL) Source Term Interim Characterization Report," DOE/ RL 2006-58, U.S. Department of Energy, Richland, Washington, 2006.

[6] M.J. Hartman, L.F. Morasch, W.D. Webber, "Hanford Site Groundwater Monitoring for Fiscal Year 2005," PNNL 15670, Pacific Northwest National Laboratory, Richland, Washington, 2006.

[7] J.P. McKinley, J.M. Zachara, J. Wan, D.E. McCready, and S.M. Heald, "Geochemical controls on contaminant uranium in vadose Hanford Formation sediments at the 200 Area and 300 Area, Hanford Site, Washington," Vadose Zone Journal, v. 6, no. 4, p. 1004-1017, 2007.

[8] D.G. Horton, G.V. Last, T.J. Gilmore, B.N. Bjornstad, and R.D. Mackley, "A catalogue of geologic data for the Hanford Site," PNNL-13653, Pacific Northwest National Laboratory, Richland, WA, 2005.

[9] S.P. Reidel, and M.A. Chamness, "Geology Data Package for the Single-Shell Tank Waste Management Areas at the Hanford Site," Pacific Northwest National Laboratory, Richland, Washington, PNNL-15955, 2007.

[10] J.M. Zachara, J. Serne, M. D. Freshley, F. Mann, F. Anderson, M. Wood, T. Jones, and D. Myers, "Geochemical processes controlling migration of tank wastes in Hanford's vadose zone," Vadose Zone Journal, v. 6, no. 4, p. 985-1003, 2007.

[11] G.V. Last, C.J. Murray, D.A. Bush, E.C. Sullivan, M.L. Rockhold, R.D. Mackley, and B.N. Bjornstad, "Standardization of borehole data to support vadose zone flow and transport modeling," Vadose Zone Journal, v. 6, no 4., p. 906-912, 2007.

[12] PNL-MA-567, Procedures for Groundwater Investigations. DO-6, DO-7, DO-8, Pacific Northwest National Laboratory, Richland, Washington, 2006.

[13] Schwartzenbach, et al., Environmental Organic Chemistry. New York: Wiley-Interscience, 1993.

[14] R. Allen-King, "Geochemical and Physical Aquifer Property Heterogeneity: a Multi-scale Sedimentologic Approach to Reactive Solute Transport," State University of New York at Buffalo, 2006.

ABSTRACTS

TABLE OF CONTENTS

Biology

*The effect of inhibitors of the multi-xenobiotic resistance protein on domoic acid disposition in Dungeness crabs and Mediterranean mussels. *Laura Almaguer* (*Gavilan College, Gilroy, CA*) *Irvin Schultz* (*Pacific Northwest National Laboratory, Richland, WA*). Select species of marine algae primarily belonging to the genus *Pseudo-nitzchia* produce the toxin domoic acid (DA), making it a naturally occurring neurotoxin that contaminates shellfish that have fed on *Pseudo-nitzchia*. People ingest the neurotoxin by eating contaminated fish and shellfish; in extreme cases it can even cause death in humans and animals alike. The contamination of shellfish with domoic acid has caused health and economic problems world wide. Some species of shellfish retain domoic acid longer than others and it is not fully understood why. It is hypothesized that the multi-xenobiotic resistance (MXR) protein(s) identified in marine shellfish, functionally similar to mammalian counterparts p-glycoprotein (pgp) and OAT-1 (organic anion transporters), are associated with the unusual interspecies differences in domoic acid. To test this hypothesis both the uptake and excretion of DA was monitored by exposing one set of mussels with known pgp and OAT-1 inhibitors, verapamil and cyclosporine. Uptake of DA was determined using static water exposures where verapamil or cyclosporine injected mussels were placed in 1 L beakers containing soluble DA. Excretion of DA was studied by reversing this protocol and injecting DA into mussels placed in seawater containing verapamil. Subsequent experiments with crabs measured the excretion of injected DA beginning 1 hr after injection with either verapamil or cyclosporine. Water, hemolymph and digestive gland tissues were then analyzed for DA using High Performance Liquid Chromatography (HPLC) with either UV or fluorescence detection. Initial results suggest neither inhibitor altered the kinetics of DA in mussels and crabs.

Evaluation of Cloning Vectors pMCSG8 and pMCSG10 to Increase Protein Solubility. *Jessica Bearden* (*University of Texas – Pan American, Edinburg, TX*) *Shiu Moy* (*Argonne National Laboratory, Argonne, IL*). A major obstacle in the high-throughput production of purified proteins, as conducted in the Protein Structure Initiative, is to routinely obtain soluble proteins using the standard cloning vector pMCSG7. It is important that cloners release soluble proteins to the purification group because insoluble proteins cannot be purified. Evaluation of cloning vectors pMCSG8 and pMCSG10 was conducted to recover soluble proteins that failed to be soluble using pMCSG7. pMCSG7 has a histidine affinity tag at the N-terminus, followed by a tobacco etch virus(TEV) protease recognition site, followed by a ligation independent cloning site, followed by another histidine tag at the C-terminus. pMCSG8 is structurally similar to pMCSG7 with the exception of a binding loop(S-loop) of the chaperone protein GroES between the histadine tag and the TEV protease recognition site, while pMCSG10 has a Glutathione-S-Transferase(GST) in place of the S-loop. Selected samples were transformed and then cloned into the desired vector. Competent *Escherichia coli* cells were induced to uptake the recombinant DNA. Expression and solubility analysis was conducted using sodium dodecyl sulfate polyacrylamide gel electrophoresis. Clones that both expressed and were soluble were then frozen down and released to the protein purification team. pMCSG8 was able to recover ten percent of the samples tested. pMCSG10 analysis is still underway. pMCSG8 results implicate incorporation of a feedback loop in the high-throughput production of proteins at the Structural Biology Center at Argonne National Laboratory.

A Cell-Free Membrane Protein Factory Fueled by Rhodobacter Extracts. *Michael Bellisario* (*University of Illinois at Urbana-Champaign, Champaign, IL*) *Phil Laible* (*Argonne National Laboratory, Argonne, IL*). Membrane proteins play critical roles in many biological processes such as energy supply, solute import and export, and signal transduction. They are also ultra-critical to human health, comprising 60–80% of current drug targets. However, producing usable quantities of these proteins for structural and functional studies is quite challenging. Here, the goal is to eliminate this difficulty by creating a cell-free protein synthesis system specially designed for membrane proteins. This coupled transcription-translation system uses extracts (the source of all the enzymes and factors necessary for transcription and translation) derived from *Rhodobacter sphaeroides* cells, and membrane vesicles are introduced to the reaction in order to accommodate the membrane proteins being synthesized. This *in vitro* method has the capability to produce milligrams of target protein in a single milliliter reaction. In comparison, previously studied *in vivo* systems only produce milligrams of protein per liter of culture. The ultimate goal is to engineer this system so that it can be used generically and economically to produce target molecules for drug discovery.

Isolation of Organelles in an Itaconic Acid Producing Anamorphous Fungus. *Darby Bennett* (*Walla Walla Community College, Walla Walla, WA*)*; Ellen Panisko* (*Pacific Northwest National Laboratory, Richland, WA*). Filamentous fungi have been identified as platform organisms by the Department of Energy (DOE) in that they can be used for several different applications including: making industrial chemicals, use in pharmaceutical drugs and treatments, and conversion of biomass into usable fuels. The ability of *Aspergillus terreus*, ATCC strain 32359, to produce itaconic acid and a method to determine how production can be improved is one focus of our research program. Itaconic acid or methylene succinic acid is an unsaturated organic compound made in a portion of the Krebs cycle which produces copolymers used in strictly non-food products. It is not known which proteins are involved in the process that allows one strain of fungus to produce high amounts of itaconic acid, while others do not make this acid, but it is thought that some of the proteins responsible that have increased expression during the hyper productive growth state are involved in substrate/product transport. To examine this theory, the components of the cell membranes and mitochondria during the non-productive and hyper productive growth states were isolated. To accomplish this, several different digestive enzymes and centrifuging techniques were used. At each stage of the process, samples were collected and examined to determine the protein concentration and cell components present using protein assays and spectrophotometry. Proteins isolated from the organelles were separated according to size by gel electrophoresis, and probed by Western analyses to determine the extent of organelle enrichment. Preliminary results show that there are more proteins present in the hyper productive state than in the non-productive state, although this may be due to an increase in initial biomass collected for the hyper productive state. Follow up analyses will examine the proteins expressed in the two disparate itaconic acid production states to identify those proteins that may be responsible for hyper productivity. If the specific proteins responsible for increased production of itaconic acid can be identified and isolated, A. terreus can be engineered to produce industrially relevant quantities of itaconic acid.

Crystallographic Studies of Two Bacterial Antibiotic Resistance Enzymes: Aminoglycoside Phosphotransferase (2'')-Ic and GES-1 ß-lactamase. *Laura Byrnes* (*Rensselaer Polytechnic Institute, Troy, NY*) *Clyde Smith* (*Stanford Linear Accelerator Center, Stanford, CA*). Guiana Extended-Spectrum-1 (GES-1) and Aminoglycoside phosphotransferase (2'')-Ic (APH(2'')-Ic) are two bacteria-produced enzymes that essentially perform the same task: they provide resistance to an array of antibiotics. Both enzymes are part of a growing resistance problem in the medical world. In order to overcome the ever-growing arsenal of antibiotic-resistance enzymes, it is necessary to understand the molecular basis of their action. Accurate structures of these proteins have become an invaluable tool to do this. Using protein crystallography techniques and X-ray diffraction, the protein structure of GES-1 bound to imipenem (an inhibitor) has been solved. Also, APH(2'')-Ic has been successfully crystallized, but its structure was unable to be solved using molecular replacement using APH(2'')-Ib as a search model. The structure of GES-1, with bound imipenem was solved to a resolution of 1.89Å, and though the inhibitor is bound with only moderate occupancy, the structure shows crucial interactions inside the active site that render the enzyme unable to complete the hydrolysis of the ß-lactam ring. The APH(2'')-Ic dataset could not be matched to the model, APH(2'')-Ib, with which it shares 25% sequence identity. The structural information gained from GES-1, and future studies using isomorphous replacement to solve the APH(2'')-Ic structure can aid directly in the creation of novel drugs to combat both of these classes of resistance enzymes.

Crystallization and Preliminary X-ray Crystallographic Analysis of the Archaeal Tryptophan Regulator, TrpY. *Jacquelyn Cafasso* (*Cornell University, Ithaca, NY*). *Mark Chance, Babu Manjasetty,* (*Brookhaven National Laboratory, Upton, NY*). The TrpY protein from the archaeon *Methanothermobacter thermautotrophicus* is a transcription regulator of the metabolically expensive tryptophan biosynthetic pathway. Although the trp genes in Bacteria, *archaea*, and *eukaryotes* share a common ancestry, diverse mechanisms regulate their expression. The TrpR repressor in *E. coli* has been extensively studied, but the structure and mechanism for repression by the TrpY regulator from archaea remains unknown. Furthermore, TrpY shows very little sequence homology with the TrpR tryptophan regulator in *E. coli*, and although bioinformatics studies indicate that the fold is conserved among other archaeal transcription regulators, the sequence

similarity to TrpY is nonetheless very low. Native crystals of TrpY were successfully grown in 0.1 M sodium acetate and 1.6 M ammonium sulfate at room temperature using the hanging-drop vapor diffusion method. Initial diffraction tests and the search for a suitable cryo-protectant were performed at beamline X3A of the National Synchrotron Light Source (NSLS). X-ray diffraction data was collected at beamline X29 of the NSLS to 2.9 Å resolution. Preliminary data analysis revealed that the crystals fall in the tetragonal space group with cell parameters a=b=87Å, c=147Å. Methods to solve the structure of TrpY using heavy atom derivatives are currently underway. Using crystallographic X-ray analysis to solve the structure is important to gain insight into the TrpY mechanism of repression as well as important features of transcription regulation and evolutionary history in the Archaea. This project is a small portion of a larger project under investigation in collaboration with the Department of Microbiology at The Ohio State University.

Hydrogen Production by the Cyanobacterium *Plectonema boryanum*: Effects of Initial Nitrate Concentration, Light Intensity, and Inhibition of Photosystem II by DCMU. *BLAINE CARTER* (*Northwest Nazarene University, Nampa, ID*) *MICHAEL HUESEMANN* (*Pacific Northwest National Laboratory, Richland, WA*). The alarming rate at which atmospheric carbon dioxide levels are increasing due to the burning of fossil fuels will have incalculable consequences if disregarded. Fuel cells, a source of energy that does not add to carbon dioxide emissions, have become an important topic of study. Although significant advances have been made related to fuel cells, the problem of cheap and renewable hydrogen production still remains. The cyanobacterium *Plectonema boryanum* has demonstrated potential as a resolution to this problem by producing hydrogen under nitrogen deficient growing conditions. *Plectonema boryanum* cultures were tested in a series of experiments to determine the effects of light intensity, initial nitrate concentration, and photosystem II inhibitor DCMU (3-(3,4-dichlorophenyl)-1,1-dimethylurea) upon hydrogen production. Cultures were grown in sterile Chu. No. 10 medium within photobioreactors constantly illuminated by halogen lights. Because the enzyme responsible for hydrogen production is sensitive to oxygen, the medium was continuously sparged with argon/CO_2 (99.7%/0.3% vol/vol) by gas dispersion tubes immersed in the culture. Hydrogen production was monitored by using a gas chromatograph equipped with a thermal conductivity detector. In the initial experiment, the effects of initial nitrate concentration were tested and results revealed cumulative hydrogen production was maximum at an initial nitrate concentration of 1 mM. A second experiment was then conducted at an initial nitrate concentration of 1 mM to determine the effects of light intensity at 50, 100, and 200 μmole/m^2·s. Cumulative hydrogen production increased with increasing light intensity. A final experiment, conducted at an initial nitrate concentration of 2 mM, tested the effects of high light intensity at 200 and 400 μmole/m^2·s. Excessive light at 400 μmole/m^2·s decreased cumulative hydrogen production. Based upon all experiments, cumulative hydrogen production rates were optimal at an initial nitrate concentration of 1 mM and a light intensity of 100 μmole/m^2·s. DCMU was shown in all experiments to severely decrease hydrogen production as time progressed. With the information acquired so far, future experiments with reducing substances could determine maximum rates of hydrogen production. If maximum hydrogen production rates proved to be large enough, *Plectonema boryanum* could be grown on an industrial scale to provide hydrogen gas as a renewable fuel.

Improving Power Density of a Microbial Fuel Cell by Optimizing Electrode Area and Substrate Delivery. *SCOTT CESAR* (*Western Michigan University, Kalamazoo, MI*); *ABHIJEET BOROLE* (*Oak Ridge National Laboratory, Oak Ridge, TN*). Microbial Fuel Cells (MFC's) are devices which use micro-organisms as catalysts to oxidize compounds such as lactate whereby electrons are released and are allowed to flow between electrodes to generate current. The box-type MFC involved used *Shewanella oneidensis* in a minimal media with lactate and a carbon felt electrode as the anode. An air cathode was used involving a platinum/carbon electrode. Improving the power density output of an air cathode MFC was the primary goal if this work. The MFC performance can be assessed by analyzing the electrical and chemical/biochemical parameters of the system. The current can be determined by monitoring the voltage across a fixed load using a voltmeter. The electrical performance of the MFC can be determined by first measuring the open circuit voltage (OCV) and current produced across a variable load resistor. Along with electrical measurements, samples of the anode solution are taken to determine the changes in biochemical characteristics of the MFC. Under no-flow conditions, the MFC stabilized at 0.177 volts. With the introduction of flow to the system, the MFC stabilized at 0.347 volts. The power density at this time was found to be 128.6 mW/m^2 with a current density of 446.4 mA/

m^2. Further improvements in power delivery are possible via a more compact design of the fuel cell and flow of the media across a three-dimensional electrode.

Wind energy educational outreach program: Bringing Wind Energy to Schools. *BRENT CUMMINGS* (*Brigham Young University – Idaho, Rexburg, ID*); *GARY SEIFERT* (*Idaho National Laboratory, Idaho Falls, ID*). Educational outreach programs play an important role in the proliferation of renewable energy sources throughout the United States. An outreach website named "Wind Energy for Educators" was developed by educators in Idaho in order to educate the public about wind energy. This website contains information on wind energy, and also has some lesson plans on wind and how to use the energy that the wind contains. By teaching students in the classroom about renewable energy and its potential they can make educated decisions in the future about whether they want to support renewable energy projects or not. They will also be aware of possible career opportunities that are available to them. As part of the outreach program a skystream wind turbine was erected at Skyline High School in Idaho Falls, Idaho. The turbine will allow the students at the high school to participate in some hands on learning. It is also located next to an interstate highway where it can be seen by the public. The data gathered about the energy produced by the turbine will be recorded and made available to students via a web site for educational purposes. Education modules that use the information gathered about the turbine are being developed. These modules will deal with subjects such as understanding what a kilowatt hour is, CO_2 emissions, sound monitoring, and others. Although the turbine will not significantly reduce the schools expenditures for energy, it will provide many useful educational opportunities.

A Rational Approach for Crystallization of Proteins in Deuterated Media. *ALEXIS RAE DEL CASTILLO* (*California State University – Channel Islands, Camarillo, CA*); *HUGH O'NEILL* (*Oak Ridge National Laboratory, Oak Ridge, TN*). Neutron crystallography is emerging as a powerful tool for the study of protein structure and dynamics. In neutron crystallography the neutrons interact weakly with the nucleus of an atom and therefore are a highly penetrating and non-destructive probe. Unlike X-rays, which interact with the electron cloud surrounding an atom, neutrons can detect lighter atoms such as hydrogen in the presence of heavier ones and differentiate between them. The aim of this study was to determine how reagents influence the crystallization behavior of proteins in order to improve the growth of crystals for neutron crystallography. In order to achieve this goal a range of proteins were selected for crystallization studies, including several proteins for which the crystallization behavior is well established, and several other targets which were over-expressed in Escherichia coli in hydrogenated and deuterated media. The recombinant proteins were purified to homogeneity by three-phase partitioning and anion exchange chromatography. The conditions for crystallization of each protein were determined using a high throughput screening platform. Conditions that produced crystals were then optimized and refined in order to produce large crystals suitable for neutron crystallographic analysis.

*The Effects of Nicotine Exposure on Cytochrome P450-Mediated Metabolism of Chlorpyrifos in Sprague-Dawley Rats. *JOSH ELSASSER* (*California State University – Fresno, Fresno, CA*); *CHARLES TIMCHALK* (*Pacific Northwest National Laboratory, Richland, WA*). Chlorpyrifos (CPF) is a common organophosphate insecticide used for pest control. CPF is metabolized to chlorpyrifos-oxon (CPF-Oxon) and 3,5,6-trichloro-2-pyridinol (TCP). The metabolite of most concern is CPF-Oxon since it is responsible for acetylcholinesterase (AChE) inhibition. The inhibition of AChE activity can adversely impact cholinergic function and if severe enough can result in central and peripheral neurotoxicity. Studies have shown that both nicotine (smoking) and ethanol (drinking) can induce cytochrome P450s (CYP450), the enzyme family responsible for the metabolism of CPF. Since the enzymatic profiles of CYP450 are expected to be altered due to nicotine exposure, this could modify the metabolism of CPF. Thus, the aims of this study are to characterize the changes in CYP450 profiles and CPF metabolism associated with nicotine induction. Rats were dosed subcutaneously (s.c.) with 1 mg of nicotine/kg body weight daily. Liver microsomes were prepared 4 hour, 24 hour, 7 day, 7 days and 4 hours, and 10 days post-dosing. Total amounts of protein and CYP450s in microsome samples were determined by spectrophotometry. *In vitro* metabolism studies were also conducted to measure the formation of CPF-Oxon and TCP using gas chromatography/mass spectrometry (GC/MS). CPF was incubated with microsomal samples in 1 mL of 50 mM HEPES buffer containing 15 mM $MgCl_2$ and 1 mM EDTA at 37°C and 1 mM NADPH was added to initiate the reaction, which was terminated after 20 minutes by

the addition of 200 µL of NaCl-saturated 2.5 N acetic acid solution. Initial analysis of the data did not provide any conclusive evidence to suggest that nicotine exposure produced substantial changes in either the amount of CYP450 or the amount of metabolites within the microsome samples. Further experimentation will be needed to identify if a change did occur particularly at the level of individual CYP450 forms. The results from this study are being used to design an *in vivo* pharmacokinetic study for the risk assessment of concurrent nicotine, ethanol and CPF exposure.

Marine Mussel Adhesive Protein Production in *Saccharomyces cerevisiae*. Kindra Engels (*Washington State University, Pullman, WA*); Frank Roberto (*Idaho National Laboratory, Idaho Falls, ID*). The adhesion proteins used by *Mytilus edulis* (blue mussel) to cling to surfaces in an aqueous environment have many features, such as strength and water resistance, that make them a potentially useful adhesive. Three *M. edulis* foot proteins (Mefp) will be the focus of this study: Mefp-1 (115 kDa), which forms a hardened sheath around the byssal threads, Mefp-2 (42–47 kDa), which adds stability near the attachment site, and Mefp-3 (5–7 kDa), which may act as an adhesion primer. Because it takes 10,000 mussels to obtain 1g of an individual native mussel adhesive protein, a more practical production method was investigated. Mussel adhesive protein genes were introduced into clones of *Saccharomyces cerevisiae*, with Mefp-1 in clone #21, Mefp-2 in clone QTB10, and Mefp-3 in clone #11. *S. cerevisiae* cultures (20 liters) were grown in a 2% galactose SC-U induction medium at 30°C with shaking and harvested by centrifugation. Growth was monitored by spectrophotometry. Cells were homogenized and lysed in an acidic breaking buffer with glass beads in a bead beater. After centrifuging again, the recombinant mussel adhesive protein in the supernatant was purified by dialysis with nanopure water and a sodium borate solution (pH 8.5). Centrifugal filter devices concentrated the proteins. Protein concentration was determined using a Bradford assay with bovine serum albumin as a standard. Samples were analyzed by electrophoresis. Results from growth curves revealed that 20 L cultures had optimal harvest times after 24 hours and cell pellet wet weights of 114.55g (#21), 102.69g (QTB10), and 185.512g (#11) were obtained. Electrophoresis of #21 and QTB10 purified proteins resulted in bands near the expected size ranges of recombinant proteins Mefp-1 and Mefp-2. In conclusion, the results suggest that adhesive protein production in *S. cerevisiae* cells is possible and that purification methods successfully concentrated the adhesive proteins. This method could potentially be used to produce recombinant adhesive protein quantities that would normally require the sacrifice of thousands of mussels. The *M. edulis* recombinant adhesive proteins obtained may be used for various studies involving the proteins' adhesive potential and further formulation development.

Phosphate Enhanced Uranium Reduction. Rachel Fairbank (*Tompkins Cortland Community College, Dryden, NY*); Anthony V. Palumbo (*Oak Ridge National Laboratory, Oak Ridge, TN*). A common contaminant found at DOE sites is uranium, which characteristically leaches into groundwater and surrounding soils. Remediation of these sites is therefore a DOE focus. Current technologies mainly consist of pump and treat technologies which have the disadvantage of being invasive and ineffective in areas with low flow velocity. Total cleanup costs using existing technologies are estimated to exceed a total of $220 billion, making it worthwhile to investigate alternative methods of uranium remediation. One focus for remediation is the stabilization of uranium through reduction of mobile U(VI) to its less soluble and immobile form U(IV). One possibility is by stimulating existing microbial communities to reduce uranium. Previous experiments had demonstrated the ability of electron donors' ethanol and methanol to stimulate bioreduction of uranium. This experiment investigated the idea of phosphate being a limiting nutrient in bioreduction of uranium. Anaerobic microcosms were created using contaminated soil from the Oak Ridge Field Research Center. Samples were analyzed at specific time points throughout the experiment using a Kinetic Phosphorescence Analyzer which measured the amount of soluble uranium. This experiment found that the addition of phosphates led to immediate removal of uranium from solution. This effect was observed to be independent of the presence of an electron donor, as a similar effect was observed in the microcosms with only phosphates added. Therefore, these results imply that reduction is due to a chemical interaction with the phosphates rather than due to stimulation of the microbial community.

Effects of Phosphate on the Bioreduction of Iron Oxyhydroxide. Kathryn Fenske (*University of Illinois at Urbana-Champaign, Urbana, IL*); Edward O'Loughlin (*Argonne National Laboratory, Argonne, IL*). Green rusts are mixed ferrous/ferric hydroxides minerals that form in suboxic environments as products of Fe(III) oxide reductions by dissimilatory iron-reducing bacteria (DIRB), and as such play an important role in Fe cycling in aquatic and terrestrial environments. DIRB can conserve energy and also support growth by coupling the oxidation of organic compounds to the reduction of Fe(III) to Fe(II) with the potential formation of Fe(II)-bearing minerals such as magnetite, siderite, and green rust. The overall processes of the formation of a specific Fe(II)-bearing mineral, such as green rust, are controlled by several factors including microbial physiology, solution chemistry, and Fe(III) mineralogy. This experiment examines the effects of phosphate on the type(s) of Fe(II)-bearing minerals resulting from the bioreduction of a Fe(III) oxyhydroxide (lepidocrocite). Experimental systems consisted of sealed serum vials containing lepidocrocite with formate provided as an electron donor. Different amounts of phosphate were added to each system and they were inoculated with Shewanella putrefaciens CN32, a model DIRB. Lepidocrocite reduction was monitored by measuring Fe(II) by the Ferrozine assay. Biomineralization products were identified by X-ray diffraction. Analyses of results indicate that green rust formed when phosphate was present at concentrations of 100 µM or higher, while magnetite formed at phosphate concentrations below 100 µM. Green rusts have recently been shown to be capable of reducing a number of organic and inorganic contaminants (including carbon tetrachloride and U(VI)). Therefore, understanding how factors such as phosphate concentration can contribute to the formation of green rusts may assist in efforts to design remediation strategies for cleanup of subsurface contamination.

Elucidating a Practical Approach to the Study of Eukaryotic Genes: Expression of Eukaryotic Zebrafish Proteins in Prokaryotic *E coli* Expression Vectors. Ashley Frank (*Elmhurst College, Elmhurst, IL*); Frank Collart (*Argonne National Laboratory, Argonne, IL*). Production of heterologous protein via expression in prokaryotic expression vectors has been extensively employed in recent years to yield significant amounts of protein for downstream characterization and analysis. The use of such vectors offers a practical, economical route for the production of protein, eliminating cost and time inefficiencies accompanying protein isolation from the native protein-producing organism. While bacterial expression systems have been optimized for cloning prokaryotic genes, further investigation is needed to optimize these systems for production of more complex eukaryotic proteins. The cell machinery of a bacterial expression system is limited with respect to the production of eukaryotic proteins as these proteins are derived from more intricate, compartmentalized cells and often require specific enzymes for post-translational modifications and protein folding. Since many of the enzymes and machinery necessary for the successful expression of eukaryotic proteins are lacking in the current bacterial expression systems, study of such proteins has been avoided using these methods. To accommodate the requirements of eukaryotic protein production in bacterial expression systems, periplasmic expression vectors have been constructed and modified using previous cytoplasmic vector templates to optimize the expression and solubility of eukaryotic proteins. Such vectors direct proteins to the periplasm where bacterial chaperones reside to aid in proper protein folding and disulfide bond formation which is required by many eukaryotic proteins, thus increasing protein solubility and recovery potential. In a study to determine a successful approach to the production of eukaryotic proteins, 96 select Zebrafish genes were amplified, cloned into two different periplasmic vectors (pBH31 and pMCSG19p), induced to express the heterologous target protein, and screened for positive expression and solubility. Results suggest that pMCSG19p, which harbors a solubility fusion tag, was superior in performance, with respect to the production of soluble proteins for these 96 targets. In addition, expression in this vector resulted in a relative increase in solubility of targets containing predicted disulfide bonds and signal peptides, suggesting that pMCSG19p may provide an effective route for the production of complex eukaryotic proteins. The solubility results for proteins produced in pBH31, however, were comparable to the solubility results of these same 96 targets produced in the cytoplasmic vector, pMCSG7, suggesting that this vector not only does not improve solubility of eukaryotic proteins, but also may not shunt the proteins to the periplasm for proper expression. Further studies employing different vector solubility tags or manipulation of cytoplasmic physiology may be required for the optimization of eukaryotic protein expression in bacterial expression systems.

Extracellular Translocation of Recombinant MtrC and OmcA by Type II Secretion System. Shirabrandy Garza (*Washington State University, Pullman, WA*); Liang Shi (*Pacific Northwest National Laboratory, Richland, WA*). Dissimilatory reduction of metal (e.g., Fe, Mn) (hydr)oxides represents a challenge for microorganisms, as their

cell envelopes are impermeable to metal (hydr)oxides that are poorly soluble in water. Outer membrane decaheme c-type cytochromes MtrC and OmcA of *Shewanella oneidensis* MR-1 are extracellular lipoproteins important for dissimilatory reduction of solid metal (hydr)oxides during anaerobic respiration. To investigate the roles of type II secretion system (T2S) in translocation of MtrC and OmcA across outer membrane, we measured the effects of deleting two T2S genes, gspD and gspG, on the secretion of recombinant MtrC and OmcA when cells were grown under anaerobic conditions. Deletion of gspD or gspG resulted in slightly yellowish supernatants of cell culture, different from the pink supernatant of wild type (wt). Subsequent analysiss with heme-staining and Western blot showed that deletion of gspD or gspG not only reduced the abundances of recombinant MtrC and OmcA in the supernatants, but also increased their abundances inside the cells. Thus, our results indicate that T2S facilitates translocation of recombinantMtrC and OmcA across outer membrane.

Metal Repartition and Expressed Genes in Spinal cord of Rats.
SERITTA HILL (*Chicago State University, Chicago, IL*)*; CHRISTINE GERIN* (*Argonne National Laboratory, Argonne, IL*). Specific metals such as Fe, Cu, and Zn have been shown to accumulate in the central nervous system (CNS) in several neurodegenerative diseases such as amyotrophic lateral sclerosis (ALS). Metal involvement has been linked to neural degeneration in late onset neurodegenerative diseases. The hypothesis is that similar cellular patterns of degeneration might occur in spinal cord injury. The first aim addresses the question of metal repartition in spinal cord of rats, using X-ray fluorescence. The second aim addresses the question of variation in expression targeted genes in spinal cord using quantitative real time polymerase chain reaction (QRT-PCR). Rats were anaesthetized with sodium pentobarbital (60 mg/1,000g) injected intraperitoneally. Spinal cord segments T9 and T13 were excised. RNA isolation was performed using TriZol protocol (Sigma). RNA was purified using RNA clean up kit (Qiagen). Two μl of the RNA sample were used to determine the optic density (OD) and the concentration in ng/μL. Three RNA dilutions were made to construct a concentration curve for c DNA and QRT-PCR. cDNA was synthesized using 10 μL of RNA followed by QRT- PCR using 11 housekeeping genes (primers). Most of our RNA OD results were 2.0 for the 260/280 ratio and for the 260/230 they were in the ranges of 1.8–2.2. The concentration of RNA samples ranged from 5.4 ng/μl to 1,200 ng/μl. OD curves illustrated that RNA absorbed the highest at 260 nm. RT-PCR demonstrated two curves for each RNA concentration and it illustrated that the c DNA with their various primers amplified properly. In conclusion the housekeeping genes were expressed in our samples. In the future the house keeping genes will be compared to our gene of interest. For example, BDNF. The Advance Photon Source (APS) beam line was used to train on cardiomyocytes in order to use it in the future to measure the sub cellular trace metals such as Zn, Fe, and Cu in our spinal cord samples. Experimental work was performed in collaboration with Argonne National Laboratory and Northwestern University.

*Successful Crystallization Leading to Structure of Protein Rv0632c from Mycobacterium tuberculosis.
JEFFREY HOHENSTEIN (*Contra Costa College, San Pablo, CA*)*; MINMIN YU* (*Lawrence Berkeley National Laboratory, Berkley, CA*). Tuberculosis (TB) is an infectious disease caused by *Mycobacterium tuberculosis* that results in over a million fatalities annually. The TB Structural Genomics Consortium (TBSGC) was formed to address diagnosis and treatment of TB by determination and analysis of the structure of proteins within tuberculosis. The protein Rv0632c was predicted to be an Enoyl-CoA Hydratase involved in fatty acid metabolism. In order to solve the structure of Rv0632c optimal crystallization conditions were sought. Random screening of crystallization conditions was conducted using Hampton Research CrystalScreen, CrystalScreen II, and PEG/Ion as well as Emerald Biosystems Wizard I, Wizard II, and Precipitant Synergy random screening kits. Crystallization was performed using the sitting drop vapor diffusion method in 96 well plates. Drops containing the native protein were 1 μL with 0.5 μL of protein solution combined with 0.5 μL of crystallization solution and a protein concentration of 5.58 mg/mL. Optimization of conditions was performed based on initial crystal hits. Crystals were screened at Advanced Lightsource beamline 5.0.2 at Lawrence Berkeley National Laboratory. The successful optimization condition included 0.2 M ammonium acetate, 30% PEG 4000, and a 0.1 M sodium acetate buffer at pH 4. The best diffraction of the initial crystal hit was good to 1.4 Å. The best diffraction of the optimized crystal was good to 1.0 Å. Bromine soaking multi-wavelength anomalous dispersion (MAD) data collected on the optimized crystal at 1.4 Å ultimately leading to an initial structure. The total time from receipt of protein to initial structure solution was within 1

month. The speed of crystallization and structure solution of this target represents a unique demonstration of the promise of high throughput protein crystallography.

The Effects of Vertically Aligned Carbon Nanofibers on Mitosis.
LINA HU (*Washington University in St Louis, St Louis, MO*); *TIM MCKNIGHT* (*Oak Ridge National Laboratory, Oak Ridge, TN*). One of the methods used to deliver DNA into a cell is microinjection, where macromolecules are directly administered into a cell, thereby overcoming a cell's physical and chemical barriers. Recently, a technique termed 'impalefection' has been developed, where high aspect ratio spikes of either carbon nanofiber or black silicon are used to impale and deliver DNA on a parallel basis to many cells at once. Morphologically, these high aspect ratio materials are similar to microinjection needles but can also be compared to asbestos fibers and vitamin B2 crystals, both of which are known to interfere with mitosis by hindering the formation of the spindle apparatus and chromosome segregation. As such, experiments were conducted to determine whether vertically aligned carbon nanofibers (VACNFs) and black silicon can cause similar interference during mitosis. A variety of tests were conducted such as live cell imaging of mitotic events following cellular impalement on these spikes and fixed cell assays following impalement and/or culture of cells upon nanoneedle arrays. Live cell imaging following nanofiber impalement showed several occurrences of mitotic arrest (metaphase checkpoint) and mitotic abort, ultimately resulting in multinucleation in the Chinese Hamster Ovary (CHO) cell line. Based on this, a series of tests were conducted in which the mitotic index and multinucleation of impaled and non-impaled CHO cells were evaluated over time. Cells were cultured in conventional dishes, upon chips of high aspect ratio structures (unimpaled), and impaled upon spikes of these structures. The mitotic index and multinucleation of the samples were scored at 16, 40, and 64 hours. Preliminary data indicates that there are statistically significant differences in multinucleation between conventional dishes and growth upon substrates of these high aspect ratio nanomaterials, as determined by the Student T-Test with a p-value of 0.05. Continued testing will determine if these differences are more pronounced with impalement of the cells. These tests will help determine whether growth and impalement on high aspect ratio substrates cause a disturbance in mitosis, and will provide an assay by which substrate modifications can be evaluated to counter these effects. Future modification of the VACNFs to minimize mitotic disturbances could possibly be applied to gene delivery and other intracellular applications of these nanostructured materials.

Functional Analysis of Different G Protein Coupled Receptors (GPCRs) in Aspergillus niger.
MONICA HU (*Massachusetts Institute of Technology, Cambridge, MA*)*; ZIYU DAI* (*Pacific Northwest National Laboratory, Richland, WA*). *Aspergillus niger* (*A. Niger*), a model industrial fungus that annually produces more than 4 million tons of citric acid globally, can grow at an extremely low pH and form small pelleted morphology, an ideal morphology for use in the industrial production of bioproducts. Understanding the molecular mechanisms of fungal morphology is a prerequisite for the improvement of bioprocess productivity via genetic engineering. G protein systems, the upstream components of the signal transduction pathway, have been found to be involved in the regulation of fungal growth and development. Previous studies have demonstrated that the G protein beta subunit and one of the alpha subunits were involved in regulation of *A. niger* morphology. In this study, the involvement of the G-protein coupled receptors in *A. niger* morphology was examined via gene deletion analysis. A polymerase chain reaction (PCR) based strategy was used to generate gene-deletion mutants in *A. niger* using the selective marker gene hygromycin B phosphotransferase. The genomic DNA was isolated from these transformants and gene replacements were confirmed by PCR. The G protein coupled receptors A, F, and H were successfully deleted via homology replacement. Single spores of those selected transformed events were isolated. The deletion effects of selected genes on citric acid production and morphology will be examined by culturing in different culture conditions. Through this and other examinations, the functions of those selected G-protein coupled receptors of *A. niger* can be better understood. This knowledge can be applied to other fungal strains used for producing different bioproducts. As a result, the morphology of these fungi can be effectively controlled for optimal bioproduct production.

Aquatic Macroinvertebrates of Wetland R at Argonne National Laboratory, Illinois: A Comparative Study of Pond Populations and Water Health.
LEAH JOHNSTON (*University of Illinois at Urbana-Champaign, Champaign, IL*)*; KIRK LAGORY* (*Argonne National Laboratory, Argonne, IL*). Wetlands are essential for sustaining

dynamic and healthy environments. The presence of wetlands has decreased during the past one hundred years due to human-caused disturbances. In order to comply with wetland protection laws, Wetland R was created to replace the 1.8 acres of natural wetlands that were destroyed during the construction of the Advanced Photon Source at Argonne National Laboratory in DuPage County, IL. Construction of Wetland R began in August 1990. The purpose of this study was to survey and compare the aquatic macroinvertebrate populations in Wetland R to those in upper Freund Pond. Upper Freund Pond is located northwest of building 617 at Argonne National Laboratory. Aquatic macroinvertebrates are used as bioindicators of water quality. Based on the populations found in both locations, the qualitative health of each was determined and compared. Samples were taken from each site using a dipnet and were sorted with a series of sieves to find specimens. Once collected, specimens were examined and identified to the genus level. The known sensitivity towards pollution levels of each genus was determined from the literature to determine the water health of each area. The water surface area was measured weekly at Wetland R. A total of 15 genera were discovered. There was a higher genus diversity present in Wetland R (10 genera) than in Freund Pond (seven genera). Of the genera discovered at each site, eight of the 10 (80%) in Wetland R and three of the seven (43%) at Freund pond were sensitive or moderately sensitive towards water pollution. Biomonitoring (the utilization of biological responses to assess environmental changes) using the sensitivity levels of the collected genera from each location indicated that the water quality at Wetland R exceeded that of Freund Pond. It is recommended that annual monitoring of aquatic macroinvertebrates in Wetland R continue. The utilization of laboratory-based chemical analysis on the water of Wetland R is recommended to provide additional information on water quality. Maintaining good water quality in Wetland R will promote high species diversity.

Engineering Novel Gene-Regulatory RNA Aptamers. *YUVRAAJ KAPOOR, LESLEY LARA* (*University of California – Berkeley, Berkeley, CA*)*; JAY KEASLING, JAMES M. CAROTHERS* (*Lawrence Berkeley National Laboratory, Berkley, CA*). Aptamers are RNA sequences that bind to target molecules and consequently regulate gene expression in a ligand-dependent fashion. They are frequently employed in nature to couple fluctuations in the concentration of a metabolite with changes in gene expression. Upon binding a small molecule, aptamers sequester the ribosome binding site [RBS] of a cis mRNA and repress translation. Synthetic aptamers eliminate the need to rely upon pre-existing biological molecules as the source of binding structure. Generation of synthetic aptamers occurs through *in vitro* selection, iterative rounds of enrichment and amplification which eventually select for an RNA molecule with high binding affinity (~100 uM) and specificity. Through a combination of directed evolution and rational design we generated functional, ligand-binding RNA structures that control the cis-expression of mRNA transcripts in response to tetramethylrhodamine (TMR), a small fluorescent dye that is cell permeable. Iterative rounds of reselections and binding assays in *in vivo* like conditions have generated 3 isolates of TMR-binding aptamers. When incorporated into constructs with self-cleaving hammerhead ribozymes, such molecules will provide general tools for simultaneously varying the expression levels of toxic intermediates in engineered pathways such as that of the anti-malarial drug, Artemisinin.

Agt1 Promoter Sequence Analysis in the Collaborative Cross Parental Mouse Strains. *JEANNA KIDWELL* (*Christopher Newport University, Newport News, VA*)*; BRYNN VOY* (*Oak Ridge National Laboratory, Oak Ridge, TN*). The Collaborative Cross (CC) is a unique mouse genetic reference population being generated at the Oak Ridge National Laboratory. This cross will consist of approximately one thousand recombinant inbred (RI) strains of mice derived from eight parental strains that were chosen for their genetic and phenotypic diversity. Each strain will contain a unique combination of alleles from the eight parental genomes, creating a population with genetic and phenotypic diversity on par with the human population and a novel resource for the study of heritable disease in humans. We are using the CC population to study the association between adipose tissue production of Angiotensinogen (Agt) on obesity and type 2 diabetes. Agt is the substrate for Angiotensin II, a bioactive hormone that regulates insulin sensitivity as well as many other physiological processes. We sequenced the Agt1 promoter region (about 1.2 kilobases upstream from Agt1) in the 8 CC parental strains in an attempt to identify regulatory polymorphisms that cause wide variation, up to 100-fold, of adipose Agt mRNA expression levels across the CC parental strains. DNA was extracted from mouse ear clips using a modified "Hot Shot" protocol (alkaline lysis followed by neutralization). The Agt promoter was amplified using Polymerase Chain Reaction with a series of six oligonucleotide primers. DNA sequencing was performed at the UTK Molecular Biology Resource Facility. Sequence analysis indicates several single nucleotide polymorphisms between the strains as well as a three base pair deletion present in three strains (A/J, NZO, and CAST) and not present in the other five strains (C57BL/6J, 129, NOD, PWK, WSB). Future experiments will be directed towards determining the impact of these polymorphisms on Agt transcription.

Amplification of Methylated DNA Sequences that Retains mCG Epigenetic Marks. *DANNY KOHUT* (*New York University, New York, NY*)*; JOHN J. DUNN* (*Brookhaven National Laboratory, Upton, NY*)*.* It has been shown that tumor cells contain an extensive amount of methylated DNA, which could be used in finding cancer before the onset of symptoms or to monitor reoccurrence. By amplifying DNA in such a way that retains methylation patterns, a small amount of DNA can be used to detect cancer. The pGEM5 vector was methylated using HpaII Methyltransferase, an enzyme that recognizes CCGG sequences and adds a methyl group to the second cytosine residue. The DNA was then cut with HpaII and MspI to check for complete methylation; the latter enzyme is able to cut methylated CmCGG sequence while the former cannot. An attempt was then made to amplify the methylated pGEM5 sequence using F29 amplification with dnmt1 Methyltransferase, but without success. Our second and novel method required HeLa DNA, which comes from a cancerous cell line, to be cut with MseI, gel purified and then joined to a synthetic DNA cassette. The purified ligation mixture was then bisulfite modified, which transforms all non-methylated cytosine residues into uracils. PCR amplification of the top strand with bisulfite-modified specific primers produced a large amount of DNA where the only remaining CG's are those that were originally methylated. M.SseI Methyltransferase will then add a methyl group to these sites to re-form mCG's, which are then affinity purified using the methyl-binding proteins MBD2b and MBD3L1 and then either hybridized to a microarray or sequenced.

Optimization of a Batchwise Immobilized Metal Affinity Chromatography Protocol. *DAVID KONOPKA* (*Kalamazoo College, Kalamazoo, MI*); *FENG YANG* (*Pacific Northwest National Laboratory, Richland, WA*). Phosphorylation plays a significant role in regulating metabolic activities in the cell. However, samples of phosphopeptides must first be enriched prior to analysis by mass spectrometry, primarily due to the very low concentration of proteins that are phosphorylated at any given time. Immobilized metal (Fe3+) affinity chromatography (IMAC) is, at present, the most promising method available. Unfortunately, the current, column-based technique is relatively slow and does not have a high throughput capacity. Development of a batchwise IMAC protocol would resolve these shortcomings. A mixture of tryptically digested beta-casein, a common phosphoprotein, and a phosphopeptide standard was used to test the batchwise IMAC protocol with various wash and elution buffers. Tryptic digestion of protein samples extracted from normal human dermal fibroblasts was also used to test the protocols. The number/signal of identified phosphopeptides from both experiments will be used to select the optimized protocol. Due to time constraints and a backlog of samples to be run on the mass spectrometer, no data has yet been obtained from this project.

Methodological analysis of an Amidohydrolase from Psychroflexus torquis and its Crystal Structure. *JENNIFER LEVIA* (*Medgar Evers College, Brooklyn, NY*)*; BROWN/D. KUMARAN* (*Brookhaven National Laboratory, Upton, NY*). Amidohydrolases, superfamily of metallo-dependent hydrolases, a large group of proteins that show conservation in their 3-dimensional fold (TIM barrel). To gain structural insights into the substrate specificity and enzymatic mechanism, one of this family member 9355a was selected for structure determination as a structural genomics target. This study will be useful in understanding this enzyme family at molecular level and will provide structural basis for designing drugs for specific target. The target amidohydrolase enzyme was crystallized using sitting drop vapor diffusion technique at room temperature. Square shaped crystals of dimensions 0.2 x 0.2 x 0.1 mm^3 were obtained in a day or two. X-ray diffraction intensities were collected at the X29 beamline of National Synchrotron Light Source (NSLS). Crystals diffract to at least 2.4 Å and belong to the tetragonal space group I41 with unit-cell parameters a=b=192.56 Å, c=277.0 Å. Assuming 12 molecules of 50,000 Da per asymmetric unit, the Matthews coefficient is 2.2 Å3 Da-1 corresponding to an estimated solvent content of 43% by volume of the unit cell. The structure determination process is in progress.

Imaging Cue-Induced Dopamine Release and Brain Activations in Behaving Animals. *COURTNEY LIEBLING* (*Smith College, Northampton, MA*); *WYNNE SCHIFFER* (*Brookhaven National Laboratory, Upton,*

NY). Much progress has been made in imaging technology that has enabled us to study molecular events in behaving animals. Given that we now have the ability to image small animals while performing a behavioral task, we have developed a new technique that combines positron emission tomography (PET) imaging with animal models of addictive behavior. This technique has advantages over other methods that measure brain metabolism and neurotransmitter release, such as microdialysis and autoradiography, in that it allows noninvasive examination of neurological processes, permits longitudinal study of the same subjects, and gives a clearer understanding of brain function rather than anatomy. Clinical PET studies in human subjects have shown that exposure to cues associated with a drug activates certain brain regions and increases striatal dopamine which displaces binding of the D2 ligand, [11C]raclopride (rac). This increase significantly correlates with subjective reports on craving. Here, we assessed brain glucose metabolism using [18F]fluorodeoxyglucose (18FDG) and measured changes in dopamine by comparing rac binding in rats conditioned to associate cocaine with a specific environment in order to determine whether animal models of addiction produce the same pattern of metabolic activations and rac displacement as that observed in human drug abusers exposed to drug-related cues. These studies were conducted simultaneously using the conditioned place preference (CPP) model. Using the microPET R4 tomograph, we showed that the specific binding of rac in dorsal and ventral striatum was significantly reduced when animals were placed in the cocaine-paired environment. The extent of this reduction positively correlated with preference scores (r2=0.925, dorsal; r2=0.844, ventral striatum). Further, changes in metabolic rates occurred during the expression of cocaine preference in areas of the brain that are associated with the expectation of a psychostimulant challenge. These results suggest that the expectation of a drug reward produces an increase in striatal dopamine release. Therefore, strategies aimed at inhibiting cue-induced striatal dopamine release in response to the expectation of a drug reward hold promising implications for the treatment of drug addiction. Additionally, this procedure of monitoring molecular events in behaving animals further advances behavioral neuroimaging technology by assessing the degree to which animal models correlate with human behavior.

Angiotensinogen Expression in Collaborative Cross Offspring.

ADAM LUNDQUIST (*Christopher Newport University, Newport News, VA*); *BRYNN H. VOY* (*Oak Ridge National Laboratory, Oak Ridge, TN*). The Collaborative Cross (CC) is an emerging population of recombinant inbred (RI) lines of mice designed to untangle complex webs of genetic interactions. The CC, now being implemented at Oak Ridge National Lab (ORNL), is being created from 8 diverse inbred strains of mice bred to produce 1,000 RI strains, with every resulting strain containing a portion of the genome from each of the 8 parental strains. The genetic and phenotypic diversity of these 1,000 RI strains will model that found in human populations, making the CC a valuable resource for dissecting the genetic contributors to complex traits such as obesity and hypertension[1]. This diversity, coupled with the known genotypes of the animals, will be utilized to map and dissect the genetics of complex traits, which are phenotypes produced from the interaction of multiple genes. We are interested in obesity a complex trait involving many genes interacting within multiple metabolic pathways. One such gene known to play a role in both obesity and hypertension is angiotensinogen, Agt. Agt is a vascular constrictor expressed in adipose tissue; its expression varies widely among the eight CC parental strains. In order to study Agt expression in the intermediate CC generations, those whose genomes have yet to be fixed by inbreeding (strict brother-sister mating for 20 generations), we extracted RNA from adipose tissue, reverse transcribed it into complementary DNA (cDNA), and utilized quantitative Polymerase Chain Reaction (qPCR) techniques to determine mRNA expression levels. Agt expression levels ranged widely (~15-fold) across the sampling of CC mice, indicating tha the diversity of this molecular trait in CC mice reflects that of a human population. Our results provide insight into the effects that mixing diverse genetic backgrounds have on Agt expression in these RI mice and will lead to future mapping of genomic loci involved in complex metabolic traits.

Non-Invasive Indexing of Red and Gray Fox Populations at Brookhaven National Laboratory.

PATRICK MALLIN (*College of William and Mary, Williamsburg, VA*); *JENNIFER HIGBIE* (*Brookhaven National Laboratory, Upton, NY*). The red fox (*Vulpes vulpes*) and the gray fox (*Urocyon cinereoargenteus*) have sympatrically inhabited the greater Long Island area over the last several hundred years. In recent years, speculation has grown regarding the population size of each species. While the red fox has historically been known to adapt well to ecological disturbances, including those of an anthropogenic nature, and is largely

considered to have a thriving population in the Long Island area, recent studies of the last thirty years suggest the gray fox populations have struggled with such anthropogenic disturbances of the last century. A previous Brookhaven National Laboratory (BNL) study in 2006 confirmed the presence of gray Fox on BNL property using non-invasive fecal DNA analysis via mitochondria DNA markers and automated camera documentation. This project further studied the extent of the gray fox presence on BNL property for the 2007 season by using the non-invasive techniques of fecal DNA extraction and automated field cameras. Gray fox presence was confirmed through both methods over the course of the study. While apparently much less common than the red fox, the gray fox species appears to be present and established on the BNL site and, presumably, in similar habitats throughout the Long Island area.

Systems Genetics: Elucidating Networks that Underlie Heritable Variation in Adipose Function and Susceptibility to Obesity.

IAN-JAMES MALM (*Macalester College, Saint Paul, MN*); *BRYNN VOY* (*Oak Ridge National Laboratory, Oak Ridge, TN*). Obesity and its co-morbidities are rampant in Western society. Excess adipose tissue not only physically stresses the organism but also disrupts homeostasis through release of adipokines, bioactive molecules produced in adipose tissue. The long-term goal is to determine the mechanisms by which heritable differences in adipose function impact risk for obesity and its consequences. Systems genetics was employed by anchoring phenotypic variation to naturally occurring genetic polymorphisms in two mouse genetic reference populations (GRP): 1) recombinant inbred BXD (C57BL/6J X DBA/2J) strains, and 2) a panel of eight genetically diverse strains that serve as progenitors for the collaborative cross (CC), an emerging GRP. Body and fat pad weights, plasma hormone profiles and adipose expression of adipokine genes were measured in males of 24 BXD strains and in both sexes of the eight CC parental strains. Current progress demonstrates: 1) adiposity is highly correlated with expression of some adipokine genes (e.g., leptin, r2= 0.626; p=5.4E-6) but not others (e.g., visfatin, r2=0.012, p=0.937); 2) a subset of tightly intercorrelated adipokines are regulated independent of adiposity; and 3) sexually dimorphic relationships exist among adipokines and adipose weight. Ongoing assay of adiposity in emerging generations of CC mice confirms that this new GRP will provide physiological diversity reflective of its genetic diversity and on par with that in a human population, highlighting its power to dissect the molecular components of complex traits. Collectively the results suggest that factors in addition to adipose mass need to be considered when predicting genetic risk for conditions co-morbid with obesity.

*Root Colonization of Prairie Plants by Extramatrical Hyphae.

CHEVON MARSH (*Governors State University, University Park, IL*); *MARY CARRINGTON* (*Argonne National Laboratory, Argonne, IL*). Arbuscular mycorrhizal (AM) fungi increase a plant's ability to capture water and essential nutrients. The fungus that extends outward from the root is the extramatrical hyphae. Prairie dock (*Silphium terebenthinaceum*), wild quinine (*Parthenium integrifolium*), and smooth blue aster (*Aster laevis*) are prairie plants associated with extramatrical hyphae. Sixteen fungal ingrowth bags from the three plant species were used to measure the extent of the extramatrical hyphae. When compared, prairie dock was expected to have the most extramatrical hyphae, smooth blue aster was expected to have the least, and wild quinine's measurements weree expected to fall somewhere in between. The results revealed that all three species were almost the same in their amount of extrametrical hyphae. This work is part of a greater study to see the success of plants in restored prairies of Illinois.

Accuracy of Sequence-Based Identifications of Filamentous Fungal Species Using ITS2 and LSU rDNA Sequences.

IVY MCDANIEL (*Scripps College, Claremont, CA*); *TAMAS TOROK* (*Lawrence Berkeley National Laboratory, Berkley, CA*). As fungi are becoming increasingly relevant to human society, the number of scientists qualified to identify fungal species using traditional methods is dwindling. Therefore, there is a need to develop tools that use standard molecular methods to accurately identify filamentous fungi at the species level. Our laboratory examined the effectiveness of making DNA sequence-based identifications of a collection of filamentous fungi by comparing the sequences of different variable regions of the ribosomal DNA to those in the NCBI Genbank database. By examining a conserved gene such as the ribosomal DNA, we hypothesized that there would be low variability among the sequence of conspecific organisms, but enough variability in the sequence of different species to clearly separate the organisms. We analyzed sequences from the D1/D2 domains of the large-subunit rDNA of 159 organisms from 85 species and 44 genera, and the ITS2 sequences of 28 organisms from 23 species and 13 genera. In both regions, the sequences

by themselves did not appear to be variable across all genera and divisions of fungi to the point that the sequences could be used as an accurate identifier of a single species.

Crystallization and Crystallography Analysis of Amidohydrolase Enzyme from the Structure Genomic Project. *Arshad Mehmood* (*Medgar Evers College, Brooklyn, NY*)*; D. Kumaran* (*Brookhaven National Laboratory, Upton, NY*). The crystal structure of an amidohydrolase (target ID 9355e) has been obtained to 2.35 Å resolution. Diffraction data were collected at the National Synchrotron facility of Brookhaven National Laboratory (beam-line X29). The crystals obtained by the sitting drop vapor diffusion method were 0.1 x 0.06 x 0.05 mm^3 in dimension. The crystals belong to the tetragonal space group P4 with unit-cell parameters a=b=144.74 Å, c =100.96 Å. In this tetragonal crystalline structure of 9355e there was one dimer per asymmetric unit. Amidohydrolase includes the families of enzymes that catalyze the cleavage of wide range of substrates bearing amide or ester functional groups at Carbon and Phosphorus centers. This enzymatic reaction is common in various metabolic processes thus it is important to understand this reaction at the molecular level. Therefore, by knowing the three-dimensional structures of these enzymes and their active sites, we can predict their function and the catalytic mechanism.

Triethyl Phosphate Degradation by INL Microorganisms. *Sara Montgomery* (*Rochester Institute of Technology, Rochester, NY*)*; Yoshiko Fujita* (*Idaho National Laboratory, Idaho Falls, ID*). Large amounts of radioactive contaminants including 90Sr and uranium have been released into the subsurface of several Department of Energy sites. Long term sequestration of these pollutants is important to limit the threat of groundwater contamination. The goal of this study is to evaluate the use of triethyl phosphate (TEP) as a reactive agent or amendment to sequester and immobilize 90Sr in phosphate minerals. TEP can be degraded by microorganisms, resulting in the release of inorganic phosphate which can then react with Sr and other metals to form poorly soluble phosphate minerals. These minerals should be stable under environmental conditions, resulting in the immobilization of the target contaminants. TEP degradation and liberation of inorganic phosphate by microbes from soil collected at the Vadose Zone Research Park at the INL were monitored in enrichments containing soil and TEP at 1 mM and 10 mM concentrations. The effect of ethanol added as a supplemental carbon and electron source was also evaluated. TEP degradation appears to occur similarly in enrichments with and without ethanol. However, fluctuations in TEP concentrations suggest that problems with measuring TEP exist. In addition, relative to TEP degradation, the phosphate released is approximately 1/1000th of the concentration of the TEP apparently degraded. The fact that this amount of phosphate is so small could be attributed to the microorganisms utilizing phosphate for growth, sorption of phosphate to sediments, and/or precipitation. There was an effort to obtain a pure microbial culture capable of degrading TEP. Visible colony growth was observed on agar plates containing 1 mM and 10 mM TEP. However, growth was also observed on agar plates without TEP, suggesting that microbes may be using the agar for growth. DNA extractions were performed on the original sediment samples and enrichments. The extracts will be subjected to phylogenetic microarray analysis to characterize the microbial communities. We conclude that TEP degradation by INL subsurface microorganisms may occur, but mass balances on the TEP and phosphate are difficult to obtain, and improved analytical methods may be needed in order to elucidate TEP degradation rates.

Semi-Automatic Segmentation for Biological Soft X-Ray Tomography. *Bradlee Nelms* (*University of Wisconsin – Madison, Madison, WI*); *Carolyn Larabell* (*Lawrence Berkeley National Laboratory, Berkley, CA*). Biological Soft X-Ray Tomography is an emerging technique to image cells in 3-dimensions with greater than 50nm resolution. While X-ray tomography can generate a wealth of data in a short period of time, the lengthy data analysis limits the rate at which research can be conducted. Important objects in X-Ray images must be identified before a computer can render them in 3D or measure their volume, surface area, or average X-ray absorption coefficient. The process of identifying relevant objects in an image is called segmentation and is currently performed manually, requiring a significant time commitment by a trained expert. To facilitate the segmentation of data collected by X-ray tomography, a framework is proposed for automating this step. First, edge-preserving smoothing is performed to reduce noise. Then, an edge detection algorithm based on the work of Canny is employed to find strong, continuous edges. Finally, an initial contour is deformed towards these edges by a vector field produced with Gradient Vector Flow. This semi-automatic pipeline was tested on 2D slices of the reconstructed volumes of

the fission yeast Schizosaccharomyces pombe. Results compare favorably with manually annotated images. Although further work is needed to develop this pipeline for 3-dimensional segmentation, these initial 2D tests suggest automation is possible for the high contrast, high signal-to-noise images yielded by X-ray tomography.

Transgenic Approaches for Functional Insigh into Plant Acyl CoA Dependent Acyltransferases. *Maria Norako* (*Kingsborough Community College, Brooklyn, NY*)*; Ghang-Jun Liu* (*Brookhaven National Laboratory, Upton, NY*). Acyl-CoA dependent acyltransferases catalyze the transfer of aliphatic and/or aromatic acyl moiety from CoA thioesters to the nucleophile of acceptor molecules. The enzymes constitute a large superfamily, namely BAHD family in plants. The numbers of BAHD family members vary accordingly in the different plant species. The biological functions of most of acyltransferases remain to be characterized. Previous study on Populus trichocarpa genomic sequences led to identification of about 94 putative acyltransferase genes. In order to further understand the biological functions of the identified putative acyltransferases, transgenic approaches are used to monitor the "loss and gain" functions of the individual acyltransferase gene. In this study, putative acyltransferases PtHCT1 and PtHCT2, the hydroxycinnamolyl-CoA: shikimate/quinate hydroxycinnamolyl transferase homologues, and PtACT45 are focused for transgenic studies. These three genes were individually cloned into binary vector pMDC85 chimeric with green fluorescent protein (GFP) gene and driven by double 35S promoter. The resultant plasmids were transferred into Agrobacterium strains EHA105 and C58C1 and confirmed by Polymerase Chain Reaction (PCR). The transformed strains were used to infect 295 pieces of tobacco leaves using leaf disc method. The co-incubated leaves were selected on hygromycin containing medium in the required conditions of light and temperature. The hygromycin resistant callus appeared around the edge of the leaves after 2 or 3 weeks. The rate of callus formation is much higher when using Agrobacterium strain EHA105 than using strain C58C1. The percentages of the callus formed are 92.8% and 82.5% respectively. The insertion of PtHCT1, PtHCT2 and PtACT45 genes were confirmed by performing genomic DNA-PCR and electrophoresis. Green fluorescence was indeed observed in the PCR-screened positive transformants under fluorescence microscope. LC-MS analyses were performed to monitor the enzymatic activity of the transgenic product. As the result, the high activity on the formation of p-coumaroyl shikimate were detected in PtHCT2- transgenic tobacco.

Carbon Sequestration in an Agricultural Ecosystem under Elevated Carbon Dioxide Levels. *Daniel Olson* (*Iowa State University, Ames, IA*); *Julie Jastrow* (*Argonne National Laboratory, Argonne, IL*). Atmospheric carbon dioxide has increased by 30 percent since the Industrial Revolution and is predicted to continue increasing at an accelerated rate. The increase in CO_2 allows terrestrial plants to grow faster and thus increases carbon inputs to the soil. Higher levels of CO_2 have shown increased carbon sequestration in deciduous forest and grassland soils, but the effect on agricultural soils requires further investigation. In 2001 a free air carbon dioxide enrichment (FACE) site was constructed in central Illinois to study the effects of elevated CO_2 conditions on a corn-soybean crop rotation. FACE allows experimental areas to be exposed to elevated levels of CO_2, while minimizing the change in sunlight, humidity, wind speed, and so forth. Soil from four FACE plots releasing CO_2 with a concentration of 550 ppm CO_2 and four rings exposed to ambient CO_2 levels (approximately 370 ppm) were sampled prior to planting in 2001 and again in April 2006. In both ambient and elevated CO_2 plots, soil carbon decreased between 2001 and 2006 based on whole soil carbon concentration; however, elevated CO_2 plots did not lose as much soil carbon as did ambient CO_2 plots. The loss of whole soil carbon over the study period is unexpected. It is most likely due to a difference in land use and management before 2001. The difference in carbon loss may be due to increased soil inputs in elevated CO_2 plots. The amount of carbon sequestered in each of the soil fractions will show where carbon loss is occurring. The change in carbon concentration of each soil fraction between 2006 and 2001 must be found. That data will indicate where carbon is sequestered in this agricultural ecosystem.

Purification and Characterization of Recombinant Aequeorea coerulescens Green Fluorescent Protein from *Escherichia coli*. Matt Peoples (*Earlham College, Richmond, IN*); Hugh O'Neill (*Oak Ridge National Laboratory, Oak Ridge, TN*). Green Fluorescent Protein (GFP) is a single chain polypeptide that forms a fluorescent chromophore by rapid cyclization and subsequent oxidation of residues Ser65-Tyr66-Gly67. It is widely used as a fluorescent tag for *in vivo* investigations. In this study an efficient procedure was developed for

the isolation and characterization of enhanced recombinant *Aequeorea coerulescens* GFP (aceGFP) that was over-expressed in *Escherichia coli* JM109. The first step employed three-phase partitioning to precipitate GFP using ammonium sulfate and tert-butanol. This was followed by dialysis and anion exchange chromatography. The purification procedure was monitored by UV/Visible absorption spectrophotometry, circular dichroism spectroscopy, fluorescence excitation/emission, and sodium dodecyl sulfate (SDS) and native polyacrylamide gel electrophoresis (PAGE). Interestingly, two variants of GFP separated during anion exchange chromatography. The first variant (GFP478) absorbed maximally at 478 nm with a fluorescence emission maximum of 505 nm. The yield was 3.04 mg GFP478/g cell paste. The second variant (GFP493) had a maximum absorbance at 493 nm and an emission maximum of 509 nm. The yield of this protein was 11.4 mg GFP493/g cell paste. Comparison of the UV/Visible and circular dichroism absorption spectra of the two isoforms indicate that the environments of their chromophores are different. Denaturing SDS-PAGE demonstrated that the lengths of their polypeptide chains are identical; however GFP493 migrated less than GFP478 by native PAGE, indicating a difference in the tertiary/quaternary structural characteristics of the two isoforms. GFP has been successfully purified from recombinant *E. coli* in good yield, and the two resulting isoforms of aceGFP have been characterized. Small angle X-ray scattering will be used to further investigate the structural properties of these two proteins in solution.

A Computational Model for Analyzing the Biochemical Pathways of Matrix Metalloproteinase (MMP) 2&9 in Collagen Type IV Proteolysis. Elizabeth O'Quinn (*Wofford College, Spartanburg, SC*)*; Kara Kruse (*Oak Ridge National Laboratory, Oak Ridge, TN*). Cardiovascular disease is the leading cause of death in first world countries. The imbalance of matrix degrading enzymes and structural proteins within the extracellular matrix of an arterial wall is a critical factor in cardiovascular disease processes. Matrix metalloproteinase-2 (MMP-2) and matrix metalloproteinase-9 (MMP-9) degradation of collagen type IV results in migration and proliferation of vascular smooth muscle cells; this can lead to further narrowing of a diseased artery. Kinetic modeling of proteolysis is an approach which can be used to understand complex systems by describing the enzyme's mechanism and behavior quantitatively. In this research project, a computational model of biochemical pathways involved in activation and inhibition of MMP-2 and MMP-9 proteolysis of collagen type IV is being developed. Separate MMP-2 and MMP-9 models have been implemented within JSim, a software application developed by the University of Washington. Since MMP-2 and MMP-9 pathways overlap, the individual models will be integrated in the future. This MMP-2 model was also implemented in JDesigner, a tool of the Systems Biology Workbench, and DEVS, a discrete event system specification, for comparison of model environments. Various experimental methods for obtaining quantitative reaction rate parameters were explored, including high pressure liquid chromatography (HPLC) and florescence polarization. By pairing HPLC separation, largely by hydrophobic property, with spectrometry techniques, protein and peptide identification and quantification is possible. Previous literature suggests the use of HPLC to measure enzymatic activity, by using traces of the product/substrate itself as an internal standard. An experimental protocol for the measurement of the enzymatic activity of MMP-2 and MMP-9 is being developed. HPLC baseline standards for the individual substrates and enzymes are currently being measured and optimized. After baseline standards are determined the MMP enzymatic activity can be determined. The HPLC experimental results will be analyzed to derive the reaction rate parameters needed by the computational model. The use of HPLC methods to analyze the enzymatic activity of MMP-2 with collagen type IV and other correlated substrates provides parameters which cannot be obtained through literature. This research is in collaboration with the Vascular Research Laboratory at the University of Tennessee Medical Center in Knoxville.

A High Throughput Method of Screening Mutant *Arabidopsis* Plants for Improved Biofuel Capacity Using Infrared Microspectroscopy. Simone Park (*State University of New York at Stony Brook, Stony Brook, NY*)*; Lisa Miller (*Brookhaven National Laboratory, Upton, NY*). Acyl-esterification is one of the most common modifications that occurs within the plant cell wall, and contributes to the covalent cross-linked polymerizations found there. These cross-linkages are found between lignocelluloses, components found in the cell wall, and contribute to the recalcitrance and complexity of the overall plant and prevent effective degradation for conversion into bioethanol. In this study, stems from 12 mutant *Arabidopsis thaliana* plants representing 6 distinct mutant lines were analyzed with

Fourier Transform Infrared (FTIR) microspectroscopy to develop a high-throughput method of screening and characterizing Arabidopsis lines. Cell wall components were extracted with ethanol in 2 ways and point spectra were taken to determine the extent of the 1,740 cm^{-1} peak corresponding to the vibrational carbonyl group characteristic of esters. Results from cluster analysis and acyl content from the microspectroscopy revealed that samples presented variabilities inherent to the complexity of the cell wall structure and to those attributed with sample preparation. Imaging of cross-sectioned stems was also performed, and it was found that the acyl content in the section was radially heterogeneous. More careful sample preparation for microspectroscopy and use of synchrotron light for imaging to gain greater spatial resolution in the cell wall will be valuable in improving this high throughput screening method.

The Surface-Mediated Unfolding Kinetics of Globular Proteins is Dependent on Molecular Weight and Temperature. Alexander Patananan (*University of California – Los Angeles, Los Angeles, CA*)*; Steven C. Goheen (*Pacific Northwest National Laboratory, Richland, WA*). The absorption and unfolding pathways of proteins on rigid surfaces are essential in numerous complex processes associated with biomedical engineering, nanotechnology, and chromatography. It is now well accepted that the kinetics of unfolding are characterized by chemical and physical interactions dependent on protein deformability and structure, as well as environmental pH, temperature, and surface chemistry. Although this fundamental process has broad implications in medicine and industry, little is known about the mechanism because of the atomic lengths and rapid time scales involved. Therefore, the unfolding kinetics of myoglobin, ß-glucosidase, and ovalbumin were investigated by adsorbing the globular proteins to non-porous cationic polymer beads. The protein fractions were adsorbed at different residence times (0, 9, 10, 20, and 30 minutes) at near-physiological conditions using a gradient elution system similar to that in high-performance liquid chromatography. The elution profiles and retention times were obtained by ultraviolet/visible spectrophotometry. A decrease in recovery was observed with time for almost all proteins and was attributed to irreversible protein unfolding on the non-porous surfaces. This data, and those of previous studies, fit a positively increasing linear trend between percent unfolding after a fixed (9 minutes) residence time (71.8%, 31.1%, and 32.1% of myoglobin, ß-glucosidase, and ovalbumin, respectively) and molecular weight. Of all the proteins examined so far, only myoglobin deviated from this trend with higher than predicted unfolding rates. Myoglobin also exhibited an increase in retention time over a wide temperature range (0°C and 55°C, 4.39 minutes and 5.74 minutes, respectively) whereas ovalbumin and ß-glucosidase did not. Further studies using a larger set of proteins are required to better understand the physiological and physiochemical implications of protein unfolding kinetics. This study confirms that surface-mediated unfolding can be described by experimental techniques, thereby allowing for the better elucidation of the relationships between the structure and function of soluble proteins as well as other macromolecules.

Structural Identification of a Glyoxalase Family Protein and Discussion of Possible Functions. Sara Patterson (*Knox College, Galesburg, IL*)*; Ruiying Wu (*Argonne National Laboratory, Argonne, IL*). At the Midwest Center for Structural Genomics (MCSG), located at Argonne National Laboratory, as well as several other research laboratories, a project to determine and catalogue all the protein structures is underway. At the MCSG, a three-step high-throughput process has been used to clone, purify, and determine the structure of protein BA3701. First, the target gene is ligated into an *E. coli* K12 vector and grown and induced in modified M9 media. Second, it was purified using Immobilized Metal Affinity Chromatography (IMAC) with a nickel column employed in the AKTA® purification robotic system. Finally, crystallization was induced by screening the protein against various conditions containing precipitants, buffers, and salts. Crystallization was successful through vapor diffusion at 16°C. The protein crystal was harvested and frozen in its mother liquor containing cryo-protectant glycerol, and its structure is determined via X-ray crystallography. Based on structural homology it is believed that the protein belongs to the glyoxalase family and super family pfam00903. It shares many similarities with bleomycin resistant proteins indicating that it perhaps acts to protect the *Bacillus anthracis* from its own antibiotics. However, further investigation is necessary to conclusively determine the function of the protein.

Expression, Purification, and Small Angle X-Ray Scattering of DNA Replication and Repair Proteins from the Hyperthermophile Sulfolobus solfataricus. Stephanie Patterson (*Del Mar College, Corpus Christi, TX*)*; Steven M. Yannone (*Lawrence Berkeley

National Laboratory, Berkley, CA). Vital molecular processes such as DNA replication, transcription, translation, and maintenance occur through transient protein interactions. Elucidating the mechanisms by which these protein complexes and interactions function could lead to treatments for diseases related to DNA damage and cell division control. In the recent decades since its introduction as a third domain, Archaea have shown to be simpler models for complicated eukaryotic processes such as DNA replication, repair, transcription, and translation. *Sulfolobus solfataricus* (*S. so*) is one such model organism. A hyperthermophile with an optimal growth temperature of 80°C, S. so protein complexes and transient interactions should be more stable at moderate temperatures, providing a means to isolate and study their structure and function. Here we provide the initial steps towards characterizing DNA-related *S. so* proteins with small angle X-ray scattering (SAXS). We focused on three *S. so* proteins: Sso0257, a cell division control/ origin recognition complex homolog, Sso0768, the small subunit of the replication factor C, and Sso3167, a Mut-T like protein. *E. coli* cells transformed with the pet21a expression vector containing the *S. so* gene of interest were grown to logarithmic phase. Protein expression was induced with 1mM Isopropyl ß-D-1-thiogalactopyranoside (IPTG). Cells were harvested by centrifugation. Proteins were extracted by sonication, then the extracts heated to denature any contaminating *E. coli* proteins. Soluble protein was purified by Ni-affinity column chromatography in a Fast Protein Liquid Chromatography (FPLC) system. *S. so* proteins were eluted with an imidazole gradient and collected as fractions, then concentrated to a range of 1–10 mg/ml. *S. so* proteins were analyzed with SAXS at multiple concentrations for both short and long exposure times. The Sso0257 sample was determined to be a 1:1 combination of monomer and dimer states. Sso0768 was found to be a complex mixture of multimeric states. Molecular envelope reconstruction from SAXS data for Sso3167 revealed a novel structural component which may function as a disordered to ordered region in the presence of its substrates and/or protein partners.

Cytochemical Investigation of Lignin Redistribution During Thermochemical Pretreatment. *Britney Pennington* (*Florida Institute of Technology, Melbourne, FL*)*; Todd Vinzant* (*National Renewable Energy Laboratory, Golden, CO*). Due to the increasing demand for oil, the United States has developed starch ethanol programs, but corn cannot support both the food and fuel industries. Cellulosic ethanol is a promising alternative to starch-based ethanol but is more difficult to generate cost-effectively because biomass is inherently resistant to degradation. Lignin, the polyphenolic compound in plant cell walls, contributes to this recalcitrance by inhibiting hydrolytic cellulases and presents an obstacle to producing bioethanol. Dilute acid pretreatment of biomass removes only a fraction of the lignin content, and yet at high temperatures, sufficient enzymatic digestion can still occur. To address this paradox, this study utilized microscopy and cytochemical stains to determine temperature's role in lignin redistribution during dilute acid pretreatment. All of the cytochemical stains used to detect lignin had evenly distributed staining patterns at 80°C but became concentrated towards the cell edges as temperatures approached 160°C. Temperature's effect on the biomass surface was also investigated using scanning electron microscopy. Starting at 140°C, half-sphere droplets appeared on the tissue surfaces and their morphologies seem to coalesce into larger spheres at higher temperatures. Round droplets were also observed using the light microscope. It has been hypothesized that the melted lignin is pushed out of the cell wall, possibly by increased hydrogen bonding between adjacent cellulose microfibrils, and forms spheres due to hydrophobic forces. Understanding lignin redistribution and its resulting implications on cell and tissue structure will help biologists explain the effects of pretreatment on biomass.

High-Throughput Purification of Novel Proteins. *Victoria Perez* (*The University of Texas – Pan American, Edinburg, TX*)*; Lour Volkart* (*Argonne National Laboratory, Argonne, IL*). A protein's three dimensional structure can shed light on many biological functions and the protein's relationship to sequence, function, and disease. The Structural Biology Center (SBC) at Argonne National Laboratory has established a protein structure determination pipeline capable of high-throughput production of purified protein and crystals. Protein structures are determined by using synchrotron X-ray crystallography. Target proteins must first be tested for their solubility and expression against a scale that determines whether the protein fits within the range best suited to be successful using the SBC protocol. Desired proteins must be highly purified before they are able to produce a high quality protein that is able to be crystallized. The SBC protein purification protocol produces milligram quantities of highly purified protein using

the high- performance chromatography workstations AKTA Xpress and IMAC 2. The implementation of the SBC protein purification protocol will be used to determine whether eight target proteins fit within the protocol's range for novel proteins. If the protein targets do not fit the protocol criteria, other methods will be explained to broaden the protocol's ability to crystallize the proteins.

Soft X-Ray Tomography at the ALS. *Allison Pymer* (*Temple University, Philadelphia, PA*) *Carolyn A. Larabell* (*Lawrence Berkeley National Laboratory, Berkley, CA*). Microscopy is a key biological research technique that allows scientists to study organisms and cells *in vivo*. Traditional visible light microscopes are limited in their maximum resolution whereas high-resolution electron microscopes require UHV environments to collect data. Newly developed X-ray microscopes at the Advanced Light Source (ALS) allow scientists to resolve hydrated cellular structures to 40 nm as a result of advances in X-ray optics, cryogenic microscope stages, and computer image reconstruction software. Scientists can study whole cells in their native environment due to this microscope, resulting in a better understanding of cell structure and function on a molecular level. For example, changes in the cell due to factors such as pharmaceuticals and disease may be observed *in vivo* without the use of dyes, stains, or other chemicals. Future advances in the methods used for X-ray tomography will assist scientists in furthering cellular studies to the molecular level.

*Root Length Colonization of Mycorrhizal Fungi in Prairie Plants. *Rita Richardson* (*Governors State University, University Park, IL*)*; Mary Carrington* (*Argonne National Laboratory, Argonne, IL*). Mycorrhizal fungi form associations with the roots of some plants while promoting growth. It has a greater association with plant species having thick, unbranched roots versus those with roots finely branched (Jastrow and Miller, 1993). It is hypothesized that roots from three prairie plant species will all have different proportions of mycorrhizal fungi colonization. The root length colonization of mycorrhizal fungi in three prairie plants: wild quinine (*Parthenium integrifolium*), smooth blue aster (*Aster laevis*), and prairie dock (*Silphium terebenthinaceum*) was studied. Roots of each of the three plant species were gathered, soaked in potassium hydroxide, and stained with trypan blue. The roots were then analyzed microscopically. The hypothesis of this study was supported by comparison of extent of root colonization by mycorrhizal fungi among prairie dock, wild quinine, and smooth blue aster. Becoming familiar with the associations between mycorrhizal fungi and different plant species may be useful when trying to increase the growth of plants.

Relative Quantitation Using Real-time Polymerase Chain Reaction Techniques (RT-PCR) to Compare Expression Levels of Genes Relevant to Pellet Formation in *Aspergillus niger*. *Torri Rinker* (*Oregon State University, Corvallis, OR*)*; Scott Baker* (*Pacific Northwest National Laboratory, Richland, WA*). Filamentous fungi have the potential to be used in industry for the conversion of complex biomass into useful products and alternate fuel sources. *Aspergillus niger* is highly efficient at producing citric acid from glucose. Due to its high productivity and the ability to control the morphological changes needed to reach most efficient production, citric acid production in *A. niger* serves as a model bioprocess for other filamentous fungi. In citric acid producing conditions, *A. niger* takes on a distinct pelleted morphology. Chitin, a polysaccharide found in the cell wall of fungi, is thought to contribute to this unique growth because of its involvement in cell wall generation. In this study, nine different chitin synthase genes along with other genes involved in pellet formation were studied in *A. niger* using Real-Time Polymerase Chain Reaction (RT-PCR). Gene expression levels in the citric acid producing strain ATCC 11414 were measured in 4 different types of media. Comparative assays were also performed on a modified strain of ATCC 11414 containing a deletion of a chitin synthase gene (csmAΔ). Relative quantitation of the RT-PCR data showed that three chitin synthases, csmA, csmB, and csmC were expressed at higher levels in citric acid producing conditions, while csmD and csmH were expressed at lower levels. Chitin synthase genes with a both myosin motor-like and cytochrome B5 domains had lower expression levels under minimal medium growth conditions than in citric acid production media. These data may indicate that such domains are important for cell wall formation in pelleted cells. Because cell wall formation is an important aspect of pelleted morphology, targeting genes that synthesize chitin, an integral component of the fungal cell wall, is an approach that may aid in obtaining pelleted morphology. From this study, it was concluded that csmA, csmB, csmC, csmD and csmH were significant contributors to pelleted morphology and will be further studied through gene deletion.

Protein Complex Interaction Assays of *Shewanella oneidensis* MR-1 Proteins and Its Relevance to Bioremediation Techniques. *Nathan Roberts* (*Marquette University, Milwaukee, WI*)*; Frank Collart* (*Argonne National Laboratory, Argonne, IL*). Identification of interacting proteins is a first step toward understanding the biological function of a protein. Mapping the protein interactions throughout a genome can define the communication network. The network can be used to predict how the organism will respond to changes in the environment. The bacterium *Shewanella oneidensis* MR-1 was used as a model organism for identification of interacting proteins. This bacterium can survive in the presence of heavy metals and its metabolic machinery can render these metals insoluble. This characteristic opens up many possibilities for *Shewanella oneidensis* or its proteins to be used in bioremediation of areas afflicted with radioactive and/or heavy metal contamination. Since very little is known about specific interacting proteins in *Shewanella oneidensis*, interacting proteins in *Escherichia coli* have been identified which contain high sequence similarity to *Shewanella oneidensis* proteins. Proteins are generally considered to have a similar function when protein sequences are 50+% identical. Open reading frames coding for proteins from *Shewanella oneidensis* were amplified from genomic DNA and cloned into *E. coli* expression vectors using molecular techniques. The proteins were screened for expression and solubility and the soluble proteins purified at a milligram scale. Each protein was expressed with an N-terminal his-tag to allow for interaction screening using a pull-down assay. This technique has allowed for mass scaling up and purification of chosen targets which then has allowed for identification of interacting proteins and further research into functionality.

A Biochemical and Computational Confirmation of ncRNAs in *E coli*. *Rebecca Roha* (*Gettysburg College, Gettyburg, PA*)*; Stephen R. Holbrook* (*Lawrence Berkeley National Laboratory, Berkley, CA*). Non-coding RNAs (ncRNAs) are transcripts that do not code for a protein, but rather functional RNA molecules in that have roles in protein manufacturing, DNA replication, cellular control and many other processes. However important, ncRNAs are difficult to study because their sequences lack clear start and stop signals, making them practically invisible on the genome scale. Bioinformatics techniques must be designed for the classification and discovery of ncRNAs. The Positive Sample only Learning Algorithm (PSoL) suggested a highly accurate machine learning algorithm to identify ncRNAs by using a support vector machine to combine many ncRNA detection signals in order to distinguish ncRNA sequences from intergenic sequences. This method identified to predict 420 ncRNA sequences in the E. coli genome. The PSoL predicted sequences were then clustered using LocARNA, folded using RNAalifold, and interpreted. Several trials were completed to test LocARNA's ability to cluster large amounts of sequences, correctly cluster identical sequences and to determine the effect of inaccurate sequences on the accurate clusters. Clusters were identified and a representative ncRNA from each was selected. For each chosen ncRNA, a Northern Analysis was completed; total E.coli RNA was extracted, the RNA was electrophoresed and transferred to a positively charged membrane, the membrane was then probed with non-isotopically labeled DNA complementary to the predicted ncRNA, hybridized, detected and developed. LocARNA successfully grouped the sequences into 9 clusters. ncRNA expression verification by Northern analysis is ongoing yet advancements have been made; DNA oligomers were successfully labeled and control RNA sequences were detected. A potential ncRNA has been identified, while further validation is necessary, a predicted sequence appears to be expressed. This work demonstrated that LocARNA is adequate clustering software for grouping predicted sequences into families. These findings are significant because they contribute to the search for a technique to identify and classify ncRNAs. Future research includes identifying more predicted ncRNAs as well as assigning the identified LocARNA clusters to known ncRNA families.

Using *In Situ* Reactors to Assess Natural Attenuation of TCE. *Alison Rope* (*Dartmouth College, Hanover, NH*)*; Deborah Newby* (*Idaho National Laboratory, Idaho Falls, ID*). Trichloroethylene (TCE) is a major groundwater contaminant in the United States. In the past it was used as a metal degreaser, a textile cleaner, and an anesthetic. Use at Test Area North 35 (TAN 35) as a metal degreaser left a large plume of the contaminant in the Snake River Plane Aquifer (SRPA). TCE is a likely human carcinogen and the EPA requires its removal from the groundwater. Many studies of the possible natural attenuation of TCE have been conducted, including extensive studies of methane oxidizing bacteria (methanotrophs) native to the SRPA. These methanotrophs degrade TCE into carbon dioxide and water using the enzyme soluble methane monooxygenase (sMMO). The degradation of TCE by aerobic

methanotroph metabolism has been well documented by a variety of enrichment studies, but an actual rate for the natural degradation rate (i.e. using an environment as closely simulated to the aquifer as possible) has never been found. We believe that TCE co-metabolism is controlled by coupled biogeochemistry (e.g., methane production and consumption) and hydrology (e.g., rate of fluid movement in primary flow paths). In order to minimize artifacts created by a laboratory environment, six flow through *in situ* reactors (FTISR) were placed into the aquifer and allowed to incubate. All reactors were packed with crushed basalt taken from the aquifer and had water pumped through at two different rates (1 m/day and 0.1 m/day) with three reactors at each flow rate. These rates were chosen specifically to simulate the environment in different parts of the aquifer. Over the eight month period, the reactors were colonized by both attached (living on the basalt surface) and planktonic (not attached) methanotrophs. The methanotrophs were allowed to colonize naturally; no chemicals or nutrients were added to the reactors. Molecular indicators of TCE co-metabolism (enzyme activity, expression of cometabolic genes and proteins) will be evident in these cells. The indicators of microbial potential and activity (sMMO expression) can be correlated with TCE degradation rates and used for refinement of computational (and site specific) models of natural attenuation. TCE degradation was analyzed over a five-day period. We will use reverse transcriptase real time PCR to determine if methanotrophs expressed the sMMO enzyme responsible for TCE oxidation.

Bystander Analyses of X-ray Microbeam Induced Gamma-H2AX Punctate Signals in the Human Mammary Epithelial Cell Line 184V. *Michelle Salcedo* (*Diablo Valley College, Pleasant Hill, CA*)*; Eleanor Blakely* (*Lawrence Berkeley National Laboratory, Berkley, CA*). Damage to DNA can be caused by direct and indirect effects of ionizing radiation absorbed by irradiated cells. Radiation damage to DNA can trigger a sequential cascade of responding DNA-repair molecules that can be visualized microscopically with the use of specific fluorescently-labelled antibodies and immunohistochemistry. The focus of my research has been to use a 12.5 keV X-ray microbeam produced at the LBNL Advanced Light Source beamline 10.3.1 to target a dose stripe of 100 microns wide on a population of 184V Human Mammary Epithelial Cells (HMEC) and to process the cell samples for DNA damage response markers as a function of time and distance from the dose stripes. This allows me to study both targeted and untargeted cells. The response of untargeted cells not in the radiation field is called a "bystander effect". Comparisons have been made after doses of either a relatively high dose stripe of 100 cGy or a relatively low dose stripe of 10 cGy. Gamma-H2AX and 53BP1 are the two DNA damage response markers I have studied. Some differences were noted in the phosphorylation response of each of these markers in the nuclei of irradiated HMEC. Gamma-H2AX and 53BP1 appear to co-localize, but with a different time course. I developed a scoring system to compare the morphological differences noted in these two DNA damage response markers in large montages of HMEC irradiated with the X-ray microbeam. Comparisons were made with unirradiated control cultures. The results indicated that a significant diversity of gamma-H2AX fluorescent signals exist in the unirradiated control possibly due to asynchronous cells varying in different stages of the cell cycle or culturing conditions. Irradiated areas expressing a high response of gamma-H2AX were an efficient indicator of the location and width of the stripe of dose, especially within the 100 cGy 10 minute montage image. Physical measurements of the stripe confirmed widths of 100 to 110 microns verifying the accuracy of the microbeam used. Histograms of different levels of intensities of gamma-H2AX expression were created using the data collected by using the devised scoring system. The data analyzed in the histograms demonstrated potentially novel fingerprints of the background fluorescent signal, the direct radiation damage effect, and the bystander effect. Future replication of this experiment is needed to validate significance of these results.

Comparison of Land Management Practices on Common Wood Nymph Butterfly Populations. *Tara Schwass* (*Western Illinois University, Macomb, IL*)*; Rod Walton* (*Fermi National Accelerator Laboratory, Batavia, IL*). Diversity of habitat and variety of wildlife has been increasing through restoration and land management techniques at Fermi National Accelerator Laboratory (Fermilab). These land management techniques are crucial to restoring and sustaining the natural habitats and native species of the area. This study examined the effects of land management techniques on the burned restored prairie, unburned restored prairie and mowed non-native grasslands and how these techniques affected local butterfly populations of *Cercyonis pegala*, the common wood nymph. Originally native to the prairie, the common wood nymph now occupies a wide range of

habitat that includes not only prairie but also non-native grasslands, open woodlands, fields, marshes, savanna, and road sides. Transect counts were used to survey the abundance of wood nymphs for each of the five sites studied. A similar study performed last year included two of the same sites studied this year. Results were analyzed using a t-test, Mann-Whitney U-test, Spearman correlation, and Pearson correlation. Our results indicated the prairie had significantly more butterflies than the non-native grasslands and also weather variables did not significantly affect butterfly counts. Our results differed greatly from the study performed last year where non-native grasslands had more butterflies than the native prairie site. These varying results are likely due to the timing of the land management techniques at the sites. However, other possible explanations for the results may be vegetation differences in growth, abundance, and density, and/or butterfly behavior. A continuation of this study should include the same sites after a new season of burning and mowing to examine long-term effects of land management techniques and also to gain a better understanding of butterfly ecology at Fermilab.

Analyzing the Structure and Function of Novel Cytochromes from a Natural Microbial Community. *Anna Siebers* (*University of California – San Diego, La Jolla, CA*)*; Michael P. Thelen* (*Lawrence Livermore National Laboratory, Livermore, CA*)*.* The Richmond mine in Iron Mountain, California, provides an unusual ecosystem suitable for the growth of microbial biofilms which produce many unique proteins. Through iron oxidation, these proteins facilitate acid mine drainage (AMD). Because this habitat is extremely acidic, survival is an extraordinary feat and the process of environmental selection is rare. In order to understand the mechanisms by which these organisms oxidize iron and gain electrons for energy, biochemical studies were applied. More specifically, column chromatography, spectrophotometry, and gel electrophoresis were used to determine the proteins present in different biofilms. Two specific locations of the mine researched were the AB drift and Ultraback C (UBC), which were both found to contain at least five different types of protein and a large amount of heme-bound cytochromes. Another application of these methods was to investigate proteins playing a major role within the community; one protein selected was cytochrome 579 (Cyt579) due to its abundance in the biofilm, iron oxidizing potential, and signature absorbance of 579 nm. The structure and function of Cyt579 could be characterized by the isolation of its heme, which was completed using column chromatography; however, one of the challenges has been liberating the heme from the column. Further research, including acid-base and temperature profiling of Cyt579 should help elucidate its structural changes within alternate environments and metabolism within the community.

Modeling Estimated Personnel Needs for a Potential Foot and Mouth Disease Outbreak. *Kirsten Simmons* (*North Carolina State University, Raleigh, NC*)*; Pam Hullinger* (*Lawrence Livermore National Laboratory, Livermore, CA*)*.* Foot and Mouth disease (FMD) is a highly contagious viral disease affecting livestock that was last detected in the US in 1929. The prevalence of FMD in other countries, as well as the current potential for this virus to be used as a form of agroterrorism has made preparations for a potential FMD outbreak a national priority. All 50 states were surveyed via e-mail, telephone and web search to obtain emergency response plans for FMD or for foreign animal diseases in general. Information from 35 states was obtained and analyzed for estimates of resources needed to respond to an outbreak. These estimates were expanded and enhanced to create a spreadsheet tool that could be used by individual states to better understand the personnel that would be needed to complete various tasks during an outbreak response. Personnel estimates were varied according to facility type and scaled by size. The estimates were then coupled to the output from FMD outbreaks simulated using the Multiscale Epidemiological/Economic Simulation and Analysis (MESA) model at Lawrence Livermore National Laboratory to assess the personnel resource demands on a response agency over the course of an outbreak response.

Testing the Enhancement of Protein Expression and Solubility by Induction Conditions. *Khouanchy Souvong* (*Knox College, Galesburg, IL*)*; Minyi Gu* (*Argonne National Laboratory, Argonne, IL*)*.* Inducing recombinant proteins in *Escherichia coli* under different conditions are shown to affect protein expression and solubility. Some proteins are expressed in insoluble forms which are much more difficult to purify; therefore, Argonne National Laboratory (ANL) is collaborating with the Midwest Center for Structural Genomics (MCSG) with the goal of finding the best conditions for increasing protein solubility to yield greater crystal production, for the most rapid and affordable protein structures. The cells were stressed and exposed to different induction conditions or with low concentration of isopropyl-ß-D-thiolgalactoside

(IPTG), with intentions of slowing protein production rate, thus have better folded protein. Clones with low solubility were subjugated through 2% ethanol in growth media, 15°C and 20°C induction temperatures, and 1 mM and 0.1 mM induction reagent IPTG. The optical density (OD) of the cells was taken before induction and before harvesting to monitor cell growth. The preliminary data showed that cells grow faster in 20°C, without ethanol. Nevertheless, the sodium dodecyl sulfate polyacrylamide gel electrophoresis (SDS-PAGE) showed samples with ethanol had a slight increase in targeted protein expression level; unfortunately, solubility level was still low with ethanol. The next step will be to continue to test with more clones, until the best conditions are found. After the optimal condition is formulated, it will then be used to screen less soluble clones to improve the clone production. This research is done with the prospects of better understanding protein function, improving human health, and for facilitating advancement in the medical field.

*Seagrass Change Associated with Land Use Trends in the Gulf of Mexico: A Historical Analysis. *Emily Stefansson* (*Everett Community College, Everett, WA*); *Ron Thom* (*Pacific Northwest National Laboratory, Richland, WA*). Seagrasses and other types of submerged aquatic vegetation (SAV) play an essential role in coastal ecosystems. By providing habitat to juvenile organisms, including a variety of endangered and commercially important species, seagrass beds are both ecologically and economically valuable. Over the past century, the health and coverage of seagrasses has declined significantly. In the Gulf of Mexico, many estuaries have lost up to 100 percent of their seagrasses within the last fifty years. While dredging, propeller scarring, over-water structures, and other forms of nearshore development have been listed as causes of seagrass loss, land use changes in the upper watershed must also be considered. Changes in watershed conditions can degrade water quality (e.g., light penetration, nutrients, temperature, salinity) in estuaries harboring SAV, which can in turn affect the ability of SAV to survive and spread. The purpose of this study was to investigate historical correlations between seagrass change and land use trends in the Gulf of Mexico, in an attempt to better understand seagrass declines in the area. Four bays within the Gulf were chosen for this analysis: Tampa Bay, Charlotte Harbor, Perdido Bay, and Galveston Bay. County-level data for each watershed was collected from the U.S. Census Bureau, U.S. Forest Service, and U.S. Department of Agriculture, concerning farmland, urban, and forest acreages in the 1900s. These data were then compared to trends in seagrass coverage, taken from existing literature and historical navigation charts dating back to the early 1900s. Overall trends showed a peak in agricultural land area during the 1950s, dramatic deforestation in the mid-1900s, and large increases in population and housing units throughout the 1900s. These major land conversions correlate with the largest seagrass losses between 1940 and the early 1980s. This may be related to increased turbidity, caused by nutrient-rich agricultural runoff and increased impervious surfaces accompanying development. As resource managers and policy makers look to restore seagrasses and the delicate ecosystems they support, an understanding of all potential stressors on key factors controlling seagrass growth is critical. Therefore these correlations provide the basis for planning and implementing future restoration and conservation efforts.

Effects of Burrow Characteristics on Temperature in Simulated Owl Burrows. *Lucy Tran* (*University of California – Los Angeles, Los Angeles, CA*)*; Corey A. Duberstein* (*Pacific Northwest National Laboratory, Richland, WA*). Western burrowing owls (*Athene cunicularia hypugaea*) are thought to be declining throughout their North American range. Reasons for their decline include the eradication of the fossorial mammals whose burrows they require and loss of habitat to urban and agricultural development. Many studies have investigated the aboveground characteristics of burrows and nest sites to determine their relationships to nest site selection, incubation, and productivity. Very little research has assessed the influence of the belowground environment on these processes. One aspect of belowground environment that may influence owls is microclimate (i.e., temperature and gas concentrations). This study examined the effects of two proximate factors that may influence owls when choosing nest sites on daily minimum and maximum temperatures within burrows: tunnel diameter and entrance aspect. Burrow temperature was recorded using DST milli™ archival temperature tags at three depths within replicate north- and south-facing simulated burrows of 7.6-, 10.2-, and 15.2-cm diameters at two sites near Richland, WA during July and August 2007. Daily minimum temperature ranged from 21.8 to 27.5°C, while daily maximum temperature varied between 26.4 and 29.5°C. Both daily minimum and maximum temperature differed between the two sites

and was affected by tunnel diameter. Daily maximum temperature was additionally affected by aspect. The observed diel temperature regimes indicate that south-facing burrows of smaller diameter may be more physiologically and reproductively advantageous for burrowing owls than north- and south-facing burrows of other sizes. Such information could be incorporated into the design and implementation of artificial burrows that would be thermally appropriate for burrowing owls.

The Structural Specificity of Recombinant Proteins from the Hyperthermophile *Sulfolobus solfataricus*. CATHERINE TREVINO (*Del Mar College, Corpus Christi, TX*); STEVE M. YANNONE (*Lawrence Berkeley National Laboratory, Berkley, CA*). The hyperthermophile archaeon *Sulfolobus solfataricus* grows optimally at 80°C and in the pH range of 2–3. The archaeon domain is most closely related to the Eukaryotes on the phylogenic tree than Eubacteria, suggesting that the DNA repair complexes of Archaea are most closely related to those of humans rather than those of other prokaryotes. These attributes and the fact that this organism's protein complexes are more stable at room temperature than mesophiles make it a good model organism. To analyze how different proteins interact with one another, the structural specificity of the protein should be known. The proteins that were investigated were cell division control 6/orc1 protein homolog, replication factor C, small subunit, phrB Deoxyribodipyrimidine photolyase, and MutT-like protein. To date, there are no structures available of the four *S. solfataricus* proteins that are being investigated. To investigate how protein-to-protein interactions occur, the four proteins from *S. Solfataricus* were harvested, extracted, purified and run through SAXS, using X-ray diffraction via cyclotron radiation. The attempts to obtain a structure in solution of the DNA repair proteins were better than predicted. Only cdc6-1, rfc, and MutT proteins showed good results when run through SAXS, phrB Deoxyribodipyrimidine photolyase was aggregated and did not give clear results. From the results gathered, cdc6 is said to be a transient complex between a monomer and a dimer. Rfc showed the protein adopts different oligmerisation states in solution. According to the PONDR and Kratky plot, MutT either has an elongation or aggregation added to the shape because there is disorder in the middle of the structure. With this data we will make crystal trays and attempt to crystallize the proteins that gave adequate results.

Purification of Chromatin-binding Protein YieF for Cancer Prodrugs. LISA WANG (*State University of New York at Stony Brook, Stony Brook, NY*); YAN-BIAO ZHANG (*Brookhaven National Laboratory, Upton, NY*). To further our understanding of the roles of YieF protein in chromate transformation and detoxification, the crystal structure of YieF protein can be observed and the binding site and activity site of the protein can be found. YieF is a bacterial enzyme from *Escherichia Coli* (*E. Coli*) with prodrug-reducing activity involved in cancer chemotherapy. Through its prodrug capabilities, the activity of YieF ultimately reduces the toxicity of chemotherapy on normal cells. YieF has chromate-reducing capabilities without redox recycling, and reduces the toxic contaminant Cr^{+6} to Cr^{+2} directly using four-electron transfer by transferring three electrons to chromate and one electron to oxygen. The plasmid pYBZ49, containing the YieF gene in a pTYB3 expression vector, was used to overproduce the YieF protein in the *E. coli* BL21(DE3) strain. Recombinant YieF was purified by using affinity chitin-binding column and size exclusion chromatography column. Crystal conditions were tested. From the crystals we routinely observed, the crystal conditions were defined and we were able to see crystals at 2 microns. Purified YieF protein was used to test different crystal formation conditions to ultimately solve the protein structure.

Expression and Purification of a Vaccinia Virus Nudix Family Decapping Enzyme. BRANDI WENGER (*Diablo Valley College, Pleasant Hill, CA*); STEPHEN HOLBROOK (*Lawrence Berkeley National Laboratory, Berkley, CA*). The Nudix (nucleoside diphosphates linked to another moiety x) hydrolase superfamily of proteins is characterized by its conserved 23 amino acid signature sequence. The motif is found among eukaryotes, bacteria, archaea and viruses. Proteins of the Nudix hydrolase superfamily perform a wide variety of functions using diverse substrates. The Nudix proteins have very low sequence conservation outside the signature and have a large amount of structural variation around a conserved structural core. Protein D10 contains this motif and is conserved in all poxviruses. In recent research, it was revealed that without the Nudix motif expressed in protein D10 of the laboratory prototype of poxviruses, vaccinia virus (VACV), the virus was unable to successfully target a host. Altering the motif in protein D10 caused VACV to lose its ability for mRNA decapping. With this ability lost, VACV no longer had the ability to suppress synthesis of cellular proteins and regulate its own gene expression. Solving the structure of protein D10 would allow

an inhibitor to be designed to prevent poxviruses from successfully targeting a host. VACV D10 was cloned and expressed in *Escherichia coli* bacterial cells as a maltose binding protein (MBP) fusion (pMalD10) and a His-tagged protein (pETD10). Although expression is low for both the fusion and tagged versions of protein D10, preliminary results indicate that purification by affinity chromatography is feasible. Further experiments are underway to improve expression and purification of protein D10 with the goal of obtaining sufficient homogeneous material to perform crystallization experiments.

The Expression and Purification of the Core Protein of the Hepatitis C Virus in *E Coli*. GLENN WERNEBURG (*State University of New York at Stony Brook, Stony Brook, NY*); MARC ALLAIRE (*Brookhaven National Laboratory, Upton, NY*). The second most fatal virus, Hepatitis C Virus (HCV) infects over 170 million people worldwide. Since only about 40% of the population responds to the current treatment, it is important to determine the structure of the HCV capsid protein which is involved in the packaging and assembly of the viral RNA. HCV is a single-stranded RNA type IV virus. Using an autoinduction method and media consisting of essential nutrients, the protein was expressed in an *E. Coli* strain. A high concentration (5.0 M) of sodium chloride salt in the lysis solution was used in the media to keep the fragment soluble. While the 1-82 amino acid (aa) 170aa, and 1-173aa protein fragments were expressed using this method, only the 1-82aa fragment was expressed in a soluble state. The 1-170aa and 1-173aa were present only in the pellet. The supernatant of the His-tagged 1-82aa protein fragment was then successfully purified on a Nickel column using imidazole to unbind it. 0.75 milligrams of pure protein was produced. Crystallization will be attempted using large quantities of this protein expressed and purified in the same way on a larger scale. The reconstitution of the capsid will also be pursued using tRNA and observed using Cryo-Electron Microscopy (Cryo-EM). In the event that the capsids are homogenous, a T-number for the symmetry of the capsid may be defined. This would be a major step in the determination of the structure of the HCV core protein and ultimately a better treatment for the virus.

High-Throughput Protein Crystallography of Mycobacterium Tuberculosis Targets. ERIK WESTLING (*City College of San Fransisco, San Fransisco, CA*); MINMIN YU (*Lawrence Berkeley National Laboratory, Berkley, CA*). High-throughput protein crystallography is an efficient method to manage researching the multitudes of proteins part of the Mycobacterium Tuberculosis bacterium. Since crystallization conditions are unpredictable, hundreds of different conditions must be arranged and observed for crystal growth. Each protein is screened through up to approximately 450 different chemical conditions. Conditions generally include a buffer of specific pH, a precipitant and salt. Experiments are created on 96 well plates. Each well corresponds to three droplets (0.2 micrometers in diameter). In each droplet, the chemical conditions are mixed with the protein. The droplets are observed routinely for crystal growth with an automated image-viewing device. In attempt to increase the quality and size of crystals, conditions in which crystals are observed to grow can be slightly altered. Changes are generally made to buffer pH and concentrations of precipitants and salts. Putting several proteins through this process at the same time will narrow down those that can crystallize in the available conditions. Of forty proteins received by our laboratory, thirty are crystallized. Eleven of those crystallized are verified to be protein crystals. Conformation of the remaining crystals is underway. This method allows research to progress for several proteins simultaneously, rather than one at a time.

Sample Preparation for Proteomic Studies on the Adaptive Evolution of *Escherichia coli*. ANGELA ZHANG (*University of Washington, Seattle, WA*); KIM HIXSON (*Pacific Northwest National Laboratory, Richland, WA*). Extensive research has been conducted on the bacterial evolution of *Escherichia coli* (*E. coli*) using comparative genomics, yet little research on microbial evolution has been done using the technology of proteomics. Recent findings have documented that mutations in the coding regions of *E. coli* may allow certain strains of the bacteria to improve their growth phenotype in initially unfavorable substrates. The intent of this project was to identify the amino acid changes that correspond with genomic mutations evoked in *E. coli* grown with glycerol or lactate as the carbon source by high throughput proteomic methods. In order for *E. coli* cell samples to be analyzed on the mass spectrometer, the cells were lysed with the Barocycler NEP 3229 to extract the proteins present. Then, the lysed *E. coli* cells were reduced and denatured with bond-breaker tris(2-carboxyethyl)phosphine and guanidine HCl, digested with trypsin, and alkylated with iodoacetamide. The digestion converted the proteins to peptides which were then cleaned up using C-18

Solid Phase Extraction columns. A Coomassie Blue Assay was used to measure protein concentration before digestion and peptide concentration was determined by a Bicinchoninic Acid Assay after C-18 clean-up. Samples were pooled into four groups according to growth substrate and injected into a strong cation exchange column (SCX) which fractionated the sample into twenty-five fractions. Each of these fractions which represent a less complex mixture will then be analyzed by a reversed phase C-18 column coupled to an ion trap mass spectrometer used to detect and identify the peptides. Due to time constraints, however, mass spectrometric analysis will not occur until after the conclusion of this internship. All identifications will go into a reference peptide database/library and the results will be compared with mutations identified by previous genomic studies. If mutations are translated into proteins, mass spectrometry can then be used to identify the various strains of *E. coli*, drastically reducing both time and money. Future work may include preparing strains of *E. coli* grown on substrates other than glycerol and lactate for proteomic analyses.

High-throughput Protein Purification. DAVID ZHANG (*University of Illinois at Urbana-Champaign, Urbana, IL); MIN ZHOU (Argonne National Laboratory, Argonne, IL*). Structural genomics is an integral part of biology, where three-dimensional structures of macromolecules are determined using X-ray crystallography. As part of the Midwest Center for Structural Genomics, the Structural Biology Center (SBC) at Argonne National Laboratory has played a key role in developing protocols for cloning, protein purification, and structure determination. These three steps of the pipeline are linked in that order. Cloning determines which proteins are soluble enough and have optimal expression so that they may then be isolated by the purification group. Cells are grown to a certain density, which are then lysed. The cell extract is then purified through nickel-ion affinity chromatography. The target protein is then concentrated and set up for crystallization in a high-throughput manner. Crystals are then transferred over to the hands of the crystallographers where structure determination takes place by the multiple-wavelength anomalous dispersion (MAD) method. In the long-term, more cost-efficient methods and tools will be used in order to solve the more difficult projects. The two main issues that impede the structural genomics program are protein solubility and expression. Protein structures, especially those of important pathogens, may reveal a lot about the mechanisms in which they perform their functions. Discovering and analyzing protein structures are a major step towards the advancement of biomedical research.

Characterization of Actin as a Cofactor for the Adenovirus Proteinase. HAN ZHU (*Massachusetts Institute of Technology, Cambridge, MA); WALTER F. MANGEL (Brookhaven National Laboratory, Upton, NY*). A good model system for the development of effective protease-inhibition based anti-viral agents (drugs) is human adenovirus (AVP), because AVP is essential for the production of infectious viruses. AVP is found to require viral cofactors, which regulate the activity of AVP in time and space, for maximal activity. Actin, one of the most abundant proteins in the cell and a major component of the cytoskeleton, is believed to be an AVP cofactor due to the high homology of its c-terminus with the 11 amino acid peptide viral cofactor pVIc. The binding of monomeric actin to AVP allows for its activation and the cleavage and degradation of the cytokeratin-18 network of a host cell, releasing newly formed virions. Using a spectrofluorometric assay with optimized buffer conditions to preserve the native structure and monomeric form of actin, insights can be gained by characterizing the binding interaction between actin and AVP. Although the reaction rates were lower than expected, assays varying the actin concentration with constant concentrations of AVP suggest tight binding between actin and AVP. The KM of the AVP-actin complex was measured to be 7 μM, very similar to the measured KM of the AVP-pVIc complex, suggesting that the binding of actin does not change substrate affinity. Rather, the binding of actin changes the properties of the enzyme itself, or the kcat (determined by VMAX). In addition, actin stimulates AVP in the presence of either one of the two viral cofactors (DNA and pVIc), allowing us to conclude that actin binds to two independent sites on AVP. Furthermore, through the use of competition assays with DNA, we were able to begin to estimate the binding affinity between actin and AVP with and without its viral cofactor pVIc. A better understanding of the interaction between actin and AVP should reveal new targets for anti-viral drug development.

Chemistry

Energetics of Electron Transfer and Charge Separation in Moderate to Low Polarity Solvents. BRIAN ALBERT (*Columbia University, New York, NY); JOHN MILLER (Brookhaven National Laboratory, Upton, NY*). Because photosynthesis occurs in a region of low polarity so that photoelectrons store their absorbed energy in new chemical bonds instead of emitting it as heat through interaction with the solvent, studying electron transfer and charge separation in low polarity solvents will have applications in new solar energy storage. These experiments combine strong electron donors (metallocenes) and strong electron acceptors (quinones) to obtain ion formation by thermal equilibria in media of moderate to low polarity. In solvents of a range of dielectric constants, the extent to which cobaltocene and various quinones formed ion pairs and separated to form free ions was measured via conductivity and UV-Vis spectroscopy. Gibbs free energy changes were calculated for both the electron transfer and charge separation reactions in various solvents using acetonitrile as a standard highly polar solvent. With known values for the ionization potential of cobaltocene and the electron affinities of the quinones, Gibbs free energy changes observed in the moderately polar solvent, tetrahydrofuran (THF), were fit to the theoretical Born solvation energy and Coulomb potential models. Predictions made for free energy changes in solvents of very low dielectric constants disagreed with experimental data because a fourth species, charge transfer complex, becomes more significant in relative concentration, thus introducing a third equilibrium. Also, molecule structure of the solvent molecule was found to affect Gibbs free energy changes of ion formation. Approximations of neutral specie, ion pair, and free ion concentrations became more difficult in low polarity solvents because of charge transfer complexes that appear as broadened peaks in UV-Vis absorption spectra as well as extremely low conductivity measurements. Observed Gibbs free energy changes were found to be significantly more unfavorable compared to redox potentials of the same reactions determined electrochemically. The difference is attributed to the stabilization caused by salt in solution required for the electrochemical method.

Selective Electrochemical Oxidation of Sodium Chloride Solution. MAX BASTOW (*Colorado College, Colorado Springs, CO); CHARLENE SANDERS (Oak Ridge National Laboratory, Oak Ridge, TN*). Activated electrodes placed in saline solution create an electric double layer composed of opposite charges, repelling ions of like charge. It is hypothesized that, due to this characteristic of the electric double layer, it is possible to inject a short anionic pulse into a saline solution that will selectively oxidize water to produce oxygen. If the pulse is short enough, it will stop before chloride ions are drawn to the electrode surface, thus avoiding production of chlorine. This would have applications to the generation of oxygen and hydrogen from sodium chloride solutions. Phosphate buffered saline (PBS) was placed into an electrolysis cell and a stimulus generator was used for controlled charge injection of an anionic pulse. This pulse was applied for 4 hours in a closed cell and chlorine production was observed by the spectrophotometric determination of hypochlorite based on its reaction with ascorbate. The same pulses were then applied to an identical cell containing PBS sparged with N_2 at 50 ml/min. A galvanic cell was used for oxygen measurements, and a Figaro gas sensor was used for hydrogen measurements. Evolution of chlorine was not observed until pulse widths greater than 200 μs were applied. At this pulse width the production of oxygen was already well established at 0.11 ± 0.01 μmol/hr. At the greatest applied pulse width of 400 μs chlorine production was at 0.053 ± 0.008 μmol/hr while oxygen production was 0.25 ± 0.01 μmol/hr. These results show that short pulses are indeed capable of oxidation of water in PBS to produce oxygen while avoiding the oxidation of chloride to chlorine.

Electrochemical Arsenic Remediation of Drinking Water in Rural Bangladesh. YOLA BAYRAM (*University of Michigan – Dearborn, Dearborn, MI); ASHOK GADGIL (Lawrence Berkeley National Laboratory, Berkley, CA*). According to the World Health Organization, in Bangladesh over 60 million people drink arsenic-laden water making it the largest case of mass poisoning in human history. Available methods of treating arsenic are too expensive, ineffective, or commonly difficult to implement, making them unsuitable for a poor or undeveloped country such as Bangladesh. Electrochemistry may provide an innovative, effective, and inexpensive method for arsenic remediation of drinking water. The method is an improvement upon a known method of using Fe(III) to remove arsenic. The Fe(III) combines with As(V), forming an insoluble complex which then can be easily filtered out. The innovative step of electrochemistry allows control over the amount of Fe(III) produced as well as electrochemical oxidation of the As(III) into reactive As(V) anion, making the method far more effective. Experiments were performed with water samples with 600ppb of total arsenic that received various amounts of current for varying durations of time. The objective is to determine the appropriate current and time necessary for an arsenic removal below 50ppb in order to meet

Bangladesh standards. It was found that a charge between 96.35C/L and 103.76C/L gave an arsenic concentration within the range or below the Bangladeshi standard. Once the process is well understood and the electrochemical variables are optimized, the method will be applied to a practical water filter. The hope is that this filter will be applied in Bangladesh and other areas affected by arsenic poisoning to provide millions of people with safe drinking water and an improved standard of living.

Metabolism of Dibromoacetic Acid and Bromochloroacetic Acid by Rat Liver Cytosol.

Anna Beiler (*Messiah College, Grantham, PA*) *Irvin Schultz* (*Pacific Northwest National Laboratory, Richland, WA*). Di-halogenated acetic acids (di-HAAs) are common by-products of municipal disinfection of drinking water and are known rodent hepatocarcinogens. Concern has been voiced by environmental and regulatory agencies about their effects in humans. In this study, the *in vitro* metabolism of two di-HAAs, dibromoacetic acid (DBAA) and bromochloroacetic acid (BCAA), was measured. The kinetics of DBAA and BCAA metabolism was studied in young male and female rat liver cytosol. The metabolism was characterized by both consumption of added substrate and formation of the initial metabolite, glyoxylate, after 1–30 minutes incubation at 37°C. Both the di-HAAs and glyoxylate were quantified by conversion to their respective methyl esters and subsequent analysis by gas chromatography-mass spectroscopy (GC-MS). BCAA is a chiral compound and its stereoisomers were analyzed using a chiral column on a GC-electron capture detector (GC-ECD). Due to technical difficulties with methylation of glyoxylate and analysis by GC-MS, conclusive data for the DBAA experiment was not found. In the BCAA incubations, the (-) BCAA stereoisomer was consumed so rapidly it was impossible to obtain a conclusive rate of metabolism. Further studies should repeat the experiment at a slower rate. Also, the method should be further developed to work more accurately on the brominated haloacids. In addition, future studies can explore the kinetics of remaining di- and tri-halogenated acids, and apply the findings to the effects on humans at the concentrations found in drinking water.

Kinetic Studies of Ammonia Borane.

Stephen Berds (*Monroe Community College, Rochester, NY*); *Wendy Shaw* (*Pacific Northwest National Laboratory, Richland, WA*). The need for effective hydrogen fuel cells (HFCs) is paramount to the success of establishing a stable energy economy based on hydrogen. At the heart of a productive HFC lies a system for efficiently storing and releasing hydrogen in a controlled fashion. One promising method for such a system is to use chemicals to store hydrogen. Ammonia borane, NH_3BH3 (AB) is both stable at room temperature and, with modest heating, able to generate hydrogen (H_2) with an H_2 to AB ratio of greater than 2:1. To better understand the effect which temperature has on the release of H_2 from AB, a gas burette system was employed to measure the amount of H_2 released from AB at set temperatures over time. AB was also loaded on MCM-41, a mesoporous scaffold, in several different mass ratios with AB to study its effect on H_2 release. It was found that the induction period which exists to release one mass equivalent of H_2 is directly dependent on the reaction temperature. The second mass equivalent of H_2 which is released does not have a separate induction period and is generated at only slightly higher temperatures than the first equivalent. The addition of MCM-41 both increased the rate of hydrogen release and eliminated the induction period for the release of the first equivalent of H_2. This research is part of a larger study being conducted by the Department of Energy's Chemical Hydrogen Storage Center for Excellence to fully characterize the mechanism and kinetics of H_2 release from AB. This work was supported by the Office of Energy Efficiency and Renewable Energy of the Department of Energy.

Electrolysis of Saline for pH Control and Oxygen Production.

Anna Besmann (*University of North Carolina at Asheville, Asheville NC*); *Eli Greenbaum* (*Oak Ridge National Laboratory, Oak Ridge, TN*). Diabetic retinopathy is a disease which causes small, fragile blood vessels to form within the retina to compensate for the normal blood vessels' inability to bring sufficient oxygen to the eye. These blood vessels are prone to hemorrhaging in the eye, causing temporary or permanent blindness. To help stop this problem before the small blood vessels can form, electrodes can be implanted into the eye to stimulate the production of oxygen in the vitreous humor. However, this also induces the formation of free chlorine, which causes the vitreous humor to become more alkaline. In order to keep the pH at a manageable level, an anode and a cathode can be implanted into the vitreous humor while a second anode connected to both electrodes by a sidearm can be implanted behind the ear. Protons will pass back and forth along the sidearm, keeping the vitreous humor from becoming too acidic or too

alkaline. Alternating between both configurations keeps the pH stable, as the internal electrodes cause a rise in pH while the sidearm electrode causes a drop in pH. In these experiments, two electrodes were put into the buffered saline itself and a third electrode into a glass sidearm filled with saline solution. To counter the problem of excessive baseline pH shift, a 2 mM solution of phosphate buffered saline (PBS) was used instead of pure saline. The solution was sparged at 25 ml/minute and heated with a water bath to 37°C to simulate the fluid motion in the vitreous humor and temperature of the human body. A DC charge of 800 µA was applied to the electrodes to stimulate the production of oxygen and a change in pH. The internal electrodes were used in three minute increments until the pH had moved one pH unit above the baseline, then the sidearm electrode was used in 1.5 minute increments to bring the pH down 2 units. Afterward, the internal electrodes were used to bring the pH back to the baseline. However, the exact amount of time needed to reach the acceptable limits of high and low pH was variable, and on occasion use of the internal electrode after using the sidearm electrode for a long period of time caused the pH to drop for unknown reasons. The next step of this process would be to repeat the experiment with a solution that is more like the vitreous humor of the eye, and eventually move on to implanting the electrodes within an actual eye.

Multiplexed Assemblies for SERS-Detection Applications.

Christina Brady (*University of California – San Diego, San Diego CA*); *Stephen Doorn* (*Los Alamos National Laboratory, Los Alamos, NM*). Raman techniques offer advantages over the well-established fluorescence in detection applications and microscopic analysis. Unlike fluorescence, Raman spectroscopy generates narrow peak widths allowing for a distinct fingerprint spectrum and easy identification of a material; however, low signal strength from Raman spectroscopy has limited its practical applications. Raman applications have increased with the use of Surface Enhanced Raman Scattering (SERS). To overcome weak signal strength, metal nanoparticles, such as gold or silver, are used as substrates for the attachment of the signal dye. Various attempts have been made to optimize the Raman signal by allowing the combination of different signal dyes for a single SERS-active nanoparticle. To achieve this, current research at Los Alamos National Laboratory involves synthesis of multiplexed nanoparticle assemblies to give a combination of signals. Silver (Ag) nanoparticles approximately 60nm in diameter were tagged with a particular Raman dye, aggregated, and silica coated. The tagged Ag particles were attached to silicon microspheres via biotin-avidin interactions in different dye ratios. Raman spectroscopy and Raman microscopy were used to measure and characterize the signal strength of the particles. Results showed that optimization of Raman signals occurred with the aggregation of Ag nanoparticles due to increased surface plasma resonance between the particles. Attachment chemistry of SERS-active nanoparticles to the silicon bead and dye combination spectra are currently being analyzed. Multiplexed nanoparticles can be used in further experiments requiring SERS-detection of different substrates simultaneously. Future synthesis of multiplex particles with different combination of dyes will allow for a larger array of dye spectra than currently available.

Synthesis of Silicon and Gold Nanoparticles.

Robert Brown, Morgan McGray (*Western Kentucky University, Bowling Green, KY*); *Marvin G. Warner* (*Pacific Northwest National Laboratory, Richland, WA 99352*). Gold and silicon nanoparticles have been widely used for their unique characteristics for various applications. By attempting to replicate other researchers' work, these syntheses were explored and expanded upon. Using sodium naphthalide in 1,2-dimethoxyethane as a reducing agent, adding silicon tetrachloride, and finally capping with octanol gives octanol-capped silicon nanoparticles. Gold nanoparticles can be synthesized through the use of hydrogen tetrachloroaurate(III) hydrate, toluene, and tetraoctylammonium bromide. With the addition of triphenylphosphine, the gold particles can be stabilized. In addition, ligand exchange reactions can be carried out with 4-trifluoromethyl-benzenethiol to produce nanoparticles with varying functionalities. It is evident that the gold nanoparticles are more easily produced and more stable then their silicon counterparts. Although we were not able to test the purity of our gold particles with 1H NMR, thin layer chromatography (TLC) showed high purity. The silicon nanoparticles were found to aggregate and were different than what was anticipated based on the reported literature preparation.

Isolation and Analysis of Above Cloud Point Precipitates in Palm and Poultry Fat Derived Biodiesels.

Rebecca Callahan (*Hendrix College, Conway, AR*); *Teresa Alleman* (*National Renewable Energy Laboratory, Golden, CO*). As the search for alternatives to petroleum based fuels continues many promising options have arisen. Vegetable

and animal fat derived biodiesels have become one viable alternative to petroleum based diesel fuel. Biodiesel can be directly substituted for petrodiesel while exhibiting less hazardous and superior environmental properties, such as its high flash point and biodegradability. Biodiesel typically has high cloud and pour points than conventional diesel. Additionally, a small fraction of biodiesels also show a precipitate formed above the cloud point. This precipitate may accumulate in storage tanks or on fuel filters inhibiting biodiesel's distribution. The identification of this precipitate may assist in finding a solution to its operability problems or an identification method of the fuels it impairs, thus enhancing the capability of biodiesel as an alternative fuel. Multiple samples of biodiesel were visually examined for the presence of precipitate at room temperature and two samples of different feed stocks were chosen for precipitate analysis, one palm and one poultry fat. Three steps were implemented to identify their precipitates. First, the mass of precipitate was increased by chilling biodiesel above its cloud point. The precipitate was then isolated from biodiesel through filtration and solvent washing. Lastly it was identified using the following analytical techniques: Fourier Transform Infrared Spectroscopy (FT-IR), Gas Chromatography Flame Ionization Detector (GC-FID) pyrolysis Molecular Beam Mass Spectrometry (py-MBMS), and proton, carbon 13 and Distortionless Enhancement by Polarization Transfer Nuclear Magnetic Resonance (H NMR and 13C NMR and DEPT NMR.) Using these methods of analysis it was determined that the two samples differed in physical appearance, yet both contained a large quantity of monoglycerides. Approximately ten percent of the samples examined in this work showed precipitation upon cooling, additional examination of biodiesels needs to be conducted to verify that this precipitation is universal to all feed stocks. Additionally, after the definitive identification of the precipitates, their impact on fuel filters must be quantified from the distributor to the vehicle.

BOB Ionic Liquids: Preparation and Properties. *Alejandra Castano (Queens College, Flushing, NY); James Wishart (Brookhaven National Laboratory, Upton, NY).* Ionic liquids (ILs) are salts that melt below 100°C. ILs are ideal alternative solvents to work with because they exhibit properties such as thermal stability, non-volatility, combustion resistance, high conductivity, and wide electrochemical windows. Owing to their non-volatility ILs do not contribute to air pollution and they are being investigated for a variety of applications as alternative solvents, including use in nuclear processes. The potential utility of ionic liquids for the processing of radioactive material is being investigated through the use of pulse radiolysis techniques. Ionic liquids containing the Bis(Oxalato)Borate (BOB-) anion are being investigated for this application, because of the neutron scavenging ability of 10boron. Calculations by others have shown that ILs containing boron can be used to handle higher concentrations of fissile material than conventional solvents without the risk of criticality. Halide salts such as 1-methyl-3-pentylimidazolium bromide (C5MIM Br) and a homologous series of pyrrolidinium, and pyridinium types were synthesized using both thermal and microwave-assisted techniques. The halide salts were prepared by reacting the amines with their corresponding alkyl halides. Boron containing ILs were prepared by metathesis reactions with sodium BOB (NaBOB). NaBOB was synthesized by reacting boric acid, oxalic acid and sodium hydroxide in water under reflux conditions. Preliminary results of pulse radiolysis experiments indicate that BOB anion scavenges radiolytically-generated solvated electrons too efficiently for BOB ILs to be stable as neat solvents for processes under ionizing radiation, as in nuclear separations. Thus, only small concentrations of borated ILs such as the BOB salts may be necessary to achieve inherent criticality protection. The salts would be most effective when dissolved in a IL co-solvent such as N-butyl-N-methylpyrrolidiunium bis(trifluoromethylsulfonyl)imide. Further characterizations such as viscosity, melting points, glass transitions, and electrochemical windows are also being investigated. Such data will provide valuable information to facilitate the broader applications of the BOB ILs.

Characterization of Silicon Carbide for Water-Splitting and Corrosion Protection. *Boris Chernomordik (University of Louisville, Louisville, KY); John Turner (National Renewable Energy Laboratory, Golden, CO).* Harnessing hydrogen as an energy carrier by means of renewable power, such as solar, is key to achieving a clean and dependable energy cycle. Direct photoelectrolysis of water with photoelectrochemical (PEC) cells is the most efficient method to collect hydrogen from water. In this study, commercial samples of the 4H polytype of silicon carbide (SiC), with n- and p-type doping, were photoelectrochemically characterized with a focus on durability for possible use as a protective coating for chemically sensitive high-efficiency PEC materials. The indirect band gap was found to agree with the literature value of 3.23eV and the bands were found to straddle the water electrolysis redox potentials, with the flat band potential vs. pH relationship exhibiting Nernstian behavior. Corrosion experiments showed that n-type SiC is susceptible to oxidative etching, while p-type SiC did not show signs of corrosion. Though the high band gap renders 4H-SiC inefficient for photoelectrolysis because it absorbs only a tiny portion of the solar spectrum, corrosion experiments suggest that p-type SiC may be durable enough to act as a protective layer in PEC cells. More experimentation in this regard is necessary, though. In addition, more research is needed into methods for incorporating SiC as a protective coating for a high conversion efficiency cell.

*Design and Development of Palladium-Iron Bimetallic Electrocatalysts for Polymer Electrolyte Fuel Cells. *Richard Cook, Jessica Price (Berea College, Berea, KY); Mark Cunningham (Argonne National Laboratory, Argonne, IL).* The path to more efficient energy sources for modes of transportation, to replace the CO_2-emitting, low efficiency internal combustion engine, has led The Department of Energy and Argonne National Laboratory to develop commercially competitive polymer electrolyte fuel cells (PEFCs). The purpose of this project is to design and develop bimetallic cathodic electrocatalysts for PEFCs with high electrochemical activity and high stability in order to replace more expensive platinum-based electrocatalysts. The bimetallic electrocatalysts reported in this study are composed of the precious metal palladium (Pd) and the base metal iron (Fe) fixed onto carbon support. The less expensive base metal, iron, is designed to comprise the core of the bimetallic alloy with a monolayer outershell consisting of palladium. The Pd-Fe electrocatalysts were synthesized by the impregnation method, utilizing $Fe(NO_3)_3$ and $Pd(NO_3)_2$ as metal precursors, producing bimetallic catalysts with a range of metal compositions. The precursor salts were reduced to the Pd-Fe bimetallic electrocatalyst in a dilute hydrogen atmosphere. Transmission electron microscopy, temperature programmed-reduction, and cyclic voltammetry, using the rotating disk electrode, were used to characterize the electrocatalysts' composition and particle size, reduction conditions for heat treatment, and catalyst stability and performance, respectively. The bimetallic catalyst with a molar ratio of 30:70 (Pd:Fe), heat treated in regen gas at 620°C for 10 hours, showed the highest activity of 65.31 mA/mgPd at 0.85V. Further research will focus on maximizing catalyst performance by optimizing heat treatment conditions to minimize particle size with a core-shell morphology. The desired end result is a bimetallic alloyed electrocatalyst that is cost efficient, has a high rate of oxygen reduction, a small particle size, and an activity of 440 mA/mg metal at 0.9V (2010 DOE target).

Seeding Nucleation for the Production of Diamond Stripper Foils. *Ryan Coleman (The University of Virginia, Charlottesville, VA); Robert W. Shaw (Oak Ridge National Laboratory, Oak Ridge, TN).* Diamond stripper foils are implemented by the Spallation Neutron Source (SNS) to convert H- to H+ at the entrance of the accumulator ring. These corrugated nanocrystalline diamond foils can currently withstand about 800°C of injected charge when exposed to the 20 Hz, 800 MeV Proton Storage Ring at Los Alamos National Laboratory. Currently, it is necessary for the stripper foils to have lifetimes in excess of 200 hours for the operational scheduling of the SNS system to be independent of foil lifetimes. In light of the scheduled power upgrade for the SNS accelerator, research in producing stripper foils with longer lifetimes is necessary for the efficient operation of the SNS facility. Essentially, the production of diamond films involves two major steps: nucleation and growth. My research has been conducted to develop a nucleation procedure that is similar to one that recently appeared in the literature. The diamond films are grown on silicon substrates, and previously, nucleation sites were created by scratching the substrate surface in a diamond slurry solution. The new nucleation process involves depositing an amorphous carbon layer on the silicon substrate and then sonicating a dense layer of nano-powder diamond particles into the amorphous layer. These diamond particles act as seeds during the growth process, and the hypothesis was that this nucleation process could produce diamond films with higher uniformity. The amorphous carbon layers were deposited on the substrate surfaces with microwave plasma assisted chemical vapor deposition, and over the course of many experiments, the deposition variables were adjusted to find the ideal conditions for seeding. The varied experiments showed that the experimental apparatus could not yield the uniformity and thickness reported in the literature. However, we have discovered that the amorphous carbon layer may not be necessary; simply seeding the silicon substrates can promote the growth of uniform diamond films. The apparatus has no independent heating source, and the substrate temperature variable is strongly coupled with the power and pressure variables. This coupling prevented reproduction of the

reported growth conditions, and the reported nucleation process could not be implemented within the confines of the apparatus. As a result, the next phase of the research project is to incorporate an independent heating source into the plasma chamber.

*Fuel Cells: Synthesis and Characterization of Sulfonated Polysulfone for Proton Exchange Membrane (PEM). *Nancy Davenport* (*Chicago State University, Chicago, IL*) *Asare Nkansah* (*Argonne National Laboratory, Argonne, IL*). Fuel cells are electrochemical energy conversion devices which convert hydrogen and oxygen into water in the process of generating electricity. The most common fuel cells are proton exchange membrane fuel cells (PEMFC). In order to develop newer proton exchange membrane (PEM) material, a monomer containing protogenic sulfonic acid groups on the pendant branches was prepared from commercially available 2,2'diallylbisphenol A via two different reactions. The course of the reaction was followed by thin layer chromatograms. This new monomer was then polymerized with 4, 4'-dichlorodiphenyl sulfone by step growth polymerization. The resulting polymer was characterized by NMR. The most striking feature of this new polysulfone was its extremely high decomposition temperature. Future work involves conductivity and viscosity measurements to determine the application of sulfonated polysulfone as (PEM) in fuel cells.

Synthesis of Dendrimeric Polysulfonic Acid for Use as a Proton Exchange Membrane. *Brian Davis* (*Chicago State University, Chicago, IL*)*; Suhas Niyogi* (*Argonne National Laboratory, Argonne, IL*). The fuel cell technology is an alternative energy/power for the future. The performance of a proton exchange membrane fuel cell is dependent upon the ability of the membrane to transport protons from the anode to the cathode. The current technology uses expensive perfluorinated sulfonated polymer like Nafion with limitations. In this work a new hyperbranched sulfonated polysulfonate was prepared for possible application as a membrane material. Due to its inherent structure and the presence of sulfonic acid groups on the outer part of the polymer it is expected to provide efficient proton transport. The monomer 2-hydroxy-4-methyl-benzene-1,3-disulfonyldichloride (HDDC) was synthesized by reacting m-cresol in large excess of chlorosulfonic acid at room temperature. The monomer was polymerized via self-condensation in a biphasic system. The polymer was hydrolyzed to free sulfonic acid to obtain water soluble product. Insoluble hyperbranched polymer was obtained by reacting with 4,4-dihydroxybiphenyl prior to hydrolysis. The polymer melted at around 215–225°C.

Physical and Chemical Properties of Polyol-Based Deicing Solutions. *Sarina Dorazio* (*Genesee Community College, Batavia, NY*)*; William D. Samuels* (*Pacific Northwest National Laboratory, Richland, WA*). The U.S. Environmental Protection Agency (EPA) regulations require an alternative for the environmentally toxic propylene glycol (PG) and organic salt based deicers currently used in the United States at an estimated 35 million kg annually. New Battelle derived polyol-based deicing solutions are a more environmentally friendly, materials friendly, and cost effective alternative to PG or organic salt based deicers for airplanes and runways. The polyol-based solutions produced are D3: Degradable by Design Deicers, which include both Airplane Deicing Fluid (ADF) and Runway Deicing Fluid (RDF). These solutions meet the criteria put forth by different U.S. regulatory agencies such as the Federal Aviation Administration (FAA), EPA, and Department of Defense (DoD). Quick, reliable and simple testing parameters are critical to the eventual use of these solutions. Due to these constraints, a number of measurements were performed between June and August 2007 on various dilutions of the certified ADF and RDF solutions in order to define certain characteristics: refractive index, pH, density, and freezing point. A freezing point apparatus was used which was assembled to meet American Society for Testing and Materials (ASTM) specifications. Freezing points and other physical tests were run on diluted certifiable fluids and the data was correlated to identify the tests that will best predict the composition and efficacy of the fluid. Various cooled solutions were investigated with respect to their ability to transfer heat both quickly and efficiently in the freezing point apparatus.

Large Scale Production, Purification, and 65Cu Solid State NMR of Azurin. *Amy Gao* (*Olin College of Engineering, Needham, MA*)*; Robert Heck* (*Pacific Northwest National Laboratory, Richland, WA*). This paper details a way to produce azurin with an efficiency over 10 times greater than previously described and demonstrates the first solid state nuclear magnetic resonance spectrum of $^{65}Cu(I)$ in a metalloprotein (Harris *et al.*, 2004). A synthetic gene for azurin based upon the DNA sequence from *P. aeruginosa* including the periplasmic targeting sequence was subcloned into a T7 overexpression vector to create the plasmid pGS-azurin, which was transformed into BL21 (DE3) competent cells. The leader sequence on the expressed protein causes it to be exported to the periplasmic space of *Escherichia coli*. Bacteria grown in a fermentation unit were induced to overexpress the azurin, which was subsequently purified through an endosmotic shock procedure followed by high performance liquid chromatography (HPLC). 1,480 mg of azurin were purified per liter of culture. $^{65}Cu(II)$ was added to apo-azurin and then reduced. The ^{65}Cu metal cofactor in azurin was observed with solid state nuclear magnetic resonance (NMR) to determine any structural variations that accompanied copper reduction. This is the first ever solid state NMR spectra of a copper(I) metalloprotein. Analysis of the NMR spectra is being used to complement hypotheses set forth by X-ray diffraction and computational calculations of electron transfer mechanisms in azurin.

Characterization of Non-platinum Electrocatalysts for Polymer Electrolyte Fuel Cells. *James Gilbert* (*University of Illinois at Chicago, Chicago, IL*)*; Xiaoping Wang* (*Argonne National Laboratory, Argonne, IL*). Two of the limiting factors for polymer electrolyte fuel cell (PEFC) development are the cost and supply availability of platinum, which is currently used as the electrocatalyst for both the oxygen reduction reaction (ORR) and the fuel oxidation reaction. The goal of this project is to develop ORR catalysts that do not contain platinum, are less expensive, and offer comparable ORR activity to platinum-based catalysts. In this work, a testing procedure was established to evaluate ORR activity by using commercial platinum and non-platinum electrocatalysts and using cyclic voltammetry with a rotating disk electrode setup that is used for correction for mass transport contribution. The non-platinum catalysts studied were different compositions of a palladium-based bimetallic system supported on carbon that were prepared by impregnation and post-temperature-programmed reduction. Their ORR activity per mass of metal catalyst was determined and compared to that of commercial catalysts. Results show that the alloying of the base metal to the palladium yields a greater activity. The best ORR activity was observed from the atomic ratio of palladium to the base metal of 1:1, with ratios of 9:1 and 3:1 showing improved activity than that of the palladium catalyst alone. This project is part of a larger effort to develop an effective, low-cost, platinum-free cathode catalyst for PEFC technologies. Future work will include a broader characterization of the palladium-based bimetallic catalyst for practical use in a PEFC, along with the study of other palladium-based bimetallic systems.

***In-Situ* Analysis of Platinum Degradation for Fuel Cell Catalysts Using Small-Angle X-Ray Scattering.** *James Gilbert* (*University of Illinois at Chicago, Chicago, IL*)*; Matt Smith* (*Argonne National Laboratory, Argonne, IL*). Catalyst durability during Polymer Electrolyte Fuel Cell (PEFC) operation remains a key challenge in developing a cost effective PEFC with an acceptable lifetime for both automotive and stationary power generation. Understanding the mechanisms of catalyst degradation is essential for furthering research toward lengthening fuel cell lifetimes. Platinum (Pt) and platinum-alloys are considered to be state-of-the-art catalysts for PEFCs. The precise method of the Pt corrosion is still unknown. However, several mechanisms have been proposed such as Pt dissolution and re-deposition (Ostwald ripening), coalescence of platinum particles via migration on the carbon support, and Pt particle agglomeration triggered by corrosion of the carbon support. Novel synthesis of nano-sized catalyst particles has improved power performance and lowered material cost. However, it is observed that the smaller the particles the faster the degradation and agglomeration via, nominally, the above mechanisms. Small Angle X-Ray Scattering (SAXS) is a powerfully accurate X-ray technique for characterizing particle size, especially between 1 and 100 nm. Thus SAXS is highly specific to the nano-sized Pt catalysts, which have been observed to aggregate to as much as 30 nm from an initial size of approximately 2–3 nm. In this study, samples of 20 wt% (2.2 nm) and 40 wt% (2.8 nm) Pt supported on commercial Vulcan XC-72 carbon were characterized *in-situ* using SAXS while cycling the potential between 0.4 and 1.4 V for up to 16 hours in an electrochemical half-cell. Particle size change was observed to increase 55% and 50% for the 20 wt% and 40 wt% Pt/C catalysts, respectively. SAXS data shows trends in particle growth correlated to cycle time and electrochemical potential. The results contained in this study have significant implications with regards to the durability of carbon-supported Pt-based nano-sized catalysts. These results also make a significant contribution to the larger effort in determining the mechanism by which Pt degrades.

Separation of Lanthanide Ions with Kläui Ligand Resin. *Trinity Granger* (*University of the Virgin Islands, St. Thomas, VI*)*; Gregg Lumetta* (*Pacific Northwest National Laboratory, Richland, WA*)*;*

Victoria Henry (*University of the Virgin Islands, St. Thomas, VI*). Separation and pre-concentration of the desired analyte is often a critical step in many radioanalytical methods. Current procedures for separating and concentrating analytes for detection are complex, and can be both expensive and time consuming. Therefore, the purpose of this research is to develop an alternative method of separating lanthanide ions through the use of an extraction chromatography resin containing a Kläui ligand salt. This research is a continuation of a concerted effort to develop new methods of detecting small concentrations of radionuclides and lanthanides using Kläui ligands. The Kläui ligands, $C_5Me_5Co(OP(OR)_2)_3^-$ (R=Me, Et, i-Pr, n-Pr) (L_{OR}^-), have unique affinity for lanthanide and actinide ions in the presence of competing metal ions. The use of 1 wt% NaL_{OR} (R=Et or n-Pr) adsorbed onto resin support has been shown to extract lanthanide ions from aqueous nitric acid solutions of different concentrations. In order to further evaluate the utility of these materials in radiochemical separation, the selectivity of the resins for the different lanthanide ions was examined by measuring the distribution coefficients (K_d) for a series of lanthanide over a range of solution conditions. Based on prior research with actinide ions, it was hypothesized that the lanthanide ions would bond strongly with the Kläui ligands. The success of this research is important, because it will assist in expanding and improving current automated radiochemical methods, which will decrease the cost of developing and implementing radiochemical methods. To date, Kd values have been determined for Eu^{+3}, Nd^{+3} and Pr^{+3} under varying nitric acid (HNO_3) concentration, using a resin consisting of 1.0 wt% NaLOPr on Amberlite XAD-7HP. The dependence of the Kd values for Eu^{+3} has also been examined as a function of the ligand-to-europium ratio and the nitrate concentration. Decreasing K_d values were obtained upon increasing the nitric acid concentration, indicating protonation of the ligand, which competes with binding of the lanthanide ions. As expected, increasing the Kläui ligand-to-europium ratio results in increasing K_d, but no conclusions could be made from these data regarding stoichiometry of the complex formed on the resin. No dependence of the K_d on the nitrate concentration was observed, supporting the notion that the HNO_3 dependence is dominated by the presence of the acidic hydronium ion (as opposed to the nitrate ion). Future work will involve the determination of the K_d values for the remainder of the lanthanide series to further assess the potential of the Kläui ligand for intra-group lanthanide separations.

Synthesis of Ionic Liquids for Toxicity Studies. *Jinhee Gwon* (*CUNY Queensborough Community College, Bayside, NY*)*; James F. Wishart* (*Brookhaven National Laboratory, Upton, NY*)*; Xing Li* (*Queensborough Community College, New York, NY*). Ionic liquids (ILs) have potential uses as green solvent alternatives due to their relative non-volatility, non-flammability, wide liquid range, and high conductivity when compared to volatile organic solvents. Understanding the possible IL toxic effects on the environment before replacing the current solvents with them is critical. Reports suggest that many ILs are toxic to organisms varying from nematodes to algae and fish. However, those studies do not indicate a relationship between the purity of the ILs and their toxic effects. This investigation explores that relationship. A series of halide salts based on N-methylpyrrolidine were successfully prepared. N-methylpyrrolidine was reacted with alkyl halides of various chain lengths to produce the corresponding quaternary ammonium halide salts. These alkyl halides include 1-Bromobutane, 1-Bromopentane, 1-Bromodecane, 1-Bromododecane, and 1-Bromooctadecane. The quaternary ammonium halide salts were purified by washing with ethylacetate and diethylether. The structures of the salts were confirmed using H-1 and C-13 Nuclear Magnetic Resonance (NMR) spectroscopy. The salts were then converted to ionic liquids bearing the phosphate (PO_{43}^-) and bis(trifluoromethylsulfon yl)imide(-NTf2) anions. These liquids were prepared in different levels of purities. Purity was checked using NMR, fluorescence and UV-visible absorbance spectroscopy. This is a part of a larger collaborative research project where other similar series of ionic liquids based on imidazolium and pyridium cations were prepared and screened for their toxicity to a variety of microorganisms.

Dynamic Dissolution Testing of Nanoporous Niobium Phosphate. *Katherine Harris* (*The College of William and Mary, Williamsburg, VA*)*; Dawn Wellman* (*Pacific Northwest National Laboratory, Richland, WA*). Leaks in storage tanks holding radioactive waste on the Hanford Site and other Department of Energy (DOE) sites have led to a need for *in situ* soil and groundwater remediation techniques. Nanoporous transition metal phosphates have been shown to be effective in reductively sequestering radionuclides, but their stability within subsurface conditions has not been evaluated. A conservative estimate of the stability of nanoporous niobium phosphate (NP-NbPO) was quantified using single-pass flow-through (SPFT) dissolution testing under the pH range of 6–9 at 90°C. The tests were run until a steady-state rate of dissolution was reached. Inductively coupled plasma-optical emission spectroscopy (ICP-OES) analysis of effluent samples indicates that at 90°C the dissolution rate of NP-NbPO, 4.31 x 10^{-7} mol m^{-2} s^{-1}, is independent of pH. The high, pH-independent stability of NP-NbPO suggests it may serve as a stable, highly effective radionuclide barrier within the subsurface environment. Further quantification of dissolution rates under the temperature range of 5° to 60°C and evaluation of the migration of NP-NbPO through the vadose zone is pending. However, preliminary results show that NP-NbPO is a promising candidate for *in situ* remediation for radionuclide-contaminated soil and groundwater.

*Comparing the properties of pyridinium and 4-dimethylamino-pyridinium ionic liquids. *Jasmine Hatcher* (*Queens College, Queens, NY*)*; James Wishart* (*Brookhaven National Laboratory, Upton, NY*). Ionic liquids, organic salts that melt below 100°C, are generally composed of a large organic cation and a relatively small inorganic anion. They have generated much interest due to their potential as alternative reaction media for a variety of applications including use in batteries, fuel cells, and for the storage and processing of nuclear waste. Ionic liquids can be designed to incorporate specific functionalities for certain uses ("task-specific ionic liquids"). The physical characterization and properties of 4 dimethylaminopyridnium (DMAP) based ionic liquids with varying functionalities in comparison to their pyridinium (py) analogues are reported here. In addition, this study examines the effect of the dimethylamino group of DMAP on the physical properties of these two series of ionic liquids. The dimethylamino group of DMAP is known to have catalytic properties and DMAP based ionic liquids are expected to have similar properties. The DMAP and pyridinium salts were synthesized using various alkylating agents such as 3-chloropropanol and 2-bromoethyl ethyl ether. The resultant halide salts were converted to ionic liquids bearing bis(trifyl)imide anion. Physical properties investigated include: viscosity, conductivity, and thermal profile. Preliminary results indicate that for both the DMAP and py systems, the ionic liquids containing alkyl groups have lower viscosities and higher conductivities at room temperature compared to those bearing hydroxyl groups. Results also suggest the presence of the dimethyl amino group on the pyridine ring has minimal effect on the conductivity and viscosity. The Butyl DMAP and Butyl Pyridinium ionic liquids had almost the same conductivity (2.12 mS/cm and 2.22 mS/cm respectively) and viscosity (9.950 cP and 9.122 cP at 850°C respectively). Future work will focus on the effect of the position of the dimethylamino group on the pyridine ring on the same properties.

A study of Nitrogen-containing complexes of Zinc(II) as photocatalysts in the production of hydrogen peroxide. *Jennifer Hayes* (*University of Wyoming, Laramie, WY*)*; Robert Disselkamp* (*Pacific Northwest National Laboratory, Richland, WA*). Hydrogen peroxide is a valuable chemical commodity and its use as a clean, easily stored, and high energy density fuel source may gain acceptance should there be efficient and sustainable methods of production from dioxygen and water using solar irradiation. The current method of manufacturing is not cost efficient and photocatalytic production from solar light is one approach that has not been explored in detail. The concentration of hydrogen peroxide produced in an ultraviolet (UV) irradiated environment using nitrogen-containing complexes of zinc(II) as photocatalysts was studied using isomers of imidazole, indazole, pyrazole, pyrazine, and phenylenediamine complexes. Three variables are at play in determining production efficiency including catalyst UV absorbance, photon output, and quantum yield. UV wavelengths between 280nm and 360nm were attained from a UV-B lamp. Sample catalyst complexes were immersed in water, aerated, and irradiated over time to initiate a redox reaction between dissolved oxygen and water using photoinduced ionization properties of the semiconductor system for electron transport. Concentration of at certain time intervals was determined by titration with potassium permanganate. Ultra-violet absorbance and percent transmittance of the photocatalyst solids were measured with a UV-VIS scanning spectrophotometer. Irradiation of multiple zinc complexes revealed Zn-5-amino indazole to have the greatest first day production of 62.63mM, 37% quantum yield for the first 24 hours. Para-phenylenediamine showed the greatest long-term production as concentrations increased for 70 hours before a decrease was measured. Isomeric forms of the catalyst's organic components did have an effect on production. Irradiation of diaminopyridine isomers indicated 2,3 and 3,4 structures were the most productive, each generating 32mM hydrogen peroxide. However, the 2,5 isomer showed no production. After 90 hours, significant decrease in was noticed in all samples, suggesting a stoichiometric rather than catalytic relationship.

In this study, Zn-indazole and certain isomers of Zn-diaminopyridine complexes seemed to be the most active among those tested, exhibiting greater production efficiency and producing the highest quantum yield based on UV-absorbance. Photocatalytic production of hydrogen peroxide using these compounds has a strong potential to be an energy and cost efficient prospect in a renewable energy economy.

Synthesis of Novel Anion Receptors for Separation. TRINA HAYES, BETHTRICE THOMPSON, KIMBERLY TUCKER (*Jackson State University, Jackson, MS*)*; BRUCE MOYER (*Oak Ridge National Laboratory, Oak Ridge, TN*). Synthesis of Novel Anion Receptors for Separations Bethtrice Thompson, Trina Hayes, Kimberly Tucker, Alamgir Hossian Jackson State University, Jackson, MS FAST Bruce Moyer, Peter Bonnesen Chemical Science Division Oak Ridge National Laboratory Many anionic species have become a major environmental and health concern. For example nitrate is an agricultural contaminant in soil and is also present in large quantities of radioactive waste. As for the health concern, nitrate that is above the U.S. Environmental Protection Agency's regulated contamination level in ground water has caused an increase in bladder cancer in women. These major concerns have led researchers to develop anions receptors that can detect, bind, separate, and remove anions from the environment. To address such needs, we have been carrying out the synthesis of monofunctional, difunctional, and trifunctional thiourea compounds and their guanidinium derivatives. We followed a multi-step synthesis in which our starting compounds are isothiocyanate and amine which are converted to the desired thioureas followed by methylation and aminolysis to afford the guanidinium derivatives. Making and breaking covalent bonds is applied to construct desired molecules. The new compounds are analyzed by NMR spectrometry. It is planned to obtain crystals from the compounds in order to determine their molecular structures by X-ray Crystallography. These receptors will be used for binding and separation of the target ionic species in complex mixtures. Binding properties of synthesized molecules for anions will be tested in different solvents using NMR spectrometry. This study will provide ground work for future cleanup and vitrification of USDOE wastes and environment streams.

Determining the Extent of Delocalization in Mixed-Valence Iron Dimers Using X-ray Absorption Spectroscopy. ALISON HOYT (*Yale University, New Haven, CT*)*; KELLY GAFFNEY (*Stanford Linear Accelerator Center, Stanford, CA*). This study examines the extent of charge delocalization in mixed valence compounds. Understanding the structure of charge delocalization is the first step in understanding the local dynamics of charge transfer. This insight has diverse applications such as the ability to mimic biological reactions and to enhance solar technology. Because of its fast time scale, synchrotron radiation was used to probe the iron K-edge for three organometallic systems. In these complexes, two bridged metal atoms share an effective charge of 5+. In a Robin-Day Class II compound, charge is localized and the two iron atoms have effective oxidation states of 2+ and 3+ respectively. For Class III delocalized compounds each metal center has an effective charge of 2.5+. Class II/III compounds exhibit characteristics of both localized and delocalized systems according to various optical spectroscopies. Synchrotron radiation was used to study charge distribution in these poorly-understood Class II/III intermediate systems. In the limit of absolute localization, spectra of the mixed valence species were expected to be a linear combination of the reduced and oxidized species. For the delocalized case, a linear combination was not expected. These two cases were used as calibration limits to determine the extent of delocalization in the unknown Class II/III compound. Results showed that synchrotron radiation classifies the Class II/III compound as localized. However, data also demonstrated that the linear combination model did not hold as expected and a revised model is necessary to better understand this phenomenon.

Investigating the microwave-assisted synthesis of ionic liquids. KIJANA KERR (*Queensborough Community College, Bayside, NY*)*; JAMES F. WISHART (*Brookhaven National Laboratory, Upton, NY*). Ionic liquids (ILs), which have gained a lot of attention as alternative solvents recently and have found industrial applications, are salts that are liquid at or near room temperature. This makes them good solvents for a range of organic and polymeric compounds. ILs typically consist of large nitrogen-containing organic cations and small inorganic anions. The need is increasing for developing synthetic procedures that are faster, more efficient, and more economical as the number of applications for ionic liquids increase. Typical advantages of microwave-assisted syntheses are to significantly reduce reaction times and increase the product yield. The microwave assisted syntheses of halide salts based on DABCO diazabicyclo[2.2.2]octane and their conversion into ionic liquids are reported here. Reaction conditions, such as the temperature, the nature of the reaction solvent and the

length of reaction time, have been varied. A comparison of these two synthetic techniques (thermal and microwave-assisted) and the physical characterization of these compounds are reported. Preliminary results show that quaternization has been achieved to produce mono- and di- substituted DABCO halide salts with different substituent groups such alkyl, ethoxy and hydroxyl. Conditions have been worked out to obtain some of these salts in high yields, particularly alkyl containing DABCO salts. Structure determination of the resulting ionic liquids was done using 1H, 13C and 31P NMR spectroscopy. Subsequent characterization, including differential scanning calorimetry (DSC), of a series of compounds is reported. Dramatic differences in melting points were observed with anion variation of DABCO compounds.

The Characterization of Gadolinium-Loaded Liquid Scintillator: An Antineutrino Detector for σ13 Measurement. TIGISTI KESETE, IKENNA OKAFOR (*Central State University, Wilberforce, OH*)*; SELEEM, RICHARD HAHN, MINFANG YEH (*Brookhaven National Laboratory, Upton, NY*). After the Sudbury Neutrino Observatory successfully observed three neutrino flavors and solved the 40-year-old solar neutrino problem, most of the neutrino experiments have been focusing on the understanding of the neutrino oscillation mechanism. Continued growth in this field depends strongly on the unknown mixing angle σ13, a fundamental neutrino parameter that is needed as an indicative guideline for next-generation neutrino experiments. The Daya Bay collaboration proposed by scientists from U.S., China, and Russia are favored for σ13 measurement because their derivations for σ13 are relatively clean and unambiguous. The gadolinium-loaded liquid scintillator (Gd-LS) is the centerpiece of the antineutrino detector, and its key required characteristics are long-term chemical stability, long attenuation length, and high photon production. Research has indicated that three carboxylic acids-3,5,5-trimethylhexanoic acid (TMHA), 2-ethylhexanoic acid (EHA), and methylvaleric acid (MVA)-could interact with inorganic Gd aqueous solution to form organometallic carboxylate that could be extracted into the organic liquid scintillator by solvent-solvent extraction. However, the Gd-LS synthesized with these acids showed different chemical properties. To characterize their effects on the antineutrino detector, this summer research focused on: (1) purifications of TMHA, EHA, and MVA to improve their optical transparencies and chemical stabilities and determination of their dissociation constants (pKa) to better understand the chemical properties of the synthesized Gd-LS, and (2) comparisons of the phosphorescence and fluorescence effects to the photon production of Gd-LS with the carboxylic acids. Experimentally, vacuum distillation was used to purify the acids, and their purification effects were monitored using Shimadzu UV-1601 absorption spectrometer by the absorbance at 430 nm. Results indicated that the attenuation lengths for TMHA, EHA, and MVA were improved from 2.7 m, 1.6 m, and 1.8 m to 7.2 m, 6.2 m, and 10.9 m, respectively. The acid-base titrations for three acids were conducted with Accumet AR25 dual-channel pH/Ion meter by fitting their differential curves (Gaussian distribution), and their pKa values were determined to be below 5. For phosphorescence and fluorescence comparisons, the light-yield data indicated that the photon production of the Gd-LS was mainly dominated by fluorescence process. The characteristics of Gd-LS synthesized with these acids are still under further analysis.

Electrochemical Remediation of Arsenic Contaminated Groundwater. KRISTIN KOWOLIK (*University of California – Berkeley, Berkeley, CA*)*; ASHOK GADGIL (*Lawrence Berkeley National Laboratory, Berkley, CA*). Millions of people worldwide do not have access to clean water. This problem is especially severe in Bangladesh where water is severely contaminated with arsenic. Chronic arsenic exposure has devastating health effects: cardiovascular diseases, cancers, and eventually death. Many methods of arsenic removal have been studied but most of these are too expensive and impractical to be implemented in poor countries such as Bangladesh. This project investigates electrochemistry as an affordable means of removing arsenic. Experiments are performed using a whisk like device made out of iron as the cathode and copper as the anode. Both electrodes are immersed in simulated groundwater spiked with an arsenic concentration of 600 ppb. During voltage application, currents of 70 mA and 110 mA are passed through the system. The water is stirred gently to ensure uniform electron distribution. While the electrochemical process is progressing, iron metal is oxidized to Fe(III). As an ionic species, iron will bind free arsenic in solution. After the desired amount of charge is passed, the treated water is allowed to precipitate for 24 hours and is then filtered by means of vacuum filtration. One of the significant major tasks of the project was to develop an experimental protocol (methods, measurement techniques, experimental conditions) to obtain proof of concept, so this process can be investigated further.

We showed that if certain conditions are met such as (1) optimal charge per volume, (2) optimal current density and (3) precipitation time of 24 hours, promising results are obtained. An initial arsenic concentration of 600 ppb can be reduced to a final concentration of 50 ppb in 2.5 L water by application of 70.08 C/L at 70 mA and 107.5 C/L at 110 mA. These results are very encouraging and provide great promise that electrochemistry is a powerful, and most importantly, an affordable tool in the remediation of arsenic from contaminated groundwater.

Integrated Electrodialysis Membrane Process for Beneficial Use of Coalbed Methane Produced Water. *Stephanie Le Clair* (*Saint Mary's College of California, Moraga, CA*); *Paula Moon* (*Argonne National Laboratory, Argonne, IL*). During oil and gas production, the water that is trapped in underground formations is brought to the surface. About 15–20 billion bbl of this water, known as produced water, is generated in the United States each year. The Colorado Energy Research Institute at the Colorado School of Mines has brought together a team of scientists and engineers to address produced water management. In support of this effort, Gas Technology Institute and Argonne National Laboratory have been collaborating in using electrodialysis (ED) to remove ions from water in the Powder River Basin (PRB) so that the water may be used for irrigation or livestock drinking water. In most states, the criteria needed for beneficial use include averages of total dissolved solids of 1,000–2,000 mg/L, a pH range of 6–8, and a sodium absorption ratio (SAR) of less than 6. In order to meet water discharge specifications, experiments were conducted with produced water from the PRB area to determine the parameters needed for the ED system. The electrodialysis membrane type, current density, stock concentrations, and power consumption were tested to find an optimum for each variable. Different post-demineralization treatments were also performed, using calcium carbonate, calcium sulfate and limestone, to determine which was the most effective at desalting the water, after the use of the ED system. Results showed that the best configuration for the ED system consisted of using of a non-selective membrane as the cation membrane, a sodium bicarbonate solution as the concentrate and a current density of 4.00 mAmps/cm^2. This setup provided the most cost-effective ED system, yielding 88.9% desalination with a modest energy input of 0.18 kWh/lb of NaCl removed. For post-treatment demineralization, limestone proved to be the most cost-effective way to lower the SAR value to below 6. These experiments showed that it should be possible to desalt the produced water up to around 80% and then treat the water with limestone to reach the water quality needed to dispose of it for beneficial use. A long term membrane stability experiment is currently underway.

Separating and Recovering Materials from Shredder Residue. *Stephanie Le Clair* (*Saint Mary's College of California, Moraga, CA*); *Joseph Pomykala, Jr.* (*Argonne National Laboratory, Argonne, IL*). Every year, 4.5 million metric tons of shredder residue — a complex heterogeneous mixture generated from shredding automobiles, electrical appliances, construction debris, and other metal-containing materials — is landfilled. Argonne National Laboratory has been developing a mechanical process to separate and recover various materials from shredder residue. The process has successfully recovered ferrous metals, nonferrous metals, a mixture of polypropylene and polyethylene, and acrylonitrile butadiene styrene. Byproducts from this process include two fractions, referred to as fines, that are on average 40% by weight of the starting shredder residue. One objective of the project was to determine the technical feasibility of separating and recovering polymers and metals from the fines. Analysis was conducted on samples from a 100 pounds experiment to complete a mass balance and determine the quantities of recoverable materials of value, such as plastics, rubber compounds and metals. The tests showed that it was technically feasible to separate and recover from the fines a polymer concentrate fraction, which accounted for 19.1% by weight of the starting shredder residue. This fraction contained 9.9 wt.% metals, 18.3 wt.% plastics, 54.5 wt.% rubber, and 17.3 wt.% others, including rocks, fibers, and foams. Future work will involve developing a method to separate and recover the metals from the polymer concentrate fraction. The plastics will then processed through the Argonne developed froth-flotation process. Another objective of the project was to determine what cleaning processes would be more successful in removing the polychlorinated biphenyls (PCBs) from the plastics. For any product recovered from shredder residue to be reintroduced into the U.S. market, it must contain a PCB concentration of less than 2 ppm. Current commercial methods to remove PCBs to below this limit are not cost effective. Benchscale tests were conducted by using washing solutions with different catalysts, two different solvents, and various thermal desorption techniques. The

plastic samples were then sent to Environmental Monitoring Technology for analysis. The received analytical results showed that none of the methods were able to remove the PCBs to a concentration below 2 ppm. The analytical results for all of the experiments have not been received yet, however. Future work will involve larger scale testing of the most promising approach.

Evaluation of relative metal nucleophilicities of diphenyldithiophosphinate ligands Using gas-phase dissociation reactions. *Christopher Leavitt* (*Wichita State University, Wichita, KS*); *Anita Gianotto* (*Idaho National Laboratory, Idaho Falls, ID*). The relative metal cation nucleophilicities of a series of unique diphenyldithiophosphinate ligands were evaluated by forming [metal-mixed ligand]- complexes, then fragmenting them using competitive collision induced dissociation. The bis(trifluoromethyl phenyl)dithiophosphinate anions are of high interest because they have demonstrated potential for exceptional separation of Am3+ from lanthanide trications. With respect to sodium and europium (III), the unmodified diphenyldithiophosphinate anion (Lu-) was compared with three different ligands, which varied in terms of the position of the trifluoromethyl (TFM) group on the phenyl rings: bis(ortho-TFM) (L1-), (ortho-TFM)(meta-TFM) (L2-), and bis(meta-TFM) (L3-). Relative to Na+, the unmodified Lu- anion was the strongest nucleophile. Comparing the TFM derivatives, the bis(ortho-TFM) derivative, L1-, was found to be the strongest nucleophile, while the bis(meta-TFM), L3-, was the weakest, and the mixed ortho,meta derivative was intermediate. Similar experiments were performed using europium nitrate complexes; ionic dissociation of these complexes always produced the anionic TFM ligands, showing again that the unmodified Lu- was the strongest nucleophile. The europium (III) nitrate complexes also underwent redox elimination of radical ligands. The tendency of the ligands to undergo oxidation and be eliminated as neutral radicals followed the same trend as the nucleophilicities for Na+, viz. Lu- > L1- > L2- > L3-.

Determination of Silica in Uranium Casting Pins Samples by Inductively Coupled Plasma-Atomic Emission Spectroscopy (ICP-AES). *Megan Longo* (*Albertson College of Idaho, Caldwell, ID*)*; Jeffrey Giglio* (*Idaho National Laboratory, Idaho Falls, ID*). An analytical method was developed for the determination of Silica (Si) in Uranium casting pins. The new method utilized an Inductively Coupled Plasma Atomic Emission Spectrometer (ICP-AES) for the determination of Si at 250.69 nm and 251.611 nm. The Si lines yielded instrument detection limits (3s) of 0.007 and 0.02 µg/mL, respectively. The method detection limits for the new analytical method are 50 µg/g in the solid. An interfering element correction had to be employed because of a spectral interference from U. The U concentration in the solutions analyzed by ICP-AES was approximately 1150 µg/mL. Spiked sample recoveries yielded complete recoveries, within the experimental error of the analysis. The new ICP-AES method was compared to a molybdenum blue colorimetric method. Results were comparable, within the experimental error of both measurements.

Variating Parameters to Increase DNA Encapsulation in Biodegradable Nanospheres for Drug Delivery Applications. *Tracey Mamma* (*Norfolk State University, Norfolk, VA*)*; Carol J. Mertz* (*Argonne National Laboratory, Argonne, IL*). Nanoparticles are submicron-sized polymeric colloidal particles that can have a therapeutic agent of interest encapsulated within, conjugated on the surface or absorbed on the surface of their polymeric matrix. In recent years, biodegradable nanospheres have become the focus of extensive research. We will evaluate the use of various solvents (primarily dichloromethane, acetone, and chloroform), in combination with different molecular weights of PLGA, to determine the most effective combination to produce high DNA encapsulation and minimal particle size. For biomedical applications these nanospheres are made of biodegradable and biocompatible polymers of poly (D, L-lactide-co-glycolide) (PGLA) and allow controlled and protected delivery of a therapeutic agent encapsulated in the polymer core. Research on the use of these polymers has shown a wide range of encapsulation efficiencies for DNA when a double emulsion (w1/o/w2) method was used. In this study, the focus is on increasing the encapsulating efficiency of DNA into biodegradable/biocompatible nanospheres for drug delivery application. When FDA approved materials are used in the manufacturing of the nanoparticles, the laboratory and animal testing phase may be shortened allowing the nanospheres to move to the human clinical trials sooner. While varying the synthesis parameters, the goal is to optimize the encapsulation of DNA while tailoring the size of the nanospheres. These particles can be tailored to target specific cellular/tissue, improve oral bioavailability, solubilize drugs for intravascular delivery, solubilize drugs for and improve the

stability of the therapeutic agents, specifically against enzymatic degradation (nucleases and proteases).

Power Density and Longevity of Solid Oxide Fuel Cells. *Amanda Manley* (*College of Dupage, Glen Ellyn, IL*)*; Richard Jarman* (*Argonne National Laboratory, Argonne, IL*). The solid oxide fuel cell (SOFCs) are an electrochemical energy conversion device. The objective of this project is to improve the power density of a solid oxide fuel cell while using components that are lower in cost and have more chemical and physical durability. Tri-layer cells were made by tape casting. They consisted of a hydrogen electrode, an electrolyte, and a porous stainless steel support layer. This design increases the stability of the hydrogen electrode while allowing more flexibility in sintering options than traditional ceramic supported SOFC, while at the same time reducing the cost of the fuel cell. The tri-layer cell was evaluated using the scanning electron microscope to determine the distribution of elements after sintering. The oxygen electrode was screen printed onto a previously sintered tri-layered cell which was then sintered again. One of the objectives was to find the optimal sintering temperature for the oxygen electrode, to minimize the potential for oxidation of the stainless steel support. The power density characteristics of the device were then measured using electro-chemical impedance spectroscopy, and cell DC polarization. By increasing the power density of SOFCs that run at a lower operating temperature they may be more widely utilized for a broader selection of applications.

Determining the Local Structure of Platinum Streptidine Using X-Ray Absorption Spectroscopy. *Michaelle Mayalu* (*Massachusetts Institute of Technology, Cambridge, MA*)*; Serena Debeer George* (*Stanford Linear Accelerator Center, Stanford, CA*). X-Ray absorption spectroscopy (XAS) is a technique that utilizes high energy X-rays commonly obtained from synchrotron radiation to determine the structure of known and unknown substances and materials. By examining the absorption vs. energy pattern, one can determine the local structure surrounding the absorbing atom. Analysis of a region of the absorption vs. energy graph called extended X-ray absorption fine structure (EXAFS) leads to information about the identity of the atoms surrounding the absorber, the number of atoms surrounding the absorber, and the distances between the absorber and neighboring atoms. Using XAS, structural descriptions of platinum streptidine, a newly synthesized platinum anti-cancer agent, have been obtained. The results show that the platinum is in fact coordinated to the streptidine, which was the main question that needed to be answered about the drug.

*Developing a Single Source Precursor for Next Generation Lithium Ion Batteries. *Toni McIntyre* (*Fayetteville State University, Fayetteville, NC*)*; Jonathan Breitzer* (*Argonne National Laboratory, Argonne, IL*). The electrical conductivity of manganese oxides make them an ideal cathode material in lithium ion batteries. Coupled with the electrochemical stability of titanium, this combination proved to be an excellent cathode with exceptional electrochemical performance. Using a single source precursor method for combining these ions demonstrated a much better performing cathode material than by physically mixing them, due to the resulting smaller crystal size and better cation mixing. The precursor $MnTiO(C_2O_4)_2$ was synthesized by first forming a stable solution of $H_2TiO(C_2O_4)_2$ and then adding a stoichiometric amount of Mn(II) to precipitate the final product. LiOH • H_2O was added and the sample was heated to 300°C to produce the desired material, $Li_2Mn_{0.5}Ti_{0.5}O_3$. $Li_2Ni_{0.5}Ti_{0.5}O_3$ can also be synthesized using this method. The ceramic sample was formed by physically grinding MnO, TiO_2, and LiOH · H_2O and heating in air at 900°C. The ratio of Ti to Mn was varied by synthesizing a precursor with Ti and $H_2C_6H_{12}N_2$ (DABCO) replacing Mn as the +2 cation. Coin cells were constructed using four different materials as the cathode laminates, lithium metal as the anode, and 1.2M $LiPF_6$ in a 3:7 %wt mixture of ethylene carbonate (EC)/diethyl carbonate (DEC) as the electrolyte. The coin cells were tested by cycling them from 4.85 V to 1.8 V with a fixed current of 0.16 mA at room temperature. The cells containing the laminates prepared using the precursor method with a 1:1 metal ratio performed better than the other batteries, with an average first cycle capacity of 350 mA·h/g. The laminates with the 2:1 (Ti to Mn) ratio had an average first cycle capacity of about 100 mA·h/g, but had a very stable cycle pattern. The physically synthesized laminate had an average first cycle capacity of about 50 mA·h/g. The compound containing only Ti had a first cycle capacity of about 0.03 mA·h/g. The precursor method of synthesizing these cathode materials proved to be more electrochemically favorable than the ceramic method. Further studies on increasing the ratio of manganese to titanium may further optimize the electrochemical performance of cathodes.

*Analysis of Some Near-Infrared Spectra of C₂Br. *Elizabeth Millings* (*Suffolk County Community College, Selden, NY*)*; Trevor Sears* (*Brookhaven National Laboratory, Upton, NY*). In combustion chemistry, the C_2H molecule has been studied extensively because it is an important intermediate and provides an example of the breakdown of the Born-Oppenheimer approximation. A related molecule, C_2Br, supplies a different view of the Born-Oppenheimer breakdown, and its rotational, vibrational, and electronic structure can be compared to C_2H. Previously, only computational studies have been reported regarding C_2Br. Its energy states and spectra were theoretically determined, and a model equation was developed to describe its rotational energy levels. Recently, a spectrum of C_2Br was accidentally detected at Brookhaven National Laboratory, and a portion of it was tentatively assigned to some P-branch rotational transitions. In this project, the spectroscopic data were further examined in an attempt to confirm the assignments, determine the rotational constants, identify spectral lines corresponding to the two bromine isotopes, and identify the band origins. To accomplish this, a LabVIEW computer program was developed and used to calculate the energy levels and predict spectra, which were then compared to the experimental near-infrared (NIR) spectra. The error between the data and the calculations was minimized by adjusting the modeling constants and testing possible assignments. A simulated spectrum was created with each new calculation enabling a set of "best fit" values to be determined. This analysis is part of a larger work investigating the chemical processes of combustion by studying the structure and dynamics of intermediate reactive species.

Novel Reduction of Monosaccharides and Disaccharides using Palladium-Carbon Catalysts. *Fiona Mills-Groninger* (*Manchester College, North Manchester, IN*)*; George Kraus* (*Ames Laboratory, Ames, IA*). Mixtures of sugars as by-products of industrial processes are difficult and expensive to separate. This will be increasingly important in the emerging cellulose ethanol industry in which large volumes of carbohydrates will be produced. By reducing the different sugars in a mixture to a single product in a single-step reaction, the resulting carbohydrate can be easily used in further processes. Reductions of carbohydrates using palladium-catalyzed reactions are documented in literature, typically with lengthy reaction times. In this study, mono- and disaccharides are reduced using a novel combination of palladium-carbon catalyst, formic acid, and concentrated sulfuric acid heated to 80°C, producing the reduced form of the simple carbohydrate after one hour. Reaction progress was determined using 300 and 400 MHz proton NMR. After successful production of the reduced sugar, the compound was acetylated using acetic anhydride and purified using TLC and flash column separation. Various acetylation conditions were attempted, and reaction efficiency was determined using the NMR spectra as well as qualitative TLC comparison. Reduction was confirmed by comparing the spectra of the carbohydrate starting material with spectra after reduction. The spectra of a-methyl-D-glucopyranoside (methoxy glucose), dextrose, D-cellobiose, and sucrose showed distinct differences from the starting material indicative of reduction. Furthermore, comparison of the spectra of reduced forms of methoxy glucose, dextrose, and cellobiose showed almost identical peaks consistent with production of a single reduced product. The complex carbohydrate cellulose acetate was unable to be reduced using this method. Future work will include optimizing conditions for acetylation as well as determining conditions for effective reduction of complex carbohydrates.

Determination of Naturally Occurring versus Process Introduced Beryllium at Lawrence Livermore National Laboratory. *Jennifer Mullins* (*Randolph-Macon Woman's College, Lynchburg, VA*)*; Ryan Kamerzell* (*Lawrence Livermore National Laboratory, Livermore, CA*). The DOE Title 10 Code of Federal Regulations, Part 850, Chronic Beryllium Disease Prevention Program defines the maximum removable surface contamination of beryllium (Be) in non-Be work areas as the higher of 0.2 µg Be/100cm^2 or the concentration of Be in soil at the point of release. Be is a naturally occurring metal and can be found on surfaces in concentrations greater than the defined DOE release limit without a process present that would introduce contamination. Until now there has been no standardized method for deciphering between naturally occurring and process introduced Be. The purpose of this research was to develop such a method by determining naturally occurring ratios of Be to other naturally occurring metals in soil at Lawrence Livermore National Laboratory (LLNL). Sixty random soil samples were collected from uncontaminated locations within the LLNL site boundary. The samples were analyzed for the concentrations of Be and 19 other metals using an Inductively Coupled Plasma Spectrometer. Aluminum (Al), nickel (Ni), and vanadium (V) were selected to calculate the naturally occurring ratios based upon

detection rates, low variability, and R-values from the Ryan-Joiner W-test for normality. Two-sided 95% upper and lower tolerance limits (UTL and LTL) were calculated for the true 95th percentile of each naturally occurring ratio: [Be]:[Al]- UTL97.5%, 95% = 5.06 x 10^{-5}, LTL2.5%, 95% = 4.35 x 10^{-5}, mean = 3.40 x 10^{-5}; [Be]:[Ni]- UTL97.5%, 95% = 1.73 x 10^{-2}, LTL2.5%, 95% = 1.30 x 10^{-2}, mean = 8.12 x 10^{-3}; and [Be]:[V]- UTL97.5%, 95% = 1.63 x 10^{-2}, LTL2.5%, 95% = 1.38 x 10^{-2}, mean = 1.05 x 10^{-2}. Sample data suggests with 95% confidence that 95% of the ratios do not exceed the true UTL when beryllium is naturally occurring. Future data can be compared to the ratios to conclude the following: (1 if the sample ratio is less than the LTL, the Be is naturally occurring, (2 if the sample ratio is greater than the LTL but less than the UTL, further investigation is required, and (3 if the sample ratio is greater than the UTL, the Be is process introduced. Other DOE sites can use this method to determine their own ratios to discriminate between naturally occurring and process introduced Be. The ability to determine this will allow for redirection of resources away from unnecessarily implementing decontamination requirements for cleaning surfaces with false contamination. Implementing this method would be fiscally responsible while not increasing employee health risk.

Simple Route to Control Nanoscale Domain Morphology in Block Copolymer Films. *ELIZABETH NETTLETON* (*University of South Dakota, Vermillion, SD); SETH DARLING* (*Argonne National Laboratory, Argonne, IL*). As demand for increasingly smaller devices grows, new efficient patterning techniques must replace traditional lithographic methods. Self-assembly presents a possible technique by which to pattern materials using a parallel, bottom-up process. Gaining control over the structure and order of self-assembled domains is critical to the success of this methodology. This study focuses on the self-assembly of thin films of polystyrene-block-poly(ferrocenyldimethylsilane) block copolymers (PS-b-PFS) on silicon nitride substrates. Upon annealing, the thin films microphase separate to form nanoscale PFS cylinders within a PS matrix. Traditionally, order in such films is improved using thermal annealing, which has drawbacks including time requirements and the possibility for thermal degradation. In this work, solvent annealing, an alternative to thermal annealing, is used. By varying solvent anneal times, either in-plane or standing cylinder domains can be achieved. In order to characterize cylinder structures, reactive ion etching was used to remove the PS matrix and the remaining PFS cylinders were imaged via atomic force microscopy (AFM). Because of the comparatively high etch resistivity of the PFS block, this block copolymer holds potential in lithographic patterning of nanowires, nanopillar arrays, and nanofluidic channels.

Development of Production and Purification Procedures for Calbindin D9k Mutants for Solid State Nuclear Magnetic Resonance Spectroscopy. *SHELLY NI* (*Stanford University, Stanford, CA); ROBERT HECK* (*Pacific Northwest National Laboratory, Richland, WA*). Calbindin, a metalloprotein with two calcium binding sites, is present in multiple species and involved in biological processes as varied as calcium transport in fruit fly neurons and mammalian intestinal calcium uptake. Despite its ubiquity, its biological roles, and binding behavior are unknown. This paper focuses on the preparation of 9 kDa calbindin for solid state nuclear magnetic resonance (ssNMR) spectroscopy. Our purified calbindin will be used for the first ssNMR experiments studying calcium within a protein. To best understand the structure and mechanisms of calbindin's binding sites, each site must be studied separately. To accomplish this, two calbindin mutants were to be prepared for ssNMR spectroscopy. Each mutant had been altered so that only one binding site retained its original structure and function. A synthetic gene was inserted into a pET expression system to produce calbindin mutants using *Escherichia coli.* After harvesting the cells, protein was purified primarily with ion exchange and gel filtration chromatography. However, several analyses using SDS-PAGE Tris-tricine and Tris-HCl gels made it evident that D9K P43M E65Q was not expressing well in *E. coli* BL21(DE3) or *E. coli* BL21(DE3) pLysS competent cells. Instead, we then purified calbindin D9K P43M, which had both binding sites intact. The ssNMR spectrum of a previously made calcium binding mutant E27Q P43M can be removed from that of calbindin D9K P43M, still allowing for study of the other calcium binding site. Though purification of the initial calbindin double mutant P43M E65Q was found unfeasible, a combination of earlier calbindin purification procedures were successfully adapted to purifying D9K P43M to homogeneity as determined by SDS-PAGE. With the aid of a fermentation unit, these methods should be easily scaled up to produce the required quantities needed for planned ssNMR experiments.

Electronic Characterization of Rare Earth-Doped. *ANDREW OLSON* (*Carleton College, Northfield, MN); DALE L. PERRY* (*Lawrence Berkeley National Laboratory, Berkley, CA*). Zinc telluride and telluride-

containing compounds have been extensively analyzed by X-ray photoelectron spectroscopy (XPS) and Auger electron spectroscopy (AES) in order to determine the chemical states and shifts in electronic energy levels of the elements present in the materials. To a lesser extent, chemical shifts of gadolinium lines in various compounds have also been studied. However, the characterization of ZnTe:Gd by XPS and AES is practically non-existent. Use of this material as a semiconductor in various applications requires that electrical contact be maintained between the material's surface and other electrical components. Buildup of oxides and other species on the surface can cause insulating effects, hampering the material's intended performance. It is, therefore, of interest to study surface reactions of the compound with air in order to identify surface product films that may adversely affect the utility of ZnTe:Gd as a multipurpose semiconductor. The current study was an initial characterization of these materials using XPS and AES. Observed spectra for the initial, "as received" surface yielded data consistent with the presence of Gd_2O_3, ZnO, and TeO_2. Spectral parameters including binding energies, spin-orbit splitting, satellite structure, and kinetic energy Auger lines of elements compared favorably to analogous features in spectra of other Zn-Te-Gd compounds. Surface charging of the material was observed and studied in conjunction with argon ion sputtering. The results indicated that insulating surface films do indeed form on these materials in air, films that can act as interfacial layers between the semiconductor material and other materials such as electrical contacts attached to the surface of the semiconductor. A future examination of this material by other characterizing methods and types of instrumentation will provide further insight into the chemistry, structure, and electronic properties of this material and shed more light on the formation of the surface layers under ambient air exposure.

Inkjet Printing of Nickel and Silver Metal Solar Cell Contacts. *ROBERT PASQUARELLI* (*Rochester Institute of Technology, Rochester, NY); CALVIN CURTIS* (*National Renewable Energy Laboratory, Golden, CO*). With about 125,000 terawatts of solar power striking the earth at any given moment, solar energy may be the only renewable energy resource with enough capacity to meet a major portion of our future energy needs. Thin-film technologies and solution deposition processes seek to reduce manufacturing costs in order to compete with conventionally coal-based electricity. Inkjet printing, as a derivative of the direct-write process, offers the potential for low-cost, materials-efficient deposition of the metals for photovoltaic contacts. Advances in contact metallizations are important because they can be employed on existing silicon technology and in future-generation devices. We report on the atmospheric, non-contact deposition of nickel (Ni) and silver (Ag) metal front contacts from metal-precursor organic inks on a Dimatix inkjet printer at 180–220°C. Near-bulk conductivity Ag contacts were successfully printed up to 4.5 μm thick and less than 125 μm wide on the silicon nitride antireflective coating of silicon solar cells. Thin, high-resolution Ni adhesion-layer lines were printed on glass and zinc oxide at 55 nm thick and 80 μm wide with a conductivity two orders magnitude less than bulk. Additionally, the ability to print multi-layered metallizations (Ag on Ni) on transparent conducting oxides was demonstrated and is promising for contacts in copper-indium-diselenide (CIS) solar cells. Future work will focus on further improving resolution, printing full contacts on devices, and investigating copper inks as a low-cost replacement for Ag contacts.

Optimal Mixed-Acid Digestion Procedures for Sediment and Tissue Using a Hot Block Heating System. *JULIA PETERSEN* (*Western Washington University, Bellingham, WA); GARY GILL* (*Pacific Northwest National Laboratory, Richland, WA*). Investigations were conducted to optimize mixed-acid digestion procedures for sediments and tissues using a hot block heating system with disposable vials. This method is more cost efficient and less labor intensive than digestion methods using high pressure heating in sealed Teflon vessels. A series of digestions were conducted using varying procedures on several Standard Reference Materials (SRMs). The acid mixtures employed included, aqua regia (3:1 nitric: hydrochloric acid), aqua regia plus hydrogen peroxide and several combinations of hydrochloric/ nitric/ hydroflouric/ boric acid patterned after the procedures used at Texas A&M University (TAMU) and for the National Status and Trends Program (National Oceanic and Atmospheric Association). The digestates were analyzed by Inductively Coupled Plasma-Optical Emission Spectrometry and percent recoveries were calculated from certified and reference values. Very few elements (Cu, Ag, and Cd) had acceptable recoveries (>90%) for the aqua regia and the aqua regia plus hydrogen peroxide digestion of sediments. The TAMU digestions showed an overall increased recovery of 7% for a collective group of 15 elements (Al, As, Ba, Be, Ca, Cu, Fe, K, Mg, Mn, Mo, Na, Sr, V and Zn)

when the procedure included a heating step after boric acid was added. Recoveries were >90% for the National Status and Trends procedures for the group of 15 elements which proved to be most comprehensive sediment method. This digestion included 2 mL HNO_3, 3 mL HCl, 2 mL HF, and 15 mL 5% boric acid with a heating step after HCl, HF and boric acid were added. For the tissue digestions, the best recoveries were observed when the sample was allowed to sit overnight with only nitric acid added at room temperature before initiating a heated mixed-acid (2 mL HNO_3, 3 mL HCl, and 2 mL of H_2O_2) digestion procedure the following day. Recoveries >90% were observed for the elements Ag, Ca, Cu, Fe, K, Mg, Mn, Na, Ni, Sr, and Zn. Further work could include the use of an Inductively Coupled Plasma-Mass Spectrometer to monitor additional elements as well as studying matrix effects on the difficulty of digestion.

Protein-Assisted Magnetite Nanoparticle Synthesis. *Timothy Pica* (*University of California at Berkeley, Berkeley, CA*); *Tanya Prozorov* (*Ames Laboratory, Ames, IA*). Uniform magnetite nanocrystals were synthesized in the presence of the biomineralization protein mms6 involved in the biomineralization of magnetite in bacterial magnetosomes. Several recombinant mms6 proteins were tested: polyhistidine-tagged full-length mms6 protein (his-mms6), a 25 amino acid segment from the C-terminus of this protein (c25-mms6), and a glutathione s-transferase enzyme-tagged mms6 protein (GST-mms6). The his-mms6 protein was reported to facilitate formation of ~30 nm, single-domain, uniform, isomorphic magnetite nanocrystals in aqueous polymeric gel, as verified by transmission electron microscopy analysis and magnetization measurements. Conjugating the proteins to activated Pluronic polymer allowed further control over particle growth. Similarly, the c25-mms6 protein was also shown to promote shape-selective formation of magnetite nanocrystals. Preliminary fast protein liquid chromatography (FPLC) studies indicated that both his-mms6 and c25-mms6 proteins were present in solution as multimers, thus potentially forming extended surfaces suitable for nucleation of magnetite. The significantly larger GST-mms6, which was found in a monomeric state and did not form multimers in solution, exhibited poor magnetite templating ability, and produced small nanoparticles lacking specific shape. This suggests that the ability of the protein to form multimers could play an important role in magnetite crystal formation, with larger numbers of protein molecules in the multimer resulting in the formation of larger magnetite nanoparticles. To test this hypothesis, we conducted magnetite synthesis in solution with various protein concentrations. In addition to synthesis in solution, we attempted synthesis on surfaces using both chemical ink-jet printing of protein solution on silicon wafers, as well as stamping the protein solution onto the surface of functionalized silicon. It was found that magnetite growth was limited to locations on the silicon wafer where protein had been stamped. The structure and placement of the formed magnetite nanoparticles were analyzed through electron microscopy and magnetic measurements. Additional magnetic analysis will offer further insight into the magnetic characteristics of mms6-assisted magnetite nanocrystals.

Characterization of GaN, In025Ga075N and In050Ga050N for Photoelectrochemical Water Splitting. *Sally Pusede* (*University of Colorado at Denver and Health Sciences Center, Denver, CO*) *Todd Deutsch* (*National Renewable Energy Laboratory, Golden, CO*). GaN, $In_{0.25}Ga_{0.75}N$ and $In_{0.50}Ga_{0.50}N$ semiconductors were characterized as possible candidates for photoelectrochemical water splitting. The band gap energies of the materials were measured and found to decrease with increasing indium content. The flatband potential (Vfb) of GaN was determined and the material's band edges verified to span the potentials of the hydrogen and oxygen evolution reactions; however, the Vfb positions of $In_{0.25}Ga_{0.75}N$ and $In_{0.50}Ga_{0.50}N$ could not be experimentally established. Two-electrode current density vs. potential measurements of both InGaN materials indicated anodic current flow at zero applied potential considerably below theoretical maxima, suggestive of photocorrosion rather than spontaneous water splitting. Where GaN was observed to be stable, $In_{0.25}Ga_{0.75}N$ and $In_{0.50}Ga_{0.50}N$ were found to be extremely susceptible to photocorrosion.

A Radiochemical Separation of Selenium and Arsenic Using a BioRad Ag1-X8 Resin Column. *Pawan Rastogi* (*Columbia University, New York, NY*) *Michael Fassbender* (*Los Alamos National Laboratory, Los Alamos, NM*). Although classified as a group 1 carcinogen by the International Agency for Research on Cancer, arsenic and its compounds have proven to have many potential uses in nuclear medicine. Isotopes of arsenic, such as 74As and 72As, have been used in Positron Emission Tomography (PET). 72As is a positron emitting isotope with a 26 hour half life (T) and mean positron energy (EB+mean) of 1.2 MeV. These characteristics lead 72As to be a promising candidate for being incorporated into radiopharmaceuticals. Such 72As-labeled radiopharmaceuticals can be used in quantitative imaging of different biochemical and physiological processes. Here the delivery route for radioarsenic is considered via the production of a radionuclide generator parent like 72Se, which, in turn, will decay into 72As. A potential portable radioarsenic generator will be of value due to transportability and efficacy in delivering the radioisotopes to hospital and university settings. The main objective in this study was to develop an As/Se separation system that could be used in the future for a radionuclide medical generator. A strongly basic anion exchange resin (BioRad Ag1-X8) column was used to separate arsenic from selenium with different concentrations of ammonium chloride (NH_4Cl). Radioarsenic was seen to elute with 0.01M NH_4Cl and 0.2M NH_4Cl. Generally all radioselenium retained on the column, but a small amount (~0.1%) was seen to elute with a 0.5M NH_4Cl eluent. The different retentions of radioarsenic and -selenium on the resin column support that more than one species of As and Se are present within the matrix. Due to time constraints speciation of the effluent was unable to be conducted. This preliminary separation of radiotracer quantities of arsenic and selenium shows much potential in developing a system fit for radionuclide generators. Future hopes include optimization of separation, characterizing the species involved in the matrix system, and development of a biologically deliverable form of the radioarsenic. The purpose of this paper is to report a method to separate arsenic from selenium using a BioRad Ag1-X8 anion exchange resin column with an ammonium chloride elution system.

Increasing Activity for Oxygen Reduction of Cathode Electro-Catalysts in Fuel Cells. *Jose Regalbuto* (*University of Illinois at Urbana-Champaign, Urbana, IL*) *D.J. Liu* (*Argonne National Laboratory, Argonne, IL*). As the search for alternatives to gasoline powered internal combustion engines intensifies, more attention is drawn to the use of fuel cells as an alternative power source. Fuel cells directly convert chemical to electrical energy, and are more efficient than internal combustion engines. The objective of our research is to identify and test new approaches in preparing electro-catalysts for use in fuel cells. We focused on two methods for the synthesis of cathode catalysts. The first was to steam activate a catalyst support before impregnating it with platinum. The second was to test a platinum free catalyst in basic media. A special emphasis was placed on using aligned carbon nanotubes as a catalyst support. Wet chemistry and gas phase vapor deposition methods were used to synthesize the catalysts. Our prepared catalysts were evaluated using standard electrochemical methods, with a focus on rotating disk electrode tests. We found that steam activation over a carbon nanotube support can improve oxygen reduction reaction (ORR) activity in acidic conditions. We also found that iron and nitrogen doped carbon nanotubes show good ORR activity in basic conditions. This work is part of a larger project to determine the feasibility of and make new catalysts for a direct ethanol fuel cell.

*Nanotechnology. *Melixa Rivera, Michelle Rosa* (*University of Puerto Rico, Mayaguez, PR*); *Luis Rivera, Luis Nunez* (*Argonne National Laboratory, Argonne, IL*). Due to its potential impact, nanotechnology has become an important part of research in fields such as physics, chemistry, and bioscience. One of the greatest advances made in nanoscience are nanoparticles which are currently being considered for drug delivery and for cancer treatment modality. Our project is focused on using PLGA (poly (lactic-co-glycolic acid)) nanoparticles for three different applications; systemic, local distribution and cellular drug delivery and for this matter these nanoparticles are being physically and chemically characterized. For the systemic application, tPA (tissue plasminogen activator), a clog buster, is the drug encapsulated in the nanoparticle. The core is surrounded by polymer with Fe_2O_3 particle which makes it magnetic and easy to move them in different directions in the body. The tPA drug is useful because it destroys blood clogs, and if we are able to deliver this drug successfully, it could save lives. For the tPA study, it is necessary to characterize the physical properties (size distribution and surface charge) and quantify the release of the drug from the nanoparticles. A spectrophotometer assay was performed to quantify the tPA released from the nanoparticles. For the local delivery application, the cancer drug encapsulated particles, the physical properties and drug release characteristics were examined and are critical for uniform distribution within a tumor. Size distributions were obtained using DLS (Dynamic light scattering) and a Zeta potential instrument. Zeta potential is a measure of the surface charge magnitude of the repulsion or attraction between particles. The 40–100 nm particles were encapsulated with a drug named TMZ (Temozolomide), used to treat two different types of brain tumor in adults: anaplastic astrocytoma and glioblastoma multiforme (GBM).

The nanoparticles were introduced in a rat's brain and using Convection Enhanced Delivery (CED)it was demonstrated that the particles were distributed uniformly along the brain. The cellular studies are based on selective liquids such as antibodies which will bind with over expressed receptors on cancer cells. The particles were ultracentrifuged to collect various size fractions which ranged from 200–250 nm and they are used for *in vitro* cell culture tests as a function of particle size. The concept of this experimental hypothesis is to see if the cancer cells can successfully uptake the nanoparticles over normal cells, and if the drug is delivered homogeneously.

Silicon Nitride for Semiconductor Photoelectrochemical Water Splitting. Joseph Ryerson (*University of Colorado, Boulder, CO*); John Turner (*National Renewable Energy Laboratory, Golden, CO*). Silicon nitride was analyzed to determine if it is an effective material to split water in direct photoelectrolysis application. Band gaps determined via photocurrent spectroscopy were found to exhibit indirect transitions between 1.54–1.75 eV. The higher end nitrogen content samples (14–16% nitrogen) fell within the band gap range effective in splitting water (1.7–2.2 eV). Flat band potentials were not negative enough to drive the hydrogen evolution reaction for these n-type films. Silicon nitride is therefore ineffective as a direct photoelectrolysis device, because its band edges are not aligned with respect to the redox potentials, a criteria necessary to generate hydrogen from water splitting. Twenty-four hour durability tests in 1M KOH revealed that this material is highly stable, as determined from post-test optical microscopic analysis, with low nitrogen contents (5%), and much less stable at higher nitrogen contents (14–16%N).

Novel Bipolar Plate for Polymer Electrolyte Membrane Fuel Cells. Lilia Santos (*College of Dupage, Glen Ellyn, IL*); J. David Carter (*Argonne National Laboratory, Argonne, IL*). Several partially fluorinated hydrocarbon polymers have been screened to form composite films as components of bipolar plates for application in proton exchange membrane fuel cells (PEMFC). Various compositions containing these polymers and graphite were scouted to prepare conductive films of about 0.4 mm thickness. A methodology was also devised to adhere these composites to the stainless steel substrate using anchoring molecules. The most promising anchor was found to be 4-[2,2,2-Trifluoro-1-(4-{2-hydroxy-3-[4-(4-oxiranylmethoxy-benzyl)-phenoxy]-propoxy}-phenyl)-1-trifluoromethyl-ethyl]-phenol both pre- and *in-situ* prepared from bis (4-glycidyloxyphenyl)methane and 4,4'(hexafluoroisopropylidene)diphenol. The composite films were consequently laminated on to 310S stainless steel plates using the anchors. These conductive composite coated plates showed excellent thermo-hydrolytic stability in boiling water for an extended period. In addition, resistance to delamination and corrosion were established by immersing these conductive plates in fairly concentrated H_2SO_4 for 10 days. Out of several compositions evaluated, initial results indicate that poly(chlorotrifluoroethylene) with 60 volume% graphite to be a superior composition. These preliminary results are encouraging and would have positive impact on the cost factor of fuel cell assembly without sacrificing performance.

Electron Transfer in Molecular Wires. Elicia Selvaggio (*Dowling College, Oakdale, NY*); John Miller (*Brookhaven National Laboratory, Upton, NY*). Conjugated oligofluorenes with two to ten monomer units (F2 to F10) were used to address fundamental questions regarding eletron capture capacity and delocalization of charge. The oligofluorenes were reacted with sodium metal in tetrahydrofuran (THF) under vacuum, and ultraviolet/visible/near infrared (UV-vis-NIR) spectroscopy was used to measure the formation of anions, dianions, trianions, and tetranions. When reacted with sodium, F2 through F10 formed anions and dianions. Trianions and tetranions were observed in F4 and larger oligofluorenes. The absorption maxima, wavelengths at the maximum absorbances, and extinction coefficients were determined for each species formed. The study indicates that oligofluorenes can capture and store multiple electrons from sodium metal, and that the negatively-charged molecules are stable in the absence of air. Results for the series indicate that the length occupied by an electron is three to five monomer units. These results are consistent with the value obtained in polyfluorene by a different method in this lab. This challenges the notion that electrons are delocalized over the entire length of a conjugated molecule, and it has implications for understanding the fundamental nature of charged molecules in conjugated systems.

Analysis of a Microbial Biofilm Matrix. Anna Siebers (*University of California – San Diego, La Jolla, CA*); Michael P. Thelen (*Lawrence Livermore National Laboratory, Livermore, CA*). A matrix comprised of cells and polymeric substance distinguishes a robust biofilm

found floating in extremely acidic waters of an iron mine in northern California. Although both components are integral to the biofilm, the extracellular polymeric substance (EPS) has not been characterized and its function in the biofilm is poorly understood. To isolate the EPS, biofilm samples were disrupted and washed with dilute sulfuric acid. EPS could then be precipitated from the acid wash with either ammonium sulfate or ethanol. This gelatinous material was analyzed using a variety of independent techniques, including solvent treatment, UV-visible spectroscopy, gel electrophoresis, elemental analysis, and glycosyl analysis (in progress). EPS was not soluble in 17.5% NaOH, indicating a cellulosic component, and dissolved completely in 2M HCl. Analysis of material precipitated with 15, 30, 60 and 75% ethanol indicated differential sedimentation, with EPS primarily in the 15 and 30% fractions. Denaturing polyacrylamide gel electrophoresis of these fractions revealed two proteins with molecular weights of ~20 kDa and 60 kDa exclusively in the 60% fraction. Also, DNA was found in the same fraction using agarose gel electrophoresis; this was corroborated by a distinct absorbance peak at 260 nm. Elemental analysis of the total EPS material indicated a chemical formula of C18H35O17N2S, consistent with a polysaccharide assignment (1:2:1 CHO). Glycosyl analysis following pyrolysis, gas chromatography and mass spectrometry will determine the carbohydrate composition of the EPS and will give insight into its electronic charge state and hydrophobicity, and perhaps explain the buoyancy of the biofilm. We propose that the EPS protects the microbial community by buffering the acidity of the mine water and facilitating the exchange of gases at the air-water interface. Therefore, understanding the role of EPS within the biofilm will lead to further characterization of this unique microbial system and help determine how the community thrives in such an extreme environment.

Dynamics of Fast Reactions in Ionic Liquids. Kathryn Sims, Kandis Stubblefield (*Howard University, Washington, DC*); James F. Wishart (*Brookhaven National Laboratory, Upton, NY*). Ionic liquids (ILs) are liquids consisting of ions and have melting points below 100°C. Used in technologies and green chemistry they are being considered as processing media in the advanced nuclear fuel cycles needed to support a sustainable nuclear power industry for the world's future energy needs. It is important to understand the radiation-induced chemistry of ILs and how it may affect the chemistry of nuclear fuel separation. The unique reactivity of the "pre-solvated" electron surfaces as an important aspect of radiation chemistry due to the slower response to charge movement in ionic liquids relative to ordinary solvents. This study explores the reactivity of pre-solvated electrons in the ionic liquid N-methyl N-butylpyrrolidinium NTf2 (P14NTf2) by measuring the kinetics of their reactions with cadmium, nitrate and selenate ions. These ions were selected because they show a wide range of reactivities with electrons in conventional solvents. The process of electron solvation, which competes with pre-solvated electron capture, is estimated by measuring the benzophenone anion solvation process because its spectroscopic properties are better suited to the available detection equipment than those of the electron. The Brookhaven National Laboratory (BNL) Laser Electron Accelerator Facility (LEAF) was used for all of the kinetics measurements performed by pulse radiolysis transient absorption spectroscopy. The C37 parameter was obtained to look at the lower concentration of benzophenone. Higher concentrations were also analyzed to allow us to look at the spectral shifts and compare them to that of the selected ions in the IL. In conclusion, we have determined the reaction kinetics of fast reactions in the IL.

Dynamic Behavior of Nicotine and Its Impact on Assessment of Human Exposure to Secondhand Smoke. Emma Smith (*Yale University, Albany, CA*); Lara Gundel (*Lawrence Berkeley National Laboratory, Berkley, CA*). Secondhand tobacco smoke (SHS) is a common toxic contaminant in indoor air. Exposure to SHS has been linked to increased risk of lung cancer, asthma and acute respiratory illness. LBNL is currently measuring concentrations of SHS in bars and restaurants in Minneapolis-St. Paul, MN, in collaboration with colleagues at the Center for Energy and Environment. The goals are to correlate exposure data with health profiles of employees and assess the effects of prolonged indoor exposure to SHS. Measured concentrations of nicotine, 3-ethenyl pyridine and pyridine are being used as tracers of exposure. Nicotine is the most common tracer due to its uniqueness to tobacco, and its metabolite, cotinine, is a useful biomarker. However, earlier work at LBNL has shown that sampling nicotine in real environments is strongly influenced by changes between emission and collection, due to its affinity for surfaces (i.e., walls, clothes, hardware) and its reactivity (i.e., oxidation, acid-base reactions). This project measured the stability of gas-phase nicotine

in humid air and pure nitrogen, and dry air and nitrogen. High purity nicotine was injected into inert Tedlar bags and heated to vaporize it. Samples were collected after one, six and twenty-four hours, and analyzed using the same methods as the MN study (active sampling onto sorbent tubes, followed by gas chromatography with nitrogen-specific detection). After accounting for sorption of nicotine to the walls of the gas bags, the results showed that gaseous nicotine in dry N_2 remained stable, but samples of nicotine in humid air produced chromatograms with the same unusual features seen in field samples from MN, as well as peaks corresponding to the oxidation products nicotinaldehyde, N-methyl formamide, myosmine and cotinine. These data strongly suggest that nicotine oxidation is expedited over time in the presence of humid air. Thus, the degradation of nicotine either in the environment or inside sampling equipment may contribute to inaccurate concentration and exposure calculations. Future experiments are needed to monitor the behavior of nicotine for longer time periods, with varying amounts of nicotine and at different temperatures.

Analysis of Compounds Produced by Biomass Burning Using High Resolution Mass Spectrometry. *JEFFREY SMITH* (*University of Washington, Seattle, WA*)*; JULIA LASKIN* (*Pacific Northwest National Laboratory, Richland, WA*). As global climate change becomes a pressing issue worldwide, it is important to identify the composition of particles emitted from biomass burning to understand the influence on our atmosphere from natural and anthropogenic pyrolysis. This study utilized high resolution mass spectrometry (MS) combined with electrospray ionization (ESI) for chemical characterization of smoke particles. The analyzed pyrolysis particles were collected on the six smallest particulate stages of a ten stage Micro-Orifice Uniform Deposit Impactor (MOUDI) using both Teflon and aluminum substrates. These substrates were then washed and filtered in solvents of both methanol and a 3:7 toluene:acetonitrile mixture. The samples were ionized using ESI, and analyzed in a high resolution hybrid linear ion trap Orbitrap instrument in both positive and negative ion modes. Tandem mass spectrometry (MS/MS) was performed for selected species to obtain more detailed structural information for specific compounds. Elemental composition was assigned to peaks based on their accurate mass-to-charge ratios. Comparison with literature data showed some overlap between the previously reported chemical components of smoke particles and species identified through the high resolution MS. Several known biomarkers for biomass pyrolysis, such as levoglucosan and dehyrdroabietic acid were observed in ESI-MS spectra. However, the high resolution MS identified many compounds not listed in existing literature publications; many of which contain nitrogen in their likely empirical assignments. These results indicate that the use of high resolution MS is a viable method for the analysis of compounds produced by biomass combustion, and can be used in conjunction with conventional approaches to obtain a more detailed characterization of the chemical composition of particulate matter emitted into the atmosphere during forest fires. Because this experiment only analyzed five biomass sources, substantial further research on a large variety of biomass burns will be needed to identify the majority of compounds produced through biomass combustion. Without first identifying the compounds produced by biomass combustion, it will not be known if these compounds pose risks to human health or potentially can affect the earth's climate.

Automation of Chromatographic Separation Procedures. *NICK STUCKERT* (*University of Wyoming, Laramie, WY*); *ROSI PAYNE* (*Pacific Northwest National Laboratory, Richland, WA*). The purpose of this paper is to provide a detailed discussion of an attempt to automate UTEVA and TRU gravity chromatographic separation procedures. These procedures are used for the chemical separation of radioactive elements prior to analysis. The problems that were encountered will be presented along with solutions and potential solutions to the problems. The methods for leak detection and resolution are presented in addition to a suite of additional minor changes. Some specific suggestions for modifications include the use of flow meters or creating an open system that relies on gravity filtration. In both cases substantial work will be required to develop a working system.

Effect of Solvent Box Size on Wide-Angle X-Ray Scattering Patterns. *HEATHER SUTTON* (*Chicago State University, Chicago, IL*)*; DAVID M. TIEDE* (*Argonne National Laboratory, Argonne, IL*). Wide-angle X-ray scattering (WAXS) has been presented as an alternative method to the use of X-ray diffraction and nuclear magnetic resonance (NMR) for experimental structural verification of solution-phase macromolecular assemblies. Use of WAXS to determine solution structure requires comparison of the experimental scattering patterns to scattering patterns produced by molecular models. One approach

for producing these models is to use structures produced during explicit solvent molecular dynamics (MD) simulations. These simulations place the solute in a bath (a box or sphere shape is most common) of explicit solvent molecules. Prior work has focused on the solute scattering, removing all solvent molecules before the X-ray scattering pattern is computed, thus ignoring all solvent scattering. The long-term goal of this work is to extend the simulation model approach by including solvent in the scattering calculation in order to investigate the structure of solvent around porphyrin solutes. However, the finite size of the simulation solvent box results in artificial X-ray scattering. The present goal of this work is to facilitate treatment of solvent in MD simulations by determining adequate solvent box size to prevent the appearance of edge scattering peaks within our range of interest in the calculated scattering pattern. Solvate baths of various sizes and shapes were created using the solvate tool in visual molecular dynamics (VMD). After equilibration, constant energy (nve) simulations were run on these solvation boxes using the CHARMM force-field. Coordinates of these simulations were Fourier transformed to produce the calculated scattering patterns. These calculated scattering patterns have shown that the edge-scattering peaks can not be eliminated by increasing the size of the solvation box. However, spherical solvation baths have an analytic form for the edge scattering allowing the "false" scattering peaks to be subtracted off. These spherical baths will be used to study the solvent/solute interactions of porphyrin systems. Additionally, this work suggests that the TIP3 water model is accurate enough to use in further simulation work. In contrast, the charmm 22 toluene parameters will need to be adjusted before being used to model toluene/porphyrin interactions. The usage of WAXS data combined with simulation will provide, for the first time, a means to achieve this re-parameterization that is directly linked to experimental data.

Electronic Characterization of Rare-Earth Doped Telluride Semiconductors. *ERIK TOPP* (*Diablo Valley College, Pleasant Hill, CA*); *DALE L. PERRY* (*Lawrence Berkeley National Laboratory, Berkley, CA*). Zinc telluride and telluride-containing compounds have been extensively analyzed by X-ray photoelectron spectroscopy (XPS) and Auger electron spectroscopy (AES) in order to determine the chemical states and shifts in electronic energy levels of the elements present in the materials. To a lesser extent, chemical shifts of gadolinium lines in various compounds have also been studied. However, the characterization of ZnTe:Gd by XPS and AES is practically non-existent. Use of this material as a semiconductor in various applications requires that electrical contact be maintained between the material's surface and other electrical components. Buildup of oxides and other species on the surface can cause insulating effects, hampering the material's intended performance. It is, therefore, of interest to study surface reactions of the compound with air in order to identify surface product films that may adversely affect the utility of ZnTe:Gd as a multipurpose semiconductor. The current study was an initial characterization of these materials using XPS and AES. Observed spectra for the initial, "as received" surface yielded data consistent with the presence of Gd_2O_3, ZnO, and TeO_2. Spectral parameters including binding energies, spin-orbit splitting, satellite structure, and kinetic energy Auger lines of elements compared favorably to analogous features in spectra of other Zn-Te-Gd compounds. Surface charging of the material was observed and studied in conjunction with argon ion sputtering. The results indicated that insulating surface films do indeed form on these materials in air, films that can act as interfacial layers between the semiconductor material and other materials such as electrical contacts attached to the surface of the semiconductor. A future examination of this material by other characterizing methods and types of instrumentation will provide further insight into the chemistry, structure, and electronic properties of this material and shed more light on the formation of the surface layers under ambient air exposure.

*Preparation and Properties of Phosphate Containing Ionic Liquids. *KATHERINE URENA* (*Queens College, Flushing, NY*)*; JAMES WISHART* (*Brookhaven National Laboratory, Upton, NY*). Research in the field of ionic liquids (ILs) continues to flourish due to their potential application in the area of green chemistry. ILs are organic salts with melting points below 100°C. Many of them exhibit melting points below room temperature and are referred to as room temperature ionic liquids. ILs are often composed of large organic cations and relatively small inorganic anions. Typical IL cations are nitrogen-containing and include imidazolium, pyridinium, and pyrrolidinium. This work focuses on the preparation and characterization of ILs based on these cations and the phosphate ($\{PO4_3\}$) anion. Data on the physical properties of phosphate ILs is lacking in the IL field. The need for specific structural types of ILs and data on their physical properties become more important as the

number of applications for ILs increase. The ILs were prepared by first preparing the quaternary ammonium halide salt precursors. The halide salts were made by reacting the tertiary amines with the alkyl halides in acetonitrile under reflux conditions. The halide salt precursors were then converted to phosphates using phosphoric acid in ethanol. The structures of the ILs were confirmed using nuclear magnetic resonance (NMR) spectroscopy. We have successfully synthesized pyrrolidinium and imidazolium based phosphate salts. Physical properties such as viscosity, conductivity and the thermal profiles of new salts will be reported.

*Effects of the Porphyrin Oxidation State on the Conformation of C-type Cytochromes. TIM VUONG (*Chicago State University, Chicago, IL*); KRISTY L. MARDIS (*Argonne National Laboratory, Argonne, IL*). The increase in natural gas and oil prices has sparked renewed interest in alternative fuel sources such as solar energy. C-type cytochromes, found in a variety of bacteria, plants, and animals are being studied as possible building blocks for solar energy devices. Their usage depends on electron transfer (ET). To make these proteins suitable for ET devices, their solution conformation must be determined. Experimental wide-angle X-ray scattering (WAXS) studies have found that the c-type cytochrome (Protein Data Bank entry 1os6), extracted from the Geobacter genome and expressed in *Escherichia coli*, has identifiably different conformations in the reduced and oxidized form. The current work seeks to determine if the Chemistry of Harvard Molecular Modeling (CHARMM) force field can reproduce the experimental scattering pattern. This protein was chosen because (1) experimental scattering data are available and (2) it has three heme sites making the effect of oxidizing or reducing the iron in the center of the site larger than for proteins with single hemes. Calculations of the scattering profile were accomplished using structures obtained from crystal structure data. These starting structures were then subjected to nanosecond scale molecular dynamics simulations in a water sphere (radius = 30 Angstroms). The scattering profiles were obtained as the Fourier transform of the atomic coordinates. The scattering profiles calculated from the ensemble of structures for both the oxidized and reduced structures were then compared to the experimental data. Preliminary results indicate that the CHARMM 22 force field does distinguish between the oxidized and reduced forms of the protein. However, longer simulations are required before the results can be directly compared to experiment. The results will indicate the ability of the CHARMM forcefield to distinguish between two proteins differing only in the charge state of the irons in the three heme groups.

Mechanization of Cadmium Sulfide Chemical Bath Deposition. DOMINIC WEBER (*Colorado School of Mines, Golden, CO*); STEVEN ROBBINS (*National Renewable Energy Laboratory, Golden, CO*). The preferred method to deposit the Cadmium Sulfide (CdS) layer for thin-film solar cell research is Chemical Bath Deposition (CBD). In order to improve the reproducibility, and thus help the understanding of the process, a machine was created to mimic the CBD process. The design of the system involved placing the substrate over a flow well, only depositing CdS on one side of the substrate. Within the machine was a pump, designed to make the chemicals flow at a designated speed across the substrate. Also included was a temperature bath, designed to heat the chemicals to the desired deposition conditions. The machine was constructed, and everything in the system was tested for functionality. Since the machine was designed to mimic the current CBD method, the processed films were compared with CdS films made by the old process. These tests involved: thickness, thickness uniformity, and optical properties. The first run of the system revealed some major uniformity issues: the film had areas of no deposition (bubbles) on the edges and the thickness varied quite a bit on the other areas of the film. The first run also revealed another major problem: waste minimization. The run required 2.5 L (for 16 in^2 of substrate) compared to 500 mL (for 13.5 in^2) in the old CBD method. The second run was devoted to waste minimization. A beaker was placed in the temperature bath to displace volume, reducing the amount of required chemicals to 1.5 L (for 36 in^2). The second run showed that a smaller amount of liquid still produced a good quality film. Further designs for the CBD machine will have to concentrate on making the flow, and therefore the film thickness uniform. Future designs will also have to keep in mind the waste management issue: a great design would be one that uses 500 mL of solution or less.

An Exploration of Ternary Compounds in RE-T-In, RE-T-Ge, and RE-T-Al Systems (RE = Ce, Nd, Lu; T = Pd, Pt, Ni): A New Ternary Indide and a Symmetry Question. JOSHUA WEBER (*Grinnell College, Grinnell, IA*); GORDON J. MILLER. SRINIVASA THIMMAIAH (*Ames Laboratory, Ames, IA*). Ternary indides containing rare-earth (RE) and transition (T) metals, RE-T-In, have exhibited unique properties, yet

the characteristics of many RE-T-In systems remain unknown. This exploration initially focused on novel Ce-T-In systems, with T = Pd, Pt, and Ni. The focus then expanded to include ternary indides with the RE metals Nd and Lu and to include ternary compounds from RE-T-Ge and RE-T-Al systems to study the effects of varying atomic size and valence electron count. All samples were synthesized by arc-melting. A Guinier powder X-ray diffractometer was used for phase identification, and select samples were further analyzed using a Bruker single crystal X-ray diffractometer. Only select crystals were analyzed because most products, including all Ce-T-In systems, contained multiple phases instead of the desired complex-structured phase. The most interesting results have come from the Lu-Ni-In and Ce-Pd-Al systems, from the phases Lu10Ni10.08(1) In19.0(1) and CePd0.93(1) Al3.08. Lu10Ni10.08(1) In19.0(1) is a new phase. It crystallizes in the tetragonal crystal system, space group P4/nmm, adopting the Ho10Ni9In20-type structure, with unit cell parameters a = 13.128(1) Å and c = 8.977(1) Å, and unit cell volume of 1547.2(3) Å3 for Z = 2. Single-crystal analysis indicates that CePd0.93(1) Al3.08 belongs to space group I4/mmm, but it has been reported (as CePd0.75Al3.25) in space group I4mm. While electronic structure calculations seem to suggest this reported solution as well, the space group is still undetermined. The RF values of the refinement were 5.13% for Lu10Ni10.08(1) In19.0(1) and 4.75% for CePd0.93(1) Al3.08. Physical measurements and electronic structure calculations will be used to study the new Lu-Ni-In compound and to resolve the space group problem of the Ce-Pd-Al compound. In future explorations, RE-T-In systems containing Nd, Lu, and other RE elements and additional RE-T-Ge and RE-T-Al systems, those systems which yielded the most interesting results, will be further investigated.

A Search for Scintillators: Ce³⁺ Doping of Alkali Gadolinium Halides and Eu2+ Doping of Barium Zinc Oxides. LATORIA WIGGINS (*North Carolina Agricultural and Technical State University, Greensboro, NC*); STEPHEN DERENZO (*Lawrence Berkeley National Laboratory, Berkley, CA*). The need for new and improved gamma ray and X-ray detectors, scintillators, is at an all time high due a progression in detection knowledge. Commonly used scintillators such as BGO and YAP have undesirable properties such as low luminosity, and slow decay times. The mission of the High Throughput Characterization and Synthesis Facility(HTCSF) is to develop scintillators with rapid decay times, high luminosities and crystal production at low costs. Discovering new scintillators required literature searches, synthesizing and the characterization of compounds. The research at hand concentrated on cerium (III) doped alkali halides and europium (II) doped barium zinc oxides. Compounds were synthesized using the ceramic method mostly performed in a nitrogen filled glove box because of the hygroscopic nature of the halides. Characterization consisted of X-ray diffraction, X-ray luminescence and pulsed X-ray measurements. Several new inorganic scintillators were founded, however, findings concerning barium zinc oxide synthesis warrant further investigation of the compound.

Computer Science

A Case Study of Efficient Social Network Simulation through General Processing on Graphics Processing Units. BRANDON AABY (*Maryville College, Maryville, TN*); KALYAN S. PERUMALLA (*Oak Ridge National Laboratory, Oak Ridge, TN*). Agent based simulation has been both a large area of study and a widely used tool for scientific research in past years. Current implementations run on standard CPUs, and with the requirement of processing ever growing data sets, higher computational speed is of the utmost importance. General processing on graphics processing units (GPGPU) is an emerging platform offering the possibility of increased speed for data sets and models that can be processed in parallel. Agent based simulation is one such candidate for performance gains in a GPGPU implementation. My research has focused on thoroughly investigating GPGPU's suitability for providing researchers with a more efficient way of conducting agent based simulation research. Studies were done using two conventional models: two-dimensional diffusion and Conway's Game of Life. I first created an optimized CPU diffusion model and, following a determination of accuracy, compared computational speed with an Open Graphics Library GPGPU implementation previously developed at Oak Ridge National Laboratory. Similarly, like studies were completed with the Game of Life. Following this strict CPU and GPGPU comparison, further comparisons and analyses were conducted with a widely used agent based simulation API, Repast. Evaluations involving Repast revolved around the premise that were GPGPU to be harnessed by researchers for agent based simulation, it must be competitive with currently used research technologies.

Results obtained with both two-dimensional diffusion and the Game of Life show significant performance gains through GPGPU. For a plethora of data sizes, it has been found that the GPU processes the models in parallel at much greater rates than both optimized CPU code and Repast. Furthermore, as both sample size and the number of iterations through the model increase, the gap between GPU and CPU performance becomes even wider. These successful studies are to now be extended by investigating new models through GPGPU and exploring compatibility with necessary agent based simulation functions, such as image generation. Nonetheless, this research has certainly shown that GPGPU has the potential to become an efficient and viable tool for researchers.

OSCAR Diskless. *WILLIAM ADERHOLDT* (*Tennessee Technological University, Cookeville, TN*); *STEPHEN L. SCOTT* (*Oak Ridge National Laboratory, Oak Ridge, TN*). OSCAR, Open Source Cluster Application Resources, is software used to create and manage high performance computing clusters. The current method of installation assumes that each compute node is equipped with a local hard disk. However, the trend in high performance computing today is leaning toward diskless clusters where compute nodes do not require local hard disks. The motivation for diskless clusters include reduced power, lower hardware costs, and improved reliability (hard disks are notoriously prone to failure). This work extends OSCAR to support the creation and management of both diskfull and diskless clusters. In order to enable diskless OSCAR nodes, a boot method known as NFS-Root is used. This means that during the bootstrap phase the compute nodes will mount their root partition via a Network File System (NFS) share, eliminating the local hard disk requirement. The way this is done, specifically, with OSCAR is to mount a small root partition containing only what is absolutely needed for the init process as read/write. All other directories are mounted as read-only from a NFS shared network folder, which is accessed by the diskless nodes in the cluster. Init is modified in order to obtain a diskless node by mounting the network shares before any other work is done. So, through creation of a NFS shared network folder, a small root partition, and modification of the init process, OSCAR is able to create and maintain both diskfull and diskless clusters. This ability aligns OSCAR with the current trends in high performance computing and creates more efficient clusters as it reduces power, lowers hardware costs, and increases reliability.

Auto-ADL (Automatic Generation of MEDM Displays Depicting Collider-Accelerator Components). *JONATHAN BECK* (*Binghamton University, Vestal, NY*); *TED D'OTTAVIO* (*Brookhaven National Laboratory, Upton, NY*). A software program called Auto-ADL was developed for use by the Collider-Accelerator Department (C-AD) at Brookhaven National Laboratory (BNL). The goal of this program is to use software automation to greatly decrease the time and tedium required to create displays using the program Motif-Based Editor & Display Manager (MEDM). Previously, the displays could take a member of the C-AD several hours to generate, as each element would have had to been added manually and each portion of the Collider-Accelerator complex can contain hundreds of magnets, detectors, and other devices of interest. To accomplish this, the user inputs the beamline section and element types of interest. This input is turned into an SQL query and data is extracted from a Sybase database using the DB_request library available at BNL, then converted to an Extensible Mark-up Language (XML) file using the XMLDom library, also available at BNL. This XML file is then converted to MEDM's native file format (ADL) and the data is displayed using MEDM. Using Auto-ADL, the user only needs to take a few seconds to select the areas and device types they would like to view, and the appropriate ADL files are produced in less than a minute, saving the C-AD hours of tedious work. Future improvements on Auto-ADL may include making the displays produced dynamic, so that new files do not need to be produced every time a new set of device types are to be displayed. This would significantly improve the speed at which a user can switch between different displays. The XML files produced by Auto-ADL may also be put to use in other programs whose development has not yet started.

Developing a Tree Search Algorithm for Track Reconstruction in the Hall A BigBite Spectrometer. *BRANDON BELEW* (*Rensselaer Polytechnic Institute, Troy, NY*); *Ole Hansen* (*Thomas Jefferson National Accelerator Facility, Newport News, VA*). In many experiments that involves particle collisions, the ability to track the paths of the particles is essential. In the Hall A BigBite Spectrometer at the Thomas Jefferson National Accelerator Facility (JLab), wire drift chambers are used to detect these paths. For each individual measurement, there is an associated hit pattern that shows which detector bins were activated by the particles traveling through the drift chamber. The track information can be reconstructed from the hit

pattern with the help of software. The current algorithm uses a brute-force method to analyze all possible ways of connecting lines through the hits. This has been sufficient thus far, but future experiments will need faster performance because the expected rates and particle multiplicities will be higher and a larger number of wire planes will be used. The HERMES Spectrometer at the Deutsches Elektronen-Synchrotron uses a much more efficient tree search algorithm. The goal of this project was to implement such an algorithm for use at JLab. The code developed for this project was written based on a general description of the HERMES algorithm. It compares the associated hit pattern to a pre-generated database of all possible patterns that could be produced by particles moving in a straight line, arranged in a branching structure of increasing resolution. This tree structure allows for logarithmic rather than linear comparison time. It has been demonstrated to work with a high level of accuracy using Monte Carlo simulations. For a sufficiently high detector resolution and reasonably low levels of simulated background noise, the algorithm was shown to very quickly match all the simulated tracks and to produce very few "ghost tracks," or false positives. In the future, this algorithm will be moved out of the testing phase and integrated with JLab's existing software to be used on a regular basis. The increased speed of this new matching algorithm will make many future experiments possible.

CCA Linear Solver Components Using SciPy. *ANDREA BERGER* (*Clarion University, Clarion, PA*); *BOYANA NORRIS* (*Argonne National Laboratory, Argonne, IL*). The Common Component Architecture (CCA) is a standard for component design used during software development that allows components to be used effectively for high performance or scientific computing. CCA also gives scientists the ability to dynamically change components during program execution. This methodology allows programmers to interact easily with code written in other languages, and supports code re-usability. Components are accessed through high-level interfaces and are designed for the scientist's specific needs. The Towards Optimal Petascale Simulation (TOPS) Interface is one of these interfaces that is used to solve systems of linear equations. TOPS solver components provide an easy common interface to parallel libraries such as PETSc, hypre, and SuperLU; however, these libraries are usually more advanced than beginners may desire to experiment with. This project demonstrates basic usage of the TOPS solver interface via a simple component implementation built on the SciPy (Scientific Python) library, which offers the advantage of being a relatively easy starting point for beginning users. To aid in the understanding of this software, Python component examples to solve systems of linear equations using SciPy were created. They will be added, along with reference documentation, to the CCA Tutorial as an initial starting point for those wishing to use the CCA software. Scientists can then run these examples to understand how the components work together. These examples will also become part of the new test bed being developed by the Computational Quality of Service working group, which is part of the CCA Forum.

Penetration Testing of ORNL.GOV. *TRISTAN BITHELL* (*University of North Carolina at Charlotte, Charlotte, NC*); *DON WILLIAMS* (*Oak Ridge National Laboratory, Oak Ridge, TN*). Today, the risk of an internet based attack is greater than ever. Google.com has become the target of hackers to be used as a tool for reconnaissance. Google is capable of revealing vulnerabilities in web sites if you know the proper search operators. Through the use of a Google API (Application Programming Interface) key one can even automate the reconnaissance process. Other tools such as spider crawlers and backend tools can also reveal vulnerable files or URL's that should have remained hidden. Also, the listing of excessive contact data can be used in a social engineering based attack. My project was to use manual searching and automated tools to attempt to locate any vulnerabilities or unprotected, sensitive data on onrl.gov or any leaked information from the lab to a newsgroup. I used Athena 2.0, Wikto, Paros, SiteDigger 2.0, and Aura in my project. During my initial setup, I found that Google no longer issues API keys so I was able to use SnakeOil Lab's Aura program to simulate an API key. I used Athena 2.0, Wikto, and Site Digger 2.0 to look for common vulnerabilities that were listed in the Google Hack Data Base at johnny. ihackstuff.com. Wikto is a multipurpose tool that I used for several tests. First I scanned the website for known vulnerable directories. Next I scanned those directories for known vulnerable files. Wikto would use an AI to assess if a URL or file existed but this tended to often return false positives and lead to URL's that did not exist. With Paros I set up my browser to redirect traffic through a local proxy server run by Paros to intercept and modify data packets. As I browsed ornl. gov, Paros would save the URL's that I visited. I then activated a spider scan on a URL to generate a list of every directory and file in the website. Though ornl.gov itself proved too massive to scan in its

entirety, I was able to complete a scan of neutrons.ornl.gov which is the website for the SNS facility. Through my penetration testing, I was able to extract various pieces of possibly sensitive information. From the results of the tests and measures taken to secure ornl.gov's data, the website will be more secure against the threat of an attack.

Performance Comparison between 10GigE and InfiniBand in High Performance Computing. *Colby Boyer* (*University of California – Berkeley, Berkeley, CA*); *Carolyn M. Connor* (*Los Alamos National Laboratory, Los Alamos, NM*). The processing power of a large computing cluster relies heavily on its ability to transmit data quickly among its numerous nodes. This requirement demands that the network interconnects have both low latency and high bandwidth. Currently, the most popular form of interconnect in high performance applications is InfiniBand (IB), because it offers both low latency and high bandwidth. The recently released 10 Gigabit Ethernet (10GigE) standard offers similar bandwidth and slightly worse latency performance as compared to the IB 4x. Despite its drawbacks, 10GigE can be more easily integrated into the common Ethernet network than IB because 10GigE uses the Ethernet protocol and IB does not. To determine 10GigE Message Passing Interface (MPI) performance, MVAPICH2 MPI benchmarks will be run over native InfiniBand and 10GigE with Remote Direct Memory Access (RDMA), and in addition MPICH2 MPI benchmarks will compare IP over IB (IPoIB) and 10GigE without RDMA. These benchmarks measure the MPI bandwidth and latency performance. The bandwidth comparison between 10 GigE with RDMA and InfiniBand are nearly equal but 10 GigE provides slightly higher bandwidth. With small message sizes the latency comparison shows IB with two to three times lower latency as compared to 10 GigE with RDMA. IPoIB and 10 GigE without RDMA both performed worse than IB and 10 GigE with RDMA, because the RDMA used by IB and 10 GigE allows for Operating System bypass (OS bypass). The poor test results of IPoIB and 10 GigE without RDMA show that OS bypass is key for high network performance. Even though the performance between IB and 10 GigE with RDMA are similar, IB still remains significantly cheaper than 10 GigE because 10 GigE is a newer technology. Future testing with production level MPI software should be conducted to determine what effect the latency difference between the two has on performance.

Notification Services for Urgent Computing. *Amy Catlett* (*Olivet Nazarene, Bourbonnais, IL*); *Pete Beckman* (*Argonne National Laboratory, Argonne, IL*). The Special PRiority and Urgent Computing Environment (SPRUCE) is a system that provides "urgent" computing capability to time-critical emergency decision support systems, such as severe weather prediction or flu modeling. For these high-priority computing jobs, scientists and administrators want to be notified about any activity, such as job submissions and completions. This project involved developing a way in which SPRUCE users can specify what kind of jobs they want to be notified about and can choose a method of notification, such as email or Short-Messaging Service (SMS). The data from a web form is added to a backend database via Web services. A trigger was implemented in order to check this database every time a job-related event occurs. If an event matches the specifications in the database, an email or SMS is sent to the corresponding people. The software to initiate this action is written in Java code and uses a MySQL database. A prototype version of this software is currently being tested. The final version of this notification service will be deployed on the SPRUCE server.

Developing a Proof-of-Concept CyberInfrastructure for the USA National Phenology Network. *Benjamin Crom* (*University of Tennessee, Knoxville, TN*); *Bruce E. Wilson* (*Oak Ridge National Laboratory, Oak Ridge, TN*). Phenology is the study of the timing of naturally recurring events, such as flower blooming, particularly those influenced by environmental changes. Phenological measurements are extremely valuable indicators of local, regional, and global climate changes. Further, phenological variations have a variety of crucial environmental and socio-economic implications. Despite this value, broadly distributed phenological measurements are almost non-existent in the USA, in contrast to some European countries. The objective of this work is to explore and evaluate different data models and data management methods needed for the development of the cyberinfrastructure for a new data resource: the USA National Phenology Network (USA-NPN). The USA-NPN will create a national repository for submitting and retrieving a wide range of phenological data, including data from existing research networks and from citizen scientist observers. For this project, we have been focusing on the data model and information management tools necessary to support the citizen scientist aspect of USA-NPN, based on existing work from the Plant Phenology Network (PPN). A key feature at this stage of the

program is for citizen scientists to enter phenological observations on any of the 38 species currently in the PPN. The USA-NPN will also require basic tools for observers to retrieve their own data and the publicly available data. We have created a simple but flexible database schema which we are testing against a range of ways the system may be used. This schema is an improvement over the current PPN tools, which use separate text files for each species. We are also working on improving the registration and authentication processes. The user is now able to create login credentials and submit personal contact information without PPN staff intervention. This reduces staff load and the revised data entry forms greatly improve the tracking of data provenance. Our current work will improve session management operations and may enable OpenID authentication. We intend to streamline the maintenance of data submission pages by eliminating the current 38 separate submission pages in favor of one master submission page driven by the underlying database. We will also add a data retrieval page which will give users access to public phenology data. The data offered by this network will contribute to a better understanding of climate change and help engage citizen scientists in climate change science.

Converting RELAP5-3D Environmental Library to Fortran 90. *Riley Cumberland* (*North Carolina State University, Raleigh, NC*); *George Mesina* (*Idaho National Laboratory, Idaho Falls, ID*). RELAP5-3D is being converted to Fortran 90 to increase code legibility and longevity. As part of that effort, the RELAP5 subdirectory called the Environmental Library (EL) has been converted to Fortran 90 with the additional requirement to increase code readability and conciseness. The EL is comprised of service subroutines that perform table look-ups, interpolations, and solutions to linear systems, among other things. To improve readability, each EL subroutine was initially restructured the commercial tool, For_Struct, which applies uniform coding style rules and reorganizes to code to eliminate jumps in logic flow paths (GO TO statements). Afterwards, manual modifications were made to further improve readability. These modifications included eliminating multiple returns, entry points and virtually every GO TO statement. Pre-compiler directives also reduce legibility; these were eliminated manually by replacing machine-specific code with machine-independent Fortran 90 intrinsics and by moving other directives into Fortran 90 modules or new subroutines. The files were further processed as groups by abstracting coding repeated in several subroutines into separate, reusable subroutines. An example of this was the many search loops reduced to two subroutines. In addition, a mnemonic subscripting system was used in many subroutines and transmitted through a new Fortran 90 module. Another improvement was rewriting the subroutines from older fixed format Fortran to the more modern free-source format. To achieve this, another pre-compiler that alters the code for 32-bit or 64-bit integer machines was eliminated by creating and using a bit-transfer subroutine of Fortran 90 constructs. Additionally, handling the declaration with a kind parameter set in a module by formatting all floating point constants as double precision was also necessary to convert to free format. The three multi-file processes improved conciseness. Measurements of improved readability and conciseness were made. The conversion process resulted in a sizable reduction in the number of line labels and GO TO statements, an indicator of readability. The number of pre-compiler directives was reduced dramatically, improving conciseness and readability. The number of comment lines increased slightly while the number of non comment lines, an indicator of conciseness, decreased slightly. This process has clearly improved the readability of the code.

Using Kepler Scientific Workflows to Automate Processing of Data from Scientific Models. *Matthew Devries* (*Vanderbilt University, Nashville, TN*); *Scott A. Klasky* (*Oak Ridge National Laboratory, Oak Ridge, TN*). As a Leadership Computing Facility, Oak Ridge National Laboratory (ORNL) is home to several large-scale scientific models that take advantage of the advanced supercomputing power available. These models generate gigabytes of data, which must be archived, processed, and transferred to other locations before the output can be analyzed. Currently, each of these steps requires the use of separate tools, each with its own syntax and options. The aim of this project is to automate these processes in such a way that researchers can easily watch the results as a model is running. This is being done with Kepler scientific workflow software, which provides a flowchart-like interface for designing a script that can be executed from the command line. Using such a workflow that had previously been designed for a scientific model, new workflows are being developed for S3D, a state of the art direct numerical solver combustion model that runs on the entire Cray XT4 system. When finished, these will automate various parts of processing the data, as well as feeding into an AJAX dashboard, being

developed separately, for real-time monitoring. For researchers using these models, this project should mean fewer tools to master and an easier time managing their data and monitoring their models as they run. On the development side, this project will provide feedback on the suitability of the Kepler software for this application, as well as possible improvements for the software and the process.

Processing Text Data and Advanced Search Capabilities for the Intelligence Community. JON DOBSON (*East Tennessee State University, Johnson City, TN*); LINE POUCHARD (*Oak Ridge National Laboratory, Oak Ridge, TN*). One of the most valuable sources of intelligence for military agencies today is open source intelligence (OSINT). OSINT embodies all publicly available information. It is becoming increasingly important to intelligence analysts as knowledge becomes globally available via the Internet. However, the problem with OSINT is that it is so time consuming and inefficient for an analyst to sort through all the available information on any given subject. The goal of this project was to use Semantic Web technologies and Natural Language Processing (NLP) to enhance the search capabilities of software tools used by intelligence analysts. The challenge behind this project was trying to avoid inheriting the search limitations that come with using only structured data or only natural language. In order to search structured data, the analyst must know exactly how the data is organized. Information Extraction based on automatic NLP techniques yields results that amount to 70% of results produced by a human. By combining the two methods with Semantic Web technologies like the Resource Description Framework (RDF), we are attempting to demonstrate that documents can be efficiently searched and cross referenced. OpenSource.gov files are automatically downloaded from an FTP server. After extracting the Extensible Markup Language (XML) files, all of the metadata is stored in a Java data structure. The text body is searched using Baseline Information Extraction (Balie) to find possible city names. For each possible city name, if it is found within a country listed in the XML metadata, then it is stored in the data structure. Finally, all of the data is used to create an RDF document, which is uploaded to a Sesame repository. Using Sesame's web interface, it is possible to query, modify, and browse all of the data in the repository. A text file was also acquired from geonames.org containing information and coordinates on over 80,000 cities. Balie was chosen for named-entity recognition because it is easy to implement and highly configurable. An alternative to Balie, called General Architecture for Text Engineering (GATE) was also considered. However, since Balie can use GATE configuration files, Balie seemed like the most flexible choice. This project focuses on combining existing tools in a way that has not been done before. There is currently no standard way to convert XML data to RDF format, but this project is a step in that direction.

FORMS-GUI: A Graphical User Interface For Input Into The Forms Simulation Tool. SEAN DOEBLER (*Drake University, Des Moines, IA*); BOYANA NORRIS (*Argonne National Laboratory, Argonne, IL*). FORMS is a nanophotonics simulation program that simulates light passing through three dimensional nano sized objects called forms. The input into the program comes in the form of a Scheme file containing all of the parameters required to run a simulation. The parameters include the objects' dimensions and positions, the material properties, the source of the waves, the characteristics of the grid, and what should be outputted by the program. The input file type makes setting up a basic simulation difficult for someone whom is unfamiliar with Scheme and also makes setting up a simulation by hand rather difficult. The FORMS-GUI program, which is based off of the two dimensional version called SHAPES-GUI, addresses this problem by visually allowing the user to define the simulation domain, place the objects on a grid, resize and move the objects through an input dialog, and change the view point to see the simulation from any angle. It also allows the user to set other parameters, which cannot be visually placed, through simple dialogs. The application will be expandable to allow the user to input or define any three dimensional object they wish to simulate.

Energy Efficiency of Desktop and Laptop Computers. MAT DOIRON (*Big Bend Community College, Moses Lake, WA*); CHARLIE VERBOOM (*Lawrence Berkeley National Laboratory, Berkley, CA*). As the number of computers in use worldwide increases, so does the demand for electricity to power them. This research focused on measuring computers typically used at Lawrence Berkeley National Laboratory in order to determine their power consumption. This included the Optiplex 745 series from Dell, ClientPro series from MPC and a custom made computer designed to run Computer-Aided Design (CAD) software. Three Dell Latitude Laptops(D600, D610, D630) were included. Measurements were taken during five different "states"; off, booting, idle, active and sleep, with a Kill-A-Watt meter. Two Operating

systems, Microsoft Windows XP Professional and Windows Vista Business were also compared to determine their impact on power use. PassMark Performance Test V 6.1, a benchmarking program, was used to evaluate the performance of the computers. It was also used to simulate the computer in an active state. It was discovered that the computer uses less energy while sitting idle than while active and significantly less while in sleep mode. Putting the computer to sleep during non-working hours would be ideal but several factors currently prevent this from taking place, including scheduled backups and remote access. New desktop computers being implemented at the lab use less energy than those currently in use despite their superior performance. The new computers are the Dell Optiplex 745 series, which were tested in three different configurations: Minitower, Small Form Factor and Ultra Small Form Factor. The three were compared to see if size or component differences affected power consumption and performance. There was very little difference between the Minitower and Small Form Factor. In contrast, the Ultra Small Form Factor used less power with reduced performance. This could be because of the external power brick and lack of dedicated graphics card. The laptops in this study consumed significantly less power than did the desktops: 22W while idle compared to 68W. This is significant because it includes the monitor. An LCD monitor uses 30W and a CRT up to 130W, which is more than the entire laptop. Windows Vista and Windows XP were also compared using identical computers. Vista performed worse and consumed more power despite the fact that it is the successor to XP. It is recommended that customers wait for the first service pack to switch to Vista if performance or power management is a major concern.

Automatically Generated Unit Testing for Large FORTRAN Models. NICK EDDS (*University of Chicago, Chicago, IL*); ROB JACOB (*Argonne National Laboratory, Argonne, IL*). Many modern climate models, such as the Community Atmosphere Model and the Weather Researching and Forecasting Model, are large models written in FORTRAN 90. There are a number of such large FORTRAN climate models, but they do not collectively adhere to any general standards. There are accepted standards of validity for much of the data they generate, but there is currently no system in place to test them against these standards. A program has been developed as part of this project that enables unit testing of these large FORTRAN climate models against the industry standards. This program parses the source files of climate models, extracts any pertinent information from each subroutine, and generates a series of testing subroutines to verify the validity of the original subroutine. The program utilizes netCDF for input and output because of its portability. Its development in ruby reflects an emphasis on ease of development rather than a need for greater efficiency. Automatic unit test generation has gained industry recognition for its usefulness, but it has not been previously applied to FORTRAN climate models, which makes this project unique. This program will allow for easier extension and improvement of the existing FORTRAN climate models.

Design and Development of a Mobile Application for Purification Database Systems. ALVINA ELSTON (*Governors State University, University Park, IL*); ANDRZEJ JOACHIMIAK (*Argonne National Laboratory, Argonne, IL*). The Midwest Center for Structural Genomics (MCSG) at Argonne National Laboratory develops and optimizes integrated methods for determination of protein structures through X-ray crystallography. The MCSG program requires entering data and procedures to common database using LIM system. The goal of the project is to design and develop a Personal Digital Assistant (PDA) application with MCSG cloning and purification databases. The PDA will exhibit the same functionality as the web page but will provide much greater convenience and accuracy on a secure network. The initial PDA application was developed by using Microsoft.NET 2003. However, the new system will be re-developed using Microsoft.NET 2005 technology. User interfaces are developed with ASP.NET Mobile forms, HTML, WML and JavaScript. Scientific logics are implemented with C++/C# programming languages and Oracle PL/SQL. Like the Web page, the PDA application uses Oracle 9i/10g databases for data storage. Current web applications are designed, implemented and upgraded for common web task and data storage in order to fit into the scale of a PDA window using most up-to-date technologies. Users can scan the data using a PDA scanner and save the data directly into the database. The major areas of work during this project are to design and implement rich mobile web content and applications across a variety of hardware platforms and hand held devices. Using the PDA interface scientists can scan the data using a PDA scanner and save the data directly into the database. When scientists enter data it prevents scientist from entering invalid and out of range data. The PDA mobile

applications are able to deliver access to anyone authorized at anytime, anyplace on any hand-held device.

*Face Recognition System. *Amarachukwu Enemuo* (*The City College of New York, New York, NY*)*; Upendra Rohatgi* (*Brookhaven National Laboratory, Upton, NY*). Biometrics, a significant component of identification technology, involves verification and identification based on an individual's biological characteristics. Universality, time invariance, uniqueness, accuracy, and acceptability are desirable characteristics biometrics must possess. Commercial biometric systems are designed to use a single biometric; however, the Integrated Biometric Recognition System (IBRS) consisting of fingerprint, voice, face, and hand Recognition Systems (RS) combines all four technologies into one system, and is platform independent. The IBRS utilizes client-server architecture, and was scheduled to be tested to determine the efficiency of its performance. To fully assess this, understanding of the underlying algorithms are essential. IBRS has three modes namely Enrollment, Identification and Verification. For face recognition, prior to the Enrollment phase, a sample of multiple face images are collected from various individuals. These set of face images become our database of known faces. (S) IBRS uses the eigenface (eigenvector) technique to recognize the face image of a client. Eigenfaces are based on the Euclidean distances of salient features on the face. These distances are measured, and stored as general templates which are used for identification of the face area on an image, and for verification. During Enrollment, a camera is used to capture fifteen sequential images of a client which are converted to grayscale images of same size in pixels. Each pixel is converted to a vector, and 15 eigenfaces are constructed from the face images of the client and stored as the client's personal template. The Identification phase, involves a 1:S comparison where "1" represents the client's face image and S is the database of known faces. Verification is a one-to-one authentication of who the client portrays himself to be. During this mode, the client's input image is compared with the stored personal template created at the enrollment stage. Face testing on IBRS was done using frontal view of face images and varied lightning. It was found out that the system is easy to use and the Enrollment, Identification and Verification modes work as expected.

Information Technology Enterprise Monitoring. *Jacob Fenske* (*Northern Illinois University, Dekalb, IL*); *Paul Domagala* (*Argonne National Laboratory, Argonne, IL*). The Information Technology (IT) Enterprise Monitoring evaluation project compares software with the goal of selecting and implementing solutions which best suit the needs of IT staff monitoring the computer & network systems at Argonne National Laboratory. A number of systems monitor the laboratory. However, a single comprehensive and consistent view of the status of the entire operation is lacking. When a problem occurs that affects multiple systems, critical time is wasted focusing on isolated events rather than identifying the root cause of the problem. By using a single monitoring system, problems can be more easily identified and fixed. The candidate software should also be able to identify potential problems and alert the staff to mitigate them before they affect operations. Benefits of monitoring system resources include long term planning. For example, drive space can be monitored over a period of time and an estimate can be made as to how much space will be needed for the following year. To aid in the evaluation, a table listing the products and the functional requirements was used. Each product was evaluated and given a score in each of the requirement categories. The outcome of this project was detailed technical information on the capabilities, reliability, performance and features of each candidate solution and a final product recommendation.

Deployment Process. *Mat Folz* (*Elmhurst College, Elmhurst, IL*); *Eric Pershey* (*Argonne National Laboratory, Argonne, IL*). In the past the steps that had to be taken to get an asset (computer, printer, etc) out onto the network and delivered would take up to one or more weeks. With this time delay people would take short cuts by skipping some steps that should not be skipped. Deliver the asset and forget were that asset was put. Never get it signed out of their name so that it would say they owned that asset. We plain on solving this be making the steps necessary to get the asset out onto the network as automated as possible. We are going to break each step into four groups and have very simple forms that the person can fill out. Have the data saved so that the data builds off of its self and does not allow for any one to skip an asset from one step to the next with out the proper information field in. With the deployment process being automated the process will take less time in certain steps and also allow CIS to keep track of all their assets.

*Mass Metabolic Model Generation (3MG) in the SEED. *Kevin Formsma* (*Hope College, Holland, MI 49423*)*; Mike Kubal* (*Argonne National Laboratory, Argonne, IL 60439*). Metabolic flux balance models of bacteria provide a cost effective means for simulating the effects of knocking out genes and modifications to the environment. A scalable methodology for the generation of accurate metabolic models for the growing number of newly sequenced genomes will provide researchers with a dynamic kernel of data with different possible applications. This research focuses on development of 3MG, a set of bioinformatics tools to automatically generate metabolic models. 3MG is built within the framework of the SEED and uses the technology of Scenarios. The SEED is a computational environment geared for the annotation of genomic data using comparative analysis. Scenarios define small metabolic tasks and provide tested reaction paths for any genome. The first step is to compute the scenarios present for the given genome and predict the inputs, outputs, and biomass to be included in the model. The predictions are supported by information obtained from published models. The ability of a new model to produce each predicted biomass component is validated using the predicted inputs and the reactions that define the scenarios. The consistency of each model is tested with a linear programming solver. The models are generated in the two file formats: Systems Biology Markup Language and Mathematical Programming System. 3MG was integrated into the RAST, a larger automated annotation pipeline within the SEED. An annotated genome, metabolic model and model analysis reports are generated for each genome submitted to the RAST pipeline. 3MG provides metabolic model generation capability on a mass scale, and has successfully generated initial flux balance models for 505 complete genomes. Future work will focus on the development of tools for the comparison of models of the same organism, and later across different organisms. Tools for the further curation of Scenarios technology to improve metabolic coverage need to be built. With metabolic models available in mass quantities, a new generation of comparative analysis of genomes will be possible.

Solving Ill-conditioned Linear Systems in High-Precision Arithmetic. *Jasmine Garner* (*Lane College, Jackson, TN*)*; Ed D'Azevedo* (*Oak Ridge National Laboratory, Oak Ridge, TN*). A linear system of equations is a set of linear equations in variables that can be represented in matrix form, where it is called the matrix coefficient of linear systems. A small change in the coefficients produces a large change in the solution and the system becomes ill-conditioned. The most efficient way for solving linear systems is the Gaussian elimination method, but this method itself is not always valid to the ill-conditioned cases. The goal of this project is to explore effective methods such as using high-extended, precision arithmetic library software for solving ill-conditioned block tridiagonal linear systems. The linear system is not too ill-conditioned but intermediate results may be ill-conditioned and can lead to instability. The idea is to use higher precision arithmetic to regain stability and accuracy. A dense direct solver using Gaussian elimination with partial pivoting from LAPACK (Linear Algebra Package) is modified to use higher precision. The solver computes a "LU" factorization where the matrix equals a lower triangular L multiplied by an upper triangular matrix U. The LAPACK is one commonly used library for performing numerical linear algebra computations. Both C++ and Fortran-90 high-level language interfaces are provided to permit one to convert an existing C++ or Fortran-90 program to use the library with only minor changes to the source code. LAPACK is written in Fortran since the language is commonly used for numerical computation. The code with extended precision was used to explore the range block sizes and number of blocks where the approach is effective by collecting runtimes and computed errors. A parameter (beta) controls scaling and conditioning of the system and as beta increases, the maximum error in solution increases as well. The measured runtimes decreases at the same rate as the number of block sizes increases in the data of fixed number of blocks. The results are summarized in plots. Although the runtimes are often lengthy, using a high-level program language to solve difficult linear equations permits faster development of large problems.

Software Development for a New OSCAR GUI that Will Support the Use of Virtual Machines. *Nathaniel Graham* (*University of New Mexico, Albuquerque, NM*)*; Stephen L. Scott* (*Oak Ridge National Laboratory, Oak Ridge, TN*). Open Source Cluster Application Resources (OSCAR) facilitates the installation, administration, and programming of Beowulf type high performance computing (HPC) clusters. OSCAR has a variety of pre-packaged applications and utilities which allow one to install and manage clusters without specific technical expertise. An expanding interest in virtualization today has shown that virtual machines are a suitable solution to address issues for

application, execution, and system management. However, the support of virtual environments in OSCAR is an ongoing effort, particularly regarding the user interface employed by OSCAR which is not currently optimized for management of virtual machines. The current OSCAR graphical user interface (GUI) was improved to better facilitate its use for managing virtual machines. The new OSCAR GUI was based on out of date OSCAR code. The project was divided into two phases: (i) the refactoring of existing code and (ii) the adaptation of the code to manage virtual environments. The base OSCAR code came from earlier GUI work that had fallen out of the main development path. That specific GUI project was never finished and was not maintained for a number of years. My first task was to modify the code to make it work with the current OSCAR architecture. It is now possible to launch the original GUI with all options available. The second phase was the adaptation of the code to virtual environments. For instance, compared to a standard execution platform, virtual environments are significantly more dynamic (virtual machines are created/destroyed on demand). For that I designed a new set of widgets for "node sets" and "package sets" management, and the mapping of virtual nodes onto physical nodes. The ultimate goal of my project was to provide a well-defined GUI for the management of virtual environments while maintaining the original Beowulf cluster installation abilities. This GUI will be integrated into OSCAR-V, the virtualized OSCAR infrastructure package, as the interface by which the user will manipulate OSCAR-V virtual environments.

Implementing Optimized and Scalable Non-Standard Matrix-Multiply Algorithms. RANDY HASSELL JR. (*Old Dominion University, Norfolk, VA*)*; RICHARD BARRETT (*Oak Ridge National Laboratory, Oak Ridge, TN*). Matrix-Multiplication is the fundamental operation for solving several algorithms including other linear algebra operations like matrix inversion, systems of linear equations, and matrix determinants. It's also used in computer graphics and digital signal processing. The Computational Materials Science Group at the Oak Ridge National Laboratory (ORNL) is developing a large-scale computer application that studies the fundamental properties of materials. The performance of this materials science code relies heavily upon the execution of matrix-multiplication. The dimension of the matrices are 32 x N, where N is currently 4K, and continues to expand to 40K. The purpose of this project is to create an optimal algorithm that performs matrix-multiplication, and to research the implementation on different computer architectures. Using the Fortran language, all the matrices are dynamically allocated, so that memory is created and destroyed without wasting any. Then, double precision random numbers fill both matrices. There are three multiplication techniques to test, a Fortran function matmul, a source file dgemm.f, and the subroutine dgemm directly from lblas during compilation. The timer used is a subroutine called gettimeofday() in the C language. The algorithm calculates the Floating Point Operations per second (FLOPS) that measure an algorithm's performance on a processor. For multiplying rectangular matrices, I am testing from 5x5 to 40Kx40K using iterations and 10 trials each. For multiplying square matrices, I am testing from 5x5 to 4Kx4K. I am compiling my algorithm with these computer processors: Intel Celeron, Pentium 4, and the Cray XD1(dmz00 & wc00). For matmul, the performance dropped as the size grew from an average of 5GFLOPS to 1 MFLOP on all processors. For dgemm.f, the dmz00 performed the best leveling around 225 MFLOPS as the size increased. For square matrices, the performance dropped as the size grew on all processors, and that is due to the increased amount of time it takes to multiply square matrices because after all, a 1Kx32 takes less time to read than a 1Kx1K. Overall, the best performance came from the wc00 using dgemm, where the performance leveled at 600 MFLOPS for the larger matrices. The implementation of the algorithm will continue on the hardware side by taking into account the layout of the memory and the transport speed from the main memory to the local cache, and then the materials code should run optimally.

Rapid Performance Assessment of Parallel Applications. JAMES HORNER (*North Central College, Naperville, IL*)*; BILL GROP (*Argonne National Laboratory, Argonne, IL*). Parallel programs and computations are difficult to profile, and of the tools available, many have deficiencies. The project seeks to build a frame work that can encompass these tools. The ability to profile parallel programs and computations will be beneficial, allowing scientists to see how there code is performing, and where it could be improved. Some of the tools studied include: TAU, Jumpshot, FPMPI2, mpiP, PAPI, Scalsca, and Pablo. These tools can be found on the internet, and are free for education, research, and non-profit use. Installation and assessment of these tools is essential to examine their usability and understand how we might incorporate their best parts into our framework. All of these tools where tested in

two basic steps. First they were installed, and then they were run. This allowed us a view of each tools compatibility with different test codes. This frame work, when completed, will benefit many scientists who use parallel programs for their computations. The goal is for others to be able to profile their code in a few hours, so they will be able to modify it to decrease runtime, and receive information from their programs faster.

Numerical Optimization of NDCX-II. SONIA OLIVIA IBARRA (*Stanford University, Stanford, CA*)*; ENRIQUE HENESTROZA (*Lawrence Berkeley National Laboratory, Berkley, CA*). The Heavy Ion Fusion Science Virtual National Laboratory group is improving upon their original design of the Neutralized Drift Compression Experiment (NDCX) at the Lawrence Berkeley National Laboratory. NDCX will help explore beam manipulation techniques in order to obtain physics limits on the compression of heavy ion beams used in creating high energy density matter and for fusion ignition conditions. The goal of the Heavy Ion Fusion group is to build NDCX which includes an injector that delivers a 100 keV lithium ion beam and an accelerator that will boost the energy up to 2.8 MeV. In order to obtain these goals in an effective manner, two computer programs are used: Mathematica and the multidimensional particle beam simulation program WARP. Mathematica and WARP help aid in the optimization of the transverse and longitudinal beam dynamics along the accelerator. This is done by finding a solenoidal field profile that produces a smooth solution to the beam envelope differential equation for various acceleration schedules. The solenoidal field parameters 100extracted from the Mathematica simulation are used as WARP input in order to simulate particles running through the accelerator. Comparisons are then made and good agreement is observed between both simulations.

Developing Standardized Interactions between a Variety of Data Sources and Generally Available Map-Display Programs. WILLIAM KARNESKY (*Columbia Basin College, Pasco, WA*)*; DAVID MILLARD (*Pacific Northwest National Laboratory, Richland, WA*). Developing Standardized Interactions between a Variety of Data Sources and Generally Available Map-Display Programs. William Karnesky (Columbia Basin College, Pasco, WA 99301) David Millard (Pacific Northwest National Laboratory, Richland, WA 99354) Richard Leigh (Pacific Northwest National Laboratory, Richland, WA 99354). Abstract: There is a wide variety of free service-based map programs aimed at the general user such as Google Earth, Google Maps, Microsoft's Virtual Earth, and NASA's World Wind. These map displays allow a user to add their own points of interest in a variety of ways including place-marks, polygons, and image overlays. There are many tools and applications that could benefit from the ability to connect their capabilities with a service-based map display. One example would be to dynamically link an Excel spreadsheet containing the location of a county's traffic control points to Google Earth. Currently there are very few generic tools that provide efficient and standardized ways to dynamically link an application's information with a service-based mapping program. This project's purpose is to identify and develop mechanisms that make it simple to link map display capabilities to an external application. PNNL's status board system called WebOSB which provides the dynamic status of user-defined information such as bridges, emergency shelters, traffic control points, etc. was used to develop an interoperability layer that will link data sources containing status information to a service-based map display capability. After a map-display interoperability layer is implemented in WebOSB, PNNL plans to continue to generalize that capability to allow a quick, seamless integration of data-oriented systems with a map display capability.

Java Table Tools for the Collider-Accelerator Department. DAVID KATZ (*Alfred State College, Alfred, NY*)*; SETH NEMESURE (*Brookhaven National Laboratory, Upton, NY*). The Collider-Accelerator Department at Brookhaven National Laboratory has a diverse set of data tables which are used to display accelerator controls system data. One program used to display the data is called "pet" (Parameter Editing Tool). There are also a mature set of database tables that store various types of information including device description data, logged data, configuration data and more. Java tools to display the data for this complex system would be very beneficial since Java is platform independent and will be able to run on any OS in the lab. The tools include a unique table structure that doesn't have dependencies on the data source (i.e., database or controls system). In order to provide this in the implementation, I looked at the different types of control system parameters and made the decision to use a hash mapped based table structure. These maps store everything from the look and feel to the layout of the data within the cells. A wrapper class contains each of these hash map arrays, thus defining the generic table structure. Two separate parsers were also written, one to parse pet files and the other to parse database tables. Both of these classes return a table

structure. In order to display the table, a Java table model, cell editor, and cell renderer were written to use the table structure with its unique key mappings. This design offers flexibility for future implementations. The intention is that this tool will allow a sophisticated interface to be quickly and easily integrated by programmers into end-user applications while also providing a clear interface for the user.

Event Based NeXus Files. *Wesley Kendall* (*University of Tennessee, Knoxville, TN*); *Peter Peterson* (*Oak Ridge National Laboratory, Oak Ridge, TN*). When gathering data from instruments across different locations, a universal file format for representing the data becomes essential. The NeXus format is a standard for representing raw data. My project involves writing a program to convert neutron event files to the standard NeXus format. The main resource to write this software is the NeXus Application Programming Interface (API). The API includes many functions for reading and writing data in the NeXus format. Currently, raw binary neutron event data is automatically converted into histogrammed NeXus files. This locks the scientist into a particular choice of histogramming parameters for the data. If the scientist wishes to perform a histogram parameter data analysis scan to find the optimal settings, a new histogram file for each parameter set needs to be generated before data analysis can proceed. An event NeXus file will allow a single file to become the source for each set in the parameter data analysis scan. Space will be significantly reduced since the original raw binary neutron data and its associated metadata will be duplicated in the event NeXus files. My program converts the raw binary neutron event data into event based NeXus files enabling the previously described flexibility. The following details further illustrate how my program operates. First, it reads in a neutron event file, which consists of pixel identification (id) numbers and pixel time of flight values. Since some detectors have different electrical set ups, the pixel id numbers will often have to be mapped to other numbers to closer match the physical detector layout. After the pixel id numbers are mapped to the appropriate number, the program then reads in a pulse id file. The file gives the exact starting times of a pulse. Adding the time of flight value of a pixel id with the corresponding pulse time gives the exact clock time of the neutron event in nanoseconds. This allows for analysis of different time slices of data. After all the steps are completed, the event based NeXus file is created. The data can then be analyzed by scientific software that is specifically made to handle the NeXus format, making analysis much more efficient.

Someone is Spoofing My IP! Research and Development of a Detection Algorithm for IP Spoofing by Using Backscatter. *Deborah Kimnach* (*Illinois Institute of Technology, Chicago, IL*); *Tamara Martin* (*Argonne National Laboratory, Argonne, IL*). Spoofing the source IP address (i.e., misrepresenting where a network communication packet came from) is a common tactic when a hacker wants to disrupt network operations. While keeping the true IP address hidden from network monitors and logs, spoofing also generates enough traffic on the network to reduce performance considerably. Most often a hacker will use it to perform a Denial-of-Service (DoS) attack to overload a server with requests. Inadvertently this use of IP spoofing will generate the phenomena commonly called "network backscatter" where responses to the spoofed packet will "return" to the spoofed IP rather than the hacker. The objective for this research and development is to devise and develop a reliable algorithm to detect the network backscatter where a hacker has spoofed an Argonne National Laboratory (ANL) IP address while performing an attack on an outside third party. The purpose and use of this research is to develop a detection tool that supports administrators in reporting the incident to ANL's ISP (Internet Service Provider) and to assist in tracking down the hacker by monitoring traffic and generating alerts. Although it has been elusive to detect and define this behavior, given some limitations of NetFlow, it has been discovered that at least two types of backscatter have easily detectable patterns. Building on the existing network monitoring scripts in place at ANL and this newfound knowledge, a script has been built, written in the Perl programming language. This script interacts with the NetFlow log files, filters them, and then alerts through email any ANL IP address that may be spoofed.

Georeferenced Image Registration of Aerial Imagery. *Jason Kotenko* (*Edinboro University of Pennsylvania, Edinboro, PA*); *Ryan Hruska* (*Idaho National Laboratory, Idaho Falls, ID*). Photography captured from unmanned aerial vehicles (UAVs) can be used in a variety of applications ranging from security to thematic analysis of geographic areas. Images taken from an aerial platform of the earth's surface must be overlaid to form a single mosaic, this is called image registration. Georeferencing is the process of accurately projecting the images onto a common reference frame. To accomplish this, invariant features were extracted from each image. The search space for

matching these features between images was narrowed through the analysis of telemetry data about the location and attitude of the UAV when the picture was taken.

PDF Forensics and Steganography Detection. *Brandon Langley* (*University of Tennessee, Knoxville, TN*); *Mike Neergaard* (*Oak Ridge National Laboratory, Oak Ridge, TN*). The Portable Document Format (PDF) is used to display two-dimensional documents in a device-independent manner. Standard PDF viewer applications, such as Adobe Acrobat, are designed to hide more information about PDF files than they display. A PDF file consists of a series of objects that are referenced whenever they are used. There are various methods of hiding content inside a PDF file so that a viewer will not display it. This makes PDF an ideal format for hiding information, because most people will view the file in a standard viewer and will not dig deeper into the structure of the file. The science of hiding this information so that only certain people know there is anything hidden is known as steganography. There is no reason for a person to go out of their way to dig into a stegonagraphic document, because nothing appears hidden to the normal eye. I am researching the different ways to hide content inside a PDF file and, in turn, the different methods of extracting hidden data from a PDF file. I am also writing a standard C++ Linux application package to aid in the extraction of any hidden data present in the file. Currently, there is no application designed to help with PDF forensics in this manner. I am using the Adobe PDF Reference (second edition) to study the complete PDF specifications, and the Poppler general public license library to help with the PDF parsing. The application first prints all metadata from the file that may be useful for a forensics investigation. This includes the author, application used to create the file, creation date, modification date, etc. In addition, this application searches for and displays any content that is hidden in the file and not viewable in a standard PDF viewer. This is a three phase process. First, the application finds every legal object that is in the file but never referenced by a page. Second, it searches for any content that is hidden between legal objects. Finally, the application looks at the instructions for displaying each page. If an object is referenced by a page, but never used in the page's actual display instructions, those objects are also considered hidden. Any hidden content is then displayed for the user. This application should aid in investigations involving computer crimes such as child pornography. If someone has criminal content hidden in a PDF file so that only they know how to view it, this application should help to expose it.

*Long Island's Interactive Weather Map and Microsoft Excel Data Entry. *Joe Lanier* (*State University of New York at Stony Brook, Stony Brook, NY*); *Victor Cassella* (*Brookhaven National Laboratory, Upton, NY*). The Long Island Interactive Weather Map was created for all personnel on site at Brookhaven National Laboratory (BNL). The primary purpose of this map is to give employees a place where they can access current weather data from all over Long Island, as well as archival data dating back from the 1940s up to the present day. Throughout weather stations across Long Island, we collected data on temperature, wind speed, direction, gusts, barometric pressure, humidity, and precipitation from old records and entered them into a large Microsoft Excel database. This data is sent via radio waves to a receiver at BNL, collected and stored as an ASCII string, fed into a MySQL database, and updated on the meteorological website once a minute. We have created a web page using the following languages: PHP, SQL, JavaScript, and HTML. This page has an image of Long Island and displays all of the towns with BNL's current weather stations. When a user hovers over any of the towns or stations, a small pop-up box appears and the current data is displayed for that town. At the bottom of the box, a link for further archive data is available for that town or station. The user can navigate through the data to get what is needed. Never before has there been such an easy, all-in-one design that has allowed users to see current and archival weather data on BNL's meteorological website. Throughout this project, the majority of the BNL weather acquisition system has been reconfigured and available to the BNL staff.

The Integration of Sub-Hourly CALPUFF and its Processors. *Katrina Lee* (*Big Bend Community College, Moses Lake, WA*); *Frederick Rutz* (*Pacific Northwest National Laboratory, Richland, WA*). CALifornia PUFF model (CALPUFF) is an Environmental Protection Agency (EPA) approved atmospheric modeling application used for the simulation of long range dispersion of airborne pollutants. CALPUFF is currently integrated into DUST TRANsport (DUSTRAN), a graphical dust dispersion modeling system. Within DUSTRAN, CALPUFF makes use of three preprocessor applications, a meteorological model, and a postprocessor application. The preprocessors condition raw topographical data for use in the models. The two models include

a meteorological model named CALifornia METeorological model (CALMET) and the atmospheric dispersion model CALPUFF. Recent upgrades released for CALPUFF components provide new support for simulations on a sub-hourly basis. These upgrades necessitate changes to how data is acquired, processed, and output at all levels of the CALPUFF integration system. Integration of these new components is necessary to allow the system to function seamlessly as a single entity, automating the time consuming and human-error prone process of editing large amounts of input data while executing each processor in order. An integrated CALPUFF system may be used as a component of a larger system, such as DUSTRAN, with minimal input from the user. Integration of the new components is complete through the pre-processors and the CALMET model, with work still to be done on CALPUFF and the postprocessor application pending full documentation. This paper describes the progress, integration methods, and models for use in DUSTRAN.

A Computational Process to Locate IS Elements and Study Horizontal Gene Transfer in Bacterial Genomes. *WALTER LEWIS* (*Cheyney University of Pennsylvania, Cheyney, PA*)*; SEAN MCCORKLE* (*Brookhaven National Laboratory, Upton, NY*). Currently there is a tremendous focus on studying how whole units of DNA are shared between species. These movable tracks of DNA, called transposons, are demarcated by shorter insertion sequence (IS) elements, which themselves are generally around 700 to 2500 bp in length, and code for proteins implicated in the transposition activity, such as transposase and intergrase. IS elements are bracketed by pairs of inverted repeats of variant length (approx. 10–30 bp), and are further embedded in a pair of short direct repeats of approximately 3–7 bp. While there is a great deal of software to automatically annotate genes and regulatory regions, there are currently no programs to identify IS elements de novo. Hundreds of completed bacterial genomes are currently available and more are constantly being added to that list, which makes it increasingly important for the computational detection of IS elements. To this end, we have developed a C++ program to locate IS elements in bacterial genomes. The process was broken down into steps in order to make it more dynamic so that one could easily examine the data in each stage of the process to detect errors, or perhaps discover something unexpected. First, all repeats (within length constraints) are reported, then these are searched for pairs of inverted repeats which have the proper orientation and distance. Positions, paired inverted repeat sequences, and interior coding sequences are reported for these IS element candidates. Lastly the interior coding sequences are examined for homology with known transposition genes. Preliminary tests on the genome of Enterobacter strain 638, recently sequenced as part of the DOE biofuels initiative, revealed 9 putative IS candidates, 6 of which were confirmed by Blastx searches of Genbank, which yielded strong homology matches to transposase and intergrase in other organisms. Further testing on an IS-rich genome, now Cupriavidus metallidurans (CH34), will allow us to optimize program parameters to improve performance. Because this process reports direct and inverted sequence pairs, which travel along with the IS element as it moves, it can be used to trace horizontal gene transfer history within or between genomes for evolutionary studies.

Modeling the Interactions among Microbial Communities under Environmental Conditions through High Density Phylogenetic Microarrays. *CURTIS LUCE* (*New Mexico State University, Las Cruces, NM*)*; TODD DESANTIS* (*Lawrence Berkeley National Laboratory, Berkley, CA*). The K-th order logical network modeling software determines significant interactions among microbes in a microbial community. Using inference of the K-th order the temporal information in the gene expression data sets provides a basis to examine interactions with a microbial community using the logical network model. In a logical network, a logical function, associated with each microbe population as a node, describes its behavior dictated by some other influential microbes. The optimal logics at each microbe node in the network will be searched so that they best explain the observed data. Determination of an optimal logic will involve parent node selection and truth-table generation. The maximum number of parents is set to a given number. If the current node shows consistent behavior during transition from one state to another given the parent nodes, then the parent nodes will be kept. The actual goodness of the transition will be calculated using the chi-square test.

Electrodymanics Simulation of the Pulse Line Ion Accelerator. *ROXANNE MARTINEZ* (*Stanford University, Stanford, CA*)*; ENRIQUE HENESTROZA* (*Lawrence Berkeley National Laboratory, Berkley, CA*). The Heavy Ion Fusion Science Virtual National Laboratory is currently studying the Pulse Line Ion Accelerator (PLIA), a slow-wave accelerator that would substantially reduce the cost of experiments for studies of high energy density matter and fusion ignition conditions. The PLIA uses a high voltage pulse at the input end of a helical pulse line structure as a means to accelerate charged particles. The high voltage pulse generates an electric field that travels across the span of the accelerator. This wave pulse can be used to accelerate the ions to energies far greater than the peak voltage which was applied to the input end of the structure. Moreover, the PLIA can axially confine the heavy ion beam bunch, making it an excellent candidate for a high intensity, short bunch injector. The electrodynamics of the system will be presented. This analysis was performed using MAFIA (MAxwell's equations by the Finite Integration Algorithm), an electromagnetic and particle dynamics code.

On Adapting the Core-Edge Fusion Code UEDGE to Use the Portable Extensible Toolkit for Scientific Computing Libraries. *MICHAEL MCCOURT* (*Illinois Institute of Technology, Chicago, IL*)*; HONG ZHANG* (*Argonne National Laboratory, Argonne, IL*). Numerically simulating nuclear fusion requires discretizing the associated physical processes and geometries, and then solving the resulting equations for the ionized and neutral gases. This project is a collaboration between physicists at Lawrence Livermore National Laboratories (LLNL) and mathematicians and computer scientists at Argonne National Laboratories (Argonne). UEDGE is a two-dimensional edge-plasma transport code developed at LLNL from 1989 to the present. After discretizing the plasma transport equations a nonlinear system must be solved at each time step to advance the system or approximate a steady state solution. Separately, ANL has developed a Portable Extensible Toolkit for Scientific Computing (PETSc) which provides access to optimized routines for solving nonlinear systems with preconditioning. The PETSc scalable nonlinear equation solvers have been adapted to be called from UEDGE subroutines. This allows UEDGE users access to the PETSc preconditioners which provide faster convergence and a more robust algorithm for some situations. Tests were run on 4 different cases with incomplete LU and algebraic multigrid preconditioners, some of which performed better than the standard UEDGE solvers.

Systems Administration: Improving Efficiency. *CARL MEHNER* (*Baylor University, Waco, TX*)*; CRAIG STACEY* (*Argonne National Laboratory, Argonne, IL*). Working as a system administrator over many computer systems is a challenging problem; the best way to ease the problem of managing these systems is to use different scripts or programs to shorten the amount of time spent doing procedural tasks that are often repeated. Web applications coupled with high-level scripting languages are advantageous solutions for administrators to increase work efficiency. An existing system for creating and managing user accounts has exceeded the assumptions of usage set forth in its planning. The goal is to create new version of this project using existing ideas, amplify extensibility, and adding new features to further increase efficiency and utility. Using PHP, Perl, and Python scripting languages interfacing with a MySQL database, a web application to manage user accounts that is extensible and supportive of multiple computing environments can be created. Completed, this system will allow for clear, straightforward, and more efficient management of user accounts over our computing systems.

Second Order Boundary Derivatives in 3D. *EMILY MITCHELL* (*University of South Carolina, Columbia, SC*)*; LEONARD GRAY* (*Oak Ridge National Laboratory, Oak Ridge, TN*). The Boundary Element Method (BEM) is a numerical technique for the solution of the partial differential equations that describe physical phenomena. The integral equation formulation contains the Green's function (fundamental solution of the differential equation) and its first derivative; as these functions are singular, singular integral evaluation is an important aspect of the BEM. A boundary integral solution provides complete knowledge of the primary function (e.g., potential for the Laplace equation, displacement for elasticity) and its normal derivative on the boundary. An algorithm for the post-processing evaluation of second order derivatives of this primary function has been developed. The integral equation expression for these derivatives contains second (hypersingular) and third order (supersingular) derivatives of the Green's function, and thus the definition and evaluation of these highly singular integrals is the key task. In this work, the difference of the interior and exterior boundary limits of the integral equation is exploited to calculate the integrals. The difference procedure effectively weakens the singularities, resulting in finite limiting values, and moreover all non-singular terms vanish. The limit calculation is made possible by partial analytic evaluation of the four-dimensional parameter space integrals. The second derivative algorithm has been implemented for the 3D Laplace and Helmholtz equations. This latter case involves a more complicated Green's function, and it was necessary to use

suitable Taylor expansions to carry out the limits. The ability to handle the Helmholtz Green's function indicates that the second derivative methods are generally applicable. The boundary element method is applicable to areas such as mechanics, acoustic and elastic wave propagation, and electromagnetism. This new second derivative algorithm should find application in many of these areas.

Reconstructing Userbase: Providing Administrative Support for Expanding Computing Environments. *Tuan Nguyen* (*Northern Illinois University, Dekalb, IL*)*; Craig Stacey* (*Argonne National Laboratory, Argonne, IL*). Userbase is a program used to query and modify the systems administration database containing information on registered users and everything associated with them. It provides a simple command-line syntax for ease of use and scripting. The Math and Computer Science division has outgrown the current Userbase in the sense that the current Userbase lacks extensive support for multiple computing environments. Additionally, some data fields are in need of database and environment reconciliation to avoid ambiguous usage and field deprecation. Rewriting Userbase focuses on the standalone back-end scripts which use the database information for tailoring user environments, the Userbase API which provides the command-line Userbase invocation, and the overall structure of the user database.

Using Math to Determine Optimal Placement for Wireless Access Points. *Kellen O'Connor* (*University of Tennessee, Knoxville, TN*)*; Don Williams* (*Oak Ridge National Laboratory, Oak Ridge, TN*). Intranet and Internet networking have become a huge part of the operating strategies of many large organizations. Many organizations use networking to keep in contact with their employees, inform their employees, and to communicate among one another. It used to be that desktop computers were the standard, and laptop computers were only for the elite, used when absolutely necessary. Now, the world of electronics is focusing on smaller, more portable devices to make it more convenient for people to travel with their devices. So, the challenge for the organizations is to continue communication with these portable devices. The main method used is Wi-Fi, or wireless. Once a novelty, wireless communication has become a necessity in any large organization. Because wireless communication is a relatively new concept, there are not really any standards in place for the placement of wireless transmitters/receivers, wireless access points (APs). The goal of this project was to determine a mathematical equation that could be used to determine signal strength at different distances from the AP, so the APs could be placed in buildings by evaluating signal strength needs in certain areas. To determine this equation, I used a handheld signal strength measuring device. I setup the AP in a central location and recorded the signal strength at distances in intervals of five feet from the AP. I first measured the signal strength five feet from the AP, then again ten feet, fifteen feet, and so forth. I recorded that data and plotted the points on a graph. Visually, it was obvious to tell that the signal strength was linearly related to the distance from the access point. I used linear regression to determine an appropriate equation to relate the two variables, distance versus signal strength, and the data fit nicely. The results of this research are quite helpful in the information technology world; however, further research could also benefit the IT professionals. There are other factors to consider when setting up a wireless network that were not taken into account here. If research is continued, it would also be useful to obtain a device designed specifically for measuring signal strength. This would allow researchers to obtain more accurate data and therefore give better, more accurate results. This research is a step in the right direction and is the beginning of creating a useful tool for the IT professional when designing a wireless network.

An Internet-Enabled Computer Simulation for Cleaning Up Contaminants In Groundwater and Soil. *Raul Ortiz, Todd Sallis* (*Governors State University, University Park, IL*)*; Eugene Yan* (*Argonne National Laboratory, Argonne, IL*). Due to the many sources that could potentially contaminate Groundwater, remedial strategies for cleaning groundwater have become increasingly important. Soil Vapor Extraction is currently the most widely used method for removing contaminants from the groundwater. Tough2 is a complex numerical simulator developed by the Lawrence Berkeley National Laboratory in 1999 and used to simulate different characteristics as they dynamically change in the groundwater. To simplify the process of using the Tough2 simulator, the integrated development environment (IDE) Visual Studio.NET was used to generate a more user friendly system. The IDE provides tools enabling convenient input pages to be created and allows for design of a database with multiple tables to store and secure input data. When different scenarios are recreated using selected data, the system will determine calculations and ultimately help improve current methods of cleaning groundwater and removing volatile organic compounds. The

main objective is to add pre-processing and post-processing features to the TOUGH2 design. The new application provides an efficient way for entering data that represents both the thermodynamic and thermo-physical properties of the mass components. Also, the application will display visualized results using the TecPlot360 plotting software.

Automatic Differentiation Optimization on Vector Arithmetic implementation on the Cell Broadband Engine Processor. *Eliseo Ramon* (*La Sierra University, Riverside, CA*); *Paul Hovland* (*Argonne National Laboratory, Argonne, IL*). The Cell Broadband Engine processor is currently the latest multi-core processor with distinctive parallel processing elements offering optimization in automatic differentiation (AD). By developing a general Scalar Vector Plus Vector library (AXPY), the Synergistic Processing Elements (SPE) can be exploited to improve runtime performance. Using single precision arithmetic on available SPE, the Cell processor can provide high runtime reductions by means of vectorization and the use of the Simple Instruction Multiple Data (SIMD) method. Furthermore, individual AXPY computations are executed in parallel which provide an independent runtime decrement. When comparing runtime estimates of single core implementation vs multiple core implementation, runtime gain occurred when data was elongated or when more stress was put on individual SPE. Although the actual computation produces reduced runtime results, the initial cost of activating the SPE requires multiple uses of the AXPY library before it results in an overall runtime gain. The most optimal result produced is an seven time speed increment. Currently this performance indicates that the Cell processor offers advantages to AD. Development of this library also indicates that other libraries can be ported to the Cell processor from a x86 structure.

FitNesse: Application of a Software Testing Framework to the Bioinformatics Resource Manager. *Jonathan Rice* (*University of Nebraska – Omaha, Omaha, NE*); *Anuj Shah* (*Pacific Northwest National Laboratory, Richland, WA*). One of the goals of a software development team is the delivery of quality software in a timely fashion. The importance of thoroughly testing a software product can never be overstated. However, testing the functionality of software, especially ones with graphical user interfaces (GUIs), is often a laborious process due to the amount of time required, difficulty of testing consistently, uncertainty of what exactly should be tested, and the lack of easy-to-use testing frameworks. Other considerations include minimal impact on existing code, a straightforward script writing process, and automated execution of test suites. The project goal was to integrate an existing automated testing framework into the Bioinformatics Resource (BRM) application to facilitate the automated testing of key functionality. Previously, testing was manual and most functionality testing occurred just prior to version releases, rather than progressively. Project development utilized the FitNesse testing tool, which allows for the creation and running of acceptance tests against GUI-based software; BRM; and the Java programming language. The ease of use, the script-based test case development and the WIKI-like execution engine make FitNesse amenable to use by non-developers. The new test environment allows convenient, consistent, and defined testing.

Systems Administration In a Scientific Laboratory Environment. *John Roberts* (*Joliet Junior College, Joliet, IL*); *Craig Stacey* (*Argonne National Laboratory, Argonne, IL*). Systems Administration is the key to a successful computing infrastructure in any environment, especially a scientific environment. Behind the scientific research in the Mathematics and Computer Science division (MCS) at Argonne National Laboratory, the systems group make all of this possible using today's highly advanced computing systems. The goals of this project were to assist in day to day systems administration duties of the MCS computing infrastructure and to support Linux, OS X and Windows workstations and servers. MCS help desk duties and divisional tape storage backup procedures were the main focus of this project. Systems administration tools were developed making use of Python, shell scripting, PHP, and HTML. Use of a workstation and hands on procedures ensured these tasks were completed efficiently and effectively. A systems administration position did not produce scientific results, instead it gave a chance to learn and improve on how the systems administration duties were carried out. Further work includes learning various tasks in order to become a more efficient administrator. Systems administration provides scientists a chance to make their research a reality.

Data Analysis and Social Collaboration. *Eugene Sandberg* (*Mississippi State University, Starville, MS*); *Dane Skow* (*Argonne National Laboratory, Argonne, IL*). This summer I am working on the TeraGrid project. TeraGrid is an open scientific discovery infrastructure

that combines resources at nine different sites to create an integrated computational resource. There are well over a thousand users that work on and use and the TeraGrid system. More information on TeraGrid can be found on the website (http://www.teragrid.org/). I have two different tasks in the TeraGrid project. First I will be doing computational analysis on all the user data since 2004 to produce histograms of various grouping of the data. My second task is to setup a social collaboration for all of the project's users. A social collaboration is an integration of networking tools that are specifically driven to better user connectivity.

Wireless Network for On-Site Housing. Jennifer Scheuerer (*Alfred State College, Alfred, NY*); AJ Temprosa (*Brookhaven National Laboratory, Upton, NY*). The implementation of a secure, functional, and reliable network is important when you are dealing with more than 2,000 users. Brookhaven National Laboratory (BNL) is in the process of upgrading the on-site apartments from Cisco 827 Routers to Cisco 857W Routers. The original network was designed to provide the scientists and visitors with network access for their accommodations. The original configuration of the Cisco 827 Routers was a Network Address Translation (NAT) on top of a Network Address Translation (NAT). This new configuration is now extending publicly routed space to the DSL router, where each apartment now has it's own IP address. In this way it is simple to track down which apartment may be out of compliance with the Computer Usage Policy. On top of wired digital subscriber line (DSL), the new routers now provide each individual apartment with a unique wireless access point (WAP). The reason for the current architecture to be redesigned is to include additional services and capabilities as requested by user community and as required by the Department of Energy's (DOE) security standards. The new design provides more functionality and security because now users are not connecting their personal wireless routers, which created many security holes in BNL network. The Cisco 857W's were configured with a baseline and deployed within the project plan. The chosen encryption method for these routers is Wi-Fi Protected Access (WPA). This was chosen as the baseline configuration due to security flaws in the previously used Wireless Equivalent Privacy (WEP). All 112 routers were deployed with a baseline configuration on the Digital Subscriber Line Access Multiplexer (DSLAM) that met all the requirements of the new architecture. The redesign of the apartment network brought on multiple additional services and features for users and it also brought the apartment network to compliance with DOE's security directives. This redesign also protects BNL from rogue wireless networks and it is now easier to quarantine machines and keep viruses from spreading onto BNL's network. BNL is committed to providing all users with reliable and fully functional network access

Two-Dimensional Storage Analysis for Peta-Scale Computing. Kyle Schochenmaier (*Iowa State University, Ames, IA*); Rob Ross (*Argonne National Laboratory, Argonne, IL*). Two projects were discussed for this summer. One was to develop a two-dimensional storage architecture for the PVFS2 file system, and another was to create a strongly automated benchmarking framework to use for future research and testing of the PVFS2 file system. As part of the first project a hierarchical storage system had to be created that would interface with the original PVFS2's model for distributing data amongst servers. This requires a new module to plug into the existing model as well as documentation and testing. The second project involves creating an extensive scripting framework that automatically tests the PVFS2 file systems performance and correctness under various settings and configurations. When both projects come to completion at summer's end, the benchmarking system will be used on future computer installations to test the performance of newly developed systems for the PVFS2 software suite, including the inclusion of the two-dimensional storage system developed here.

Enhancing Network Security by a Centralized and Standardized Dynamic Event Log Data Collection Method. Mark Seal (*Walters State Community College, Morristown, TN*); Don Williams (*Oak Ridge National Laboratory, Oak Ridge, TN*). Event logs are at the core of network security. Without the tracking and logging ability that event logs allow, there would be no accountability of the security of the network. The logs allow the detection of worms and viruses via monitoring system resources and processes, detection of port scans by monitoring the dropped port requests by the firewall, detection of brute force password cracking by the number of failed login events, and the ability to start a trace on the agent when a security event is recorded. It is imperative that the logs from each machine are parsed and the relevant information passed on to a central log server (syslog) where the information can be analyzed and trend analysis preformed. The problem faced is that Windows does not have a single log that collects all of the required data; instead the data must be collected in segments. In addition, both XP and Vista are both being used as operating systems. Each of these OS's has different ways of storing the logs, requiring different data collection methods. XP uses evt format as the logging method while Vista uses an evtx format. XP logs may be ported to the syslog server while Vista requires that either an event viewer or a data collection program (e.g. LogParser) be used. The development of the new Windows event log data collection protocol centers around three core concepts: scalability, control, uniformity. The chosen method of collection of data by using Powershell scripts meets all three core concepts. Powershell may be installed on both XP and Vista machines, while coming mounted on the upcoming Window Server 2008. Scripting in Powershell allows for the full control of the event log data. The data can be parsed by content as well as being stripped of superfluous data for storage and trending in the syslog server. In addition, the data will be supplied to the syslog in real-time, allowing for real-time trend analysis and alerting protocols. Powershell scripting also creates a uniform event log data collection protocol as that Linux system logs are parsed by scripts. Powershell, which is based on the Korn Shell model, will be easier for cyber security to modify and maintain the core scripting code. This project will increase the security of the network by allowing for data collection of the system logs of Windows machines while decreasing the response time of the cyber-security team by allowing for real-time data comparison between Linux and Window machines.

Flocking-Based Document Clustering on the Graphics Processing Unit. Jesse St. Charles (*University of Tennessee at Chattanooga, Chattanooga, TN*); Xiaohui Cui (*Oak Ridge National Laboratory, Oak Ridge, TN*). Analyzing and grouping documents by content is a complex problem. One explored method of solving this problem borrows from nature, imitating the flocking behavior of birds. Each bird represents a single document and flies toward other documents that are similar to it. One limitation of this method of document clustering is its complexity O(n2). As the number of documents grows, it becomes increasingly difficult to receive results in a reasonable amount of time. However, flocking behavior, along with most naturally inspired algorithms such as ant colony optimization and particle swarm optimization, are highly parallel and have found increased performance on expensive cluster computers. In the last few years, the graphics processing unit (GPU) has received attention for its ability to solve highly-parallel and semi-parallel problems much faster than the traditional sequential processor. Some applications see a huge increase in performance on this new platform. The cost of these high-performance devices is also marginal when compared with the price of cluster machines. In this paper, we have conducted research to exploit this architecture and apply its strengths to the document flocking problem. Our results highlight the potential benefit the GPU brings to all naturally inspired algorithms. Using the CUDA platform from NIVIDA®, we developed a document flocking implementation to be run on the NIVIDA® GEFORCE 8800. Additionally, we developed a similar but sequential implementation of the same algorithm to be run on a desktop CPU. We tested the performance of each on groups of news articles ranging in size from 200 to 3,000 documents. The results of these tests were very significant. Performance gains ranged from three to nearly five times improvement of the GPU over the CPU implementation. This dramatic improvement in runtime makes the GPU a potentially revolutionary platform for document clustering algorithms.

PTFrame: An Extensible Framework for Automating Parallel Performance Tools. Michael Sullivan (*George Mason University, Fairfax, VA*); William Gropp (*Argonne National Laboratory, Argonne, IL*). The hardware needed to build petascale supercomputers exists today, and such systems will soon be in use worldwide. However, writing programs which realize the full potential of these massively parallel systems remains a challenge. Program assessment — the evaluation of the performance and scalability of parallel applications — is critical for writing powerful parallel code, but demands a great deal of time and labor. Although there are various tools available which aid in understanding different aspects of program performance, there is no one tool which gives a complete characterization of parallel code, including the potential scalability of applications. Furthermore, the available tools, as a whole, may be prohibitively difficult to learn and run manually. The PTFrame framework is designed to create an extensible meta-tool which utilizes existing performance tools to aid with program assessment. Written in the Python programming language, PTFrame is highly configurable, allowing it to be adapted to various build systems and target platforms. The PTFrame framework utilizes the strengths of the existing performance tools and automates the repeated compilation and execution of programs in order to reduce the time required to provide a description of the performance properties of parallel code.

PTFrame may reduce the time required to characterize parallel code. This, in turn, could aid in the development of code which is able to scale to hundreds of thousands of nodes in order to utilize the processing power of future petascale supercomputers.

Cyber Security at Oak Ridge National Laboratory. BOBBY SWEET (*Roane State Community College, Oak Ridge, TN*); VICTO HAZLEWOOD (*Oak Ridge National Laboratory, Oak Ridge, TN*). The Office of the Chief Information Officer (OCIO) has the responsibility to ensure that all information technology (IT) is managed to all statutory, regulatory, and organizational requirements which can be found in the Certification and Accreditation package which documents the Oak Ridge National Laboratory (ORNL) Cyber Security Program Plan. In the case of ORNL, who has over ten thousand computer systems, there are systems that will not comply with these standards for a variety of operational and other reasons. The OCIO ensures that computing resources are managed to requirements with some mitigation in place for systems where the requirements could not be met. In many cases, a security plan will provide the basis for the mitigation for systems or collections of systems that cannot meet all the requirements. Security planning was our main emphasis this summer. There were approximately two-hundred forty systems at the start of this summer that needed a security plan in place, if they were going to stay on the ORNL network. A process needed to be developed and implemented to address the two-hundred forty systems and their required security plans in the most efficient manner within a limited amount of time. Four security planning meetings were given to communicate the security planning process. It is expected that these meetings will be held each month to keep up with new systems that might not meet requirements and require a security plan. Three questionnaires were created for the different control categories to help the owners of the devices. The three different control categories were moderate with enhanced, moderate, and low. The categories are determined by the sensitivity of information each of these systems would hold (moderate with enhanced requiring the most controls of the three). The classes have been completed and the resources have been distributed to the system owners and administrators to start their security plan process. The ORNL security planning project has been developed and is being implemented. The security planning process will continue to be improved in the effort to protect the devices that are not able to satisfy all cyber security requirements. This project is designed to protect the devices making them as safe as possible from intruders or unauthorized access by providing a mitigation strategy when a device cannot implement one or more required cyber security requirements.

A New Build System for the Common Component Architecture. DANIEL TAYLOR (*Edinboro University of Pennsylvania, Edinboro, PA*); BOYANA NORRIS (*Argonne National Laboratory, Argonne, IL*). The Common Component Architecture (CCA) is a set of tools to allow researchers to easily link together multiple scientific software components, to create custom application to run on large compute clusters. Specifically, the components allow code written in C/C+, Java, Python, and Fortran to be linked using a standard scientific definition language. Contractor is an installation system written in Python that allows developers to write complex build and package configuration swith dependencies and options. The CCA tools are complex and require many dependencies to build properly. A new build system based on Contractor, but with many improvements, was created to simplify the process of getting and using the CCA tools. It replaces the old build scripts with a robust, easy-to-use, automated configuration and installation, including a graphical client to configure the build. As a result, releases can be built with few changes to the build system, the build system can manage complex configurations eliminating manual configuration, and it can report errors back to the CCA team to facilitate fixing bugs. Most importantly, the new build system lets developers work with the CCA tools quickly and easily without focusing on mundane computer science details.

*Test and Evaluation of the Decision Evaluation in Complex Risk Networked Systems (DECERNS) Software. BRIAN TUCKER (*SCCC, Selden, NY*); TERRY SULLIVAN (*Brookhaven National Laboratory, Upton, NY*). Environmental management requires decision support tools that are able to integrate multiple sources of technical information and evaluate options based on multiple criteria. Decision Evaluation in Complex Risk Networked Systems (DECERNS) is a web-based software system being developed with the objective of providing a methodology, computer models, and software tools to facilitate decision making in the field of sustainable land use. The system includes geographic information system (GIS) tools for mapping and data analysis along with risk models, economic analysis tools for evaluating costs, and tools for incorporating social choices into the decision

process. The main advantage of DECERNS as opposed to existing decision support systems is its ability to integrate different models and measures as well as decision-maker values using Multi-Criteria Decision Analysis (MCDA) tools. The objective of this work is to perform extensive quality assurance testing of the system reliability, system functionality, and user interface to ensure the system can be deployed and used as desired. Testing was performed using Java version 1.6.01 under Microsoft Windows XP Professional. In addition, work included software development of Java applications for graphical display of MCDA results to rank and compare alternatives. The GIS map viewing function has been extensively tested and comments are being incorporated. At this time the full functionality of DECERNS has not been implemented. The next release will incorporate these comments and add the MCDA tools including the graphical display developed. This version will also undergo quality assurance testing as part of this program. Once the full functionality of this system is completed, it will be a valuable tool for environmental management.

Development of a Model for Electrical Distribution Utility Switching Analysis. SHAWN WALTON (*Big Bend Community College, Moses Lake, WA*); CLINT GERKENSMEYER (*Pacific Northwest National Laboratory, Richland, WA*). The ability to assess and respond to a situation is imperative in the operation of an electric utility. Electric utility dispatchers are required to reconfigure the system on a daily basis, but may not always have the necessary instructions or data to make correct decisions. The goal of this project was to create a Model for Electrical Distribution Utility Switching Analysis (MEDUSA). The model was created using Invensys Wonderware, Practical Extraction and Report Language (PERL) scripts, and a Structured Query Language (SQL) database. PERL and SQL were used to create simulated electrical line values, including amps and volts, for two distribution lines. Using Wonderware, a graphical user interface was created to represent the distribution line system including breakers, loads, connecting lines, and switches. This interface allows the dispatcher to manipulate any combination of breakers and switches and view the resulting configuration and estimated system measurements. Once the configuration is simulated and optimized, the switches can either be operated directly from the MEDUSA dashboard or instructions can be given to a lineman to operate them manually. All possible breaker/switch configurations were tested and proved. The graphical interface was designed to be visually clutter-free and utilized color schemes native to the industry. MEDUSA demonstrates the effectiveness of providing situational awareness to distribution system dispatchers by allowing them to simulate the new switch configuration and analyze the resulting data in real time without risk to the system. Further development of this program could benefit from eliminating the current Wonderware shell and utilizing the C++ language. This would improve the ability to easily modify or add to the system. Integration of actual system measurements and the modeling of an entire distribution system would also need to be addressed for this application to be utilized by the industry.

Consolidating Three Data Sources into a Centralized Data Repository That Can Be Accessed by Multiple Systems. TASHA WHEATLEY (*Clarion University, Clarion, PA*); MARK BAYLESS (*Pacific Northwest National Laboratory, Richland, WA*). The purpose of the system is to pull data from three different Lotus Domino application databases, Office of Science Application System (Edulink), SEE Application System (OFP), and SEE Request System (SEE), into a centralized location. The Edulink system provides and controls all online applications filed for DOE internships at any of the national laboratories while OFP merely contains applications for internal Pacific Northwest National Laboratory (PNNL) internships. In addition the SEE system allows PNNL mentors to request an intern that applied for an internship through either the Edulink or OFP systems. Before being pulled into the private Intern Tracking System database, the original system used the SEE System to pull information from the Edulink and OFP systems. Because of complexities in how data was being pulled together by the SEE system from the Edulink and OFP systems, modifications were needed to address data integrity issues. The new design provides a Domino agent that executes daily to compile the necessary data from the three databases. Once the data is compiled, a Microsoft SQL Server scheduled job runs to load the data from Domino into SQL Server tables, providing any final data scrubbing such as converting dates in varchar format to date/time format. A SQL Server view was also created so the Data Repository (Op Warehouse) can pull and store the data; thus, allowing several internal systems to access the data from a central source. This is ideal because it ensures consistent data among the systems. In the next couple of years the applications are going to be moved from Domino to a .NET application,

which is another reason why these modifications needed to occur. Whenever the new applications are created, the hope is to ensure that all necessary information is available for all systems.

DHS Analyst Software Implimentation. *Christopher Whitehouse* (*Big Bend Community College, Moses Lake, WA*); *Mary Sue Hoxie* (*Pacific Northwest National Laboratory, Richland, WA*). The objective is to see how analytical programs such as Collaborative Analytical Tool (CAT), ProSPECT, IN-SPIRE, and Analyst Notebook (ANB) will help in analyzing investigative data. Before any of the tools could be used we needed to convert the data into a usable format, plain text. My lab partner, Sherwin Hunte, created a program to automate extraction of a PDF (portable document format) file into separate smaller PDF files. After converting all the documents we imported the data into the separate programs. I used CAT to index all of the files related to the data. These files included Excel, Access, Adobe Acrobat, and text documents. CAT is very useful because it can index several different file types and group them into different data sets. I also imported the data into the ANB program and created timelines for the data. This was a very useful tool except after importing the data it requires a lot of the organizing of the timeline by hand. These analytical programs simplify looking at data that is convoluted. They allow us to visually search through and cross reference the data. These programs also make it a lot easier to find specific information and reference it as needed to support or refute Hypotheses, which allows for stronger hypotheses and better understanding of the data being analyzed. Though the way the data is gathered may need revising, I do think these tools would be helpful to any analyst working with convoluted or disjoined data.

A Case Study of the Performance of Speculative Asynchronous Simulation on Parallel Computers. *Patrick Wilkerson* (*Austin Peay State University, Clarksville, TN*); *Kalyan Perumalla* (*Oak Ridge National Laboratory, Oak Ridge, TN*). Modern supercomputers use thousands of processors running in parallel to achieve their high computational speeds. However, on such large processor counts, communication and synchronization operations can waste valuable processor time. Communication involves processors exchanging intermediate computed data that needs to be shared by processors at runtime. Synchronization involves processors ensuring the mutual orderings of operations across processors are correct. In this work, we investigated the runtime efficiency of two methods that are aimed at reducing communication and synchronization costs, respectively, namely, asynchronous updates and speculative execution. The experimental investigation is performed on a parallel finite difference time domain (FDTD) simulation developed at ORNL, which has wide applicability in simulating various physical system phenomena. It uses an iterative algorithm to reduce communication by allowing messages to be asynchronously sent when the change in values on a given processor is greater than some threshold value. We conducted research to develop an empirical performance study of the algorithm. The first part of asynchronous updates is accomplished by exploring the effect of threshold-based communication on overall runtime of the parallel simulation, with the number of processors increasing. A significant improvement in performance on up to 64 processors was observed when using the asynchronous update scheme, due to reduced communication. We are currently working on the synchronization aspect of the problem, to relieve the tight coupling among processors, using "speculative execution" with sophisticated "rollback" techniques being developed in an ORNL Laboratory Directed Research and Development (LDRD) project. In speculative execution, processors are allowed to progress without having to wait for other processors, but any violations in ordering of computations are detected and corrected using rollback techniques. Further research is being done to implement a rollback mechanism necessary for optimized parallel execution. Preliminary results on a special case of the synchronization mechanism show improved speedup over and above the gains of asynchronous updates on up to 64 processors. We are working towards implementing the more general rollback method and expect to complete the performance study on the generalized asynchronous speculative execution.

Vascular Smooth Muscle Cell Migration Modeling. *Matthew Woerner* (*Tufts University, Medford, MA*); *Jim Nutaro* (*Oak Ridge National Laboratory, Oak Ridge, TN*). The migration of vascular smooth muscle cells is a catalyst for intimal hyperplasia, the thickening of the arterial walls in response to an injury in the blood vessel. Cell migration can be quantified using Boyden Chamber experiments. A model by Jabbarzadeh and Abrams model is used in designing this model. While this model is based on Jabbarzadeh and Abram's model, our model contains several differences. In this algorithm, eukaryotic cells were modeled, instead of bacterial prokaryotic cells in their model, which slightly changed the nature of how cells move. A hybrid model, a model containing both discrete and continuous parts, was developed to simulate Boyden Chamber experiments in order to better understand cell migration. The hybrid nature of this model accounts for motion of individual cells, diffusion of the chemoattractant, and the interaction between the chemoattractant and cells. This model is being built using a C++ code and a discrete event system specification (DEVS). In the future this model will provide the foundation to aid in predicting the appearance of intimal hyperplasia following balloon angioplasty.

Two Case Studies of Reversibility in Computational Methods. *John Wright* (*Mercer University, Macon, GA*); *Kalyan S. Perumalla* (*Oak Ridge National Laboratory, Oak Ridge, TN*). Currently state-saving is employed in many large simulations to realize rollback. Reverse computation is a recently proposed method which computes previous states instead of saving them. This approach can be beneficial on large machines as computing power is abundantly available and is possibly more efficient than retrieval from memory. This project investigates the reversibility of the well known Newton-Raphson root finding method and the possibility of developing a reversible interface for the Level 1 (vector) operations found in the Basic Linear Algebra Subprograms (BLAS) library. The mechanics of Newton-Raphson were studied and an algorithm was developed to reverse each iteration in the forward method. The reverse method involves finding the root of a derived function and forward Newton-Raphson is used on the derived function. Consequently, reverse Newton-Raphson gains the strengths and weaknesses found in Newton-Raphson. The reverse method has produced favorable results on functions that converge with forward Newton-Raphson. Unfortunately the forward method behaves unpredictably when multiple roots, periodic behavior, local minima, etc. exist in the target function and the reverse method will also produce unpredictable behavior in these cases. Further research is needed to handle unpredictability in certain functions in the reverse method. Routines in the BLAS Level 1 were analyzed and candidates were chosen based on the need for reversibility. Only those routines which modify input values require reversal. Reverse routines were developed for Givens rotation, vector scale, vector swap, and vector scale and update (saxpy). The reverse routines have shown identical scaling to their forward counterparts, however some problems concerning precision need to be resolved. Further work is needed to improve the interface to realize transparent reversibility for the vector copy operation. The forward BLAS library will need to be modified to implement copy reversibility.

Extending the MPI-Serial Library to Support Derived Datatypes. *John Yackovich* (*Shippensburg University of Pennsylvania, Shippensburg, PA*); *Robert Jacob* (*Argonne National Laboratory, Argonne, IL*). The Message-Passing Interface (MPI) standard is widely used to manage communication between networks of processors working on a single problem. MPI defines a set of derived data type constructors for the C and Fortran languages to enable the communication of multiple pieces of information simultaneously between processors, thus minimizing both the overhead of these communications and the effort required by the user. There is a compatibility library implementation of the MPI standard called MPI-Serial that aids in testing MPI-based codes on smaller, single-processor systems. To support a greater subset of the MPI standard, functionality for the MPI derived data types has been implemented in MPI-Serial for use with C and Fortran programs. In addition, a test suite has been developed to aid the performance of MPI-Serial that focuses on successful operation of MPI-based programs in a single-processor environment.

Engineering

Analyzing the Response of Frisch-Ring CdZnTe Radiation Detectors. *Najeb Abdul-Jabbar* (*University of Michigan, Ann Arbor, MI*); *Aleksey Bolotnikov* (*Brookhaven National Laboratory, Upton, NY*). Cadmium Zinc telluride (CdZnTe or CZT) is a direct band gap semiconductor that has very promising qualities as a material for gamma-ray radiation detectors. Unlike the traditional high purity Germanium detectors, which require cryogenic cooling, CZT devices have yielded high detection efficiency and exceptional energy resolution while operating at ambient temperatures. This makes them particularly appealing for national security applications such as explosives detection. It is known that CZT detector performance is dependent on two common factors: CZT crystal defects (mainly Te inclusions present in the crystal structure) and surface irregularities that may cause polarization or electric field defocusing. Using infrared microscopy (with

magnification up to x10), Te inclusions on the order of micrometers can be identified. X-ray mapping techniques at Brookhaven's National Synchrotron Light Source (NSLS) are utilized to analyze CZT surface irregularities at a maximum resolution of 10 μm steps. To determine CZT detector performance, pulse height spectra and correlation curves are obtained using Cs-137 and Ge-68 sources. Results show that CZT crystals with a low concentration of Te inclusions measuring greater than ~10–20 μm in diameter consistently yielded excellent spectral response (the best detector tested had an energy resolution of ~1.1%). Polarization was not observed in any of the samples; however an aberrant defocusing effect was discovered that diminished detector energy resolution by roughly 25%. The research involved in this project is part of a general effort to correlate CZT detector performance with the material properties of CZT.

Bio-Oil Stability Increase by Minimizing Ash through Pretreatment. *Dustin Bales* (*University of Missouri – Rolla, Rolla, MO*)*; Justinus Satrio* (*Ames Laboratory, Ames, IA*). Bio Oil is created through the fast pyrolysis of biomass process, and can be used for production of commodity chemicals and is being researched as a fuel. Bio-Oil is preferable over biomass as a fuel because it is much more energy dense and easier to transport. Bio-Oil created by fast pyrolysis tends to be unstable in long term storage because the fast pyrolysis process has a short reaction time, which does not allow thermodynamic equilibrium to be reached immediately after production. It has been determined that this is partly due to high alkali ash content. Alkali metals (ash) act as a catalyst in the destabilizing reactions. Hence, alkali reduction causes increased stability. It is hypothesized that certain biomass pretreatments could reduce this alkali content before the sample is pyrolized into bio-oil, specifically boiling water and boiling acid. The objective of this research is to discover what effect these biomass pretreatments have on alkali content. Experiments have been designed to test the ash reduction properties of boiling corn stover for 60 minutes in water and 1%, 2.5%, and 5% phosphoric acid solutions with corn stover biomass feedstock. Samples that have gone through the torrefaction process then the boiling pretreatment will also be used to discover any affect torrefaction has on alkali content. Torrefaction is a low-temperature thermo-chemical pretreatment that breaks down hemi-cellulose in an inert atmosphere and also acts as an excellent drying process. Phosphoric acid is used because of its ability to breakdown hemi-cellulose, hypothetically releasing locked-in alkali and increasing Levoglucosan content. Simple ash analyses of the untreated and treated biomass show a maximum of 52% reduction with 5% phosphoric acid treatment with rinse. Torrified biomass showed a maximum of a 72% ash reduction after a 2.5% acid treatment. Scanning Electron Microscope with Energy Dispersive X-Ray Spectrometry gives a breakdown of the components of biomass ash, char ash, and bio-oil ash. Largest percentages other than oxygen were Silicon, Silicon, and Iron, respectively. Fiber analysis shows a steady decrease in hemi-cellulose with increasing acid concentration. Future work must be done to discover the mechanism by which the Phosphoric Acid removes ash, and to test the pretreated biomass in the actual pyrolysis process.

Design for Increased Functionality of the Hot Cells inside the Radiochemical Engineering Development Center. *Brent Beatty* (*University of Tennessee, Knoxville, TN*); *Jeffrey Binder* (*Oak Ridge National Laboratory, Oak Ridge, TN*). The Radiochemical Engineering Development Center (REDC) has been the United States' main production center for transcurium elements since operations began in 1966. Together with the neighboring High Flux Isotope Reactor (HFIR) these facilities produce transuranium elements for commercial and research purposes. The facilities' technologies and capabilities gained through a vast production history allow for an ideal test bed for Global Nuclear Energy Partnership's (GNEP) Coupled End to End (CETE) demonstration. The purpose of the demonstration is to perform mechanical and chemical processes on actual spent nuclear fuel, which will confirm the projected material flow and performance data and with extensive experimental data. While the specialized support infrastructure for hot cell processing has been in place for forty years, there are still design improvements to the current operational flow necessary to fully accommodate all aspects of the demonstration and to enhance future capabilities of the facility to attract new projects. Many of the cubicles have not been updated in several years and were designed primarily for targets and fuel elements from HFIR. The CETE demonstration will be performed on many different fuel pins and assemblies from many reactor designs. In order to accommodate this larger variety of experimental components, I designed and coordinated fabrication of a new "disconnect well" and the associated "containment thimble" for the remote hot cell welder. These modifications will

double the length of components that may be processed in the hot cell. This design adds functionality and increases the flexibility required to process the diverse fuel components with minimal impact on the safety specifications and operational requirements and uses materials that did not require new certification for use in REDC. Due to the increased load that will be on the "disconnect well" flange, a calculation was made confirming the ability of the new design to support the added load. The increased moment of the assembly required an updated seismic analysis which was performed and documented in the facility handbook. As the world accepts Nuclear Energy, facilities like REDC have an important and unique role in demonstrating and validating new advanced chemical processes. There are many additional updates and improvements that will have to be made similar to the redesigned "disconnect well" discussed here in order to fully modernize this key facility.

Development of a Visualization Program Used in Computational Simulations of Nanomaterials. *Jana Black* (*University of Tennessee, Knoxville, TN*); *Peter Cummings* (*Oak Ridge National Laboratory, Oak Ridge, TN*). Nanoscience offers many scientific opportunities; it also poses significant experimental challenges since it deals with matter in the size range of 1 to 100 nanometers. Theory and simulation are crucial to nanoscience since experimental measurements and observations made at the nanoscale are often impossible to interpret without a theoretical model. Oak Ridge National Laboratory's (ORNL's) Center for Nanophase Materials Sciences (CNMS), in particular the Nanomaterials Theory Institute (NTI), is involved extensively in the development of programs and tools for nanoscale simulations at various time and length scales. NTI maintains a high-performance visualization cluster and 16-node visualization wall in addition to its multi-teraflop computational clusters. The goal of this project is to develop a complex tool that can be used to visualize, at high resolution, the trajectories obtained from various types of molecular modeling such as *ab initio*, molecular dynamics, or Monte Carlo. The specific data used as an example in this study is from molecular dynamics simulations of pulling apart a gold nanowire. My role in the project is to write a program to drive two major visualization packages which are already installed on the NTI visualization clusters, VisIt and Visual Molecular Dynamics (VMD), so that high-resolution animations can be created from the simulation trajectories. VisIt is designed to visualize very large parallel data in the terascale range. VMD is designed to visualize molecular biological systems. Neither program is ideal for this project, but both encourage users to modify the source code and/or write scripts so the program will better meet their needs. In this particular study, it was considered best to run the visualization simultaneously with 16 copies of either VMD or VisIt, one per node, using 16 sets of simulation data collected at various conditions. I have written scripts to synchronize them. The scripts label the atoms according to their instantaneous temperatures and vividly display the evolution of the system. The visualization helps to interpret the physical process of pulling apart a gold nanowire at the molecular level. This project serves as a trial step in the molecular visualization of complex systems using the NTI facilities; it is one step toward the ultimate goal of developing comprehensive simulation and animation tools of various stages at CNMS to interpret/guide experimental efforts.

Performance-Based Brake Testing: A Quantitative Analysis of Brake Wear within the Trucking Industry. *Amanda Blagg* (*Pensacola Christian College, Pensacola, FL*); *Gary Capps* (*Oak Ridge National Laboratory, Oak Ridge, TN*). Little is known about the brake performance of commercial motor vehicles within the United States since the current method of inspection is visual and subjective. However, brake life and wear are of great interest to the transportation community, because faulty brakes are both a primary cause of collisions in the trucking industry and a significant expense to trucking companies. In order to assess brake performance, aftermarket brake drums and shoes will be supplied to four industry partners who maintain fleets of class-8 vehicles. Tankers, dry-box vans, dump trucks, and motor coaches will be tested to provide data for each category of heavy vehicles. Each vehicle will be tested on a performance-based brake tester (PBBT) which has been installed at the Greene County Inspection Station on I-81 in Tennessee. Testing will take place at regular intervals varying from weekly to monthly and will continue over the brake life, which may range anywhere from 8 to 18 months. The PBBT's in-ground roller dynamometers will objectively evaluate braking force of each wheel end. Since this braking force is proportional to vehicle weight, artificial axle loading will provide 80% of the gross axle weight rating through hydraulically-operated hooks. As brake force is also dependent upon air pressure, transducers will be used to measure air pressure available in the brake line. To determine wear over brake life,

---

the thickness of brake pads will also be measured with a caliper and the ovality and eccentricity of brake drums will be measured with a digital indicator before and after the testing period. I wrote the test plan for the experiment, researched equipment used to make initial measurements of eccentricity, and conducted initial tests on the PBBT. The results from this experiment will provide a previously unavailable performance curve for brakes across several industries and will lay groundwork for future studies in which the PBBT may be utilized as a diagnostic tool for faulty brakes.

Development of 40% Energy Saving Home. JACOB BONAR (*University of Tennessee, Knoxville, TN*); JEFFREY E. CHRISTIAN (*Oak Ridge National Laboratory, Oak Ridge, TN*). The demand for energy continues to rise throughout the world. One place that everyone can reduce energy consumption is in their home. This is especially true of new homes built with energy efficiency in mind. The goal of my research is to show that a new home can operate with a total energy savings of 40%. The major areas to look closely at are building tightness, appliances installed in the home, and the proper sizing of the Heating, Ventilation, and Air Conditioning (HVAC) system. I will gather the necessary data to prepare a report for the fifth Zero Energy Home, ZEH5. The report concerning only the top floor of ZEH5 will cover how to build a house that has an energy savings totaling 40%. Included in the report detailing ZEH5 will be my write up describing the HVAC sizing using Manual J 8th Edition analysis, which I will conduct for ZEH5. I will work with Jeff Christian to measure and document the airflow rates in ZEH5 distribution system using a flow hood and the whole house air tightness using a blower door. In addition to these sections, an Energy Gauge packet will also be included in the documentation. One major part of the Energy Gauge packet and associated write up will be a comparison between the ZEH5 and the Building America benchmark home. After looking at the energy consumption for a physical year, ZEH5 consumed a daily average of $0.66/day. This is lower than ZEH1-4 homes that consumed between $0.75-$1.01. Two more homes are in development that will continue the research towards a true Zero Energy Home.

Acoustic Array for Wind Turbine Noise Analysis. CHRISTOPHER BONILHA (*Univeristy of Colorado, Boulder, CO*); IAN TSE (*Cornell University, Ithaca, NY*); PATRICK MORIARTY (*National Renewable Energy Laboratory, Golden, CO*). Locating and characterizing sources of noise from wind turbines can greatly aid in the design and production of quieter, more publicly accepted machines for renewable power generation. An acoustic array is a device comprised of an arrangement of microphones that when coupled with an algorithm, can locate sources of noise. In 2006, The National Renewable Energy Laboratory (NREL) partnered with the University of Colorado at Boulder to construct a prototype acoustic array as a proof of concept. Issues arose in both the original hardware and software components which needed troubleshooting and correction before the capabilities of the array could be determined. Tests showed that erroneous signals being outputted by the array were caused by the original data acquisition (DAQ) hardware's inability to handle the high volume of data samples. A robust, differential-referenced, simultaneous-sampling DAQ was purchased to replace the old DAQ, resolving the data acquisition issues. The low-quality microphones had inconsistent frequency responses that contributed to the erroneous results. It was also determined that the signal-to-noise ratio could be significantly improved with better microphone arrangements and with the doubling of the number of microphones on the array. The beamforming algorithm that computes the sound pressure levels emanating from a given plane of interest was originally written incorrectly and very inefficiently. A new program was written to perform the beamforming algorithm on the recorded audio signals and produce plots to facilitate easier analysis. Simulations were performed to analyze how array parameters contribute to the performance of the array. After hardware upgrades and the software revisions, the array was subjected to a series of simulations and tests to determine its capabilities. The array was unable to detect a monopole sound source roughly 4 meters away. Further tests should be done on an array with more microphones of better quality and also with a source that is both louder and positioned at probable turbine locations.

Electrical Systems Analysis of Off-Site Groundwater Treatment Facilities to Determine Arc Flash Hazard. JOHN BOUCHER (*Middlebury College, Middlebury, VT*); ALAN RAPHAEL (*Brookhaven National Laboratory, Upton, NY*). Before an arc flash accident prompted Brookhaven National Laboratory (BNL) to devise the Arc Flash Analysis Project, a project designed to achieve a complete electrical systems analysis of all BNL systems and buildings, many of BNL's older facilities had not been inspected to determine if they satisfied the National Fire Protection Association's "Standard for

Electrical Safety in the Workplace" (NFPA 70E–2004). The following study examined the electrical systems of BNL's Off-Site Water Treatment Facilities for their compliance with NFPA 70E–2004 and so was only a piece of the comprehensive Arc Flash Analysis Project. Electrical information such as equipment layout, manufacturing, and operating information for all electrical components such as panels, fuses, and circuit breakers, as well as cable sizes, types, and approximate lengths was obtained by manually inspecting and tracing out the water treatment facilities' electrical systems. Using SKM PTW Power Tools Software (PTW), this information was organized, illustrated, and then analyzed to establish the electrical systems' susceptibility to and energy available for arc flash. The work done for this study produced single-line electrical diagrams via PTW containing all electrical equipment down through the lowest rated panels (480 Volt or 208 Volt) to any 3 phase 480 Volt or 3 phase 208 Volt/225 Amp or greater equipment for the facilities. With the supplied information in the single-line diagrams, PTW was used to compute information such as arc flash incident energy level at each equipment location, the flash protection boundary, and the recommended Personal Protective Equipment (PPE) at these locations. This study sought to achieve greater safety for those working on the concerned electrical systems by providing recommendations for necessary PPE for electrical workers, collecting data to be archived, managed, updated as necessary, and made accessible to facility engineers for future electrical work, and affixing up-to-date arc flash warning labels to all appropriate electrical equipment.

A Comparison between Sludge Sedimentation Rates and Dispersion Characteristics of No. 2 Oil and Biodiesel. CHRISTOPHER BROWN (*Clarkson University, Potsdam, NY*); THOMAS BUTCHER (*Brookhaven National Laboratory, Upton, NY*). Biodiesel made to American Society for Testing and Material (ASTM) standards, D6751, is a renewable fuel source that within the fuel industry is criticized as being a solvent. When blended with petroleum-based fuels in tanks with contaminants such as carbon deposits, the Fatty Acid Methyl Esters (FAME or biodiesel) are accused of introducing contaminants into solution with the fuel. This leads to filter plugging and fuel starved equipment. In order to attain a greater knowledge of the fuel solvency characteristics of biodiesel, data was collected from testing sedimentation rates, particle size and particle distribution. To test sedimentation rates, clean fuel samples of biodiesel and No. 2 oil were thoroughly mixed with sludge (carbon deposits from No. 2 oil tank bottoms). After being uniformly mixed, each fuel sample was allowed to settle for set time intervals, and then centrifuged. To measure particle size and distribution a laser based optical probe measured the chord length of particles and distribution of particles in solution. When reviewing the sludge particle sedimentation rates, it was evident that the particles required a greater period of time to settle out of the biodiesel fuel sample compared to the No. 2 fuel oil sample. Furthermore, although the settling rate is longer for biodiesel, the same amount of sediment precipitated from the fuel. When analyzing the results from the laser based optical probe, the particle chord length and particle distribution was identical when comparing biodiesel to No. 2 fuel oil. The results that have been gathered imply a significant breakthrough on the industries diagnosis of biodiesel's solvency. The data suggests that biodiesel has the same solvency characteristics as No. 2 fuel oil and that biodiesel is a better dispersant. Biodiesel disperses the sediment particles in the fuel and suspends them longer than No. 2 fuel oil, allowing the contaminants a greater amount of time to be carried to the fuel filter. This finding will allow any necessary changes to be made to in-line fuel filtration.

Electromagnetic Interference from the ILC Beams. LAVONDA BROWN (*Norfolk State University, Norfolk, VA*); GARY BOWER (*Stanford Linear Accelerator Center, Stanford, CA*). Electromagnetic interference is an emerging problem of the future. This investigation analyzed the data collected from airborne radiation waves that caused electronic devices to fail. This investigation was set up at SLAC in End Station A and the data collected from the electromagnetic waves were received from antennas. In order to calibrate the antennas it required a signal generator to transmit the signals to the antenna and a digital oscilloscope to receive the radiation waves from the other antenna. The signal generator that was used was only able to generate signals between 1.00 and 1.45 GHz; therefore, the calibrations were not able to be completed. Instead, excel was used to create a curve fitting for the attenuation factors that were already factory calibrated. The function from the curve fitting was then used to extend the calibrations on the biconical and yagi antennas. A fast Fourier Transform was then run in Matlab on the radiation waves received by the oscilloscope; in addition, the attenuation factors were calculated into the program to show the

actual amplitudes of these radiation waves. For future research, the antennas will be manually calibrated and the results will be reanalyzed.

In Situ Measurement of Stresses in Carburized Gears via Neutron Diffraction. *JEFFREY BUNN* (*University of Tennessee at Martin, Martin, TN*); *CAMDEN HUBBARD* (*Oak Ridge National Laboratory, Oak Ridge, TN*). Carburized gears are characterized by a very hard outer layer that contains chemistry, phase, and microstructure gradients. X-rays have been used in the past to attain measurements of residual stresses, but X-ray diffraction is limited to near surface stress measurements due to attenuation. X-ray diffraction also has difficulty reaching the critical stress regions of a gear tooth due to beam interference from the complex geometry. This research seeks to develop experimental methods for measuring the stresses/strains in carburized gears at locations unattainable by X-rays and to do this as a function of applied load on the gear tooth. Experiments are being performed to determine if neutron diffraction can be used as an alternative to X-ray diffraction to measure the total stresses. Total stresses consist of both the residual stresses imparted during the carburization process and the load induced stresses resulting from power transmission. The experiments are being performed at the Neutron Residual Stress mapping Facility (NRSF2) at the High Flux Isotope Reactor (HFIR). In neutron diffraction, a powder sample is normally used to determine the unstressed lattice spacing or d_0. In carburized components, d_0 can not be determined from a single powdered sample because of the non-homogeneous material in the carburized region. As an alternative to using a powder sample, a method commonly used in X-ray diffraction known as the $\sin^2\psi$ method is being studied to determine if it can be used with neutron diffraction to accurately quantify d_0 in the carburized region. If successful, the $\sin^2\psi$ method will be used to determine d_0 at a number of points in the carburized region. Neutron diffraction methods will then be used to measure the d-space at each of the points for which d_0 was determined. The combination of d-space and d_0 at each point will enable the strains and stresses to be determined at the measurement points. The measurement of the d-space in a loaded gear is being facilitated with a Static Load Application Device (SLAD). This device was designed to statically load the gears as well as be compatible with the equipment at NRSF2. Stress analysis was done on the SLAD to ensure that the device would not exceed strength values found in engineering design standards.

Leak Detection Device. *ELISABETH BYRD* (*Georgia Institute of Technology, Atlanta, GA*); *DAVE LOUSTEAU* (*Oak Ridge National Laboratory, Oak Ridge, TN*). When mercury is sensed between the mercury vessel and water shroud in the Spallation Neutron Source target, a leak exists and the target has to be removed from operation. To improve future targets, the front of the target is examined to determine the cause and location of the leak. Most likely, a leak will be visible, but if not, a leak detection device needs to be available. My work was to model and design a leak detection device that would enable the inside of the target to be pressurized while coated with a chemical that will bubble when the air seeps through the cracks, revealing the location of the leak. I was first given an assembly that included a table with a simulated flange serving as the top, which would hold the target. The assembly also included a lid that is placed on the top of the target to seal it. The entire leak detection device will be radioactive after use; therefore, one goal is to minimize the amount of material when designing the assembly. There is a boot already in the hot cell, which was made to provide shielding for the front end of the target when it is being removed. I used this boot instead of the table so that no waste would be created and nothing new would have to be designed or manufactured with the exception of a part connecting the flange to the boot. This new part was designed to accommodate the racetrack shape on the top of the boot and the circular shape of the flange. The initial adapting part model used a blend from the racetrack shape to the circular top. Unfortunately, this direct approach would be both difficult and expensive to manufacture. I then modeled a more manufacturing friendly part using the racetrack shape as the dominant feature and then attached wings on the top to accommodate the circular flange. This way, the manufacturer could use sheet metal to form the racetrack shape and then weld a piece of sheet metal to the top, which would form the wings. The stress on the part was calculated using the finite element analysis tool, Mechanica. Mechanica indicated that it can withstand loads much greater than the 900-pound force that will be applied from the weight of the target and seal assembly. In addition to learning a new modeling program, this challenge taught me to include from the outset design concerns for manufacturing, robot assembly, and end waste management.

Surveying and Mapping for a Localized GIS. *INDIA CALHOUN* (*Savannah State University, Savannah, GA*); *BRIAN FUSS* (*Stanford Linear Accelerator Center, Stanford, CA*). The Alignment Engineering Group (AEG) is responsible for an extensive array of alignment and positioning activities at the Stanford Linear Accelerator Center (SLAC). In particular, the location of accelerator components using specialized tools and data adjustment procedures are the center mission(s) of the group. My established goals for this project are to accurately measure a set of buildings known as Forte Apache to produce a 3-dimensional CAD drawing that will be used to create a 2-dimensional Geographic Information Systems (GIS). Computer Aided Design (CAD) is the use of a wide range of computer-based tools that assist engineers, architects and other design professionals in their design activities [5]. Overall, in the project, I will construct a 2-dimensional GIS that can be used to analyze relationships between features.

Assessment of a Residential Style Oil-Fired Boiler as a Host for a Thermophotovoltaic Combined Heat and Power System. *JULIAN CARPENTER* (*Alfred State College, Alfred, NY*); *Thomas Butcher* (*Brookhaven National Laboratory, Upton, NY*). Combustion of number 2 heating oil is intrinsically emissive, more so than natural gas, propane or butane. Therefore, oil combustion is a good candidate for power generation using thermophotovoltaic (TPV) cells. In order to test the viability of current residential oil heat technology as a host for TPV combined heat and power generation (CHP), a prototype oil fired TPV CHP system must be built, tested, and characterized. Previous work has shown potential for sufficient power densities using a small 1 cm^2 GaSb TPV array with a residential boiler, however, the effects of the much larger array (99 cm^2) on achievable power density, and the effects of system geometry, firing rate, combustion conditions and the use of silicon carbide (SiC) emitters is not known. One small and one large (99 cm^2) GaSb TPV arrays were tested with various configurations in a modified residential style boiler capable of firing at 0.5 to 0.85 gallon per hour (gph). The use of a reticulated SiC emitter as well as the effect of firing conditions, burner output, and system geometry were varied and measurements of short circuit current (Isc) and open circuit voltage (Voc) were taken to measure power output. It was determined that a large pore SiC foam emitter improved power output, although the pressure drop across the foam plate was problematic. Varying the distance from cell to emitter, the size of the cell, boiler combustion chamber insulation, amount of excess air, and firing rate were found to substantially impact the power output of the TPV cell. Power densities of approximately 1.3 W/cm^2 were achieved with the single cell array, and 0.85 W/cm^2 with the 99 cell array. Future work should investigate ways to boost power output to over 2 W/cm^2, in an effort to provide more than enough power for a stand-alone oil fired boiler TPV CHP system.

Use of RF and Digital Signal Processing for Beam Position Monitoring. *SARA CARR* (*Rochester Institute of Technology, Rochester, NY*); *JOHN MUSSON* (*Thomas Jefferson National Accelerator Facility, Newport News, VA*). A Beam Position Monitor (BPM) is a useful device because it accurately detects the location of an electron beam at very low current. A BPM coupled with a Beam Current Monitor (BCM), located in Hall A of the Continuous Electron Beam Accelerator Facility (CEBAF), originates the analog signal on three channels: an X-position, a Y-position, and a current channel. The BPM detects the output voltage proportional to the product of current and position, while the BCM detects the voltage proportional to current. It was believed that the quotient of the two signals would result in the position of the beam. The purpose of this project was to attain a good resolution by optimizing signal-to-noise ratio; this was accomplished by limiting the bandwidth of the noise. With the use of RF signaling and digital filtering, the bandwidth was configured using a Field Programmable Gate Array (FPGA), a small integrated microprocessor. Using Altera Analog Hardware Description Language (AHDL) a coded block diagram of digital logic was programmed onto the chip. Once the bandwidth was limited to the desired frequency, the current channel was divided into the X-position channel resulting in the beam's position on that plane. It was shown that a low current run of 50 nA could be detected with 100 μm of resolution by limiting the bandwidth to 5 kHz. This was accomplished with a series of digital filters that were able to cut the frequency with a method called decimation. In order to detect different magnitudes of current, there was a second filtering path with a bandwidth of 100 kHz, that measured current runs up to 40 μA. The design of the system can easily be tailored to the needs of Users by implementing different firmware to the FPGA, which is both time and cost effective.

Oxidation Characterization and Resistance of Nb-Cr-W Super Alloys at Elevated Temperatures. *Daniel Castro* (*University of Texas at El Paso, El Paso, TX*); *Ken Natesan* (*Argonne National Laboratory, Argonne, IL*). The importance of turbine engines in aerospace and energy sectors of industry has lead to the research of high temperature low oxidation super alloys for turbine engine component fabrication. An interest in niobium based super alloys has developed because of its high service temperature capability and oxidation resistance when alloyed with chromium and tungsten. The goal of this project is to evaluate Niobium based super alloys when exposed to high temperatures. Samples from two separate alloy compositions were oxidized at temperatures ranging from 700°C–1,400°C. The characterization of the oxide layers of the samples was critical due to little or no research performed on the oxide scale of Nb-Cr-W super alloys. It was thought that the primary oxide formed on this alloy after high temperature exposure was Nb_2O_4, however, Nb_2O_4 carries a distinct geometrical shape (spherical and cylindrical) but oxides of a different geometry and chemical composition were identified. By using a JOEL JSM-6400 Scanning Electron Microscope (SEM) and Energy Dispersive X-ray Spectroscopy (EDS), the oxides on the alloys were characterized as being chromium rich as opposed to niobium rich (Nb_2O_4) in previous alloys with less chromium in the initial chemical composition. The identified oxide layer has never been seen previously and carries no distinct geometrical form, rather, it has a scale type of appearance. The oxide layer appears only at the surface of the metal samples because these are the only areas exposed to oxygen during heat treatment. With an increase in exposure temperature, the oxide becomes more pronounced under the SEM and the oxide layer penetrates deeper into the sample thus reacting with more chromium in the metal. In the resolve of this research, identifying a new oxide formation and mechanism has affirmed the need for more oxidation research in Nb-Cr-W alloys. Future study on the chromium rich oxide layer and its mechanical properties will determine the feasibility of the Nb-Cr-W super alloys in turbine engine components.

Sampling and Analysis Methods for Microbial Fuel Cells. *Scott Cesar* (*Western Michigan University, Kalamazoo, MI*); *Abhijeet Borole* (*Oak Ridge National Laboratory, Oak Ridge, TN*). Microbial Fuel Cells (MFC's) are devices which use micro-organisms as catalysts to oxidize compounds such as glucose whereby electrons are released and are allowed to flow between electrodes developing a potential difference from which usable power may be drawn. MFC's are quite simple when viewed yet quite complex when analyzed. Many factors need to be steadily sampled and analyzed to determine different parameters within the system. Direct monitoring of system electrical characteristics with a voltmeter gives open circuit voltage (OCV) and current output at a given load. A variable-load resistor was employed to obtain a power density curve in which overall power of the system was determined. The most recent method involves electrode cycling to obtain higher output of the total system. Along with electrical measurements, samples of anode and cathode solutions are taken to determine the performance of the MFC's. Spectroscopy was used to derive optical density measurements for determining cell concentrations and also for determining differing iron concentrations in solution. The solution pH was also monitored for biological stabilization. High Pressure Liquid Chromatography (HPLC) was used for glucose and organic acids analysis. The results have shown that a mediator was required for conduction of electrons from the microbes to the electrode surface under the conditions tested. Iron was used as a mediator, since it is cheaply available. From iron analysis, it was found that iron (III) is electro-sorped on the electrode surface after electron donation. Electrode cycling was used to maximize power output under these conditions. Further work to facilitate increased rate of iron desorption is needed to enable stable power output.

Evaluation and Recommendation of Advanced Laser Power and Laser Energy Meters for Potential Acquisition. *Timothy Cheers* (*Southwest Tennessee Community College, Memphis, TN*); *Mark Ludwig* (*Lawrence Livermore National Laboratory, Livermore, CA*). Lasers are powerful research tools but pose significant safety issues if not monitored and controlled appropriately. The ever evolving world of technology has developed smaller, more advanced meters used to monitor power-energy emissions from lasers. These devices are called laser power and laser energy meters. The Hazards Control Department (HCD) uses power and energy meters to verify output of lasers, reclassify lasers as needed, and conduct accident investigations should one occur. Due to their safety applications, the HCD power-energy meters are calibrated to National Institute of Science and Technology standards and are an integral component of Lawrence Livermore National Laboratory's (LLNL) laser safety program. LLNL HCD has not updated these meters for many years. The purchase of updated equipment would enhance HCD's capability and efficiency in supporting LLNL laser users in the performance of critical laser measurements. The newer more advanced power-energy meters were researched and companies solicited for loaner units. A test plan and meter rating spreadsheet tool was developed for evaluating the instruments based on their capability to meet LLNL laser system performance needs (e.g., maximum power-energy levels, total range, pulse width, and laser repetition rate). The usability factors as determined by the researchers, compatibility with LLNL data transfer devices, cost, maintenance and calibration requirements, performance history at other facilities, etc. were taken into account. Three companies arranged to loan units for LLNL's evaluation. Limited testing with researchers was completed on the units received. Based on the rating results and budget constraints, a single laser power and energy meter was selected. Using this rating spreadsheet, selecting the most suitable meter has become a more efficient and valid process, which will be useful for future meter evaluations. This work was performed under the auspices of the U.S. Department of Energy by University of California, Lawrence Livermore National Laboratory under Contract W-7405-Eng-48.

Effective Queue Distributions in Video Streaming: A User Perspective. *R. Benjamin Clay* (*Virginia Tech, Blacksburg, VA*); *Sami Ayyorgun* (*Los Alamos National Laboratory, Los Alamos, NM*). Queuing theory and buffer control are areas of great interest as networks become large and unmanageable. Specifically, guaranteeing a quality of service (QoS) in a large, uncontrolled network such as the internet is important from both a business perspective (selling a service at a specified QoS) and a user perspective. In order to ensure that data reaches the intended target at the intended rate, stochastic rate control algorithms can be used to guarantee a service within a given probability. To this end, previous work has determined and elaborated upon mathematical methods to achieve optimum buffer control given a generic packet-based data source. Our work extends these algorithms to streaming video, using subjective analysis to determine the appropriate equations and values to make the rate control transparent to the end user. To do so, a server-client implementation has been built on top of the popular opensource video player (VLC). The rate control algorithms specified in previous work are built as the core of the server application, modifying VLC's User Datagram Protocol (UDP) streaming server component. The client is another copy of VLC, operating as a UDP streaming client. Preliminary results indicate correlation between decay rate and video quality for those distributions that employ a decay rate.

Friction Factors Appropriate to the Application of Ultra-Filtration to Radioactive Waste. *Adriana Contreras, Marc Stevens* (*Nicholls State University, Thibodaux, LA*); *Reid Peterson* (*Pacific Northwest National Laboratory, Richland,WA*). The U.S. Department of Energy's Hanford Site was developed during World War II to produce weapons-grade plutonium. This and other activities resulted in 60,000 metric tons of waste stored in 177 underground storage tanks (UST). Some of these USTs have leaked into the subsurface. Because of this and other environmental concerns, DOE and Bechtel National, Inc. (BNI) are designing a Waste Treatment and Immobilization Plant (WTP) to treat the radioactive waste. A critical element of the WTP is an ultra-filtration process (UFP) that separates the radioactive slurry into high-level waste (HLW) and low-activity waste (LAW) forms. However, the productivity of the UFP in terms of HLW and LAW is in question and one approach to addressing production maximization is to understand the conditions to maximize permeate rates. This is predicated on understanding the relationship between axial velocity and pressure drop, which is the subject of this research. There are several approaches to modeling v versus Δp. For example, researchers at Savannah River National Laboratory compared the Blasius model to experimental data collected from the Filtration Research Engineering Demonstration apparatus. They observed that the Blasius model under-predicted the data. Our approach is to use the Darcy-Weisbach equation, which includes a friction factor that has been determined using Prandtl's Mixing-Length Theory. The friction factor is a function of Reynold's number (Re) and a parametrically defined coefficient B. This B coefficient is possibly a function of several non-dimensional numbers. The results show that the appropriate model for B is a function of Cp (coefficient of pressure) and length divided by diameter. Our results also show that one model works well for a particular apparatus when treating diluted slurries, but it is not as effective when applied to more prototypical slurries. Different models are developed for more prototypical slurries on the 07 Cell Unit Filtration Systems for low and high solids, which may be an influence of the fluids behavior from Newtonian to non-Newtonian. Through our understanding of this basic science, a better knowledge base will be formed to assess the productivity of the UFP, which helps the Pacific

Northwest National Laboratory's goal to give research and development support to DOE and BNI.

Optical Detection Techniques of Solid and Liquid Explosives. *Christopher D'Ambrose* (*Cooper Union, New York, NY*); *Biays Bowerman* (*Brookhaven National Laboratory, Upton, N*Y). Explosives present a current threat for both soldiers and civilians. Therefore, it is necessary to possess the ability to detect both solid and liquid explosives. It is also important to be able to detect the explosives from a safe distance in order to minimize the risk of injury or even death. This research paper focuses on the standoff detection of explosive materials by using optical techniques, such as some of the various methods of Raman spectroscopy and light detection and ranging (LIDAR). Raman involves excitation of a sample with a laser and subsequent measurement of scattered radiation that is dependent on vibrational states of the molecules of interest. LIDAR requires a light source that transmits radiation to a target and then measures the time difference of backscattered radiation in order to identify the location of the substance. Variations of the LIDAR technique can be used for chemical identification. The Internet provided some of the literature for the research on this topic. The types of websites that were used include science websites, government websites, military websites, and online news articles. Also, companies that design and sell explosive detection devices supplied the specifications of various products that are commercially available. Books from the Research Library at Brookhaven National Laboratory provided technological descriptions of Raman spectroscopy and LIDAR. Scientific journals contributed valuable information on the use of Raman spectroscopy and LIDAR for explosive detection. This research paper is a collection of useful information about explosive detection in order to make this topic easier to understand and quicker to learn about. The main purpose of this research was to explain the advantages and disadvantages of both Raman spectroscopy and LIDAR in the area of standoff explosive detection. Therefore, the reader is able to analyze the possibility of the future development and the field deployment of these detection techniques.

Ensuring Co-planarity of Tiled Optical Surfaces. *Michael Dawson-Haggerty* (*Tufts University, Medford, MA*); *Paul O'Connor* (*Brookhaven National Laboratory, Upton, NY*). The Large Synoptic Survey Telescope (LSST) is designed to have an extremely large field of view, 9.62 square degrees, nearly 50 times the area of the full moon. The digital camera used to record the images provided by such a large field needs to be enormous. The focal plane of the camera is a circular area 60 cm in diameter, covered in a tiled surface of 4 cm square CCD imaging chips, which provide the digital image for analysis. Although the area is large, the tiled sensors need to be coplanar to within plus or minus five microns, as the light is converging on a very specific, precise point. To do this, the tiles are grouped into 3x3 arrays called 'rafts' which can be constructed individually. The rafts are scanned with a laser confocal displacement meter mounted onto an x-y gantry system. The displacement meter is scanned over the raft surface, and a 3D model can be made of the raft. Tilt and vertical displacement of each CCD can be assessed, and extremely thin foil shims of known thickness can be inserted to compensate. The scan is repeated until all silicon sensor surfaces are within tolerances. This allows the effectiveness of thin-foil spacers to be assessed, as well as the overall feasibility of the precision requirements for the tiled surface, a greater precision then has been attempted previously. This work is a small portion of a much larger project being researched to develop the LSST optical and mechanical systems, and once completed will play a large part in ensuring a clear and focused image.

Hexapod as a Goniometer System. *Michael Dibiccari* (*Rensselaer Polytechnic Institute, Troy, NY*); *Elaine Dimasi* (*Brookhaven National Laboratory, Upton, NY*). A hexapod is a device consisting of two platforms conjoined by six diagonal legs of variable length. By changing the lengths of these legs, it is possible for the upper platform to experience independent or simultaneous translation in any of three dimensions, as well as independent or simultaneous changes in roll, pitch, or yaw. A hexapod mounted atop a rotation stage can be a viable replacement for the three or four ring goniometer systems being used for small angle X-Ray scattering experiments at the National Synchrotron Light Source (NSLS) at Brookhaven National Laboratory (BNL). For this project, these legs consist of ultra-high-vacuum (UHV) rated piezoelectric nanostepping linear motors, which are monitored by optical encoders. The hexapod system in this project is mounted to a rotation stage which is also manipulated by UHV rated piezoelectric nanostepping motors. The manufacturer of this hexapod claims up to 5nm precision for the motors, 50nm precision for its upper platform, a 28mm linear working envelope, pitch yaw and roll range of ±18°, and maximum Z stroke of 55mm. This hexapod system manipulates roll, pitch, and yaw similarly to an eulerian cradle, where axes of rotation for successive rotations are carried on in an enforced order of rotations. In this way, rotation commands sent to this hexapod commute; the order in which they are issued does not effect the resulting position of the sample stage on the top platform. This hexapod system is controlled as a socket device through Certified Scientific Software's SPEC X-Ray Diffractometer software interface. This interface is currently used to control other devices at the NSLS at BNL including the four-ring euler cradle this hexapod system is being designed to replace. The hexapod and rotation stage goniometer system is to be implemented in the beamline X9 of Brookhaven National Laboratory's NSLS. This system is also very promising for the upcoming NSLS-II. Because the NSLS-II beam cross-section is very small, great care must be taken to assure that the sample does not shift out of the beam path during the experiment. A hexapod system such as this has rarely been used as a goniometer system, and should allow for increased precision over the three or four ring goniometer system currently in use for small angle X-Ray scattering experiments.

Characterization of a Mobile Oscillatory Fatigue Operator for Wind Turbine Blade Testing. *Pearl Donohoo* (*Franklin W. Olin College of Engineering, Needham, MA*); *Jason Cotrell* (*National Renewable Energy Laboratory, Golden, CO*). Laboratory testing of wind turbine blades is required to meet wind turbine design standards, reduce machine cost, and reduce the technical and financial risk of deploying mass-produced wind turbine models. Fatigue testing at the National Wind Technology Center (NWTC) is currently conducted using Universal Resonance Excitation (UREX) technology. In a UREX test, the blade is mounted to a rigid stand and hydraulic exciters mounted to the blade are used to excite the blade to its resonant frequency. A drawback to UREX technology is that mounting hydraulic systems to the blade is difficult and requires a relatively long set-up period. The author has analyzed an alternative testing technology called the Mobile Oscillatory Fatigue Operator (MOFO). The MOFO uses an oscillating blade test-stand rather than a rigid stand, avoiding the need to place hydraulic systems on the blade. The MOFO will be demonstrated by converting an existing test-stand at the NWTC to an oscillating stand that can test blades up to 25 m in length. To obtain the loads necessary to design the MOFO, the system motion is modeled using rigid body and lumped mass dynamics models. Preliminary modeling indicates the existing stand can be converted to a MOFO relatively easily. However, the blade dynamic models suggest that blade bending moment distributions are significantly different for UREX and MOFO testing. More sophisticated models are required to assess the implication of this difference on the accuracy of the test.

Four-Cylinder, 22L Direct-Injection, Omnivorous Engine Project. *Emily Dringenberg* (*Kansas State University, Manhattan, KS*)*; Steve Ciatti* (*Argonne National Laboratory, Argonne, IL*). Concerns associated with petroleum dependency, increasingly stringent emission standards, and the effect of personal transportation on our environment demand that researchers explore the capabilities of renewable energy sources. Ethanol is a fuel of primary investigation; it is being looked to as a promising step toward energy independence. Related research is being done in the Transportation Technology R&D Center at Argonne National Laboratory where researchers are using an Opel 2.2L EcoTec Engine (GM L850) to study variable ethanol-gasoline fuel blends and their effect on engine performance, efficiency, and emissions. The in-line 4-cylinder GM engine is designed to run on gasoline fuel. It has not been altered to run using ethanol fuel, but the cylinder head has been modified to include a pressure transducer for each cylinder. The pressure transducers directly measure the pressure in each combustion chamber. Heat release analysis, which characterizes combustion behavior, can be derived from these pressure measurements. Additional sensors measure other engine variables, such as temperatures, pressures, and flow rates. A Horiba MEXA-7100D emissions bench is being used to analyze the engine-out emissions. Preliminary data relating to engine performance, efficiency, and emissions for gasoline, E10 (10% ethanol and 90% gasoline by volume), and E20 have been collected, and data for E50 and E85 will follow. From this preliminary information, general trends regarding fuel consumption, engine efficiency, and emissions were observed. With increased amounts of ethanol, improved engine efficiency and a reduction in mid-load emissions were observed. Using this information as a baseline, researchers hope to continue research to find an optimized configuration for different fuel blends.

Heavy Truck Duty Cycle Data Collection. *Fiona Dunne* (*University of California – Santa Barbara, Santa Barbara, CA*)*; Gary Capps* (*Oak Ridge National Laboratory, Oak Ridge, TN*). Real-world data on Class-8 truck operation is necessary for fuel efficiency studies as well as for use in vehicle powertrain design software. To gather this data, six Class-8 trucks were instrumented with a data acquisition system (DAS) and a set of sensors to monitor numerous vehicle performance parameters from engine to tires, as well as weather conditions, road slope, and load weight over a one year period. First, the truck's J1939 vehicle network was tested to learn what vehicle performance information was available on it, and how to retrieve the data of interest. The other sensors and DAS were then installed on each truck, and all data was recorded to the DAS as the trucks then continued in regular operation. During operation, data was checked weekly for errors to determine whether the equipment was functioning correctly. By checking the data, it was discovered that weather sensors began failing from water entry due to unexpected pressure washing of the trucks. Load weight data was found to be inaccurate, as truck drivers had not correctly calibrated the weighing system. Road slope and vehicle network data results were as expected. It was concluded that weather sensors should be covered during pressure washing, and an alternative method for calibrating the weighing system was devised. It was also concluded that the method used to obtain road slope, a derivation from GPS vertical and ground velocity data, was adequate. Finally, it was determined that no changes needed to be made in the method of communication with the vehicle network. Data will continue to be checked for errors throughout the remainder of the one year test, and changes will be made as necessary.

Determining the Ability to Monitor the Viability of Transplant Rat Glioma Cells with an Optically Enhanced Catheter. *Rachel Dyer* (*St. Olaf College, Northfieldm, MN*)*; Boyd M. Evans III* (*Oak Ridge National Laboratory, Oak Ridge, TN*). Approximately fifty thousand cases of Parkinson's Disease are diagnosed within the United States each year. This debilitating disease results from the dissolution of dopamine-dependent communication between the substantia nigra and the striatum of the brain. Cellular replacement therapy, in which stem cells are introduced to supplant dead or stressed cells, has shown promise in animal models. However, the viability of transplanted cells and their survival rate is poorly accounted for by early tests. A novel design coupling a surgical catheter with fiber optic technology provides a tissue delivery platform that can monitor cell viability with sensing techniques widely accepted in the medical industry. The goal of this work is to monitor the health of transplant cells in real time at the final point of delivery using the optically enhanced catheter. Rat glioma cells were separately labeled with CellTracker Orange (CTO) (Invitrogen) and JC1 stain from BioVision's MitoCapture Mitochondrial Apoptosis Detection Kit and fluorescence was characterized by confocal microscopy. CTO exhibited a single emission peak at 570 nm upon excitation with a 488 nm argon laser. JC1 exhibited two emission peaks corresponding to fluorescence of viable cells and apoptotic cells, 595 and 540 nm respectively. JC1 was used to monitor the viability of cells under apoptotic conditions induced by incubating JC1-labeled cells with carbonyl cyanide 3-chlorophenylhydrazone or etoposide. Observation of fluorescence using a mercury fluorescence microscope over a four hour period demonstrated JC1's ability to shift in color to reflect cell viability. To detect cell movement through the catheter, cells were labeled with CTO, excited by an argon ion laser with a 501 nm wavelength and a peak emission at 570 nm was detected by an Ocean Optics spectrometer. JC1 was also used to detect the movement and the viability of cells through the catheter. Cells excited by an argon ion laser with a 488 nm wavelength exhibited emission peaks at 540 and 595 nm, demonstrating the ability to detect both viable and apoptotic cells at the final point of delivery. From the detection of rat glioma cells labeled with CTO and JC1 using the diagnostic catheter, and the characterized response of JC1-labeled cells to apoptotic conditions, it can be concluded that these fluorescent probes are suitable for tracking and monitoring the viability of transplant cells through the optically enhanced catheter.

Superconducting Magnets. *Aly Elayat* (*University of Illinois, Urbana, IL*)*; Juan Lizarazo* (*Lawrence Berkeley National Laboratory, Berkley, CA*). Supercon is a research group that deals with the fabrication of superconducting magnets. One of the goals of the group is to upgrade the Data Acquisition System (DAQ) to increase flexibility for the user and get more precise results while testing. The DAQ includes the Strain Gage System which is used to examine fluctuation in temperature and pressure that occur while testing the magnet. Several voltage taps are located on the coils which monitor the voltage drop across a certain resistance that helps us identify such fluctuations.

Keeping the fluctuations at a minimum is an ideal goal of the group. Supercon was looking to build a switch box that enables the user to supply current to numerous strain gages located on a magnet. I had to design this switch box to be user friendly, cost-effective, and meet all specification needed. The design provides the flexibility that allows the user to use up to 12 current sources to supply power to multiple daisy chained strain gages. This flexibility allowes more precise results while testing. Researches can now supply current to specific strain gages located on the magnet to measure their fluctuations in temperature and pressure.

*An Assessment of the Implications of 10CFR851 on the Vacuum Systems at the National Synchrotron Light Source. *Michael Espinoza* (*State University of New York at Stony Brook, Stony Brook, NY*); *Ed Haas* (*Brookhaven National Laboratory, Upton, NY*). As of February 9, 2007, the U.S. Department of Energy required that its facilities are compliant with Section 10 of the Code of Federal Regulations, part 851 (10CFR851). One of the new rules is the requirement to treat vacuum vessels as pressure vessels due to their susceptibility to backfill pressurization. The consequence of treating vacuum vessel as pressure vessels is that they must potentially comply with the American Society of Mechanical Engineers (ASME) Boiler and Pressure Vessel (B&PV) Codes which formerly were not used for vacuum systems, specifically Section VIII of the B&PV code. At the National Synchrotron Light Source, electrons circulating in the accelerators produce photons in the beam lines for research. The electrons and photons are contained within vacuum chambers and beam pipes. Most beam line segments having sources of pressure, such as water or a gas, and were inspected to see if added safety devices were needed. If needed, ASME-compliant safety devices shall be identified, sized, and located according to ASME code. All of these codes are divided into smaller sub-sections, in which only some are applicable to vacuum systems. These codes require safety pressure relief devices on vessels where over-pressurization could result in a failure mode. After developing and programming the necessary equations using Excel spreadsheets, a study of each beam line was undertaken. Of highest concern were pressure sources that penetrated into the vacuum space within components such as monochromators, slits, and beryllium windows. Cooling water sources connected to make-up water, nitrogen, helium, and process gas sources were examined and the pressure and flow information was calculated. Each isolatable section with a potential pressure source required a pressure relief device. Within each segment, the weakest component was generally identified. Glass view ports and beryllium windows for example were usually the components which would be expected to fail at the lowest internal pressure. The spreadsheet calculated the pressure relief requirements and output graphs of flow rate and pressure verses time. This effort assures that NSLS is compliant with 10CFR851 and its vacuum systems are safe.

Effects of Humidity in Inlet Air on a Proton Exchange Membrane (PEM) Fuel Cell. *Andrew Fasano* (*Farmingdale State College, Farmingdale, NY*)*; Devinder Mahajan* (*Brookhaven National Laboratory, Upton, NY*). Air humidification plays a crucial role in the performance of polymer electrolyte membrane (PEM) fuel cells. The present study aims to determine the effect of relative humidity on the cathode side that will produce optimal fuel cell performance at various power levels. Usually, increasing air humidity improves fuel cell performance until it reaches an optimal operating condition. If humidity continues to increase beyond this point, the fuel cell experiences flooding due to the isolation of the catalyst surface from the reactant gases which causes considerable power degradation of the fuel cell. The recorded data shows that air humidification at relatively low temperature levels tends to hinder the cell performance due to its saturation with water. When current levels are increased, an increase in inlet air humidity causes the cell to initially drop in performance due to a certain degree of catalyst flooding at low temperature. However, as the cell begins to increase in temperature, the humidification of inlet air results in a slight recovery of power in the cell output. In conclusion, at room and low temperatures humidification of the inlet air to the PEM fuel cell exhibits a negative effect on the cell power output due to partial flooding. But as the fuel cell continued to operate, the temperature increased that allowed the initial flooding to subside and power escalation was observed.

Effect of Chemistry on the Life and Performance of High-Power Lithium-Ion Cells. *Magdalena Furczon* (*University of Illinois at Chicago, Chicago, IL*)*; Daniel Abraham* (*Ames Laboratory, Ames, IA*). High-power battery technology is key to the commercial success of hybrid electric vehicles (HEVs). These vehicles combine the advantages of the extended driving range and rapid refuelling capability

of a conventional vehicle with the increased fuel economy and reduced exhaust gases of an electric vehicle. The relatively high specific-energy and specific-power characteristics of rechargeable lithium-ion batteries make them an attractive alternative to the nickel metal-hydride batteries used in hybrid vehicles currently in the market. The goal of this project is to determine the suitability of various electrode-electrolyte combinations for HEV applications. The cells typically contain a layered oxide-based positive electrode, a graphite-based negative electrode, and an electrolyte containing an organic solvent and lithium-bearing salts (such as $LiPF_6$). Project activities to date have involved investigation of the effect of alternative salts, such as $LiF_2B(C_2O_4)$ and $LiB(C_2O_4)_2$, on cell cycling performance. Experiments were conducted on ~2 mAh coin cells and on ~35 mAh cells containing a lithium-tin reference electrode. The cells were electrochemically cycled or subjected to above-ambient temperatures (up to 55°C). Capacity and impedance measurements were made periodically to determine the deterioration of cell performance with age. Initial data indicate that cells containing the $LiF_2B(C_2O_4)$ salt show better long-term performance than do cells containing the $LiPF_6$ and $LiB(C_2O_4)_2$ salts.

Electrolysis and Pressure Driven Flow for Temperature Gradient Focusing. *ELLIS GARAI* (*University of California – Los Angeles, Los Angeles, CA*)*; KEVIN NESS* (*Lawrence Livermore National Laboratory, Livermore, CA*). Bio-warfare detection systems are a necessary means of maintaining national security. In order for a detection system to be practical and largely deployed it should be easy to use, affordable, portable, low power, rapid, accurate, and autonomous. Currently, bio-warfare detection instrumentation do not meet the aforementioned specifications due to the lack of automated front-end sample preparation(FESP). FESP consists of purifying, concentrating, and separating 'complex' environmental samples in order to improve the downstream detection assays performance. Temperature gradient focusing(TGF) has been identified as a novel microfluidic technique to aid in the necessary autonomous FESP. TGF is the balance of an advective flux and an electrophoretic flux, in the presence of a temperature gradient, to ensure focusing only occurs at a unique spatial location along the axis of the microchannel. The main factors influencing the stability during TGF are a stable flow field and a stable electric field within the microfluidic system; therefore, these parameters must be tightly controlled. Electrolysis greatly influences these parameters; any gas formation within a channel can perturb both the flow and at the very least perturb the electric field. An in-line gas management system was devised to overcome this obstacle. Several approaches were taken to address this issue. The first was to remove the gas forming at the electrode through a porous gas permeable Teflon material while under vacuum. The second consisted of a large sealed air/liquid electrode reservoir, through which bubbles would float to the surface. With certain disadvantages in the first two, a final, more promising approach to directly isolate the gas formation was chosen. By using a proton permissible material (Nafion), gas generated at the electrode is isolated from the TGF flow line and swept down a separate line using a constant running buffer. In addition to electrolysis altering the flow field, generating a stable flow at the ~100 nL/minute range was another hurdle. Commercial pumping technology has an ~10% variation in the flow rate at any given time. By using a high resolution flow sensor and a dynamically controlled pressure source, in combination with a custom PID control scheme, a stable flow rate of less than 1% change (~1 nL/minute) was attained. Through this tighter control over important TGF parameters improvements in purification, separation, and concentration effects are realized.

Practical DNA-based Clinical Diagnostics. *DAVID GEB* (*University of California – Los Angeles, Los Angeles, CA*)*; TORSTEN STAAB* (*Los Alamos National Laboratory, Los Alamos, NM*). The development of a disposable test cartridge for DNA-based clinical diagnostics will afford a better alternative to current protein-based tests. DNA-based clinical diagnostics is significantly more accurate than the protein-based alternative. Moreover, a cheap, effective, disposable test cartridge will allow this technology to be accessible to more patients. The development of this test cartridge involves designing, prototyping, assembling, and testing its mechanical components. After the completion of the project, a user-friendly, affordable, and accurate device will be the result. Its technology will provide a solution for clinical diagnostics in physician offices worldwide.

Scrubbing of Sulfur Dioxide Byproducts of a Hydrogen Production System. *LINDSEY GOODMAN* (*Georgia Institute of Technology, Atlanta, GA*)*; GREG KRUMDICK* (*Argonne National Laboratory, Argonne, IL*). The design of an SO_2 scrubber was necessary for a hydrogen sulfide (H_2S) to hydrogen conversion system that is currently being developed at Argonne National

Laboratory. It has been previously shown that hydrogen can be produced by reacting hydrogen sulfide (H_2S) gas with a molten metal, producing sulfur dioxide (SO_2) as a byproduct. Because large quantities of SO_2 will be generated by this new conversion system, a method had to be devised to further break down this compound into environmentally neutral substances. The process of SO_2 removal is called Flue Gas Desulfurization, or scrubbing, and is done with an apparatus called a scrubber. Described in the following paper is the process engineering of this small scrubber system. A wet Venturi ejector type system was chosen. A liquid jet eductor nozzle was implemented as the scrubbing device. The chosen scrubbing reagent was a solution of 20% concentration of sodium hydroxide (NaOH, or caustic). A heat exchange system was employed to ensure the correct operating temperature. Control methods were used to ensure proper concentration of NaOH solution. It was estimated that for one six hour batch of the H_2S conversion process, the scrubber will remove approximately 200 pounds of SO_2, generate about 282,000 BTU of heat, and consume roughly 130 gallons of 20% caustic solution. Once the H_2S conversion system is complete, the scrubber will be tested and adjusted accordingly.

Binding Superhydrophobic Powder to Surfaces for Dielectric Purposes. *MARY HADLEY* (*Vanderbilt University, Nashville, TN*)*; ENIS TUNCER* (*Oak Ridge National Laboratory, Oak Ridge, TN*). Outdoor insulators used in high voltage transmission lines and substations are constantly under environmental stress leading to power interruptions, flashovers, etc. One common occurrence in polluted areas is excess water collecting on insulators promoting dry band arcing. It has been shown that hydrophobic materials are the solution to avoiding this event. These materials do not interact with water molecules forcing them to bead up instead of collecting into films. This unique surface quality also makes the hydrophobic materials self-cleaning in wet environments. Traditional hydrophobic materials for outdoor insulation have been silicone rubber based materials. Recently other material formulations with fluor based compounds have been proposed. In this study, a superhydrophobic (SH) material made of a glass-based powder is investigated. The material alone does not adhere to surfaces, so research was performed to find a polymer that will bind the particles to a surface while maintaining SH qualities. Test surfaces were prepared by making six solutions of SH powder, a binder, and an alcohol solvent and then dispensing the solution onto plastic and glass slides. Binders tested were polyvinyl butyral resin (PVB), polymethyl methacrylate (PMMA), Rhoplex Fastrack X-tended Seasonal Range resin (XSR), and Araldite resin. Hydrophobicity was tested by measuring the radii of water droplets to calculate contact angles and wettability by recording radii of droplets over time. The surfaces were also observed for scratch resistance, adhesion, and cohesion. Three mixtures showed high angles of approximately 130° to 133°. PVB surfaces had high wettability and poor cohesion, and surfaces made with a higher ratio of binder had poor adhesion. The resin and XSR surfaces maintained some scratch resistance. These tests prove the best surface investigated in this research is made with 0.8 g of SH powder and 0.4 g of XSR. It repels water for an extended time and maintains the highest contact angle at 133°. This surface is not deemed SH because its contact angle is below 150°, but this mixture is most able to remain hydrophobic. The particle mixture forms a consistent film and adheres well to surfaces, but only fair scratch resistance makes it imperfect for potential application. These results are part of ongoing research to determine polymers that bind to particles and withstand environmental conditions experienced in polluted areas.

Implications of Exhaust Stream Sampling Conditions for Measurement of Gas and Particle Emissions from Natural Gas Appliances. *ADAM HALL* (*Bowdoin College, Brunswick, ME*)*; BRETT SINGER* (*Lawrence Berkeley National Laboratory, Berkley, CA*). Accurate measurement of ultra-fine particle and gaseous emissions from natural gas fueled appliances are needed to quantify the potential health and environmental impacts of airborne emissions that may result from use of new gas supplies. In order to quantify differences in emissions between natural gas derived from liquefied natural gas versus conventional gas supplies a variety of used appliances will be accessed and operated. Concentrations of carbon dioxide, oxides of nitrogen, carbon monoxide, oxygen, and ultra-fine particles in the exhaust of these appliances are to be measured. Making such measurements requires that samples of the appliances' exhaust be captured and delivered to a number of gas and particle analysis instruments. This sampling must not interfere with the normal operation of the appliance and must preserve the composition of the exhaust for measurement. Concern has been expressed that in drawing up these emissions the sampling system may change the airflow around

the flame, possibly having effects on the levels of pollutants produced by the burner. Experiments were conducted to assess how the elevation of the exhaust hood relative to the stovetop burner impacts emissions formation. Hood elevation did not affect gaseous emissions appreciably. However, increased hood elevation lead to an increase in particle formation of roughly an order of magnitude. This suggests that even though the exhaust hood does not affect flame performance directly, it does impact characteristics of the exhaust stream, such as temperature, which have a measurable effect on particle formation. This finding illustrates the importance of designing our experimental system to reflect conditions in the consumer setting in all parameters relevant to pollutant formation.

Application of Modern X-ray Techniques to Common Industrial Materials: Measuring the Local Density of Compressed Cellulose Fibers by Ultra Small Angle X-Ray Scattering. *Joshua Hammons* (*Texas Tech University, Lubbock, TX*); *Jan Ilavsky* (*Argonne National Laboratory, Argonne, IL*). Cellulose Fibers have a wide range of applications from simple typing paper to cleaning and personal hygiene products. In many applications the density of the cellulose fibers is very important to ensure the quality of the product. The dimensions of the lamellae fibers are on the order of 1 micron in thickness and several millimeters long. Several other techniques can be employed such as BET analysis and SEM imaging; however, these techniques are very time consuming for large samples and may require cutting of the sample so that individual sections can be evaluated separately. Ultra small angle scattering (USAXS) allows small angle scattering (SAS) data to be obtained from large volumes of samples up to a few cubic mm. A complete 3-dimensional statistical representation of relatively large volumes of samples can be obtained in approximately 20 to 30 minutes for each sample point. Additionally, as many as 100 different USAXS scans can be performed with little to no interaction required by the experimenter at the Advanced Photon Source Beamline 32-ID. The motivation of this research is to evaluate the ability of USAXS to differentiate between varying levels of cellulose density. SAS data obtained from USAXS experiments span up to 4 decades, in Q, of useful data. Therefore, fiber and void sizes, ranging from 1 nm to just over 1 μm can be evaluated. The correlation between the SAS data and density is due to additional hydrogen bonding between fibers, induced by compression, which result in the reduced shared surface area between the cellulose fibers and voids. The reduced surface area is extracted by the Porod constant, obtained from SAS data. All of the data obtained from 52 USAXS experiments indicate that variation in the SAS data can be directly correlated to the density of the cellulose fibers. Some recommendations for future USAXS experiments were also developed. Small angle scattering data obtained from the sample sheets indicated some multiple scattering affects at low Q. For this reason, future USAXS experiments, on similar samples, should be performed at either energies greater than 18 keV or samples thinner than 2 mm. Additionally, the SAS data can be evaluated at much smaller intervals by decreasing the X-ray beam size. In this manner, a complete map of the fluctuation in density can be made for very large industrial samples, comprised of compressed cellulose fibers.

Air Filter Pricing Analysis for a Business to Business or Indefinite Quantity Agreement (Alternative). *Matthew Hardman* (*University of Idaho, Moscow, ID*); *Dale Schielke* (*Pacific Northwest National Laboratory, Richland, WA*). As the number and breadth of the facilities under Pacific Northwest National Laboratory (PNNL) control increase, the need and importance of cost estimates for maintenance of these facilities also increases. As with any business, the cost to maintain operation of its facilities can be a daunting task. The price analysis on air filters for a 'cutting edge' research facility such as PNNL is difficult to achieve since many non-traditional, higher rated filters are needed. In response to the growing difficulty in managing many systems, electronic databases complete with inventories, work orders, preventative maintenance, and purchasing capabilities are being built. One such program which the Facilities and Operations Directorate (F&O) at PNNL uses is MAXIMO, developed by mro software. MAXIMO contains a purchasing capability which can be set up with a business to business (B2B) agreement or indefinite quantity (IDQ) agreement. A B2B agreement is a contract between two businesses for the sale of products directly between the two entities. PNNL wants to set up a B2B or IDQ agreement for air filters as a pilot for using the full capabilities of MAXIMO purchasing capabilities in the future. Using MAXIMO report capabilities, descriptive reports were made for all air filters currently used at PNNL. Microsoft Excel files were then produced and sent out to previous vendors for pricing information. After gathering the pricing information into files, the information was then entered into MAXIMO.

These files along with inventories were compared to determine which filters were eligible for excessing. Once the excessing was underway, work on a B2B began. If requirements for a B2B cannot be met, an IDQ will then be set up. This work towards a B2B or IDQ will help create a system in which filters are ordered for "just in time delivery". This kind of system will help with storage costs since not as many air filters will need to be stored on a regular basis. Overall, implementing a B2B or IDQ system will reduce cost and increase the efficiency of the maintenance work, therefore saving money, on mechanical systems here at PNNL.

Thermochemical Ethanol via Indirect Gasification of Lignocellulosic Biomass with Methanol and Dimethyl Ether Intermediates. *Michelle Harris* (*Colorado School of Mines, Golden, CO*); *Steven Phillips* (*National Renewable Energy Laboratory, Golden, CO*). Thermochemical gasification is a process where a carbonaceous feed is partially oxidized to a gas-phase fuel (syngas) consisting mostly of carbon monoxide (CO) and hydrogen (H_2) gases. Syngas can be converted to fuels such as ethanol, methanol, or dimethyl ether (DME) via a catalytic process called synthesis. A 2007 report by S. Phillips, A. Aden, J. Jechura, and D. Dayton at the National Renewable Energy Laboratory (NREL) provided a detailed techno- economic evaluation of a 2,000 tonne wood to ethanol process via gasification and synthesis. The present study evaluates a new scenario that consists of five of these small plants producing methanol or DME from wood, and a larger plant producing ethanol via the methanol or DME collected from the smaller plants. Achieving improved economy of scale for the large ethanol production plant is the reasoning behind this new study. The mass and energy calculations needed for this study were done using the computer simulation program ASPEN®, which models chemical and industrial processes, with the original ASPEN simulation designed by Phillips *et al.* modified to meet the new specifications. The cost of production (COP) of each of the products (methanol, DME, or ethanol) was determined to assess the feasibility of the new scenario versus the original process. The COP was calculated using a Discounted Cash Flow Rate of Return (DCFROR) method programmed in Microsoft® EXCEL. The COP, in units of $/MM Btu and $/gal ethanol equivalent, ranged from $8.73–$10.20/MM BTU and $0.67–$0.78/gal for the methanol and DME scenarios. The methanol to ethanol process used in this study produced ethanol at a COP of $1.26/gal, which is significantly higher than the $1.01/gal from the Phillips *et al.* study. Future research will continue to work on the scenarios involving DME and other process configurations to optimize the industrial plants to achieve their greatest efficiency and to decrease the cost of production.

Alternative Fuels Data Center: Fleet Reports, Databases and Website Redesign. *Brett Hoag* (*University of Colorado, Boulder, CO*); *Johanna Levene* (*National Renewable Energy Laboratory, Golden, CO*). The Alternative Fuels Data Center (AFDC) is online collection of data, including more than 3,000 documents and several interactive tools. The AFDC collaborates with the U.S. Department of Energy's (DOE) Clean Cities Program as well as the Energy Policy Act of 1992 (EPAct) fleet programs. Federal fleet location reports for EPAct were processed using excel, geocoding software and cgi scripts that evaluated the received data to the data located in the AFDC (AFDC) Alternative Fuel Station Locator Database. A total of 15,267 unique fleet locations were processed resulting in an addition of 73,841 vehicles to the AFDC Database. The updating process of the Related Links Database used several different debugging procedures and techniques, as well as work with Oracle database maintenance software. The Clean Cities Success Stories Database update process required extensive work contacting organizations, writing and editing summaries about organizations that are currently implementing alternative fuels within their fleet. During the updating process 131 individual organizations were contacted, resulting in a new Success Stories Database that had 15 new organization summaries as a base. Debugging procedures and techniques were also applied to several online tools available for fleets as well as the public. The Make/Model Application, Flex-Fuel Fleet Vehicle Cost Calculator and the AFDC Laws and Incentives page were debugged for potential problems that new users may experience. The research was conducted to aid in the development of the new AFDC website that has a planned launch date of September 30, 2007.

Updating Tank Information in Current Site Key Plans. *Alexander Hoimes* (*Pennsylvania State University, State College, PA*); *Jason Remien, Peter Pohlot* (*Brookhaven National Laboratory, Upton, NY*). All buildings on the Brookhaven National Laboratory site are represented in drawings known as Key Plans, which are blueprints drawn in AutoCAD. Several years ago a number of upgrades to the infrastructure of the lab were completed, most notably an upgrade to

the aging tank system present at the lab. The tank system consists of chemical, oil, water, and hazardous waste storage. Some of the current key plans have tank layers, and some are missing this layer. A layer refers to specific part of a drawing in AutoCAD that can be shown or hidden by turning the layer on and off. This feature allows one to draw very complex drawings with multiple layers, but at the same time can provide a clear view of the drawing and the specific point of interest when needed. This project corrected the current key plans by updating the tank layer in each plan. A list of updated tanks was available, but the measurements and exact positions must be measured at each site and physically be changed in the Key Plan of each building. So far the updating of the tank layer is on schedule, with a projected completion at the beginning of August. This project is intended to keep the Key Plans up to date, which is essential for the ongoing planning, development, and maintenance of Brookhaven National Laboratory.

Diffractive Optics at Soft X-Ray Wavelengths. *Terence Holloway* (*Norfolk State University, Norfolk, VA*)*; Yanwei Liu, David Atwood* (*Lawrence Berkeley National Laboratory, Berkley, CA*). The Center for X-Ray Optics (CXRO) at Lawrence Berkeley National Laboratory works to advance the science and technology of short-wave optical systems through applications using extreme ultraviolet light (EUV) and Soft X-Ray wavelengths that range from 1 nm–50 nm. The short wavelength radiation is generated by a machine known as a synchrotron. The synchrotron used in our experiment, operated by Lawrence Berkeley National Laboratory, is the Advance Light Source (ALS). At these wavelengths there are a large number of atomic resonances which cause the absorption of radiation over short distances (in nanometers or micrometers) in most materials. As a result, conventional devices which operate in the optical region of the electromagnetic spectrum are no longer applicable at these short wavelengths. CXRO specializes in two classes of optics that operate at EUV/Soft X-ray wavelengths, reflective multilayer coatings and diffractive optics. This SULI research project places emphasis on nanometer scale diffractive optics. It begins by creating programs for the optical devices using Matlab. A Graphical User Interface (GUI) was created to generate desired patterns for the optics chosen by the user. The GUI runs a simulation of diffractive soft X-ray optics based on electromagnetic wave propagation. The simulation will give us a good idea of how the experiments performed in the ALS will result. After running the simulation, we performed actual synchrotron experiments using those specialized optics at ALS beamline 12.0.2.

Modeling of an Aerosol Collection Inlet for Interior Monitoring. *Robert Igel* (*Bradley University, Peoria, IL*)*; David Decroix* (*Los Alamos National Laboratory, Los Alamos, NM*). The dispersion of biological agents into populated environments is a serious terrorist threat faced by the United States. Possible targets of biological terrorism include densely populated areas such as stadiums and public transportation systems. Los Alamos National Laboratory wants to be able to collect air samples in these areas using an aerosol inlet for a collection device that has been designed to be installed in the HVAC system of densely-populated buildings. The inlet was designed to collect particles less than 10 μm. Preliminary testing has been performed on this design; however, a more complete understanding of the inlet was desired. The purpose of this research was to model the same inlet using the Fluent computational fluid dynamics solver to provide more conclusive collection efficiency results and determine the flow characteristics caused by the inlet. The 3-D model of the design, its mesh, and its boundary conditions were constructed in Gambit. This file was then exported into the Fluent solver, where flow conditions — turbulence, flow rate, and particulate size — were specified. Several wind tunnel tests were run varying the free stream velocity between 2 and 8 km/hr and particulate sizes of 8, 12, and 20 μm. The results of these experiments show that the inlet will collect the vast majority of the 8-μm particles, only a small percentage of the 12-μm particles, and none of the 20-μm particles. However to determine the streamlines and other flow properties of the inlet geometry and its overall efficiency, computational simulations have been run. The results from this research will better enable the detection of biological agents harmful to building occupants.

Improving the Documentation of Findings and Corrections. *Philip Irminger* (*Pellissippi State Technical Community College, Knoxville, TN*); *John Czachowski* (*Oak Ridge National Laboratory, Oak Ridge, TN*). Currently at ORNL, there is a program in place known as the Operational Awareness Program (OAP). This program is designed to help ensure that regulations are being followed in the various laboratory spaces, and that proper safety measures are being addressed to help protect all those involved. The OAP team has members consisting of Subject Matter Experts (SME), and also DOE representatives.

Using a variety of SME's allows for a vast variety of knowledge of the various hazards which may be present including chemical, electrical, and environmental. During the OAP inspection, findings are found and documented including violations, possible hazards, and also noteworthy practices. In the past, documenting these findings has been documented via confirmation in writing; however I have been tasked with assisting in documentation of these findings via photographs. I will assemble pictures of the findings both before and after corrective actions have taken place. Through assembling these photographs the corrective actions that have taken place will be relayed to the OAP team to document resolution of the findings. By following this procedure, there is no doubt about the corrective actions that have been completed. It also allows for reference photographs for similar issues in other sections of the laboratory. Through the use of this documentation of the OAP assessments, there will be a reliable and effective way of documenting the corrective actions which have taken place to resolve any issues found during the inspection.

Transmission IR Microscopy of CdZnTe Crystals for Nuclear Radiation Detectors. *Jesse James* (*Tennessee Technological University, Cookeville, TN*)*; Aleksey Bolotnikov* (*Brookhaven National Laboratory, Upton, NY*). The key problem of CdZnTe (CZT) crystals is trying to find a correlation between defects or inclusions found in the layers within the crystal itself and, trying to prove that inclusions affect the responsiveness of CZT detectors. Along with other projects investigating CZT defects using highly collimated X-ray beams and the spectral response of CZT detectors, this research seeks to discover an optimal and efficient way of analyzing the uniformity of CZT crystals. Using a highly sensitive camera taking infrared beams of the given CZT detector and correct amount of light exposure, five points of position on the crystal (10mm x 5mm x 5mm crystals dimensions) were taken. Using the Interactive Data Language (IDL) program was created to identify the defects accurately and precisely to have sufficient data for the examination of results. The results are correlated to the full width half maximum (FWHM) at 1,000V bias and to the concentration threshold of inclusions that was >20 μm in diameter. Approximately half of the detectors that were tested have had moderate to good quality detector response. However, their has been many defects in the crystals such as twins, dislocations, grain-boundaries, precipitates, and >20 μm inclusions. The structural non-uniformity of CdZnTe crystals around Te Inclusion is responsible for electron transport non-uniformity and diminished energy resolution of large-volume CdZnTe coplanar-grid detectors. This work is expected to be completed at the end of 2007 in making CZT detectors more robust and less expensive compared with other detectors.

Scheduling. *Darren Johnson* (*Brigham Young University – Idaho, Rexburg, ID*); *Rick Staten* (*Idaho National Laboratory, Idaho Falls, ID*). I was tasked to perform data entry work on Excel spreadsheets and Primavera Project Manager Gant Charts. I worked on several projects, most of which pertained to the testing of new fuels. My tasks were to create logical connections between series of activities. These activities were individual steps within a project and when tied together they create a logical sequential order that can be followed in order to finish a project correctly and on time. The projects I have been working on are both on-going and future projects that may not be started yet. This is a continuum report that will be on-going after I leave Idaho National Laboratory.

Ultrasonic Evaluation of Bolt Elongation. *Kyle Johnson* (*Washington State University, Pullman, WA*); *Morris Good* (*Pacific Northwest National Laboratory, Richland, WA*). The automotive industry has an interest to improve measurement consistency of clamp load when using threaded fasteners. Several early studies were done in support of this effort to acquire ultrasonic elongation measurements to estimate bolt clamp load for an automotive application. The first study correlated bolt elongation with measurements obtained with a 7 MHz transducer bonded to the bolt head. The second study placed unfocused immersion transducers with varying frequency and diameter above the bolt head and empirically evaluated the pulse-echo signal from the other end of the bolt as a function of these parameters. A third study looked at a limited variety of coupling materials. Data showed that bolt elongation correlated well with the change of the ultrasonic time-of-flight for the case that the transducer was bonded to the bolt head, that selection of frequency and transducer diameter affected the signal to noise ratio, and that membranes used in combination with an applied force were capable of coupling ultrasound between a transducer and a bolt head. Future research should continue the examination of coupling materials and use this information to examine measurement stability during the tightening process. This document contains Battelle-Business Sensitive

Information and, since it is transmitted in advance of patent clearance, is made available in confidence under the protections of 35 U.S.C. § 205 solely for use in performance of work under contracts with the U.S. Department of Energy. This document is not to be published nor its contents otherwise disseminated or used for purposes other than specified above before patent approval for such release or use has been secured, upon request, from Intellectual Property Legal Services, Pacific Northwest National Laboratory, Richland, Washington 99352.

Gas retention and release in the presence of an Anti-Foaming Agent during the nuclear Waste Treatment Process. *Wesley Johnson* (*Bevill State Community College, Fayette, AL*); *Consuelo Guzman-Leong* (*Pacific Northwest National Laboratory, Richland, WA*). Nuclear waste stored at the Hanford site in Richland, Washington, will be vitrified in order to dispose of the waste in an environmentally sound manner. Hydrogen gas generated by radiolysis within waste processing tanks in the Waste Treatment Plant (WTP) could combust under some upset conditions, posing a significant safety concern. The Anti-Foaming Agent (AFA) research team utilized a Quarter Scale Lag Storage system to facilitate gas hold-up and release testing in simulated waste materials mixed using a hybrid system comprised of pulse jet-mixers (PJMs) and spargers. We utilized PJMs and spargers because they are the most effective method of mixing, requiring the least amount of maintenance. Mixing the waste creates larger bubbles than the bubbles from the waste itself and these larger bubbles, in connection with the actual mixing, allow for the release of the gases at the surface of the waste. This waste is an assortment of varying by-products exhibiting non-Newtonian rheology which determines how and when gases will be released. Data collected will address potential hazards during pretreatment processes by determining whether or not a significant portion of potentially flammable gases will be released during the mixing phase and whether or not an alternative AFA must be utilized in order to minimize gas retention. My team administered a series of tests to collect data for extrapolation to full scale operations. One series consists of water visualization tests with and without AFA, another of clay, a third of simulant with and without AFA, a fourth of simulant using research-determined, bounding yield stress for gas retention or ~13 Pa. — depending on which of the two is lower — with AFA or an alternative AFA, and a final series of simulant with an alternative AFA. Varying yield stresses of ~ 3, 13, and 30 Pa. were used in the clay and simulant testing series because previous research suggested that the AFA impact upon gas retention differed depending on the yield stress of the simulant. Our team employed hydrogen peroxide as the most effective method of generating gas bubbles for testing without introducing significant error to the research. Results are not available because testing is in progress. Our team's information will be used to determine appropriately safe working conditions as they pertain to gases escaping during the waste treatment and if a different type of AFA is necessary to also reduce dangers.

Green Processes: Synthesis of Higher Oxygenates Using Transition Metal Catalysts in Aqueous Phase. *Sheena Joseph* (*State University of New York at Stony Brook, Stony Brook, NY*); *Devinder Mahajan* (*Brookhaven National Laboratory, Upton, NY*). Biomass can be converted to useful fuels and chemicals by two methods: biological and thermochemical. Certain microorganisms that process simple sugars as a carbon source mediate the biological route, seen in the well-established fermentation pathway to ethanol. The thermochemical route is a two-step process that involves biomass gasification to yield synthesis gas (or syngas), a mixture of carbon monoxide and hydrogen and catalytic conversion of syngas into higher oxygenates. This pathway requires development of highly efficient catalysts to achieve total carbon utility and produce biofuels economically. Since methanol can be produced selectively and in high yield by catalyzed reaction of syngas at low temperatures, catalysts that efficiently convert methanol into C2+ oxygenates are being investigated. A supported Rh catalyst, Rhodium on alumina, was evaluated at 200°C for activity because Rh-based catalysts are known to promote methanol homologation (carbon-carbon coupling) into ethanol at 200°C. However, in the present work, Rh on alumina was observed to yield dimethyl ether at 200°C. A ruthenium catalyst operating in an aqueous phase under moderate conditions was also evaluated. The reactions were conducted in a 300 mL Parr batch reactor fitted with gas and liquid sampling ports. The fate of the catalysts was monitored *in situ* using gas chromatography and infrared spectroscopy. The ruthenium catalyst, $Ru_3(CO)_{12}$, was also observed to yield dimethyl ether at 200°C. Dimethyl ether is currently considered an attractive replacement for diesel fuel. More work is underway to further study these systems for biomass to fuels conversion.

A New Routing Protocol for Connectivity in *Ad Hoc* Networks. *Tyler Karrels* (*University of Wisconsin – Madison, Madison, WI*); *Sami Ayyorgun* (*Los Alamos National Laboratory, Los Alamos, NM*). TCP/IP routing is the standard for static wired networks, but TCP/IP cannot quickly adjust to changes in network topology that can occur in wireless *ad hoc* networks. A wireless *ad hoc* network's topology is dynamic because hosts eventually lose power, hosts' transmission ranges may vary over time, hosts may become damaged, or hosts may enter or exit the network's transmission range. These problems require new routing paths to be established to maintain network connectivity. The purpose of our research at Los Alamos National Laboratory (LANL) is to improve, or at least maintain, connectivity between hosts even when the network topology is drastically altered. We propose a new routing protocol called Neighbor Monitoring (NM) that creates multiple paths to the network sink and monitors these paths to decide which is optimal. Network simulations have been conducted in Matlab using a simulator developed for this research. For a comparison to existing routing algorithms, Dynamic Source (DSR) and Load Balance (LB) routing algorithms have been implemented in addition to NM routing. Simulations are being run with networks of varying size and topology. The three topologies used are grid, random, and degree based. Preliminary results for small networks have shown that DSR and LB algorithms perform better than NM in a grid network topology and no node failures. It is expected that NM routing will be more resilient by quickly repairing routes. It is also expected that NM routing will establish quicker routes even when a network is heavily loaded.

Dirty Bomb Simulation Experiment: Usability, Control Condition Selection, and Composite Mission Performance. *Tim Klein* (*Oregon State University, Corvallis, OR*); *David Bruemmer* (*Idaho National Laboratory, Idaho Falls, ID*). To further the understanding and evaluation of the problems of usability, control condition selection, and composite mission success related to human robot interaction in high stress conditions, a dirty bomb experiment and simulation field study was conducted in an as-near-as-possible real world situation. This paper focuses on the simulation portion of the study with emphasis on the theory that the robot performing under semi autonomous control conditions will show improved holistic performance when compared to manual control conditions. The simulation utilized the current control conditions and interface methods available to the robot system. In the simulation, the participants were asked to find three simulated radioactive sources using the two control conditions, the Shared control using a joystick providing continuous operator control or the newer semi-autonomous Target control. Both control conditions use the robot intelligence kernel (RIK) developed by the Robotic and Human Systems Group at the Idaho National Laboratory for optimized mission success along with environment and robot system safety protection. The data collection came from three different techniques, logged communications from the RIK, participant self evaluation questionnaires, and administrator observations. The greatest differences found during data analysis appear in the participant evaluation characteristics of input and workload demands and the perceptions of control and understanding, shown by comparison and statistical tests of the control conditions. The results show that with an approximate difference of 92 seconds there is no statistically significant difference between the control conditions with respect to the average time taken to complete the task. The results of the holistic composite performance equation, represented by the non control condition specific performance characteristics, favor the Target control condition in which the participants felt less demand and had a higher feeling of mission performance and control. As a design tool, the simulation provides a useful adjunct to field studies and provides insightful evidence, if not entirely conclusive, to continue the development of the Target control condition for use in urban search and rescue, situations involving object detection, and in reducing human exposure during environmentally hazardous missions.

Conceptual Design of a New Large Scale Wind Turbine Drive Train Testing Facility. *Scott Lambert* (*University of Colorado, Boulder, CO*); *Jason Cotrell* (*National Renewable Energy Laboratory, Golden, CO*). Laboratory testing of wind turbine drive trains is an important way to validate designs, test reliability, debug systems, and verify computer and analytical models. The large physical size and high torque requirements of modern wind turbines present engineers with unique manufacturing and testing challenges. The 2.5 MW drive train testing facility at the National Renewable Energy Laboratories (NREL) in Colorado is one of a few facilities capable of testing multi-megawatt wind turbine drive trains. The rapid growth of wind turbine size has outpaced the facility's capacity to test very large wind turbine systems. The goal of the research described in this report is to identify possible configurations, assess the technical challenges, and investigate the

costs for a new, larger, 12 MW drivetrain test facility. The identification of potential dynamometer configurations was conducted by examining large test facilities in use overseas, and through consultation with industry. Several conceptual designs were modeled using computer aided design software and a preliminary engineering analysis for each concept was conducted. Readily-available components that could be used in this project and suppliers capable of assisting with engineering and manufacturing of limited production components were identified. The concepts where then judged against each other on the basis of cost, component availability, and relative ease of implementation. This research shows that configurations using large custom built gearboxes and motors are expensive and require long lead times due to technical obstacles in engineering and manufacturing. Concepts using large custom components show higher overall system costs than those using multiples of smaller, more readily-available components that distribute the high torque loads over several load paths. While initial estimates show that these distributed-load systems have considerable potential for cost savings, further investigation into these concepts is required to assess the risks involved. Furthermore, the results of this study indicate that concepts such as single motor and gearbox combinations suitable for use in smaller scale test bench systems do not scale well up to 12 MW, and do not offer the same setup and configuration flexibility that is possible with distributed load concepts.

*Simulation of Shearing in Dense Granular Flows. BRIAN LANGSTRAAT (*Central College, Pella, IA*)*; SHANKAR SUBRAMANIAM (*Ames Laboratory, Ames, IA*). Understanding the response of granular matter to mechanical loading is essential to many applications in science and engineering, such as avalanches and hopper flows. The constitutive behavior of pure solids or fluids is well understood by researchers. However, the mechanical response of granular matter, which can exhibit fluid-like or solid-like behavior depending on the loading conditions and volume fraction, is not well understood. In this work, computer simulations of interactions between individual particles that constitute the granular matter are used to test continuum models of granular flow. We use the Large-scale Atomic/Molecular Massively Parallel Simulator (LAMMPS) which was developed at Sandia National Laboratories to simulate the dynamics of a large number of particles. The response of granular matter to plane shear between two parallel plates is chosen as a canonical test problem. The LAMMPS simulation data is analyzed to understand the evolution and steady-state profiles of volume fraction, average velocity, granular temperature, and stress. Glass beads are simulated with a volume fraction of 0.46. Three shear rates are tested corresponding to the slow frictional, transitional, and intermediate regimes. The sheared particles tend to form striated layers in planes parallel to the shearing surfaces. The simulations reveal that the center layers are very dense with high stress and a linear change in velocity. Also, the granular temperature is low within the center layers. We conclude that in the dense, central layers of the sheared granular flow there are less velocity fluctuations. This research is part of a larger project that will help to further the understanding of dense granular flows.

Wireless Roadside Inspection Proof-of-Concept Test. MARY LASCURAIN (*Pensacola Christian College, Pensacola, FL*); GARY CAPPS (*Oak Ridge National Laboratory, Oak Ridge, TN*). Safety inspections are performed on commercial vehicles to promote safety on the roadways, but these inspections are limited due to their labor-intensive nature. The use of a wireless inspection method could dramatically increase the number of safety inspections by allowing enforcement personnel to check driver licensing, medical card, carrier, and weight information without requiring the driver to stop. This proof-of-concept test examines the feasibility, effectiveness, and limitations of the wireless inspection method. PeopleNet, a producer of current electronic on-board recorder technology, designed a system to produce a Safety Data Message Set (SDMS) containing the desired information. This SDMS data was compared to similar data obtained through an independent monitoring system comprised of an eDAQ-lite, VBOX III, Air-Weigh, and custom software. The ability to send and receive an SDMS at varying truck orientations (in 45-degree increments), distances (100 ft to 400 ft), and frequencies (5.9 GHz and 2.4 GHz) was tested under static conditions. SDMS transmission from the instrumented truck to a roadside unit and mobile enforcement vehicle (MEV) was tested at various relative speeds in the dynamic portion of testing. Tests were performed at 2.4 GHz as well as 5.9 GHz, and two different antenna types (dome and stick) were used. Most of the test data for the SDMS files was accurate. However, due to software problems in the PeopleNet system, over an hour was required for some driver status changes to be reflected in the SDMS. The best reception under static conditions was found to be to either side, slightly ahead of

the instrumented truck. Reception was best on the right side, where the antenna was located. The dynamic tests indicated that the dome-type antenna had better reception at 2.4 GHz, while the stick antenna performed better at 5.9 GHz. The use of a tripod for the antenna mount increased the reception for both antennas. Files were successfully transferred at various speeds (up to 55 mph). This proof-of-concept test demonstrated the feasibility of a wireless inspection method while identifying areas in which further testing would be beneficial. Further research should include more extensive testing to determine ideal antenna height, the most appropriate frequency, and the optimum mounting locations for both trucks and MEVs. Additionally, the effects of terrain, other vehicle interference, and weather will need to be well understood.

Polyhydroxyl Fullerene with Silicotungstic Acid Hydrate to Create a Composite and Integrate With Nafion® Polymer to Create a Proton Exchange Membrane. JOSHUA LAU (*Colorado School of Mines, Golden, CO*)*; JOHN A. TURNER (*National Renewable Energy Laboratory, Golden, CO*). The U.S. Department of Energy's (DOE) goal is to have a membrane for the PEM that will operate at 120–150°C and a relative humidity (RH) of 25% or less by the year 2010. Proton exchange membranes (PEMs) for fuel cell applications have current limitations on the materials and capabilities of the membrane as is. There has been research to modify the perfluorosulfonic acid (PFSA) polymer based membranes, most notably, Nafion®, by doping PFSA membranes with different compounds, such as heteropoly acids (HPAs), to increase the conductivity of the membranes, and with other particles to improve the longevity of the membranes at high temperatures and low relative humidity. In this research, a combination of polyhydroxyl fullerene (PHF), a fullerene derivative, and silicotungstic acid hydrate (HSiW), were combined in two separate solutions and mole ratios of one-to-one and one-to-four, respectively, to create a composite. Infrared spectroscopy (IR) was conducted on the composite at various stages of the process. The results showed that the resulting compound differed from the starting material. An *in-situ* method of mixing of the two compounds on a stir plate in mole equivalent ratios of one-to-one, one-to-two, one-to-three, and one-to-four in the DuPont DE2820 polymer matrix was done in order to make membranes. Three controls were also cast at the same time to get base conductivities for comparison. The conductivities of the *in-situ* mixed membranes of the controls were found to have conductivity values of 132 ± 15 mS·cm^{-1}, 23.4 ± 0.2 mS·cm^{-1}, and 156 ± 15 mS·cm^{-1} for PHF; 129 ± 18 mS·cm^{-1}, 21.5 ± 3.0 mS·cm^{-1}, and 150 ± 21 mS·cm^{-1} for HSiW; and 130 ± 8 mS·cm^{-1}, 24.2 ± 4.4 mS·cm^{-1}, and 162 ± 2 mS·cm^{-1} for DuPont DE2820. The mole ratio conductivities had average values 146 ± 20 mS·cm^{-1}, 26.6 ± 22 mS·cm^{-1}, and 194 ± 20 mS·cm^{-1}. All of the values were at 60°C 100%RH, 80°C 50%RH, and 80°C 100%RH, respectively. The values are promising compared to Nafion® which is well known and reported. It is also interesting that added separately, the materials actually had worse conductivity than that of the pure DuPont DE2820, but when the materials were combined, the conductivity was greater in all cases.

An Ergonomics Guide to Pipette Selection and Use. MONICA LICHTY (*University of Michigan, Ann Arbor, MI*); IRA JANOWITZ (*Lawrence Berkeley National Laboratory, Berkley, CA*). The ergonomics of laboratory environments has not been developed as thoroughly as that of computer workstations and there is not much current guidance on ergonomics attributes of common laboratory equipment for the scientific community. This means that scientists and technicians are in great danger of developing upper extremity cumulative trauma disorders (CTDs) such as tendonitis and carpal tunnel syndrome from their regular activities. The focus of this project was on providing a usable guide to pipette and pipet controller selection for the employees at the Lawrence Berkeley National Laboratory (LBNL) to facilitate purchasing decisions and reduce the rate and severity of injuries associated with manual pipetting. The first step in the development was to become familiar with the pipette models that are commercially available. Interviews were conducted to learn which qualities of a pipette are important to users. Insight was also gained into the ways in which pipettes are held and operated through observation. Once a final list of attributes was determined, meetings were held with pipette manufacturer representatives to obtain demonstration products for assessment and to learn about the different product lines. The main quantitative measurements were: weight, plunger force, tip ejection force, blowout force, maximum thumb displacement, girth, and overall length from the thumb support to the end of the tip ejector sleeve. Other qualities were recorded such as autoclavability, electronic program options, and charging method of the pipettes. A section of comments was developed based on user input and ergonomics

factors including handle comfort, display legibility, and ease of volume adjustment. The guide will be available in two versions. The quick reference guide is comprised of product ratings in a variety of categories including weight/balance, grip comfort, and control forces. The extended user guide includes all of the quantitative information obtained as well as free-form comments about the products. Both versions of the guide will be available online to all employees of LBNL. The guides also come with a set of tips on posture, workstation layout, and task design to address the task as a system of interacting factors rather than solely a tool design issue. Although the guides provide an increased level of assistance to consumers, they will only remain relevant if they are updated on a regular basis to include new products and improvements.

Development of a Vacuum Monte Carlo Code. REYNALDO LOPEZ (*University of California – Los Angeles, Los Angeles, CA*)*; MATTHAEUS LEITNER* (*Lawrence Berkeley National Laboratory, Berkley, CA*). This paper presents the initial development of a three-dimensional Monte Carlo computer code that calculates the vacuum pressure of a sample cylindrical pipe vacuum vessel. The implementation of a basic Monte Carlo molecule-tracing algorithm is discussed. The pressure distribution is determined by tracing particles through the vessel structure; converting the trajectory lengths to molecular residency time by using the average molecular velocity. Simulations with various molecule sample sizes are implemented and compared to conventional analytical vacuum formulas. First code results calculate a correct parabolic pressure profile. Future work will include the development of a new geometry module for 3D CAD data, and the implementation of different surface conditions.

Studies of Cadmium Zinc Telluride (CZT) Defects with Highly Collimated X-ray Beams. ALEXANDER LURYI (*Cornell University, Ithaca, NY*)*; ALEKSEY BOLOTNIKOV* (*Brookhaven National Laboratory, Upton, NY*). Cadmium Zinc Telluride (CZT), an alloy of cadmium telluride and zinc telluride, is a wide bandgap semiconductor which has shown great potential in gamma radiation detection. While detectors that use other materials, such as germanium, must be cooled with liquid nitrogen to function usefully, CZT detectors have the distinct advantage of being able to operate at room temperature. In addition, since the creation of electron-hole pairs in CZT requires very little energy, CZT detectors take far less power to operate. However, it is hypothesized that the presence of tellurium (Te) inclusions in CZT crystals inhibits detector performance. The purpose of this work was to correlate the presence of these inclusions with decreased CZT detector quality. This was accomplished in three steps: first, crystals were scanned using infrared microscopy. Since CZT is transparent to infrared light, inclusions were easily visible in an infrared light source. Next, detectors were built out of these scanned crystals and their spectral responses were measured in the presence of a Cesium-137 source. Finally, the crystals were tested with a collimated X-ray beam to determine the significance of the defocusing effect, in which a nonuniform electric field causes charge to curve outward to the surfaces of the crystal. Comparisons between infrared imaging and pulse-height spectra showed a weak but implicative direct correlation between Te inclusion density and the absorption peak's full-width half maximum. The X-ray analyses provide further insight into each crystal's response by producing a pulse-height spectrum for a multitude of small areas of the crystal surface. This experiment demonstrated a phenomenon in which a crystal's response is best at its longitudinal center and decreases dramatically around its edges. The department of homeland security has expressed interest in CZT development and these results may foster significant advances in radiation detection.

Vehicle Immobilization Technology Evaluation Project. JOSEPH MASSIMINI (*Purdue University, West Lafayette, IN*); GARY CAPPS (*Oak Ridge National Laboratory, Oak Ridge, TN*). Since September 11, 2001, the Federal Motor Carrier Safety Administration (FMCSA) has been actively investigating methods to improve safety, security, and efficiency through the Hazardous Materials Safety and Security Technology Operational Test. The purpose of that Operational Test was to quantify the security costs and benefits of an operational concept that applies technology and improved enforcement procedures to hazardous materials (hazmat) transportation. In 2005, the House of Representatives Conference Report 108-792 stated that further testing of technologies, including vehicle immobilization is necessary. The present Vehicle Immobilization Technology (VIT) Evaluation Project has been conducted to support the Congressional directive, and has built on the experience and lessons learned from previous field operational tests. A VIT is any technology that prevents a highway vehicle from reaching its destination. There are two types of VITs. Vehicle Disabling Technologies (VDTs) prevent the motion of a

stopped vehicle, and Vehicle Shutdown Technologies (VSTs) stop a moving vehicle. These devices typically work through communication between a dispatch office and the vehicle's on-board computer system, and use GPS and/or cellular technology. The VIT evaluation project used information from the FMCSA Operational Test to compile a list of vendors of VIT technologies. As available, companies provided ORNL public information that they had about their products for review. Visits were conducted to selected companies in the United States. In February 2007, six companies demonstrated their products to ORNL and members of the federal government at Michelin North America's Laurens Proving Grounds near Laurens, South Carolina. A test track was used to allow moving vehicles to be shutdown safely in a secured area. Test vehicles were outfitted with sensors to collect kinematics data for evaluation. In March 2007, a workshop was held at the annual Commercial Vehicle Safety Alliance (CVSA) conference in Atlanta, Georgia where the use of VITs was discussed, and an open forum elicited input from attendees. Information collected from these events were used to create a report that contained best practices for hazmat carrier utilization and a concept of operation for law enforcement so that the safety and efficiency of VIT usage can be emphasized. The final report will be sent to Congress for their review and further consideration.

Development of the New AutoCAD Layering Standard. THOMAS MCMILLIN (*Columbia Basin College, Pasco, WA*); SHAUNA ANDERSON (*Pacific Northwest National Laboratory, Richland, WA*). The Engineering and Design Services group of the Facilities and Operations directorate at the Pacific Northwest National Laboratory design and draft their projects on the AutoCAD program that is put out by Autodesk. The need for a standard layering system is critical to stay organized and consistent. Layers are used in AutoCAD to differentiate between types of objects. Most of the drawings that are drafted contain different disciplines in them such as, architectural and electrical. There is a National CAD Standard already developed; however there is an over-abundance of layers that fall outside the scope of what would be used. It was decided to use a modified version of the general layout of the national standard. The research team investigated all of the disciplines that are used at Pacific Northwest National Laboratory. Then layer names were developed in a matrix, using the Microsoft Excel program. After verifying the new matrix, the layer names were transferred into the AutoCAD program. Line types, line weights, and colors were added to the layers. Layers were organized by discipline and systems to be incorporated into drawings as they are needed. After the addition of 744 layers into the program, the comprehensive layering standard was unparallel to any of the standards that were in place. There will now be very little that is drawn which does not have a layer assigned to it. If there is something drawn that does not fit one of the other layer categories, a miscellaneous layer exists. As a living document, the AutoCAD layering scheme can be reviewed and revised when needed. This project not only provides a greater understanding of what goes into an official drawing, it lays a foundation for consistent drawings within the Engineering and Design Services group for many years to come.

Analysis of Interstate Weigh Station Viewer Performance. RAMON COLON MENDOZA (*Florida International University, Miami, FL*)*; DAVID E. HILL* (*Oak Ridge National Laboratory, Oak Ridge, TN*). After the 9-11 attacks, the United States has increased its focus on developing technologies designed to warn us in the event of another attack, and to prevent these attacks from happening. The Sensor Net research group at ORNL is participating in this effort by developing systems to give critical real-time information to federal, state, and local emergency response decision makers. Sensor Net's Southeastern Transportation Corridor Pilot (SETCP) Project utilizes interstate weigh stations not only to weigh the passing trucks but also to check for Gamma and Neutron radiation inside the truck without the aid of a human in close proximity. My role is to characterize and analyze the data from the South Carolina weigh station on I-26W and the Tennessee weigh station on I-40 E. The purpose is to find patterns in the truck traffic as well as to find patterns of inconsistency that the system makes repeatedly. Also I analyze the improvement after the repairs. Inconsistence patterns are found by analyzing the data, looking for missing information, and how often it happens. Traffic Patterns are found by grouping all the data and making graphs and charts that show the flow of the traffic, the kind of truck traffic, the number of alarms, as well as other information. It has been found that Monday, Tuesday, Wednesday, and Thursday the truck traffic is heaviest. Both the component to determine truck length and the component to read each truck's license plate were inaccurate, but have now been fixed as a result of my data analysis.

Dense Ceramic Membranes for Hydrogen Production. *Stephen Menke* (*University of Illinois at Urbana-Champaign, Urbana, IL*)*; U. Balachandran* (*Argonne National Laboratory, Argonne, IL*)*.* It is known that the ceramic compound $SrFeCo_{0.5}O_x$ (SFC2) can be used as an oxygen transport membrane (OTM) to produce hydrogen through water dissociation. The primary challenge for this project was the development of OTMs that transport oxygen at an industrially significant rate. Several factors affect oxygen flux through a membrane including membrane thickness, temperature, and water partial pressure (pH_2O). Previous studies with thick membranes (1.76 ~ 0.21 mm) show that oxygen flux through the membrane increases as membrane thickness decreases. To try and further increase oxygen flux, SFC2 membranes of thickness 20 ~ 30 μm were made. Porous layers made of SFC2 were added on both sides of the membrane to maximize surface reaction kinetics. Membranes were sealed in a reactor assembly to conduct pH_2O dependence measurements as well as compare thickness dependence measurements. A hydrogen production rate of 6.5 cm^3/min-cm^2 was obtained with a thin film membrane at 900°C, 49 vol% H_2O/N_2//80% H_2/He. The hydrogen production rates obtained were similar to previous measurements conducted on a 0.21 mm disk without porous layers. SEM characterization was then performed and indicated differences in the dense layer microstructure when sintered in hydrogen vs. air. Further work should be allotted to better understanding the microstructure of SFC2 as its composition plays an important role in determining the hydrogen production rate.

Analysis of Renewable Energy Deployment in Colorado by 2030. *Russell Muren* (*University of California at Berkeley, Berkeley, CA*)*; Chuck Kutscher* (*National Renewable Energy Laboratory, Golden, CO*)*.* Currently most utilities in the state of Colorado are subject to the 20% renewable portfolio standard (RPS) passed by voters in 2004 and expanded by the state legislature in 2007. However, because of bonuses and exemptions written into the law, the true required renewable energy penetration is only 12.3%. This makes this law less then adequate for addressing climate change. This study aims to assess the real renewable energy and carbon impacts of the current RPS and investigates the benefits of increasing the RPS to true 20% and 30% values. To this end a user input-driven predictive Excel model was developed to find the proper technology spread, electrical outputs, and carbon reduction for each RPS. It was found that while all the RPS variants are technically feasible based on available renewable resources, only the 30% RPS meets the carbon reductions that are thought necessary to avoid the worst impacts of climate change. Based on the results of this report the current RPS does not offer an effective avenue to reduce fossil fuel and carbon reduction. Furthermore, if the goal of the current Colorado legislature and administration is carbon reduction, a 30% RPS is the most acceptable avenue.

Reactants Flow Field Design Optimization For Hydrogen and Direct Methanol Fuel Cells. *Glenn Musano* (*Farmingdale State College, Farmingdale, NY*)*; Devinder Mahajan* (*Brookhaven National Laboratory, Upton, NY*)*.* Fuel cells are considered to be a clean and reliable power source, converting hydrogen to electricity and water by means of a catalyst. The channels' pattern that the reactants flow through, contribute to the overall efficiency of the fuel cell. Graphite fuel cell bipolar plates using the standard flow pattern was considered a reference of comparison for two alternate patterns that operated at 30°C.The alternate flow patterns are newly designed to conserve humidity within the cell, help humidify the cell membrane and maintain efficient power output. Each experimental cell was tested with hydrogen and methanol to determine the pattern with the optimal performance for each fuel. These alternate flow patterns have demonstrated a 20% increase in maximum power output. The pattern with the highest power density will be utilized to build a fourth cell using thermal sprayed aluminum bipolar plates to examine the effect of metallic plates on the cell performance. Thermal sprayed aluminum bipolar plates have been compared to graphite in an earlier work and determined to be more efficient. The success of the new flow pattern will be determined by incorporating it in the future design of a one kW fuel cell system and comparing the output power density of this new metallic fuel cell to the commercially available systems operating with the old flow pattern.

*High-Throughput Protein Crystallography. *Tuyet Nguyen* (*Contra Costa College, San Pablo, CA*)*; Minmin Yu* (*Lawrence Berkeley National Laboratory, Berkley, CA*)*.* Proteins are the building blocks of living cells and control much of the biochemical processes that are important to all life. Different kinds of protein play different roles in the body. Because structure of proteins is essential to understand the natural function of cells, our goal is to identify the structures of the full complement of proteins, using X-ray crystallography. Using the computer system, the diffracted patterns of the protein crystal can be translated into a 3-D structure. The research group focuses mainly in producing protein crystals. Before setting plates to crystallize protein, the first step was to do cloning and purifying protein if necessary. In the process of protein purification, cells were added to lyses buffer sonicated to break the cells. The supernatant, which contained protein of interest, would be obtained after centrifuging the lysate. Later, the supernatant was run through Ni-NTA Chromatography to purify the protein and was done further purification using gel filtration column. After we got purified protein, a crystallization process was obtained using vapor diffusive method with sitting drop. Series of protein solutions were set up in droplet in a 96-well plate and let to crystallize for a certain time. During the time that protein was crystallizing, a close follow up viewing plate was taking place. Then the crystallization condition and crystal viewing results were entered into CLIMS database. We tried to find possible crystallization conditions from initial crystal hits. The initial hits of crystal formation leads to further optimization for obtaining high quality crystal that can give the best result in diffraction. The selective protein crystals were harvested and tested on the synchrotron beam line. Minmin Yu directly did the X-ray crystallography process. The crystals were mostly analyzed with the synchrotron at the Advance Light Source (ALS) of Lawrence Berkeley National Laboratory. Various proteins that are analyzed at this lab are for the Integrated Center Structure and Function Innovation, and TB Structural Genomic Consortium.

Forced Convection Heat Transfer in Cooling Channels Enhanced with Copper Wire-Coil Inserts. *William O'Brien* (*University of Rhode Island, Kingston, RI*)*; Jeff Collins* (*Argonne National Laboratory, Argonne, IL*)*.* Front end high-heat-load components of the insertion devices and bending magnets at the Advanced Photon Source are cooled with deionized (DI) water flowing through channels which have oxygen free copper (OFC) wire-coils inserted into them, enhancing the forced convection heat transfer. The convective heat transfer coefficient within these cooling channels is studied to optimize operational parameters. Data collected is reduced to several empirical relationships and prepared for publication to an international heat and mass transfer audience. Several OFC heat transfer test tubes are used, each with a 0.375 inch approach diameter, made to accommodate the 13.5 inch long OFC wire-coil inserts. A matrix of OFC wire-coil inserts is fabricated in house with wire diameters ranging from 0.035–0.125 inches and different coil pitches ranging from 0.091–1.00 inches. Water is deionized, sterilized, filtered, and sent through a slip stream flow system with circuits designed to test flow rates across laminar, transitional, and fully rough turbulent flow regimes. Flow rate and temperature readings are collected and reduced to dimensionless quantities used to develop forced convection heat transfer empirical equations correlating channel size, wire diameter, wire-coil pitch, mechanical fluid properties, and bulk fluid velocity of the DI water through turbulent flow. The correlation established will provide thermal engineers functions that predict coil pitch and wire size based upon design geometry and heat transfer needs.

Humidity Control Instrumentation: Sensing and Generation. *Obafemi Otelaja* (*Howard University, Washington, DC*); *Lin Yang* (*Brookhaven National Laboratory, Upton, NY*). The hydration level of open samples used in X-ray scattering experiments is changed by varying the relative humidity (RH) in a temperature controlled, aluminum sample chamber. The traditional relative humidity sensors used in these sample chambers usually have a slow response, and they are susceptible to damage at very high RH. The aim of this work is to realize a precise and durable method for humidity control using chilled mirror dew point hygrometer for RH sensing, divided-flow volumetric mix ratio technique for RH generation, and a newly designed temperature controlled and monitored sample chamber. By flowing helium gas, of predetermined flow rate, through a fritted gas dispersion tube into a flask containing temperature controlled water, the wet gas leaving the flask would be saturated at the water temperature. The wet gas is mixed with dry helium, also of predetermined flow rate, and the mixture is maintained at the saturation temperature and flown through the chilled mirror sensor into the sample chamber. From the chilled mirror sensor, we could obtain the dew point temperature, and with a four-wire surface platinum resistance temperature detector (PRTD) placed inside the sample chamber; we could obtain the sample temperature. Hence, we could determine the relative humidity in the sample chamber as a ratio of actual vapor pressure to saturated vapor pressure, since vapor pressure and saturated vapor pressure depend on dew point and sample temperature respectively.

Investigating Further Applications of Electric Power Grid Data Visualization Using GreenGrid Software. *Jeff Otto* (*The University of Idaho, Moscow, ID*)*; Kevin Schneider* (*Pacific Northwest National Laboratory, Richland, WA*). Clear and concise system reports are essential for the proper operation of the nation's electricity infrastructure. The GreenGrid visualization program was developed to give system operators and planning engineers an effective visualization of the nation's electricity infrastructure. Using this program in real-time will allow system operators to detect the presence and location of potential system vulnerabilities. With the existence of potential system vulnerabilities identified, the operators will gain a better situational awareness, be able to reduce the occurrence of blackouts and mitigate their impact when they do occur. While GreenGrid shows promise, it is still in the prototype phase and requires validation. Research was conducted to identify where GreenGrid would be of the most use as a visualization tool. Tests were conducted by comparing the visualization of power system characteristics under both normal and stressed conditions. GreenGrid was ultimately shown to produce distinct visual indications of increased power flow through constrained transmission areas. The evidence produced by this experiment further solidifies GreenGrid's position as a truly novel and useful visualization program.

Effect of Deposition Temperature on the Crystallinity and Resistivity of ZnO Films by Atomic Layer Deposition Using DEZ and H$_2$O. *Victor Oyeyemi* (*Goshen College, Goshen, IN*)*; Jeffrey Elam* (*Argonne National Laboratory, Argonne, IL*). ZnO films were deposited by atomic layer deposition using diethyl zinc (DEZ) and ozone as precursors. The depositions were done at temperatures ranging from 50°C to 350°C, and the effect of the different temperatures on growth rate, film morphology, crystallinity and resistivity characterized. It was found that ZnO exhibits linear growth with respect to the number of ALD cycles, and with a rate that increases with increasing deposition temperature; the rate for the 150°C deposition being 0.6Å/cycle. Surface roughening increases with temperature. Scanning electron microscopy shows grain sizes that get bigger with temperature. Also, there is a ZnO (002) preferred crystal orientation. The film resistivity decreases with growth temperature for temperatures less than 300°C but increase sharply for higher temperatures. The minimum resistivity of 0.04O was recorded for the 250°C film. Measurement of carrier mobility of the films shows a near inverse relationship with resistivity.

A Piping Flow Diagram: Verifying the Nitrogen Supply System for Argonne National Laboratory Building 212. *Sophia Pan* (*Swarthmore College, Swarthmore, PA*)*; Elizabeth Grom* (*Argonne National Laboratory, Argonne, IL*). There is a significant need to maintain accurate records for configuration management of nuclear facilities at Argonne National Laboratory. Building 212 at Argonne National Laboratory contains the Alpha-Gamma Hot Cell Facility that is presently used to handle and process radioactive material. An important aspect of creating safe working conditions is the maintenance of an inert atmosphere within the hot cell, due to the storage of pyrophoric material. This project involves the verification and updating of the system schematic for the existing safety-significant nitrogen supply system piping and valves showing the flow of nitrogen into Building 212 as well as for an H-wing as-built document of the nitrogen storage tanks and vaporizers. The updated nitrogen flow schematic includes drawings of pipe lines, the numbered valve system, which controls the flow of nitrogen gas into the building, and two nitrogen tanks — a main and auxiliary tank — that hold the nitrogen supply. The H-wing as-built includes the two nitrogen tank plan views as well as two detailed elevated views. When the updated schematic and H-wing as-built are approved, they will be added to the Document Control Center archives in Building 214. It is important to keep careful records of system as-built diagrams for routine maintenance, system updates, or in the event of an emergency at the laboratory.

Post Occupancy Evaluation Review of Six Sustainably-Designed Buildings. *Anna Passernig* (*University of California – San Diego, La Jolla, CA*)*; Kim Fowler* (*Pacific Northwest National Laboratory, Richland, WA*). Post occupancy evaluations (POEs) are used to measure the impact of a building compared to a baseline. This report analyzes POE energy and water data for six sustainably-designed government buildings compared to design expectations, and industry standards for energy and water use. A considerable amount of literature is available focused on the design and construction of "sustainably-designed" buildings. With hundreds of buildings in operation and thousands of buildings pursuing sustainable design strategies, investors want to know how well these buildings perform. Sustainable design is integrated design balancing the impacts on cost, the environment, and the occupants. Integrated design incorporates resource-efficient construction, renovation, operation, maintenance,

and demolition. Currently, it is assumed that if a building meets the sustainable design standards, that it will be a "better" building than a "typically" designed building. POE studies offer an opportunity to analyze the performance of these buildings. Although the sample size for this study was limited, it was observed that the sustainably-designed buildings were performing better than "typical" buildings in many cases, and some performed even better than expected. There are many extenuating factors impacting building operations and these factors need to be investigated further before definitive statements can be made. However, with the awareness of the magnitude of impact that buildings have on the environment, designing, constructing, and operating sustainable buildings has the potential of significantly lessening the anthropomorphic environmental impact.

AirMagnet System Installation: Securing and Assuring the Advanced Photon Source Wireless Network. *Marya Pearson* (*Norfolk State University, Norfolk, VA*); *Ken Sidorowicz* (*Argonne National Laboratory, Argonne, IL*). Using a wireless network in a government research enterprise raises concerns of security breaches, signal interference, and internet connectivity. Initially, the wireless network at the Advanced Photon Source (APS) was vulnerable because efficient managing tools were not available. The AirMagnet system, manufactured by AirMagnet Incorporated, is a security software utility which provides a secure overview of the wireless network. New AirMagnet technology detects and reduces wireless vulnerabilities at the APS through a system of monitoring software and spectrum sensors. Following the system's installation on the APS site, spectrum evaluations were conducted to gather information on the network's performance. AirMagnet's survey-planner feature was used to scan the ring and each floor of APS for radio frequency signal data. In response to user complaints of poor internet connection, spectrum analyzer and laptop analyzer were enabled to identify devices that were affecting the wireless signal. The survey-planner's RF signal distribution prompted adjustments to the signal strength and the access point channel allocations. Information gathered using spectrum analyzer and laptop analyzer implicated unknown rogues and channel interference affecting the network. In addition, the programs offered troubleshooting solutions for each alarm. Subsequently, the spectrum evaluations improved the wireless network environment. Using the AirMagnet system as an administrative tool minimized speculation and time-consuming tasks related to network problem-solving.

Air Transport of Commercial Spent Nuclear Fuel (SNF) Assemblies. *Giancarlo Pena* (*Florida International University, Miami, FL*); *Jonathan M. Haire* (*Oak Ridge National Laboratory, Oak Ridge, TN*). The world is experiencing transformations as energy prices increase, and nuclear technology is not an exception. However, the method of transporting spent nuclear fuel (SNF) has not changed in decades. Currently in the U.S., SNF casks are shipped by train, truck, and ship. This work examined the technical feasibility of transporting SNF casks by aircraft. Air transport of research reactor SNF has already occurred between countries because of geographical and political reasons. It is concluded that air transport of commercial spent nuclear power reactor fuel is feasible in the U.S. with as many as 21 fuel assemblies shipped at one time. The major constraint that limits the number of SNF assemblies is the lift weight of the aircraft. This study uses the maximum aircraft payload as 154 tons — the net payload of the Boeing 747-8 air freighter. Existing casks from different private companies were analyzed. Sensitivity analyses were performed for transporting different numbers of SNF assemblies. The smaller the number of SNF casks transported, the lower the cask weight. Shielding analyses were conducted using ORNL computer codes CAPSIZE, SCOPE, and SCALE, the objective when using these codes was to optimize the amount of radiation shielding, while meeting regulatory radiation dose requirements. Impact crash analyses were conducted with CTH code to demonstrate crash compliance regulations. Recently, the U.S Department of Energy (DOE) submitted a license application for a permanent geological repository in Yucca Mountain, Nevada. The cost of air shipments of SNF assemblies to surface storage for SNF at Yucca Mountain is less than the costs of building the proposed railway spur to the Yucca Mountain geologic repository. Nuclear power is essential if the world intends to reduce the levels of greenhouse gases that warm the earth and by adopting this method of transporting SNF, time and costs will be reduced.

Evaluation of Technologies for Protected Asset Management. *Ben Peters* (*Maryville College, Maryville, TN*); *Chris A. Pickett* (*Oak Ridge National Laboratory, Oak Ridge, TN*). Protected asset management is a valuable concept that incorporates rigorous accountability and various layers of security. Both of these aspects

are necessary to create a robust protected asset management system (PAMS). Radio frequency identification (RFID) tags were tested for basic accountability purposes, and seals were tested for asset security. The RFID tag system tested for accountability was based on an IEEE standard called RuBee. The RuBee system uses a low frequency RF-tag, antenna, and reader to aid in locating and tracking assets. Multiple RuBee antenna designs and sizes were tested to determine the best configuration for monitoring assets in a room. The best design appeared to be a single-loop antenna that consisted of three connected coils. To test this configuration tags were placed in the antenna's field to check whether the tag was seen in various positions throughout the room. Preliminary results indicate that this antenna design adequately detects tags throughout the entire area and could possibly be used in the future as a piece of an effective PAMS. The security aspect of a PAMS was tested using Russian rope seals. This seal consists of a seal body, metal connecting rope, and a plastic optical insert that possesses a serial number that is read and stored by an automatic seal identifier. A test group of ten seals was used to determine the ease of use, time for set-up, and overall performance of the seals. These seals were first assembled and attached to a metal storage drum. They were then stored in the automatic seal identifier's memory and checked three times daily. Some design issues with the seal body and plastic optical insert need to be resolved before the seals are actually used in the field. More testing needs to be conducted in order to develop more specific recommendations for the improvement of both systems and to determine their possible uses in protected asset management.

Comparison of Commercial Office Buildings Using the NC3 Database. *Kimberly Petty* (*Washington State University, Pullman WA*)*; Emily Rauch* (*Pacific Northwest National Laboratory, Richland, WA*)*. The effects of global climate change and the significant use of energy in the building sector of the United States has caused huge concern and prompted shifts to more sustainable building practices. In order to track the nations' progress in improving building practices, analysis of current building practices must be done to create a benchmark. The National Commercial Construction Characteristics (NC3) database was formed in 2001 to provide such a benchmark by including building data from construction plans ranging from 1996-2007. Information collected includes general building information, envelope data, heating ventilation and air conditioning (HVAC) data, water heating data, and light fixture data. This information is gathered from design plans out for bid in the United States using the Dodgeview software that enables the user to perform take-offs from construction plans. With the information available in the NC3 database, an analysis comparing old and new office buildings was done to determine changes in the construction industry. Results showed that some changes have occurred within the eleven year time span. Differences were seen in the types of windows, wall and roof frames, water heating and HVAC fuel types, cooling distribution equipment, and lighting technology types. These suggest that the construction industry is starting to incorporate newer technologies and methods that will improve building function, increase energy efficiency, and help protect our natural resources.

Improving Roadway Safety by Implementing Wireless Inspection Systems for Tractor Trailers. *Randall Plate* (*Cedarville University, Cedarville, OH*)*; Gary Capps* (*Oak Ridge National Laboratory, Oak Ridge, TN*)*. According to the Federal Motor Carrier Safety Administration (FMCSA) there were over 144,000 large trucks involved in fatal and non-fatal crashes in 2005. Their Large Truck Crash Causation Study revealed that 56 percent of fatal truck crashes are due to truck-driver error and the majority of vehicle failure-related crashes are due to brake failure. Safety inspections can help prevent such occurrences by identifying drivers who have driven too long or trucks that are unsafe. However, with over 8 million commercial trucks (10,000 lbs. or greater) on U.S. roads today, officials are limited by the lengthy manual inspection process to performing only about 3 million safety inspections per year and see a violation rate of approximately 72 percent. It is estimated that an electronic device that could collect vehicle and driver information electronically and wirelessly transmit this inspection data to the roadside could greatly expedite the inspection process, thereby increasing the number of safety inspections carried out each year to approximately that of weight inspections: about 82 million. The present project is the first of three phases of Oak Ridge National Laboratory's Wireless Roadside Inspection program. It will begin examination of the technical and legal issues surrounding the implementation of a Universal Wireless Inspection System (UWIS), assemble prototype technology, test the functionality of this equipment, and report on the feasibility of implementing such a device in commercial vehicles. This UWIS will be capable of accepting driver input for identification purposes and hours of service recording, as well as information from the vehicle's onboard data bus (J-1708 and/or J-1939) to monitor vehicle status. It will then format this information and transmit it to either the roadside or a patrol car via a pair of wireless transceivers. Software that will be used at the receiving end to collect the data from the transceiver and display it for inspection officials is also currently being developed. FMCSA's Federal Motor Carrier Safety Regulations as well as information gathered from the Tennessee Department of Transportation will guide the development of this technology by providing data set content and operational requirements. Proof of concept testing is scheduled to begin in June of 2007, with a full field operational test to follow in 2008.

*Electricity Market Complex Adaptive System (EMCAS) as a Tool for Teaching Undergraduates about Power Market, Environmental Policies and Renewable Energy. *Angel Reyes, Luis Rodriguez* (*University of Puerto Rico, Mayaguez, PR*)*; Eduardo I. Ortiz-Rivera* (*Argonne National Laboratory, Argonne, IL*)*. Electricity Market Complex Adaptive Systems (EMCAS) is the next generation energy and environmental market simulation tool developed recently by Argonne National Laboratories. EMCAS simulates the behavior of restructured power market participants using an agent-based complex adaptive systems approach. EMCAS provides an agent based framework to capture and investigate the complex interactions between the physical infrastructures and the economic behavior of market participants that are a trademark of the newly emerging markets. As an introduction for the EMCAS software simple cases were studied in order to understand the capabilities of this analytical tool. The eleven node and the central European cases were hypothetical cases in which the main functions of EMCAS were studied. After that, the simple market of Puerto Rico's grid was studied using EMCAS to analyze how the system behaves. Also, the effect of the Hurricane George and the Palo Seco's power plant fire on the system of the Puerto Rico Electric Power Authority was analyzed. Future studies will include the analysis and the development of the system in the next couple of years, the effect of adding new transmission lines in the transmission system and the addition of renewable energy sources in the island's power system. Electricity Market Complex Adaptive Systems (EMCAS) is the next generation energy and environmental market simulation tool developed recently by Argonne National Laboratories. EMCAS simulates the behavior of restructured power market participants using an agent-based complex adaptive systems approach. EMCAS provides an agent based framework to capture and investigate the complex interactions between the physical infrastructures and the economic behavior of market participants that are a trademark of the newly emerging markets. As an introduction for the EMCAS software simple cases were studied in order to understand the capabilities of this analytical tool. The eleven node and the central European cases were hypothetical cases in which the main functions of EMCAS were studied. After that, the simple market of Puerto Rico's grid was studied using EMCAS to analyze how the system behaves. Also, the effect of the Hurricane George and the Palo Seco's power plant fire on the system of the Puerto Rico Electric Power Authority was analyzed. Future studies will include the analysis and the development of the system in the next couple of years, the effect of adding new transmission lines in the transmission system and the addition of renewable energy sources in the island's power system.

Platform for Secure Remote Access to Sensors through an Ethernet Network. *Nathan Rowe* (*University of Tennessee, Knoxville, TN*)*; Chris Pickett* (*Oak Ridge National Laboratory, Oak Ridge, TN*)*. In Nuclear Material Safeguards, sensors are frequently used to verify material attributes during processing, transportation, and storage. The ability to remotely read and configure these sensors, with confidence in the security and accuracy of the transmission would significantly reduce the need for on-site inspections. A compact and secure sensor platform was designed by the student to meet these needs. The sensor platform measures 56 by 24 by 22 mm and provides secure communications, general purpose I/O ports, a dedicated bus for interfacing with various types of sensors, and is fully web enabled. The system is powered over Ethernet, which not only minimizes installation complexity and cost, but also allows the sensors to be distributed away from customary power sources. Support for encryption and authentication protocols at the sensor ensure that the platform is suitable for high security deployments. A compatible Geiger Mueller radiation detector sensor board was also designed by the student to serve as a proof of concept demonstration. The design shows promise for use in many distributed sensor applications. Remaining steps include further testing of the platform, improved end user software, and further development of compatible sensor packages, including a potential radio frequency based design.

Use of Hollow Fiber Membranes in Liquid-liquid Extraction of Ethanol from Corn Fermentation Broth. *Neha Rustagi* (*University of Maryland, College Park, MD*)*; Seth Snyder* (*Argonne National Laboratory, Argonne, IL*)*.* Fermentation of dextrose produced by enzymatic reactions with corn starch is one of the essential steps in ethanol production from corn, and filtration of ethanol from the fermentation broth is subsequently necessary for ethanol recovery. Currently, separation of the ethanol from the fermentation broth is typically accomplished with pervaporation; however, a less energy intensive process that also yields higher ethanol recovery is the use of ionic liquid to perform liquid-liquid extraction of the ethanol in a device known as a membrane contactor. In this project, the use of hydrophobic hollow fiber membranes in a membrane contactor to filter out ethanol and ionic liquid from a fermentation broth is being investigated. The hydrophobicity of the membranes is intended to prevent passage of water and other dissolved materials in the fermentation broth; thus, only the ionic liquid and ethanol should pass, and the ionic liquid will subsequently be removed from the ethanol with distillation. Hollow fiber membranes are expected to yield greater flux than the flat sheet membranes currently in use due to their significant surface area. The flux through the membranes will be assessed by measuring the volume of permeate produced in a given amount of time; ideally, the flow will be around $5.258 * 10^{-8} m^3/s$, which is around 3% of the total influx of fermentation broth into the contactor. The pressure output by the pump in the membrane contactor will be adjusted to help produce this flow. The effectiveness of the membrane as a filter will be assessed by use of high performance liquid chromatography (HPLC) to detect the presence of unwanted substances in the permeate. Ideally, the permeate will only contain the ionic liquid 1-butyl-1-methylpyrrolidinium and ethanol. The membranes to be tested were chosen based on their pore sizes or molecular weight cutoff values. The pores in the membrane should block the passage of bacteria, which is around 5 μm in length and $6 * 10^8$ kilodaltons in weight. The flow rate and ability of the membrane to filter bacteria and fermentation broth out of the feed solution will determine the hollow fiber membrane's effectiveness in the contactor unit.

Well-to-Wheel Analysis of Renewable Fuels in Hybrid and Plug-In Hybrid Vehicles. *Christine Ryan* (*University of Colorado, Boulder, CO*)*; Mathew Thornton* (*National Renewable Energy Laboratory, Golden, CO*)*.* Well-to-Wheel (WTW) analyses have been used for a number of years to understand the energy and environmental impacts of various types of fuel and vehicle systems. As the issues of reducing America's dependence on petroleum and decreasing transportation sector emissions become increasingly important so do WTW analyses on the vehicle and fuel systems of the future in order to understand appropriate pathways. Plug-In Hybrid Electric Vehicle (PHEV) technology and renewable biomass fuels have the potential to significantly reduce the petroleum consumption of the transportation sector and in turn the United States as a whole. Using the Greenhouse gases, Regulated Emissions, and Energy use in Transportation (GREET) model developed by Argonne National Laboratory, WTW analyses were conducted for 12 vehicle/fuel systems. Baseline spark-ignition (SI) and baseline compression-ignition (CI) engines were compared to HEV and PHEV vehicles using various fuels; reformulated gasoline (RFG), low-sulfur diesel (LSD), 20% biodiesel blend (BD20), and 85% ethanol blend (E85). The result of using E85 and B20 shows an over all reduction in the use of fossil fuels, in both HEV and PHEV models when compared to the baseline RFG vehicle, and this reduction is larger when renewable fuels are used. The largest reduction was seen with a HEV vehicle paired with E85 fuel. PHEV vehicles also saw reductions in fossil fuel use, with a PHEV40 reducing the fossil fuel use more when compared to an HEV using RFG fuel. PHEVs have greater petroleum reductions than HEV vehicles with all fuel types used. Emissions from PHEV and HEV models differ as fuels change. The greatest reduction in CO_2 emissions was seen with E85 fuel used in an HEV, with a reduction of 58.7% .

Evaluating the efficacy of mustard (*Sinapis alba*) seed meal as an organic control method for invasive Harding grass. *Gregory Rybka* (*Pennsylvania State University, University Park, PA*)*; Robert Van Buskirk* (*Lawrence Berkeley National Laboratory, Berkley, CA*)*.* Biodiesel is widely viewed as an alternative to fossil-based fuels. The production of oil for biodiesel by pressing mustard seed has been studied and found to be feasible though the process has shown to be uneconomical. White mustard meal (*Sinapis alba*) contains glucosinolates (GLS) which when hydrolyzed break down into toxins to various plants, such as ionic isothyocianate and thyociante. The research reported in this study considers using the remaining mustard seed meal as an organic bioherbicide to control Harding grass, an invasive plant in California. A randomized complete block experimental design was employed in field trials, involving four treatments of mustard meal applied at varying rates of 0.5 t/acre, 1 t/acre, 4 t/acre and 0 t/acre (the control). The treatments were applied to two plots each with 16 subplots, where one plot had above ground (AG) biomass removed prior to application and on the other no removal took place. The subplots were initially characterized by the quantity of Harding grass per unit area, at 20%, 40%, 60% and 80% coverage. On all subplots water was applied exclusively by rainfall and totaled 1.5 inches. After six weeks, the Harding grass was removed and weighed; the water content of the removed grass was measured in order to determine the AG biomass for each subplot. The average AG biomass of all treated plots and that at each application rate were larger than that for their respective control subplots, though using an analysis of variance the data sets were not found to be statistically different. The initial and final measurements of Harding grass were also found to have discrepancies as they were negatively correlated for the control plots, indicating an issue with the use of both area and mass measurements. Due to the lack of statistically significant evidence it is not possible to draw conclusions on the potential of mustard meal as economically supporting mustard seed as a source for alternative fuel.

Applied Material and Energy Evaluation for Biomass Gasification. *Isaac Sachs-Quintana* (*New Mexico Institute of Mining and Technology, Socorro, NM*)*; Calvin Feik* (*National Renewable Energy Laboratory, Golden, CO*)*.* As gasoline prices continue to climb, and the price of corn increases, the thermochemical conversion of lignocellulosic biomass into fuels becomes more economical. Economic modeling is the primary tool for assessing the feasibility of biomass conversion processes. Material and energy balances on experimental data are needed to validate the theoretical economic models. Material and energy balances were performed on a pilot scale biomass gasification plant. The plant's gasifier, thermal cracker, and tar reformer were considered. Usable data was extracted from the pilot plant's data acquisition system. Differentiation and integration were performed to achieve a basis of calculation. Input and output flows were compared, and material and energy closures were executed. The average material closure for the gasifier, thermal cracker, and tar reformer were 74.34% ± 28.77%, 97.71% ± 3.129%, 100.1% ± 15.05%, respectively. The average energy closures for the thermal cracker and the tar reformer are 107.9% and 101.3% respectively. At the moment, an energy closure for the gasifier cannot be determined because of insufficient data. The experimental data for the tar reformer and thermal cracker can readily be used for validating economic models. The gasifier data cannot. Additional tests in the pilot plant are required to obtain more accurate material and energy streams.

Temperature Distribution in a Hydrogen Fuel Cell Stack. *Robert Schulz Jr.* (*State University of New York at Farmingdale College, Farmingdale, NY*)*; Devinder Mahajan* (*Brookhaven National Laboratory, Upton, NY*)*.* With global warming and energy resource shortages continuing to threaten our environment and national economy, fuel cells hold an excellent potential for a clean and reliable source of energy. Hydrogen fuel cells will help maintaining a healthy environment by eliminating harmful emissions and reducing the green house effect. The main objective of this project is to obtain an empirical formula for the relationship between the power output of this stack and the operating internal bipolar plates' temperature. This formula will be utilized in producing an efficient and cost effective design of the power stacks' cooling system. Three different bipolar plates located in the front, middle and end of the fuel cell stack were fitted with five thermocouples to each plate, to monitor the stack temperature in real-time as it operates at various power levels. Lab View, a Data Acquisition System, was connected to these fifteen thermocouples to collect and record the stack's internal temperature. The bipolar plates were fabricated with 40 cm^2 active area and the stack was supplied with hydrogen and air at a stoichiometry value of 3. The current was increased in increments of 0.1 amps and the resulting voltage, power, and 15 thermocouple temperature readings were recorded. This process was continued until the voltage almost dropped to zero. The experimental stack average temperature followed the expected trend and showed steady increase with the applied electric load; however, the fuel cell stack temperature was limited to 80°C to prevent Membrane Electrode Assembly (MEA) damage. In conclusion, the designed cooling system should help maintain a steady state environment for the cell stack. The cooling system will consist of 2 or more electric fans that will help to increase the heat transfer from the cell, reducing the temperature. This process will be used to find the ideal current, voltage, and power levels that will maximize the cell stack's performance while maintaining a relative cooling process of the cell stack.

Plug-in Hybrid Electric Vehicle and Hybrid Electric Vehicle Emissions under FTP and US06 Cycles at High, Ambient, and Low Temperatures. MATTHEW SEIDMAN (*California State Polytechnic University, Pomona, CA*)*; TONY MARKEL (*National Renewable Energy Laboratory, Golden, CO*).* The concept of a Plug-in Hybrid Electric Vehicle (PHEV) is to displace consumption of gasoline by using electricity from the vehicles large battery pack, to power the vehicle as much as possible with minimal engine operation. This paper assesses the PHEV emissions and operation. Currently, testing of vehicle emissions is done using the federal standard FTP4 cycle on a dynamometer at ambient (75°F) temperatures. Research was also completed using the US06 cycle. Furthermore, research was completed at high (95°F) and low (20°F) temperatures. Initial dynamometer testing was performed on a stock Toyota Prius under the standard FTP4 cycle, and the more demanding US06 cycle. Each cycle was run at 95°F, 75°F, and 20°F. The testing was repeated with the same Prius retrofitted with an EnergyCS Plug-in Hybrid Electric system. The results of the testing confirm that the stock Prius meets Super-Ultra Low Emission Vehicle requirements under current testing procedures, while the PHEV Prius under current testing procedures were greater than Super-Ultra Low Emission Vehicle requirements, but still met Ultra Low Emission Vehicle requirements. Research points to the catalyst temperature being a critical factor in meeting emission requirements. Initial engine emissions pass through with minimal conversion until the catalyst is heated to typical operating temperatures of 300–400°C. PHEVs also have trouble maintaining the minimum catalyst temperature throughout the entire test because the engine is turned off when the battery can support the load. It has been observed in both HEVs and PHEVs that the catalyst is intermittently unable to reduce nitrogen oxide emissions, which causes further emission releases. Research needs to be done to combat the initial emission spikes caused by a cold catalyst. Research also needs to be done to improve the reduction of nitrogen oxides by the catalyst system.

AC Losses in YBCO Superconducting Cables. DANIEL SIMS (*Tennessee Technological University, Cookeville, TN*)*; ROBERT DUCKWORTH (*Oak Ridge National Laboratory, Oak Ridge, TN*).* To better supply power to dense urban areas, superconducting power cables are one solution that can accomplish this within existing electrical ductwork. While "first generation" Bi-Sr-Ca-Cu-O (BSCCO) tapes are currently being used in several demonstration cable projects around the world, its cost may limit the market penetration of commercial superconducting cables. As a potential low cost alternative, "second generation" Y-Ba-Cu-O (YBCO) tapes has started to meet and exceed the current-carrying performance of BSCCO tapes with lengths greater than 100 m and could be used in superconducting cables in the near future. AC loss, which is the amount of heat generation of a superconducting cable under ac current, is a critical design parameter since it directly impacts the size of the cryogenic refrigeration system and thus impacts the overall cost. The goal of this project is to make a technical evaluation of current YBCO tape architectures, which are currently being supplied in the United States by American Superconductor (AMSC) and SuperPower (SP). Prototype cables with lengths of 1.25 m and former diameters of 3.81 cm were made from the 4-mm wide YBCO tapes to evaluate the effect of the tape architecture on ac loss. A well-established electrical measurement method and a thermal measurement method were employed to accurately characterize each cable. A finite element model was used to make sure that the heater used in the thermal method was sized appropriately to match the heat generated by the cable. As a measure of the cable performance, the critical current was measured under dc conditions and was found to be 5380 A for the AMSC cable and 4400 A for the SP cable, which agreed well with the single tape critical current for each type of YBCO. With respect to the measured electrical ac loss at 3 kArms, the AMSC cable was 3 W/m, while the SP cable was 6 W/m. While this might indicate some advantage to AMSC YBCO tapes, comparing the ac loss in each cable as a function of the ratio of the peak current to the cable critical current showed the functional dependence of each cable to be similar as the current approached 3 kArms. Comparing the ac loss measurement methods, differences between the thermal and electrical ac loss measurements suggest refinement of the thermometry is needed and is currently under further investigation.

Preliminary form and footprint studies for the integrative design of NREL Research Support Facility. MICHAEL SMITH (*Portland State University, Portland, OR*)*; PAUL TORCELLINI (*National Renewable Energy Laboratory, Golden, CO*).* Commercial buildings currently account for 18% of annual U.S. energy consumption. The U.S. Department of Energy (DOE) has established the goal of achieving market viable commercial zero-energy buildings by 2025. A net zero-energy building

(ZEB) is a building with significantly reduced energy demand through efficiency improvements such that the remaining energy needs can be supplied with onsite renewable technologies. Building design problems are inherently multivariate and multi-objective, encompassing a large number of parameters to consider. Balances must be researched and found to maximize an overall net gain in performance. A whole-building or integrative design approach takes into account the interactions among the subsystems of a building and requires collaboration through interdisciplinary design teams which includes key players throughout the building process. On March 16th, 2007, the DOE approved $73 million to design and construct a new administrative building termed the Research Support Facility (RSF). DOE and NREL view this as an opportunity to create a national showcase how aggressive energy efficiency goals can be achieved. The studies covered in this report are intended to provide recommendations for key players involved in the process of designing the RSF. The studies are focused on early-phase preliminary design decisions. The emphasis is on examining the effects of building form and footprint on the energy performance of a building. This assessment is simulation-based, systems integration analysis using NREL's Opt-E-Plus software based on DOE's EnergyPlus building simulation program to model the energy performance of different options for the RSF. The results are analyzed to develop recommendations for optimal building shapes that take into account trade offs between energy use for heating, cooling and lighting. The recommended floor plate is roughly rectangular with an aspect ratio of 2.5, floor-to-floor height of 12.5 ft, and the longer walls of the building facing north and south. Meeting the RSF's goal of energy use intensity of 25 kBtu/ft^2•yr should be possible as long as typical energy efficient measures are applied, plug loads do not exceed 0.5 W/ft^2, and installed lighting loads are around 0.7 W/ft2.

Revising the Building Combined Heat and Power (BCHP) Screening Tool. RODNEY SMITH (*University of Tennessee, Knoxville, TN*)*; F. ED PIERCE (*Oak Ridge National Laboratory, Oak Ridge, TN*).* The United States Government created the Federal Energy Management Program (FEMP) in order to reduce the electricity consumption of its agencies. One method by which the program meets this goal is development and application of combined heat and power (CHP), or cogeneration, technology. In a typical CHP system, the waste heat from an on-site turbine or engine is recovered and used for heating the surrounding building or area. In order to assess the economic feasibility of this technology, a screening must be performed that simulates the layout and energy usage of a candidate site. ORNL uses a computer program called the BCHP Screening Tool for this purpose. However, the particular version of this software in use at the lab is lacking in its capabilities and appearance. Thus it has been my goal to revise the source code of this program so as to remove as many such deficiencies as possible. The revisions made can be divided into three categories: debugging, reformatting, and upgrading. First, debugging efforts primarily focused on avoiding error messages that were called inappropriately or at inconvenient times, such as when certain pieces of equipment were omitted. Next were reformatting changes, which included revising the system font and layout to something more modern and rearranging objects where space limitations had cut off words or lines. Finally, upgrading changes made the program more user-friendly, such as by allowing single-case simulations and adding additional user-defined parameters. Work is still in progress, as the screening tool is inherently dated by its Visual Basic/FORTRAN architecture. Future developments may include interaction with Excel-based input forms and further modification of the program's appearance.

Effect of Oxygen Annealing on Substrates for Complex Oxide Film Growth. RYAN SMITH (*Case Western Reserve University, Cleveland, OH*)*; HANS CHRISTEN (*Oak Ridge National Laboratory, Oak Ridge, TN*).* In this investigation, the optimum annealing conditions (temperature and atmosphere) yielding atomically flat surfaces on the crystalline material NdGaO$_3$ were examined. This material is used as substrate for thin-film pulsed laser deposition (PLD) of various complex oxide films, including, for example, Yttrium Barium Copper Oxide (YBCO), a high-temperature superconductor (HTSC) based on the perovskite crystal structure. Since their discovery over 20 years ago, HTSCs have been thoroughly investigated because they exhibit superconducting properties (zero resistance) above the boiling point of liquid nitrogen (77 K). Thin films of these materials have shown improved superconducting properties, which are highly dependant on the defect structure of the film. Recently, new complex oxide substrates for YBCO deposition have been investigated, including LSAT ((La,Sr)(Al,Ta)O$_3$) and NdGaO$_3$, because of their similar thermal expansion coefficient, good dielectric properties, and small lattice parameter mismatch with YBCO compared to traditional sapphire

substrates. Such a perovskite substrate with atomically flat terraced surface terminated in regular unit-cell high steps is essential for high quality epitaxial YBCO films with low or controllable defect density and optimal superconducting properties, as well as for other metal-oxide films (ferroelectrics, colossal magnetoresistive (CMR) materials, etc.). Perovskite-type ABO_3 crystals with at least two cation species, like $NdGaO_3$, can terminate in either "A-site" (AO) or "B-site" (BO_2) layers on the crystal surface. Unlike most substrates considered for oxide film growth (e.g., $SrTiO_3$), thermal annealing of NdGaO3 results in an A-site layer termination. Studies of YBCO film deposition have shown that A-site layer termination prevents the segregation of deleterious copper precipitates, and thus such substrates are highly desirable for HTSC growth. Single crystal (001) $NdGaO_3$ substrates were thus annealed in air and oxygen, and the resulting surface morphologies were investigated by atomic force microscopy (AFM). The optimum annealing conditions for annealing were found to be 1100°C for 1 hour in an argon (or other inert gas) atmosphere, although annealing in air yields acceptable results.

Fabrication of an Emergency Shutdown System for a Hydrogen Production System. *Kurt Stuart* (*Monmouth College, Monmouth, IL*); *Greg K. Krumdick* (*Argonne National Laboratory, Argonne, IL*). Hydrogen sulfide (H_2S) gas is a toxic byproduct of the petroleum and mining industry with little to no commercial value. Hydrogen sulfide is considered a broad-spectrum poison that affects the respiratory system. Exposure to levels as little as 100 ppm can lead to eye damage, olfactory nerve paralyzation, and at 500 ppm can lead to pulmonary edema, loss of breathing and death. This experimental process involves the use of high concentrations of H_2S. In order to run experiments safely, a sophisticated emergency shutdown system needed to be designed and fabricated. This system requires sensors for the various gasses used in the process, including H_2S, Sulfur Dioxide, Methane, and Hydrogen as well as alarms and control equipment to automatically shut down the system if a critically toxic gas exceeds a safe limit. The system also monitors airflow throughout the hoods used in this experiment to ensure it is at a level to allow the experiment to be safely conducted. The shutdown system also includes an emergency shutdown button that can be depressed to shut the system down in the case of a general emergency. Currently, the system includes gas sensors for H_2S located in the ventilation ductwork, an airflow sensor, and an emergency shutdown button mounted on the main control panel. This emergency shutdown system demonstrates the high level of safety taken into consideration to protect workers from the hazards of this experiment.

A Networked Control/Data Acquisition System Based on the ColdFire Microprocessor. *Ilya Sukhanov* (*State University of New York at Stony Brook, Stony Brook, NY*); *Edward Kistenev* (*Brookhaven National Laboratory, Upton, NY*). Nose Cone Colorimeter Control (N3C) is a highly dynamic system used for slow data acquisition (DAQ), remote system control, and environmental monitoring. The N3C project utilizes an embedded ColdFire processor with the Quadros real time operating system (RTOS) which acts as a bridge between an array of hardware devices and remote-controlling machines over the TCP/IP network protocol. The requirements of this project were to build a network-capable device to program field-programmable gate array (FPGA) devices such as Xilinx and Altera. While such network-FPGA-programmers are available on the market they all only do one task, our specification called for a way to interface with other buses of the system and DAQ. N3C utilizes the feature rich ColdFire microprocessor which allows for easy access to a number of buses such as I2C, QSPI, UART, JTAG and GPIO. With the help of the N3C client one can quickly develop custom tools to remotely interface with devices via these buses. In the case of the Nose Cone Colorimeter, N3C is used to interface with most of the buses supported by ColdFire, JTAG is utilized for FPGA configuration and the systems slow control, I2C as a bridge to a Dallas 1-Wire bus which in turn is used for environmental monitoring and control, QSPI for slow DAQ read out. The N3C system is controlled via a simple control protocol over TCP and data-stream is transferred over UDP to reduce the network overhead at the cost of reliability. During the course of this project we've optimized Quadros RTOS supplied TCP/IP stack (a modified OpenTCP implementation) for our applications resulting in a ten-fold performance increase. This optimization makes it feasible to use N3C as a slow (2 MBytes/s) DAQ system. For further improvement we plan to implement a compression schema into our DAQ system. While we have only tested compression on a desktop machine the results are promising. Utilizing a variant of Hashemian coding described in the paper entitled "Condensed Table of Huffman coding, a New Approach to Efficient Decoding" by Reza Hashemian, it is possible to compress data just as well as with Huffman coding but decompression requires less memory and time. Built with

flexibility in mind, N3C was developed to work on two versions of the ColdFire processor, the MCF5282 and MCF523x. Such flexibility allows for easy integration of new features and utilization of this system in projects other than the Nose Cone Colorimeter Upgrade.

Development of a Mathematical Model for Intimal Hyperplasia Due to Vascular Injury. *Nathan Summers* (*University of Tennessee, Knoxville, TN*); *Richard Ward* (*Oak Ridge National Laboratory, Oak Ridge, TN*). Intimal hyperplasia (IH) is the thickening of the arterial wall in response to an injury of the blood vessel. IH results from the migration of vascular smooth muscle cells (VSMCs) from the medial to the intimal layer of the blood vessel wall and is believed to be directed by biochemical concentration gradients, a process known as chemotaxis. The primary chemotactic biochemical appears to be platelet-derived growth factor (PDGF) which is produced by platelets adhering to the arterial wall and macrophages invading the intima. The induced migration can be quantified using individual cell tracking or through cell population assays. The parameters for individual cell assays, such as average cell speed and persistence time (the average amount of time the cell takes before it changes direction), can be related mathematically to the parameters of the cell population assays, such as the random motility coefficient (similar to a Brownian diffusion coefficient) and the chemotaxis coefficient (the directed diffusion coefficient). One of the goals of this research was to quantify this relationship using data obtained through literature searches and data obtained from experiments conducted by the Vascular Research Laboratory (VRL) of the University of Tennessee Graduate School of Medicine, Knoxville. However, the needed data from the VRL has not yet been made available, making it impossible to fully quantify the algebraic model for this relationship. It is also believed that the receptors on the cell surface of VSMCs play a key role not only in detecting but also in processing the information from the PDGF biochemical gradient. The second goal of this research was to incorporate VSMC receptor mechanics into a hybrid model (a combination of a discrete model for cellular migration and a continuous model for biochemical diffusion) of VSMC migration driven by chemoattractants. This was accomplished by writing a C++ code modeling the role cell receptors play in the cellular response due to the effect of PDGF. The ultimate goal of this research is to augment a hybrid cell migration model with receptor mechanics to study the possible deleterious affects of balloon angioplasty and the effects of hormone replacement therapy on the outcome of this procedure.

Improving Efficiency of Washington Commercial Buildings. *Danny Taasevigen* (*Montana State University, Bozeman, MT*); *Srinivas Katipamula* (*Pacific Northwest National Laboratory, Richland, WA*). Commercial buildings in Washington are currently the fastest growing electricity-consuming sector using roughly 36 percent of the state's electric energy at a cost of about $1.7 billion annually. As a result of inefficient operations of heating, ventilation, and air conditioning (HVAC) units, experts estimate that about 10 to 30 percent of this energy is wasted. To recover this wasted energy, Battelle has targeted large and small commercial buildings for re-tuning. Large commercial buildings (greater than 100,000 square feet) use sophisticated building automation systems (BASs) to manage a wide range of building equipment. These systems need periodic tuning to ensure maximum efficiency, which HVAC service providers will provide through training from Battelle. Small commercial buildings (less than 50,000 square feet) typically lack sophisticated controls, so Pacific Northwest National Laboratory(PNNL) has developed a low cost, wireless sensing control and conditioning monitoring technology that will be implemented onto these buildings' packaged rooftop units. There were two successful contributions made to the project this summer. First, specified commercial buildings provided past utility bills (March 2006 to February 2007), which allowed recording of past electric energy consumption. Then, with recorded temperature data for the corresponding month, a regression analysis was performed for each building, comparing energy consumption versus temperature. These pre-installation performance models will allow for the calculation of the baseline energy use at the end of the project. Once the buildings are re-tuned by Battelle trained service providers, monitoring will commence for the same time period. This will allow for a comparison with pre-re-tuning data, which will then provide necessary data for a savings analysis. For the small commercial buildings' wireless sensing controls, a mounting technology was designed to hold the sensor secure while attached onto the side of the HVAC unit. These sensors will monitor the unit's performance and alert service providers of maintenance issues that need attention. These contributions aid in the projects' aim at reducing and monitoring energy use in Washington buildings.

Optimization of the Hydrolysis Reaction in the Copper-Chloride Thermochemical Cycle. DAVID TAGLER (*University of Notre Dame, Notre Dame, IN*); MICHELE LEWIS (*Argonne National Laboratory, Argonne, IL*). Several thermochemical cycles, which generate no greenhouse gases, are currently being developed to efficiently produce hydrogen. The copper-chloride (Cu-Cl) thermochemical cycle is exceptionally promising because it has been designed to operate at the relatively low peak temperature of 550°C. This project specifically focuses on the thermal hydrolysis reaction of cupric chloride, $2CuCl_2$ (s) + H_2O (g) → Cu_2OCl_2 (s) + 2HCl (g), from 365°C to 385°C at atmospheric pressure. The goal of this project is to determine the optimum operating conditions (temperature, steam to copper molar ratio, space velocity, and reaction time) to maximize the products of this reaction. Using argon as an inert carrier gas, steam is transported at 100 to 500 ml/min through a 38 cm long vertical reactor tube. $CuCl_2$ samples ranging from 300 to 500 mg are placed in a 13 mm inside-diameter crucible positioned 17.3 cm from the top of the reactor tube. Space velocities range from 10,000 to 75,000 hr^{-1}, reaction times range from 30 to 60 mins, and steam to copper molar ratios range from 17 to 66. Inductively Coupled Plasma-Atomic Emission Spectroscopy (ICP-AES) is used to analyze the solid products of the reaction. Analysis of the results shows that the composition of Cu_2OCl_2 most strongly depends on the space velocity. The mass conversion of $CuCl_2$ to Cu_2OCl_2 was optimized from 50% to about 90%. The decomposition of $CuCl_2$ to CuCl was 8%. Future studies will analyze the effect of varying the bed length to diameter ratio (L/D), sample surface area, reactor design, and transport gas.

Vulnerability Assessment of Earth Dams Subjected to Extreme Loads Using Finite Element Analysis. DONALD TEMPINSON (*Southern Illinois University Carbondale, Carbondale, IL*); NIKOLAOS SIMOS (*Brookhaven National Laboratory, Upton, NY*). A major problem facing earth dams is that their response to seismic loads as well as other high-rate, extreme loads is difficult to assess due to the fact that a lot of the knowledge gained about seismic and other dynamic-type loading has been acquired only recently and after these earth dams were designed and constructed. One of the important areas of concern is slope failure of the embankment that can cause the dam to fail. Also of concern is the possibility of water seepage through the dam, which will weaken the structure over time. The complexity of the seismic loads, the unique geometric and material properties of the dam, and the complicated nature of soils make it difficult to assess a dam's vulnerability. To overcome this obstacle, state of the art computational techniques such as finite element analysis must be utilized to assess the vulnerability of these dams. The use of a general finite element analysis program, such as ANSYS and LS-DYNA, allows the modeling of complex structures and loads. The results from the analysis of these structures can identify possible weaknesses and allow corrective measures to be taken. Due to the sensitive nature of the research being conducted, exact results cannot be shared.

Implementing and Testing a Data Acquisition System for Use with the BigBite Spectrometer. BRENT TERRES (*Old Dominion University, Norfolk, VA*); ROBERT MICHAELS (*Thomas Jefferson National Accelerator Facility, Newport News, VA*). Nuclear physics experimentation relies on particle detectors whose analog signals must be digitized and archived by a data acquisition (DAQ) system. A DAQ system must digitize, format, and store all required data from an experiment so that it can be retrieved later for in depth analysis. At the Jefferson National Accelerator Facility, DAQ systems are implemented using the CEBAF Online Data Acquisition (CODA) system, a set of hardware and software devices developed specifically for nuclear physics experimentation. This project involved the implementation and testing of a new multi-crate DAQ for the BigBite Spectrometer, in Hall A at Jefferson Lab, to be used for a series of experiments to run in 2008. A trigger supervisor, a custom device that coordinates and synchronizes the data, was implemented. Next, deadtime, the time during which the hardware is busy and cannot record data, was minimized for application with the BigBite spectrometer and was found to be consistent with expectation. Finally, an analysis program was created that quickly checked the data for missing or extra hits, verified the synchronization of the data, and measure the deadtime. It was determined that a functioning DAQ system could be built for use with the BigBite spectrometer that would both meet the specification and make use of two design standards for redundancy. Also, it was determined that the DAQ system would be suitable for use with the BigBite Spectrometer. The DAQ system developed meets and exceeds the specifications required by the experiment. A properly functioning DAQ system will provide researchers with a high quantity of precise data when using the BigBite detector.

The Multicomponent Crystallization Analysis of Biodiesel at Cloud Point. KAITLIN THOMASSEN (*State University of New York at Geneseo, Geneseo, NY*); C.R. KRISHNA (*Brookhaven National Laboratory, Upton, NY*). Fatty Acid Methyl Ester (FAME), known as biodiesel, is a renewable fuel source, that when lowered in temperature crystallizes, forming a wax like solid. When compared to petroleum based distillate fuels, biodiesel reaches its cloud point between 20°C to 35°C higher depending upon the source feedstock used for production. Biodiesel is also composed of many components based on the source material from which it is made (vegetable oils such as soy, canola, palm oil etc., waste cooking oil such as yellow grease, and animal lard such as tallow), hence the importance of multicomponent crystallization studies. In order to achieve a deeper understanding of this elevated crystallization temperature, an analysis of the multicomponent crystal size, distribution, and growth rate was needed. Using a laser based optical probe that measures the chord length of particles in a liquid, the crystal size and distribution was measured at cloud point from biodiesel fuel samples derived from various feedstocks. When analyzing the crystal growth rate, it was observed for soy that there was no crystal formation, or nucleation, until cloud point was reached. For tallow however, there was nucleation observed before the cloud point. Once crystal formation occurred, the growth rate was rapid in both fuels. The crystal size distribution was similar to a bell curve, peaking with a maximum particle occurrence of roughly 8 microns. Although maximum crystal size observed was about 250 microns, the majority of crystals fell between the range of 2.5 through 21.5 microns. The agglomeration point was clearly detectable in both fuels. In soy there was a significant crystal count decrease in the 1–5 micron particle range. At this same point the 10–23 micron particle range increased surpassing the 1–5 micron crystal count. In Tallow, this transition was not as sharp. The data that has been gathered applies to several areas of interest in the industry. One of the most pertinent applications is Cold Filter Plugging Point (CFPP). The CFPP is the lowest possible temperature at which fuel can flow through a filter, at a specified flow rate, before the filter is considered clogged. The multicomponent crystallization data can be applied towards CFPP research along with research to develop additives that can improve cold flow properties. Additionally, with this data, it is possible to remove the crystal formation at the agglomeration point through filtration procedures as a means to lower cloud point temperatures. If the solution for cold flow properties of biodiesel can be ascertained, biodiesel would be a viable alternative energy source.

*Design and Implementation of a Sulfur Hexafluoride Gas Transfer System for the Free Electron Laser (FEL) Gun Test Stand. BRIAN TUCKER (*Virginia Tech, Blacksburg, VA*); KEVIN JORDAN (*Thomas Jefferson National Accelerator Facility, Newport News, VA*). Jefferson Laboratory's Free Electron Laser (FEL) program is currently developing a photocathode test gun to benchmark the performance of new gun technology for eventual use in free electron lasers. The gun uses a 500 kV DC high voltage power supply (HVPS) that connects to a high voltage stack held in a pressure vessel. When the HVPS is being used, the vessel is filled with pressurized sulfur hexafluoride (SF_6), a non-toxic, non-flammable gas that suppresses electrical discharges. Because a full vessel of SF_6 costs approximately $4,000, the gas needs to be recycled so that the vessel can be opened without loss of gas. The goal of this project is to develop a system to transfer gas between the pressure vessel and a storage bag without significant loss of gas or contamination. A similar system has been used in the FEL vault for the past eight years. Analyzing the old design revealed ways to improve the gas transfer process. These improvements were used to select the new system's components. Finally, designs were made to fit the system into the Gun Test Stand vault and to mount the components to the wall. The resulting design improves the old system by implementing a more user friendly layout, automating the entire process, and taking advantage of more advanced pumps and valves. Improving the recycling of SF_6 saves time and money, while helping to ensure smooth gun operation and make HVPS maintenance routine. For now, the new system will serve as an important part of the testing process for the photocathode test gun. Eventually, the changes will be used to upgrade the system in the FEL vault.

Updating and Creating New Documentation for the PHENIX Gas Distribution System. JEFFREY TYLER (*Northeastern University, Boston, MA*); DON LYNCH (*Brookhaven National Laboratory, Upton, NY*). The Physics High Energy Nuclear Interaction eXperiment (PHENIX) at Brookhaven National Laboratory (BNL) utilizes an extensive gas distribution system which supplies custom mixed gases to the various subsystems involved in the experiment. In compliance with Department of Energy (DOE) standards, it is important to have accurate and up-to-date documentation on all aspects of this gas system.

The gas system is constantly being updated with new components, gases, and mixing racks, and because of this, it is difficult to keep documentation current. As a state-of-the-art laboratory with over 4,000 annual guest users, safety is of paramount importance and it is imperative to communicate information efficiently. In order to properly document the gas distribution system all current documentation was collected, updated, and organized. This updated documentation includes Microsoft Excel spreadsheets for each gas system which lists information regarding their components, AutoCAD schematic drawings of both the gas pad and the gas mixing house, and a 3D assembly of the gas pad using Autodesk Inventor. These updated documents along with current PHENIX procedures provide a thorough and up-to-date set of documentation for the gas distribution system. This updated system allows for BNL's plethora of guest users to easily navigate through the PHENIX gas system documentation therefore creating a safer and more efficient work environment.

LabView Data Acquisition Programs Applied to Enhance Heat Transfer Experiments. MARIBEL VALDEZ (*Illinois Institute of Technology, Chicago, IL*)*; JEFF COLLINS* (*Argonne National Laboratory, Argonne, IL*). The Advanced Photon Source (APS) X-ray beam at Argonne National Laboratory provides luminous X-rays for diverse scientific experiments. The surface used to stop the beam is made of Glidcop (Aluminum oxide strengthened copper) and it is limited to 300°C and 450 MPa. Currently, the APS wants to increase the intensity of the beam thus two enhanced heat transfer experiments were employed to promote longevity of the beam strike surface. The first experiment tests a method currently implemented in the facility which uses round water-cooling passages containing wire coil inserts. These cooling passages are located above and beneath the beam strike surface and drastically improve convective heat transfer. The second experiment tests a future beam strike surface material, pyrolytic graphite, which has anisotropic properties that will reduce stresses provoked by thermal gradients. To ensure experimental reproducibility and provide an improved user-friendly interface, data acquisition and reduction programs have been implemented using LabVIEW software. This software easily acquires experimental data, reduces the raw data, and calculates non-dimensional coefficients (Prandtl's number Reynolds number, Biot number, Nusselt number and friction factors) needed to produce generalized correlations of the heat transfer process thereby enhancing data representation. Data reduction software provides a module to process and repeat high temperature heat transfer experiments. It will subsequently introduce new experiments to improve the cooling process. The APS beam strike surface is limited by thermo-mechanical design criteria. However, by promoting enhanced heat transfer experiments, safe operation and longevity of the X-ray beam life are promoted.

Development of EnergyPlus Utility to Batch Simulate Building Energy Performance on a National Scale. JAYSON VALENCIA (*University of Washington, Seattle, WA*)*; JAMES DIRKS* (*Pacific Northwest National Laboratory, Richland, WA*). EnergyPlus is a simulation program that requires a large number of details to fully define and model a building. Hundreds or even thousands of lines in a text file are needed to run the EnergyPlus simulation depending on the size of the building. To manually create these files is a time consuming process that would not be practical when trying to create input files for thousands of buildings needed to simulate national building energy performance. To streamline the process needed to create the input files for EnergyPlus, two methods were created to work in conjunction with the National Renewable Energy Laboratory (NREL) Preprocessor; this reduced the hundreds of inputs needed to define a building in EnergyPlus to a small set of high-level parameters. The first method uses Java routines to perform all of the preprocessing on a Windows machine while the second method carries out all of the preprocessing on the Linux cluster by using an in-house built utility called Generalized Parametrics (GPARM). A comma delimited (CSV) input file is created to define the high-level parameters for any number of buildings. Each method then takes this CSV file and uses the data entered for each parameter to populate an extensible markup language (XML) file used by the NREL Preprocessor to automatically prepare EnergyPlus input data files (idf) using automatic building routines and macro templates. Using a Linux utility called "make", the idf files can then be automatically run through the Linux cluster and the desired data from each building can be aggregated into one table to be analyzed. Creating a large number of EnergyPlus input files results in the ability to batch simulate building energy performance and scale the result to national energy consumption estimates.

Spatiotemporal Variability in Soil Radon Fluxes to the Atmosphere. COURTNEY WARD (*California State University – Chico, Chico, CA*)*; MARC FISCHER* (*Lawrence Berkeley National Laboratory, Berkley, CA*). Because of its ubiquitous release on land, radon is often used as a natural tracer of air transport. This study focuses on the use of radon to infer regional-scale fluxes of CO_2 and specifically characterization of the variability in the flux of radon from a wide range of soils. Currently, it is erroneously assumed that radon is independent of space and time, with a uniform flux rate of 1 atom cm^{-2} s^{-1}. A more detailed source term is highly desirable to improve validation of atmospheric transport models since the quality of validation is directly proportional to the quality of the radon source term used. To explore the variability in surface radon flux, measurements were conducted using a closed loop flux chamber and radon specific detector system. Measured radon fluxes ranged from 0.159 to 3.89 atoms cm^{-2} s^{-1}. Soil radon flux was also modeled both analytically and with a transient, finite-element model (Rn3D). Radon fluxes obtained from the numerical model under conditions of purely diffusive transport and a steady state radon flux obtained under conditions of a constant soil pressure gradient were compared to see the effects of different soil properties. Soil properties had strong impacts on both diffusive and advective flux in the model simulations. Simulated soil radon fluxes ranged from 0.106 to 4.46 atoms cm^{-2} s^{-1} depending on the soil moisture, permeability, porosity, radium content, and pressure gradient. Simulated flux rates support the hypothesis of large variability in soil radon fluxes to the atmosphere. These results suggest that in order to accurately estimate regional-scale fluxes of CO_2 one must consider the impacts of soil parameters and incorporate those into the estimated flux rates.

Conversion of Geothermal Silica into Value-Added Nano-Sized Materials. ZHAN HANG YANG (*State University of New York at Stony Brook, Stony Brook, NY*)*; DEVINDER MAHAJAN* (*Brookhaven National Laboratory, Upton, NY*). Geothermal brines store natural heat that can be harnessed to produce thermal and electrical power. Unlike fossil fuels, it is a promising, sustainable natural resource with negligible CO_2, SO_2 and NO_x emissions. The circulating hot fluids below the Earth's surface dissolve minerals and metals like silica, lithium, zinc and manganese from the rocks they travel through. The presence of silica (SiO_2) and other chemicals is a major concern during power production from geothermal brines because it causes scaling and corrosion. The recovery of silica is highly desirable to reduce scaling and to offset the cost of power production. This research project is undertaken to investigate the conversion of silica of high purity into nano-sized, value-added materials such as silicon carbide (SiC) and silicon nitride. Sonication or ultrasound irradiation is employed since this technique is known to produce nanoparticles *in-situ*. The method involves cavitations, and within the cavities high pressures and high temperatures are generated that can be harnessed to drive chemical reactions. A carbonaceous source, dextrose or graphite, was sonicated with silica to yield silicon carbide. The product was characterized by X-ray diffraction (XRD) and Fourier Transform Infrared Spectroscopy (FTIR). The XRD patterns of collected solids suggested the presence of three different polytypes of silicon carbide, along with unreacted starting materials. The FTIR measurements showed the appearances of two new peaks at 1,015 and 815 cm- that are probably due to ν(Si-O-C) and ν(Si-C) stretching, respectively. The vibrations are tentative evidence of silicon carbide formation and possible indicator of the extent of reaction.

LabView Data Acquisition Programs Applied to Enhance Heat Transfer Experiments. PRISCILLA ZELLARCHAFFERS (*Illinois Institute of Technology, Chicago, IL*)*; BHARAT* (*Argonne National Laboratory, Argonne, IL*). The Advanced Photon Source (APS) X-ray beam at Argonne National Laboratory provides luminous X-rays for diverse scientific experiments. The surface used to stop the beam is made of Glidcop (Aluminum oxide strengthened copper) and it is limited to 300°C and 450 MPa. Currently, the APS wants to increase the intensity of the beam thus two enhanced heat transfer experiments were employed to promote longevity of the beam strike surface. The first experiment tests a method currently implemented in the facility which uses round water-cooling passages containing wire coil inserts. These cooling passages are located above and beneath the beam strike surface and drastically improve convective heat transfer. The second experiment tests a future beam strike surface material, pyrolytic graphite, which has anisotropic properties that will reduce stresses provoked by thermal gradients. To ensure experimental reproducibility and provide an improved user-friendly interface, data acquisition and reduction programs have been implemented using LabVIEW software. This software easily acquires experimental data, reduces the raw

data, and calculates non-dimensional coefficients (Prandtl's number Reynolds number, Biot number, Nusselt number and friction factors) needed to produce generalized correlations of the heat transfer process thereby enhancing data representation. Data reduction software provides a module to process and repeat high temperature heat transfer experiments. It will subsequently introduce new experiments to improve the cooling process. The APS beam strike surface is limited by thermo-mechanical design criteria. However, by promoting enhanced heat transfer experiments, safe operation and longevity of the X-ray beam life are promoted.

Environmental Science

An Enclosure Study to Investigate the Causes of the decline of Southern Leopard Frogs (*Rana sphenocephala*) on Long Island. *Duncan Adams* (*Earlham College, Richmond, IN*); *Jeremy Feinberg* (*Brookhaven National Laboratory, Upton, NY*). Around the world amphibian species are declining at unprecedented rates due to a variety of causes. Some, such as habitat loss, are readily observable, while some amphibian declines are not as well understood. The southern leopard frog (*Rana sphenocephala*) is an anuran native to much of the eastern United States, including Long Island, New York. Formerly one of the most visible and abundant frog species on Long Island, it has declined over the last 30 to 50 years to the point that there has not been a confirmed sighting since 1998. This possible extirpation could be due to habitat loss, environmental contamination, disease, invasive vegetation, interspecific competition, or any combination of these factors. In order to test these hypotheses leopard frog tadpoles were used as bio indicators. Leopard frog eggs were collected from southern New Jersey and placed in screen enclosures located in Long Island wetlands. Measurements of the tadpoles will be collected weekly and dead tadpoles tested for disease and toxicity. Tadpole growth and survival rates for the different conditions will indicate the relative importance of competition, disease, and plant community to the leopard frog. In following years similar experiments will be done to test the same and other factors in southern leopard frog decline on Long Island. The use of leopard frog tadpoles as bio-indicators this year and subsequent findings will help to identify possible sites of relic populations, as well as allowing the design of more effective conservation efforts for southern leopard frogs and similar species.

Characterization of the Sunset Semi-Continuous Carbon Aerosol Analyzer. *Jace Bauer* (*Purdue University, West Lafayette, IN*) *Xiao-Ying Yu* (*Pacific Northwest National Laboratory, Richland, WA*). Atmospheric carbonaceous aerosols play a key role in climate forcing and global change. *In-situ* quantification of carbonaceous aerosols is therefore essential to reduce uncertainty in climate change models as well as for long-term monitoring by government agencies. The field deployable Sunset Semi-Continuous Organic Carbon/Elemental Carbon Aerosol Analyzer (Sunset OCEC) utilizes a modified National Institute for Occupational Safety and Health (NIOSH) thermal-optical method to determine total carbon (TC), organic carbon (OC), and elemental carbon (EC). It can provide *in-situ* semi-continuous measurements on an hourly basis; however, its performance is not yet fully characterized. Two collocated Sunset OCECs, identified as 'Unit A' and 'Unit B,' were used to characterize the relative standard deviation (RSD) and limit of detection (LOD) between June 23 and July 9, 2007 in Richland, WA. A high efficiency particulate air (HEPA) filter was utilized to determine the LODs of both instruments. The RSDs between the two Sunset OCECs are 9.1% for TC, 13.0% for optical OC, and 9.0% for thermal OC, indicating good precision between the instruments. In addition, the RSD for thermal EC is 29.0%, while optical EC is 48.3%. The LOD for Unit A is approximately 0.21 µgC/m3 for TC, optical OC, and thermal OC and ~0.004 µgC/m^3 for optical and thermal EC. Similarly, Unit B has an LOD of ~0.29 µgC/m^3 for TC, optical OC, and thermal OC, 0.018 µgC/m^3 for optical EC, and 0.004 µgC/m^3 for thermal EC. Several factors may have contributed to the poor RSDs of thermal and optical EC. First, the low EC mass loading at this location caused uncertainty in the measurements. Second, Unit B EC measurements were affected by a leakage in the oxygen valve. Third, the non-dispersive infrared detector in Unit B displayed excessive "noise," resulting in scattered optical EC measurements, which consequently worsened the comparison between Unit A and Unit B. Improved RSDs of all OC and EC parameters are expected after Unit B is repaired. Future work should reevaluate the precision of the Sunset OCECs and investigate the difference in various thermal-optical protocols on OCEC quantification.

Impacts of Mercury Emissions from Coal-Fired Power Plants in Western Pennsylvania. *Michele Bender* (*Mount Saint Mary College, Newburgh, NY*)*; Carlos Bu* (*Monroe Community College, Rochester, NY*)*; John Heiser, Terry Sullivan* (*Brookhaven National Laboratory, Upton, NY*). Mercury, a neurotoxin, is toxic to humans, especially in the brain, nervous system, kidney, and liver. Power plants are the biggest source of mercury emissions in the United States. When fully implemented by the U.S. Environmental Protection Agency (EPA), the Clean Air Interstate Rule and the Clean Air Mercury Rule will lead to a reduction in mercury emissions from coal-fired power plants by 70% to 15 tons per year by 2018. The EPA estimates that due to these higher restrictions mercury deposition will be reduced 8% on average in the eastern United States. A concern exists that the deposition of mercury near power plants will be much greater than average, leading to a "hot spot" where exposure may be greater than desired. For this study, a "hot spot" is defined as an area no less than four square miles with a mercury concentration higher than the average by one standard deviation. The goal of this study is to determine the effect of three coal-fired power plants on the surrounding environment in western Pennsylvania. During the growing season, oak leaves collect deposited mercury from the power-plant emissions and have a large surface area to collect mercury. The study focused on oak leaves from leaf litter within a five-mile radius of each power plant. Sample collection began with mapping of the area around the power plants to determine easy access locations within circular sampling rings, and collection of oak leaves from the leaf litter at the sampling locations. The samples collected were dried, ground into small particles, and processed using a Direct Mercury Analyzer to calculate the mercury content in the samples. After the results were collected, the data was analyzed to determine if "hot spots" occurred. The results did not indicate a "hot spot" in the region near the power plant. However, the information shows a possible effect of the power plants increasing mercury concentration in a southeast direction, consistent with the prevailing wind pattern. The data shows a possible correlation of elevation increasing deposition, but the data is not conclusive. Therefore, the power plants had little impact on the presence of a "hot spot" on the surrounding area.

Post-Breeding Dispersal and Terrestrial Habitat Use by Woodhouse's Toad (*Bufo woodhousii*) on the Hanford Reach National Monument. *Shannon Blackburn* (*Western Washington University, Bellingham, WA*)*; James Becker* (*Pacific Northwest National Laboratory, Richland, WA*). Anurans serve as key biological indicators of environmental health due to their use of both terrestrial and aquatic habitats and permeable skin. However, knowledge regarding terrestrial habitat use is relatively unknown. The purpose of this study was to evaluate the post-breeding dispersal, aestivation locations, and identify terrestrial habitat use of Woodhouse's toads (*Bufo woodhousii*) at the Hanford Reach National Monument. We used radio-telemetry to track the movements of thirty-two Woodhouse's toads from July 13th–August 20th, 2007 at two pools after cessation of most breeding activity. We found that during late-breeding season and summer aestivation, adult Woodhouse's toads utilize a variety of different environments; temporary and permanent pools, wetlands, and dry upland areas up to 1.12 km away from the breeding site. The observed mean distance, the sum of linear movements between locations, was 479 m and toad movement was not significantly correlated with snout-vent-length (R2=0.0588). The toads were observed burying in fine sand, silts, and clays in exposed areas, underneath vegetation litter, and in small animal burrows. Woodhouse's toads had significantly shorter movements at the pool with a dense community of tall grasses than at the pool with a drier, anthropogenic-modified habitat.

Study of Chloride Mass Balance Preparations. *Chase Bovaird* (*The George Washington University, Washington, DC*)*; Jeff Serne* (*Pacific Northwest National Laboratory, Richland, WA*). Chloride Mass Balance (CMB) is an inexpensive and effective way to estimate groundwater recharge in arid or semi-arid environments. CMB analysis is important to the Hanford Site in its ongoing environmental cleanup efforts, in that estimation of contaminant flow is important to regulators. Past studies have resulted in data that show an increase in chloride concentration when 1:1 water extracts are prepared by oven drying or when the water is allowed a prolonged contact time with the sediment. Using 1:1 water extract method with air dried and oven dried sediments, chloride analyses were performed with an ion-chromatograph mass spectrometer (IC-MS). Analysis with IC-MS was also performed on 1:1 sediment-water extracts after contact times of 1, 3, and 7 days. Expected results, commensurate with assumptions made in CMB analysis should show neither chloride loss from porewater from oven drying sediment nor an increase. Further, there should be no increase

or decrease in chloride concentration in the water extracts with increasing contact time. This project is part of a larger work on CMB and should help in standardizing/optimizing the procedure. Preliminary results show that there are several complications in steps used to obtain the water extract and in the analysis of chloride that are making the application of CMB problematical for Hanford environments where recharge rates are larger than a few mm/yr. Further, the Hanford sediments may be a source or readily leachable chloride during the water extract process that is not present in the actual porewater

Increasing the Accuracy of Global Irradiance Calculations: An Analysis of Responsivities and Correction Methods. *Liza Boyle* (*University of the Pacific, Stockton, CA*)*; Stephen Wilcox* (*National Renewable Energy Laboratory, Golden, CO*)*.* In an effort to make solar radiation data more accurate for solar energy system and climate change research there have been many advances in solar radiometer calibration leading to the creation of several different pyranometer responsivities and correction methods. Here we study the accuracy of four responsivities — "responsivity (45⁰)", "responsivity function", "responsivity (45°) corrected", and "responsivity function corrected" — and three correction methods — "Reda" (which relates directly to the two corrected responsivities), "Dutton", and "Full." Data was gathered from the National Renewable Energy Laboratory and Atmospheric Radiation Measurement program, Southern Great Plains sites, over a two and half year period. The average difference, or deltas, between a reference irradiance, determined from independent direct and diffuse irradiances, and the irradiance calculated from pyranometer data using these different methods was examined. The averages and standard deviations of these deltas indicate the accuracy and precision of the pyranometer data. Analysis of data showed that the "responsivity function" reduced the zenith angle dependence apparent in the "responsivity (45°)", decreasing the overall standard deviation of the deltas from 15.15 W/m^2 to 11.74 W/m^2. Average deltas decreased from 4.40 W/m^2 to 1.46 W/m^2 by using the "responsivity function". Analysis also showed that "responsivity (45°) corrected" slightly decreased the average delta of the "responsivity (45°)" data from 4.40 W/m^2 to 1.56 W/m^2, while keeping the scatter relatively constant, 15.15 W/m^2 to 13.45 W/m^2 respectively. The "responsivity function corrected" slightly increased the average delta of the "responsivity function" data from 1.46 W/m^2 to 1.51 W/m^2, while keeping the scatter relatively constant, 11.74 W/m^2 to 12.31 W/m^2 respectively. When applied to "responsivity (45°)" data, the "Dutton" and the "Full" methods reduced the average delta from 4.40 W/m^2 to 0.23 W/m^2 and 0.97 W/m^2 respectively, but increased scatter from 15.15 W/m^2 to 16.26 W/m^2 and 16.13 W/m^2 respectively. These results indicate that that "responsivity function" and "responsivity function corrected" have the greatest accuracy and least uncertainty. Further studies are needed to understand why the "Dutton" and "Full" methods increase scatter, understand all of the trends revealed in the data, and compare other responsivities and correction methods with those analyzed in this study.

Characterization and Performance of the Zonal Exposure to Broadband RAdiation (ZEBRA) Shadowband. *Sarah Braden* (*Northwestern University, Evanston IL*)*; Daryl Myers* (*National Renewable Energy Laboratory, Golden, CO*)*.* Cost-effective measurement of solar radiation resources is a worldwide problem. The Zonal Exposure to Broadband RAdiation (ZEBRA) shadowband was developed by Michael J. Brooks at the University of KwaZulu-Natal (UKZN) in Durban, South Africa, to reduce the cost of providing widespread data for solar resource assessment and climate change. The shadowband consists of regularly spaced perforations, allowing alternate measurement of diffuse and global radiation throughout the day. A pyranometer equipped with the ZEBRA shadowband is used to independently measure diffuse and global irradiance. Clear sky direct irradiance may be calculated without relying on a moving shadowband or other instruments. With the aid of an absolute cavity radiometer, or other reference pyrheliometer, the ZEBRA can provide shade-unshade calibration for pyranometers. This project characterizes and investigates the accuracy of the ZEBRA shadowband for data acquisition and pyranometer calibration. Data from National Renewable Energy Laboratory (NREL) Solar Radiation Research Laboratory (SRRL) and UKZN was used to develop an algorithm to reconstruct global and diffuse clear sky profiles, test the shade-unshade pyranometer calibration method, derive and verify responsivity values, investigate thermal offset correction, calculate a shadowband correction factor, perform an uncertainty analysis, compare derived and reference data, study site dependence (using experimental results from southern and northern-hemisphere trials), and investigate performance under partly cloudy and overcast conditions. The

combined statistical (2-sigma) and bias calculated uncertainty is about +/- 17 W/m² for diffuse irradiances and +/- 50 W/m² for global and direct irradiances. Comparisons of ZEBRA data with reference data have average empirical uncertainty of approximately +/- 30 W/m² or better for direct estimates, +/- 20 W/m² for global, and +/- 15 W/m² for diffuse. Our results demonstrate that the ZEBRA has the potential for use in mainstream radiation resource assessment as an alternative to multiple expensive instruments. The ZEBRA concept also has the potential to work for other types of radiometers. Further work may include the development of a software package for processing ZEBRA data as discussed here.

*Population Assessment of the New York State Threatened *Enneacanthus obesus* (Banded Sunfish) Conducted in Zeke's Pond and the Peconic River. *Tyra Bunch, Carmen Maldonado* (*Southern University at New Orleans, New Orleans, LA*)*; Tim Green* (*Brookhaven National Laboratory, Upton, NY*)*. Enneacanthus obesus* (Banded sunfish), the smallest species of sunfish inhabiting rivers, lakes, and ponds along the Atlantic coast, has been declared a threatened species in the state of New York. Approximately 200 sunfish were relocated to Zeke's Pond in 2004 during the remediation of the Peconic River, which runs through Brookhaven's property. However, in 2005 a drought nearly eliminated the relocated sunfish population. A population assessment was conducted in the Peconic River, and Zeke's pond, which is found on the eastern most point of Brookhaven's grounds. To capture and assess a sampling of the sunfish population, a seine net, a dip net, a bucket, a measuring tape, a pen, and an all weather writing tablet were utilized. The first step was to complete a survey of the aquatic vegetation by calculating the amount of vegetation in the immediate area that was to be seined. The sunfish were collected from the seine net, stored in the bucket, counted, measured, and then returned safely back to the water. No sunfish were found in the Peconic River. An area of approximately 25,785.5 ft.² was covered in Zeke's Pond during a series of thirteen visits resulting in a total of eighty seines. Final fish counts yielded 369 sunfish, 66 catfish, and 13 pumpkinseeds. The estimated total population is 4,027, which is 4% of the previous study's count of 95,900.Further studies are necessary to document the life cycle and population trends of the Enneacanthus obesus.

*Effects on Soils after Burning Prairie Ecosystem. *Paloma Martina Cuartero* (*Contra Costa College, San Pablo, CA*)*; Margaret Torn* (*Lawrence Berkeley National Laboratory, Berkley, CA*)*.* Soil respiration is one of the many ways C is released in the atmosphere in form of CO_2. And since soils are the largest reservoir of carbon on land, where it accumulates roughly three times compared to that of the aboveground biomass and just about twice that of the atmosphere (Eswaran *et al.* 1993), the smallest change in soil carbon cycling worldwide can lead to major global climate change. Although fire is used to manage prairie ecosystem, wildfire is also a common event with effects on C balance that are not well understood. This study explains how burning affects C balance in the terrestrial ecosystem by comparing the C properties of burned and unburned soils. As expected, the C content of soil is much higher in the top surface soil where decomposition of organic matters occurs. Our data for the unburned soils shows C accumulates over time. However, burning prairie ecosystem allows C to escape from soils (in form of CO_2) causing a change of flux between the soil and the atmosphere. The total C lost is approximately 0.50 kg/m².

Exploration of a Real Options Analysis of the Nuclear Waste Issue. *Benjamin DeJonge* (*State University of New York at Brockport, Brockport, NY*); *David Lepoire* (*Argonne National Laboratory, Argonne, IL*)*.* The question of how to assess energy criteria in a rapidly evolving world economy is nothing new, however it has recently captured more public attention due to changing political and environmental factors. For example, fossil burning power plants emit large amounts of greenhouse gasses. While all energy sources have pros and cons; for example, nuclear power has virtually no carbon emissions, but introduces problems in proliferation, waste (spent nuclear fuel — SNF), and accident issues, various research efforts and strategies have been proposed to reduce these problems. However, these research and environmental issues also require economical analyses to help determine the value of pursuing a particular technological path, such as the development and utilization of a closed-fuel cycle in which SNF is reprocessed and recycled to meet rapidly increasing energy demand while also potentially reducing risks. Real options analysis (ROA) addresses assessment in quickly changing situations with large uncertainties for actions that might be irreversible. ROA is applicable in determining the value of SNF reprocessing because the situation is one in which environmental assessments, technology, regulations, markets, and scientific understanding quickly evolve. An existing ROA based

discrete binomial lattice model on renewable energy was implemented in Microsoft Excel. The model was modified in order to better assess the value of SNF reprocessing with specific parameter values, nuclear growth assumptions, uranium price fluctuations, and various funding scenarios. A ROA value of about $9 billion was calculated, given that the initial price of uranium was 268 $/kg, with a government funding. This value indicates that with the simplified assumptions in this model it would be economically favorable to continue with consideration of reprocessing technologies. The sensitivity to the interest rate, the time to deploy, and the demand for nuclear fuel were investigated. Future work could address the inclusion of: more options (e.g., deploying in multiple phases), environmental costs (e.g., consideration of risk reduction), detailed data on potential plans, and modeling specific research efforts. Given the uncertainty in environmental, economic, and international politics, the U.S. is in a position to seriously consider reprocessing as a potential domestic and international energy source through the GNEP program. This technique could facilitate and communicate these decisions.

Effects of Naturally Occurring Ions on Arsenic Remediation in Bangladesh.
Emily Desley-Bloom (*Contra Costa College, San Pablo, CA*); *Ashok Gadgil* (*Lawrence Berkeley National Laboratory, Berkley, CA*). Bangladeshis have been drinking arsenic contaminated water for over 20 years. Methods involving electrochemistry are being developed to improve the drinking water in Bangladesh. Few comprehensive studies have been performed on the naturally occurring ions found in Bangladesh, but a review of the available literature is essential to understand the potential effect such ions could have on remediation strategies employed in Bangladesh. In the following review, it was determined that phosphate had the greatest potential for interference, but it will not be a problem since the average concentration of phosphate in Bangladesh is less than was in the studies. However, regions with high concentrations of these ions, an increased amount of iron hydroxides may be required to effectively remove arsenic from groundwater. The following report details the effects of various ions on arsenic removal via complexation with iron hydroxides.

Testing Vegetation Sampling Methods of Central Pine Barren Freshwater Wetlands in Preparation of the Wetland Protocol.
Emily Efstration (*University of Delaware, Newark, DE*)*; Ariana Breisch* (*Brookhaven National Laboratory, Upton, NY*). The current health of the freshwater wetlands of the Long Island Central Pine Barrens is unknown. In order to determine the health of the wetlands, a protocol must be established to determine a baseline. The baseline will then aid in monitoring future wetland conditions. Several bioassemblages of the wetland community will be examined because each element has an affect on the overall health of the wetland. Vegetation is an element that plays a major role in determining the health of the wetlands. It is the primary source of energy flow in the wetland ecosystem and forms the foundation of the wetland food chain. No other life forms are able to exist without the presence of vegetation. Plants, both dead and alive, form a structural habitat for many species to live and thrive in. Not only does vegetation affect taxonomic groups, but it also has a major impact on the wetland's water and soil quality. Therefore, vegetation is very important for the survival of the entire wetland community and must be closely monitored. By reading bioassessment case studies of Florida, Michigan, Minnesota, North Dakota, Oregon, Wisconsin and Maryland, different methods for analyzing wetland vegetation were collected and examined. Information on how to carry out various analytical techniques of vegetation was gathered and organized. The techniques that best suited our purpose, along with the necessary equipment, were taken into the Pine Barren Wetlands to be tested. Many different methods for analyzing the wetland vegetation was carried out in and around the wetland ponds of Long Island. The procedures that were the most practical and informative for the wetlands being assessed were noted. Many methods that were tested did not apply to the Pine Barren wetlands being examined because many of the case studies established permanent plots. Since the wetlands being studied will be on public lands, permanent plots were not a viable option. Upon investigating different methods of vegetative analysis, it was found that the case studies were very helpful, but many of the procedures were altered in order to accommodate the ponds being studied. Further investigation must be conducted in order to determine the precise vegetative methods that will be used to examine plants of the freshwater wetlands in the Long Island Pine Barrens.

Energy, Carbon and Climate: Projections to 2025.
Alison Erlenbach (*University of Florida, Gainesville, FL*)*; T.J. Blasing* (*Oak Ridge National Laboratory, Oak Ridge, TN*). Energy demands and associated carbon emissions in the U.S. are expected to increase in the foreseeable future. Policies to reduce fossil-fuel consumption and carbon emissions must consider present and future energy needs, and fuels available to most economically meet those needs, both of which show appreciable inter-regional differences. The National Energy Modeling System (NEMS), a product of the Energy Information Administration of the U.S. Department of Energy, projects this growth based on various economic factors for the country as a whole, and within each of the nine census divisions of the country. In this study, we summarized output from the NEMS for each census division, including projected regional carbon emissions which we calculated based on NEMS-projected energy statistics. To consider climate-change effects on energy demand, we used the results of an earlier study in which a Parallel Climate Model-Integrate BIosphere Simulator (PCM-IBIS) was used to drive the NEMS using different climate change scenarios. Base-case (no climate change) projections show varying increases in energy consumption and carbon emissions for each region, as their populations increase at varying rates. Carbon emissions do not increase proportionately to energy demands, but instead depend on the fuel types each region uses, and is projected to use, as well as the proportion of energy supplied by electricity. Electric generation is inherently an inefficient use of thermal energy; only about one-third of the thermal energy produced can be converted to electricity. The remainder is identified as "electricity-related loss" in the NEMS. Approximately 20% of U.S. carbon dioxide emissions result from this "lost" thermal energy. Effects of simulated climate warming, compared to the base case, were to decrease national energy demand. However, projected carbon emissions increased because reduced carbon from heating was outweighed by the increase in carbon emissions for electricity used for cooling. Regional carbon emissions increased at varying rates, being heavily dependent on the fraction of energy that is electricity and on the fuel types used to generate electricity. Policies to mitigate carbon emissions should consider regional differences in projected demands and in economically available fuels, as well as differences in regional potentials of renewable energy sources and of technologies that reduce wasted thermal energy.

Soil and Water Assessment Tool for a Population Viability Analysis of the Endangered Shortnose Sturgeon (*Acipenser brevirostrum*).
Kendall Ernst (*Stanford University, Stanford, CA*); *Yetta Jager* (*Oak Ridge National Laboratory, Oak Ridge, TN*). The shortnose sturgeon is a federally endangered fish species found in the Ogeechee River System (ORS). Efforts are being made to ensure the persistence and support the expansion of the species; among these efforts is an increased awareness of the affect of land use on sturgeon habitat. The land use on and around the watersheds of a river have a direct impact on the water quality of the river, raising the question of how altering land uses will improve sturgeon chances of persistence. To answer this question, a Population Viability Analysis (PVA), in this case a computer model receiving inputs of water quality and hydrodynamics, will model individual sturgeon and provide information regarding extinction risk over an extended period of time. For the purpose of providing input, three models for the ORS will be implemented using the Water Quality Analysis Simulation Program (WASP), the Environmental Fluid Dynamics Code (EFDC), and the Soil and Water Assessment Tool (SWAT), which are respectively a water quality model, a river hydrodynamics model, and a watershed and water quality model. During the first year of the PVA project, the SWAT model has been most heavily emphasized because of its utility in discriminating among watershed influences on water quality. The EFDC and WASP models will be used later in the project when tidal variations will be considered within the ORS. SWAT requires several types of input to produce results. These are: land cover data, soils data, a digital elevation model (DEM), and stream flow lines. At this point in the project the model has been run, however, the model has not been calibrated. The process of calibration is as follows: the model is run with the current data, the results of the simulation are then compared to real data collected in the field, the input data is altered or upgraded, and the process is repeated until model output closely resembles real data. The ORS runs through a Fort Stewart military base as well as urban development and upstream agriculture. The goal of the model is to differentiate between the water quality contributions of the military base and urban land, as well as experimenting with the alteration of current land uses to see the effects on the water quality of the ORS, and then use each result in the PVA model. The model is part of a three year project, including the acquisition of several more datasets from the ORS through field work.

Effects of Climate Change on the Leaf Gene Expression of Avena barbata in a California Grassland Ecosystem.
Laleh Esmaili (*Gavilan College, Gilroy, CA*)*; Gary L. Andersen* (*Lawrence Berkeley National Laboratory, Berkley, CA*). Global climate changes

are impacting the environmental conditions of many ecosystems. In order to develop an informed understanding of the effects of climatic changes on a grassland ecosystem, a study was conducted to examine plant response to altered rainfall pattern and increase nitrogen availability. *Avena barbata*, an abundant species in many Californian annual grasslands, was grown on natural soil in a climate-controlled greenhouse and submitted to three precipitation treatments (low, ambient and high rainfall) and two levels of nitrogen (ambient and addition of NH_4NO_3). The transcript abundance of three genes of interest (RbcS, GS1 and GS2) was studied in leaf samples collected from *A. barbata* plants at peak physiology. The changes in rainfall patterns did not have a significant effect on the total RNA content from *A. barbata* leaves or leaf gene expression except for GS1. Fertilization of the ambient soil conditions with NH_4NO_3 significantly increased the leaf RNA content and also lead to increased transcript levels for RbcS and GS2. The results suggest that *A. barbata* plants grown under high nitrogen availability respond by changing their gene expression possibly to increase the rate of photosynthesis and growth. This data will be used together with biochemistry and physiology data in a model to predict ecosystem response to climate change.

Relationship Between Water Flowpaths, Water Content, and Particle Size in Partially-Saturated Sediment Samples. *Luxi Fang* (*Furman University, Greenville, SC*); *Melanie Mayes* (*Oak Ridge National Laboratory, Oak Ridge, TN*). The transport and fate of nuclear processing wastes in unsaturated sediments at U.S. Department of Energy's Hanford Site in Richland, WA is of concern due to the proximity of the Columbia River. Intact cores (0.2 m x 0.2 m) were collected to study the effect of sedimentary layering on the hydrologic and geochemical processes controlling contaminant transport. The goal of this project was to study the relationship between water content, particle size, and flowpaths in the cores as inferred using a dye tracer (Brilliant Blue FCF). The dyes are predicted to follow the water flowpaths and to be found in the most conductive flowpaths. Kinetic studies determined the rate of dye interaction with two types of soil samples, Hanford Coarse (HC) and Hanford Dike (HD). We used dye concentrations of up to 5g/L and set them for different equilibration time periods. An isotherm batch study was performed in order to determine the distribution of dye among sediment and solution at different concentrations. Solution samples were analyzed using UV-visible wavelength spectrophotometry in order to quantify dye concentrations. This data was plugged into the convective-dispersive equation to predict the transport of dye through the intact cores and to determine when to dissect the core. We prepared a dye tracer for the dissection of HC and HD cores at the highest concentration (5g/L). We dissembled the cores before any dye was visible in the effluent. The cores were dissected into approximately 9 horizontal layers at 5 different depths, while photographing the appearance of the dye. We found the mass wetness of each sample. Since HD and HC are horizontally-oriented cores where the beds are parallel to the direction of flow, we determined particle size analysis across cores at one depth. The water content and particle size were related to water flow paths as inferred by the presence of the dye. The distribution of dye showed significant preferential water flow and solute transport for both samples, even though HC sample appeared to be homogeneous. For the HD sample that consisted of distinct sand and clay layers, the transport was controlled by visible layering. A relationship between moisture content and preferential flowpaths was found for HC. The finding suggests that the transport of the contaminants in the unsaturated Hanford sediments may be mainly controlled by water content and particle size.

*Vertical Transport in the Urban Atmospheric Dispersion Test. *Ramon Fernandez* (*State University of New York at Stony Brook, Stony Brook, NY*); *John Heiser* (*Brookhaven National Laboratory, Upton, NY*). Part of the Urban Dispersion Program (UDP) is to investigate the behavior of vertical transport of gases around the rooftop of buildings of New York City (NYC). The research emphasis of the vertical transport component focuses on how the regional winds affect the movement and distribution of tracers along NYC's rooftop buildings. To carry out the project, Brookhaven National Laboratory scientists and environmental engineers released six different perfluorocarbon tracers, which are non-toxic harmless gases and have a range sensitivity up to parts per quadrillion (10–15). Air samplers were placed on NYC's rooftops during six intensive operating periods (IOPs) of the field project, which took place during February, 2005. These IOPs generally ran from 7 am until 2 pm of that same day. Data were collected and analyzed to validate tracer movement patterns by comparing the ground level tracer concentrations to the rooftops tracer concentration. As part of the validation process, we compared tracer concentrations as a function of time and distance. We have used tracers that have similar transport

characteristics so that as they follow each other we can have a 3-D model validation.

*Poor litter quality under elevated atmospheric carbon dioxide concentrations reduces aquatic macroinvertebrate colonization of decomposing leaf litter in streams. *Vanessa Garcia* (*California State University – Fresno, Fresno, CA*); *Aimee T. Classen* (*Oak Ridge National Laboratory, Oak Ridge, TN*). Levels of atmospheric CO_2 have increased since the industrial revolution and are expected to continue to rise. Previous work has shown that leaf litter produced by trees grown under elevated levels of atmospheric CO_2 is of lower quality (increased carbon (C) to nitrogen (N) ratios) relative to leaves grown under ambient CO_2 levels. While many studies have focused on how this change in quality may alter terrestrial decomposition, few have investigated how it may alter invertebrate decomposition of leaves in streams. Our objective was to determine whether a decline in leaf litter quality (i.e, an in increase in litter C:N) due to elevated atmospheric $[CO_2]$ would decrease the number of invertebrates that fed on leaf litter in streams. Leaf litter used in this experiment was collected from the Oak Ridge National Laboratory (ORNL) Free Air Carbon Enrichment (FACE) site in early September, 2006 after leaf senescence. Leaf litter from each ring was combined by treatment (ambient or elevated) and placed into mesh decomposition bags. Bags were submerged in a first order stream on the Oak Ridge reservation and removed at five different time periods between January and May 2007. Upon returning to the laboratory, samples were processed to remove litter invertebrates. Results indicate that, over time, there are less aquatic invertebrates on leaves grown under elevated atmospheric $[CO_2]$. These results suggest that stream macroinvertebrates prefer to colonize and feed on leaf litter of higher quality (i.e., litter grown under ambient CO_2 conditions).

A GIS Mapping Inventory of New York's Lake Ontario Ordnance Works for the Benefit of Environmental Decision Making. *Kyla Gregoire* (*Florida State University, Tallahassee, FL*); *Lisa Durham* (*Argonne National Laboratory, Argonne, IL*). Lake Ontario Ordinance Works (LOOW) of Niagara County, New York was, in 1942, home to a trinitrotoluene (TNT) production plant. From 1944 to the early 1950s, the Manhattan Engineering District (MED) used the site to store radioactive residue from the processing of uranium ore. Current remediation efforts, which began in 1970, focus on the implementation of risk-based environmental assessment (RBES) to determine future land use and appropriate clean-up criteria. Discontinuities in technology and the level of detail among the 50 years of LOOW documentation often make it difficult to use and combine the various historical maps, photos, and documents. Such discontinuities can impede the decision-making process for site remediation and closure. To eliminate this remediation obstacle, the ESRI Arc Geographic Information Systems (ArcGIS) program was employed to catalog historic, spatial layers relating to the site. All historic, hard-copy physical map layers such as parcel boundaries, utility lines, and structures were first cataloged in Excel spreadsheets. They were subsequently cross-referenced to the available layers of the electronic record. In this manner, the final GIS inventory will be compiled as a complete replica of the original, hard copy, historic record. Attention was paid to detail such as uniform coordinate systems and the evolution of site layers over 50 years, which ensures consistency and readability among maps. The end product will be a GIS dataset of physical, hydrologic, and ecologic maps related to the site and surrounding area. This product will aid in determining clean-up criteria for the LOOW site media, comparing remedial alternatives, and ultimately designing remediation and site closure strategies. Further, it will communicate remedial efforts and progress among all LOOW stakeholders. Similar GIS cataloging techniques could be employed for remedial decision-making and environmental communication of contaminated sites nationally and globally.

Testing of Nanoporous Niobium Thiophosphates for the Removal of Heavy Metals from Water and Waste Streams. *Kyla Gregoire* (*Florida State University, Tallahassee, FL*); *Dawn Wellman* (*Pacific Northwest National Laboratory, Richland, WA*). Current methods of offshore oil drilling and coal energy production result in waste streams with elevated levels of toxic metals including mercury, lead and cadmium. The ability to efficiently remove these metals from production waters would reduce the risk of bioaccumulation in humans and wildlife. Recent advances in the field of nanotechnology indicate that nanoporous metals are effective sorbents for removing contaminants from aqueous solutions. In this investigation we present the development of nanoporous niobium thiophosphate (NP-NbTPO), and the results of static batch sorption tests to quantify the ability of nanoporous thiophosphates to sequester mercury, lead and cadmium from aqueous solutions. Results demonstrate that nanoporous niobium

thiophosphate materials provide a loading capacity of ~700 mg/g for mercury and Kd values 1.28 x 10^6 mL/g for lead and 1.54 x 10^5 mL/g for cadmium.

Elevated Atmospheric [CO$_2$] Concentrations Do Not Alter Net Nitrogen Mineralization Rates in a [CO$_2$] Enriched Sweetgum Forest. CAITLIN GUTHRIE (*Pomona College, Claremont, CA*)*;* AIMEE T. CLASSEN (*Oak Ridge National Laboratory, Oak Ridge, TN*). Carbon dioxide concentrations ([CO$_2$]) in the atmosphere have increased by 36% in the last 250 years. Previous research has demonstrated that elevated levels of atmospheric [CO$_2$] can increase plant production. However, to maintain an increased level of growth, trees must acquire higher levels of soil nutrients. Thus, nutrient availability might ultimately constrain the response of forests to elevated [CO$_2$]. In particular, nitrogen (N) often limits plant production in terrestrial ecosystems, and understanding how soil N cycling responds to elevated [CO$_2$] in forests will enable scientists to make better predictions of how forests will respond to climatic changes in the future. I took advantage of a long-term experiment at Oak Ridge National Laboratory (ORNL) manipulating atmospheric [CO$_2$] to test the prediction that elevated [CO$_2$] would decrease net N mineralization. Net N mineralization is the amount of N that microbes have transformed from an organic form to an inorganic form that is available to plants (minus the N taken up for use in microbial biosynthesis). The ORNL, Free-Air [CO$_2$] Enrichment (FACE) facility was constructed on a sweetgum plantation planted in 1988. There are five 25-m rings (two elevated rings where the target concentration is 550 ppm CO$_2$, and three ambient rings) and the treatments have been running since 1998. I inserted N mineralization soil cores into each of the rings in June and July, 2007, and let them incubate for 30 days each. Results indicate that there is no difference in net N mineralization rates, net N nitrification rates, or leaching between elevated and ambient plots. However, there was a significant decrease in net N mineralization rates for both treatments from June to July. These results may indicate that increased forest production under elevated [CO$_2$] has not altered the net amount of N available for tree uptake at ORNL FACE. Alternatively, the lack of response to elevated [CO$_2$], and concurrent temporal response could reflect the low levels of precipitation (the third lowest on record since 1895) observed over the course of this study. More work is needed to illuminate the effects of elevated [CO$_2$] on soil N cycling and its effects on forest production at this site.

Estimating Evaporative Transpiration in Wetlands of the San Joaquin Valley. ADAM HALL (*Bowdoin College, Brunswick, ME*)*;* NIGEL QUINN (*Lawrence Berkeley National Laboratory, Berkley, CA*). Since the water resources of Central California are intensively used in agricultural and municipal contexts water resources available for managed wetlands are very limited and must be carefully managed. Modeling patterns of evaporation and transpiration, collectively referred to as ET, is an important step in managing irrigation regimes with the goals of limiting evapo-concentration of salts and maintaining high levels of water quality with the greatest possible water use efficiency. In agricultural systems water needs are often estimated by reference to potential ET (ETo) values, the ET of a well watered pasture plot. ETo data is readily available from weather stations reporting to the California Irrigation Management Information System from locations throughout the state. The relationship between ET and ETo in agricultural systems is well understood. This relationship is less well understood for wetlands because of the complex vegetation and moisture dynamics within these systems. A Bowen Ratio Energy Balance Station was deployed to a wetland near Los Banos to estimate ET using a Bowen Ratio Energy Balance Equation. Micro-meteorological sensors measure incoming and outgoing energy fluxes through air and soil and estimate the latent heat flux of the system, which is proportional to ET. Our estimates of ET are compared to ETo values reported to the CIMIS network. Wetland ET and ETo values do not correlate well. The dynamic nature of wetland plant communities and water resources create more complex patterns of ET than those observed at ETo plots where water resources and plant communities are intentionally held constant. Modeling of wetland ET based on ETo data will must account for seasonal changes in soil moisture and plant community composition and distribution. This research contributes to a larger project of understanding the relationships between irrigation timing, water use, water quality, and plant communities. A variety of methods, including soil salinity surveys and remote sensing estimates of plant community distributions will be integrated to model wetland moisture and plant community dynamics with the aim of improving wetland best management practices and water use efficiency while sustaining valuable wetland habitat.

Linking Microbial Diversity and Geochemistry of Uranium-Contaminated Groundwater. DANIELLE HALL (*University of Michigan – Dearborn, Dearborn, MI*); CHRISTOPHER SCHADT (*Oak Ridge National Laboratory, Oak Ridge, TN*). Microbes control many of the important geochemical processes that occur in the environment. They utilize and produce nutrients that are involved in eutrophication and are even capable of cleansing the environment by degrading a vast variety of chemical compounds. In this study, microbial communities were assessed based on clone libraries of 16S rDNA genes from the Department of Energy Field Research Center. The samples were collected from four different sites (GW-835, GW-836, FW-113-47, and FW-215-49) containing varying levels of pH (3 to 7), nitrate (44 to 23,400 mg/l-1) and uranium (0.73 to 60.36 mg/l-1). Community DNA was extracted by grinding the samples with sterile sand and liquid nitrogen. The resulting DNA was purified then amplified using polymerase chain reaction (PCR) with 16S ribosomal primers. The 16S ribosomal genes were cloned using a PCR 2.1 vector and then transformed in *E. coli* cells. The clones were then screened by PCR and sequenced. The sequence data were analyzed for each clone library using BioEdit, DOTUR, LIBSHUFF, and RDP Classifier. Results indicated that bacterial diversity correlated with the geochemistry of groundwater. Bacterial diversity was highest at the site with a neutral pH and containing the lowest concentrations of nitrate and uranium (GW-836). The diversity decreased with declining pH values and increasing concentrations of nitrate and uranium. This difference reflects not only the diversity measurements and indices of nucleotide sequences but also LIBSHUFF analysis of clone libraries. The clones consisted primarily of sequences closely related to the phylum Proteobacteria, with site FW-113-47 almost exclusively containing this phylum. Firmicutes, Bacteroidetes, and Chloroflexi were also very prevalent bacterial groups in all samples except FW-113-47. The microbial community information gained from this study and previous studies at the site can be used to develop predictive multivariate and Geographical Information System (GIS) based models for microbial populations at the FRC. This will allow for better understanding of what organisms are likely to occur where and when based on geochemistry, and how these relate to bioremediation processes at the site.

*Studying the Soil of an Intentionally Burned Field to Understand More about the Effects of Wildfires and Climate Change on the Carbon. ALFREDO HERNANDEZ (*Contra Costa College, San Pablo, CA*)*;* MARGARET TORN (*Lawrence Berkeley National Laboratory, Berkley, CA*). To learn more about the amount of carbon and nitrogen in 20 different plots taken in El Reno, Oklahoma, and to understand more about the carbon cycle and the involvement of wildfires, especially in the prairie fields of Oklahoma, different cores were taken from the fields and studied by depth. Comparison of carbon to nitrogen ratios of burned and unburned surface soil was one way to approach this question. Since carbon to nitrogen ratios are important for plants and microorganisms in soil, the amount of carbon and nitrogen with depth was also important. The results showed no significant difference in the carbon to nitrogen ratio in comparison of burned and unburned field. The ratio is also similar as you go down with depth in co with depth in comparing all the cores.

Elevated Atmospheric Carbon Dioxide Effects on Agricultural Soil Carbon Using Free-Air Concentration Enrichment. LIZ HOFREITER (*Bradley University, Peoria, IL*)*;* JULIE D. JASTROW (*Argonne National Laboratory, Argonne, IL*). Increasing atmospheric carbon dioxide (CO$_2$) has raised concerns that global climate change will result in adverse consequences including a loss of ecosystem biodiversity. In attempts to offset rising CO$_2$ levels, carbon (C) sequestration potential in agricultural ecosystems is being examined to determine if agricultural soil will act as a sink for future C emissions. This study examined the effects of CO$_2$ enrichment on soil C storage in maize (Zea maize L.) and soybean (Glycine max L.) rotation agro-ecosystems in Champaign, Illinois over a seven year period. Free air concentration enrichment was used to elevate CO$_2$ in four crop rings 70 m in diameter. An identical set-up was established for an additional four control rings held at normal atmospheric CO$_2$ levels. Core samples 25 cm deep were collected from all eight rings and fractionated into particulate organic matter (POM), microaggregates >53 µm, silt, and clay. Microaggregates >53 µm were further fractionated, isolating intra-aggregate POM, silt, and clay. Fractions were dried and processed through the Carlo Erba to find percent C by gas chromatography. The C distribution dropped in all soil fractions in both control and elevated rings by less than 2 mg C/g soil between 2001 (when pre-experiment samples were taken) and 2007. Percent carbon also decreased in all soil rings (control and elevated) ranging from -0.0736% to -0.9905%, with the exception of

ring five (elevated) which increased by 0.0339%. The nominal change of C can be attributed to slow soil organic matter accretion. Although past studies show increases in root biomass in elevated CO_2 rings, only a fraction of C in root biomass is translated to soil organic carbon, resulting in a slight accumulation of soil C, which may take more than 7–10 years to detect. A greater time period is needed before future studies are conducted to compare soil C accumulation to initial 2001 values.

Air Quality Impacts of Gas Appliance Usage. TRANG HUYNH (*DePaul University, Chicago, IL*)*;* BRETT SINGER (*Lawrence Berkeley National Laboratory, Berkley, CA*). Liquefied natural gas (LNG) from the Pacific Rim is being considered for use in Californian homes to supplement domestic natural gas supplies. Because the composition of natural gas varies depending on the origin of the gas supplies and the process of purification used by gas companies, studies are being performed to determine if this new source of natural gas can be introduced safely and efficiently into Californian homes. To determine the health and environmental impacts of LNG, NO_x, CO_2, and CO and fine particle concentrations (below 1×10^7 particles/cm^3) were collected through an exhaust hood and measured using gas and particle analyzers during gas appliance usage. Before LNG fuel sources can be tested, it is necessary to develop a method for determining conditions for optimal appliance performance and minimal particle emissions during appliance usage using current natural gas supplies to compare with future experiments with LNG. Currently, studies are being performed to determine the effect of cleaning ovens on the amount of particles that form during oven usage. The concentration of particles measured during oven usage varied (approximately 1×10^7 to 1×10^4 particles/cm^3) by oven temperature setting and by oven model. Following cleaning, oven particle concentrations decreased by an order of magnitude. These results will be used to develop a standardized method of conditioning appliances and to study gas appliance performance in a range of conditions to compare with future experimental studies using LNG.

Heterogeneity of Aquifer Materials and Spatial Variability in the Carbon Tetrachloride Plume in the 200-West Area, Hanford Site. TAMARA JEPPSON (*Utah State University, Logan, UT*)*;* GEORGE V. LAST (*Pacific Northwest National Laboratory, Richland, WA*). The migration and transformation of groundwater contamination is affected by the physical and chemical heterogeneity of the lithofacies that make up aquifer material. At the 200 West area of Washington State's Hanford Site a plume of carbon tetrachloride (CCl_4) is located in the unconfined aquifer. Remediation of the plume requires accurate models of the subsurface that show the lithofacies and their affect on the migration of CCl_4 in the aquifer. To add detail to previous models a 2.87 km long transect along the eastern part of the 200 West area was chosen. The transect passes through eight wells; the borehole and geophysical logs from these wells were standardize and interpreted to create a geologic cross section showing the depth and continuity of the lithofacies. Depth discrete measurements of the concentration of CCl_4 and chloroform ($CHCl_3$), which forms as a result of the dechlorination of CCl_4, were used to infer the extent of the contaminant plume. The high concentrations of $CHCl_3$ occur in the same areas of the cross section as the high concentrations of CCl_4, their correlation suggests that geochemical reactions maybe causing the dechlorination of the CCl_4. A comparison of the contaminant concentrations and stratigraphy shows that the highest concentrations of the CCl_4 and $CHCl_3$ occur around and are confined by fine grained layers. Within the fine-grained layers the concentration of $CHCl_3$ is higher than it is outside of the layer indicating that reduced zones and iron-containing sediments, needed for the dechlorination of CCl_4, may be present in high amounts in these layers. In the southwest end of the cross section there are high concentrations of CCl_4 and $CHCl_3$ that apparently do not occur near a fine grained layer. This difference implies that there maybe reduced, iron-containing sediments within the coarse-grained layers as well as the fine-grained layers The influence of reduced zones and fine-grained layers on the contaminant plume indicates that improved understanding of the spatial variability of these reactions should improve fate and transport predictions and lead to better remediation decisions.

*Long Island's Interactive Weather Map and Microsoft Excel Data Entry. KATIE JOHNSON (*St. Joseph's College, Patchogue, NY*)*;* JOE LANIER (*State University of New York at Stony Brook, Stony Brook, NY*); VICTOR CASSELLA (*Brookhaven National Laboratory, Upton, NY*). The Long Island Interactive Weather Map was created for all personnel on site at Brookhaven National Laboratory (BNL). The primary purpose of this map is to give employees a place where they can access current weather data from all over Long Island, as well as archival data dating back from the 1940s up to the present day. Throughout weather stations across Long Island, we collected data on temperature, wind speed, direction, gusts, barometric pressure, humidity, and precipitation from old records and entered them into a large Microsoft Excel database. This data is sent via radio waves to a receiver at BNL, collected and stored as an ASCII string, fed into a MySQL database, and updated on the meteorological website once a minute. We have created a web page using the following languages: PHP, SQL, JavaScript, and HTML. This page has an image of Long Island and displays all of the towns with BNL's current weather stations. When a user hovers over any of the towns or stations, a small pop-up box appears and the current data is displayed for that town. At the bottom of the box, a link for further archive data is available for that town or station. The user can navigate through the data to get what is needed. Never before has there been such an easy, all-in-one design that has allowed users to see current and archival weather data on BNL's meteorological website. Throughout this project, the majority of the BNL weather acquisition system has been reconfigured and available to the BNL staff.

Improving Efficiency of Storage Gas Water Heaters. DEREK KING (*Laney College, Oakland, CA*)*;* JIM LUTZ (*Lawrence Berkeley National Laboratory, Berkley, CA*). The energy required for water heating accounts for approximately 25% of national residential natural gas consumption. In California that figure is closer to 40%. With water heating using such a substantial portion of valuable natural gas resources, water heating appliance efficiencies deserve some scrutiny. What is referred to as "standby losses" are addressed in this study. Typical storage gas water heaters have a flue for combustion exhaust located along the center of the storage tank. When the burner is inactive, ambient air flows through the flue. The cooler air absorbs heat from the storage tank and rises out of the exhaust vent. Fresh air is drawn in through openings at the base of the heater. This cycle continues until the stored water falls below the preset maintenance temperature and the burner is activated. Consequently, more fuel must be spent to maintain a store of hot water to keep up with the standby losses. Several alternative designs have been proposed to address this energy loss mechanism and remain competitively priced for consumers. The Department of Energy's 24 hour efficiency test will be used to compare performance of an off-the-shelf storage gas water heater and the alternative prototypes. The prototypes that demonstrate an improvement in heating efficiency could then be further developed for the consumer market.

The Application of Surface Enhanced Raman Scattering (SERS) to Pollen Identification. BRADLEY LANDGRAF (*Allegheny College, Meadville, PA*)*;* MENG-DAWN CHENG (*Oak Ridge National Laboratory, Oak Ridge, TN*). The current method of pollen identification — collecting pollen grains on filters, examining each grain with a microscope, and comparing the grain with a reference — is a timely and tedious process in need of modernization. Raman spectroscopy can be used to identify pollen species, but this method suffers from a low signal strength that can make identification difficult. To address this low signal, a technique known as Surface Enhanced Raman Scattering (SERS) was developed. SERS involves the adsorption of nanometallic particles or surfaces (silver, gold, or copper) to analyte molecules. While SERS has been used to identify a number of biomolecules, little work has implemented SERS in pollen identification. Accordingly, this study focused on finding a synthesis and adsorption method that yielded the most effective signal enhancing silver nanoparticles. The syntheses involved the reduction of silver nitrate ($AgNO_3$) with either sodium citrate ($Na_3C_6H_5O_7$) or sodium borohydride ($NaBH_4$) to yield elemental silver (Ag_0) nanoparticles. Several techniques were used to adsorb the nanoparticles to the pollen grains, such as air-drying and aerosolization. The pollen grains of interest were from three species of plants — common ragweed (*Ambrosia artemisiifolia*), eastern white pine (*Pinus strobus*), and smooth tag alder (*Alnus incana ssp. rugosa*) — indigenous to the eastern U.S. and known for their allergenicity. Spectra for each pollen species were obtained and compared to Raman spectra taken without SERS to see which synthesis and adsorption method provided the best Raman signal enhancement. The $NaBH_4$-synthesized silver applied by aerosolization produced the best spectra by eliminating some of the background noise associated with Raman spectroscopy, however, no significant enhancement occurred with either synthesis. Aerosolizing the silver colloid was the most effective application method, as all other means of application caused too much silver to be adsorbed to the pollen grains. Future research involving alternative silver nanoparticles syntheses, whether or not gold or copper may be more effective, and the mechanization of aerosol application to the pollen should be completed, as SERS is a technique that could

play an integral role in developing an analytical instrument capable of identifying pollen grains *in situ* and in real time.

*Redesign of the Personal Air Sample (PAS). Miguel Lopez (*State University of New York at Stony Brook, Stony Brook, NY*); Damoon Moin (*Sacramento City College, Sacramento, CA*); John Heiser (*Brookhaven National Laboratory, Upton, NY*). The Personal Air Sampler (PAS), a versatile air-sampling instrument used to identify many chemical particulates, is used at Brookhaven National Lab (BNL) to capture Perflurocarbon Tracer Samples (PFT). PFTs, along with the PAS, are used for personal dose assessment studies, atmospheric dispersion studies and nuclear control room infiltration measurements. The first PAS was a pocket-sized air sampling unit which held a Capillary Adsorbent Tracer Sampler (CATS) tube for sampling tracers. The pump flow rate for the older unit was set via a variable resistor and using an external flow meter. In the field the pump flow rate proved to be unstable and varied greatly. This instability in the flow rate resulted in the air volume sampled being highly varied from sample to sample. A secondary tracer analysis was required to determine the sample volume and this result in much greater analytical expense, time delays and greater uncertainties in the data. A new design for the PAS was developed that allows control of the pump flow rate via mass flow determination. In addition to the mass flow measurement component, the new PAS uses a programmable micro-computer (ATMEGA128L) to control the pump speed, allow programmability of flow rate, sample time, data logging and to display the PAS parameters (pump flow rate, battery power, and temperature inside the unit) on a liquid crystal display. Programming is accomplished using a personal computer and a mini-USB interface connection. One additional feature of the new PAS is a sensor that tells the main computer when the CATS is inserted or removed. We are in the process of building and testing these new devices. The new design will allow us to get more accurate data with better QA/QC management and are a major upgrade to the old units.

Analysis of Meteorological Observations Over the Former USSR, 1950–2000. Garrett Marino (*Massachusetts Institute of Technology, Cambridge, MA*); Dale P. Kaiser (*Oak Ridge National Laboratory, Oak Ridge, TN*). Climate change studies require the processing and analysis of large compilations of meteorological data. Past studies investigated trends in meteorological variables over the former Soviet Union using data from a 223-station network spanning 1936–1990. A newly-acquired update to the database includes data through 2000. The database has been made available through cooperation between the two principal climate data centers of the United States and the former Soviet Union: the National Climatic Data Center, in Asheville, North Carolina and the All-Russian Research Institute of Hydrometeorological Information — World Data Centre in Obninsk, Russia. Station records consist of 6- and 3-hourly observations of 25 meteorological variables including temperature, precipitation, cloud amount and type, pressure, humidity, and wind speed and direction. The 6-hourly observations extend from 1936 through 1965; 3-hourly observations extend from 1966 through 2000. To ensure high data quality, extensive quality assurance (QA) checks examined the data for completeness, reasonableness, and accuracy. We found significant gaps in some records from observational gaps or measurement values deemed erroneous. Also, World War II and the breakup of the Soviet Union affected some records' completeness. Therefore, this analysis examined the period 1950–2000 for 125 stations. Total and low cloud amount, frequencies of various cloud types, and air temperature were all extracted from the dataset and plotted by station to assess variability and any long-term trends. The results showed that trends found by previous researchers using data through 1990 have continued through 2000. Total cloud cover significantly increased (95% confidence level) at 0.2%/decade despite a significant decrease in low cloud cover of 1.1%/dec. Meanwhile, low level stratiform clouds significantly decreased by 1.6%/dec and cumulus clouds significantly increased at 1.4%/dec. Stratiform clouds are associated with atmospheric stability and frontal passages. A warmer planet and the resultant reduction of both the meridional temperature gradient and atmospheric stability may be causing these cloud trends. Air temperature did exhibit a significant increase of 0.2°C/dec. The Russian database represents a wealth of meteorological information for a large and climatologically important portion of the earth's land area, and should prove useful for a wide variety of additional regional climate change studies.

Sediment Phosphate Desorption Kinetics. Jolene Mattson (*Laney College, Oakland, CA*); Willliam Stringfellow (*Lawrence Berkeley National Laboratory, Berkley, CA*). Phosphate, as a main component in fertilizer, is heavily used in the Central Valley farmlands of California. Phosphate can negatively impact aquatic ecosystems such as the

San Joaquin River (SJR), by stimulating elevated algal growth. This study sought to determine if suspended and bed sediments could act as a significant source of phosphate to the SJR watershed. It was hypothesized that agriculturally derived sediments would have high desorption rates, and reach equilibrium in 24 hours. Rapid equilibrium is required for sediment to act as nutrient reservoirs for algae growth since algae grow with a doubling time of less than 24 hours in the SJR. Sediment samples were collected from two sources: Ramona Lake, an open surface freshwater wetland which receives agricultural sediment, and the San Luis Drain (SLD), a major drainage for irrigation runoff in the SJR valley. Two studies were conducted examining desorption of phosphate from these sediments in simplified water-sediment flux environmental models. Water samples were collected, filtered, and analyzed according to the Ascorbic Acid method using a UV/VIS spectrometer. Sediment mass desorption rates under mixed, aerobic conditions indicative of suspended sediments, were not rapid, 39.4 and 16.0<µ>g PO_4-P/kg dry sed/hour for Ramona Lake and SLD respectively. The time required to reach equilibrium was longer than the hypothesized length of 24 hours. At high sediment water ratios equilibrium was not reached until after 400 hours. In an attempt to reach equilibrium more rapidly, the second aerobic experiment was run with sediments at lower concentrations, and aqueous phosphate concentrations reached equilibrium with sediments only after 250 hours. Ramona Lake sediments again showed a faster average mass desorption rate than SLD sediments, with averages being 54.3 and 10.3<µ>g PO_4-P/kg dry sed/hour respectively. The differences between sediment mass desorption rates could be variation of total phosphate and organic carbon contained in the two sediments and are under investigation. Under anoxic, layered conditions, indicative of bed sediments, Ramona Lake sediments had good initial desorption reproducibility. Initial area desorption rates showed significant desorption of phosphate, averaging 19.8mg PO_4-P/m^2hour. Results of this study indicate that sediments serve as a reservoir for phosphate, but rates of desorption are lower than expected, and will not support exponential algal growth at high biomass densities.

Educating Communities of Industrial Contaminants and Health Effects. Margaret McKie (*Loyola College in Maryland, Baltimore, MD*); Margaret MacDonell (*Argonne National Laboratory, Argonne, IL*). An overall project of educating communities on safe contaminant levels and health effects concerning these contaminants is being realized through two different applications. The Research Institute of Industrial Science and Technology (RIST) in South Korea has requested the occupational and health-related toxicity values and key health effects of a list of more than 50 contaminants released into the air during the steel making process, to compare with the current output of these chemicals from a local steel company. Toxicity values from governmental and other scientific agencies were compiled into tables. These tables will serve as a foundation for a database for the communities, making them easily accessible by the responsible industry managers and the community, and other agencies in the future. The toxicity values will give the company a mark to measure their own values against, to see if they are within a safe range and to prioritize their future pollution mitigation plans. Another application of this project that puts knowledge of toxicity values into use concerns mercury and other chemicals used in the gold mining process. The purpose of this project is to educate gold shop owners and local artisans of the dangers when working with mercury and cyanide when producing gold. A prototype of a website was started to get the information to local people via teachers and trainers. The goal of this program is to develop health based information and facilitate training through easy to understand lessons. Outlines of chemical fact sheets that address mercury and cyanide have been created so that employers and the community can have a quick reference for the health effects of these chemicals. Nearly 20 resources used to create the fact sheets and website were put into a matrix delineating the most prominent topic and key content, so readers can navigate through the literature more easily. A business plan was outlined in order to support the wider use of mercury retorts to reduce airborne releases throughout the world of small gold mining. Through the education of workers and employers the Environmental Protection Agency hopes to create a safer working and living environment in these regions. Both applications have similar goals which are to notify communities of the toxicity and possible health effects of contaminants in the air and water, so educated decisions concerning health and the environment can be made.

*Measurement of Aerosol Absorption Using Photothermal Interferometry: Folded Jamin Interferometer. William McMahon (*SCCC, Selden, NY*); Arthur Sedlacek (*Brookhaven National*

Laboratory, Upton, NY). While the role of greenhouse gases (GHG) on global climate change is well understood the contribution of aerosols to climate change is much more uncertain. For example, depending upon their optical properties, aerosols can either offset GHG effects (through scattering) or contribute to global warming (through absorption). As a result, there is a need for improved measurements that will better quantify the role of aerosols on our climate. The Photothermal Interferometer (PTI) is an instrument designed to measure aerosol absorption. In its present configuration the PTI measures aerosol absorption at one wavelength incorporating a Lock-In Amplifier in a Phase Sensitive Detection (PSD) technique. However, climate modelers require aerosol absorption data at several wavelengths, in which case an LIA would need to be dedicated to each wavelength. To meet this requirement upgrades to the control and data acquisition system of the PTI unit must be made. Specifically, using an Analog to Digital Converter (ADC) card combined with the Fast Fourier Transform (FFT) technique several wavelengths can be separated and analyzed simultaneously. This FFT technique would replace the PSD technique eliminating the need for multiple LIA's. Preliminary measurements verified 1) A strong correlation between the LIA and FFT techniques, and 2) The linear response of PTI signal to concentration of absorbing gas.

Just in Time Data Retrieval Using Python. ELVIRA MEZA (*City University of Seattle, Bellevue, WA*); LANCE VAIL (*Pacific Northwest National Laboratory, Richland, WA*). Vail and Skaggs (2002) describe the conceptual design of a system to improve natural resources management in the Columbia River Basin. A key feature of this proposed system is the need to access data from distributed servers on a "just in time" basis. This capability is essential to ensure that the system's ability to fulfill the system's requirements related to accountability, accessibility, and adaptability are achieved. The system is composed of toolboxes related to decision support, model management, and data management. The functionality of the data management toolbox requires a reliable and flexible capability to for distributed data management. The project described herein was to evaluate the utility of the Python programming language to develop tools for a wide range of platforms that can perform the "just in time" data access and filtering.

Simulating Land Competition for Biomass Energy, Forestry and Agriculture:G-FALUM, Global Forestry and Agricultural Land Use Model. ZHENG MI (*Colorado College, Colorado Springs, CO*); ANTHONY KING (*Oak Ridge National Laboratory, Oak Ridge, TN*). This research addresses the competition for land to simultaneously satisfy growing biomass energy, forestry and agricultural demands as part of sustainable energy and carbon management strategies within the context of CarMan, a global carbon management analysis model. A review of existing land use models (FASOM, AgLU and KLUM) identified insufficiencies for addressing biomass energy land-use in CarMan. In response we developed a new Global Forestry and Agricultural Land-Use Model, G-FALUM. G-FALUM is designed to simulate the competition for land from biomass energy, forestry and agricultural production over a period of 100 years. Numerical optimization methods in Mathematica are used to model the virtual land owners' decisions to allocate land to different forestry and agricultural products. It allows plants used as biomass feedstock for renewable energy production to be included in either/both forestry and agricultural product lists, so that biomass energy production directly competes for land with other forestry and agricultural products based on their varied profitability. Three different scenarios were designed to test the land allocation component of G-FALUM. The first scenario demonstrates that the model properly simulates decreasing return to land scale and can avoid the problem of devoting all the land to a single monoculture of most profitable product. The second and the third scenarios assign a high yield to pulpwood biomass feedstock (poplar, willow) that competes for land with a low yield forestry product (natural forest), a medium yield agricultural product (potato) and the option of idling the land (not planting anything). The model rationally favors the high yield pulpwood by allocating more land for this use, and assigning significantly less land to the rest of possible land uses. When the simulation starts with a skewed land use allocation that devotes all the land to pulpwood plantation (scenario 2), the model's virtual land owner develops this monoculture forest into a land with 69.9% pulpwood, 1.4% potato and 28.7% of natural forest land in 15 time steps (time step unit is a year). Beginning at the 8th time step, the land share converges towards the stable share in the 15th time step with an error of 1%. In the third scenario, the model starts with a monoculture of potato. After 25 time steps, the virtual land owner

develops the land into 70.0% pulpwood, 1.4% potato and 28.6% natural forest land.

Using Macroinvertebrates as Biological Indicators of Selenium Contamination at the Monticello Mill Tailings Site, Utah. BEN MILLER (*Birmingham-Southern College, Birmingham, AL*); ROBIN DURHAM (*Pacific Northwest National Laboratory, Richland, WA*). Following the removal of mill tailings at the Monticello Mill Tailings Site (MMTS) in Utah, selenium has become a contaminant of concern, and has the potential to bioaccumulate throughout the food web. During remediation efforts at the MMTS, all waste, or tailings, remaining from the milling process was transported offsite. Mitigation activities after the excavation of tailings included establishing a series of wetlands along Montezuma Creek. During the excavation process, a layer of seleniferous shale was exposed, causing selenium (Se) to leach into these wetlands. As with any micronutrient, excess concentrations of Se are toxic to biological systems. At the MMTS, Se concentrations now exceed ecological risk guidelines as reported by the U.S. Department of Energy (DOE) and the U.S. Fish and Wildlife Service (FWS). Of particular concern are the area's migratory birds. Because they are at the highest trophic level, bioaccumulation of Se in their prey — aquatic macroinvertebrates — is magnified in the birds. Aquatic macroinvertebrates were collected in May 2007 using kick nets in Wetland 3 and the sediment pond, two areas at the MMTS shown in past studies to have elevated levels of Se. Hester-Dendy artificial substrate samplers were also deployed in the sediment pond to obtain a representative sample of macroinvertebrates. Macroinvertebrates were characterized based on feeding groups, and then analyzed for total Se using hydride generation flow injection atomic absorption spectroscopy. The Se accumulated in the macroinvertebrates, as well as the Se monitored in sediment and water samples, was compared to ecological risk guidelines. The probable oxidation state of the dominant species of Se was extrapolated through modeling on The Geochemist's Workbench 6.0 (GWB). Results indicate that total Se concentration in macroinvertebrate tissues sampled in 2005 and 2006 exceeds ecological risk guidelines set by FWS. In addition, GWB6.0 modeling suggests that the dominant oxidation state of Se present is selenite, a particularly mobile inorganic species, making a compelling case for the reassessment of mitigation strategies at the MMTS. Results for 2007 are forthcoming.

Effects of Radiotransmitters on Woodhouse's Toad. BROCK MILLER (*Washington State University, Pullman, WA*); JAMES BECKER (*Pacific Northwest National Laboratory, Richland, WA*). Radio telemetry is being used to study the post-breeding dispersal and home range of woodhouse's toad (*Bufo woodhousii*) on the Hanford Reach in southeastern Washington. However, little is actually known about whether transmitters attached to anurans affect their mobility and ability to avoid predation. Most studies assume that attaching transmitters causes little to no effect on anuran behaviors. We conducted an experiment designed to determine if the attachment of radio transmitters on anurans affects their ability to successfully bury in loose soil. Experiments were conducted using Woodhouse's toads collected at night. Timed tests were conducted of individual toads burying under controlled conditions during daylight hours of the following day. Three treatments were assigned to each toad consisting of the transmitter positioned, 1) on the posterior and 2) on the anterior side of the individual, and 3) with a control where no transmitter was attached. Results indicated that the capability of the toads to bury and the amount of time spent burying were not different with and without transmitters. In this experiment transmitters that were less than 10% of the toad's total biomass appeared to have no negative effects on burying ability.

Response of N Metabolism in Aspen Grown at Elevated Atmospheric Carbon Dioxide under Fully Open-Air Field Conditions. CRYSTAL MILNE (*Walla Walla College, College Place, WA*); ALISTAIR ROGERS (*Brookhaven National Laboratory, Upton, NY*). Atmospheric carbon dioxide levels ([CO_2]) have risen substantially since the beginning of the industrial revolution, and are projected to continue to rise in this century. Since CO_2 is the carbon source for photosynthetic organisms, understanding the effects of sustained elevated [CO_2] is critical to predicting the future of biological ecosystems and agricultural crops. Although the availability of more carbon increases photosynthesis, plant growth requires a complex C:N balance and may be limited by the accessible nitrogen supply. As a result of initial increased growth and, therefore, increased nitrogen assimilation, nitrogen may become sequestered in long-lived plants and in the soil as organic matter. In these forms, nitrogen is not available for assimilation by plants as soil nitrogen, and further plant growth may be impacted by progressive nitrogen limitation. To study the interaction between carbon

assimilation and nitrogen metabolism, *Populus tremuloides* (aspen) were grown at ambient [CO_2] and under elevated [CO_2] conditions using free-air CO_2 enrichment technology. The activities of five key enzymes involved in nitrogen metabolism were measured from aspen leaf tissue using robotized, microplate-based, cycling assays. Statistical analysis of the enzyme activities indicates no significant interactions between the two clones, two treatments, nor the clones and the treatments. The only exception was an interaction between the treatment and clone in isocitrate dehydrogenase. A power analysis to determine assay sensitivity found an 85% chance of detecting a 20% difference in enzyme activity at elevated [CO_2], using a = 0.1 to further reduce the chance of type II errors. This preliminary data provides no evidence that nitrogen limitation is occurring under elevated CO_2 in a 10-year-old fast-growing aspen forest. However, these early results are part of a more comprehensive analysis that includes additional metabolic indicators of nitrogen limitation, and it is important to wait until this analysis is completed before drawing further conclusions.

Assessing Benthic Macroinvertebrate Sampling Procedures for the Development of the Freshwater Wetland Health Monitoring Protocols of Long Island's Central Pine Barrens. *Sarah Miloski* (*State University of New York at Brockport, Brockport, NY*); *Ariana Breisch* (*Brookhaven National Laboratory, Upton, NY*). While wetlands, among the most productive ecosystems in the world, are often called the nurseries of life, little is known about the current health status of Long Island's freshwater wetlands. Such vital systems should be monitored over time to determine the health of the wetlands. However, before gathering data in the field, it is necessary to assess and choose methods that will obtain the most representative results. Appropriately designed protocols will achieve the goals of establishing baseline data of the current wetland health and provide land managers with the data they require to make management decisions to optimize the health of the wetlands under their supervision. Monitoring methods need to be consistent, informative, and replicable in order to be comparable to future data. Benthic macroinvertebrates are crucial indicators of wetland health, since the number and type of species present yield significant information regarding water quality. In this research, appropriate procedures for sampling these organisms were reviewed and assessed using protocols developed by other states, such as Ohio and Florida. These protocols were adjusted to accommodate the unique conditions of the wetlands of Long Island's Central Pine Barrens. To test the protocols, invertebrates were acquired using a d-frame dip net to sweep various wetland habitats. Invertebrates were then randomly chosen from an observation tray and identified in the field. Several protocols called for a sample total of 100 organisms. This task consumed time that could have been allotted to other aspects of the protocol. Therefore, the benthic macroinvertebrates encountered were noted as present, thus providing a list of organisms that existed in the wetland. When this list is compared to data collected during the revisit of a site, the absence of a formerly present organism provides information about the current state of the wetland and how it has changed. Despite a low amount of diversity while sampling, there was a plethora of adult Odonates in the wetland. This occurrence would support the existence of a substantial supply of microorganisms, such as algae and periphyton. It was concluded that simply monitoring benthic macroinvertebrates may not be an informative way of monitoring the aquatic organisms. Therefore, for the wetland protocol of Long Island's Central Pine Barrens, further analysis should delve into a smaller scale of aquatic biota, such as periphyton and algae.

Development of an *In-Situ* Data Logging System for Multiple Trace Gas Analyzers. *John Mioduszewski* (*Edinboro University of Pennsylvania, Edinboro, PA*); *Xiao-Ying Yu* (*Pacific Northwest National Laboratory, Richland, WA*). A field deployable *in-situ* data logging system was developed at Pacific Northwest National Laboratory for trace gases including carbon monoxide (CO), ozone (O_3), sulfur dioxide (SO_2), and nitrogen oxides including nitric oxide, nitrogen dioxide, and odd nitrogens ($NO/NO_2/NO_x$). On-line data acquisition and calibration are essential to analysis of observables and data integrity. As such, a program was written to control the communication between the data logger and each analyzer in Logger Net, a program used to communicate with the data logger. Analog outputs were collected by a CR-23X Campbell data logger between July 2, 2007 and August 7, 2007 in Richland, WA, with data being averaged every minute. A dynamic calibrator was used to calibrate the instruments using a gas standard with NIST certified concentration. The National Oceanic and Atmospheric Administration's HYSPLIT model was used to create a backward and forward trajectory of air during an episode of peak O_3 to determine pollutant sources and sinks. Data collected through the duration of the sampling period revealed several observations.

Concentrations of all trace gases were low, due in part to the scarcity of pollutant sources in the region. Preliminary results indicate that the SO_2 readings were considerably lower than the more common mixing ratios of 1–20 ppb in rural-suburban environments. NO, NO_2, and NO_x averaged 0.3, 12.2, and 12.8 ppb, respectively, while the average CO was 228.5 ppb. Typical O_3 in similar environments peaks at 80–150 ppb, but the highest mixing ratio of O_3 observed was less than 45 ppb. HYSPLIT offered no apparent source for additional pollutants during the high O_3 episode, but increased photochemistry due to high temperatures would explain the increase in O_3. The development of the data logging and display system for key trace gas species is an essential measurement capability. It will facilitate future field deployment either on the ground or aboard aircraft with minor modifications. The calibration coefficients determined in this study would provide useful references of the instrument performance characteristics. In addition, the continuous data collected could potentially be a unique data set to study atmospheric chemistry of key trace gas species in a non-urban environment.

Investigating Metal Concentrations in the Tissue and Shells of Bivalves *Crassostrea virginica* and *Geukensia demissa* in NY Hudson River Estuary and Long Island Sound Using Synchrotron Radiation. *Soren Murray* (*Kingsborough Community College, Brooklyn, NY*); *Keith Jones* (*Brookhaven National Laboratory, Upton, NY*). Bivalves are shellfish that filter feed by straining suspended food particles in the water. Heavy metals and other contaminants found in the silt in the water they filter are absorbed and reflected in their shells and tissues. Many government and non-government groups have teamed up to bring them back to the Hudson Estuary and Long Island Sound for their monitoring and filtering capabilities. In Mayor Bloomberg's Sustainable Development report for 2007, he proposed putting mussel farms in the Hendrix Creeks water treatment plant discharge which would allow the water to be filtered and monitored. Synchrotron radiation, because of its detection sensitivity, spatial resolution, and multi-element detection, can be used to determine the concentrations and locations of the contaminating elements; shells indicating multi-year time span and soft tissue indicating the compounds deposited in the sediment that may be recycled back into the environment when the bivalve dies. Samples of eastern oysters *Crassostrea virginica* and ribbed mussels *Geukensia demissa* shell and tissue were taken from New York's Hudson Estuary, Long Island Sound, known contaminated and known uncontaminated locations. The gills, adductor muscles, feet, and digestive track were dissected and then analyzed at the National Synchrotron Light Source using the x26a beamline. The results are being analyzed for contaminating element correlations between different locations. Growth patterns of the shell indicate, depending on the elements locations in the shell, the time the bivalve ingested the elements. Present and previous contamination levels will be recorded and observed giving researchers an indication of water quality and whether it's improving or declining. Once the contamination levels are definitive a course of action to clean the waters can be formed. Experiments and analysis are still in progress.

Three-year Analysis of the Habitat of the Henslow's Sparrow Compared to Randomly Selected Grassland Areas. *Virag Nanavati* (*University of Illinois at Chicago, Chicago, IL*); *Rod Walton* (*Fermi National Accelerator Laboratory, Batavia, IL*). Henslow's Sparrows (Ammodramus henslowii) are endangered prairie birds, and grasshopper sparrows (Ammodramus savannarum) are rare birds in illinois. Historically, grasslands throughout the state provided these birds with a suitable habitat. However, due to the loss of grasslands, the population of these birds is declining. This longitudinal study is being conducted to improve understanding of the habitat preference of the henslow's sparrow and grasshopper sparrow. This, in turn, will help the fermilab land managers to develop a restoration plan. In this study, we found Henslow's Sparrows at twenty-three sites and found grasshopper sparrows at two sites. Due to such a small sample, the grasshopper sparrow's data was not analyzed. A vegetation survey using the point-quarter study methodology was done at each bird location. The emphasis of the vegetation survey was to characterize the general physical structure of the habitat rather than studying the exact species of plants. Random quadrats near each nesting site were surveyed for maximum plant height and duff height. Visual estimates were also carried out to determine the average vegetation height, percent of grass, forbs, bare ground, and duff. A similar vegetation survey was also carried out at sixteen random sites on the fermilab campus to serve as a control. Statistical analysis found that Henslow's Sparrows are very particular about their habitat. They prefer an average maximum plant height of 90–100 cm, an average plant height of 40–55 cm and average duff height between 4.5–7.5 cm.

The henslow's sparrow is also particular about the ground cover in its habitat. It prefers ground cover ranging from 45%–60%, forbs cover from 15%–25%, duff cover that ranges around 25% and minimal bare ground. From the data during the three years of this study, the henslow's sparrow's consistent preference of habitat has become clear.

Paving an Environmentally Friendly Road to Fusion. *Doreen Nuzzolese* (*The College of New Jersey, Ewing NJ*)*; Carl Szathmary* (*Princeton Plasma Physics Laboratory, Princeton, NJ*). Princeton Plasma Physics Laboratory (PPPL) strives to sustain fusion power as a reliable and environmentally safe energy source. First, with the tokamak fusion test reactor, then the national spherical torus experiment, and now the national compact stellerator experiment, pppl comes closer and closer to achieving their goal. However, these experiments use harmful substances, such as deuterium and tritium, and it is imperative that these substances not get released into the surrounding air and water. It is the responsibility of PPPL's princeton environmental analytical radiological laboratory (pearl) to protect the environment and ensure safety. To do so, radio-chemists in the pearl perform tests on air and water samples taken from areas surrounding the laboratory. Before being released into the environment, wastewater is tested through either chemical oxygen demand (COD), testing for organic matter, or alkaline distillation purification, followed by liquid scintillation analysis, testing for tritium. Air samples are tested for tritium through the differential atmospheric tritium sampler system. All test results are fed into a fiscal year report and kept on file. If any one sample shows evidence of harmful substances, it is immediately removed from site and cured before disposal. Therefore, while advancing fusion, PPPL poses no health threat, but rather advocates safe scientific practices. In conclusion, PPPL is on its way to safely revolutionizing energy through fusion, an inexpensive, inexhaustible fuel that will be sure to have an immense global impact.

Evaluating Health Effects and Technology Options for Communities with Environmental Contaminants. *Angela Parker* (*Norfolk State University, Norfolk, VA*)*; Margaret M. MacDonell* (*Argonne National Laboratory, Argonne, IL*). The research supports two projects, both of which address an overarching theme of evaluating health effects and technology options for communities with environmental contaminants. Both of these projects will be used to guide mitigation programs in designated areas of the world. Basic information was compiled, organized and synthesized in order to support the programs being designed to protect the health of those individuals and their communities within targeted areas. Contributions to these projects include evaluating key exposure and toxicity values from a number of agency sources, both for the public and workers, including the Environmental Protection Agency, Agency for Toxic Substances & Disease Registry, and Occupational Safety & Health Administration. A large quantity of information has been extracted on more than 30 chemicals of interest to prepare the project database. This database will be used to provide the Research Institute of Industrial Science and Technology (RIST) scientists with detection targets for upcoming environmental sampling programs in the steel making industrial area. The information in the database has also been synthesized to outline a management prioritization tool to help highlight those chemicals that should be addressed first by upcoming studies. Also, a preliminary evaluation of current technology was conducted in order to compare two chemicals of interest (mercury and cyanide) for artisanal gold miners in many communities throughout the world and their respective effects on human health and the environment. In addition, this scientific information is being translated into educational outreach materials for both a website and health fact sheets to promote awareness of the hazards for the local public.

*Initial Characterization of Soil Cultivated with Switchgrass at Milan, TN. *Melissa Payton* (*California State University – Fresno, Fresno, CA*)*; Julie Jastrow* (*Argonne National Laboratory, Argonne, IL*). Greenhouse gases, such as carbon dioxide, have been increasing in the atmosphere due to anthropogenic activities. Scientists have been researching ways to remediate this increase through carbon sequestration. The Department of Energy's Consortium for Research on Enhancing Carbon Sequestration in Terrestrial Ecosystems (CSiTE) focuses on studying carbon sequestration in terrestrial ecosystems cultivated with the bioenergy crop, Panicum virgatum (switchgrass). Switchgrass in belowground ecosystems has the ability to sequester and allocate carbon from carbon dioxide into the soil. This study focused on investigating the relationship between soil organic carbon (SOC) and different switchgrass cultivars. Another focus of this study included determining fine and coarse particulate organic matter (POM), clay, and silt fractions of the soil at 0–5 cm, 5–10 cm, and 10–15 cm depths as well as the carbon and nitrogen ratios (C:N) between

fractions. Soil samples were fractionated according to size through wet sieving and centrifuging. Nitrogen and carbon percentages were measured for each fraction at the 0–5cm depth utilizing automated carbon and nitrogen analyzers. Results revealed that differences existed in the amount of soil organic carbon cultivated with the different switchgrass cultivars, and soil was composed of primarily silt (74–76%). Clay percentages increased and POM percentages decreased as the depth of the soil increased. The highest carbon and nitrogen concentrations at the 0–5 cm depth occurred in the clay and silt fractions. This study also revealed that the coarse POM in the 0–5 cm soil depth had the highest C:N ratio. The differences between SOC and switchgrass cultivar revealed in this study indicate that there may be one switchgrass cultivar that sequesters the most amount of carbon. Future research needs to focus on measuring the nitrogen and carbon percentages at 5–10 cm and 10–15 cm depths, and determining the role soil microaggregates play in storing carbon.

Long Island Pine Barren Ponds: Water Quality. *Shakera Pinder* (*Tallahassee Community College, Tallahassee, FL*)*; Tim Green* (*Brookhaven National Laboratory, Upton, NY*). Ponds in the Pine Barren complex at Brookhaven National Laboratory (BNL), Near Road Ponds (NRP), Calverton Ponds (CP), Sears Bellows County Park Ponds (SBP), and ponds of the Long Pond Greenbelt (GP) of Suffolk County, NY were studied. A Magellan eXplorist 200 Global Positioning System (GPS) was used to mark each pond. A YSI 650 MDS Probe was used to measure the real-time data on temperature, pH, dissolved oxygen (DO), conductivity, and turbidity of the water. This study is specifically focused on the alkalinity, the acidity, and the buffering capabilities of ponds within the Pine Barrens. We have collected three random surface water samples directly into 500 mL Nalgene bottles and one random water sample at approximately two feet deep, from each pond for a total of 33 ponds located on and around BNL's site and of Suffolk County, NY, using a Plano Horizontal Polycarbonate Water Sampler. Water samples were analyzed using HACH Digital Titrator and TitraVer Solutions and were tested for acidity, alkalinity, calcium (Ca) and magnesium (Mg) hardness, and total hardness. The water temperature of each pond was greatly affected because some ponds were shaded by surrounding forest trees, while other ponds were directly exposed to the Sun. One of the goals of this project was to obtain the results of the physico-chemical analyses of water samples and focus on the most pressing water quality of pond problems in Long Island, NY. This study also provides a look at the variations of pH within each pond and how they are affected by the atmospheric acid deposition. The results of this research show that there is no correlation between near-road ponds and off-road ponds. Results of this study will assist ecologists on how to manage the habitats of wildlife in the Long Island Pine Barren ponds.

Examining the Relationship between Soil Carbon Stability and Mineral Surface Reactivity in an Ultisol from the Tennessee Valley. *Rachel Porras* (*California State University – East Bay, Hayward, CA*)*; Margaret S. Torn* (*Lawrence Berkeley National Laboratory, Berkley, CA*). Soil Organic Matter (SOM) represents a major reservoir of biosphere carbon which may be chemically or biologically transformed to atmospheric CO_2 as well as other greenhouse gases. Despite its importance in maintenance of ecosystem integrity and critical role in regulation of climate system stability, the actual physicochemical and biotic factors that govern the partitioning and long-term stabilization of organic matter within the soil environment remain poorly understood. SOM stability derives principally from physical protection within aggregates and association with reactive mineral surfaces. Mineral associated C is believed to be irreversibly bound. However, evidence from recent ^{14}C studies of mineral stabilized OM appears to indicate that the mineral fraction contains a more labile carbon component that is capable of actively exchanging over time. In this this preliminary experiment radiocarbon measurements were utilized to assess the size and relative stability of two operationally defined SOM pools within the dense mineral fraction of a carbonaceous soil (Ultisol) in an effort to gain insight into the capacity of the mineral fraction of these soils to actively adsorb and stabilize organic inputs. AMS results obtained for the 0–15 cm depth class were contrary to initial predictions. The dense fraction (rho> 2.4 g cm^{-3}) contained a greater concentration of pulse-derived 14C than the lower density fraction. The trend observed for the 0–15 cm depth is reversed in the 15–30 cm depth for all treatments with the 1.7–2.4 g cm^{-3} fraction exhibiting a greater concentration of pulse-derived [14]C. Measured soil $\Delta^{14}C$ indicates greater retention of rhizospheric inputs by both fractions. The $\Delta^{14}C$ measured for the litter treated plots was similar in magnitude to that of the control. The effect of depth and treatment were found to be highly significant on

measured $\Delta^{14}C$ ($P<0.001$). The effect of density on $\Delta^{14}C$ was also found to be significant across treatments. Although additional analyses are necessary to quantify labile C in the two density fractions, characterize mineralogic composition, and assess mineral surface reactivity, these results indicate that the method utilized successfully isolated two SOM pools from the dense fraction with differing chemical properties and C stabilization efficiencies.

*Climatological Impacts of Extreme Naturally Occurring Fire Events Associated with the Alaskan Summer of 2004. Jessica Ragazzi (*St. Joseph's College, Patchogue, NY*); Richard Wagener (*Brookhaven National Laboratory, Upton, NY*). Besides their important role in the forest ecology, fires are also expected to have a large impact on weather and climate. Climatotological impacts are expected to be the largest in the arctic regions due to these high intensity fires. Previous studies have shown that the composition of smoke particles produced by the fires depends on the type of fire and its temperature. Fires create their own local weather and the most intense fires lift smoke particles high into the atmosphere where they can reside a long period of time and are transported great distances by high altitude winds. The summer of 2004 in Alaska had been a most unusual season, characterized by dry spells and various periods of intense lightning strikes. In two days alone, seventeen thousand strikes were recorded. These events triggered tremendous fires across the state, in the end leaving six million acres burned. This study Used Moderate Resolution Imaging Spectroradiometer (MODIS) and Multi-angle Imaging Spectro-radiometer (MISR) satellite data to calculate the area of these fires. An analysis of the trajectories of these smoke plumes using an atmospheric transport model (HYSPLIT-HYbrid Single-Particle Lagrangian Integrated Trajectory) needed to be enacted in order to select those fires whose plumes pass over the *in-situ* Aerosol Observation System (AOS) operated by National Oceanic and Atmospheric Administration in Barrow, AK. The site is collocated with the DOE's Atmospheric Radiation Measurement's Climate Research Facility whose complement of instruments allows ground-based aerosol measurements. These *in-situ* and ground-based remote sensing measurements are combined with the MODIS aerosol retrieval products to estimate the direct radiative impact of these high intensity wild-fires. Several potential indirect effects investigated include the effects of smoke particles on cloud formation, cloud properties (droplet size, life-time), and the effect of soot particles on surface albedo by direct modification of the albedo of Alaskan glaciers and the potential for accelerated melting. This project explored only some of the effects of fires on climate. Further research may be done in order to obtain information on additional short or long term effects.

*Evaluation of Operating Conditions when Measuring Gaseous Ammonia Using a Tunable Diode Laser Absorption Spectrometer (TDLAS). Khatera Rahmani (*Brooklyn College, Brooklyn, NY*) Arthur Sedlacek (*Brookhaven National Laboratory, Upton, NY*). Ammonia (NH_3) is the only alkaline in the atmosphere. It is highly-reactive and is commonly found in concentrations of 1ppb in ambient air (but can readily approach concentrations in the 1,000s of ppb when near sources). In addition to the role that NH_3 plays in the biochemical cycles of nitrogen, it also plays a role in aerosol formation by reacting with atmospheric NO_x and SO_x. The resulting aerosols have been observed to play a role in global climate change. The high sensitivity and fast response time of the TDLAS makes it a good candidate for measuring gaseous NH_3. Although the TDLAS is highly sensitive and can measure concentrations of NH_3 can stick to the inner walls of the tubing used to inject in the air sample into the instrument. Typically, tubing made out of Teflon (PFA) is used, however very little research has been done to determine if Teflon is the most inert material with respect to NH_3. Therefore, a series of experiments were performed on a known concentration of NH_3 of flowed through various tubing materials (Teflon, copper, stainless steel, glass). Under dry air conditions, stainless steel held up the least amount of NH_3. In contrast,Teflon resulted in the greatest loss of NH_3. The tubing was also heated (40°C) under dry conditions and negligible changed in the loss of NH_3 was observed. An important finding in this study was that with increased flow rates, the measured concentration of NH_3 agreed more closely to that calculated for a permeation source, possibly due to the decrease in residence time of NH_3 in the tubing. Decreased residence time leads to less diffusion of NH_3 in the inlet system. Inlet conditions were then evaluated under humidified conditions using ambient air from outdoors to dilute the NH_3 source. With relative humidity above 50%, NH_3 loss was observed with all tubing material. Least amount of NH_3 loss was observed with Teflon (9% loss), while greater loss was observed with stainless steel (11% loss) and copper (15% loss). The loss of NH_3 under humidified conditions is presumably due to NH_3

diffusing into the condensed water on the inner walls of the tubing. These preliminary studies have shown that humidity, and flow rate have a significant effect on the accuracy of measurements of ambient NH_3 concentration. With further research, loss of NH_3 in inlet systems can be quantified to aid in the process of monitoring ambient NH_3 concentrations to evaluate overall environmental health.

The Use of Mark-Recapture to Estimate Odonate Populations at Vernal Pools at Brookhaven National Laboratory. Dianna Rodriguez (*State University of New York at Old Westbury, Old Westbury, NY*); Timothy Green (*Brookhaven National Laboratory, Upton, NY*). Dragonflies are insects of the order Odonata, suborder Anisoptera. In the state of New York there are 60 known, documented species of odonates of the 3,000 species known worldwide. Odonates are important because they play a role in maintaining the delicate ecosystems of vernal pools and other bodies of water such as marshes, streams, and wetlands. Monitoring and tracking odonates can present much difficulty due to their numerous population, migration, extraordinary flight speed, and relatively short life span. The use of a tracking system is needed in order to keep accounts of odinate species populations that are being monitored and observed. With the use of a simple form of the mark-recapture method, odonates are caught using nets, numbers are drawn on their wings then released. The study was conducted for ten weeks at three ponds. Surveys were also conducted at each of the three ponds once a week. These surveys provide an account of all species visibly present and their apparent abundance. From the use of mark-recapture, 525 dragonflies were captured and marked with 18 recaptured at least once. Once all data was collected the program Noremark was used to make population estimates. Two population estimates were generated for each pond. The program estimated about 629 dragonflies inhabiting pond 7, 2,700 dragonflies inhabiting 9 O'clock pond, and inconclusive results for Meadow Marsh. The surveys have shown that there are at least ten common species amongst all three ponds, and the most abundant species at the ponds have changed in the past eight and a half weeks. It has also been observed that a species, the Band-Winged Meadowhawk (Sympetrum semicinctum), which has not been previously documented as part of Brookhaven National Labs (BNL) Odonate population, has gained a significant abundance during weeks five through eight. These studies are indicators of pond health and speciation, and have thus far shown that the ponds at Brookhaven Lab are clean and habitable because of the great abundance of these sensitive insects. This research is part of an ongoing project that was started in 2003 to observe the Odonate populations of the BNL campus and will be continued until an accurate account of species is created. Future studies may include the effects of hydroperiod on Odonate populations and abundance.

The Effects of Mixed Obscurant Aerosols of Carbon Fiber, Graphite Flake, and Fog Oil on Wildlife. Margarita Rodriguez (*Sacramento City College, Sacramento, CA*); Crystal Driver (*Pacific Northwest National Laboratory, Richland, WA*). U.S. Army installations have responsibility for matching military mission activities with ecological compatibility of the land and natural resources, including balancing military-essential functions and preservation of Threatened and Endangered Species (TES). Among the operations critical for supporting Warfighter readiness and battlefield protection, is training with smoke and obscurants to conceal troop movements and mechanized equipment. The Army has a developed smoke/obscurant generation system that can counter heat and radar sensors as well as visual detection using by producing a mixed plume of graphite flake, carbon fiber and fog oil, respectively. As a result of training, environmental releases of these mixed obscurant aerosols may accompany troop readiness exercises, thereby providing the Army with the need to identify and plan for environmental requirements of their actions. The objectives of this study are to determine the inhalation and oral toxicity of a mixed obscurant of carbon fiber, graphite flake, and fog oil on wildlife species under simulated field conditions. Current tests being conducted are investigating the impact of obscurants on birds and tortoises. The animals receive inhalation exposures at field relevant concentrations in the environmental wind tunnel at the PNNL Aerosol Research Facility and then returned to their home pens where they are maintained in simulated natural habitats. A separate group of tortoises are maintained in naturalized habitats to which carbon fiber was deposited on food sources at field relevant rates per unit area. Behavioral and health effects are being monitored during and post exposure. Data from these tests will provide information for general and site-specific risk assessments and management of carbon fiber-graphite-fog oil generations and training activities. This is an ongoing project, thus the results are still pending. In the near future, this similar experiment will be with bats.

Uranium Sorption Kinetics on Synthetic Goethite and Hanford Fine Sediment. *Amy Sessions* (*Northern Arizona University, Flagstaff, AZ*); *Wooyong Um* (*Pacific Northwest National Laboratory, Richland, WA*). The Hanford site located in southeastern Washington State, is among the most contaminated sites in the DOE complex where at least seven distinct uranium plumes have been identified within the Hanford site subsurface. The purpose of testing sorption conditions is to determine the mobil-ity of uranium within the Hanford area natural setting. Desirable rates for sequestering uranium would favor rapid adsorption rates, and slower desorption rates. Batch experiments were con-ducted on a Hanford Fine Sediment (HFS) and synthetic goethite (FeOOH) to determine sorption kinetics. A series of solutions with varying pH and atmospheric conditions were prepared for desorption tests to determine the effect of background conditions on the solids ability to sorb uranium species. ICP-MS analysis quantified the amount of uranium in solution samples. The goe-thite adsorbed fifty percent more uranium than the HFS. Uranium sorption and desorption on both solids fit a pseudo second order reaction rates for adsorption and desorption.

*Climate Change: A Systems Perspective on Research at Pacific Northwest National Laboratory. *Caitlin Shenk* (*Lehigh University, Bethlehem, PA*)*; Charlette A. Geffen* (*Pacific Northwest National Laboratory, Richland, WA*). Many aspects of the natural environment and human society are significantly affected by changes in climate. The impacts of climate change on both natural and social systems will be pervasive and complex, and are becoming increasingly apparent. As one of today's most important and pressing environmental issues, climate change demands the expansion of fundamental scientific knowledge and the incorporation of this knowledge into practical mitigation and adaptation strategies. In order to examine and articulate the critical linkages between earth, energy, and social systems involved in addressing the climate change issue, an investigation and synthesis of current research efforts at Pacific Northwest National Laboratory (PNNL) in Richland, Wash. was conducted. Research initiatives and programs from divisions across the laboratory were examined, and information was synthesized to create an initial platform for the development of a comprehensive PNNL climate research policy and public image. PNNL's research capabilities were divided into three categories of scientific and social interest based on gaps in knowledge about three major climate change questions. First is a question of climate change sensitivity: how sensitive are climate mechanisms to change? Second is a question of climate change impacts: how well can these changes, and the impacts of these changes, be predicted? Third is a question of climate change response: what, if anything, can be done to mitigate the impact on climate or adapt to the changes? By providing a useful composite of current issues and trends related to climate change, this project articulates the integral role of PNNL in climate research and provides a foundation for continued discussion of current and future scientific needs.

Spatial Distribution of Iridovirus in the Eastern Box Turtle Population at Brookhaven National Laboratory: Implications for Transmittance Based on Home Range Size. *Sarah Snyder* (*Unity College, Unity, ME*)*; Valorie Titus* (*Brookhaven National Laboratory, Upton, NY*). There are currently four recognized genera of the icosohedrally symmetric iridoviruses that infect both invertebrates (Iridovirus and Chlorirdovirus) and poikilothermic vertebrates (Lymphocystivirus and Ranavirus). Ranaviruses have only been documented in a relatively few number of reptiles when compared to the number of viruses that have been documented in amphibians and fish. Recent detection of ranaviruses in five species of chelonians, including a virus outbreak in a population of Eastern box turtles (Terrapene carolina carolina) at Brookhaven National Laboratory, is especially alarming. This discovery poses a threat to box turtles in surrounding areas since the species is listed as special concern in the state of New York. This is a continuing study to ascertain the current distribution of infected turtles at Brookhaven National Laboratory. Turtles were sampled during 2006 and 2007 using systematic transect searching. Cloacal and oral samples were collected from each turtle encountered and DNA was isolated from swabs using DNeasy kit protocols. PCR was used to amplify virus DNA and products were subsequently run on 0.8% agarose gels to determine the presence or absence of Ranavirus. Ranavirus was detected in a liver tissue sample and oral swab obtained from one turtle collected during the summer of 2006. This turtle exhibited advanced symptoms of viral infection including an aural abscess and later died. These results preliminarily suggest that swab sampling and PCR testing may not be adequate methods for detecting ranavirus in pre-symptomatic turtles, yielding falsely negative results from turtles sampled during the early stages of infection. To further

explore the potential transmission of the Ranavirus within the box turtle population, determining individual home range size specific to turtles at the study site was necessary. Radiotransmitters were attached to five box turtles inhabiting the area of Ranavirus discovery and their daily movements were recorded for two summers. Geographic Information Systems was used to digitally map turtle movements and estimate home range size by creating minimum convex polygons. Home ranges of individual turtles are not significantly different from one another, varying between 1.8 ha and 8.2 ha, which is comparable to home range sizes found in other studies. Home ranges also grossly overlap which suggests favorable conditions for virus spread, depending on encounter rates and mode of transmission.

Development and Optimization of Growth Media for *Anaeromyxobacter dehalogenans* 2CP-C. *Allison Spencer* (*Whitman College, Walla Walla, WA*); *David Culley* (*Pacific Northwest National Laboratory, Richland, WA*). Bioremediation has great potential for containing and neutralizing toxic materials present in the environment. *Anaeromyxobacter dehalogenans*' ability to reduce different halogenated compounds makes it a prime candidate for environmental cleanup. Efficient growth conditions are essential for timely, cost-effective collection of the *Anaeromyxobacter* biomass necessary for genetic studies of this organism. The increased growth rate of *Anaeromyxobacter dehalogenans* 2CP-C based on spectrophotometric assay of optical density was achieved by identifying nutritional growth requirements and determining optimal concentrations in a defined media. All *Anaeromyxobacter* cells were grown anaerobically from freezer stock at 37°C in 22mL Balsch tubes without shaking. Cultures were grown in 10 mLs media with a headspace of 90:10 N_2:CO_2. Experimentation commenced using a defined DCB-1 media which was continually modified as results were obtained. The optical density indicating peak cell concentrations resulted from the addition of 30mM Fumarate and 0.5 uM Cysteine with a 40 fold decrease in Selenium and Tungsten concentrations previously used in a defined DCB-A media. Heat labile vitamins, trace minerals, Sodium Acetate, Sodium Fumarate, Selenium and Tungsten were added after autoclaving. The optical density of cell cultures increased from a maximum value of 0.077 after 16 days under standard conditions to a final density of 0.722 with the altered nutrients under identical growing conditions. This increase in optical density is proportional to a ten fold increase in cell biomass.

*Comparative Ecological Study: Long Island Pine Barren Ponds, NY. *Ha'wanna St. Cyr, Latonya Stemley* (*Southern University at New Orleans, New Orleans, LA*)*; Tim Green, Murty Kambhampati* (*Brookhaven National Laboratory, Upton, NY*). The purpose of this research was to collect scientific ecological data on water and sediments from the Long Island Pine Barren Ponds including the ponds on Brookhaven National Laboratory (BNL) site and to compare results between the on-site (Zone-I) and off-site (Zone-II) ponds. The specific objectives were to: (a) analyze samples for physico-chemical factors; (b) compile and analyze data statistically; and (c) to identify the interrelationships between abiotic factors in ponds of two zones. We have collected 99 surface water and sediment samples (0°C for 36–48 hours to obtain moisture. Majority of the water and sediments were acidic and nutrient poor. Soil texture is mostly either sand or silt. Moisture content varied between 20.98±10.35 to 50.02±6.13% in NRP and BNL samples, respectively. Sediment ANOVA results indicated positive and negative significances ($P<0.05$ and $P<0.01$) between elements, aluminum (Al), iron (Fe), lead (Pb), and chromium (Cr). In conclusion, the Long Island Pine Barren pond water and sediments are acidic and nutrient poor. Sendiments have higher concentrations of metals (Al and Fe) in general.

Characterization of the Structure of Cation-Doped Bacteriogenic Uranium Oxides Using X-Ray Diffraction. *Jonathan Stahlman* (*Carnegie Mellon University, Pittsburgh, PA*)*; John Bargar* (*Stanford Linear Accelerator Center, Stanford, CA*). Remediation of uranium contamination in subsurface groundwater has become imperative as previous research and manufacturing involving radionuclides has led to contamination of groundwater sources. A possible *in situ* solution for sequestration of uranium is a bacterial process in which *Shewanella oneidensis* MR-1 reduces the soluble (and thus mobile) U(VI) oxidation state into the less mobile UO_2 crystalline phase. However, the long term stability of the UO_2 compound must be studied as oxidative conditions could return it back into the U(VI) state. Incorporation of other cations into the structure during manufacture of the UO_2 could alter the dissolution behavior. A wide angle X-ray scattering (WAXS) experiment was performed to determine whether or not calcium, manganese, and magnesium are incorporated into this structure. If so, the substituted atoms would cause a contraction or expansion in the

lattice because of their differing size, causing the lattice constant to be altered. After several stages of data reduction, the WAXS diffraction peaks were fit using the Le Bail fit method in order to determine the lattice constant. Initial results suggest that there may be incorporation of manganese into the UO_2 structure due to a .03 Å decrease in lattice constant, but more data is needed to confirm this. The calcium and magnesium doped samples showed little to no change in the lattice constant, indicating no significant incorporation into the structure. Most importantly, this experiment revealed an artifact of the cleaning process used to remove the bacteria from the sample. It appears the NaOH used to clean the samples is contracting the lattice also by ~.03 Å, but no physical explanation is offered as of yet.

*Evaluating Electrical Conductivity Measurements to Determine Water Flow Rates. RAY TUGMAN (*California State University – Fresno, Fresno, CA*); EARL MATTSON (*Idaho National Laboratory, Idaho Falls, ID*). Centrifuges are used to measure hydraulic properties and solute transport in porous medias. Although the centrifuge is attractive due to the large centrifugal force that it can apply, a major drawback of the centrifuge method is the difficulty of measuring flow rates while the test is in progress. To overcome this limitation, Idaho National Laboratory (INL) scientists are investigating if water flow rate can be determined through the analysis of electrical conductivity measurements in the effluent cup. A prototype electrical conductivity meter was designed and built that can continuously record and transmit electrical conductivity measurements of the effluent while the centrifuge is spinning. The objective of this work is to evaluate the feasibility of the electrical conductivity prototype as to its ability to measure flow rate. If we know the initial volume, the initial electrical conductivity, the electrical conductivity at any given time and the input conductivity, we can calculate the cumulative flux. By plotting the cumulative flux as a function of time, we will produce a graph whose slope is equivalent to the flow rate. In the steady flow tests, the flow rate determined by the cumulative flux of the actual flow rate was constant throughout the experiment and within approximately 2.5% of the actual flow rate. The cumulative flux appears to be nosier in the latter ½ of the data set . In the variable flow test, the calculated cumulative flux predicts the correct shape of the measured cumulative flux curve; however, the calculated cumulative efflux is biased slightly high. This electrical conductivity meter needs further evaluation in the following areas: 1) the effects of mixing in the centrifuge ; 2) long term probe drift-how much will the probe drift during experiments lasting several days; 3) optimization of solution initial volumes and concentrations.

The Effects of Hydrologic Conditions on the Distribution of Plant Species in a Mitigated Wetland at Argonne National Laboratory, Illinois. MEAGAN TURNER (*Washington State University, Pullman, WA*); KIRK LAGORY (*Argonne National Laboratory, Argonne, IL*). During the construction of the Advanced Photon Source (APS) in 1990 at Argonne National Laboratory in DuPage County, Illinois, three small wetlands totaling 1.8 acres were destroyed. To comply with the no-net-loss policy under the Clean Water Act, a mitigation wetland (Wetland R) was created south of the APS facility. Monitoring of Wetland R began in 1992 and continued annually for five years. In 2002, monitoring started again and has continued through 2007. The purpose of this study was to examine changes in Wetland R with a specific focus on the distribution of species in relation to hydrologic conditions. Percent cover of plant species was determined in 50 quadrats at randomly selected locations along transects throughout the wetland. Each plant species' origin (native, non-native), coefficient of conservatism, and wetland status were recorded. Species were placed in hydrology classes determined by the number of days water was recorded in a quadrat. Overall, the distribution of plant species in 2007 was similar to that in 2005. The distribution of plants according to hydrology was also similar for the two studies except for two species: *Eleocharis erythropoda* and *Boltonia latisquama*. In 2005, 70% of *E. erythropoda* was found in quadrats covered in water greater than 40% of the time. In 2007, 100% of *E. erythropoda* was found in quadrats with no standing water present during 2006 and 2007. In 2005, the majority of *B. latisquama* was found in quadrats covered in water for 1–40% of the time. In 2007, the percentage found in quadrats with no water reached 96%. The hydrology of wetlands strongly affects species composition and richness. It is suggested that Wetland R continued to be monitored for diversity and the distribution of species, especially obligate wetland species, be monitored for changes in response to changing water levels.

The oak savanna. ASHLEY WENTLAND (*University of Illinois at Chicago, Chicago, IL*); ROD WALTON (*Fermi National Accelerator Laboratory, Batavia, IL*). The oak savanna, a mixture of prairie grasses, forbs and scattered tress, mainly oaks, was one of the major natural communities of the Midwest. Today, they are a top concern for restoration. Our objective was to document and characterize the tree population and age structure of the oak savanna by examining relative density, relative frequency, and relative cover for most common species. We conducted tree research in the remnant savanna on Fermi National Accelerator Laboratory's property using the point-centered quarter method. We also prepared soil samples for analyses by First Environmental Laboratories, Inc. in Naperville, Illinois. Ca++ and Mg++ concentrations were identified for each soil sample. The north side of the savanna has a high tree and vegetation density compared to the south side where there is an abundance of open space and prairie grass. Bur Oak (*Q. macrocarpa*) is by far the most important species in the savanna. However, the basswood (*T. Americana*), white ash (*F. Americana*), and black cherry (*P. serotina*) are slowly dominating the oak savanna at Fermilab, which poses a problem. The data suggest that the north side of the savanna is degraded compared to the description of the healthier side of the savanna. The savanna is being invaded by trees and vegetation and may convert into a woodland if nothing is done. Some possible strategies indicated by our results that may help aid restoration are: removing the invasive tree species, planting more oak species and prairie grasses, and carrying out fires to control the density of vegetation.

Stratigraphic Control on CCl_4 and $CHCl_3$ Concentrations. KELSEY WINSOR (*Smith College, Northampton, MA*); GEORGE V. LAST (*Pacific Northwest National Laboratory, Richland, WA*). An extensive subsurface contaminant plume of carbon tetrachloride (CCl_4) is the focus of a remedial effort in the 200 West Area of Washington State's Hanford Site. Remediation requires a high-resolution model of the region's spatially variable lithofacies and of the effect these units have on CCl_4 migration through the unconfined aquifer. To increase detail of previous models, a transect was chosen along the primary groundwater flow path in the most heavily contaminated area. Borehole logs of wells along this 3.7 km-long transect were systematized and used to create a cross section displaying lithofacies depth and continuity. Natural and spectral gamma geophysical logs were examined to pinpoint the depths of geologic units. Depth discrete concentrations of CCl_4 and its reductive dechlorination product, chloroform ($CHCl_3$), were overlain on this cross section. Comparison of stratigraphy to contaminant levels shows that peaks in CCl_4 concentration occur in thin, fine-grained layers and that other fine-grained layers frequently form lower boundaries to regions of high concentration. Peaks in CCl_4 concentrations are frequently located at different depths from those of $CHCl_3$, suggesting that these concentrations are affected by dechlorination of CCl_4. Transformation of CCl_4 to $CHCl_3$ appears to be more prevalent within reduced, iron-containing sediments. Influence of thin, fine-grained layers within the larger aquifer unit indicates that characterization of contamination in this locality should consider subsurface geology with at least as much resolution as provided in this study.

General Sciences

High Order Network Analysis in Power and Pulsed Power of the AGS Main Magnet System. GRACE KING (*University of California – Los Angeles, Los Angeles, CA*); ARLENE ZHANG (*Brookhaven National Laboratory, Upton, NY*). Particle accelerator systems like the Brookhaven's Alternating Gradient System (AGS) function on the basis of a high-order network complex of dipole magnets. Comprehensive analysis of this network is essential to the continual success of main magnet system operations. Until now, the limits of current processing technologies have hindered the effective examination of the magnet system's behavior, whose ladder-style characterization can reach hundreds of degrees in its equivalent polynomial form. Previous analysis, which involved the simplification of the circuit system, failed to reflect the nature of its true complexity. Frequency decomposition, aided by the circuit simulation software, Microcap VIII, is a new approach that is able to take advantage of present computer processing capabilities. Presently, distinct circuit models have been simulated and various transient analysis runs have been conducted successfully. Further analysis with the application of transmission-line and ladder-network theory on simulated data should demonstrate the effectiveness of frequency decomposition. The development of this method has greatly facilitated the investigation of present magnet network properties as well as the exploration of new phenomena that may arise from future simulation studies.

Analysis of Mixture Experiments Using Slack Variable and Mixture Approaches. SAMANTHA LANDMESSER (*University of Tennessee, Knoxville, TN*); GREG F. PIEPEL (*Pacific Northwest National*

Laboratory, Richland, WA). In a mixture experiment, the response variable depends on the proportions of the components, which must sum to one. Because of this constraint, standard polynomial models cannot be used to analyze mixture experiment data. To get around this, some researchers ignore one of the components and use standard polynomial models in the remaining components. Because the component proportions must sum to one, the ignored component (referred to as the "slack variable" (SV)) makes up the remaining proportion of the mixture. In the literature, there have been many examples of researchers using the SV approach instead of a mixture approach. We have analyzed several of these examples using both approaches. For screening examples, we fit full linear models and identified which components were important using both approaches. In six screening examples, the mixture approach revealed that the SV had a significant effect on the response. For the quadratic examples, we used stepwise regression to develop reduced quadratic models for the SV approach, and partial quadratic mixture (PQM) models for the mixture approach. In three examples, the PQM models identified the SV and/or one of its quadratic blending terms as having a significant effect on the response variable. Hence, by completely ignoring a component's effect on the response, SV analysis carries an inherent risk of wrong conclusions. There are fewer possible reduced quadratic SV models than possible PQM models because the reduced quadratic models are a subset of the class of PQM models. As a result, the PQM models will always fit the data as well as, or better than, the best reduced quadratic SV model. Our research concludes that it is better to analyze mixture experiments using methods specifically developed for them instead of using standard methods with the SV approach.

Planning for the Future: Updating Energy Forecasting Techniques. *CATHERINE SAMPSON* (*Western Washington University, Bellingham, WA*); *TODD SAMUEL* (*Pacific Northwest National Laboratory, Richland, WA*). Every year the Energy Information Administration publishes a document known as the Annual Energy Outlook (AEO), which provides analysis and forecasts of world energy markets through the year 2025. The results of this publication are used in the decision making processes of policy makers and public and private investors alike, and are the most comprehensive energy forecasts currently available. However, the National Energy Modeling System (NEMS), the program used to produce these forecasts, is riddled with minor flaws that may have major impacts on the applications of the AEO results. Though built using a detailed, modular structure, NEMS can only be run deterministically on a scenario by scenario basis. Further, NEMS models display an asymmetric loss function, making the results ambiguous to users whose loss function is not identical to that of modelers'. That is why the Department of Energy and the National Renewable Energy Laboratory are commissioning a new model for forecasting energy use. Known as the Stochastic Energy Deployment System (SEDS), this model will improve on current energy modeling mechanisms by providing for full probabilistic treatment of uncertainties. SEDS is in development under experts from several national laboratories, and will be designed on Analytica, a commercially available software package offering a user-friendly format. Hopefully, SEDS will be able to provide forecasts with better representations of the various possible futures of energy markets than are currently available.

Testing the Multiwavelet Representation of Functions. *OWEN WORLEY* (*Dartmouth College, Hanover, NH*); *GEORGE FANN* (*Oak Ridge National Laboratory, Oak Ridge, TN*). The multiwavelet transformation of functions is one of the most promising methods for analyzing and performing operations on them. The multiwavelet expansion represents functions in terms of a basis of discontinuous multiwavelet functions, which are nonzero over a unit domain. In particular, representations of the Green's function of operators of partial differential equations, constructed in multiwavelet bases, can be proven, in many cases, to be sparse and nearly diagonal. Thus, the computational complexity of the application of these operators is linear or nearly linear with respect to the problem size, and so is very attractive as a method of solution. As in the development of any complex software, testing must be done to assure that the transformed function behaves correctly with respect to basic algebraic and calculus operations. This testing is done by creating and inputting a variety of functions into a program, calculating the multiwavelet representation of these functions, applying a number of operators to both the original and transformed functions, and comparing the results, demonstrating that operating on the multiwavelet representation is numerically stable and achieves the required accuracy. Said testing demonstrated that the transformed functions do behave correctly with respect to the algebra and calculus operations tested to a high degree of accuracy. Also, as the tests

were scaled to higher numbers of processors, the completion times decreased in a smooth log curve. These results were expected, but in obtaining them, debugging was performed and problems were identified and worked around. Further testing should be performed on functions represented with a higher wavelet order, and testing should generally be done as the code is modified and improved. The Joule program, written by George Fann and Robert Harrison, performs the multiwavelet transformation which is tested. The paper, Adaptive Solution of Partial Differential Equations in Multiwavelet Bases, by B. Alpert et al, provides background on multiwavelet transformations.

Materials Sciences

The Effects of Amorphous Carbon Coating of Standard Modified Graphite and Soft Carbon on Anode Properties for Li Ion Batteries. *DAVID ABRAM* (*University of Illinois, Urbana, IL*); *JUN LIU* (*Argonne National Laboratory, Argonne, IL*). Hybrid electric vehicles are gaining popularity to increase fuel efficiency and lessen dependency on oil. The battery used is predominantly nickel metal hydride, but there is a push to use Li ion batteries due primarily to their higher gravimetric and volumetric energy density. Improvements in anode quality can be made, and six Hitachi anodes consisting of blank soft carbon and surface modified graphite as well as the same materials with an amorphous carbon coating were examined. Formation cycles were run for half cells against lithium and full cells against $LiNi_{1/3}Co_{1/3}Mn_{1/3}O_2$. Hybrid pulse power characterization tests were run to determine the area specific impedance at various depths of discharge for the full cells. The half cell formation cycles showed that the charge capacity neared the theoretical capacity limit for graphite of 372 mAh/g while the capacity was much lower for soft carbon at around 220 mAh/g. The coating increased the capacity by 4% and reduced the area specific impedance by 36% for the soft carbon. The effects at the same particle size of 20 microns were inconclusive for the graphite, but there was a 25% decrease in area specific impedance when the particle size was decreased. The effect of the coating on the performance of the soft carbon was visibly beneficial while the effects for the graphite may have been due more to particle size. A new test involving a 10 micron graphite blank and a larger electrode area will be done in the future to closer examine the phenomena.

High Activity Fuel Cell Catalysts via Mesoporous Nanocomposite Polymers. *GREGORY BAKER* (*Pennsylvania State University, University Park, PA*); *ERIC COCHRAN* (*Ames Laboratory, Ames, IA*). Hydrogen fuel cells have the potential to improve the way we propel our vehicles. Catalyst particles within cathode catalyst layer (CCL) promote the reaction of protons, electrons, and oxygen, producing water, which must be removed. The current CCL design suffers from poor mass transport properties, limiting the efficiency of the present-day hydrogen fuel cell. The current structure is a combination of different materials put together to achieve these goals but lacks the order needed to achieve the desired efficiency. In this research, we investigated the development of a novel CCL design that will significantly increase the transport of reactants to active catalyst sites. The first step towards this design was the synthesis of a new catalyst support, based on single-wall carbon nanotubes (SWCNTs), that integrates electon and proton conductivity into a single particle. First, pristine SWCNTs were functionalized with an aniline derivative compound using a solvent free technique. Then, azide-terminated polystyrene was "click-coupled" to the alkyne group. This SWCNT-graft-polystyrene was then sulfonated; this created negatively charged regions in the polymer, which facilitated the deposition of platinum nanoparticles through the reduction of platinum salts. After sulfonation the polymer is also proton-conductive. Thermogravimetric analysis analyzed the effectiveness of the grafting reactions. Nuclear magnetic resonance spectroscopy demonstrated that the proper products were prepared during the synthesis of the aniline derivative and also to ensure that azide terminated polystyrene was achieved. Transmission electron microscopy determined the effectiveness of the decoration with platinum.

Oxidation Characterization of Chromium Tungsten Niobium Superalloys. *AMANDA BASTIDOS* (*University of Texas at El Paso, El Paso, TX*); *KEN NATESAN* (*Argonne National Laboratory, Argonne, IL*). The past 50 years of metallurgical and materials engineering has brought about much more technologically advanced materials and alloys. One of the dilemmas with current alloys used in high temperature environments is the temperature limit seems to peak at 1,000°C. The overall goal of this research project is to characterize the oxidation layers of a chromium tungsten niobium (CrWNb) superalloy in short term oxidation (STO) experiments and long term oxidation (LTO) experiments in high temperature environments (700–1,400°C).

The STO samples undergo heat treatment in the furnace for 24 hours from 700–1,400°C in increments of 100 degrees and subsequently furnace cooled. Plots of weight gain per total surface area vs. oxidation temperature are obtained from the data. The LTO experiment follows the same set of procedures as the STO with the change from 24 hours to 168 hours; plots of weight gain per total surface area vs. oxidation time are obtained from the data. At temperatures between 700–900°C, the samples were primarily powder as opposed to temperatures 1,000°C and above where the samples maintained their solid forms. To characterize the oxidation layers of the CrWNb samples, scanning electron microscopy (SEM) and energy dispersive spectrometry (EDS) were be performed. If the research is successful, the application of this superalloy will be in gas turbines, combustion liners, fossil-fuel fired combustion systems, turbine blades, etc.

Photovoltaic Properties of Epitaxially Grown Bismuth Ferrite. SOURAV BASU (*University of California at Berkeley, Berkeley, CA*); RAMAMOORTHY RAMESH (*Lawrence Berkeley National Laboratory, Berkley, CA*). Photovoltaic properties of epitaxially grown (111) $BiFeO_3$ (a ferroelectric material) were investigated under a 100 mW/cm^2 solar simulator light source and tunable halogen source. Photo-excited carriers were extracted through transparent Indium Tin Oxide (ITO) top electrodes. Carrier migration was through-film, in the direction of intrinsic polarization. Current densities observed under solar spectrum at no applied field exceeded 1 mA/cm^2 for certain samples, much higher than previously observed in photovoltaic ferroelectric materials. All films were grown by Pulsed Laser Deposition (PLD). Annealing of samples in varying partial pressures of oxygen was conducted post-deposition to introduce oxygen vacancies and consequently improve the conductivity of the $BiFeO_3$ films. The magnitude of the photocurrent was observed to be directly proportional to the conductivity of the migration pathway. Traditionally, photovoltaic ferroelectric materials have been prevented from being used in energy conversion primarily because of their low current density output. By observing current densities in excess of 1 mA/cm^2 (on the order of magnitude of current densities produced by many photovoltaic semiconductors), we demonstrate the possibility for the use of $BiFeO_3$ in direct energy conversion. In addition, preliminary results involving wavelength dependence of photocurrent indicate the presence of the absorption edge near a wavelength corresponding to $BiFeO_3$'s theoretically predicted bandgap. In addition, future research involving the multiferroic properties of $BiFeO_3$ could present the possibility of optically controlled magnetization.

Doping of TiO_2 (with C and S) for Visible-light Absorption. ROHIT BIYANI (*Washington State University, Pullman, WA*); THEVA THEVUTHASAN (*Pacific Northwest National Laboratory, Richland, WA*). Hydrogen proves to be a very clean and efficient fuel source; unfortunately obtaining large quantities of it is not cheap. One of the potential methods of obtaining hydrogen involves photocatalytic splitting of water molecules with Ultraviolet light using Titanium Oxide (TiO_2) as the catalyst. However, an Ultraviolet light source is expensive; a cost efficient substitute is visible light or sunlight. Band engineering of TiO_2 single crystals with appropriate dopants can facilitate photocatalytic activity for visible-light absorption. Anion dopants such as nitrogen, carbon and sulfur have been implanted into the TiO_2 substrate, and it has been demonstrated that some of these implanted materials can absorb visible light for photochemistry. Our overall objective is to develop fundamental scientific understanding about the mechanisms associated with photochemistry in these materials. In this study, we used ion accelerator to implant C and S dopants in single crystal TiO_2 (110) samples and to investigate the structural changes in the materials. The samples were implanted at various temperatures and doses, the lattice site location of the dopants were analyzed using ion beam capabilities. The implanted TiO_2 substrates were characterized using Nuclear Reaction Analysis (NRA), Rutherford Backscattering Spectrometry (RBS), and Proton Induced X-ray Emission (PIXE) methods in random and channeling geometries. Although PIXE is extremely sensitive to trace elements, S quantification could not be made using PIXE due to the domination of the signal from Ti. The signal from S could not be collected without too many uncertainties. The RBS along channeling and random geometries showed that the greater the temperature of implantation, the less the damage was on the surface. Also a lower carbon dose at a high temperature of 900°C shows some substitutional behavior of the carbon atoms replacing possibly oxygen in the TiO_2 lattice. The samples were finally annealed at 900°C in air for several hours and as expected, the implantation damage was significantly reduced in the annealed samples. In addition, the angular yield curves show that the C atoms moved to interstitial positions during annealing. Further experiments are necessary to understand the influence of C dose on this behavior of C location in TiO_2 lattice.

High Storage Density Capacitors Fabricated Using Atomic Layer Deposition. ANDREA BLUMENTRITT (*LeTourneau University, Longview, TX*); JEFFREY ELAM (*Argonne National Laboratory, Argonne, IL*). Capacitors are devices which store charge and consist of an insulator between two conducting layers. Capacitors with high energy storage densities are extremely attractive as replacements for conventional batteries in electric and hybrid vehicles. This project sought to design and build high storage density capacitors with small insulator thicknesses and large surface areas-two factors that increase capacitance. The conducting and insulating layers were deposited by atomic layer deposition (ALD), a thin-film process which coats atomic monolayers of material through sequential self-limiting reactions. ALD is extremely useful for this application because it can deposit very uniform layers on high surface area substrates. Anodic aluminum oxide (AAO) membranes were used as the high surface area substrate material. Circular AAO membranes with a diameter of 13 mm and a thickness of 60 μm were used. These contained 200 nm pores which closed down to 20 nm at one end of the disc and had a pore density of 109/cm^2. The AAOs were placed in the ALD reactor and coated with layers of aluminum-doped zinc oxide (AZO, a conductor), aluminum oxide (Al_2O_3, an insulator), and again with AZO. A piece of silicon was also placed in the reactor as a baseline for measuring film thickness. After analysis by an ellipsometer, thicknesses of the final trial were recorded to be 20 nm for each AZO layer and 30 nm of Al_2O_3. Using a scanning electron microscope, thorough and even coatings of each layer were observed. More tests are still needed in order to measure capacitance and capacitance density, but the preliminary results suggest that forming a capacitor on a high surface area AAO can produce devices with greater capacitance densities than what is currently being made with similar technology.

***In Situ* Measurement of Stresses in Carburized Gears via Neutron Diffraction.** BRYAN BOGGS (*University of Tennessee at Martin, Martin, TN*); CAMDEN HUBBARD (*Oak Ridge National Laboratory, Oak Ridge, TN*). Carburized gears are characterized by a very hard outer layer that contains chemistry, phase, and microstructure gradients. X-rays have been used in the past to attain measurements of residual stresses, but X-ray diffraction is limited to near surface stress measurements due to attenuation. X-ray diffraction also has difficulty reaching the critical stress regions of a gear tooth due to beam interference from the complex geometry. This research seeks to develop experimental methods for measuring the stresses/strains in carburized gears at locations unattainable by X-rays and to do this as a function of applied load on the gear tooth. Experiments are being performed to determine if neutron diffraction can be used as an alternative to X-ray diffraction to measure the total stresses. Total stresses consist of both the residual stresses imparted during the carburization process and the load induced stresses resulting from power transmission. The experiments are being performed at the Neutron Residual Stress mapping Facility (NRSF2) at the High Flux Isotope Reactor (HFIR). In neutron diffraction, a powder sample is normally used to determine the unstressed lattice spacing or d_0. In carburized components, d_0 can not be determined from a single powdered sample because of the non-homogeneous material in the carburized region. As an alternative to using a powder sample, a method commonly used in X-ray diffraction known as the sin2σ method is being studied to determine if it can be used with neutron diffraction to accurately quantify d_0 in the carburized region. If successful, the sin2σ method will be used to determine d_0 at a number of points in the carburized region. Neutron diffraction methods will then be used to measure the d-space at each of the points for which d_0 was determined. The combination of d-space and d_0 at each point will enable the strains and stresses to be determined at the measurement points. The measurement of the d-space in a loaded gear is being facilitated with a Static Load Application Device (SLAD). This device was designed to statically load the gears as well as be compatible with the equipment at NRSF2. Stress analysis was done on the SLAD to ensure that the device would not exceed strength values found in engineering design standards.

Redox Reactions wiith Single-Walled Carbon Nanotubes. SOFIANE BOUKHALFA (*University of Illinois at Urbana-Champaign, Urbana, IL*); STEPHEN DOORN (*Los Alamos National Laboratory, Los Alamos, NM*). Single walled carbon nanotubes (SWNT) have been under close scrutiny by the scientific community since their discovery in 1992 due to their surprising material properties. SWNT synthesis can be achieved in numerous ways. However, these methods result in a wide spectrum of chiralities of nanotubes. In order to more efficiently use these novel materials, individual chiralities must be isolated.

To achieve this, a reduction-oxidation chemistry approach is used. Redox reagents of different electro-chemical potentials were added to solutions of SWNT in surfactant. Spectroscopy (absorbance and fluorescence) measurements were taken in order to monitor the effects of electron transfer between the SWNTs and the salts. Once chiral-specific doping can be achieved, isolation of these individual chiralities of SWNTs is planned through the use of ultracentrifugation. 20μL of each redox reagent was added to 3mL SWNT in surfactant solution while spectroscopy measurements were taken every 7 seconds in order to map out chiralities. Using a Fermi level map of the chiralities as a model, it was determined that the electro-chemical potential of the reagents directly affected the chiralities which were quenched during the experiments. Interaction between the salt and the surfactants is characterized by aggregation of the SWNTs; in the current redox reactions such aggregation, which broadens the spectroscopic signals, is not observed. Thus, a direct correlation was determined between the electro-chemical potential of the redox reagent and its effects on the nanotube solutions. This work establishes a future guideline for new work in the isolation of individual chiralities of nanotubes.

Spallation Neutron Source (SNS). *Yan-Jiun Chen* (*National Taiwan University, Taipei, Taiwan*); *Robert W. Shaw* (*Oak Ridge National Laboratory, Oak Ridge, TN*). The Spallation Neutron Source (SNS) uses a Multi-Turn Charge-Exchange Injection to form short pulses of protons in its accumulator ring. Carbon stripper foils are used in this process for removing electrons from the incoming H-Linac beam. Testing at various facilities has shown diamond stripper foils have an expected lifetime of more than 100 hours, five times that of evaporated carbon ones. Longer lifetimes can reduce beam downtime for replacement. This project involves producing diamond foils for the SNS and other accelerators. Diamond foils are grown via microwave plasma enhanced Chemical Vapor Deposition (CVD) on patterned silicon substrates. Substrates are patterned using photolithography, and etched chemically to produce corrugations 5~7 μm deep around the edges for mechanical stability of films. To enhance nucleation, the substrate surface is abraded with diamond powder slurry in an ultrasonic bath. Subsequently, 1~2 μm thick nano-crystalline diamond films are grown on the substrates under 1,000 W of microwave power and 130 torr with a gas mixture of 2% CH_4, 8% H_2, and 90% Ar. The substrate is then partially removed with a 1:1:1 mixture of hydrofluoric acid, acetic acid, and nitric acid, leaving a silicon edge for support of the foil. The main focus of the project is to optimize the performance of these diamond foils. Recently, foil areas have been increased by 57% to minimize beam loss, and foil thickness has been increased to maximize efficiency. Scanning electron microscopy (SEM) of the foils has revealed imperfections in the films, including black spots and pits. Black spots have not been proven to affect performance. Nevertheless, they can be successfully removed by etching away the surface of the film in a pure H_2 plasma. They are also suppressed with a lower growth pressure. Pits, ranging from 1 μm~10 μm wide, are suspected to cause loss of stripping efficiency and may result in holes or weak spots in foils. These pits are mainly caused by dust particles during the patterning of the substrates. Special attention is now paid to the preparation of substrates to minimize these occurrences. A cloudy visual appearance signifies uneven nucleation densities and/or substrate roughness. As a result, adjustments to the duration of ultrasonic abrasion are being made. Further testing in the SNS will reveal whether these measures lead to greater efficiency and longer lifetimes of foils.

X-ray Absorption Spectroscopy of Yb³⁺-Doped Optical Fibers. *Robert Citron* (*The University of Chicago, Chicago, IL*); *Arthur J. Kropf* (*Argonne National Laboratory, Argonne, IL*). Optical fibers doped with Ytterbium-3+ have become increasingly common in fiber lasers and amplifiers. Yb-doped fibers provide the capability to produce high power and short pulses at specific wavelengths, resulting in highly effective gain media. However, little is known about the local structure, distribution, and chemical coordination of Yb^{3+} in the fibers. This information is necessary to improve the manufacturing process and optical qualities of the fibers. Five fibers doped with Yb^{3+} were studied using Extended X-ray Absorption Fine Structure (EXAFS) spectroscopy and X-ray Absorption Near Edge Spectroscopy (XANES), in addition to Yb^{3+} mapping. The Yb^{3+} distribution in each fiber core was mapped with 2D and 1D intensity scans, which measured X-ray fluorescence over the scan areas. Two of the five fibers examined showed highly irregular Yb^{3+} distributions in the core center. In four of the five fibers Yb^{3+} was detected outside of the given fiber core dimensions, suggesting possible Yb^{3+} diffusion from the core, manufacturing error, or both. X-ray absorption spectroscopy (XAS) analysis has so far proven inconclusive, but did show that the fibers had differing EXAFS spectra. The Yb^{3+} distribution mapping proved highly useful, but additional modeling and examination of fiber preforms must be conducted to improve XAS analysis, which has been shown to have great potential for the study of similar optical fibers.

Production of Pure Phase Multiferroic Materials by High Oxygen Pressure Annealing Processes *Matthew Cromwell* (*Brigham Young University – Idaho, Rexburg, ID*); *R.W. McCallum* (*Ames Laboratory, Ames, IA*). This study aims to form multiferroic materials from Rare Earth compounds and Manganese oxides. The desired composition is RMn_2O_5 (R = Rare Earth). Multiferroic materials import stems from simultaneous ferromagnetic and ferroelectric characteristics. Because of their dual nature, multiferroic materials could be utilized in various technologies. Understanding the properties and behavior of their crystal systems is critical to the eventual application of such materials, yet producing a pure single phase is still problematic. This must be done by reacting highly stable R_2O_3 with Mn-O, which remain stable in air to 1200°C. Existing phase diagrams for the given system indicate that increasing partial pressure of Oxygen (PO_2) greatly improves the kinetics of the phase transition. However, at such temperatures and pressure, standard materials soften and fail. Oxygen also presents a problem, being highly corrosive in nature. A furnace chamber maintaining up to 1000°C with 10 bar PO_2 was built from Hainesalloy-230, a high-nickel superalloy. This pressurized system was installed and various safety considerations and procedures were negotiated in bringing this into operation. A series of experiments varying annealing conditions were then performed to study the effect of changing PO_2. Two sets of samples were made from the same mixture and run at 900°C and 1000°C for twenty hours. Within each set, four pressures (in bar) were applied — 9.3, 3, 1 and 0.2. Results were examined by X-Ray Diffraction (XRD) to determine composition. XRD showed the content of desired phase increased significantly at higher temperature and also with increasing PO_2. Increasing temperature by 100°C produced double the desired phase over the 20 hour test. Still significant was the increase due to PO_2 which lifted the desired phase from 60% to 72%. This affirms the importance of PO_2 in this phase system. In further study, the effect of PO_2 over greater time intervals and elevated temperatures may be instructive in obtaining pure phase materials.

Zirconium Oxide Nanostructures Prepared by Anodic Oxidation. *Ying Yi Dang* (*Columbia University, New York, NY*); *M. Parans Paranthaman* (*Oak Ridge National Laboratory, Oak Ridge, TN*). Zirconium oxide is an advanced ceramic material highly useful for structural and electrical applications because of its high strength, fracture toughness, chemical and thermal stability, and biocompatibility. If highly-ordered porous zirconium oxide membranes can be successfully formed, this will expand its real-world applications, such as further enhancing solid-oxide fuel cell technology. Recent studies have achieved various morphologies of porous zirconium oxide via anodization, but they have yet to create a porous layer where nanoholes are formed in a highly ordered array. In this study, electrochemical methods were used for zirconium oxide synthesis due to its advantages over other kinds of coating techniques, and because the thickness and morphology of the ceramic films can be easily tuned by the electrochemical parameters, such as electrolyte solutions and processing conditions, such as pH, voltage, and duration. The effects of additional steps such as pre-annealing and post-annealing were also examined. Results demonstrate the formation of anodic porous zirconium oxide with diverse morphologies, such as sponge-like layers, porous arrays with nanoholes ranging from 40 to 75 nm, and nanotube layers. X-ray powder diffraction analysis indicates a cubic crystallographic structure in the zirconium oxide. It was noted that increased voltage improved the ability of the membrane to stay adhered to the zirconium substrate, whereas lower voltages caused a propensity for the oxide film to flake off. Further studies are needed to control and confine these morphologies to specific parameter windows, and to investigate other important characteristics such as ionic conductivity.

X-ray Absorption Fine-Structure Spectroscopy of a Platinum-Nickel Catalyst X-ray Absorption Fine-Structure Spectroscopy of a Platinum-Nickel Catalyst for a Direct Methanol Fuel Cell. *Jarod Delhotal* (*Sauk Valley Community College, Dixon, IL*); *Carlo Segre* (*Argonne National Laboratory, Argonne, IL*). Direct methanol fuel cell (DMFC) technology is approaching the point where it may solve many energy problems for portable power. However, there are still several obstacles that must be overcome before DMFCs become a viable energy solution. To better understand the structure of a platinum-nickel catalyst, researchers used X-ray absorption fine-structure (XAFS) spectroscopy to analyze the first-shell structure of a platinum-nickel cathode catalyst for a DMFC. The nanoparticle catalyst was supported by a carbon base and pressed into a proton-permeable membrane to

form a membrane electrode assembly (MEA). The dry MEA was then scanned at both nickel K edge and platinum L3 edge energy ranges. Surprisingly, it was discovered that the nickel atom's most abundant near neighboring atom was oxygen at 2.07 Angstroms (Å), while a nickel neighbor was also found at 2.63 Å. From the platinum edge, a platinum neighbor was found at 2.69 Å and a nickel neighbor at 2.62 Å. Similar results were found for a wet MEA that was taken directly out of the DMFC. Nickel was found to have an oxygen neighbor at 2.04 Å and a nickel neighbor at 2.60 Å. The platinum edge spectrum for the wet MEA showed a platinum neighbor at 2.69 Å and a nickel neighbor at 2.63 Å. Further analysis is being conducted to determine the structure of the catalyst while it is in operation in a DMFC. A comparison of these findings will help scientists to understand the structural behavior of the catalyst while it is in use. This will lead to a better understanding of fuel cell catalysis, and could accelerate the development of fuel cell technology.

Data Processing and Analysis for the Superconductivity Program. *Michael Duitsman* (*University of Evansville, Evansville, IN*); *Victor Maroni* (*Argonne National Laboratory, Argonne, IL*). The Superconductivity for Electric Systems Program at Argonne is performing detailed characterization studies on $Y_1Ba_2Cu_3O_7$ (YBCO) superconducting films deposited on long-length metal-substrate tapes. One of the important research tools used in this research is Raman micro-spectroscopy. With Raman spectroscopy it is possible to determine phase composition and texture quality of the YBCO films. A large number of Raman spectra have been collected for this program. Each spectrum has to be processed to remove background noise, so that a representative Raman spectrum extrapolated to a horizontal baseline can be obtained for further analysis. Various types of computer programs are available to carry out these tasks. In this report the use of one such series of programs, the GRAMS series, is discussed. The work is focused on processing groups of spectra obtained from YBCO tapes for which the processing time and temperature were varied from end to end. The tape was then diagonally milled in intervals throughout its length, so that the effects of baking could be observed throughout the depth of the superconducting film. The samples were analyzed by applying the software for baselining, noise smoothing, spectral subtraction, and curve-fitting of such spectra. It is clear that baking, as well as the introduction of rare earth elements, has a significant effect on the performance of superconducting films.

Single Component Variation of Low Activity Tank Waste to Determine Chemical and Physical Behavior on Molten Ionic Salt. *Shaelah Easterday* (*Gonzaga University, Spokane, WA*); *Michael Schweiger* (*Pacific Northwest National Laboratory, Richland, WA*). Bulk vitrification is a process used to safely contain Low Activity Waste (LAW) on the Hanford Site into a vitreous waste form. This is done by heating the LAW mixed with glass-forming minerals in a large melting container lined with Castable Refractory Block (CRB). At temperatures above 275–325°C, sodium nitrate and sodium nitrite (NO_3+NO_2) in the LAW form Molten Ionic Salt (MIS) that penetrates the CRB. When this occurs, the MIS may be able to leach from the CRB into the environment. Feeds were prepared by drying a liquid LAW simulant with glass-forming minerals. The LAW composition was varied, one component at a time. Feeds were placed in silica crucibles of a similar porosity as the CRB, and heated to 500°C at 5°C/minute and held for 30 minutes. The feed was removed, and the crucibles were heated from 650°C to 1,000°C at 7°C/minute and held at 1,000°C for 60 minutes. To determine MIS penetration, the crucibles were weighed before and after each heat treatment. It was found that by replacing NO_3+NO_2 with any component but sulfate, MIS migration decreased. Replacing NO_3+NO_2 with sulfate had no effect on MIS migration. Acetate and chromate decreased MIS migration more than other components. This project provides important data for the Bulk Vitrification of LAW on the Hanford Site by allowing to asses the response of MIS migration in melter feeds to composition variations of the waste.

Degradation of Organic Light Emitting Diodes. *Eric Ellenoff* (*Stanford University, Stanford, CA*); *Joseph Berry* (*National Renewable Energy Laboratory, Golden, CO*). Organic light emitting diodes (OLEDs) currently degrade much faster than standard inorganic light emitting diodes. In order to improve OLEDs' lifetimes, it is necessary to measure their degradation in a controlled environment to determine what mechanism is responsible. A measurement setup was constructed to characterize the decay of an OLED's IV curve, emission intensity, and emission spectrum. A baseline for device performance and degradation was established by measuring their performance in a glovebox where they were surrounded by Argon with water and oxygen kept below 0.1 ppm. A second set of devices was tested outside of the glovebox in a prototype for a portable encapsulation device designed and built at NREL known as a "puck". By comparing the degradation of these devices to the set which was kept in the glovebox, we were able to determine how effective the puck was at protecting OLEDs. Over the course of a 165-hour test, the intensity of the OLED tested in the glovebox fell by 62% which indicates a half life of 115.5 hours. The relative emission of light at each wavelength remained constant throughout this test. The OLED which was tested in a puck degraded much more rapidly: it lost half of its intensity after every 19 hours of use, and degraded even when not in use. Furthermore, as the OLED became dimmer, its emission spectrum shifted, resulting in significantly less light being emitted between 540 nm and 660 nm. For these reasons, the puck proved to be inadequate for encapsulating devices. A second-generation test would feature the ability to leak controlled concentrations of reactants such as oxygen and water vapor to the device.

Synthesis of Microporous Materials Using Amino Triazoles. *Laura Engerer* (*Valparaiso University, Valparaiso, IN*); *John Schlueter* (*Argonne National Laboratory, Argonne, IL*). Microporous materials (MM) are commonly used in separation and storage of hydrogen fuel for energy applications. The objective of this project is to synthesize MM using zinc and copper ions and triazole ligands by a solvothermal process. Various combinations of Zn and Cu were mixed with 3-amino-1,2,4-triazole (AmTAZ) and 3,5-diamino-1,2,4-triazole (DamTAZ) and carbonate, oxalate, cyanate, thiocyanate, dicyanamide, and tricyanomethanide anions in a water/ethanol mix. They were heat treated to 80, 120, and 140°C with reaction times ranging from one day to two weeks. The materials were characterized by X-ray diffraction and gas adsorption techniques. From the X-ray powder diffraction patterns, most samples were crystalline in nature, whereas a few appeared to be amorphous. Based on the diffraction patterns, modifications were made to the original protocol aiming at eliminating multiple phases and to grow single-crystals. Analysis of the powder patterns provided a few trends. Copper ions were too easily reduced and therefore produce multiple phases in each experiment. This indicated that copper ions are undesirable for this particular system. Zinc has been shown to produce promising structures before this project and remains the most promising metal ion. Initially the DAmTAZ ligand did not show as much promise as its AmTAZ counterpart as none of the powders that were crystalline in nature contained DAmTAZ. Of the other anions incorporated into the framework the oxalate anion tended to combine with just the metal ion causing it to form crystals of the starting material. A few different combinations produced single crystals, but of these only two were appropriate for single crystal X-ray diffraction. The first structure was $K_2[Zn_5AmTAZ_4(Oxalate)_4]_{0.6}(H_2O)$. This structure is similar in contents but not structure to one of the materials previously synthesized in this project. The second is $[Zn_2(DamTAZ)_2(OH)(OH_2)](NO)_3$. This second one is the first to be synthesized with the DAmTAZ ligand. Future inquiries should take pH into account and experiment with solvent size.

Cross-Sectional Polishing for Solar Cell Device Characterization. *Nathan Fast* (*California State University – Northridge, Northridge, CA*); *Bhushan Sopori* (*National Renewable Energy Laboratory, Golden, CO*). Fabrication of high efficiency solar cells requires a method to study the effects of new processes on the interactions and physical structure within a cell. An improved method for cross-sectional polishing of large areas of solar cells is described. This method produces a highly planar surface compared to the conventional way of preparing a sample by cleaving. The traditional method of cleaving or fracturing a sample works well for single crystalline wafers, however, creates undesirable surface morphologies for polycrystalline wafers or multi-layered devices such as finished solar cells. The discontinuities caused by the fracture mechanics of non-homogeneous samples create patterns that make it difficult to characterize the true nature of the materials under study. Solar cells cross-sectioned by this improved technique can be characterized by very high resolution electron-beam and optical imaging to measure the alloyed regions of front and back contacts, thickness of backsurface field, and other important physical properties of solar cells. In this method, a standard polycrystalline Si solar cell sample is prepared in a specially designed polishing chuck and secured with wax. The sample is sequentially mechanically polished by progressively decreasing the polishing grit size with chemical mechanical polishing (CMP) used as the last step. Optical microscope and scanning electron microscope (SEM) micrographs showing the planar results of this progressive polishing method are presented showing the improvement over the cleaving technique. This large area cross-sectioning permits statistically significant evaluation of many areas of the cell. The planarity of the sample edge makes it possible to perform a variety of atomic force microscope (AFM), conductive atomic force microscope

(CAFM), scanning Kelvin probe microscope (SKPM) and other scanning analyses over large areas in addition to more localized investigations such as with SEM.

Bending Kirkpatrick-Baez Mirrors for Neutron Focusing. *Anthony Fields, Jay Patel* (*South Carolina State University, Orangeburg, SC*)*; Gene E. Ice* (*Oak Ridge National Laboratory, Oak Ridge, TN*). Neutron scattering is useful for analyzing the atomic structure and defect density of materials. Because neutrons have spin, an isotope-dependent scattering cross-section and are penetrating, neutron beams are particularly well suited for the study of magnetic materials, bulk materials and for the study of low Z or mixed Z structures. Several techniques for directing a beam of neutrons to a sample are available. While guide tubes and collimators work well for large sample sizes, focusing becomes increasingly important as the neutron probe dimension and sample sizes become small. The importance of high-performance nondispersive focusing optics for neutrons has just recently been recognized. In micro-focus experiments, we consider the need for convenient wavelength tuning and/or broad bandpass beams. This favors achromatic methods based on specular reflection. The Elliptical Kirkpatrick-Baez (KB) scheme offers the best flexibility and neutron gathering power, and can nondispersively image neutrons to small spots with high intensity and source-limited brilliance. The KB geometry uses crossed mirrors in grazing-incidence. With perfect elliptical KB mirrors, spherical aberration can be eliminated. We have adopted techniques for producing elliptical neutron mirrors by controlled bending. The need to control the slope errors in the mirrors is very important. The mirrors, the bending control mechanism, and supports are integrated as a unit. Both mirrors are attached to, and bent by a leaf spring mechanism. We have used a laser beam to simulate a thermal neutron beam for system calibrations; we determine the radius of curvature of the mirror as a function of bender settings (coupling force). Results show changes in the focal length (and subsequently in the radius of curvature) with micrometer setting. From these results we can determine the optimum radius of curvature of the mirrors for minimum slope errors. The mirror in the vertical plane sags under gravity and therefore, introduces a mixture of defocus and spherical aberration. We have designed passive corrections by a series of springs under the mirror. A computer program has been written to calculate the gravitational curvatures and slope errors as a function of the number of support springs and loading conditions. Simulation results show that the effect of one spring alone reduces the slope errors by a factor of 10 and with three spring supports, slope errors are reduced by over a factor of 100.

Blends of Thiophene-Based Dendrimers with Titania Nanoparticles for Use in Organic Photovoltaic Devices. *Talia Gershon* (*Massachusetts Institute of Technology, Cambridge, MA*)*; David Ginley* (*National Renewable Energy Laboratory, Golden, CO*). Dendrimers (small branched organic molecules) offer an exciting alternative to typical semiconducting polymers in organic photovoltaic applications, as they are monodisperse and have virtually independently tunable optical, electronic, and architectural properties. Similarly, metal oxide nanoparticles offer a tunable, high-mobility alternative to the established organic electron acceptors. Since nanoparticles are many times larger than typical organic acceptors they may also help address issues in domain size limitations that appear in fullerene-based bulk heterojunctions. To explore these advantages a unique blend of the thiophene-based dendrimer, 4G1-3S, and anatase titania nanoparticles has been studied for use in organic photovoltaic devices. The charge transfer between these two materials was monitored as a function of solvent, drying conditions, and device architecture. Changes in film domain size and morphology were observed via SEM and AFM images. Devices were made under a variety of conditions via solution processing in air. Although no photocurrent was consistently extracted, several key conclusions were drawn regarding how these materials interact, which point toward the realization of a successful device.

Accelerated Wear Testing of Ultrananocrystalline Diamond-Coated Pump Seals. *Lindsey Goodman* (*Binghamton University, Binghamton, NY*)*; Greg Krumdick* (*Argonne National Laboratory, Argonne, IL*). The performance of industrial chemical pumps can depend directly on the performance of the seals installed within the pumps. Using a chemical vapor deposition process developed at Argonne National Laboratory, scientists can coat standard pump seals with a thin layer of Ultrananocrystalline Diamond (UNCD™). Prior laboratory tests conducted at Argonne found that when subjected to identical conditions as uncoated seals, UNCD™-coated seals show increased energy efficiency and dramatically increased seal life expectancy. The objective of the experiment described in this paper was to design a system that can be used to verify these findings by subjecting UNCD™ coated and uncoated seals to accelerated wear conditions. The experimental protocol requires the pumping of an abrasive slurry of diatomaceous earth for 100 consecutive hours. Prior to their installation into the abrasive pump testing system, Raman spectroscopy and surface profilometry was used to analyze and characterize the surfaces of uncoated and UNCD™-coated seals. Before performing a complete 100 hour test with both identical pumps, the system was evaluated for robustness and durability using only the pump containing the uncoated seal. Critical temperatures, pressures, and flows were continuously recorded while abrasives were pumped for 100 hours. Upon completion of the test, components of the test system were inspected for damage due to the abrasives. Accelerated wear was found on system parts, requiring design modifications to the experimental system. Analysis was performed on the uncoated seal. Wear on this seal was evaluated by comparison between pre and post-experimental surface profile analyses. When system modifications are complete, both UNCD-coated and uncoated seals will be subjected to identical accelerated wear conditions. Wear on the seals will be compared using surface profilometry and Raman spectroscopy.

Optimization of Spray-Coated Organic Photovoltaics. *Renee Green* (*University of Pittsburgh, Pittsburgh, PA*)*; Garry Rumbles* (*National Renewable Energy Laboratory, Golden, CO*). Organic photovoltaic devices, traditionally spin-coated, were made via an airbrush spray-deposition technique from a 1:1 poly(3-hexylthiophene) (P3HT) and [6,6]-phenyl-C61 butyric acid methyl ester (PCBM) blend in dilute (1 mg/ml each) solution. Devices were tested for dependence on solvent boiling point and annealing temperature. Working devices resulted from solutions prepared in chloroform, toluene, chlorobenzene, and para-xylene, with an initial maximum power conversion efficiency of over 2% (average 1.787%) from a p-xylene solution. Chlorobenzene was selected for use in further studies due to its small statistical spread of device efficiencies, high-quality smooth films, and comparable (1.15%) efficiency values. Annealing the device active layer at 120°C resulted in the highest power conversion efficiency among annealing temperatures ranging from 90°C to 200°C. Spray-coating is ideal for its ability to deposit highly dilute solutions, create multilayer organic devices, and expand the range of available analysis techniques by permitting the creation of high-quality thick films.

Development of an ASTM Graphite Oxidation Test Method. *Tyler Guldan* (*The University of Tennessee, Knoxville, TN*)*; Timothy D. Burchell* (*Oak Ridge National Laboratory, Oak Ridge, TN*). Graphite, one of the three allotropes of carbon, is a very useful material because of its unique chemical structure and properties such as mechanical strength, chemical inertness, and electrical conductivity. In order to advance our knowledge of various graphite brands, further research must be conducted to gain a greater insight into the process and effects of oxidation on graphite properties. Although the key processes and controlling elements of graphite oxidation have been identified, the behavior of this material during and after oxidation is not well established. Knowledge of this behavior is crucial in understanding what happens to the various graphite components in nuclear reactors. Thermogravimetric analysis in a vertical furnace of large samples of NBG-18 graphite at the Oak Ridge National Laboratory (ORNL) has been used to characterize the oxidation resistance of this material, and to increase the scientific understanding of the relationship between the rate of oxidation and the flow rates of gases, temperature, and the intrinsic reactivity of graphite. This helps to identify the more oxidation resistant forms of graphite. In addition, comparative analysis of data collected on other graphite materials has been conducted, in order to identify a more expedient procedure for analysis of graphite oxidation data. The information gathered from these experiments and calculations is geared towards the development of an American Society for Testing and Materials (ASTM) test method for the oxidation of graphite. More research on all of the types of graphite is needed, but such results suggest that the current ORNL procedure using the vertical tube furnace may become a reliable ASTM test method.

Friction and Wear of Steel in Commercial Gear Oils. *Joel Hernandez* (*University of Puerto Rico, Mayagüez, PR*); *Robert A. Erck* (*Argonne National Laboratory, Argonne, IL*). Friction is one of the principal causes of lower efficiency of mechanical systems. Friction also produces wear, which has an impact of millions of dollars per year to the industry and transportation. To reduce the effect of wear and reduce friction, new lubricants for transportation systems, like motor and transmission oils and their additives, are being synthesized and tested. Using a CSEM ball-on-disk tribometer, the performance of a commercial gear oils was tested in a range of temperatures from 250°C to 1,000°C. For the test, a flat 8620 steel surface was slid

against a 0.5 inch diameter type 52100 steel ball; a light bulb with an on-off controller was used to raise and control the temperature in the system. Over the course of five-hour tests, all the samples behaved different from oil to oil, some of them rising and lowering its friction coefficient (μ) with the changes of temperature, the same happened with wear. For two of the five oils, the μ at the start and the end was constant regardless the test temperature; for the other three oils the friction coefficient had no noticeable change with the rise in temperature. These three oils lowered its μ faster with proportionally with an increment in temperature. By using surface mapping microscopy, we analyzed the shape of the scars and measured the volume of material loss. It was found that the behavior of oils do not followed any concrete pattern with the rise of temperature; it can be caused by the formula use for the oil fabrication and the additives presents in them.

Slag Penetration in Coal Gasifier Refractories. *Brent Hicks* (*Brigham Young University, Provo, UT*); *S.K. Sundaram* (*Pacific Northwest National Laboratory, Richland, WA*). Coal gasification is a process used to convert coal in the presence of water, elevated temperature, high pressure, and a reducing atmosphere into high-value chemicals and fuels. A gasifier refractory lining protects the stainless steel shell of the gasifier from elevated temperatures and corrosive coal slag. Refractories composed primarily of Cr_2O_3 have been found the most resistant to slag corrosion, but they still fail to meet their targeted operational lifetime of three years. Experimental data on the slag-refractory interaction is necessary to develop models to 1) identify critical conditions at which refractory corrosion sharply increases 2) predict the service life of a gasifier refractory, and 3) discover processes/techniques to protect the refractories for extended life. Laboratory tests were conducted to determine the penetration depth of three slags representative of a wide variety of coals in the United States into five high-chrome refractories. The slags were pressed into pellets, placed inside a core-drilled refractory sample, and heat-treated in a controlled atmosphere furnace. Variables tested were refractory-slag combinations, different maximum temperatures and partial pressures of O_2, and thermal cycling between temperature extremes found in commercial gasifiers. Slag penetration depths were measured from spliced optical images of each refractory. Samples heated to 1,470°C for 2 hrs had average penetration depths ranging from 1.99±0.15 mm to approximately 27 mm; compare to 1.53±0.26 mm to 8.47±0.34 mm for samples heat-treated at 1,310°C for 2 hrs and 8.55±0.55 mm to approximately 26.2 mm for samples thermally cycled three times between 1,150°C and 1,550°C. AUREX 95P, a high-chrome refractory containing 3.3wt% P_2O_5, showed the least slag penetration of all studied conditions. P_2O_5 likely reacts with the slags to increase their viscosity and restrict molten slag penetration. Results indicate that lower temperatures correspond to less slag penetration; the slag is less fluid at 1,310°C than at 1,470°C. Scanning electron microscopy will be used to verify slag penetration depths for AUREX 95P because it was difficult to distinguish slag from P_2O_5 with optical microscopy.

Establishment of Manganese Oxide and Lanthanum Oxide as Atomic Layer Deposition Materials for Lanthanum Strontium Manganate (LSM) Electrodes. *David Honegger* (*Lewis & Clark College, Portland, OR*); *Jeffrey Elam* (*Argonne National Laboratory, Argonne, IL*). Nanostructured electrodes coated with thin LSM films show promise for increasing the efficiency of solid-oxide fuel cells by dramatically increasing the reactive surface area. Although the ability of atomic layer deposition (ALD) to conformally coat high-aspect-ratio substrates with monolayer control makes the process ideal for LSM deposition on these porous structures, ALD deposition of the individual materials that make up LSM, manganese oxide, lanthanum oxide and strontium oxide, is still in the pioneering phase. Moreover, the creation of LSM requires that the deposition conditions (e.g., substrate temperature) for the constituent materials be compatible. This study explored the deposition environments of manganese oxide and lanthanum oxide, and then found suitable conditions under which lanthanum manganate could be deposited. The results were confirmed with spectroscopic ellipsometry, X-ray fluorescence and an *in situ* quartz-crystal microbalance. Manganese oxide films were deposited on silicon in a substrate temperature range of 100°C to 300°C by using bis(ethylcyclopentadienyl) manganese [$Mn(EtCp)_2$] and de-ionized water as reactants. Lanthanum oxide films were successfully deposited on silicon as well in a substrate temperature range of 175°C to 300°C by using tris(i-propylcyclopentadienyl) lanthanum [$La(IpCp)_3$] and ozone as reactants, creating a convenient temperature window of 175°C to 300°C in which to attempt lanthanum manganate deposition. Lanthanum manganate films were then deposited by alternating the exposure of the reactants between $La(IpCp)_3/O_3$ and $Mn(EtCp)_2/H_2O$. Film composition was controlled by altering the ratio of reactant exposures to the substrate. Successful growth of lanthanum manganate paves the way for LSM deposition via strontium-doping, and the eventual optimization of its electrical properties for use in solid oxide fuel cells.

The Optimization of Atomic Layer Deposition Parameters for Zinc Oxide and Aluminum-Doped Zinc Oxide Films as Transparent Conducting Oxides in Dye-Sensitized Solar Cells. *David Honegger* (*Lewis & Clark College, Portland, OR*); *Gregory Krumdick* (*Argonne National Laboratory, Argonne, IL*). Severely low efficiencies have outweighed the benefits of low-cost and the manufacturing ease of dye-sensitized solar cells (DSSCs). However, recent nano-scale developments are unlocking new possibilities and rekindling considerable interest in these solar cells. Novel high-aspect-ratio substrates are being fabricated to support more light-harvesting dye and create a more direct path for electrons in the DSSC photovoltaic circuit, but the enhanced efficiencies are still too low for widespread application. The deposition of thin transparent conducting oxide (TCO) films, such as zinc oxide (ZnO) and aluminum-doped zinc oxide (AZO), on the surface of these substrates can increase DSSC efficiency by providing a more efficient electron transport. Therefore, the effects of deposition parameters on the optical and electrical properties of thin TCO coatings on high-aspect-ratio substrates need to be studied in order to create an optimal film. This study measured the resistivities and optical transmittances of ZnO and AZO films on anodic aluminum oxide membranes using atomic layer deposition, a thin-film deposition technique involving a binary sequence of self-limiting surface reactions. Spectroscopic ellipsometry, spectrophotometry, and four-point probe resistance measurements were used to study the effects of varying oxidizer strengths (H_2O, H_2O_2, and O_3) and deposition temperatures (50–200°C). Results have confirmed that a weaker oxidizer such as H_2O, as well as a higher deposition temperature, creates a significantly more conductive film. Optical transmittance, however, trends in the opposite direction; stronger oxidizers such as O_3 and deposition at lower temperatures lead to more transparent films. These observations suggest that both deposition temperature and oxidizer strength affect the number of oxygen vacancies in n-type conductive ZnO films. Also, the 5% aluminum AZO films were observed to enhance the conductivity of ZnO without compromising a significant amount of optical transmittance. In conclusion, AZO films are seen as advantageous over ZnO films as TCOs, but the optimal choice of oxidizer and deposition temperature will depend upon the relative influences of conductivity and transparency on the overall efficiency of the DSSC. Further studies on the effects of annealing the films after deposition would be advantageous to a more complete understanding of the potential ZnO and AZO films have as TCOs in nanostructured DSSCs.

The Effect of Metal Deposition on the Electro-Optical Properties of Single Wall Carbon Nanotube Networks. *John Hunt* (*University of Tennessee, Knoxville, TN*); *Ilia Ivanov* (*Oak Ridge National Laboratory, Oak Ridge, TN*). Single wall carbon nanotube (SWNT) networks exhibit high flexibility and optical transparency which make them perfect candidates to replace brittle and expensive indium tin oxide (ITO) as electrodes in displays. However, SWNT networks do not have the excellent conductivity of individual carbon nanotubes due to the high resistance of nanotube bundles and nanotube-to-nanotube junctions. The focus of this research project was to explore the deposition of metals on SWNT networks as a means to improve their conductivity, without sacrificing transparency. SWNT networks were deposited on the surface of glass and varying amounts, ranging from 1 to 10 nm, of Au, Pt and Pd were deposited via physical vapor deposition. The optical absorbance and sheet conductivity of SWNT networks were measured for each metal loading. Small metal loadings (~1nm) were found to increase conductivity by approximately 50% with a 6% average increase in absorbance. Analysis of absorbance and conductivity measurements both indicated electronic interactions occurring between SWNTs and deposited metal. Temperature-resistance measurements were used to determine the nature of this interaction, which was shown to be the reduction of barrier hopping resistance at nanotube-nanotube junctions.

Atomic Layer Deposition of Alumina on High Surface Area Silica Powders. *Trang Huynh* (*DePaul University, Chicago, IL*); *Jeffrey Elam* (*Argonne National Laboratory, Argonne, IL*). Alumina is a transparent insulating oxide which is widely used as a catalyst support layer. Thin films of alumina can be grown by atomic layer deposition (ALD) down to the nanoscale of one monolayer per reaction cycle by using trimethylaluminum and water. The purpose of this project was to determine whether nanoporous silica powders with high surface areas could be uniformly coated with alumina by the ALD method

such that full saturation could occur. X-ray fluorescence and direct weight measurements were used to determine the growth rate of alumina with respect to the number of reaction cycles during growth. In order to better understand the surface chemistry of these powders, the properties of the alumina coated powders were analyzed using scanning electron microscopy and energy dispersive analysis of X-rays (EDAX) measurements. These measurements revealed uniform infiltration of the high surface area powder by the ALD alumina coating. There is future interest in growing cobalt oxide on silica powders by ALD for its potential use as a catalyst in nanoporous membranes using alumina as a support.

In-Situ Stress Measurement for MOCVD Growth of High Efficiency Lattice-Mismatched Solar Cells.

ALEJANDRO LEVANDER (*Pennsylvania State University, State College, PA*)*; JOHN GEISZ (*National Renewable Energy Laboratory, Golden, CO*). Dislocations, formed in order to relieve stress, act as sites for nonradiative electron/hole pair recombination, which reduces the efficiency of photovoltaics. Stress forms as a result of mechanical and thermal mechanisms during the metal-organic chemical vapor deposition growth process. Mechanical stress is the result of depositing lattice-mismatched (LMM) layers on top of one another and thermal stress results from a thermal gradient within the sample and depositing layers with different thermal expansion coefficients on top of one another. To reduce the number of dislocations in the active layer when using LMM materials, compositionally step-graded layers and a buffer layer are placed between the two LMM materials. In order to achieve a better understanding of the effect of stress on the active layer, the buffer composition, and therefore lattice constant, was varied to change the stress on the active layer. The *in-situ* stress and *ex-situ* strain were characterized using a multi-beam optical stress sensor and X-ray diffractometry respectively. The quality of the photovoltaic devices was measured using a solar simulator and quantum efficiency instrument. Samples with near zero stress or small amounts of compressive stress in the active layer had the highest open-circuit voltages and efficiencies. Tensile stress in the active layer significantly degraded performance. The biaxial modulus was calculated from a stress v. strain curve, but several sources of error exist. The band gap of the active layer increased with increasing stress, despite the composition remaining constant. Future work will concentrate on the effect of dopant type on stress development and dislocation formation in the graded layer.

Quasielectrostatic Carbon Orientation for Lithium-Ion Battery Applications.

CLIFF MCCOLD (*Vanderbilt University, Nashville, TN*); JANE Y. HOWE (*Oak Ridge National Laboratory, Oak Ridge, TN*). In Quasielectrostatic Carbon Orientation (QCO) processing, carbon precursor materials are thermally treated while subject to an alternating current (AC) electric field with the goal of producing carbon materials with oriented graphene sheets. To provide proof-of-principle, QCO-treated samples are characterized to determine if conductive graphene sheets composed of bonded carbon atoms can be aligned in the direction of the electric field. Carbons with oriented graphene sheets could potentially be used in lithium-ion battery anodes, permitting higher charge rates, greater maximum current, and higher power density. A tube furnace was used to raise the temperature of the precursor material in an inert argon atmosphere. The material was held in a rig between top and bottom capacitor plates at different voltages, which applied the field during the entire 24-hour thermal processing. Variables included precursor materials (Mitsubishi AR mesophase pitch, phenolic resin), highest temperature (280°C, 650°C), AC field frequency (200 Hz, 10 kHz, 700 kHz), and electric field strength (no field, 2.4 kV/cm, 6.0 kV/cm). Created samples underwent X-ray diffraction and impedance spectrometry to determine if desired graphene sheet orientation was achieved. Results indicated that AR mesophase pitch does not respond to QCO processing at softening temperature (280°C). Severe foaming of AR mesophase pitch under numerous run conditions up to carbonization temperature (650°C) excluded carbonized samples from both characterization techniques. Phenolic resin samples showed QCO treatment-dependant results at carbonization temperature, but data was from too small a sample population to see clearly defined trends. Future work includes extensive sample creation under various QCO field frequencies. The ability to apply a stronger field (6.0 kV/cm and higher) was only recently developed by minimizing capacitor plate separation, and many samples remain to be created using stronger field conditions. Isotropic pitch and cellulose are potential future precursor materials. Created samples must be analyzed using the X-ray diffraction and impedance spectrometry, and scanning electron microscopy will also be used for future analysis. Once a clear trend in data is observed, the appropriate precursor material and run conditions will be used to create samples for direct lithium-ion battery anode testing.

Safety Barrier Program to Protect Experimenters in the Event of Pressure Cell Explosion.

RACHEL MORRIS (*Maryville College, Maryville, TN*)*; LAKEISHA WALKER, LOUIS SANTODONATO (*Oak Ridge National Laboratory, Oak Ridge, TN*). In neutron scattering research, high pressure experimentation with pressure cells is becoming more prevalent. Although this particular type of experimentation can provide a plethora of information regarding solutions to geophysical issues as well as hydrogen storage designs, material analysis at high pressure can be very dangerous. For this reason, scientists need to take precaution for ensuring their safety when using pressure cells under extreme conditions. Since pressure cell fragments can be projected if the cell ruptures or explodes, a safety barrier should be constructed to contain the hazard. Therefore, I have written a program in Visual Basic for Applications using a Microsoft Excel spreadsheet interface to help determine an appropriate and cost-efficient safety barrier. The logic of the program is not only based on calculations derived from the equations of motion in physics for radial distance and velocity, but it is also based on equations of acceleration involving the thickness and density of the cell initially and the amount of pressure used in the experiment. These calculations are the basis for determining how fast an infinitesimal fragment (in the worst case, the entire cell) will be traveling at any given distance from the initial starting position of the cell. The primary purpose of the program is to use a model of velocity versus distance to aid in determining the dimensions for a safety barrier that will be impenetrable for the largest fragment traveling at the highest velocity. Although any cell can be modeled with this program (provided the user supplies certain values for variables), the Titanium Zirconium (TiZr) alloy cell is exampled in this paper, which has a pressure equivalent to 200×10^6 Pa, a density of 5,230 kg/m^3, a thickness of 0.0039751 m, and an initial radius of 0.003175 m. The TiZr cell was modeled for 35 steps for 0.000036 s, until the radial distance of the fragment reached 0.123 m and the velocity reached 195 m/s. Thus, the projected and desired results were achieved using the program, and the construction of the barrier will occur in fall 2007.

Model Based Illumination Optimization for a 003-Numerical Aperture Extreme Ultraviolet Lithography Tool.

JONATHAN NATION (*University of Arizona – Tucson, Tucson, AZ*); PATRICK NAULLEAU (*Lawrence Berkeley National Laboratory, Berkley, CA*). There have been many recent advances in high numerical aperture (NA) extreme ultraviolet (EUV) lithography systems. The 0.3-NA Micro Exposure Tool (MET) at the Advanced Light Source (ALS) currently utilizes a programmable coherence illuminator system with the capability of creating different pupil fills. It is well known that illumination settings can be tailored to optimize printing performance for particular features. The optimal illumination settings, however, depend not only on the feature type but also on the specifics of the pupil function, including phase (or aberrations) and amplitude (or pupil obscurations). In order to maximize the productivity of the MET, the best possible pupil fill should be chosen for the feature type being imaged in each experiment. In this research, aerial image modeling software is used to study the optimal illumination conditions for the SEMATECH Berkeley MET tool as a function of feature size and type taking into consideration the known pupil function of the optic. The metrics of maximum contrast over a 50 nm focus range and depth of focus with contrast greater than 0.5 are used to gauge the performance of each pupil fill tested. We will present the best annular, dipole, and monopole pupil fills for each feature type as well as for each individual feature size. Experiments relying on only one feature size will obtain the greatest improvement in contrast and depth of focus by using the presented pupil fills, at the possible expense of losing quality of other feature sizes. The results are also directly compared to the default annular 0.35–0.55 setting used in the commercial implementations of the MET tool. Initial results for annular pupil fills reveal that improvements of up to 12% in each metric can be obtained.

Terahertz Spectroscopy of Chalcogenide Glasses.

JEFFREY NEUMANN (*University of Michigan, Ann Arbor, MI*); S.K. SUNDARAM (*Pacific Northwest National Laboratory, Richland, WA*). Chalcogenide glasses are well known for having technologically significant optical properties such as high transparency in the infrared regime (some being transparent in the visible region), non-linear optical properties, semiconducting properties, and photomodifiable properties which make them attractive for applications in chemical and remote sensing. However, their properties in the terahertz (THz) regime are not reported in the literature. With the recent advances in the area of THz imaging and spectroscopy, advanced tools are now available to characterize this family of materials. Selected chalcogenide glasses were

characterized using a THz spectrometer that covers a frequency range of 172–265 GHz and the data is presented here. Using a terahertz wave generator, terahertz waves were transmitted through a sample and then detected on the other side. Each sample produced a unique output displaying the magnitude of transmission across the frequency range. Software was used to fit the Fresnel expressions for complex transmission to the resulting graphs to determine the transmission, refractive index, and dielectric constants of each sample. The results showed that transmission of terahertz waves show a marked decrease as the waves move up into a higher frequency range. This decline is also varied in connection with the refractive index and whether it was increasing or decreasing.

Heat-Reflective Paint for Deck Surfaces of Naval Vessels. *Emily Ottenweller* (*University of St. Francis, Fort Wayne, IN*)*; Rick Lowden* (*Oak Ridge National Laboratory, Oak Ridge, TN*). The new V-22 Osprey aircraft has the capability to vertically take off from and land on the deck of an aircraft carrier. During take off and landing, the hot exhaust from the Osprey aircraft engines impinges directly onto the deck of the ship. The deck surfaces were not designed to handle high temperatures and thus warp from the excess heat. Insulating paints that use special ceramic additives have been developed to improve the energy efficiency of buildings and structures. The decks of naval vessels are coated with paints that include ceramic grit to make them non-skid. It was hypothesized that the insulating additives could be used to replace the non-skid grit and create a paint that could protect the deck from the hot exhaust. Ceramic particles were added to an epoxy-based surface coating to alter the layer's thermal properties, i.e. to reflect, absorb or conduct heat. The ceramic additives include Bionic Bubbles which are hollow microspheres derived from fly ash, Insuladd particles which are hollow ceramic mircospheres invented by NASA, and silicon carbide platelets. The test specimens were ½ inch thick steel plates to which paints with different additives were applied. The plates were heated using a heat gun to simulate the exhaust of the aircraft and temperature distributions on the backside of the painted specimens were measured. The temperature distributions for the plates coated using paints with additives were compared to results for bare metal, paint with no additive, and the standard non-skid deck coating. The plate with the highest concentration of Bionic Bubbles was the most effective in reducing the temperature of the plate; however, the layer is likely too fragile for the application. The deck coating must not only be insulating but also robust and non-skid. It appears that the ceramic additives will need to be modified to best suit the needs of this application.

Developing Minimally Resistive and Highly Transparent Conduction Oxides Films by Atomic Layer Deposition. *Victor Oyeyemi* (*Goshen College, Goshen, IN*); *Jeffrey Elam* (*Argonne National Laboratory, Argonne, IL*). Zinc oxide (ZnO) and indium oxide (In$_2$O$_3$) are important members of the group of oxides known as transparent conducting oxides (TCOs), which are used in thin film coatings for such applications as energy-conserving windows, surface electrodes for flat panel displays and solar panels, and invisible security shields in windows. The electrical and optical properties of these oxides depend on the method of preparation and can also be modified by the incorporation of dopant materials. ZnO and In$_2$O$_3$ films can be prepared in various ways including spray pyrolysis, sputtering, chemical vapor deposition and pulsed laser deposition. Researchers at Argonne National Laboratory are investigating a new technology known as atomic layer deposition (ALD), which uses the self-limiting surface reactions of the precursors (reactants), sequentially applied to the surface, to generate thin films one molecular layer at a time. Thus, film thickness can be controlled with precision on an Angstrom level. In particular, ALD is more advantageous to traditional methods because it produces films that are smooth and conformal. This report presents a study to develop TCO films that are both more conductive and transparent than what is currently available. There are two parts to the study. The first part involves establishing the growth rate, morphology, and crystalline structure of ZnO films produced by the ALD of diethyl zinc and ozone precursors, and how these properties are affected by the growth temperature. The effect of aluminum doping on the ZnO film resistivity was also examined. The second part of the study examined the effect of zinc doping on the resistivity, transparency, and crystalline structure of ALD grown In$_2$O$_3$ films, as well as how these properties depend on growth temperature. The pure zinc oxide films deposited at 150°C were shown to have a linear growth rate of ~0.46Å/cycle and a resistivity of 0.26–0.6 Ocm. Contrary to expectations, the aluminum-doped ZnO films deposited at 200°C were found to have a strictly increasing resistivity with respect

to doping level. Investigation remains ongoing to obtain a complete picture of the properties outlined above.

Control of Carbon Nanofiber Alignment During Growth in Plasma Enhanced Chemical Vapor Deposition Processes. *Ryan Pearce* (*University of Tennessee, Knoxville, TN*); *Michael Simpson* (*Oak Ridge National Laboratory, Oak Ridge, TN*). Carbon nanofibers are just recently coming under scrutiny with a number of potential uses such as gene delivery arrays and neuronal interfaces. Nanonfibers have a stacked "herringbone" structure, giving them a very high aspect ratio, which is what lends them such a great range of possible applications. Carbon nanofibers are typically grown using a process called "Plasma Enhanced Chemical Vapor Deposition" (PECVD). In this process, a silicon wafer with nickel deposited on it in a specific pattern is placed on a heater in a vacuum chamber. The heat is turned on and ammonia (NH$_3$) and Acetylene (C$_2$H$_2$) are introduced into the chamber at a specific pressure and flow rate. A plasma is induced which causes the carbon from the C$_2$H$_2$ to deposit on the nickel dots, forming the carbon nanofibers. This process forms vertically aligned carbon nanofibers. Our project aims to find a technique to control the alignment of the nanofibers during growth. The way we do this is by changing the method whereby gas is introduced into the system. Classically, the gas flows into the chamber perpendicular to and far away from the surface of the wafer, so that only the ratio of gases affects the growth, and not the flow rate. What we do is place a nozzle directly over the wafer so that the gas flows directly over it. We devise an optimal regimen for growth where we only vary the total flow, keeping the ratio of gases constant. After growth, we observe the wafer under a scanning electron microscope. We have found that nanofibers respond to the variations in flow by tilting along the flow. There are some aspects of this study that require further investigation. First, we need to determine the correlation between angle of tilt and flow rate, which can be done by setting up a series of experiments keeping the total flow variable in a stepped sequence and measuring the resulting angle formed by the nanofibers and the substrate. Then, flow ratio needs to be varied to determine the resulting effects. Another method of creating tilt in nanofibers is through variance in the electric field during PECVD. Towards the edge of the field, this causes the nanofibers to "bend." This technique is impractical, however, as only the fibers grown on the very edges of the field are affected. Our study is fundamental in understanding how to control nanofiber growth, which will lead to an overall better understanding of nanoscale fabrication.

Self-Assembly of Au Nanorods. *Eric Petersen* (*Harvard University, Cambridge, MA*); *Jin Wang* (*Argonne National Laboratory, Argonne, IL*). The packing of Au nanorods into ordered arrays was studied. A seed-mediated growth process was used to synthesize Au nanorods in surfactant with lengths of approximately 30 nm (aspect ratio ~4). UV-visible spectophotometry and transmission electron microscopy were used to characterize the nanorod dimensions. The behavior of the nanorods under an applied dc electric field of 5,000 V/m was monitored *in situ* by small angle X-ray scattering and two-photon photoluminescence microscopy. Scanning electron microscopy was used to observe the nanorod arrays left behind on the electrode surface after the field was turned off. Results indicate that a net positive charge remains on the Au nanorods after synthesis. This charge encourages the formation of two types of ordered nanorod domains; one with the longitudinal dimension oriented along the field lines, the other with it oriented normal to the field lines. Future research will investigate charge properties of Au nanorods in organic solution, and on different types of electrodes, with the objective of understanding their electrical behavior. This understanding may be applied to create large scale domains of Au nanorods with a single orientation, for a wide array of device applications.

Compiling and Organizing RIMS-Related Data. *Walter Pettus* (*Hillsdale College, Hillsdale, MI*); *Michael R. Savina* (*Argonne National Laboratory, Argonne, IL*). Investigation of microscopic silicon carbide grains found in meteorites has revealed isotopic ratios which closely match the predicted values based on the nucleosynthesis models, but are unlike anywhere in the solar system. This has led scientists to classify the grains as presolar, having been unchanged since their creation in stars before the formation of our solar system. Using Resonant Ionization Mass Spectrometry (RIMS) at Argonne, investigations into heavier elements have been made possible. The existing data associated with this project was scattered throughout many published articles and several electronic files. In order to expedite the processes of research and analysis, it was necessary to organize all the available data into searchable databases. The first phase was to gather all the RIMS data along with corresponding

standards and laser information and to sort it into a Microsoft Access database. The second phase was to organize the data collected regarding the Titanium:Sapphire laser cavity configurations so that when tuning the lasers back to the same wavelength in the future, an optic arrangement could be quickly recreated to optimize power. Finally the RIMS data was reformatted and exported so that it could be combined with the online database of all presolar grain data that Washington University in St. Louis is constructing. The databases that have been created hold the formatting so that all future data obtained can be easily entered and the databases maintained with all the available data.

Cd_2SnO_4 and ZnMgO: Ternary Transparent Conducting Oxides for Thin Film CdTe and CuInGaSe$_2$ Solar Cells. *Hannah Ray* (*Wesleyan University, Middletown, CT*); *Xiaonan Li* (*National Renewable Energy Laboratory, Golden, CO*). The compounds cadmium stannate (Cd_2SnO_4) and zinc magnesium oxide alloy ($Zn_{1-x}Mg_xO$) are ternary transparent conducting oxides (TCOs) that are promising for use in thin film solar cells. When used in place of the commonly used TCO tin oxide (SnO_2), Cd_2SnO_4 enhances small-scale cadmium telluride (CdTe) solar cell performance. To scale up the deposition area and rate of Cd_2SnO_4, metal organic chemical vapor deposition is used. The commonly used precursors for cadmium oxide and SnO_2 have incompatible deposition temperatures; thus, a different tin oxide precursor with a lower deposition temperature must be found to be used with dimethyl cadmium. A literature search was performed, and tin (II) acetylacetonate was deemed best for this application. Zinc oxide (ZnO) is commonly used in copper indium gallium diselenide (CIGS) solar cells. Alloying ZnO with the insulator magnesium oxide (MgO) allows for band gap (Eg) engineering. However, adding MgO to a ZnO alloy detracts from the film's electrical conductivity. In this study, a gradient of ZnO:Al and MgO was deposited using RF magnetron sputtering by two ZnO:Al and MgO targets, creating the zinc magnesium oxide alloy $Zn_{1-x}Mg_xO$. Magnesium (Mg) content of the films varied from 3–30%. The optical and electronic properties of the film were measured every centimeter along the gradient. It was determined that the electrical properties of the $Zn_{1-x}Mg_xO$ alloys are only acceptable for use in a solar cell when the proportion of Mg in the sample is less than 3.5% (xg ($Zn_{1-x}Mg_xO$) = 1.72x + Eg (ZnO) with the amount of Mg in the alloy. At Mg content between 0–7%, the band gap was higher than this fit line due to the Burstein-Moss effect. As Mg content increased in this region, Eg due to the Burstein-Moss effect decreased until the effect disappeared at x = 0.07. Increasing the deposition temperature improved the electronic conductivity of the films. Increasing the temperature had no effect on the band gap when the Mg content was greater than 7%, but when Mg content was less than 7%, Eg increased with temperature.

Synthesis and Integration of Carbon Nanofibers for Nanobiological Applications. *Patricia Reynolds* (*University of Toledo, Toledo, OH*); *Michael L. Simpson* (*Oak Ridge National Laboratory, Oak Ridge, TN*). Recent advances in the controlled synthesis of nanomaterials are enabling new approaches for probing biological system functionality at the nanoscale. Several CNMS projects incorporate one such nanomaterial, carbon nanofibers, as functional elements. Applications include the use of carbon nanofibers as nanoelectrodes, as means for gene delivery, and as the principle component of biomimetic membranes. Current efforts make use of vertically aligned carbon nanofibers (VACNF) as suspension supports for lipid bilayers (LBL). There are two main purposes; one is to develop techniques to form LBL structures and secondly to use them as a platform to study integral membrane proteins and their interactions using neutron scattering. Carbon nanofibers are synthesized in a plasma enhanced chemical vapor deposition process from metal (nickel) catalyst, and the vertical alignment results from the applied electric field during synthesis. The growth process allows for controlled synthesis as the parameters (e.g., length, diameter, shape, position, and chemical composition) of individual nanofibers can be selected by definition of catalyst properties and growth conditions. LBLs are composed of phospholipid head groups which are hydrophilic and hydrocarbon centers which are hydrophobic. To fabricate hybrid structures composed of VACNF arrays with deposited LBLs, small unilamellar lipid vesicles were generated through the sonication of LBLs, deposited on VACNF arrays, and heated to 35 degrees C for 30 minutes to encourage layer development. Atomic Force Microscopy was used to map the VACNF array surface both before and after LBL deposition, and encouraging initial results were acquired to show a change in surface topography that is indicative of the formation of a LBL on the nanofibers. The next step in this work is to image these

hybrid structures with neutron scattering to validate the presence of a suspended LBL on the surface of carbon nanofibers.

Elaboration on the Hexagonal Grid and Spiral Method for Data Collection via Pole Figures. *Anthony Rizzie* (*Ball State University, Muncie, IN*); *Thomas Watkins* (*Oak Ridge National Laboratory, Oak Ridge, TN*). A pole figure provides a representation of the distribution of a particular set of atomic planes for data acquired through diffraction and is used for analyzing crystallographic texture or preferred orientation. Pole figures are constructed from a collection of data points, each with a prescribed azimuthal angle (phi) and sample tilt angle (chi) (as specified by the goniometer) and measured intensity (counts or counts per second). Traditionally, the Schulz method (5°x5° grid) is employed to acquire the necessary data, but this leads to a high concentration of data points for small chi values, low concentration for large chi values, and consequently an inefficient use of time. Two alternative data collection methods, the hexagonal grid and spiral, have been previously proposed but only tersely documented in terms of both construction and implementation. The goal, therefore, is to provide a practical description of the mathematics required to implement the hexagonal and spiral data collection schemes. Applying the concepts of equal area and stereographic projections and geometry, spreadsheets were created to formulaically develop hexagonal and spiral grids, which are then related to angular movements of the goniometer. Using the generated data points, the hexagonal grid and spiral methods were programmed by "brute force" into the existing X-ray software and employed to collect data for a sample of aluminum foil. The resulting (111) pole figures compared favorably to typical rolling textures for aluminum foil collected with the conventional Schulz method. The hexagonal grid has been shown to reduce the number of data points and time needed to complete a pole figure, while providing equal area sampling. The spiral method was shown to use only a quarter as many data points as the 5° x 5° grid. In the future, LabVIEW software will be utilized to develop programs for collecting data using both the hexagonal grid and spiral methods and then convert the data back to the conventional 5° x 5° grid.

Synthesis of leucite nanocrystals through glass hydration and sol-gel method. *Elisa Sanchez* (*San Antonio Community College, San Antonio, TX*); *Pavel Hrma* (*Pacific Northwest National Laboratory, Richland, WA*). Leucite ($KAlSi_2O_6$), a potassium alumino-silicate, has been widely used as a principal component in porcelain-fused-to-metal restorations to match the thermal expansion coefficient (CTE) of dental porcelain with the CTE of the metal. The combination of porcelain and metal creates a strong and durable restoration that is highly biocompatible and wear-resistant but lacks the natural translucency of enamel. The low strength and fracture toughness of natural looking all-ceramic restorations have restricted their widespread use in aesthetic dentistry. The introduction of nanoleucite porcelain might make the all-ceramic restorations possible. It was found that the fracture toughness and flexural strength of the leucite porcelain can be significantly increased by controlling the amount, particle size, and distribution of the leucite crystals in the porcelain matrix. The objective of this study was to synthesize nanocrystals of leucite via glass hydration and sol-gel method where the silica sol was mixed either with potassium aluminate for a basic synthesis or with potassium nitrate and aluminum nitrate for an acidic synthesis. The synthesized powders were analyzed with X-ray diffraction (XRD) to determine the concentration of leucite, and with scanning electron microscopy and energy dispersive spectroscopy (SEM-EDS) to determine the crystal size of leucite. Differential thermal analyses and thermogravimetric analyses were used to study the phase changes in amorphous gels leading to the formation of leucite. Preliminary results of XRD analyses of the glass hydration samples show crystal formation. The concentration of leucite increases with temperature, time, and added volume of water. Average crystal size as determined by SEM was approximately 1 μm. At the time of this report, sol-gel data collection is ongoing, but nearing completion. Preliminary results of this study suggest a promising trend toward synthesis of nano-sized particles of leucite using both tested methods.

Uniform Height, Self-Organized Pb/In Islands Grown on Si(111) 7 x 7 Interfaces. *George Scott* (*Northwestern University, Evanston, IL*); *Michael Tringides* (*Ames Laboratory, Ames, IA*). The ability to grow uniform height self-organized nanostructures is made possible by Quantum Size Effects (QSE) and could have applications in the technology sector. Pb deposited epitaxially onto different Si(111) interfaces ((7 x 7), Beta Phase-sqrt(3)xsqrt(3), Alpha Phase-sqrt(3)xsqrt(3) etc) produced islands of uniform heights but In on Si(111) 7 x 7 did not. These initial Si(111) interfaces are prepared by depositing small amounts of Pb or In under ultra-high vacuum (UHV)

conditions. After these initial 2-D phases are prepared, deposition is followed by the element of interest (Pb or In) to form epitaxial nanostructure islands. Good height uniformity was found when In was deposited on the Pb Alpha Phase-sqrt(3)xsqrt(3) phase when fcc In(111) islands are present. In order to gain insight into the kinetics that could lead to similar behavior in other Pb-In mixed systems, Pb was deposited on In sqrt(31)xsqrt(31). Spot profile analysis — low-energy electron diffraction (SPA-LEED) was the primary method used in the uniform height experiments because of the ability to observe a large sample area. From the diffraction intensity profiles, uniform heights existed only when Pb was present in the system. Scanning tunneling microscopy (STM) was also used to build height histograms and verify the diffraction results.

Combinatorial Study of $Zn_x Sn_{1-x} O_y$: a Transparent Conducting Oxide. *Diana Silva (University of Colorado, Boulder, CO); Maikel Van Hest (National Renewable Energy Laboratory, Golden, CO).* Zinc-tin-oxide (ZTO) libraries were co-sputtered from ZnO and SnO_2 by RF magnetron sputtering onto Eagle 2000 glass substrates at temperatures ranging from room temperature to 550°C and analyzed with combinatorial analytical techniques. Samples were deposited in pure argon and in a mixture of argon and hydrogen with 4% and 2% hydrogen. ZTO films were found to be amorphous at a tin content ranging from 30 to 70% when deposited in pure argon gas at 550°C. ZTO films were also amorphous when deposited in a mixture of argon/hydrogen with 4% and 2% hydrogen at 550°C. ZTO films deposited in pure argon had a maximum conductivity of 134 S/cm at a 70% tin content and an optical transparency with transmission 85%. While, ZTO films deposited in a mixture of argon and hydrogen 2% had an optical transparency with transmission 85% across the visible spectrum and a maximum conductivity of only 92 S/cm observed at 75 at % tin content. Thin films of zinc-tin-oxide deposited in a mixture of argon and hydrogen with 4% and 2% hydrogen, did not improve conductivity and optical properties as expected. Key words: zinc tin oxide, transparent conducting oxides, amorphous.

The Effects of Polymers on the Rheology and Green Strength of the Feedstock in Titanium Injection Molding (TIM). *Juan Teran (Estrella Mountain Community College, Avondale, AZ); Kevin L. Simmons (Pacific Northwest National Laboratory, Richland, WA).* When implementing naphthalene as a patented primary ingredient in our binder system, it is imperative that we understand and assess the characteristic differences that polymers have on the torque values and green strength of the overall mixing with titanium hydride powder. Knowing how to influence the torque values during the initial mixing between the binder and powder will give us a better chance of molding a complex geometrical shape, since increasing the powder volume is known to increase the torque value and decrease the mold capacity of the mix. By keeping the volume for all binder constituents' equal, and changing the chemistry for one of the constituents, in this case acetamide, low density polyethylene, and polyethylene glycol, the results of these experiments can provide insight on the effects that these alternative constituents have on the feedstock's rheological properties as well as its green strength. Each individual run was carefully mixed and monitored in a Haake Rheocord Fisions 90 torque rheometer and their torque values were recorded in Newton-meters. All mixes were conducted in the same manner and were allowed to reach their lowest torque value within a forty minute time limit. Acetamide, when in mixture with stearic acid and naphthalene, produces the lowest torque and injection molds but does not have enough green strength to be handled and sintered. The polymer mixtures produced different torque values that were slightly higher than that of acetamides but can be injection molded nicely with suitable green strength to pass through the sintering stage. This work was focused on analyzing the effects that specific polymers have on the feedstock traits, in anticipation of finding one adequate enough to increase its probability of entering the fourth stage in the TIM process. The use of polymers in the naptha-based binder is necessary; they provide key properties to the feedstock that allow it to pass through the entire TIM operation. Ongoing research and development continues in the areas of binder development, molding conditions, and proper heat treatment during the de-binding and sintering phase to improve the overall success rate in the production of viable parts in the TIM process.

The Effect of MnO on the Thermal, Mechanical and Interfacial Reaction of a SOFC Sealing Glass with Metallic Interconnect Materials. *Jameson Thornton (Santa Rosa Junior College, Santa Rosa, CA); Yeong-Shoung Chou (Pacific Northwest National Laboratory, Richland, WA).* This paper will discuss the effect of MnO on the thermal and mechanical properties of a novel solid oxide fuel cell (SOFC) sealing glass (YSO77), both in the as-cast and short-

crystallized forms. MnO has been chosen as a "trapper" due to its potential ability to react with Cr, a major source for degradation of SOFCs. In the as-cast glass, both the glass transition and softening temperature decreased with increasing MnO. In the short-crystallized glasses, the softening temperature generally decreased with increasing MnO, and the presence of softening point suggested remaining glassy phases after short crystallization. The effect of MnO on the coefficient of thermal expansion (CTE) showed no distinct trend. Elastic properties of Young's and shear modulus decreased with increasing MnO for both the as-cast and short-crystallized glass.. The elastic properties in the crystallized glasses were generally higher than those of their as cast counterparts. The density of the glasses decreased with increasing MnO content, and was lower in the crystallized counterparts when compared to the as-cast glasses. The CTE seemed to fluctuate in both sets of glasses without and logical pattern. These fluctuations are still not understood and may require further investigation if the CTE of these glasses becomes a primary concern. But since MnO was chosen for its chemical interest and not its physical properties for this study these are not of general concern. The properties of the new glasses are adequate to be used in further SOFC applications, and the glass with 6 mol% MnO will be further investigated under actual conditions as a sealant.

Synthesis and Characterization of Nickel Oxide and Vanadium Oxide Nanostructures. *Amanda Tiano (University of Tennessee, Knoxville, TN); Stanislaus S. Wong (Brookhaven National Laboratory, Upton, NY).* In the field of nanotechnology, transition metals have attracted research interest because of their electronic and magnetic capabilities. Nickel(II) oxide (NiO), an antiferromagnetic material and p-type semiconductor, has been a large focus in research due to its diverse applications, such as catalysis, electrochromic devices, gas sensors, and magnetic films, making it an attractive material for the fabrication of nanodevices. Vanadium oxide (VO_2), like NiO, has also appealed to researchers because it undergoes a semiconductor-to-metal transition, known as a Mott transition, at 68°C. Below this temperature, VO_2 maintains monoclinic (M) phase and above converts to the metallic (R) phase. Since the Mott transition is also associated with reversible changes in optical, magnetic, and electrical properties as well as structure, VO_2 is also appealing for a variety of applications from energy storage to catalysis. NiO nanocrystals formed with and without the presence of a surfactant via thermal decomposition at 830°C in molten NaCl of two different precursors: nickel(III) oxide (Ni_2O_3) and nickel oxalate ($NiC_2O_4 \cdot 2H_2O$). These precursors formed quasi-circular particles measured as 283 ± 135 nm and 287 ± 100 nm in size, respectively. NiO nanosheets, 355 ± 166 nm in diameter and 44 ± 12 nm in thickness, were also formed by hydrothermal treatment of nickel acetate, $Ni(CH_3COO)_2 \cdot 4H_2O$, to generate nickel hydroxide with subsequent thermal decomposition at 400°C. Monoclinic VO_2 (B) nanorods, (width: 185± 37 nm, length: 1.4 ± 0.4 μm) were synthesized by hydrothermal treatment of V_2O_5. Subsequent thermal decomposition at 340°C in air produced V_2O_5 nanoparticles (107 ± 26 nm) while heating at 500°C in a flowing argon atmosphere produced larger monoclinic VO_2 (M) rod-like particles (width: 0.98 ± 0.38 μm, length: 6.8 ± 2.2 μm). The products were characterized using X-ray diffraction (XRD), scanning electron microscopy (SEM), transmission electron microscopy (TEM), and a magnetic property measurement system (MPMS). We have confirmed the presence of nickel oxide and vanadium oxides with XRD and determined size, shape and morphology with SEM. We have begun analysis with the MPMS but the current signal intensity associated with our samples has thus far been too weak for adequate interpretation. Through characterization, we can conclude the successful synthesis of nickel oxides and several forms vanadium oxide nanostructures by both molten salt and hydrothermal methods.

Semiconductor-Nanoparticle-(Poly)Ionic Liquid Composite. *Veronika Vajdova (University of Chicago, Chicago, IL); Millicent Firestone (Argonne National Laboratory, Argonne, IL).* The design, synthesis, and characterization of a hierarchically ordered composite whose structure and optical properties can be reversibly switched by adjustment of solvent conditions are described. Semiconductor cadmium sulfide (CdS)-nanoparticle containing ionic liquid-derived polymers were synthesized in a single step by UV irradiation of a Cd^{2+}-ion-precursor-doped, self-assembled ionic liquid gel, 1-decyl-3-vinylimidazolium chloride. Several approaches to preparing semiconductor ionic liquid derived polymer composites have been studied. In the first approach, a Cd^{2+} impregnated polymer is swollen in ethanol (EtOH), and then immersed in a sodium sulfide (Na_2S) solution to generate the encapsulated CdS nanoparticles. In the second approach, the Cd^{2+} impregnated polymer is directly swollen

in a methanol-Na_2S solution. Both procedures yield transparent polymers with a light yellow to orange color. The yellow color, after photopolymerization of the binary mixtures with UV irradiation for two hours, indicates formation of CdS nanoparticles. The properties of the *in-situ* synthesized CdS nanoparticles were determined by UV-Vis and photoluminescence spectroscopy. Optical spectroscopy of the CdS-polymer composite shows a dramatic increase in the absorption at 450 nm. Moreover, this CdS impregnated polymer exhibits a fluorescence band located at 473 nm, whereas the control polymer showed no distinct bands. The polymerization described in this paper yields a material with improved mechanical properties, which can be both readily processed and applied in technologically relevant applications and environments.

Microbiologically Influenced Corrosion in Oil Pipelines: Causes and Effective Treatments. BRENDEN VAN SLYKE (*State University of New York at Stony Brook, Stony Brook, NY*); BRENDEN VAN SLYKE (*Brookhaven National Laboratory, Upton, NY*). Microbiologically Influenced Corrosion (MIC) is a serious problem in the oil industry. During oil extraction, especially secondary recovery, water may become mixed with the oil. This water can harbor microorganisms, that when not controlled can cause serious corrosion due to their metabolic processes. Two particularly damaging and widespread forms of bacteria involved in MIC are sulfate reducing bacteria (SRB) and acid producing bacteria (APB). The initial phase of this project was literature research into the causes and mechanisms for MIC. Then this information was applied to examining photographs and replicas of a pipeline suffering from possible MIC. Based on this examination, information on different treatment options were researched. The literature research aspects of the project were undertaken using electronic media such as the Internet and online journals, correspondence with industry officials and scientific researchers, and printed material. Literature research into the causes of MIC led to two distinct areas of interest. The first of these was the human factor, which dealt with poor maintenance and improper use of biocides allowing bacteria to proliferate in the system. On the bacteria side, the SRB and APB formed colonies with themselves and other non-corrosive bacteria. The bacteria can influence corrosion by the production of corrosive metabolites, hydrogen sulfide in the case of SRB and organic acids with APB present. SRB also can stimulate the development of iron sulfide deposits, which increase corrosion by enlarging the cathode. Furthermore, acids produced by APB can also complex with metal ions at the anode, removing them and accelerating the corrosion reaction. The replica casting were made from actual corroded oil pipe using Struers Repliset kits. These were then sputter coated using an Anatech Hummer VII to show more contrast. After examining the photographic evidence and replicas three types of corrosion were suspected. Two cases of MIC, one each by SRB and APB, were determined. One sample showed inorganic carbon dioxide corrosion and a fourth section exhibited an undetermined form of corrosion. The most important factor in limiting MIC is keeping oil pipelines clean and as water free as possible. Biocides containing glutaraldehyde as the active agent and quaternary ammonium compounds to break up biofilms are suggested. This project is part of a larger investigation into oil pipeline corrosion, which is ongoing.

Effect of Chemistry Variations on the Microstructure and Mechanical Properties of Creep Strength Enhanced Ferritic Steels. KEELY WILSON (*Michigan Technological University, Houghton, MI*); JOHN SHINGLEDECKER (*Oak Ridge National Laboratory, Oak Ridge, TN*). Grades 91, 92, and 122 steels (9–12% Chromium) are known as Creep Strength Enhanced Ferritic steels. These grades of steel are finding increased usage in the pressure retention components of advanced fossil energy systems (Ultrasupercritical Steam Boilers, Heat Recovery Steam Generators, etc.) because of their superior performance in high temperature, high stress environments. The chemical specifications for these grades are very broad, which may affect the mechanical properties and long-term performance of the alloy in service. Ideally in the normalized and tempered condition, Gr 91, 92, and 122, will have fully martensitic structures with no ferrite forming. In an earlier study, two compositions of each grade were produced by varying the amounts of austenite formers (C, Mn, Ni, N) and ferrite formers (Si, Cr, Mo, V, Nb) within the current specification range. These chemistry changes were guided by computational thermodynamics to alter the intercritical temperatures, the temperatures at which steel changes phase, and to cause the formation of ferrite under standard processing conditions. In this study, the mechanical properties of these samples were evaluated, and are compared to literature results for commercially produced material. High temperature (650°C) creep tests were run with loads ranging from 100 to 140 MPa for times exceeding 1,000 hours. Tensile tests were run at both high temperature (650°C) and room temperature (25°C). Digital Imaging software was used to analyze the steel microstructures to determine the amount of martensite and ferrite present in each alloy. It was found that both the tensile strength and the creep strength of the alloys decreased substantially with the presence of ferrite in the material. This critical finding clearly shows that the specification range for these alloys is too broad which may result in commercially produced materials with properties far from expectations. A limited evaluation of thermodynamic predictions and microstructural findings was also conducted. The data collected in this study, combined with data from other tests, such as long term creep tests, thermo-mechanical simulation, and thermodynamic modeling will later be used to create more specific standards for Gr 91, 92 and 122 alloys.

Synthesis of Calix[4]cyclohexanol to Serve as an Electron Trap. BENJAMIN ZALISKO (*Elmhurst College, Elmhurst, IL*)*;* JOHN A. SCHLUETER (*Argonne National Laboratory, Argonne, IL*). Electrons are known to be trapped between positive charges of liquid water and alcohol molecules without being incorporated into the molecules' electron shells. Seeking to trap an electron within a single molecule, calix[2]cyclohexanol should be synthesized by hydrogenation of calix[4]arene at 200 psi and 90°C, resulting in calix[2]cyclohexanone. This should be followed by reduction with $NaBH_4$ to produce calix[2]cyclohexanol. Using an electron donor (Na metal or electrolysis), an electron should become trapped between the partially positive, tetrahedral hydrogen atoms of the internal hydroxyl groups of calix[2]cyclohexanol. This trapped electron's presence will be confirmed by its ability to retain magnetic spin with electron spin resonance spectroscopy. Acting as a capacitor, this electron trap will retain electron spin efficiently and could lead to further studies of conduction, electron spintronics, and even new media for micro processing.

Cadmium-doped SiO_2 Nanoparticle Label for the Electrochemical Immunodetection of Protein IgG. XIAOHAI ZHANG (*University of Washington, Seattle, WA*); JUN WANG (*Pacific Northwest National Laboratory, Richland, WA*). Semiconducting nanoparticles have garnered enormous attention in the field of biosensor development within the past decade. Due to recent advancements in the control of their growth size and shape, nanoparticles such as silica MCM-41, which have unique structural functionalities, are now an applicable material in creating novel methods of bio-detection. In this report, an amperometric biosensor using biochemically modified silica nanoparticles was developed for the detection of protein IgG via sandwich immunoassay. This novel electrochemical immunosensor is based on the encapsulation of Cadmium ions within mesoporous aluminosilicate nanoparticles (SiNPs) MCM-41. The synthesized silica NPs — antibody conjugates were then characterized with electrochemical detection as well as UV spectrum analysis. Preliminary tests have confirmed that Cadmium ions were immobilized inside the mesoporous shell of the silica NPs; they've also shown that the protein antibodies were successfully conjugated. In these experiments, the performance of the electrochemical immunosensor was evaluated via carbon Screen Printed Electrodes (SPE), and a detection sensitivity of 10 ppm was achieved. This report has shown that SiNPs has great potential for future research and development of electrochemical bio-sensors; however, optimizations in its synthesis method are still required to increase the detection limit. Cadmium labeled silica NPs offers a viable approach for the rapid, simple, and cost-effective analysis of biological samples.

Medical and Health Sciences

Determining the Optical Properties of Biological Tissue Samples Using an Integrating Sphere Method. MARCUS ALLEGOOD (*North Georgia College and State University, Dahlonega, GA*); JUSTIN S. BABA (*Oak Ridge National Laboratory, Oak Ridge, TN*). Wavelength dependent light interaction with biological tissue can be described using three parameters: the scattering and absorption coefficients and the cosine of the average scattering angle (g). To accurately determine these optical properties for different types of tissue at specific wavelengths would be beneficial for a variety of different biomedical applications. The goal of this project was to take a user defined g-value and determine the remaining two parameters for a specified range of wavelengths. In order to collect the needed data for all the wavelengths in a timely and accurate manner, a fully automated computer program and process was developed. Using a single integrating sphere method, scattered light intensity inside the sphere was recorded via a spectrometer as either transmitted or reflected light from the tissue sample. LabVIEW was used to write programs to collect raw intensity

data from the spectrometer, to convert the data into a format for C code execution, and to compute the optical properties based on the collected data. To make the process fully automated, the LabVIEW and C code programs were linked together into one single program to allow data to be passed between the two efficiently. The automated program was tested using a tissue mimicking phantom and determination of the absorption and scattering coefficients showed excellent agreement with theory. Future work and the final phase of testing will entail examining actual biological tissue with known optical properties to check for accuracy before proceeding to utilize the system for its intended purpose. Ultimately, the data collection process and algorithms developed through this effort will be applied to build models for light interaction with biological tissue samples.

Vigabatrin-Induced Weight Loss and Locomotor Sensitivity in Normal and Obese Animals. STEFANIE AQUILINA (*Cornell University, Ithaca, NY*); STEPHEN DEWEY (*Brookhaven National Laboratory, Upton, NY*). Vigabatrin, an irreversible inhibitor of GABA-transaminase, decreases dopamine in the central nervous system (CNS). Recent studies suggest that much like drugs of abuse, food increases brain dopamine in obese human volunteers. Combined with previous work using a host of addictive substances, this study focused on an examination of food intake and body weight in an animal model of obesity (Zucker rats). Dopamine is implicated in behaviors associated with addictive drugs, including cocaine, nicotine, amphetamines, alcohol, heroin, and a handful of illicit drug combinations. Unlike other prescription drugs, short-term Vigabatrin use does not appear to have any significant and potentially dangerous side effects. Two minor side effects were thought to include weight fluctuations, as well as locomotor depression. Weight and food intake in normal (adolescent Sprague Dawley rodents) and an animal model of obesity (genetically altered adolescent and adult Zucker fatty rodents) were measured during a period of two sub-chronic Vigabatrin administrations. In addition, locomotor behavior boxes were used to analyze the activity in control animals and those treated with Vigabatrin. Upon treatment with a high dose (150 mg/kg) of Vigabatrin (active enantiomer) in normal rodents, significant weight loss was noted. Treatment in obese rodents, however, resulted in a significantly slower rate of weight gain. These weight loss trends appear dose-dependent (with more extreme weight fluctuations occurring as a result of higher doses of Vigabatrin). However, locomotor sensitivity was not significantly different between Vigabatrin treated and saline treated animals. Thus, locomotor depression does not appear to be a side effect of Vigabatrin. Furthermore, adult rodents treated daily with 300 mg/kg of Vigabatrin (racemic) lost nearly 10% of their body weight in a period of only four days. These studies suggest that Vigabatrin may be an effective treatment for obesity. Additional studies at The University of Pennsylvania, University of California Los Angeles, and Louisiana State University are currently ongoing in human subjects using multiple doses of Vigabatrin and several treatment protocols.

Conflict Resolution is Impaired in Currently Withdrawn Cocaine Addicted Individuals. BAABA BLANKSON (*State University of New York at Stony Brook, Stony Brook, NY*); RITA GOLDSTEIN (*Brookhaven National Laboratory, Upton, NY*). Individuals with cocaine use disorders (iwCUD=CUD) experience neuropsychological impairments that encompass attention and executive function deficits, possibly due to structural and functional changes in prefrontal cortical brain regions. The Attention Network Test (ANT), a computerized reaction time task, has been developed to measure three of these attention and executive function networks: alerting (associated with right hemisphere frontal and parietal regions), orienting (associated with subcortical regions), and executive control (associated with the prefrontal cortex, particularly the anterior cingulate cortex). Our study used the ANT to examine 1) differences between CUD and healthy control subjects in attention and executive function; and 2) the effect of urine status (positive or negative for cocaine use within 72 hours) on attention and executive function in the CUD group. The ANT was administered as part of a larger neuropsychological battery to 84 individuals with current CUD [55 positive (CUD+), 29 negative (CUD-)] and 75 healthy control subjects matched on gender, age, and years of education, but not on race, general intellectual functioning, socioeconomic status, state depression and history of cigarette smoking. Results of three separate ANOVAs revealed a significant group difference in executive control [[$F_{(2, 156)}$ = 5.8, p < 0.004; pairwise comparisons: controls faster than both cocaine subgroups, an effect that reached significance for CUD-, p < .004, M±SD = 127.5±47.8 for controls vs. 149.4±64.5 for CUD+ vs. 169.8±76.5 for CUD-], but not in orienting [$F_{(2, 158)}$ = 1.0, p > 0.4] or alerting [$F_{(2, 157)}$ = 0.2, p > 0.8]. The executive control effect remained significant after controlling (with ANCOVA) for general intellectual functioning, the only non-matched variable that correlated with executive control (p < 0.03). The current results suggest that the ability to resolve a cognitive conflict may be uniquely impaired in CUD and expressed primarily during acute withdrawal. Possible explanations may encompass the self-medicating hypothesis (i.e., where cocaine use ameliorates an underlying cognitive deficit in CUD) or the effects of acute withdrawal symptoms on neuropsychological function. The effects of longer abstinence periods and other drug use variables on ANT conflict in CUD remain to be established. Future studies need to also explore the role of the anterior cingulate cortex in underlying this cognitive conflict resolution performance deficit in drug addiction.

Measurement of Methamphetamine-Induced Cue Response in Rodents Using MicroPET. JOSEPH CARRION (*The City College of New York, New York, NY*); WYNNE SCHIFFER (*Brookhaven National Laboratory, Upton, NY*). Methamphetamine (Meth) has seen an increase in use among eighth to twelfth graders. The effects of Meth are similar to amphetamine but even more potent and addictive to the central nervous system. A behavioral model of craving with metabolic imaging using Micro Positron Emission Tomography (MicroPET) was used to determine brain region activation due to drug craving in response to specific stimuli. Conditioned Place Preference (CPP) is an established method of assessing drug-paired environmental responses: Cravings. Twelve male Sprague-Dawley rodents were injected with 5 mg/kg Meth or saline and placed in distinct CPP chambers on alternating days. One day after the 10th Meth pairing, the CPP test was performed while the animal's preference was measured in a drug-free state. From these results, the preference score was calculated as time spent in the saline-paired chamber minus time spent in the Meth-paired chamber. Two days after the last Meth-pairing, animals received an intraperitoneal (i.p.) injection of 18-Fluorodeoxyglucose (18-FDG), and were placed in the Meth-paired chamber. After 45 minutes of FDG uptake, animals were anesthetized and scanned in the MicroPET for 10 minutes. The animals were allowed to rest for one day. Following the rest period, the animals were injected with 18FDG and placed in the saline-paired chamber. The same protocol was followed for all 12 rodents. There was a significant preference for the Meth paired chamber (conditioned animals spent 461 sec in the Meth paired chamber compared to 260 sec in the saline paired chamber, p=0.002). Brain 18FDG data were analyzed using Statistical Parametric Mapping (SPM) and Region of Interest (ROI) methodologies correlated with a preference score. There were significant (p

The Radiosynthesis of 6-(18Fluoroacetamido)-1-Hexanoicanilide for Positron Emission Tomography Imaging of Histone Deacetylases in the Brain. SHANIKA COLLINS (*Medgar Evers College, Brooklyn, NY*); JOANNA FOWLER (*Brookhaven National Laboratory, Upton, NY*). The substrate 6-(18Fluoroacetamido)-1-hexanoicanilide (18F-FAHA) may be useful in measuring the level of histone deacetylase (HDAC) expression and activity in cancer patients via Positron Emission Tomography (PET) imaging and also in studying gene expression in the brain. Inhibition of HDACs triggers growth arrest, differentiation and apoptosis in tumor cells. To evaluate the HDAC expression in the brain and other organs *in vivo*, before and during the use of inhibitors, FAHA was developed as a substrate for the HDAC to allow for non-invasive whole body imaging of the HDAC. Our objective is to prepare 18F labeled FAHA to image HDAC in the brain *in vivo* using PET imaging. FAHA was prepared by the reaction of 6-amino hexanoic acid with thionyl chloride in dichloroethane followed by addition of aniline. The resulting product, compound 1, was then treated with bromoacetyl bromide in the presence of triethylamine to afford compound 2 which was fluorinated using tetrabutylammonium fluoride to give our unlabeled reference compound. The bromine substituted compound will serve as a precursor to 18F-FAHAwhich will be used together with the HDAC inhibitor, suberoylanilide hydroxamic acid for PET imaging of the HDAC expression and activity in the brains of baboons. These studies will form the groundwork for future PET studies in humans to understand the relationship between genes, brain chemistry and behavior.

Dose-Dependent Conditioned Place Preference Response and Locomotor Activity in Methamphetamine-Treated Animals. REEMA DALAL (*New York University, New York, NY*); STEPHEN DEWEY (*Brookhaven National Laboratory, Upton, NY*). Previous behavioral studies indicate that animals exposed to methamphetamine (METH) often associate and prefer specific environments with their exposure, a behavior termed conditioned place preference. The conditioned place preference (CPP) paradigm is a commonly used technique to evaluate the positive or negative reinforcement values of different drugs. These studies closely parallel behavioral responses reported by human substance abusers. In the present study, the procedure

involved several drug pairings where the animals, adolescent male Sprague-Dawley rats, were exposed to different doses of METH in distinct chambers containing well-defined tactile, visual, and/or olfactory cues. Following randomization of the animals, the goal was to expand previous studies, demonstrating that rats will express a CPP to METH exposure by determining a dose-response. For these CPP studies, three groups of animals were exposed to METH at concentrations of 2.5, 5.0, or 10.0 mg/kg. Following twenty consecutive days of pairings (alternating with saline), animals were given access to both chambers in a drug-free state (saline injection). The amount of time spent in the METH-paired chamber was recorded, and was used as an indicator of preference. Further, the locomotor activity was monitored each day and the values obtained on the test day were compared against those obtained for the pre-test. This analysis indicated a significant increase from low-dose to high-dose administration, demonstrating that methamphetamine produced a significant, dose-dependent CPP. Further studies using different concentrations are currently ongoing in a continuing effort to better understand the locomotor and behavioral effects of METH.

Patterning a PDMS Scaffold Towards Wound Healing. *TEJAS DOSHI* (*Wofford College, Spartanburg, SC*); *BARBARA BECKERMAN, APRIL MCMILLAN, BOYD EVANS* (*Oak Ridge National Laboratory, Oak Ridge, TN*). One of the most important functions of skin is to act as a barrier against pathogens. This function is compromised when a person suffers a partial-thickness or full-thickness wound. The wound triggers a healing cascade that consists of three phases: inflammation, proliferation, and tissue remodeling. The rate of wound healing determines if scars form and how quickly skin can regain its purpose to serve as a barrier. Depending on the severity of the wound, the healing process may last from a few days to several months or longer. During the last thirty years, there has been much interest and research in applying micro and nano-scaled technologies to increase the rate of wound healing. These technologies include patterning and functionalization of implantable materials. Patterning involves changing the surface topography of a substrate. Functionalization involves attaching different functional groups or signaling proteins to a substrate. The purpose of this research is to determine a method to increase the rate of wound healing using these micro and nano-scaled technologies. Extensive literature searches were conducted to determine appropriate methods for patterning and functionalizing a scaffold. Polydimethylsiloxane (PDMS) was chosen as the scaffold for the experiments because it has been shown to be biocompatible with the human body. Self-assembled polystyrene-block-polyacrylic acid (PS-b-PAA) diblock copolymer micelles act as the template for patterning PDMS. The goal was to achieve regular, evenly spaced patterns. However, the micelles formed bifurcated striations which did not allow patterning of PDMS. This result is attributed to using PS-b-PAA with a higher molecular mass than described in previous literature. A close substitute was used because the vendor no longer sells the PS-b-PAA described in the referenced experiment. Assuming that the micelles form regular, evenly spaced patterns in future experiments, dermal fibroblasts will be seeded onto molded scaffolds to determine if a patterned surface can best be used to increase proliferation of skin cells so as to also increase the rate of wound healing. Cell proliferation will be measured via a Coulter Counter device. The substrate will also be functionalized with different signaling proteins to induce a greater rate of wound healing. These experiments are the initial stage of a long-term goal to create a therapeutic material that will increase the rate of wound healing.

Biodistribution and Metabolism Studies of 14C-Ethanol in Mice. *MEL PILAR ESPAILLAT* (*Farmingdale State College, Farmingdale, NY*); *ANDREW GIFFORD* (*Brookhaven National Laboratory, Upton, NY*). Ethanol acts as a central nervous system depressant; it is rapidly absorbed by the body, and approximately 90% is metabolized, almost entirely in the liver. The intermediate metabolites of ethanol are believed to be involved in its toxicological properties. The mechanism of ethanol toxicity and its interaction with tissue have not been well understood because of lack of fundamental knowledge about both the pharmacokinetics of ethanol and its metabolism in the human body. This work seeks to study the rate of metabolism of ethanol in different tissues and provide preliminary data for future PET studies to directly measure the distribution and pharmacokinetics of ethanol in human subjects. Mice were injected with approximately 2.0×10^{-3} microcuries of 14C-Ethanol and then were sacrificed at 5, 15, and 60 minute intervals after injection. Plasma and various organs were collected and assayed for carbon-14 under acidic and basic conditions. In the present study a high concentrations non-volatile material was found in the liver, consistent with the role of this organ in metabolizing ethanol.

However, it is notable that other organs were also found to accumulate both ethanol and non-volatile metabolites, although it is not possible to say whether this represents accumulation of circulating radiolabeled metabolites from liver metabolism of ethanol or is due to local metabolism of the radiolabeled ethanol. This work is a small portion of a much larger project being researched to investigate the distribution and pharmacokinetics of ethanol in human subjects.

Effect of Stroke on Regional Distribution of Aromatase and NMDA Receptors in the Female Rat Brain. *CANDACE GIRARD* (*Mount Holyoke College, South Hadley, MA*); *ANAT BIEGON* (*Brookhaven National Laboratory, Upton, NY*). The production of estrogens from precursor androgens is catalyzed by the enzyme aromatase (AR), which under normal circumstances, is restricted to specific neuronal locations. The N-methyl-D-aspartate receptor (NMDAR) is one of the three major subtypes of glutamate receptors, which under normal circumstances, plays a critical role in synaptic plasticity mechanisms. Experimental data suggests that AR activity and NMDARs may be involved in neurodegenerative processes following brain injury. Recent studies have indicated that brain insults can induce brain AR expression and decrease brain NMDAR's. However, the long term effect of stroke w/respect to AR and NMDAR distribution has not been investigated. Middle cerebral artery occlusion (MCAo) in female rats induced stroke and was confirmed in the left hemisphere by MRI and histology. Stroke rats were sacrificed 2 or 4 weeks post MCAo and brain tissue processed for autoradiography. Five control brains (w/surgery; w/o stroke) and five experimental brains (w/surgery; w/stroke) were used in these experiments. Using quantitative *in vitro* autoradiography, AR distribution was investigated with [11C]-vorozole and NMDA distribution with [3H]-MK-801. Regional densities of autoradiograms were quantified with standard image analysis software. The [11C]-vorozole autoradiograms did not show specific or increased binding in our stroke animals. This may be due to the low AR expression in young females and/or a short-lived (<2 weeks) increase in aromatase. The [3H]-MK-801 autoradiograms showed similar regional bainding density in control rats at 2 and 4 weeks. In stroke animals, binding density was decreased at 2 weeks after surgery compared to controls as well as to stroke rats 4 weeks after surgery. These effects were more pronounced in brain regions adjacent to the stroke. The most significant increase in binding between 2 and 4 weeks after stroke was found to be in the frontal cortex (~20%) and denate gyrus (~28%). Binding in the left caudate putamen was significantly lower in experimental rats (~18%). These results, if upheld in a larger series, suggest that hippocampal and cortical NMDAR reduction induced by MCAo is transient, which is in line with the transient nature of many cognitive symptoms often seen in the acute phase after a stroke. This also suggests that damage to the caudate putamen may be sustained or irreversible, in line with the long term nature of motor deficits among MCAo stroke patients.

Microbeam Radiation Therapy: Applying The Method to Spinal Cord Research in Rats. *MEAGAN GREEN* (*La Salle University, Philadelphia, PA*); *F. AVRAHAM DILMANIAN* (*Brookhaven National Laboratory, Upton, NY*). Presently there are no established methods for stimulating the regeneration of the glial system in animals, yet it is known that the system repairs itself after minor injuries. It has previously been shown that the glial system recovers from irradiation with high dose planes of thin synchrotron x rays. In this experiment we are interested in seeing if irradiation treatment will not only cause recovery of the glial system but also locomotive ability as well. Here we produced contusion injury in the rat spinal cord and irradiated the site with arrays of parallel X-ray microplanar beams. The New York University (NYU) impactor was used to produce contusions to the T9 spinal region once the cord section was exposed by a laminectomy. The injury temporarily paralyzed the rats from the T9 region down. The rats were treated with antibiotics and were placed on heating pads to maintain a steady homeostasis after surgery. They were then irradiated with arrays of thin, parallel x rays (microbeams) at the National Synchrotron Light Source (NSLS). On the day before the irradiations the rats were scored using the Basso et al scale to rank their locomotor ability post surgery yet pre- irradiation. The range is 0–21, with 0 being the worst and fully paralyzed and 21 being the best and fully functional. After the irradiations the rats were scored every four days to test how quickly they were recovering. Within the first two weeks after irradiation the rats' performance appears to improve quickly, yet then it slows down drastically. We saw rapid improvement within the first 14 days after irradiation. On the day of irradiation two of the rats had a score of 3 and two of the rats had a score of 8. On day 14 after the initial irradiation, the two rats with the lower scores, achieved a score of 9.5. The two rats with the higher scored achieved a score of 13. Because of the lack

of unirradiated controls in this primary study, the interpretation of the results will have to wait until such controls are studied and scored.

National University Consortium Capability Catalog Development. *Michalena Grosshans* (*Ohio Northern University, Ada, OH*)*; Roger Mayes* (*Idaho National Laboratory, Idaho Falls, ID*)*.* The Idaho National Laboratory (INL) established a National University Consortium (NUC) to enhance collaboration with university faculty and further integrate university research and development with INL programs. Five Academic Centers of Excellence (ACE), each with a different focus that aligns with the INL mission, have also been established. The NUC schools and the respective ACEs are as follows: Massachusetts Institute of Technology (Advanced Reactor Fuels and Materials Technology), North Carolina State University (Simulation and Modeling), The Ohio State University (Instrumentation & Control and Reactor Safety), Oregon State University (Thermal Fluids and Reactor Safety) and the University of New Mexico (Non-Proliferation Science and Technology). To facilitate collaboration between university and INL researchers, the INL created a catalog of unique equipment, laboratories, projects, software, computers, libraries etc., at each NUC facility, all connected to points of contact. The catalog features data organized by Research Focus, Subcategory, Keywords, Institution, Location, College, Department, Function/Capability, Description, Resource Type, Collaborators/Sponsors/Partners, URL, Point of Contact including phone number and e-mail, and Notes/Miscellaneous Information. The research foci were identified by the ACEs and aligned with the laboratory's strategic plan. During this effort, information available on each university's website was researched thoroughly and gaps in the information were identified. Faculty and researchers at each university have been asked to fill in the gaps. However, most requests are pending response. The catalog is currently configured as an Excel spreadsheet which will later provide INL researchers with an online, searchable database. To maintain this catalog, continual updates will be needed to keep information current. Future efforts will also capture the capabilities of the INL to make the database useful for university researchers. Documentation to support these efforts is available in the form of a user's guide which provides insight as to how the spreadsheet was generated and organized. This will allow someone else to continue project development and potentially help end users improve the quality of their searches.

Δ9-THC Chronic Exposure in Adolescent Rats: Effects on Cocaine Conditioned Place Preference. *Yu Fen Hwang* (*State University of New York at Stony Brook, Stony Brook, NY*); *Peter Thanos* (*Brookhaven National Laboratory, Upton, NY*)*.* Epidemiological studies have shown that use of marijuana during early adolescence is associated with a higher risk for other substance abuse disorders. The extent to which this represents neuroadaptation responses secondary to Δ9-THC (delta-9-tetrahydrocannbinol, main psychoactive ingredient of marijuana), exposure versus genetic vulnerability that underlies high risk with experimentation with drugs in general is unclear. In this study we investigated if chronic exposure of Δ9-THC during the adolescence period in the rat affected the reinforcing responses to cocaine (assessed with condition place preference). Male Sprague Dawley rats (age 3–4 weeks) were administered daily with either Δ9-THC (0.75 and 2 mg/kg) or saline for 21 days. The day after the last injection, we started the Conditioned Place Preference (CPP) segment of the study: [day 1: preconditioning; days 2–9 conditioning phase {cocaine (5 and 10 mg/kg) and saline on alternate days}; day 10: test day]. The results showed that Δ9-THC pretreatment rats resulted in decreased CPP for cocaine (5 mg/kg or 10 mg/kg) On the other hand there were no differences between the group on cocaine induced dose-dependent increases in locomotor activity. These results provide evidence of that exposure to THC during the adolescent period changes the sensitivity to cocaine-induced conditioning. The extent to which this generalizes to conditioning to other drug but also non-drug reinforcers requires further investigation.

Microbeam Radiation Therapy: Treating the 9LGS Rat Brain Tumor. *Nicolle Lanier* (*Suffolk County Community College, Selden, NY*)*; Avraham Dilmanian* (*Brookhaven National Laboratory, Upton, NY*)*.* In conventional radiation therapy the limitation in delivering the adequate dose to the tumor is the damage to the normal surrounding tissue. Microbeam radiation therapy (MRT) is an experimental method that uses arrays of parallel, thin (< 100 μm) planes of synchrotron-generated X-rays (called microbeams, or microplanar beams). It allows the normal tissue, including the central nervous system (CNS), to recover from these irradiations at doses many times higher than doses from the conventional beams that severely damage the tissue. The effect has been attributed primarily to the quick recovery of the microvasculature due to the survival of angiogenic cells between the microbeams. Additionally, at very high doses, single-direction microbeam irradiation kills the tumor in a single session without damaging the surrounding normal tissues, an effect called "the preferential tumoricidal effect of microbeams". However, our recent studies showed that the CNS also tolerates beams as thick as 0.68 mm. We used an array of thick microbeams in a method called "stereotactic microbeam radiation therapy (SMRT)" to treat the rat brain tumor 9L gliosarcoma (9LGS). This method uses irradiations from ten different angles, all crossing the tumor. The rats were irradiated with SMRT at day 15–17 after inoculation (usually done at day 14). Following the irradiation the rats were weighed and otherwise observed daily. The parameters registered were a) if the rat was lethargic, b) if there is any sign of dry blood around the rat's eyes or nose (which are indications of intracranial pressure produced by the tumor), c) if the rat shows epilation over the head where the radiation was aimed, and d) if the rat shows any sign of abnormal behavior (including vocalization upon touch). As of today, 45 days post-inoculation, three of the 15 rats are alive and gaining weight. We plan to repeat the study, this time irradiating the rats at day 14. Research was supported by grants from NIH, Georgetown University, and from the brain tumor foundations of "Musella," "Lauren's First and Goal," and "Have a Chance."

*Synthesis of Suberoyl Anilide Hydroxamic Acid for Positron Emission Tomography Studies of its Inhibitory Effect in Histone. *Frank Ogero* (*Medgar Evers College, Brooklyn, NY*); *Kwesi Amoa* (*Brookhaven National Laboratory, Upton, NY*). Suberoyl anilide hydroxamic acid (SAHA) is a potent inhibitor of cell proliferation. Cell proliferation is caused by the transcriptional role of histone deacetylase (HDAC) an enzyme that influence tumorigenesis of cells. Our research involves synthesizing SAHA via a two-step process. The initial step involved the reaction of suberic acid monomethyl ester with aniline to afford methyl-8-anilino-8-oxooctanoate. This compound was then treated with hydroxylamine to afford the desired compound. SAHA and (18Flouroacetamido)-1-hexanoic acid (18FAHA), a radiotracer for HDAC, will be used to verify the Positron Emission Tomography (PET) image with 18FAHA represents HDAC binding. More specifically, if SAHA blocks the uptake of 18FAHA, this will serve as evidence that the image represents HDAC in the brain. These studies will form the groundwork for future PET studies in humans to understand the relationship between genes, brain chemistry and behavior.

Microbeam Radiation Therapy: Dose Distribution Calculations and Mathematical Modeling. *Jennifer Ong* (*University of Illinois at Urbana-Champaign, Urbana, IL*)*; F. Avraham Dilmanian* (*Brookhaven National Laboratory, Upton, NY*)*.* Microbeam radiation therapy (MRT) uses arrays of parallel, thin, synchrotron-generated X-ray beams, which, when administered at high dosages, spare normal tissues while damaging tumor tissues, thus exhibiting a "preferential tumoricidal" effect. Implementing MRT in a new stereotactic geometry (SMRT) of cylindrical pencil beams in circular arrays concentrates radiation on the tumor by positioning it at the crossing of ten arrays while exposing surrounding normal tissue merely to single arrays, thereby maximizing absorbed dose to the tumor and minimizing damage to healthy tissues. The irradiation port positions for the new geometry were calculated using the computer program Matlab and then applied to the rat brain tumor model experiments conducted at the National Synchrotron Light Source (NSLS). The Monte Carlo code MCNP5 was then employed to simulate the absorbed radiation dose profiles resulting from a 309-microbeam SMRT array with radius 1.5cm in a spherical water phantom model of a human brain and tumor. Superimposing a volumetric mesh tally of 150 μm x 150 μm x 1 cm voxels on the phantom and using a photomultiplier in order to obtain absorbed dose from 1 billion incident photon events yielded relative errors. In order to utilize SMRT geometry in animal model experiments and ultimately on human carcinoma, determination of the beam port angles, as well as an analysis of the spatial distribution of the dose in exposed tissues, is needed.

A Review of Empirical Methods for the Derivation of Parameters in a Theoretical Model of Matrix Metalloproteinase 2 & 9 Proteolysis of Collagen Type IV. *Elizabeth O'Quinn* (*Wofford College, Spartanburg, SC*); *Kara Kruse* (*Oak Ridge National Laboratory, Oak Ridge, TN*). Cardiovascular disease is the leading cause of death in first world countries. An imbalance of matrix degrading enzymes and structural proteins within the extracellular matrix of an arterial wall is a critical factor in cardiovascular disease processes. An increase in matrix metalloproteinase-2 (MMP-2) and matrix metalloproteinase-9 (MMP-9), as part of the inflammatory process, results in degradation of collagen type IV influencing the migration and proliferation of vascular smooth muscle cells; this can lead to further narrowing of a diseased artery. Kinetic modeling of

proteolysis is an approach which can be used to understand complex systems by describing enzymatic mechanisms, cellular processes, and the system's behavior quantitatively. In this research project, a computational model of the biochemical pathways involved in activation and inhibition of MMP-2 and MMP-9 proteolysis of collagen type IV is being developed from empirical data and published data. Separate and integrated models of MMP-2 and MMP-9 pathways have been implemented within JSim, a software application developed by the University of Washington. In addition to the enzyme model a cellular migration model is also being developed for the simulation of VSMC migration and will be explored further. The utilization of reverse-phase high pressure liquid chromatography (HPLC) methods for obtaining quantitative reaction rate parameters are being explored for the estimation of parameters not previously published in the literature. By pairing HPLC separation with spectrometry techniques, protein and peptide identification and quantification are possible. Experimental protocols for the measurement of the enzymatic activity of MMP-2 and MMP-9 proteolysis of collagen type IV are being developed to obtain empirical data. These experimental results are then analyzed to derive the rate parameters needed in the computational model. The use of HPLC methods to analyze the enzymatic activity and cellular activity provides parameters which cannot be obtained through literature. This research is in collaboration with the Vascular Research Laboratory at the University of Tennessee Medical Center in Knoxville.

RS-GVG blocks methamphetamine-triggered reinstatement of the expression of methamphetamine-induced conditioned place preference. *Jessica Pai* (*New York University, New York, NY*); *Stephen Dewey, Wynne Schiffer* (*Brookhaven National Laboratory, Upton, NY*). This study investigated the effects of RS-GVG on the reinstatement of the methamphetamine (METH)-induced expression of conditioned place preference (CPP) in adolescent male Sprague-Dawley rats. The expression of a CPP response correlating to dosage was first examined by subjecting three groups of animals (n=8) to 30-minute pairings of METH (2.5, 5.0, and 10 mg/kg, respectively) with one chamber and 30-minute pairings of saline in the other on alternate days over a 20-day period. Following completion of the METH regimen, a CPP response was established. Subsequent daily testing identified the rate of extinction for each group. On test days, animals received saline and were permitted free access to both chambers for 20 minutes. The amount of time spent in the METH-paired chamber was used to determine the conditioning score. This test was performed until the expression of the CPP response was extinguished (defined as 5 consecutive days without a significant CPP, p < 0.05).

Food Stimulation in a Rat Model of Obesity: Food Seeking Behavior as Assessed by Nose-Poke Activity and Locomotor Responses in the Open-Field. *Lisa Robison* (*Colgate University, Hamilton, NY*); *Peter Thanos* (*Brookhaven National Laboratory, Upton, NY*). Food intake is regulated by factors that modulate caloric requirements, as well as food's reinforcing properties. Apart from genetic factors, there are also environmental factors that play a very important role in obesity, including society, culture, stress, food palatability and food availability, as well as food-related cues. Previously, we showed that exposure to an appetitive food stimulus had significant effects on brain glucose in both humans (Wang, *et al.*, 2001) and rodents (Michaelides, *et al.*, 2006). In this study we examine the effect of genetically-induced obesity and food restriction on seeking and learned behavior before and after classical conditioning of a food (bacon) olfactory stimulus. Zucker Obese (Ob) and Lean (Le) rats were divided into 4 groups: i) Ob *ad lib* fed, ii) Ob food restricted (70% of *ad lib*), iii) Le *ad lib* fed and iv) Le food restricted rats. Leptin-receptor deficiency mixed with an unrestricted diet showed the greatest significant amount of novelty-seeking.

Molecular Cloning of Epitope-Tagged Mitochondria Fission and Fusion Genes. *Joly Shah* (*Tallahassee Community College, Tallahassee, FL*); *Andrew Gifford* (*Brookhaven National Laboratory, Upton, NY*). There are two different types of proteins in mammalian cells Drp-1 and fis-1 which are involved in mitochondria fission. In contrast, there are three different types of proteins in mammalian cells OPA-1, Mfn-1 and Mfn-2 which are essential for fusion of mitochondria. But the central idea of this project is to make epitope tagged Drp1 or OPA1 DNA constructs to study these proteins in cultured cells. Epitope are short stretch of peptides that are antigenic. Proteins attached with epitope can be detected by antibody that recognizes epitope. To make these constructs, we will use DNA recombination and molecular cloning methods. Molecular cloning is the process of generating genetically identical copies of DNA. We will first obtain cDNA clone information of these genes will be purified by using Drp-1 and OPA-1 proteins, in order to receive genetically identical copies of DNA fragments. It is

also necessary to use DNA recombination method to make epitope Flag tagged Drp-1 and OPA-1 in pFLAG-CMV1 vector by growing some bacteria. In order to grow bacteria Precision Scientific Thelco oven was use. To purified plasmid DNA the QIAprep Spin miniprep kit and a centrifuge machine was use. Polymerase Chain Reaction machine was also use in order to isolate fragment of DNA. Fisher Biotech machine was use to find pure DNA and vector. By using this technique DNA was cut and paste in vector to let it grow in clones. Moreover, molecular cloning book was use for the more procedure. The project is still continuing, therefore the result will indicate in future. In conclusion, cloning DNA fragment known as molecular cloning. The purpose of growing DNA is to have large quantities of identical copies of DNA for experiments.

Optical Detection of Cocaine-Induced Brain Function Changes in the Rat Brain *in vivo*. *Melissa Tully* (*State University of New York at Stony Brook, Stony Brook, NY*); *Congwu Du* (*Brookhaven National Laboratory, Upton, NY*). Cocaine abuse increases the risk of life-threatening neurological complications, has vasocontrictive properties and also decreases the metabolism. However, the exact pathophysiological mechanisms underlying cocaine's neurotoxic effects remain incompletely understood. We have developed a multi-wavelength spectroscope (MWS) to simultaneously measure the changes in blood volume (CBV) and tissue oxygenation (StO$_2$) from the brain surface. We also have developed a Laser-Doppler Speckle Contrast Imaging (LDSCI) for detecting the local cerebral blood flow (LCBF) changes in the living rat brain with a high spatiotemporal resolution. In this study, we applied these new optical techniques and combined them with Laser Doppler flowmetry (LDF) to systematically characterize the effects of cocaine on cerebral blood flow (CBF), CBV, and StO$_2$ as functions of time in response to cocaine administration, as well to identify the spatial feature of cocaine-induced LCBF changes in the somatosensory cortex of the living brain. Three groups of rats were used in parallel to study the changes in CBF, CBV and StO$_2$, nd LCBF distribution in response to cocaine administration using the optical systems of LDF, MWS and LDSCI, respectively. Each rat was anesthetized, intubated, and mechanically ventilated, and the physiological parameters, including the heart rate (ECG), respiration rate, mean arterial blood pressure (MABP) and body temperature, were monitored. A craniotomy was then performed above the left somatosensory cortex. An optical fiber-based probe, from MWS or LDF, or a CCD camera of LDSCI was then mounted upon the exposed brain surface. The back-scattered photons from the cortical surface were collected by the optical probe/camera continuously before and after the cocaine administration. The changes of CBF, CBV, StO$_2$, and LCBF were determined as functions of time Our preliminary results show that the cocaine induced a transient changes in CBF, CBV, and StO$_2$. The changes in CBF recovered to the baseline within 10–12 minutes whereas the changes in CBV and StO$_2$ in the brain were relatively longer lasting (>20 minutes). Interestingly, using the LDSCI system, the beta-chloralose anesthetized rats have shown increased blood flow in large vessels and decreased flow in capillaries or the microcirculation within the tissue bed in response to the cocaine administration. These results explored the temporal and spatial features of the cerebrovascular effects of cocaine on the brain, which might provide a better understanding of etiology of cocaine related, stroke and transient ischemic attacks.

A Personality Profile of Cocaine Addicted Individuals. *Catherine Urban* (*State University of New York at Geneseo, Geneseo, NY*); *Rita Goldstein* (*Brookhaven National Laboratory, Upton, NY*). Impairments in higher executive function, such as inhibitory control and decision-making, characterize cocaine addicted individuals; however, the contribution to these cognitive functions of personality traits is not well established. The current study therefore examined differences in personality traits between healthy control subjects and cocaine addicted individuals and the extent to which these differences may be affected by recent cocaine use. Sixty-six cocaine addicted individuals [20 testing negative (CUD-) and 46 testing positive (CUD+) for cocaine in urine, indicative of drug use within 72-hours] and 66 gender-, age-, and education-matched healthy control subjects were administered the Multidimensional Personality Questionnaire (MPQ) as part of a larger neuropsychological battery. The MPQ measures three trait super-factors, each comprised of 3–4 lower order subscales; differences between the groups were examined with four separate MANOVAs. Results revealed significant group differences on all three super-factors such that cocaine abuse was associated with lower positive emotionality [F(2,131) = 3.8, p < .0001], higher negative emotionality [F(2,131) = 5.0, p < .0001], and decreased constraint [F(2,131) = 3.1, p < .001]. These differences were driven by lower social closeness especially

U.S. Department of Energy Journal of Undergraduate Research

in the cocaine positive subgroup [Mean±SEM=12.3±0.6 for CUD+ vs. 14.0±0.8 for CUD- vs. 15.7±0.5 for controls], higher aggression especially in the cocaine negative subgroup [Mean±SEM=5.7±0.5 for CUD+ vs. 6.7±1.0 for CUD- vs. 3.4±0.4 for controls], and lower self-control in the cocaine positive subgroup [Mean±SEM=14.1±0.7 for CUD+ vs. 16.0±1.1 for CUD- vs. 17.7±0.5 for controls]. These effects remained significant after controlling (with ANCOVAs) for state depression and other demographic variables that differed between the groups. These results suggest significant differences between healthy control subjects and individuals addicted to cocaine in trait measures of personality. Together, the higher negative emotionality (aggression), lower positive emotionality (social closeness) and lower self-control may predispose the addicted individuals to relapse and compulsive drug use, especially under socially stressful situations. The underlying cognitive and neurobiological substrates remain to be elucidated.

Analysis of the Biological Effects of Aspirated Carbon Nanohorn Particles in Mice Using Scanning Near-Field Ultrasound Holography. KATHERINE VENMAR (*Denison University, Granville, OH*); THOMAS THUNDAT (*Oak Ridge National Laboratory, Oak Ridge, TN*). Engineered nanomaterials, because of their enhanced physicochemical properties compared to their bulk form, are finding an increasingly important role in many potential commercial applications. However, the health effects of nanomaterials are not well understood or thoroughly investigated. Therefore, more studies are needed to examine different types of nanomaterials and the biological responses they invoke. The purpose of this research was to examine the effects of aspirating single-walled carbon nanohorns (SWCNHs) *in vivo* using mice. Bronchoalveolar lavage (BAL) and blood samples were collected from two experimental groups, the nanohorn exposed, and the control mice. Three mice from both groups were sacrificed 24 hours and 7 days after aspiration. Gross examination of the number of macrophages versus activated macrophages in BAL samples from the exposed and the control mice suggested a possible pro-inflammatory response to the carbon nanohorns. Employing a unique detection technique, Scanning Near-Field Ultrasound Holography, carbon nanohorns were discovered bound to cell membranes, inside cells, and near cells in both the red blood cells and BAL sample cells. The positioning of carbon nanohorns inside the cells not bound to a membrane suggests that they entered the cell through a process other than phagocytosis. Furthermore, the red blood cells (RBC) in all the exposed blood samples exhibited a distorted phenotype. Such distortions could possibly lead to various pulmonary diseases. From their ability to permeate membranes, cause pro-inflammatory responses, and distort the phenotype of red blood cells, it can be concluded that carbon nanohorns may pose a biological threat.

Chronic THC Exposure: Effects on Sucrose Conditioned Place Preference in Adolescent Rats. ANNA VERDE (*State University of New York at Stony Brook, Stony Brook, NY*); PANAYOTIS (PETER) THANOS (*Brookhaven National Laboratory, Upton, NY*). The psychoactive constituent in marijuana Δ9-tetrahydrocannabinol (THC) pharmacologically activates the mesolimbic reward pathways. Similarly highly palatable foods also activate the reward circuitry of the brain. Specifically, administration of THC has been shown to influence the intake of sweet foods. The effect of THC in adolescence hasn't been looked at yet. Adolescence may be characterized as a period when a significant amount of neurobiological and development changes occur. Drug abuse during an early neurodevelopmental period may impact the reward potential and consumption of foods or drugs later in life. Therefore, the goal of the present study was to examine the effect of chronic THC administration during adolescence on the reward potential of sucrose using a conditioned place preference (CPP) paradigm. During the exposure period, 4 week old male Sprague Dawley rats were divided into 3 groups to receive a daily i.p. injection for 3 weeks of either: 1) vehicle (saline) 2) low dose THC (0.75 mg/kg) 3) high dose THC (2 mg/kg). Next, all rats started CPP after the last day of treatment. The CPP timeline encompassed the following: Day 1: Habituation, Days 2–9: Conditioning Phase (10 sucrose pellets on even days and no sucrose on odd days), and Day 10: Test Day. These findings will help gain insight on the impact of chronic THC exposure during a neurodevelopmental period on the subsequent reward potential of natural rewards. Finally these sucrose CPP results will be compared to CPP results to drugs in similar THC pretreated rats (Hwang *et al.*, 2006).

The Role of Bootstrap Resampling to Improve Signal-to-Noise Ratio in PET Images. JOHN ZABROSKI (*St. Joseph's College, Patchogue, NY*); JEAN LOGAN (*Brookhaven National Laboratory, Upton, NY*). Positron Emission Tomography (PET) imaging helps determine the effects of genetic variation, disease, behavior, and drug administration on living systems at the cellular level. However, the amount of information gained from these images is limited by noise due to poor counting statistics related to the half-life of the radiotracer used and the amount injected, which is limited by regulations placed on radiation exposure to human subjects. For some radiotracers this noise also limits the ability to create parametric images for each subject since an image is constructed by assigning the biochemical parameter to each voxel. Group parametric images may overcome these factors, eliminating error due to poor counting statistics by using discrete time-frame averaging (DFA) before assigning the biochemical parameter to the group image. However, the statistical significance that would otherwise be obtained through individual parametric images cannot be determined with a group parametric image, because there is only one image per group. To overcome this, bootstrap re-sampling was used to create additional datasets-bootstrap samples. The initial trial used data collected from the PET radiotracer [11C]-Clorgyline (CLG), which binds to the enzyme monoamine oxidase A (MAO-A). Simulated data was generated from the measured plasma input functions using model parameters (K1, k2, k3) derived from a region of interest analysis of the thalamus where k3 represents binding of tracer to MAO-A and K1 and k2 represent transfer between plasma and tissue. By introducing different levels of random noise to this data we can simulate time-activity curves at the voxel level. Using DFA we then attempted to increase the signal-to-noise. For each simulation, standard error was calculated. Also, each simulation was compared to a bootstrapped standard error, with the number of bootstrap samples necessary to obtain a stable estimate of the standard error systematically determined. Our analysis shows that bootstrap resampling plays a useful role in determining statistics associated with the DFA process. Bootstrap resampling was closest to the true value of the voxel at the highest noise level (a = 8.0). Now that we have tested the validity of DFA in conjunction with bootstrap resampling, the next step is to generate bootstrap parametric images, allowing an assessment of the statistical significance of group differences.

Nuclear Sciences

Investigate How Different Operating Conditions or Different Reactors Produce Different Fission Product Nuclides, Using ORIGEN Code. DAVID ASKINS (*Kansas State University, Manhattan, KS*); CHARLES WEBER (*Oak Ridge National Laboratory, Oak Ridge, TN*). There are many questions in today's age when it comes to the problem of radioactive nuclear waste. With the several different types of engineered nuclear reactors in existence around the world, there are many varied output nuclides that are generated as a result of the broad range of running conditions in certain types of reactors. To determine the theoretical output nuclides ORIGEN/ARP code was used. It is a sequence in SCALE that serves as a fast and user-friendly method of performing nuclear irradiation and decay calculations, using problem-dependent cross sections. All possible reactor types were run with different variables, such as burnup, average power, fuel assembly, enrichment of fuel, percentage of time the reactor was powered up, and the amount of cycles. Once the variables were plugged in, the nuclide output products were taken and compared to those of the same type of reactor under different conditions, and to those of different reactors under different situations and similar circumstances. They were evaluated by first finding the average amount of a nuclide for a single reactor, and then measured up to different reactors by finding either the percent difference between the two nuclides, or the ratio between them. Each reactor type was compared to each of the other reactor types. Following this, the main differences were identified to recognize trends, if any, in the various output products related to the varying reactors. To accomplish this task, for each reactor, several different cases were run, keeping the burnup value the same, while varying the average power and running period. Following the running of each specific case, an executable file, 71process, was created to output all possible fission-product nuclides and their respective weights in gram-atoms. These results were then used to generate Excel spreadsheets with the ratios of how many parts of a given element are produced by one reactor, as compared to another. These ratios were then analyzed for certain trends of nuclides between reactors. At this time no results have been obtained. With nuclear power becoming ever more present in today's power industry, we are inevitably faced with the problem of spent fuel accumulating. Furthermore, with the ever-present threat of nuclear waste falling into the wrong hands, it is essential to be able to identify where such nuclear waste came from. To achieve tangible results, more research should be conducted.

Characterization of Neutron Spectra from Coulombic Deuteron Breakup. *Brad Barquest* (*University of California at Berkeley, Berkeley, CA*); *Peggy McMahan* (*Lawrence Berkeley National Laboratory, Berkley, CA*). A source of tunable, quasi-monoenergetic neutrons is under development at the 88-Inch Cyclotron at Lawrence Berkeley National Laboratory (LBNL). The neutrons are produced through breakup of deuterons in a nuclear coulombic field. As neutrons from both direct nuclear reactions and coulomb-induced breakup contribute to the outgoing flux, characterization of the neutron spectra as a function of deuteron energy, target material and angle are needed to determine the relative contributions from the two channels. 29 MeV deuterons impinged upon a Ta foil, and the residual beam was dumped in an adjacent room. Measurements were taken at 25°, 35°, and 45° with respect to the target in the lab frame, and time-of-flight (TOF) techniques were used to determine the neutron energies. Results demonstrate a decreasing flux with increasing lab angle for neutrons with energy greater than or equal to 10 MeV, which is consistent with coulombic breakup. Further comparison with theory is necessary to determine the extent of direct reaction contributions.

Combating Nuisance Alarms Caused by "Ship Effect" in ^{3}He Based Neutron Detection Radiation Portal Monitors. *Elise Buckley, Anna Oliveri* (*Juniata College, Huntington, PA*)*; James Ely* (*Pacific Northwest National Laboratory, Richland, WA*). The "ship effect" occurs when high-energy neutrons produced by cosmic rays strike bulk materials and produce a burst of neutrons. These ship effect neutrons can present unique challenges in ongoing efforts to interdict illicit nuclear trafficking at border crossings. ^{3}He neutron proportional counters, the neutron detection component in deployed radiation portal monitors (RPM), can generate false positives due to these neutron spikes, leading to cumbersome and time-consuming secondary radiation scans. This work explores methods to mitigate these nuisance alarms through a better understanding of how this effect is manifested in different materials, the role of a target materials' neutron density, and data analysis techniques to account for its effects. We used a mobile RPM equipped with ^{3}He tubes to detect the neutron flux from several commercial products containing naturally occurring radioactive materials (NORM), including ceramic tile, fertilizer, rock salt, cat litter, and lead. We compared the mass density and neutron density of these materials to their neutron count rates, finding a linear relationship between neutron density and neutron flux. High neutron density materials were found to be a greater source of ship effect neutrons. While neutrons from illicit nuclear sources such as plutonium are Poisson in their temporal frequency distribution, those from background are not. We found that ship effect neutrons deviated from a Poisson distribution when binned over 0.1 second time intervals, however if the neutron flux was averaged instead over 2.0 second time intervals the ship effect neutron spikes were washed out, recovering a Poisson distribution. These findings provide underlying knowledge regarding ship effect neutrons emanating from some common bulk materials, and suggest a data analysis algorithm to distinguish between innocent ship effect neutrons and more worrisome neutron-emitting illegal sources.

Fabrication Manual for the Fuels and Applied Science Building. *Megan Dixon* (*University of Idaho, Moscow, ID*); *Jared M. Wight* (*Idaho National Laboratory, Idaho Falls, ID*). The Fuels and Applied Science Building (FASB) in the Materials and Fuels Complex (MFC) at the Idaho National Laboratory (INL) is a radiological facility where significant scientific research and development occur. This summer, INL research facilities were scheduled for several inspections in preparation for an upcoming Department of Energy (DOE) safety audit. Groundwork for these inspections included both paperwork and physical preparation which impacted the majority of FASB researchers and postponed the originally planned summer research activity entirely. The majority of the research occurring in FASB is conducted for the Reduced Enrichment for Research and Test Reactors (RERTR) fuel development program. The RERTR program is tasked to convert civilian research and test reactors worldwide from High Enriched Uranium (HEU) to Low Enriched Uranium (LEU). This research includes the development of advanced high-density LEU fuels. The program has developed a uranium-molybdenum monolithic fuel foil and is currently developing techniques to clad the fuel in aluminum. Friction Bonding (FB) is a bonding process used to clad the uranium alloy foils. Friction bonding works by applying pressure with a rotating tool. This generates heat, softens the material, and creates a bond by producing a plastic flow of metal on both sides of the fuel plate. Another cladding process, Hot Isostatic Pressing (HIP), uses high temperature and pressure to bond the metallic fuels to the cladding. Other work for the RERTR program includes development of high-density dispersion fuels using the same type of fuel alloy. The

dispersion process consists of many steps including: production of uranium alloy powder, compaction with aluminum powder, and the hot rolling of the compacts in an aluminum frame to form a fuel plate. Process information about the various RERTR projects was acquired from appropriate researchers and compiled to create a poster which will be placed inside FASB to educate visitors about the projects being conducted.

Nuclear Material Shipments: The Challenge of Material Transfers Using Certified Containers. *Matthew Duchene* (*University of Illinois, Urbana, IL*); *Terri Bray* (*Argonne National Laboratory, Argonne, IL*). In a continuing effort to develop safe nuclear technology, Argonne National Laboratory and the U.S. Department of Energy (DOE) utilize a variety of approved shipping containers to transport nuclear fuel and radioactive waste to various facilities across the country. As many of these shipping casks become old and outdated, the DOE will decommission a large number of different cask models for safety purposes. The rapid decommissioning of so many containers presents a great challenge for all government and private run institutions. The model T-2 shipping cask, which is used heavily by Argonne for hot cell material movement, is one of the many casks being retired. Due to this development, Argonne will require a new model shipping container to transport irradiated nuclear material from the onsite decommissioned reactors and hot cell facility to other national facilities for storage and waste management. In order to conduct procedures in the future, the Nuclear Operations Division at Argonne must find a certified shipping cask that is not slated to be retired, will be effective in the movement of the laboratory's nuclear material, and does not exceed the structural and safety limits of the laboratory's facilities. After a detailed literature search, the T-3 cask is the best option for offsite material transfers if the material is first relocated from the hot cell to a staging point in the Argonne building 200 M-wing.

Photoelectrochemically Splitting Water Using TiO_2 Nanotubes. *Latoya Harrison* (*Prairie View A&M University, Prairie View, TX*)*; Costas Tsouris* (*Oak Ridge National Laboratory, Oak Ridge, TN*). Fossil fuels, burned for energy, are polluting the earth's ecosystem. Hydrogen is a non-polluting fuel that could be used, instead of fossil fuels. The question is how one can efficiently produce hydrogen. The purpose of this project is to photoelectrochemically split water to produce hydrogen. The concept is to use light to split water molecules into hydrogen at the cathode and oxygen at the anode. The experimental system used in this study consists of a power source attached to a titania (TiO_2) nanotubes anode and a platinum cathode. Ultraviolet (UV) light irradiation of the anode is used to reduce the amount of electrical force required by the electrolytic process. An aqueous solution containing 1M sulfuric acid completes the circuit. The specific contribution of this work tests the hypothesis that a film of TiO_2 nanotubes synthesized at Oak Ridge National Laboratory can be used as a photoactive anode with improved efficiency. This hypothesis is being tested through a set of experiments using different anodes. We used: amorphous TiO_2, rutile crystalline TiO_2, and anatase crystalline TiO_2 nanotubes. We found that, in all cases, photoillumination of the anode increases the produced current. The TiO_2 anatase crystalline structure produced the highest increased in photocurrent. Higher produced currents led to higher hydrogen production. TiO_2 anatase nanostructures showed the highest photo efficiency, about 0.3 percent, of the total light energy used in the experiments.

A Physical Description of Fission Product Behavior in Fuels for Advanced Power Reactors. *Gary Kaganas* (*Florida International University, Miami, FL*)*; Jeff Rest* (*Argonne National Laboratory, Argonne, IL*). The Global Nuclear Energy Partnership (GNEP) is considering a list of reactors and nuclear fuels as part of its chartered initiative. Because many of the candidate materials have not been explored experimentally under the conditions of interest, and in order to economize on program costs, analytical support in the form of combined first principle and mechanistic modeling is highly desirable. The present work is a compilation of mechanistic models developed in order to describe the fission product behavior of irradiated nuclear fuel. The mechanistic nature of the model development allows for the possibility of describing a range of nuclear fuels under varying operating conditions. Key sources include the mechanistic FASTGRASS code and the Dispersion Analysis Research Tool (DART). Described behavior mechanisms are divided into subdivisions treating fundamental materials processes under normal operation as well as the effect of transient heating conditions on these processes. Model topics discussed include intra- and intergranular gas-atom and bubble diffusion, bubble nucleation and growth, gas-atom re-solution, fuel swelling and fission gas release. In addition, the effect of an evolving microstructure on these processes (e.g., irradiation-induced

recrystallization) is considered. The uranium-alloy fuel, U-xPu-Zr, is investigated and behavior mechanisms are proposed for swelling in the α-, intermediate- and γ-uranium zones of this fuel. The work reviews the FASTGRASS kinetic/mechanistic description of volatile fission products and, separately, the basis for the DART calculation of bubble behavior in amorphous fuels. Development areas and applications for physical nuclear fuel models are identified.

Transportation of Nuclear Fuel Rods in Building 212.
JASON McCALL (*University of Missouri – Rolla, Rolla, MO*)*; TERRI BRAY* (*Argonne National Laboratory, Argonne, IL*). Under a directive from DOE, the Alpha Gamma Hot Cell Facility (AGHCF) in Building 212 at Argonne must empty all nuclear material by 2011. To meet this deadline the DOE has given the Nuclear Operations Division (NOD) four years to transport all the nuclear material out of the AGHCF. Fissile Inventory Management System (FIMS) is a program developed at Argonne with the purpose of tracking all the nuclear material in the AGHCF. FIMS lists information ranging from the composition of a material to the dimensions of that material. This program was used to prepare material for shipments. Shipments of material are transported in aluminum tubes. A conservative number for the amount of tubes that must be shipped is 241; this estimate was generated by careful analysis of the dimensions of the material. The casks Argonne currently uses to ship tubes are the T-2 casks each of which houses twelve tubes. However, the T-2 casks are currently in the decommissioning process, and by the year 2008 the T-2 casks will be allowed for onsite usage only. NOD therefore must find a cask that will replace the T-2 casks and allow the material in the AGHCF to be removed within the DOE's allotted time frame.

Sensitivity Improvement In Low-Profile Distributed Detector Systems For Tracking Sources In Transit.
TENILLE MEDLEY (*University of Illinois at Chicago, Chicago, IL*)*; RICHARD VILIM* (*Argonne National Laboratory, Argonne, IL*). The RadTrac real-time detection and tracking software runs on a laptop computer networked to gammaradiation detectors. A probabilistic estimate for source position is generated by combining measured count rate data with a first-principles stochastic model for the space and time dependence of count rates and knowledge of detector intrinsic efficiency. Recent development work has focused on improving RadTrac sensitivity in lowcount rate situations. A method has been developed for processing count rates by energy according to that part of the energy spectrum with the greatest signal-to-noise ratio. In addition a method has been developed that places constraints on the solution that are physically appropriate when count rates approach background. In both instances experiments with a weak source confirmed the uncertainty in estimated position is reduced.

Similarity of Critical Experiment Using Sensitivity Analysis.
ALLISON MILLER (*University of New Mexico, Albuquerque, NM*)*; BRAD REARDEN* (*Oak Ridge National Laboratory, Oak Ridge, TN*). Validation of nuclear critical safety calculations is required to establish the relationship between calculated keff values and reality. From the International Handbook of Evaluated Criticality Safety Benchmark Experiments (IHECSBE), critical experiments were examined. Benchmark experiments that were similar in composition to that of the criticality safety model were modeled with the use of the same version of computer code, nuclear data and modeling assumptions as in the criticality safety model. The SCALE 5.1 TSUNAMI -3D is a code in which the sensitivity of the nuclear data is calculated. This sensitivity defines how the keff of a model or system will be affected for a given change in a specific nuclide. The goal was to obtain data for the sensitivity analysis for each benchmark experiment and compare these results to those of criticality safety model. For the purpose of code validation, direct perturbation calculations were preformed. A new prototypic SCALE module is being beta-tested to perform the direct perturbation (DP) calculations, named TSUNAMI -DP. The expectation is that this module will release with SCALE 6 in 2008. TSUNAMI -DP generates the direct perturbation Critical Safety Analysis Sequences (CSAS) files. The CSAS output files are then examined to validate the TSUNAMI -3D sensitivity results. Once it is seen that the TSUNAMI -3D results and the direct perturbation results are within 5% of one another, the sensitivity data files are compared to those of the cask models; using the TSUNAMI -IP module. TSUNAMI -IP generates a final value that shows how similar the two models are. TSUNAMI-IP generates a final value, which states the similarity between the criticality safety model and the benchmark experiment model. The majority of the critical experiments that were modeled were not similar to those of the criticality safety model, and therefore will not be applicable. Continual work is being done to obtain more critical benchmark experiments that are applicable to that of the criticality safety model.

Variance Reduction for Radiation Transport Using Delta-f Methods.
IAN PERCEL (*University of Illinois at Urbana-Champaign, Urbana, IL*)*; RICK NEBEL* (*Los Alamos National Laboratory, Los Alamos, NM*). Radiation hydrodynamics is employed by physicists to describe the behavior of fluids that are strongly coupled to a radiation field. This is particularly important in analyzing astrophysical phenomena. Direct Simulation Monte Carlo is one of the few numerical tools available for solving realistic problems in radiation hydrodynamics. Since M. Kotschenreuther's work in 1988, the delta-f method has dramatically reduced the variance observed in Monte Carlo solutions to problems in plasma physics. Recently, researchers at Lawrence Livermore National Laboratory (LLNL) have considered using a similar technique in radiation transport. The new algorithm being studied at Los Alamos National Laboratory (LANL) includes the LLNL algorithm as a special case. The LANL equilibrium term results from using the standard asymptotic expansion to include diffusion as well as the Local Thermal Equilibrium component that the LLNL algorithm is restricted to. The weighting function is evolved using a difference equation for the total time derivative of the distribution. The connection to the weighting function is established by using a Klimontovich representation of the system. In this research, the proposed change has been formally proven to provide a valid extension of the delta-f method. The derivation also implies the existence of an alternate evaluation method that may provide a check on the diffusion approximation. If efficiency gains observed in plasma physics simulations hold, the new algorithm should show a dramatic improvement over the LLNL algorithm. Specifically, the new algorithm may offer as large a gain in efficiency over the LLNL algorithm as the LLNL algorithm demonstrates when compared with analog methods. A comparison of the two algorithms has not been completed and continuing work should provide a basis for further improvements. This algorithm may offer significantly more accurate radiation transport calculations than have been possible to date. Initial numerical results will be presented.

Semi-Automation of Data Analysis of RTBT Wire Scanners.
FEDRICK REYNOLDS (*Tennessee State University, Nashville, TN*)*; TED WILLIAMS* (*Oak Ridge National Laboratory, Oak Ridge, TN*). The Spallation Neutron Source (SNS) is the most powerful pulsed source of neutrons in the world. SNS consists of a Linear Accelerator (Linac) that accelerates negatively charged hydrogen ions (H-) throughout the various regions of the Linac to approximately 88% of the speed of light. However, the region that is focused on is the Ring to Target Beam Transport (RTBT). In this region, the beam is transported to the mercury target to produce neutrons that are used for research. During the transport, the size of the beam is increased, and to produce the maximum amount of neutrons the beam size and orientation is essential. To ensure that the neutron production is efficient as possible, the analyzation of data from wire scanners in the RTBT is necessary. When analyzing data, it is common to perform the tasks of eliminating outliers and noise caused by various things. These tasks are many times tedious and time consuming. Therefore, the task was to modify an existing program that would make the analyzation less wearisome, and include buttons that would subtract noise and store important values that would be produced from the analyzation. These buttons were created and placed in the program RTBT Wizard, a program that analyzes wire scanner data from the RTBT region of the Linac. These buttons, "Clear Data," "Percent of Range," and "Fit and Store" provides the user with an easy step-by-step process of analyzing data. The "Clear" button clears a table holding data while allowing the user to import another set of data to be analyzed. The "Percent Range" button is used to subtract background noise from being analyzed. This is essential because the background noise can cause the beam size calculations to be thrown off, therefore causing over-adjustments by the Linac operators. The "Fit and Store" button, fits the data with a Gaussian profile and stores the values of amplitude and sigma. These values determine the beam size and within the program the orientation and shape of the beam can be calculated with these same figures. These modifications, while minor on a visible level, were much needed, and will prove to become great assets for the operators.

Reviving and Upgrading of the eP Device.
IDAYKIS RODRIGUEZ (*Florida International University, Miami, FL*)*; DOUGLAS W. HIGINBOTHAM* (*Thomas Jefferson National Accelerator Facility, Newport News, VA*). At Thomas Jefferson National Accelerator Facility, an electron beam is used to probe the fundamental properties of the nucleus. In these experiments, it is essential to know the precise energy of the beam. An important instrument along the beamline to measure the beam energy is the eP device. The device measures the scattered electron angle and the recoil proton angle of an elastic collision. From these angle measurements, the beam energy can be calculated. The eP device

components such as computer software, controls, and mechanical parts needed to be upgraded and/or replaced in order for the eP device to be operational again. A research study was conducted of the current hydrogen target and its properties as well as alternate targets for better performance. An analysis was also done on potential changes to the position of the electron and proton detectors for the 12 GeV upgrade because eP can only measure energies up to 5.5 GeV. Calculations show that for the new energy upgrade, electron detectors need to be positioned at 50 above and below the beamline to measure the energy of 11 GeV. Another two proton detectors need to be placed at an angle of 49.20 above and below the beamline to measure energies of 6.6 GeV and 8.8 GeV. With these changes the eP device will measure the range of new energies from 2.2 GeV to 11GeV. From the target research studies it was found that a carbon nanotube mixture with polypropylene could be the ideal target for the eP device because of its high thermal conductivity and its high hydrogen content. The changes made to the eP device demonstrate the importance of continued research and new technologies.

Using the Fissile Inventory Management System to Identify Hazardous Radioactive Materials for Transportation out of Alpha-Gamma Hot Cell Facility. *Mark Sakowski* (*Purdue University, West Lafayette, IN); Terry Bray* (*Argonne National Laboratory, Argonne, IL*). During its 43-year history, the Alpha-Gamma Hot Cell Facility (AGHCF) has accumulated 142 kg of uranium and plutonium from previous nuclear reactor research. While research no longer takes place in the AGHCF as a result of its crowded and potentially hazardous workplace, the Department of Energy recently required that the AGHCF be decontaminated and decommissioned in the next four years. All irradiated materials will be transferred from Argonne to appropriate repositories. To carry out this plan, the AGHCF uses a sample tracking database program known as the Fissile Inventory Management System (FIMS) where detailed information of each item in the AGHCF is provided. Consolidating two FIMS data tables provided a single universal data spreadsheet that allowing several analyses of irradiated materials inside the AGHCF; these include volume of fuel elements inside, reactor type and origin, and plutonium and uranium content. Furthermore Argonne uses the T-2 cask for shipments of irradiated reactor fuel elements. The T-2 has strict limits on weight, decay heat, and quantity of hazardous material, so careful planning is necessary. The goal is to retrieve the radioactive material inside the AGHCF and to package the T-2 cask safely and efficiently while maximizing the amount of fissile material to be shipped out to the respective repositories. In addition research for new prototype casks to use for shipments after the T-2's expiration is ongoing.

Applicability of Steady RANS Turbulence Models for Simulation of 7-Pin Wire Wrapped Fuel Pins. *Jeffrey Smith* (*Kansas State University, Manhattan, KS); David Pointer* (*Argonne National Laboratory, Argonne, IL*). In response to the goals outlined by the U.S. Department of Energy's Global Nuclear Energy Partnership program, Argonne National Laboratory has initiated an effort to create an integrated multi-physics multi-resolution thermal hydraulic simulation tool package for the evaluation of nuclear power plant design and safety. As part of this effort, the applicability of a variety of thermal hydraulic analysis methods for the prediction of heat transfer and fluid dynamics in the wire-wrapped fuel-rod bundles found in a fast reactor core is composed is being assessed. The work described herein provides an initial assessment of the predictive capabilities of steady RANS turbulence models for this application using the general purpose commercial computational fluid dynamics code Star-CD. A 7-pin wire wrapped fuel rod bundle based on the dimensions of fuel elements in the concept Advanced Burner Test Reactor was simulated using the standard high Reynolds number k-ε model, standard high Reynolds number k-ε model with a Norris & Reynolds two layer wall treatment, the RNG formulation of the high Reynolds number k-ε model, and a six equation algebraic Reynolds Stress Model. The turbulent kinetic energy and velocity magnitude predictions were compared for each case. Among the k-ε formulations, the RNG formulation of the high Reynolds number k-ε model results in the most distinctive change in predicted flow features in comparison to the baseline high Reynolds number k-ε model.

Monitoring Patient Motion During Head Single Photon Emission Computed Tomography Imaging. *Gevorg Stepanyan* (*Hampden-Sydney College, Hampden Sydney, VA); Stan Majewski* (*Thomas Jefferson National Accelerator Facility, Newport News, VA*). Patient motion during head single photon emission computed tomography (SPECT) could adversely affect the resolution in diagnostic imaging. The sudden movements compromise the high spatial resolution capabilities of the SPECT imager. To eliminate the image degradation

through shifts in the six degrees of freedom, a motion compensation technique is required. The goal of this project is to provide real time tracking with sub-millimeter accuracy of patient motion. The Vicra system uses two infrared (IR) position sensors that track passive IR reflections. The Vicra system was placed to track the retro reflective markers positioned on the head of the patient. This stereo-infrared system provided excellent results from the tracking, of the six degrees of freedom, with errors well within the proposed limits. The 3D root mean square error was 0.101 mm. The full width at half max error was lower then that of the SPECT gamma camera. Analysis of other methods of patient motion tracking suggests that regular stereo-optical tracking systems do not provide the accuracy and repeatability that the Vicra system does. The data obtained using the Vicra system can be utilized for patient motion compensation during SPECT image reconstruction. Image reconstruction allows for an accurate diagnostic of the administered radiopharmaceutical source. The specific goal of this project is to assist in monitoring 131Iodine treatment of glioblastoma multiform using a high resolution SPECT gamma camera.

Thermodynamic Analysis of ITER's Cooling Water System. *Shawn Wachter* (*Pittsburg State University, Pittsburg, KS); Juan Ferrada* (*Oak Ridge National Laboratory, Oak Ridge, TN*). ITER, the International Thermonuclear Experimental Reactor, is currently being constructed in Cadarache, France by an international consortium including the United States. FlowITER is a simulations package designed at Oak Ridge National Laboratories to study the operations of ITER's cooling water system. ITER is an experimental magnetic confinement fusion reactor designed to produce plasmas capable of sustaining controlled fusion reactions. It is expected to be the first reactor to produce up to five times more thermal energy in steady state operations than is consumed through auxiliary heating, and is forecast to sustain steady state operations for a 500 second fusion pulse. Water will be used as the cooling fluid in the reactor and will transfer heat, or power, away from the reactor. As it is an experimental reactor, the cooling water system will not actually generate electricity but rather will transfer power to a heat rejection system. The United States is responsible for the design and construction of the cooling water system. The focus of our project is to design a software package capable of accurately simulating the operations of the cooling water system. The simulation platform is FlowJava, which is written in Java, and the participating models are written in Python. The tokamak's coolant subsystems include the Divertor / Limiter system, the Primary First Wall / Blanket system, the Neutral Beam Injector system, and the Vacuum Vessel system. By accurately modeling the behavior of the various cooling systems, problems can be predicted in the design stage and construction delays can be avoided.

Designing and Implementing Graphical User Information (GUI) Components for the Automation of the Analysis of RTBT Wire Scanners' Data. *Karla Ward* (*Tennessee State University, Nashville, TN); Ted Williams* (*Oak Ridge National Laboratory, Oak Ridge, TN*). Spallation Neutron Source (SNS) located at Oak Ridge National Laboratory (ORNL) is home to the world's highest-energy-pulsed H-ion particle accelerator. The accelerator sends an intense proton pulse to a heavy atomic nucleus of mercury to produce neutron-scattering. Within the accelerator complex are five different sections that work together to result in this neutron-scattering: the linac, the high energy beam transport (HEBT), the ring, the ring to target beam transport (RTBT), and the mercury target. The Linac accelerates the beam to 90% of the speed of light. The HEBT transports the beam from the linac to the ring. The ring stores the protons and the RTBT transports the beam to the mercury target, which gets bombarded by the beam at 60 times per second. The RTBT region of the accelerator is of particular importance currently because this is where data is taken that relate to the size and horizontal and vertical position of the beam before it reaches the target. Wire scanners perform the process of taking the data from the RTBT and placing it into a file to be analyzed, and with the help of a computer program the operators of the accelerator analyze this data. To speed up the analysis of data from the RTBT wire scanners, the analysis program rtbtwizard was modified to improve and enhance the functionality between the user and the data processing routines. Specifically these modifications included the addition of "Cut, Fit and Store All", "Percent Range", "Noise Subtraction", and "Clear Data Table" buttons into an already existing panel. The activation of these buttons produce a series of actions which include automatic Gaussian fitting, storing analyzed data, finding and eliminating the noise floor, and clearing the data table. These modifications resulted in a more efficient procedure for the operators of the accelerator to analyze the size and position of the beam on the target. This in turn improves the probability

that there will be a reduction in activation at the target, damage to the nose cone of the target, and ensure maximum neutron production.

Database Management Systems for the Inventory of Nuclear Materials. REBECCA WARD (*McDaniel College, Westminster, MD*); ARTHUR A. FRIGO (*Argonne National Laboratory, Argonne, IL*). Argonne National Laboratory observes stringent inventory practices with regards to nuclear materials as promulgated in the Code of Federal Regulations (10 CFR 830, 10 CFR 835). The Department of Energy also provides specific guidelines for complying with the codes and sets forth instructions for transporting, storing, and accounting for nuclear materials of security concern. The ability to ensure the implementation of these policies depends on the accuracy with which the inventory of nuclear materials is maintained. Several privately-developed databases are used to track nuclear material inventories at Argonne. The goal of this project is to provide an in-depth examination of Argonne databases as well as databases developed by other national laboratories and the private sector. This paper recommends a comprehensive nuclear materials database that meets the needs of the user, meets the appropriate information technology requirements, and reliably tracks information about nuclear materials. The following databases are considered and evaluated in detail in this paper: Argonne Chemical Engineering Division (CMT) Radionuclide Inventory Database, Local Area Nuclear Materials Accountability Software (LANMAS), Argonne Fissile Inventory Management System (FIMS), Argonne Waste Management System, and the Argonne Sealed Source Inventory Database (SSID). In addition, a comparable database from Oak Ridge National Laboratory was considered, as well as IsoStock©, a commercial software bundle produced by the Gillett Partnership; however, due to space restrictions, details about these other databases are not reported. Information about each database was gathered through dialogue with the architect and the primary users, as well as from available written documentation. The CMT Radionuclide Inventory Database was found to be the most user-friendly and comprehensive tracking system. With a few improvements, this system could be adopted to serve as the inventory database for all nuclear materials at Argonne.

Criticality Evaluation of Plutonium-239 Moderated by High-Density Polyethylene in Stainless Steel and Aluminum Containers Suitable for Non-Exclusive Use Transport. TIMOTHY WATSON (*Rensselaer Polytechnic Institute, Troy, NY*); JOHN SCORBY (*Lawrence Livermore National Laboratory, Livermore, CA*). Research is conducted at the Joint Actinide Shock Physics Experimental Facility (JASPER) on the effects of high pressure and temperature environments on 239Pu, in support of the stockpile stewardship program. Once an experiment has been completed, it is necessary to transport the end products for interim storage or final disposition. Federal shipping regulations for non-exclusive use transportation have an exemption allowance when no more than 180 grams of fissile material are present in at least 360 kilograms of contiguous non-fissile material. This allowance exempts the shipper from the requirement to establish and assign a Criticality Safety Index for a package. To evaluate the general applicability and conservatism of this exemption criterion, a worst-case scenario of 180g 239Pu was modeled using one of Lawrence Livermore National Laboratory's in-house Monte Carlo transport codes known as COG 10. The geometry consisted of 239Pu spheres homogenously mixed with high-density polyethylene surrounded by a cube of either stainless steel 304 or aluminum. An optimized geometry for both cube materials and hydrogen-to-fissile isotope (H/X) ratio were determined for a single unit. Infinite and finite 3D arrays of these optimized units were then simulated to determine if the systems would exceed criticality. Completion of these simulations showed that the optimal H/X ratio for the most reactive units ranged from 800 to 1600. A single unit of either cube material would not reach criticality. An infinite array was determined to reach criticality. A lower loading of 100 g of 239Pu was then considered and found to be subcritical in an infinite array with either Al or steel. The offsetting of spheres in their respective cubes was also simulated and showed a considerable decrease in the number of close-packed units needed to reach criticality. These results call into question the general applicability of current regulations for fissile material transport, which under the modeled circumstances may not be sufficient in preventing a critical system. However, a conservative approach was taken in all assumptions and such idealized configurations would most likely not be achieved in more realistic loadings. Additional modeling should be conducted to verify these findings to ensure the transportation requirements are appropriately conservative.

Hydrodynamics of a Centrifugal Contactor. MEECKRAL WILLIAMS (*Prairie View A&M University, Prairie View, TX*); COSTAS TSOURIS (*Oak Ridge National Laboratory, Oak Ridge, TN*). Countries producing nuclear energy have an interest in nuclear fuel reprocessing, a chemical procedure that extracts fissile materials such as uranium-233, uranium-235, and plutonium-239 from fission products and other materials in the spent nuclear reactor fuels. The goal is to recycle materials that are useful for further nuclear energy production. Centrifugal contactors are used in many plants for the reprocessing of fissile materials. By the use of centrifugal force, the contactor has the advantages of intensive mixing, rapid phase separation, and chemical separation by liquid-liquid extraction in a single unit operation. Two immiscible fluids of different densities, usually an aqueous and an organic fluid, are fed into the contactor to obtain two-phase mixing and extraction. The objective of this work is to determine flow patterns and dispersion properties, such as drop size distributions, in a four-inch diameter centrifugal contactor. The two fluids used here are water and dodecane at flow rate ratios ranging between 1:5 and 5:1. The total flow rate is on the order of 600 mL/min, and the agitation speed is up to 3600 rotations per minute. Once the dispersion is formed, a sample is taken into a light scattering cell where cetyl trimethyl ammonium bromide (CTAB) solution is initially located. The CTAB is a surfactant that stabilizes the droplets to prevent coalescence. Results of particle size measurements obtained by the LS130 light scattering instrument from Coulter have shown that only small droplets can be measured by this method because large drops escape fast to the top of the cell due to buoyancy, even though the sample in the cell is stirred. Video photography using a camera that operates at fast shutter speed and frame recording was employed to visually observe the dispersion in the contactor through an optically transparent wall. Video images reveal details of the drop size, air bubble entrainment, and flow dynamics of the mixing zone. Video imaging has the advantage of direct visualization of the droplets; however, the disadvantage is that it is difficult to distinguish bubbles from droplets. It is hypothesized that, because the difference in the refractive index is greater for air and water or dodecane than for water and dodecane, air bubbles appear sharper on the video images. Drop size measurements are obtained from the images through a size calibration procedure. The size of drops ranges between 1 µm and 500 µm.

238U Fission Ion Chamber for Neutron Dosimetry at the 88-Inch Cyclotron. BRENT WILSON (*University of California – Davis, Davis, CA*); PEGGY MCMAHAN (*Lawrence Berkeley National Laboratory, Berkley, CA*). Neutrons are difficult to detect directly due to a neutral charge; however, there are several different ways to measure neutron flux density indirectly. This paper investigates testing a commercial 238U fission ion chamber to measure neutron flux density, as well as conducting efficiency measurements using two sets of three activation foils (27Al, 58Ni, and 59Co) at different locations to sample beam uniformity at the 88-Inch Cyclotron at Lawrence Berkeley National Laboratory. Fast, monoenergetic neutrons in the energy range of 5 to 30 MeV are under development at the facility through deuteron break-up, for radiation effects testing and cross-section measurements for a variety of applications. Through comparisons with absolute fluxes obtained using activation foils, and energy spectra obtained using the time-of-flight method, efficiency for both monoenergetic and white spectrum neutrons can be calculated. Preliminary neutron flux density measurements indicate 1.44×10^7 neutrons per second per cm^2 per steradian were collected by the fission ion chamber for 30 minutes using a 38 MeV deuteron beam with 50 nanoamps of current. Preliminary activation foil data results indicate the center activation foils received roughly 20% more beam than the side foils, separated by a distance of 1.2 cm.

Physics

Establishing Atmospheric Background Ion Levels for the Stand-Off Detection of Ion Sources. MARC PENALVER AGUILA (*St. Olaf College, Northfield, MN*); CHARLES GENTILE (*Princeton Plasma Physics Laboratory, Princeton, NJ*). Airborne ion counts can be used to estimate the source and intensity of combustive and electrostatic activity. To determine the minimum threshold for stand-off detection of ion sources, it is necessary to establish the background levels of ions in the lower atmosphere. Source detection depends on the ability to distinguish between regular background variations and exceptional activity. Natural occurrences such as the diurnal cycle, clouds passing overhead, or changing weather conditions all may contribute to increased ion formation. Gerdien condensers, which draw a constant stream of air through an electric field, were used for sampling atmospheric ions. All samples were taken through the exhaust of a

fume hood. Due to a possible thermal response from the operational amplifiers used to magnify the signal, the electronics were calibrated for temperature. An analysis of frequency of ion level variation was performed. Abnormal weather phenomena were noted and correlated to ion levels. Finally ion sources were placed in the hood to determine the sensitivity of the gerdiens. The electronics were found to have a minimal thermal response within the range of temperatures observed during the experiments. No multiplier or offset was needed to normalize the data. Fourier analysis revealed that the diurnal cycle was the only regular period linked to a variation in ion levels. A significant change in ion levels was associated with a thunderstorm. Moreover, the gerdiens were found to be highly sensitive to ions drawn through a fume hood. Nearby ion sources could easily be detected by the gerdiens, despite regular temperature and diurnal variations. The range of detection of known activity merits further investigation, as does the discrimination of sources by ion polarity. Possible applications of ion sensors include off-site and stand off detection of motor vehicles, abnormal laboratory conditions, and other ionizing sources.

Monte-Carlo Based Simulation of Double-Image Granvitational Lensing by Cosmic Strings ERIC ALBIN (*California State Polytechnic University, San Luis Obispo, CA*); GEORGE SMOOT (*Lawrence Berkeley National Laboratory, Berkley, CA*). Cosmic Strings have yet to be observed, but they are still experimentally sought after. The simulation of a Cosmic String lensing event signal is invaluable for testing detection criteria. Light sources from I-band survey flexible image transport system (FITS) images taken by the Advanced Camera for Surveys (ACS) aboard the Hubble Space Telescope (HST) are identified using the open-source astronomical software Source Extractor v2.2.2. All identified sources are then pseudo-randomly assigned redshift based on a parameterization of the measured redshift distribution as a function of source absolute magnitudes. Each identified source is also isolated from the FITS image file so that a particular Cosmic Strings can be simulated by re-integrating selected isolated sources back into the FITS image assuming a λCDM cosmology with Ωm = 0.3. Simulations are limited to perfectly straight Cosmic Strings which span across the entire FITS image used as well as to strongly-lensed events. Simulated Cosmic String lensing event signals are then applied towards calculating detection efficiencies in v1.0 data from the Great Observatories Origins Deep Survey (GOODS).

Concept to Employ Magnetohydrodynamic Conversion in a Two Gigawatt Inertial Fusion Energy Direct Drive Power ReactorMagnetohydrodynamic Conversion in a Two Gigawatt Inertial Fusion Energy Direct Drive Power Reactor. BRETT ANDERSON (*Southern University, Baton Rouge, LA*); D. PETER SIDDONS (*Brookhaven National Laboratory, Upton, NY*). A two gigawatt Inertial Fusion Energy (IFE) direct drive power reactor, currently in conceptual design, injects deuterium-tritium targets into the reactor chamber at the rate of five hertz and uniformly illuminates each target with ultraviolet laser light, resulting in detonation. The conceptual design of this IFE reactor may provide an opportunity to directly harness the power in the post detonation ion fields. This can be accomplished by utilizing a magnetic cusp field to guide the ions into collectors located in the equatorial and polar regions of the reactor. The shaped ion fields resulting from this magnetic intervention configuration pose a distinct challenge, as their intensity may have the potential to damage certain areas within the ion collectors. One method of addressing this challenge is to employ magnetohydrodynamic (MHD) conversion to transform the internal energy of the ion fields directly into electrical energy, a process that would also attenuate the strength of the fields. In order to analyze the potential of MHD conversion in IFE, previous work on MHD conversion in other applications is examined in the context of this proposed IFE reactor configuration. Other conversion techniques are also investigated, including Compact Fusion Advanced Rankine II (CFARII) MHD conversion, radio frequency (RF) particle deceleration, and direct conversion. Analysis reveals that MHD conversion may be a promising solution depending on the intensity of the ion fields. However, a number of engineering and operational concerns need to be addressed; for example, the materials need to be able to withstand extreme conditions. In addition, some elements of the other methods for energy conversion could be incorporated into an MHD conversion design. The next logical step in the development of this aspect of the IFE reactor would be a scaled experimental test facility where material tests and methods can be advanced. This work is in support of efforts to develop an efficient, economical, and clean fusion energy source.

3 Inch Double GEM for X-Ray Fluorescent Detector. DERREK ANDERSON, JANEL GRAY (*Southern University, Baton Rouge, LA*); D. PETER SIDDONS (*Brookhaven National Laboratory, Upton, NY*). Two

3-inch diameter gas electron multipliers (GEM) are used to build a high gain X-Ray gas detector for Extended X-Ray Absorption Fine Structures (EXAFS). The X-Ray ionizes the gas and the electrons are drifted towards the first GEM. The strong electric field in the GEM multiplies electrons by impact ionization. The second stage GEM further amplifies the electrons by the same process. The advantage of the double GEM is to provide two stages of electron amplification. This improves the signal magnitude without the introduction of noise. The charge collected from the second GEM is connected to a Keithley Amplifier. We have tested the Double GEM to detect dilute amounts of Mn and Fe in an arbitrary tree leaf.

HELIOS Detector Simulations with Geant4. NATANIA ANTLER (*Massachusetts Institute of Technology, Cambridge, MA*); BIRGER BACK (*Argonne National Laboratory, Argonne, IL*). This is a crucial period in the construction of the Helical Orbit Spectrometer (HELIOS) which is scheduled to be completed by the winter of 2008. HELIOS will be used to study particles emerging from collisions with a radioactive beam from the Argonne Tandem Linear Accelerator (ATLAS) at Argonne National Laboratory. It is important to determine the tolerance of the spectrometer before it turns on in 2008, in order to assess the feasibility of proposed experiments. The inverse kinematic reactions in the magnetic field, that make this detector unique, were modeled using Geant4, a simulation toolkit developed at the European Organization for Nuclear Research (CERN). Spectrometer tolerance was modeled for various detector geometries and incident particles. Additional simulations model the specific kinematics of reactions to be studied in the detector, such as the benchmark reaction d(132Sn,p)133Sn. These investigations helped to qualify measurement uncertainties associated with different aspects of the spectrometer design. Further simulations of reactions to be studied by HELIOS, as well as the addition of a realistic field map into the Geant4 model will be the next steps for this project.

Simulation of a Laser Plasma Accelerator Operating in the Bubble Regime and Using Laser Assisted Injection. JOHN BAILEY, III (*University of Alabama in Huntsville, Huntsville, AL*) YUELIN LI (*Argonne National Laboratory, Argonne, IL*). Laser Wake Field Acceleration (LWFA) is an area that shows great promise in its potential to drastically reduce the size and cost of particle accelerators. Recent experimental work has demonstrated a method of controlling injection, and thereby final beam energies. In this research the 3D particle-in-cell (PIC) code VORPAL is used to conduct LWFA simulations. The first set of simulations endeavors to provide a self-consistent computational explanation of the recent controlled injection experiment. Based on this, the second set looks at the effects of the injection pulse duration on the beam's properties. It is found, as expected, that a longer injection pulse causes more particles to be trapped in the bubble; thus causing a more severe beam loading effect (effects which reduce the highest beam energy achievable). Unexpectedly, however, the effect is also found to significantly reduce the energy spread.

Fast Track Finding in the International Linear Collider's Proposed SiD Detector. DAVID BAKER (*Carnegie Mellon University, Pittsburgh, PA*); NORMAN GRAF (*Stanford Linear Accelerator Center, Stanford, CA*). A fast track finder is presented which, unlike its more efficient, more computationally costly $O(n^3)$ time counterparts, tracks particles in $O(n)$ time (for n being the number of hits). Developed as a tool for processing data from the International Linear Collider's (ILC) proposed SiD detector, development of this fast track finder began with that proposed by Pablo Yepes in 1996 [1] and adjusted to accommodate the changes in geometry of the SiD detector. First, space within the detector is voxellated, with hits assigned to voxels according to their γ, 0, and η coordinates. A hit on the outermost layer is selected, and a "sample space" is built from the hits in the selected hit's surrounding voxels. The hit in the sample space with the smallest distance to the first is then selected, and the sample space recalculated for this hit. This process continues until the list of hits becomes large enough, at which point the helical circle in the x, y plane is conformally mapped to a line in the x', y' plane, and hits are chosen from the sample spaces of the previous fit by selecting the hits which fit a line to the previously selected points with the smallest x^2. Track finding terminates when the innermost layer has been reached or no hit in the sample space fits those previously selected to an acceptable x^2. Again, a hit on the outermost layer is selected and the process repeats until no assignable hits remain. The algorithm proved to be very efficient on artificial diagnostic events, such as one hundred muons scattered at momenta of 1 GeV/c to 10 GeV/c. Unfortunately, when tracking simulated events corresponding to actual physics, the track finder's efficiency decreased drastically (mostly due to signal noise), though future data cleaning programs could noticeably increase its efficiency on these events.

Quark and Antiquark Distributions in the Proton. *Rona Banai* (*Cornell University, Ithaca, NY*)*; Paul E. Reimer* (*Argonne National Laboratory, Argonne, IL*). Quark distributions in the proton cannot be determine theoretically, but require experimental measurements. Data are lacking for the large-x region, where one quark carries most of the momentum of the proton. Experiment 866 completed at Fermilab measured data for the Drell-Yan cross section for pp and pd interactions, which is sensitive to the quark distributions of the interacting hadrons. By examining the data from 175,000 dimuon events in the range (4.2 = M = 16.85 GeV and -0.05 = xF = 0.8), we are able to examine the light quark and anti-quark distributions in the nucleon. In the experiment both hydrogen and deuterium targets were used in order to solve for the absolute quark distributions in the proton and the neutron. In this project we verified the cross section determined as a function of (xF, M) and determined the functional dependence on (x1, x2). The Monte Carlo data show a general agreement with the next-to-leading order experimental data demonstrating an understanding of the theory behind the experiment. Through a comparison of the experimental data to the Monte Carlo results and next-to-leading order cross section calculations, a better determination of the parton distributions will be achieved.

Measuring Strain Using X-Ray Diffraction. *James Belasco* (*Villanova University, Villanova, PA*); *Apurva Mehta* (*Stanford Linear Accelerator Center, Stanford, CA*). Determining the strain in a material has often been a crucial component in determining the mechanical behavior and integrity of a structural component. While continuum mechanics provides a foundation for dealing with strain on the bulk scale, how a material responds to strain at the very local level-the understanding of which is fundamental to the development of a cohesive framework for the behavior of strained material-is still not well understood. One of the critical components in determination of the behavior of materials under strain at a local scale is an understanding how global average deformation, as a response to an externally applied load, gets distributed locally. This is critical and very poorly understood for a polycrystalline materials-the material of choice for a large variety of structural components. We studied this problem for BCC iron using X-ray diffraction. By using a nanocrystalline iron sample and taking X-ray diffraction patterns at different load levels and at different rotation angles, a complete 2nd rank strain tensor was determined for the three sets of crystallites with three distinct crystallographic orientations. The determination of the strain tensors subsequently allowed the calculation of the elastic modulus along each crystallographic plane. When compared to measured values from single crystal for the corresponding crystal orientations, the data from our polycrystalline sample demonstrated a higher degree of correlation to the single crystal data than expected. The crystallographic planes demonstrated a high degree of anisotropy. Therefore, to maintain displacement continuity, there must be a secondary mode of strain accommodation in a regime that is conventionally thought to be purely elastic.

*Analysis of the Directivity of a Defective R-F (Radio-Frequency) Coupler Using a Network Analyzer. *Zephra Bell* (*Southern University and A&M College, Baton Rouge, LA*)*; Terrence Reese* (*Fermi National Accelerator Laboratory, Batavia, IL*). The R-F couplers that we tested were used in a project called HINS at Fermi National Accelerator Laboratory (Fermilab). HINS stands for High Intensity Neutrino Sources. These couplers are arranged in a transmission line at Fermilab. The couplers are crucial for the transfer of power in an R-F cavity. However, one of the couplers in the transmission line seemed to be defective. The high power signal down the "line" in the reflected power was too low from that in the forward port. It was measured to be only 13 dB when it should have been 60 dB. Therefore, initially, three different methods were used to test the defective coupler: 1) The connector cables attenuation was measured. Connector cables are used to attach the port of the coupler to other pieces of the R-F cavity. The cable attenuation and the reflection load were good. This meant that the coupler did not have power flowing through faulty cables. 2) Low power in the switch was generated. This still reflected a low signal of 13 dB. 3) Finally, the coupler was physically removed and tested directly. It still reflected a low signal of 13 dB. Hence, the coupler was brought to our team to see if we could determine the defects of the coupler through rigorous testing of the ports and internal modifications.

Analysis of X-Ray Spectra Emitted from the VENUS ECR Ion Source. *Janilee Benitez* (*California State University – East Bay, Hayward, CA*)*; Daniela Leitner* (*Lawrence Berkeley National Laboratory, Berkley, CA*). The Versatile Electron Cyclotron resonance ion source for Nuclear Science, VENUS, produces its record breaking ion beam currents and high charge state distributions because it uses strong magnetic fields to confine the plasma and high microwave frequencies to heat it. The magnetic fields are produced using liquid helium cooled superconducting coils. While in operation, VENUS produces significant quantities of bremsstrahlung, in the form of X-rays, through two processes: 1) electron-ion collisions within the plasma, and 2) electrons are lost from the plasma and collide with the plasma chamber wall and release energy. The energy lost by electron collisions with the chamber wall presents a significant heat load on the cryostat needed to keep the coils superconducting. In order for VENUS to reach its maximum operating potential at 10kW of 28GHz microwave heating frequency, the heat load posed by the emitted bremsstrahlung must be understood. A code has been written, using the Python programming language, to analyze the recorded bremsstrahlung spectra. The code outputs a spectral temperature and total integrated count number corresponding to each spectra. Bremsstrahlung spectra are analyzed and compared by varying two parameters: 1) the heating frequency, 18 and 28GHz, and 2) the magnetic field gradient, 44% and 70%, at the electron resonant zone.

Effects of Elemental Impurities on TiNiSn Solution Growths. *Thomas Brenner* (*Carleton College, Northfield, MN*); *Paul Canfield* (*Ames Laboratory, Ames, IA*). The intermetallic compound TiNiSn has been of interest to researchers because of its semiconducting and thermoelectric properties. We attempted to determine the effects of constituent element purity on the growth and electrical properties of TiNiSn single crystals. We grew TiNiSn single crystals from a Sn flux, each time varying the purity of our constituent elements. In order to test the hypothesis that chlorine impurities affect the crystal formation and electrical properties of TiNiSn, we added nickel chloride powder to the starting elements for several growths. Qualitative differences in crystal growth were observed, and secondary compounds were identified by X-ray diffraction whenever possible. Resistivity measurements were made between 2 and 375 K on TiNiSn crystals from each growth, so that the effect of elemental purity on resistivity could be determined. Using the resistivity data, we calculated the semiconducting gap for each sample. Lower purity Ti led to variation in growth products, but changing Sn and Ni purity did not produce variation. The addition of nickel chloride produced several changes in the growth. For all samples room temperature semiconducting gaps were between 110 and 180 meV. No trends were observed in either gap energy or resistivity with respect to elemental purity.

Testing an Algorithm to Find Cosmic Strings in the CMB. *Heather Busk* (*Ventura College,Ventura,CA*); *George Smoot* (*Lawrence Berkeley National Laboratory, Berkley, CA*). A number of theories, such as Grand Unified Theories (GUTs) and superstring theories, predict that cosmic strings would have formed shortly after the Big Bang. They may even continue to exist today. Since most of the predictions of these theories could only be observed at much higher energies than are produced on Earth, strings provide one of the few ways to test the theories. Eunwha Jeong and George Smoot developed a technique to search the Cosmic Microwave Background (CMB) for strings, by looking for a temperature jump (step) across a moving string, via the Kaiser-Stebbins effect. I simulated a square patch of the CMB containing a temperature step, using normally distributed random numbers. I then implemented the algorithm to calculate the properties of the patch. I tested how well the algorithm returned the correct values for a range of input values for the background temperature (T0), temperature step (σ), standard deviation of random noise (sG), and patch size (n). The preliminary results suggest that there is a small decrease in the accuracy for increasing background temperatures. This is most noticeable for the calculated T0, fraction of blueshifted pixels, and sG. Increasing n significantly improves the results, while accuracy decays with a larger sG. The results had large errors for low Δ, but they attenuated with increasing T0.

Characterizing the Noise Performance of the KPiX ASIC Readout Chip. *Jerome Carman* (*Cabrillo College, Aptos, CA*); *Timothy Knight Nelson* (*Stanford Linear Accelerator Center, Stanford, CA*). KPiX is a prototype front-end readout chip designed for the Silicon Detector Design Concept for the International Linear Collider (ILC). It is targeted at readout of the outer tracker and the silicon-tungsten calorimeter and is under consideration for the hadronic calorimeter and muon systems. This chip takes advantage of the ILC timing structure by implementing pulsed-power operation to reduce power and cooling requirements and buffered readout to minimize material. Successful implementation of this chip requires optimal noise performance, of which there are two measures. The first is the noise on the output signal, previously measured at 1500e-, which is much larger than the anticipated 500e-. The other is the noise on the trigger logic branch, which determines where thresholds must be set in order to eliminate noise hits, thus

defining the smallest signals to which the chip can be sensitive. A test procedure has been developed to measure the noise in the trigger branch by scanning across the pedestal in trigger threshold and taking self-triggered data to measure the accept rate at each threshold. This technique measures the integral of the pedestal shape. Shifts in the pedestal mean from injection of known calibration charges are used to normalize the distribution in units of charge. The shape of the pedestal is fit well by a Gaussian, the width of which is determined to be 2480e-, far in excess of the expected noise. The variation of the noise as a function of several key parameters was studied, but no significant source has been clearly isolated. However, several problems have been identified that are being addressed or are under further investigation. Meanwhile, the techniques developed here will be critical in ultimately verifying the performance goals of the KPiX chip.

Computational Development of H-Ion Sources for the Spallation Neutron Source. Justin Carmichael (*Worcester Polytechnic Institute, Worcester, MA*); Robert F. Welton (*Oak Ridge National Laboratory, Oak Ridge, TN*). The U.S. Spallation Neutron Source (SNS) requires a high power H- ion source in order to achieve the desired neutron flux. Over the next several years, the SNS will require substantially higher average H- beam current than can be produced from conventional H- ion sources including our baseline source. H- currents of 70–100 mA with an RMS emittance of 0.20–0.35 π mm mrad and a ~7% duty-factor will be needed for the SNS power upgrade project. Presently, external antenna sources, based on Al_2O_3 plasma chambers, have been developed which have been shown to produce beam currents of 25–35 mA with a duty-factor of 2–3%. Computer simulations employing the Finite Element Method (FEM) with coupled fluid dynamic, heat transfer, and thermal stress and deformation capabilities have been performed to investigate the design of the plasma chambers operating at higher duty-factors. These simulations show that a plasma chamber made from AlN can be designed to meet the full duty-factor requirement. In order to meet the beam current requirements, efforts are being made to (i) increase source plasma density by using magnetic confinement and (ii) improve the efficiency of ion extraction from the plasma. Towards these ends simulations are being performed using LORENTZ for magnetic field modeling and COSMOS for thermal analysis of the electron dumping electrode. An AlN plasma chamber, a solenoid confinement magnet and an electron dumping electrode have been designed. It is anticipated that substantially greater beam currents can be achieved with these improvements to the ion source.

Analysis of Consistency in Channel Pedestal Readings for the Track Imaging Cerenkov Experiment (TrICE) Camera as a Function of Temperature and Time. Ana Chachian (*Florida International University, Miami, FL*); Karen Byrum (*Argonne National Laboratory, Argonne, IL*). Track Imaging Cerenkov Experiment (TrICE) is a telescope prototype on site at Argonne National Laboratory. Its camera is composed of an array of 16 high definition multi-anode photomultiplier tubes (MAPMTs) that give an angular pixel spacing (0.08 deg) better than most existing Cerenkov shower detecting telescopes (~0.15 deg). The TrICE telescope is a testbed for the development of a next-generation gamma-ray telescope. TrICE has been observing cosmic rays since earlier this year. The stability of the TrICE camera performance was analyzed through the study of background noise pedestals recorded by its channels to determine if these are constant under the background sky. The method involved generating histograms that compared the pedestal signals for each channel over different days, times, and temperatures, using a C++ interfaced with Root macro. The results of this analysis concluded that the pedestal means were constant over a variety of conditions and are therefore reliable to reproduce accurate Cerenkov signals. The result of this analysis is the first step in understanding the data taken by the camera. Further steps to this end include research of each channel's gain as a function of these pedestal fluctuations.

Calculation of Divertor Thermal Response as a Function of Material Composition in the National Spherical Torus Experiment. Michael Chaffin (*Reed College, Portland, OR*); Rajesh Maingi (*Princeton Plasma Physics Laboratory, Princeton, NJ*). Present tokamak designs use a magnetic divertor to deposit heat from the edge plasma onto Plasma Facing Components (PFCs) designed to remove the heat. Studying how this heat is distributed under various discharge conditions gives insight into how heat deposition can be optimized, and how different materials respond to plasma heating. In the National Spherical Torus eXperiment (NSTX), infrared cameras are used to measure divertor surface temperature, from which heat flux is computed using a one dimensional (1D) semi-infinite slab model with constant thermal conductivity. Here, a 1D simulation of the PFCs incorporating

material-dependent thermal properties is used to compute heat flux profiles resolved across time and tile thickness. The PFC response to a given heat flux is also computed, and comparisons of resulting temperature profiles are made for a variety of materials including ATJ graphite (a low thermal expansion coefficient polycrystalline graphite presently in the NSTX divertor), pyrolytic graphite, molybdenum, and tungsten. The relatively high conductivity of pyrolytic graphite allows for greater thermal penetration of the PFCs, resulting in much lower temperatures at the PFC boundary. Using pyrolytic graphite instead of ATJ graphite in future fusion devices would mitigate the effects of higher flux deposition onto the PFCs. Further study is needed to determine the appropriateness of using high conductivity materials in particular reactor designs.

Extensions to DivGeo, a Graphical Tool for Editing 2D Edge Plasma Computational Meshes Extensions to DivGeo, a Graphical Tool for Editing 2D Edge Plasma Quasi-Orthogonal Computational Meshes. Alan Chin (*Princeton University, Princeton, NJ*); Daren P. Stotler (*Princeton Plasma Physics Laboratory, Princeton, NJ*). Transport of plasma and neutral particles across magnetic flux surfaces in tokamak fusion experiments is a highly complex dynamical system of much practical interest in designing efficient fusion reactors. Codes that have been written to simulate the behavior of such systems include B2 and Eirene, used to model plasma and neutral transport behavior, respectively, in the divertors of ITER, and DEGAS 2, used to model neutral transport during Gas Puff Imaging experiments on the National Spherical Torus eXperiment (NSTX), both of which approximate the plasma region by 2D computational meshes that are designed to be quasi-orthogonal to the poloidal magnetic flux surfaces inside the tokamak. Because the distribution of mesh cells and the topology of the mesh are specific to each experiment, a customized mesh must be created for each study undertaken. DivGeo (DG) is a graphical user interface used, in combination with mesh-generating codes such as Carre and Sonnet, to create and modify such meshes. Using the C programming language and GNU utilities in a Red Hat Linux environment, the source code of DG was modified and subjected to testing by the author and users of DG at Princeton Plasma Physics Laboratory (PPPL) and ITER. After the modifications, DG was now able to be compiled using the freely available Open Motif 2.x graphics library, which allowed it to run reliably on the Linux machines at PPPL. In addition, several new features were added to DG, including an auto-save feature, the ability to recognize concave mesh cells and the segment of the reactor determining the outer bound of the mesh, and the ability to view the mesh at arbitrary angles and aspect ratios. Together, these improvements allow precisely tailored and general meshes to be generated more quickly and easily, accelerating the progress of computational studies on tokamak plasmas.

Characterizing Surface Layers in Nitinol Using X-ray Photoelectron Spectroscopy. Rebecca Christopfel (*Western Washington University, Bellingahm, WA*); Apurva Mehta (*Stanford Linear Accelerator Center, Stanford, CA*). Nitinol is a shape memory alloy whose properties allow for large reversible deformations and a return to its original geometry. This nickel-titanium alloy has become a material used widely in the biomedical field as a stent to open up collapsed arteries. Both ambient and biological conditions cause surface oxidation in these devices which in turn changes its biocompatibility. Depending on the type and abundance of the chemical species on or near the surface, highly toxic metal ions can leak into the body causing cell damage or even cell death. Thus, biocompatibility of such devices is crucial. By using highly surface sensitive X-ray photoelectron spectroscopy to probe the surface of these structures, it is possible to decipher both layer composition and layer thickness. Two different samples, both of which were mechanically polished with one then exposed to a phosphate buffered saline solution to mimic the chemical properties of blood, were investigated. It was found that the latter sample had a slightly thicker oxide layer and more significantly a phosphate layer very near the surface suggesting toxic metal components are well contained within the sample. These are considerable indications of a biocompatible device.

*Study of KS Production with the BaBar Experiment. Thomas Colvin (*The Ohio State University, Columbus, OH*); Jochen Dingfelder (*Stanford Linear Accelerator Center, Stanford, CA 94025*). We study the inclusive production of short-lived neutral kaons KS with the BaBar experiment at the Stanford Linear Accelerator Center. The study is based on a sample of 383 million B-Bbar pairs produced in e+e- collisions at the Y(4S) resonance, in which one B meson has been fully reconstructed. We select a clean sample of KS mesons and compare kinematic spectra for data and simulation. We find that the simulation overestimates the total production rate of KSand we see differences in

the shape of the KS momentum spectra. We derive correction factors for different momentum intervals to bring the simulation into better agreement with the observed data.

Construction and Commissioning of a Micro-Mott Polarimeter for Photocathode Research and Development. *April Cook* (*Monmouth College, Monmouth, IL*); *Marcy Stutzman* (*Thomas Jefferson National Accelerator Facility, Newport News, VA*). Thomas Jefferson National Accelerator Facility uses polarized electrons to further the understanding of the atomic nucleus. The polarized source produces electrons by directing laser light onto a specially prepared gallium arsenide (GaAs) photocathode. During the course of this project, an off-beamline micro-Mott polarimeter has been built and commissioned within the Source Lab for photocathode research and development. A polarimeter measures the polarization, or spin direction, of electrons. The micro-Mott runs at 30 keV and can be used directly in the Source Lab, off of the main accelerator beamline. Construction of the Mott system began with a polarized source, which consists of a vacuum chamber complete with a cesiator and nitrogen triflouride (NF_3) to activate the photocathode, residual gas analyzer (RGA), ultra-high vacuum pumps, an electrostatic deflector to bend the electron beam 90°, and electrostatic lenses. The polarimeter is housed in an adjacent vacuum chamber. The circularly polarized laser light enters the polarized source, hits the GaAs photocathode, and liberates polarized electrons. The original longitudinally-polarized electrons are transformed into transversely-polarized electrons by the electrostatic bend. They are then directed onto a gold target inside the Mott and scattered for data analysis. The polarized source has been commissioned, achieving photoemission from the activated GaAs crystal, and the electrostatic optics have been tuned to direct the electrons onto the gold target. Nearly ten percent of the electrons from the photocathode reach the target, giving adequate current for polarization measurement. The micro-Mott polarimeter will aid in photocathode research and pre-qualification of material for use in the injector.

*Photo-Excitation of RF Magnetron Sputter Grown SrRuO3 Observed by Electron Crystallography. *Brian Cooper* (*Temple University, Philadelphia, PA*); *Ivan Bozovic, Vladimir Butko* (*Brookhaven National Laboratory, Upton, NY*). Strongly-correlated electron systems such as high temperature superconductivity, colossal magnetoresistance, and heavy fermion systems are still not well understood by solid state physicists. Since the conventional free electron approximation breaks down in these strongly-correlated systems, it is imperative that experimentalists examine all aspects of materials that exhibit these properties. To better understand the effects of photo-excitation on the strongly-correlated electron systems of some perovskite crystals, we are attempting to grow thin films of $SrRuO_3$ (SRO) on substrates of $LaSrAIO_4$ (LSAO) and $SrTiO_3$ (STO) using RF magnetron sputtering. The impetus for growing SRO films arose from data gathered during ultra-fast electron crystallography (UEC) performed on epitaxially grown oxygen doped $La_2CuO_{4+\delta}$ (LCO). Since a charge mismatch exists between the planes of the crystal, a significant electric field exists between the planes of the crystal. During UEC the lattice constants of LCO increased to amounts that would require equivalent thermal energy transfers associated with temperatures around 2500 K. This prompted us to believe that this effect could be a result of the strong electric field present between the planes of LCO. Since SRO is electrically neutral between its planes, but represents a strongly-correlated electron system with a nearly identical crystal structure (perovskite), it is ideal for comparative study. In order to grow SRO, firstly wafers of commercially grown LSAO (or STO) are coated with photo-resist, covered with an etched quartz mask, and undergo lithography. Then using an argon ion (Ar^+) mill, a highly collimated beam of Ar^+ is used to remove layers from the substrate. After troughs approximately 600 Å in depth are cut out of the substrates and the photo-resist washed away with acetone, the substrates are deposited with the SRO. After various modus operandi used to characterize the films of SRO are performed, we will send these samples to the California Institute of Technology to undergo UEC. We expect to see an ameliorated effect (if any at all) in the SRO films, but even if the effect is still prominent, the results will shed further light on the effects of photo-excitation on highly-correlated electron systems of perovskites.

Vibration Analysis of a Cryocooler for CDMS. *Lauren Coutant* (*University of Illinois, Champaign-Urbana, IL*); *Dan Bauer* (*Fermi National Accelerator Laboratory, Batavia, IL*). A new pulse tube cryocooler was obtained by the Cryogenic Dark Matter Search (CDMS) research group with the intent of replacing their Gifford-McMahon cryocooler which is currently installed at their research site in the

Soudan Mine. A study was done on the new cryocooler to determine its vibration spectrum. More analysis needs to be completed to accurately compare the two cryocoolers, but it appears that the new pulse tube system has less intense vibrations. In addition to measuring vibrations, vibration reduction methods were investigated. Installing flexible materials in the cryocooler is the reduction method recommended for the CDMS project.

Simulation of Neutron Backgrounds from the ILC Extraction Line Beam Dump. *Siva Darbha* (*University of Toronto, Toronto, ON*) *Takashi Maruyama* (*Stanford Linear Accelerator Center, Stanford, CA*). The operation of the International Linear Collider (ILC) as a precision measurement machine is dependent upon the quality of the charge-coupled device (CCD) silicon vertex detector. A neutron flux of 1,010 neutrons/cm^2 incident upon the vertex detector will degrade its performance by causing displacement damage in the silicon. One source of a neutron background arises from the dumping of the spent electron and positron beams into the extraction line beam dumps. The Monte Carlo program FLUKA was used to simulate the collision of the electron beam with the dump and to determine the resulting neutron fluence at the interaction point (IP). A collimator and tunnel were added and their effect on the fluence was analyzed. A neutron source was then generated and directed along the extraction line towards a model of the BeamCal, vertex detector, and beampipe to determine the neutron fluence in the silicon layers of the detector. Scattering in the BeamCal and beampipe was studied by manipulating the composition of the BeamCal. The fluence in the first silicon layer for the current tungsten BeamCal geometry was corrected according to a 1 MeV equivalent silicon displacement damage to obtain a comparable value for the damage done to the CCD vertex detector. The IP fluence was determined to be $3.65*10^{10}$ +/- $2.34*10^{10}$ neutrons/cm^2/year when the tunnel and collimator were in place, with no appreciable increase in statistics when the tunnel was removed. The BeamCal was discovered to act as a collimator by significantly impeding the flow of neutrons towards the detector. The majority of damage done to the first layer of the detector was found to come from neutrons with a direct line of sight from the quadrupole, with only a small fraction scattering off of the beampipe and into the detector. The 1 MeV equivalent neutron fluence was determined to be $1.85*10^9$ neutrons/cm^2/year when the positron beam was considered, or $9.27*10^8$ neutrons/cm^2/year by one beam alone, which contributes 18.5% of the threshold value in one year. Future work will improve the detector model by adding the endcap sections of the silicon detector, and will study in detail the neutron scattering off of the tunnel walls. Other sources of neutron backgrounds will also be analyzed, including electron-positron pairs, Beamstrahlung photons, and radiative Bhabha scattering, in order to obtain a complete picture of the overall neutron damage done to the vertex detector.

Analysis of the CDF II Data in Search of the Higgs Boson Decaying to Two Photons. *Callie Demay* (*University of Illinois, Urbana-Champaign, IL*); *Craig Group* (*Fermi National Accelerator Laboratory, Batavia, IL*). Although the Standard Model is accurate, the one fundamental aspect needed to complete the model, a massive particle called the Higgs Boson, has not yet been discovered. In this investigation, we searched for a non-Standard Model, fermiophobic Higgs, which would decay to two photons. This decay mode is predicted to have a very small branching fraction according to the Standard Model; however, some models predict a higher branching fraction. We initially optimized selection criteria in order to become as sensitive as possible to the signal region. Using the 2fb-1 of data provided by Fermilab's Tevatron and collected by the Collider Detector at Fermilab (CDF) experiment, we were unable to see a signal for the Higgs; therefore, the focus of our research shifted to placing a limit on the cross section for the Higgs in the fermiophobic model. We were able to place a lower limit of 99 GeV on the mass of the fermiophobic Higgs. This limit is currently the best in the world for a hadron collider. The previous limits at Fermilab included one by CDF at 82 GeV, and one by DZero at about 90 GeV. However, the world's best limit of 109.7 GeV was placed by the Large Electron-Positron Collider (LEP) in Switzerland. Although we were not able to find a Higgs signal, the techniques used to improve sensitivity to photon events will be useful in the next generation of collider experiments, which will be more sensitive to the small branching fraction of diphoton events.

Measurement of Charge Diffusion in a Thick, High Resistivity Charge-Coupled Device. *Anna Derbakova* (*University of North Carolina at Chapel Hill, Chapel Hill, NC*)*; Peter Takacs* (*Brookhaven National Laboratory, Upton, NY*). When a diffraction-limited point source of light is focused onto a charge-coupled device (CCD), the recorded image becomes blurred due to a number of effects, one of which is the lateral diffusion of photogenerated charge within the

semiconductor material. The quality of the signal is characterized by the point spread function (PSF) which measures the amount of blurring that is present. The PSF of the present system is a convolution of a known contribution of the pixel array geometry as well as the charge diffusion within the silicon wafer, which can be controlled by varying the applied electric field. The purpose of this experiment was to use two different methods to measure the charge diffusion coefficient of a high resolution prototype CCD which will later form the basis of the CCD camera in the Large Synoptic Survey Telescope (LSST). In the first method, a light spot from a diode laser coupled to a 4 μm optical fiber was projected onto the surface of a CCD. The spot size was characterized via a knife-edge scan technique. An autofocus mechanism was developed to keep the micron-size spot focused on the surface, and images were acquired as the point source was stepped across the CCD in sub-pixel increments. By summing the intensity in a fixed pixel window as the light spot is scanned across the edge of the window, the charge diffusion width can be obtained ("virtual knife-edge" technique). Subtracting the known input light-spot size in quadrature from the width of the fit to the virtual knife edge scans results in an estimate of the diffusion width of 5.95 μm when the electric field in the sensor is 5 kV/cm. In the second method, a Michelson interferometer with a motorized tilt adjustment mirror mount was constructed and used to project a sinusoidal interference pattern with a variable spatial frequency onto the surface of the detector. The intensity readout of the detector was fit with a sinusoidal curve to extract the amplitude and calculate the modulation of the image, Mi. This process was shown to work and in the future will be repeated for a range of spatial frequencies to characterize Mi(v) and obtain the MTF. The charge diffusion coefficient will then be obtained by deconvolving the known Sinc function contribution of the CCD pixel array and the Gaussian diffusion function from the MTF. The results from each method will serve as a cross check in determining the actual intrinsic sensor performance.

Definition of a Twelve-Point Polygonal SAA Boundary for the GLAST Mission.

Sabra Djomehri (*University of California – Santa Cruz, Santa Cruz, CA*); *Markus Ackermann* (*Stanford Linear Accelerator Center, Stanford, CA*). The Gamma-Ray Large Area Space Telescope (GLAST), set to launch in early 2008, detects gamma rays within a huge energy range of 100 MeV–300 GeV. Background cosmic radiation interferes with such detection resulting in confusion over distinguishing cosmic from gamma rays encountered. This quandary is resolved by encasing GLAST's Large Area Telescope (LAT) with an Anti-Coincidence Detector (ACD), a device which identifies and vetoes charged particles. The ACD accomplishes this through plastic scintillator tiles; when cosmic rays strike, photons produced induce currents in Photomulitplier Tubes (PMTs) attached to these tiles. However, as GLAST orbits Earth at altitudes ~550km and latitudes between -26° and 26°, it will confront the South Atlantic Anomaly (SAA), a region of high particle flux caused by trapped radiation in the geomagnetic field. Since the SAA flux would degrade the sensitivity of the ACD's PMTs over time, a determined boundary enclosing this region need be attained, signaling when to lower the voltage on the PMTs as a protective measure. The operational constraints on such a boundary require a convex SAA polygon with twelve edges, whose area is minimal ensuring GLAST has maximum observation time. The AP8 and PSB97 models describing the behavior of trapped radiation were used in analyzing the SAA and defining a convex SAA boundary of twelve sides. The smallest possible boundary was found to cover 14.58% of GLAST's observation time. Further analysis of defining a boundary safety margin to account for inaccuracies in the models reveals if the total SAA hull area is increased by ~20%, the loss of total observational area is < 5%. These twelve coordinates defining the SAA flux region are ready for implementation by the GLAST satellite.

Flux Jumps in Nb$_3$Sn Superconducting Accelerator Magnets and Implications for a Current Dependent Quench Protection System.

Conor Donnelly (*University of Pennsylvania, Philadelphia, PA*); *Said Rahimzadeh-Kalaleh* (*Embry-Riddle Aeronautical University, Daytona Beach, FL*); *Giorgio Ambrosio, Michael Tartaglia* (*Fermi National Accelerator Laboratory, Batavia, IL*). With the upcoming inauguration of the Large Hadron Collider (LHC), the practical limit in the performance of Niobium Titanium (NbTi) superconductors will be reached based on the properties of the material. Fermi National Accelerator Laboratory has been developing a new generation of superconducting accelerator magnets based on Niobium Tin (Nb$_3$Sn) intended for a luminosity upgrade to the LHC. The performance of these magnets has been found to be below the expected level due to thermomagnetic instabilities present in the superconductor. In order to develop better magnets for future machines, it is essential to fully understand these instabilities, which are characterized by

fast voltage excursions or spikes. For this purpose, a new software application was developed to automate the analysis of voltage spikes in superconducting Nb$_3$Sn magnets. Using the new software, the current dependence of spike amplitudes was determined, which demonstrated the possibility to use a current dependent quench protection threshold. Such a threshold could avoid premature system trips at low current due to non-quenching voltage spikes. This work presents quantitative and analytical studies on voltage spikes arising from flux jumps in superconducting Nb$_3$Sn magnets as well as the features of the software developed for the analysis.

Testing a Novel Laser Polarimeter Design.

Joan Dreiling (*Fort Hays State University, Hays, KS*); *Marcy Stutzman* (*Thomas Jefferson National Accelerator Facility, Newport News, VA*). Polarized electron beams are used at Thomas Jefferson National Accelerator Facility to study the properties of nuclei. When circularly polarized light of the appropriate wavelength illuminates a gallium arsenide cathode, polarized electrons are emitted. Right-hand circularly polarized light excites electrons of one spin polarization state, and left-hand circularly polarized light excites the opposite spin polarization state. The polarization of the electrons is typically measured with complex polarimeters, either in the lab or in the accelerator and experimental halls. A novel polarimetry technique was explored to determine if a simple optical setup could be used to measure polarization of the electron beam from a gallium arsenide cathode. A pump and probe system similar to those in atomic absorption spectroscopy was employed. A circularly polarized pump laser was used in an attempt to deplete one polarization state of the crystal, while the probe laser was varied between the same and opposite circular polarizations. If the pump laser depleted one polarization state, the probe laser would cause additional photocurrent only when the two lasers had opposite polarizations. It was found that the photocurrent did not vary when the polarization of the probe laser was changed. The absence of a statistically significant difference in photocurrent suggests that depletion of electron states was not achieved. Therefore, this proposed easy and low cost method of polarimetry is not feasible, and the more complex polarimeters are still required when knowledge of electron beam polarization is needed.

Improved Calculations of Particle Orbit Times in Tokamaks.

Alexander Egan (*University of Pennsylvania, Philadelphia, PA*); *Jonathan Menard* (*Princeton Plasma Physics Laboratory, Princeton, NJ*). Stabilizing the resistive wall mode is important to maximize the plasma pressure in tokamaks and spherical tori. Rotational stabilization of the RWM is predicted from kinetic damping theory to depend strongly on particle bounce and transit times. Previous analytic calculations of bounce and transit times have assumed high aspect ratio and circular flux surfaces. For the low aspect ratio and strongly shaped plasmas of the National Spherical Torus Experiment, recently developed calculations of the particle orbit times in general geometry find that the commonly used analytic approximation is inaccurate by as much as a factor of two. However, the analytic formula is convenient since it is based on a relatively simple elliptic integral function. General geometry extensions to the existing analytic theory are being pursued for RWM stability and other applications. It is expected that some short series of elliptic integral terms added to the current model will concisely capture the aforementioned deviation. This simple form would greatly reduce the computational overhead currently required for accurate bounce and transit time calculations. Applications of this result will include the enhancement of RWM modeling in the widely used MARS stability code.

Coil Configurations Study for Bi-2212 Subscale Magnets.

Christopher English (*Texas A&M University, College Station, TX*); *Helene Felice* (*Lawrence Berkeley National Laboratory, Berkley, CA*). The Superconducting Magnet Group at Lawrence Berkeley National Laboratory is developing subscale magnets consisting of Bi-2212 (Bi$_2$St$_2$Ca-Cu$_2$O$_x$) racetrack coils as part of its subscale program. Several configurations are being considered: the stand-alone racetrack, subscale common coil, subscale dipole, and subscale hybrid dipole. In order to prepare for the assembly and testing of these magnets, a study has been carried out to determine the short sample current (Iss) and the Lorentz forces for each configuration. OPERA 3D has been used to determine the field distributions on the coils. The maximum field on the conductor determined the load line of each subscale magnet. The intersection of these load lines with the engineering critical current density versus magnetic field curve (JEC(B)) for Bi-2212 round wire subsequently determined the Iss. The results show little variation in the Iss of each configuration due to the small slope of the JCE(B) in the field range of 5–10 T. The Lorentz forces, also determined with OPERA 3D, have been analyzed by defining the magnetic pressure on the

coils. Results from the analysis show that a possible testing sequence for the subscale program could be the stand-alone racetrack, subscale common coil, subscale dipole, and finally the subscale hybrid dipole, in order of increasing magnetic pressure. Future simulations for hybrid dipoles based on varying the current in the Nb_3Sn from the current in the Bi-2212 coil are recommended.

Fast Vertexing Studies for the STAR Experiment at RHIC. *Michael Erickstad* (*University of Minnesota, Minneapolis, MN*)*; Howard Matis* (*Lawrence Berkeley National Laboratory, Berkley, CA*)*. On-line or fast vertexing (the real-time determination of the position of a collision) can be used as a trigger in data acquisition. Triggers are used in experiments to select specific classes of events and to reduce the storage of uninteresting events. Fast vertexing, when combined with fast secondary vertexing, also enables a detector to focus on certain physics topics (i.e. B-tagging, a method of determining the presence of a bottom quark based on decay length, the distance of travel before decay). The goal of this project was to test the effectiveness of a few potential fast vertexing algorithms for use with the proposed Heavy Flavor Tracker (HFT) detector at the Solenoidal Tracker at RHIC (Relativistic Heavy Ion Collider) (STAR) experiment. Simulations, which use simulated event data to predict the efficiency of these algorithms, were created. This code was written in the C++ programming language. The layers of the HFT have a cylindrical geometry and coordinate system with the beam-line as the Z-axis. The collisions take place along the beam-line. The most effective algorithm, which was tested, separates the hits (on two detector layers) into groups in Φ and then uses all combinations of two hits (one on each layer) to fill and fit a histogram of the Z intercept values for a line through the two points. It was determined that this method of using linear approximation can measure the collision vertex to a s of 430 ± 20 μm for central Au + Au events, 950 ± 20 μm for minimum-bias Au+Au collisions and 6,100 ± 200 μm for p + p events, when used with the Silicone Strip Detector and the Intermediate Silicone Tracker. It was also found that using this method with the two layers of the Pixel detector can approximate a vertex to 113 ± 7 μm for central Au + Au events, 507 ± 30 μm for minimum-bias Au+Au collisions and 1310 ± 90 μm for p + p events. Each simulation had incident particles at 200 GeV/A. A Pixel detector can achieve these results with this algorithm, if it detects particles with a suitable technology possessing no significant pile-up. These results indicate that this algorithm has a potential for implementation in the STAR experiment, for quick identification of the vertex, as well as for use in B-tagging and other decay length based particle identification methods.

Characterization of a Microchannel Plate Photomultiplier Tube for Use in Picosecond Time-of-Flight Detectors. *Camden Ertley* (*University of Akron, Akron, OH*)*; Karen Byrum* (*Argonne National Laboratory, Argonne, IL*)*. Particle accelerators use time-of-flight (TOF) detectors to distinguish between lighter and heavier particles of the same momentum. Current TOF detectors have a timing resolution of ~100 picoseconds. A higher-precision TOF detector would allow more accurate measurement of the particles' energy in a detector such as the Collider Detector at Fermilab. The purpose of this project was to test the timing resolution of the Burle Planacon microchannel plate photomultiplier tube (MCPPMT) in a laser test stand. The laser test stand consisted of a Hamamatsu picosecond laser pulsar and lenses to focus the laser on the MCPPMT. The timing resolution of the MCPPMT was found to be 70 picoseconds when in a single-photoelectron mode and 32 picoseconds when the number of photoelectrons was high, ~150. A dark box containing a light-emitting diode, filter wheel, and reference photomultiplier tube was used to test the gain and response of the MCPPMT. The diode and filter wheel were used to control the amount of light used to illuminate single pixels of the MCP. The output was recorded and put into a histogramming program. The gain and number of photoelectrons were calculated from these data. The next step for this research is to determine the timing resolution between two MCPPMTs. The ultimate goal is to develop a TOF detector with a 1-picosecond resolution.

Scanning 3rd-Order Cross Correlator to Measure Contrast of Ultrashort Laser Pulses. *Eugene Evans* (*University of California – Berkeley, Berkeley, CA*)*; Wim Leemans* (*Lawrence Berkeley National Laboratory, Berkley, CA*)*. The measurement of laser contrast and the identification of undesirable beam features in high peak power pulse lasers is a key aspect of the development and use of such lasers in the Lasers, Optical Accelerator Systems Integrated Studies (LOASIS) Program. The Scanning 3rd-Order Cross Correlator (S3OCC), a robust and accurate instrument based on the principles of third-order cross-correlation, has been developed to analyze ultrashort laser pulses. The instrument allows laser contrast measurement and pulse artifact

detection in a femtosecond-scale time regime by cross-correlating the pulse with itself in nonlinear crystals. The S3OCC is composed of a number of optics, several nonlinear crystals, a motor-actuated delay stage, and a photomultiplier tube (PMT). Scans of an 800 nm infrared beam from the LOASIS Ti:Sapphire laser used for laser wakefield acceleration were performed to calibrate the zero position of the delay stage, confirm the detection and amplitude of intentionally induced beam artifacts, and characterize the linear range of the PMT and transimpedance amplifier. A new LabVIEW-based control system was also designed and implemented. As a result, the S3OCC can consistently measure the correct position and amplitude of pulse artifacts such as pre- and post-pulses, allowing the device to measure laser contrast with almost seven orders of magnitude dynamic range. However, calibration data also revealed nonlinear responses in the PMT-amplifier system, suggesting that the operating characteristics of each component should be investigated separately to determine the origin of the nonlinearities.

Shielded Active Integrators for Use in Plasma Magnetic Field Diagnostics. *Ian Faust* (*University of Michigan, Ann Arbor, MI*)*; Tom Intrator* (*Los Alamos National Laboratory, Los Alamos, NM*)*. The Field Reversed Experiment (FRX-L) at Los Alamos National Laboratory confines deuterium plasma in a compact toroidal shape known as a Field Reversed Configuration (FRC). The characterization of the plasma necessitates the analysis of its magnetic fields. Through the use of Faraday's induction law, an electrical signal from a "b-dot" probe must be integrated accurately to understand the strength and nature of the induced magnetic field. Integration of the signal is done precisely using an analog active integrator. It allows for substantial gains, automatic zeroing of the baseline integrated signal, and no signal drop reducing the error. Data accuracy is preserved through diligent shielding from electromagnetic interference. This was done by mounting the cards within a standard rack chassis isolated in a faraday cage-like arrangement. The design has been optimized to reduce cross-interference, ease repairs and reduce temperatures. The overall error and noise fluctuations are expected to be reduced significantly by many orders of magnitude. Magnetic signal analyses, which comprise the primary diagnostic for the FRC, require one to difference two integrated dB/dt signals. This differential integrator provides a simple way to do this electronically without manually zeroing out integrating signals. The increased precision will allow for better characterization of the plasma in the upcoming tests on FRX-L. Depending on the time scales and characteristics of future plasmas, adjustments to longer timescales and greater shielding will necessitate modification of the active integrator.

*A Systematic Study of the Effect of Magnetized Oxygen on a Photon Beam. *Alishia Ferrell* (*Florida A&M University, Tallahassee, FL*)*; Joseph Heard* (*Community College of Philadelphia, Philadelphia, PA*)*; Rachael Millings* (*Suffolk County Community College, Selden, NY*)*; Carol Y. Scarlett* (*Brookhaven National Laboratory, Upton, NY*)*. A systematic study of the effects of oxygen oscillation on a laser beam propagating through an electromagnetic field (EMF) was deemed necessary due to the physical set up of the main experiment concerning space time curvature. The control or "shunt" measurements for the main experiment were made by propagating the laser outside of a vacuum chamber along side a super conducting magnet. However, this caused the beam to travel extremely close to the lead wires. This raised the question, "Was the oxygen movement being created by EMF deviating the laser beam enough to corrupt the control data". In order to see if the oxygen was significantly changing the data a systematic study had to be done. To perform this systematic study a 514 nm helium neon laser generator, several focusing and defocusing optical lenses, a quad cell photo-receiver, and a quadrapole magnet capable of oscillating its current were used. After doing a number of calibrations on the photo receiver we were able to ramp a 10 Amp electromagnetic field using alternating current through a quadrapole on the averages of events given. While the light was hitting the photo-receiver data was being collected from a data acquisition system. Once the data was done being colleted it was converted into text files. With these numbers a FORTRAN program was created using fast Fourier transforms (fft), which showed that there was a bit of movement in the X direction which caused a noticeable signal. Further studies must be done so that we can insure that this signal that we see is not just by coincidence.

Coarsening of Superconducting Froths. *Andrew Fidler* (*Albion College, Albion, MI*)*; Ruslan Prozorov* (*Ames Laboratory, Ames, IA*)*. The structure and dynamics of foams and froths has been a subject of intense interest due to the desire to understand the behavior of complex systems, when topological complexity prohibits exact derivations based on minimum energy arguments. Though exact solutions have

proven unattainable, general laws that govern the overall structural evolution have been developed. This is particularity true in the case of two-dimensional foams consisting of arrays of polygonal shaped cells with three edges per vertex. The mathematics for describing the cellular evolution in this system has proven to be surprisingly simple in form, and it applies only to the system as a whole. This gives a hope that, while the behavior of individual cells may be difficult to analyze, the overall system can be described by relatively simple rules. Using magneto-optical imaging, it was recently demonstrated that the intermediate state in superconducting lead exhibits patterns that appears to be very similar to soap foams. While visually alike, physically these systems are quite different. In conventional foams the foaming agent is always some form of matter, while in the intermediate state in lead the structure is characterized by superconducting and normal state regions. In this project, we have investigated these analogies and seen whether the general equations mentioned above apply equally as well to magnetic superconducting foams. It has been determined that laws describing foam evolution, such as von Neumann's law, work remarkably well for superconducting froth, but some parameters are different when compared to conventional foams. The biggest difference between these two systems is the agent that provides the foaming in superconducting lead, the superconducting region, decreasing as the field evolves, whereas in conventional soaps the amount of the foaming agent is constant. Nevertheless, the statistics of the polygons and structural dependence on the applied magnetic field and temperature have proven to be analogous to time. Topological transformations of the cells have also proven to be identical to conventional foams. This new type of superconducting foam could prove to help greatly to the insight into the general physics of foams, since the structure can be controlled to a greater extent by reversible manipulation of magnetic field and temperature, which is impossible in case of conventional foams where time cannot be reversed.

Parameterization of Polarized ^{3}He Quasi-Elastic Scattering Cross Sections. *Octavian Geagla* (*University of Virginia, Charlottesville, VA*)*; Xiaochao Zheng* (*Thomas Jefferson National Accelerator Facility, Newport News, VA*). The substructure of the atom can be revealed in electron scattering experiments through the analysis of the scattering cross-section. The scattering can be determined as elastic, quasi-elastic, and inelastic from the relative size of the energy loss of the electron and the four-momentum transfer squared of the virtual photon. In quasi-elastic scattering, each proton and neutron reacts to the electron beam independently. In order to apply radiative corrections to the ^{3}He nucleus, an accurate parameterization of these cross-sectional data are needed. Current world parameterizations do not have access to polarized quasi-elastic scattering cross-sections for the ^{3}He nucleus, but instead use data from other nuclei and combine them with theoretical predictions for the polarized ^{3}He nucleus. However, ^{3}He nuclear effects are neglected. This leads to great discrepancies and uncertainties in the results. In order to perform the parameterization, various computational methods were used to create a physical model of the scattering using magnetic and electric form factors which would not neglect the ^{3}He nuclear effects. The Jefferson Lab National Accelerator Facility data were fit to various nonlinear distribution models and the best fits were found for each beam energy. A global fit was created by fitting the parameters of these distributions. These results can be used to predict polarized quasi-elastic cross sections for unmeasured kinematics and for applying radiative corrections where such parameterizations are needed.

Imaging Diagnostic Systems for the Spallation Neutron Source. *Kathleen Goetz* (*Middlebury College, Middlebury, VT*)*; Tom Shea* (*Oak Ridge National Laboratory, Oak Ridge, TN*). Since the start of commissioning, imaging beam diagnostics have been utilized widely at the Spallation Neutron Source (SNS) as quick intuitive diagnostic measures and for the calibration of other diagnostic instrumentation. Because other imaging systems such as the Video Foil Monitor proved indispensable, there was a drive to create new systems such as the temporary Target Viewscreen (TVS) and the Small Angle Neutron Scattering (SANS) Neutron Beam Stop Monitor (NBSM). My work on the TVS was performed over three semesters, with this summer's focus being on system documentation. Although the temporary TVS, a system that my mentor and I designed and implemented, has already served its purpose and has been decommissioned, my work on the project continues in the form of a paper and presentation at the International Accelerator Applications conference that was at the end of July 2007. I am also part of a team that is working on plans for a second generation Target Viewscreen to be implemented next year. The NBSM is a new project with initial design work to be completed by the end of August 2007. Earlier this summer, I performed calculations to estimate the light that will be collected by the second generation TVS and NBSM optics. Presently, my work on the NBSM includes an as yet to be completed experiment at HFIR to look into the types of optics required for a successful system. I am also currently designing the experimental set up.

Study of Pedestal Fluctuations of Channels in the Track Imaging Cherenkov Experiment Camera. *Emily Gospodarczyk* (*Sauk Valley Community College, Dixon, IL*)*; Karen Byrum* (*Argonne National Laboratory, Argonne, IL*). The Track Imaging Cherenkov Experiment (TrICE) is a prototype telescope on-site at Argonne National Laboratory. It is designed to measure the composition of cosmic rays through the detection of direct Cherenkov radiation. TrICE is exploring the capabilities of a camera composed of a 4×4 array of 16-channel Hamamatsu R8900 multianode photomultiplier tubes (MaPMTs) and their corresponding electronics. The higher angular resolution explored in the TrICE prototype telescope can be applied to the next generation of high energy gamma-ray telescopes. The objective of the research was to study TrICE pedestal data and look for pedestal fluctuations in each channel over the time structure of an event. Data was recorded at a rate of 53 MHz (or 19 ns sampling). Each event contained a snapshot of eight 19ns time slices of PMT signals. By programming in C++ interfaced with the ROOT graphics language, a macro was written that calculates the mean ADC counts for each time slice for each channel. The code created a plot of the mean ADC counts for all time slices, each represented by a different marker and superimposed. The result of running the code on individual pedestal files illustrated that the pedestal remained relatively consistent between time slices. A further examination compared the Gaussian means of each time slice for channel one. The results proved that the Gaussian means for all the time slices fell within a small range and within the standard deviation. Subsequent steps should involve analyzing multiple pedestal files and looking for variations in pedestal as a function of time and temperature.

How to Control a 7,000 Ton Giant with Your Fingertips: An Interactive 3D Visualization of the ATLAS Experiment. *Emily Greenberg* (*Dartmouth College, Hanover, NH*)*; Michael Barnett, Joao Pequenao* (*Lawrence Berkeley National Laboratory, Berkley, CA*). ATLAS, the particle detector currently under construction at CERN, Geneva, Switzerland, is scheduled to begin observing collisions between protons accelerated by the LHC (Large Hadron Collider) in 2008. In an effort to make the exciting events occurring at CERN accessible to students, interested members of the public, and fellow scientists, the ATLAS Collaboration is working to develop AMELIA (ATLAS Multimedia Educational Lab for Interactive Analysis), a real-time educational 3D visualization program featuring the ATLAS detector. Supported by the DOE, NSF, and CERN, AMELIA is expected to enter classrooms with the debut of the ATLAS detector next year. Before interacting with a 3D detector, AMELIA users will be able to learn basic concepts about particle physics and ATLAS through dynamic multimedia and written references. They will then enter a virtual environment where they can visualize an event and select tracks produced by the detected particles in order to analyze real and simulated collision data. After users have analyzed collision data and have found an interesting event, they will be invited to share their findings with the scientific community at a website that displays the analyses done by AMELIA users and provides links to related sites and web-based educational tools. AMELIA is being developed in C++ using wxWidgets, Mozilla, and the Irrlicht 3d Engine, a library typically used in the computer video game industry for real-time 3D graphics. Progress was made on the development of a streamlined interactive interface and menu, as well as the conceptualization of a pedagogical structure to ensure that the program will be comprehensible and engaging for users of differing interest levels and backgrounds.

Measurement of Copper Deposition Rate and Uniformity Utilizing Electron Cyclotron Resonance Plasma Sputtering Techniques. *Kelly Greenland* (*Lock Haven University of Pennsylvania, Lock Haven, PA*)*; Andrew Zwicker* (*Princeton Plasma Physics Laboratory, Princeton, NJ*). ECR (electron cyclotron resonance) plasma is used in processing such as circuit manufacturing and thin-film deposition due to its ability to produce more energetic, more dense, and more uniform plasma than other techniques. In this project, an ECR plasma, with argon as the base gas, was used to sputter copper on to silicon wafers at various pressures, powers, and geometries, and then analyzed using a scanning electron microscope to determine the thickness, uniformity and contamination of the copper layer. In addition, a spectroscopic method was developed to measure the electron temperature of the plasma by taking the intensity of certain spectral lines in the light emitted from the plasma. Typical plasma parameters were microwave

power of 2500 watts, a target bias of 125 volts, and an argon pressure of 0.46 mTorr. Measurements deduced that these conditions deposited 360 angstroms per minute of copper onto a three inch round wafer sample, and the plasma temperature was found to be approximately 7.88 eV. These results will aid in additional research, including replacing the copper target with a graphite target in order to apply ultra-hard thin films for high performance applications such as laser windows and heat resistant circuit boards.

Analysis of the Particle Identification Capabilities of the Proposed Helical Orbit Spectrometer (HELIOS). ZACHARY GRELEWICZ (*University of Chicago, Chicago, IL*)*; *BIRGER BACK (*Argonne National Laboratory, Argonne, IL*). In order to study nuclear reactions involving short lived nuclei, inverse kinematic reactions must be used. Therefore, a novel spectrometer, HELIOS, has been designed to optimize the detection of particles in inverse kinematic reactions. In principle, the cyclotron period of an ejectile traveling along a helical orbit in a uniform magnetic field corresponds to a unique charge-to-mass ratio. However, if the ejectile is intercepted before completing a full period, the extended geometry of the detector may be used to determine not only a charge-to-mass ratio, but a unique mass. Using the Geant4 toolkit provided by the European Organization for Nuclear Research (CERN), as well as analytical techniques, the data collected by the detector from proton, deuteron, triton, helium-3, and alpha particle ejectiles were simulated. Then a program for identifying particles based on time-of-flight, energy of impact, and distance traveled along the axis of the detector, as well as an analysis of the characteristics of unidentifiable particles, was developed using the C++ programming language, with visualizations provided by CERN's ROOT system. It was found that successful particle identification depends most strongly on the lab angle of the ejected particles, with different lab angle ranges and acceptances for the five particles. Most particles may be identified by their location in the phase space, with few areas of phase space containing overlapping particles.

VISION Simplified Interface for Education. JOSEPH GRIMM (*Brigham Young University – Idaho, Rexburg, Idaho*); JACOB J. JACOBSON (*Idaho National Laboratory, Idaho Falls, ID*). VISION (Verifiable Fuel Cycle Simulation Model), a dynamic model of the US commercial nuclear fuel cycle, allows the user to manipulate the parameters of the model to analyze multiple nuclear fuel cycle scenarios. The model was created in a program called Powersim with inputs and outputs through Excel. Analysis is possible using the output graphs, charts, and tables in Powersim and Excel. There is an advanced version of VISION which allows the user to run the fuel cycle via three methods: base cases, manual mode, and user defined base cases. The base case mode allows the user to click on one of more than 60 base case scenarios; following the selection the remaining variables are set automatically. Manual Mode allows the user to set parameters via seven different interface pages in which there are multiple graphs, table inputs, slider bars and buttons. User defined base cases allow the user to set all of the parameters through the Excel input files which is extremely complex. Due to the advanced nature of the VISION interface it was unable to meet the needs of potential educational institutions for use in fuel cycle classes. Therefore it became necessary to create a simplified version of the VISION interface in order for it to be usable and understandable within an educational setting such as a college classroom or elsewhere outside of the INL. Using the capabilities of Powersim in which VISION was created, my task was to take the four base case scenarios and the three fuel cycle parameters chosen by my mentor and create a new simplified educationally friendly user interface. The four base cases would set all of the parameters within the model automatically for the user except for the three parameters shown on the interface screen. The new interface allows the user to use the VISION model without having to go through the gauntlet of setting all the user inputs. Thus they can concentrate on the system behavior rather on the modeling environment. The new interface is going to be in use this fall by five major universities in their fuel cycle classes within their nuclear programs.

Sediment Depth Measurement Using Conventional Ultrasound Techniques in Support of Scaled Mixing Tests Related to the Hanford Site Waste Treatment Plant. ABBY HEIEREN (*University of Idaho, Moscow, ID*); RICHARD PAPPAS (*Pacific Northwest National Laboratory, Richland, WA*). The Waste Treatment Plant (WTP) model has proposed mixing waste in tanks using pulse-jet mixers. To help determine mixing effectiveness of the design, two ultrasonic techniques were proposed: the Ultrasonic Doppler Velocimeter (UDV) and conventional ultrasonic pulse-echo techniques. The UDV device is designed to quantify the motion of particles suspended in fluids. The classic pulse-echo method determines position of stationary boundaries based on reflections due to acoustic impedance mismatches. The applicability of an ultrasound-based monitoring system to ascertain the presence of particle build-up on the bottom of pulse-jet mixing (PJM) tanks required further proof-of-concept through quantitative investigations. To establish the applicability of the pulse-echo method, a 2.25 MHz transducer with a plastic-matched wearplate was mounted on an acrylic, 16-in diameter, hemispherical bowl with 3.175 mm wall thickness with 25.4 mm acrylic standoff. Sound velocity through acrylic and water could be determined using partial sound reflections before collecting the following particle data: 2.68 mm/µs and 1.48 mm/µs respectively. Glass beads of diameter 60–80 µm, 150–212 µm, and 600–850 µm were then added to the water individually, retrieved, and combined, to simulate mixing process parameters, while approximating sediment depth and measuring time-of-flight. If the transducer was able to determine the layer of particles, the oscilloscope would show a static-dynamic interface, which could be verified by perturbing the sediment surface. Surface perturbation was not observed using the 2.25 MHz transducer with 600–850 µm bead size. Lower frequency transducers were tested, and a 1.0 MHz transducer was then introduced to achieve improved penetration while maintaining suitable sensitivity. The velocity of sound through each type of particle and combination were approximated to determine sediment depth within the bench-top simulation. Analyzed data represented accuracy and applicability of the conventional method for monitoring the PJM tanks. The ultrasound monitoring system (the UDV approach coupled with conventional ultrasonic methods) was determined to be suitable for this application in a bench-top scenario. If the ultrasound monitoring system is determined viable for the WTP project, future developments will incorporate performance features that are responsive to PJM test requirements.

A Comparative Study of GEM Foils from Tech Etch and CERN. JONATHAN HERSTOFF (*Muhlenberg College, Allentown, PA*); CRAIG WOODY (*Brookhaven National Laboratory, Upton, NY*). Gas Electron Multipliers (GEMs) were originally developed at CERN and are now being used in applications such as charged particle tracking. They consist of a thin polyimide foil which is copper clad on both sides and contain a large number of small holes extending through the foil. When high voltage is applied across the copper electrodes, a large electric field is developed inside the holes, which is used to produce gas gain. Different methods of manufacturing these GEMs can potentially be determinative of how the GEMs behave under high voltage. In this study, a company called Tech Etch produced three different batches of foils, each using a different chemical etching method. Although the measurements of gain versus time were varied widely from foil to foil, contrary to what was expected, there does appear to be a correlation between the size of the holes and the performance of the GEM. In general, foils with holes that have a larger polyimide area exposed tended to exhibit poorer gain stability than those with less exposed polyimide.

*Detection of Ultra High Energy Cosmic Rays Using Radar. STEVEN HICK (*State University of New York at Stony Brook, Stony Brook, NY*); HELIO TAKAI (*Brookhaven National Laboratory, Upton, NY*). Ultra High Energy Cosmic Rays (UHECR) are constantly bombarding our planet from unknown sources outside the solar system and uncovering their mysteries can provide insight into the origins and evolution of the universe. The Mixed Apparatus for Radar Investigation of Cosmic-rays of High Ionization (MARIACHI) project is a collaborative effort between research scientists, educators, and students that will explore UHECR. Understanding UHECR will be a major accomplishment in the physics community since the energies they produce are orders of magnitude higher than energies we can produce on earth with current particle accelerators. MARIACHI will scatter radio waves off ionization trails that are created when UHECR interact with our atmosphere, and will be detecting these signals using scintillator arrays that are strategically located across Long Island. Along with the scintillator arrays, antennas will be constructed and used for the detection of UHECR, and calibrating these antennas will be a major step forward for MARIACHI. The design for an antenna is a simple double dipole, which we have been experimenting with all summer. Designing, calibrating, and implementing the antennas as a compliment to the scintillator arrays is a main goal for the project. Furthermore, MARIACHI will be developing ways to subtract unwanted background information from meteors and other sources that try and mask the detection of UHECR. The MARIACHI project is still in its initial phases and there is a high risk involved since it is unknown whether or not it's possible to use radar for UHECR detection. Although there is this risk factor the concept of MARIACHI is highly seductive since the forward scattering technique is extremely inexpensive, which allows for a wide

range of users to participate. The project is mainly concerned with pure scientific research, but is unique in the fact that research scientists, educators, and students are all participants. Detecting UHECR and extracting maximal information from the MARIACHI project has promise and potential for opening many new doors in physics and education.

PDF Contributions and Parity Violation at High Bjorken x. *Timothy Hobbs* (*The University of Chicago, Chicago, IL*)*; Wally Melnitchouk* (*Thomas Jefferson National Accelerator Facility, Newport News, VA*). In recent decades, leptonic deep inelastic scattering (DIS) has been widely used to probe nucleon structure. Despite continued success, a number of surprising results have complicated the original picture of a quark-dominated nucleon. Among the most significant recent studies of parton distributions, the European Muon Collaboration (EMC) and NuTeV at Fermilab have challenged these old assumptions in nuclear structure. Problematically, precision data characterizing the d-quark parton distribution function (PDF) and the PDF ratio d/u at high values (i.e., > 0.7) of the momentum fraction (Bjorken x) are fairly incomplete. Calculations of the d/u PDF ratio contribution to parity-violating asymmetries in unpolarized DIS are performed for a range of values of the square momentum transfer Q2; for completeness, calculations involve several PDF models and target/polarization schemes for the neutral/electromagnetic interference current. So far, models demonstrate a significant dependence of beam asymmetries upon the d/u PDF ratio — a confirmation of theoretical expectation. This evaluation of PDF effects through d/u concurs with and expands earlier findings in nucleon structure, thereby driving further interest and tests of the Quark-Parton Model (QPM). Moreover, these calculations complement a discussion of parity and charge symmetry violation with implications for ongoing study in sub-nuclear theory.

The Kaon Charge Ratio in Accelerator Experiments. *Andrew Hoffman* (*Yale University, New Haven, CT*); *Maury Goodman* (*Argonne National Laboratory, Argonne, IL*). Charged kaons (K^+ and K^-) are a type of particle that can be produced from various high-energy proton-nucleus interactions due to both cosmic rays and accelerators. Kaons can decay into muons (which are seen by detectors), so the K^+/K^- ratio affects the muon charge ratio. A search was conducted for articles relevant to the kaon charge ratio to compare accelerator results to the Main Injector Neutrino Oscillation Search (MINOS) Far Detector (FD) interpretation from cosmic ray muons for the ratio of production rates ($K^+/K^- \approx 2$). Most accelerator experiments that were found used colliding proton beams to produce the kaons, whereas one used a proton beam incident on a carbon target and another the collisions of lead ions. Protons colliding with air would be ideal for studying the atmospheric muon charge ratio, but few of these experiments have been done. The accelerator results are consistent with kaon and pion charge ratios that increase with Feynman x (a scaling variable closely related to laboratory momentum); it appears that the K^+/K^- ratio is most consistent with MINOS for x ≈ 0.15–0.20. Several of the experiments used such a value, whereas one used a lower one and others used a range of values. There is a parameterization of the kaon charge ratio vs. xR ≈ x that seems rather consistent with the accelerator results. The muon and kaon charge ratios are important for neutrino physics because decays and interactions of these particles can produce either neutrinos or antineutrinos, depending on the charge of the parent particle. Since it has been shown that the muon charge ratio and neutrino-antineutrino ratio are closely related in the atmosphere, the muon and kaon charge ratios will be useful for interpreting results from neutrino detectors such as the MINOS FD.

Structure of ZnO Nanorods Using X-Ray Diffraction. *Marci Howdyshell* (*Albion College, Albion, MI*); *Michael Toney* (*Stanford Linear Accelerator Center, Stanford, CA*). Many properties of zinc oxide, including wide bandgap semiconductivity, photoconductivity, and chemical sensing, make it a very promising material for areas such as optoelectronics and sensors. This research involves analysis of the formation, or nucleation, of zinc oxide by electrochemical deposition in order to gain a better understanding of the effect of different controlled parameters on the subsequently formed nanostructures. Electrochemical deposition involves the application of a potential to an electrolytic solution containing the species of interest, which causes the ions within to precipitate on one of the electrodes. While there are other ways of forming zinc oxide, this particular process is done at relatively low temperatures, and with the high amount of X-ray flux available at SSRL it is possible to observe such nucleation *in situ*. Additionally, several parameters can be controlled using the X-ray synchrotron; the concentration of Zn^{2+} and the potential applied were controlled during this project. The research involved both gathering the X-ray diffraction data on SSRL beamline 11-3, and analyzing it using fit2d, Origin 6.0 and Microsoft Excel. A time series showed that both the in-plane

and out-of-plane components of the ZnO nanorods grew steadily at approximately the same rate throughout deposition. Additionally, analysis of post-scans showed that as potential goes from less negative to more negative, the resulting nanostructures become more oriented.

Using "R" to Analyze Radio Signals. *Candice Humpherys* (*Brigham Young University – Idaho, Rexburg, ID*); *Helio Takai* (*Brookhaven National Laboratory, Upton, NY*). Radio data from a distant transmitter is being collected by a MARIACHI (Mixed Apparatus for Radio Investigation of Cosmic rays of High Ionization) antenna in an attempt to understand the background signals to cosmic ray showers. Part of these background signals are meteors. To understand and then analyze these signals, we have elected to use the statistical package "R". "R" has many advantages over other statistical packages such as: it is open-sourced software, it can run on multiple platforms, it can run in batch mode and can be used to constantly monitor data that is being acquired by the MARIACHI antenna. Data is written to a text file every hour and this data must then be read in to "R" to run analysis. The intent of MARIACHI is to post graphs of the meteor data on the internet each hour. To accomplish this, I wrote a script in the programming environment of "R" that reads in each text file and creates graphs that display when meteors occurred. Analysis of this data will begin as soon as we gather enough data in to "R". Information about the amplitude and width (time duration) of the meteor signals is also recorded. Analysis of this information has begun, and a strong correlation between amplitude and width has been found. Analysis of the average signal width will also commence when enough data is gathered. One thing that I am working to accomplish before the average signal width analysis becomes meaningful is to distinguish between meteor signals and airplane signals and exclude the latter ones, which have a much longer width than meteors. The purpose of collecting and studying this meteor data, and the main goal of the MARIACHI project is to determine if studying cosmic rays by scattered radio signals is feasible.

Ultraviolet Induced Motion of a Fluorescent Dust Cloud in an Argon Direct Current Glow Discharge Plasma. *Michael Hvasta* (*The College of New Jersey, Ewing, NJ*); *Andrew Zwicker* (*Princeton Plasma Physics Laboratory, Princeton, NJ*). Dusty plasmas consist of electrons, ions, neutrals and comparatively large particles (dust). In man-made plasmas this dust may represent impurities in a tokamak or in plasma processing. In astronomical plasmas this dust forms structures such as planetary rings and comet tails. To study dusty plasma dynamics an experiment was designed in which a silica (< 2 mA) when the cloud is exposed to the UV (100 watts, λ = 365 nm) the mixture fluoresces, moves ~2 mm towards the light source and begins rotating in a clockwise manner (as seen from the cathode). By using a Charge-Coupled Device camera, dust clouds with diameters ranging from 6–10 mm have been observed with particle rotational velocities in excess of 3 mm/s near their periphery. Particle velocities decrease towards the center of the cloud. By calibrating a UV lamp and adjusting the relative intensity of the UV with a variable transformer it was found that both translational and rotational velocities are a function of UV intensity. Additionally, it was determined that bulk cloud rotation is not seen when the dust tray is electrically floated while bulk translation is. This ongoing experiment represents a novel way to control and localize contamination efficiently in man-made plasmas as well as a pathway to better understanding UV-bathed plasma systems in space.

Analysis of Beta-Decay of 51,52K. *Emily Jackson* (*Knox College, Galesburg, IL*); *Michael Carpenter* (*Argonne National Laboratory, Argonne, IL*). The beta decay of 51,52 K has been analyzed from data taken at TRIUMF (TRI-University Meson Facility) in Vancouver, Canada. The high purity Ge detectors were calibrated with respect to energy and efficiency using standard calibration sources (152Eu, 133Ba, and 57Co). The peaks in the beta decay spectra from the two K isotopes were identified and the energy and intensity were fitted. These results were compared to a table of energy and intensity published in a paper by F. Perrot *et al.* to check for consistency: they were found to agree with the published results. From another data set obtained at the ATLAS accelerator at Argonne with the Gammasphere array, the level scheme for 52Ti was established and expanded a great deal in comparison to the known level scheme. Any further research into the neutron-rich nuclei will require a more powerful accelerator than the accelerator used in this experiment in addition to a radioactive beam.

*Development of an Apparatus for Analysis of Monolayers by Grazing Incidence X-ray Diffraction (GIXD) and Brewster Angle Microscopy (BAM). *Morgan Jacobs* (*University of California – Berkeley, Berkeley, CA*); *James Viccaro* (*Argonne National*

Laboratory, Argonne, IL). The simultaneous use of grazing incidence X-ray diffraction (GIXD) and Brewster angle microscopy (BAM) is a powerful tool in imaging surfactant-water interfaces in Langmuir troughs. The use of both techniques allow imaging on both the angstrom and the micron scale. Previously, each technique has been used individually, however, due to the geometrical limitations of the Langmuir trough, it is difficult to use both techniques simultaneously. X-ray diffraction requires that the surfactant be in an inert atmosphere and BAM requires that a microscope be placed close to the surface being analyzed. The BAM setup previously used at Argonne National Laboratory has served as a starting point from which to make modifications. The trough is not large enough to contain the BAM microscope in its entirety, and it is therefore not possible to seal the trough. As such, an inert atmosphere is no longer practical. It may be possible to place the BAM microscope outside of the trough, using a coherent fiber optic bundle to transport the light from the inside of the trough to the microscope. However, there are a few issues that one must consider when using fiber optics. Foremost among these are collecting enough light, keeping high enough resolution, and maintaining polarization. The purpose of this project is to develop an apparatus based on an investigation of these problems. The IG-163 wound fiber optic bundle from Schott Fiber Optics seems like a promising candidate for our setup as it does seem to fit our criteria, but some testing will be required to determine whether or not it will be suitable.

Optical and Mechanical Design Features of the Qweak Main Detector. *Elliott Johnson* (*North Dakota State University, Fargo, ND*)*; James Spencer* (*Stanford Linear Accelerator Center, Stanford, CA*)*.* Photonic Band-Gap (PBG) fibers are a periodic array of optical materials arranged in a lattice called a photonic crystal. The use of PBG fibers for particle acceleration is being studied by the Advanced Accelerator Research Department (AARD) at Stanford Linear Accelerator Center. By introducing defects in such fibers, e.g., removing one or more capillaries from a hexagonal lattice, spatially confined modes suitable for particle acceleration may be created. The AARD has acquired several test samples of PBG fiber arrays with varying refractive index, capillary size, and length from an external vendor for testing. The PBGs were inspected with a microscope and characteristics of the capillaries including radii, spacing, and errors in construction were determined. Transmission tests were performed on these samples using a broad-range spectrophotometer. In addition, detailed E-field simulations of different PBG configurations were done using the CUDOS and RSOFT codes. Several accelerating modes for different configurations were found and studied in detail.

Designing the Gamma Calorimeters for the Future International Linear Collider. *Eric Jones* (*State University of New York at Stony Brook, Stony Brook, NY*)*; William Morse* (*Brookhaven National Laboratory, Upton, NY*). The electron-positron beams of the future International Linear Collider (ILC) must be monitored by utilizing feedback measurements of the bunch characteristics in order to keep them properly aligned for the optimum resulting luminosity once they collide. The Gamma Calorimeter (GamCal) is one of the proposed calorimeter designs to be placed in the very-forward region of the ILC that will be used to gather information about the beam interactions in order to maintain this alignment. It will measure the energy of photons produced by so-called beamstrahlung, a process which results from the intensification of the electromagnetic fields of the bunches as they pass through each other; however, their energy will not be measured directly. The beamstrahlung photons will first be converted into electron-positron pairs by directing them into a 10–5 m thick diamond foil, and then the positrons will be magnetically deflected into a detector grid that will measure their energy. In order to obtain a quantity proportional to the luminosity, this information will then be combined with information from the Beam Calorimeter (BeamCal) that will detect the pair particles produced in the collisions. We have used Daniel Schulte's simulation program, the Generator of Unwanted Interactions for Numerical Experiment Analysis Program, Interfaced with Geometry and Tracking (GEANT) (GUINEA-PIG), in order to understand the effects of changing important collision parameters such as the beam offset, the incoming beam angles, and the bunch lengths on the produced pair particles and beamstrahlung photons. The resulting GUINEA-PIG data were analyzed using the program Physics Analysis Workstation (PAW) and Excel. The photon energy and angular distributions will be used to optimize the detector placement in the GamCal, while other output data shall be used to determine if the luminosity can be optimized without data from the BeamCal during preliminary runs of the beams. Future studies shall also determine how well the converting foil will survive when the beams fail to interact, as the electron-positron beams are intense enough to punch holes through the foil, and these holes will decrease the acceptance of our detector. What we understand now are the number and energy acceptances for nominal bunch parameters with varying offsets and incoming angles, and that the foil should remain reliable to about 1% error.

Elemental Analysis of a Shrub-Steppe Soil. *Rachael Kaluzny* (*Western Michigan University, Kalamazoo, MI*); *James McKinely* (*Pacific Northwest National Laboratory, Richland, WA*). Scanning electron microscopy is an important research tool used widely today in areas such as medical evaluation, forensics evidence examination, and scientific research. Electron microscopes use a beam of highly energetic electrons to examine objects on a microscopic scale. This examination can yield: topography, morphology, composition, and crystallographic structure. Advanced automation on the ASPEX Personal Scanning Electron Microscope (PSEM) 3025 was used to acquire elemental data on a shrub-steppe soil sample obtained from the Yakima Valley near Sunnyside, WA. The PSEM 3025 was designed for semi-automated imaging and analysis of inorganic specimens in the millimeter to sub-micron range. The shrub-steppe soil was analyzed at 20 kV with a working distance of 18.4 mm and an emission current of 112 µA. The automated run performed energy dispersive X-ray spectroscopy (EDS) on each particle. EDS is a technique based on characteristic X-ray peaks which are generated when an electron beam interacts with the specimen. Characteristic X-rays are produced for each element present in the region being analyzed. Comparison of the intensities of X-ray peaks are then used to verify the relative abundance of each element in the analyzed region. A total of 6611 particles were analyzed on the soil sample. Rule files were developed to define membership classes based on chemical properties and elemental ratios. Particles were grouped into the defined classes as the data was being acquired. From these results it can be seen that the shrub-steppe sample consists primarily of silicates containing iron, aluminum, and calcium. This is consistent with the composition of silt loam soils in the Yakima Valley.

Improving LER Coupling and Increasing PEP-II Luminosity with Model-Independent Analysis. *Lacey Kitch* (*Massachusetts Institute of Technology, Cambridge, MA*); *Yiton Yan* (*Stanford Linear Accelerator Center, Stanford, CA*)*.* The PEP-II storage ring at SLAC houses electrons (in the High-Energy Ring, or HER) and positrons (in the Low-Energy Ring, or LER) for collision. The goal of this project was to improve the linear optics of the LER in order to decrease coupling, thereby decreasing emittance and increasing luminosity. To do this, we first took turn by turn BPM (Beam Position Monitor) data of a single positron bunch at two betatron resonance excitations, extracted orbits from this data using Model-Independent Analysis, and from these orbits formed a virtual model of the accelerator. We then took this virtual model and found an accelerator configuration which we predicted would, by creating vertical symmetric sextupole bumps and adjusting the strengths of several key quadrupole magnets, improve the coupling and decrease the emittance in the LER. We dialed this configuration into the LER and observed the coupling, emittance, and luminosity. Coupling immediately improved, as predicted, and the y emittance dropped by a dramatic 40%. After the HER was adjusted to match the LER at the Interaction Point (IP), we saw a 10% increase in luminosity, from 10.2 x 10^{33} cm^{-2}sec^{-1} to 11.2 x 10^{33} cm^{-2}sec^{-1}, and achieved a record peak specific luminosity.

Plateauing Cosmic Ray Detectors to Achieve Optimum Operating Voltage. *Elissa Knoff* (*Northwestern University, Evanston, IL*); *Robert Peterson* (*Fermi National Accelerator Laboratory, Batavia, IL*). Through QuarkNet, students across the country have access to cosmic ray detectors in their high school classrooms. These detectors operate using scintillator and a photomultiplier tube (PMT). A data acquisition (DAQ) board counts cosmic ray hits from the counters. Through an online e-Lab, students can analyze and share their data. In order to collect viable data, the PMTs should operate at their plateau voltages. In these plateau ranges, the number of counts per minute remains relatively constant with small changes in PMT voltage. We sought to plateau the counters in the test array and to clarify the plateauing procedure itself. In order to most effectively plateau the counters, the counters should be stacked and programmed to record the number of coincident hits as well as their singles rates. We also changed the threshold value that a signal must exceed in order to record a hit and replateaued the counters. For counter 1, counter 2, and counter 3, we found plateau voltages around 1V. The singles rate plateau was very small, while the coincidence plateau was very long. The plateau voltages corresponded to a singles rate of 700–850 counts per minute. We found very little effect of changing the threshold voltages. Our chosen plateau voltages produced good performance studies on the

e-Lab. Keeping in mind the nature of the experiments conducted by the high school students, we recommend a streamlined plateauing process. Because changing the threshold did not drastically affect the plateau voltage or the performance study, students should choose a threshold value, construct plateau graphs, and analyze their data using a performance study. Even if the counters operate slightly off their plateau voltage, they should deliver good performance studies and return reliable results.

Functionalized Particles As Templates for Nanoparticles Self-Assembly. CHRIS KNOROWSKI (*Virginia Tech, Blacksburg, VA*); ALEX TRAVESSET (*Ames Laboratory, Ames, IA*). Block copolymer solutions or melts exhibit an amazing variety of phases and structures with vast possibilities for the design of novel materials A promising design strategy is the transfer of a polymer structure to an inorganic component present in solution, where the goal is to obtain a self-assembled inorganic crystal exhibiting the mesoscopic order imposed by the polymeric phase, which serves as a template. Establishing general conditions for successful templating is therefore a major theoretical challenge, with fundamental implications for both basic and applied science. In this paper we investigate general conditions leading to successful templating by considering a generic pluronic coexisting with inorganic particles, which herein will be referred as nanoparticles. We assume that nanoparticles tend to crystallize and thus attract each other with a characteristic attractive energy ξN. We also functionalize the ends of the polymer with an affinity for the nanoparticles to facilitate template thus introducing a new energy scale ξF, which is the energy gain for nanoparticles to bind to the functionalized group. We use a short ABA triblock copolymer where the A blocks are hydrophilic and the B blocks are hydrophobic, and model the water implicitly. Using course grained MD simulations we investigate the region where this triblock copolymer forms a hexagonal phase. When the nanoparticles are added to the system an extraordinary variety of exotic phases are realized as we vary the attractive ξN and ξF forces. Over a large range we see a double gyroid with the nanoparticles forming one gyroid (space group 1a3d) and the hydrophobic blocks forming another gyroid which interlock around each other. Over a small region we see a perforated lamellar with hexagonal ordering, with the nanoparticles and the hydrophobic blocks forming alternating planes. The hydrophobic forming the perforated lamellar and the nanoparticle Lamellar connecting through the perforations in the hydrophobic plane. As we continued to increase both values of ξN and ξF we see a noncentrosymetric double gyroid (space group I4_132). There are also several areas where coexistence between phases occur and many regions where further exploration could reveal new phases of the diagram.

Studies of Flux Pinning in Superconducting $YBa_2Cu_3O_7$ Disks. ANGELA KOU (*Columbia University, New York, NY*); SÖREN PRESTEMON (*Lawrence Berkeley National Laboratory, Berkley, CA*). $YBa_2Cu_3O_7$ (YBCO) is a high temperature superconductor that has been shown to pin high magnetic fields when it is placed in an applied field greater than its lower critical magnetic field, Hc1 and less than its higher critical magnetic field, Hc_2. The pinning properties of a bulk YBCO sample are studied in order to probe its ability to pin uniform high magnetic fields for extended periods of time. The YBCO sample was field cooled from 100 K to 13 K using a ^{3}He cryostat in an applied magnetic field of 5 T. A Hall probe was used to monitor the field within the sample. The sample was found to trap a maximum field of 3.5 T. Flux jumps were observed during ramping down of the applied field. Flux creep was observed in the sample; the sample showed a loss of less than 0.1% of the trapped field over a period of 120 s. The slow rate of degradation of the field over time demonstrates the possibility of using bulk samples of YBCO as "permanent magnets". Finally the trapped field decreased with increasing temperature and lost all trapped field above 100°K, indicating that for this sample the critical temperature is 104°K. Critical state models were used to model the trapped field within the sample. This work is part of an ongoing project to investigate the feasibility of using bulk YBCO with trapped fields as the source of a uniform magnetic field in condensed matter scattering experiments.

ILC Electron Source Injector Simulations. MANU LAKSHMANAN (*Cornell University, Ithaca, NY*); AXEL BRACHMANN (*Stanford Linear Accelerator Center, Stanford, CA*). As part of the global project aimed at proposing an efficient design for the ILC (International Linear Collider), we simulated possible setups for the electron source injector, which will provide insight into how the electron injector for the ILC should be designed in order to efficiently accelerate the electron beams through the bunching system. This study uses three types of software: E-Gun to simulate electron beam emission, Superfish to calculate solenoidal magnetic fields, and GPT (General Particle Tracer) to trace charged particles after emission through magnetic fields and subharmonic bunchers. We performed simulations of the electron source injector using various electron gun bias voltages (140 kV–200 kV), emitted beam lengths (500 ps–1 ns) and radii (7 mm–10 mm), and electromagnetic field strengths of the first subharmonic buncher (5–20 MV/m). The results of the simulations show that for the current setup of the ILC, a modest electron gun bias voltage (~140 kV) is sufficient to achieve the required bunching of the beam in the injector. Extensive simulations of parameters also involving the second subharmonic buncher should be performed in order to gain more insight into possible efficient designs for the ILC electron source injector.

Building X-ray Diffraction Calibration Software. JOSHUA LANDE (*Marlboro College, Marlboro, VT*); SAMUEL WEBB (*Stanford Linear Accelerator Center, Stanford, CA*). X-ray diffraction is a technique used to analyze the structure of crystals. It records the interference pattern created when X-rays travel through a crystal. Three dimensional structure can be inferred from these two dimensional diffraction patterns. Before the patterns can be analyzed, diffraction data must be precisely calibrated. Calibration is used to determine the experimental parameters of the particular experiment. This is done by fitting the experimental parameters to the diffraction pattern of a well understood crystal. Fit2D is a software package commonly used to do this calibration but it leaves much to be desired. In particular, it does not give very much control over the calibration of the data, requires a significant amount of manual input, does not allow for the calibration of highly tilted geometries, does not properly explain the assumptions that it is making, and cannot be modified. We build code to do this calibration while at the same time overcoming the limitations of Fit2D. This paper describes the development of the calibration software and the assumptions that are made in doing the calibration.

Designing an LED Monitoring System for the FMS. JONATHAN LANGDON (*State University of New York at Stony Brook, Stony Brook, NY*); LES BLAND (*Brookhaven National Laboratory, Upton, NY*). The Forward Meson Spectrometer (FMS) at Brookhaven National Laboratory's STAR Experiment is composed of lead glass cells which are used to detect photons produced in high energy collisions of gold nuclei or protons. In past iterations of the FMS, panels of fiber optics were used to provide light from light emitting diodes (LEDs) as a calibration signal. This test signal could be observed as an event distribution within the data, far removed from other physical events. For the FMS, the goal is to create a more comprehensive and adaptable LED testing system. Unlike previous iterations, the goal is provide variable light sources to cell clusters allowing for patterns of light to be used instead of simply pulses of light. This would provide a means for proofing the functionality of the FMS's triggering system. To accomplish this, a type of microchip, known as a Field Programmable Gate Array (FPGA), will be installed to control the LED output. FPGAs are also known as programmable logic chips, since one can use a computer to define its behavior after it has been implemented. Making use of an FPGA development kit in conjunction with an "integrated software environment" (ISE), known as Xilinx ISE Webpack, a functioning system for controlling the light panels has been developed. However, in addition to the hardware aspect, it has also been necessary to develop graphical interface tools for loading light pattern instructions in real time. This was accomplished by way of Microsoft's "Visual Basic. NET 2005 Express" interactive development environment (IDE). The final product, known as the "Light Panel Control System," is the product of by directional development, starting from the computer out to the development board and from the FPGA back.

Bunch by Bunch Profiling with a Rotating X-Ray Mask. CHRISTOPHER LEE (*University of California – San Diego, La Jolla, CA*); ALAN FISHER (*Stanford Linear Accelerator Center, Stanford, CA*). It is desirable to monitor the cross sections of each positron bunch in the Low Energy Ring (LER) storage rings of the Positron Electron Project II (PEP-II) located at the Stanford Linear Accelerator Center. One method is to pass the X-rays given off by each bunch through a scintillator, thereby studying a visible image. A rotating X-ray mask with three slots scans the beam image in three different orientations, allowing us to mechanically collect data to characterize and profile each image. Progress was made in designing the X-ray mask, researching and procuring parts, as well as advancing project plans. However, due to time constraints and difficulties in procuring special parts, the full system was not completed. A simpler setup was built to test the hardware as well as the feasibility of characterizing a circular image with a rotating mask. A blinking green light emitting diode (LED) simulated a single positron bunch stored in the LER ring. The selected hardware handled this simulation setup well and produced data that led to a reasonable estimation of the LED image diameter.

Measurement of Density of Polarized ³He Target Cell Using Laser Interferometer. *Andrew Leister* (*The College of William and Mary, Williamsburg, VA*); *Jian-Ping Chen* (*Thomas Jefferson National Accelerator Facility, Newport News, VA*). As scientists continue to learn more about fundamental matter, they are trying to fully understand the structure of nucleons (protons and neutrons). One of the difficulties in studying the neutron structure is that the isolated neutron decays after approximately ten minutes and is therefore not ideal for experimentation. Fortunately, it has been found that the structure of polarized Helium-3 (³He) allows it to serve as an effective polarized neutron target for studying neutron spin-structure. This is because the spins of the two protons in ³He are anti-aligned about 90% of the time. Therefore the remaining spin is derived entirely from the neutron. There are several factors that determine the maximum polarization of a target ³He cell, one of the key factors being the density of the cell. The focus of this study is to determine an accurate value for the density of a target ³He cell, "Aaron". To calculate the density, a laser with a specified frequency range was projected through the ³He target cell while the intensity was read by a photo-diode. This data was then read by the LabView and Root programs which generated a Lorentzian curve to fit the data. One of the parameters of this Lorentzian curve is directly proportional to the density of the cell. It was found that the density of the target cell was 8.547 ± .333 amagats (amg) at sufficiently high temperatures. Since the density of the cell is now known, the maximum polarization of the cell can be determined. With this value known, there is greater knowledge of the characteristics of "Aaron" and the results of further experiments with the cell can be understood more fully. This will ultimately lead to a deeper understanding of the spin-structure of nucleons.

Effect of Biotin Density on 2D Streptavidin Crystallization on Lipid Monolayers at the Liquid-Vapor Interface. *Matthew Lohr* (*Pennsylvania State University, University Park, PA*); *Masafumi Fukuto* (*Brookhaven National Laboratory, Upton, NY*). Phospholipid monolayers at the gas-liquid interface are interesting because of their ability to act as templates for two-dimensional (2D) crystallization of various proteins. Such behavior could lead to utilization for assembly of practical bio-nanostructures. Previously studied examples of this phenomenon include the crystallization of streptavidin through binding with biotinylated phospholipids. In this study, we examine the effect of biotin surface density on streptavidin crystallization by observing the behavior of streptavidin at an ionic subphase-vapor interface coated with a phospholipid monolayer comprised of a binary mixture of dimyristoylphosphatidylcholine (DMPC) and biotin-capped dipalymitoylphosphotidylethanolamine (DPPE-x-Biotin). We monitor the formation of 2D streptavidin domains on lipid surfaces using Brewster-angle microscopy (BAM) over 20 hours. The mean molecular area of lipids is fixed at 75 Å²/lipid, and the mole fraction of DPPE-x-Biotin ranges from 100% to 0.01%. These observations have yielded several distinct regimes for crystallization behavior. At 8% DPPE-x-Biotin composition and above (937.5 Å² per biotin and below), bowtie-shaped crystal domains form almost immediately after injection of streptavidin, grow with time, and eventually cover the entire surface of the sample. At 5% and 4.3% DPPE-x-Biotin composition (1,500 and 1,744 Å² per biotin), crystal domains only partially cover the available sample surface. At 3.9% and 3.5% DPPE-x-Biotin composition (1,923 and 2,142 Å² per biotin), several crystal domains are observed, but they are not uniformly distributed over the entire surface. At 3% DPPE-x-Biotin and below (2500 Å² per biotin or larger), the surface shows no crystal domains that can be discerned by BAM (=10 µm). According to previous diffraction studies of streptavidin crystals under similar conditions, the proteins arrange in two-dimensional unit cells with an average of 1,610 Å² per biotin binding site. This observation and our BAM studies provide strong evidence that in order for the 2D crystallization of streptavidin to take place, the surface density of biotin linkers must be comparable to or larger than the binding site density in the 2D crystal. This observation may be key to understanding the mechanisms behind streptavidin's crystallization behavior. These results supplement ongoing studies of streptavidin crystallization, including X-ray and optical studies of the effects of subphase pH.

The Assembly and Testing of the BigBite Hadron Detector System. *Gordon Lott* (*Virginia Tech, Blacksburg, VA*); *Douglas Higinbotham* (*Thomas Jefferson National Accelerator Facility, Newport News, VA*). Scintillator detectors are a basic part of nuclear and high energy physics research. When a charged particle passes through a scintillator, it creates photons. The photons travel to the ends of the scintillator and into photomultiplier tubes (PMTs) which turn the photons into an electric pulse. The BigBite Hadron particle detector package has a scintillator plane made of two layers of 24 scintillator

bars. This project focuses on this detector package which will be used in a Thomas Jefferson National Accelerator Facility Hall A experiment next year and its scintillator plane and electronics needed to be assembled. All the PMTs were connected to labeled high voltage (HV) cables and signal cables. The signal cables were connected to a series of nuclear instrument modules (NIM) which amplify the signal and convert the analog signal to a digital signal. The different NIM modules needed for logic and triggering were arranged and cabled in an organized fashion for easy troubleshooting and repair. The HV cables were connected to LeCroy high voltage supplies. The whole system was tested with cosmic rays to find problems. This assembly and testing put the detector in complete working order and verified the quality of the set up. The prepared package can now be moved into Hall A for the experiment.

Ion Beam Analysis for the Investigation of Bozzolo-Ferrante-Smith Predictions of Interface Stability. *Kasey Lund* (*Montana State University, Bozeman, MT*); *Shuttha Shutthanandan* (*Pacific Northwest National Laboratory, Richland, WA*). The world of nanotechnology is upon us. Today there are a myriad of techniques for growing thin films only nanometers thick. With all the knowledge we have of the laws of physics, we still do not fully understand the interactions of thin metal-metal structures. Currently there is a large effort to grow films with flat, chemically abrupt interfaces that would be applicable to industries making thin film sensors and magnetic data storage devices. One model, known as the Bozzolo-Ferrante-Smith (BFS) model, predicts that a thin layer of either titanium or vanadium can be used to suppress the interdiffusion of aluminum and iron at the Al-Fe interface. Studies of Ti behavior have already been performed, however little is know about the behavior of V. In order to contribute more information to this comprehensive model that would reliably predict atomic behavior at the nano scale, a thin layer of vanadium was deposited between iron and aluminum. Using an RF magnetron sputtering chamber, different combinations of Al, Fe, and V layers were deposited onto a silicon substrate. The samples were analyzed with Rutherford Backscattering Spectroscopy (RBS) to identify the thickness of the layers and to look for interdiffusion between layers, and with X-ray Reflectivity (XRR) to complement the RBS data. The samples were then annealed for various times and reanalyzed with the same techniques. From the RBS and XRR it can be seen that diffusion occurs at the Al-Fe interface during growth and that the diffusion layer will increase after annealing. When Ti was placed between Al and Fe, the Ti hindered the interdiffusion of Al and Fe before and after the annealing up to 350°C. However, the V did little to suppress the interdiffusion before or after the annealing. The BFS model correctly predicted the behavior of the Al/Ti/Fe structure, but it was incorrect with regards to the behavior of V. With these results it can be seen that the BFS predictions are not completely correct. Future experiments will be conducted to further improve the BFS calculations.

Noise Studies in ATLAS Pixel Detector Endcap A. *Kevin Lung* (*University of California at Berkeley, Berkeley, CA*); *Wei-Ming Yao* (*Lawrence Berkeley National Laboratory, Berkley, CA*). In order to improve the results of the ATLAS detector data, it is necessary to remove noise from the data sample before running other analyses. The noise removal involves the definition of hot pixels. These hot pixels are indicative of noise because they have registered data more often than is expected for the typical cosmic ray signal. The goal of this noise removal is to achieve the most noise suppression, resulting in a more clearly defined signal. The noise suppression is measured through the module occupancy, the number of pixel hits per pixel per module per event readout. For this study, a noise occupancy on the order of 10^{-10} is obtained for Run 1129, which is much lower than the 10^{-7} noise occupancy of the MC simulation. Evidently, this order of noise occupancy shows a large magnitude of noise suppression as compared to the signal occupancy on the order of 10^{-7}.

What the Formation of the First Stars Left in its Wake. *Christene Lynch* (*Gettysburg College, Gettysburg, PA*); *Marcelo Alvarez* (*Stanford Linear Accelerator Center, Stanford, CA*). The formation of the first stars marked a crucial transition in the formation of structure in the universe. Through their feedback effects, which include ionization by their radiation and the supernovae or black holes formed at the end of their lives, they were able to influence the evolution of their surroundings. In this paper we present a new visualization and use analytical calculations in order to study the influence of these first stars. The visualization was created using both Enzo, a simulation program that uses adaptive mesh refinement, and Amira, a 3D volume rending program. The visualization allows for a better understanding of the impact these stars had on their surroundings and conveys the importance of these stars to a broader audience. The analytical

calculations used investigate the possibility that black holes left by the first stars could be seeds for the 109 solar mass black holes seen as quasars at redshift z~6. We found that if a remnant black hole was to begin Eddington accretion at z~20 they will be able to form the 109 solar mass quasars by z~6 but that there is likely to be a delay in the onset of accretion onto the seed black hole because of the radiative feedback of its progenitor. Future, more detailed, numerical calculations will be necessary to understand whether the black holes left by the first stars could possibly be seeds for quasar formation.

Determining the Components of an Iron Beam at the NASA Space Radiation Laboratory. *JENNIFER MABANTA* (*St. Joseph's College, Patchogue, NY*)*; MICHAEL SIVERTZ* (*Brookhaven National Laboratory, Upton, NY*). Before extended space missions can occur, protective measures must be put in place for astronauts since prolonged exposure to radiation fields can have adverse effects. The purpose of the research done at the NASA Space Radiation Laboratory (NSRL) at Brookhaven National Laboratory (BNL) is to gain a better understanding of the cosmic rays in space and develop the most efficient countermeasure for the voyagers. Proton and heavy-ion beams from the BNL Booster accelerator are directed along a beam line to NSRL. These beams mimic cosmic rays providing a controlled area in which to study the effects of the rays. The most harmful of the rays is iron and the least destructive and most abundant is hydrogen. Of particular interest to NASA are the iron beams as they are the most destructive form of radiation facing astronauts. Since completely shielding them from these heavy beams would not be feasible given the constraints in space, scientists are seeking to utilize the process of fragmentation in their shielding methods. Fragmentation is the way in which heavy ions break up into lighter less dangerous ions. In order to study this process, it is necessary to measure the components within the beam. To achieve this, a scintillator detector is placed within the beam. However, the response of this scintillator is not linear with the deposited energy; it follows a relation known as Birk's Law. In order to study the different components of the beam, the response function of the scintillator must be determined. Once this response function is made linear, each elemental ion within the iron beam is more easily identified. To create the best fit, the fewest number of parameters must be used while still keeping the value of chi squared at a minimum. Using the spreadsheet software Excel, a fitting routine was created that could be implemented on each of the components of the iron beam from hydrogen to iron. Using this routine, the centroids for the peak of each element was determined and used to develop the response function. A second order polynomial was found to be adequate to fit the response of the scintillator, $y = 0.000121x^2 + 1.0x$. A comparison of the scintillator response function before and after unfolding shows that the response can be portrayed as a linear function within a given range. Using this function, scientists will be better able to characterize the iron beam in order to develop the best shielding methods for harmful space radiation.

*Implicit Simulation for Beam Problems. *KAM MAK* (*Contra Costa College, San Pablo, CA*)*; ALEX FRIEDMAN* (*Lawrence Berkeley National Laboratory, Berkley, CA*). Experimental facilities that generate particle beams are expensive, while computers are getting more powerful. Computer simulation using the methods of computational plasma physics has become a reliable and effective approach to understanding beam behavior. Such simulation enables analysis of more realistic situations than are analytically tractable, so that researchers can explain the behavior of an existing machine, improve its performance, and predict the performance of a future machine. The research group in the Heavy Ion Fusion Science Virtual National Laboratory (HIFS-VNL) at Lawrence Berkeley National Laboratory (LBNL) develops and uses plasma and beam simulation programs. The most adaptable and reliable tools for the study of plasma behavior are Particle In Cell (PIC) simulations, in which a few thousand to many million particles are used to model the beam and/or plasma. These particles follow the Newton-Lorentz equations of motion in fields governed by Maxwell's equation. However, traditional PIC codes require use of a time step shorter than the plasma period to maintain numerical stability. When plasma oscillations are not important and a larger time step is required, implicit methods can maintain the stability and model the macroscopic behavior. In such methods, the particle positions at the advanced time level depend on their accelerations due to the electric field at that time level. But that field itself depends on the density of particles at their new positions. A direct method for obtaining this field solves a modifed field equation which takes account of the effect of that field on itself through the particle motion. After the predicted field is known, the particles are advanced to the new time level. In this project we combined several old codes into a modern 1-D implicit test-bed, and

made the new code user-steerable using the Python language, linked to Fortran by the Forthon system. We then studied the performance of various algorithms on a plasma expansion problem, and studied the behavior of a test electron in an electrostatic potential well that models the well caused by an ion beam. Regimes of reliable algorithmic performance were clarified.

Simulation of Electron Trajectories Inside an Annular Dielectric. *JULIE MANAGAN* (*Vanderbilt University, Nashville, TN*)*; JOHN R. HARRIS* (*Lawrence Livermore National Laboratory, Livermore, CA*). Development of a compact Dielectric Wall Accelerator (DWA) is desirable for scientific and medical applications such as proton therapy, but requires vacuum insulators to withstand electric fields (E-field) near 100-MV/m without surface flashover. It is believed that flashover is caused by secondary electron emission avalanches (SEEA), requiring field-emitted electrons to re-strike the insulator surface. In a fast voltage pulse, changing E-field creates a displacement current and induces a magnetic field (B-field), which will influence the trajectories of field-emitted electrons. This may cause them to strike the insulator, triggering SEEA. In a previous study, B-field simulations showed this effect for particles emitted from the exterior of a cylindrical dielectric. This abstract describes a study simulating the B-field effect on electrons emitted from the interior of an annular dielectric capped by disc electrodes. The particle-in-cell code LSP was used to simulate field-emitted electrons under the E and B-fields created on the rising edge of a trapezoidal voltage pulse, while varying outer diameter, inner diameter, dielectric constant, emission time, voltage pulse length, and emission energy. Since conventional flashover research does not account for B-field effects due to displacement current, the code was modified so that the B-field could be eliminated, and all tests were run with and without it. The sign and strength of the B-field determined particle motion: when the E-field had a positive rate of change the B-field deflected electrons away from the surface, but when it had a negative rate of change the B-field deflected electrons toward the surface. Ringing appeared at the end of the voltage ramp, creating a negative rate of change in the E-field. Variations in timing and geometry influenced the fields seen by the particles and changed their trajectories accordingly. Where no B-field was present, the electrons traveled within 1 mm of the surface. Under most conditions, the B-field deflected electrons away from the interior surface during the rising edge of the voltage pulse, which is opposite to its effect on the exterior surface. This benefits the DWA system by decreasing possible triggers of SEEA. This study improved understanding of vacuum insulators, and will aid development of materials that are better suited to the high E-fields of the DWA.

Experimental Study of Effects due to Perturbations on Boundary Conditions to Couette Flows. *FREDERICK MANLEY* (*University of Illinois, Champaign, IL*)*; HANTAO JI* (*Princeton Plasma Physics Laboratory, Princeton, NJ*). When fluid flows between two independently rotating cylinders at low aspect ratios (the ratio of the height to the difference in radii), the flow is seen to deviate substantially from ideal Couette flow due to Ekman circulation along the end caps. In the case where the end caps are attached to the outer cylinder, fluid with less angular momentum is advected into the bulk flow, which decreases the mean velocity as predicted by the ideal case. In order to study the stability of Ekman circulation, an experiment was devised to perturb the Ekman boundary layer by modifying the inner cylinder. Water flows between an aluminum inner cylinder and acrylic outer cylinder and its velocity is measured using a Laser Doppler Velocimeter (LDV) scanned radially from underneath to obtain 2-D velocity profiles. The robustness of the Ekman layer was studied against perturbations of varying magnitudes. Though perturbing the inner cylinder boundary did produce profiles closer to the ideal Couette case, the Ekman layer proved to be more robust than predicted. Both a 7-mm offset and four o-rings placed on the inner cylinder were needed to produce profiles resembling the ideal Couette case. A new apparatus will be built with a larger aspect ratio to observe the effects of similar perturbations on the less stable Ekman flow. In the future, less viscous fluids may be used to determine the effects of larger Reynolds numbers on Ekman stability.

United States A Toroidal Large Hadron Collider Apparatus (US Atlas) Load Test Scheduler. *MICHAEL MAY* (*Loyola College in Maryland, Baltimore, MD*); *JAY PACKARD* (*Brookhaven National Laboratory, Upton, NY*). United States A Toroidal Large Hadron Collider Apparatus (US Atlas) Load Test Scheduler was created by the United States Department of Energy (DOE) at Brookhaven National Laboratory (BNL) to allow users to make a reservation to test the local input/output (I/O) performance at a site (farm) as would be seen by an ATLAS user or analysis job. To accomplish this, the Java programming language, on the eclipse console, was used along with hibernate

mapping and MySQL database. In this way a user can request a reservation to run a test on a site inserting the start date, end date, farm name, cluster name, node name, and the submitter's distinct number and an administrator can search the requests for a reservation and approve or deny the reservation. This project allows for an organized way to make a reservation to perform a load test on a site to measure the I/O performance.

Calculation of Charge-Changing Cross Sections of Ions or Atoms Colliding with Fast Ions Using Classical Trajectory Method. *Harrison Mebane* (*Harvard University, Cambridge, MA*)*; Igor Kaganovich* (*Princeton Plasma Physics Laboratory, Princeton, NJ*). Evaluation of ion-atom charge-changing cross sections is needed for many accelerator applications. Ions lose energy when passing through background gasses, beam transport lines, and detectors. A classical trajectory Monte Carlo simulation has been used to calculate ionization and charge exchange cross sections. For benchmarking purposes, an extensive study has been performed for the simple case of hydrogen and helium targets in collisions with various ions. To improve computational efficiency, several integration methods, including Runge-Kutta with adaptive stepsize and Bulirsch-Stoer with Stoermer's Rule, were compared. The algorithm was also upgraded to simulate the trajectories of two electrons for a helium target. Despite the fact that the simulation only accounts for classical mechanics, the calculations are comparable to experimental results for projectile velocities in the region corresponding to the vicinity of the maximum cross section. The accuracy of a purely classical simulation allows for simpler and faster calculations of cross sections in the vicinity of maximum cross section, avoiding slower and more complex quantum mechanical calculations. In the future, support will be added for simulations of multiple electron trajectories in more complicated targets, and the algorithms will be further refined to improve speed and accuracy.

Rietveld Full Profile Refinement of MnO and MnAs. *Dalgis Mesa, Rahul Patel* (*Florida International University, Miami, FL*)*; Jaime Fernandez-Baca* (*Oak Ridge National Laboratory, Oak Ridge, TN*). In the present study, elastic neutron scattering was used to obtain a powder diffraction pattern for MnO at the Wide Angle Neutron Diffractometer (WAND) located at the High Flux Isotope Reactor (HFIR) at Oak Ridge National Laboratory (ORNL). The diffraction pattern obtained from the sample was analyzed using the Rietveld method of full profile refinement in order to refine the relevant crystallographic parameters of the specimen. The Rietveld method is based on a least squares fit of the full diffraction pattern to a model that takes into account the crystallographic as well as the instrumental parameters to calculate the full profile. The latter includes the Caglioti resolution parameters ($U = 2.36$, $V = -1.18$, $W = 0.43$) and the wavelength (λ) of 0.1476 nm. As a resource, the Inorganic Crystal Structure Database (ICSD) was used to obtain the initial crystallographic parameters for MnAs [1] and MnO [2]. The following crystallographic parameters were refined for MnO using the software program FullProf©: lattice constant values (a, b, c) of (4.44, 4.44, 4.44) and individual isotropic thermal parameters (B - factor) with an initial default value (D.V.) of 1. The results yielded a percent change of 0.53 for the lattice constant while a 52.48 and 44.40 for the B - factors of Mn and O respectively. For MnAs, the refined crystallographic parameters included the lattice constants (3.72, 3.72, 5.72), the atomic occupancies (D.V.), as well as the B-factors (D.V.). The percentage change for the refined parameters for MnAs were of (0.26, 0.26, 0.30) for the cell parameters, 54 and 36 for the atomic occupancy of Mn and As respectively, and the obtained values for the B-factors were 4.38 and 3.25 for Mn and As correspondingly. The experimental procedure and results will be discussed in detail along with new ideas for possible improvement of the present study.

Long-Term X-ray Variability of NGC 4945. *Amara Miller* (*University of California – Davis, Davis, CA*)*; Grzegorz Madejski* (*Stanford Linear Accelerator Center, Stanford, CA*). Though short-term X-ray variability has been studied for the active galaxy NGC 4945, long-term studies promise to contribute to our understanding of the processes involved in accretion onto supermassive black holes. In order to understand the relationship between black hole mass and breaks in the power spectral density (PSD), the long-term X-ray variability of NGC 4945 was studied over the energy range 8-30 keV. Observations occurred over the year 2006 using the Rossi X-ray Timing Explorer. The data was reduced using the package FTOOLS, most notably the scripts Rex and faxbary. Light curves were produced and a PSD was obtained using a Fast Fourier Transform algorithm. Preliminary studies of the light curve show greater X-ray variability at higher frequencies. This result complements previous studies of NGC 4945 by Martin Mueller. However, the PSD produced must go through further study before accurate results can be

obtained. A way to account for the window function of the PSD must be found before the behavior at lower frequencies can be studied with accuracy and the relationship between black hole mass and the break in NGC 4945's PSD can be better understood. Further work includes exploration into ways to subtract the window function from the PSD, as well as a closer analysis of the PSD produced by averaging the data into logarithmic bins. The possibility of a better way to bin the data should be considered so that the window function would be minimized.

Density Measurements of a ^{3}He Target Cell *Sara Mohon* (*College of William and Mary, Williamsburg, VA*); *Jian-Ping Chen* (*Thomas Jefferson National Accelerator Facility, Newport News, VA*). The discovery and study of elementary particles in nature has always been attractive to scientists. The spin structure of a neutron is one such popular study and typically involves collisions between a high energy electron beam and a neutron target. At the Thomas Jefferson National Accelerator Facility (TJNAF) in Virginia, glass cells full of Helium-3 (^{3}He) serve as effective polarized neutron targets in its particle accelerator. A nucleus of ^{3}He has two protons and one neutron. Typically, ninety percent of a ^{3}He sample has two protons with opposite spins so that the overall spin of the nucleus is determined by the spin of the neutron. Before experiments can begin, characteristics of the cell must be measured and determined including its ^{3}He density. The purpose of this project was to describe how to measure the density of ^{3}He target cells. A laser and optics setup was used to measure how much laser light the ^{3}He would absorb within the target cell at certain frequencies and temperatures. At each temperature, the data was curve-fitted using Root, and statistically analyzed to give a density measurement. As expected, the wider the absorption, the larger the density of ^{3}He within the cell. Also, the density of the cell was larger at higher temperatures. These density measurements will be used to calculate the cell's maximum polarization, correct data measurements from the particle accelerator experiment, and help further investigate the spin structure of the neutron. In the future, improvements concerning cell alignment in the oven should be made to provide more accurate results.

Studies of a Free Electron Laser Driven by a Laser-Plasma Accelerator. *Andrea Montgomery* (*Butler University, Indianapolis, IN*); *Carl B. Schroeder* (*Lawrence Berkeley National Laboratory, Berkley, CA*). A free electron laser (FEL) uses an undulator, a set of alternating magnets producing a periodic magnetic field, to stimulate emission of coherent radiation from a relativistic electron beam. The Lasers, Optical Accelerator Systems Integrated Studies (LOASIS) group at Lawrence Berkeley National Laboratory (LBNL) will use an innovative laser-plasma wakefield accelerator to produce an electron beam to drive a proposed FEL. In order to optimize the FEL performance, the dependence on electron beam and undulator parameters must be understood. Numerical modeling of the FEL using the simulation code GINGER predicts the experimental results for given input parameters. Among the parameters studied were electron beam energy spread, emittance, and mismatch with the undulator focusing. Vacuum-chamber wakefields were also simulated to study their effect on FEL performance. Energy spread was found to be the most influential factor, with output FEL radiation power sharply decreasing for relative energy spreads greater than 0.33%. Vacuum chamber wakefields and beam mismatch had little effect on the simulated LOASIS FEL at the currents considered. This study concludes that continued improvement of the laser-plasma wakefield accelerator electron beam will allow the LOASIS FEL to operate in an optimal regime, producing high-quality XUV and X-ray pulses.

Electronic Structure of Nanowire Arrays. *Sam Ocko* (*Brown University, Providence, RI*); *Wei Ku* (*Brookhaven National Laboratory, Upton, NY*). It has recently been proposed that electrons will localize in the intersections of nanowires. This is purely a quantum effect, originating from the wave nature of electrons, as there is no attractive potential to keep them in the intersection. This phenomenon of localization is very important because it might provide the basis for a functional device which uses localization to exhibit useful properties such as ferromagnetism, anti-ferromagnetic insulation, and perhaps even superconductivity. We investigate the electronic structure of an array of nanowires using a piece of software we have written, which uses self-adaptive bi-orthogonal wavelet basis to model the electrons' wave functions. Instead of trying to solve Schrödinger's equations directly and treating the problem as an eigen-value equation, we use a functional minimization method which uses conjugate gradient and steepest descent methods. The program we have developed is easily extensible, as other systems can be applied simply through changing the energy functional, which makes our program able to model many-body effects and solve other Quantum Mechanical systems. Our

program has successfully demonstrated phenomena of localization and showed that the strength of localization is inversely proportional to the diameter of the wires. In application, a grid of nanowires could be possibly be printed on a piece of silicon, with complete control over the properties of the grid. Through properly choosing the diameter of the nanowires and the density of the grid, we could control the kinetic energy and electron interaction of the nanowires. Through modulating the gate voltage, we can tune the number of electrons in the grid. A grid of nanowires whose properties are chosen carefully might show many interesting electrical properties, including ferromagnetism, anti-ferromagnetic insulation, and perhaps even superconductivity, which we hope to investigate further.

Frequency Quadrupled DUV Laser for Ytterbium^{2+} Spectroscopy. *John Ogren* (*The University of New Mexico, Albuquerque, NM*)*; Justin Torgerson* (*Los Alamos National Laboratory, Los Alamos, NM*). In the case presented, Ytterbium^{2+} (Yb^{2+}) was being sought in a linear RF trap. In order to detect and then laser cool the Ytterbium^{2+}, the 1S0 to 3P1 transition at 252 nm was chosen due to the fast transition period of 231 ns. In order to excite this transition a laser system at 252 nm was needed that was widely tunable and had a narrow linewidth. There were no commercially produced laser systems that fulfill these requirements. The proposed solution to this problem was to frequency quadruple a commercially available Titanium-Sapphire (Ti-Sapph) laser from 1,008 nm to 252 nm. The titanium doped sapphire crystal was within a monolithic block resonator (MBR) and, when lasing, was tunable over a wide range of wavelengths (approximately 700 nm to 1,100 nm) with a linewidth of approximately 100 kHz. This provided the necessary flexibility needed for the spectroscopic and cooling applications. A Potassium Niobate (KNbO$_3$) crystal was mounted within the MBR cavity and frequency doubled the initial Ti-Sapph beam from 1,008 nm to 504 nm. The resulting beam was then doubled again using an external doubling cavity with a ß-Barium Borate crystal (BBO). Currently, 12 W from a Diode Pumped Solid-State Continuous Wave (DPSS CW) laser, operating at 532 nm, pumps the MBR which produces roughly 50 mW at 503 nm through the KNbO$_3$. As of recently, 2 mW of power has been output from the BBO. In addition, the linewidth is no more than 400 kHz and is tunable over several GHz. These excellent results encourage the use of frequency quadrupling techniques to retain the original characteristics of commercial lasers while fitting the system to the specific needs and goals of a project.

Module Alignment and Resolution Studies for ATLAS Pixel Detector Endcap A. *Ana Ovcharova* (*University of California – Berkeley, Berkeley, CA*)*; Wei-Ming Yao* (*Lawrence Berkeley National Laboratory, Berkley, CA*). Endcap A, a component of the ATLAS Pixel Detector, constitutes of 144 modules mounted onto three disks, whose centers lie on the Large Hadron Collider (LHC) beam pipe. Each module contains 47,232 rectangular pixels, which are individually connected to a readout system. When in operation, the pixels containing sufficient charge deposited by particles are read out and the obtained information is used to reconstruct the paths of particles passing through the detector. Through offline analysis of data collected from cosmic muons passing through Endcap A, the current study investigates the relative alignment of the modules using the areas of overlap between adjacent modules. The method used is parallel to the one used in a previous study of the alignment, however, the current results incorporate masking of noise identified on Endcap A in order to determine more precisely the resolution of the detector. The analysis involves considering the module as a rigid body with 4 allowed degrees of freedom, including translation in x, y, z local coordinates of the module and rotation around z. The parameters (alignment constants) obtained in this manner indicate quantitatively the deviation of the position of each module, relative to an adjacent module, from the nominal detector geometry. The alignment constants are determined by examining the mean distance between the actual positions of clusters on one module and their expected positions as seen from an adjacent module. Comparing the values of the parameters to these obtained by surveying the geometry of Endcap A during assembly shows good agreement. Using the obtained alignment constants, the values of the mean distances are recalculated. The resolution obtained by plotting the recalculated values is 16.5 ± 0.2 µm and 118 ± 1 µm in short and long pixel dimension respectively. Resolution varies according to the number of pixels that are triggered by a passing particle. For two pixels triggered simultaneously, the resolution is 13.8 ± 0.3µm, compared to 14.7 ± 0.4 µm for a single pixel. This method has proven itself efficient with the limited data available. When ATLAS is in operation in 2008, more data will provide sufficient statistics to increase the accuracy of the results.

Development of Integrated PV Reporting System. *Mariano Padilla* (*Fullerton College, Fullerton, CA*)*; Willem Blokland* (*Oak Ridge National Laboratory, Oak Ridge, TN*). The Spallation Neutron Source (SNS) at Oak Ridge National Laboratory is a state of the art accelerator-based neutron source. Neutron-scattering research helps develop new materials for superconductors, magnets and plastics. SNS uses a hydrogen ion pulse beam to bombard a mercury isotope target to produce the neutrons. Operators control the accelerator complex by using console screens that can display and set Process variables (PV) from the Input/Output Controller (IOC) devices. Reports on the statistics of the accelerator operation are needed to evaluate the performance of the accelerator. Providing time sensitive and accurate reports of the overall health of the accelerator in an automated, efficient and intuitive manner is an important necessity. The reporting system requirements are to provide an intuitive multi-platform and web-browser based user interface, integration with Oracle, e-mail systems and Portable Document Format (PDF) generation. The reporting system provides the user with a web-based interface to setup specific PVs to acquire, how to process, and how to publish the results. An integrated reporting system is developed using PHP, Java, Javascript, Java Server Pages (JSP) and Business Intelligence and Reporting Tools (BIRT) for ECLIPSE Integrated Development Environment (IDE). The Oracle database already in production use at SNS is the primary storage location for the data collected from the PV's at a rate up to 1 Hz. The integrated reporting system will provide physicists, operators and engineers with a simple platform to monitor, analyze, and report on the operation of the SNS accelerator.

HHFW Propagation and Heating in NSTX. *Jeffrey Parker* (*Cornell University, Ithaca, NY*)*; Cynthia Phillips,* (*Princeton Plasma Physics Laboratory, Princeton, NJ*). Recent experiments on the National Spherical Torus Experiment (NSTX), a fusion research device, show that the high harmonic fast wave (HHFW) core heating efficiency depends on the antenna phasing and plasma conditions. Power losses in the edge due to rf sheath formation or other parasitic absorption processes could occur if the waves propagate nearly parallel to the wall in the edge regions and intersect nearby vessel structures. To investigate this possibility, the 3D HHFW propagation in NSTX has been studied both analytically and numerically with the ray tracing code GENRAY. Initial calculations show that for certain values of the launched parallel wave number and magnetic field, the waves in NSTX are launched at a shallow angle to the vessel wall. In contrast, for ion cyclotron radio frequency (ICRF) heating in the Alcator C-Mod device at MIT or the not yet built ITER test reactor, the initial ray trajectories tend to be more radially oriented. Comparisons of the GENRAY results with 2D TORIC full wave simulations for the power deposition will also be discussed.

Search for Scintillators in Barium Compounds: Europium Doping of Barium Titanates and Barium Zirconates and Cerium Doping of Barium Gadolinium Halides. *Shameka Parms* (*North Carolina Agricultural and Technical State University, Greensboro, NC*)*; Stephen Derenzo* (*Lawrence Berkeley National Laboratory, Berkley, CA*). Scintillators are most commonly known in the world of medical imaging for their role in detecting radiation emitting from the body. They are also used to detect radiation from dangerous sources; providing security for American citizens. As security issues becomes more important, the demand on the research team increases and the push to develop new and improve existing radiation detectors speeds up. The High Throughput Synthesis and Characterization Facility (HTSCF) allows for the researchers to increase production and screening of possible scintillators. Several scintillators are currently being used in industry, however more ideal scintillators are needed to meet growing concerns. The goal is to find dense, highly luminous scintillators exhibiting fast decay times. In this manuscript we report the results of this high throughput search for scintillators in the following families: Ba-Ti-O, Ba-Zr-O, and BaGdX$_4$ (where X= Cl, Br, and I). Three new scintillators were found during this search but further work needs to be done on these compounds.

Construction of a Monitoring System for the Solenoidal Tracker At RHIC (STAR) Forward Meson Spectrometer (FMS). *Shawn Perez* (*State University of New York at Stony Brook, Stony Brook, NY*)*; Les Bland* (*Brookhaven National Laboratory, Upton, NY*). The Forward Meson Spectrometer (FMS) at Brookhaven National Laboratory, consists of a matrix of lead-glass bars viewed by photomultiplier tubes that surround the colliding beam axis. The FMS detects the two photons associated swith the decay of a p0 meson, or other photons, electrons or positrons produced in the collisions. The pseudo rapidity -ln(tan(σ/2) dependence of particle production can be analyzed to explore parton distributions within the proton. We are currently

designing an LED light pulsing system which will be used to monitor the performance of these 1264 lead-glass detectors. Using Very High Speed Integrated Circuit (VHSIC) Hardware Description Language (VHDL) to program the Field Programmable Gate Array (FPGA) via the Xilinx ISE WebPack development environment, the goal is to have the LED Panel mimic events generated from the proton–proton collisions by pulsing different patterns of light with amplitude control into the FMS. The aspect of this project that I have been assisting with is the PC Board design, which integrates the electronic components with the necessary circuitry and mechanics for the monitoring system to function. The software required for this design are Microsoft Office Visio 2007 to generate the block diagram of the processes between the electronics, Cadence OrCAD Capture Schematic to represent the systems circuitry, and PADS — PCB 2007 which is the PC board layout tool manufactured by Mentor Graphics. The LED monitoring system once completed, will provide a means of testing the FMS and monitoring its performance during RHIC operations.

Simulating Beam Passage Through the Injection Chicane of the Spallation Neutron Source. *Matthew Perkett* (*Denison University, Granville, OH*)*; Jeff Holmes* (*Oak Ridge National Laboratory, Oak Ridge, TN*). The Spallation Neutron Source (SNS) is an accelerator-based neutron source that will become the most powerful device of its kind when full power of 1.4 MW is achieved in 2009. Such a powerful source has a correspondingly small tolerance for uncontrolled beam loss, which leads to activation of the facility and longer maintenance times. To meet radiation requirements at such high energies, only 1/10,000 of the particles can be lost due to collision with the beam pipe. According to recent measurements, the area with the worst beam loss is in the injection chicane and beam dump line. Due to a structural flaw, this region will eventually need to undergo physical modification, so it is critical to accurately track the particles' paths. Previous studies have been conducted using a piece-wise symplectic magnetic field approximation, but it is now essential to track particles with greater precision using a 3D multipole expansion representation for the magnetic field. To achieve this, a large portion of time was devoted to coding, testing, and adding C++ modules to the new Python wrapper of the Objective Ring Beam Injection and Tracking code (pyORBIT). PyORBIT is an accelerator physics code that utilizes a Message Passing Interface (MPI) for parallel computing capabilities, which is being developed at ORNL and used by accelerator facilities worldwide. Multiple benchmarks completed in the weeks leading to the final measurements agreed well with results calculated by hand. Tracking a Gaussian distribution of particles with SNS injection parameters from the primary stripping foil to the secondary stripping foil at a kinetic energy of 1.0 GeV resulted in a physically realized position and momentum confirming code integrity. It was found that the 3D magnetic field produced 66mm separation between H0 and H- components while the piece-wise symplectic only found a 61 mm separation. This higher separation could account for a greater difficulty getting the beam to enter the dump line and the observed high losses in that region. The next logical project will be to utilize the new modules in pyORBIT for a 3D magnetic field from the secondary foil down the dump line.

Electron Cyclotron Resonance Ion Source Interlock Design. *Francisco Ramirez* (*Yuba Community Colllege, Marysville, CA*); *Richard Pardo* (*Argonne National Laboratory, Argonne, IL*). ATLAS (Argonne Tandem Linac Accelerator System), is a series of machines whose purpose is to accelerate ions and deliver them to several targets. ATLAS has two electron cyclotron resonance (ECR) ion sources. In the event of a failure, several of the ECR source components which includes solenoids, voltage sources, radiofrequency generators, and magnets can damage themselves as well as other machinery or workers around the source. A digital interlock is to be designed so that the source cannot damage itself or humans working around it. This interlock device is a digital circuit constructed of small electronic circuits called logic gates, which are simple electrically controlled switches. This interlock circuit will receive inputs indicating water flow, temperature among other conditions and the interlock will shut down the source or the appropriate component if any failure is detected in any of these inputs. A panic button will be provided which will shut down the source in case of an emergency. In addition, a reset button will be included in the interlock system; its purpose will be to allow the interlock system to function again after a failure has occurred or the panic button has been pressed. This interlock is to be designed in two different ways, TTL (Transistor-Transistor Logic) and Relay logic. This device's TTL circuit is still being designed, having its frame and part of its relay logic already built.

Analysis of Nuclear Semi-Inclusive Deep Inelastic Scattering Events for Charged Pions Using FORTRAN. *Bryan Ramson* (*Howard University, Washington, DC*); *Kawtar Hafidi* (*Argonne National Laboratory, Argonne, IL*). Because of the nature of the strong interaction, it is impossible to directly observe free quarks. Therefore their fundamental properties must be studied through the results of deep-inelastic scattering of electrons off stationary nuclei. The Continuous Electron Beam Accelerator (CEBA) at the Thomas Jefferson National Accelerator Facility (JLab) provides an electron beam of sufficient energy (5.014 GeV) to study such reactions. The electron beam was used on targets of deuterium, carbon, iron, and lead. Particles produced in the reactions were detected by the CEBA Large Acceptance Spectrometer (CLAS) and analysis of the data is being conducted through collaboration of teams from JLab and Argonne National Laboratory. One area of analysis is the production of pions in the nuclear medium and the relationship that their production have with the properties of quark propagation in the nuclear medium. The analysis was not completed.

Automation of the Vacuum System along the Advanced Penning Trap Beam Line. *Layra Reza* (*University of Texas at El Paso, El Paso, TX*); *Guy Savard* (*Argonne National Laboratory, Argonne, IL*). A key component in the Canadian Penning Trap (CPT) mass spectrometer, located in the Argonne Tandem-Linear Accelerator System, is an Advanced Penning Trap (APT) filled with gas, the purpose of which is to purify an ion sample before mass measurements. The APT is one of few components where gas is required; however, high precision mass measurements must take place in an ultra high vacuum (UHV) environment, including the APT, to avoid contamination of the ions. An UHV environment is required continuously, even when operators are not present. Then, the goal of the project is to have complete automation of the APT beam line in a way that is fast and error free. The achievement of high vacuum involves a vacuum system composed of ion and thermocouple gauges, mechanical and turbomolecular pumps and pneumatic and solenoid valves. These components can be automated with the use of a Programmable Logic Controller (PLC). To achieve automation in the APT experimental setup, several steps need to be completed. First, a procedure for the safe operation of all the components has been created, a detailed list of components has been constructed, and the missing parts have been ordered. Moreover, a program in ladder logic mode has been written to control the system and avoid both operator and instrumental errors that might damage the system or its components. The project will continue until all new components are installed and wired into the PLC.

Roughness Analysis of Variously Polished Niobium Surfaces. *Guilhem Ribeill* (*North Carolina State University, Raleigh, NC*)*; Charles Reece* (*Thomas Jefferson National Accelerator Facility, Newport News, VA*). Niobium superconducting radio frequency (SRF) cavities have gained widespread use in accelerator systems. It has been shown that surface roughness is a determining factor in the cavities' efficiency and maximum accelerating potential achievable through this technology. Irregularities in the surface can lead to spot heating, undesirable local electrical field enhancement and electron multipacting. Surface quality is typically ensured through the use of acid etching in a Buffered Chemical Polish (BCP) bath and electropolishing (EP). In this study, the effects of these techniques on surface morphology have been investigated in depth. The surface of niobium samples polished using different combinations of these techniques has been characterized through atomic force microscopy (AFM) and stylus profilometry across a range of length scales. The surface morphology was analyzed using spectral techniques to determine roughness and characteristic dimensions. Furthermore, electrical impedance spectroscopy (EIS) was used to investigate the electrical properties of the niobium-acid interaction during electropolishing. Experimentation has shown that the spectral method is a valuable tool that provides quantitative information about surface roughness at different length scales, and has explored the use of EIS in electropolishing. It has demonstrated that light BCP pretreatment and lower electrolyte temperature favors a smoother electropolish. These results will allow for the design of a superior polishing process for niobium SRF cavities and therefore increased accelerator operating efficiency and power.

Calibration of the Camera of the LSST. *Andrew Scacco* (*University of Colorado, Boulder, CO*)*; David Burke* (*Stanford Linear Accelerator Center, Stanford, CA*). The camera of the Large Synoptic Survey Telescope (LSST) is analyzed theoretically using the ZEMAX optical design software. The purpose of this analysis is to have a theoretical model for the testing and calibration of the optics before they are installed in the telescope. The most effective way to perform this testing and calibration is also investigated. The calibration of the lenses and

sensors in the telescope will be performed using either a highly focused laser beam or a filtered quartz lamp with a monochromator, enabling very precise measurements to be made. The image the light source produces on the focal plane of the camera will be compared to the image predicted by the ZEMAX software and the optics and sensors for the camera will be adjusted until the desired agreement is reached. The minimal size of the spot produced by the light source is determined for a large sampling of angles and locations on the focal plane. A spot size that matches the spot size of the point spread function (PSF) of the telescope can be produced for light that strikes the focal plane at its center or for light that strikes the focal plane parallel to the optical axis of the camera, but not for light that strikes the focal plane off center at a significant angle. This work is a starting point for the testing and calibration of the LSST camera, which will be implemented and modified as necessary as the camera is built, assembled and tested.

Super-Hydrophobic Behavior on Nano-Structured Surfaces.
DANIEL SCHAEFFER (*Brigham Young University – Idaho, Rexburg, ID*); *JOHN T. SIMPSON* (*Oak Ridge National Laboratory, Oak Ridge, TN*). Super-hydrophobic behavior has been observed in various natural occurrences such as the leaves of the lotus plant and has been thoroughly studied over the past few years. Water repellant properties of water drops on uniform arrays of vertically aligned nano-cones were investigated to determine the highest achievable contact angle (a measure of water drop repellency), which is measured from the reference plane on which the drop sits to the tangent line of the point at which the water drop makes contact with the reference plane. At low aspect ratios (height versus width of the nano-cones), surface tension pulls the water into the nano-cone array, resulting in a wetted surface. Higher aspect ratios reverse the effect of the surface tension, resulting in a larger contact angle that causes water drops to roll off the surface. Fiber drawing, bundling, and redrawing are used to produce the structured array glass composite surface. Triple-drawn fibers are fused together, annealed, and sliced into thin wafers. The surface of the composite glass is etched with H_2O:NH_4F:HF etching solutions to form nano-cones through a differential etching process and then coated with a fluorinated self-assembled monolayer. Cone aspect ratios can be varied through changes in the chemistry and concentration of the etching acid solution. Super-hydrophobic behavior occurs at contact angles >150° and it is predicted and measured that optimal behavior is achieved when the aspect ratio is 4:1, which displays contact angles =175°. Super-hydrophobic behavior on uniform arrays of vertically aligned nano-cones demonstrates synthetic fabrication of super-hydrophobic surfaces is genuinely achievable by this process.

Validating the Computer Simulation of the Effects of Secondary Neutrals on the Motional Stark Effect Diagnostic Gas-Filled-Torus Calibration. *WILLIAM SCHUMAKER* (*Lawrence Technological University, Southfield, MI*); *HOWARD YUH* (*Princeton Plasma Physics Laboratory, Princeton, NJ*). The motional Stark effect (MSE) diagnostic, an important method of determining the magnetic field pitch angle in tokamak plasmas, measures the polarization angle of light emitted from injected neutral atoms that are affected by Stark splitting due to the Lorentz electric field. A common procedure of injecting a neutral beam into a gas-filled-torus with known magnetic fields in vacuum is one technique used to calibrate MSE diagnostics on many tokamak devices. The usefulness of this calibration has been limited on many installations due to anomalies in the measured pitch angles. Recently, this anomaly was explained as a consequence of beam neutrals that ionize after collisions, travel along the magnetic field lines, re-neutralize via a charge exchange, and rapidly produce emission spectra. Under certain conditions, these secondary neutrals emit hydrogen-alpha spectra that have the proper Doppler shift to pass through the MSE optical filters yet have a different polarization angle than those from the primary beam neutrals, thus contaminating the pitch angle measurement. In an effort to study these contaminations, computer code had previously been written to simulate the gas-filled-torus calibration of the MSE diagnostic on the National Spherical Torus Experiment (NSTX). To characterize the effects of secondary neutrals on the MSE gas-filled-torus calibration technique, new programming modules were written to extend the code to simulate other tokamak geometries and neutral beams. Several consistency checks involving numerical integration were meticulously performed on the modules, ensuring that they had been implemented correctly. Using these new modules, a sensitivity study involving various gas pressures, beam injection angles, magnetic field pitch angles, and system resolutions is in the process of validating the code against respective experimental data. If successful, this validation will help resolve a significant calibration issue with a major diagnostic used in current tokamak fusion research.

CMOS Monolithic Pixel Sensors with In-Pixel CDS and Fast Readout for the ILC Vertex Tracker. *TERRI SCOTT* (*New York University, New York, NY*); *MARCO BATTAGLIA* (*Lawrence Berkeley National Laboratory, Berkley, CA*). The International Linear Collider (ILC) Vertex Tracker requires detectors of new design in order to meet its physics requirements in terms of material, accuracy and readout speed. The detectors must be sufficiently thin, in order that incident particles may pass through several layers of sensors without substantial scattering. Readout should be fast enough that occupancy caused by machine-induced background does not spoil the track pattern recognition. Monolithic silicon pixel sensors provide a solution to these constraints due to their high resolution and ability to be thinned to several tens of micrometers. One detector currently under testing is the LDRD2 chip, designed and developed at the Lawrence Berkeley National Laboratory. The detector features 20 x 20 μm pixels with in-pixel charge storage for correlated double sampling, a technique by which the difference is taken between a reference and the pixel signal voltage. Half of the chip utilizes 5 x 5 μm diodes, and 3 x 3 μm diodes in the second half. To characterize its performance, lab tests were conducted using a pulsed laser and a Fe55 X-ray source. In particular, the chip was readout at several frequencies to determine the effect of the readout speed and the charge integration time on efficiency and noise. It was found that the LDRD2 chip responds to both laser pulses and incident X-rays at readout frequencies up to the highest design frequency of 25 MHz. This work is part of an ongoing R&D program at LBNL which will continue to investigate the LDRD2 and further generations of pixel sensors.

Scintillation in CF$_4$ Gas Due to the Passage of Highly Ionizing Particles. *JOHN SINSHEIMER* (*The Ohio State University, Columbus, OH*); *CRAIG WOODY* (*Brookhaven National Laboratory, Upton, NY*). The Hadron Blind Detector (HBD) in the Pioneering High Energy Nuclear Interaction Experiment (PHENIX) at Brookhaven National Laboratory's Relativistic Heavy Ion Collider (RHIC) utilizes Cherenkov radiation produced in CF$_4$ gas for the detection of electron pairs. During a RHIC collision, both electrons and many heavy particles pass through the HBD. The passage of heavy particles through CF$_4$ creates background scintillation light. A measurement of this background scintillation, in terms of photon yield per MeV deposited, will allow for better analysis of data produced by the HBD and may be applicable for other Cherenkov detectors around the world. In this study, scintillation light was produced in CF$_4$ gas using Americium-241 for an alpha particle source. As alpha particles traverse a known distance through the gas, a known portion of the total light produced is absorbed by a CsI photocathode. Photoelectrons are emitted from the CsI and then drawn in and multiplied by a triple Gas Electron Multiple (GEM) to produce a measurable signal. By measuring the gain of the GEMs and the energy each alpha particle deposits in the gas, one can compute the photon yield per MeV of deposited energy. Measurements and calculations show 110 photons produced per MeV over 4p solid angle.

Silicon Photo Multiplier for Scintillation Hodoscope. *ERIK SKAU* (*North Carolina State University, Raleigh, NC*); *STEPAN STEPANYAN* (*Thomas Jefferson National Accelerator Facility, Newport News, VA*). Photon counting is a key component in many high energy physics experiments. With the silicon photo multiplier (SiPM), a type of multi-pixel photon counter (MPPC), previous obstacles such as magnetic fields are being surmounted. Though operating at a relatively low voltage (~70V), high gain (~106) should be expected of a SiPM. The focus of this study was to determine if the efficiency of a SiPM with 1mm active area is suitable for charged particle detection in a scintillator layer, read out via green wavelength shifting fiber. A test setup was designed to study the efficiency of a Hamamatsu SiPM system. By situating a SiPM on the end of the green wavelength shifting fiber attached to a scintillator, the MPPC was able to detect the light generated by charged particles passing through the scintillators. Experiments demonstrated that the efficiency of the SiPM setup was an acceptable value. The one millimeter active area is sufficient for detecting photons from a scintillator to wavelength shifting fiber system. With the advantage of being unaffected by magnetic fields, unlike photomultiplier tubes, MPPCs may quickly become an alternative. With the diversity of newly developed MPPC available, scientists are now able to extend previous experimental boundaries.

Observing Water Uptake in NaCl Nanoparticles Using Non-Contact AFM. *MATTHEW STRASBERG* (*Cornell University, Ithaca, NY*); *ANTONIO CHECCO* (*Brookhaven National Laboratory, Upton, NY*). Aerosol particles (nano- and micron-sized particles suspended in air) affect atmospheric radiation and cloud microphysics. A correct description of their behavior is crucial to accurate climate modeling. The processes of aerosol "aging" (a phenomenon in which non-

hygroscopic particles become hygroscopic) and aerosol deliquescence (the water uptake of hygroscopic aerosols and their eventual transition to liquid state) are of particular interest. Understanding these processes may improve climate models as well as elucidate the physics of nanoscale wetting. This experiment demonstrates the use of Non-contact Atomic Force Microscopy for studying the initial stages of water uptake and eventual deliquescence of Sodium Chloride nanoparticles deposited on a silicon substrate. These exploratory studies will eventually be extended to other aerosol particles that are relevant to atmospheric science.

Assembly of a Time-Correlated Single Photon Counting Experimental Setup. SEAN SWEETNAM (*Carleton College, Northfield, MN*); RANDY ELLINGSON (*National Renewable Energy Laboratory, Golden, CO*). Recent developments in nanotechnology have created materials capable of improving the efficiency of solar cells, provided the basic photophysics involved are well understood. To properly characterize and understand the charge carrier processes which occur in nanomaterials, it is necessary to use very fast light gathering techniques, with time resolutions as small as tens of picoseconds. Time-Correlated Single Photon Counting (TCSPC) is such a technique, capable of providing sufficiently fast time resolution to resolve important process in materials by utilizing fast response mechanisms of detectors and electronic components, and by using efficient trigger timing. TCSPC also extends the range of observable photoluminescence with its long wavelength and low power detection capabilities. The goal of the work discussed in this paper is to develop a TCSPC system unique in its time resolution and range of detection. In this paper the principles and components of TCSPC are described, and the preparation of a TCSPC experimental setup is discussed, in particular noting the systematic errors encountered and their solutions. The system was run with a Tsunami Ti:Sapphire laser operating at 864–868 nm with a Si Avalanche Photodiode (APD) detector, yielding a time resolution of less than 800 ps. Emission lifetime measurements of 3.6 nm diameter PbS quantum dots with this setup yield a lifetime greater than 1300 ns; this value varied for different emission wavelengths 965–1030 nm. Because the time resolution is more than three orders of magnitude shorter than the lifetime of PbS quantum dots, it is concluded that the system is sufficiently fast for typical carrier lifetime characterization. Further development of the system will be necessary to improve the time resolution and infrared capabilities of the system; in particular the inclusion of an InGaAs APD in the system will decrease the time resolution, and increase the detection range to as far as 1,600 nm. A flexible setup permitting fast switches between the InGaAs and Si detectors will increase the usefulness of the setup by increasing the full range of sensitivity to 400–1,600 nm. Further experimentation will be necessary to determine the cause of the emission lifetime variation associated with emission wavelength.

Large Hadron Collider. BOYAN TABAKOV (*University of California – Berkeley, Berkeley, CA*); WEI-MING YAO (*Lawrence Berkeley National Laboratory, Berkley, CA*). As the Large Hadron Collider is due to start operating in 2008, final performance tests are carried out to confirm the working parameters of its components. The alignment of the middle disk of Endcap A of the Pixel Detector of ATLAS is examined using data from test runs with cosmic muons. In the data, the x and y coordinates of the points of intersection of a particle trajectory with the disks were previously recorded. Based on records for the first and last disks, the position of an expected intersection point on the middle disk is calculated. The differences Δx and Δy between the coordinates of the expected and the actual intersection points are attributed to a hypothetical misalignment. With the help of geometrical arguments, a linear transformation that uses as parameters the offsets x0, y0, and z0 and the displacements due to rotations alpha,beta, and gamma about the principal axes is developed to represent the misalignment. If the transformation is applied to the actual coordinates of an intersection point on the middle disk with the right parameter values, the actual point would be sent into the expected point. Hence, the values for the six parameters that provide the closest match between actual data and expected coordinates can be found from Δx and Δy by x^2 minimization. The preliminary conclusion is that the disk is perfectly aligned. The relatively high systematic uncertainties and x^2 values are subject to current research.

Soil Activation from Alternating Gradient Synchrotron and Booster. JULIA TILLES (*University of Massachusetts Amherst, Amherst, MA*); KIN YIP (*Brookhaven National Laboratory, Upton, NY*). At the Brookhaven National Laboratory (BNL), the soil shielding at the Alternating Gradient Synchrotron (AGS) and its Booster counterpart contains some spots that have been subjected to more radiation than others. In keeping with BNL's efforts to acknowledge the environmental

effects of the lab's operations, the soil radiation levels in those hot spots will be put on record. Protons, making up the beam of AGS and the Booster, are collided with a steel target in simulation. The three-dimensional geometry of the present beam dump of AGS and the past beam dump of the Booster, where excess beam particles were dumped, was used. The simulated radiation levels in the surrounding environment were mapped in two-dimensional plots. A Monte Carlo simulation program, developed at Los Alamos National Laboratory, called MCNPX (Monte Carlo Neutral Particles X-tended) was used. The end result is the compilation of several two-dimensional plots, each of which overlays the simulated radiation levels upon the blueprint of the respective site and plane. The information gathered will go on file for public access.

Conceptual Design for a 2 GW Inertial Fusion Energy Direct-Drive Power Reactor Employing a Mechanical Vacuum Pumping System. KELSEY TRESEMER (*George Fox University, Newberg, OR*); CHARLES GENTILE (*Princeton Plasma Physics Laboratory, Princeton, NJ*). Presented is a conceptual design for a 2 gigawatt Inertial Fusion Energy (IFE) direct-drive power reactor. The reactor operates at 5 Hz, consuming approximately 450,000 tritium-deuterium targets/day, injected at speeds greater than 100 m/s into the target chamber and uniformly illuminated by laser light, leading to detonation. Resulting post-detonation ions are directed away from the first wall of the target chamber and into equatorial and polar caches using a magnetically-induced cusp field. The reactor is designed to breed and recycle fuel through the use of breeder blankets and a fuel recovery system. To minimize target-particle interference, the chamber will be kept at less than 0.5 millitorr through the use of turbomolecular pumps (TMPs) and corresponding mechanical backing pumps. Initially, these pumps were dry-bearing TMPs, however an investigation was performed comparing bearing-based TMP's to magnetically-levitated TMPs, revealing other vacuum pump options. All pumps were evaluated based on a wide range of specifications, the most crucial being the maximum hydrogen pumping speed, greatest mean time between failure (MTBF), and the least amount of oil (if any) present in the vacuum system. Information collected from journal articles, industry, and operational TMP experience in other fusion related venues indicate that the employment of magnetically-levitated TMP's appears to be a superior vacuum pumping solution in the IFE environment. Thus, as a direct result of this research, magnetically levitated TMPs will be adopted into the IFE reactor design.

The Effects of Measurement Errors on Neutrino Angular Resolution in the IceCube Neutrino Detector. LESLIE UPTON (*Hampton University, Hampton, VA*); AZRIEL GOLDSCHMIDT (*Lawrence Berkeley National Laboratory, Berkley, CA*). The IceCube collaboration is actively pursuing neutrino detection to study astrophysical sources. These neutrinos are identified by the secondary muons detected within the IceCube detector array. The muon track is reconstructed using the information provided by the time information of Cherenkov photon illuminated digital optical modules (DOMs) within the detector. However, it is imperative to calculate how different measurement errors affect the reconstruction of the muon. A Monte Carlo simulation was developed in order to study these effects on the resolution of the muon reconstruction. The simulation, developed in ROOT, creates a muon in an array detector and uses time information from illuminated DOMs and Minuit to reconstruct the parameters of the muon without any knowledge of the original coordinates of the muon. Minuit provides precise results, with spikes around zero for the space angle between the original and reconstructed muon tracks. There are correlations between the number of illuminated DOMs, muon track length, and the angular resolution of the reconstructed track. Further work includes exploring photon statistics, energy dependence and more precise DOM information.

Application to Determine and Control Twiss Parameters of the SNS Accelerator Beam. JENS VON DER LINDEN (*University of Pennsylvania, Philadelphia, PA*); SARAH COUSINEAU (*Oak Ridge National Laboratory, Oak Ridge, TN*). The accelerator ion beam at the Spallation Neutron Source (SNS) is repeatedly focused and defocused by a series of quadruple magnets as it travels to the target to create neutrons by means of spallation. Physicists are interested in characterizing the accelerator beam in order to understand and improve the focusing and transport of the beam. Wire scans are employed to measure the traverse density profile of the beam. With a minimum of three distinct wire scans, the ion beam Twiss parameters, which characterize the phase space properties of the beam, can be determined. In this project, a Graphical User Interface (GUI) Application was developed in JAVA to automate the determination of Twiss parameters from the wire scan data files and to determine

how quadruples should be varied to change the Twiss parameters at multiple arbitrary locations. The software is coded within the XAL framework, an existing JAVA library developed at the SNS accelerator which is used for all GUI-based physics software applications. A major contribution of the JAVA GUI developed in this project is that it is generally applicable to any area of the accelerator containing a minimum of three wire scanners. Existing applications were tied to specific parts of the accelerator. Twiss results can be saved and compared through graphing and averaging. As the SNS is a high intensity accelerator which requires strict control over the beam losses, it is very important that the beam in the accelerator be transported according to the optimum design configuration. Any deviation from the optimum transport configuration can lead to beam loss that can limit the obtainable beam power in the accelerator. This application will aid in measuring the beam state at any point in the accelerator, and will subsequently allow a user to make adjustments to the beam state in order to restore the optimum configuration and ensure well controlled beam transport.

Measurements of High-Field THz Induced Photocurrents in Semiconductors. Michael Wiczer (*University of Illinois, Urbana, IL*); Aaron Lindenberg (*Stanford Linear Accelerator Center, Stanford, CA*). THz pulses have provided a useful tool for probing, with time resolution, the free carriers in a system. The development of methods to produce intense THz radiation has been slow since spectroscopists and condensed matter physicists first began probing materials with THz pulses. We have developed a method for producing intense ultra-short THz pulses, which have full width half maximum of 300 fs — approximately a half cycle of THz radiation. These intense half cycle pulses (HCPs) allow us to use THz radiation not only as a probe of the free carriers in a system but also as a source of excitation to alter a system in some way. In particular, HPCs perturb free carriers considerably in short time scales but show minimal effect to individual free carriers over long time. By exposing the semiconductor indium antimonide (InSb) to our intense THz HCP radiation, we have observed non-linear optical effects which suggest the generation of new free carriers by below band-gap THz photons. This generation of free carriers appears to be caused by an avalanche multiplication process, which should amplify the number of free carriers already in the system and then induce a current in the timescale of our THz pulse. This amplification on such a short timescale suggests the possibility of an ultra-fast detector of weak above band-gap radiation. We constructed a device which detects these currents by painting an electrode structure on the surface of the semiconductor. The currents induced across the electrodes by this avalanche multiplication process were measured and compared with other measurements of this non-linear optical process. We successfully measured THz induced currents in InSb, which indicate promise towards the development of an ultra-fast detector, and we gain insight into a possible physical explanation of the THz induced free carriers we observe in InSb.

Characterization of the Magnetic Field of a Large-Bore Superconducting Solenoid Magnet. Jack Winkelbauer (*Western Michigan University, Kalamazoo, MI*); Birger Back (*Argonne National Laboratory, Argonne, IL*). At Argonne National Lab a new type of spectrometer is being developed, the HELIcal Orbit Spectrometer (HELIOS). HELIOS utilizes a 90 cm bore superconducting Magnetic Resonance Imaging (MRI) magnet. To ensure that the magnet will be adequate for the project, the magnetic field will be mapped. Of particular importance is the field's homogeneity and axis of symmetry. To map the magnetic field in this cylindrical region (345 cm long, 90 cm diameter), an apparatus was designed and built to position a gaussmeter probe in precise cylindrical coordinates. In order to efficiently collect this data, a program was created using the graphical programming software, Labview. This field mapping data will eventually be applied to existing simulations to improve predictions.

Finding Variable Stars. Daniel Wong (*University of California – Berkeley, Berkeley, CA*); Cecilia Aragon (*Lawrence Berkeley National Laboratory, Berkley, CA*). The the Nearby Supernova Factory (SNF) seeks to observe several hundred type Ia supernovae, but their search is partially impeded by the presence of variable stars in the images they collect. To aid in their search, we tried to develop a catalog of known variable stars using their archival data, consisting of over 1 million images with 1.5 billion photometric measurements. By comparing magnitudes measured on different dates, variability could be detected and a classification could be assigned to each star. Early versions of our selection algorithm were able to detect variability in a subset of stars that we gave as input. Upon closer inspection, we found that the apparent variability in the candidates was most likely due to calibration errors, rather than intrinsic variability. To calibrate the data we supplied to our algorithm, we used the United States Naval Observatory catalog as a reference. We supposed that the difference between our instrument magnitudes (a quantity known as magi) and those listed in the catalog (known as magc to differentiate from magi) would be about constant with respect to each image. Upon reexamination, we found that a non-constant relationship existed between the difference in magnitude and magc. To describe this relationship, we developed an iterative fitting technique to be carried out separately for each image. We did not attempt to develop a physical model to describe this relationship, as an empirical understanding would have been sufficient for our variability study. To evaluate our new calibration technique, we reexamined the candidates previously selected by our algorithm. We found that many of the oddities of the original light curves were removed as a result of our new calibration technique. To see if our new technique provided consistent improvement, we compared the standard deviation in magnitude for each star caused by the original calibration technique with that of the new technique which we had developed. The reason to do this is that most stars are not variable; hence, the best calibration technique should minimize the standard deviation through all magnitude ranges. We would have considered our new technique to be a success if we could improve (i.e. decrease) the spread in all magnitude ranges. Although there was a marked improvement in the one case we examined closely, the overall improvement was not as significant. Further investigations on why this occurred should be conducted in the future.

Ohmic Heating of Gallium Arsenide Photocathodes. Matt Wood (*Fort Hays State University, Hays, KS*); Marcy L. Stutzman (*Thomas Jefferson National Accelerator Facility, Newport News, VA*). The polarized electron beam at Thomas Jefferson National Accelerator Facility (Jefferson Lab) is produced using photoemission from a gallium arsenide (GaAs) cathode. To turn a GaAs crystal into a photocathode, it must be heated to above 500°C to clean the surface, then "activated" using chemicals applied to the surface. At Jefferson Lab, the crystal is heated by conduction using commercial heaters; however, because of a lack of resources, universities and smaller government labs must heat crystals through ohmic heating by passing current through the crystal. These labs have not been successful in using special strained GaAs crystals that can provide high polarization. The goal of this project was to determine if ohmically heating high polarization GaAs crystals can produce a quantum efficiency that is comparable to crystals heated conductively. The two heating methods were compared in the same vacuum conditions, and the effectiveness of each was assessed by monitoring the photoemission from each cathode. The resistive heating method was found to be comparable to the conductive heating method for high polarization crystals. As expected, the vacuum quality and thermal conductivity are the likely reasons that other labs have not had success with high polarization crystals. This suggests that in order to produce high polarization electron beams, other labs need to focus on improving the quality of their vacuum.

Electron Cloud Modeling for the Positron Damping Ring Wigglers in the International Linear Collider. Jennifer Yu (*Cornell University, Ithaca, NY*); C.M. Celata (*Lawrence Berkeley National Laboratory, Berkley, CA*). The positron-electron collisions in the ILC must be simple, clean, and precise. However, the presence of an electron cloud in the positron damping ring would lead to a positron beam with unfavorable behavior and position. The research conducted for the Center of Beam Physics looked at the formation of the electron clouds using computer simulations, specifically in the wiggler section of the ring. The wiggler section is two hundred meters of magnetic dipoles that produce vertical fields of alternating sign. In the wigglers, the accelerated beam emits intense synchrotron radiation. When it hits the chamber walls, the radiation initiates the build-up of electrons. These primary electrons, trapped in the wigglers, also hit the vacuum walls and make even more electrons, called secondary electrons. The secondary electrons also produce electrons as the positron beam attracts the electron cloud and swings it to the opposite wall. The electron cloud can send the beam off track so the beam misses its collision or worse, hits the chamber walls. The electrons can also give the positron beam energy, which can make it harder to focus the beam. The research conducted tracked the formation of the electron clouds using Posinst, a benchmarked 2D code, and Warp, a code with both 2D and 3D capabilities. A 3D code is needed to follow the electrons in the changing magnetic fields of the ILC wiggler. However, as a first step, the research aimed to match the results of 2D Posinst-like Warp with Posinst, which has been checked with numerous electron cloud experiments and against other benchmarked codes. The agreement of 2D-Warp and Posinst shows the accuracy and precision of Warp and will lead to electron cloud modeling with 3D Warp. The computer

simulations in 3D Warp will track the electron cloud in the ILC wiggler and will help find limiting parameters for the cloud.

Effect of Pipes in a Tank to be Purged of Oxygen. *Laura Zantout (University of Minnesota, Minneapolis, MN); Stephen Pordes (Fermi National Accelerator Laboratory, Batavia, IL).* To produce a viable 50-kton LArTPC (liquid argon time projection chamber), as proposed, the liquid argon within must reach a purity level of 10 ppt oxygen. The purpose of the Daisy experiment is to determine if pipes used as structural components inside this detector would trap air and cause virtual leaks. A 2-cubic-foot tank filled with 50 half-inch diameter pipes was used to simulate the structure that would be within the detector. As argon flowed through the tank, oxygen levels were monitored both on the gas outlet and within using monitors of various sensitivities. Several variations were run: with an internal fan, without a fan, and with one end of the pipes capped. Plots of percent oxygen vs. time for all of the runs were fit well by perfect mixing equations. This suggests that oxygen was not trapped in the pipes, but instead diffused out quickly. Other turbulence (such as convection currents) may have also accounted for some mixing, especially in the capped run. It appears that building a structure of much longer pipes will not contaminate the liquid argon inside a detector via virtual leaks, as long as mixing through diffusion is given time to progress, or sped up by a fan.

Research and Development of Solution SAXS Data Analysis Methods. *Juliette Zerick (University of Mary Washington, Fredericksburg, VA); Kenneth Frankel (Lawrence Berkeley National Laboratory, Berkley, CA).* The analysis of solution small angle X-ray scattering (SAXS) data is made difficult by the lack of vigorous and open source data reduction tools. Although singular value decomposition (SVD) has proven effective and practical in the analysis of SAXS data, it is not robust to experimental noise. Additional techniques must be utilized to extract meaningful results from a dataset; autocorrelation tests, chi-square tests for goodness of fit, visual inspection, and other methods are used for this purpose. However, little research has been done on the mathematical justification for their use. In this paper, the soundness and effectiveness of the application of these methods to experimental data were evaluated. It was found that all methods used were either unsupported by the mathematics or were insufficient to resolve the number of components in solution. Therefore, in an attempt to reduce the effects of experimental noise on the application of SVD, two new "pruning" methods were developed and tested on experimental SAXS data. By "pruning" from the dataset points that exhibited a small signal-to-noise ratio, or contained experimental error beyond a defined threshold, the application of SVD to the truncated dataset resolved the number of components in solution with greater accuracy than previous methods alone. The research and development of these methods were performed in order to enhance currently-used techniques and assist in the data analysis of two projects: Structural Cell Biology of DNA Repair Machines (SBDR) and Molecular Assemblies, Genes, and Genomics Integrated Efficiently (MAGGIE). The preliminary results of this undertaking will be released to the SAXS community to spur development of better data analysis methods. The software implementation of the recommended methods will be released under the GNU General Public License (open source), available at the Structurally-Integrated Biology for Life Sciences (SIBYLS) beamline website.

Simulating Multipacting in Tapered Waveguides Using Xing RK4. *Dan Zou (University of Wisconsin – Madison, Madison, WI); Haipeng Wang (Thomas Jefferson National Accelerator Facility, Newport News, VA).* Radio frequency (RF) waveguides propagate and couple high RF power that is used to accelerate charged particles over short distances. Under certain resonant conditions in the waveguide, this high power can lead to undesirable discharging, or multipacting, consuming the RF power and possibly damaging the waveguide. One method of preventing multipaction is by avoiding these specific resonant conditions, which are most efficiently found by using appropriate computer simulation software. Xing RK4, written in FORTRAN, is one such software, though originally limited to rectangular waveguide analysis. The purpose of this study was to port Xing RK4 to C++, then to expand it to analyze multipaction in tapered waveguides. Expansion of Xing focused primarily on deriving appropriate empirical and analytic formulae for the electromagnetic (EM) fields within tapered structures. The majority of other necessary functions were inherited from the original code, slightly modified to accommodate the new geometry. EM field implementation was not completed due to time constraints and complexity of the analysis. Once completed, however, Xing RK4's new capabilities will allow scientists to determine the resonant conditions to avoid when using tapered RF waveguides and to benchmark other

simulation codes. Additional accuracy may be achieved through further fine-tuning of the analytic formulae.

1-D Simulations of Metallic Foams Heated by Ion Beam Energy Deposition. *Alex Zylstra (Pomona College, Claremont, CA); John Barnard (Lawrence Berkeley National Laboratory, Berkley, CA).* One dimensional simulations of various initial average density aluminum foams (modeled as slabs of solid metal separated by low density regions) heated by volumetric energy deposition have been conducted with a Lagrangian hydrodynamics code, DISH (Deeply Simplified Hydrodynamics by R. More), using a van der Waals equation of state (EOS). The resulting behavior has been described to facilitate the design of future warm dense matter (WDM) experiments. Deposition in the simulations ranges from 15 to 30 kJ/g total energy and from 0.075 to 0.9 ns total pulse length, resulting in temperatures from 1 to 4 eV. The peak temperature reached in the foam was found to be greater than linearly dependent on the energy deposition, increasing with increasing density to a peak at approximately 75% solid initial average density and decreasing rapidly with increasing density beyond that peak, and essentially independent of the pulse length for pulse lengths shorter than the macro hydro time, approximately 1 ns. The peak pressure increases rapidly with increasing density, increases with increasing energy, and is roughly independent of the pulse length for lengths on the order of the macro hydro time. For pulse lengths of approximately the hydro time for one slab of the foam (~0.1 ns) an increase in the maximum pressure is observed. The expansion velocity is proportional to the density for pulses on the order of the hydro time of one slab of the foam; for longer pulses a dramatic increase in the expansion velocity is observed at approximately 75% solid density initial. We find that the homogenization time of the foam increases with increasing pulse length, and the remaining inhomogeneities in the homogenized foam decrease with increasing density. These results will help future experiments examine the equation of state in the WDM regime.

Science Policy

Strategic Planning for the Neutron Sciences Directorate: The Suggested Guidelines for the Content and Layout of the Annual Report. *Kelley Coffman (Vanderbilt University, Nashville, TN); Al Ekkebus (Oak Ridge National Laboratory, Oak Ridge, TN).* The Oak Ridge National Laboratory Neutron Sciences Directorate (NScD) encompasses two world-class user facilities for studying materials with neutron scattering — the Spallation Neutron Source (SNS) and the High Flux Isotope Reactor (HFIR). As the Neutron Sciences' facilities emerge into a competitive worldwide market, a need exists for outreach to the scientific community. The larger component of my project involves outreach to a variety of audiences through scientific writing and creative design. More specifically, I headed the strategic planning of several neutron sciences publications such as scientific application fact sheets, a user orientation packet, and the future annual report. An annual report highlights achievements, developments, and operations of each facility and will be a requirement of the NScD once both facilities become operational. In conjunction with my strategic planning project, I formulated suggestions for the content and layout of the publication after engaging in research methods such as benchmarking, surveying, and outlining. The first step in outlining the report involved formulating a table of contents, which required benchmarking other top neutron facilities' reports. Additionally, I interviewed and surveyed NScD staff and scientists as well as the public and internal websites to integrate the missions and priorities into my suggestions. This also resulted in an array of perspectives on which aspects of the design should be emphasized. I then compiled an outline of my suggestions for content combining both tried and unique approaches to each section such as the page lengths, the groups to consult for information in each section, and the topics to address. In addition, I designed sample layout pages to illustrate my recommendations using advanced design software. The suggestions formulated for the NScD annual report strive to bridge the need for public outreach with representing two world-class neutron facilities.

Collaboration and Implementation of Disruptive Technologies in the Emergency Response Environment (I-ReSCUE). *Carter Dedrick (University of Memphis, Memphis, TN); Donald E. Vinson (Oak Ridge National Laboratory, Oak Ridge, TN).* Emergency response operation and networks are naturally collaborative in nature; however, due to recent catastrophic events and legislation, these networks have been encouraged to become more centralized. There is ongoing research at Oak Ridge National Laboratory involving the adaptation of existing technologies to National Security solutions. The goals for my

part of the project are to describe ways in which beneficial Disruptive Technologies act as a decentralizing force within the emergency response environment on a local level, diagram the overall emergency response environment and propose a theory for an improved planning and response tool. This is accomplished through literature review, interviews, and analysis of current response tools available. Research was conducted to develop theory for an interactive emergency response program to be constructed on an existing platform and explore how Disruptive Technologies can best be utilized. Compartmentalization of resources within emergency response cultures result in slow growth of innovations within the emergency response environment. Research into the connections of these networks is mapped and the ideal response network discussed. Requirements include management of interagency agreements, the ability to expand vertically and horizontally as needed for response to changing events, and include non-profit representatives. Collaboration in emergency response networks is currently carried out, and can be mapped on vertical as well as horizontal axes. The vertical collaboration axis begins with the local EMA (emergency management agency) and expands upward as events grow larger to include the state and Federal EMA. The horizontal collaboration axis shows the relationship between nonprofit and other NGOs (non-governmental organizations) to the vertical collaboration within the public sector EMA. Collaboration is best facilitated by policies that allow responders to create connections as opposed to those that merely limit abilities. Disruptive Technologies must be embraced and utilized on a wide and daily basis in order to be useful in the event of an emergency.

Impact Assessment of Plug-In Hybrid Electric Vehicles.

ALEXANDER EXARHOS (*Grinnell College, Grinnell, IA*)*; MICHAEL KINTNER-MEYER* (*Pacific Northwest National Laboratory, Richland, WA*). Plug-in hybrid electric vehicles (PHEVs) have been considered and analyzed as a means of reducing dependency on foreign petroleum and reducing greenhouse gas emissions. PHEVs store energy supplied by the power grid in an onboard battery to support the vehicle to drive only on electricity or in an electric-assist mode that utilizes both the electric motor and the internal gasoline engine. PHEVs overcome the limited driving range shortcoming that limited the market acceptance of electric vehicles in the 90s by using the gasoline engine for distances that exceed the battery's driving range. A brief study was conducted that analyzed the impacts of PHEVs on the gasoline consumption and CO_2 emissions in the US. The analysis was based on a spreadsheet tool that models the effects of a set of PHEV penetration scenarios with varying market shares (25, 50, and 100 percent) of the light duty vehicle fleet (i.e., cars, pickup trucks, vans, sport utility vehicles). The same tool was also used to explore policy options that would achieve a stabilization of CO_2 emissions in the Northwest. The results showed that PHEVs could have a significant impact on reducing CO_2 emissions and on reducing gasoline consumption. This tool also showed that emissions and consumption could be stabilized if the fleet average fuel economy were to grow at the same rate as the fleet, resulting in 34 miles per gallon by 2050 if started in 2018. Similarly, CO_2 emission stabilization can also be achieved with a PHEV penetration trajectory that accurately off-sets the incremental emissions from a growing future vehicle stock. The potential of PHEVs to reduce gasoline consumption and harmful emissions emphasizes the environmental benefits of this emerging technology, and it sets the stage for future research into the technical problems facing PHEVs.

Evaluation of Compliance with Safe Standard Practices and Uses of Class II Biological Safety Cabinets Used in Biosafety Level 2 Laboratories.

PETER HOANG (*Dominican University of California, San Rafael, CA*)*; LESLIE A. HOFHERR* (*Lawrence Livermore National Laboratory, Livermore, CA*). Biosafety Level 2 (BSL-2) laboratories contain operations involving biological risk agents such as infectious microorganisms associated with various human diseases that are of moderate potential hazard to lab personnel and the environment. When working with these agents, there is a risk from aerosol or splash production of biohazardous materials that can contaminate laboratory personnel, their work area, and the environment. Safety regulations, requirements, and guidelines developed by the Center for Disease Control & Prevention (CDC) and the National Institute of Health (NIH) recommend the use of physical containment devices to help minimize such exposure during BSL-2 operations. Biological safety cabinets (BSC) are one of the most effective primary barriers for such hazards. Based on these national documents along with the biosafety requirements and guidelines contained in the Lawrence Livermore National Laboratory (LLNL) Environmental Safety and Health Manual (ES&HM), a compliance survey was created to assess how well LLNL personnel implement appropriate BSC safety etiquette and procedures.

The survey's questions consisted of topics chosen at the discretion of the surveyor. Eight researchers from eight of the forty-seven LLNL BSL-2 facilities were interviewed and their operations and workplaces were evaluated. All eight of the operations reviewed in this assessment had at least one or more practices or controls that deviated from the guidelines or requirements stated in the LLNL and national safety documents of both the CDC and NIH. The most common issues identified included improper personal protective equipment (PPE) decontamination and disposal, lack of maintenance of the ultraviolet lamp, lack of a proper sharps container inside the BSC, lack of procedure for checking airflow, and lack of High Efficiency Particulate Air (HEPA) filter maintenance. The findings of this survey indicate that enhanced worker training and additional assurance evaluations along with more detailed guidelines in the ES&HM may be warranted. The survey results in the areas of decontamination and maintenance may serve to guide more detailed assessments in the future to identify additional actions that may help improve BSL-2 safety practices and procedures while using a BSC. This work was performed under the auspices of the U.S. Department of Energy by University of California, Lawrence Livermore National Laboratory under Contract W-7405-Eng-48.

Lifecycle Determination for Industrial Hygiene Portable Safety Equipment.

JORDAN KLINGSPORN (*University of Wisconsin – Green Bay, Green Bay, WI*)*; GORDON MILLER* (*Lawrence Livermore National Laboratory, Livermore, CA*). A policy for industrial hygiene instrument lifecycle assessment is necessary to ensure quality equipment is maintained, sufficient instrument capability is provided, and maintenance and replacement costs are not excessive. Such a policy is needed to ensure laboratory resources are optimized during times of increasing fiscal constraints and high regulatory scrutiny. While formalized lifecycle assessment guidance and strategies are common for facility structures, capital equipment, and consumer products such as automobiles, home electronics, and appliances, such guidance is not readily available for smaller scale equipment such as portable safety instrumentation. A combination quantitative and qualitative approach was investigated to develop a defensible and transparent basis for performing lifecycle assessments to support an industrial hygiene instrument replacement policy. Several factors were compiled to aid in predicting the lifetime of an instrument using instrument performance history reviews, operational conditions, recommendations from manufacturers, and feedback from equipment users throughout the Department of Energy complex. Some of the primary factors that were found to impact instrument lifetime are: changes in equipment technology, cost effectiveness of replacement compared to repair, availability of parts and factory calibration services, total cost of replacement, performance history, and equipment replacement costs being justified by increased efficiency and/or capability. Utilizing the compiled data, a spreadsheet tool was developed to apply the lifetime factors to prioritizing current instrumentation for replacement, as well as determine longer-term replacement budget strategies. The instrument lifetime factors and policy developed by this effort were nominally intended for portable industrial hygiene instrumentation, but they could be readily applied to instruments with different functions. The Lawrence Livermore National Laboratory Industrial Hygiene Instrument Laboratory will use these factors, tools, and policy drafted by this research as part of their operational strategy to help ensure quality safety equipment is maintained while minimizing costs. This work was performed under the auspices of the U.S. Department of Energy by University of California, Lawrence Livermore National Laboratory under Contract W-7405-Eng-48. UCRL-ABS-233244.

Best Educational Practices for Modern Day Teachers.

MEGAN REBEN (*St. Joseph's College, Patchogue, NY*)*; GAIL DONOGHUE* (*Brookhaven National Laboratory, Upton, NY*). For as long as there have been teachers, there have been those who sought the best ways to educate our children. In order to stay ahead in this changing world, it is increasingly important to provide quality education to as many students as possible. In order to find or develop the most effective method of introducing educational material to students at the elementary level, this study intends to use peer reviewed articles and subsequent results concerning the types of teaching methods in question. By referencing the conclusions of previously published studies, the results are meant to show a complete and accurate detailing of each of the methods strong and weak points. Presently, the results are not conclusive due to several factors, including cost effective versus educational effectiveness issues. The success of any particular method is interpretive because the techniques used to teach are not solely judged by their ability to allow the student to retain the most knowledge. Some examples of practices that are proven to

give students an edge up are cooperated learning and even outreach programs like the one Brookhaven National Laboratory provides. The purpose of this study is to uncover the most effective method to be used in classrooms which will allow each and every student to reach his or her full potential. That being the case, it is important to develop some kind of progress report to correlate the techniques used and the advancement of the students.

Successful Integration of Staff and Users into Oak Ridge National Laboratory's Neutron Sciences Directorate. *Jennifer Stinnett* (*University of Tennessee, Knoxville, TN*)*; Chrissi Schnell* (*Oak Ridge National Laboratory, Oak Ridge, TN*). For any scientific research laboratory to become one of the foremost facilities, it is crucial to attract and retain the best employees. To do this, a laboratory must be attractive to employees not only within their field of research, but also with the way they present their community and its resources. Oak Ridge National Laboratory (ORNL) is no exception. My project involves researching and exploring different methods to help attract new staff and users and to then help integrate them into ORNL, and more specifically to my project, the Neutron Sciences Directorate (NScD). Previously, the NScD was relying on a website that provided inadequate information to incoming employees and visitors. The scope of information provided was minimal and the coverage was lacking. As part of my project, I surveyed, gathered and organized new information, and enhanced the content of the present information. Based on the needs expressed by new staff, the information ranged from how to get a social security card to a list of local movie theaters. The information collected was vast and varied, but was all relevant and informative, and was information of interest to new and/or international persons. My project also consisted of building a new web community for NScD employees. For this I used Publisher, Photoshop and PowerPoint. The community, tentatively entitled "Friendship Web" allows employees to connect to one another outside the office. Employees voluntarily register and create their own page; complete with a picture, contact information, and any optional personal information they wish to include. They are then able to select their interests/talents/activities from a database, which are also listed on their page. This allows NScD employees to log on and find colleagues with shared interests; helping foster stronger relationships and a healthier work environment. It is also crucial to helping new employees feel welcome, and can prove resourceful when needing to locate employees who speak certain languages for translation purposes. The final part of my project consists of photographically documenting the NScD. Upon completion of this portion, new organization charts will be constructed, and locating and identifying people will be easier than the current method, which is solely on the internet and is not comprehensive. My project makes the transition into ORNL's NScD seamless, and also creates a better work environment for those already employed.

Waste Management

Construction of a Functional Replica of the Transfer Chute in the Clean Transfer Area of the Alpha-Gamma Hot Cell Facility. *Eric Becker* (*University of Illinois, Urbana-Champaign, IL*); *Donal Preuss* (*Argonne National Laboratory, Argonne IL*). The Clean Transfer Area (CTA) is part of the Alpha-Gamma Hot Cell Facility (AGHCF) where 7-gallon drums containing Remote-Handled Transuranics (RH-TRU) are transferred to 30-gallon drums. The drums are lined with plastic pouches that are subsequently vacuum sealed and tightly covered for transportation off-site following the AGHCF-OPS-305 RH-TRU 30-gal Waste Drum Outloading procedure. The CTA is radioactively contaminated, however, making practicing the Waste Drum Outloading procedure in it unsafe. Workers may receive more than the allowed radiation dosage if they are in the CTA for long periods of time. The purpose of building a replica of the transfer chute in the CTA is to provide a safe environment for the radiation workers to practice the Waste Drum Outloading procedure while still using an accurate model of the structure they will be working with. The transfer chute in the CTA was measured both from the inside and outside using a sextant. The controlled area where the replica was constructed was also assessed for usable parts and existing structures. The final step in acquiring the necessary measurements was researching the parts that needed to be ordered from outside sources. The replica design was then drawn and reviewed by the Assistant Facility Manager of the AGHCF, in addition to a Cognizant Systems Engineer. The specified materials were then ordered, both from outside vendors and from the Argonne Central Shops. A procedure outlining the necessary materials, tools, and assembly steps was written to equip the persons responsible to complete the replica accurately, efficiently, and safely. Once the materials arrived, they were moved to the assembly area where the

replica would be constructed. Construction proceeded as outlined in the assembly procedure, and completed on-time (July 16, 2007), allowing the radiological workers time to practice the operation before the actual outloading takes place. The execution of the assembly procedure was also documented in order for later disassembly and reassembly to take place.
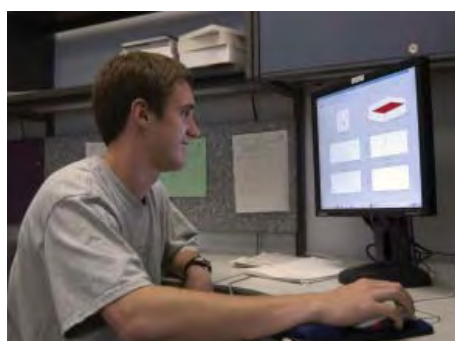
Scientists at the Department of Energy Office of Science's Ames Laboratory seek solutions to energy-related problems through the exploration of chemical, engineering, materials and mathematical sciences, and physics.

Established in the 1940s with the successful development of the most efficient process to produce high-purity uranium metal for atomic energy, Ames Lab now pursues much broader priorities than the materials research that has given the Lab international credibility.

Responding to issues of national concern, Lab scientists are actively involved in innovative research, science education programs, the development of applied technologies, and the quick transfer of such technologies to industry. Uniquely integrated within a university environment, the Lab stimulates creative thought and encourages scientific discovery, providing solutions to complex problems and educating tomorrow's scientific talent.

Ames Laboratory is located in Ames, Iowa, on the campus of Iowa State University. Iowa State's 2,000-acre, park-like campus is home to more than 25,000 students. Ames is approximately 30 minutes north of Des Moines, Iowa's capital city.

Argonne National Laboratory descends from the University of Chicago's Metallurgical Laboratory, part of the World War Two Manhattan Project. The laboratory has about 2,900 employees, including about 1,000 scientists and engineers. Argonne occupies 1,500 wooded acres in DuPage County, Illinois, about 25 miles southwest of Chicago's Loop. Argonne research falls into broad categories:

- Basic science seeks solutions to a wide variety of scientific challenges. This includes experimental and theoretical work in biology, chemistry, high energy and nuclear physics, materials science, and mathematics and computer science.
- Scientific facilities help advance America's scientific leadership and prepare the nation for the future. These facilities are used by scientists thousands of scientists and students from the U.S. and abroad. The laboratory is also home to the Advanced Photon Source, the Center for Nanoscale Materials, the Intense Pulsed Neutron Source, and the Argonne Tandem Linear Accelerator System.
- Energy resources programs help insure a reliable supply of efficient and clean energy for the future. Argonne scientists and engineers are developing advanced batteries and fuel cells, as well as advanced electric power generation and storage systems.
- Environmental management includes work on managing and solving the nation's environmental problems and promoting environmental stewardship.
- National Security has increased in significance in recent years for the nation and for Argonne research. Argonne capabilities developed over the years for other purposes are helping to counter the threats of terrorism.

Argonne's Division of Educational Programs provides workforce development for faculty and students from universities to regional K-12 schools.

Established in 1947, Brookhaven National Laboratory is a Department of Energy, Office of Science multidisciplinary laboratory managed by Brookhaven Science Associates, a company founded by Battelle and Stony Brook University. Home to six Nobel Prizes, Brookhaven conducts research in the physical, biomedical, and environmental sciences, as well as in energy technologies and national security.

Located on a 5,300-acre site on eastern Long Island, New York, Brookhaven builds and operates major scientific facilities available to university, industry and government researchers. Among those facilities are the world's newest accelerator for nuclear physics research, the Relativistic Heavy Ion Collider (RHIC), and the National Synchrotron Light Source (pictured here) where approximately 2,500 researchers use beams of light, from x-rays to ultraviolet and infrared, to study materials as diverse as computer chips and proteins. In the near future, the Center for Functional Nanomaterials will be built at Brookhaven, one of five Department of Energy centers where researchers will study materials on the scale of a billionth of a meter, or only a few atoms.

A wide variety of both basic and applied research is conducted at Brookhaven. For instance, scientists are investigating the building blocks of matter using RHIC, the roots of drug addiction and brain metabolism using positron emission tomography, the effects of space radiation on astronauts using the newly built NASA Space Radiation Laboratory, and the effects of increased carbon dioxide in ecosystems. Brookhaven researchers also develop new technologies as varied as detectors for national security and oil burners with improved efficiency.
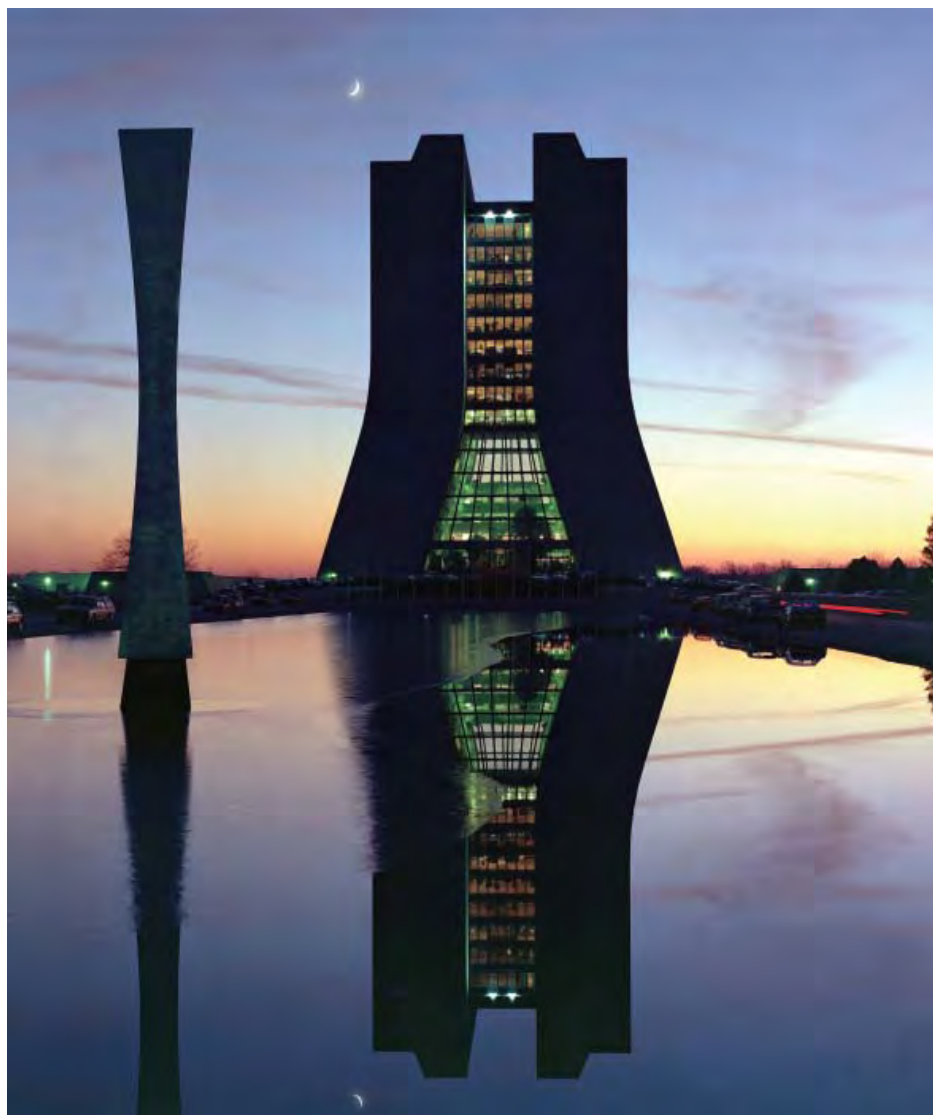
Fermi National Accelerator Laboratory (Fermilab) is one of the world's foremost laboratories dedicated to high-energy physics research. It is operated for the Department of Energy Office of Science by a consortium of 90 research-oriented universities. More than 3,000 scientists from around the world use Fermilab for their experiments.

Fermilab is located on a 6,800-acre site about 35 miles west of Chicago, Illinois. The laboratory is home to the Tevatron Collider, the world's highest-energy particle accelerator. Two large detectors analyze the Tevatron's proton-antiproton collisions to unveil the fundamental forces and particles of the universe. Scientists at Fermilab discovered the bottom quark and the top quark, and first observed the tau neutrino.

Fermilab operates the world's most powerful proton beam for creating neutrinos. The Center for Particle Astrophysics at Fermilab includes groups studying cosmic rays, supernovae, dark energy and other phenomena.
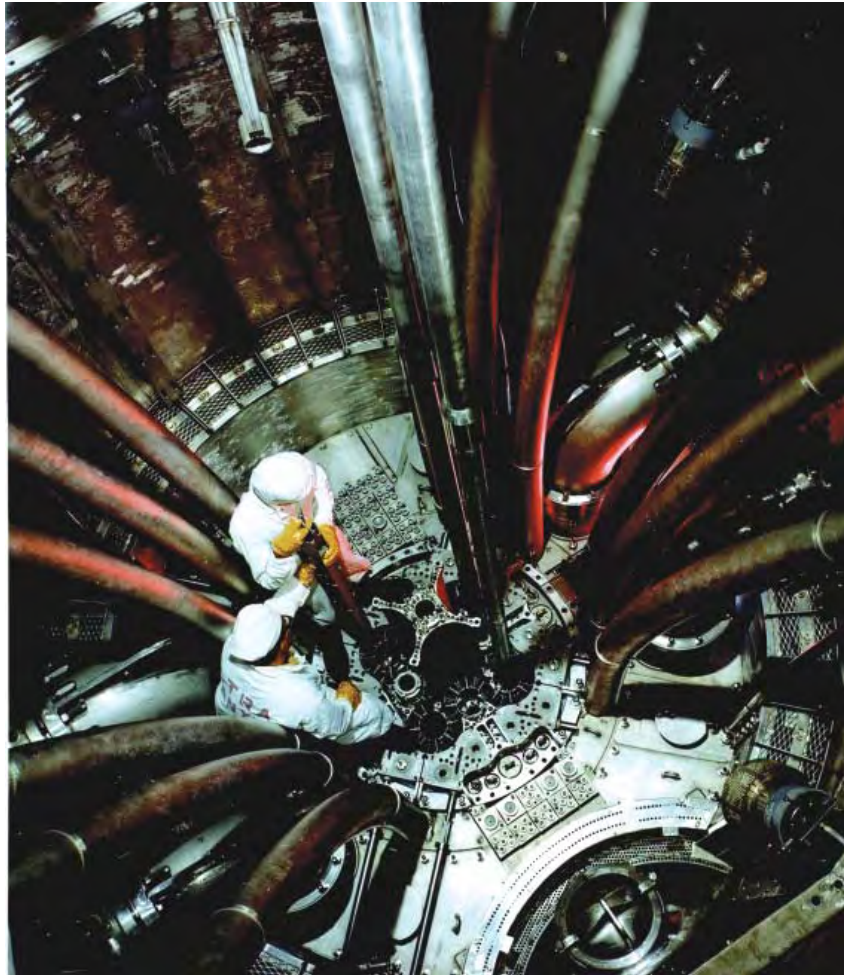
In operation since 1949, The Idaho National Laboratory (INL) is a science-based, applied engineering National Laboratory dedicated to supporting the U.S. Department of Energy's missions in nuclear and energy research, science, and national defense.

INL stands out as a unique national and international resource. Notably, the Lab has been formally designated as the nation's command center for advanced civilian nuclear technology research and development, and is home to the unparalleled Critical Infrastructure Test Range, with assets as diverse as an isolable electric grid and wireless test bed. Leveraging these and numerous other distinguishing features, the Lab and its more than 3,300 scientists, engineers and support personnel build on the potential and promise of the theoretical for the benefit of the real world.

Located in southeast Idaho, INL covers 890 square miles of the Snake River Plain between Idaho Falls and Arco, Idaho. Offices and laboratories are also in the city of Idaho Falls (population 50,000), located about two hours from Grand Teton and Yellowstone national parks and other areas offering prime recreational opportunities.

Lawrence Berkeley National Laboratory's (LBNL) research and development includes new energy technologies and environmental solutions with a focus on energy efficiency, electric reliability, carbon management and global climate change, and fusion. Frontier research experiences exist in nanoscience, genomics and cancer research, advanced computing, and observing matter and energy at the most fundamental level in the universe.

Ernest Orlando Lawrence founded the Berkeley Lab in 1931. Lawrence is most commonly known for his invention of the cyclotron, which led to a Golden Age of particle physics—the foundation of modern nuclear science—and revolutionary discoveries about the nature of the universe. Berkeley Lab's Advanced Light Source is its premier national user facility centrally located on the lab site overlooking the San Francisco Bay.
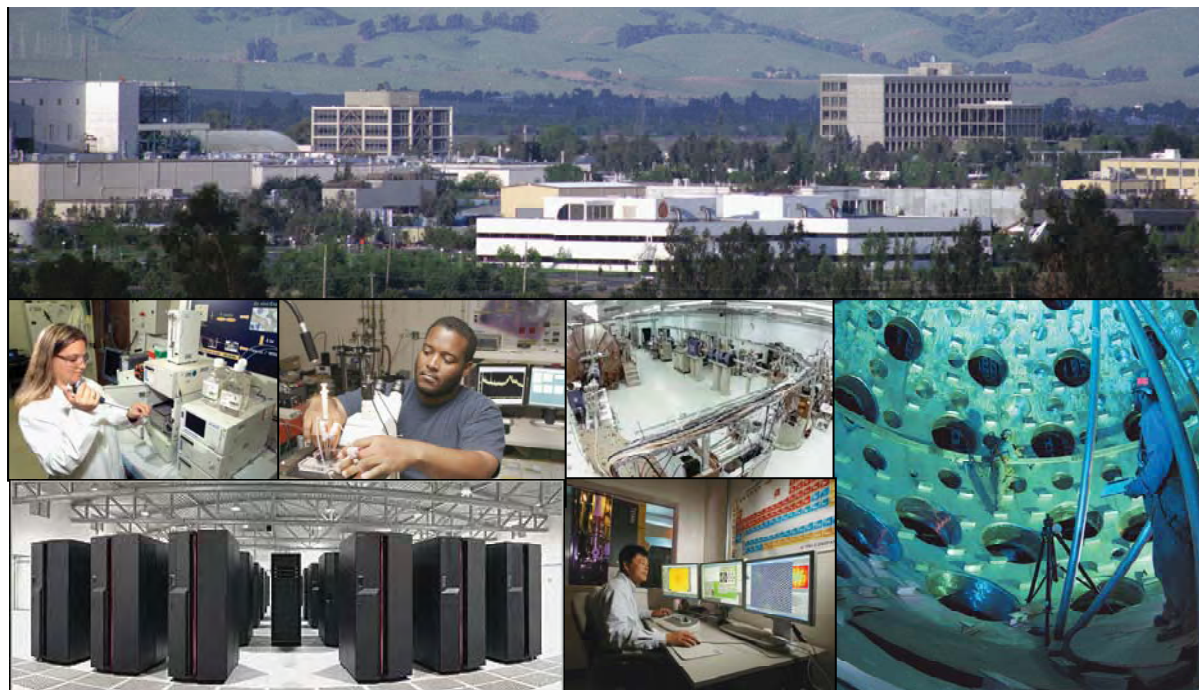
Lawrence Livermore National Laboratory (LLNL) applies cutting-edge science and engineering to enhance the nation's security. When LLNL was founded in 1952, the consuming national security concern was the nuclear arsenal of the Soviet Union and, for years, our energies, talents and resources were focused on that threat. Today, new perils have arisen that are radically different and vastly more complex, and we are directing our world-class scientific and technological resources against these threats. Assuring the safety, security, and reliability of the nation's nuclear weapon stockpile continues to be the foremost responsibility of LLNL. We are also pushing the frontiers of science and technology to make breakthroughs that will be enable us to meet future needs in national and global security, energy and environment, and economic competitiveness.

LLNL is home to some of the world's most powerful supercomputers, including BlueGene/L, first on the TOP500 list of supercomputers with a sustained world-record speed of 478.2 teraflops. LLNL also supports unique experimental facilities, including the Center for Accelerator Mass Spectrometry, the High Explosives Applications Facility, and the 192-beam National Ignition Facility, which is the world's largest laser system. Our researchers typically work in multi-disciplinary teams, where experts in physical and life sciences, engineering, and computations collaborate to devise and demonstrate solutions to nationally important problems.

LLNL offers numerous opportunities for outstanding scholars and postdoctoral fellows to complement their academic endeavors and enable them to work on exciting areas of research using our advanced experimental facilities and computing resources. Laboratory scientists, many of whom are leading experts in their fields, guide and collaborate with student researchers and have earned numerous commendations as outstanding mentors.

On the local level, the Laboratory offers a wide array of student science enrichment and teacher development programs tied to LLNL science and technology that benefit more than 25,000 K-12 students and teachers each year. Programs include college-accredited teacher research academies and research internships, community science lectures, a science and engineering project competition, tours for school groups, and special educational outreach events.

LLNL is located on a mile-square site at the eastern edge of the Livermore Valley, roughly an hour from San Francisco, two hours from the Pacific Ocean, and three hours from the Sierra Nevada mountains. The Laboratory is managed for the Department of Energy's National Nuclear Security Administration by Lawrence Livermore National Security LLC, a consortium of Bechtel National, University of California, Babcock & Wilcox, Washington Division of URS Corporation, and Battelle.

The Los Alamos National Laboratory (LANL), located in the Jemez Mountains of northern New Mexico, offers the opportunity for students to work at a multi-disciplinary, world-class research facility while enjoying a truly unique environment. Long known for its artistic community, northern New Mexico also offers a variety of exciting outdoor recreational opportunities, including rock climbing and hiking in the adjacent mountains and canyons, proximity to the Rocky Mountains, and exceptional skiing opportunities at many nearby locations.

We offer a diverse research experience for undergraduate and graduate students as a means of assuring the continued vibrancy of the science, engineering, and technology at the laboratory. Serve your internship with us and you will have the opportunity to work in a team environment with some of the world's top scientists and engineers on critical issues involving our national security, environment, infrastructure, and security. We offer internship opportunities in areas that include: Biology, Chemistry, Computer Science, Physics, Mathematics, Materials Science, Environmental Science, and Engineering: Chemical, Civil, Computer, Electrical, Mechanical, Nuclear, and Software.

If you are a problem solver and independent thinker, a team player, a good communicator, like a hands-on approach, and are self-motivated, we offer you the challenge of an internship at Los Alamos National Laboratory.

Habitat House

The National Renewable Energy Laboratory (NREL) is the Department of Energy's primary National Laboratory for renewable energy and energy efficiency research and development. From harvesting energy from the sun and wind, to advancing automotive systems, to developing biodegradable plastics from corn stalks, NREL develops renewable energy and energy efficiency technologies and practices, advances related science and engineering, and transfers research knowledge and innovations to address the nation's energy and environmental goals. NREL takes its research to the community through projects such as building Zero Energy Habitat for Humanity Homes, education outreach, teacher workshops and sponsoring interns.

NREL research has been recognized with 40 R&D 100 Awards, ranking first among National Laboratories per researcher, as well as numerous honors from R&D, Discover, and Popular Science magazines and leading scientific organizations. Scientist mentors work with over 200 interns annually in developing the future workforce.

Innovative, challenging and dynamic—that's our culture. If you are interested in a research internship with an institution that believes creativity and individual uniqueness is at the core of our success, then explore your options at: www.nrel.gov. We value intern talent that adds to the rich pool of research findings produced by NREL each year. Intern accomplishments include:

• More than 27 students have been selected by the Office of Science to present major NREL research at the AAAS.

• More than 50 past student interns have been hired on to join the NREL family.

• Teacher researchers have produced over 50 renewable energy lessons for the classroom. Two student/scientist patents have evolved from internships.

• NREL's Office of Education Programs partners with over 75 universities through-out the nation.

NREL's main 327-acre site is in Golden, Colorado, just west of Denver. The Laboratory also operates the National Wind Technology Center on 307 acres about 20 miles north of Golden, adjacent to the Department of Energy's Rocky Flats Environmental Test Site. We are an equal opportunity employer committed to diversity.

Oak Ridge National Laboratory (ORNL) is the Department of Energy's largest science and energy laboratory. Managed since April 2000 by a partnership of the University of Tennessee and Battelle, ORNL was established in 1943 as part of the secret Manhattan Project to pioneer a method for producing and separating plutonium. Today ORNL has a research portfolio in excess of $1.3 billion, a staff of more than 4,200 and approximately 3,000 guest researchers (undergraduates, graduate students, postgraduates, teachers, and faculty) who spend two weeks or longer each year in Oak Ridge. The recently completed $1.4 billion Spallation Neutron Source, located adjacent to the new Center for Nanophase Materials Sciences, is rapidly making Oak Ridge one of the world's foremost locations for the study of materials. ORNL's National Leadership Computing Facility now houses the world's most powerful open science supercomputer and soon will house a computer capable of a mind-boggling 1,000 trillion calculations per second. Each of these facilities will work closely with ORNL's new Bioenergy Science Center, funded by DOE to develop breakthrough technologies for cellulosic ethanol.

Since 2000, UT-Battelle has provided more than $8 million in support of math and science education, economic development, and corporate volunteerism in the greater Oak Ridge region as well as various civic, cultural and public awareness activities related to the Department of Energy's mission.

PACIFIC NORTHWEST NATIONAL LABORATORY
RICHLAND, WASHINGTON

Pacific Northwest National Laboratory (PNNL), on the sunny eastern side of Washington State, is one of the U.S. Department of Energy's (DOE) ten national laboratories, managed by DOE's Office of Science. PNNL also performs research for other DOE offices as well as government agencies, universities, and industry to deliver breakthrough science and technology to meet today's national needs. PNNL is home to the William R. Wiley Environmental Molecular Sciences Laboratory, a DOE Office of Science national science user facility. PNNL also operates a marine research facility in western Washington.

Our Laboratory 1) provides the facilities, unique scientific equipment, and world-renowned scientists/engineers to strengthen U.S. scientific foundations for fundamental research and innovation; 2) prevents and counters acts of terrorism through applied research in information analysis, cyber security, and non-proliferation of weapons of mass destruction; 3) increases U.S. energy capacity and reduces dependence on imported oil through research of hydrogen and biomass-based fuels; and 4) reduces the effects of energy generation and use on the environment.

We champion science, technology, engineering and mathematics (STEM) education from "grade school to grad school" in order to support the "college and workforce ready" agenda of the Nation, DOE, our region and local communities. We help to develop and educate the scientists and engineers of tomorrow. We strive to impact STEM education by acting as a catalyst for sustainable positive change on national, regional and local levels. This includes providing thought leadership, creating business-in education partnerships, participating in scalable initiatives, and advancing the progress of existing programs that have proven results, but require additional resources and partnerships to broaden their impact.

The Laboratory consistently attracts some of the world's leading scientific talent and engages them in our education programs. Student research opportunities at PNNL include, but are not limited to, appointments in atmospheric science and global change, computational sciences, experimental chemistry, marine sciences, molecular biology, environmental studies, remediation, environmental microbiology, wildlife and fisheries biology, materials research, process science and engineering, economics and political science.

PNNL is located at the confluence of the Columbia, Snake and Yakima rivers within driving distance of the Blue and Cascade mountain ranges. The region is known for year round outdoor recreational opportunities, fine wines, and the community's commitment to the arts.
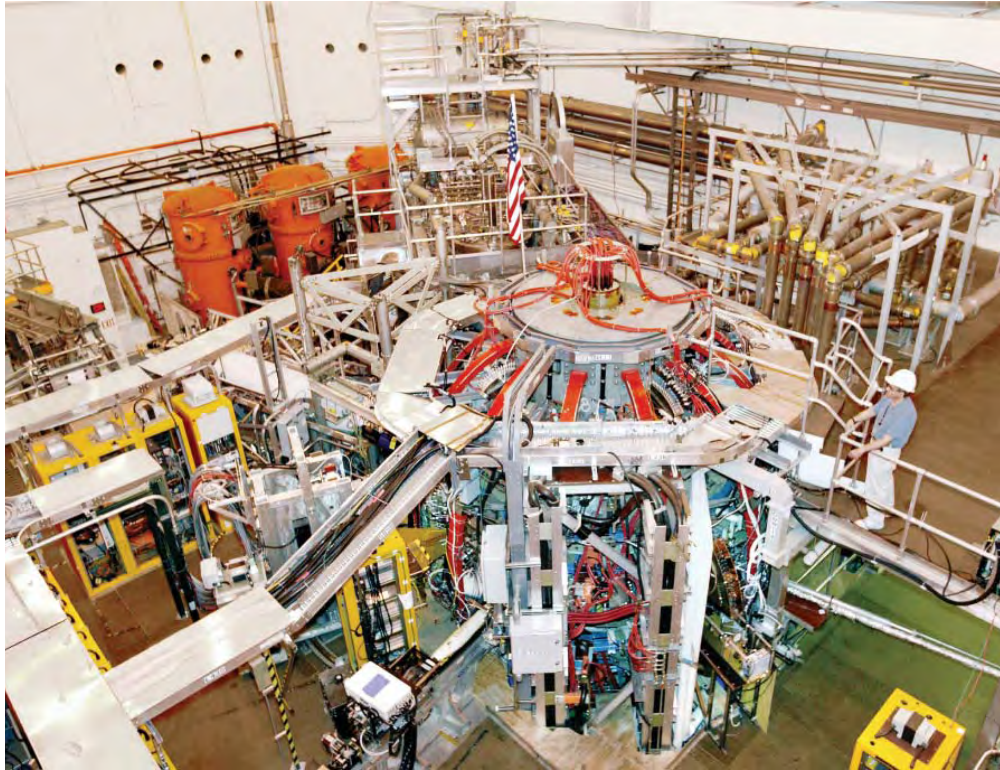
The world's reliance on fossil fuels is imperiling our environment. Fusion, the energy source of the sun and the stars, offers an inexhaustible alternative. A fusion-powered electric generator would not produce hydrocarbon emissions, greenhouse gases, or long-lived radioactive waste; nor would it emit chemicals that cause acid rain. Consequently, the U.S. Department of Energy (DOE) Office of Science has made the development of commercial fusion power one of its highest priorities.

DOE's Princeton Plasma Physics Laboratory (PPPL) is one of the world's leading facilities for fusion R&D. Currently the PPPL is operating the National Spherical Torus Experiment (pictured above) and is building the National Compact Stellarator Experiment, both use magnetic fields to confine hot ionized gas (plasma) that serves as the fusion fuel. PPPL's theoretical physicists are developing computational physics models that can predict how various plasma configurations will perform, saving time and money.

PPPL experimental physicists collaborate with their colleagues worldwide in a free, mutually beneficial, exchange of information. Princeton researchers and engineers are using knowledge and skills gained in fusion research to solve other problems, including the development of plasma-based propulsion systems for space vehicles, studies of plasma phenomena that occur in the sun's corona and the earth's magnetosphere, and support for research on the development of smart materials for artificial muscles.

PPPL is located about three miles from Princeton University's main campus in Princeton, NJ. The Laboratory interacts with the nearby community through its tour program, speakers bureau, and most extensively through its Science Education Program (SEP). The goal of the PPPL SEP is to combine the core research activities of PPPL with science education programs to create a center of excellence for students and teachers. To achieve its goals, the SEP strives to: (1) contribute to the training of the next generation of scientists and engineers, (2) collaborate with K–12 teachers on ways to improve science teaching using an inquiry-based approach to learning, and (3) improve the scientific literacy of the community at large. These initiatives, led by SEP staff in conjunction with PPPL volunteers, master teachers, and local education experts, create significant learning opportunities for undergraduate college students and K–12 teachers and students.
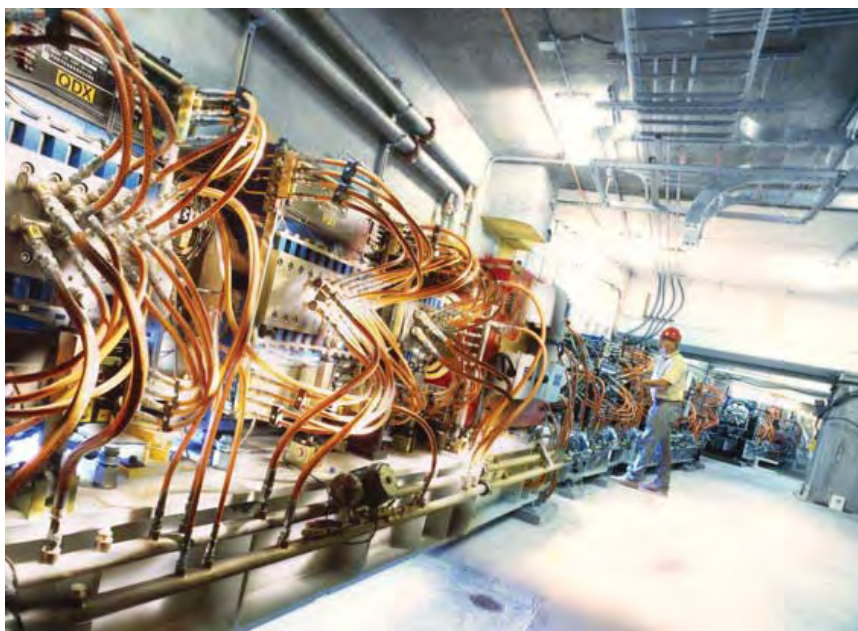
The Stanford Linear Accelerator Center (SLAC) is one of the world's leading laboratories for research in high-energy physics (HEP), particle astrophysics and cosmology, and synchrotron radiation research.

SLAC's HEP program seeks answers to fundamental questions about the ultimate structure of matter and the forces between these fundamental particles. The BABAR experiment investigates matter/anti-matter asymmetry and is the current focus of the HEP program. In addition, a vigorous R&D program is focused on realizing the next generation electron collider — the International Linear Collider, as part of a world-wide effort.

The Kavli Institute at SLAC for Particle Astrophysics and Cosmology bridges theoretical and experimental physics communities, and brings their combined strengths to bear on some of the most challenging and fascinating problems in particle astrophysics and cosmology to help us understand the birth and evolution of the universe.

The Stanford Synchrotron Radiation Laboratory (SSRL) at SLAC, provides high intensity x-ray beams for molecular and atomic scale studies in physics, biology, chemistry, medicine, and environmental science. The Linac Coherent Light Source (LCLS), a facility to provide even more intense x-ray capability is now under construction. Pioneering experiments at LCLS will advance our understanding of everything from the hidden physics inside planets, to how proteins function as the engines of life, to building nanotechnology devices for the backbone of future industry and technology.

The Thomas Jefferson National Acceleration Facility, or Jefferson Lab, is a nuclear physics research laboratory located in Newport News, Virginia. Nuclear physics research scientists who use Jefferson Lab are on a journey of discovery into the nucleus of the atom. Their goal is to develop a roadmap of matter that helps unlock the secrets of how the universe is put together. Nuclear physics funding from the Department of Energy provides Jefferson Lab with leading-edge instrumentation, world-class facilities and training and support for the people involved in these pursuits. Forefront nuclear physics research conducted at Jefferson Lab provides solid foundations for other fields. The accumulation of new results and the intellectual training of new generations of scientists foster important advances in medicine, chemistry and other sciences.

Scientists at Jefferson Lab use the Continuous Electron Beam Accelerator Facility — the first large-scale application of superconducting radiofrequency technology — to conduct physics experiments. Using accelerated electron beams, experimenters probe the sub-nuclear realm. Using this same technology, Jefferson Lab has built the world's brightest high average power Free Electron Laser that offers unique capabilities for defense, industry, basic research and medicine.

Faculty Student Team (FaST) from Columbia Basin Community College at Pacific Northwest National Laboratory (PNNL) working on analytical methods development which may include extraction, isolation, and analysis of intact natural or man-made products, metabolites, and degradation products.

FaST Team from the University of the U.S. Virgin Islands at PNNL working on a subset of a larger effort to develop automated radiochemical methods. Separation and pre-concentration of the desired analyte is often a critical step in radioanalytical methods. Current methods for separating and concentrating analytes for detection often involve complex wet chemical methods.

The Department of Energy (DOE) and National Science Foundation (NSF) are collaborating to promote the development of human resources in science, technology, engineering and mathematics (STEM). Students in NSF programs who are accepted as participants in a DOE National Laboratory take part in a hands-on and mentor-facilitated research internship, and receive supplemental support from NSF. The stipend that students receive helps defray the cost of housing and travel to and from the laboratory.

One NSF program that offers this type of student supplemental support is the Scholarships in Science, Technology, Engineering, and Mathematics (S-STEM) program. The S-STEM program makes grants to institutions of higher education to support scholarships for academically talented, financially needy students. The scholarships assist them in entering the workforce, pursuing further education following completion of an associate, baccalaureate, or graduate degree in a science and engineering discipline, and extending research opportunities in DOE National Laboratories. Grantee institutions are responsible for selecting scholarship recipients and managing the S-STEM project at the institution.

Research that NSF-funded students have performed at the DOE National Laboratories is wide in scope and across many disciplines. Several hands-on projects in which students have participated include measuring ammonia gas concentrations in a tunable diode laser absorption spectrometer and max-

Community College Institute (CCI) participant at PNNL, Sarina Dorazio from Genesee Community College, participated in investigations into the chemical and physical properties of glycerol based deicing solutions.

imizing its operating conditions, studying oligofluorines and their ability to capture electrons, using fiber optic lighting systems to mitigate the effects of shading caused by overwater structures on migrating juvenile salmon, developing software for ground-water monitoring and clean-up and writing visualization software to track pollution and its effects on the environment.

For many students in these NSF programs, the authentic research experience at the DOE National Laboratories proves invaluable to their careers as middle-school and high-school teachers, graduate students, scientists and engineers.

Index of Authors

A

Aaby, Brandon 175
Abdul-Jabbar, Najeb 186
Abraham, Daniel 192
Abram, David 220
Ackermann, Markus 244
Adams, Duncan 207
Aderholdt, William 176
Aguila, Marc Penalver 239
Albert, Brian 163
Albin, Eric 240
Allaire, Marc 162
Allegood, Marcus S. 230
Alleman, Teresa 164
Almaguer, Laura 151
Alvarez, Marcelo 251
Ambrosio, Giorgio 244
Amoa, Kwesi 233
Andersen, Gary L. 209
Anderson, Brett 240
Anderson, Derrek 240
Anderson, Shauna 198
Antler, Natania 240
Aquilina, Stefanie 231
Aragon, Cecilia 258
Askins, David 235
Atwood, David 195
Ayyorgun, Sami 190, 196

B

Baba, Justin S. 8, 230
Back, Birger 240, 247, 258
Bailey, III, John 240
Baker, David 240
Baker, Gregory 220
Baker, Scott 159
Balachandran, U. 199
Bales, Dustin 187
Banai, Rona 241
Bargar, John 218
Barnard, John 259
Barnett, Michael 246
Barquest, Brad 236
Barrett, Richard 180
Bastidos, Amanda 220
Bastow, Max 163
Basu, Sourav 221
Battaglia, Marco 256
Bauer, Dan 243
Bauer, Jace 207
Bayless, Mark 185
Bayram, Yola 163

Bearden, Jessica 151
Beatty, Brent 187
Beck, Jonathan 176
Becker, Eric 261
Becker, James 207, 214
Beckerman, Barbara 232
Beckman, Pete 177
Beiler, Anna 164
Belasco, James 241
Belew, Brandon 176
Bell, Zephra 241
Bellisario, Michael 151
Bender, Michele 207
Benitez, Janilee 15, 241
Bennett, Darby 151
Berds, Stephen 164
Berger, Andrea 176
Berry, Joseph 223
Besmann, Anna 164
Bharat 206
Bhuiyan, M.S. 48
Biegon, Anat 232
Binder, Jeffrey 187
Bithell, Tristan 176
Biyani, Rohit 221
Black, Jana 187
Blackburn, Shannon 207
Blagg, Amanda 187
Blakely, Eleanor 160
Bland, Les 250, 254
Blankson, Baaba 231
Blasing, T.J. 209
Blokland, Willem 254
Blumentritt, Andrea 221
Boggs, Bryan 221
Bolotnikov, Aleksey 186, 195, 198
Bonar, Jacob 188
Bonilha, Christopher 188
Borole, Abhijeet 152, 190
Boucher, John 188
Boukhalfa, Sofiane 221
Bovaird, Chase 207
Bower, Gary 188
Bowerman, Biays 191
Boyer, Colby 177
Boyle, Liza 208
Bozovic, Ivan 243
Brachmann, Axel 250
Braden, Sarah 208
Brady, Christina 164
Bray, Terri 236, 237
Bray, Terry 238
Breisch, Ariana 209, 215

Gerin, Christine 154
Gerkensmeyer, Clint 185
Gershon, Talia 224
Gianotto, Anita 169
Gifford, Andrew 232, 234
Giglio, Jeffrey 169
Gilbert, James 166
Gill, Gary 171
Ginley, David 224
Girard, Candace 232
Goetz, Kathleen 246
Goheen, Steven C. 97, 158
Goldschmidt, Azriel 257
Goldstein, Rita 231, 234
Good, Morris 195
Goodman, Lindsey 193, 224
Goodman, Maury 248
Gospodarczyk, Emily 246
Graf, Norman 240
Graham, Nathaniel 179
Granger, Trinity 166
Gray, Janel 240
Gray, Leonard 182
Green, Meagan 232
Green, Renee 224
Green, Timothy 208, 216, 217, 218
Greenbaum, Eli 164
Greenberg, Emily 246
Greenland, Kelly 246
Gregoire, Kyla 210
Grelewicz, Zachary 247
Grimm, Joseph 247
Grom, Elizabeth 200
Grop, Bill 180
Gropp, William 184
Grosshans, Michalena 233
Group, Craig 243
Gu, Minyi 161
Guldan, Tyler 224
Gundel, Lara 173
Guthrie, Caitlin 211
Guzman-Leong, Consuelo 196
Gwon, Jinhee 167

H

Haas, Ed 192
Hadley, Mary 193
Hafidi, Kawtar 255
Hahn, Richard 168
Haire, Jonathan M. 200
Hall, Adam 193, 211
Hall, Danielle 211
Hammel, Michal 105
Hammons, Joshua 194
Hansen, Ole 176
Hardman, Matthew 194

Harris, John R. 252
Harris, Katherine 167
Harris, Michelle 194
Harrison, Latoya 236
Hassell Jr., Randy 180
Hatcher, Jasmine 167
Hatherill, J. Robert 105
Hayes, Jennifer 167
Hayes, Trina 168
Hazlewood, Victo 185
Heard, Joseph 245
Heck, Robert W. 68, 166, 171
Heieren, Abby 247
Heiser, John 207, 210, 213
Henestroza, Enrique 180, 182
Hernandez, Alfredo 211
Hernandez, Joel 224
Herstoff, Jonathan 247
Hick, Steven 247
Hicks, Brent 225
Higbie, Jennifer 156
Higinbotham, Douglas W. 119, 237, 251
Hill, David E. 198
Hill, Seritta 154
Hixson, Kim 162
Hoag, Brett 194
Hoang, Peter 260
Hobbs, Timothy 248
Hoffman, Andrew 248
Hofherr, Leslie A. 260
Hofreiter, Liz 211
Hohenstein, Jeffrey 154
Hoimes, Alexander 194
Holbrook, Stephen R. 160, 162
Holloway, Terence 195
Holmes, Jeff 255
Honegger, David 225
Hope College 179
Horner, James 180
Hovland, Paul 183
Howdyshell, Marci 248
Howe, Jane Y. 226
Hoxie, Mary Sue 186
Hoyt, Alison 168
Hrma, Pavel 228
Hruska, Ryan 181
Hu, Lina 154
Hu, Monica 154
Hubbard, Camden 189, 221
Huesemann, Michael 23, 152
Hullinger, Pam 161
Humpherys, Candice 248
Hunt, John 225
Hura, Greg L. 105
Huynh, Trang 212, 225
Hvasta, Michael George 74, 248
Hwang, Yu Fen 233

I

Ibarra, Sonia Olivia 180
Ice, Gene E. 224
Igel, Robert 195
Ilavsky, Jan 194
Intrator, Tom 245
Irminger, Philip 195
Ivanov, Ilia 225

J

Jackson, Emily 248
Jacob, Robert 178, 186
Jacobs, Morgan 248
Jacobson, Jacob J. 247
Jager, Yetta 209
James, Jesse 195
Janowitz, Ira 197
Jarman, Richard 170
Jastrow, Julie D. 157, 211, 216
Jeffrey Elam 225
Jeppson, Tamara 212
Ji, Hantao 252
Joachimiak, Andrzej 178
Johnson, Darren 195
Johnson, Elliott 249
Johnson, Katie 212
Johnson, Kyle 195
Johnson, Wesley 196
Johnston, Leah 154
Jones, Eric 249
Jones, Keith 215
Jordan, Kevin 205
Joseph, Sheena 196

K

Kaganas, Gary 236
Kaganovich, Igor 253
Kaiser, Dale P. 213
Kaluzny, Rachael 249
Kambhampati, Murty 218
Kamerzell, Ryan 170
Kapoor, Yuvraaj 155
Karnesky, William 180
Karrels, Tyler 196
Katipamula, Srinivas 204
Katz, David 180
Keasling, Jay 155
Keller, Lewis 54
Kendall, Wesley 181
Kerr, Kijana 168
Kesete, Tigisti 168
Kidwell, Jeanna 155
Kimnach, Deborah 181
King, Anthony 214
King, Derek 212

King, Grace 219
Kintner-Meyer, Michael 260
Kistenev, Edward 204
Kitch, Lacey 249
Klasky, Scott A. 177
Klein, Tim 196
Klingsporn, Jordan 260
Knoff, Elissa 249
Knorowski, Chris 250
Kohut, Danny 155
Konopka, David 155
Kotenko, Jason 181
Kou, Angela 250
Kowolik, Kristin 168
Kraus, George 170
Krishna, C.R. 205
Kropf, Arthur J. 222
Kropf, Jeremy 39
Krumdick, Gregory K. 193, 204, 224, 225
Kruse, Kara 158, 233
Ku, Wei 253
Kubal, Mike 179
Kumaran, D. 155, 157
Kutscher, Chuck 199

L

Lagory, Kirk 154, 219
Laible, Phil 151
Lakshmanan, Manu 250
Lambert, Scott 196
Lande, Joshua 250
Landgraf, Bradley 212
Landmesser, Samantha 219
Langdon, Jonathan 250
Langley, Brandon 181
Langstraat, Brian 197
Lanier, Joe 181
Lanier, Nicolle 233
Lara, Lesley 155
Larabell, Carolyn A. 157, 159
Langdon, Jonathan 250
Langley, Brandon 181
Langstraat, Brian 197
Lanier, Joe 181
Lanier, Nicolle 233
Lara, Lesley 155
Larabell, Carolyn A. 157, 159
Lascurain, Mary 197
Laskin, Julia 174
Last, George V. 144, 212, 219
Lau, Joshua 197
Leavitt, Christopher 169
Le Clair, Stephanie 169
Lee, Christopher 250
Lee, Katrina 181
Leemans, Wim 245

Leister, Andrew 251
Leitner, Daniela 15, 241
Leitner, Matthaeus 198
Lepoire, David 208
Levander, Alejandro 226
Levene, Johanna 194
Levia, Jennifer 155
Lewis, Michele 205
Lewis, Walter 182
Li, Xiaonan 228
Li, Yuelin 240
Lichty, Monica 197
Liebling, Courtney 155
Lindenberg, Aaron 138, 258
Liu, D.J. 172
Liu, Ghang-Jun 157
Liu, Jun 220
Liu, Yanwei 195
Lizarazo, Juan 192
Logan, Jean 235
Lohr, Matthew 251
Longo, Megan 169
Lopez, Miguel 213
Lopez, Reynaldo 198
Lott, Gordon 251
Lousteau, Dave 189
Lowden, Rick 227
Luce, Curtis 182
Ludwig, Mark 190
Lumetta, Gregg 166
Lund, Kasey 251
Lundquist, Adam 156
Lung, Kevin 251
Luryi, Alexander 198
Lutz, Jim 212
Lynch, Christene 251
Lynch, Don 205

M

Mabanta, Jennifer 252
MacDonell, Margaret M. 213, 216
Madejski, Grzegorz 253
Mahajan, Devinder 192, 196, 199, 202, 206
Maingi, Rajesh 242
Majewski, Stan 238
Mak, Kam 252
Maldonado, Carmen 208
Mallin, Patrick 156
Malm, Ian-James 156
Mamma, Tracey 169
Managan, Julie 252
Mangel, Walter F. 163
Manjasetty, Babu 151
Manley, Amanda 170
Manley, Frederick 252
Mardis, Kristy L. 175

Marino, Garrett 213
Markel, Tony 124, 203
Maroni, Victor 223
Marsh, Chevon 156
Martin, Tamara 181
Martinez, Roxanne 182
Maruyama, Takashi 54, 243
Massimini, Joseph 198
Matis, Howard 245
Mattson, Earl 219
Mattson, Jolene 213
May, Michael 252
Mayalu, Michaelle 170
Mayes, Melanie 210
Mayes, Roger 233
McCall, Jason 237
McCallum, R.W. 222
McCold, Cliff 226
McCorkle, Sean 182
McCourt, Michael 182
McDaniel, Ivy 156
McGray, Morgan 164
McIntyre, Toni 170
McKie, Margaret 213
McKinely, James 249
McKnight, Tim 154
McMahan, Peggy 236, 239
McMahon, William 213
McMillan, April 232
McMillin, Thomas 198
Mebane, Harrison 253
Medley, Tenille 237
Mehmood, Arshad 157
Mehner, Carl 182
Mehta, Apurva 33, 241, 242
Melnitchouk, Wally 248
Menard, Jonathan 244
Mendoza, Ramon Colon 198
Menke, Stephen 199
Mertz, Carol J. 169
Mesa, Dalgis 253
Mesina, George 177
Meza, Elvira 214
Mi, Zheng 214
Michaels, Robert 205
Millard, David 180
Miller, Allison 237
Miller, Amara 253
Miller, Ben 214
Miller, Brock 214
Miller, Gordon J. 175, 260
Miller, John 163, 173
Miller, Lisa 158
Millings, Elizabeth 170
Millings, Rachael 245
Mills-Groninger, Fiona 170
Milne, Crystal 214

Miloski, Sarah 215
Mioduszewski, John 215
Mitchell, Emily 182
Mohon, Sara 253
Moin, Damoon 213
Montgomery, Andrea 84, 253
Montgomery, Sara 157
Moon, Paula 169
Moriarty, Patrick 188
Morris, Rachel 226
Morse, William 249
Moy, Shiu 151
Moyer, Bruce 168
Mullins, Jennifer 170
Muren, Russell 199
Murray, Soren 215
Musano, Glenn 199
Musson, John 189
Myers, Daryl 208

N

Nanavati, Virag 215
Natesan, Ken 190, 220
Nation, Jonathan 226
Naulleau, Patrick 226
Nebel, Rick 237
Neergaard, Mike 181
Nelms, Bradlee 157
Nemesure, Seth 180
Ness, Kevin 193
Nettleton, Elizabeth 171
Neumann, Jeffrey 226
Newby, Deborah 160
Nguyen, Tuan 183
Nguyen, Tuyet 199
Ni, Shelly 171
Niyogi, Suhas 166
Nkansah, Asare 166
Norako, Maria 157
Norris, Boyana 176, 178, 185
Nunez, Luis 172
Nutaro, Jim 186
Nuzzolese, Doreen 216

O

O'Brien, William 199
O'Connor, Kellen 183
O'Connor, Paul 191
O'Loughlin, Edward 153
O'Neill, Hugh 152, 157
O'Quinn, Elizabeth 158, 233
Ocko, Sam 253
Ogero, Frank 233
Ogren, John 254
Okafor, Ikenna 168
Oliveri, Anna 236

Olivet Nazarene 177
Olson, Andrew 171
Olson, Daniel 157
Ong, Jennifer 233
Ortiz, Raul 183
Ortiz-Rivera, Eduardo I. 201
Otelaja, Obafemi 199
Ottenweller, Emily 227
Otto, Jeff 200
Ovcharova, Ana 254
Oyeyemi, Victor 200, 227

P

Packard, Jay 252
Padilla, Mariano 254
Pai, Jessica 234
Palumbo, Anthony V. 153
Pan, Sophia 200
Panisko, Ellen 151
Pappas, Richard 247
Paranthaman, M. Parans 48, 222
Pardo, Richard 255
Park, Simone 158
Parker, Angela 216
Parker, Jeffrey 254
Parms, Shameka 254
Pasquarelli, Robert 91, 171
Passernig, Anna 200
Patananan, Alexander N. 97, 158
Patel, Jay 224
Patel, Rahul 253
Patterson, Sara 158
Patterson, Stephanie M. 105, 158
Patton, Robert M. 132
Payne, Rosi 174
Payton, Melissa 216
Pearce, Ryan 227
Pearson, Marya 200
Pena, Giancarlo 200
Pennington, Britney 159
Peoples, Matt 157
Pequenao, Joao 246
Percel, Ian 237
Perez, Shawn 254
Perez, Victoria 159
Perkett, Matthew 255
Perry, Dale L. 171, 174
Pershey, Eric 179
Perumalla, Kalyan S. 175, 186
Peters, Ben 200
Petersen, Eric 227
Petersen, Julia 171
Peterson, Peter 181
Peterson, Reid 190
Peterson, Robert 249
Pettus, Walter 227

Petty, Kimberly 201
Phillips, Cynthia 254
Phillips, Steven 194
Pica, Timothy 172
Pickett, Chris A. 200, 201
Piepel, Greg F. 219
Pierce, F. Ed 203
Pinder, Shakera 216
Plate, Randall 201
Pohlot, Peter 194
Pointer, David 238
Pomykala, Jr., Joseph 169
Pordes, Stephen 259
Porras, Rachel 216
Potok, Thomas E. 132
Pouchard, Line 178
Prestemon, Soren 250
Preuss, Donal 261
Price, Jessica 165
Prozorov, Ruslan 245
Prozorov, Tanya 172
Pusede, Sally 172
Pymer, Allison 159

Q

Quinn, Nigel 211

R

Ragazzi, Jessica 217
Rahimzadeh-Kalaleh, Said 244
Rahmani, Khatera 217
Ramesh, Ramamoorthy 221
Ramirez, Francisco 255
Ramon, Eliseo 183
Ramson, Bryan 255
Raphael, Alan 188
Rastogi, Pawan 172
Rauch, Emily 201
Ray, Hannah 228
Rearden, Brad 237
Reben, Megan 260
Reece, Charles 114, 255
Reese, Terrence 241
Regalbuto, Jose 172
Reimer, Paul E. 241
Remien, Jason 194
Rest, Jeff 236
Reyes, Angel 201
Reynolds, Fedrick 237
Reynolds, Patricia 228
Reza, Layra 255
Ribeill, Guilhem 114, 255
Rice, Jonathan 183
Richardson, Rita 159
Rinker, Torri 159
Rivera, Luis 172

Rivera, Melixa 172
Rizzie, Anthony 228
Robbins, Steven 175
Roberto, Frank 153
Roberts, John 183
Roberts, Nathan 160
Robison, Lisa 234
Rodriguez, Dianna 217
Rodriguez, Idaykis 119, 237
Rodriguez, Luis 201
Rodriguez, Margarita 217
Rogers, Alistair 214
Roha, Rebecca 160
Rohatgi, Upendra 179
Rope, Alison 160
Rosa, Michelle 172
Ross, Rob 184
Rowe, Nathan 201
Rumbles, Garry 224
Rustagi, Neha 202
Rutz, Frederick 181
Ryan, Christine 202
Rybka, Gregory 202
Ryerson, Joseph 173

S

Sachs-Quintana, Isaac 202
Sakowski, Mark 238
Salcedo, Michelle 160
Sallis, Todd 183
Sampson, Catherine 220
Samuel, Todd 220
Samuels, William D. 166
Sanchez, Elisa 228
Sandberg, Eugene 183
Sanders, Charlene 163
Santodonato, Louis 226
Santos, Lilia 173
Satrio, Justinus 187
Savard, Guy 255
Savina, Michael R. 227
Scacco, Andrew 255
Scarlett, Carol Y. 245
Schadt, Christopher 211
Schaeffer, Daniel 256
Scheuerer, Jennifer 184
Schielke, Dale 194
Schiffer, Wynne 155, 231, 234
Schlueter, John A. 223, 230
Schneider, Kevin 200
Schnell, Chrissi 261
Schochenmaier, Kyle 184
Schroeder, Carl B. 84, 253
Schultz, Irvin 151, 164
Schulz Jr., Robert 202
Schumaker, William 256

Index of Schools

A

Albertson College of Idaho 169
Albion College 245, 248
Alfred State College 180, 184, 189
Allegheny College 212
Austin Peay State University 186

B

Ball State University 228
Baylor University 182
Berea College 165
Bevill State Community College 196
Big Bend Community College 178, 181, 185, 186
Binghamton University 176, 224
Birmingham-Southern College 214
Bowdoin College 193, 211
Bradley University 195, 211
Brigham Young University 225
Brigham Young University – Idaho 152, 195, 222, 247, 248, 256
Brooklyn College 217
Brown University 253
Butler University 84, 253

C

Cabrillo College 241
California State Polytechnic University 240
California State Polytechnic University, Pomona 124, 203
California State University – Channel Islands 152
California State University – Chico 206
California State University – East Bay 216, 241
California State University – Fresno 152, 210, 216, 219
California State University – Northridge 223
Carleton College 171, 241, 257
Carnegie Mellon University 218, 240
Case Western Reserve University 203
Cedarville University 201
Central College 197
Central State University 168
Cheyney University of Pennsylvania 182
Chicago State University 154, 166, 174, 175
Christopher Newport University 155, 156
City College of New York, The 179, 231
City College of San Fransisco 162
City University of Seattle 214
Clarion University 176, 185
Clarkson University 188
Colgate University 234
College of Dupage 170, 173
College of New Jersey, The 74, 216, 248
College of William and Mary, The 156, 167, 251, 253
Colorado College 163, 214
Colorado School of Mines 175, 194, 197

Columbia / D / E / F / G

Columbia Basin College 180, 198
Columbia University 48, 163, 172, 222, 250
Community College of Philadelphia 245
Contra Costa College 154, 199, 208, 209, 211, 252
Cooper Union 191
Cornell University 151, 188, 198, 231, 241, 250, 254, 256, 258
CUNY Queensborough Community College 167

D

Dartmouth College 160, 220, 246
Del Mar College 105, 158, 162
Denison University 235, 255
DePaul University 212, 225
Diablo Valley College 160, 162, 174
Dominican University of California 260
Dowling College 173
Drake University 178

E

Earlham College 157, 207
East Tennessee State University 178
Edinboro University of Pennsylvania 181, 185, 215
Elmhurst College 153, 179, 230
Embry-Riddle Aeronautical University 244
Estrella Mountain Community College 229
Everett Community College 161

F

Farmingdale State College 192, 199, 232
Fayetteville State University 170
Florida A&M University 245
Florida Institute of Technology 159
Florida International University 119, 198, 200, 236, 237, 242, 253
Florida State University 210
Fort Hays State University 244, 258
Franklin W. Olin College of Engineering 62, 191
Fullerton College 254
Furman University 210

G

Gavilan College 151, 209
Genesee Community College 166
George Fox University 257
George Mason University 184
George Washington University, The 207
Georgia Institute of Technology 189, 193
Gettysburg College 160, 251
Gonzaga University 223
Goshen College 200, 227
Governors State University 156, 159, 178, 183
Grinnell College 175, 260

H

Hampden-Sydney College 238
Hampton University 257
Harvard University 227, 253
Hendrix College 164
Hillsdale College 227
Howard University 173, 199, 255

I

Illinois Institute of Technology 181, 182, 206
Iowa State University 157, 184

J

Jackson State University 168
Joliet Junior College 183
Juniata College 236

K

Kalamazoo College 155
Kansas State University 191, 235, 238
Kingsborough Community College 157, 215
Knox College 158, 161, 248

L

Lane College 179
Laney College 212, 213
La Salle University 232
La Sierra University 183
Lawrence Technological University 256
Lehigh University 218
LeTourneau University 221
Lewis & Clark College 225
Lock Haven University of Pennsylvania 246
Loyola College in Maryland 213, 252

M

Macalester College 156
Manchester College 170
Marlboro College 250
Marquette University 160
Maryville College 175, 200, 226
Massachusetts Institute of Technology 154, 163, 170, 213, 224, 240, 249
McDaniel College 239
Medgar Evers College 155, 157, 231, 233
Mercer University 186
Messiah College 164
Michigan Technological University 230
Middlebury College 188, 246
Mississippi State University 183
Monmouth College 204, 243
Monroe Community College 164, 207
Montana State University 204, 251
Mount Holyoke College 232

Mount Saint Mary College 207
Muhlenberg College 247

N

National Taiwan University 222
New Mexico Institute of Mining and Technology 202
New Mexico State University 182
New York University 155, 231, 234, 256
Nicholls State University 190
Norfolk State University 169, 188, 195, 200, 216
North Carolina Agricultural and Technical State University 175, 254
North Carolina State University 114, 161, 177, 255, 256
North Central College 180
North Dakota State University 249
Northeastern University 205
Northern Arizona University 218
Northern Illinois University 179, 183
North Georgia College and State University 8, 230
Northwestern University 208, 228, 249
Northwest Nazarene University 23, 152

O

Ohio Northern University 233
Ohio State University, The 242, 256
Old Dominion University 180, 205
Olin College 68
Olin College of Engineering 166
Oregon State University 159, 196

P

Pellissippi State Technical Community College 195
Pennsylvania State University 194, 202, 220, 226, 251
Pensacola Christian College 187, 197
Pittsburg State University 238
Pomona College 211, 259
Portland State University 203
Prairie View A&M University 236, 239
Princeton University 242
Purdue University 198, 207, 238

Q

Queensborough Community College 168
Queens College 165, 167, 174

R

Randolph-Macon Woman's College 170
Reed College 242
Rensselaer Polytechnic Institute 151, 176, 191, 239
Roane State Community College 185
Rochester Institute of Technology 91, 157, 171, 189

S

Sacramento City College 213, 217

W

Y